

Optical thin films and coatings

Related titles:

Printed films: Materials science and applications in sensors, electronics and photonics
(ISBN 978-1-84569-988-8)

Organic light-emitting diodes (OLEDs)
(ISBN 978-0-85709-425-4)

Carbon nanotubes and graphene for photonic applications
(ISBN 978-0-85709-417-9)

Details of these books and a complete list of titles from Woodhead Publishing can be obtained by:

- visiting our web site at www.woodheadpublishing.com
- contacting Customer Services (e-mail: sales@woodheadpublishing.com; fax: +44 (0) 1223 832819; tel.: +44 (0) 1223 499140 ext. 130; address: Woodhead Publishing Limited, 80, High Street, Sawston, Cambridge CB22 3HJ, UK)
- in North America, contacting our US office (e-mail: usmarketing@woodheadpublishing.com; tel.: (215) 928 9112; address: Woodhead Publishing, 1518 Walnut Street, Suite 1100, Philadelphia, PA 19102-3406, USA)

If you would like e-versions of our content, please visit our online platform: www.woodheadpublishingonline.com. Please recommend it to your librarian so that everyone in your institution can benefit from the wealth of content on the site.

We are always happy to receive suggestions for new books from potential editors. To enquire about contributing to our Electronic and Optical Materials series, please send your name, contact address and details of the topic(s) you are interested in to laura.pugh@woodheadpublishing.com. We look forward to hearing from you.

The team responsible for publishing this book:

Commissioning Editor: Laura Pugh

Publications Coordinator: Emily Cole

Project Editor: Elizabeth Moss

Editorial and Production Manager: Mary Campbell

Production Editor: Richard Fairclough

Freelance Project Manager: Newgen Knowledge Works Pvt Ltd

Copyeditor: Newgen Knowledge Works Pvt Ltd

Proofreader: Newgen Knowledge Works Pvt Ltd

Cover Designer: Terry Callanan

Woodhead Publishing Series in Electronic and Optical Materials:
Number 49

Optical thin films and coatings

From materials to applications

Edited by
Angela Piegari and François Flory



Oxford Cambridge Philadelphia New Delhi

Published by Woodhead Publishing Limited,
80 High Street, Sawston, Cambridge CB22 3HJ, UK
www.woodheadpublishing.com
www.woodheadpublishingonline.com

Woodhead Publishing, 1518 Walnut Street, Suite 1100, Philadelphia,
PA 19102-3406, USA

Woodhead Publishing India Private Limited, 303 Vardaan House, 7/28 Ansari Road,
Daryaganj, New Delhi – 110002, India
www.woodheadpublishingindia.com

First published 2013, Woodhead Publishing Limited

© Woodhead Publishing Limited, 2013. Note: the publisher has made every effort to ensure that permission for copyright material has been obtained by authors wishing to use such material. The authors and the publisher will be glad to hear from any copyright holder it has not been possible to contact.

The authors have asserted their moral rights.

This book contains information obtained from authentic and highly regarded sources. Reprinted material is quoted with permission, and sources are indicated. Reasonable efforts have been made to publish reliable data and information, but the authors and the publisher cannot assume responsibility for the validity of all materials. Neither the authors nor the publisher, nor anyone else associated with this publication, shall be liable for any loss, damage or liability directly or indirectly caused or alleged to be caused by this book.

Neither this book nor any part may be reproduced or transmitted in any form or by any means, electronic or mechanical, including photocopying, microfilming and recording, or by any information storage or retrieval system, without permission in writing from Woodhead Publishing Limited.

The consent of Woodhead Publishing Limited does not extend to copying for general distribution, for promotion, for creating new works, or for resale. Specific permission must be obtained in writing from Woodhead Publishing Limited for such copying.

Trademark notice: Product or corporate names may be trademarks or registered trademarks, and are used only for identification and explanation, without intent to infringe.

British Library Cataloguing in Publication Data
A catalogue record for this book is available from the British Library.

Library of Congress Control Number: 2013942628

ISBN 978-0-85709-594-7 (print)

ISBN 978-0-85709-731-6 (online)

ISSN 2050-1501 Woodhead Publishing Series in Electronic and Optical Materials (print)

ISSN 2050-151X Woodhead Publishing Series in Electronic and Optical Materials (online)

The publisher's policy is to use permanent paper from mills that operate a sustainable forestry policy, and which has been manufactured from pulp which is processed using acid-free and elemental chlorine-free practices. Furthermore, the publisher ensures that the text paper and cover board used have met acceptable environmental accreditation standards.

Typeset by Newgen Knowledge Works Pvt Ltd, India
Printed by TJ International Limited, Padstow, Cornwall, UK

Contents

<i>Contributor contact details</i>	xv
<i>Woodhead Publishing Series in Electronic and Optical Materials</i>	xxi
<i>Preface</i>	xxv
Part I Design and manufacturing of optical thin films and coatings	1
1 Recent developments in deposition techniques for optical thin films and coatings	3
H. ANGUS MACLEOD, Thin Film Center Inc., USA	
1.1 Introduction	3
1.2 Early processes for the deposition of optical coatings	4
1.3 The energetic processes	6
1.4 Cathodic arc evaporation	16
1.5 Pulsed laser deposition	17
1.6 Chemical vapor deposition	17
1.7 Atomic layer deposition	18
1.8 Sol-gel processes	19
1.9 Etching	20
1.10 Other techniques	20
1.11 Conclusion	21
1.12 References	21
2 Design of complex optical coatings	26
P. G. VERLY, National Research Council Canada, Canada	
2.1 Introduction	26
2.2 Modern numerical thin film synthesis techniques	28
2.3 Manufacturability issues	38
2.4 Hybrid design	41

vi	Contents	
2.5	Conclusion	51
2.6	Acknowledgements	51
2.7	References	52
3	Optical monitoring strategies for optical coating manufacturing	62
	A. V. TIKHONRAVOV, M. K. TRUBETSKOV and	
	T. V. AMOTCHKINA, Moscow State University, Russia	
3.1	Introduction	62
3.2	Classification of optical monitoring strategies	65
3.3	Turning point optical monitoring and error self-compensation effect	67
3.4	Level monitoring: passive and active monochromatic monitoring strategies	73
3.5	Direct broad band optical monitoring	82
3.6	Indirect optical monitoring strategies	85
3.7	Conclusion	90
3.8	References	91
4	Production strategies for high-precision optical coatings	94
	H. EHLERS and D. RISTAU, Laser Zentrum Hannover, Germany	
4.1	Introduction	94
4.2	Basic concept of deterministic production	96
4.3	Optical broad band monitoring	99
4.4	Virtual deposition system	105
4.5	Direct on-line correction tools	110
4.6	Design stability in production processes	111
4.7	Deposition control of coating systems with continuous refractive index variation	117
4.8	Conclusion	125
4.9	References	127
Part II	Unconventional features of optical thin films and coatings	131
5	Complex materials with plasmonic effects for optical thin film applications	133
	A. SYTCHKOVA, ENEA Optical Coatings Laboratory, Italy	
5.1	Introduction	133

5.2	Physics of some classes of novel materials for plasmonic applications	135
5.3	Ceramic matrix with embedded metal nanostructures	137
5.4	Searching for alternative plasmonic materials	146
5.5	Characterization of novel materials with plasmonic effects	152
5.6	Conclusion	162
5.7	References	163
6	Scattering properties of random structures in thin films	177
	G. BERGINC, Thales, France and A. A. MARADUDIN, University of California, Irvine, USA	
6.1	Introduction	177
6.2	Numerical solution of reduced Rayleigh equations for scattering of light from dielectric films with one-dimensional rough surfaces	179
6.3	Reduced Rayleigh equations for the scattering of p- and s-polarized light from, and its transmission through, a film with two one-dimensional rough surfaces	192
6.4	Numerical solution of the reduced Rayleigh equation for the scattering of light from a two-dimensional randomly rough penetrable surface	208
6.5	Scattering of light from a dielectric film with a two-dimensional randomly rough surface deposited on a planar metal substrate	212
6.6	Analytical methods for the scattering from a three-dimensional film with randomly rough surfaces	219
6.7	Theoretical methods for the scattering of polarized light from randomly rough interfaces and random media	240
6.8	Applications	271
6.9	Conclusion	279
6.10	References	280
6.11	Appendices	286
7	Optical properties of thin film materials at short wavelengths	290
	J. LARRUQUERT, Instituto de Óptica-Consejo Superior de Investigaciones Científicas, Spain	
7.1	Introduction	290
7.2	Material behaviour over the spectrum	291
7.3	Reflection and transmission in absorbing materials	294

7.4	The optical constants of materials at short wavelengths	299
7.5	Link between n and k : Kramers-Kronig analysis	316
7.6	Experimental determination of optical constants	317
7.7	Specifics of optical coatings at short wavelengths	320
7.8	Conclusion	342
7.9	Acknowledgements	343
7.10	References	343
8	Controlling thermal radiation from surfaces	357
	C. G. RIBBING, Uppsala University, Sweden	
8.1	Introduction	357
8.2	Blackbody radiation	359
8.3	Emissivity	363
8.4	Optically selective coatings	368
8.5	Conclusion	387
8.6	References	387
9	Color in optical coatings	391
	C. OLEARI, University of Parma, Italy	
9.1	Introduction	391
9.2	The development of the understanding of interference color	392
9.3	Overview of basic colorimetry	402
9.4	Optical coating colorimetry	413
9.5	Conclusion	422
9.6	Acknowledgements	422
9.7	References	422
Part III	Novel materials for optical thin films and coatings	425
10	Organic optical coatings	427
	T. NEUBERT and M. VERGÖHL, Fraunhofer Institute for Surface Engineering and Thin Films – IST, Germany	
10.1	Introduction	427
10.2	Specific properties of organic layers	428
10.3	Optical coatings with organic layers	431

10.4	Deposition techniques	432
10.5	Composites	443
10.6	Conclusion	445
10.7	References	446
11	Surface multiplasmonics with periodically non-homogeneous thin films	450
	M. FARYAD and A. LAKHTAKIA, Department of Engineering Science and Mechanics, Pennsylvania State University, USA	
11.1	Introduction	450
11.2	Historical development	451
11.3	Periodically non-homogeneous dielectric materials	453
11.4	Canonical boundary-value problem	456
11.5	Grating-coupled configuration	466
11.6	Turbadar–Kretschmann–Raether (TKR) configuration	476
11.7	Conclusion	482
11.8	Future research	485
11.9	Sources of further information and advice	486
11.10	References	486
12	Optical thin films containing quantum dots	493
	F. FLORY, Y.-J. CHEN and H.-J. LIN, Ecole Centrale Marseille, France	
12.1	Introduction	493
12.2	Applications of quantum dots	494
12.3	Modeling the electronic properties of multiple quantum wells	497
12.4	Numerical results	498
12.5	Realization of thin films containing quantum dots	502
12.6	Characterization of thin films containing quantum dots	503
12.7	Refractive index of layers containing quantum dots and of quantum dots alone	509
12.8	Conclusion	512
12.9	Acknowledgements	513
12.10	References	513

Part IV Applications of optical thin films and coatings	517
13 Optical coatings on plastic for antireflection purposes	519
U. SCHULZ, Fraunhofer Institute of Applied Optics and Precision Engineering, IOF, Germany and R. W. SCHAFFER, Evaporated Coatings Inc., USA	
13.1 Introduction	519
13.2 Transparent polymer materials for optics	520
13.3 Plastics in vacuum coating processes	522
13.4 Antireflection methods	528
13.5 Conclusion	534
13.6 Sources of further information and advice	534
13.7 References	535
14 Protective coatings for optical surfaces	540
T. W. BOENTORO, Fraunhofer Institute for Surface Engineering and Thin Films-IST, Germany and B. SZYSZKA, Institute for High-Frequency and Semiconductor System Technologies, Berlin, Germany	
14.1 Introduction	540
14.2 Testing methods	545
14.3 Coating design	551
14.4 Application examples	555
14.5 Conclusion	560
14.6 References	560
15 Optical coatings for displays and lighting	564
C.-C. LEE, and C.-C. KUO, National Central University, Taiwan	
15.1 Introduction	564
15.2 Optical coatings for flat panel display (FPD)	565
15.3 Optical coatings for projectors	567
15.4 Optical coatings for projectors using light emitting diode (LED) light source	573
15.5 Optical coating for automobiles head up display (HUD)	584
15.6 Optical coatings for LEDs	587
15.7 Conclusion	589
15.8 Acknowledgements	591
15.9 References	591

16	Innovative approaches in thin film photovoltaic cells L. ESCOUBAS, J. J. SIMON and J. LE ROUZO, Aix-Marseille Université, IM2NP, France and V. BERMUDEZ, Nexcis, France	596
16.1	Introduction	596
16.2	Inorganic nanostructures for photovoltaic solar cells	599
16.3	Organic thin film solar cells	606
16.4	Copper indium gallium diselenide thin film solar cells	612
16.5	Conclusion	623
16.6	References	624
17	Optical coatings for security and authentication devices B. BALOUKAS and L. MARTINU, Department of Engineering Physics, École Polytechnique de Montréal, Canada	631
17.1	Introduction	631
17.2	Basic principles and structures currently applied	633
17.3	Specific optical effects suitable for security devices	641
17.4	Active devices	650
17.5	Film functionality and structurally controlled optical coatings	653
17.6	Conclusion	655
17.7	References	656
18	Optical coatings for high-intensity femtosecond lasers V. PERVAK, Ludwig-Maximilians-University, Germany	664
18.1	Introduction	664
18.2	Mirror design approaches	666
18.3	The highest possible value of group delay dispersion (GDD)	676
18.4	Production of dispersive mirrors	677
18.5	Pulse compression with dispersive mirrors	678
18.6	Measurement of group delay with white light interferometer	681
18.7	Application of dispersive mirrors in high-intensity lasers	685
18.8	Conclusion	688
18.9	References	689

19	Optical coatings for large facilities	695
	C. GRÈZES-BESSET and G. CHAUVEAU, Department of Thin Film Coatings, CILAS, France	
19.1	Introduction	695
19.2	Domains of applications and major programs	695
19.3	Review of technological solutions	702
19.4	Thin film uniformity: key problem	705
19.5	Focus on large magnetron sputtering facility	707
19.6	Highlight on two major programs	710
19.7	Conclusion	714
19.8	References	714
20	Optical coatings for automotive and building applications	718
	C. H. STOESSEL, Southwall Technologies, USA	
20.1	Introduction	718
20.2	The role of thermal control in glazing	719
20.3	Window coating types by functionality	722
20.4	Glazing types: monolithic, laminated, and multi-cavity glazing designs	726
20.5	Coatings on glass substrates	727
20.6	Coatings on polymer substrates	729
20.7	Special considerations for applications	732
20.8	Conclusion	736
20.9	Future trends	737
20.10	Sources of further information and advice	738
20.11	Acknowledgements	739
20.12	References	739
21	Transparent conductive thin films	741
	C. BRIGHT, Bright Thin Film Solutions, USA	
21.1	Introduction	741
21.2	Conductivity fundamentals	745
21.3	Control of optoelectronic properties	751
21.4	Beyond optoelectronic properties	753
21.5	Traditional applications	753
21.6	Recent applications	767
21.7	Future applications	775
21.8	Conclusion	779

21.9	Sources of further information and advice	785
21.10	References	785
22	Optical coatings in the space environment	789
	D. WERNHAM, The European Space Agency, The Netherlands	
22.1	Introduction	789
22.2	The space environment	790
22.3	Contamination	798
22.4	Product assurance for space coatings	803
22.5	Conclusion	807
22.6	Acknowledgements	807
22.7	References	808
	<i>Index</i>	<i>811</i>

Contributor contact details

(* = main contact)

Editors:

Angela Piegari*

E-mail: angela.piegari@enea.it

François Flory

E-mail: francois.flory@centrale-marseille.fr

Chapter 1

H. Angus Macleod

Thin Film Center Inc.

2745 E Via Rotunda

Tucson, AZ 85716-5227, USA

E-mail: angus@thinfilmcenter.com

Chapter 2

Pierre G. Verly

National Research Council of

Canada Information and

Communications Technologies

1200 Montreal Rd

Bldg M50

Ottawa, ON, K1A 0R6

E-mail: Pierre.Verly@nrc-cnrc.gc.ca

Chapter 3

Alexander.V.Tikhonravov* and

Tatiana.V.Amotchkina

Research Computing Center

Moscow State University

Leninskie Gory,

Moscow, 119992, Russian

Federation

E-mail: tikh@srcc.msu.ru

Michael. K. Trubetskov

Max-Planck-Institut für

Quantenoptik,

Hans-Kopfermann-Strasse 1,

D-85748 Garching, Germany

and

Research Computing Center

Moscow State University

Leninskie Gory

Moscow, 119992

Russian Federation

Chapter 4

H. Ehlers* and D. Ristau

Laser Components Department

Laser Zentrum Hannover e.V.

Hollerithallee 8

30419 Hannover

Germany

E-mail: h.ehlers@lzh.de

and

D. Ristau
Institut für Quantenoptik
Leibniz Universität Hannover
Welfengarten 1
30167 Hannover
Germany

E-mail: d.ristau@lzh.de

Chapter 5

Anna Sytchkova
ENEA Optical Coatings
Laboratory
via Anguillarese 301
00123 Rome, Italy

E-mail: anna.sytchkova@enea.it

Chapter 6

Gerard Berginc*
Thales
2, avenue Gay-Lussac
78995 Elancourt Cedex
France

E-mail: gerard.berginc@fr.thalesgroup.com

and

Alexei A. Maradudin
Department of Physics and
Astronomy
University of California
Irvine
CA 92697, USA

E-mail: aamaradu@uci.edu

Chapter 7

Juan I. Larruquert
Instituto de Optica-Consejo
Superior de Investigaciones
Científicas
Serrano 144
28006, Madrid-Spain

E-mail: larruquert@io.cfmac.csic.es

Chapter 8

Carl G. Ribbing
The Ångström Laboratory
Uppsala University
Box 534
SE-75121 Uppsala
Sweden

E-mail: CG.Ribbing@angstrom.uu.se

Chapter 9

Claudio Oleari
Dipartimento di Fisica e di Scienze
della terra
Università di Parma
Campus, Parco Area delle Scienze
7/A
43100 Parma, Italy

E-mail: claudio.oleari@fis.unipr.it

Chapter 10

Thomas Neubert and Michael
Vergöhl*
Fraunhofer Institute for Surface
Engineering and Thin Films
(IST),
Bienroder Weg 54E

38108 Braunschweig
Germany

E-mail: michael.vergoehl@ist.
fraunhofer.de

Chapter 11

Muhammad Faryad and Akhlesh
Lakhtakia*
NanoMM—Nanoengineered
Metamaterials Group,
Department of Engineering Science
and Mechanics
212 EES Building
Pennsylvania State University
University Park, PA 16802, USA
E-mail: akhlesh@psu.edu

Chapter 12

François Flory,* Yu-Jen Chen and
Hung-Ju Lin
Ecole Centrale Marseille
IM2NP- Institute of Materials,
Microelectronics and
Nanosciences of Provence
38 rue Joliot Curie
13451 Marseille Cedex 20
France
E-mail: francois.flory@centrale-
marseille.fr

and

Yu-Jen Chen and Hung-Ju Lin
Thin Film Technology Center
National Central University
300, Chung-Da Rd.
Chung-Li, 32001, Taiwan
E-mail: tfanalysis@gmail.com;
comander_leader@yahoo.com.tw

Chapter 13

Ulrike Schulz*
Fraunhofer Institute of
Applied Optics and Precision
Engineering, IOF
A.-Einstein-Str. 7
07745 Jena, Germany
E-mail: ulrike.schulz@iof.
fraunhofer.de

Robert W. Schaffer
Evaporated Coatings Inc.
2365 Maryland Road
Willow Grove
PA 19090, USA

E-mail: rschaffer@evapcoat.com

Chapter 14

T. W. Boentoro and Bernd Szyszka*
Fraunhofer Institute for Surface
Engineering and Thin Films-IST
Bienroder Weg 54E, 38108
Braunschweig, Germany

E-mail: tjhay-weyna.boentoro@ist.
fraunhofer.de

and

Bernd Szyszka
TU Berlin
Institute for High-Frequency
and Semiconductor System
Technologies
Technology of thin-film devices
c/o Sec. HFT 5–2
Einsteinufer 25, 10587 Berlin,
Germany
E-mail: bernd.szyszka@tu-berlin.de

Chapter 15

Cheng-Chung Lee* and Chien-Cheng Kuo
Thin Film Technology Center
Department of Optics and Photonics
National Central University
300 Chung-Da Rd. Chung-Li, 320 Taiwan
E-mail: cclee@dop.ncu.edu.tw

Chapter 16

Ludovic Escoubas,* Jean-Jacques Simon and Judikael Le Rouzo
Aix-Marseille Université
IM2NP (UMR CNRS 7334)
Faculté des Sciences
Campus de Saint Jérôme
Avenue Escadrille Normandie Niemen
F-13397 Marseille Cedex, France
E-mail: ludovic.escoubas@univ-amu.fr

Veronica Bermudez
Nexcis
Avenue Célestin Coq
PA de Rousset
13790 Rousset
France

Chapter 17

Ludvik Martinu* and Bill Baloukas
Department of Engineering Physics
École Polytechnique de Montréal,
P.O. Box 6079
succursale Centre-ville

Montréal
Québec H3C 3A7, Canada
E-mail: ludvik.martinu@polymtl.ca
and bill.baloukas@polymtl.ca

Chapter 18

Volodymyr Pervak
Ludwig Maximilians University
Laboratory for Attosecond Physics
Am Coulombwall 1
D-85748 Garching, Germany
E-mail: vladimir.pervak@lmu.de

Chapter 19

Catherine Grèzes-Basset* and Grégory Chauveau
Department of Thin Film Coatings
CILAS
ZI St Mitre
Avenue de la Roche Fourcade
Aubagne 13400, France
E-mail: grezes-basset@cilas.com

Chapter 20

Chris H. Stoessel
Southwall Technologies
3788 Fabian Way
Palo Alto, CA94303, USA
E-mail: cstoessel@southwall.com

Chapter 21

Clark I. Bright
Bright Thin Film Solutions
7850 N. Silverbell Rd. 114–107
Tucson, AZ 85743, USA
E-mail: brightcrew@aol.com

Chapter 22

Denny Wernham
European Space Research and
Technology Centre (ESTEC),
The European Space Agency (ESA-
ESTEC)

Keplerlaan 1
Noordwijk
The Netherlands
E-mail: denny.wernham@esa.int

Woodhead Publishing Series in Electronic and Optical Materials

- 1 Circuit analysis**
J. E. Whitehouse
- 2 Signal processing in electronic communications: For engineers and mathematicians**
M. J. Chapman, D. P. Goodall and N. C. Steele
- 3 Pattern recognition and image processing**
D. Luo
- 4 Digital filters and signal processing in electronic engineering: Theory, applications, architecture, code**
S. M. Bozic and R. J. Chance
- 5 Cable engineering for local area networks**
B. J. Elliott
- 6 Designing a structured cabling system to ISO 11801: Cross-referenced to European CENELEC and American Standards**
Second edition
B. J. Elliott
- 7 Microscopy techniques for materials science**
A. Clarke and C. Eberhardt
- 8 Materials for energy conversion devices**
Edited by C. C. Sorrell, J. Nowotny and S. Sugihara
- 9 Digital image processing: Mathematical and computational methods**
Second edition
J. M. Blackledge
- 10 Nanolithography and patterning techniques in microelectronics**
Edited by D. Bucknall
- 11 Digital signal processing: Mathematical and computational methods, software development and applications**
Second edition
J. M. Blackledge
- 12 Handbook of advanced dielectric, piezoelectric and ferroelectric materials: Synthesis, properties and applications**
Edited by Z.-G. Ye

- 13 **Materials for fuel cells**
Edited by M. Gasik
- 14 **Solid-state hydrogen storage: Materials and chemistry**
Edited by G. Walker
- 15 **Laser cooling of solids**
S. V. Petrushkin and V. V. Samartsev
- 16 **Polymer electrolytes: Fundamentals and applications**
Edited by C. A. C. Sequeira and D. A. F. Santos
- 17 **Advanced piezoelectric materials: Science and technology**
Edited by K. Uchino
- 18 **Optical switches: Materials and design**
Edited by S. J. Chua and B. Li
- 19 **Advanced adhesives in electronics: Materials, properties and applications**
Edited by M. O. Alam and C. Bailey
- 20 **Thin film growth: Physics, materials science and applications**
Edited by Z. Cao
- 21 **Electromigration in thin films and electronic devices: Materials and reliability**
Edited by C.-U. Kim
- 22 **In situ characterization of thin film growth**
Edited by G. Koster and G. Rijnders
- 23 **Silicon-germanium (SiGe) nanostructures: Production, properties and applications in electronics**
Edited by Y. Shiraki and N. Usami
- 24 **High-temperature superconductors**
Edited by X. G. Qiu
- 25 **Introduction to the physics of nanoelectronics**
S. G. Tan and M. B. A. Jalil
- 26 **Printed films: Materials science and applications in sensors, electronics and photonics**
Edited by M. Prudenziali and J. Hormadaly
- 27 **Laser growth and processing of photonic devices**
Edited by N. A. Vainos
- 28 **Quantum optics with semiconductor nanostructures**
Edited by F. Jahnke
- 29 **Ultrasonic transducers: Materials and design for sensors, actuators and medical applications**
Edited by K. Nakamura
- 30 **Waste electrical and electronic equipment (WEEE) handbook**
Edited by V. Goodship and A. Stevles
- 31 **Applications of ATILA FEM software to smart materials: Case studies in designing devices**
Edited by K. Uchino and J.-C. Debus

- 32 **MEMS for automotive and aerospace applications**
Edited by M. Kraft and N. M. White
- 33 **Semiconductor lasers: Fundamentals and applications**
Edited by A. Baranov and E. Tournie
- 34 **Handbook of terahertz technology for imaging, sensing and communications**
Edited by D. Saeedkia
- 35 **Handbook of solid-state lasers: Materials, systems and applications**
Edited by B. Denker and E. Shklovsky
- 36 **Organic light-emitting diodes (OLEDs): Materials, devices and applications**
Edited by A. Buckley
- 37 **Lasers for medical applications: Diagnostics, therapy and surgery**
Edited by H. Jelínková
- 38 **Semiconductor gas sensors**
Edited by R. Jaaniso and O. K. Tan
- 39 **Handbook of organic materials for optical and optoelectronic devices: Properties and applications**
Edited by O. Ostroverkhova
- 40 **Metallic films for electronic, optical and magnetic applications: Structure, processing and properties**
Edited by K. Barmak and K. Coffey
- 41 **Handbook of laser welding technologies**
Edited by S. Katayama
- 42 **Nanolithography: The art of fabricating nanoelectronics, nanophotonics and nanobiology devices and systems**
Edited by M. Feldman
- 43 **Laser spectroscopy for sensing: Fundamentals, techniques and applications**
Edited by M. Baudelet
- 44 **Chalcogenide glasses: Preparation, properties and applications**
Edited by J.-L. Adam and X. Zhang
- 45 **Handbook of MEMS for wireless and mobile applications**
Edited by D. Uttamchandani
- 46 **Subsea optics and imaging**
Edited by J. Watson and O. Zielinski
- 47 **Carbon nanotubes and graphene for photonic applications**
Edited by S. Yamashita, Y. Saito and J. H. Choi
- 48 **Optical biomimetics: Materials and applications**
Edited by M. Large
- 49 **Optical thin films and coatings**
Edited by A. Piegari and F. Flory
- 50 **Computer design of diffractive optics**
Edited by V. A. Soifer

51 Smart sensors and MEMS: Intelligent devices and microsystems for industrial applications

Edited by S. Nihtianov and A. L. Estepa

52 Fundamentals of femtosecond optics

S. A. Kozlov and V. V. Samartsev

53 Nanostructured semiconductor oxides for the next generation of electronics and functional devices: Production, properties and applications

S. Zhuiykov

Preface

The field of optical coatings was thoroughly investigated in the last century and the optical effects of thin films were known even before then, as described by Newton and other scientists in the eighteenth century. The anti-reflection effect of a single layer on glass was first discovered by Fraunhofer in 1817 but the real development of simple antireflection coatings using vacuum deposition techniques was made in the 1930s, both in Europe and the United States. The understanding of optical interference in thin films and the development of the formalism for the propagation of electromagnetic waves through a layered medium paved the way for designing and producing multilayer coatings in the years following. The deposition under vacuum of metal films for obtaining high-reflectance mirrors was also developed at the industrial level in the first half of the twentieth century, even though mirrors were known long before that, and metal-dielectric filters started to be produced at that time as well.

Since then, much progress has been made in coating design, owing to both the fast development of computers and the implementation of dedicated software. At the same time, the improvements in the technologies for deposition of thin films have allowed ever more reliable coating manufacturing.

Nowadays optical coatings are considered an important sector of optical components and often they represent the critical part of entire optical systems, therefore significant efforts are dedicated to improve their performance. Applications can be found in many areas: lasers, smart windows, clean energy, environmental monitoring, telecommunications, astronomy, aerospace, displays and lighting, and anti-counterfeiting devices are only some examples of a long list. As there is an increasing demand for optics in many fields, the range of applications for optical thin films and coatings is widening more and more.

Thin-film optical coatings is an active field of research and innovative breakthroughs are continuously being made, especially in investigations on new materials and structuring of the coating morphology. The development of heterogeneous nanostructures is enlarging the use of thin films and this area is now part of nanophotonics.

A number of books have already been published on both optical coating design and thin-film deposition techniques, as well as on characterization methods, and there is a vast literature on these topics. Thus we decided to dedicate this book mainly to developments on thin-film materials and applications, for optics and related fields.

The book is divided in four parts. The initial chapters in Part I are devoted to classical topics and give a short review of each subject, including new advances. A survey of deposition techniques for optical thin films opens the book (Chapter 1), followed by a description of the methods of design of complex optical coatings (Chapter 2), these being two subjects of central relevance in each approach to optical coatings. Then, the monitoring of coating fabrication (Chapter 3) and the production technologies for high-precision coatings (Chapter 4) are described, with a look at historical developments and new strategies.

Part II is dedicated to some special features of optical thin films and coatings, like plasmonic effects for optical applications (Chapter 5), scattering in random structures (Chapter 6), thin film properties at short wavelengths (Chapter 7), thermal radiation control (Chapter 8) and color effects (Chapter 9).

Part III follows with some recent developments on film materials, starting with organic films and coatings (Chapter 10); then an overview of surface multiplasmonics with non-homogeneous thin films is given (Chapter 11) and finally a description of optical films containing quantum dots (Chapter 12) closes this part of the book.

The chapters from 13 to 22, in Part IV, are dedicated to applications and represent almost half of the book. They cover different fields, even though they are not exhaustive of all possible areas in which optical thin films can be useful. This last part of the book starts with antireflection coatings on plastic (Chapter 13) and protective coatings for optical surfaces (Chapter 14), then continues with applications in displays and lighting (Chapter 15), photovoltaic cells (Chapter 16) and security devices (Chapter 17). The next two chapters (Chapter 18 and Chapter 19) are dedicated, respectively, to the application of coatings in high-intensity femtosecond lasers and to coatings in large facilities involving lasers and space.

The last chapters give an overview on automotive and building applications (Chapter 20), transparent conductive coatings (Chapter 21) and the behavior of optical coatings in space (Chapter 22).

It is difficult to include in a single book all the interesting applications, such as for example: optical sensors, optical coatings for telecommunications, optics for art conservation, biological and medical applications, and more. Therefore a selection has necessarily been made. Moreover, characterization methods are not specifically dealt with, even though they are of great importance in this field not only to control the optical properties but

also to test the environmental resistance of coatings; there are many types of characterization methods for thin films and coatings and some of them are described in different chapters.

The diffusion nowadays of multimedia and the possibility of downloading from the web single chapters of the book, means that each chapter should be self-contained. As a consequence, some overlaps can be found between several chapters. For example optical monitoring strategies are described in both Chapters 3 and 4, plasmonics is present in the title of Chapters 5 and 11, organic thin films are mentioned in Chapters 10 and 16 and solar cells in Chapters 2 and 16, transparent conductive coatings appear in Chapters 20, 21 and others as well. However, even when similar topics are described by more than one author, the approach is substantially different and complementary. More details can be found in the contents of each chapter, which will be accessible through the web.

The authors come from both research institutes and industry, thus a combination of theoretical contributions and practical views can be seen throughout the whole book. All contributors are renowned specialists in their fields and many of them, as well as the editors, have been working in the area of optical thin films for more than thirty years. Several chapters are authored by experts who took part in the early developments in the specific sectors, and published many fundamental works.

We hope the book will be useful for scientists and technical people, providing an overview of the key role of optical coatings in different fields and stimulating the reader's interest to go deeper in each topic, taking advantage of the bibliographic material in all chapters.

The potential readers of this book may be physicists, chemists and engineers, including senior students, interested in both research developments and practical applications. Newcomers to the field of optical thin films and coatings could be attracted by the extremely wide range of applications, while specialists of a particular field could find information on the new trends in their area of interest.

We wish to thank all authors for their valuable contributions and efforts and we are also grateful to the Publishers for their assistance during the preparation of the book.

*Angela Piegari
Rome, Italy
Francois Flory
Marseille, France
March 2013*

Recent developments in deposition techniques for optical thin films and coatings

H. ANGUS MACLEOD, Thin Film Center Inc., USA

DOI: 10.1533/9780857097316.1.3

Abstract: The most significant processes for optical coating manufacture are variants of vacuum deposition. Thermal evaporation is the traditional process and still of great importance but in the last two decades there has been a major shift to the energetic processes, primarily ion and plasma-assisted deposition and various forms of sputtering. Vacuum processes are very flexible and so dominate short-run production but various forms of pulsed chemical vapor deposition are just starting to appear in long runs of very specialized components. There is also a wide range of other viable and occasionally used techniques, with various degrees of promise, ranging from arc evaporation to liquid deposition.

Key words: optical coating manufacture, deposition processes, vacuum deposition.

1.1 Introduction

A thin-film optical coating is a treatment intended to modify, in a prescribed way, the properties of the surface that supports it, and the deposition of the coating, therefore, begins with this surface. Although the coating may be expected to present a range of different properties, environmental, thermal, chemical, even acoustical, the primary objective is most frequently a set of desired specular optical properties which alter the quality of the light manipulated by the surface but leave its direction unchanged. This is the nature of the bulk of the coatings considered in this book. A glance at the chapter headings will demonstrate the enormously wide range of possible coating types. For such coatings the surface must be smooth in optical terms. In other words, departures from perfection should be of a size that is orders of magnitude less than the wavelength of the light. We assume that this is the case. Our coatings then consists of one or more thin layers of chosen materials that together exhibit the properties that we require, usually by a combination of interference and the intrinsic properties of the materials. Sometimes the materials may themselves be altered from their natural state by engineering their microstructure and this is dealt with elsewhere in this book.

The forces that hold thin films together and attach them to their surfaces are all short range, from one atom to the next. These forces are exceedingly strong but have quite short range and so a monomolecular layer of contaminant can block the bonds completely. Thus, not only is the smoothness of the surface important but its cleanliness is even more so.

There are so many processes that are or have been used for the deposition of optical coatings that a complete list is beyond us. Probably one of the earliest was the production of mirrors during the later Roman Empire by pouring molten lead over glass. Enough lead adhered to the glass to increase considerably its reflectance but the glass tended to shatter under this treatment and so the mirrors were small and irregularly shaped. An improved technique originating in the fifteenth century was a tin amalgam coating that, coupled with the enormous simultaneous improvements in the quality of flat glass allowed mirrors of essentially modern quality to be produced. Chemical silvering was developed in the middle of the nineteenth century and was the preferred technique for front-surface mirrors until the 1930s. At the same time, great progress was made in photographic processes culminating in the Lipmann emulsion that, when developed, was essentially a thin-film interference filter. Artificial tarnishing of glass surfaces to reduce their reflectance was also practiced to an extent in the nineteenth century. However, apart from the front-surface mirror coatings, there was little need for optical coatings until the increasing complexity of optical instruments and systems in the early twentieth century demanded improved surface properties, especially the reduction of reflectance that greatly improved transmittance at the same time as removing glare and ghost images. Vacuum deposition was generally adopted as the preferred process. By the middle of the twentieth century the field of optical coatings was growing rapidly. Much was happening in optics, but the advent of the laser was probably the most significant event and lasers need coatings. The unprecedented expansion of optics in the second half of the twentieth century took optical coatings with it and the expansion still continues in the twenty-first century.

Today, vacuum deposition is still the major process for the production of optical coatings but while thermal evaporation has been the primary process for many years, we are now seeing much more use of alternative vacuum processes and even some processes that do not depend on vacuum.

1.2 Early processes for the deposition of optical coatings

In 1912 Pohl and Pringsheim published a paper on the deposition of metallic mirrors through a process they called vacuum distillation (Pohl and Pringsheim, 1912). This laid out the principles of what became known as thermal evaporation. Thermal evaporation is quite simple. Material is

heated under vacuum until it boils, and the resulting vapor then condenses on the substrates to be coated, which are held at temperatures well below the freezing temperature of the evaporated material. The material, the evaporant, immediately forms a thin solid film. Although Pohl and Pringsheim's paper dealt with metals, it was clear that dielectrics and semiconductors could be equally well deposited by this technique. The technique became quite generally used for optical coatings in the 1930s and it is still of considerable importance. The thickness of the deposited film tends to follow the same rules as illumination, inverse square law coupled with the cosines of incident and emission angles and the uniformity required for any but the simplest single-layer antireflection coatings requires movement of the substrates during deposition to even out the layer thickness. The movement is usually fairly simple involving single or double rotation of the structure holding the substrates.

Early dielectric coatings produced by the thermal evaporation technique exhibited two serious problems. They were not particularly resistant to abrasion, and their spectral characteristics tended to be slightly unstable, usually settling down after a shift to longer wavelengths. This behavior was often termed settling. In the 1940s it was found possible to considerably improve the abrasion resistance by heating the substrates during deposition (Lyon, 1946) and so that was the first major development in the technique. Radiant heating is normal.

The early evaporation sources were crucibles of refractory metal, like molybdenum, tantalum or tungsten, heated by passing a current through them. The sources tended to be elongated with lands at the ends for attaching electrodes. The appearance was similar to that of a boat and so the sources, inevitably, are known as boats. Boat sources are still used, but often suffer from corrosive interaction with the heated charge. They are also often run at temperatures close to their melting points when they can distort and change the distribution of vapor. There has therefore been a gradual shift towards electron-beam heating. The electron beam source normally consists of a metallic crucible, usually copper, with perhaps a suitable lining, which is water-cooled. The charge in the crucible is heated by directing a beam of energetic electrons onto it. Beam current can be several ampères and the voltage several kilovolts and so the heat delivered to the charge is massive and capable of melting virtually anything. Interaction with the crucible is inhibited by its water cooling. The electron source is a hot filament that would also suffer from corrosion were it exposed to the evaporant. It is therefore buried in the structure of the source and the electron beam is bent through at least 180° by the magnetic field of a, usually permanent, magnet with pole pieces that run along the side of the source. This helps to focus the beam. Additional, small, electromagnets are frequently included to vary the beam position and the pattern of its movement over the surface

of the charge. Although the electron beam source is rather more expensive than the boat source, it has reached the stage of development where its stability and reliability keep the running costs low and the yield of acceptable products high.

Experiments on both metals and dielectrics by Movchan and Demshishin (Movchan and Demchishin, 1969) in the late 1960s eventually showed that the important parameter in this heating was the ratio of the temperature of the substrate to the melting temperature of the evaporant. Evaporated thin films have a columnar microstructure and the packing of the columns is of critical importance in determining the film properties. They identified three growth zones. Zone One with a ratio for dielectrics below around 0.22–0.26 gives loose dendritic columns with poor mechanical properties, particularly abrasion resistance. A larger ratio of roughly up to 0.45–0.5 yields Zone Two where the columnar structure becomes very close packed with improved abrasion resistance and stability. With ratios above around 0.5 we have Zone Three where the columns tend to be replaced with what appear to be small recrystallized grains. For optical coatings, Zone Two is much to be preferred. Films produced in Zone Three usually show significant scattering losses and, in any case, the temperature required for the many refractory materials that are employed is too high for normal deposition equipment. This structural zone model is of enormous help in understanding film properties and it has been developed and elaborated (Thornton, 1974) over the years and is still a topic of investigation (Anders, 2010). For instance the importance of the energy of the arriving evaporant has been recognized. A transition zone between Zone One and Zone Two has been identified (Thornton, 1974).

By the end of the 1970s capillary condensation of atmospheric moisture in the pores in between the columns had been shown to be the major cause of the drifting or settling of the optical coatings (Koch, 1965; Macleod and Richmond, 1976; Ogura and Macleod, 1976; Lee, 1983). There were some hints (Motovilov *et al.*, 1974; Hirsch and Varga, 1978) that what were later classified as the energetic processes might offer some improvement.

1.3 The energetic processes

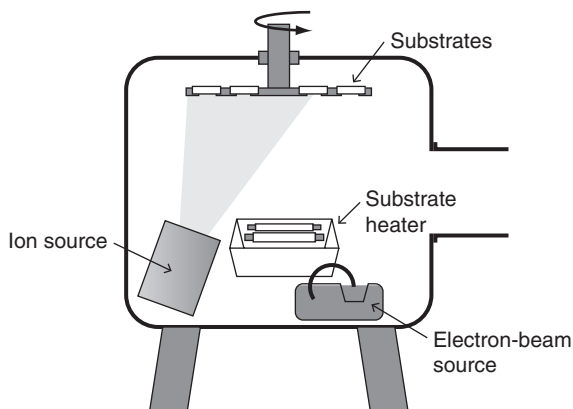
The energetic processes are so called because they involve the addition of kinetic energy to the condensation process. This additional energy can be supplied in different ways. It may be that of the evaporant itself or may be derived from bombardment by specially generated beams of energetic ions. The energetic processes share the property of increasing the solidity, density and, often, adhesion of the growing films.

Movchan and Demchishin had explained the origin of the universal columnar structure of thermally evaporated thin films as the limited mobility of the condensing species, and this has been confirmed by computer modeling

that began with the pioneering work of Dirks and Leamy (1977) and has been detailed by Jacobson (1988). The original ideas of the possible mechanism for the densification inherent in the energetic processes were that the bombardment was somehow increasing the mobility of the condensing material, perhaps through a form of annealing due to thermal spikes caused by the collisions (Hirsch and Varga, 1980). However, computer simulations tended to show that the densification was due to momentum transfer rather than thermal spikes (Müller, 1986a, 1986b) although thermal spikes could contribute to a sealing of some of the porous voids in the films. Experiments then confirmed that the primary mechanism for densification is momentum transfer (Targove and Macleod, 1988; Targove *et al.*, 1988).

1.3.1 Ion-assisted deposition

The simplest of the energetic processes is termed ion-assisted deposition, or IAD. This is thermal evaporation with additional ion bombardment of the growing film (Fig. 1.1). Broad-beam ion sources had been developed originally by NASA as possible propulsion engines for outer space. They were rapidly adopted by industry, primarily for ion-beam etching in the semiconductor industry, and so were readily available for incorporation in optical coating machines (Harper *et al.*, 1982; Kaufman *et al.*, 1982a, 1982b). The broad-beam sources, mainly of the Kauffmann type could be incorporated into thermal evaporation machines with little modification. The ions extracted from the source, with energy usually around a few hundred



1.1 Sketch of a typical arrangement for ion-assisted deposition. The broad-beam ion source does not always irradiate the entire substrate carrier but the rotating substrate carrier moves the substrates through the ion beam each rotation (Courtesy of Thin Film Center).

electron volts, are positive and so would rapidly charge any dielectric material preventing further bombardment. Sufficient electrons to neutralize this charge are therefore added to the extracted beams yielding what is usually termed a neutral ion beam. In the early work, mostly argon was used as the bombarding species but, as we shall see, a much wider range is used today. It was soon demonstrated that the bombardment in ion-assisted deposition could so improve the solidity of films so as to remove completely their moisture sensitivity (Martin *et al.*, 1983). The absence of moisture induced shifts and, also because of the high packing density, the more stable optical constants, were major reasons for the rapid adoption of ion-assisted deposition by industry.

There are several advantages in ion-assisted deposition over many of the other energetic processes. Probably the most significant, at least in the early days, is not so much a technical as a financial one. Conversion from thermal evaporation, the almost universal technique for optical coatings at that time, was relatively inexpensive. It consisted of the addition of an ion source with its associated power supply and so did not involve the scrapping of an existing, expensive, machine. A second, technical, advantage is that the bombardment parameters can be adjusted completely independently of the other deposition parameters. The Kaufman source with its extraction grid yields a quite tight distribution of ion energies making it especially attractive for research.

The refractory oxides represent a very important class of materials. There is a general tendency for these materials to lose some oxygen in the evaporation process and the resulting vacancies cause absorption. The oxygen can be restored by adding oxygen to the background atmosphere of the machine in a process termed reactive evaporation. Reactive evaporation can even produce stoichiometric oxides by the evaporation of metals in an oxygen atmosphere. A fine degree of judgment is called for in the reactive process. Not enough oxygen and the absorption remains, although reduced; too much oxygen and the packing of the thin film suffers with all the accompanying consequences. Then many nitrides, particularly of silicon and aluminum, are useful optical materials, but straightforward reactive evaporation fails. The nitrogen is not sufficiently reactive.

The reactivity of oxygen and nitrogen can be greatly increased by passing it through the ion source. Pure oxygen can be rather too reactive when in the ionization chamber of the source so that it reacts with its structure and especially with the hot filament of the Kaufman type. Oxygen, if it is to be passed through the ion source, is usually diluted by mixing it with the argon stream. Nitrogen, however, derives great benefit from passage through the source and becomes sufficiently reactive to produce highly transparent and high-quality nitride films (Netterfield *et al.*, 1986; Targove *et al.*, 1987; Hwangbo *et al.*, 1989).

There are many variants of what is essentially ion-assisted deposition that differ principally in the details of the design of the source. An ion source is one in which ions, usually positive ions, are extracted, often by means of a grid, and that has been the primary thrust of the description so far. A plasma source is one in which the entire plasma is permitted to emerge from the source. The electrons in the plasma are very mobile and tend to escape leaving a positively charged plasma that repels the positive ions so that they then bombard the growing film. This is usually termed plasma ion-assisted deposition to distinguish it from ion-assisted deposition.

The major recent development is a move to radio frequency (13.56 MHz) (Anders, 2005; Hagedorn *et al.*, 2008) or even microwave (2.45 GHz) (Sakudo, 1998; Anders, 2005) excitation of the plasma in the source. This reduces the level of impurities in the ion beam and also permits much longer operation of the source before any necessary maintenance.

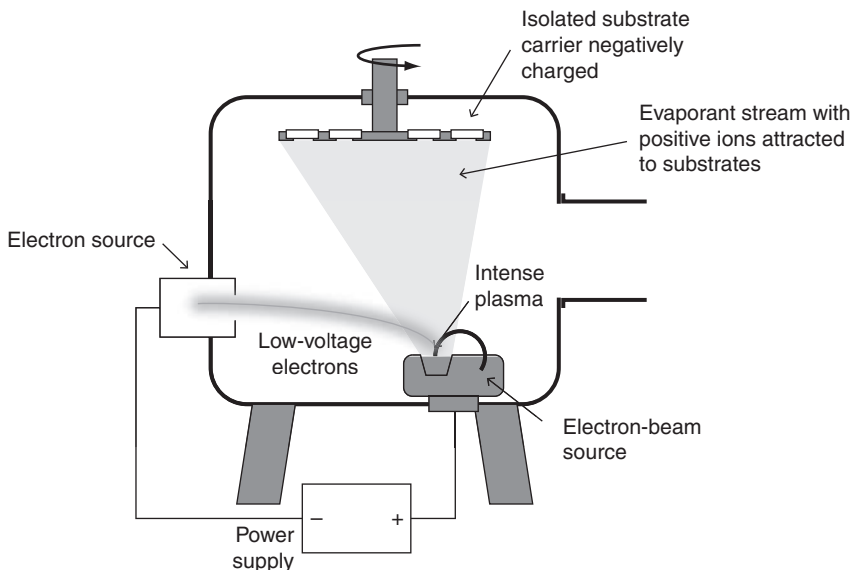
The fluorides with their enormously wide range of transparency from the far infrared to the extreme ultraviolet are very attractive thin film materials that are much used. Unfortunately, the bombardment inherent in the energetic processes tends to damage the material by preferential removal of fluorine. Small losses of fluorine can be tolerated because the vacancies are usually healed by oxygen and optical absorption is then minimized. With larger fluorine loss, however, an oxyfluoride can form that has normally rather poorer durability, more constricted regions of transparency, and elevated refractive index. All this implies that bombardment of the fluorides in energetic deposition must be severely limited. Gentle bombardment is beneficial and has been shown to improve adhesion, increase packing density and inhibit oxidation but not nearly to the extent of the improvements found in the oxides and nitrides (Saxe, 1985; Messerly, 1987; Targove, 1987).

1.3.2 Ion plating

Ion plating is a somewhat imprecise term used for a variety of processes. In its original form it was intended to replace electroplating (Mattox, 1967) and it has achieved a high degree of success in that role. In that application it consists of a thermal evaporation source and a metallic substrate holder with a glow discharge between them sustained by several thousand volts, the anode being the source and the cathode the substrate holder, an arrangement known as high-voltage ion plating. The original idea was that the positive ions would be attracted from the plasma to bombard and coat the substrates. Hard, tough deposits with excellent throw are, in fact, produced. It is now clear that the process is much more complex (Mattox, 1979) and there can be large differences between the various forms of implementation. The degree of ionization in high-voltage ion plating is usually quite

small and the major effect is the bombardment of the growing film by energetic particles, mostly neutral and that have gained energy from collisions in the discharge. These energetic particles, largely of the evaporant, form the growing film and, in transferring momentum, compact it as in ion-assisted deposition. The improved throwing power appears to be largely because of the accompanying gas scattering. This high-voltage form of ion plating has not been much used for optical coatings although Reid and colleagues did produce remarkably tough zinc sulfide layers for use in the infrared (Reid *et al.*, 1979).

Reactive low-voltage ion plating (Moll *et al.*, 1986; Pulker, 1992; Pulker and Guenther, 1995) is a more common ion plating system for optical coating deposition (Fig. 1.2). It consists of a thermal evaporation machine with an electron-beam source containing a metal or sub-oxide that is sufficiently conducting. This source is insulated from the structure of the machine and is connected to the positive pole of a DC power supply which provides large current at a few hundred volts. The negative side of the power supply is connected to a plasma chamber, also isolated from the machine, which provides an intense beam of low-voltage electrons. These are attracted to the electron-beam source where an intense plasma forms above the evaporating surface. The substrate carrier is also electrically isolated from the machine, and the electrons that are very mobile, charge it negatively, attracting positive ions from the plasma. These positive ions consist of source material and



1.2 Reactive low-voltage ion plating. (Source: After Pulker and Guenther (1995). Courtesy of Thin Film Center.)

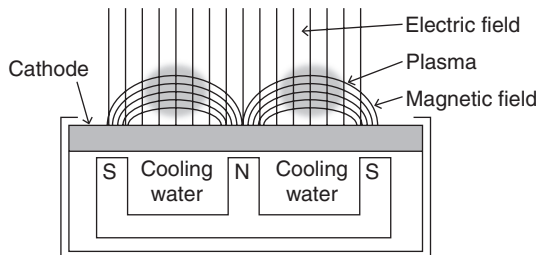
they impinge on, and form part of, the growing film with all the densification that comes from the transfer of momentum. For transparent films additional oxygen is added to the plasma to make the process reactive. Alternatively, nitrogen can be added either to create an oxynitride or a nitride, all with excellent optical properties (Bovard *et al.*, 1989).

1.3.3 Sputtering

Sputtering is probably the oldest of the energetic processes. It dates back to the middle of the nineteenth century (Grove, 1852) but it was not much used in the production of optical coatings until the second half of the twentieth century. In its simplest form it consists of an evacuated chamber containing a metallic anode and cathode. These are so arranged as to maintain a glow discharge in the residual gas in a chamber. A voltage of a few kV together with a pressure of around 1 Pa or greater (0.01 mbar) gives a very rough idea of what might be required. Positive ions from the discharge are attracted to the cathode and bombard it with elevated energy. Transfer of momentum from the bombarding ions to the molecules of the cathode causes collision cascades that end with the ejection of molecules from the cathode with considerable kinetic energy. Although it is not always possible, for best results the atomic weight of the bombarding species should be similar to that of the target material maximizing the momentum transfer. There is only quite small ionization of the sputtered material and ideally these molecules travel in straight lines to impinge on the anode, or substrate, and form there a thin solid film. The momentum transfer from the arriving material promotes a dense microstructure in the film.

There are some problems that cause departure from the ideal situation. The first is that, as described, the process works only for conducting metals. If we replace the metallic anode and cathode with dielectrics then the surfaces quickly charge and inhibit any further sputtering. To prevent this suppression of the sputtering process the surfaces must be discharged. The capacitance of a dielectric surface is minuscule and the rate of charging exceptionally high. Since the rate of discharging must be equally high, we are led to the process known as radio frequency in which the plasma is created by a radio frequency field rather than zero frequency. The process works well and has been and is used for optical coating deposition. However, there are many more problems associated with radio-frequency processes than with zero frequency and so in optical coating the process tends to be used in special cases rather than applied generally.

A second problem is that, with the simple system described, the plasma is in the way of the sputtered material. The resultant scattering reduces the energy of the condensing material and, therefore, acts against the desired



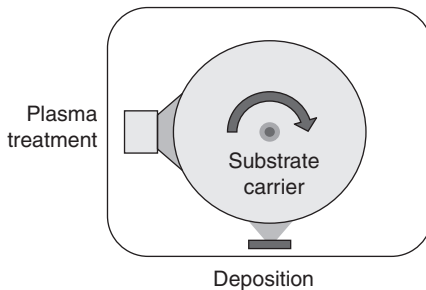
1.3 Schematic cross-section of a planar magnetron cathode showing the crossed electric and magnetic fields with the resulting plasma. The area of the cathode under the plasma is the part mainly eroded and is known as the racetrack because of its shape (Courtesy of Thin Film Center).

densification. Magnetron sputtering (Kelly and Arnell, 2000) can achieve an order of magnitude lower pressure, say 0.1 Pa (0.001 mbar) compared with the 1 Pa or greater in traditional sputtering together with a reduction in the necessary voltage to some hundreds of volts instead of some kilovolts. In magnetron sputtering the electrons are forced into cycloidal paths by the addition of a magnetic field. Permanent magnets with alternating poles are fixed behind the cathodes (usually plane) so that at a short distance, 10–20 mm perhaps, above the cathode surface the electric field and the magnetic field are crossed (Fig. 1.3). In that region the plasma forms because of the enhanced ionization due to the longer cycloidal path of the electrons. The plasma is somewhat limited in its extent and so too is the erosion region. On plane rectangular cathodes, the erosion region looks like a map of a racetrack and so the term racetrack is normally used to describe it.

Reactive sputtering represents a way of overcoming the problem of dielectrics. Many dielectrics are metal oxides or sometimes metal nitrides. In such cases the cathode can be left as the desired metal and reaction can be arranged by adding the necessary oxygen or nitrogen to the background gas. The discharge activates the reacting gas so that its reaction with the growing film is virtually complete and high-quality dielectrics result. Unfortunately the process is not as successful with fluorides. Fluorine is preferentially sputtered and lost, either from the growing film or from a fluoride target, just as in the ion-assisted processes. Although reactive processes involving added fluorine and fluorine compounds have been pursued in the research laboratory with some degree of success, such processes have not so far been seen as sufficiently reliable to be adopted generally in production.

Unfortunately, in reactive sputtering, the reacting gas tends to react not simply with the growing film but with the sputtering target as well. In magnetron sputtering this results in a build-up of insulating material known as target poisoning. In the racetrack any insulating material is rapidly removed by the bombardment. It does cause some hysteresis in the electrical characteristics that has to be dealt with in the control system, but it is outside the racetrack that serious problems occur. The thin dielectric layer acts as a capacitor which charges up as the positive ions arrive. Because the coating is thin, the capacitance is high and the charge represents considerable energy. This energy is released from time to time in a capacitor failure and the very high stored energy causes an arc that is frequently powerful enough to melt local regions of the cathode, causing ejection of metallic globules, many of which arrive at the substrate. Fortunately the high capacitance implies a long time constant so that discharging the capacitors can be carried out at relatively low frequencies, a few tens of kilohertz. Special power supplies that periodically reverse their polarity to discharge the capacitors represent one common solution. Recently, however, a technique known by several different terms has gained much ground in optical coating. Mid-frequency sputtering, or dual magnetron sputtering, involves two similar magnetrons attached to opposite sides of a power supply operating at around 40 kHz. This implies that every half cycle the rôles of the magnetrons switch from cathode to anode and vice versa. This effectively discharges the capacitors and solves another problem that can occur with reactive sputtering known as the disappearing anode. The anode in the normal sputtering process is often the structure of the machine or, sometimes, a rod or similar element introduced to act as anode. The anode gradually becomes coated with an insulating film just like the regular substrates and its effectiveness eventually vanishes. In mid-frequency sputtering, the alternate target is the anode, and so the problem is solved. Mid-frequency sputtering was introduced originally for coating large areas, usually of glass, but in the past decade it has been adopted by precision optical coating.

Target poisoning can be eliminated by scrubbing the whole surface of the cathode by the ions from the plasma. This implies moving the plasma, or moving the surface, or both. In the cylindrical rotating magnetron source the target becomes cylindrical and is rotated around the permanent magnets. This has the additional advantage of smoothing out the eroded area so that the racetrack disappears and cathode utilization is much more efficient. Small cylindrical magnetrons have penetrated into the precision optical field, particularly in the mid-frequency configuration. Although they do not suffer from the poisoning effects of reactive deposition, they can experience the disappearing anode and this is eliminated by the mid frequency technique.



1.4 The arrangement of source and treatment stations in alternating ion plating. The substrate carrier rotates rapidly past each so that as each small increments of film is added it is immediately treated but the two stages are separated so that they do not interfere with each other. (Source: After Schiller *et al.* (1975). Courtesy of Thin Film Center.)

A paper describing a process called alternating ion plating (Fig. 1.4) appeared in 1975 (Schiller *et al.*, 1975). Although, at the time, it was not aimed at optical coatings and did not attract any unusual level of interest, nevertheless its effect on the field has been fundamental and far reaching. The idea is simple. The plasma treatment of the growing film that exists in ion plating, ion-assisted deposition, sputtering and other reactive energetic processes, interferes with the deposition process. Since the effect of the ion bombardment reaches a certain, small, depth in the film it would be better to add an increment of film, bombard it, add another increment, and bombard that and so on. Provided the increments are small enough the effect will be the same as the continuous process. This technique can readily be implemented by mounting the substrates on a cylindrical drum and rotating the drum so that the substrates pass the source and then pass the treatment stage and so on. This geometry with its different treatment stages has been widely adopted for the energetic processes.

Radical assisted sputtering (RAS) is a particularly interesting new process (developed by Shincron Co. Ltd) that uses this geometry (Song *et al.*, 2000; Nagae *et al.*, 2001; Song and Sakurai, 2004). Here the treatment phase applies atomic oxygen to the growing film. The oxygen is exceedingly reactive and the oxidation, therefore, very efficient. Films of exceptionally high optical quality are produced.

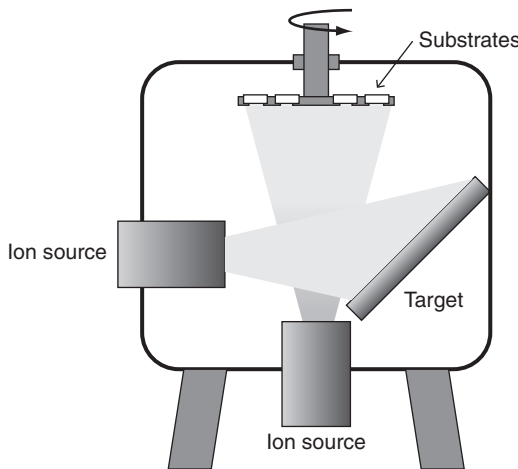
Closed field magnetron sputtering (Applied Multilayers LLC) uses a similar cylindrical intermittent deposition system but here the plasma treatment exists around the entire cylinder. This is achieved by arranging the ring of magnetron targets around the cylinder so that the permanent magnets show alternating poles. If one magnetron shows NSN, that next to it will show SNS and so on. This creates a magnetic confinement system that

spreads the plasma right round the cylindrical substrate carrier and so the plasma treatment is exceedingly efficient. High quality optical coatings have been demonstrated (Gibson *et al.*, 2008a, 2008b).

Intermittent deposition and treatment can also be achieved with a flat circular substrate carrier. The advantage here is that with a horizontal carrier the substrates can be held in place by gravity, to face the lower sources and plasma stages in the usual way. It is then a much more straightforward operation to load the carrier robotically without exposing it to the atmosphere. This is the principle of the Helios sputtering system (Leybold Optics GmbH).

A recent variant of magnetron sputtering is known as high power impulse magnetron sputtering with a somewhat variable acronym but usually HIPIMS (Kelly and Bradley, 2009). Here the process is pulsed at such high pulse power that a highly ionized metal flux results that has been likened to the output of a cathodic arc. The resulting films possess improved adhesion and are dense and smooth and exhibit, at low temperatures, structures that are associated with much higher temperatures. The pulsing is at a quite low frequency, generally less than 1 kHz, and the pulse duration of a few hundred microseconds does not overheat the targets so that even quite thermally sensitive substrates can be coated. Although the process has not so far been much employed in optical applications, there is evidence that suggests it should offer advantages there also. Titanium dioxide, for example, sputtered from a ceramic $\text{TiO}_{1.8}$ target has been shown to exhibit higher refractive index than with competing processes. Sarakinos and colleagues achieved indices of 2.45 and 2.48 at 550 nm compared with 2.38 in DC Magnetron sputtering (Sarakinos *et al.*, 2007).

Ion-beam sputtering solves many of the problems associated with the different sputtering processes by using a neutral ion beam derived from a broad-beam source to sputter the target material. Purely dielectric material can be sputtered in this way because there is no target charging problem. That the plasma from which the ions are derived is in a separate chamber, the body of the ion source, implies that the intervening plasma of the usual sputter process is completely removed. Travel of sputtered material from target to substrate is therefore completely unimpeded. The result is films of exceptionally high quality. Often a second ion source is used directly to bombard the growing film in what is termed dual ion-beam sputtering (Fig. 1.5). This second ion treatment is primarily for additional control of the film properties, particularly intrinsic stress. The process is rather slower than the other forms of sputtering and the useful coated area somewhat smaller, but because of the high quality of the films and its intrinsic accuracy, it has become one of the more important processes for high performance coatings.



1.5 Schematic of a dual ion-beam sputtering machine. One ion source bombards the target and is responsible for the sputtering. The second ion beam (vertical in the arrangement illustrated) directly bombardsthe growing film (Courtesy of Thin Film Center).

1.4 Cathodic arc evaporation

Cathodic arc evaporation (Martin *et al.*, 1991) involves a low-voltage and high-current arc that is struck between an electrode and a conducting cathode. The cross-sectional area of the arc is small and so, therefore, is the area of its impingement on the cathode resulting in a very high local temperature that can be as high as 15 000°C. Evaporated material leaves the cathode with very high energy and is also highly ionized. The cathode spot moves over the surface of the cathode, often in what seems like a random motion. Sometimes a magnetic system may be employed to move the spot in a regular raster scan.

The main application of the process has been in the coating of cutting tools and there it has been very successful. It has not significantly penetrated the optical thin film field as yet although the few results reported have been impressive (n of 2.735 for TiO₂ at 633 nm for example (Martin *et al.*, 1991)). A common problem with the simple cathodic arc is the ejection of molten droplets of material that if permitted to reach the growing film will act as scattering defects, a major problem for optical applications. For optical purposes, therefore, the evaporated material can be passed through a filter that, relying on the charged nature of the evaporant, magnetically alters its direction to separate it from the unwanted particles (Fulton, 1999). An interesting arrangement adds ion bombardment to the process in the manner of ion-assisted deposition. The process is known as ion assisted filtered cathodic arc evaporation (IFCAD) (Fulton, 1999).

1.5 Pulsed laser deposition

High target temperatures over a limited area are also achievable by irradiation by pulsed high-power lasers. The acronym appears to have settled down to pulsed laser deposition (PLD) corresponding to the title of this section. Probably the earliest use of this technique in connection with optical coatings was that of Smith and Turner in 1965 (Smith and Turner, 1965) who used a pulsed ruby laser. They had hoped that the stoichiometry of various semiconductor compounds and alloys might be maintained in the resulting films but only a few of their materials showed the same composition as the sources. This may have been partly due to their use of targets of powder in crucibles and perhaps the lower pulse energy available at that time. Difficulties were experienced with materials transparent in the visible region. Not surprisingly they found that some absorption at the ruby laser wavelength was required and some of the powders had to be mixed with a small amount of carbon to achieve this.

The laser, even in recent studies, must be placed outside the chamber and its output introduced through an optical system the final element of which, frequently a mirror, is exposed to the evaporant. Coating can be a problem and sometimes the element is arranged to rotate from time to time to expose once again a clear aperture. Smith and Turner reported that they found that their pulses caused the deposited material to re-evaporate, clearing the aperture quite effectively.

Since then, all kinds of high-power lasers have been employed from the ultraviolet to the far infrared. The high fields associated with the very high power and short pulses overcome the transparency problem by simply causing breakdown in the target material and pulsed laser deposition is now a quite viable technique for the deposition of all kinds of optical coatings (Cheung *et al.*, 1992). It has not, however, reached the mainstream and is used primarily for those rather special applications where it has advantages over other techniques. The process can be manipulated to achieve excellent stoichiometry of otherwise difficult alloys, and films can exhibit high optical performance. Recent reports, for example, have concerned zirconium dioxide and hafnium dioxide with excellent transparency (Tang *et al.*, 2010; Zhang *et al.*, 2011) and vanadium dioxide (Briggs *et al.*, 2010) a thermally-switched agile material exhibiting semiconductor properties below the transition temperature of approximately 68°C and metallic properties above.

1.6 Chemical vapor deposition

In chemical vapor deposition (CVD) precursors interact chemically to produce the final thin-film product (Choy, 2003). The precursors are transported into a reaction chamber entrained in a carrier gas stream. In this

reactor vessel they are induced to react, the reaction product – the thin-film material – being added to the growing film. In traditional chemical vapor deposition the reaction was triggered by a hot substrate and this technique is still occasionally used. A problem with this process is that an efficient reaction will usually produce material at too fast a rate to be accommodated by the growing film resulting in a rather loose deposit with little mechanical strength and poor optical properties. Thermal chemical vapor deposition, therefore, prefers reactions that are not too favorable. Since impurities in such cases often exhibit faster reactions, traditional thermal chemical vapor deposition required reactants of very high purity.

A more usual approach nowadays is to use more efficient reactants but to arrange triggering of the reaction in short pulses (Segner, 1995). The interval between pulses permits the necessary accommodation of the material in the film resulting in high optical quality and high packing density. Although it has been shown possible to pulse the entry of the reactants into a thermal chemical vapor deposition process (Westmoreland, 1993; Choy, 2003), the preferred technique is to trigger the reaction by a pulsed radio frequency or microwave frequency plasma. The process is known by various names with their different acronyms. Plasma impulse chemical vapor deposition (PICVD) is a common designation.

An interesting combination of microwave and radio frequency excitation of the plasma in the production of a narrowband rejection filter entirely of silicon nitride with packing density variation to change the index is described in Vernhes *et al.* (2004).

Uniformity in chemical vapor deposition is largely a function of the flow pattern in the reactor and usually each different substrate shape requires a different reactor design. This limits the usefulness of chemical vapor deposition in small batch production. It is primarily used, therefore, for long production runs of identical products where the reactor design is stable. A good example is the production of cold mirrors. The 50 mm parabolic reflectors that surround quartz halogen projection lamps carry a cold mirror and, although the reflector-source combination was originally intended for projectors it has found its way into almost all forms of lighting. The market is estimated to be in the hundreds of million parts per year and so the cold mirror represents the kind of long production run that is ideal for chemical vapor deposition. See Bach and Krause (1997) for an account of the process developed by the Schott Group.

1.7 Atomic layer deposition

A related process is atomic layer deposition (ALD) (Alasaarela *et al.*, 2009; Maula *et al.*, 2009). Here the precursors are introduced in alternate pulses into the reactor. Each pulse results in a thin layer over the substrates. The

vapor pressure of the material is such that evaporation of any excess leaves what can be roughly considered as a monomolecular layer behind. The second precursor then reacts with the material on the substrate, excess again evaporating away. The process is slow because the reactor has to be purged between each precursor pulse but it has the enormous advantage of being able to coat quite complex shapes with a high degree of uniformity. Since the thickness increments, although small, are quite regular, the control of layer thickness becomes one of counting cycles and complete automation is straightforward and normal.

Titanium oxide is readily deposited using precursors of TiCl_4 and water, and Al_2O_3 using trimethylaluminum (TMA: $\text{Al}_2(\text{CH}_3)_6$) and water (Maula *et al.*, 2009) and good optical quality is achieved. SiO_2 is rather more difficult. A good reliable process similar to the TiO_2 and Al_2O_3 processes would probably trigger much greater use in optics. Some success has been achieved with SiO_2 films doped with Al_2O_3 in a rather complex arrangement using trimethylaluminum and tris(tert-butoxy)silanol ($(\text{Bu}^{\prime}\text{O})_3\text{SiOH}$). The index is only slightly elevated over pure SiO_2 (Hausmann *et al.*, 2002).

1.8 Sol-gel processes

Sol-gel processes, as the name suggests, involve a solution that is transformed into a gel and then deposited on a surface (Thomas, 1993). The starting material is a metal alkoxide dissolved in a suitable solvent, often ethanol. The addition of a little water hydrolyzes the material so that it forms a polymeric material, helped usually by making the solution slightly acidic. The resulting material is a loose gel with liquid filled pores that can be applied to a surface by dipping. Removal of the liquid and densification of the material is achieved by heat treatment; the higher the temperature, the denser the resulting film. Temperatures of 600°C , sometimes even up to 1000°C , may be employed if complete densification is required. However, often lower temperatures are used so as to maintain some pre-structure with the idea of reducing the index of the film making it more suitable as an antireflection coating. TEOS (tetraethylorthosilicate, $\text{Si}(\text{OC}_2\text{H}_5)_4$) for silica films and titanium tetraethoxide [$\text{Ti}(\text{OC}_2\text{H}_5)_4$] for titanium oxide are typical starting materials. Multilayer coatings can be produced but mixing of materials is a problem that implies at least drying in between each deposition and so the most usual coating is an inhomogeneous single layer of porous silica, the inhomogeneity improving the antireflecting performance.

There are two main reasons why this process is of interest. First, discrete layer broad-band antireflection coatings for silica present considerable difficulties because of the lack of very low index materials. Second, the laser damage threshold of sol-gel materials is found to be exceptionally high (Thomas, 1993).

A serious disadvantage that limits their use as antireflection coatings is that in uncontrolled environments, the pores take up moisture and other contaminants so that their index can vary with time. They are much used in connection with very large lasers operated in tightly controlled environments.

1.9 Etching

The oldest process of all is not a deposition process but a removal one. In the early 1800s, Fraunhofer (1888) reported a reduction in the reflectance of glass surfaces after an acid treatment intended to mimic the corrosive effect of the environment. Then in 1904, H. D. Taylor patented (Taylor, 1904) an etching process for the reduction of surface reflection. The etching process was revisited from time to time with Minot (1976) achieving spectacularly broad coatings on borosilicate glasses by first applying a high temperature soak to separate the glass components followed by an acid treatment to leach out all but the silica skeleton that then formed a coating with low reflectance over the region 350 nm to 2.5 μm . Later Spiller and colleagues (1980) in 1980 published an account of how bombardment of plastic surfaces by energetic (2 MeV) ions of helium or carbon followed by etching by a solution of NaOH produced arrays of needle-like features that acted as efficient antireflection coatings. Recently Schulz and colleagues (2007, 2011) have revived the idea of etching techniques in a particularly simple yet effective plasma surface treatment for plastic materials. PMMA, for example, is a particularly frustrating plastic to coat and this new treatment handles PMMA very well. The surfaces are treated with an argon-oxygen plasma in a machine normally used for plasma ion assisted deposition. The latest work has included hybrid coatings where inorganic layers make up part of a multilayer antireflection coating with a final organic layer, melamine, plasma-treated to give the low index, 1.2, necessary for low reflectance over a wide angle range.

1.10 Other techniques

We have covered the principal techniques that are currently used for optical coating deposition but there are so many more that, depending on circumstances, are occasionally employed that it is impossible to cover them all in a chapter of this length. Spinning, spraying, plasma polymerization, electroplating, electrophoresis, anodization, Langmuir-Blodgett techniques involving picking up a floating monomolecular layer, molecular beam epitaxy, even processes based on the Lipmann emulsion (Ives, 1917) are just some of them.

1.11 Conclusion

We can recognize the beginnings of the field of optical coatings in early metallic coatings for mirrors but it was the twentieth century and the development of vacuum processes, particularly thermal evaporation that permitted the enormous and necessary expansion of optical coatings into virtually every aspect of optics. Thermal evaporation is still an important process but it has been joined by an array of different techniques, so broad as to make a complete account of every single process currently used in some way for optical coatings, impossibly large. This chapter has emphasized the more usual techniques but has also attempted to mention some that, although much less frequently met in practice, nevertheless have clear potential. The major trend that can be recognized in all this is the proliferation of techniques all of which bring their different advantages that lend them to particular optical coating needs. The one thing that can be said with certainty is that there is no one single best technique. The demands of the particular application are the primary driver for the choice of method. Looking into the future is an uncertain activity, but we can surely expect continuous development and extension of the deposition processes to meet the ever increasingly demanding needs of optics as a whole.

1.12 References

- Alasaarela, T., Maula, J. and Sneck, S. (2009). Optical coating of glass tubes by atomic layer deposition. 52nd Annual Technical Conference Proceedings, Santa Clara. Society of Vacuum Coaters, 478–482.
- Anders, A. (2005). Plasma and ion sources in large area coatings: A review. *Surface & Coatings Technology*, **200**, 1893–1906.
- Anders, A. (2010). A structure zone diagram including plasma-based deposition and ion etching. *Thin Solid Films*, **518**, 4087–4090.
- Bach, H. and Krause, D. (eds.) (1997). *Thin Films on Glass*, Berlin, Heidelberg: Springer-Verlag.
- Bovard, B. B., Ramm, J., Hora, R. and Hanselmann, F. (1989). Silicon nitride thin films by low voltage reactive ion plating: optical properties and composition. *Applied Optics*, **28**, 4436–4441.
- Briggs, R. M., Pryce, I. M. and Atwater, H. A. (2010). Compact silicon photonic waveguide modulator based on the vanadium dioxide metal-insulator phase transition. *Optics Express*, **18**, 11192–11201.
- Cheung, J. T., Sankur, H. and Chang, T. (1992). Applications of pulsed laser deposition to optics. *Optics and Photonics News*, **3**, 24–27.
- Choy, K. L. (2003). Chemical vapour deposition of coatings. *Progress in Materials Science*, **48**, 57–170.
- Dirks, A. G. and Leamy, H. J. (1977). Columnar microstructure in vapor-deposited thin films. *Thin Solid Films*, **47**, 219–233.

- Fraunhofer, J. V. (1888). Versuche über die Ursachen des Anlaufens und Mattwerdens des Glases und die Mittel, denselben zuvorzukommen. *Joseph von Fraunhofer's Gesammelte Schriften*. München: Verlag der Königlich Bayerischen Akademie der Wissenschaften.
- Fulton, M. L. (1999). New Ion-assisted Filtered Cathodic Arc Deposition (IFCAD) technology for producing advanced thin-films on temperature-sensitive substrates. *Proceedings of SPIE*, **3789**, 29–37.
- Gibson, D. R., Brinkley, I., Waddell, E. M. and Walls, J. M. (2008a). Closed field magnetron sputtering: new generation sputtering process for optical coatings. *Proceedings of SPIE*, **7101**, 710108 1–12.
- Gibson, D. R., Brinkley, I. T., Waddell, E. M. and Walls, J. M. (2008b). Closed field magnetron sputter deposition of carbides and nitrides for optical applications. *51st Annual Technical Conference Proceedings*. Chicago: Society of Vacuum Coaters.
- Grove, W. R. (1852). On the electro-chemical polarity of gases. *Philosophical Transactions of the Royal Society*, **B142**, 87–101.
- Hagedorn, H., Klosch, M., Reus, H. and Zoeller, A. (2008). Plasma ion-assisted deposition with radio frequency powered plasma sources. *Proceedings of the Society of Photo-Optical Instrumentation Engineers*, **7101**, 710109–1 to 710109–6.
- Harper, J. M. E., Cuomo, J. J. and Kaufman, H. R. (1982). Technology and applications of broad-beam ion sources used in sputtering. Part II. Applications. *Journal of Vacuum Science and Technology*, **21**, 737–756.
- Hausmann, D., Becker, J., Wang, S. and Gordon, R. G. (2002). Rapid vapor deposition of highly conformal silica nanolaminates. *Science*, **298**, 402–406.
- Hirsch, E. H. and Varga, I. K. (1978). The effect of ion irradiation on the adherence of germanium films. *Thin Solid Films*, **52**, 445–452.
- Hirsch, E. H. and Varga, I. K. (1980). Thin film annealing by ion bombardment. *Thin Solid Films*, **69**, 99–105.
- Hwangbo, C. K., Lingg, L. J., Lehan, J. P., Macleod, H. A. and Suits, F. (1989). Reactive ion-assisted deposition of aluminum oxynitride thin films. *Applied Optics*, **28**, 2779–2784.
- Ives, H. E. (1917). Lippmann color photographs as sources of monochromatic illumination in photometry and optical pyrometry. *Journal of the Optical Society of America*, **1**, 49–63.
- Jacobson, M. R. (ed.) (1988). Modeling of optical thin films. *Proceedings of SPIE*, **821**, 233.
- Kaufman, H. R., Cuomo, J. J. and Harper, J. M. E. (1982a). Technology and applications of broad-beam ion sources used in sputtering. Part I Ion source technology (Note: Part II listed under Harper). *Journal of Vacuum Science and Technology*, **21**, 725–736.
- Kaufman, H. R., Harper, J. M. E. and Cuomo, J. J. (1982b). Developments in broad-beam, ion-source technology and applications. *Journal of Vacuum Science and Technology*, **21**, 764–767.
- Kelly, P. J. and Arnell, R. D. (2000). Magnetron sputtering: A review of recent developments and applications. *Vacuum*, **56**, 159–172.
- Kelly, P. J. and Bradley, J. W. (2009). Pulsed magnetron sputtering – process overview and applications. *Journal of Optoelectronics and Advanced Materials*, **11**, 1101–1107.

- Koch, H. (1965). Optische Untersuchungen zur Wasserdampfsorption in Aufdampfschichten (inbesondere in MgF₂ Schichten). *Physica Status Solidi*, **12**, 533–543.
- Lee, C. C. (1983). *Moisture adsorption and optical instability in thin film coatings*. PhD Dissertation, University of Arizona.
- Lyon, D. A. (1946). *Method for coating optical elements*. US patent 2,398,382. April 16, 1946.
- Macleod, H. A. and Richmond, D. (1976). Moisture penetration patterns in thin films. *Thin Solid Films*, **37**, 163–169.
- Martin, P. J., Macleod, H. A., Netterfield, R. P., Pacey, C. G. and Sainty, W. G. (1983). Ion-beam-assisted deposition of thin films. *Applied Optics*, **22**, 178–184.
- Martin, P. J., Netterfield, R. P., Kinder, T. J. and Descôtes, L. (1991). Deposition of TiN, TiC, and TiO₂ films by filtered arc evaporation. *Surface & Coatings Technology*, **49**, 239–243.
- Mattox, D. M. (1967). *Apparatus for coating a cathodically biassed substrate from plasma of ionized coating material*. USA patent 3,329,601.
- Mattox, D. M. (1979). Mechanisms of ion plating. *Proceedings of International Conference on Ion Plating and Allied Techniques (IPAT 79)*, London. Edinburgh: CEP Consultants Ltd.
- Maula, J., Alasaarela, T. and Sneck, S. (2009). Atomic Layer Deposition (ALD) for optical coatings. *52nd Annual Technical Conference Proceedings, Santa Clara*. Society of Vacuum Coaters, 486–491.
- Messerly, M. J. (1987). *Ion-beam analysis of optical coatings*. PhD Dissertation, University of Arizona.
- Minot, M. J. (1976). Single-layer, gradient refractive index antireflection films effective from 0.35 to 2.5 micrometers. *Journal of the Optical Society of America*, **66**, 515–519.
- Moll, E., Pulker, H. K. and Haag, W. (1986). *Method and apparatus for the reactive vapor deposition of layers of oxides, nitrides, oxynitrides and carbides on a substrate*. USA patent 4,619,748. October 28, 1986.
- Motovilov, O. A., Lavrischev, A. P. and Smirnov, A. N. (1974). Stable narrow-band interference filters for the visible region. *Soviet Journal of Optical Technology*, **41**, 278–279.
- Movchan, B. A. and Demchishin, A. V. (1969). Study of the structure and properties of thick vacuum condensates of nickel, titanium, tungsten, aluminium oxide and zirconium dioxide. *Fiz Metal Metalloved*, **28**, 653–660.
- Müller, K.-H. (1986a). Model for ion-assisted thin-film densification. *Journal of Applied Physics*, **59**, 2803–2807.
- Müller, K.-H. (1986b). Monte Carlo calculation for structural modifications in ion-assisted thin film deposition due to thermal spikes. *Journal of Vacuum Science and Technology A*, **4**, 184–188.
- Nagae, E., Sakurai, T. and Matsumoto, S. (2001). RAS (Radical Assisted Sputtering) system and its application on depositing optical thin films. *Topical Meeting on Optical Interference Coatings*, Banff, Canada. Optical Society of America, MB5.
- Netterfield, R. P., Martin, P. J. and Sainty, W. G. (1986). Synthesis of silicon nitride and silicon oxide films by ion-assisted deposition. *Applied Optics*, **25**, 3808–3809.

- Ogura, S. and Macleod, H. A. (1976). Water sorption phenomena in optical thin films. *Thin Solid Films*, **34**, 371–375.
- Pohl, R. and Pringsheim, P. (1912). Über der Herstellung von Metallspiegeln durch Destillation im Vakuum. *Verhandlungen Deutsche Physikalische Gesellschaft*, **14**, 506–507.
- Pulker, H. K. (1992). Ion plating as an industrial manufacturing method. *Journal of Vacuum Science and Technology*, **10**, 1669–1674.
- Pulker, H. K. and Guenther, K. H. (1995). Reactive physical vapor deposition processes. In: Flory, F. R. (ed.) *Thin Films for Optical Systems*. New York, Basel, Hong Kong: Marcel Dekker, Inc.
- Reid, I. M., Macleod, H. A., Henderson, E. and Carter, M. J. (1979). The ion plating of optical thin films for the infrared. *Proceedings of International Conference on Ion Plating and Allied Techniques (IPAT 79)*, London, July 1979. Edinburgh: CEP Consultants Ltd.
- Sakudo, N. (1998). Microwave ion sources for material processing. *Review of Scientific Instruments*, **69**, 825–830.
- Sarakinos, K., Alami, J. and Wuttig, M. (2007). Process characteristics and film properties upon growth of TiO_x films by high power pulsed magnetron sputtering. *Journal of Physics D*, **40**, 2108–2114.
- Saxe, S. G. (1985). *Ion-induced processes in optical coatings*. PhD Dissertation, University of Arizona.
- Schiller, S., Heisig, U. and Goedicke, G. (1975). Alternating ion plating – A method of high-rate ion vapor deposition. *Journal of Vacuum Science and Technology*, **12**, 858–864.
- Schulz, U., Munzert, P., Leitel, R., Wendling, I., Kaiser, N. and Tünnermann, A. (2007). Antireflection of transparent polymers by advanced plasma etching procedures. *Optics Express*, **15**, 13108–13113.
- Schulz, U., Präfke, C., Gödeker, C., Kaiser, N. and Tünnermann, A. (2011). Plasma-etched organic layers for antireflection purposes. *Applied Optics*, **50**, C31–C35.
- Segner, J. (1995). Plasma impulse chemical vapor deposition. In: Flory, F. R. (ed.) *Thin Films for Optical Systems*. New York, Basel, Hong Kong: Marcel Dekker, Inc., 203–229.
- Smith, H. M. and Turner, A. F. (1965). Vacuum deposited thin films using a ruby laser. *Applied Optics*, **4**, 147–148.
- Song, Y. and Sakurai, T. (2004). High-rate, low-temperature radical-assisted sputtering coater and its applications for depositing high-performance optical filters. *Vacuum*, **74**, 409–415.
- Song, Y., Sakurai, T., Maruta, K., Matusita, A., Matsumoto, S., Saisho, S. and Kikuchi, K. (2000). Optical and structural properties of dense SiO_2 , Ta_2O_5 and Nb_2O_5 thin-films deposited by indirectly reactive sputtering technique. *Vacuum*, **59**, 755–763.
- Spiller, E., Haller, I., Feder, R., Baglin, J. E. E. and Hammer, W. N. (1980). Graded-index AR surfaces produced by ion implantation on plastic materials. *Applied Optics*, **19**, 3022–3026.
- Tang, W. T., Ying, Z. F., Hu, Z. G., Li, W. W., Sun, J., Xu, N. and Wu, J. D. (2010). Synthesis and characterization of HfO_2 and ZrO_2 thin films deposited by plasma assisted reactive pulsed laser deposition at low temperature. *Thin Solid Films*, **518**, 5442–5446.

- Targove, J. D. (1987). *The ion-assisted deposition of optical thin films*. PhD Dissertation, University of Arizona.
- Targove, J. D., Lingg, L. J., Lehan, J. P., Hwangbo, C. K., Macleod, H. A., Leavitt, J. A. and McIntyre, L. C., Jr. (1987). Preparation of aluminum nitride and oxynitride thin films by ion-assisted deposition. *Materials Modification and Growth using Ion Beams Symposium*, Anaheim, CA, USA. Materials Research Society, Pittsburgh, PA, USA, 311–316.
- Targove, J. D., Lingg, L. J. and Macleod, H. A. (1988) Verification of momentum transfer as the dominant densifying mechanism in ion-assisted deposition. *Optical Interference Coatings*, Tucson, AZ, USA. Optical Society of America, 268–271.
- Targove, J. D. and Macleod, H. A. (1988). Verification of momentum transfer as the dominant densifying mechanism in ion-assisted deposition. *Applied Optics*, **27**, 3779–3781.
- Taylor, H. D. (1904). *Lenses*. United Kingdom patent 29561.
- Thomas, I. M. (1993). Sol-gel coatings for high power laser optics: Past present and future. *Proceedings of the Society of Photo-Optical Instrumentation Engineers*, **2114**, 232–243.
- Thornton, J. A. (1974). Influence of apparatus geometry and deposition conditions on the structure and topography of thick sputtered coatings. *Journal of Vacuum Science and Technology*, **11**, 666–670.
- Vernhes, R., Zabeida, O., Klemburg-Sapieha, J. E. and Martinu, L. (2004). Single-material inhomogeneous optical filters based on microstructural gradients in plasma-deposited silicon nitride. *Applied Optics*, **43**, 97–103.
- Westmoreland, D. (1993). *CVD method for semiconductor manufacture using rapid thermal pulses*. USA patent 5,227,331. July 13, 1993.
- Zhang, W., Gan, J., Hu, Z., Yu, W., Li, Q., Sun, J., Xu, N., Wu, J. and Ying, Z. (2011). Infrared and Raman spectroscopic studies of optically transparent zirconia (ZrO_2) films deposited by plasma-assisted reactive pulsed laser deposition. *Applied Spectroscopy*, **65**, 522–527.

Design of complex optical coatings

P. G. VERLY, National Research Council Canada, Canada

DOI: 10.1533/9780857097316.1.26

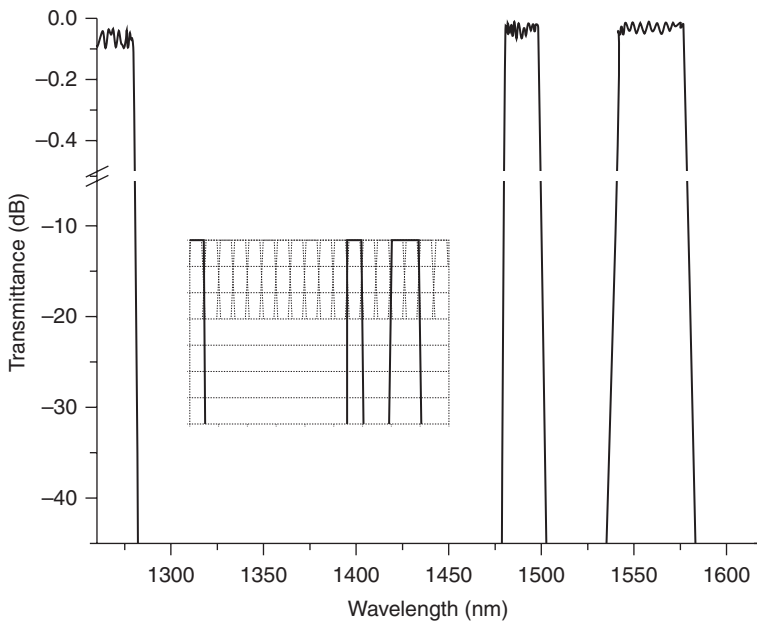
Abstract: Thin film design is loosely subdivided in two categories: refinement and synthesis, where synthesis refers to different ways of generating potentially complex solutions virtually from scratch, without the need for special starting designs. This chapter first reviews several successful thin film synthesis approaches. It then discusses the desensitization of the solutions to manufacturing errors and gives several examples of hybrid situations outside the classical framework, where the interference in the coating is not the only concern or where the geometry of the problem significantly complicates the modeling.

Key words: thin film design and synthesis, error desensitization, waveguide facet coating, resonant grating coating, solar cell design.

2.1 Introduction

Optical thin films are of increasing importance in nearly all technological fields dealing with light, from instrumentation to communications, data processing, energy, medicine, consumer goods, anti-counterfeiting and so forth. Design is an important part of the work supported by remarkable advances in deposition. Interference filters consisting of hundreds and even thousands of layers that could only be dreamed of not so long ago are now commercially available or have been made (Hendrix *et al.*, 2008). Figure 2.1 shows the measured transmittance of a triple band coarse wavelength demultiplexing filter (CWDM) of the latest generation. This type of filter is used to separate channels for short-range optical communications, such as in the fiber optics backbone for 4th generation wireless networks. The multi-band operation helps reduce the number of filters, the insertion loss and the packaged device size. Such filters are challenging to design and manufacture.

Thin films, design is documented by an extensive literature. Besides papers, quite a few books and chapters have been published with major contributions by pioneers of the field (Thelen, 1989; Furman and Tikhonravov, 1992; Willey, 1996; Kochergin, 2003; Baumeister, 2004; Macleod, 2010; Cushing, 2011). Powerful software is commercially available or freely accessible and institutions develop their own code (Dobrowolski, 1997; Kruschwitz, 2003;



2.1 Measured transmittance of a triple band coarse wavelength demultiplexing filter (CWDM) of the latest generation, designed to transmit three separate channels centered at 1270, 1490 and 1560 nm. The inset shows the passbands in relation to the channels. (Courtesy of Iridian Spectral Technologies.)

Larouche and Martinu, 2008). Thin films, design courses and short courses are regularly scheduled in universities or at conferences. The Optical Society of America (OSA), the International Society for Optical Engineering (SPIE) and the Society of Vacuum Coaters (SVC) are among the most important scientific societies in the field.

Thin film design is usually divided in two categories: refinement and synthesis. The distinction between the two is not black and white and there is no firm agreement on the definitions. Typically refinement refers to a situation where a good starting design is optimized by a suitable numerical algorithm. Usually the sequence of layers and materials is selected from the start and the optimization is mostly applied to the layer thicknesses. Synthesis is more flexible and requires less *a priori* knowledge of the solution. For example, it is possible to start the synthesis of complex multilayer or rugate filters from a single layer (rugates have a gradual refractive index variation with thickness as opposed to abrupt steps in conventional multilayers). Refinement is frequently part of the synthesis process but not always.

Synthesis techniques can be semi-analytical or purely numerical. Examples of semi-analytical approaches are those based on equivalent layers, buffer

layers, polynomial synthesis, effective interfaces, admittance diagrams and so forth described by Thelen (1989), Macleod (2010) and Cushing (2011). The designs obtained in this way are frequently composed of groups of quarter-wave layers (their optical thickness nt is equal to a quarter wavelength, where n is the refractive index and t the thickness). Quite sophisticated filters can be designed in this way. Such filters are often easier to manufacture than highly optimized purely numerical designs.

Early numerical synthesis approaches include Dobrowolski's comprehensive search, gradual evolution and minus filter methods, Southwell's flip-flop technique and Tang's statistical search (Dobrowolski, 1965, 1981, 1997; Tang and Zheng, 1982; Southwell, 1985). The comprehensive search systematically explores the parameter space of a small set of layer thicknesses and materials. Gradual evolution consists in progressively adding together groups of layers generated in this way. In the flip-flop technique, a design composed of two dielectric materials is subdivided into many thin layers. The refractive index of each layer is successively flipped and the best configuration is retained. Dobrowolski generalized the approach to three materials including the possibility of metals (Dobrowolski and Kemp, 1992). Tang's approach is an early global optimization approach where the designs are generated by statistical sampling of the layer parameter space. The sampling is limited to regions where the merit value characterizing the residual spectral errors stays below a certain level, which is progressively decreased toward, in principle, the lowest minimum.

This paper is organized in three main sections. Section 2.2 is concerned with three of the most successful numerical thin film synthesis approaches and with global optimization. Section 2.3 deals with the manufacturability of complex filter designs, or the reduction of their sensitivity to deposition errors. Section 2.4 gives examples of hybrid design – waveguide coatings, resonant grating filters and solar cells – where the interference in the coating is not the only concern or where the geometry of the problem significantly complicates the modeling. Finally other topics of interest and an outlook on future research are presented in the conclusion.

2.2 Modern numerical thin film synthesis techniques

This section describes three of the most successful numerical thin film synthesis approaches and gives an outline of global optimization.

2.2.1 Fourier transform method

The Fourier transform (FT) method is probably the first truly successful approach able to generate practical dielectric filter designs for arbitrary

spectral shapes. A similar formulation was used for many years in the synthesis of inhomogeneous transmission lines (Bolinder, 1950). The application to thin films began in the 1960s and 1970s (Delano, 1967; Sossi, 1974; Dobrowolski and Lowe, 1978). As its name suggests, the approach is based on an approximate FT relationship

$$\ln\left(\frac{n(x)}{n_0}\right) = \frac{j}{\pi} \int \frac{\tilde{Q}(\sigma)}{\sigma} e^{-j2\pi\sigma x} d\sigma \quad [2.1]$$

between the logarithm of a refractive index profile $n(x)$ and a complex function $\tilde{Q}(\sigma)$ of its transmittance or reflectance. The variable

$$x = 2 \int_0^z n(z) dz \quad [2.2]$$

is an optical thickness coordinate measured from the center of the system (otherwise the phase must be shifted), z is the usual thickness, $\sigma = 1/\lambda$ is the wavenumber (inverse wavelength) and n_0 is a constant used to center the refractive indices in the proper range. In principle $n(x)$ should be non-absorbing and non-dispersive but there are ways to partially overcome this limitation. The approach is primarily intended for filters with a gradual variation of the refractive index (rugate filters). However it can also be applied to conventional multilayers composed of homogeneous films. For simplicity we will assume that the light is at normal incidence. At oblique incidence n should be replaced by an admittance ($n\cos\theta$ or $n/\cos\theta$ depending on the polarization of the light, where θ is the angle of propagation), and x by an effective thickness ($n\cos\theta$).

It can be shown from Maxwell's equations that the complex transmission coefficient (for the field amplitude) of an immersed optical filter (with identical substrate and ambient media) can be expressed as an infinite series of nested integrals (Sossi, 1974; Verly *et al.*, 1989)

$$\frac{1}{t(\sigma)} = e^{-j2\pi\sigma x} \left\{ 1 + \int_0^x d\tilde{Q}(x_1, \sigma) \int_0^{x_1} d\tilde{Q}^*(x_2, \sigma) + \int \int \int \dots + \dots \right\} \quad [2.3]$$

where $d\tilde{Q}$ is the integrand of

$$\tilde{Q}(\sigma) = \int \frac{1}{2n} \frac{dn}{dx} e^{j2\pi\sigma x} dx \quad [2.4]$$

and $d\tilde{Q}^*$ is its complex conjugate (n is assumed real). There is a similar expression for r/t where r is the reflection coefficient. $1/t$ and r/t are functions with special mathematical properties in thin film theory (Furman and Tikhonravov, 1992; Tikhonravov, 1993).

Equations [2.3] and [2.4] establish a relationship between $\tilde{Q}(\sigma)$ and the spectral properties of the film. In the Fourier transform method, it is assumed that $\tilde{Q}(\sigma)$ is small and the terms higher than second order are neglected. Physically the integrals represent the internal reflections due to the refractive index changes at different depths x in the film ($1/n dn/dx$ is a Fresnel reflection coefficient). The multiple internal reflections are ignored (two are retained in the calculation of the transmitted light, one for the reflected light).

Many analytical forms of the Q-function have been proposed such as (Delano, 1967; Sossi, 1974; Bovard, 1988; Verly *et al.*, 1989):

$$\begin{aligned} Q &= \sqrt{1-T} = \sqrt{R} \\ Q &= \sqrt{\frac{1}{T-1}} \\ Q &= \sqrt{\ln\left(\frac{1}{T}\right)} \\ \tilde{Q} &= \frac{r}{t} \end{aligned} \quad [2.5]$$

where $R = rr^*$ is the reflectance and T the transmittance of the coating (for the light intensity or power). Q is the modulus of the complex Q-function expressed as:

$$\tilde{Q}(\sigma) = Q(\sigma)e^{i\phi(\sigma)} \quad [2.6]$$

It is easy to verify that the different forms of Q agree when R is small but otherwise diverge, sometimes a lot. The last form, sometimes called Delano's Q-function, suggests that the phase ϕ should approximately be equal to $\arg(r/t)$. However the phases are rarely specified, especially not in this form. This is a degree of freedom that can be exploited, in particular to control the shape of the index profile, an important consideration in the presence of index constraints. Filters of surprisingly high reflectance can be designed by proper choice of the Q-function and its phase (Verly *et al.*, 1989; Verly, 2011).

In principle Equation [2.1] provides a very simple way of synthesizing a dielectric filter of specified transmittance or reflectance. However there are difficulties. One is the approximate nature of the Q-functions. Second, a

sufficient part of the spectral region where the reflectance is non-zero must be known. For example it is impossible to design an antireflection (AR) coating just by knowing that the reflectance should be zero in some wavelength region. The reflectance of most coatings, in particular when they are not immersed, is non-zero outside the main region of interest. Third, errors are introduced when constraints are imposed on the refractive indices and overall thickness. The Q-phase ϕ helps address this problem (Verly and Dobrowolski, 1990; Druessel *et al.*, 1993). Surprisingly good rugate reflectors can be designed by phase optimization alone (Verly, 2011).

Several variants of an iterative procedure have been proposed for the compensation of these limitations (Sossi, 1974; Fabricius, 1992b; Cheng *et al.*, 2008a). The approach implemented at the National Research Council of Canada (NRC) applies successive corrections to the complex Q-function (Verly and Dobrowolski, 1990):

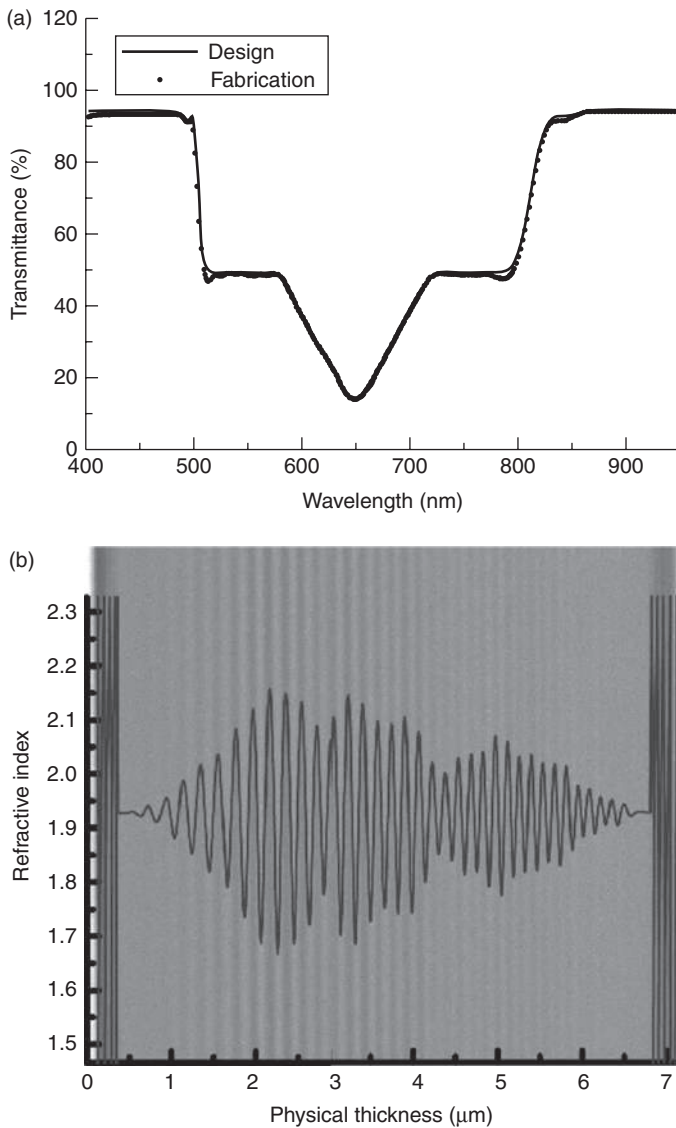
$$\Delta\tilde{Q} = [Q(T_D - Q(T))]e^{i\psi} \quad [2.7]$$

$$\psi = \arg\left(\frac{r}{t}\right)$$

where T_D is the specified transmittance and T , t and r are calculated values obtained from $n(x)$. The calculations are performed by the standard matrix approach after subdividing $n(x)$ in thin layers. The progress is monitored through a standard merit function, for example, the root-mean-square (RMS) residual transmittance error. The material dispersion and losses that are ignored in the Fourier transforms can indirectly be introduced in the matrix calculations (Fabricius, 1992a; Bulkin *et al.*, 1996; Verly, 2008). A scaling procedure can also be applied to the target transmittance (Bovard, 1993; Poitras *et al.*, 2002; Larouche and Martinu, 2007).

Equation [2.7] increments the Q-phase $\phi(\sigma)$ in a direction consistent with Delano's Q-function r/t . Numerical experimentation shows that using the $\arg(r/t)$ of a good solution as initial phase consistently yields good results. However as mentioned, this phase is usually unknown at first. Multiple filter solutions of essentially the same reflectance in the region of interest but different phases are usually possible, from which the most suitable for fabrication can be selected (Verly and Dobrowolski, 1990; Verly *et al.*, 1993). Alternatively it is possible to ignore the phase and start from a completely arbitrary starting design, for example a constant refractive index. The refinement of $\Delta\tilde{Q}$ or \tilde{Q} is also possible for improved accuracy (Verly, 1996, 2011).

In spite of its limitations the Fourier transform method generates useful rugate and multilayer designs. Figure 2.2 gives an example of a rugate filter that was recently designed and fabricated (Cheng *et al.*, 2008b). The calculations are fast. Typically the synthesized solutions gradually evolve



2.2 Comparison of the designed and measured transmittance of a rugate filter designed by the Fourier transform method (Cheng *et al.*, 2008b). The calculated refractive index profile is superposed on a SEM picture. The filter is immersed between two quartz plates. Discrete layers at both ends suppress the ripples due to the reflections at the outer interfaces. (Source: Reproduced with permission of the SPIE.)

in quasi-multilayers when the refractive index (or admittance) modulation reaches its limits (Verly *et al.*, 1992; Verly, 1996). This is in agreement with the Maximum Principle which states that the optimum solutions should be two-material multilayers in these type of problems (Furman and Tikhonravov, 1992). The hybrid solutions can easily be converted to true multilayers or used as advanced starting designs for refinement.

Finally, the Fourier transform approach has interesting by-products. Frequency filtering is particularly useful: insight is gained when the spectral contributions of different parts of a design are identified (Verly, 1995, 2011). The elimination of the high (spectral and spatial) frequencies helps reduce the number of thin layers that are notoriously difficult to deposit. It is possible to synthesize surprisingly good AR coatings simply by eliminating the Fourier frequencies of an arbitrary starting design in the desired spectral region (Verly, 1994, 2009). Other applications include the thickness estimation of reflecting filters (Verly, 2007) and thin film characterization (Swart and Lacquet, 1990; Verly, 1998a).

2.2.2 Inhomogeneous refinement

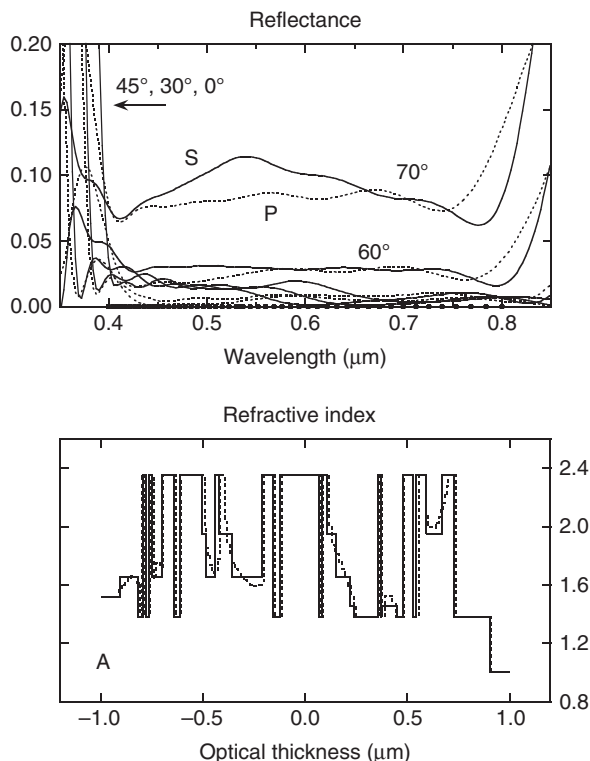
Unfortunately the Fourier transform method only applies to light arriving at a single angle in a single polarization (refractive index or admittance profiles). The approach discussed in this section removes this limitation. The solutions are simply subdivided in thin layers whose refractive indices and optional thicknesses are refined (Snedaker, 1982; Verly *et al.*, 1997; Verly, 1998b; Tikhonravov *et al.*, 2006). This is an example where the distinction between refinement and synthesis is somewhat ambiguous. However, in this case the starting design can be quite elementary. Apart from a rough estimation of the overall optical thickness, no special assumption is needed about the number of layers, sequence of materials and so forth. The thickness estimation can be progressively adjusted if necessary. As in the Fourier approach the solutions typically start as rugates and progressively evolve in hybrid multilayers. The most useful materials can be selected by examination.

This approach is mostly used for the synthesis of dielectric filters. Material dispersion and losses are easily introduced by considering the film materials as adjustable mixtures. In principle it is possible to optimize the extinction coefficient (imaginary part of the refractive index expressed in complex form $n-ik$ when the material is lossy) independently from the real part n . However the practical realization of the resulting fictitious materials might be a challenge. This design option exists in commercial software. Because of the large number of parameters typically involved, special consideration has to be given to the speed and accuracy of the calculations. In the NRC implementation the gradients used in the optimization routines are

calculated from exact analytical formulas and repetitive matrix calculations are avoided.

Figure 2.3 gives an example of a broadband wide-angle, non-polarizing antireflection coating synthesized for angles of incidence $\theta = 0^\circ, 30^\circ, 45^\circ, 60^\circ$ and 70° in air (Verly, 1998b). The refractive index profile represented by a dashed line is strongly inhomogeneous. This is understandable because the maximum contrast of the p-polarization admittance $n/\cos\theta$ is obtained with intermediate refractive indices when $\theta > 40^\circ$. The index profile represented by a solid line has been converted to a five-material multilayer of nearly the same reflectance.

With some precautions the synthesis of purely rugate filters is also possible. As seen in Fig. 2.3, homogeneous layers are created when the refractive-index or admittance modulation reaches its limits. In Tikhonravov *et al.*



2.3 Broadband, wide-angle, non-polarizing AR coating designed by inhomogeneous refinement for $0^\circ, 30^\circ, 45^\circ, 60^\circ$ and 70° angles of incidence in air. Bottom: semi-rugate and five-material multilayer solutions (Verly, 1998b). Top: reflectance in the s and p polarizations of the semi-rugate solution. (Source: Reproduced with permission of the Optical Society of America.)

(2006) a regularization term is added to a standard merit function (RMS reflectance) to ensure the smoothness of the refractive index. An additional penalty term forces the refractive indices to stay within bounds. Trade-offs are necessary between the index smoothness and the optical performance. A simple alternative approach based on a combination of inhomogeneous refinement and Fourier techniques is described in Verly (2008).

2.2.3 Needle method

The needle method is probably the best known and most successful thin film synthesis technique (Furman and Tikhonravov, 1992; Sullivan and Dobrowolski, 1996; Tikhonravov *et al.*, 1996). It is widely implemented in commercial thin film design software and hardly needs a presentation. Briefly, it consists of inserting very thin layers (needles) in a multilayer system in order to improve its spectral performance. Needle(s) of the most appropriate available material are inserted in optimum position(s). The modified multilayer is refined and the whole procedure repeated as needed. In the so-called gradual evolution mode (not to be confused with Dobrowolski's approach) the design's overall thickness is artificially increased from time to time by appending a layer of compatible material, usually on the substrate side, when no useful progress can be made otherwise.

A variant has been proposed where the needle refractive indices are also refined (Verly, 2001). The optimum needle indices are calculated by parabolic interpolation (three points), so that the perturbation function for the determination of the needle positions has to be calculated only twice (for two needle indices, the third one being the unperturbed layer index). Hybrid solutions similar to those obtained by inhomogeneous refinement have been demonstrated. The two approaches behave differently and complement each other. For example inhomogeneous refinement quickly gives a general idea of the design structure while needles tend to be more efficient for tuning the design in the end.

A disadvantage of the needle approach is the frequent proliferation of thin layers. Simple procedures for their removal have been described and are implemented in commercial software (Tikhonravov and Trubetskoy, 2007). Trade-offs must be made between the spectral performance and the minimum acceptable layer thickness.

Larouche and Martinu (2006) proposed a related approach where instead of needles small index steps are inserted in appropriate positions. The refractive indices and thicknesses are refined. The justification is that it might be easier to fabricate thicker layers of intermediate indices than thin layers of two materials. The multi-material solutions can be converted to two materials by a standard Herpin transformation (Dobrowolski and Piotrowski, 1982).

2.2.4 Global optimization

Global optimization is an important subfield of numerical analysis where the objective is to find the lowest minimum (highest maximum) of a function in a complicated parameter landscape (Rinnooy Kan and Timmer, 1987; Schoen, 1991; Panos *et al.*, 2002). Such calculations are common in areas requiring complex mathematical modeling or data analysis, like molecular dynamics, image and pattern recognition, artificial intelligence, traffic control, environmental and risk management, finances, etc.

Many search strategies are possible. A common trait is that they do not immediately descend toward an accessible minimum. There is a possibility of going uphill to increase the chances of finding the best possible result. Conceptually, the simplest strategy is to look at all the possibilities. However this quickly becomes impractical as the numbers of unknowns increases. Statistical searches are more effective but the global minimum is then found with a finite probability.

Global optimization has had a limited popularity in thin films since its introduction in the field several decades ago (Dobrowolski, 1965; Tang and Zheng, 1982; Wild and Buhay, 1986). There is a common perception that the calculations are slow. In addition the solutions are global in a parameter space that has to be properly set up and may require progressive adjustments (e.g. the tolerances or number of layers). Nevertheless interesting results have been obtained and the advances in computing power makes this type of approach more attractive. Several algorithms applied to thin films are briefly described below. All are stochastic (random parameter moves).

Simulated annealing is inspired by the metallurgical process where a metal is heated to a high temperature and progressively cooled down to allow a re-arrangement of the atomic structure (Schoen, 1991; Boudet *et al.*, 1996). Uphill moves $\Delta M > 0$ in the parameter space are allowed with a probability modeled on Boltzman's distribution

$$p = \exp\left(-\frac{\Delta M}{kT}\right) \quad [2.8]$$

where ΔM is the change in the merit value, k is Boltzman's constant, T the temperature and p must be greater than a random number between 0 and 1. Downhill moves $\Delta M < 0$ are always accepted. For a given T the algorithm can thus freely move among local minima of depths less than approximately kT . T is initially set to a high value and progressively decreased according to an annealing schedule.

The approach is computationally intensive and sensitive to the cooling strategy and the way of proposing the random moves (Morf and Kunz, 1988;

Hobson and Baldwin, 2004). A zone melting approach has been proposed where the annealing is successively applied to parts of the design (Morf and Kunz, 1990). Modifications are possible where the random searches are adapted to the topography using previous history or it is made more difficult to wander away from a deep minimum (Dobrowolski and Kemp, 1990; Cheng *et al.*, 2006).

Genetic algorithms imitate the evolution of living populations in nature (Eisenhamer *et al.*, 1993; Rabinovitch and Toker, 1994; Martin *et al.*, 1995). Successive generations of individuals (designs) are produced by operators that mimic genetic mechanisms: (i) selection: clones of randomly selected individuals are generated with a probability that depends on the merit value (reproduction of the fittest); (ii) recombination: random individuals share their genes (e.g. layer thicknesses); (iii) mutation: some individuals suffer random perturbations. Variants of this general scheme are possible (Oulton and Adjiman, 2006; Shokooh-Saremi and Magnusson, 2007). In memetic optimization, the new individuals are subjected to a quick partial refinement claimed to substantially increase the computation speed (Yakovlev and Tempea, 2002).

Genetic algorithms have been applied to the design of filters of increasing complexity over the years: X-ray coatings (Binda and Zocchi, 2004; Al-Marzoug and Hodgson, 2008; Wang, 2008), broadband omni-directional reflectors and anti-reflection coatings (Jiang *et al.*, 2008; Poxson *et al.*, 2009), solar cells (Schubert *et al.*, 2008), dispersive mirrors for femtosecond lasers (Yakovlev and Tempea, 2002), polarizing beam splitters (Shokooh-Saremi *et al.*, 2004), etc. The choice of a proper starting design and a limitation of the number of optimized parameters helps. Jiang *et al.* (2008) report calculation times of the order of a hundred hours on a recent PC computer.

Clustering methods coupled with local searches are claimed to be among the best for global optimization (Schoen, 1991; Maroosi and Amiri, 2010). Essentially random starting designs are regrouped according to the region of attraction of local minima. The location and shape of the regions of attraction are identified. A new local search is pursued only if it does not belong to an existing region of attraction. Sampling, clustering and local search are repeated until no new minimum can be found.

Different clustering approaches are possible (Abul Hasan and Ramakrishnan, 2011). One approach inspired from respiratory system modeling (Csendes *et al.*, 1986) was recently applied with success to thin film synthesis. Several complex designs obtained in this way in combination with the needle method placed highly in successive thin film design contests organized at the Topical meeting on Optical Interference Coatings (OIC), a key conference in the field. The designs are a wideband wide-angle AR coating with robustness to simulated manufacturing errors, a minimum-shift immersed short-pass filter and a non-polarizing filter (Tilsch and Hendrix,

2008; Hendrix and Oliver, 2011). The designs consist of up to 214 layers of several materials selected from a list. A metal-dielectric filter showing three different colors in transmission and reflection from the front and the back side is also reported (Badoil *et al.*, 2008; Dobrowolski *et al.*, 2008). It is worth mentioning that designs of comparable and sometimes better performance were obtained by more conventional thin film synthesis techniques.

Particle swarm optimization (PSO) is a robust evolutionary strategy inspired by the social behavior of animal species living in large colonies like birds, ants or fish. It is interesting that it was first proposed not by mathematicians, but by a social psychologist and an electrical engineer (Kennedy and Eberhart, 1995). The algorithm finds the optimal solution by moving the particles in the search space. Each particle (design) is first assigned a random position and velocity. It keeps track of its own best position p_{best} and the group's best position g_{best} (or the local best position l_{best} of its neighbours). The particle velocity is progressively deflected by adding to it random-length components in the direction of the best locations. The particle inertia or unperturbed part of the speed is given a progressively decreasing weight with respect to the changes learned from previous experience.

The application of this technique to thin films also appears to be fairly recent. A solar absorber designed in this way was submitted to the thin film design contest of the OIC 2010 conference (Hendrix and Oliver, 2011). The designers mention that they let a high-end PC computer with dual quad-core Xeon processors run for 2 months. The design of interference filters or solar cells with diffracting structures is also reported in the recent literature (Shokooh-Saremi and Magnusson, 2007; Mutitu *et al.*, 2008; Pond and Kawano, 2010). Pond reports the optimization of two different types of solar cells by PSO in conjunction with FTDT (finite-difference time-domain) computations – a plasmonic thin film silicon cell with a metal-island film and an organic cell where one interface of the active layer is patterned with a grating. The reported CPU time for the fully vectorial calculations is a few hours on a PC computer. A 15% improvement over the unpatterned case is reported.

Global optimization is also used in the modeling of ellipsometric or spectrophotometric data for the characterization of thin films optical constants (Djurisic *et al.*, 2000; Gao *et al.*, 2011). Gao's paper gives an interesting comparison of several global approaches and links to open-source software.

2.3 Manufacturability issues

With current thin film design software it is often relatively straightforward to find solutions when the only concern is the spectral performance. A more interesting challenge is to find solutions that are sufficiently simple

and resilient to manufacturing errors. Apart from the random or systematic noise created by the deposition equipment (rate fluctuations, shutter delays, etc.), thickness errors are strongly dependent on the film growth monitoring method. A layer monitored optically can be almost insensitive to thickness variations at the time of its deposition and become sensitive in the finished product (Poitras, 2005). Switching between different monitoring methods can be useful. Some monitoring approaches have error compensation mechanisms while at other times the errors accumulate (Macleod and Pelletier, 1977; Tikhonravov *et al.*, 2011). Several automated deposition processes reoptimize the deposited filter in real time when errors are detected (Sullivan *et al.*, 2000; Wilbrandt *et al.*, 2010). For these reasons the control of the deposition errors at the design stage is not easy and requires a good understanding of the deposition process.

The most common practice is to generate a design for pure spectral performance and check its error sensitivity in the end. The easiest way is to add uncorrelated random errors to the layer thicknesses and/or indices. More sophisticated simulations add the random errors to parameters more representative of the deposition process, such as a simulated monitoring signal, deposition rate(s), shutter delay(s), etc. (Tikhonravov and Trubetskoy, 2005).

Designs generated by analytical procedures are commonly perceived to be more robust than purely numerical constructions. Natural solutions that fulfill the specifications without too much tweaking are often preferred when sophisticated deposition automation is not available. Sometimes simple measures like suppressing thin layers, switching materials or even reversing a design help.

The most direct way of reducing the error sensitivity is to add a penalty term to the merit function (Dobrowolski, 1981; Dobrowolski *et al.*, 1989):

$$F = F_0 + \alpha \sum_i w_i \frac{\partial F}{\partial x_i} \quad [2.9]$$

In this equation x_i can be any layer construction parameter, F_0 is the unperturbed merit value, the w_i 's are weights representing the expected error levels and α is an adjustable constant ($0 < \alpha < 1$) used to control trade-offs between the spectral performance and the error control. Tikhonravov *et al.* (2003) proposed a variant where a second order term is added to the Taylor series. The second-order equation can be simplified so that

$$F = F_0 + \alpha_2 \sum_i \left(w_i \frac{\partial F}{\partial x_i} \right)^2 \quad [2.10]$$

Equation [2.10] is implemented in commercial software and has successfully been used in the desensitization of challenging filters (Pervak *et al.*, 2007).

To my knowledge Zheng and Tang (1987) were the first to report an automatic design technique simulating an actual deposition environment. In their work the penalty term in the merit function is a yield, or proportion of randomly perturbed designs that are within specifications. The random errors are applied to monitoring signals in reflection and transmission. The designs are generated using the global optimization approach mentioned earlier (Tang and Zheng, 1982).

Other types of statistical calculations have been reported, frequently in combination with global optimization. Greiner (1996) applies a genetic algorithm to a noisy merit function (statistical average) to desensitize an AR coating with respect to reflectance and color variation. Yakovlev and Tempea (2002) generate chirped mirrors for dispersion control in femtosecond lasers by using a memetic algorithm. The robustness of a few select designs is improved by a perturbative gradient descent (a gradient for noisy functions) similar to one used for feedback control in adaptive optics. Nohadani *et al.* (2008) desensitize a double-chirped 208-layer mirror pair for use in a few-cycle Ti:sapphire mode locked laser. They minimize the worst-case scenario corresponding to random parameters changes within a certain radius of a central design. In a subsequent paper the design with the best yield is identified on the optimization path followed when the robust design is reoptimized in a standard way, without the error considerations (Birge *et al.*, 2011).

A different approach was recently proposed where multiple designs located in a small neighbourhood of a pivotal design are simultaneously synthesized by a modified needle method (Pervak *et al.*, 2009, 2011; Trubetskoy and Tikhonravov, 2010). The collection of designs called a cloud is subjected to small random errors and refreshed from time to time. The needle(s) are inserted in each design. The method was successfully applied to different types of filters including challenging dispersion compensating mirrors for ultrafast optics. As a bonus it was found that the peaks of the electric field intensity were reduced, potentially improving the laser damage threshold of the mirrors.

Three recent editions of a thin film design contest organized at the topical meeting on Optical Interference Coatings (OIC) highlight the difficulties of reducing the error sensitivity of challenging designs (Baumeister, 2000; Thelen *et al.*, 2002; Tilsch *et al.*, 2006). The proposed challenges were a dual band AR coating for the visible and the near infrared, a gain flattening filter for erbium doped fiber amplifiers (EDFA) and a broadband, wide-angle AR coating (BBAAR) subjected to simulated manufacturing errors. Constraints were imposed on the available materials (up to five), the maximum number of layers, maximum overall thickness and the minimum layer

thickness. Approaches based on the needle method, global optimization and undisclosed proprietary software are mentioned.

Gain flattening filters are challenging because the specified spectral curve has sharp variations in a narrow spectral region requiring many precisely deposited layers. The filter proposed at the OIC had to flatten the EDFA gain to a fraction of a decibel and the yield had to be maximized when the filter was submitted to simulated random thickness errors (Thelen *et al.*, 2002). Verly (2002) observed that thicker, loosely optimized solutions were the most stable. A correlation was found between the convergence speed and the error stability. Efforts were made to maintain a high convergence rate by limiting the optimization to the most effective layers. A standard merit function was used. The error stability was monitored through the convergence and by regularly checking that the error sensitivity did not shift to resonant cavities in the design. The best solution achieved a 98% yield with 152 layers of SiO_2 and Ta_2O_5 .

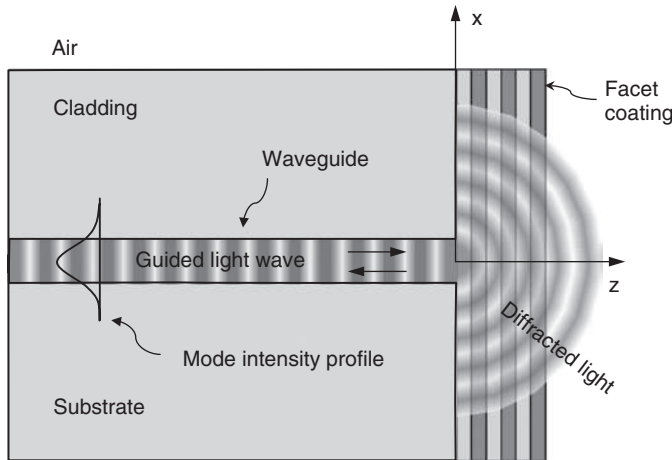
2.4 Hybrid design

This section gives some examples of hybrid situations where factors beyond the usual optical interference in planar thin film stacks are involved.

2.4.1 Waveguide coatings

Coatings are frequently applied to the end facets of optoelectronic devices such as semiconductor lasers, optical amplifiers and super-luminescent light emitting diodes. This is an interesting design problem because the coatings are commonly deposited on the end of a waveguide. A simplified two-dimensional geometry is schematically illustrated in Fig. 2.4. The incident light is a guided mode propagating in the z direction. It has a characteristic transverse light distribution concentrated in the waveguide core and an axial propagation constant determined by the waveguide geometry. Past the facet the light stops being guided and diffracts. The returning light spot that has to be coupled back in the waveguide is distorted and excites a superposition of the supported guided and radiation modes (forming a complete set of orthogonal functions). The quantity of interest is the mode reflectance, or fraction of the light coupled back in the same guided mode as before but propagating in the reverse direction. Exact calculations are possible but time consuming especially for coating design. Approximate approaches deliver good results when suitable conditions are met.

Vassallo proposed an approach where a thin fictitious layer of constant index n_{eq} is inserted between the waveguide facet and the coating (Vassallo, 1985, 1988). When the equivalent index n_{eq} is properly matched the mode enters the thin layer without reflection or distortion and becomes



2.4 Simplified representation of a waveguide facet coating.

a diffracting cone of light, a more conventional geometry for thin film calculations. Assuming for simplicity a transverse electric (TE) mode in the geometry of Fig. 2.4, the matching condition is:

$$n_{\text{eq}}^2 = \frac{\int n^2(x) |E_0(x)|^2 dx}{\int |E_0(x)|^2 dx} \quad [2.11]$$

where $E_0(x)$ is the modal electric field pointing in the y direction and $n(x)$ is the refractive index profile of the waveguide. The cone of light is converted to a superposition of plane waves by a Fourier transform:

$$E_0(x) = \int \hat{E}_0(k_x) e^{ik_x x} dk_x \quad [2.12]$$

where k_x is the transverse propagation constant in the x direction in medium n_{eq} . The total reflected field $E_r(x)$ at the facet is the superposition of the reflected plane waves. The mode reflectance is found by projecting $E_r(x)$ on the mode of interest (using the mode orthogonality):

$$R = \frac{\int E_r(x) E_0^*(x) dx}{\int |E_0(x)|^2 dx} \quad [2.13]$$

Generalizations to transverse magnetic (TM) modes (H field in the direction of the y axis) and 3D geometries have been published (Vassallo, 1988,

1990). Angled facets help to reduce the mode reflectance further but the transmitted light is deflected which is not always acceptable. This theory is valid in the case of small $dn(x)$ (weak waveguiding).

Kendall proposed a modification where the waveguide radiation modes are included to ensure better consistency of the field matching at the facet (Kendall *et al.*, 1993; Xu *et al.*, 1995; Reed *et al.*, 1996). The radiation modes are approximated by a superposition of plane waves in a homogeneous medium of appropriate refractive index (free-space radiation modes). Improved results are reported. This theory also requires waveguides with a small $dn(x)$.

Vukovic studied waveguides buried at a shallow depth where the small $dn(x)$ assumption is no longer valid because the thin cladding does not completely isolate the modal field from the air above (Vukovic *et al.*, 1998, 2000). The top corner of the coated facet generates non-negligible diffraction effects. A modification of Kendall's model is proposed where the homogeneous medium for the free-space radiation modes is split in two half spaces.

Orobetchouk *et al.* (1997) developed a model where the small $dn(x)$ assumption is not necessary. The plane waves in the modal field decomposition all have the same longitudinal wave vector $k_z = Nk_0$ where $k_0 = 2\pi/\lambda$ is the free-space wavenumber and N the mode effective index. Each plane wave is assumed to propagate in a different medium of equivalent index n_{eq} where

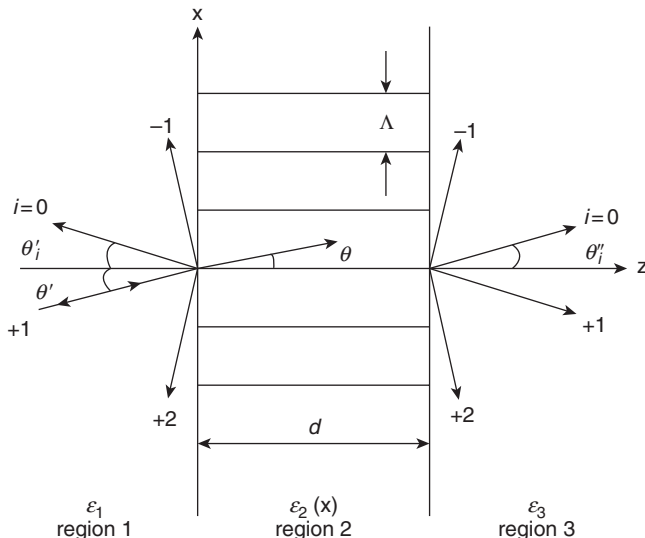
$$(n_{eq}k)^2 = k_x^2 + k_z^2 \quad [2.14]$$

There is no diffraction. The plane wave superposition reverts to the mode at any point along the waveguide axis. The approach is applicable to tilted facets and sharp bends in 3D waveguides of high-index contrast.

Rigorous calculations in 3D geometries greatly increase the difficulties. Parallel computations using multi-core CPUs or multiple computers make the situation more tractable (Labukhin and Li, 2005). Different approaches based on FDTD calculations, mode matching, the beam propagation method etc., have been published (Vassallo, 1997, 1998; Wiechmann *et al.*, 2003; Obayya, 2006; Schmid *et al.*, 2007; Strain and Sorel, 2010).

2.4.2 Structured coatings

It is notoriously more difficult to achieve narrow spectral bands in reflection than in transmission with thin films. The opposite is true when resonant gratings are incorporated in a multilayer stack (Vincent and Nevière, 1979; Wang *et al.*, 1990; Magnusson and Wang, 1992). Hybrid filters of this



2.5 Planar grating diffraction model showing the reflected and transmitted harmonics. The 0th harmonics are the specularly reflected and transmitted waves. (Source: Reproduced with permission of the Optical Society of America (Wang *et al.*, 1990).)

type have attracted interest for several decades (Moharam and Gaylord, 1981; Wang and Magnusson, 1993; Rigneault *et al.*, 1999; Escoubas *et al.*, 2001; Boyko *et al.*, 2008; Sergeant *et al.*, 2009; Wang and Menon, 2012). In their simplest expression the filters consist of a single layer with a periodic refractive index variation. For simplicity let us consider a two-dimensional geometry (Fig. 2.5). The periodicity splits the incident plane wave in multiple harmonics that propagate at angles determined by Bragg's condition or decay exponentially in the z direction. In homogeneous media or layers the harmonics are plane waves with propagation constants in the x and z directions given by

$$\begin{aligned} k_{xm} &= k_x + mK \quad m = 0, 1, 2, 3, \dots \\ k_{zm} &= \pm\sqrt{n^2 k^2 - k_{xm}^2} \\ k_x &= k_0 \sin \theta_0 \\ K &= \frac{2\pi}{\Lambda} \end{aligned} \quad [2.15]$$

where k_x belongs to the incident light, K is the grating constant, Λ the grating period, n the refractive index, k_0 the vacuum wave vector and θ_0 the angle of incidence in air. In the grating layer the harmonics coupled by the periodicity have a varying amplitude $S_m(z)$. The problem is solved by substitution of

the electromagnetic fields (sum of harmonics, also called a Bloch wave) in Maxwell's equations and applying the boundary conditions. The differential equations can be solved numerically (FDTD, etc.) or by a rigorous coupled wave approach, where the problem is reduced to a set of coupled differential equations. For a sinusoidal grating of relative permittivity $\varepsilon(x) = \varepsilon_0 + \Delta\varepsilon$ and $\cos(Kx) = n^2(x)$, one has (Moharam and Gaylord, 1981; Wang *et al.*, 1990):

$$\frac{d^2S_m}{dz^2} = A_m \frac{dS_m}{dZ} + B_m S_m + C_m (S_{m-1} + S_{m+1}). \quad [2.16]$$

A_m , B_m and C_m are constants depending on the geometry and C_m describes the coupling between adjacent harmonics, proportional to $\Delta\varepsilon/\varepsilon_0$.

A situation of particular interest occurs when the ± 1 harmonics of a plane wave arriving at normal incidence ($\theta_0 = 0$) are coupled to counter-propagating guided modes of the grating layer ($+x$ and $-x$ directions). For weak gratings ($\Delta\varepsilon/\varepsilon \ll 1$) the mode is essentially the same as in a homogeneous layer of average index. The mode's propagation constant k_x must satisfy the waveguide dispersion equation, a transverse resonance condition for the plane wave trapped by total internal reflection in the guiding layer (the round trip phase shift in the z direction must be a multiple of 2π radians).

According to Equation [2.15] the guided harmonics are such that $k_{x1} = -k_{x,-1} = K$. They are coupled to each other (reflected in the x direction) by a second order Bragg condition and coupled to plane waves radiating power in the z direction by a first order Bragg condition. Such waveguide modes losing energy as they propagate are called leaky modes. The net result of these resonances is a rapid variation of the transmittance or reflectance of the grating layer for light propagating in the z direction as the wavelength (or angle of incidence) is varied. The situation is subtle. Slow leaks are essential in order to generate enough guided light. The leaks increase the imaginary part of k_{xm} and create a stop band in the k_{xm} vs k Brillouin diagram. The grating reflectance has narrow peaks at wavelengths corresponding to the edges of this stop band (not the middle, where the leak would increase). The peak at one edge disappears for symmetry reasons when the incident light is at normal incidence and the grating is symmetrical (Vincent and Nevière, 1979). Otherwise there are two peaks (Avrutskii *et al.*, 1986; Ding and Magnusson, 2004b). This property is used to design filters with more complex spectral shapes.

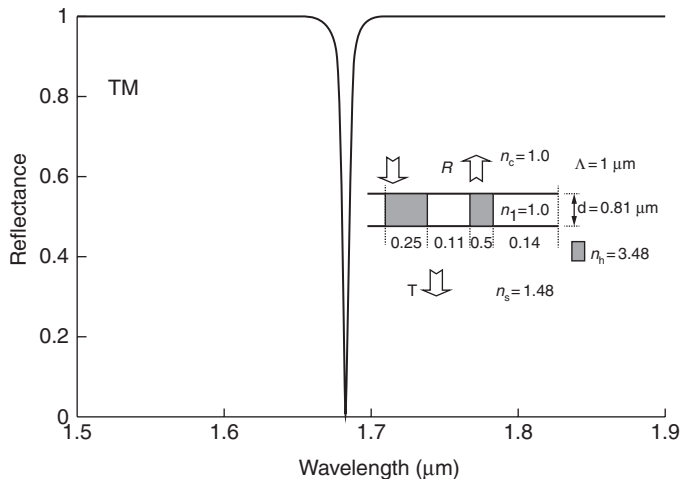
Strong coupling increases the leaks and broadens the peak(s). The shape of the spectral variations also depends on the layer structure in which the grating is embedded. Narrowband reflection filters are obtained when the grating is embedded in an AR coating. The AR provides the low reflectance background and the grating provides the narrow reflectance peak (Magnusson and Wang, 1992; Lemarchand *et al.*, 1997).

Variations are possible where the gratings have more elaborate periodicities, multiple gratings are stacked, the light couples to more than one waveguide mode, or a combination of these effects. Different types of filters have been demonstrated including narrow band reflectors with reduced angular sensitivity (Lemarchand *et al.*, 1998), bandpass filters, polarizers and polarization independent filters (Ding and Magnusson, 2004a; Shokooh-Saremi and Magnusson, 2010b), wide band reflectors (Shokooh-Saremi and Magnusson, 2010a), etc. Figures 2.6 and 2.7 illustrate a narrowband and two wideband resonant grating filters. Besides filters, the applications include optoelectronic devices, ultra sensitive bio or chemical sensors, absorption enhancement in solar cells, security devices, tunable filters, display components, etc. (Magnusson *et al.*, 2003; Ding and Magnusson, 2004a).

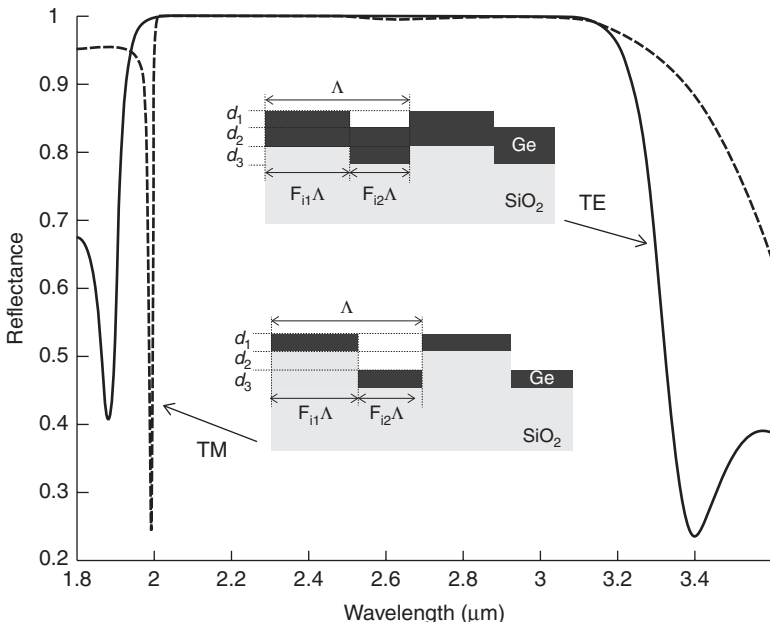
The two-dimensional weak grating model presented above has the advantage of providing physical insight. Strong gratings and 3D geometries (photonic crystals) significantly complicate the situation and require rigorous vectorial calculations.

2.4.3 Solar cells

Solar cells are a subject of intense research motivated by the urgency of developing renewable and less polluting energy sources. Thin film cells



2.6 Narrow-band reflectance spectrum of a silicon on quartz resonant grating filter in the TM polarization (Ding and Magnusson, 2004a). The grating parameters are shown in the inset. The H field is parallel to the grating lines. (Source: Reproduced with permission of the Optical Society of America.)



2.7 Wideband reflectance spectrum of two Ge/SiO_2 resonant gratings respectively in the TE and TM polarizations (Shokooh-Saremi *et al.*, 2010). The triple-level grating geometries are sketched in the inset. TE and TM refer to the polarization of the guided light (E or H field parallel to the grating lines). (Source: Reproduced with permission of the Optical Society of America.)

require less expensive material than the crystalline ones but have more limitations in terms of charge generation and transport. The material properties, fabrication limitations and light trapping strategies have a profound influence on the designs.

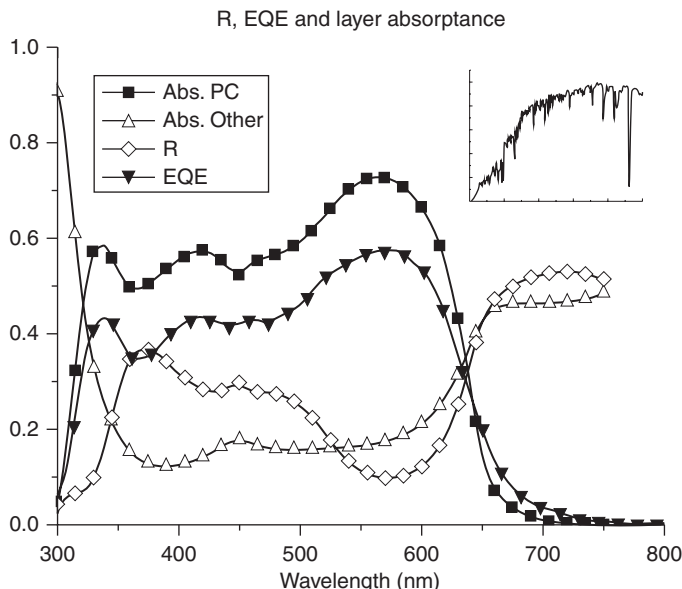
The main components of a solar cell are an active layer where light is absorbed and electric charges are generated, and electrodes to collect the charges. One electrode is transparent (e.g. Indium tin oxide (ITO)) while the other is usually opaque metal. Interfacial layers are often necessary to facilitate charge transport and for other reasons. The energy levels of the layer materials are arranged so that the electrons and holes separate and drift to their collection sites before they have time to recombine. In solar cells based on organic polymers the charges are generated in the form of bound electron-hole pairs called excitons. The charges are separated at the junction between a hole-transporting (donor-like) and an electron-transporting (acceptor-like) material. This interface must be in close proximity of the light absorption sites because the exciton diffusion length is very short, of the order of 10–20 nm

only (Duché *et al.*, 2012). The mobility of the separated charges is about ten times higher. An effective strategy consists in blending the donor and acceptor materials on a fine scale in order to form narrow elongated pathways leading to the collection sites (bulk-heterojunction materials). The efficiency of the photon to collected charge conversion can be highly nonuniform along the depth of the active layer(s), leading to semi-active or dead regions. Fabrication constraints such as suitable layer materials, roughness, homogeneity, reproducibility, limits on the acceptable thicknesses, cost considerations and so forth put severe constraints on the design possibilities. Serious consideration must be given to these issues when the optical interference is optimized.

Figure 2.8 illustrates the simulation of an organic bulk-heterojunction cell:

Glass / ITO (150 nm) / PEDOT:PSS (50 nm) / PCDTBT:PC₆₀BM (75 nm) / Lithium fluoride (LiF) (1 nm) / Al

and a comparison with experimental results (Chu *et al.*, 2009). The second and third layers are polymers processed from solution and spun-coated on



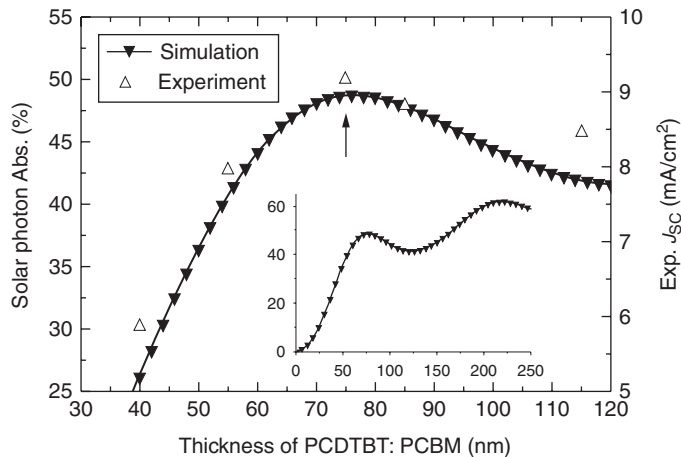
2.8 Simulation of the absorption in the organic bulk-heterojunction solar cell described in the text. (Abs. PC): absorptance of the active PCDTBT:PC₆₀BM layer of 75 nm thickness; (Abs. Other): cumulative absorptance of the other layers and the glass substrate; (R): reflectance; (EQE): measured external quantum efficiency. The inset shows the AM 1.5 solar photon flux in the same wavelength range. (Source: Adapted from Chu *et al.* (2009), with permission of *Applied Physics Letters*.)

commercial ITO. The PCDTBT:PC₆₀BM is a blend of a donor and acceptor material forming the active layer. The PEDOT:PSS and the LiF are interfacial layers. The simulated absorptance of the active layer (absorbed photon per incident photon) is roughly proportional to the measured EQE (external quantum efficiency, or collected electron per incident photon). The ratio of these two quantities (internal quantum efficiency or IQE) characterizes the efficiency of the absorbed photon to charge conversion. The calculated reflectance and the cumulative absorptance in the rest of the cell (glass substrate and other layers) represent light that does not participate in the current generation. In this case only the active layer thickness was optimized due to fabrication constraints. The figure inset shows that the photon flux in the AM 1.5 solar spectrum (plotted in the same wavelength range) drops rapidly for wavelengths below 450 nm where the active layer still absorbs.

Figure 2.9 illustrates the effect of varying the active-layer thickness on the measured short-circuit current J_{sc} and the simulated solar photon absorptance (SPA) in the active layer:

$$\text{SPA} = \frac{\int S(\lambda)A(\lambda)d\lambda}{\int S(\lambda)d\lambda} \quad [2.17]$$

In this equation $A(\lambda)$ is the layer absorptance and $S(\lambda)$ the solar photon spectrum. The fluctuations of the SPA with thickness are due to the optical



2.9 Effect of changing the active layer thickness on the measured short circuit current and simulated solar photon absorption (SPA) in the active layer of the cell described in Fig 2.8 (arrow). The inset shows the first two maxima of the SPA curve plotted in an extended thickness range. (Source: Adapted from Chu *et al.* (2009), with permission of *Applied Physics Letters*.)

interference. The current and SPA follow similar trends near the first maximum of the curves. The arrow corresponds to the cell simulated in Fig. 2.8. The second, higher SPA maximum visible in the inset was ruled out because of charge transport issues. A similar cell with thinner PEDOT:PSS (preferred from an optical point of view) achieved a respectable measured power conversion efficiency (PCE) of 5.7%.

These cells have stability issues associated with the degradation of the electrodes over time. Significant improvements are possible with inverted cells where the current direction is reversed (Chu *et al.*, 2012):

Glass / ITO / ZnO-NC / PDTSTPD-PC₇₁BM / Molybdenum oxyde (MoOx) / Ag.

The ZnO-NC is a nanocrystal film acting as electron transporting layer. A measured PCE of 6.7% is reported. The materials characterization, design and simulation of such cells can be challenging (Ameri *et al.*, 2008).

Efforts are under way to extend the absorption of organic solar cells in the infrared. One way to do this is by stacking two or more cells that absorb light in different wavelength regions (Persson and Inganäs, 2006; Kim *et al.*, 2007; Dennler *et al.*, 2008; Ameri *et al.*, 2009). The cells should be balanced because the current is limited by weakest link.

Bi-layer geometries where the donors and acceptors are in separate layers are also investigated. The very narrow active region requires careful optimization of the optical interference and a good understanding of the charge generation and transport properties. The quantity maximized in the design is the current J_{sc} , calculated from differential equations taking into account the charge generation rate (absorbed photons), recombination (life time), diffusion and drift due to charge density variations and built-in electric fields (Pettersson *et al.*, 1999; Monestier *et al.*, 2008). Bulk-heterojunction cells also benefit from such calculations (Monestier *et al.*, 2007; You and Zhang, 2009).

Ways of trapping the light in the active layer are investigated especially when its thickness is reduced to promote the charge transport properties. A common strategy is to scatter the light into guided modes of the cell structure by means of gratings, photonic crystal structures or random roughness (Zeng *et al.*, 2006; Mutitu *et al.*, 2008; Seassal *et al.*, 2008; Escoubas *et al.*, 2011; Raman *et al.*, 2011; Duché *et al.*, 2012). The dimensions of the scatterers can be optimized in order to generate resonances in the spectral regions where the intrinsic absorption of the active material is weak. A high density of Bloch modes is necessary to ensure that the improvements are not limited to a narrow spectral region. Plasmonic structures made of metallic nanoparticles are also investigated for their ability to generate high electromagnetic fields in the vicinity of the metal (Catchpole and Polman, 2008; Flory *et al.*, 2011; Vedraine *et al.*, 2011). Chapter 16 gives more details on solar cell design.

2.5 Conclusion

It is frequently heard that thin film design is the easy part of the work. A number of proven design techniques and breakthroughs such as the needle method greatly facilitate the designer's task. Nevertheless there are still many challenges. It has become a tradition at the topical meeting on Optical Interference Coatings organized by the Optical Society of America to propose cutting-edge design problems to the thin films community (Thelen and Langfeld, 1992; Baumeister, 2000; Thelen *et al.*, 2002; Tilsch *et al.*, 2006; Tilsch and Hendrix, 2008; Hendrix and Oliver, 2011).

This chapter reviews tools that are available for the solution of difficult design problems and presents some situations outside the classical framework. The desensitization to manufacturing errors is an important topic of practical interest requiring a good understanding of the deposition process. Attempts have been made at simulating the effect of realistic deposition errors (monitoring signals, rate fluctuations or other relevant parameters) on designs optimized mostly for spectral performance. Other approaches incorporate simplified deposition error models in the design algorithms. It is difficult to do both at the same time and this is still largely an open question.

The chapter also presents examples of hybrid situations where more than the interference in the coating is involved, or where the geometry of the problem significantly complicates the modeling, such as waveguide coatings, resonant grating filters and solar cells. Solar cells in particular are a subject of intense research. Rigorous modeling has to take into account charge generation and transport issues, accidental scattering or intentional diffraction by photonics structures, and so forth, in addition to the optical interference. Many questions are still unanswered.

The availability of parallel computing stimulates the interest in computer-intensive modeling. Clearly design requires many times more computing power than the simulation of an already known structure. There is no doubt that this is a direction for the future. Metamaterials, novel material mixtures, cermets, photonic crystals and devices, exotic wavelength regions, birefringence and so forth open opportunities of interesting design work.

2.6 Acknowledgements

The author wishes to thank George Dobrowolski for useful comments and Brian Sullivan from Iridian Spectral Technologies for providing the challenging, hot-off-the-press filter example illustrated in Fig. 2.1.

2.7 References

- Abul Hasan, M. and Ramakrishnan, S. (2011), A survey: hybrid evolutionary algorithms for cluster analysis, *Artif Intell Rev*, **36**, 179–204.
- Al-Marzoug, S. M. and Hodgson, R. J. (2008), Optimization of multilayer mirrors at 13.4 nm with more than two materials, *Appl Opt*, **47**, 2155–2160.
- Ameri, T., Dennler, G., Lungenschmied, C. and Brabec, C. J. (2009), Organic tandem solar cells: a review, *Energy Environ Sci*, **2**, 347–363.
- Ameri, T., Dennler, G., Waldauf, C., Denk, P., Forberich, K., Scharber, M. C., Brabec, C. J. and Hingerl, K. (2008), Realization, characterization, and optical modeling of inverted bulk-heterojunction organic solar cells, *J Appl Phys*, **103**, 084506_1–084506_6.
- Avrutskii, I. A., Golubenko, G. A., Sychugov, V. A. and Tishchenko, A. V. (1986), Spectral and laser characteristics of a mirror with a corrugated waveguide on its surface, *Soviet J Quantum Electron*, **16**, 1063.
- Badoil, B., Lemarchand, F., Cathelinaud, M. and Lequime, M. (2008), Manufacturing of an absorbing filter controlled with a broadband optical monitoring, *Opt Express*, **16**, 12008–12017.
- Baumeister, P. (2000), Evaluation of the solutions for two design problems presented at the 1998 Optical Interference Coatings Conference, *Appl Opt*, **39**, 2230–2234.
- Baumeister, P. W. (2004), *Optical Coating Technology*, Bellingham (WA), SPIE – The International Society for Optical Engineering.
- Binda, P. D. and Zocchi, F. E. (2004), ‘Genetic algorithm optimization of x-ray multilayer coatings’, *Advances in Computational Methods for X-Ray and Neutron Optics*, Denver (CO), Proc SPIE – The International Society for Optical Engineering, **5536**, 97–108.
- Birge, J. R., Kärtner, F. X. and Nohadani, O. (2011), Improving thin-film manufacturing yield with robust optimization, *Appl Opt*, **50**, C36–C40.
- Bolinder, F. (1950), Fourier transforms in the theory of inhomogeneous transmission lines, *Proc IRE*, **38**, 1216–1224.
- Boudet, T., Chaton, P., Herault, L., Gonon, G., Jouanet, L. and Keller, P. (1996), Thin-film designs by simulated annealing, *Appl Opt*, **35**, 6219–6226.
- Bovard, B. G. (1988), Fourier transform technique applied to quarterwave optical coatings, *Appl Opt*, **27**, 3062–3063.
- Bovard, B. G. (1993), Rugate filter theory: an overview, *Appl Opt*, **32**, 5427–5442.
- Boyko, O., Lemarchand, F., Talneau, A., Fehrembach, A.-L. and Sentenac, A. (2008), Resonant gratings for narrow band pass filtering applications, *Advances in Optical Thin Films III*, Glasgow, Proc SPIE – The International Society for Optical Engineering, **7101**, 71011B-9.
- Bulkin, P. V., Swart, P. L. and Lacquet, B. M. (1996), Fourier-transform design and electron cyclotron resonance plasma-enhanced deposition of lossy graded-index optical coatings, *Appl Opt*, **35**, 4413–4419.
- Catchpole, K. R. and Polman, A. (2008), Plasmonic solar cells, *Opt Express*, **16**, 21793–21800.
- Cheng, X., Fan, B., Dobrowolski, J. A., Wang, L. and Wang, Z. (2008a), Gradient-index optical filter synthesis with controllable and predictable refractive index profiles, *Opt Express*, **16**, 2315–2321.

- Cheng, X., Fan, B., Haruo, T. and Wang, Z. (2008b), 'Optical and structural properties of $\text{Nb}_x\text{Si}_y\text{O}$ composite films prepared by metallic co-sputtering process', *Proc SPIE - The International Society for Optical Engineering*, **7101**, 71011G1–71011G8.
- Cheng, X., Wang, Z., Zhang, Z., Wang, F. and Chen, L. (2006), Design of X-ray super-mirrors using simulated annealing algorithm, *Opt Commun*, **265**, 197–206.
- Chu, T.-Y., Alem, S., Verly, P. G., Wakim, S., Lu, J., Tao, Y., Beaupré, S., Leclerc, M., Belanger, F., Desilets, D., Rodman, S., Waller, D. and Gaudiana, R. (2009), Highly efficient polycarbazole-based organic photovoltaic devices, *Appl Phys Lett*, **95**, 063304–3.
- Chu, T. Y., Tsang, S. W., Zhou, J., Verly, P. G., Lu, J., Beaupré, S., Leclerc, M. and Tao, Y. (2012), High-efficiency inverted solar cells based on a low bandgap polymer with excellent air stability, *Sol Energ Mat Sol Cells*, **96**, 155–159.
- Csendes, V., Daroczy, B. and Hanos, Z. (1986), Nonlinear parameter estimation by global optimization: comparison of local search methods in respiratory system modelling, in Prékopa, A., Szelezsáán, J. and Strazicky, B. (eds.), *System Modeling and Optimization*, Berlin, Springer Verlag, 188–192.
- Cushing, D. (2011), *Enhanced Optical Filter Design*, Bellingham (WA), SPIE Press.
- Delano, E. (1967), Fourier synthesis of multilayer filters, *J Opt Soc Am*, **57**, 1529–1532.
- Dennler, G., Scharber, M. C., Ameri, T., Denk, P., Forberich, K., Waldauf, C. and Brabec, C. J. (2008), Design rules for donors in bulk-heterojunction tandem solar cells? Towards 15% energy-conversion efficiency, *Adv Mater*, **20**, 579–583.
- Ding, Y. and Magnusson, R. (2004a), Resonant leaky-mode spectral-band engineering and device applications, *Opt Express*, **12**, 5661–5674.
- Ding, Y. and Magnusson, R. (2004b), Use of nondegenerate resonant leaky modes to fashion diverse optical spectra, *Opt Express*, **12**, 1885–1891.
- Djurisic, A. B., Fritz, T., Leo, K. and Li, E. H. (2000), Improved method for determination of optical constants of organic thin films from reflection and transmission measurements, *Appl Opt*, **39**, 1174–1182.
- Dobrowolski, J. A. (1965), Completely automatic synthesis of optical thin film systems, *Appl Opt*, **4**, 937–946.
- Dobrowolski, J. A. (1981), Versatile computer program for absorbing optical thin-film systems, *Appl Opt*, **20**, 74–81.
- Dobrowolski, J. A. (1997), Numerical methods for optical thin films, *Optic Photon News*, **8**, 24–33.
- Dobrowolski, J. A., Browning, S., Jacobson, M. and Nadal, M. (2008), 2007 topical meeting on optical interference coatings: manufacturing problem, *Appl Opt*, **47**, C231–C245.
- Dobrowolski, J. A., Ho, F. C., Belkind, A. and Koss, V. A. (1989), Merit functions for more effective thin film calculations, *Appl Opt*, **28**, 2824–2831.
- Dobrowolski, J. A. and Kemp, R. A. (1990), Refinement of optical multilayer systems with different optimization procedures, *Appl Opt*, **29**, 2876–2893.
- Dobrowolski, J. A. and Kemp, R. A. (1992), Flip-flop thin-film design program with enhanced capabilities, *Appl Opt*, **31**, 3807–3812.
- Dobrowolski, J. A. and Lowe, D. (1978), Optical thin film synthesis program based on the use of Fourier transforms, *Appl Opt*, **17**, 3039–3050.

- Dobrowolski, J. A. and Piotrowski, S. H. C. (1982), Refractive index as a variable in the numerical design of optical thin film systems, *Appl Opt*, **21**, 1502–1511.
- Druessel, J., Grantham, J. and Haaland, P. (1993), Optimal phase modulation for gradient-index optical filters, *Opt Lett*, **18**, 1583.
- Duché, D., Escoubas, L., Simon, J. J., Gourgon, C., Masclaux, C., Torchio, P., Le Rouzo, J. and Flory, F. (2012), Photonic crystals for improving light absorption in organic solar cells, in Freundlich, A. and Guillemoles, J.F. (eds.), *Physics, Simulation, and Photonic Engineering of Photovoltaic Devices*, 1 ed, San Francisco, California, USA, SPIE, **8256**, 82561K-8.
- Eisenhamer, T., Lazarov, M., Leutbecher, M., Schöffel, U. and Sizmann, R. (1993), Optimization of interference filters with genetic algorithms applied to silver-based heat mirrors, *Appl Opt*, **32**, 6310–6315.
- Escoubas, L., Flory, F. O., Lemarchand, F., Drouard, E., Roux, L., Tisserand, S. and Albrand, G. (2001), Fabry-Perot multilayers for enhancing the diffraction efficiency of ion-implanted gratings, *Appl Opt*, **40**, 1587–1592.
- Escoubas, L., Simon, J. J., Torchio, P., Duché, D., Vedraine, S., Vervisch, W., Le Rouzo, J., Flory, F., Rivière, G., Yeabiyo, G. and Derbal, H. (2011), Bringing some photonic structures for solar cells to the fore, *Appl Opt*, **50**, C329–C339.
- Fabricius, H. (1992a), Gradient-index filters: conversion into a two-index solution by taking into account dispersion, *Appl Opt*, **31**, 5216–5220.
- Fabricius, H. (1992b), Gradient-index filters: designing filters with steep skirts, high reflection, and quintic matching layers, *Appl Opt*, **31**, 5191–5196.
- Flory, F., Escoubas, L. and Berginc, G. (2011), Optical properties of nanostructured materials: a review, *J Nanophotonics*, **5**, 052502–1.
- Furman, S. A. and Tikhonravov, A. V. (1992), *Optics of Multilayer Systems*, Gif-sur-Yvette (France), Editions frontiere.
- Gao, L., Lemarchand, F. and Lequime, M. (2011), Application of global optimization algorithms for optical thin film index determination from spectro-photometric analysis, in Lequime, M., MacLeod, H. A., Ristau, D. (Eds.), *Advances in Optical Thin Films IV*, Marseille, France, Proc SPIE – The International Society for Optical Engineering, **8168**, 81680B1–17.
- Greiner, H. (1996), Robust optical coating design with evolutionary strategies, *Appl Opt*, **35**, 5477–5483.
- Hendrix, K. and Oliver, J. (2011), Optical interference coatings design contest 2010: solar absorber and Fabry-Perot etalon, *Appl Opt*, **50**, C286–C300.
- Hendrix, K. D., Hulse, C. A., Ockenfuss, G. J. and Sargent, R. B. (2008), Demonstration of narrowband notch and multi-notch filters, in Kruschwitz, J. D. T. and Ellison, M. J. (Eds.), *Advances in Thin-Film Coatings for Optical Applications V*, San Diego (CA), Proc SPIE – The International Society for Optical Engineering, **7067**, 706702–14.
- Hobson, M. P. and Baldwin, J. E. (2004), Markov-chain Monte Carlo approach to the design of multilayer thin-film optical coatings, *Appl Opt*, **43**, 2651–2660.
- Jiang, L., Zheng, G., Shi, L., Yuan, J. and Li, X. (2008), Broad omnidirectional reflectors design using genetic algorithm, *Opt Commun*, **281**, 4882–4888.
- Kendall, P. C., Roberts, D. A., Robson, P. N., Adams, M. J. and Robertson, M. J. (1993), Semiconductor laser facet reflectivities using free-space radiation modes, *Optoelectronics, IEE Proc J*, **140**, 49–55.

- Kennedy, J. and Eberhart, R. (1995), 'Particle swarm optimization', *IEEE Proc, International Conference on Neural Networks*, **4**, 1942–1948.
- Kim, J. Y., Lee, K., Coates, N. E., Moses, D., Nguyen, T.-Q., Dante, M. and Heeger, A. J. (2007), Efficient tandem polymer solar cells fabricated by all-solution processing, *Science*, **317**, 222–225.
- Kochergin, V. (2003), *Omnidirectional Optical Filters*, Norwell, MA, Kluwer Academic Publishers.
- Kruschwitz, J. D. T. (2003), Software tools speed optical thin-film design, *Laser Focus World*, **39**(6), 157–166.
- Labukhin, D. and Li, X. (2005), Three-dimensional finite-difference time-domain simulation of facet reflection through parallel computing, *J Computational Electron*, **4**, 15–19.
- Larouche, S. and Martinu, L. (2006), 'A new step method for the synthesis of optical filters with arbitrary indices', *49th Annual Technical Conference Proceedings (2006)*, Soc. Vacuum Coaters, **49**, 305–308.
- Larouche, S. and Martinu, L. (2007), Dispersion implementation in optical filter design by the Fourier transform method using correction factors, *Appl Opt*, **46**, 7436–7441.
- Larouche, S. and Martinu, L. (2008), OpenFilters: open-source software for the design, optimization, and synthesis of optical filters, *Appl Opt*, **47**, C219–C230.
- Lemarchand, F., Giovannini, H. and Sentenac, A. (1997), Interest of hybrid structures for thin-film design: multilayered subwavelength microgratings, in Hall, R. L. (Ed.), *Optical Thin Films V: New Developments*, San Diego (CA), Proc SPIE – The International Society for Optical Engineering, **3133**, 58–64.
- Lemarchand, F., Sentenac, A. and Giovannini, H. (1998), Increasing the angular tolerance of resonant grating filters with doubly periodic structures, *Opt Lett*, **23**, 1149–1151.
- Macleod, H. A. (2010), *Thin-film Optical Filters*, Fourth edition. New York, CRC Press.
- Macleod, H. A. and Pelletier, E. (1977), Error compensation mechanisms in some thin-film monitoring systems, *Optica Acta*, **24**, 907–930.
- Magnusson, R., Ding, Y., Lee, K. J., Shin, D., Priambodo, P. S., Young, P. P. and Maldonado, T. A. (2003), Photonic devices enabled by waveguide-mode resonance effects in periodically modulated films, in Eldada, L. A. (Ed.), *Nano- and Micro-Optics for Information Systems*, San Diego (CA), Proc SPIE – The International Society for Optical Engineering, **5225**, 20–34.
- Magnusson, R. and Wang, S. S. (1992), New principle for optical filters, *Appl Phys Lett*, **61**, 1022–1024.
- Maroosi, A. and Amiri, B. (2010), A new clustering algorithm based on hybrid global optimization based on a dynamical systems approach algorithm, *Expert Syst Appl*, **37**, 5645–5652.
- Martin, S., Rivory, J. and Schoenauer, M. (1995), Synthesis of optical multilayer systems using genetic algorithms, *Appl Opt*, **34**, 2247–2254.
- Moharam, M. G. and Gaylord, T. K. (1981), Rigorous coupled-wave analysis of planar-grating diffraction, *J Opt Soc Am*, **71**, 811–818.
- Monestier, F., Simon, J. J., Torchio, P., Escoubas, L., Flory, F., Bailly, S., De Bettignies, R., Guillerez, S. and Defranoux, C. (2007), Modeling the short-circuit current

- density of polymer solar cells based on P3HT:PCBM blend, *Sol Energ Mat Sol Cells*, **91**, 405–410.
- Monestier, F., Simon, J. J., Torchio, P., Escoubas, L., Ratier, B., Hojeij, W., Lucas, B., Moliton, A., Cathelinaud, M., Defranoux, C. and Flory, F. (2008), Optical modeling of organic solar cells based on CuPc and C60, *Appl Opt*, **47**, C251–C256.
- Morf, R. and Kunz, R. E. (1988), Dielectric filter optimization by simulated thermal annealing, *Thin films technologies III*, Bellingham (WA), *Proc SPIE – The International Society for Optical Engineering*, **1019**, 211–217.
- Morf, R. H. and Kunz, R. E. (1990), ‘Dielectric filter optimization by simulated thermal annealing: a simulated zone-melting approach’, *Optical Thin Films and Applications*, Bellingham (WA), *Proc SPIE – The International Society for Optical Engineering*, **1270**, 11–17.
- Mutitu, J. G., Shi, S., Chen, C., Creazzo, T., Barnett, A., Honsberg, C. and Prather, D. W. (2008), Thin film solar cell design based on photonic crystal and diffractive grating structures, *Opt Express*, **16**, 15238–15248.
- Nohadani, O., Birge, J. R., Kartner, F. X. and Bertsimas, D. J. (2008), Robust chirped mirrors, *Appl Opt*, **47**, 2630–2636.
- Obayya, S. S. A. (2006), Scalar finite-element analysis of optical-fiber facets, *J Lightwave Tech*, **24**, 2115–2121.
- Orobouchouk, R., Laval, S., Pascal, D. and Koster, A. (1997), Analysis of integrated optical waveguide mirrors, *J Lightwave Tech*, **15**, 815–820.
- Oulton, R. F. and Adjiman, C. S. (2006), Global optimization and modeling techniques for planar multilayered dielectric structures, *Appl Opt*, **45**, 5910–5922.
- Panos, M., Pardalos, H. and Romeijn, E. (2002), *Handbook of Global Optimization, Volume 2*, Dordrecht, Kluwer Academic Publishers.
- Persson, N.-K. and Inganäs, O. (2006), Organic tandem solar cells – modelling and predictions, *Sol Energ Mat Sol Cells*, **90**, 3491–3507.
- Pervak, V., Tikhonravov, A. V., Trubetskoy, M. K., Naumov, S., Krausz, F. and Apolonski, A. (2007), 1.5-octave chirped mirror for pulse compression down to sub-3 fs, *Appl Phys B: Lasers Optics*, **87**, 5–12.
- Pervak, V., Trubetskoy, M. and Tikhonravov, A. (2009), Design consideration for high damage threshold UV-Vis-IR mirrors, in Exarhos, G. J., Gruzdev, V. E., Ristau, D., Soileau, M. J. and Stolz, C. J. (Eds.), *Laser-Induced Damage in Optical Materials: 2009*, Bellingham (WA), *Proc SPIE – The International Society for Optical Engineering*, **7504**, 75040A1–10.
- Pervak, V., Trubetskoy, M. K. and Tikhonravov, A. V. (2011), Robust synthesis of dispersive mirrors, *Opt Express*, **19**, 2371–2380.
- Pettersson, L. A. A., Roman, L. S. and Inganäs, O. (1999), Modeling photocurrent action spectra of photovoltaic devices based on organic thin films, *J Appl Phys*, **86**, 487–496.
- Poitras, D. (2005), ‘Dealing with sensitivity variations during the manufacture of optical coating’, *SVC, Society of Vacuum Coaters – 48th Annual Technical Conference*, Denver, CO, United States, 23–28 April 2005, 354–358.
- Poitras, D., Larouche, S. and Martinu, L. (2002), Design and plasma deposition of dispersion-corrected multiband rugate filters, *Appl Opt*, **41**, 5249–5255.
- Pond, J. and Kawano, M. (2010), Virtual prototyping and optimization of novel solar cell designs, in Schriemer, H. P. and Kleiman, R. N. (Eds.), *Photonics North 2010*, Bellingham (WA), *Proc SPIE – The International Society for Optical Engineering*, **7750**, 775028–1–6.

- Poxson, D. J., Schubert, M. F., Mont, F. W., Schubert, E. F. and Kim, J. K. (2009), Broadband omnidirectional antireflection coatings optimized by genetic algorithm, *Opt Lett*, **34**, 728–730.
- Rabinovitch, K. and Toker, G. (1994), ‘Genetic algorithm and thin-film design’, San Diego (CA), *Proc SPIE – The International Society for Optical Engineering*, **2262**, 163–174.
- Raman, A., Yu, Z. and Fan, S. (2011), Dielectric nanostructures for broadband light trapping in organic solar cells, *Opt Express*, **19**, 19015–19026.
- Reed, M., Benson, T. M., Kendall, P. C. and Sewell, P. (1996), Antireflection-coated angled facet design, *IEE Proc – Optoelectronics*, **143**, 214–220.
- Rigneault, I., Lemarchand, F., Sentenac, A. and Giovannini, H. (1999), Strong extraction coefficient for sources located inside waveguide grating structures, *J Optics A: Pure and Appl Opt*, **1**, 507–511.
- Rinnooy Kan, A. and Timmer, G. (1987), Stochastic global optimization methods part I: Clustering methods, *Math Program*, **39**, 27–56.
- Schmid, J. H., Cheben, P., Janz, S., Lapointe, J., Post, E. and Xu, D. X. (2007), Gradient-index antireflective subwavelength structures for planar waveguide facets, *Opt Lett*, **32**, 1794–1796.
- Schoen, F. (1991), Stochastic techniques for global optimization: a survey of recent advances, *J Global Optimization*, **1**, 207–228.
- Schubert, M. F., Mont, F. W., Chhajed, S., Poxson, D. J., Kim, J. K. and Schubert, E. F. (2008), Design of multilayer antireflection coatings made from co-sputtered and low-refractive-index materials by genetic algorithm, *Opt Express*, **16**, 5290–5298.
- Seassal, C., Park, Y., Fave, A., Drouard, E., Fourmond, E., Kaminski, A., Lemit, M., Letartre, X. and Viktorovitch, P. (2008), ‘Photonic crystal assisted ultra-thin silicon photovoltaic solar cell’, in Gombert, A. (Ed.), *Photonics for Solar Energy Systems II*, Bellingham (WA), *Proc SPIE – The International Society for Optical Engineering*, **7002**, 700207–1–8.
- Sergeant, N. P., Agrawal, M. and Peumans, P. (2009), Design of selective coatings for solar thermal applications using subwavelength metal-dielectric structures, in Tsai, B. K. (Ed.), *Optical Modeling and Measurements for Solar Energy Systems III*, Bellingham (WA), *Proc SPIE – The International Society for Optical Engineering*, **7410**, 74100C1–10.
- Shokooh-Saremi, M. and Magnusson, R. (2007), Particle swarm optimization and its application to the design of diffraction grating filters, *Opt Lett*, **32**, 894–896.
- Shokooh-Saremi, M. and Magnusson, R. (2010a), Leaky-mode resonant reflectors with extreme bandwidths, *Opt Lett*, **35**, 1121–1123.
- Shokooh-Saremi, M. and Magnusson, R. (2010b), New nonpolarizing resonant beam splitters, *IEEE Photonics J*, **2**, 670–676.
- Shokooh-Saremi, M., Nourian, M., Mirsalehi, M. M. and Keshmiri, S. H. (2004), Design of multilayer polarizing beam splitters using genetic algorithm, *Opt Commun*, **233**, 57–65.
- Snedaker, C. G. (1982), New numerical thin-film synthesis technique, *J Opt Soc Am*, **72**, 1732.
- Sossi, L. (1974), A method for the synthesis of multilayer dielectric interference coatings, *Eesti NSV Tead Akad Toim Fuus Mat*, **23**, 229–237.
- Southwell, W. H. (1985), Coating design using very thin high- and low-index layers, *Appl Opt*, **24**, 457–460.

- Strain, M. and Sorel, M. (2010), Curved facet 90° turning mirrors for integrated optical technologies, *Electron Lett*, **46**, 360–362.
- Sullivan, B. T., Clarke, G. A., Akiyama, T., Osborne, N., Ranger, M., Dobrowolski, J. A., Howe, L., Matsumoto, A., Song, Y. and Kikuchi, K. (2000), High-rate automated deposition system for the manufacture of complex multilayer coatings, *Appl Opt*, **39**, 157–167.
- Sullivan, B. T. and Dobrowolski, J. A. (1996), Implementation of a numerical needle method for thin-film design, *Appl Opt*, **35**, 5484–5492.
- Swart, P. and Lacquet, B. (1990), A new algorithm for layer thickness and index step estimation in multi-layer hetero-epitaxial structures, *J Electron Mater*, **19**, 1383–1394.
- Tang, J. F. and Zheng, Q. (1982), Automatic design of optical thin-film systems – merit function and numerical optimization method, *J Opt Soc Am*, **72**, 1522–1528.
- Thelen, A. (1989), *Design of Optical Interference Coatings*, New York, McGraw Hill.
- Thelen, A. and Langfeld, R. (1992), Coating design contest: Antireflection coating for lenses to be used with normal and infrared photographic film, *Thin films for optical systems*, Bellingham (WA), *Proc SPIE – The International Society for Optical Engineering*, **1782**, 552–601.
- Thelen, A., Tikhonravov, A. V., Trubetskoy, M. K., Tilsch, M. and Brauneck, U. (2002), Topical Meeting on Optical Interference Coatings (OIC '2001): design contest results, *Appl Opt*, **41**, 3022–3038.
- Tikhonravov, A. V. (1993), Some theoretical aspects of thin-film optics and their applications, *Appl Opt*, **32**, 5417–5426.
- Tikhonravov, A. V. and Trubetskoy, M. K. (2005), Computational manufacturing as a bridge between design and production, *Appl Opt*, **44**, 6877–6884.
- Tikhonravov, A. V. and Trubetskoy, M. K. (2007), Modern status and prospects of the development of methods of designing multilayer optical coatings, *J Opt Technol*, **74**, 845–850.
- Tikhonravov, A. V., Trubetskoy, M. K. and Debell, G. W. (1996), Application of the needle optimization technique to the design of optical coatings, *Appl Opt*, **35**, 5493–5508.
- Tikhonravov, A. V., Trubetskoy, M. K., Amotchkina, T. V. and Tikhonravov, A. A. (2003), ‘Application of advanced optimization concepts to the design of high quality optical coatings’, in Righini, G. C. and Consortini, A. (Eds.), *19th Congress of the International Commission for Optics: Optics for the Quality of Life*, Bellingham (WA), *Proc SPIE – The International Society for Optical Engineering*, **4829**, 1061–1062.
- Tikhonravov, A. V., Trubetskoy, M. K., Amotchkina, T. V., A. Kokarev, M., Kaiser, N., Stenzel, O., Wilbrandt, S. and Gäbler, D. (2006), New optimization algorithm for the synthesis of rugate optical coatings, *Appl Opt*, **45**, 1515–1524.
- Tikhonravov, A. V., Trubetskoy, M. K. and Amotchkina, T. V. (2011), Investigation of the error self-compensation effect associated with broadband optical monitoring, *Appl Opt*, **50**, C111–C116.
- Tilsch, M. and Hendrix, K. (2008), Optical Interference Coatings Design Contest 2007: triple bandpass filter and nonpolarizing beam splitter, *Appl Opt*, **47**, C55–C69.
- Tilsch, M., Hendrix, K. and Verly, P. G. (2006), Optical Interference Coatings Design Contest 2004, *Appl Opt-OT*, **45**, 1544–1554.

- Trubetskoy, M., K. and Tikhonravov, A., V. (2010), 'Robust synthesis of multilayer coatings', *Optical Interference Coatings*, Optical Society of America, OSA Technical Digest, TuA4-1:3.
- Vassallo, C. (1985), Rigorous and approximate calculations of antireflection layer parameters for travelling-wave diode laser amplifiers, *Electron Lett*, **21**, 333–334.
- Vassallo, C. (1988), Reflectivity of multielectric coatings deposited on the end facet of a weakly guiding dielectric slab waveguide, *J Opt Soc Am A*, **5**, 1918–1928.
- Vassallo, C. (1990), Theory and practical calculation of antireflection coatings on semiconductor laser diode optical amplifiers, *IEE Proc Part J, Optoelectronics*, **137**, 193–202.
- Vassallo, C. (1997), Difficulty with vectorial BPM, *Electron Lett*, **33**, 61–62.
- Vassallo, C. (1998), Finite-difference derivation of the reflectivity at output facets of dielectric waveguides with a highly diverging output beam, *JOSA A: Optics and Image Science and Vision*, **15**, 717–726.
- Vedraine, S., Torchio, P., Duche, D., Flory, F., Simon, J.-J., Le Rouzo, J. and Escoubas, L. (2011), Intrinsic absorption of plasmonic structures for organic solar cells, *Sol Energ Mat Sol Cells*, **95**(1), S57–S64.
- Verly, P. G. (1994), 'Fourier transform technique with frequency filtering for anti-reflection coating design', Bellingham (WA), *Proc SPIE – The International Society for Optical Engineering*, **2253**, 161–167.
- Verly, P. G. (1995), Fourier transform technique with frequency filtering for optical thin-film design, *Appl Opt*, **34**, 688–694.
- Verly, P. G. (1996), Fourier transform technique with refinement in the frequency domain for the synthesis of optical thin films, *Appl Opt*, **35**, 5148–5154.
- Verly, P. G. (1998a), 'Fourier transform approach for thin film characterization', *Technical Digest, Topical Meeting on Optical Interference Coatings*, Washington D.C., Optical Society of America, OSA Technical Digest Series, TUB1 1–2.
- Verly, P. G. (1998b), Optical coating synthesis by simultaneous refractive-index and thickness refinement of inhomogeneous films, *Appl Opt*, **37**, 7327–7333.
- Verly, P. G. (2001), Modified needle method with simultaneous thickness and refractive-index refinement for the synthesis of inhomogeneous and multilayer optical thin films, *Appl Opt*, **40**, 5718–5725.
- Verly, P. G. (2002), Design of a robust thin-film interference filter for erbium-doped fiber amplifier gain equalization, *Appl Opt-OT*, **41**, 3092–3096.
- Verly, P. G. (2007), Fourier transform approach for thickness estimation of reflecting interference filters. 2. Generalized theory, *Appl Opt*, **46**, 76–83.
- Verly, P. G. (2008), Hybrid approach for rugate filter design, *Appl Opt*, **47**, C172–C178.
- Verly, P. G. (2009), 'Antireflection coating design by fourier frequency filtering with frequency range adjustments', *52nd Annual Technical Conference Proceedings*, Society of Vacuum Coaters, 35–39.
- Verly, P. G. (2011), Optimum phase for rugate filter synthesis by Fourier transforms, *Appl Opt*, **50**, C124–C128.
- Verly, P. G. and Dobrowolski, J. A. (1990), Iterative correction process for optical thin film synthesis with the Fourier transform method, *Appl Opt*, **29**, 3672–3684.

- Verly, P. G., Dobrowolski, J. A., Wild, W. J. and Burton, R. L. (1989), Synthesis of high rejection filters with the Fourier transform method, *Appl Opt*, **28**, 2864–2875.
- Verly, P. G., Dobrowolski, J. A. and Willey, R. R. (1992), Fourier-transform method for the design of wideband antireflection coatings, *Appl Opt*, **31**, 3836–3846.
- Verly, P. G., Tikhonravov, A. V. and Poezd, A. D. (1993), Multiple solutions to the synthesis of graded index optical coatings, in Dobrowolski, J. A. and Verly, P. G. (Eds.), *Inhomogeneous and Quasi-Inhomogeneous Coatings*, Bellingham (WA), *Proc SPIE – The International Society for Optical Engineering*, **2046**, 9–16.
- Verly, P. G., Tikhonravov, A. V. and Trubetskoy, M. K. (1997), Efficient refinement algorithm for the synthesis of inhomogeneous optical coatings, *Appl Opt*, **36**, 1487–1495.
- Vincent, P. and Nevière, M. (1979), Corrugated dielectric waveguides: a numerical study of the second-order stop bands, *Appl Phys A Mater Sci Process*, **20**, 345–351.
- Vukovic, A., Sewell, P., Benson, T. M. and Kendall, P. C. (1998), Degraded facet performance caused by edge proximity, *Electron Lett*, **34**, 1939–1940.
- Vukovic, A., Sewell, P., Benson, T. M. and Kendall, P. C. (2000), Advances in facet design for buried lasers and amplifiers, *IEEE J Selected Topics Quantum Electronics*, **6**, 175–184.
- Wang, P. and Menon, R. (2012), Simulation and optimization of 1-D periodic dielectric nanostructures for light-trapping, *Opt Express*, **20**, 1849–1855.
- Wang, S. S. and Magnusson, R. (1993), Theory and applications of guided-mode resonance filters, *Appl Opt*, **32**, 2606–2613.
- Wang, S. S., Magnusson, R., Bagby, J. S. and Moharam, M. G. (1990), Guided-mode resonances in planar dielectric-layer diffraction gratings, *J Opt Soc Am A*, **7**, 1470–1474.
- Wang, Z. (2008), ‘Non-periodic multilayer coatings in EUV, soft X-ray and X-ray range’, in Kaiser Norbert, Lequime Michel and Macleod, H. A. (Eds.), *Advances in Optical Thin Films III*, Bellingham (WA), *Proc SPIE – The International Society for Optical Engineering*, **7101**, 710110–1–10.
- Wiechmann, S., Heider, H. J. and Müller, J. (2003), Analysis and design of integrated optical mirrors in planar waveguide technology, *J. Lightwave Technol*, **21**, 1584.
- Wilbrandt, S., Stenzel, O. and Kaiser, N. (2010), All-oxide broadband antireflection coatings by plasma ion assisted deposition: design, simulation, manufacturing and re-optimization, *Opt Express*, **18**, 19732–19742.
- Wild, W. J. and Buhay, H. (1986), Thin-film multilayer design optimization using a Monte Carlo approach, *Opt Lett*, **11**, 745–747.
- Willey, R. R. (1996), *Practical Design and Production of Optical Thin Films*, New York, M. Dekker, 56.
- Xu, J., Yevick, D. and Gallant, M. (1995), Approximate methods for modal reflectivity at optical waveguide facets, *J Opt Soc Am A*, **12**, 725–728.
- Yakovlev, V. and Tempea, G. (2002), Optimization of chirped mirrors, *Appl Opt*, **41**, 6514–6520.
- You, H. L. and Zhang, C. F. (2009), Influence of optical interference and carrier lifetime on the short circuit current density of organic bulk heterojunction solar cells, *Chinese Physics B*, **18**, 349–356.

- Zeng, L., Yi, Y., Hong, C., Liu, J., Feng, N., Duan, X., Kimerling, L. C. and Alamariu, B. A. (2006), Efficiency enhancement in Si solar cells by textured photonic crystal back reflector, *Appl Phys Lett*, **89**, 111111–111113.
- Zheng, Y.-F. and Tang, J.-F. (1987), New automatic design technique for optical coatings, *Appl Opt*, **26**, 1546–1549.

Optical monitoring strategies for optical coating manufacturing

A. V. TIKHONRAOV, Moscow State University, Russia,
M. K. TRUBETSKOV, Max-Planck Institute of Quantum Optics, Germany and Moscow State University, Russia and
T. V. AMOTCHKINA, Moscow State University, Russia

DOI: 10.1533/9780857097316.1.62

Abstract: Optical monitoring strategies are especially important for the reliable control of deposition processes because they allow one to monitor optical thicknesses of coating layers, which are the most important production parameters. The chapter discusses broad band and monochromatic monitoring strategies, direct and indirect monitoring approaches, passive and active monitoring strategies. In the case of monochromatic monitoring, special attention is devoted to turning point and level monitoring. The most essential effects connected with optical monitoring, such as error self-compensation effect and cumulative effect of thickness errors, are considered.

Key words: optical monitoring strategies, broad band monitoring, monochromatic monitoring, error self-compensation effect, cumulative effect of thickness errors.

3.1 Introduction

With the amazing progress achieved in the theoretical design of optical coatings, a reliable monitoring of thin film multilayer deposition becomes a key element in the optical coating design-production chain. The introduction of new energetic and highly stable deposition processes allows, in some application areas, monitoring of thin film thicknesses by time (Pervak *et al.*, 2007). Quartz crystal monitoring of thin film coating production is also widely employed in the case of stable deposition processes (Macleod, 2001). Nevertheless the interest in optical monitoring strategies has been only increased with the new developments in deposition technologies. This is obviously connected to the fact that such strategies monitor optical thicknesses of coating layers and not their physical thicknesses. Macleod (1981) wrote that this had always been considered as a strong argument in support of optical monitoring strategies. Indeed, an attentive study of the basics of

thin film theory shows that only thin film optical thicknesses are physically sensible and are entirely responsible for the optical properties of a coating (Furman and Tikhonravov, 1992).

Optical monitoring of thin film coating production has almost been as long a history as thin film optics itself. Macleod (2001, p. 500) mentions the early paper devoted to this subject (Banning, 1947) where a table allowing the monitoring of film optical thickness in quarter wave units by a color of reflected light was presented. Practically all early works on optical monitoring were connected to the production of multilayers with quarter wave optical thicknesses of their layers. For such multilayers reflectance/transmittance is monitored at a central wavelength which is four times quarter wave optical thickness. A monitoring signal reaches its maxima or minima exactly at an instant when a new quarter wave portion of layer optical thickness is deposited. Monitoring of reflectance/transmittance extrema in early days of thin film optics was done by a vacuum plant operator and a 5% accuracy of layer thickness monitoring was typical for a trained operator (Macleod, 2002, p. 503).

Reflectance/transmittance extrema are often referred to as turning points of monitoring signal and the optical monitoring technique in which a layer deposition is terminated at an extremum of monitoring signal is usually called turning value monitoring (Macleod, 2002) or turning point monitoring (Baumeister, 2004).

A great advantage of this technique is an existence of a strong error self-compensation effect associated with direct optical monitoring of narrow band pass filters at their central wavelengths (Bousquet *et al.*, 1972; Macleod, 1972). This effect was discovered both empirically and by means of computer simulations. Macleod (1972) wrote: 'The results of the first computer runs were very surprising. Turning value monitoring gave the enormous thickness errors which were expected, but the computed performance of the filters was found still to be satisfactory'. A physical explanation for the error self-compensation effect was provided only three decades later when the interest to turning point monitoring was revived in connection with a boom in production of filters for wavelength division multiplexing (WDM) applications (Tikhonravov and Trubetskoy, 2002).

Turning point optical monitoring is useful for the production of multilayers with quarter wave layer optical thicknesses but it has no obvious and physically sensible advantage in the case of multilayers with non-quarter wave layer optical thicknesses. For such multilayers so-called level monitoring is often used (Macleod, 1981; Zhao, 1985). When level monitoring is applied, a layer deposition is terminated when reflectance/transmittance at a specially chosen monitoring wavelength reaches a certain theoretically predicted level, which is called termination level. There is a great variety of monochromatic monitoring strategies exploring level monitoring. These

strategies may employ direct monitoring of one of the samples produced in a vacuum chamber or may use separate monitoring chips for indirect monitoring of a coating production. They may differ in specifications of sequences of monitoring wavelengths for various layers of a coating and they may explore corrections of termination levels in a course of coating production. The most promising trends in current developments of monochromatic monitoring strategies are considered in this chapter.

Nowadays broad band optical monitoring attracts more and more attention from optical coating engineers. The first broad band monitoring systems were used for optical coating production in the late seventies of the last century (Vidal *et al.*, 1978, 1979; Vidal and Pelletier, 1979). In these early works, considerable efforts were applied to overcome problems connected with insufficient performances of computers and spectrophotometric instrumentation of those days. Tremendous progress in modern computers performance and the development of photodiode arrays and CCD (charge-coupled device) detectors opened new horizons for applications of broad band monitoring systems. An attractive feature of broad band optical monitoring is its much lower sensitivity to random errors in measurement data as compared to monochromatic optical monitoring (Tikhonravov *et al.*, 2006a). Several authors also supposed that some sort of error self-compensation effect is inherent in broad band optical monitoring (Vidal *et al.*, 1978; Macleod, 1981) and indeed the existence of this effect was recently proved (Tikhonravov *et al.*, 2011).

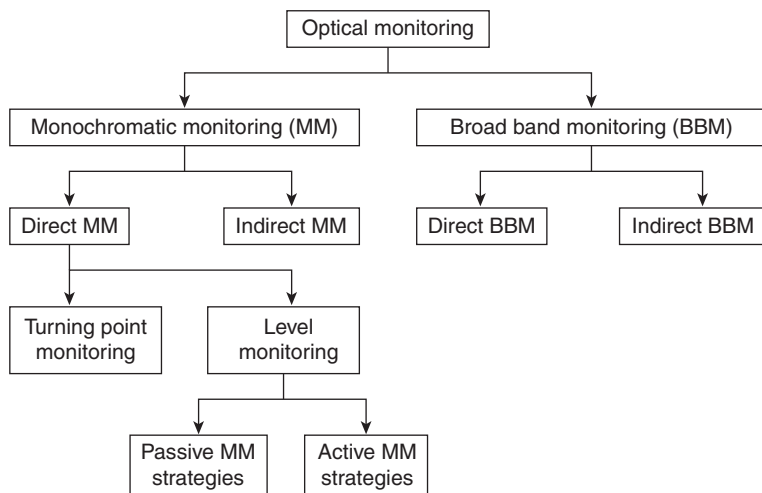
The most part of modern broad band optical monitoring devices are intended for direct monitoring of one of the samples produced in a vacuum chamber (Ristau *et al.*, 2006, 2008; Badoil *et al.*, 2007; Stenzel *et al.*, 2008). Along with many attractive features, direct optical monitoring may also have a serious disadvantage connected with the cumulative effect of thickness errors that reduces an accuracy of layer thickness monitoring when the number of deposited layers becomes big enough (Macleod, 2002, p. 509). To prevent the accumulation of errors with the growing number of deposited layers, indirect broad band monitoring systems with several monitoring chips can be used (Li and Yen, 1989; Sullivan and Dobrowolski, 1992; Zhupanov *et al.*, 2009). Pro et contra of various broad band optical monitoring approaches are discussed in this chapter.

A choice of monitoring technique and a selection of monitoring strategy for optical coating production is very much application dependent. This was clearly demonstrated by Sullivan and Dobrowolski (1992, 1993). Nowadays we have a much wider set of optical monitoring instrumentation, optical monitoring approaches and optical monitoring algorithms for processing on-line monitoring data than two decades ago. Knowing advantages and disadvantages of different optical monitoring strategies is a key to choosing a strategy that is most suitable for a particular application.

3.2 Classification of optical monitoring strategies

It is obvious from the introduction to this chapter that there is a great number of various optical monitoring strategies. The classification of the main types of these strategies is useful for a better orientation in their variety and it was discussed by several authors (Macleod, 1981; Willey, 1989; Sullivan and Dobrowolski, 1992). A primary subdivision is the subdivision into monochromatic monitoring (MM) and broad band monitoring (BBM) strategies. It is then essential to distinguish between direct and indirect strategies. In the case of direct monitoring, reflectance/transmittance measurements are performed on at least one of the coatings to be produced while, in the case of indirect monitoring, layer thicknesses are monitored on one or several separate witness chips. As pointed out by Macleod (1981) the main advantage of direct monitoring strategies is that we monitor the deposition on exactly one of the samples to be produced. In this chapter we pay special attention to the basic ideas and properties of direct MM and BBM strategies because these ideas and properties also form a basis for indirect optical monitoring strategies.

The classification of optical monitoring strategies is illustrated by Fig. 3.1. As discussed in the Introduction, direct MM strategies are subdivided into turning point optical monitoring and level monitoring. It was also proposed to further divide level monitoring strategies into passive and active ones (Tikhonravov *et al.*, 2006b). The term passive is applied to those strategies that are entirely specified prior to starting the coating deposition and in which neither the sequence of monitoring wavelengths nor the termination



3.1 Schematic illustrating main subdivisions of optical monitoring strategies.

levels are changed in the course of a coating production. In contrast, active strategies can use information obtained during the coating deposition to correct a course of a monitoring procedure. For example, reflectance/transmittance extrema passed during a layer deposition can be used for correcting reflectance/transmittance levels used for terminating layer depositions (Zhao, 1985; Laan, 1986). Monitoring strategies involving on-line re-optimizations of coating designs (Holm, 1978; Li and Yen, 1989; Sullivan and Dobrowolski, 1992) should also be considered as active strategies.

All monitoring strategies have their advantages and disadvantages. The main advantage of direct optical monitoring has been already mentioned but now it is necessary to discuss the main problem connected with this type of monitoring. Unfortunately, practically all direct monitoring strategies may give rise to a strong cumulative effect of thickness errors. This is connected to the fact that small errors in early layers affect monitoring of later layers (Macleod, 2002, p. 506). A detailed study of cumulative effect of thickness errors has been performed both for monochromatic (Tikhonravov *et al.*, 2006b) and broad band (Tikhonravov *et al.*, 2006a) optical monitoring and it was shown that total errors in layer thicknesses may be many times higher than direct errors in layer thicknesses made during the depositions of individual layers. With the total number of coating layers exceeding two-three dozens, the cumulative effect may lead to a total failure of the monitoring procedure.

The main reason for using indirect monitoring strategies is to prevent a rapid development of the cumulative effect of thickness errors due to limiting numbers of layers deposited on separate witness chips. At the same time, there is a principal objection towards indirect strategies connected with the fact that layers on witness chips do not have exactly the same thicknesses as layers on produced coatings (Macleod, 2002, p. 507). All indirect monitoring strategies require accurate calibrations of optical monitoring devices. The ratio of the layer thickness on witness chip to the layer thickness on produced sample is called calibration factor. Calibration factors are typically different for different thin film materials. They are also different for different deposition plants and different monitoring arrangements. For this reason, they should be accurately determined for each specific production environment.

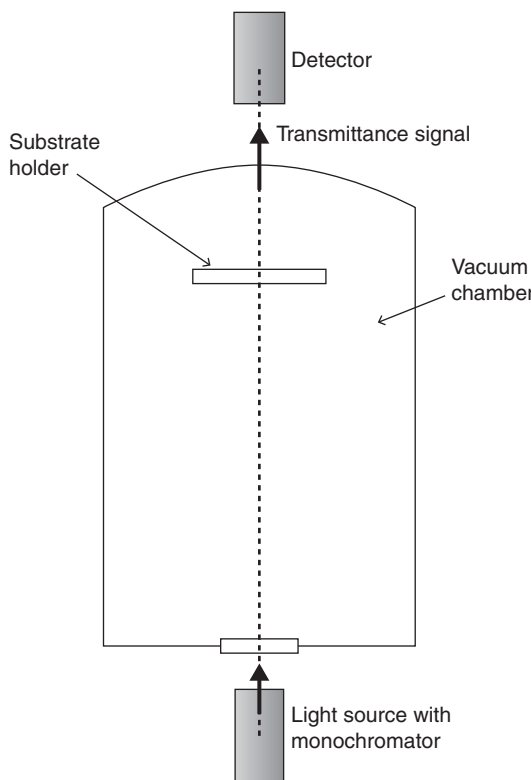
A commonly used approach to determining calibration factors is a preliminary deposition of relatively thick single layers of all thin film materials that will be used for coating production. Optical characterization of single layers on witness chips and produced samples is then performed in order to find thicknesses of these layers. It was shown in studies devoted to optical characterization that thin film optical thickness is always determined with much better accuracy than thin film physical thickness (Tikhonravov *et al.*, 2003). Thus it is better to specify calibration factors in terms of layer optical

thicknesses rather than in terms of layer physical thicknesses. Such definition of calibration factors is also correspondent with the essence of optical monitoring.

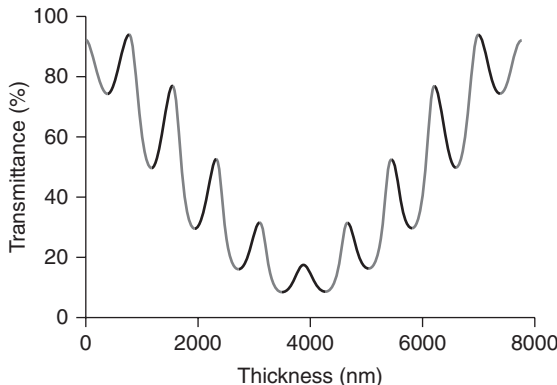
It is necessary to add one more note on the determination of calibration factors. Unfortunately these factors are not always stable and may vary from one deposition run to another. For this reason it may be useful to perform a permanent refinement of calibration factors. This can be done with the help of reverse engineering software based on the post-production optical characterization of produced optical coatings (Oliver *et al.*, 2001; Friedrich *et al.*, 2010).

3.3 Turning point optical monitoring and error self-compensation effect

Schematic of a possible arrangement for turning point optical monitoring is presented in Fig. 3.2.



3.2 Schematic of a possible arrangement for turning point optical monitoring.

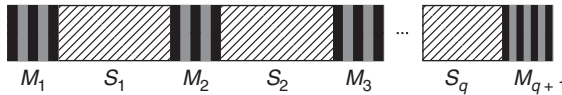


3.3 Transmittance of the 19-layer Fabry-Perot filter vs optical thickness of this filter: filter central wavelength is 1550 nm.

Consider monitoring of a simple Fabry-Perot filter having 19 layers and described by the design formula HLHLHLHLH2LHLHLHLHLH. Assume for calculations that refractive indices of high and low index layers are 2.065 and 1.465, respectively. The filter is supposed to be deposited on a glass substrate. Let the filter central wavelength be equal to 1550 nm. Figure 3.3 shows how the filter transmittance at the central wavelength of 1550 nm is expected to vary versus the optical thickness of deposited filter in the absence of measurement and production errors.

When the first high index quarter wave layer is deposited, the filter transmittance varies from its maximum to the minimum value which is achieved exactly when a layer with quarter wave optical thickness is deposited. The monitoring signal extremum values are referred to as turning points. For the next low index layer the filter transmittance varies from the achieved minimum value to the maximum value which again corresponds to the instant when the next quarter wave portion of optical thickness is deposited. The layer number ten is the so-called spacer layer for which optical thickness is two quarter waves. For this reason the deposition of this layer should be terminated when the second turning point of the monitoring signal (transmittance minimum) is achieved.

The essence of turning point monitoring is terminating layer depositions at instants when monitoring signal extrema are achieved. Due to inevitable errors in measurement data it is rather difficult to accurately determine instants corresponding to these extrema. In order to raise an accuracy of turning point determination a special processing of measurement data can be applied. Giacomo and Jacquinot (1952) were first to apply such processing on instrumentation level. They developed a system for measuring reflectance derivative versus wavelength instead of reflectance. At turning points this derivative goes through zero and varies most rapidly which helps to determine termination instants more accurately.



3.4 A general schematic of multi-cavity narrow band pass filter.

Now for raising an accuracy of turning point determination a computational processing of measurement data is usually applied.

With all possible precautions for raising an accuracy of turning point determination a relative accuracy of layer thickness control could not be better than one – several per cents. If thickness errors of such level were not correlated by the monitoring procedure, then it would be impossible to produce practically all narrow band pass filters for modern applications. Turning point monitoring has a special meaning for production of various filters for WDM applications. All these filters are multi-cavity resonance multilayer structures. For this reason we consider a physical mechanism of the error self-compensation effect for the general case of a filter with multiple spacer layers or, which is the same, with multiple resonance cavities.

A general schematic of multi-cavity narrow band pass filter is presented in Fig. 3.4. This filter has q spacer layers marked as S_1, \dots, S_q and $q + 1$ quarter wave mirrors marked as M_1, \dots, M_{q+1} . Optical thicknesses of spacer layers are integer times half wave optical thickness. Respective integers are called orders of spacer layers. All filters of the presented type are resonance structures with multiple resonance cavities formed by spacer layers and mirrors surrounding these layers (Thelen, 1989; Baumeister, 2004). It is known from the theory (Baumeister, 2004) that the filter spectral transmittance near the filter central wavelength is entirely specified by the number of filter cavities (spacer layers), reflectivities of filter mirrors and phase properties of filter cavities. For the filter central wavelength the full change of the phase for the wave making a full circle inside a spacer layer is integer times 2π . This is a condition of resonance inside a spacer layer. The filter spectral performance is destroyed as soon as the resonance condition is destroyed in at least one of the spacer layers.

The full change of the phase for the wave making a full circle inside a spacer layer is specified by the optical thickness of this spacer layer and phase shifts on reflection from surrounding mirrors. Even small errors in the optical thickness of a spacer lead to violating the resonance condition and as a sequence to the degradation of filter spectral performance. This fact was discovered computationally for Fabry-Perot filters many years ago (Lissberger, 1959).

Consider now errors in thicknesses of quarter wave mirrors. It is known from the theory (Furman and Tikhonravov, 1992) that these errors have only a very small effect on the mirror reflectivity near the mirror central

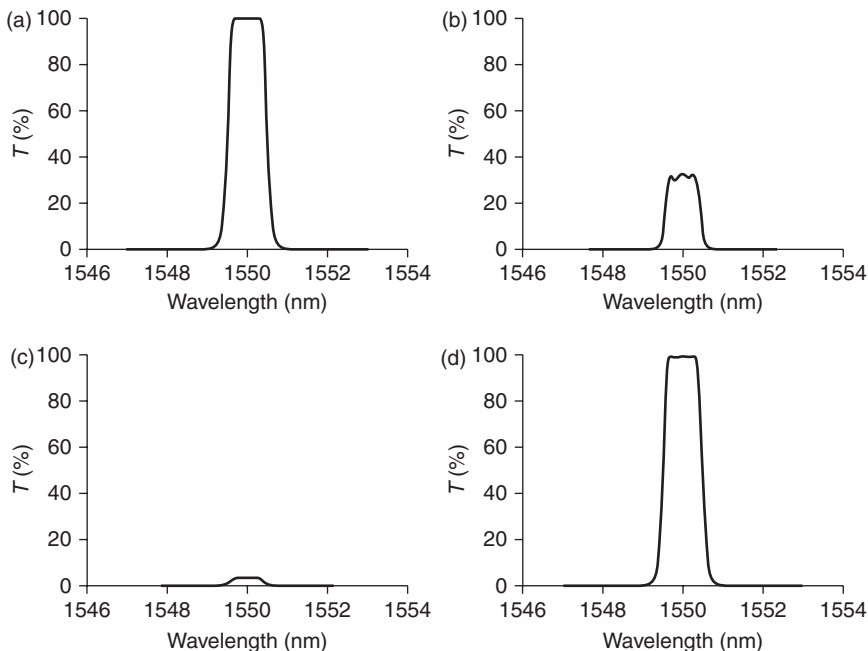
wavelength. At the same time these errors change the phase shift on reflection significantly. This means that they also affect phase properties of filter cavities. A general conclusion is that thickness errors affect spectral performance of the filter through violating resonance conditions in filter cavities.

It was rigorously proved (Tikhonravov and Trubetskoy, 2002) that terminating layer depositions at turning points adjusts errors in thicknesses of filter layers so that resonance conditions in filter cavities are fulfilled. Thus from a physical point of view the error self-compensation effect is nothing else but maintaining phase properties of filter cavities. It is clear therefore that an accurate control of turning points for mirror layers following spacer layers is especially important. The highest effect on phase properties is caused by variations of thicknesses of layers that follow immediately after spacer layers. This will be additionally demonstrated a little bit later.

To illustrate the error self-compensation effect, consider a four-cavity filter for WDM applications. This filter uses the same high index and low index materials as the Fabry-Perot filter discussed above. It has 122 layers and is described by the design formula $(HL)^7 6H(LH)^{14} L16H(LH)^{14} L16H(LH)^{14} L6H(LH)^7 L0.385H 1.283 L$. Note that only the last two design layers are non-quarter wave layers. They serve as an antireflection coating at the top of the WDM filter design.

The spectral transmittance of ideal filter with no errors in layer thicknesses is shown in Fig. 3.5a. Figure 3.5b shows what happens with the filter transmittance when there is only one +3% relative error in the thickness of the layer number 12. Additional +0.5% error in the thickness of the first spacer layer (layer number 15) leads to a full degradation of the filter transmittance near 1550 nm (see Fig. 3.5c). Figure 3.5d shows that both errors in layers number 12 and 15 can be entirely compensated by a proper variation of the thickness of layer number 16 that follows immediately after the spacer layer (thickness of this layer was reduced for 5.7%). Turning point optical monitoring performs such compensation automatically.

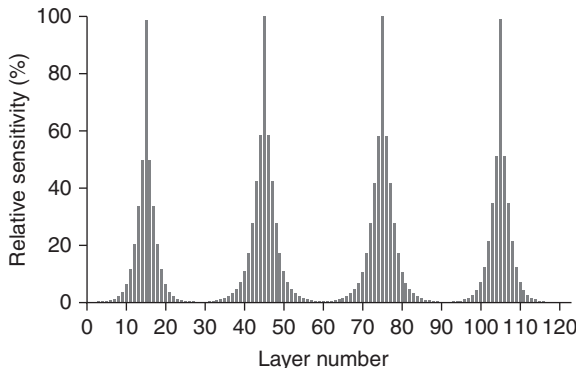
It is clear from a physical point of view that spectral performance of a narrow band pass filter is most sensitive to errors in thicknesses of spacer layers and nearby mirror layers. This fact is confirmed by the computational error analysis. Let us apply equal relative errors to all filter layers one by one. For each test we calculate root mean square deviations of the transmittances of filters with thickness errors from the transmittance of ideal filter with no errors. Denote these r.m.s. deviations as D_1, D_2, \dots, D_m where m is the total number of filter layers. Let D_{\max} be their maximum value. We assign 100% sensitivity to the layer with D_{\max} deviation. All other layers are ranged with respect to this layer so that their sensitivities are taken equal to $D_j / D_{\max} \cdot 100\%$ where j is the layer number.



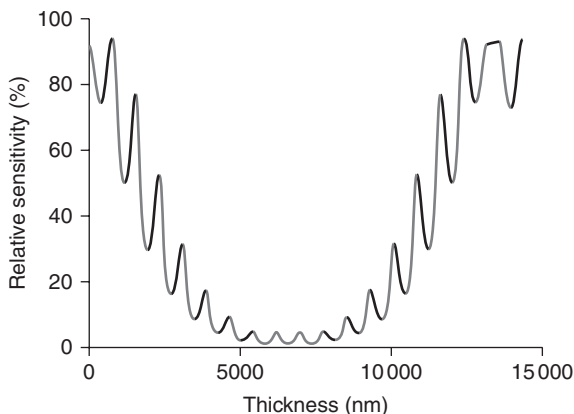
3.5 Illustration of the error self-compensation effect: (a) transmittance of the ideal four-cavity WDM filter with no errors in layer thicknesses; (b) transmittance of the same filter with only one +3% relative error in the thickness of the layer number 12; (c) transmittance of the same filter with +3% relative error in the thickness of layer number 12 and +0.5% error in the thickness of the first spacer layer (layer number 15); (d) transmittance of the same filter when +3% error in the thickness of layer number 12 and +0.5% error in the thickness of the layer number 15 are compensated by -5.7% error in the thickness of the layer number 16.

Figure 3.6 presents results of the error sensitivity analysis for the 122-layer WDM filter considered above. One can see that indeed most sensitive to thickness errors are spacer layers (layers number 15, 45, 75 and 105) and nearby mirror layers. Fortunately turning point optical monitoring provides a self-compensation of errors in thicknesses of these layers. It is also worth noting that errors in layers located far from spacer layers are not that critical. This note may be useful for planning monitoring strategy for multi-cavity WDM filters.

Figure 3.7 presents transmittance of the discussed four-cavity WDM filter at its central wavelength for the first 32 layers of this filter. One can see that the variation of monitoring signal for the layer number 30 is very small. During the deposition of this layer the filter transmittance varies only for 0.8% from the minimum value of 92.3% to the maximum value of 93.1%.



3.6 Error sensitivity analysis for the 122-layer four-cavity WDM filter.



3.7 Transmittance of the four-cavity WDM filter versus optical thickness of the first 32 layers of this filter.

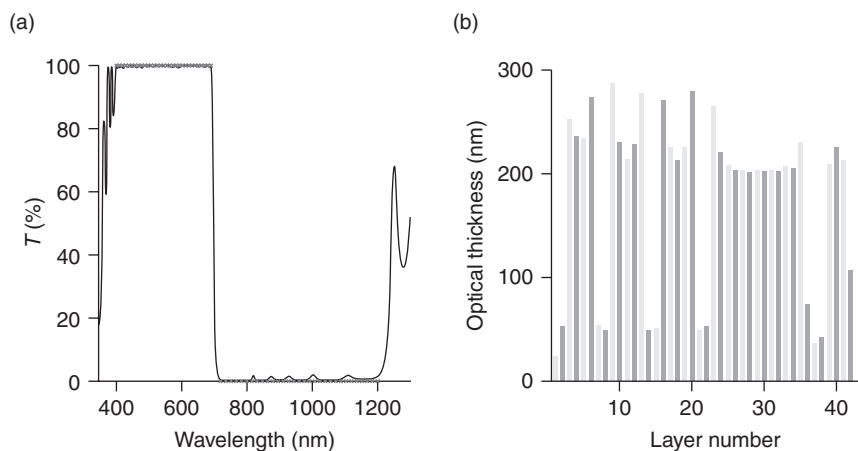
In the presence of measurement errors it is very difficult to monitor thicknesses of such layers optically. It is however not necessary to deposit all filter layers using turning point optical monitoring. Instead of this mixed monitoring strategy can be used.

Note that layer number 30 is located exactly between two filter spacer layers (see Fig. 3.6). Intermediate layers of this type are often referred to as coupling layers (Macleod, 2002, p. 518). It is seen from Fig. 3.6 that a thickness error in this layer is not critical. Instead of using an optical monitor, one can control the deposition of coupling layers using time monitoring or quartz crystal monitoring. These types of monitoring can also be used for the deposition of the last two layers of the considered filter. Recall that these are non-quarter wave layers serving as an antireflection coating.

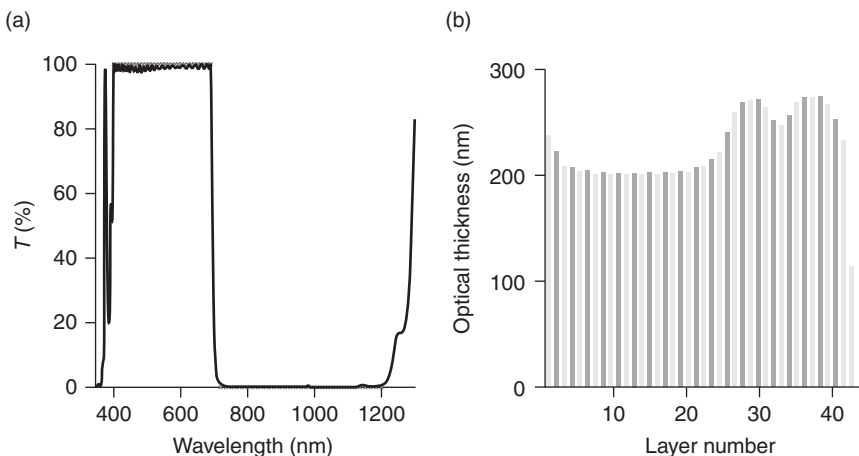
3.4 Level monitoring: passive and active monochromatic monitoring strategies

We start discussing level monitoring with what we call passive monitoring strategies. Recall that this term is applied to those strategies that are entirely specified prior to starting the deposition and neither sequences of monitoring wavelengths nor termination levels are changed in the course of a coating production. A passive level monitoring strategy is entirely specified by a monitoring spreadsheet where monitoring wavelengths and termination levels are indicated for all coating layers. Examples of monitoring spreadsheets corresponding to different monitoring strategies are provided below.

In this section we consider monitoring spreadsheets for two model design examples of a hot mirror with a high transmittance in visible and high reflectance in the infrared spectral band up to 1200 nm. Spectral transmittances of the designs are shown in Figs 3.8a and 3.9a. Optical thicknesses of design layers are presented in Figs 3.8b and 3.9b. Odd layers of both designs are high index layers with refractive indices 2.35 and even layers are low index layers with refractive indices 1.45. Refractive index of the substrates is 1.52. Discussion of modern design approaches is out of the scope of this chapter but it is necessary to make one note in the contest of choosing monitoring strategies. In many cases modern design techniques enable an optical coating engineer to obtain multiple solutions to a design problem (Tikhonravov *et al.*, 2007a). Multiple solutions with acceptable and almost equivalent spectral properties may have very different structural properties. This fact is illustrated by Figs 3.8 and 3.9. The first design depicted in Fig. 3.8b has several thin layers with optical thicknesses of about 20–50 nm while optical thicknesses of nearly all layers of the second design are higher than 200 nm



3.8 Spectral transmittance (a) and layer optical thicknesses (b) of the 42-layer hot mirror design.



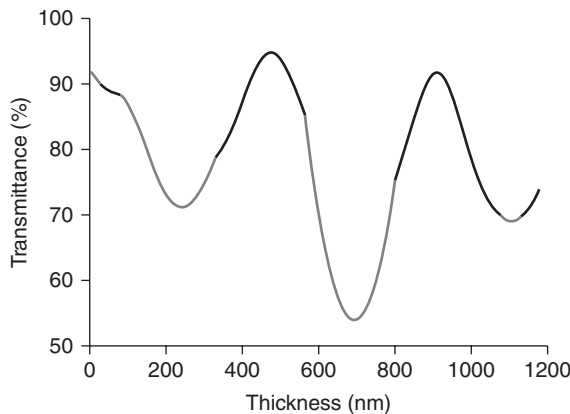
3.9 Spectral transmittance (a) and layer optical thicknesses (b) of the 40-layer hot mirror design.

Table 3.1 Monitoring spreadsheet for the 42-layer hot mirror design: rows corresponding to the first eight layers are shown

#	Material	Ph.th. (nm)	Chip	Layer number	Correction factor	Wavelength (nm)	Response (%)
1	H	10.03	1	1	1.0	700	91.8
2	L	35.66	1	2	1.0	700	90.3
3	H	107.7	1	3	1.0	700	88.6
4	L	162.5	1	4	1.0	700	78.6
5	H	99.77	1	5	1.0	700	85.3
6	L	189.3	1	6	1.0	700	75.3
7	H	23.12	1	7	1.0	700	70.3
8	L	33.74	1	8	1.0	700	69.7

and only the last layer has optical thickness of 113.6 nm (see Fig. 3.9b). It will be seen that an application of some monitoring strategies requires specific structural properties of a design. Thus an optimal choice of monitoring strategy is always correlated with a choice of optical coating design.

Table 3.1 presents the first eight rows of the monitoring spreadsheet for the 42-layer hot mirror design. The monitoring signal is coating transmittance at normal incidence. The first column of the table shows layer numbers starting from the substrate, the second column indicates abbreviations for layer refractive indices (H = high and L = low indices) and the third column gives physical thicknesses of layers. Columns 4–6 can be used for specifications of indirect monitoring strategies and will be discussed in Section 3.6. Monitoring wavelengths for coating layers are indicated in the seventh column. In this particular case we have the same monitoring wavelength



3.10 Monitoring signal (normal incidence transmittance) for the first eight layers of the 42-layer hot mirror: monitoring wavelength is 700 nm.

of 700 nm for all coating layers. The eighth column presents theoretically predicted variations of monitoring signal during layer depositions. The first values in all rows of this column are transmittance levels at the starts of layer deposition. The last values are transmittance levels at the ends of layer depositions, i.e., termination levels. In some rows there are also bold values in between the above ones. These are minima and maxima transmittance levels that are expected to be achieved during layer depositions. A special meaning of these values will be discussed later in connection with active monitoring strategies. A trace of the monitoring signal for the first eight layers corresponding to Table 3.1 is shown in Fig. 3.10.

Difficulties associated with optical monitoring of thin layers are immediately seen from Fig. 3.10. One can see that variations of the monitoring signal for the layers number 1, 2, 7 are less than 2%. In the presence of measurement errors it is difficult to monitor such small variations reliably and thus high errors in thicknesses of these layers are possible. Thus, in general, designs with no thin layers are preferable for applying optical monitoring strategies. For this reason in the following part of this section we proceed with the discussion of optical monitoring strategies using the 40-layer hot mirror design with no thin layers as an example.

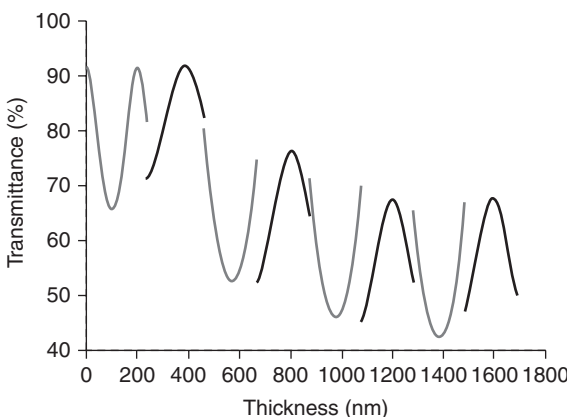
The choice of a sequence of monitoring wavelengths for all coating layers is one of the key issues in specifying optical monitoring strategy. One of the rigorously defined monitoring strategies is based on the choice of the so-called most sensitive monitoring wavelengths (Holm, 1978; Sullivan and Dobrowolski, 1992). The most sensitive wavelength is the wavelength from a monitoring spectral band where the derivative of monitoring signal versus layer thickness achieves its maximum value at the end of layer deposition.

A sequence of the most sensitive monitoring wavelengths can be easily calculated for a given coating design.

Table 3.2 presents the first eight rows of the monitoring spreadsheet corresponding to the strategy based on the choice of the most sensitive wavelengths for the 40-layer hot mirror design. Columns of the Table 3.2 are used as discussed above for Table 3.1. As before the monitoring signal is coating transmittance at normal incidence. The most sensitive monitoring wavelengths for coating layers have been chosen in the monitoring spectral band from 400 to 900 nm. A trace of the monitoring signal for the first eight design layers is shown in Fig. 3.11. One can see that the monitoring signal is now discontinuous. All discontinuities correspond to layer boundaries and are connected with changing of monitoring wavelength from layer to layer (see Table 3.2).

Table 3.2 Monitoring spreadsheet for the 40-layer hot mirror design: monitoring strategy based on the choice of the most sensitive wavelength, rows corresponding to the first eight layers are shown

#	Material	Ph.th. (nm)	Chip	Layer number	Correction factor	Wavelength (nm)	Response (%)
1	H	101.1	1	1	1.0	400	91.8 65.7 91.8 81.8
2	L	152.9	1	2	1.0	700	71.5 91.9 82.5
3	H	88.65	1	3	1.0	652	80.4 52.7 74.6
4	L	142.9	1	4	1.0	713	52.4 76.4 64.5
5	H	86.38	1	5	1.0	666	71.3 46.1 69.6
6	L	141.0	1	6	1.0	698	45.3 67.4 52.5
7	H	85.55	1	7	1.0	672	65.5 42.5 66.9
8	L	140.1	1	8	1.0	688	47.1 67.7 50.2



3.11 Monitoring signal (normal incidence transmittance) for the first eight layers of the 40-layer hot mirror: monitoring strategy based on the choice of the most sensitive wavelength.

The discussed strategy is based on the belief that choosing the most sensitive monitoring wavelength allows one to minimize thickness errors caused by errors in measurement data. This is however true only to a certain extent. Let us perform a simplified consideration of thickness errors which nevertheless will allow us to reveal the main problem associated with direct optical monitoring. Consider only random errors in transmittance measurement data and let us neglect all other factors that may cause errors in layer thicknesses. Suppose that at the end of the first layer deposition we have transmittance measured with an error $\delta T_{\text{meas}}^{(1)}$. This error will cause an error in the thickness of the first layer which is (Tikhonravov *et al.*, 2006b)

$$\delta d_1 = - \left[\frac{1}{\partial T^{(1)}/\partial d_1} \right] \delta T_{\text{meas}}^{(1)} \quad [3.1]$$

Here $\partial T^{(1)}/\partial d_1$ is the derivative of the transmittance of the first coating layer versus its thickness at the end of a layer deposition.

In the case of random measurement errors it is natural to suppose that they are distributed by the normal law. Denote σ_{meas} as a standard deviation of random errors in transmittance data. For the sake of simplicity assume that this value depends neither on the monitoring wavelength nor on the monitoring time. We shall refer to σ_{meas} as level of errors in measurement data. It follows from Equation [3.1] that the expected thickness error is also a random error distributed by the normal law. Its mean value is zero and its standard deviation is

$$\sigma_1 = \left| \frac{1}{\partial T^{(1)}/\partial d_1} \right| \sigma_{\text{meas}} \quad [3.2]$$

The value σ_1 and analogous values below will be called expected levels of errors in layer thicknesses. One can see that the expected error in the thickness of the first layer is minimized when the monitoring wavelength for this layer is chosen so as to maximize the modulus of the transmittance derivative $\partial T^{(1)}/\partial d_1$. This is nothing else but the choice of the most sensitive monitoring wavelength.

The monitoring strategy based on the choice of the most sensitive monitoring wavelength would be the best level monitoring strategy if there were no influence of errors in preceding layers on the accuracy of subsequent layers monitoring. Unfortunately, in the case of direct optical monitoring, errors in all preceding layers affect monitoring of all subsequent layers. Consider as an

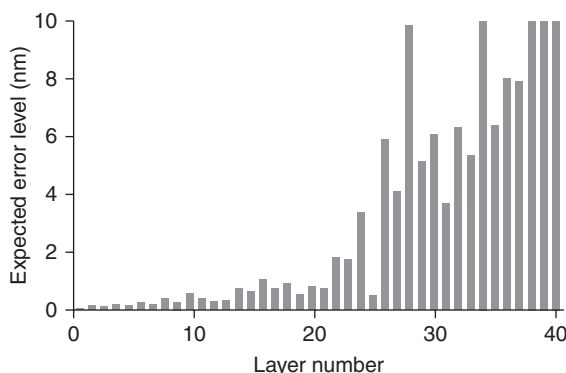
example monitoring of the second layer. The expected error in the thickness of the second layer is expressed by the equation (Tikhonravov *et al.*, 2006b):

$$\delta d_2 = -\left[\frac{1}{\partial T^{(2)}/\partial d_2} \right] \left[\delta T_{\text{meas}}^{(2)} + \frac{\partial T^{(2)}}{\partial d_1} \delta d_1 \right] \quad [3.3]$$

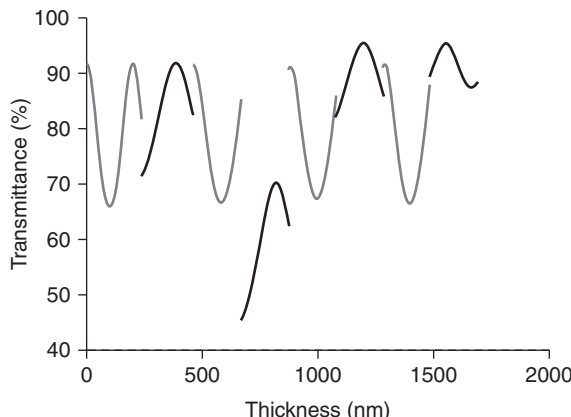
Here $\delta T_{\text{meas}}^{(2)}$ is the measurement error at the end of the second layer deposition, $\partial T^{(2)}/\partial d_1$ and $\partial T^{(2)}/\partial d_2$ are derivatives of the transmittance of the two-layer system vs thicknesses of the first and second layers that are also calculated at the end of the second layer deposition.

Equation [3.3] is basically different from Equation [3.1] because now we have an additional term in the second brackets representing the influence of the first layer error on the accuracy of monitoring of the second layer. Suppose that at the monitoring wavelength the modulus of the derivative $\partial T^{(2)}/\partial d_1$ is large. This means that there is a strong influence of errors in the first layer on the quality of monitoring of the second layer. In this situation the choice of the most sensitive monitoring wavelength, i.e., the wavelength where we have the largest modulus of the derivative $\partial T^{(2)}/\partial d_2$ is not necessarily the best choice.

Equation [3.3] represents what is called cumulative effect of thickness errors. A detailed investigation of this effect was performed by Tikhonravov *et al.* (2006b). Results of this study allow estimating of cumulative effect of thickness errors for any direct monochromatic monitoring strategy. Figure 3.12 shows expected levels of errors in the thicknesses of layers of the 40-layer hot mirror design when the monitoring strategy based on the



3.12 Expected levels of errors in thickness of layers of the 40-layer hot mirror in the case of monitoring strategy based on the choice of the most sensitive monitoring wavelengths: the level of random errors in transmittance data is 0.05%.



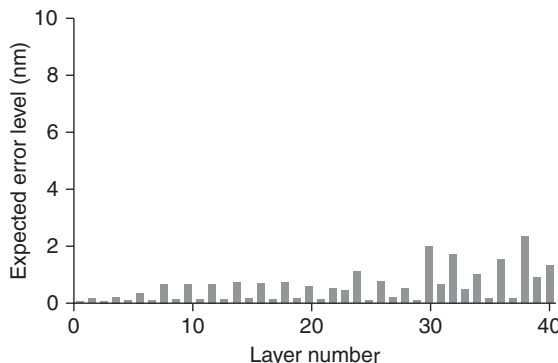
3.13 Monitoring signal (normal incidence transmittance) for the first eight layers of the 40-layer hot mirror: monitoring strategy aimed at minimizing the cumulative effect of thickness errors.

choice of the most sensitive monitoring wavelengths is applied. The level of random errors in transmittance data for this figure is equal to 0.05%. One can observe a rapid development of the cumulative effect with the growing number of coating layers. Note that for the last layers the expected errors were truncated at the 10 nm level.

Starting from layer number two, instead of choosing the most sensitive monitoring wavelength one can try to choose for each coating layer a compromise wavelength that will minimize the cumulative effect of thickness errors. The algorithm for calculating such compromise wavelengths has been developed (Tikhonravov *et al.*, 2006b) and we shall refer to the respective strategy as to the strategy aimed at minimizing the cumulative effect.

Figure 3.13 presents a monitoring signal for the first eight layers of the 40-layer hot mirror design when the monitoring strategy aimed at minimizing the cumulative effect is applied. The compromise monitoring wavelengths for this strategy have been chosen in the monitoring spectral band from 400 to 900 nm. One can see that starting from layer number two the monitoring signal in Fig. 3.13 differs from that in Fig. 3.11 which is connected with different choices of monitoring wavelengths.

Figure 3.14 shows expected levels of errors in the thicknesses of layers of the 40-layer hot mirror design when the monitoring strategy aimed at minimizing the cumulative effect of thickness errors is applied. The level of random errors in transmittance data for this figure is 0.05% as before. One can see that expected thickness errors are much smaller than in the case of monitoring strategy based on the choice of the most sensitive wavelengths. Nevertheless the development of the cumulative effect of thickness errors is still observed for the last coating layers.

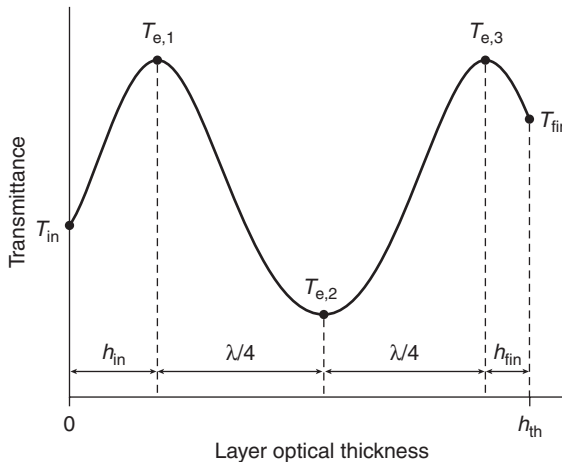


3.14 Expected levels of errors in thickness of layers of the 40-layer hot mirror in the case of monitoring strategy aimed at minimizing the cumulative effect of thickness errors: the level of random errors in transmittance data is 0.05%.

Above we considered only one factor causing errors in thicknesses of deposited coatings. In fact there is a long list of error factors that may cause production errors (Van der Laan, 1986; Tikhonravov and Trubetskoy, 2005). These are deviations of the refractive indices of thin film materials from layer to layer, bulk inhomogeneities of coating layers, thickness errors caused by inaccuracies in closing shutters terminating layer depositions, etc. The cumulative effect of thickness errors may cause an avalanche growth of thickness errors. As a result a real monitoring signal may be quite different to that predicted by the monitoring spreadsheet. Additionally calibration drifts of optical monitoring devices and fluctuations of a monitoring signal caused by fluctuations in light intensities due to various factors may also cause deviations in a monitoring signal. Active monochromatic monitoring strategies may help to overcome these problems.

One of the first active monitoring strategies was discussed by Van der Laan (1986). It was proposed to use monitoring signal extrema registered during layer depositions for the on-line correction of termination levels. In fact all active optical monitoring strategies explore this idea of using monitoring signal extrema for correcting termination levels.

Different active monitoring strategies differ in algorithms for correcting termination levels. A substantial progress in these algorithms has been achieved in recent years (Lee *et al.*, 2005; Chun *et al.*, 2006; Tikhonravov and Trubetskoy, 2007; Tikhonravov *et al.*, 2007b). Detailed descriptions of mathematical formulas of these algorithms are rather long and we refer an interested reader to the original works. Below we provide only a short description of main ideas of one of these algorithms (Tikhonravov and Trubetskoy, 2007). The main feature of this algorithm is that it allows one to entirely eliminate a cumulative effect of thickness errors. Under certain



3.15 Monitoring signal for a coating layer with several signal extrema passed during a layer deposition.

conditions a thickness of any new layer can be monitored independently of thickness errors made in preceding layers.

Consider monitoring of a coating layer with an optical thickness that is big enough for registering one or several monitoring signal extrema during a layer deposition. A schematic of monitoring signal for such layer is presented in Fig. 3.15. In this figure monitoring signal extrema are denoted as $T_{e,1}, \dots, T_{e,3}$. T_{in} and T_{fin} are monitoring signals at the start and at the end of layer deposition, h_{in} is a portion of layer optical thickness deposited at an instant when the first monitoring signal extremum is registered, and h_{fin} is a portion of layer optical thickness deposited between the instant corresponding to the last registered monitoring signal extremum and the end of layer deposition.

Due to errors in thicknesses of previously deposited layers all monitoring signal values indicated in Fig. 3.15 may be quite different from respective values indicated in the monitoring spreadsheet specified before coating deposition. Our goal is to correct the termination level T_{fin} so that an optical thickness of the considered layer can be controlled accurately and independently of thickness errors in preceding layers.

Portions of layer optical thickness deposited between two instants corresponding to two adjacent monitoring signal extrema are all equal to a quarter of monitoring wavelength. Therefore the layer optical thickness h can be represented in the form

$$h = h_{in} + (m - 1) \frac{\lambda}{4} + h_{fin} \quad [3.4]$$

where m is the number of monitoring signal extrema registered during the layer deposition.

Now we are able to outline the main steps of the termination level correction algorithm. It is rigorously proved (Tikhonravov and Trubetskoy, 2007) that knowing initial monitoring signal value T_{in} and the first monitoring signal extremum $T_{e,1}$, we are able to calculate the initial portion of layer optical thickness h_{in} . As soon as we know this value the final portion of layer optical thickness h_{fin} providing the required layer optical thickness h is calculated from Equation [3.4]. Knowing this value and the value of the last registered monitoring signal extremum $T_{e,3}$ we can calculate a new termination level T_{fin} . The calculation of a new termination level can be performed on-line immediately after registering the last monitoring signal extremum.

It is seen from the above considerations that for the application of described algorithm at least one monitoring signal extremum should be registered during the layer deposition. This requires that all coating layers have sufficient optical thicknesses. This demand relates to all active monochromatic monitoring strategies. For this reason optical coating designs with no thin layers may be preferable from the production point of view. One can see in Figs 3.11 and 3.13 that the 40-layer hot mirror design has layers that are thick enough to achieve monitoring signal extrema during layer depositions.

3.5 Direct broad band optical monitoring

An obvious trend of recent years is a growing interest in directing broad band optical monitoring. Several groups in different countries have been reporting a considerable progress in the development of broad band monitoring instrumentation and algorithmic tools for processing on-line monitoring data (Badoil *et al.*, 2007; Ristau *et al.*, 2008; Friedrich *et al.*, 2010). We cannot discuss here all features of the recently proposed strategies. For specific details it is better to refer to original publications as well as to the Chapter 4 of this book where one of these strategies is discussed in detail. In this section the main focus is devoted to basic principles, and advantages and disadvantages of direct broad band optical monitoring strategies.

One of the most attractive features of all broad band optical monitoring techniques is their low sensitivity to random errors in measurement data (Tikhonravov *et al.*, 2002). Tikhonravov *et al.* (2006a) performed a statistical analysis of the influence of errors of different types and, in particular, of random errors in measurement data on the accuracy of layer thickness monitoring. If only random errors in measurement data are considered then an expected level of errors in the thickness of the first layer is

$$\sigma(\beta_1) = \frac{\sigma_{\text{meas}}}{\left[\sum_{\{\lambda_k\}} (\partial T^{(1)} / \partial d_1)^2 \right]^{1/2}} \quad [3.5]$$

Here $\partial T^{(1)} / \partial d_1$ are the derivatives of the transmittance of the first coating layer versus its thickness calculated at the end of layer disposition for all wavelengths where broad band monitoring data are measured. The set of monitoring wavelengths is designated as $\{\lambda_k\}$ and the summation in Equation [3.5] is performed along all these wavelengths. For simplicity in Equation [3.5] we assume the level of random errors in measurement data σ_{meas} is the same in all monitoring spectral band. As in the previous section it is supposed that random errors have a normal distribution.

Modern monitoring devices record measurement data at many hundreds and even thousands of monitoring wavelengths. Thus there is a great number of terms in the sum of the denominator in Equation [3.5] and consequently this denominator is many times higher than the denominator in Equation [3.2] estimating a level of thickness errors in the case of monochromatic monitoring data. Analogous results for thickness errors originating from random errors in measurement data are obtained for all other coating layers (Tikhonravov *et al.*, 2006a). So it is theoretically proved that random errors in measurement data are not that dangerous for broad band optical monitoring as they are for monochromatic optical monitoring.

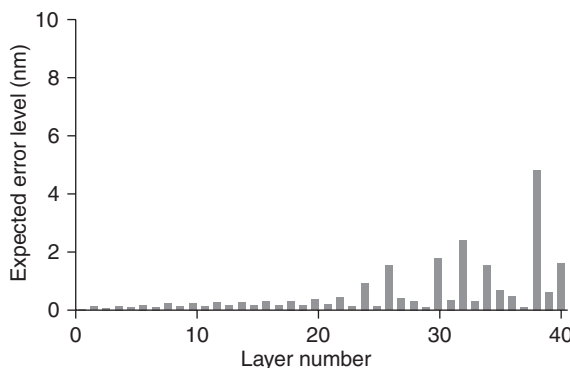
On the contrary with random errors, systematic errors in measurement data are extremely dangerous for all optical monitoring strategies. Such errors are always associated with calibration drifts of optical monitoring devices and permanent re-calibrations of these devices were proved to be necessary for a successful application of broad band optical monitoring (Sullivan and Dobrowolski, 1992). It is useful to perform re-calibrations before recording every new set of broad band measurement data. For calibrating the spectrometer it is typical to leave an empty position in the substrate holder and to record signals for this empty position and for an opaque position on the rotating calotte (Ristau *et al.*, 2002).

Along with low sensitivity to random errors there is another attractive feature of direct broad band optical monitoring. Already in the first works devoted to this subject (Vidal *et al.* 1978, 1979; Vidal and Pelletier, 1979), it was noted that some sort of error self-compensation mechanism is inherent in broad band optical monitoring. An existence of this effect was supposed to be based on results of computer simulations of depositions of relatively simple non-quarter wave coatings. A detailed investigation of the error self-compensation effect associated with direct broad band optical monitoring was performed only recently (Tikhonravov *et al.*, 2011). It was confirmed

for coatings of different types (hot mirrors, cold mirrors, band pass filters, narrow band pass filters, multi-line filters) that the effect is really present. It was also found that whether the effect is strong or not depends not only on the type of optical coating but also on the choice of specific design of coating of a given type. Thus it may be useful to perform a pre-production investigation of multiple designs with close spectral properties for choosing one that is most suitable for production with broad band optical monitoring. We discuss this issue in more detail at the end of the section.

Obviously an error self-compensation effect is possible only if thickness errors in coating layers are correlated by monitoring procedure. All direct optical monitoring procedures correlate thickness errors due to the fact that errors in preceding layers affect an accuracy of monitoring of subsequent layers through variations of a monitoring signal connected with already made errors. But there is also a serious problem associated with correlation of errors. This is a cumulative effect of thickness errors. A detailed investigation of this effect for the case of direct broad band optical monitoring was presented by Tikhonravov *et al.* (2006a). In this study various error factors were considered and formulas allowing pre-production estimation of thickness errors caused by these factors were derived.

As an example Fig. 3.16 presents expected levels of errors in thicknesses of the 40-layer hot mirror (see Section 3.4) in the case of broad band optical monitoring with transmittance data measured at 501 spectral points in the wavelength range from 400 to 900 nm. For calculating expected levels of thickness errors in Fig. 3.16 only random errors in transmittance data with 0.5% level were specified. This was done for comparing effects of random errors in the cases of monochromatic monitoring and broad band monitoring.



3.16 Expected levels of errors in thicknesses of the 40-layer hot mirror in the case of broad band monitoring in the range 400–900 nm: the level of random measurement errors is 0.5%.

Expected levels of errors in the thicknesses of layers of the 40-layer hot mirror design in the case of monochromatic monitoring strategy based on the choice of the most sensitive monitoring wavelengths were presented in Fig. 3.12. Recall that the level of random errors in transmittance data for this figure was equal to 0.05%. The level of random errors in broad band monitoring data in the case of Fig. 3.16 is ten times higher than this value. At the same time levels of thickness errors in Fig. 3.16 are several times less than in Fig. 3.12. This vividly demonstrates a low sensitivity of broad band optical monitoring to random errors in measurement data.

A cumulative effect of thickness errors is clearly observed in Fig. 3.16. It is possible to estimate expected levels of thickness errors also for other factors causing production errors, such as systematic drifts of measurements data, direct thickness errors made in individual layers due to inaccuracies of closing shutters, instabilities of deposition rates, etc. (Tikhonravov *et al.*, 2006a). A cumulative effect of thickness errors is observed in all situations. For the 40-layer hot mirror designs it becomes especially strong after depositing half of its layers.

In the case of direct broad band optical monitoring there are two main approaches to overcoming problems associated with the cumulative effect of thickness errors. The first one is including on-line re-optimization in optical monitoring strategies (Li and Yen, 1989; Sullivan and Dobrowolski, 1992; Tikhonravov and Trubetskoy, 2004; Ristau *et al.*, 2008; Friedrich *et al.*, 2010; Schlichting *et al.*, 2011). The second one is pre-production choice of the most manufacturable design from a set of possible theoretical designs (Tikhonravov and Trubetskoy, 2002; Friedrich *et al.*, 2010). Both approaches widely explore such powerful research tool as computational manufacturing of optical coatings (Tikhonravov and Trubetskoy, 2005). In fact computational manufacturing, or computer simulation of deposition and monitoring processes, was used as a powerful tool for optimizing broad band optical monitoring strategies from the very early days of their elaboration (Vidal *et al.*, 1978).

3.6 Indirect optical monitoring strategies

The main reason for using indirect optical monitoring strategies is reducing the number of layers monitored on a single witness chip and, as a consequence, preventing a rapid development of cumulative effect of thickness errors caused by monitoring of a large number of layers on a single substrate (Sullivan and Dobrowolski, 1992). Choosing an optimal indirect monitoring strategy is still an open question because a great variety of such strategies potentially exist. In the case of monochromatic monitoring one can vary a number of witness chips being used, numbers of layers monitored on various chips and monitoring wavelengths. As an example

Table 3.3 Monitoring spreadsheet for the 40-layer hot mirror design: indirect monitoring strategy using a new witness chip for monitoring of each new pair of high and low index layers, rows corresponding to the first eight layers are shown

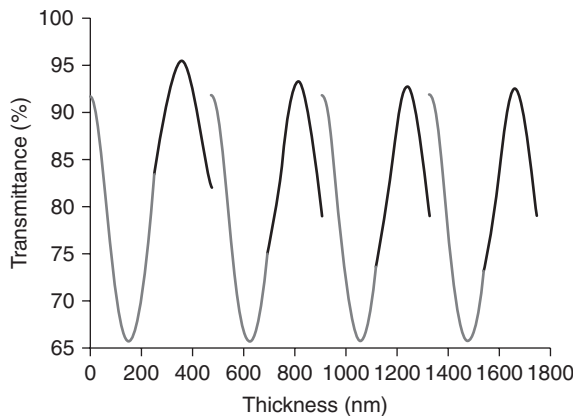
#	Material	Ph.th. (nm)	Chip	Layer number	Correction factor	Wavelength (nm)	Response (%)
1	H	101.1	1	1	1.05	600	91.8 65.7 83.4
2	L	152.9	1	2	1.02	600	83.4 95.5 82.1
3	H	88.65	2	1	1.05	600	91.8 65.7 75.0
4	L	142.9	2	2	1.02	600	75.0 93.3 79.1
5	H	86.38	3	1	1.05	600	91.8 65.7 73.6
6	L	141.0	3	2	1.02	600	73.6 92.8 79.0
7	H	85.55	4	1	1.05	600	91.8 65.7 73.1
8	L	140.1	4	2	1.02	600	73.1 92.6 79.1

we consider only one possible indirect monochromatic monitoring strategy. This strategy is specified for the 40-layer hot mirror discussed in the previous sections.

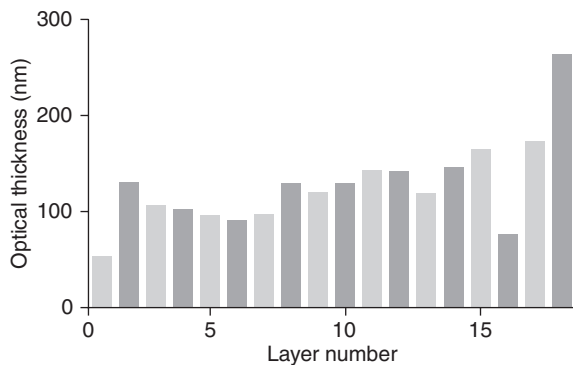
Table 3.3 presents the first eight rows of the monitoring spreadsheet corresponding to the indirect strategy using a new witness chip for monitoring of each new pair of high and low index layers. The number of a witness chip being used is indicated in the fourth column of the table. The fifth column shows layer numbers on particular chips. The sixth column presents calibration factors for high and low index layers. All other columns are used as described above for Tables 3.1 and 3.2.

As in Tables 3.1 and 3.2 the monitoring signal is coating transmittance at normal incidence. The calibration factors indicated in the sixth column of Table 3.3 are used to recalculate thicknesses of design layers to the thicknesses of layers on witness chips and then to calculate traces of monitoring signals for all witness chips. These traces for the first four chips are shown in Fig. 3.17.

A strong argument against using indirect monitoring strategies is a necessity to know accurately calibration factors for recalculating thicknesses of coating layers (Macleod, 2002, p. 507). Zöller *et al.* (2011) have presented a very promising monitoring arrangement that allows one to combine advantages of direct and indirect optical monitoring. They placed a witness chips changer on the rotating substrate holder where produced samples are located. Due to this arrangement a pre-production calibration of witness chips is not required anymore. The changer may have up to four witness chips and they can be changed after depositing of a part of coating layers in order to prevent a rapid development of the error accumulation effect. A successful application of this new device with the monochromatic monitor has been demonstrated and it has been indicated that the witness chip changer can be used in combination with broad band optical monitors as well (Zöller *et al.*, 2011).



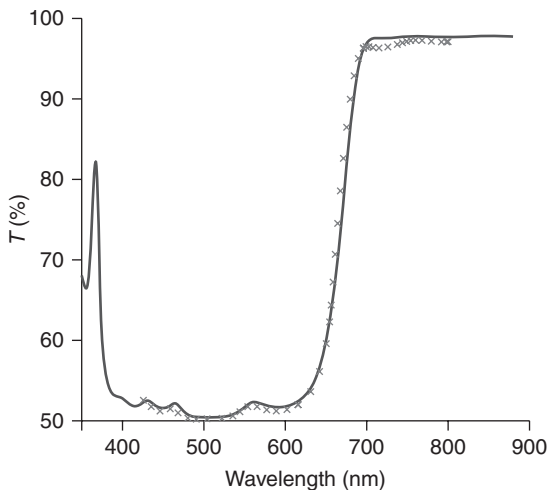
3.17 Traces of monitoring signal (transmittance) for the first four witness chips used for indirect monitoring of the 40-layer hot mirror.



3.18 Layer optical thicknesses of the 18-layer filter with TiO_2 odd layers (light bars) and SiO_2 even layers (dark bars).

It is typical for indirect monitoring strategies to use witness chips for monitoring of subsequent groups of coating layers (Li and Yen, 1989; Zöller *et al.*, 2011). However, only one possible approach and other strategies may be useful. The original indirect broad band monitoring strategy where different witness chips are used to monitor not groups of subsequent layers but layers chosen from a design in a special manner has been recently presented (Zhupanov *et al.*, 2009). An application of this strategy was demonstrated for the 18-layer filter with layer optical thicknesses shown in Fig. 3.18. Odd and even layers of the filter are respectively titanium dioxide and silica dioxide layers. They are denoted below as H and L layers. Theoretical transmittance of the filter is shown by solid curve in Fig. 3.19.

The described monitoring strategy is specified by establishing a correspondence between layers of deposited coating and layers of witness chips



3.19 Theoretical transmittance of the 18-layer filter (solid curve) and measured transmittance of the produced filter (crosses).

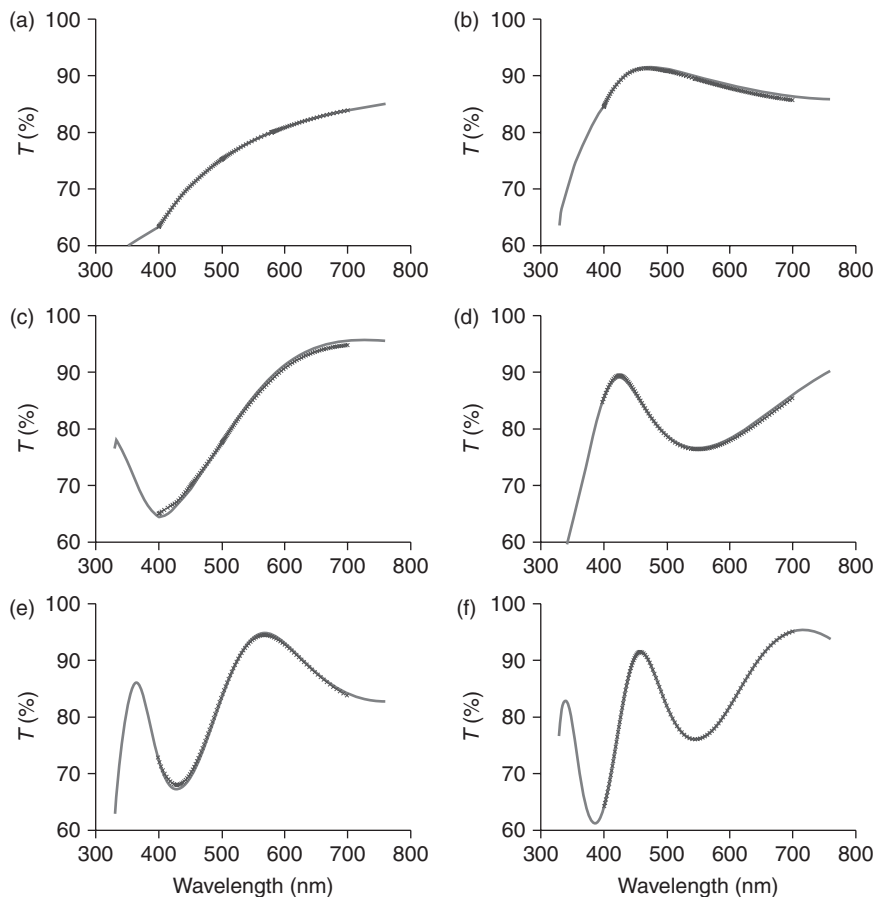
Table 3.4 Assignment of witness chips for monitoring of different filter layers

T-slide 1	T-slide 2	T-slide 3	T-slide 4
1, H	3, H	11, H	13, H
2, L	5, H	12, L	15, H
4, L	7, H	14, L	17, H
6, L	9, H	16, L	
8, L		18, L	
10, L			

used for thickness monitoring. Witness chips are numbered according to an order in which they are brought to a measurement position for the first time. Table 3.4 presents the strategy used for depositing the 18-layer filter. The first witness chip is used for monitoring the first filter layer (high index layer) and then for monitoring five low index layers with numbers 2, 4, 6, 8, 10. The second witness chip is used for monitoring four high index layers with numbers 3, 5, 7, 9 and so on. In the course of the filter production, the first two layers are monitored using the witness chip 1. For monitoring of the third layer this chip is replaced by the chip 2, but then the witness chip 1 is again placed to the measurement position and is used for monitoring the fourth filter layer. It is clearly seen from Table 3.4 how all subsequent layers are monitored.

Of course it is possible to assign monitored layers to witness chips in a different way and thus to specify a different monitoring strategy. It was already

mentioned that choosing of an optimal strategy is still an open question. Nevertheless some useful recommendations for specifying strategies of the considered type have been provided (Zhupanov *et al.*, 2009). It is recommended to monitor low index layers not on a bare witness chip but on a chip that has been already used for monitoring of a high index layer. This increases the contrast between a refractive index of a low index layer and effective admittance of an underlying chip. Increasing this contrast facilitates accurate monitoring of thicknesses of low index layers. A deposition of layers of one material on a particular witness chip is also recommended because this also increases an accuracy of optical monitoring. A physical explanation of this fact has been provided by Zhupanov *et al.* (2009).



3.20 Predicted transmittances (solid curves) and actually measured transmittances (crosses) of the witness chip used for monitoring layers 1, 2, 4, 6, 8, 10.

Figure 3.20a–3.20f shows theoretically predicted transmittances (solid curves) and actually measured transmittances of the witness chip 1 at the ends of depositions of filter layers with numbers 1, 2, 4, 6, 8 and 10. The transmittance of the manufactured 18-layer filter is shown in Fig. 3.19 by crosses.

3.7 Conclusion

Up to now a great variety of optical monitoring strategies has been proposed. Unfortunately there is no single universal strategy providing an accurate thickness monitoring in all situations. The choice of monitoring approach is dependent on the production environment as well as on the type of optical coating that one wants to manufacture. The classification of monitoring strategies provided in this chapter may help one to make a proper choice. It is also important to know pro et contra of direct and indirect monitoring approaches, of passive and active monitoring strategies. For some types of optical coatings a choice of monitoring strategy should be correlated with a choice of optimization technique used for constructing an optical coating design. Multi-cavity narrow band pass filters with steep transmittance slopes are the most obvious examples of such coatings. If one wants to explore the powerful error self-compensation effect associated with turning point optical monitoring of such filters then it is necessary to employ a special optimization technique that allows one to design filters with quarter wave and multiple quarter wave optical thicknesses of its layers (Tikhonravov and Trubetskoy, 2002).

In this chapter all main groups of optical monitoring strategies based on spectrophotometric measurement data have been discussed. Additionally it should be mentioned that there are also monitoring approaches based on exploring ellipsometric measurement data. An overview of these approaches was recently provided by Dligatch (2010). The most impressive demonstration of potentialities of *in situ* ellipsometric monitoring is a successful deposition of a complex notch filter with 79 layers (Dligatch *et al.*, 2004). Nevertheless monitoring strategies based on *in situ* ellipsometric data have not been discussed in detail in this chapter for two tightly connected reasons. First of all these strategies are used on a much smaller scale than spectrophotometric monitoring strategies. Second, a technical implementation of *in situ* ellipsometric measurements is more difficult than implementation of *in situ* photometric measurements because it is necessary to perform a system alignment on a rotating substrate and to overcome problems connected with the substrate wobble (Dligatch *et al.*, 2004).

It has been already mentioned several times that all monitoring strategies have their advantages and disadvantages. Combining the advantages of different strategies has therefore a great potential for raising the accuracy of thickness monitoring. As an example of combined strategies, we have

discussed monitoring of WDM filters. The most part of WDM filter layers can be monitored using turning point monitoring while the coupling layers and the outermost antireflection layers can be monitored using different approaches. In the future one should expect much wider implementation of combined strategies, in particular, combining broad band monitoring approaches with monochromatic monitoring approaches.

An essential advantage of *in situ* ellipsometric measurements is the ability to determine a film refractive index along with a film thickness (Chtanov *et al.*, 2010; Rademacher *et al.*, 2011). The refractive index of films may vary from layer to layer (Dligatch, 2010) and *in situ* determination of refractive indices may help to raise an accuracy of optical monitoring. It is therefore important to develop spectrophotometric monitoring strategies and reliable algorithms for spectrophotometric data analysis that can provide a simultaneous *in situ* determination of layer refractive indices and layer thicknesses. In many application areas there is a great demand for the production of complex optical coatings that require high accuracy monitoring of layer parameters and there is no doubt that a great progress in optical monitoring techniques should be expected in the near future.

3.8 References

- Banning, M. (1947) 'Practical methods of making and using multilayer filters', *Journal of the Optical Society of America*, **37**, 792–795.
- Baumeister, Ph. (2004) *Optical Coating Technology*, SPIE, Washington.
- Bousquet, P., Fournier, A., Kowalczyk, R., Pelletier, E. and Roche, P. (1972) 'Optical filters: monitoring process allowing the auto-correction of thickness errors', *Thin Solid Films*, **13**, 285–290.
- Chtanov, A., Dligatch, S. and Gross, M. (2010) 'Multi-Wavelength Laser Ellipsometer for *in situ* Monitoring of Optical Coatings,' in *Optical Interference Coatings*, OSA Technical Digest (Optical Society of America), paper TuC7.
- Chun, C., Kwon Hwangbo, C. and Sup Kim, J. (2006) 'Optical monitoring of non-quarterwave layers of dielectric multilayer filters using optical admittance', *Optics Express*, **14**, 2473–2480.
- Dligatch, S., Netterfield, R. and Martin, B. (2004) 'Application of *in-situ* ellipsometry to the fabrication of multi-layer optical coatings with sub-nanometre accuracy', *Thin Solid Films*, **455–456**, 376–379.
- Dligatch, S. (2010) '*In situ* ellipsometric monitoring of complex multilayer designs', *Chinese Optics Letters*, **8**, 44–48.
- Friedrich, K., Wilbrandt, S., Stenzel, O., Kaiser, N. and Hoffman, K.H. (2010) 'Computational manufacturing of optical interference coatings: method, simulation results, and comparison with experiment', *Applied Optics*, **49**, 3150–3162.
- Furman, Sh. and Tikhonravov, A. (1992) *Basics of Optics of Multilayer Systems*, Edition Frontieres, Gif-sur-Yvette.
- Giacomo, P. and Jacquinot, P. (1952) 'Localisation pr'écise d'un maximum ou d'un minimum de transmission en fonction de la longeur d'onde. Application à la pr'éparation des couches minces', *Journal de Physique et le Radium*, **13**, 59A–64A.

- Holm, C. (1978) 'Optical thin film production with continuous reoptimization of layer thicknesses', *Applied Optics*, **18**, 1978–1982.
- Laan, C. (1986) 'Optical monitoring of nonquarterwave stacks', *Applied Optics*, **25**, 757–760.
- Lee, C.-C., Wu, K., Kuo, C.-C. and Chen, S.-H. (2005) 'Improvement of the optical coating process by cutting layers with sensitive monitoring wavelengths', *Optics Express*, **13**, 4854–4861.
- Lissberger, P. (1959) 'Properties of all-dielectric interference filters. I. A new method of calculation', *Journal of the Optical Society of America*, **49**, 121–122.
- Li, L. and Yen, Y. (1989) 'Wideband monitoring and measuring system for optical coatings', *Applied Optics*, **28**, 2890–2894.
- Macleod, A. (1972) 'Turning value monitoring of narrow-band all-dielectric thin-film optical filters', *Optica Acta*, **19**, 1–28.
- Macleod, A. (1981) 'Monitoring of optical coatings', *Applied Optics*, **20**, 82–89.
- Macleod, A. (2001) *Thin-Film Optical Filters*, Third Edition (Series in Optics and Optoelectronics), Bristol and Philadelphia, Institute of Physics Publishing.
- Oliver, J., Tikhonravov, A., Trubetskoy, M., Kochikov, I. and Smith, D. (2001), 'Real-Time characterization and optimization of e-beam evaporated optical coatings', *Optical Interference Coatings (OIC) 2001, OSA Technical Digest Series*, ME8.
- Pervak, V., Tikhonravov, A., Trubetskoy, M., Pistner, J., Krausz, F. and Apolonski, A. (2007) 'Band filters: 2-material technology versus rugate', *Applied Optics*, **46**, 1190–1193.
- Rademacher, D., Vergöhl, M. and Richter, U., (2011) 'In situ thickness determination of multilayered structures using single wavelength ellipsometry and reverse engineering', *Applied Optics*, **50**, C222–C227.
- Ristau, D., Ehlers, H., Gross, T. and Lappschies, M. (2006) 'Optical broadband monitoring of conventional and ion processes', *Applied Optics*, **45**, 1495–1501.
- Ristau, D., Ehlers, H., Schlichting, S. and Lappschies, M. (2008) 'State of art in deterministic production of optical thin films', *Proceedings of SPIE*, **7101**, 71010C-1–71010C-13.
- Schlichting, S., Heinrich, K., Ehlers, H. and Ristau, D. (2011) 'Online re-optimization as a powerful part of enhanced strategies in optical broadband monitoring', *Proceedings of SPIE*, **8168**, 81681E.
- Stenzel, O., Wilbrandt, S., Fasold, D. and Kaiser, N. (2008) 'A hybrid in situ monitoring strategy for optical coating deposition: application to the preparation of chirped dielectric mirrors', *Journal of Optics A: Pure and Applied Optics*, **10**, 1–8.
- Sullivan, B. and Dobrowolski, J. (1992) 'Deposition error compensation for optical multilayer coatings. I. Theoretical description', *Applied Optics*, **31**, 3821–3835.
- Sullivan, B. and Dobrowolski, J. (1993) 'Deposition error compensation for optical multilayer coatings. II. Experimental results – sputtering system', *Applied Optics*, **32**, 2351–2360.
- Thelen, A. (1989) *Design of Optical Interference Coatings*, McGraw-Hill, New York.
- Tikhonravov, A. and Trubetskoy, M. (2002) 'Automated design and sensitivity analysis of wavelength-division multiplexing filters', *Applied Optics*, **41**, 3176–3182.
- Tikhonravov, A. and Trubetskoy, M. (2004) 'On-line characterization and reoptimization of optical coatings', *Proceedings of SPIE*, **5250**, 406–413.
- Tikhonravov, A. and Trubetskoy, M. (2005) 'Computational manufacturing as a bridge between design and production', *Applied Optics*, **44**, 6877–6884.

- Tikhonravov, A. and Trubetskoy, M. (2007) 'Elimination of cumulative effect of thickness errors in monochromatic monitoring of optical coating production: theory', *Applied Optics*, **46**, 2084–2090.
- Tikhonravov, A., Trubetskoy, M., Kokarev, M., Amotchkina, T. and Duparré, A. (2002) 'Effect of systematic errors in spectral photometric data on the accuracy of determination of optical parameters of dielectric thin films', *Applied Optics*, **41**, 2555–2560.
- Tikhonravov, A., Trubetskoy, M. and DeBell, G. (2003) 'On the accuracy of optical thin film parameter determination based on spectrophotometric data', *Proceedings of SPIE*, **5188**, 190–199.
- Tikhonravov, A., Trubetskoy, M. and Amotchkina, T. (2006a) 'Investigation of the effect of accumulation of thickness errors in optical coating production using broadband optical monitoring', *Applied Optics*, **45**, 7026–7034.
- Tikhonravov, A., Trubetskoy, M. and Amotchkina, T. (2006b) 'Statistical approach to choosing a strategy of monochromatic monitoring of optical coating production', *Applied Optics*, **45**, 7863–7870.
- Tikhonravov, A., Trubetskoy, M. and DeBell, G. (2007a) 'Optical coating design approaches based on the needle optimization technique', *Applied Optics*, **46**, 704–710.
- Tikhonravov, A., Trubetskoy, M. and Amotchkina, T. (2007b) 'Elimination of cumulative effect of thickness errors in monochromatic monitoring of optical coating production: theory', *Applied Optics*, **46**, 6936–6944.
- Tikhonravov, A., Trubetskoy, M. and Amotchkina, T. (2011) 'Investigation of the error self-compensation effect associated with broadband optical monitoring', *Applied Optics*, **50**, C111–C116.
- Vidal, B., Fournier A. and Pelletier, E. (1978) 'Optical monitoring of nonquarterwave multilayer filters', *Applied Optics*, **17**, 1038–1047.
- Vidal, B. and Pelletier, V. (1979) 'Nonquarterwave multilayer filters: optical monitoring with a minicomputer allowing correction of thickness errors', *Applied Optics*, **18**, 3857–3862.
- Vidal, B., Fournier, A. and Pelletier, E. (1979) 'Wideband optical monitoring of non-quarterwave multilayer filters', *Applied Optics*, **18**, 3851–3856.
- Willey, R. (1989) 'Optical thickness monitoring sensitivity improvement using graphical methods', *Applied Optics*, **26**, 729–737.
- Zhao, F. (1985) 'Monitoring of periodic multilayers by the level method', *Applied Optics*, **24**, 3339–3342.
- Zhupanov, V., Klyuev, E., Alekseev, S., Kozlov, I., Trubetskoy M., Kokarev, M. and Tikhonravov, A. (2009) 'Indirect broadband optical monitoring with multiple witness substrates', *Applied Optics*, **48**, 2315–2320.
- Zöller, A., Hagedorn, H., Weinrich, W. and Wirth, E. (2011) 'Testglass changer for direct optical monitoring', *Proceedings of SPIE*, **8168**, 81681J.

Production strategies for high-precision optical coatings

H. EHLERS and D. RISTAU,
Laser Zentrum Hannover, Germany

DOI: 10.1533/9780857097316.1.94

Abstract: This chapter is dedicated to advanced monitoring and control concepts for deposition processes employed in the production of optical coatings. After a motivation before the background of recent challenges in optical coating technologies and their application, an introduction will be given into implementations of optical broad band monitoring concepts as well as related instruments to simulate deposition processes and to detect errors during a deposition run. Also, selected examples will be outlined to support the versatility of these new approaches. Finally, a section will be concentrated on ternary oxides as material mixtures and rugate filters produced by co-deposition processes.

Key words: broad band optical monitoring, virtual deposition processes, reverse engineering, on-line error detection and correction, ternary oxides, co-deposition, rugate filters.

4.1 Introduction

Trends in modern photonics clearly indicate the need for optical components with ever increasing quality and demanding spectral transfer properties. In this context, laser technology can be considered as an important pacemaker with an enormous economic and innovation potential. Looking back just two decades into the past, most commercial laser systems contained a few discrete optical components with typical sizes in the centimeter range specified for a single wavelength or constricted spectral range. Nowadays, systems with orders of magnitude higher performance are assembled to highest compactness with a large variety of special optical components individually tailored in their functioning and geometry to the requirements of the laser and its manufacturing process. This development can be considered as representative for many other fields in modern optics including communication technology, precise measurement methods or consumer products. As a consequence, new challenges are also imposed on the production of optical coatings, not only in respect to the quality, precision and difficult specifications

covering broader spectral ranges. Even more, the market position of a coating factory will sensitively depend on the flexibility and diversification of the implemented production chain and coating processes allowing for the delivery of special coatings in small quantities within short times.

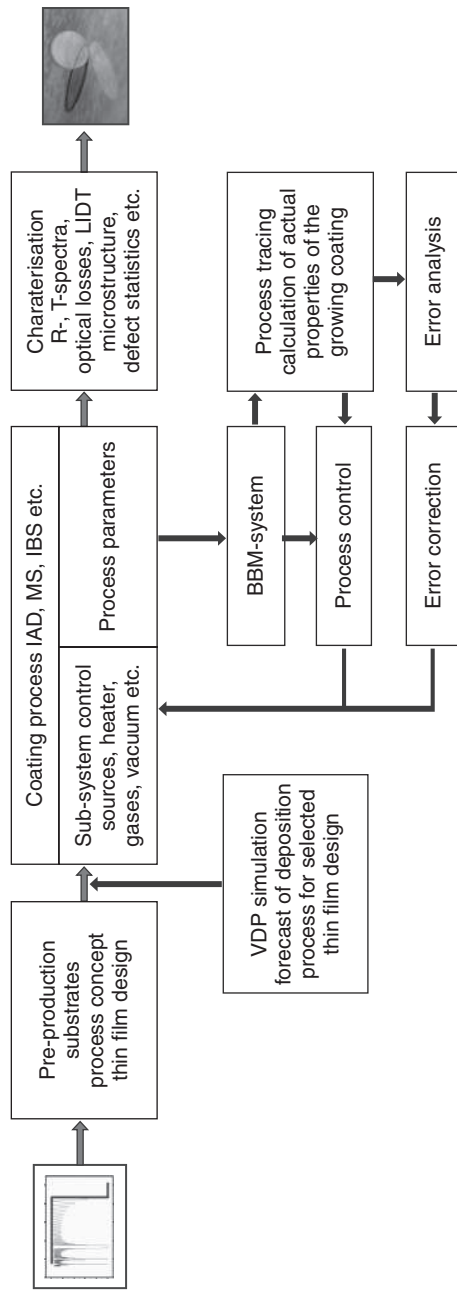
Before this general background new production strategies have to be implemented in optical coating technology that allow for direct manufacturing in a linear chain. In contrast to conventional production concepts, which are often based on optimization cycles involving several deposition runs until the specified quality is reached, advanced approaches have to combine coating design and evaluation tools with stable and well controlled deposition processes in order to achieve highest economic efficiency and shortest product development times. Following the line from the customer enquiry to the final product, the first step comprises the selection of materials and the conception of the coating design. In an innovative fabrication process, the design phase should be followed by an evaluation of the envisioned coating system to exclude problematic designs and to minimize the risk of production failures. Apart from conventional evaluation techniques, which just perform an analysis in view of random variations of coating parameters, progressive software environments facilitate an immediate prediction of the coating result. Such virtual deposition programs are based on multiple simulations of the deposition process in combination with the actually applied control systems including optical parameters and major sources of errors observed in routine operation of the individual deposition systems. For the subsequent coating production, stable ion assisted or sputtering processes are suitable which are controlled by precise on-line monitoring devices. Besides single wavelength optical techniques, the analysis of the transmission or reflection spectra of the growing coating system measured directly on the product over a broad wavelength range within short time intervals during the coating processes gains importance for achieving highest precision in layer thickness. These novel devices, which are often known as optical Broad Band Monitors (BBM), allow also for a combination of the *in situ* analysis with data from additional sensors integrated in the deposition plant to improve the sensitivity and reliability of optical thickness control. Furthermore, they offer the possibility to implement error detection and correction tools which identify upcoming problems in the deposition sequence and even propose adapted design solutions to bring the running deposition process to a successful ending. With this outlined production strategy, optical coating production will move away from the former 'black magic art' towards a deterministic manufacturing technique with high efficiency and flexibility.

Obviously, present optical coating production still has not reached this ideal situation, and further efforts are necessary in research and industry to master the ever increasing challenges of modern photonics. However, on the basis

of advanced measurement devices, fast and inexpensive computer systems as well as enormous progress in the development of stable ion deposition processes, the fundamental scheme for the deterministic production of optical coatings could be implemented during the last decade. In the following chapter major aspects of this development are summarized and discussed. In the first section deterministic production strategies will be outlined in detail, and selected coating processes will be considered in respect to the special requirements of novel thin film production schemes. The following part is dedicated to the technical basis including advanced on-line monitoring systems in combination with additional sensors and examples for a modern software environment comprising virtual deposition schemes, on-line error detection and correction tools. The section will be concluded with the discussion of an extended experiment oriented to a demonstration of the advantages of the novel deterministic coating process. The third section highlights some new developments in the field of material mixtures and the related production of rugate filters. A brief review on the production of ternary oxides of reproducible stoichiometry with an adapted ion beam sputtering (IBS) process will be presented. After a glance onto the advantages of material mixtures the production and control of rugate filters will be discussed and illustrated with a few examples. The chapter will be closed with a summary and outlook onto the future prospective of deterministic coating production.

4.2 Basic concept of deterministic production

The fundamental idea of deterministic production strategies has already been outlined in the introduction. For further illustration, Fig. 4.1 depicts the major steps of conventional production with iteration cycles in contrast to the novel deterministic approach. The additional ingredients for an implementation of the advanced concept are grouped in the lower half of Fig. 4.1 and incorporate a software environment for the simulation of deposition processes (virtual deposition process, VDP), an advanced monitoring device represented by a BBM-system and the corresponding process tracing algorithm in conjunction with on-line error handling tools. In a typical functioning scheme of these units, the BBM-system monitors the spectral characteristics of the growing layer system and formats data files for the process tracing algorithm. The tracing system contains a routine which extracts the thickness and often also the dispersion of the momentarily growing single layer in time intervals according to the rotation time of the substrate holder. As an example for detecting the switching point of the actual layer an additional algorithm is integrated that compares the state of the layer to the expected spectral performance for the completed layer. Additional data transfer takes place between the process tracing system and the error analysis as well as correction tools which are also linked to the system control



4.1 Production cycle for coated optical components. In many cases, the production cycle has to be performed several times in order to reach the required specifications defined by the client. For the deterministic production of optical coatings, a linear production chain is realised without iteration cycles. The optimization of the coating system is accomplished during the deposition on the basis of adapted *in situ* monitoring strategies (units in the lower half). MS, magnetron sputtering; LiDT: laser induced damage threshold.

unit of the deposition plant. In case of a deposition failure, the error correction system can automatically modify the sequence of the remaining layers in the process tracing program to compensate for the detected deviations. A further expansion stage for an improvement in precision and reliability, which is not illustrated in Fig. 4.1, may comprise links of the process tracing system to other process sensors like a crystal microbalance, mass spectrometer or a plasma monitor.

Besides the units depicted in Fig. 4.1, the employed deposition processes are of key importance for a successful implementation of deterministic production strategies. Since the applied monitoring concepts are directly targeted on the spectral transfer characteristics of the coating system directly under the gas atmosphere at low pressure during the running deposition process, a change of the coating properties after venting would reduce the reproducibility. Therefore, conventional thermal evaporation processes, which often suffer from water adsorption effects typical for produced relatively porous coatings, are not well suited to BBM-control methods. However for some special applications, for example involving fluoride materials for coatings in the deep ultraviolet/vacuum ultraviolet (DUV/VUV)-spectral range, spectral monitoring offers advantages for the quality management and is occasionally employed in coating production without a link to process control (Ristau, *et al.*, 2006). In contrast to this, modern ion assisted deposition processes are qualified for manufacturing dense and stable coatings with only small variations in their optical properties. Nowadays, the corresponding commercial deposition plants for precision optics are often equipped with BBM-devices directly integrated in the process control scheme, and they are routinely employed in industrial production (Sullivan, 2010). Especially, sputter processes benefit from their intrinsic high process stability and a superior homogeneity of the refractive index in the depth of the layers. As a consequence, simple time control for depositing a defined layer thickness was sufficient for most sputter systems in the past. In conjunction with optical monitoring and particularly BBM-devices, sputtering reaches a very high precision in coating thickness down to the level of a single atomic layer.

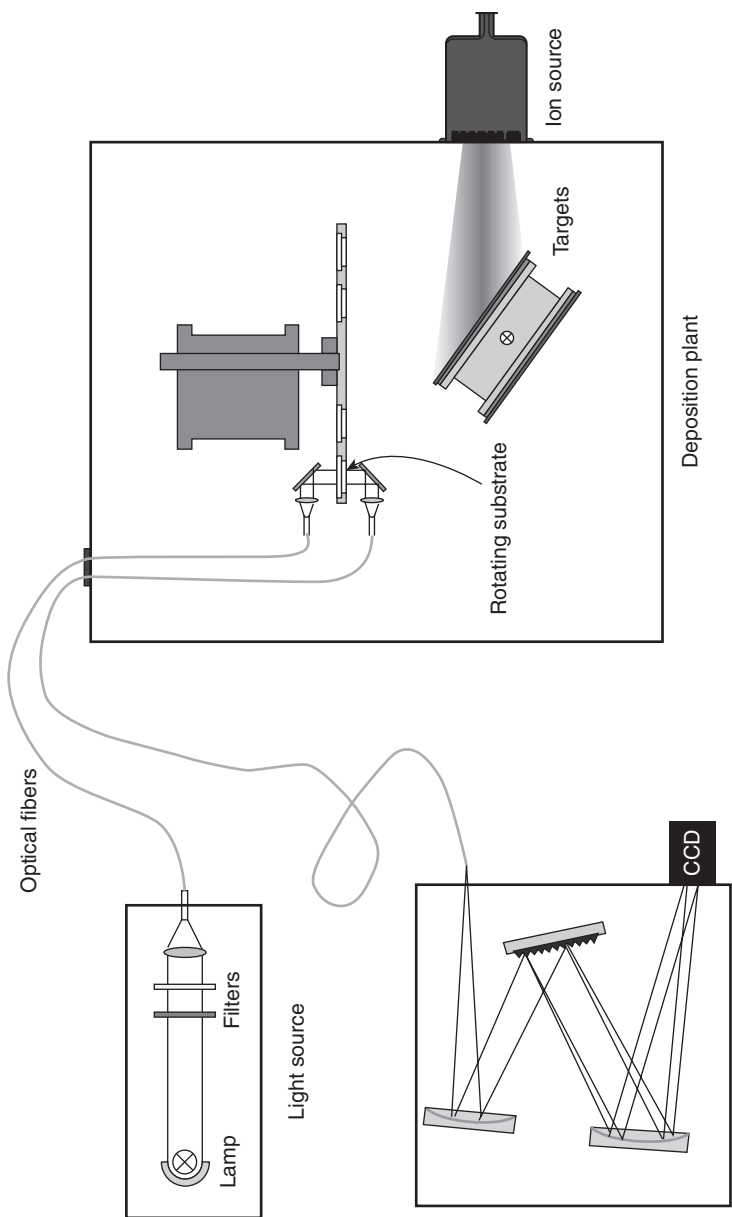
For example, recent research in magnetron sputtering demonstrated an outstanding reliability of these processes for the production of very complex coating systems including filters for fluorescence spectroscopy (Lappschies *et al.*, 2011) or chirped mirrors for ultra-short pulse lasers (Pervak, 2010). In this connection, also the enormous capability of conventional sputtering to produce complex layer stacks of many hundred or even a few thousand single layers (Tilsch *et al.*, 2010) has to be mentioned. On the other hand, ion beam sputtering is known for the production of coatings of excellent optical quality with lowest defect concentration. Since the deposition rates are still relatively limited and only few parameters have to be controlled, IBS-concepts are very well suited to sophisticated BBM-control techniques and reach an outstanding flexibility as well as precision for manufacturing of

complex coating systems (Ristau and Groß, 2005; Ristau, 2010). During the last years, IBS-processes could be also extended to the production of coatings with defined material mixtures (Lappschies *et al.*, 2005) and to rugate filters (Starke and Ristau, 2011), featuring IBS as an interesting concept for future oriented deterministic coating production concepts. Nevertheless, optical coating processes are treated in the present book in all aspects and therefore, the following part will be concentrated on details of the additional components necessary for deterministic production techniques. These will be described for exemplary systems which are being used partly in industrial production and research of optical thin film systems.

4.3 Optical broad band monitoring

The technological evolution of monitoring the transfer characteristics of growing coatings during deposition can be traced back to the beginning of 1970s. At that time semi-automatic monochromators were coupled to the deposition plant for repetitively measuring the spectral characteristics of a test glass in the center of the substrate holder (Vidal *et al.*, 1978, 1979). This pioneering work of the group at the former Ecole Nationale Supérieure de Physique Marseille in France stimulated and was paralleled by several other research activities in Canada (Powell *et al.*, 1986), the United States (van Milligen and Macleod, 1985), Australia (Netterfield *et al.*, 1988) and Italy (Emiliani *et al.*, 1988) during the 1980s. Limited by the relatively low performance of computer systems available back then, only fractions or selected data points of the measured spectra could be evaluated. An extended analysis of the growing layer system was even more inconvenient, because the deposition processes had to be interrupted to allow for the needed calculation times. However in the next decade, direct spectral monitoring found first applications in industrial production environments (Bauer and Nüssler, 1994), especially in conjunction with ion beam sputtering (Tilsch *et al.*, 1994) as a low rate process rendering sufficient time for data processing. In this time period also first control algorithms for a switching of the layers on the basis of the measured spectrophotometric data were developed, and considerable research work was concentrated on a deeper understanding of the error budgets for a direct spectrophotometric deposition control (Sullivan and Dobrowolski, 1993).

Supported by enormous improvement of compact spectrophotometers with high-speed CCD cameras and the rapid growths of available cost-efficient computer power, new sophisticated on-line spectrometers could be integrated in deposition systems during the last decade. These systems feature data acquisition times for a spectrum covering a wavelength range from 350 to 1100 nm in a few milliseconds and therefore, allow for a direct monitoring of the actual product synchronized to the rotation of the substrate holder during deposition (Starke *et al.*, 2000; Lappschies *et al.*, 2004b). A typical set-up



4.2 Basic arrangement for on optical broad band monitoring system coupled to a deposition process (ion beam sputtering).

for a BBM-device operating in transmission mode is depicted in Fig. 4.2 for an IBS-process. In the basic version, the measurement radiation is generated by a tungsten lamp and coupled into a fiber which transfers the radiation to the measurement channel in the deposition plant. After collimation by a lens, the radiation passes the product on the moving substrate holder and is guided by a second fiber to the spectrophotometer. Depending on the desired spectral resolution and accuracy, spectrophotometers can be selected from large variety of commercially available systems. For an economic approach, a compact single card device with fixed grating and an adapted CCD-line detector can be employed, which is directly coupled to a computer system. Recording and data acquisition of spectra can be performed for preselected positions on a fixed radius of the calotte. In this configuration several products can be monitored and furthermore, a calibration can be performed during each revolution of the calotte. For this purpose, a 100% spectrum of an empty position and a spectrum of an area with zero transmittance are measured and taken as the normalization basis for the product spectra.

In Table 4.1 representative specifications of BBM-systems used in industry and research are compiled. The UV-BBM-system in column 1 is operated with a D₂-discharge lamp and allows for only relatively long data acquisition times not suited to direct monitoring. However, even though the UV-BBM represented in the second column of Table 4.1 is monitoring a fixed test glass, an improvement in coating precision especially for coatings used in excimer laser technology could be achieved (Günster *et al.*, 2001; Ristau and Günster, 2003). In contrast to this, the device often favored in industrial production (column 3 of Table 4.1) offers sufficient precision balanced with short data acquisition times. The BBM-system specified with low relative measurement error and moderate spectral resolution in column 4 had been developed for research in high precision IBS-processes (Lappschies *et al.*, 2004b). The last column outlines the performance which can be probably achieved within the further development of BBM-system for deposition control. Besides improved accuracy and data acquisition

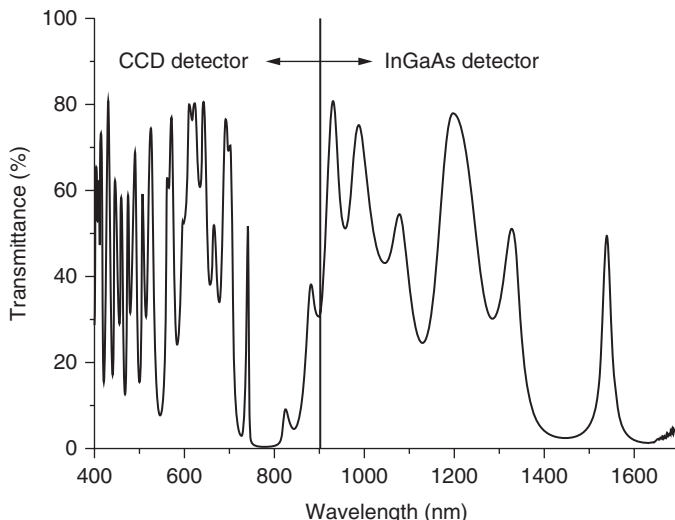
Table 4.1 Selected specifications of typical optical BBM-systems applied in research and industry for deposition control (innovative system: under development).

Specification	UV-BBM in research	BBM-system in industry	BBM-system in research	Innovative BBM-system
Wavelength range	140–200 nm	350–1100 nm	520–980 nm	200–2500 nm
Wavelength resolution	2 nm	2–7 nm	1 nm	< 1 nm
Accuracy ΔT	1–1.5%	1%	0.2%	< 0.1%
Acquisition time	> 100 ms	10 ms	50 ms	< 10 ms

Note: The last column indicates a BBM-system presently under development for an improved deterministic coating production.

speed, the system covers a spectral band of more than three octaves and should enable an advanced precision. A coarse argument for this expected enhancement in switching accuracy may be based on the number of independent data points within the measured spectra which increases with the spectral range of the measurement device. In this context, a further analysis and also experience gained during the application of BBM-systems indicate that a major criterion for the accuracy of a BBM-controlled process can be found in the integral variation of the spectra for the respective thickness increments. For example, the sum of the squared variations at all wavelength points in the spectra measured before and after deposition of a certain layer thickness can be considered as a quantity describing the dynamic behavior of the spectra with thickness variation. Obviously, designs with higher spectral dynamics in respect to thickness variations allow for a better switching of the layers than designs with only minute dynamics, where small changes lead to high uncertainties in the thickness values derived from the spectra. This is also a further allegation for an extension of the spectral range for BBM-systems which automatically results in covering additional features in the measured spectra, especially if higher orders are taken into account at the short wavelength edge of the detection range. The technical implementation of such BBM-systems with measurement ranges extended down to 200 nm in the UV can be only performed with light sources delivering sufficient radiation power in the UV-range (Ristau *et al.*, 2008). An example for a NIR extended spectrum measured with an advanced BBM operating over a range from 380 to 1700 nm is depicted in Fig. 4.3. This system comprises a combination of two spectrometer arrangements with a Silicon CCD-chip and an InGaAs-array as detector elements. Technical problems to be solved on the way to BBM featuring more than three octaves in bandwidth from UV to NIR include the adapted splitting and combination of the measurement radiation, the synchronization of spectrometer systems with the motion of the calotte, as well as the calibration of the spectra.

As a further option for an improvement in the precision of BBM-devices measurement channels allowing for the synchronous acquisition of the transmission and reflection of the coating has been investigated. For example, the integration of an Ulbricht sphere in the coating plant can be considered as an interesting approach to mitigate the relatively marked directional variation of the measurement beam reflected by the coating. In the ideal case, the measured power signal of an Ulbricht sphere arrangement is invariant in respect to the direction of incidence tolerating strong geometrical changes in the reflected beam. The additional recording of reflectance spectra allows for an on-line determination of optical absorption complementing the thickness calculation algorithms.



4.3 Transmittance spectrum of a multilayer system measured by an advanced BBM-system with a detection range from 380 to 1700 nm. The spectral region between 380 and 900 nm is covered by a CCD array, and the long wavelengths part in the NIR is recorded with an InGaAs array.

In principle, optical monitoring is not limited to a simple recording of conventional spectra during the deposition. Alternatively ellipsometric techniques can be considered, that enable the spectrally resolved measurement of the polarization state of light reflected by the growing coatings. Corresponding devices with conventional ellipsometers, but also specially developed systems, were studied during the last decades. Before this background the work of E. Masetti dedicated to an arrangement without moving parts in the polarization analyzing channels has to be mentioned (Masetti *et al.*, 1996). The major innovation of this technique was the introduction of special filters separating the polarization modes of the measurement radiation. Recent results for the control magnetron sputtering with ellipsometry were published by a German group in 2010 (Rademacher *et al.*, 2011). However, most publications in the field of ellipsometric control of deposition processes are dedicated to single wavelength methods, because the practical application of spectrally resolved ellipsometric measurements precludes a static coating sample on account of the long data acquisition times of present ellipsometers.

If highest sensitivity, stability and reproducibility are demanded, today BBM-devices are often connected to other sensors installed in the coating plants. These multi-sensor approaches result in the need for advanced hybrid monitoring concepts which require adapted control algorithms. In the following, the focus is on *in situ* layer thickness determination. Therefore, examples aiming mainly at process stability aspects like connections to plasma monitoring or mass spectrometry devices are not considered.

Basically, hybrid layer thickness monitoring concepts can be divided into two categories. In the first case, multiple monitoring techniques are applied sequentially for the end-point detection in different layers in one multilayer stack. As a consequence, a strategy defining the optimal monitoring technique for each layer has to be developed prior to the deposition process. Common examples are combinations of optical monitoring and quartz crystal microbalances or time-based thickness monitors. In these approaches often only critical layers in terms of the precision of the optical monitoring algorithm, for instance very thin layers, are terminated by the non-optical monitoring systems. It has to be mentioned that in addition to the pure sequential application of the different measurement concepts cross-system calibrations are possible. For example, the accuracy of the quartz crystal microbalance tooling or of the time-based monitor can be enhanced by data of optical measurements of the already finished layers. In the opposite direction, the optical process tracing can be verified by separate consistency checks on basis of logged data from non-optical terminated layers.

In contrast to the previous sequential application of the different monitoring systems, the data of more than one monitoring technique are evaluated simultaneously in the second category of hybrid monitoring approaches. Consequently, in this true hybrid monitoring case, each layer of a multi-layer stack is terminated based on an algorithm processing the signals of different monitoring systems. In extension of the example above, a BBM-system and a quartz crystal microbalance can be combined in a true hybrid way. For instance, this combination opens up the possibility of guiding the BBM algorithm by the crystal microbalance data in case of critical thicknesses resulting in low spectral dynamics (see Section 4.3). More in detail, the thickness measurements by crystal microbalance influence the starting values for the numerical minimization procedure of the BMM-system for fitting the theoretical to the measured transmittance spectra (Ehlers *et al.*, 2010). This hybrid approach is particularly advantageous if minor deviations in the already deposited layers accumulate to larger discrepancies between the measured spectra of the current layer and the theoretical spectra, which are calculated on the basis of error-free thicknesses of the underlying layers. In this case, points of ambiguous solutions can occur for the pure BBM tracing algorithm while the layer thickness increases. However, implementing the hybrid process control, the guiding of the tracing algorithm by the crystal microbalance values allows for passing the described critical positions successfully. Nevertheless, the layer is finally terminated by the high-precision optical BBM-system taking advantage of positive effects like error self-compensation.

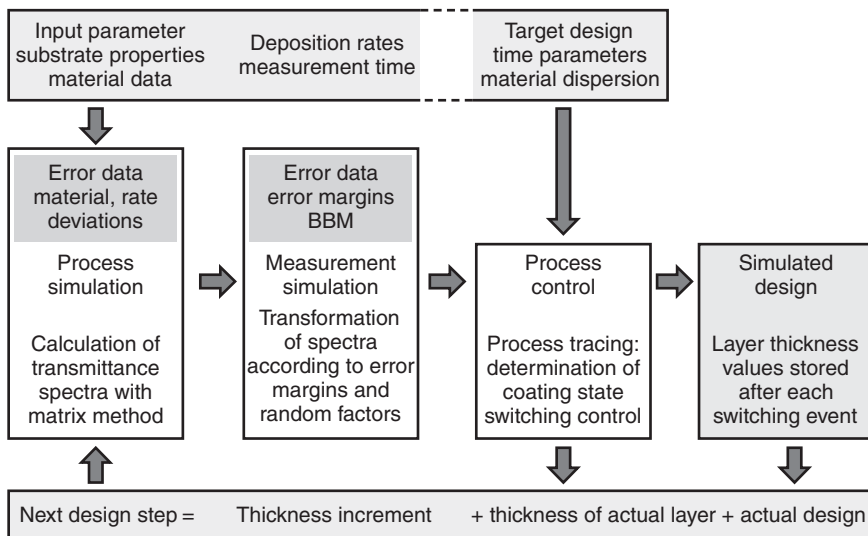
Furthermore, the hybrid combination of different monitoring systems offers the possibility to realize advanced error handling strategies. In such configurations the operator can often define various individual conditions

and actions with a high flexibility. For instance, the deposition process can be adjusted or paused automatically if a certain relative or absolute layer thickness deviation level between different simultaneously working monitoring systems is exceeded. Also, rules triggered by specific error events can be established to reverse the roles in a master-slave configuration of two monitoring systems, e.g. switching to crystal microbalance control if negative rate values are calculated by the BBM algorithm. In addition, thickness levels for switching from crystal microbalance to optical monitoring can be defined to provide a minimum layer thickness for the evaluation of the optical measurements.

In summary, the presented advanced monitoring concepts can enhance precision and yield in the production of complex multilayer stacks without a need for developing design dependent individual monitoring strategies. Practical examples of the benefits of a true hybrid monitoring approach will be given in Section 4.6.

4.4 Virtual deposition system

The evaluation of a synthesized design in respect to its stability in production was always a key issue in optical thin film technology. Typical concepts for a first assessment of the design stability include algorithms performing random variations of the thickness values within predefined limits and a subsequent calculation of the transfer spectra. These algorithms are repeated several times for all layers of the design resulting in estimated confidentiality intervals for the individual thickness values and corresponding tolerance bands for the spectra. More sophisticated techniques also involve variations in the dispersion of the single layers in the design in dependence on their position in the layer structure. Accordingly, a limited comprehension of coating processes can be achieved on the basis of the individual dispersion variations, which are expected to differ significantly for instance, between conventional evaporation or ion beam sputtering. Generally, these algorithms form an integral part of modern commercial design synthesis packages and allow for a first estimation of the design stability. However, in most cases comparisons between the estimated error budget and results observed in practice reveal severe deficiencies of the employed random algorithms. As a consequence advanced tools, that directly perform a simulation of deposition runs controlled by defined techniques, have been developed during the last few years. Typical approaches consist of an algorithm emulating the deposition plant and a further computer program imitating the control system, which may contain a quartz crystal balance, a single wavelength optical monitor (Zöller *et al.*, 2008), or even a BBM as measurement system (Ehlers *et al.*, 2010). These simulation tools, often referred to as ‘virtual deposition system’ VDP (Ristau *et al.*, 2008), can be devised with high flexibility in respect



4.4 Diagram for a virtual deposition process (VDP) with a BBM-system for deposition control. The fundamental structure consists of three units simulating the deposition process and the measurement channel of the on-line monitoring device. These two parts form the virtual deposition system. The virtual deposition control unit is illustrated in the left half of the diagram for a BBM-system.

to the deposition process, the measurement system or the process tracing algorithm. In the following, the typical functioning of VDP-concepts comprising the emulation of the deposition plant, the on-line monitoring device and the process tracing algorithms will be described for a BBM-system as central on-line monitor (see Fig. 4.4). Finally, results for dielectric filter system will be illustrated as an example for a typical application (Ehlers *et al.*, 2010, 2011).

4.4.1 Deposition system

In a typical VDP concept the major outcome of the algorithm emulating the deposition system consists of spectra for the different phases of the process. For that reason, the mathematical kernel of the deposition system emulator consists of a layer matrix program calculating spectra for a layer structure formulated according to the progress of the deposition run. At the beginning of the simulation, the first layer of the intended design is considered, and a spectrum is calculated for the first thickness increment from dispersion data of the substrate and the involved layer material. The size of the thickness increment is depending on the deposition rate and the measurement scheme

applied in the control system. In case of a quartz crystal balance, the thickness increment would be defined by the sampling time of the frequency read out. For an optical system operated in direct monitoring mode, the thickness increment would amount to the deposition rate multiplied by the revolution time of the calotte. Considering these generic relations, the counting basis for the progress of the simulated layer structure is the time interval between the consecutive measurements of the control system. In the further course of the simulation, the corresponding time counter is continually incremented, and a spectrum is calculated for the layer thickness at each time step. For the first layer, this procedure will be stopped and the reached layer thickness will be stored, once the control system identified the switching point. After that, the second layer data are loaded into the layer matrix program and the spectra are calculated again until the switching point is indicated. This track will be followed until the last layer is simulated, and the result of the VDP-process can be read out as the thickness values stored for each layer at the switching points. The specific properties of the considered deposition processes are accounted for by the input parameters for the deposition emulation routine including variations or trends in the dispersion data and deposition rates of the materials. Also, additional routines are integrated in the program to simulate effects of error sources generated by technical deficiencies in the system. For highest flexibility and modularity, the deposition emulator is configured to transmission control protocol/internet protocol (TCP/IP)-interface for data communication between the other components of the VDP system.

4.4.2 On-line measurement system

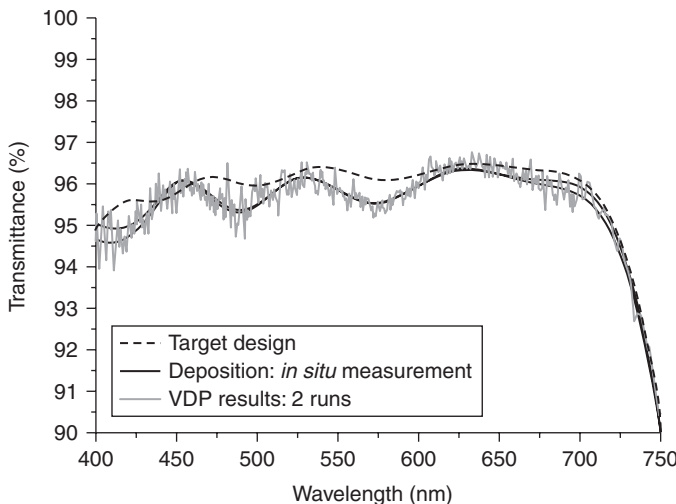
The procedure representing the on-line measurement system loads the emulated spectra from the deposition system via the TCP/IP-interface and performs an adapted transformation according to the specific errors of the measurement systems. For instance, prominent errors to be primarily considered for a BBM-system include systematic components induced by the limited spectral resolution as well as absolute deviations in the wavelength position and transmittance. Further random variations have to be taken into account representing the noise of the system and aberrations in the calibration routines. The simulation routine for the BBM measurement stamps the effects of the mentioned errors on the ideal spectra calculated by the deposition emulator and formats the data for the subsequent process tracing algorithm. As a consequence of the TCP/IP-interface, the measurement simulation routine can be replaced by any other program module representing a quartz crystal device, single wavelength monitoring or other specific process observing instruments related to the development of coating design.

4.4.3 Process tracing algorithm

If the interfaces of the VDP components are devised in an appropriate way, the respective original process tracing software package used in the deposition plant can be directly employed. In the case of the BBM-system the corresponding program can be transferred from the deposition plant, where it is operated with the spectrometer system, to the VDP system without any alterations (see process control box in Fig. 4.4). As a consequence, the user interface and all options of the software package are part of the BBM VDP device and can be operated identically to the situation at the real plant. The major functioning of the tracing algorithm is implemented in a least squares fit algorithm which deduces the actual thickness of the current layer from the measured spectrum (Starke *et al.*, 2000). In the special environment of the VDP system, the measured spectra are given by the data simulated by the VDP on-line measurement system. Since the process tracing algorithm is identical to the application tool, all input data describing the target design, the substrate and the deposition materials are considered in the tracing routines. The current layer thickness calculated by the least squares fit algorithm is compared to the value according to the termination point of the layer during each time step of the VDP routine. At a certain small distance to the target thickness, the control system switches to a time counting mode in order to enable termination of the layer at any instance in-between to consecutive time steps of the deposition emulator. After reaching the termination point, the deposition emulator is stopped, and the thickness value, which is corrected by the additional minute amount introduced by the time counting switching mode, is stored as the actual thickness value of simulated design.

4.4.4 Application example for a VDP analysis

A major prerequisite for an efficient application of VDP procedures is a set of error and material data which has to be gained from the routine operation of the individual deposition plants. For example, deviations in dispersion and deposition rates are critically dependent on the process concept used for the production of a certain coating design. As a consequence of the relatively low error margins, valid results are expected for stable processes as ion assisted deposition or ion beam sputtering. In Fig. 4.5 results for a broad band anti-reflection design with 16 layers of the materials TiO₂ and SiO₂ are illustrated precluding an ion beam sputtering process. Target specifications of the design range from 400 to 700 nm. The spectrum calculated directly from the design is depicted by the dashed black curve in Fig. 4.5 and compared to the result of a VDP-analysis on the basis of deviation parameters



4.5 Spectra of a broad band anti-reflection coating deposited in ion beam sputtering process with the materials TiO_2 and SiO_2 . The spectrum of the target design (dashed black curve) is compared to the results of the process simulation using the virtual deposition system (solid black curves, two VDP runs) and the produced coating system (*in situ* spectrum, grey curve).

for the employed ion beam sputtering plant (solid black curves, two simulation runs). Obviously, the VDP-analysis leads to small but noteworthy differences in the spectral behavior which are also reflected by the simulated design with some layer thickness values diverging from the target design. Since the observed error margins conform to the specified tolerance band, the coating was produced yielding the *in situ* spectrum indicated by the grey curve in Fig. 4.5. The good agreement between spectral behavior forecasted by the VDP analysis and the produced layer system clearly demonstrates the versatility of this novel pre-production evaluation tool.

Summarizing, experience gained during several years of application of VDP concepts in research and also within an industrial network indicate that the risk for the production of a certain layer designs can be estimated on a relatively reliable basis for a large variety of deposition systems and complex layer designs. In most cases the produced coating systems deviate only by a small amount from the spectral characteristics forecasted by the VDP analysis, whereas larger differences are often observed for the target designs. For example, experimental investigations even reproduce the position in a problematic design, where the critical aberration is predicted by the VDP process. A corresponding study will be summarized in a subsequent section of this chapter.

4.5 Direct on-line correction tools

Direct on-line error detection and correction tools complement the described combination of advanced monitoring concepts and virtual deposition systems in an ideal way. The basic idea of a computer based on-line re-optimization of the layer thicknesses as well as a first implementation in optical coating production can be dated back to the late 1970s (Holm, 1979). In a first step, the evolution of layer thickness errors has to be traced by an error detection tool. In the given case of optical broad band monitoring the deviations between the measured spectra of the growing layers and the theoretical target spectra have to be evaluated. The necessary calculations can be performed by applying different algorithms, of which two are most common. On the one hand, only the last measured spectrum can be used to calculate the thickness of the corresponding last layer, while the thicknesses of the underlying layers are kept constant. This type of calculation is implemented in the so called sequential algorithm. On the other hand, one measured spectrum for each already deposited layer of the growing stack can be evaluated by an algorithm at once to calculate the thicknesses of all deposited layers. This simultaneous analysis of all measurements is done by the so called triangular algorithm. Due to the broader experimental data base of the triangular algorithm, a better reliability can be expected, which could be demonstrated in an experimental study (Amotchkina *et al.*, 2011).

The above described approaches provide information about the thickness deviations of the already deposited layers derived from on-line measurements. Regarding the BBM-control, the calculated thicknesses can substitute the theoretical values in the multilayer design to process the remaining layers under conditions as close to reality as possible. However, with respect to the aim of an on-line correction tool, it is crucial to classify the evaluated errors and to determine a critical error level for an automated intervention. Consequently, in the next step the impact of the errors on the expected spectral performance of the complete layer system has to be calculated. Depending on the specifications the need for a re-optimization of the multilayer design has to be checked. In the subsequent re-optimization procedure, the thicknesses of the remaining layers have to be refined, while the thicknesses of the already deposited layers are taken from the previous deviation calculations. If a modified design fulfills all specifications, the process control replaces the original design and the BBM-system traces the process on basis of the new thicknesses for all layers. In rare cases of high deviations, additional layers are required to fulfill the specifications. This further feature can be provided by the on-line correction tool as a selectable option. Generally, the specifications processed by the correction tool are not limited to transmittance and reflectance values. For instance, also

absorption, phase, group delay, or group delay dispersion requirements can be defined as specific target values.

Furthermore, the VDP system described in the previous sections can be integrated into the re-optimization procedure to automatically benchmark different refined designs with respect to their design stability within the process. It has to be mentioned that the chosen algorithms in combination with the available hardware have to be fast enough to perform all calculations on-line, normally before the finish of the current layer.

In addition to the described evaluation of layer thickness deviations, an optional on-line analysis of deviations in the wavelength dependent refractive indices and extinction coefficients is possible. However, due to the limited information contained in the measured transmittance data these on-line multi-parameter fits have to be done carefully. In practice, the re-optimization should be restricted to a layer thickness variation by default, which is no significant limitation in case of stable deposition processes. Nevertheless, in certain cases for selected layer configurations e.g. an on-line refinement of the dispersion data can be advantageous. Altogether, these versatile tools are currently under intense development, first promising approaches are available (Schlichting *et al.*, 2011).

In summary, the direct on-line correction tools coupled to enhanced BBM-systems enable a further increase in yield as well as in precision of complex optical coatings. In most cases the resulting re-optimized design differs only slightly from the theoretical starting design that would not have been deposited successfully without the application of an on-line correction tool. A concrete experimental example of re-optimization results will be given in the next section.

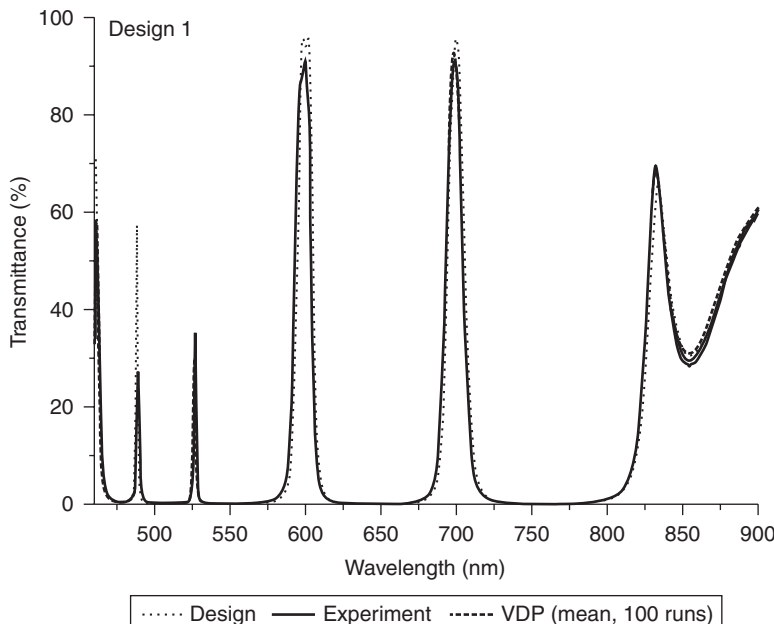
4.6 Design stability in production processes

In the following, selected results of an experimental study are summarized to give an overview of the potential of different monitoring conditions. The evaluated techniques comprise monitoring by a BBM-system and a hybrid BBM configuration as well as the application of a VDP system and a direct on-line correction tool. All coatings were manufactured by an ion assisted deposition process (IAD) on a commercial Leybold SYRUSpro 1100 machine equipped with a Leybold APSpro plasma source.

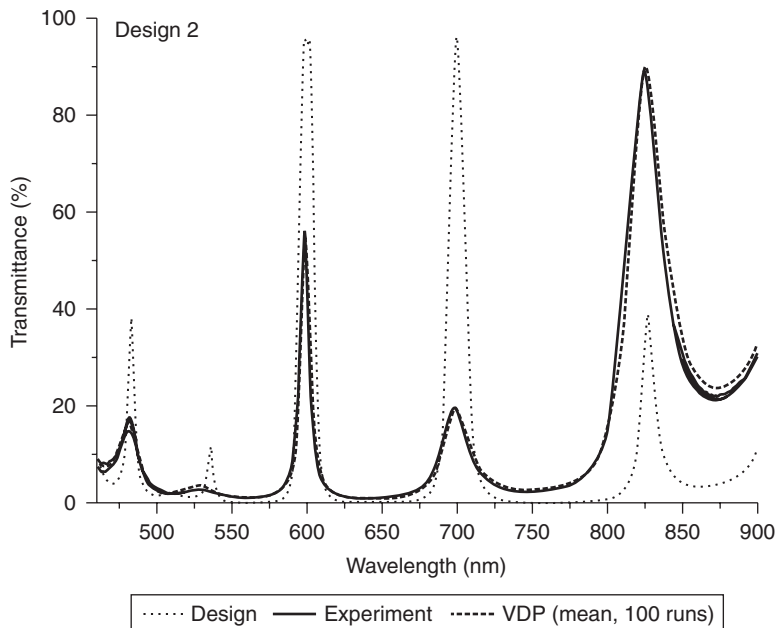
Following the production chain, the selection of an appropriate design is the first step. Therefore, the VDP system is applied in the beginning to choose the most stable multilayer design. Within the experimental study a double bandpass filter with transmittance peaks at wavelengths around 600 and 700 nm was chosen as demonstrator. Initially, two alternative designs for $\text{TiO}_2/\text{SiO}_2$ stacks were calculated by a thin film design software. Both of them show nearly identical transmission/reflection in the relevant

spectral range from 550 to 800 nm. Furthermore, both of them include 31 layers with similar proportions of TiO_2 and SiO_2 as well as a total thickness of $\sim 2.6 \mu\text{m}$. Regarding design stability aspects under process conditions it can be stated that none of the designs contains a layer with a thickness below 30 nm.

In Section 4.4 basic examples of algorithms for design stability analysis were introduced. However, in case of the two given double bandpass filter designs random variations of the layer thicknesses result in no significant differences. Only a slightly higher stability is predicted for the second design. Also, the analysis of the dynamic behavior of the transmittance spectra with increasing layer thickness reveals no further information. Again, the second design only shows minor advantages over the first one. In contrast, the VDP approach based on the BBM monitoring software results in considerable differences between the two designs. In Fig. 4.6 the simulated transmittance spectra of design 1 are plotted in comparison to the theoretical target spectrum. To take the reproducibility into account 100 virtual deposition runs were performed. All simulations were done using the SYRUSpro 1100 machine specific error sets and show a high reproducibility with a maximum standard deviation of 0.3% in the transmittance peaks. Therefore, the mean



4.6 Theoretical transmittance target spectrum of design 1 in comparison to corresponding simulated and measured transmittance spectra.



4.7 Theoretical transmittance target spectrum of design 2 in comparison to corresponding simulated and measured transmittance spectra.

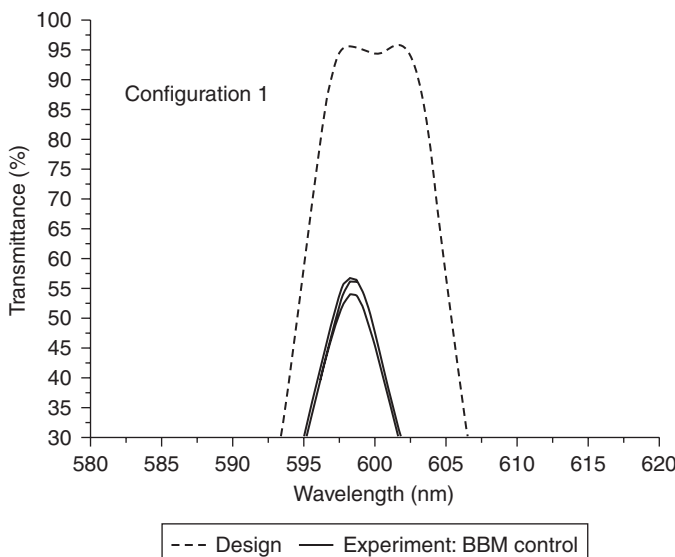
simulated transmittance is depicted in Fig. 4.6. To validate the calculated VPD results comparable real deposition runs are necessary. In addition, Fig. 4.6 shows the result of three BBM controlled depositions runs for the first design. Obviously, the simulated results are in a good agreement with the measured transmittance data, which indicate good reproducibility, too. Looking at Fig. 4.7, the difference in performance of design 2 compared to design 1 is evident. Again, the theoretical target spectrum and the VDP as well as the experimental results are plotted. Due to the large target deviations, the second design could be identified as much more unstable under production conditions. This result was predicted by the VDP runs and also confirmed by the real deposition runs.

As described above, the intention of this section is to compare different monitoring concepts with respect to their precision and stability in layer thickness control. Most likely, in production, the first design would be the preferred choice because yield is an important factor. However, in view of this section a more challenging design is preferable. Therefore, all following examples will refer to the second design and concentrate on the transmittance in the passband centered at wavelength of about 600 nm. More in

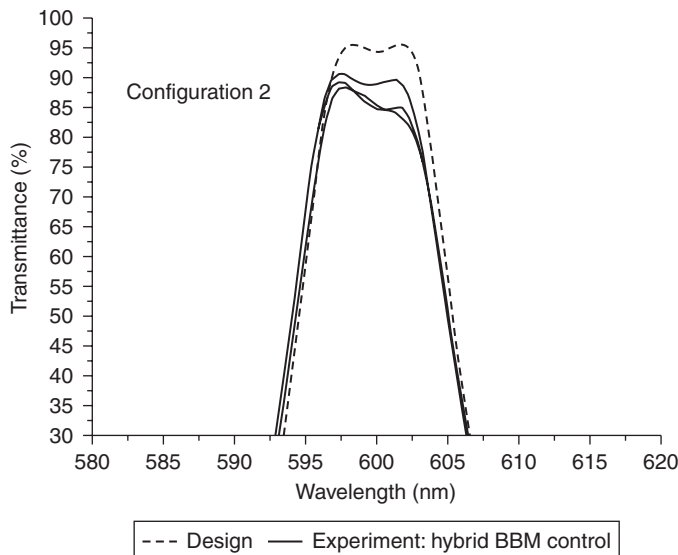
detail, five different control configurations were applied to evaluate their performance:

1. process monitored by BBM-system (see Section 4.3),
2. process monitored by hybrid combination of a BBM-system and a quartz crystal microbalance (see Section 4.3),
3. process monitored by BBM-control in combination with a direct on-line correction tool (see Section 4.5),
4. process monitored by BBM-system after a refinement of deposition and material parameters by a VDP analysis based on the preceding experimental results (see Section 4.4) and
5. process monitored by a simultaneous application of all the above described tools.

The results of example 1 in Fig. 4.8 are based on the BBM-control and therefore Fig. 4.8 shows a detail of Fig. 4.7. Instead of the aimed transmittance of ~95% in maximum, only ~55% are reached in the three deposition runs due to strong error accumulation effects resulting from the problematic design. In contrast, Fig. 4.9 documents a much higher transmittance. In this second example, a hybrid BBM monitoring system that includes a quartz crystal microbalance as described in Section 4.3 was applied. But deviations of more



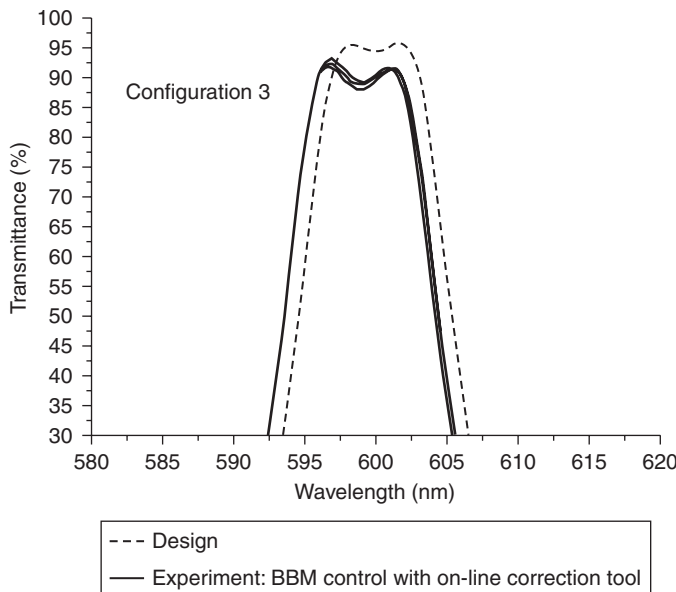
4.8 Process monitored by BBM-system (example 1), measured transmittance spectra (three deposition runs) in comparison to the theoretical target spectrum.



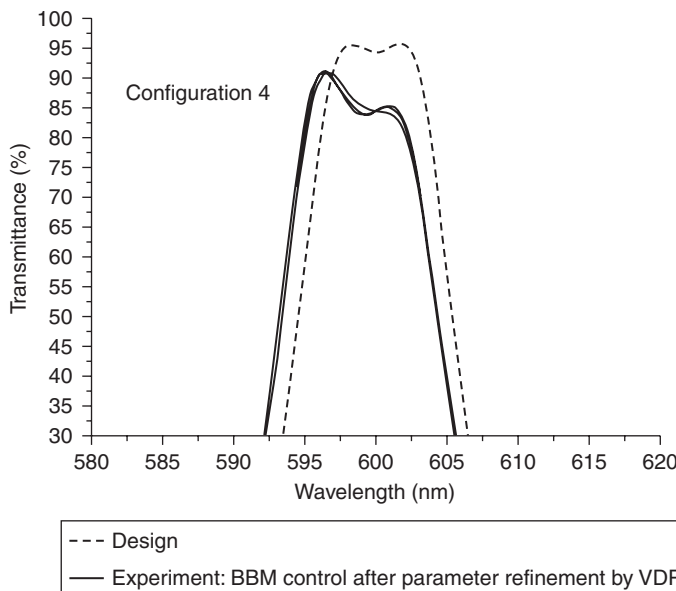
4.9 Process monitored by hybrid combination of a BBM-system and a quartz crystal microbalance (example 2), measured transmittance spectra (three deposition runs) in comparison to the theoretical target spectrum.

than 5% from the spectral target deviations are still evident in all three deposition runs. As an optional extension the connection of the BBM to a direct on-line correction tool was introduced in Section 4.5. Corresponding results are depicted as example 3 in Fig. 4.10. Again, the transmittance curves of the four experimental runs are much closer to the target transmittance than the results of example 1 and exhibit a high reproducibility. Furthermore, the versatility of the VDP system was applied to perform different parameter refinement simulation runs in example 4. As a data base for this analysis the spectral results from the preceding examples were used. It can be seen in Fig. 4.11 that the VDP refined parameters enabled the BBM without the help of any additional tool to a higher precision compared to the first runs in Fig. 4.8. Finally, as a state-of-the-art approach all the above-mentioned tools were simultaneously applied to monitor the deposition in example 5. Consequently, these experiments resulted in the best agreement between measured and calculated transmittance which is shown in Fig. 4.12. In this context, it has to be pointed out again that these small deviations were achieved although design 2 was identified as very unstable under optical broad band monitoring.

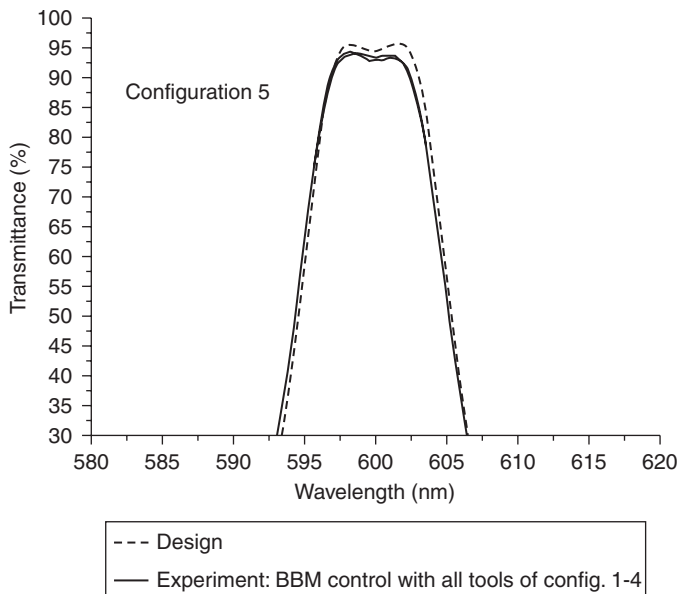
In conclusion, each of the described extensions to pure broad band monitoring allow for a clear improvement in precision and yield. Nevertheless, an advantageous combination of two or more of these tools can even increase these enhancements.



4.10 Process monitored by BBM-system with a direct on-line correction tool (example 3), measured transmittance spectra (four deposition runs) in comparison to the theoretical target spectrum.



4.11 Process monitored by BBM-system after a VDP parameter refinement (example 4), measured transmittance spectra (three deposition runs) in comparison to the theoretical target spectrum.



4.12 Process monitored by a simultaneous application of all presented tools (example 5), measured transmittance spectra (two deposition runs) in comparison to the theoretical target spectrum.

4.7 Deposition control of coating systems with continuous refractive index variation

In principle, layer structures comprising a sequence of discrete layers with constant optical properties, which are commonly processed in optical thin film technology, represent only a very special class of coatings. For a more general consideration, functional optical coatings may be understood as a structure with any arbitrary continuous variation of the refractive index in the depth. In this context, an ideal antireflective coating can be realised on the basis of coating structures with a refractive index decreasing constantly from the substrate value down to the refractive index of the environment. Long before mankind existed, such structures evolved in nature and are presently in the focus of many scientific studies. Still among the most prominent topics the ‘moth eye effect’ can be found, which was first described by Bernhard (Bernhard, 1967) and which is treated in more detail in Chapter 13 of this book. As a rough estimation, the nanostructure on the cornea of moth eyes can be interpreted as a gradient in density of a transparent material with a pertinent continuous decrease in refractive index. The antireflective effect of this system is remarkable in respect to wavelengths covering the entire visible spectral range as well as to the broad regime of angles of incidence.

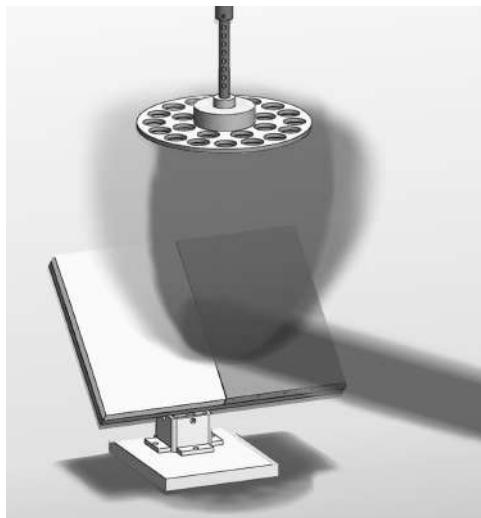
Besides constant optical performance over broad operation ranges including the suppression of spectral sidebands, additional advantages in temperature and laser stability were expected for gradual systems. Therefore, part of the research work on gradual systems, which can be traced back to early 1980s (Ristau *et al.*, 1988), is motivated by demands on the laser power handling capability of optical coatings. In this connection, optical coatings with a continuous variation of the refractive index are often referred to as ‘Rugate Filters’, a term initially reserved for structures with a sinusoidal oscillation in refraction. Even though attempts of closed formulations for the optical transfer properties of the media with a refractive index gradient are studied since more than one century (Schlick, 1904; Schröder, 1941), a solution for structures with an arbitrary variation could not be found until now. Besides most advanced techniques based on Fourier transformation algorithms (Verly *et al.*, 1989), most of the approaches for the description of the spectral behavior of rugate filters comprise a fractioning of the continuous system in very thin discrete layers with a refractive index given by the average value at the respective position in the structure (Southwell, 1985) and a subsequent calculation of the transfer properties using the common matrix formalism for optical thin films. Presently, this ‘quasi-rugate filter’-approach represents the only available method that integrates the dispersion behavior of the involved coating materials.

4.7.1 Production of material mixtures

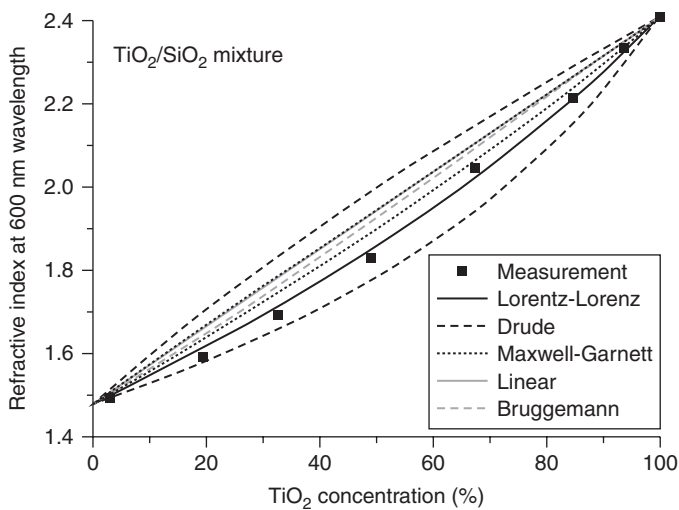
Before the background of the expected superior properties of rugate filters, a large variety of investigations in appropriate production strategies has been performed in optical thin film technology. The fundamental building block is a controllable transition between defined index values within a certain layer thickness. For the technical implementation of such transitions, mixing of two materials by co-deposition or processes with two reactive gas components can be employed. As typical concept involving two reactive gases, the production of $(\text{SiO}_2)_x(\text{Si}_3\text{N}_4)_{1-x}$ layers with defined composition ratio x has been studied for sputter processes and found applications for antireflection coatings on laser diode facets (Katagiri and Ukita, 1990) among others. As a consequence of the relatively low flexibility of oxynitrides, the majority of research activities are dedicated to co-deposition processes of ternary oxide compounds that allow for low optical losses and a high dynamic in refractive indices. In conventional e-beam deposition systems, switching of the e-beam between two crucibles represents a simple principle where the mixing ratio is adjusted by dwell time of the e-beam on the materials. More advanced concepts involve the application of two separate e-beam evaporation sources with independent rate control (Sagebiel, 1983; Ristau *et al.*,

1988). In most cases, these co-deposition processes suffer from stoichiometric deficiencies in the compounds induced by the relatively delicate supply of the reactive gas. Also, strong variations in the material composition often cannot be avoided for a small content of one material as a consequence of the poor stability of the evaporation sources operated at their low rate limits. An additional disadvantage can be attributed to the specific emission characteristics of the e-beam sources in conjunction with the low energy of the adatoms forming the co-deposited layer. Electron microscopic investigations in the layer structure of coatings grown on substrates mounted on a rotating calotte reveal the formation of a nanolaminate instead of a homogeneous mixture of the involved materials. This effect is explained by the consecutive adatom fluxes seen by the growing layer passing the emission zones of the two material sources during rotation (Leitel *et al.*, 2005). This problem can be avoided by a geometric superposition of the material fluxes from the material sources. Also, RF magnetron sputter techniques have been considered for the production of rugate filters (Rickers *et al.*, 2006) employing two separate sputter sources in an activated reactive process. Major challenges related especially to co-sputtering of oxide materials include the control of the reactive atmosphere to maintain the oxidation state of the two different target surfaces.

IBS with a zone target offers several advantages in respect to process stability and quality of the produced coatings (Chao *et al.*, 1999; Lappschies *et al.*, 2005). The fundamental principle of this process strategy is depicted in Fig. 4.13 and comprises the three components: ion source, target and substrate holder of a typical ion beam sputtering arrangement. In contrast to conventional IBS-systems, the multiple target mount is replaced by a zone target that can be positioned in front of the ion source. In dependence on the position, the ion beam interacts simultaneously with surface areas of the two adjacent materials, and the material composition in the emitted sputter flux is related to the interrogated target area fractions as well as the respective sputtering rates. Consequently, the material composition and the corresponding refractive index of the growing layer can be simply adjusted between the two refractive indices of the pure target materials by positioning of the target. A more detailed analysis of the layer formation process indicates an inhomogeneous distribution of the two materials in the sputter flux from the target as observed for the competing e-beam and magnetron processes. However, since the material fluxes from the two zones are directly located side by side and the energy of the sputtered adatoms allows for high mobility on the growing layer, a nearly homogeneous intermixing of the two material components is achieved in the layer structure. Selected effective media theories have been applied to model the dependence of the refractive index of produced oxide mixtures on the material composition (Amotchkina *et al.*,

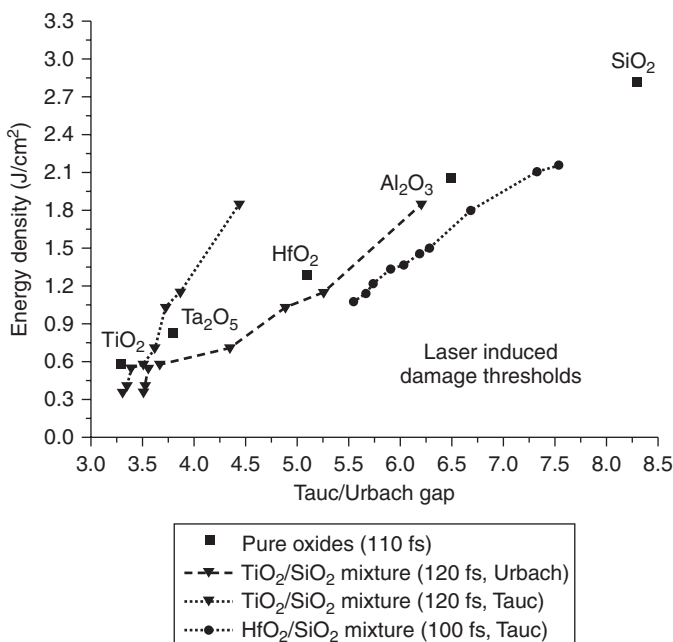


4.13 Schematic operation principle of Ion Sputtering Process with a zone target. The ion beam is directed to the target from the lower right corner. The substrate holder is positioned above the target, which can be moved left and right to adjust the mixture ratio of the sputtered materials.



4.14 Comparison of results for selected effective media theories (Lorentz-Lorenz, Drude, Maxwell-Garnett, linear model, Bruggemann) to the measured refractive indices of TiO₂/SiO₂-films co-deposited in an IBS-process. The concentration of TiO₂ was determined on the basis of EDX-measurements (Lapschies, 2009).

2007; Lappschies, 2009). Among the approaches (see Fig. 4.14) considered for mixed layers of $\text{TiO}_2/\text{SiO}_2$, best accordance to the measured refractive index data was found for the Lorentz-Lorenz model. Another interesting observation was a clear variation of the band gap energy for mixed layers between the values of the pure materials. Opposite to the expectation, defined band gap energies could be assigned to the mixtures indicating that the produced mixed coatings represent a new class of materials with individual properties. This outcome is supported by extended investigations in the properties of these ternary oxide coatings. For example, laser induced damage thresholds (LIDTs) of ternary oxides and pure materials were determined in the femtosecond (fs)-regime (see Fig. 4.15) with an ultra-short pulse laser system operating at a wavelength of 780 nm. In contrast to the nanosecond (ns)-regime, where laser induced damage phenomena are dominated by inclusions and often exhibit a pronounced statistical behavior, laser induced damage by ultra-short pulses is nearly deterministic in nature and governed by the material properties. Models describing the fs damage mechanisms often involve rate equations for the



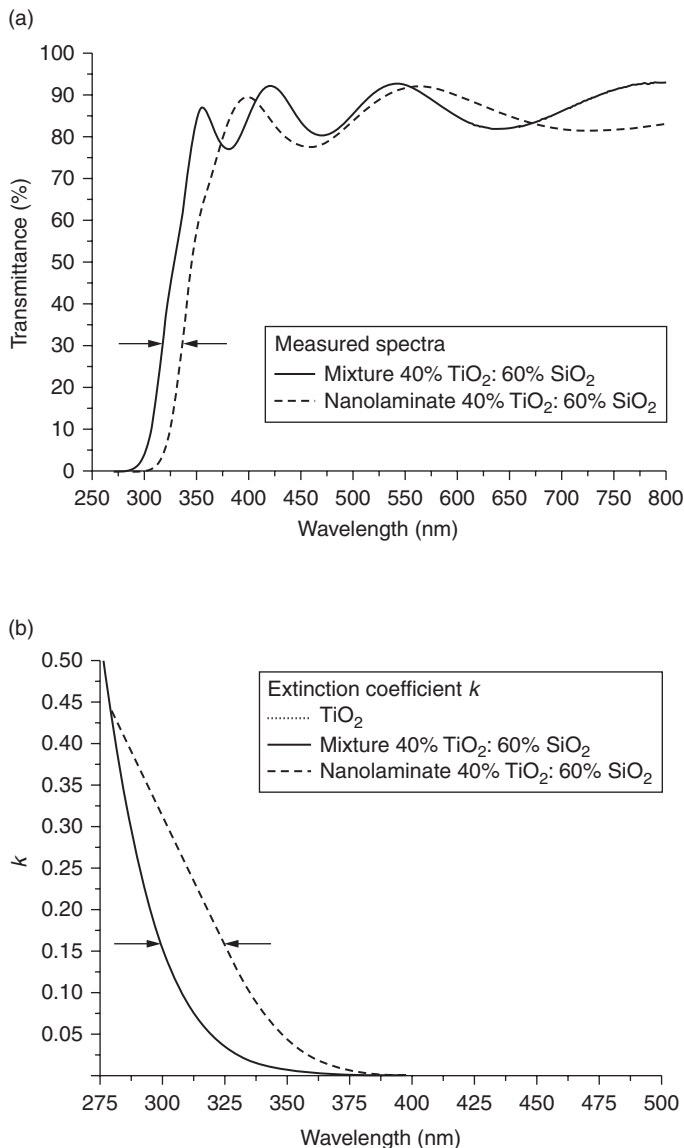
4.15 Laser induced damage thresholds. (Source: Data from Jasapara *et al.* (2001), Nguyen *et al.*, 2007 and Jensen *et al.*, 2010) of pure oxide materials and ternary compounds of $\text{TiO}_2/\text{SiO}_2$ and $\text{HfO}_2/\text{SiO}_2$ as a function of band gap energies (Ristau, 2011).

development of a critical electron density in the conduction band, which are directly related to the band gap energy of the materials (Jupé *et al.*, 2009). Modeling the LIDT-values of the pure materials in respect to their band gap energy, a specific correlation can be found which is reflected by the corresponding measurement values (LIDT for TiO_2 , Ta_2O_5 , HfO_2 , Al_2O_3 and SiO_2 in Fig. 4.15). A comparison of these data to the threshold values of the ternary compounds evidently corroborates the assumption, that these mixtures can be considered as a new class of individual materials with adjustable refractive indices and band gap energies.

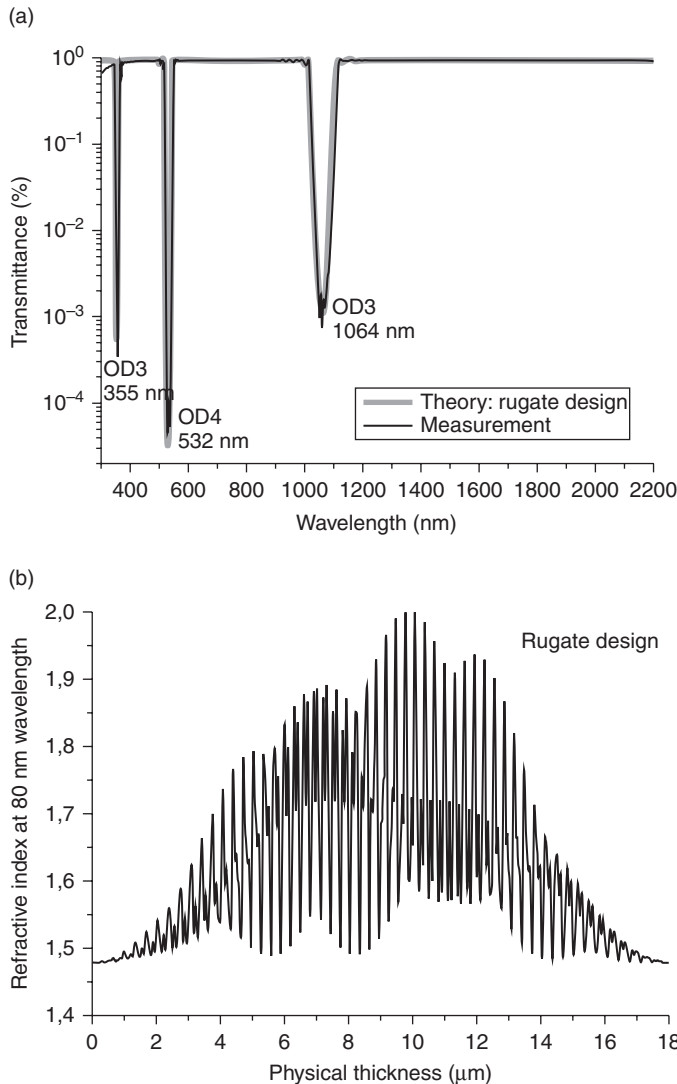
This experimental finding is additionally supported by a study of nanolaminates in comparison to co-deposited single layers. As an example (Lappschies *et al.*, 2007), a nanolaminate consisting of 50 alternate thin films of the materials TiO_2 and SiO_2 was produced with an ion beam sputtering process to form a 2 QWOT layer for the wavelength 1.064 nm. This corresponds to a geometric layer thickness of 4.6 nm for the TiO_2 - and 7.2 nm for the SiO_2 -layers, respectively. The spectrum measured for this nanolaminate is depicted in Fig. 4.16a. In a second experiment, a single layer was deposited with the same material contents ratio as the stack by co-deposition involving the described IBS-process with a zone target (Fig. 4.16a). Evaluating the measured spectrum of the co-deposited layer, again the particularity of ternary oxides can be observed. Obviously (see Fig. 4.16a), the transmittance limit of the co-sputtered layer is shifted towards shorter wavelengths, and the spectral behavior of the extinction coefficients (Fig. 4.16b) also indicates a band gap shifted by nearly 20 nm into the UV-region. This pertinent shift of the band gap towards shorter wavelengths opens the way towards the improvement of high power laser coating systems for the UV-spectral range. For instance, the development of excimer lasers and frequency conversion schemes operating between 240 and 270 nm may significantly benefit from ternary layer materials consisting of the deposition materials HfO_2 , Al_2O_3 and SiO_2 . Considering also further experimental results indicating improved temperature stability up to 600°C of ternary compounds, this new class of materials has a high potential for the optimization of coatings with high laser induced damage thresholds on the basis of appropriate positioning of ternary compounds in the layer system according to the internal distribution of the electric field strength. Recent studies (Mende *et al.*, 2011) in such optimization strategies to enhance the power handling capability of high reflectors reveal clear improvements for the wavelength 355 nm of the frequency converted Nd:YAG-laser.

4.7.2 Deposition control of rugate filters

Before the background of the experimental results for discrete material mixtures, IBS processes with a zone target can be considered as a



4.16 Measured transmittance spectrum of a stack with 50 discrete alternate layers of TiO₂ and SiO₂ (nanolaminate) compared to a single mixture layer of the same material composition and nearly the same thickness (a, both: ion beam sputtering). The related extinction coefficients in comparison to pure TiO₂ are depicted in (b). Both graphs indicate a clear shift of the band gap to lower wavelengths for the co-deposited layer (Lappschies *et al.*, 2007).



4.17 (a) Theoretical and realized spectrum of a quasi rugate filter for laser protection goggles. The coating system was produced with an IBS-process employing a BBM-system for controlling the position of the zone target of $\text{Ta}_2\text{O}_5/\text{SiO}_2$. (b) The refractive index step function followed by the BBM-tracing algorithm during deposition is illustrated.

promising strategy for the reproducible production of rugate filters with complex variations in the refractive index profile. As main ingredients for a stable production of such structures, the thorough control of the refractive indices and the positioning of refractive index values in the

depth of the layers have to be harnessed. In principle, an ideally continuous variation of the refractive index can be achieved by a steady motion of the zone target in front of the ion beam. However, such a strategy would imply an absolutely reproducible matching of the attained refractive index values with the target position which cannot be perfectly realized in practice. As a consequence of target erosion and intermediate oxidation effects, minute deviations in the refractive index are observed for a certain position of the zone target. This problem can be solved to an acceptable extent on the basis of the quasi rugate deposition technique. In this approach the continuous variation of the refractive index is approximated by a series of very thin discrete layers with adapted refractive index (Lappschies *et al.*, 2004a, 2005). An example is illustrated in Fig. 4.17b for a coating to be adapted for laser protection goggles against radiation of the Nd:YAG-laser operating at the wavelength 1064 nm as well as its harmonics at 532 and 355 nm. A rugate filter design was selected because nearly undistorted spectral transmittance had to be reached for visible range (see Fig. 4.17a). In the present case, the refractive index profile had been resolved into a series of 1854 layers with 726 refractive index steps accumulating to a total thickness of 18.1 μm . Even though the average thickness of the constituent layers is in the range of less than 10 nm, the BBM-system described before can be employed for controlling of the deposition process after adaptation to the zone target option. In contrast to the control of conventional processes, the BBM device moves the zone target to next position instead of switching a shutter for layer termination. The underlying software algorithms for the determination of the switching point can be directly transferred to the control of rugate filters and allow for a compensation of small variations in the refractive index for each target position. In this configuration, the position control is regularly performed in refractive index steps of typically $\Delta n = 0.05$ which can be adjusted with a reproducibility of approximately $\Delta n \approx 0.02$. Applying this control method, a good agreement between the spectrum of the realized quasi rugate filter system and the calculated spectral performance could be achieved (see Fig. 4.17a).

4.8 Conclusion

Advanced monitoring and control concepts of high-precision optical coatings gain more and more importance on the way toward deterministic production in modern optical fabrication. The routine implementation of a variety of recently developed control approaches and tools could be realized by intensive research efforts over the last years. In most cases direct optical *in situ* measurements, in particular, sophisticated optical broad band monitors form the basis of these versatile and modular concepts.

Today, virtual deposition systems often replace classic design stability analysis tools, which are based only on design thickness variations. In contrast, the VDP concepts are process as well as process control specific and reproduce e.g. error accumulation or compensation effects inherently. They are not only advantageous for a reliable pre-production design stability analysis but also as a comprehensive and flexible reverse engineering tool for minimizing process development and error identification times.

Direct on-line correction tools can be automatically activated if critical layer thickness or dispersion data deviations occur. These software modules initialize design refinement algorithms, which calculate re-optimized designs that differ only slightly from the original target designs in most cases. But in contrast to the original designs failing in these critical process runs the automatically re-optimized target designs result directly in a significantly higher rate of yield. In addition, the increased yield is complemented by a gain in precision and flexibility of the manufacturing process.

Advanced hybrid monitoring concepts are a further proven approach to enhance precision and yield for complex multilayer structures. On the one hand, the conventional sequential application of different optical or non-optical thickness monitoring systems for one multilayer stack can be extended by superior cross calibration routines. On the other hand, recent true hybrid monitoring concepts can evaluate the measured data of more than one system simultaneously for a precise and fail-safe endpoint detection.

A maximum impact on precision, flexibility and yield is achieved if the approaches summarized above are combined within a production environment. As shown by the practical examples, even extremely critical multilayer designs can be deposited successfully, if multiple advanced monitoring and control concepts are applied. However, this multi-concept approach requires not necessarily a complex hardware basis as could be demonstrated. All discussed approaches allow for a rapid manufacturing without the need for developing multilayer design dependent individual monitoring strategies.

Material mixtures produced by co-deposition processes and rugate filters with an arbitrary continuous variation of the refractive index in the depth are a particular challenge for adapted production strategies. Ternary oxides as material mixtures represent a new class of materials with individual properties and can be applied to realize rugate filters, which offer new degrees of freedom in the design of optical coatings. However, based on an ion beam sputtering process with a zone-target, quasi rugate filters can be successfully manufactured under optical broad band monitoring. In the quasi rugate filters very thin discrete layers with very small refractive index steps substitute the continuous variation of the refractive index.

Besides further technological improvements in the control devices and software environments, an advanced approach towards deterministic production processes would involve a direct modeling of thin film growth. In

this visionary concept, theoretical calculations on the basis of molecular dynamic techniques and quantum mechanics may be employed to determine the structural and optical properties of the growing coating from the specific parameters of a deposition process. Vice versa, a forecast of the needed process parameters to achieve a certain set of coating properties may come into reach for harnessing high quality optical coating production according to future demands.

4.9 References

- Amotchkina, T. V., Ristau, D., Lappschies, M., Jupé, M., Tikhonravov, A. V. and Trubetskoy, M. K. (2007). 'Optical properties of $\text{TiO}_2 - \text{SiO}_2$ mixture thin films produced by ion-beam sputtering', *Optical Interference Coatings*, OSA Technical Digest, TuA8.
- Amotchkina, T.V., Trubetskoy, M.K., Pervak, V., Schlichting, S., Ehlers, H., Ristau, D. and Tikhonravov, A.V. (2011). 'Comparison of algorithms used for optical characterization of multilayer optical coatings', *Applied Optics*, **50**, 3389–3395.
- Bauer, H.H. and Nüssler, E. (1994). 'In-situ optical multichannel spectrometer system', *SPIE*, **2253**, 423–431.
- Bernhard, C. G. (1967). 'Structural and functional adaptation in a visual system', *Endeavor*, **26**, 79–84.
- Chao, S., Wang, W.-H., Hu, M.-Y. and Wang, L.-C. (1999). 'Characteristics of ion-beam-sputtered high-refractive-index $\text{TiO}_2\text{-SiO}_2$ mixed films', *Journal of the Optical Society of America A*, **16**(6), 1477–1483.
- Ehlers, H., Schlichting, S., Schmitz, C. and Ristau, D. (2010). 'Adaptive manufacturing of high precision optics based on virtual deposition and hybrid process control techniques', *Chinese Optics Letters*, **8**, 62–66.
- Ehlers, H., Schlichting, S., Schmitz, C. and Ristau, D. (2011). From independent thickness monitoring to adaptive manufacturing: advanced deposition control of complex optical coatings, [8168–71], in Macleod, A., Lequime, M. and Ristau, D. (eds.), *Advances in Optical Thin Films IV* Marseille, France, 5–7 September, *Proceedings of SPIE*, Vol. **8168**.
- Emiliani, G., Piegari, A. and Masetti, E. (1988). 'Fast scan spectrometer for monitoring of thin film optical properties', *SPIE*, **1012**, 35–46.
- Günster, St., Kadkhoda, P. and Ristau, D. (2001). 'Online spectrophotometric characterisation of $\text{MgF}_2/\text{LaF}_3$ – fluoride multilayer coatings production', *Proceedings of the Conference on Optical Interference Coatings*, OSA Technical Digest p. ME9–1, 2001.
- Holm, C. (1979). 'Optical thin film production with continuous reoptimization of layer thicknesses', *Applied Optics*, **18**, 1978–1982.
- Jasapara, J., Nampoothiri, A.V.V., Rudolph, W., Ristau, D. and Starke, K. (2001). 'Femtosecond laser pulse induced breakdown in dielectric thin films', *Physical Review B*, **63**(4), 045117.
- Jensen, L., Mende, M., Blaschke, H., Ristau, D., Nguyen, D., Emmert, L. and Rudolph, W. (2010). Investigations on $\text{SiO}_2/\text{HfO}_2$ mixtures for nanosecond and femtosecond pulses, in Exarhos, G. J., Gruzdev, V. E., Menapace, J. A., Ristau, D. and

- M. J. Soileau (eds.), Proceedings of the 42nd Annual Symposium on Optical Materials for High Power Lasers, *Proceedings of SPIE*, vol. **7842**.
- Jupé, M., Jensen, L., Melninkaitis, A., Sirutkaitis, V. and Ristau, D. (2009). ‘Calculations and experimental demonstration of multi-photon absorption governing fs laser-induced damage in titania’, *Optic Express*, **17**(15), 12269–12278.
- Katagiri, Y. and Ukita, H. (1990). ‘Ion beam sputtered $(\text{SiO}_2)_x(\text{Si}_3\text{N}_4)_{1-x}$ antireflection coatings on laser facets produced using $\text{O}_2\text{-N}_2$ discharges’, *Applied Optics*, **29**(34), 5074–5079.
- Lappschies, M. (2009). Rugate Filter und Mischschichten für optische Hochleistungskomponenten, dissertation, Leibniz Universität Hannover.
- Lappschies, M., Görtz, B. and Ristau, D. (2004a). ‘Application of optical broad band monitoring to quasi-rugate filters by ion beam sputtering’, *Applied Optics*, **45**(7), 1502–1506.
- Lappschies, M., Görtz, B. and Ristau, D. (2005). Optical monitoring of rugate filters. In Mazuray, L. and Wartmann, R. (eds.), Optical Design and Engineering II, *Proc. of SPIE*, vol. **5963**, 1Z1–1Z9.
- Lappschies, M., Groß, T., Ehlers, H. and Ristau, D. (2004b). ‘Broadband optical monitoring for the deposition of complex coatings’, *Proceedings of the Conference on ‘Advances in Optical Thin Films’*, St. Etienne, France, SPIE Vol. **5250**, 637–645.
- Lappschies, M., Jupé, M. and Ristau, D. (2007). ‘Extension of ion beam sputtered oxide mixtures into the UV spectral range’, *Optical Interference Coatings*, OSA Technical Digest, TuA7.
- Lappschies, M., Schallenberg, U. and Jakobs, S. (2011). Exclusive examples of high-performance thin-film optical filters for fluorescence spectroscopy made by plasma-assisted reactive magnetron sputtering, Advances in Optical Thin Films IV, in Lequime, M., Macleod, H. A., Ristau, D. (eds.), *Proceedings of SPIE*, **8168**, 81680Y.
- Leitel, R., Stenzel, O., Wilbrandt, S., Gäbler, D., Janicki, V. and Kaiser, N. (2005). ‘Fabrication and characterization of rugate structures composed of SiO_2 and Nb_2O_5 ’, *Optics and Precision Engineering*, **13**(4), 505–511.
- Masetti, E., Montecchi, M., Larciprete, R. and Cozzi, S. (1996). ‘In situ monitoring of film deposition with an ellipsometer based on a four-detector photopolarimeter’, *Applied Optics*, **35**(28), 5626–5629.
- Mende, M., Jensen, L. O., Blaschke, H., Ehlers, H. and Ristau, D. (2011). Laser-induced damage of pure and mixture material high reflectors for 355-nm and 1064-nm wavelength, [8168–73], in Macleod, A., Lequime, M. and Ristau, D. (eds.), Conference on Advances in Optical Thin Films IV, *Proceedings of SPIE*, Vol. **8168**, 816821.
- van Milligen, F.J. and Macleod, H.A. (1985). ‘Development of an automated scanning monochromator for monitoring thin films’, *Applied Optics*, **24**(12), 1799.
- Netterfield, R.P., Martin, P.J. and Müller, K.-H. (1988). ‘In-situ optical monitoring of thin film deposition’, *SPIE*, **1012**, 10–15.
- Nguyen, D. N., Cravetchi, I., Rudolph, W., Jupe, M., Lappschies, M., Starke, K. and Ristau, D. (2007). ‘Experimental and theoretical studies of subpicosecond laser damage in $\text{Ti}_x\text{Si}_{1-x}\text{O}_2$ composite films’, in Exarhos, G. J., Guenther, A. H., Lewis, K. L., Ristau, D., Soileau, M. J. and Stolz, C. J. (eds.), Proceedings of the 39th Annual Symposium on Optical Materials for High Power Lasers, *Proceedings of SPIE*, Vol. **6720**, 64031A.

- Pervak, V. (2010). 'Recent development and new ideas in the field of dispersive multilayer optics', *Optical Interference Coatings*, OSA Technical Digest, FB1.
- Powell, I., Zwinkels, J. C. M., Robertson, A. R. (1986). 'Development of optical monitor for control of thin-film deposition', *Applied Optics*, **25**(20), 3645.
- Rademacher, D., Vergöhl, M. and Richter, U. (2011). 'In situ thickness determination of multilayered structures using single wavelength ellipsometry and reverse engineering', *Applied Optics*, **50**(9), C222–C227.
- Rickers, C., Polenzky, C. and Vergöhl, M. (2006). 'Deposition of rugate filters by magnetron sputtering technology', Proceedings of the 6th International Conference on Coatings on Glass and Plastics, 18–22 June 2006, Dresden, Germany.
- Ristau, D. (2010). 'Ion beam sputtering – state of the art and industrial application', Proceedings of the 8th International Conference on Coatings on Glass and Plastics, 203–208.
- Ristau, D. (2011). 'Optical thin films with high laser stability', Proceedings of the 54th Annual Technical Conference Proceedings of the Society of Vacuum Coaters, Chicago, IL, ISSN 0737–5921, 276–282.
- Ristau, D. and Groß, T. (2005). 'Ion beam sputter coatings for laser technology', in Mazuray, L. and Wartmann, R. (eds.), Optical Design and Engineering II, *Proceedings of SPIE*, Vol. **5963**, 315–326.
- Ristau, D. and Günster, St. (2003). 'Optimization of optical coatings for the UV/VUV-range', Proceedings of the Conference on Advanced Characterization Techniques for Optics, Semiconductors, and Nanotechnologies, San Diego, USA, *SPIE* Vol. **5188**, 80–95.
- Ristau, D., Groß, T., Lappschies, M. and Ehlers, H. (2006). 'Optical broadband monitoring of conventional and ion processes', *Applied Optics*, **45**(7), 1495–1501.
- Ristau, D., Lappschies, M., Schlichting, S. and Ehlers, H. (2008). 'State of the art in deterministic production', in Kaiser, N. and Lequime, M. and Macleod, H. A. (eds.), Advances in Optical Thin Films III, Glasgow, UK, 2–3 September. *Proceedings of SPIE*, Vol. **7101**, 71010C–71010C-14.
- Ristau, D., Schink, H., Mittendorf, F., Akhtar, S. M. J., Ebert, J. and Welling, H. (1988). 'Laser induced damage of dielectric systems with gradual interfaces at 1.064 μm', in Bennett, H. E., Guenther, A. H., Newnam, B. E. and Soileau, M. J. (eds.), Proceedings of the Conference on Laser-Induced Damage in Optical Materials NIST Spec. Publ. No.775, Boulder, USA, 26–28 October, 414–426.
- Sagebiel, A. (1983). Appareil pour le control d'un processus de coévaporation pour le double canon à electron. Academie de Montpellier.
- Schlichting, S., Heinrich, K., Ehlers, H. and Ristau, D. (2011). 'Online re-optimization as a powerful part of enhanced strategies in optical broadband monitoring', *Proceedings of SPIE*, Vol. **8168**, 81681E.
- Schlick, M. (1904). *Über die Reflexion des Lichtes in einer inhomogenen Schicht*. Dissertation, Berlin.
- Schröder, H. (1941). 'Bemerkung zur Theorie des Lichtdurchgangs durch inhomogene durchsichtige Schichten', *Annalen der Physik*, **5**(39), 55.
- Southwell, W. H. (1985). 'Coating design using very thin high- and low-index layers', *Applied Optics*, **24**(4), 457.
- Starke, K. and Ristau, D. (2011). Highly stability optical coatings by employing gradient index designs, *Proceedings of the 54th Annual Technical Conference Proceedings of the Society of Vacuum Coaters*, Chicago, IL, ISSN 0737–5921, pp. 463–467.

- Starke, K., Groß, T. and Ristau, D. (2000). 'Rapid prototyping of optical thin film filters', *Conference Optical and Infrared Thin Films, SPIE*, **4094**, 83–92.
- Stenzel, O., Wilbrandt, S., Stenzel, O. and Kaiser, N. (2010). DE 102009012756 (A1) Method for measuring optical characteristics of movable probe in coating installation, involves measuring intensity of transmitted beam by probe at transmission detector.
- Sullivan, B. T. (2010). An overview of optical monitoring techniques, *Optical Interference Coatings*, OSA Technical Digest, TuC1.
- Sullivan, B. T. and Dobrowolski, J. A. (1993). 'Deposition error compensation for optical multilayer coatings: II. Experimental results-sputtering system', *Applied Optics*, **32**(13), 2351.
- Tilsch, M. K., Grigoris, M. and Ockenfuss, G. J. (2010). 'Manufacturing of precision optical coatings', *Chinese Optics Letters*, April 30, **8**, Supplement, 38–43.
- Tilsch, M., Scheuer, V., Staub, J. and Tschudi, T. (1994). 'Direct optical monitoring instrument with double detection system for the control of multilayer systems from the visible to the near infrared', *SPIE*, **2253**, 414–422.
- Verly, P. G., Dobrowolsky, J. A., Wild, W. J. and Burton, R. L. (1989). 'Synthesis of high rejection filters with the Fourier transform method', *Applied Optics*, **28**, 2864–2875.
- Vidal, B., Fournier, A. and Pelletier, E. (1978). 'Optical monitoring of nonquarterwave multilayer filters', *Applied Optics*, **17**(7), 1038.
- Vidal, B., Fournier, A. and Pelletier, E. (1979). 'Wideband optical monitoring of non-quarterwave multilayer filters', *Applied Optics*, **18**(22), 3851.
- Zöller, A., Boos, M., Hagedorn, H. and Romanov, B. (2008). 'Computer simulation of coating processes with monochromatic monitoring', in Kaiser, N., Lequime, M. and Macleod, H. A. (eds.), *Proceedings of the SPIE, Advances in Optical Thin Films III*, Vol. **7101**, 71010G–71010G-7.

Complex materials with plasmonic effects for optical thin film applications

A. SYTCKOVA, ENEA Optical Coatings Laboratory, Italy

DOI: 10.1533/9780857097316.2.133

Abstract: Plasmonic materials are complex nanostructures that can be designed and manufactured to significantly alter electromagnetic radiation in ways not available to traditional thin film devices. These new materials offer measurement and characterization challenges to determine their unique properties and improve our understanding of the underlying physics of nanostructured materials. Applications of plasmonics ranging from unique filters for spectral control to hyperbolic and negative refractive index materials enabling novel photonic devices are all very active areas of research today.

Key words: plasmonics, metamaterials, optical coatings, characterization, modeling.

5.1 Introduction

At the beginning of the 1960s McAlister and Stern¹ demonstrated that absorption bands in reflection and transmission spectra of very thin metal films illuminated by *p*-polarized light at oblique incidence are due to excited resonances normal to the film plane. Such collective longitudinal optical modes were previously theoretically explained by Ritchie² after the experimental observation of Ferrell in electron energy loss spectroscopy of a thin metal slab.³ So-called Ferrell modes in metals are known nowadays also as volume or bulk plasmons; they are collective oscillations of free electrons at a frequency ω_p that can propagate in a material when its dielectric function $\varepsilon_c(\omega_p)$ approaches zero.

Bulk plasmon is a radiative mode decaying after excitation by spontaneous emission or due to collision damping. But if coupled to the incident photon, this mode becomes propagating with the wave vector of the photon and forms so-called plasmon polariton (PP). In continuous metal films (or semiconductor in free-electron regime), PPs are not forbidden only if they are surface-bound; they are known as surface plasmon polaritons (SPPs) or simply, surface plasmons (SPs).⁴ Surface plasmons may exist in a conductor

only if its dielectric function ε_c has a negative real part $\varepsilon'_c \equiv \text{Re } \varepsilon_c < 0$, and these SPs have a well-pronounced resonance appearance when the optical losses in the material are low, that means when the imaginary part of the dielectric function is small $\varepsilon''_c \equiv \text{Im } \varepsilon_c \ll -\text{Re } \varepsilon_c$. In different ranges of optical spectrum, either metals or semiconductors may satisfy these two criteria simultaneously and thus be good plasmonic materials. Various types of collective electron excitations may be rigorously described like the many-body dynamical electronic response of solids to electromagnetic radiation.⁵

SPs can be excited at a plane dielectric-conductor interface by means of matching techniques like prism or grating, and at some well-determined conditions on incidence angle and dielectric function properties of both interfacing materials. With change of the conductor's geometry, i.e. when moving from planar to spherical shape, the incidence angle ceases to determine resonance excitation, for symmetrical reasons. Localized SP resonances (LSPRs) known also as localized SPPs, localized SPs or Mie PPs, can be excited at the surface of metal or semiconductor particles embedded in a less conducting host material even at arbitrary incidence. This phenomenon determines colors of artistic glasses with metal particle suspension, the effect known and exploited since antiquity.⁶

Plasmonic materials shaped into tiny volumes called nanoparticles (NPs) and embedded in a host matrix of another material, or introduced as ultrathin films into multilayers, are subject of an intense research in the last decade.^{7,8} If the inclusions are periodically organized, it is common to speak about metamaterials (MMs). Continuously increasing interest in such composites is due to their outstanding capability to concentrate electro-mechanical energy at optical frequencies onto nanoscale overcoming the theoretical limits for optical confinement valid for electromagnetic energy.⁹ The enhancement it enables provides a unique platform for next-generation photonic devices^{10,11} and ensures technologic revolution in many fields of life science.¹² By variation of NP doping,¹³ size and shape,^{14,15} as well as by a suitable choice of host,¹⁶ substrate¹⁷ or gain¹⁸ material, novel artificial materials with particular optical properties may be engineered thanks to a proper tuning of SPs, localized or propagating.

Various bottom-up and top-down synthesis methodologies are used for creation of thin films with NPs, including lithographic techniques,^{19,20} focused-ion-beam milling,²¹ electrochemical methods,²² self-assembling from colloidal solutions^{23,24} and direct laser writing.²⁵ Physical vapor deposition (PVD) methods are common for many applications too, as despite a relatively poor control on NP size and the spacing they provide, these methods have the advantages of being compatible with most substrates of technological interest and with most technologies for nanoplasmonic device manufacturing. Same PVD methods, i.e. sputtering,²⁶ thermal and

electron-beam evaporation,²⁷ laser ablation,²⁸ etc., are used for fabrication of multilayer devices with ultrathin metal film with SP properties. An extensive review of different fabrication methods of MMs has been compiled by Boltasseva and Shalaev.²⁹

In this chapter we overview recent results on modeling and characterization of novel materials with plasmonic properties useful for thin film applications.

5.2 Physics of some classes of novel materials for plasmonic applications

Either propagating or localized, SPs are waves on the surface of a conductor (metal or semiconductor) interfaced with another less conducting material (semiconductor or dielectric). Therefore, to understand the optical properties of plasmonic media it is essential to know the physical properties of their basic constituent materials.

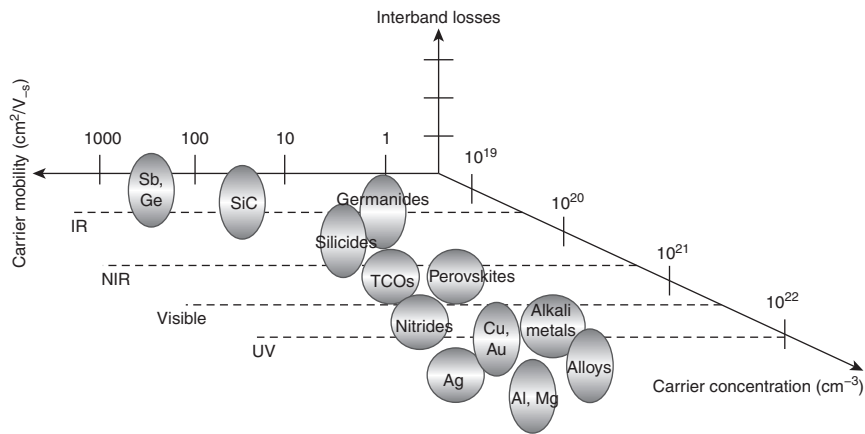
Notice that nanostructured inclusions change radically the dispersion relation of the original host material. In fact, thanks to this, MMs are media with *ad hoc* engineered photonic density of states.³⁰

In the visible and infrared regions most of MMs are strongly dispersive, and the origin of this dispersion is mostly ascribed to the conductor component. Conversely, what determines dramatically the optical performance of a multilayer stack with an ultrathin continuous or semi-continuous layer(s) of a conductor material, are the optical properties of the conductor material. To the optical properties of dielectrics many classical textbooks are dedicated and, as far as the key-materials for plasmonic materials are conductors, let us focus our attention onto optical features of metals and semiconductors.

Macroscopically, the complex dielectric function $\epsilon_c(\omega) = \epsilon'_c + i\epsilon''_c = (n + ik)^2$ totally describes the electronic response of a conductor to the electromagnetic wave with frequency ω . Here n is the material refractive index and k is its extinction coefficient. The modified Drude approximation is normally used to model the dielectric function of a conductor:

$$\epsilon_c(\omega) = \epsilon_\infty - \frac{\omega_p^2}{\omega(\omega + i\gamma)} \quad \omega_p^2 = \frac{Ne^2}{\epsilon_0 m^*} \quad [5.1]$$

Here γ is phenomenological damping term, ω_p is plasma frequency, N is conduction electron density, m^* is the effective optical mass of conduction electrons and ϵ_0 is permittivity of vacuum. The offset ϵ_∞ is ‘core polarizability’ of the material that encompasses contributions due to the interband transitions of bound electrons (single particle excitations from valence to conduction bands). This term is taken equal to unit for metals in free-electron regime



5.1 Carrier concentration and mobility, together with interband transition losses can be optimized by a proper choice of material for a given application. The heights of the bubbles representing main plasmonic materials indicate their interband losses in the corresponding part of the spectrum. (Source: Figure similar to that in Reference 31. Copyright 2011, AAAS.)

(classical Drude model), while it is a not-unit parameter for description of conductors at higher frequencies.

As we see, to guarantee a negative dielectric permittivity, the carrier concentration should be high enough. To ensure good plasmonic performance not only the sign of ϵ'_c is important, but also the low level of losses, that means high mobility of the carriers and low interband losses (we will consider in detail this issue below). The ideal conductor for plasmonics would have the corresponding indicator maximally left-shifted along the carrier mobility axis, and positioned on the horizontal zero-interband-transition plane,³¹ Fig. 5.1.

More precisely, from the point of view of electronic features, to be good for plasmonic applications a material should possess four main properties:³² (i) the energy bands at the Fermi level must have the gradient sufficiently high to ensure an appropriate ω_p ; (ii) all scattering types (including electron-electron, electron-phonon, surface and defect interactions) represented by γ , must be low so that $\gamma \ll \omega_p$; (iii) the ‘core polarizability’ ϵ_∞ must be low; (iv) the ratio ω_g/ω_p , where ω_g is the optical gap, should be proportional to the sharpness of the band edge $\epsilon_c''(\omega_g)$. Notice, that interband transitions provoke screening in real conductors, thus shifting the plasma frequency from the value ω_p . Therefore, the condition (iv) also means that the screened plasma frequency ω_s should be well-separated from the optical gap, i.e. the ratio ω_g/ω_s must be low.

5.3 Ceramic matrix with embedded metal nanostructures

This section considers the influence of geometrical factors on the optical properties of plasmonic material. They are essentially four: the size and the shape of inclusions, the particle interdistance and the type of their distribution within the host material, either periodic or random.

First of all, we shall distinguish between the case of NP inclusions distributed within the volume of the host material, either a bulk or a thin film, and, on the other hand, the case of stratified structures containing layers with NP inclusions or thin metallic layers, in particular, ultrathin (partially) percolated metallic layers. Only the case of metal layers deals with propagating SPs (or SPPs), while for all the structures localized SPs (LSPs) are inherent.

Size scale of sub-wavelength metal particles determines the theoretical approach proper for calculation of the electromagnetic field in the material. While for the systems with NP size much smaller than the light wavelength, but larger than the mean free path of the oscillating electrons (typically about 30–50 nm), the quasi-static approximation may be successfully used to describe polarizability of a metallic sphere, for smaller or bigger particles significant corrections are needed. In particular, retardation results in larger particles bring to a corrected expression³³ for the material polarizability, while for much smaller NPs purely classical model is not valid anymore as far as quantum effects begin to set in.

To get an idea what particle sizes we are speaking about, let us refer to silver nanospheres, the simplest NP geometry. For the spheres of radius a such that $10 \text{ nm} < a \ll \lambda$ the quasi-static approach is valid.⁴ For larger particles the phenomena to take into account are the depolarization field inside the NPs on one hand,³⁴ the radiation damping caused by the radioactive decay of electron oscillations into photons on the other hand,³⁵ as well as non-radiative decay due to intraband excitations within the conduction band and interband transitions.³⁶

For smaller particles, having $a < 10 \text{ nm}$ so-called ‘chemical interface damping’ due to elastic scattering at particle surface must be considered.³⁷ For even smaller particles with $a \leq 1 \text{ nm}$ a combination occurs of the large concentration of conduction electrons typical for metals ($v \approx 10^{23} \text{ cm}^{-3}$) with the small absolute number of electrons $N \approx va^3$. This results in comparability of the energy increase of an electron excited by a photon with its kinetic energy, i.e. $hc/(\lambda N) \sim k_B T$, where T is the temperature and k_B is the Boltzmann constant. Therefore, for such small particles, plasmons as collective oscillations of electrons cannot represent adequately the mechanisms of light-matter interaction, and multiple-particle excitations should be considered using the language of quantum mechanics.³⁷

Interparticle distance δ scales with the particle size, naturally. For well-separated NPs (with $a \ll \delta$) the dipolar approximation is valid for the description of LSP coupling. The dipole interaction has significantly different behavior for the case of closely positioned NPs ($\delta \ll \lambda$) and for the case of well-separated NPs. In the first case the far field follows δ^{-3} dependence caused by the prevailing near-field character of the interaction, and strong field localization in interparticle gaps takes place,³⁸ while for well-separated NPs the interference pattern is observable in the near-field, the far field behaves with the distance dependence of δ^{-1} , and the interspacing $\delta \sim 3a$ results sufficient to enter in the regime of essentially isolated NPs.³⁹

5.3.1 Materials with quantum dots

When the size of NP inclusions in a medium is comparable with the de Broglie wavelength of electron, it is common to speak about quantum dots (QDs) in a host matrix. Localized SPs (LSPs) of metal QDs are charge density oscillations of metal free electrons in resonance with the driving electromagnetic field of the incident light. For a given host matrix where QDs are embedded, the LSP resonance (LSPR) frequency is tunable by the QD size and geometry, but mainly depends on free electron density of the metal, value modulated by the high frequency dielectric constant ϵ_{∞} .⁴⁰

Either QDs are distributed randomly⁴¹ or periodically,⁴² depending on application, the peculiarity of such nanostructured materials consists in the fact that the SP oscillations should be considered in terms of quantum mechanics, for example applying quantum wells as first theoretical model.^{43,44} In fact, conventional plasmons in a nanohole array or a metal strip were experimentally proved to possess properties that are essentially quantum, like entanglement⁴⁵ and squeezing.⁴⁶ Within the quantum mechanics approach, the squared modulus of the electron wavefunction provides probability of the electron or hole density distribution. For a series of coupled periodic wells, the energy levels of the single well are split, and we deal with energy bands when the number of coupled wells becomes large. The electrons can be localized or delocalized, like in molecules, if the wells are not equidistant. For the nanostructures with elementary geometries that support elementary plasmons, a hybridization model was developed by Prodan *et al.*⁴⁷ as an electromagnetic analog of molecular orbital theory.

The importance of QD geometries for future nanoscale quantum information processing⁴⁸ or fundamental research of quantum effects,⁴⁹ is determined by the ability of these isolated broadband emitters to interact exceptionally well with plasmons in bigger nanostructures. Near a metallic nanowire, an excited QD with high probability emits spontaneously a single photon into the plasmonic mode and, despite the decoherence expected due

to electron collisions, the plasmon will carry the quantum bit of the exciting photon and transmit it in the back-conversion into photon. Controlled addressing of QDs by nanowire plasmons becomes possible.⁵⁰ Moreover, the emission wavelength of QDs may be tuned over dozens of nanometers by employing SPPs.⁵¹ Furthermore, novel architectures for enhanced three-dimensional quantum confinement like QDs embedded in wells are under extensive study for QD photodetectors for the IR.⁵² A short comprehensive overview on new frontiers achievable with quantum plasmonics may be found in Jacob and Shalaev.⁵³ Most of these effects are important for near-field applications, while far field appropriate homogenization theories are suitable for description of materials with QD inclusions, as we will see in Sections 5.5.2 and 5.5.3, respectively.

5.3.2 Metal nanoclusters in periodic arrays (metamaterials)

Subwavelength plasmonic structures arranged into periodic arrays act as the functional units of an artificially created medium, which has unusual properties in interaction with electromagnetic radiation. Upon proper engineering, so-called metamaterials (MMs) can possess behavior that is unattainable in nature, like negative refraction index,^{54,55} the giant chiral⁵⁶ and the ‘trapped rainbow’⁵⁷ effects, the ability for electromagnetic cloaking,⁵⁸ or the ability to concentrate light extremely⁵⁹ and even to funnel energy within subwavelength slit with no reflection⁶⁰ as well as many others. The beginning of the theoretical research in the field dates back to the end of 1960s,⁶¹ and until now theoretical aspects remain the prevalent subject of publications on metamaterials, mainly due to difficulty in MMs manufacturing. A tremendous variety of geometries have been proposed for MMs depending on applications, from noble-metal nanorods⁶² to nanoholes,⁶³ nanowires⁶⁴ and to nanorice⁶⁵ that combines the advantages of noble-metal nanoshells with those of dielectric NPs.

Among the variety of already existing or future applications enabled by MMs, optical filtering takes a special place. Perhaps, one of the first types of optical filters essentially using metal-dielectric subwavelength structures are 2D MM structures of metal-dielectric gratings for filtering light polarization.⁶⁶ Among recent developments in the field of polarization spectral filtering a multiband stereoMM-based polarization filter may be cited.⁶⁷ It uses chiral structures of twisted asymmetrical split-ring resonators rendering ripple-free transmission peaks of over 60% in a wide GHz range.

Band-pass filtering with MMs is a relatively new vision of the classical problem of spectral selection. At GHz wavelengths, a planar MM was proposed some years ago⁶⁸ having properties of electromagnetically induced

transparency analogously to the classical nonlinear quantum phenomenon. While in the classical approach⁶⁹ an opaque medium is rendered transparent in a narrow spectral range utilizing quantum interference of a pump and a probe laser beam tuned at different transitions, in the proposed MM a double fish-scale metallic pattern induces the resonant splitting of the incident radiation, resulting in two separated modes, each corresponding to dipole-like oscillations in both layers of the MM structure. This leads to high energy concentration between the layers, i.e. to trapped-mode resonance. In the far fields, a narrow transmission resonance with long pulse delay is hence observable. However, the in-band transmission level of this MM is about 20% and, combined with high outer-band transmission, this persuades stacking of such planar MM slabs in order to increase the bandwidth and maximum transmitted intensity. The resulting media are appealing candidates for ultracompact broad-band delay lines operating at prescribed wavelength to employ in optical communication field.

In the far infrared (terahertz, THz) range, MM-based filter devices operate by controlling the fundamental inductive-capacitive (LC) resonance in split ring resonator (SRR) based oscillators. To enhance the sensitivity of the SRRs aiming to have advantages in narrowband filtering, there have been invented different mechanisms to excite sharper LC resonance response with high quality factor.⁷⁰ Very recently a mirrored arrangement of asymmetric single SRRs (ASRs) was proposed⁷¹ that dramatically enhances the quality factor of the LC resonance so that it prospects to suppress radiation losses in terahertz, microwave and infrared plasmonic MMs. While in a regular non-mirrored arrangement, the surface current modes are all oriented in phase and the light scattered by individual ASRs interferes constructively, in the proposed arrangement the surface currents are oppositely oriented for neighboring ASRs. This leads to the cancellation of the net dipole moment accompanied by destructive interference of the scattered fields. The proposed design outperforms similar non-mirrored super cell geometries by almost three times.

On the other hand, cloaking devices, bandstop filtering and broadband absorption applications require broad-range filters. Realization of broadband metamaterials in the THz range was proposed either as a multiple stacked MM-layer configuration⁷² or, alternatively, through a planar single layer with nested multiple interconnected rings in succession within a single gap SRR.⁷³ In this latter approach, mode redistribution in the rings results in reduced effective inductance and hence is responsible for the resonance linewidth broadening (by a factor of four in this study, without altering the resonance minima significantly) as well as for the resonance blue shifting. Recently, an ultra-broad 3 dB and sharp-transition band-pass THz filter was projected and realized.⁷⁴ Essentially 3D geometries of these structures have ensured transmission of over 82%. In this range also dichroic mirrors

were fabricated⁷⁵ despite the employment of MMs for this type of devices is less common.

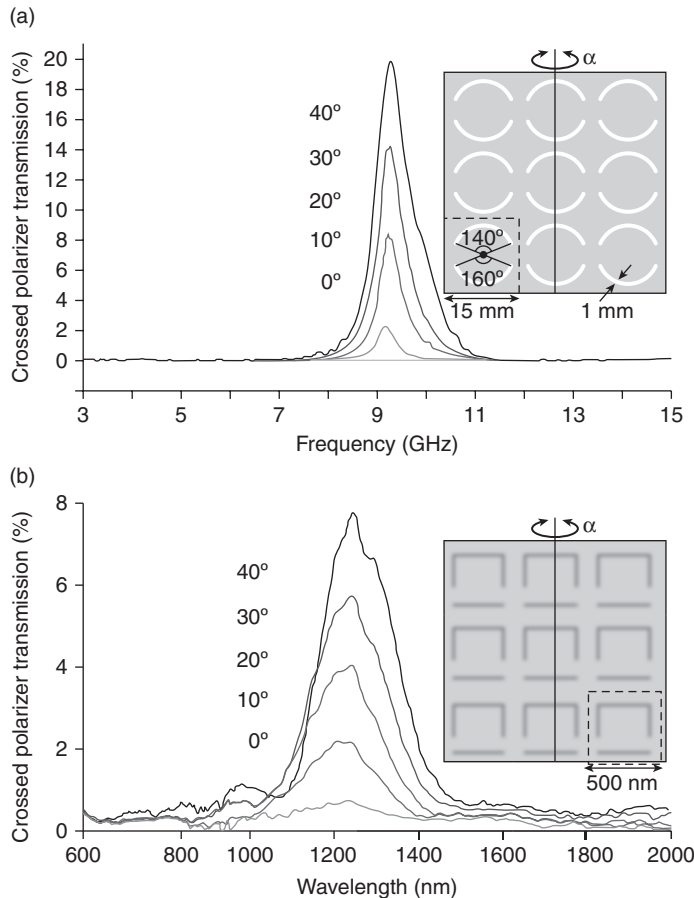
For the near-infrared (NIR) and visible range, only very few pioneer works concerning MM-based optical filtering have been published up to now. This is probably due to the high quality of conventional optical multilayers, which goodness is sufficient for many applications. Nonetheless, side ripples and limited acceptance angle may often represent a problem, one that might be solved using plasmonic MMs. The main reason for few results for the shorter wavelength ranges is undoubtedly the difficulty of fabricating NPs, which for the visible should be much smaller than micron-size inclusions required for the THz range and millimeter-size ones for GHz. As an example we cite a novel MM polarization spectral filter proposed recently.⁷⁶ Here a metal film patterned at the subwavelength scale has polarization properties enabling narrow-band ripple-free transmission peak. Isoindex materials for microwaves and NIR were realized, see Fig. 5.2. Notwithstanding their low peak transmission value (of only 8% in the NIR) the approach is interesting also due to omnidirectional character of such device.

Wu and Shvets⁷⁷ have latterly proposed a simple theoretical model for designing MM-based broadband absorbers in the NIR. It describes the optical response of the coating through the series of circuit models employed for each subunit of the patterned gold on the dielectric surface. Subunit size variety results in almost 100% absorbance over a broad range around 1500 nm. Validity of the proposed model relies on short propagation range of SPs.

The alignment and control of the distance between the particles represents the main challenge in MMs fabrication, and from this point of view, ‘negative’ geometries like fishnets⁷⁸ are preferable. Nevertheless, a dozen years of successful practical realizations have been undoubtedly demonstrated that plasmonics has become a pervasive technology offering an unprecedented level of synergy between optics and electronic.⁷⁹

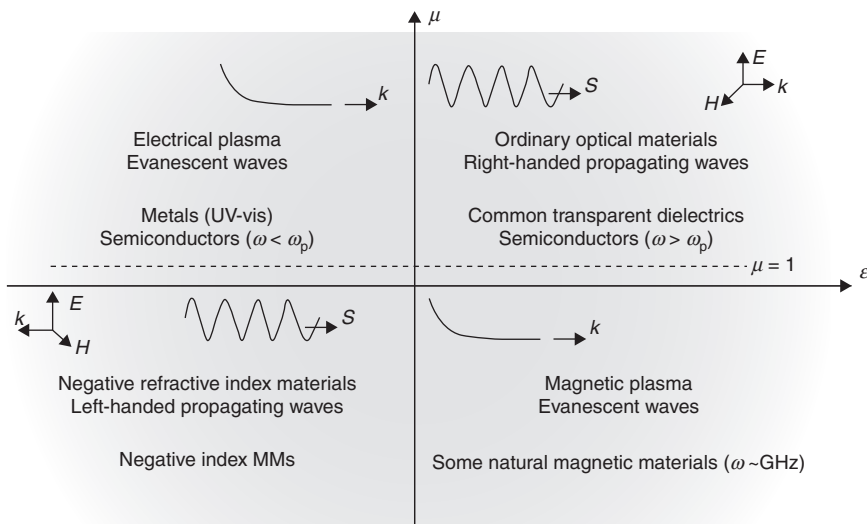
The realm of MMs falls into the three-fourths of possible combinations of signs for real dielectric permittivity and magnetic permeability.⁸⁰ See Fig. 5.3, where nonmagnetic optical materials corresponds the dashed line $\mu = 1$. On the other hand, the question on the sign of refractive index is not an evident issue for these materials with physically unusual behavior. To solve the problem unambiguously, Govyadinov *et al.*⁸¹ proposed to link firmly the sign of the refractive index to the wavevector direction for the modes, and derived an approach for imposing causality in active and passive materials.

Vast literature on the subject is available, much of that the reader may find in the reference list to this chapter, including comprehensive monographs and reviews. Here we have referred only some basic information relevant to the scope of employment in thin film optics. It should be noted in particular



5.2 Transmission of MM-based isoindex filters for microwaves (a) and NIR (b) at various incidence angles. The insets show types of MM patterns. (Source: Reprinted with permission from Reference 76. Copyright 2011 by the American Institute of Physics.)

that the inclusions, either ‘positive’ like nanorods or nanoshells, or ‘negative’ like nanoholes, are assumed to be large on the microscale, i.e. the first level of homogenization should be allowed that consists of the description of the MM structural units in terms of their bulk dielectric permittivity and magnetic permeability. On the other hand, these structural units are small compared to the wavelength of the optical or microwave range they are thought to be employed in. Therefore, the electromagnetic radiation fails to resolve the MM structure rendering possible the second level of homogenization; hence the retrieval of the MM effective parameters is based on the optical parameters of the constituent materials, see Section 5.5.3.



5.3 Classification of materials based on their dielectric and magnetic properties. The dashed line corresponds to non-magnetic materials, $\mu = 1$. S is the Poynting vector.

5.3.3 Effect of small random disorders and imperfections in metamaterials

Real metamaterials show optical responses different from theoretical responses due to inherent limitations in the fabrication process. Disorders and imperfections often make the measured losses higher than theoretically predicted. An infinite periodic arrangement of lossless inclusions theoretically cancels out the scattering from each individual NP yielding a perfect, lossless metamaterial,⁸² as if it should happen in one- or three-dimensional lattices of closely packed NPs,⁸³ but the measured permittivity and permeability result higher either due to deviations of particle size from the ideal, or due to array alignment deficiency. Experimental efforts in realization of better metamaterials poses a problem of qualitative and quantitative modeling of realistic devices not free from manufacturing imperfections in order to provide an idea of which type of imperfections have the most effect and how the electromagnetic response of the device may be prevented through an improved design. A theory of quantification of the first-order small random and uncontrollable disorder in the periodic arrays of plasmonic NPs has been proposed by Alù and Engheta.⁸⁴ They have shown that the main disorder effect consists of additional radiation

losses for the guided mode and have proposed extension of these results to the general class of periodic metamaterials.

5.3.4 Composites of random elements

Composites of randomly oriented elements with inclusions of sizes statistically distributed around a chosen design value do not require implementation of expensive manufacturing techniques like focused ion-beam or e-beam lithography. Their relatively low-cost production is useful for many applications where large surfaces should be coated or rather big slabs of 3D material are needed. The PVD methods are widely implemented for creation of such thin film structures.

Many interesting devices created using such comparatively simple approaches are reported in literature, being a great number of them aimed to improve light energy harvesting or manipulation. For example, recently an omnidirectional transparent conducting-metal-based plasmonic composite was proposed by Elbahri *et al.*⁸⁵ The minimization of reflection of the reported coating composed of a stack of a gold film and a silver/polymer nanocomposite fabricated by sputtering on glass substrate, is achieved by means of symmetric plasmonic coupling under impedance matching condition in the visible range.

Elezzabi *et al.*⁸⁶ proposed a random composite governed by non-resonant interactions for which the group refractive index can be increased to be larger than the refractive indices of both the dielectric host material and that of metal inclusions. Customized novel photonic materials with atypical optical constants may be created easily by mixing two materials microparticles. Dense ensembles of subwavelength-sized constituents cannot be described by standard homogenization theories (see Section 5.5.3) and was only qualitatively explained by the authors considering near-field particle–plasmon interaction.

On the other hand, proper processing and deposition method adjustment help to tailor better the size and shape of NPs prepared by sputtering. Bruno *et al.*⁸⁷ used a two-step sputtering processing to control the nucleation and position of gold NPs on silicon substrate thanks to intermediate treatment of the sample with oxygen plasma.

5.3.5 Coatings containing thin and ultrathin metal layers and metamaterials

A particular case of periodically alternating layers of a metal with permittivity ϵ_1 and a dielectric with permittivity ϵ_2 , in fractions f_1 and f_2 , respectively, is a simple but important example of an artificial anisotropic composite. Its

effective permittivity ϵ may be calculated by effective medium approximation model (EMA, see Sections 5.5.3 and 5.5.4) with modification for the shape effect:

$$f_1 \frac{\epsilon_1 - \epsilon}{\epsilon_1 - \xi\epsilon} + f_2 \frac{\epsilon_2 - \epsilon}{\epsilon_2 - \xi\epsilon} = 0 \quad [5.2]$$

Parameter ξ is the screening factor of the material with respect to the external fields: for the electric field parallel to the layers (*p*-polarization) $\xi \rightarrow \infty$ and $\epsilon \rightarrow \epsilon_l = f_1\epsilon_1 + f_2\epsilon_2$, while for the electric field perpendicular to the layers (*s*-polarization) $\xi \rightarrow 0$ and $\epsilon \rightarrow \epsilon_{\perp} = \epsilon_1\epsilon_2/(f_2\epsilon_1 + f_1\epsilon_2)$. So-called Wiener bounds⁸⁸ ϵ_l and ϵ_{\perp} are useful for estimation of the possible permittivity values achievable with given constituent materials in various fractions in a multilayer stack. The extreme values of ϵ are of great potential interest for photonic nanocircuits,⁸⁹ epsilon-infinity materials being perfect conducting wires for optical displacement currents, and epsilon-near-zero (ENZ) media being excellent insulators. Moreover, ENZ materials find a vast field of application for creation of ‘lenses’ that may effectively redirect the energy from a source and reshape the radiation phase pattern at will, not being limited in shape and size unlikely to standard lenses.⁹⁰ Covering with ENZ materials may also drastically reduce scattering from dielectric and even conducting objects making these objects practically invisible (electromagnetic cloaking).⁵⁸

In interference coatings, single or double metal layers embedded in a particularly designed dielectric stack give rise to so-called induced transmittance filters⁹¹ suitable to be implemented in the construction of modern portable spectrometers.⁹² Reliable deposition of such thin-film devices enables their optimal performance⁹³ and should take into account not only the process of optical monitoring but also the peculiarities of the metal-dielectric interface.⁹⁴

Being embedded into multilayer coatings, layers with plasmonic inclusions make possible effective narrow-band Fabry-Perot (FP) filtering. Hsu and Wu⁹⁵ reported an FP design with a negative-refractive-index MM and calculated that unlikely to conventional FP designs, the spectral response of such a filter strongly depends on the MM layer thickness.

Ultrathin semicontinuous metal films give rise to random metal-dielectric composites with interesting properties. Such composites may be used as transparent electrodes for a wide range of applications,²⁶ or make possible surface-enhanced Raman spectroscopy,⁹⁶ thanks to giant local electric field fluctuations (so-called Anderson localization⁹⁷ or hot-spots) that achieve their maximum at a certain pre-percolation state.⁹⁸ Random metal-dielectric films have also found extensive use in many fields, among which photovoltaics⁹⁹ should be mentioned. Light-to-current and current-to-light

coupling (photon drag effect) in plasmonic systems with thin metal layers where SPPs are controllable by external DC current,¹⁰⁰ and may find application in plasmonic nanocircuitry, where advantages of fast photonics are combined with compact electronics.

5.4 Searching for alternative plasmonic materials

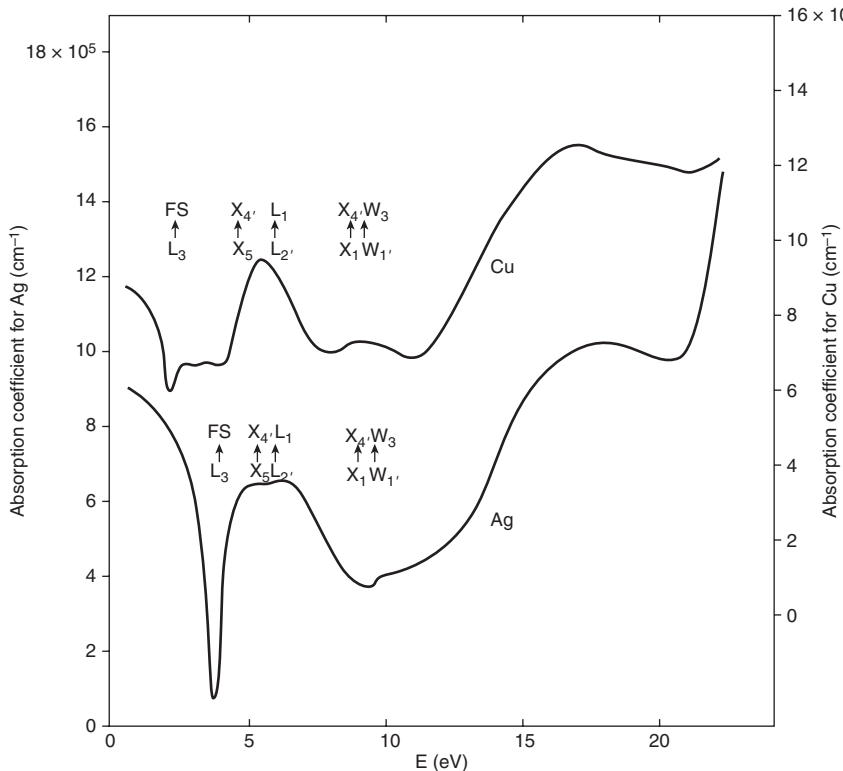
Metals are traditional materials used for plasmonic applications, but even those of highest conductivity exhibit high losses in the optical range. Low-loss plasmonic materials research is required therefore.^{31,101} To determine the proficiency of a material to perform in particular plasmonic application a series of metrics have been elaborated by Arnold and Blaber.¹⁰² Despite multiplicity of possible geometries determining particular quality factor Q , in the quasi-static limit with presumed low loss level, two main cases may be formulated: for localized SP $Q_{\text{LSP}} = -\epsilon_c' / \epsilon_c'' = k/2n$, and for extended modes, i.e. SP polaritons $Q_{\text{SPP}} = \epsilon_c'^2 / \epsilon_c'' = k^3/2n$. Therefore, not only the loss issue, i.e. the ϵ_c'' value, is important to render a material good for plasmonic applications, but also an appropriate value of the ϵ_c' . Thus, the ability to tune the real part of the dielectric permittivity when engineering a novel plasmonic material should be considered simultaneously with the problem of material loss diminishing.

The losses in materials in the optical range are due to interband transitions of electrons to empty levels of higher energy caused by absorption of photons of the incident light. Figure 5.4 illustrates the impact of interband transitions onto losses in two noble metals, copper and silver.¹⁰³ For example, in copper, the electrons can either shift from the filled L₃ band to Fermi surface (peak at 2.1 eV) or undergo L₂→L₁ and X₅→X_{4'} transitions (peak at 5.2 eV). Unfortunately, the nanogeometries additionally increase the interband transitions worsening plasmonic response of the metals. Slightly higher ω_p/ω_s ratio of silver compared to gold and copper ensures better performance of silver nanostructures. For example, in the case of gold the interband contributions to absorption present in a wide range from 1.8 to 2.35 eV¹⁰⁴ not only red-shift the observable LSPR to 2.4 eV,¹⁰⁵ but also strongly damp, hence broaden the SPR band, Fig. 5.5.

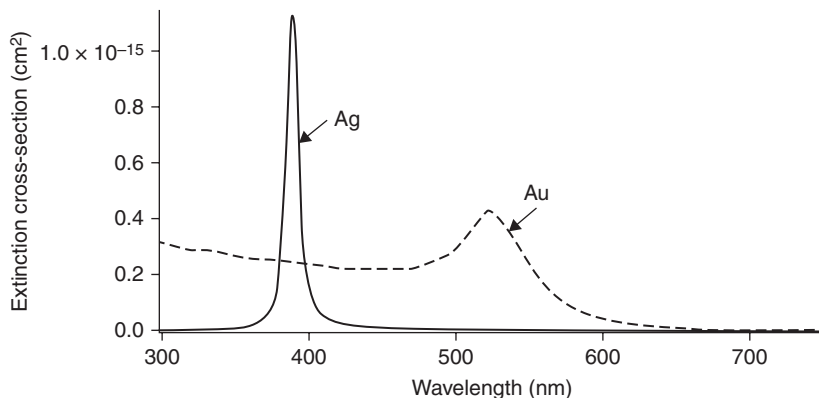
In the last decade unconventional materials have been theoretically studied³² to face the problem in the context of interband transitions, and some of the projected doped metals, alloys and compounds were realized.

5.4.1 Alloys and intermetallics: novel metal materials

Among a vast variety of metals, only those having free electron character are of interest for plasmonic applications, but in nature, the choice of



5.4 Absorption spectra of copper and silver. Contributions form free-electron losses and interband transition losses are indicated. FS stands for 'Fermi Surface'. (Source: Reprinted with permission from Reference 103. Copyright 1962 by the American Physical Society.)



5.5 Extinction spectra of silver (solid) and gold (dashed) 20 nm nanospheres in water calculated by Mie theory. (Source: Figure similar to that in Reference 152. Copyright 2012 by Elsevier.)

free electron metals is extremely limited. Therefore, besides those conventional metals, novel metals are searched for implementation in plasmonic devices, both for reasons of costs and for chemical as well as plasmonic performance.

As far as optical metrics are concerned, there exists superior alternatives to noble metals (gold, silver and copper) in terms of the dielectric function. Alkali metals would be ideal from the optical performance point of view, but they are chemically reactive, hence are problematic to handle, while the durability of a device based on such materials may be severely compromised. So that is for the alkali-noble intermetallic compounds too, among which potassium gold (KAu) was theoretically demonstrated³² to have zero interband losses below its unscreened plasma frequency at 1.54 eV, the value practically worsened down to 0.5 eV by Drude losses, however. That is why both silver and gold are almost exclusively used in plasmonics nowadays: at the same time they are more chemically stable (gold is even inert) and have a strong plasmonic performance.

Copper would be a good alternative to more expensive gold and silver thanks also to its ε_c'' comparable with that of gold in 600–750 nm range, but ease of copper oxidation affects dramatically the SP modes. Nevertheless, the LSP resonance peak of copper is comparable with that of gold and silver in sharpness and width.¹⁰⁷

In the blue and UV range, aluminum is better than noble metals, as its ε_c'' remains relatively low for wavelengths shorter than 200 nm where its ε_c' is negative, while for silver and gold the latter is true only down to 326 and 207 nm, respectively. But again, chemically, aluminum is easily oxidized: the native oxide of 2.5–3 nm red-shifts the LSP resonance frequency from 10.5 to 6.5 eV.¹⁰⁸ Despite the induced challenges in manufacturing, aluminum has been used in plasmonic devices in the UV-blue range for SPP propagation¹⁰⁹ and LSPR employment.¹¹⁰ Similar behavior has another plasmonic metal interesting for the UV, magnesium, which exhibits SPR peak at 7 eV shifted to 5 eV upon air oxidation.

Among alternative metals being explored for plasmonic applications, gallium was demonstrated to be attractive for employment in quaternary-logical resonatorless optical memory elements.¹¹¹ SPR of this metal is sufficiently stable against oxidation even in nanoshapes (red-shift is about 0.3–0.6 eV) and it yields two plasmon modes, the transverse and longitudinal, that can be tuned in a very wide spectral range, from the UV to the near-IR.¹¹² Gallium NPs coupled with some semiconductors enable plasmon-enhanced solid-state devices working in the UV-vis-NIR range.¹¹³

Random mixtures of silver, gold, aluminum and copper were studied by Sharma and Mohr¹¹⁴ who suggested in particular the tunability of a SP-based fiber optic sensor by non-stoichiometric alloying of Al with its best signal-to-noise ratio and Au with its best sensitivity. Unfortunately, clustering or

stoichiometric alloying present in all these alloys origin single electron excitations that have dramatic consequences for the SPR quality.

Blobb *et al.*¹¹⁵ have demonstrated a blue-shift of the optical gap of gold by alloying it with cadmium that has caused an improved absorption efficiency of Au-Cd NPs compared to ones of pure Au accompanied, however, by an unwanted disruption in the originally optimal IR behavior of pure gold. In general, using *n*-type doping of noble metals by bivalent transition metals, like zinc or cadmium, an increase of plasma frequency may be obtained, hence a shift of the interband transition threshold. Such ‘band engineering’ is considered a promising technique for the improvement of noble metals’ plasmonic performance for a chosen spectral range.

A comprehensive review of recent achievements in the field may be found in the work of Blaber *et al.*,¹¹⁶ where noble and transition elementary metals and alloys are compared to binary and ternary intermetallics as well as to silicides. Materials with simple crystal structures and low lying d electronic states are thought to be most promising plasmonic alternatives to gold and silver.

As for ultrathin metal layers implemented in plasmonic multilayers, besides doping and alloying, ion sputtering represents a way to modify the surface of a metal film changing hence its SP properties via induction of magnetic¹¹⁷ and optical¹¹⁸ anisotropies, structural variation¹¹⁹ and surface morphology modification, in particular by patterning.¹²⁰ Electronic properties of sputtering-modified silver evaporated on Cu(111) surface were compared with those of Ar⁺-sputtered bulk Ag(100) surface.¹²¹ Similarly to the above cited case of Au-Al alloying, a blue-shift of the band gap was accompanied by SP broadening due to the induced additional single-particle transitions.

5.4.2 Semiconductors for plasmonics

Generally speaking, the SP tuning is a very attractive issue. One of the most recent works in this field considers a multilayer device which allows the mechanical control of SP propagation properties by means of a simple modification on an inner air gap thickness between two SP-supporting layers, one made of gold and another made of silicon.¹²² It is worth noting, however, that when for the metals such a control is limited to electrical biasing¹²³ or mechanical external forces, the world of semiconductors adds more flexibility in the SP management.

Compound semiconductors may be easily tuned, within certain limits, for a desirable value of the dielectric function. For example, in the case of oxides such a tuning is possible by doping adjustment or by oxidation state. ‘Active’ tuning by photocarrier generation or by direct dopant

injection or by thermal excitation is one more intriguing property of semiconductor-based plasmonic materials. In their pioneer work on this topic Gómez Rivas *et al.*¹²⁴ demonstrated such active tuning of the carrier density via modification of the Bragg scattering of terahertz SPPs on a InSb grating by thermal excitation of free carriers. At temperatures lower than 100°C the SPP propagation was switched completely off at certain frequencies.

Good for plasmonic applications are semiconductors having a high plasma frequency that guarantees $\varepsilon_c' < 0$ in the NIR and visible range, and with a large bandgap that ensures minimum interband transition losses. In semiconductors, interband transitions can be either direct or indirect, depending on the material type. While for direct bandgap semiconductors the bandgap corresponds to the onset of interband transitions, for indirect bandgap semiconductors transitions may be caused by the photons with energies higher than bandgap by means of various mechanisms of absorption like trap-assisted transitions, transitions between impurity levels, or due to generation of exitons. Any of such mechanisms can be described in terms of Lorentz oscillator model: the dielectric function dispersion in the vicinity of the absorption peak due to transition $l \rightarrow k$ is:¹²⁵

$$\varepsilon_{lk}(\omega) = \frac{f_{lk} \omega_{p,lk}^2}{\omega_{lk}^2 - \omega^2 - i\omega\gamma_{lk}} \quad [5.3]$$

where f_{lk} is the oscillator strength, ω_{lk} is the resonant frequency corresponding to the energy difference between the levels, $\omega_{p,lk}$ is the plasma frequency defined similarly to Equation [5.1] but with N being the concentration of electrons in the lower occupied state. The damping factor γ_{lk} accounts for the peak width. The sum of all allowed Lorentzian terms gives a reasonable approximation for the dielectric function of a semiconductor.

Aside the optical performance and tunability, compatibility with standard nanofabrication and integration technologies should be taken into account as a factor of suitability of a material for plasmonic applications.

It is easier to find good plasmonic semiconductors at longer wavelengths, where some of them are either intrinsically plasmonic thanks to sufficiently high carrier mobility and concentration, or may exhibit negative real permittivity in phonon resonance.¹²⁶ For the mid-IR silicon carbide¹²⁷ has been shown to be suitable for superlensing, while some arsenides like highly doped InGaAs and intrinsic AlInAs were used for fabrication of all-semiconductor MM with negative refraction.¹²⁸ For the NIR applications wide-band heavily doped oxides should be considered almost exclusively. They are so-called transparent conductive oxides (TCOs) like ITO (Sn-doped In_2O_3), or AZO and GZO (Al- and Ga-doped ZnO). TCOs are useful for many applications

like epsilon-near-zero (ENZ) materials, MMs with hyperbolic dispersion and SPP waveguides.¹²⁹

Pioneer works of Franzen *et al.*^{130,131} opened the way to an extensive study of TCOs like plasmonic materials. In particular, for waveguiding applications the characteristic penetration depth to the dielectric (d) or conductor (c) medium $l_{d,c} = \text{Im}(\lambda/2\pi)\sqrt{(\epsilon_d + \epsilon_c)/\epsilon_{d,c}^2}$ determines the SPP compactness. This means that at telecom wavelengths ($\lambda \sim 1550$ nm) good SPP-supporting materials with planar geometry may appear only with implementation of alternative to noble metals materials like TCOs¹³² as for silver and gold SPPs cease to be compact after 539 and 660 nm, respectively. Tunability of ITO NPs from 1618 nm to >2200 nm by changing the concentration of Sn doping from 3 to 30 mol% was demonstrated by Kanehara *et al.*,¹³³ where the shortest SPR wavelength was reached for the 10% Sn-doping, known as the optimal value of tin solubility in indium oxide matrix. On the other hand, TCOs start to bring to the visible-range plasmonics their advantageous properties like low losses and optical function flexibility upon doping: a unity-order refractive index change (1.39 at 800 nm) upon applied external field was reported by Feigenbaum *et al.*¹³⁴ in TCOs implemented in metal-oxide-semiconductor heterostructure with conducting oxide as the active material.

Transition-metal nitrides like GaN, TiN and ZrN may substitute metals traditionally employed in the visible.¹³⁵ The influence of the polarity of hexagonal wurtzite semiconductors (GaN, ZnO, SiC) onto SPR performance of the metal NPs was studied by Wu *et al.*¹³⁶ Formation, geometry and dynamics of gallium and gold NPs on the surface of polar semiconductors were shown to be influenced by the interface potential between the substrate and the NPs. Therefore, tailoring of the semiconductor surface charge was indicated as an intrinsic method for tuning the SPR resonance of metal NPs on a polar semiconductor.

Notice, that besides noble metal QDs implemented traditionally, recently, also semiconductors were reported by Luther *et al.*¹³⁴ to be employed for plasmonics in the form of QDs. QDs of copper sulfide were shown to exhibit LSPR in the NIR when enough free carriers are introduced via dopants and vacancies. While properties of noble metal QDs may be engineered by their shape and size and then remain locked-in permanently, the frequency and intensity of LSPR in semiconductor QDs can be dynamically tuned by doping, temperature and phase transition.

Semiconductor plasmonics develops rapidly also for photovoltaics. Gratings of five materials employable for enhancement of broadband absorption of thin-film solar cells namely, Ag, Au, Al, and Si and SiO₂, were recently theoretically compared in a recent study,¹³⁷ and silicon strips were predicted to provide a four-times the enhancement of short-circuit currents due to much lower ohmic losses.

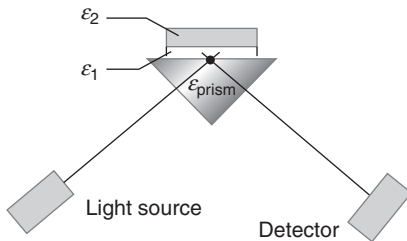
5.5 Characterization of novel materials with plasmonic effects

Characterization of materials refers to probing of internal material structure and properties using external techniques. Interaction of complex materials having plasmonic properties with external electromagnetic radiation imposes use of suitable measurement techniques as well as adequate data interpretation, specific for the case. Depending on the effects under study, near- or far-field material properties should be considered, hence necessary measurement tools should be applied followed by consistent modeling of microscopic or macroscopic properties of the media. Here we overview the main methods for characterization of complex plasmonic materials, including instrumentation and modeling approaches.

5.5.1 Optical characterization techniques for complex materials

Characterization of a material with nano-inclusions (NPs or thin layers) typically employs tools providing information on the material's optical and morphological (geometrical) features. Depending on whether one is interested in the near-field or in the far-field responses of the material, the emphasis may be put on to this or that characterization method. For the geometrical characterization the prevailing approach is the scanning probe microscopy (SPM) with its variants of atomic force microscopy (AFM) and scanning tunneling microscopy (STM). Cross-sectional geometrical analysis of multilayer stacks is possible by means of transmission electron microscopy (TEM). Near field optical properties of complex materials with plasmonic properties may be measured either by another type of SPM, the scanning near-field optical microscopy (SNOM), or by other microscopies giving access to determination of local parameters, like confocal microscopy and multiphoton microscopy. Surface enhanced Raman spectroscopy (SERS) should be also mentioned as one of the most popular tools for the localized optical characterization.

While a good synthetic description of the most common of the above mentioned measurement techniques (SNOM, SERS and geometrical methods) applied to materials with subwavelength inclusions may be found in many reviews (see for example Fu¹³⁸) we will focus our attention on the optical methods for macroscopic measurements, as they are more common for the society of optical-coating researchers. In Section 5.5.4 an example of spectral-ellipsometric analysis of a plasmonic structure will be considered, whereas below we will briefly describe the principles of another technique widely employed for SP observation so-called attenuated total reflectance (ATR) measurement.



5.6 Schematic representation of attenuated total reflectance measurement. To select *p*-polarization, a polarizer is introduced on the path of either the incident or reflected beam (not shown). For the Kretschmann configuration $\epsilon_1 = \epsilon_c$ and $\epsilon_2 = \epsilon_{\text{gap}}$ while for the Otto configuration $\epsilon_1 = \epsilon_{\text{gap}}$ and $\epsilon_2 = \epsilon_c$. The ATR condition is $k_x^2 = k_0^2(\epsilon_c \epsilon_{\text{gap}} / \epsilon_c + \epsilon_{\text{gap}})$, where k_x is the component of the wave-vector parallel to the surface, and k_0 is the magnitude of free-space wave-vector. Notice that to obtain total reflection conditions the condition $\epsilon_{\text{prism}} > \epsilon_{\text{gap}}$ should be satisfied.

Imprints of SPs are observable in the far field as absorption bands in the acquired optical spectra at a proper illumination. To excite an SP at the metal surface, it is necessary to match the wave-vector of the incident light with the wave-vector of surface collective oscillations. In the 1960s^{139,140} for the observation of SPs excited at the interface between a conductor and a dielectric, Otto and Kretschmann proposed the two optical configurations enabling matching of the wave-vectors by means of a prism put into contact with the studied surface, see Fig. 5.6. Then, in the conditions of total reflectance, at the interface between the prism and the sample, an attenuation of the reflected intensity occurs when the light couples to the surface plasmons of a metal layer covering the sample (Otto configuration) or the prism (Kretschmann configuration). The depth, bandwidth and shape of the reflectance curve dip are conditioned by the thicknesses of the metal and dielectric layers, the optical constants of the materials, surface roughness and the sample-prism distance. Enhanced tools combining ATR with ellipsometry (total-internal-reflection ellipsometry, TIRE) may provide higher sensitivity to plasmonic properties of materials.¹⁴¹

Commercial or *ad hoc*-constructed optical benches like spectrophotometers or ellipsometers allow far-field measurements for retrieval of macroscopic optical functions of a composite. It is well-known that to retrieve the macroscopic optical functions of natural materials, typically complex amplitude reflection (*r*) and transmission (*t*) coefficients are sufficient,¹⁴² obtainable, for example, from ellipsometric angles Ψ and Δ . For materials with anisotropic properties the situation is more complicated as for them different polarization states are coupled and therefore the generalized ellipsometry approach is required, where either Jones or Mueller matrix is measured.¹⁴³

Notice that ellipsometry in its generalized and total-internal-reflection forms (GE and TIRE) enables observation of any plasmonic resonance of a media: volume plasmons (Ferrell modes), SPPs and LSPRs.¹⁰⁶ On the other hand, for non-magnetic ($\mu = 1$) isotropic materials the refractive index n and extinction coefficient k may be retrieved from relatively simple spectrophotometric measurement of intensity reflectance (R) and transmittance (T), or even from one of them when, for example, the sample is not transparent. In this last case a Kramers-Kronig analysis should be performed,¹⁴⁴ but the spectral range of the measurement should be sufficiently wide.

5.5.2 Local properties of nanostructured materials

Analytical solution of Maxwell equations for description of extinction (absorption + scattering) spectra of spherical particles dates back to 1908.¹⁴⁵ Although the famous Mie theory remains of great interest,³⁷ new shapes of NPs suitable for various applications make indispensable further development of near-field semi-analytical¹⁴⁶ and numerical modeling. Among most used numerical methods are the Modified Long Wavelength Approximation (MLWA),¹⁴⁷ the multiple multipole method,¹⁴⁸ the Finite-Difference Time-Domain (FDTD) method,¹⁴⁹ and especially, the Discrete Dipole Approximation (DDA).^{150,151} The theoretical advances in this area were reported by Kelly *et al.*¹⁵

The above theories do not consider however the particle–particle interaction, and to the problem of plasmonic coupling in nanostructures a large amount of modern studies are dedicated. The polarization, orientation and distance dependence of the near-field plasmonic coupling was discussed by Jain and El-Sayed¹⁵² for a series of nanogeometries including nanospheres, nanorods and nanoshells. Importance of rigorous analytical techniques in studying collective phenomena in complex plasmonic arrays was demonstrated by Natarov *et al.*¹⁵³ Optical forces between coupled plasmonic NPs near metal interfaces were investigated by van Vlack *et al.*¹⁵⁴ by non-perturbatively calculating the scattering electric field via a Green function technique which includes particle interaction of all orders.

On the other hand, simplified approximations have been elaborated too. Langguth and Giessen¹⁵⁵ report a simple and efficient multiple dipole approximation model, which can account for not only SP in single objects, but for their coupling of complex plasmonic systems too. A simple fitting approach to interpret Fano-like spectral features in the nanostructure far-field spectra and to relate them to near-field intensity profiles was proposed by Gallinet and Martin.¹⁵⁶ This approach provides a useful tool for experimental spectra interpretation, as well as for design of plasmonic and photonic devices exploiting the Fano effect.

Quantitative analysis of strong coupling between plasmonic copper nanogap and silicon photonic waveguides was performed by Salas-Montiel *et al.*¹⁵⁷ The phenomenon was observed by near-field scanning optical microscope, and hence modeled to explain the registered signal, providing characteristics such as near-field distribution or effective indices.

Besides the link to macroscopically observable optical features of plasmonic nanostructures, their local properties themselves are always increasing attraction for creation of novel devices for time-resolved measurements,¹⁵⁸ surface-enhanced Raman spectroscopy,¹⁵⁹ superlenses,¹⁶⁰ spectroscopy on chip⁵⁶ and many others. The sensitivity of plasmonic NPs to local refractive index variation was studied by Piliarik *et al.*¹⁶¹

5.5.3 Effective macroscopic parameters

Modeling of the optical response to incident electromagnetic radiation of complex materials with plasmonic properties, including MMs and coatings with either composite materials or ultrathin conductor layers, opens the possibility of simulating the behavior of devices based on such materials designed for a wavelength much larger than the mean inclusion size or plasmonic layer thickness. For this purpose it is indispensable to know the *effective macroscopic* optical functions of such artificial materials that means to solve the inverse problem of determination of the complex effective permittivity ϵ and the complex magnetic permeability μ from the measurement data. Effective macroscopic optical functions are obtainable using so-called homogenization approaches, and in Section 5.3 the approximation limits for such methods were considered.

The two homogenization models most used in practice are the Maxwell-Garnett theory (MGT)¹⁶² and Bruggeman effective medium approximation (EMA).¹⁶³ These classic homogenization theories are based on the Clausius-Mossotti relation,¹²⁴ which offers an essential link between macroscopic and microscopic parameters of a medium. Notice that MGT provides a reasonable approximation only for substantially asymmetrical mixtures where one of the components is treated as a host and the others are low-fraction inclusions. What makes EMA the most well-known mean-field theory, widely used even to modern plasmonic applications,¹⁶⁴ is that it is applicable to composites with fractions in arbitrary proportion.

Nowadays, the interest in the MGT and EMA is justified by their versatility and straightforward applicability to many random geometries for which the experimental observations that result are described adequately. For example, an easy-to-handle model based on MGT for layered composites of metal NPs embedded into dielectric matrix was recently proposed by Protopapa.¹⁶⁵ It allows the retrieval of the main features of the inclusions in

terms of their shape (in terms of a fitting scalar parameter), size and geometric distribution with a reasonable experimental agreement.¹⁶⁶ An advanced version of EMA taking into account nonlocal effects neglected by the standard one was proposed by Elser *et al.*¹⁶⁷

The most general effective medium approach was proposed in the end of 1970s¹⁶⁸ and known as Bergman-Milton representation. In this method, the geometrical features of complex plasmonic composites are taken into account not just by the macroscopic depolarization factor, but by defining geometrical functions to which a set of spectral density functions are correlated, and these latest are used for the fit.¹⁶⁹

These averaging methods however, often fail to describe adequately the exotic inclusions in artificial materials.¹⁷⁰ For MMs a specific protocol for extraction of effective parameters was elaborated by Smith *et al.*,¹⁷¹ the authors of the first demonstrated negative-index material, since improved by them¹⁷² and other researchers.¹⁷³ The proposed inversion of the classical relations for the reflection (r) and transmission (t) coefficients in terms of refractive index n and impedance Z ($\epsilon = n/Z$, $\mu = nZ$), gives for a slab of homogenous material with thickness d :

$$n = \pm \cos^{-1} \left(\frac{1 - r^2 - t^2}{2t} \right) \quad Z = \pm \sqrt{\frac{(1+r)^2 - t^2}{(1-r)^2 - t^2}} \quad [5.4]$$

The choice of the sign in these solutions is ruled by the conditions $\text{Re}(Z) > 0$ and $\text{Im}(n) > 0$ for a causal and passive medium.

Similarly to the classical approaches, these generalized Clausius-Mossotti methods, however, remain limited to the description of a medium by permittivity and permeability, while complex scatterers embedded in MMs have an electromagnetic response that is not sufficiently described with ϵ and μ tensors. Such bianisotropic media require additional parameters relating the complexity of the electric and magnetic fields in the material, like magnetoelectric coefficients. Thus, that is for an alternative method^{174,175} based on averaging of inclusions over a planar sheet with the consequent consideration of a Bloch-lattice-type layer interaction. Within these approaches, however, basic passivity and causality constraints¹⁷⁶ may be easily violated when the optical functions are modeled in the vicinity of inclusion resonances, due to a strong spatial dispersion not taken into account properly as demonstrated by Alù.¹⁷⁷

An alternative description of composite media made of only dielectrics is a Floquet-type representation¹⁷⁸ based on the generalized permittivity tensor $\hat{\epsilon}(\omega, \vec{k})$ that is spatially dispersive (\vec{k} is the wave-vector). The generalized permittivity tensor includes all polarization effects hence is suitable for

description of artificial or bianisotropic effects including artificial magnetism. To simplify linking these effects with weak spatial dispersion effects, the preferable description of a medium is in terms of local permeability or chirality parameters.¹⁷⁹

Among other widely used approaches, the bianisotropic parameter retrieval method proposed by Kriegler *et al.*¹⁸⁰ should be mentioned. For randomly distributed inclusions, 2D and 3D footprinting methods for geometry modeling followed by finite-difference time domain (FDTD) calculation was shown to yield results in quantitative agreement with the experimentally measured far-field spectra of real samples.¹⁸¹

An extension of the rigorous Floquet-type representation to magnetodielectric MMs has been proposed recently for periodic structures by Alù.¹⁸² This theory takes into consideration complex interaction among inclusions via coupling of their polarization properties. The analysis showed that not only magnetoelectric coupling arising at the inclusion level contributes to bianisotropy description of a MM, but also a weak spatial dispersion effect at the lattice level, which appears because of inherent asymmetry introduced by phase propagation across a finite unit cell of the MM. This latter contribution was demonstrated to be inherent to any bianisotropic media and not only to media with asymmetric or noncentered inclusions as was thought before.¹⁸³ Both types of magnetoelectric coupling appear through polarization terms in the expressions for averaged dielectric \mathbf{D}_{av} and magnetic \mathbf{B}_{av} displacements:

$$\mathbf{D}_{av} = \epsilon_0 \mathbf{E}_{av} + \mathbf{P}_{av} = \epsilon_{eff} \mathbf{E}_{av} - (\chi_{eff}^e + \chi_{eff}^o) \boldsymbol{\beta} \times \mathbf{H}_{av} \quad [5.4a]$$

$$\mathbf{B}_{av} = \mu_0 \mathbf{H}_{av} + \mathbf{M}_{av} = \mu_{eff} \mathbf{H}_{av} - (\chi_{eff}^e + \chi_{eff}^o) \boldsymbol{\beta} \times \mathbf{E}_{av}, \quad [5.4b]$$

where \mathbf{E}_{av} and \mathbf{H}_{av} are averaged electric and magnetic fields, \mathbf{P}_{av} and \mathbf{M}_{av} are averaged polarization and magnetic vectors, respectively, $\boldsymbol{\beta}$ is the propagation eigenvector, ϵ_0 and μ_0 are the background permittivity and permeability.

The effective parameters χ_{eff}^e and χ_{eff}^o corresponding to the coupling at inclusion and lattice levels, respectively, together with the effective permittivity ϵ_{eff} and effective permeability μ_{eff} , totally describe the macroscopic response of a MM as a bulk to an arbitrary electromagnetic excitation. The inconsistency and lack of physical meaning for the results obtainable with classic homogenization theories applied to MMs in the way like natural materials are treated,^{184,185} were shown to originate from omitting *a priori* the spatial dispersion contribution χ_{eff}^o , even at the wavelengths where this term is not negligible. A numeric comparison of effective optical parameters for three specific MM geometries has allowed emphasis on the difference of this homogenization approach and other available techniques.

At the end of this section let us mention a recent review¹⁸⁶ on the methods of electromagnetic characterization and homogenization developed for nanostructured MMs for their linear properties. Besides a review overlook, in this work a concept of *characteristic material parameters* (CMP) is proposed, which is more restrictive than the concept of effective material parameters. CMP are parameters satisfying basic physical limitations and applicable to different wave processes, in particular satisfying Maxwell's boundary conditions for macroscopic fields at the surface of a material. For effective material parameters, this last is true with very high accuracy when we consider natural materials which fails for MMs. The pitfalls related to incorrect utilization and interpretation of effective parameters are explained too.

5.5.4 Complex materials and ultrathin metals in multilayers

When a plasmonic material is embedded in a multilayer structure, the problem of the determination of its effective optical parameters may be posed in two different ways, depending on geometrical properties of the coating. Either a total response of the structure may be searched for, if the layers are ultrathin and the coating is intended as an in-one-piece device,¹⁸⁷ or, in a more classical fashion, each of the composing layers should be treated as a film having its own complex dielectric functions, hence the rigorous Fresnel coefficient calculus with the matrix method should be used.^{91,141} In both cases, proper modeling is required for the plasmonic material optical functions as well as of its interfaces with adjacent media.

Ni *et al.*¹⁸⁷ compare four methods for modeling the dispersion relations of loss-compensated and active hyperbolic metamaterials with permittivity along one axis is negative, while the permittivities along two other directions are positive. This material is considered as a single slab, being in practice composed of ultrathin alternating layers of a metal (20 nm thick silver) and a dielectric (40 nm thick organic dye Rh800 mixed with epoxy). The constituent materials were considered to have a fixed experimentally found refractive index and extinction coefficient, while their layers were ideal, i.e. isotropic, homogenous and having plane-parallel surfaces and fixed thicknesses. The rigorous method of matrix calculations providing an exact solution for complex dielectric anisotropic permittivity of the multi-layer device was compared in this work with another three methods, namely, spatial harmonic analysis (SHA),¹⁸⁸ standard EMA and a more advanced EMA method¹⁶⁶ that takes into account the nonlocal effects neglected by the latter. The SHA method was shown to be in a perfect agreement with

the matrix calculations, both yielding the results of high accuracy for a sufficiently dense numeric mesh. On the other hand, in agreement with their physical nature, hence applicability, the EMA methods provided results with significant errors in effective permittivity calculation for thick layers or for those with high metal-to-dielectric thickness ratio, as well as for oblique incidence. Moreover, while the advanced EMA gave the results close within 3% to the exact values in most considered cases, the standard EMA was shown to produce errors as high as 50% already for the layers as thick as one-twelfth of the wavelength. Both EMA methods overestimate the imaginary parts of the permittivities in the active region of the spectrum for the implemented dye-doped dielectric.

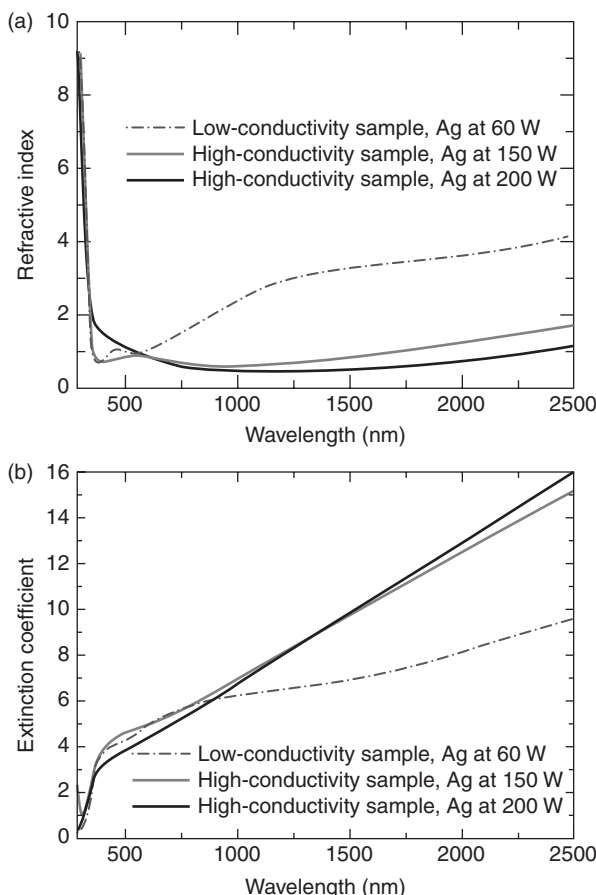
The effect of the interface roughness in such hyperbolic MMs may be crucial. For a multilayer metal-insulator stack, Shivanand *et al.*¹⁸⁹ have recently compared the numerically simulated effective parallel and perpendicular dielectric constants and analytical homogenization results as a function of wavelength and number of periods. A 0.2 μm thick slab made of 10 periods of Ag/ZnO with various roughness values was prepared and analysed. The homogenized dielectric constants (especially ϵ_{\perp}) were shown to be very sensitive to interlayer roughness. High roughness hence invalidates the performance of lenses for imaging with sub-wavelength resolution due to loss of stack anisotropy.

Homogenization with EMA remains so far the model of choice for reliable characterization of ultrathin metal film materials embedded in a dielectric stacks²⁶ or of metal-dielectric composites where a dielectric matrix embeds conductor inclusions.¹⁶⁵ To simulate the dielectric function of metal nanoinclusions, recently a nonparametric technique was compared with multiple oscillator technique.¹⁹⁰ For the description of some types of metal-dielectric composites prepared by e-beam evaporation at different deposition conditions, hence yielding different metal film granularity, the two approaches, different from both mathematical and physical point of view, were shown to be consistent.

Angularly resolved spectroscopic ellipsometry may be used to provide data for reliable retrieval of a complex dielectric function of a conductor layer with plasmonic features in a stack. Sytchkova *et al.*²⁶ studied the radio frequency (r.f.) sputtered transparent electrodes made of silver layers sandwiched between two dielectric layers (aluminium-doped zinc oxide, AZO) and having thickness varying from 8 to 14 nm obtained at various r.f. power values. Silver films were proposed to be considered to have different effective permittivities upon deposition conditions (see Fig. 5.7), as soon as they had different morphologies too. The refractive index and extinction coefficient of the silver layers were modeled by an ensemble of Lorentz and Drude oscillators, while the EMA was applied for description of the rough interfaces with

AZO layers. Two examples of ellipsometric spectra for low- and high-energy deposited Ag layers are given in Fig. 5.8, where the imprints of Ferrell modes and SP absorption bands are observable. Indeed, the optical constants of three silver types differ significantly, being that of 200 W-sample most similar to bulk Ag, whereas 60 W-sample has LSPR bands in the k -curve, corroborated by low conductivity of this partially percolated layer, see Fig. 5.7.

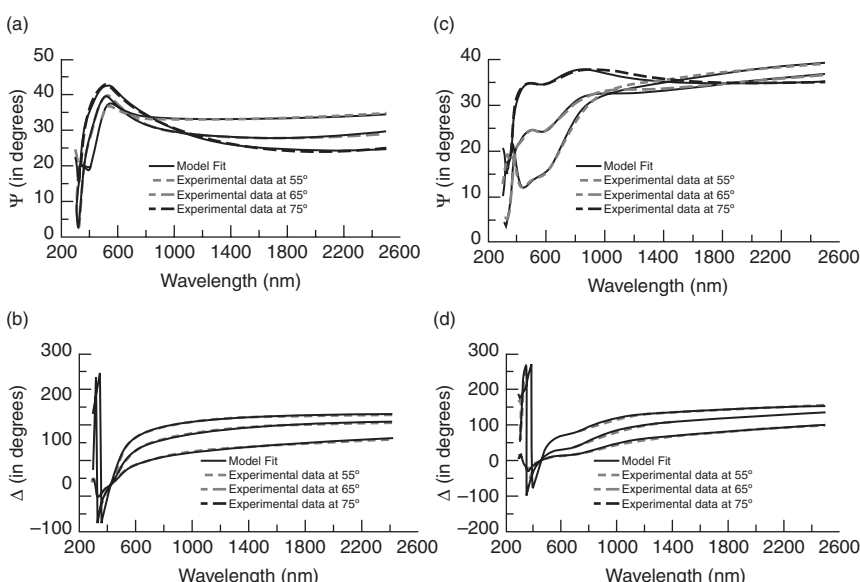
For metal films well below percolation threshold, a similar ellipsometric study was performed earlier by Toudert *et al.*¹⁹¹ for silver nanoclusters sandwiched between two silicon nitride layers. Basing their conclusion on Yamaguchi dipolar model for collective optical response of metal clusters,¹⁹² Toudert and co-workers found that the SP spectral position is mainly



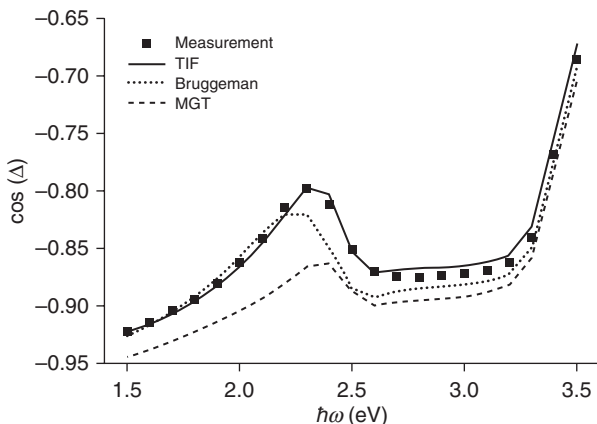
5.7 The refractive index (top) and extinction coefficient (bottom) of silver ultrathin layers within AZO/Ag/AZO transparent electrodes prepared by sputtering at various r.f. power values: 60, 150 and 200 W.

affected by the average shape of the clusters, while their size, shape distribution and electromagnetic interaction appear to have weaker influence. Haarmans and Bedeaux¹⁹³ showed in fact that noble metal films with particle coverage below 50% are well described by dipole and quadrupole terms in expansion of the problem of interaction between an ensemble of identical particles and incident light. A multipole expansion of this problem has the name of ‘thin island film’ (TIF) theory and was proposed by Bedeaux and Vlieger.¹⁹⁴ TIF theory was shown¹⁴³ to be the only correctly evaluating ellipsometric phase (angle Δ) response measured for gold 13.6 nm-NPs on silicon substrate with coverage of 12%, if compared to MGT and EMA, Fig. 5.9.

In the infrared region, spectroscopic ellipsometry was employed to study layered structures composed of polar semiconductor materials.¹⁹⁵ GaAs homo- and hetero-structures with various types of resonances in the spectral data were studied. Bulk and surface polaritons, together with Fano and Brewster modes were successfully modeled to fit experimental Ψ and Δ curves.



5.8 Typical ellipsometric spectra of two AZO/Ag/AZO samples: (a) and (b) are ellipsometric angles for the sample with Ag deposited at 60 W, while (c) and (d) correspond to those of 200 W. Despite equal nominal thickness of all layers, the graphs show different character of features corresponding to the different types of absorption bands of SPs.



5.9 Measured and theoretical dependence of cosine of ellipsometric angle Δ on photon energy for a silicon substrate covered at 12% by 13.6 nm diameter gold colloids. Notice that Bruggeman's EMA predicts a larger red-shift of the resonance peak, while MGT forecasts it correctly, but underestimates the overall change in Δ . (Source: Reprinted with permission from Reference 106. Copyright 2011 by Elsevier.)

5.6 Conclusion

Generally speaking, not only metal NPs exhibit LSPR, and not only ultra-thin metal layers support SPPs. Nanoshapes of any material, as long as their interface possesses a significant number of free carriers, either electrons or holes, may work as plasmonic media. Besides metals, semiconductors, alloys and intermetallics considered in this review, there exist other categories of alternative plasmonic materials like graphene,¹⁹⁶ ceramics¹⁹⁷ or organic materials,¹⁹⁸ which, however, are less advantageous, at least in the present state of the art, in terms of both optical performance and fabrication and integration compatibility.^{134,199}

As we saw, nanotechnology has enabled almost arbitrary control of electromagnetic waves leading to trapped rainbows, superlensing, or anomalous refraction. Moreover, hybrid devices with exotic properties may be engineered when semiconductors and metal NPs are both used, like invisible photodetector.²⁰⁰ Negative index MMs may be engineered to enable nonlinear effects like second harmonic generation²⁰¹ or quadratic and even cubic²⁰² optical parametric amplification, which can be used moreover for loss compensation in MMs.²⁰³ Either embedded into multilayer coatings⁹³ or alone-deposited on a substrate,^{76,77} MMs make possible effective narrow-band and polarization ripple-free filtering with tunable bandwidth and throughput efficiency anywhere from optical range to microwaves operating with wide

acceptance angle. Additionally, plasmonic coupling may be rendered easier than conventional prism and grating approaches using MMs themselves: a gradient-index meta-surface for linking free propagating waves and surface waves was recently proposed,²⁰⁴ creating a valid alternative to traditional coupling methods. This material combines a thin gradient-index MM layer with a perfect electric conductor, and such a combination induces reflection-phase gradient and compensates the momentum mismatch between the two wave types with nearly 100% efficiency. The idea was experimentally confirmed in the microwave range both by near- and far-field measurements and may pave the way for creation of novel types of SP couplers, light absorbers or antireflection surfaces.

The materials used for all these novel exciting applications require adequate characterization methods both in near- and far-field that we have endeavored to overview in this chapter. With the development in the field, new conductors and new characterization methods will arise. Materials from the hottest frontiers of condensed-matter physics might induce further progress in plasmonics. Who knows if awkward cousins of metals dubbed ‘orthogonal metals’,²⁰⁵ indistinguishable from the Fermi liquids²⁰⁶ in conductivity and thermodynamics, but having sharply distinct one-electron properties, might bring to a revolutionary vision into the topic once implemented for creation of complex materials? Might this new kind of possible conducting phases of matter show itself to be a new, exciting puzzle for plasmonic applications?

5.7 References

1. A.J. McAlister and E.A. Stern, ‘Plasma resonance absorption in thin metal films’, *Phys. Rev.* **132** (1963) 1599–1602. DOI:10.1103/PhysRev.132.1599
2. R.H. Ritchie, ‘Plasma losses by fast electrons in thin films’, *Phys. Rev.* **106** (1957) 1214–1222. DOI:10.1103/PhysRev.106.874
3. R.A. Ferrell, ‘Predicted radiation of plasma oscillations in metal films’, *Phys. Rev.* **111** (1958) 874–881. DOI:10.1103/PhysRev.106.874
4. S.A. Maier, *Plasmonics* (2006) (Berlin: Springer).
5. J.M. Pitarke, V.M. Silkin, E.V. Chulkov and P.M. Echenique, ‘Theory of surface plasmons and surface plasmon polaritons’, *Rep. Prog. Phys.* **70** (2007) 1–87. DOI:10.1088/0034-4885/70/1/R01
6. I. Freestone, N. Meeks, M. Sax and C. Higgitt, ‘The Lycurgus cup – a Roman nanotechnology’, *Gold Bull.* **40** (2007) 270–277. DOI:10.1007/BF03215599
7. J. Zhang and L. Zhang, ‘Nanostructures for surface plasmons’, *Adv. Opt. Photon.* **4** (2012) 157–321. DOI: 10.1364/AOP.4.000157
8. M.A. Garcia, ‘Surface plasmons in metallic nanoparticles: fundamentals and applications’, *J. Phys. D: Appl. Phys.* **44** (2011) 283001. DOI:10.1088/0022-3727/44/28/283001
9. M.I. Stockman, ‘Nanoplasmonics: past, present, and glimpse into future’, *Opt. Express* **19** (2011) 22029–22106. DOI:10.1364/OE.19.022029

10. S.A. Maier and A.H. Atwater, 'Plasmonics: localization and guiding of electromagnetic energy in metal-dielectric structures', *J. Appl. Phys.* **98** (2005) 011101. DOI: 10.1063/1.1951057
11. L. Feng and Y. Fainman, 'Manipulation of plasmonics from nano to micro scale' in *Plasmonics and Plasmonic Metamaterials*, eds. G. Schevts and I. Tsukerman, (2001) (World Scientific).
12. T. Pradeep and Anshup, 'Noble nanoparticles for water purification: a critical review', *Thin Solid Films* **517** (2009) 6441–6478. DOI: 10.1016/j.tsf.2009.03.195
13. J.M. Luther, P.K. Jain, T. Ewers and A.P. Alivisatos, 'Localized surface plasmon resonances arising from free carriers in doped quantum dots', *Nature Mat.* **10** (2011) 361–366. DOI: 10.1038/NMAT3004
14. E. Kazuma, K. Matsubara, K.L. Kelly, N. Sakai and T. Tatsuma, 'Bi- and uniaxially oriented growth and plasmon resonance properties of anisotropic Ag nanoparticles on single crystalline TiO₂ surfaces', *J. Phys. Chem. Lett.* **C** **113** (2009) 4758–4762. DOI: 10.1021/jp900749x
15. K.L. Kelly, E. Coronado, L.L. Zhao and G.C. Schatz, 'The optical properties of metal nanoparticles: the influence of size, shape, and dielectric environment', *J. Phys. Chem. B* **107** (2003) 668–677. DOI: 10.1021/jp02673y
16. S. Kubo, A. Diaz, Y. Tang, T.S. Mayer, I.C. Khoo and T.E. Mallouk, 'Tunability of the refractive index of gold nanoparticle dispersions', *Nano Lett.* **7** (2007) 3438–3433. DOI: 10.21/nl071893x
17. Z.Y. Sheng and V.V. Varadan, 'Tuning the effective properties of metamaterials by changing the substrate properties', *J. Appl. Phys.* **101** (2007) 014909. DOI: 10.1063/1.2407275
18. M.P. Nezhad, K. Tetz and Y. Fainman, 'Gain assisted propagation of surface plasmon polaritons on planar metallic waveguides', *Opt. Express* **12** (2004) 4072–4079. DOI: 10.1364/OPEX.12.004072
19. P.K. Jain, W. Huang and M.A. El-Sayed, 'On the universal scaling behavior of the distance decay of plasmon coupling in metal nanoparticle pairs: a plasmon ruler equation', *Nano Lett.* **7** (2007) 2080–2088. DOI: 10.1021/nl071008a
20. R.H. Pedersen, A. Boltasseva, D.M. Johansen, T. Nielsen, K.B. Jorgensen, K. Leosson, J. Erland and A. Kristensen, 'Nanoimprinted reflecting gratings for long-range surface plasmon polaritons', *Microelectr. Eng.* **84** (2007) 895–898. DOI: 10.1016/j.mee.2007.01.110
21. C. Enkrich, R. Perez-Willard, D. Gerthsen, J.F. Zhou, T. Koschny, C.M. Soukoulis, M. Wegener and S. Linden, 'Focused-ion-beam nanofabrication of near-infrared magnetic metamaterials', *Adv. Mater.* **17** (2005) 2547–2549. DOI: 10.1002/adma.200500804
22. Y.-Y. Yu, S.-S. Chang, C.-L. Lee and C.R.C. Wang, 'Gold nanorods: electrochemical synthesis and optical properties', *J. Phys. Chem. B* **101** (1997) 6661–6664. DOI: 10.1021/jp971656q
23. P.T. Hammond, 'Form and function in multilayer assembly: new applications at the nanoscale', *Adv. Mater.* **16** (2004) 1271–1293. DOI: 10.1002/adma.200400760
24. J.A. Fan, C. Wu, K. Bao, R. Bardhan, N.J. Halas, V.N. Manoharan, P. Nordlander, G. Shvets and F. Capasso, 'Self-assembled plasmonic nanoparticle clusters', *Science* **328** (2010) 1135–1138. DOI: 10.1126/science.1187949
25. F. Formanek, N. Takeyasu, T. Tanaka, K. Chiyoda, A. Ishikawa and S. Kawata, 'Three-dimensional fabrication of metallic nanostructures over large areas by

- two-photon polymerization', *Opt. Express* **14** (2006) 800–809. DOI: 10.1364/OPEX.14.000800
- 26. A. Sytchkova, M.L. Grilli, A. Rinaldi, S. Vedraime, P. Torchio, A. Piegaro and F. Flory, 'R.F. sputtered Al:ZnO-Ag transparent conductor: A plasmonic nanostructure with enhanced optical and electrical properties', *J. Appl. Phys.* **114** (2013) 094509. DOI: 10.1063/1.4820266
 - 27. D.R. Sahu, S.-Y. Lin and J.-L. Huang, 'Investigation of conductive and transparent Al-doped ZnO/Ag/Al-doped ZnO multilayer coatings by electron beam evaporation', *Thin Solid Films* **516** (2008) 4728–4732. DOI: 10.1016/j.tsf.2007.08.089
 - 28. S.H. Ko, Y. Choi, D.J. Hwang, C.P. Grigoropoulos, J. Chung and D. Poulikakos, 'Nanosecond laser ablation of gold nanoparticle films', *Appl. Phys. Lett.* **89** (2006) 141126. DOI: 10.1063/1.2360241
 - 29. A. Boltasseva and V.M. Shalaev, 'Fabrication of optical negative-index metamaterials: recent advances and outlook', *Metamaterials* **2** (2008) 1–17. DOI: 10.1016/j.metmat.2008.03.004
 - 30. Z. Jacob, J.-Y. Kim, G.V. Naik, A. Boltasseva, E.E. Narimanov and V.M. Shalaev, 'Engineering photonic density of states using metamaterials', *Appl. Phys. B* **100** (2010) 215–218. DOI: 10.1007/s00340-010-4096-5
 - 31. A. Boltasseva and H.A. Atwater, 'Low-loss plasmonic metamaterials', *Science* **331** (2011) 290–291. DOI: 10.1126/science.1198258
 - 32. M.G. Blaber, M.D. Arnold and M.J. Ford, 'Designing materials for plasmonic systems: the alkali-noble intermetallics', *J. Phys.: Condens. Matter.* **22** (2010) 095501. DOI: 10.1088/0953-8984/22/9/095501
 - 33. H. Kuwata, H. Tamaru, K. Esumi and K. Miyano, 'Resonant light scattering from metal nanoparticles: practical analysis beyond Rayleigh approximation', *Appl. Phys. Lett.* **83** (2003) 4625–4627. DOI: 10.1063/1.1630351
 - 34. M. Meier and A. Wokaun, 'Enhanced fields on large metal particles: dynamic depolarization', *Opt. Lett.* **8** (1983) 581–583. DOI: 10.1364/OL.8.000058
 - 35. T. Kokkinakis and K. Alexopoulos, 'Observation of radiative decay of surface plasmons in small silver particles', *Phys. Rev. Lett.* **28** (1972) 1632–1634. DOI: 10.1103/PhysRevLett.28.1632
 - 36. S. Link and M.A. El-Sayed, 'Shape and size dependence of radiative, non-radiative and photothermal properties of gold nanocrystals', *Int. Rev. Phys. Chem.* **19** (2000) 409–453. DOI: 10.1080/01442350050034180
 - 37. U. Kreibig and M. Vollmer, *Optical Properties of Metal Clusters*, Springer Series in Material Science 25; Springer, Berlin (1995).
 - 38. J.R. Krenn, A. Dereux, J.C. Weeber, E. Bourillot, Y. Lacroute, J.P. Goudonnet, G. Schider, W. Gotschy, A. Leitner, F.R. Aussenegg and C. Girard, 'Squeezing the optical near-field zone by plasmon coupling of metallic nanoparticles', *Phys. Rev. Lett.* **82** (1999) 2590–2593. DOI: 10.1103/PhysRevLett.82.2590
 - 39. S.A. Maier, M.L. Brongersma, P.G. Kik and H.A. Atwater, 'Observation of near-field coupling in metal nanoparticle chains using far-field polarization spectroscopy', *Phys. Rev. B* **65** (2002) 193408. DOI: 10.1103/PhysRevB.65.193408
 - 40. J. Pérez-Juste, I. Pastoriza-Santos, L.M. Liz-Marzán and P. Mulvaney, 'Gold nanorods: synthesis, characterization and applications', *Coord. Chem. Rev.* **249** (2005) 1870–1901. DOI: 10.1016/j.ccr.2005.01.030
 - 41. M. Ficcadenti, N. Pinto, L. Morresi, R. Murri, L. Serenelli, M. Tucci, M. Falconieri, A.K. Sytchkova, M.L. Grilli, A. Mittiga, M. Izzi, L. Pirozzi and S.R. Jadkar, 'Si

- quantum dots for solar cell fabrication', *Mater. Sci. Eng. B* **159–160** (2009) 66–69. DOI: 10.1016/j.mseb.2008.10.054
42. S.A. Maier, P.G. Kik, A.H. Atwater, S. Meltzer, E. Harel, B.E. Koel and A.A.G. Requicha, 'Local detection of electromagnetic energy transport below the diffraction limit in metal nanoparticle plasmon waveguides', *Nature Mat.* **2** (2003), 229–232. DOI:10.1038/nmat852
43. F. Flory, L. Escoubas and G. Berginc, 'Optical properties of nanostructured materials: a review', *J. Nanophotonics* **5** (2011) 052502. DOI: 10.1117/1.3609266
44. F. Flory, Y.-J. Chen, C.-C. Lee, L. Escoubas, J.-J. Simon, P. Torchio, J. Le Rouzo, S. Vedraine, H. Derbal-Habak, I. Shupyk, Y. Didane and J. Ackermann, 'Optical properties of dielectric thin films including quantum dots', *Appl. Opt.* **50** (2011) C129. DOI: 10.1364/AO.50.00C129
45. S. Fasel, F. Robin, E. Moreno, D. Emi, N. Gisin and H. Zbinden, 'Energy-time entanglement preservation in plasmon-assisted light transmission', *Phys. Rev. Lett.* **94** (2005) 110501. DOI: 10.1103/PhysRevLett.94.110501
46. A. Huck, S. Smolka, P. Lodahl, A.S. Serensen, A. Boltasseva, J. Janousek and U.L. Andersen, 'Demonstration of quadrature-squeezed surface plasmons in a gold waveguide', *Phys. Rev. Lett.* **102** (2009) 246802. DOI: 10.1103/PhysRevLett.102.246802
47. E. Prodan, C. Radloff, N.J. Halas and P. Nordlander, 'A hybridization model for the plasmon response of complex nanostructures', *Science* **302** (2003) 419–422. DOI: 10.1126/science.1089171
48. A.V. Akimov, A. Mukherjee, C.L. Yu, D.E. Chang, A.S. Zibrov, P.R. Hemmer, H. Park and M.D. Lukin, 'Generation of single optical plasmons in metallic nanowires coupled to quantum dots', *Nature* **450** (2007) 402–406. DOI: 10.1038/nature06230
49. D.E. Gómez, K.C. Vernon, P. Mulvaney and T.J. Davis, 'Surface plasmon mediated strong exiton-photon coupling in semiconductor nanocrystals', *Nano Lett.* **10** (2010) 274–278. DOI: 10.1021/nl903455z
50. C. Gruber, P. Kusar, A. Hohenau and J.R. Krenn, 'Controlled addressing of quantum dots by nanowire plasmons', *Appl. Phys. Lett.* **100** (2012) 231102. DOI: 10.1063/1.4725490
51. R.J. Moerland, H.T. Recola, G. Sharma, A.-P. Eskelinen, A.I. Väkeväinen and P. Törmä, 'Surface plasmon polariton-controlled tunable quantum-dot emission', *Appl. Phys. Lett.* **100** (2012) 221111. DOI: 10.1063/1.4724327
52. S. Sengupta, J.O. Kim, A.V. Barve, S. Adhikary, Y.D. Sharma, N. Gautam, S.J. Lee, S.K. Noh, S. Chakrabarti and S. Krishna, 'Sub-monolayer quantum dots in confinement enhanced dots-in-a-well heterostructure', *Appl. Phys. Lett.* **100** (2012) 191111. DOI: 10.1063/1.4711214
53. Z. Jacob and V.M. Shalaev, 'Plasmonics goes quantum', *Science* **334** (2011) 463–464. DOI: 10.1126/science.1211736
54. S. Anantha Ramakrishna, 'Physics of negative refractive index materials', *Rep. Prog. Phys.* **68** (2005) 449–521. DOI: 10.1088/0034-4885/68/2/R06
55. V.M. Shalaev, 'Optical negative-index materials', *Nat. Photonics* **1** (2007) 41–48. DOI: 10.1126/science.1139266
56. E. Plum, V. A. Fedotov, A. S. Schwanecke, N. I. Zheludev and Y. Chen, 'Giant optical gyrotropy due to electromagnetic coupling', *Appl. Phys. Lett.* **90** (2007) 223113. DOI:10.1088/0034-4885/68/2/R06

57. V.N. Smolyaninova, I.I. Smolyaninov, A.V. Kildishev and V.M. Shalaev, 'Trapped rainbow techniques for spectroscopy on chip and fluorescence enhancement', *Appl. Phys. B* **106** (2012) 577–581. DOI: 10.1007/s00340-011-4856-x
58. J.B. Pendry, D. Schurig and D.R. Smith, 'Controlling electromagnetic fields', *Science* **312** (2006) 1780–1782. W. Cai and V. Shalaev, 'Transformation optics and electromagnetic cloak of invisibility', in *Optical Metamaterials: Fundamentals and Applications*, Springer Science + Business Media, LLC 2010. DOI: 10.1007/978-1-4419-1151-3_9
59. J.A. Schuller, E.S. Barnard, W. Cai, Y.C. Jun, J.S. White and M.L. Brongersma, 'Plasmonics for extreme light concentration and manipulation', *Nat. Mater.* **9** (2010) 193–205. DOI: 10.1038/NMAT2630
60. C. Argyropoulos, G. D'Aguanno, N. Mattiucci, N. Akozbek, M.J. Bloemer and A. Alù, 'Matching and funneling light at the plasmonic Brewster angle', *Phys. Rev. B* **85** (2012) 024304. DOI: 10.1103/PhysRevB.85.024304
61. V.G. Veselago, 'Электродинамика веществ с одновременно отрицательными значениями ϵ и μ ', *Usp. Fiz. Nauk* **92** (1967) 517. V.G. Veselago, 'The electrodynamics of substances with simultaneously negative values of ϵ and μ ', *Sov. Fiz. – Usp.* **10** (1968) 509.
62. S. Link and M. El-Sayed, 'Spectral properties and relaxation dynamics of surface plasmon electronic oscillations in gold and silver nanodots and nanorods', *J. Phys. Chem. B* **103** (1999) 8410–8426. DOI: 10.1021/jp9917648
63. A. Lesuffleur, I. Kumar and R. Gordon, 'Enhanced second harmonic generation from nanoscale double-hole arrays in a gold film', *Appl. Phys. Lett.* **88** (2006) 261104. DOI: 10.1063/1.2218057
64. Y. Peng and K. Kempa, 'Controlling light propagation with nanowires', *Appl. Phys. Lett.* **100** (2012) 171903. DOI: 10.1063/1.4704193. S. Rehwald, M. Berndt, F. Katzenberg, S. Schwieger, E. Runge, K. Schierbaum and D. Zerulla, 'Tunable nanowires: an additional degree of freedom in plasmonics', *Phys. Rev. B* **76** (2007) 085420. DOI: 10.1103/PhysRevB.76. 085420
65. H. Wang, D.W. Brandl, F. Le, P. Nordlander and N.J. Halas, 'Nanorice: a hybrid plasmonic nanostructure', *Nano Lett.* **6** (2006) 827–832. DOI: 10.1021/nl060209w
66. Z. Sun, X. Zuo and J. Li, 'Optical transmission through multilayered ultrathin metal gratings', *Plasmonics* **6** (2011) 745–751. DOI: 10.1007/s11468-011-9259-7 (nd references 1–12 within).
67. J.H. Shi, H.F. Ma, W.X. Jiang and T.J. Cui, 'Multiband stereomaterial-based polarization spectral filter', *Phys. Rev. B* **86** (2012) 035103. DOI: 10.1103/PhysRevB.86.035103
68. N. Papasimakis, V.A. Fedotov, N.I. Zheludev and S.L. Prosvirin, 'Metamaterial analog of electromagnetically induced transparency', *Phys. Rev. Lett.* **101** (2008) 253903. DOI: 10.1103/PhysRevLett.101. 253903
69. S.E. Harris, J.E. Field and A. Imamoglu, 'Nonlinear optical processes using electromagnetically induced transparency', *Phys. Rev. Lett.* **64** (1990) 1107–1110. DOI: 10.1103/PhysRevLett.64. 1107
70. M.T. Reiten, D. Roy Chowdhury, J. Zhou, A.J. Taylor, J.F. O'Hara and A.K. Azad, 'Resonance tuning behaviour in closely spaced inhomogeneous bilayer metamaterials', *Appl. Phys. Lett.* **98** (2011) 131105. DOI: 10.1063/1.3566978
71. I. Al-Naib, R. Singh, C. Rockstuhl, F. Lederer, S. Delprat, D. Rocheleau, M. Chaker, T. Ozaki and R. Morandotti, 'Excitation of a high-Q subradiant res-

- onance mode in mirrored single-gap asymmetric split ring resonator terahertz metamaterials', *Appl. Phys. Lett.* **101** ((2012) 071108. DOI: 10.1063/1.4745790
72. N.R. Han, Z.C. Chen, C.S. Lim, B. Ng and M.H. Hong, 'Broadband multi-layer terahertz metamaterials fabrication and characterization on flexible substrates', *Opt. Express* **19**(8) (2011) 6990–6998. DOI: 10.1364/OE.19.006990
 73. D.R. Chowdhury, R. Singh, M. Reiten, H.-T. Chen, Taylor, A.J., O'Hara and A.K. Azad, 'A broadband planar terahertz metamaterial with nested structure', *Opt. Express* **19**(17) (2011) 15817–15823. DOI: 10.1364/OE.19.015817
 74. T-T. Yeh, S. Genovesi, A. Monorchio, E. Prati, F. Costa, T.-Y. Huang and T.-J. Yen, 'Ultra-broad and sharp-transition terahertz filters by hybridizing multiple resonance mode in monolithic metamaterial', *Opt. Express* **20**(7) (2012) 7580–7589. DOI: 10.1364/OE.20.007580
 75. M. Lu, W. Li and E.R. Brown, 'Second-order bandpass terahertz filter achieved by multilayer complementary metamaterial structures', *Opt. Lett.* **36**(7) (2011) 1071–1073. DOI: 10.1364/OL.36.001071
 76. N.I. Zheludev, E. Plum and V.A. Fedotov, 'Metamaterial polarization spectral filter: isolated transmission line at any prescribed wavelength', *Appl. Phys. Lett.* **99** (2011) 171915. DOI: 10.1063/1.3656286
 77. C. Wu and G. Shvets, 'Design of metamaterial surfaces with broadband absorbance', *Opt. Lett.* **37** (2012) 308. DOI: 10.1364/OL.37.000308
 78. J. Valentine, S. Zhang, T. Zentgraf, E. Ulin-Avila, D.A. Genov, G. Bartal and X. Zhang, 'Three-dimensional optical metamaterial with a negative refractive index', *Nature* **455** (2008) 376–379. DOI: 10.1038/nature07247
 79. H. Chen, C.T. Chan and P. Shen, 'Transformation optics and metamaterials', *Nat. Mater.* **9** (2010) 387–396. DOI: 10.1038/NMAT2743
 80. J.B. Pendry, 'Focus issue: negative refraction and metamaterials', *Opt. Express* **11** (2003) 639. DOI: 10.1364/OE.11.000639
 81. A.A. Govyadinov, V.A. Podolskiy and M.A. Noginov, 'Active metamaterials: sign of refractive index and gain assisted dispersion management', *Appl. Phys. Lett.* **91** (2007) 191103. DOI: 10.1063/1.2800309
 82. P.A. Belov and C. Simovski, 'Homogenization of electromagnetic crystals formed by uniaxial resonant scatterers', *Phys. Rev. E* **72** (2005) 026615 (1–15). DOI: 10.1103/PhysRevE.72.026615
 83. A. Alù and N. Engheta, 'Three-dimensional nanotransmission lines at optical frequencies: a recipe for broadband negative-refraction optical metamaterials', *Phys. Rev. B* **75** (2007) 024304 (1–20). DOI: 10.1103/PhysRevB.75.024304
 84. A. Alù and N. Engheta, 'Effect of small random disorders and imperfections on the performance of arrays of plasmonic nanoparticles', *New J. Phys.* **12** (2010) 013015. DOI: 10.1088/1367-2630/12/1/013015
 85. M. Elbahri, M.K. Hedayati, V.S.K. Chakravadhanula, M. Jamali, T. Strunkus, V. Zaporozhchenko and F. Faupel, 'Omnidirectional transparent conducting-metal-based plasmonic nanocomposite', *Adv. Mater.* **23** (2011) 1993–1997. DOI: 10.1002/adma.201003811
 86. A.Y. Elezzabi, K.J. Chau, C.A. Baron and P. Maraghechi, 'A plasmonic random composite with atypical refractive index', *Opt. Express* **17** (2009) 1016–1022. DOI: 10.1364/OE.17.001016
 87. G. Bruno, G.V. Bianco, M.M. Giangregorio, A. Sacchetti, P. Capezzuto and M. Losurdo, 'A two-step plasma processing for gold nanoparticles supported on silicon near-infrared plasmonics', *Appl. Phys. Lett.* **96** (2010) 043104. DOI: 10.1063/1.3291670

88. O. Wiener, Die Theorie des Mischkörpers für das Feld der stationären Stromung', *Abh. Math-Phys. Klasse Königlich Sächsischen Des Wiss* **32** (1912) 509–604.
89. N. Engheta, Circuits with light at nanoscales: optical nanocircuits inspired by metamaterials', *Science* **317** (2007) 1698–1702. DOI: 10.1126/science.1133268
90. A. Alù, M.G. Silveirinha, A. Salandrino and N. Engheta, Epsilon-near-zero metamaterials and electromagnetic sources: tailoring the radiation phase pattern', *Phys. Rev. B* **75** (2007) 155410. DOI: 10.1103/PhysRevB.75.155410
91. H.A. Macleod, *Thin Film Optical Filters*, 3rd edition, CRC Press (2001). ISBN 0750306882, 9780750306881
92. A. Piegari, J. Bulir and A.K. Sytchkova, 'Variable narrow-band transmission filters for spectrometry from space. 2. Fabrication process', *Appl. Opt.* **47** (2008), C151–C156. DOI: 10.1364/AO.47.00C151
93. A. Sytchkova, 'Reliable deposition of induced transmission filters with a single metal layer', *Appl. Opt.* **50** (2011) C90–C94. DOI: 10.1364/AO.50.000C90
94. E. Masetti, J. Bulir, S. Gagliardi, V. Janicki, A. Krasilnikova Sytchkova, C. Coluzza and G. Di Santo, 'Ellipsometric and XPS analysis of the interface between silver and SiO₂, TiO₂ and SiNx thin films', *Thin Solid Films* **455–456** (2004) 468–472. DOI: 10.1016/j.tsf.2003.11.244
95. H.-T. Hsu and C.-J. Wu, 'Design rules for a Fabry-Perot narrow band transmission filter containing a metamaterial negative-index defect', *Prog. Electromagn. Res. Lett.* **9** (2009) 101–107. DOI: 10.2528/PIERL09032803
96. F. Brouers, S. Blacher, A.N. Lagarkov, A.K. Sarychev, P. Gadenne and V.M. Shalaev, 'Theory of giant Raman scattering from semicontinuous metal films', *Phys. Rev. B* **55** (1997) 13234–13245. DOI: 10.1103/PhysRevB.55.13234
97. P.W. Anderson, 'Absence of diffusion in certain random lattices', *Phys. Rev.* **109** (1958) 1492–1505. DOI: 10.1103/PhysRev.109.1492
98. V. Krachmalnikov, E. Castanie, Y.D. Wilde and R. Carminati, 'Fluctuations of the local density of states probe localized surface plasmons on disordered metal films', *Phys. Rev. Lett.* **105** (2010) 183901. DOI: 10.1103/PhysRevLett.105.183901
99. H.A. Atwater and A. Polman, 'Plasmonics for improved photovoltaic devices', *Nature Mater.* **9** (2010) 205. DOI: 10.1038/nmat2629
100. N. Noginova, A.V. Yakim, J. Soimo, L. Gu and M.A. Noginov, 'Light-to-current and current-to-light coupling in plasmonic systems', *Phys. Rev. B* **84** (2011) 035447. DOI: 10.1103/PhysRevB.84.035447
101. P.R. West, S. Ishii, G.V. Naik, N.K. Emani, V.M. Shalaev and A. Boltasseva, 'Searching for better plasmonic materials', *Laser Photonics Rev.* **4** (2010) 798–808. DOI: 10.1002/lpor.200900055
102. M.D. Arnold and M.G. Blaber, 'Optical performance and metallic absorption in nanoplasmonic systems', *Opt. Express* **17** (2009) 3835–3847. DOI: 10.1364/OE.17.003835
103. H. Ehrenreich and H.R. Philipp, 'Optical properties of Ag and Cu', *Phys. Rev.* **128** (1962) 1622–1629. DOI: 10.1103/PhysRev.128.1622
104. B. Balamurugan and T. Maruyama, 'Evidence of an enhanced interband absorption in Au nanoparticles: Size-dependent electronic structure and optical properties', *Appl. Phys. Lett.* **87** (2005) 145105 (1–3). DOI: 10.1063/1.2077834
105. M.M. Alvarez, J.T. Khouri, G. Schaaff, M.N. Shafiqullin, I. Vezmar and R.L. Whetten, 'Optical absorption spectra of nanocrystal gold molecules', *J. Phys. Chem. B* **101** (1997) 3706–3712. DOI: 10.1021/jp962922n

106. T.W.H. Oates, H. Wormeerter and H. Arwin, ‘Characterization of plasmonic effects in thin films and metamaterials using spectroscopic ellipsometry’, *Prog. Surf. Sci.* **86** (2011) 328–376. DOI: 10.1016/j.progsurf.2011.08.004
107. G.H. Chan, J. Zhao, E.M. Hick, G.C. Schatz and R.P. Van Duyne, ‘Plasmonic properties of copper nanoparticles fabricated by nanosphere lithography’, *Nano Lett.* **7** (2007) 1947–1952. DOI: 10.1021/nl070648a
108. G.H. Chan, J. Zhao, G.C. Schatz and R. Duyne, ‘Localized surface plasmon resonance spectroscopy of triangular aluminum nanoparticles’, *J. Phys. Chem. C* **112** (2008) 13958–13963. DOI: 10.1021/jp804088z
109. J.C. Quail, J.G. Rako and H.J. Simon, ‘Long-range surface-plasmon modes in silver and aluminum films’, *Opt. Lett.* **8** (1983) 377–379. DOI: 10.1364/OL.8.000377
110. A. Taguchi, N. Hayazawa, K. Furusawa, H. Ishitobi and S. Kawata, ‘Deep-UV tip-enhanced Raman scattering’, *J. Raman Spectrosc.* **40** (2009) 1324–1330. DOI: 10.1002/jrs.2287
111. B.F. Soares, M.V. Bashevoy, F. Jonsson, K.F. MacDonald and N.I. Zheludev, ‘Polymorphic nanoparticles as all-optical memory elements’, *Opt. Express* **14** (2006) 10652. DOI: 10.1364/OE.14.010652
112. P. Wu, T.H. Kim, M. Losurdo, G. Bruno, H.O. Everitt and A.S. Brown, ‘Real-time plasmon resonance tuning of liquid Ga nanoparticles by in situ spectroscopic ellipsometry’, *Appl. Phys. Lett.* **90** (2007) 103119. DOI: 10.1063/1.2712508
113. J. Bao, M.A. Zimmler, F. Capasso, X. Wang and Z.F. Ren, ‘Broadband ZnO single-nanowire light-emitting diode’, *Nano Lett.* **6** (2006) 1719–1722. DOI: 10.1021/nl061080t
114. A.K. Sharma and G.J. Mohr, ‘On the performance of surface plasmon resonance based fibre opticsensorwithdifferentbimetallicnanoparticlealloycombinations’, *J. Phys. D: Appl. Phys.* **41** (2008) 055106. DOI: 10.1088/0022-3727/41/5/055106
115. D.A. Blobb, G. Zhu, M. Mayy, A.V. Gavrilenko, P. Mead, V.I. Gavrilenko and M.A. Noginov, ‘Engineering of low-loss metal for nanoplasmonic and metamaterials applications’, *Appl. Phys. Lett.* **95** (2009) 151102. DOI: 10.1063/1.3237179
116. M.G. Blaber, M.D. Arnold and M.J. Ford, ‘A review of the optical properties of alloys and intermetallics for plasmonics’, *J. Phys.: Condens. Matter.* **22** (2010) 143201. DOI: 10.1088/0953-8984/22/14/143201
117. M.O. Liedke, B. Liedke, A. Keller, B. Hillebrands, A. Mücklich, S. Facsko and J. Fassbender, ‘Induced anisotropies in exchange-coupled systems on rippled substrates’, *Phys. Rev. B* **75** (2007) 220407. DOI: 10.1103/PhysRevB.75.220407
118. T.W.H. Oats, A. Keller, S. Facsko and A. Mücklich, ‘Aligned silver nanoparticles on rippled silicon templates exhibiting anisotropic plasmon absorption’, *Plasmonics* **2** (2007) 47–50. DOI: 10.1007/s11468-007-9025-z
119. A. Toma, B. Šetina Batič, D. Chiappe, C. Boragno, U. Valbusa, M. Godec, M. Jenko and F. Bautier de Mongeot, ‘Patterning polycrystalline thin films by defocused ion beam: the influence of initial morphology on the evolution of self-organized nanostructures’, *J. Appl. Phys.* **104** (2008) 104313. DOI: 10.1063/1.3021100
120. F. Everts, H. Wormeester and B. Poelsema, ‘Optical anisotropy induced by ion bombardment of Ag(001)’, *Phys. Rev. B* **78** (2008) 155419. DOI: 10.1103/PhysRevB.78.155419

121. A. Politano and G. Chiarello, 'Sputtering-induced modification of the electronic properties of Ag/Cu(111)', *J. Phys.: Appl. Phys.* **43** (2010) 085302. DOI: 10.1088/0022-3727/43/8/085302
122. D. Armand, G. Taguchi and Y. Kadoya, 'Mechanical active control of surface plasmon properties', *Opt. Express* **20** (2012) 9523–9534. DOI: 10.1364/OE.20.009523
123. H.-T. Chen, H. Lu, A.K. Azad, R.D. Averitt, A.C. Gossard, S.A. Trugman, J.F. O'Hara and A.J. Taylor, 'Electronic control of extraordinary terahertz transmission through subwavelength metal hole arrays', *Opt. Express* **16** (2008) 7641–7648. DOI: 10.1364/OE.16.007641
124. J. Gómez Rivas, M. Kuttge, H. Kurz, P. Haring Bolivar and J.A. Sánchez-Gil, 'Low-frequency active surface plasmon optics on semiconductors', *Appl. Phys. Lett.* **88** (2006) 082106. DOI: 10.1063/1.2177348
125. J.D. Jackson, *Classical Electrodynamics* New York: Wiley, (1998).
126. E.D. Palik, *Handbook of Optical Constants of Solids* San Diego: Academic Press (1998).
127. T. Taubner, D. Korobkin, Y. Urzhumov, G. Shvets and R. Hillenbrand, 'Near-field microscopy through a SiC superlens', *Science* **313** (2006) 1595. DOI: 10.1126/science.1131025
128. A.J. Hoffman, L. Alekseyev, S.S. Howard, K.J. Franz, D. Wasserman, V.A. Podolskiy, E.E. Narimanov, D.L. Sivco and C. Gmachl, 'Negative refraction in semiconductor metamaterials', *Nat. Mater.* **6** (2007) 946–950. DOI: 10.1038/nmat2033
129. G.V. Naik and A. Boltasseva, 'A comparative study of semiconductor-based plasmonic metamaterials', *Metamaterials* **5** (2011) 1–7. DOI: 10.1016/j.metmat.2010.11.001
130. S. Franzen, 'Surface plasmon polaritons and screened plasma absorption in indium tin oxide compared to silver and gold', *J. Phys. Chem.* **112** (2008) 6027–6032. DOI: 10.1021/jp7097813
131. C. Rhodes, S. Franzen, J.-P. Maria, M. Losego, D.N. Leonard, B. Laughlin, G. Duscher and S. Weibel, 'Surface plasmon resonance in conducting metal oxides', *J. Appl. Phys.* **100** (2006) 054905. DOI: 10.1063/1.2222070
132. M.A. Noginov, L.Gu, J. Livenere, G. Zu, A.K. Pradhan, R. Mundle, M. Bahoura, Barnakov, Y.A., and V.A. Podolskiy, 'Transparent conductive oxides: plasmonic materials for telecom wavelengths', *Appl. Phys. Lett.* **99** (2011) 021101. DOI: 10.1063/1.3604792
133. M. Kanehara, H. Koike, T. Yoshinaga and T. Teranishi, 'Indium tin oxide nanoparticles with compositionally tunable surface plasmon resonance frequencies in the near-IR region', *J. Am. Chem. Soc.* **131** (2009) 17736–17737. DOI: 10.1021/ja9064415
134. E. Feigenbaum, K. Diest and H.A. Atwater, 'Unity-order index change in transparent conducting oxides at visible frequencies', *Nano Lett.* **10** (2010) 2111–2116. DOI: 10.1021/nl1006307
135. G.V. Naik, J. Kim and A. Boltasseva, 'Oxides and nitrides as alternative plasmonic materials in the optical range', *Opt. Mat. Express* **1** (2011) 1090–1099. DOI: 10.1364/OME.1.001090
136. P.C. Wu, M. Losurdo, T.-H. Kim, M. Giangregorio, G. Bruno, H.O. Everitt and A.S.Brown, 'Plasmonic gallium nanoparticles on polar semiconductors:

- interplay between nanoparticle wetting, localized surface plasmon dynamics, and interface charge', *Langmuir* **25** (2009) 924–930. DOI:10.1021/la802678y
137. M.B. Dühring, N.A. Mortensen and O. Sigmund, 'Plasmonic versus dielectric enhancement in thin-film solar cells', *Appl. Phys. Lett.* **100** (2012) 211914. DOI: 10.1063/1.4719203
 138. Y. Fu, *Subwavelength Optics: Theory and Technology* Bentham Science Publisher (2010).
 139. A. Otto, 'Excitation of nonradiative surface plasma waves by the method of frustrated reflection', *Z. Physik.* **216** (1968) 398–410.
 140. E. Kretschmann and H. Raether, 'Radiative decay of nonradiative surface plasmons excited by light', *Z. Naturforschung* **23A** (1968) 2135–2136.
 141. H. Arwin, M. Poksinski and K. Johansen, 'Total internal reflection ellipsometry: principles and applications', *Appl. Optics* **43**(15) (2004) 3028–3036. DOI: 10.1364/AO.43.003028
 142. O.S. Heavens, *Optical Properties of Thin Solid Films* London: Butterworth (1955).
 143. A. Krasilnikova Sytchkova, 'Measurement of optical constants of thin films by non conventional ellipsometry, photothermal deflection spectroscopy and plasmon resonance spectroscopy', in *Proceedings of SPIE 7101, Advances in Optical Thin Films III*, Eds. N.Kaiser, M.Lequime, H.A. Macleod, 7101–7129 (2008). DOI: 10.1117/12.797660
 144. D.M. Roessler, 'Kramers-Kronig analysis of reflection data', *Br. J. Appl. Phys. B* **16** (1965) 195104. DOI: 10.1088/0508–3443/16/8/310
 145. G. Mie, 'Beitrage zer Optik truber Meiden speziell kolloidaler Metallosungen [Contributions to the optics of turbid media, particularly of colloidal metal solutions]', *Ann. Phys.* **25** (1908) 377–445.
 146. N.V. Voshchinnikov and V.G. Faraonov, 'Optical properties of spheroidal particles', *Astrophys. Space Sci.* **204** (1993) 19–86. DOI: 10.1007/BF00658095
 147. W.H. Yang, G.C. Schatz and R.P. van Duyne, 'Discrete dipole approximation for calculating extinction and Raman intensities for small particles with arbitrary shapes', *J. Chem. Phys.* **103** (1995) 869–876. DOI: 10.1063/1.469787
 148. E. Moreno, D. Erni, C. Hafner and R. Vahldieck, 'Multiple multipole method with automatic multipole setting applied to the simulation of surface plasmons in metallic nanostructures', *J. Opt. Soc. A* **19** (2002) 101–111. DOI: 10.1364/JOSAA.19.000101
 149. A. Taflove, *Computational Electrodynamics: The Finite-difference Time-domain Method*. Boston: Artech House (1995), p. 509.
 150. E.M. Purcell and C.R. Pennypacker, 'Scattering and absorption of light by non-spherical dielectric grains', *Astrophys. J.* **186** (1973) 705–714.
 151. K.L. Kelly, T.R. Jensen, A.A. Lazarides and G.C. Schatz, 'Modeling metal nanoparticle optical properties', in *Metal Nanoparticles: Synthesis, Characterization and Applications*, Eds. D. Feldheim and C. Foss, New York: Marcell-Dekker (2002), p.89.
 152. P.K. Jain and M.A. El-Sayed, 'Plasmonic coupling in noble metal nanostructures', *Chem. Phys. Lett.* **487** (2010) 153–164. DOI: 10.1016/j.cplett.2010.01.062
 153. D.M. Natarov, V.O. Byelobrov, R. Sauleau, T.M. Benson and A.I. Nosich, 'Periodically-induced effects in the scattering and absorption of light by infinite and finite gratings of circular silver nanowires', *Opt. Express* **19** (2011) 22176–22190. DOI: 10.1364/OE.19.022176

154. C. van Vlack, P. Yao and S. Hughes, 'Optical forces between coupled plasmonic nano-particles near metal surfaces and negative index material waveguides', *Phys. Rev. B* **83** (2011) 245404. DOI:10.1103/PhysRevB.83.245404
155. L. Langguth and H. Giessen, 'Coupling strength of complex plasmonic structures in the multiple dipole approximation', *Opt. Express* **19** (2011) 22156–22166. DOI: 10.1364/OE.19.022156
156. B. Gallinet and O.J.F. Martin, 'The relation between near-field and far-field properties of plasmonic Fano resonances', *Opt. Express* **19** (2011) 22167–22175. DOI: 10.1364/OE.19.022167
157. R. Salas-Montiel, A. Apuzzo, C. Delacour, Z. Sedaghat, A. Bruyant, P. Grosse, A. Chelnokov and G. Lerondel, 'Quantitative analysis and near-field observation of strong coupling between plasmonic nanogap and silicon waveguides', *Appl. Phys. Lett.* **100** (2012) 231109. DOI: 10.1063/1.4725511
158. G.V. Hartland, 'Coherent vibrational motion in metal particles: Determination of the vibrational amplitude and excitation mechanism', *J. Chem. Phys.* **116** (2002) 8048. DOI: 10.1063/1.1469021
159. J.C. Hulteen and R.P. van Duyne, 'Nanosphere lithography: a materials general fabrication process for periodic particle array surfaces', *J. Vac. Sci. Technol. A* **13** (1995) 1553. DOI: 10.1116/1.579726
160. Z.L. Liu, V.M. Shalaev and A.V. Kildishev, 'Coupling effect in a near-field object-superlens system', *Appl. Phys. A* **107** (2012) 83–88. DOI: 10.1007/s00339-012-6780-2
161. M. Piliarik, P. Kvasnicka, N. Galler, J.R. Kren and J. Homola, 'Local refractive index sensitivity of plasmonic nanoparticles', *Opt. Express* **19** (2011) 9213–9220. DOI: 10.1364/OE.19.009213
162. J.C. Maxwell Garnett, 'Colours in metal glasses and metallic films', *Phil. Trans. R. Soc. Lond.* **203** (1904) 385–420.
163. D.A.G. Bruggeman, 'Calculation of various physical constants in heterogeneous substances. I. Dielectricity constants and conductivity of mixed bodies from isotropic substances', *Annalen der Physik* **24** (1935), 636–664.
164. J. Fu, B. Park and Y. Zhao, 'Nanorod-mediated surface resonance sensor based on effective medium theory', *Appl. Opt.* **48** (2009) 4637–4649. DOI: 10.1364/AO.48.004637
165. M.L. Protopapa, 'Surface plasmon resonance of metal nanoparticles sandwiched between dielectric layers: theoretical modelling', *Appl. Opt.* **48** (2009) 778–785. DOI: 10.1364/AO.48.000778
166. M.L. Protopapa, A. Rizzo, M. Re and L. Pilloni, 'Layered silvernanoparticles embedded in a BaF₂ matrix: optical characterization', *Appl. Opt.* **48** (2009) 6662–6669. DOI: 10.1364/AO.48.006662
167. J. Elser, V.A. Podolskiy, I. Salakhutdinov and I. Avrutsky, 'Nonlocal effects in effective-medium response of nanolayered metamaterials', *Appl. Phys. Lett.* **90** (2007) 191109. DOI: 10.1063/1.2737935
168. D.J. Bergman, 'Dielectric constant of a composite material – a problem in classical physics', *Phys. Rep.* **43** (1978) 377–407. DOI: 10.1016/0370-1573(78)90009-1
169. G.W. Milton, *The Theory of Composites*, Cambridge monographs on applied and computational mathematics, Cambridge: Cambridge University Press (2002).
170. N. Engheta and R.W. Ziolkowski, Eds., *Electromagnetic Metamaterials: Physics and Engineering Explorations*, New York: John Wiley and Sons (2006).

171. D.R. Smith, S. Schultz, P. Markos and C.M. Soukoulis, 'Determination of effective permittivity and permeability of metamaterials from reflection and transmission coefficients', *Phys. Rev. B* **65** (2002) 195104. DOI: 10.1103/PhysRevB.65.195104
172. D.R. Smith, D.C. Vier, T. Koschny and C.M. Soukoulis, 'Electromagnetic parameter retrieval from inhomogeneous metamaterials', *Phys. Rev. E* **71** (2005) 036617 DOI: 10.1103/PhysRevE.71.036617
173. X.D. Chen, T.M. Grzegorczyk, B.I. Wu, J. Pacheco and J.A. Kong, 'Robust method to retrieve the constitutive effective parameters of metamaterials', *Phys. Rev. E* **70** (2004) 016608. DOI: 10.1103/PhysRevE.70.016608
174. C.R. Simovski and S. He, 'Frequency range and explicit expressions for negative permittivity and permeability for an isotropic medium formed by a lattice of perfectly conducting Ω particles', *Phys. Lett. A* **311** (2003) 254. DOI: 10.1016/S0375-9601(03)00494-8
175. C. Fietz and G. Shvets, 'Current-driven metamaterial homogenization', *Physica B* **495** (2010) 2930. DOI: 10.1016/j.physb.2010.01.006
176. L. Landau and E. Lifschitz, *Electrodynamics of Continuous Media* Elsevier, Butterworth-Heinemann; Jordan Hill, Oxford (1984).
177. A. Alù, 'Restoring the physical meaning of metamaterial constitutive parameters', *Phys. Rev. B* **83** (2011) 081102(R). DOI: 10.1103/PhysRevB.83.081102
178. M.G. Silveirinha, D.J. Baena, L. Jelinek and R. Marques, 'Nonlocal homogenization of an array of cubic particles made of resonant rings', *Metamaterials* **3** (2009) 115. DOI: 10.1016/j.metmat.2009.08.004
179. V.M. Agranovich, Y.R. Shen, R.H. Baughman and A.A. Zakhidov, 'Linear and nonlinear wave propagation in negative refraction metamaterials', *Phys. Rev. B* **69** (2004) 165112. DOI: 10.1103/PhysRevB.69.165112
180. C.E. Kriegler, M.S. Rill, S. Linden and M. Wegener, 'Bianisotropic photonic metamaterials', *IEEE J. Sel. Top. Quant. Electron.* **16** (2010) 367. DOI: 10.1109/JSTQE.2009.2020809
181. M.D. Thoreson, J. Fang, A.V. Kildishev, L.J. Prokopeva, P. Nyga, U.K. Chettiar, V.M. Shalaev and V.P. Drachev, 'Fabrication and realistic modeling of three-dimensional metal-dielectric composites', *J. Nanophotonics* **5** (2011) 051513. DOI: 10.1117/1.3590208
182. A. Alù, 'First-principles homogenization theory for periodic metamaterials', *Phys. Rev. B* **84** (2011) 075153. DOI: 10.1103/PhysRevB.84.075153
183. R. Marques, F. Medina and R. Rafii-El-Idrissi, 'Role of bianisotropy in negative permeability and left-handed metamaterials', *Phys. Rev. B* **65** (2002) 144440. DOI: 10.1103/PhysRevB.65.144440
184. S. O'Brien and J.B. Pendry, 'Magnetic activity at infrared frequencies in structured metallic photonic crystals', *J. Phys. Condens. Mater.* **14** (2002) 6383. DOI: 10.1088/0953-8984/14/25/307
185. T. Koschny, P. Markos, D.R. Smith and C.M. Soukoulis, 'Resonant and anti-resonant frequency dependence of the effective parameters of metamaterials', *Phys. Rev. E* **68** (2003) 065602. DOI: 10.1103/PhysRevE.68.065602
186. C.R. Simovski, 'On electromagnetic characterization and homogenization of nanostructured metamaterials', *J. Opt.* **13** (2011) 013001. DOI: 10.1088/2040-8978/13/1/013001

187. X. Ni, S. Ishii, M.D. Thoreson, V.M. Shalaev, S. Han, S. Lee and A.V. Kildishev, 'Loss-compensated and active hyperbolic metamaterials', *Opt. Express* **19** (2011) 25242. DOI: 10.1364/OE.19.025242
188. X. Ni, Z. Liu, A. Boltasseva and A.V. Kildishev, 'The validation of the parallel three-dimensional solver for analysis of optical plasmonic bi-periodic multi-layer nanostructures', *Appl. Phys. A-Mater.* **100** (2010) 365–374. DOI 10.1007/s00339-010-5865-z
189. Shivanand, A. Ludwig and K.J. Webb, 'Impact of surface roughness on the effective dielectric constants and subwavelength image resolution of metal-insulator stack lenses', *Opt. Lett.* **37** (2012) 4317. DOI: 10.1364/OL.37.004317
190. T.A. Amotchkina, M.K. Trubetskoy, A.V. Tikhonravov, V. Janicki, J. Sancho-Parramon and H. Zorc, 'Comparison of two techniques for reliable characterization of thin metal-dielectric films', *Appl. Opt.* **50** (2011) 6189. DOI: 10.1364/AO.50.006189
191. J. Toudert, D. Babonneau, L. Simonot, S. Camelio and T. Girardeau, 'Quantitative modeling of surface plasmon resonances of metal nano-clusters sandwiched between dielectric layers: the influence of nano-cluster size, shape and organization', *Nanotechnol.* **19** (2008) 125709. DOI:10.1088/0957-4484/19/12/125709
192. T. Yamaguchi, S. Yoshida and A. Kinbara, 'Anomalous optical absorption of aggregated silver films', *Thin Solid Films* **18** (1973) 63–70. DOI: 10.1016/0040-6090(73)90221-6
193. M.T. Haarmans and D. Bedeaux, 'The polarizability and the optical properties of lattices and random distributions of small metal spheres on a substrate', *Thin Solid Films* **224** (1993) 117–131. DOI: 10.1016/0040-6090(93)90468-5
194. D.Bedeaux and J.Vlieger, 'A phenomenological theory of the dielectric properties of thin films', *Physica* **67** (1973) 55–73. DOI: 10.1016/0031-8914(73)90022-0
195. M. Schubert, 'Infrared ellipsometry on semiconductor layer structures', *STMP* 209, Berlin, Heidelberg: Springer-Verlag, (2004), pp. 45–65.
196. S. Thongrattanarisi, I. Silveiro and F.J. Garcia de Abajo, 'Plasmons in electrostatically doped graphene', *Appl. Phys. Lett.* **100** (2012) 201105. DOI: 10.1063/1.4714688
197. G. Naik and A. Boltasseva, 'Ceramic plasmonic components for optical metamaterials', *Quantum Electronics and Laser Science Conference*, Optical Society of America (2011).
198. G. Zhu, L.Gu, J.Kitur, A. Urbas, J. Vella and M. Noginov, 'Organic materials with negative and controllable electric permittivity', *Quantum Electronics and Laser Science Conference*, Optical Society of America (2011).
199. P.Tassin, T. Koschny, M. Kafesaki and C.M. Soukoulis, 'A comparison of grapheme, superconductors and metals as conductors for metamaterials and plasmonics', *Nat. Photonics* **6** (2012) 259–264. DOI: 10.1038/nphoton.2012.27
200. P.Fan, U.K. Chettiar, L.Cao, F.Afshinmanesh, N. Engheta and M.L. Brongersma, 'An invisible metal-semiconductor photodetector', *Nat. Photonics* **6** (2012) 380–385. DOI: 10.1038/nphoton.2012.108
201. I.V. Shadrivov, A.A. Zharov and Y.S. Kivshar, 'Second-harmonic generation in non-linear left-handed materials', *J. Opt. Soc. Am. B* **23** (2006) 529–534. DOI: 10.1364/JOSAB.23.000529

202. A.B. Kozyrev, H. Kim and D.W. van der Weide, 'Parametric amplification in left-handed transmission line media', *Appl. Phys. Lett.* **88** (2006) 264101. DOI: 10.1063/1.2214136
203. A.K. Popov and V.M. Shalaev, 'Compensating losses in negative-index metamaterials by optical parametric amplification', *Opt. Lett.* **31** (2006) 2169. DOI: 10.1364/OL.31.002169
204. S. Sun, Q. He, S. Xiao, Q. Xu, X. Li and L. Zhou, 'A gradient-index meta-surface as a bridge linking propagating waves and surface waves', *Nat. Mater.* **11** (2012) 426–431. DOI: 10.1038/NMAT3292
205. R. Nandkishore, M.A. Metlitski and T. Senthil, 'Orthogonal metals: the simplest non-Fermi liquids', *Phys. Rev. B* **86** (2012) 045128. DOI:10.1103/PhysRevB.86.045128
206. A.J. Schofield, 'Non-fermi liquids', *Contemp. Phys.* **40** (1999) 95–115. DOI:10.1080/001075199181602

6

Scattering properties of random structures in thin films

G. BERGINC, Thales, France and
A. A. MARADUDIN, University of California, Irvine, USA

DOI: 10.1533/9780857097316.2.177

Abstract: The scattering of electromagnetic waves from films with randomly rough surfaces and/or volume disorder is discussed in this chapter. One or both of the surfaces of the film are rough. The surface roughness considered is either one-dimensional or two-dimensional, while the volume disorder is three-dimensional. Advances in computational approaches to the solution of these scattering problems, with an emphasis on multiple-scattering phenomena are described, and results obtained by these approaches are presented. Examples of applications of the results of calculations of scattering from rough surfaces of, and volume disorder in, films are presented with a focus on remote sensing.

Key words: random roughness of film surfaces, volume disorder in films, computational methods in scattering from random films, multiple scattering, reduced Rayleigh equations, small-slope approximation.

6.1 Introduction

The main objective of this chapter is to outline the scattering properties of random structures and to introduce the reader to the phenomena associated with multiple scattering. We consider rough surfaces, random films and random media with rough boundaries. Our second aim is to bring the advances of scattering modeling from random structures as close as possible to the non-traditional phenomena of scattering properties for polarized electromagnetic waves. Following the fabrication of random structures, their optical scattering properties must be determined. This review will now shift from characterization techniques and coating design to computational and theoretical modeling. Theoretically, the classical optical behavior of a random structure is governed by Maxwell's equations. This chapter outlines improvements in analytic and numerical solutions of Maxwell's equations for random structure scattering and observations of interesting new phenomena. This chapter consists of eight sections. Following the Introduction,

Section 6.2 is devoted to numerical solutions of reduced Rayleigh equations for the scattering of light from dielectric films with one-dimensional rough surfaces. We present solutions for a layered two-dimensional system with one randomly rough surface. The solution is based on a numerical approach to the solution of the reduced Rayleigh equations. With the method of reduced Rayleigh equations, we can eliminate the field within the scattering medium and simplify the theoretical studies of the light scattering from a structure with rough boundaries. With this new development, satellite peaks that appear on both sides of the well-known enhanced backscattering peak can be investigated with precision for strongly rough surfaces where the small-perturbation method is inapplicable. In Section 6.3, we consider a two-dimensional system with two one-dimensional randomly rough surfaces. This challenging and relatively unexplored problem is solved, and multiple-scattering effects such as enhanced backscattering, enhanced transmission and the existence of satellite peaks are analyzed. In Section 6.4, we present a rigorous calculation of the electromagnetic field scattered from a two-dimensional randomly rough surface. Numerical calculations of the scattering of light from this kind of surface have been carried out by a variety of approaches, but such calculations remain time-consuming and need improvements. A new approach to the calculation of the light is described in this section. It is based on a purely numerical solution of the reduced Rayleigh equations. The complex problem of the scattering of light from a dielectric film with a two-dimensional randomly rough surface deposited on a planar metal substrate is treated in Section 6.5. In this section we consider a three-dimensional system. Until now this system has been solved only by analytic methods. We describe a non-perturbative, purely numerical solution of the reduced Rayleigh equation for the case where the dielectric film has a two-dimensional randomly rough surface and a planar interface with a metallic substrate. Analysis of satellite peaks can be performed. Section 6.6 deals with analytical methods for the scattering of light from a three-dimensional film with randomly rough interfaces. In this section, we introduce the small-slope approximation and the small perturbation method for a two-dimensional randomly rough surface. We present the most advanced form of the small-perturbation method where the amplitudes of the scattered field are expanded in powers of the surface profile function through terms of third order. The *small-slope approximation* (SSA) is a new formulation that makes a bridge between the well-known Kirchhoff approximation and the *small-perturbation method* (SPM). We give the complete expressions for the scattering matrices and the cross-sections for the different polarization states by introducing the Mueller matrices. In this section, we consider a generalization of the small-slope approximation to a three-dimensional layer bounded by two randomly rough surfaces which is an unexplored problem. We introduce the development of the SSA series with the third-order SPM

kernel. The new terms introduced in the SSA development describe the coupling between the two rough surfaces. With this new formulation, it is now possible to study theoretically the scattering of light from three-dimensional films with rough boundaries for a large spectrum of roughness. In Section 6.7, we make the three-dimensional problem more complex by considering discrete scatterers in the dielectric film. This section is devoted to a theory of transport. In this section, we introduce a new formulation based on a unified Bethe-Salpeter equation which enables obtaining a general expression for the scattered field whatever the choice of the scattering operators used at the randomly rough boundaries. We present a multiple-scattering theory for a random slab bounded by randomly rough surfaces, and we explore the relationships between the different parameters of the random medium and the rough surfaces and the polarized scattered intensity. This section is perhaps the most mathematical one of the chapter, since it contains the derivation and the demonstration of the perturbative solution of the Bethe-Salpeter equation for the polarized scattering from a random slab with a randomly rough surface. This section also treats the coherence effects of multiple scattering and the coupling between the random medium and the rough interfaces. We can observe the effect of backscattering enhancement brought about by the discrete scatterers. The final section contains concluding remarks.

We hope that the topics covered in this chapter will give an overview of new methods in scattering modeling and unconventional features of light behavior in random structures.

6.2 Numerical solution of reduced Rayleigh equations for scattering of light from dielectric films with one-dimensional rough surfaces

In several papers the scattering of light from a layered system, one of whose interfaces is a one-dimensional randomly rough interface, has been studied theoretically. It was found in these studies that if the system supports at least two (and not many more) guided waves at the frequency of the incident light, features can be present in the angular dependence of the intensity of the light scattered incoherently (diffusely) in addition to the well-known enhanced backscattering peak,^{1,2} which appears in the retroreflection direction. These features are peaks on both sides of the enhanced backscattering peak, and have come to be called satellite peaks. They are the result of the coherent interference of multiple-scattered guided waves with the frequency of the incident light, but with different wavenumbers, that are excited by the incident light through the roughness of the single rough interface.^{3–6} These theoretical studies were carried out for the scattering of p- and s-polarized light from a dielectric film with a one-dimensional randomly rough surface, deposited on the planar surface of a perfect conductor.^{3–6}

Similar effects were found in the angular dependence of the intensity of light transmitted through a multilayer system. The scattering of p-polarized light from, and its transmission through, a thin metal film whose illuminated surface was a one-dimensional randomly rough surface, while its back surface was planar, also displayed satellite peaks^{7,8} in addition to the enhanced transmission peak in the antispecular direction.⁹

The results of these investigations showed that if the scattering system supports N surface or guided waves, where $N \geq 2$, whose wavenumbers at the frequency ω of the incident light are $q_1(\omega)$, $q_2(\omega)$, ..., $q_N(\omega)$, satellite peaks should be seen in the contribution to the mean differential reflection or transmission coefficient from the light scattered incoherently at angles of scattering θ_s or transmission θ_t , given by^{3,4,8}

$$\sin \theta_{s,t}^{(n,m)} = -\sin \theta_0 \pm \frac{c}{\omega} [q_n(\omega) - q_m(\omega)] \quad (n \neq m), \quad [6.1]$$

where θ_0 is the angle of incidence, c is the speed of light in vacuum, and n and m are integers that label the surface or guided waves, and take the values 1, 2, ..., N . The maximum number N , of satellite peaks that can be present is twice the number of combinations of N objects taken two at a time, namely $N_s = 2N!/[(N-2)!2!]$. However, some of the possible combinations may not give rise to a satellite peak. This happens when the absolute value of the right-hand side of Equation [6.1] is greater than unity. Then the corresponding peak lies in the nonradiative region of the optical spectrum. Moreover, among the real satellite peaks that should appear in the radiative region, not all may be intense enough to be observable.

The methods used in these studies of satellite peaks ranged from small-amplitude perturbation theory^{4,6-8} through many-body perturbation theory,^{3,4,8} the stochastic functional approach,⁵ to computer simulations.^{4,7,8} The small amplitude perturbation calculations carried out in References [4,6-8] yielded solutions of the reduced Rayleigh equation for the scattering or transmission problem being studied. In this approach the electromagnetic field inside the dielectric or metallic film is eliminated from the calculations, so that only a single one-dimensional integral equation for the scattering or transmission amplitude needs to be solved. It is this equation that is solved by small-amplitude perturbation theory.

For scattering from weakly rough surfaces small-amplitude perturbation theory yields good results, but it is inapplicable to scattering from strongly rough surfaces. For such surfaces computer simulation calculations need to be used, but they yield poor results for weakly rough surfaces. Thus there is an intermediate range of surface roughness where a different calculational approach is needed. A nonperturbative, purely numerical, solution

of the reduced Rayleigh equations is one such approach.^{10,11} The numerical approaches to the solution of the reduced Rayleigh equations in References [10] and [11] were different, and may be of interest in themselves. We describe them in this section, and present some results obtained by their use.

6.2.1 A film with a one-dimensional randomly rough vacuum-dielectric interface deposited on the planar surface of a perfect conductor

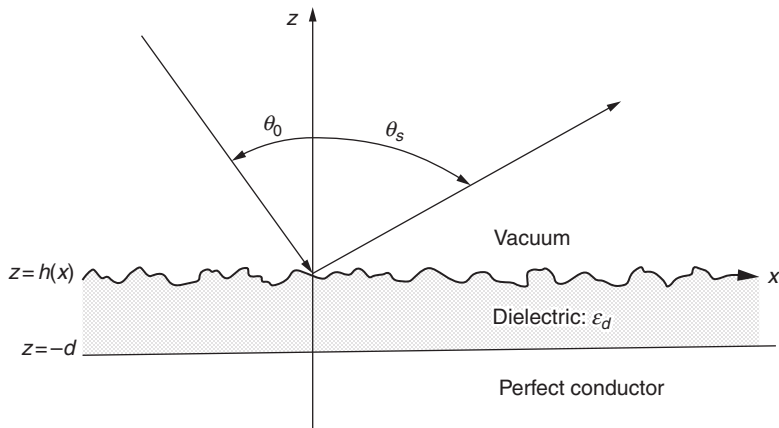
In the first case we consider, the physical system consists of a vacuum in the region $z > h(x)$, a dielectric film whose dielectric constant is ϵ_d in the region $-d < z < h(x)$, and a perfect conductor in the region $z < -d$ (Fig. 6.1). The surface profile function $h(x)$ is assumed to be a single-valued function of x that is differentiable with respect to x , and constitutes a zero-mean, stationary, Gaussian random process defined by

$$\langle h(x)h(x') \rangle = \sigma^2 w(|x-x'|). \quad [6.2]$$

The angle brackets here denote an average over an ensemble of realizations of the surface profile function, while $\sigma = \langle h^2(x) \rangle^{1/2}$ is the rms height of the surface.

In what follows we will also need the power spectrum of the surface roughness $g(|k|)$, which is given by the Fourier transform of the surface height autocorrelation function $w(|x|)$:

$$g(|k|) = \int_{-\infty}^{\infty} dx w(|x|) \exp(-ikx). \quad [6.3]$$



6.1 The scattering system studied in Section 6.2.1.

Realizations of the random surface profile are generated by the use of a filtering method based on the power spectrum.¹²

This structure is illuminated from the region $z > h(x)$ by a p- or s-polarized plane wave of frequency ω , whose plane of incidence is the xz plane. There is no cross-polarized scattering in this geometry. The electromagnetic fields in this structure are given by

$$\mathbf{H}(\mathbf{r}; t) = (0, \Phi_p(x, z | \omega), 0) \exp(-i\omega t) \quad [6.4a]$$

in p-polarization, and

$$\mathbf{E}(\mathbf{r}; t) = (0, \Phi_s(x, z | \omega), 0) \exp(-i\omega t) \quad [6.4b]$$

in s-polarization, where $\mathbf{r} = (x, y, z)$. In the region $z > h(x)$ the field amplitude $\Phi_v(x, z | \omega)$ ($v = p, s$) is the sum of an incident field and a Rayleigh expansion of the scattered field,

$$\begin{aligned} \Phi_v(x, z | \omega) = & \exp[ikx - i\alpha_0(k, \omega)z] \\ & + \int_{-\infty}^{\infty} \frac{dq}{2\pi} R_v(q | k) \exp[iqx + i\alpha_0(q, \omega)]z \end{aligned} \quad [6.5]$$

where $\alpha_0(q, \omega) = [(\omega/c)^2 - q^2]^{\frac{1}{2}}$, with $\text{Re}\alpha_0(q, \omega) > 0$, $\text{Im}\alpha_0(q, \omega) > 0$. The angles of incidence θ_0 and scattering θ_s are measured counterclockwise and clockwise from the positive z axis, respectively, and are related to the wave-numbers k and q by

$$k = \left(\frac{\omega}{c} \right) \sin \theta_0, \quad q = \left(\frac{\omega}{c} \right) \sin \theta_s. \quad [6.6]$$

The scattering amplitude $R_v(q | k)$ is the solution of the reduced Rayleigh equation^{4,6}

$$\int_{-\infty}^{\infty} \frac{dq}{2\pi} M_v^{(+)}(p | q) R_v(q | k) = -M_v^{(-)}(p | k), \quad [6.7]$$

where

$$\begin{aligned} M_v^{(\pm)}(p | q) = & e^{i\alpha(p, \omega)d} \frac{[pq \mp \alpha(p, \omega)\alpha_0(q, \omega)]^{\mu}}{\alpha(p, \omega) \pm \alpha_0(q, \omega)} I(\alpha(p, \omega) \pm \alpha_0(q, \omega) | p - q) \\ & - e^{-i\alpha(p, \omega)d} \frac{[-pq \pm \alpha(p, \omega)\alpha_0(q, \omega)]^{\mu}}{-\alpha(p, \omega) \pm \alpha_0(q, \omega)} I(-\alpha(p, \omega) \pm \alpha_0(q, \omega) | p - q) \end{aligned} \quad [6.8]$$

and

$$I(\gamma | Q) = \int_{-\infty}^{\infty} dx \exp(-iQx) \exp[i\gamma h(x)]. \quad [6.9]$$

The function $\alpha(q, \omega)$ in Equation [6.8] is defined by $\alpha(q, \omega) = [\epsilon_d(\omega/c)^2 - q^2]^{\frac{1}{2}}$, with $\text{Re}\alpha(q, \omega) > 0$, $\text{Im}\alpha(q, \omega) > 0$. The exponent μ is unity in the case of p-polarization, and zero in the case of s-polarization.

To solve Equation [6.6], in Reference [10] a random surface profile function $h(x)$ was first generated numerically by a standard method¹² for x in the interval $-L/2 < x < L/2$. This segment was then replicated periodically to cover the entire x axis. The resulting surface is that of a classical grating with a period L , with a complicated profile within each period. The function $I(\gamma | Q)$ defined by Equation [6.9] now becomes

$$I(\gamma | Q) = \sum_{s=-\infty}^{\infty} 2\pi\delta(Q - (2\pi s/L)) I_s(\gamma), \quad [6.10]$$

where

$$I_s(\gamma) = \frac{1}{L} \int_{-L/2}^{L/2} dx \exp\left(-i\frac{2\pi s}{L}x\right) \exp[i\gamma h(x)]. \quad [6.11]$$

In order that the Floquet-Bloch theorem be satisfied, the scattering amplitude $R_v(q|k)$ must be expressed in the form

$$R_v(q | k) = \sum_{s=-\infty}^{\infty} 2\pi\delta(q - k - (2\pi s/L)) R_s^{(v)}, \quad [6.12]$$

where $R_s^{(v)}$ is the amplitude of the s th Bragg beam in the diffracted field. On substituting Equations [6.10] and [6.12] into Equation [6.7] we obtain the equation satisfied by the $\{R_s^{(v)}\}$,

$$\sum_{n=-\infty}^{\infty} m_{v,m-n}^{(+)}(k_m | k_n) R_n^{(v)} = m_{v,m}^{(-)}(k_m | k_0), \quad m = 0, \pm 1, \pm 2, \dots \quad [6.13]$$

where we have introduced the notation $k_m = k + (2\pi m/L)$, and

$$\begin{aligned} m_{v,s}^{(\pm)}(p | q) &= e^{i\alpha(p,\omega)d} \frac{[pq \mp \alpha(p,\omega)\alpha_0(q,\omega)]^\mu}{\alpha(p,\omega) \pm \alpha_0(q,\omega)} I_s(\alpha(p,\omega) \pm \alpha_0(q,\omega)) \\ &\quad - e^{-ia(p,\omega)d} \frac{[-pq \mp \alpha(p,\omega)\alpha_0(q,\omega)]^\mu}{-\alpha(p,\omega) \pm \alpha_0(q,\omega)} I_s(-\alpha(p,\omega) \pm \alpha_0(q,\omega)). \end{aligned} \quad [6.14]$$

In the solution of the system of Equations [6.13] the indices m and n are restricted to take the values $0, \pm 1, \pm 2, \dots, \pm N$, to produce a finite order matrix equation for the amplitudes of a finite number of Bragg beams, both propagating and evanescent. The propagating beams are those for which $\alpha_0(k_s, \omega)$ is real.

The Fourier coefficient $I_s(\gamma)$ is calculated by writing it as

$$\begin{aligned} I_s(\gamma) &= \delta_{s,0} + \frac{1}{L} \int_{-L/2}^{L/2} dx e^{-i\frac{2\pi s}{L}x} (e^{i\gamma h(x)} - 1) \\ &\equiv \delta_{s,0} + \frac{1}{L} \sum_{n=1}^N \frac{(i\gamma)^n}{n!} \int_{-L/2}^{L/2} dx e^{-i\frac{2\pi s}{L}x} h^n(x) \\ &\equiv \delta_{s,0} + \sum_{n=1}^N \frac{(i\gamma)^n}{n!} A_{sn}, \end{aligned} \quad [6.15]$$

where

$$\begin{aligned} A_{sn} &= \frac{1}{L} \int_{-L/2}^{L/2} dx e^{-i\frac{2\pi s}{L}x} h^n(x) \\ &\equiv \frac{(-1)^s}{l'} \sum_{l=0}^{l'-1} e^{-i(2\pi sl/l')} h^n(x_l). \end{aligned} \quad [6.16]$$

Here $x_l = -L/2 + l\Delta x$ with $\Delta x = L/l'$. In the calculations carried out in Reference [10] the value of l' used was $l' = 8000$. For values of the rms height of the roughness up to $\sigma = 60$ nm, retaining 18 terms in the expansion Equation [6.15] was sufficient to obtain convergent results.

The differential reflection coefficient, that is, the fraction of the total time-averaged flux incident on the surface that is scattered into the angular interval $\Delta_\theta = \theta_{s+1} - \theta_s \equiv \lambda / (L \cos \theta_s)$ about the direction of the s th diffraction beam is¹⁰

$$\frac{\partial R_v}{\partial \theta_s} = \frac{L}{\lambda} \frac{\cos^2 \theta_s}{\cos \theta_0} |R_s^{(v)}|^2, \quad [6.17]$$

where $\lambda = 2\pi c/\omega$ is the wavelength of the incident light. We see that if $L \cos \theta_s/\lambda$ is sufficiently large, the scattering angles θ_s can be regarded as being essentially continuously distributed. As we are dealing with scattering from a random surface, it is the average of the mean differential reflection coefficient over the ensemble of realizations of the surface profile that we need to calculate. To study nonspecular effects it is the contribution to the mean differential reflection coefficient from the light that has been scattered incoherently (diffusely) that is of interest. It is given by¹⁰

$$\left\langle \frac{\partial R_v}{\partial \theta_s} \right\rangle_{\text{incoh}} = \frac{L}{\lambda} \frac{\cos^2 \theta_s}{\cos \theta_0} [\langle |R_s^{(v)}|^2 \rangle - |\langle R_s^{(v)} \rangle|^2]. \quad [6.18]$$

Only propagating beams contribute to this function.

The surface profile function $h(x)$ was generated on the basis of the power spectrum devised by West and O'Donnell¹³ for use in fabricating the weakly rough random surface used in their studies of the enhanced backscattering of p- and s-polarized light from vacuum-metal interfaces by the surface plasmon polariton mechanism.¹ This power spectrum is

$$g(|k|) = \frac{\pi}{k_+ - k_-} [\theta(k - k_-)\theta(k_+ - k) + \theta(-k_- - k)\theta(k + k_+)], \quad [6.19]$$

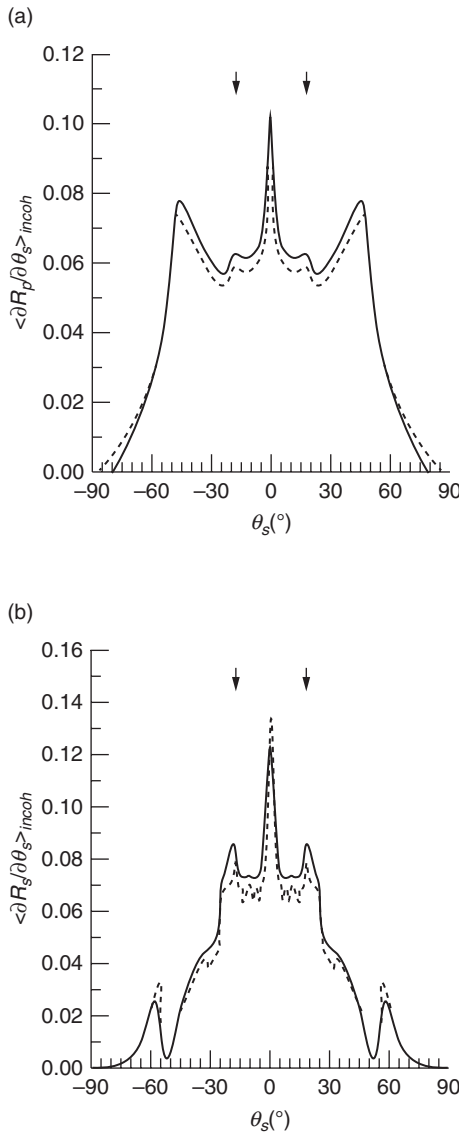
where $\theta(x)$ is the Heaviside unit step function, and

$$k_{\pm} = k_{sp}(\omega) \pm \frac{\omega}{c} \sin \theta_{\max}. \quad [6.20]$$

Here $\pm k_{sp}(\omega)$ are the wavenumbers of the forward and backward propagating surface plasmon polaritons at a planar vacuum-metal interface whose frequency is that of the incident field. The significance of the angle θ_{\max} is that if the angle of incidence θ_0 is in the interval $(-\theta_{\max}, \theta_{\max})$, the incident light can excite both the forward and backward propagating surface plasmon polaritons through the surface roughness. Similarly, if the scattering angle θ_s is in the interval $(-\theta_{\max}, \theta_{\max})$, the excited surface plasmon polaritons will be converted into scattered volume waves in the vacuum region above the surface. Moreover, with this power spectrum, when angles of incidence and scattering satisfy $|q - k| < k_-$, single-scattering processes will not contribute to $\langle \partial R_v / \partial \theta_s \rangle_{\text{incoh}}$.¹⁰

The power spectrum Equation [6.19] was used in the present calculations with values of k_- and k_+ chosen in such a way as to enhance the excitation of selected guided waves supported by the scattering structure.

In Fig. 6.2 we present results of calculations carried out in the manner described. The wavelength of the incident light is $\lambda = 632.8$ nm. The period of the rough surface is $L = 160.1\lambda = 101343.3$ nm. The number of Bragg beams kept in the solution of the matrix Equation [6.13] was 801; the number of propagating Bragg beams was 321. The plots were obtained by averaging results from $N_p = 2000$ realizations of the surface profile function. Even with the large number of surface profiles the results obtained (the broken curve in each figure) are noisy. Consequently, they were convolved



6.2 The contribution to the mean differential reflection coefficient from the incoherent component of the scattered light when a plane wave is incident normally from vacuum on the one-dimensional randomly rough surface of a dielectric film deposited on the planar surface of a perfect conductor. (a) p-polarization; (b) s-polarization.¹⁰

with a Gaussian function of 1° width, and the results are plotted as continuous curves in each figure.

In Fig. 6.2a $\langle \partial R_p / \partial \theta_s \rangle_{\text{incoh}}$ is plotted as a function of θ_s when p-polarized light is incident normally ($\theta_0 = 0^\circ$) on the scattering structure. The mean thickness of the dielectric film $d = 380$ nm, and its dielectric constant $\epsilon_d = 5.6644 + i0.1$. In the absence of roughness and absorption this scattering structure supports three guided waves whose wavenumbers are $q_1(\omega) = 2.34(\omega/c)$, $q_2(\omega) = 2.04(\omega/c)$ and $q_3 = 1.32(\omega/c)$. The maximum number of satellite peaks possible is therefore six. From Equation [6.1] it follows that they should occur at scattering angles $\theta_s^{(1,2)} = \pm 17.46^\circ$ and $\theta_s^{(2,3)} = \pm 46.05^\circ$, while $\theta_s^{(1,3)}$ is in the nonradiative region.

In obtaining the result plotted in Fig. 6.2a it was assumed that the rms height of the roughness is $\sigma = 30$ nm, and the values of k_- and k_+ are $k_- = 1.61(\omega/c)$ and $k_+ = 2.76(\omega/c)$. With these choices for k_- and k_+ the incident light can directly excite only the guided waves with wavenumbers $q_1(\omega)$ and $q_2(\omega)$. Thus, only the satellite peaks at the scattering angles $\theta_s^{(1,2)} = \pm 17.46^\circ$ should be present in $\langle \partial R_p / \partial \theta_s \rangle_{\text{incoh}}$. Satellite peaks at both of these angles are seen in both the raw and smoothed data in Fig. 6.2a. There is no contribution from single-scattering processes to the result plotted in this figure. The height of the enhanced backscattering peak (at $\theta_s = 0^\circ$) is therefore nearly twice the height of the background at its position, as is expected.¹⁴

In Fig. 6.2b we present a plot of $\langle \partial R_s / \partial \theta_s \rangle_{\text{incoh}}$ as a function of θ_s when s-polarized light is incident normally on the scattering structure. The mean thickness of the dielectric film is now $d = 500$ nm. The dielectric constant of the film is $\epsilon_d = 2.689 + i0.01$. The rms height of the surface is again 30 nm, and the values of k_- and k_+ are $k_- = 0.82(\omega/c)$ and $k_+ = 1.97(\omega/c)$. This structure supports two guided waves whose wavenumbers are $q_1(\omega) = 1.5466(\omega/c)$ and $q_2(\omega) = 1.2423(\omega/c)$,⁴ in the absence of roughness and absorption. Thus this power spectrum is nonzero in a range of wavenumbers that contains both $q_1(\omega)$ and $q_2(\omega)$. According to Equation [6.1] satellite peaks should be present in the result plotted in Fig. 6.2b at scattering angles $\theta_s^{(1,2)} = \pm 17.7^\circ$. Both of these peaks are present in the result presented in this figure, together with a very prominent enhanced backscattering peak. Single-scattering processes do not contribute to $\langle \partial R_s / \partial \theta_s \rangle_{\text{incoh}}$ for scattering angles $|\theta_s| < 55.1^\circ$. Therefore, the three peaks present in these results are due to multiple-scattering processes.

It should be noted that the satellite peaks present in the mean differential reflection coefficient for s-polarized incident light are stronger and more sharply defined than those in the mean differential reflection coefficient for p-polarized incident light. This may make satellite peaks easier to observe experimentally in s-polarization than in p-polarization.

6.2.2 A film with a planar vacuum-dielectric interface deposited on a one-dimensional randomly rough perfectly conducting surface

The second scattering structure we consider consists of a vacuum in the region $z > d$, a dielectric film whose dielectric constant is ϵ_d in the region $h(x) < z < d$, and a perfect conductor in the region $z < h(x)$ (Fig. 6.3). The surface profile function $h(x)$ possesses the properties described in Section 6.2.1.

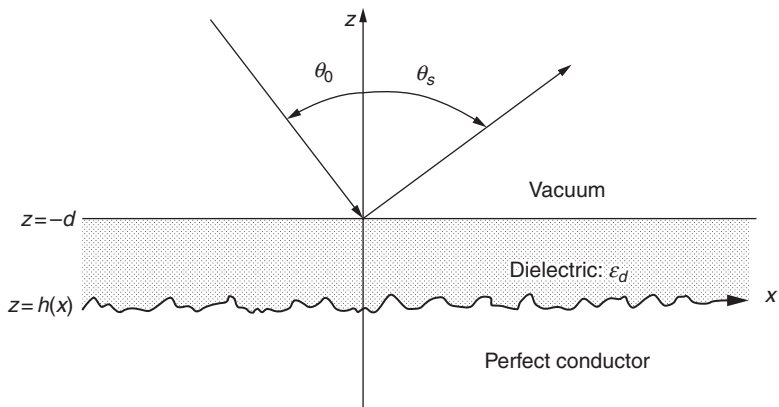
This structure is illuminated from the region $z > d$ by a p- or s-polarized plane wave of frequency ω , whose plane of incidence is the xz plane. The electromagnetic fields in this structure are given by Equation [6.4], and the field amplitude $\Phi_v(x, z|\omega)$ ($v = p, s$) entering them in the region $z > d$ is given by Equation [6.5].

The scattering amplitude $R_v(q|k)$ is the solution of the reduced Rayleigh equation¹¹

$$\int_{-\infty}^{\infty} \frac{dq}{2\pi} M_v^{(+)}(p|q) R_v(q|k) = M_v^{(-)}(p|k), \quad [6.21]$$

where for p-polarization

$$\begin{aligned} M_p^{(\pm)}(p|q) = & \pm e^{\pm i\alpha_0(q,\omega)d} \frac{\epsilon_d(\omega/c)^2 - pq}{\alpha(q,\omega)} \\ & \times [e^{-i\alpha(q,\omega)d} \frac{\alpha(q,\omega) \pm \epsilon_d \alpha_0(q,\omega)}{\alpha(q,\omega)} I(\alpha(q,\omega)|p-q) \\ & + e^{i\alpha(q,\omega)d} \frac{\alpha(q,\omega) \mp \epsilon_d \alpha_0(q,\omega)}{-\alpha(q,\omega)} I(-\alpha(q,\omega)|p-q)] \end{aligned} \quad [6.22a]$$



6.3 The scattering system studied in Section 6.2.2.

and for s-polarization

$$\begin{aligned} M_s^{(+)}(p|q) = & \pm e^{\pm i\alpha_0(q,\omega)d} [e^{-i\alpha(q,\omega)d} \frac{\alpha(q,\omega) \pm \alpha_0(q,\omega)}{\alpha(q,\omega)} I(\alpha(q,\omega)|p-q) \\ & - e^{i\alpha(q,\omega)d} \frac{\alpha(q,\omega) \mp \alpha_0(q,\omega)}{-\alpha(q,\omega)} I(-a(q,\omega)|p-q)]. \end{aligned} \quad [6.22b]$$

The contribution to the mean differential reflection coefficient from the light scattered incoherently from this structure is given in terms of the scattering amplitude $R_v(q|k)$ by

$$\left\langle \frac{\partial R_v}{\partial \theta_s} \right\rangle_{\text{incoh}} = \frac{1}{L} \left(\frac{\omega}{2\pi c} \right) \cos^2 \theta_s [\langle |R_v(q|k)|^2 \rangle - \langle \langle R_v(q|k) \rangle \rangle^2] \quad [6.23]$$

where L is now the length of the x axis covered by the rough surface. The angles of incidence and scattering, θ_0 and θ_s , respectively, are given in terms of the wavenumbers k and q by Equations [6.6].

Equation [6.21] was solved by replacing the infinite limits of integration by finite limits given by $q = \pm Q/2$, where $Q \gg (\omega/c)$. With a finite length of the x axis covered by the rough surface, $L \gg \lambda$, Equation [6.21] can now be discretized by a standard numerical quadrature scheme, and a system of linear equations is obtained:

$$\frac{h_q}{2\pi} \sum_{n=-N_q/2}^{N_q/2} w_n M_v^{(+)}(p_m|q_n) R_v(q_n|k) = M_v^{(-)}(p_m|k) \quad m = -\frac{N_q}{2}, \dots, \frac{N_q}{2}, \quad [6.24]$$

where $N_q + 1$ is the number of discretization points in q space, $h_q = Q/N_q$ is the corresponding discretization length, and $\{w_n\}$ are the weights in the quadrature scheme used. The abscissas $\{q_n\}$ are defined by

$$q_n = nh_q, \quad n = -\frac{N_q}{2}, \dots, \frac{N_q}{2}. \quad [6.25]$$

The quadrature scheme used in these calculations is an $O(h_q^4)$ method with $w_1 = w_N = 3/8$, $w_2 = w_{N-1} = 7/6$, $w_3 = w_{N-2} = 23/24$, and with all the other weights equal to unity.¹⁵

The function $I(\gamma|q)$ is now given by

$$I(\gamma|Q) = \int_{-L/2}^{L/2} dx \exp(-iqx) \exp[i\gamma h(x)]. \quad [6.26]$$

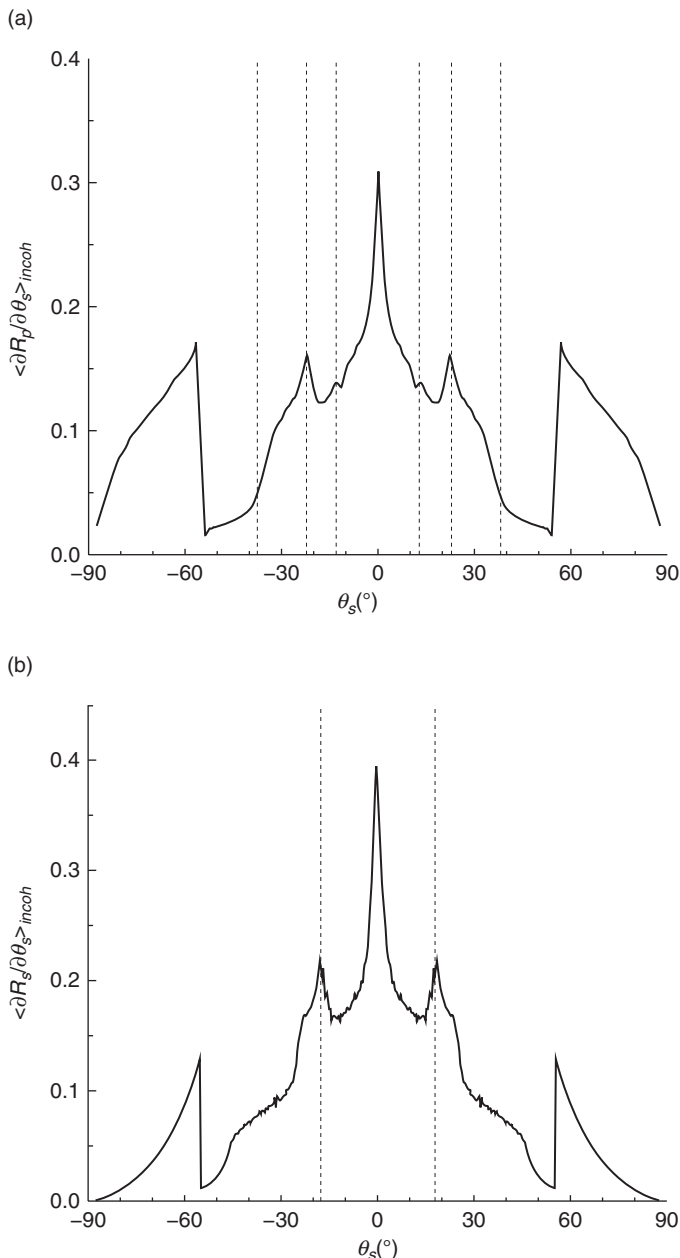
Since we have finite cutoffs of the q integration in Equation [6.21] at $|q| = Q/2$, it follows from Equations [6.21] and [6.22] that wavenumbers $p-q$ in the range $(-Q, Q)$ are needed in the calculation of this integral. Because this integral is evaluated by discretizing the x variable and using the (discrete) Fourier transform, the value of Q is controlled by the spatial discretization length h_x of the problem. To resolve wavenumbers up to Q one has from the Nyquist sampling theorem¹⁶ that the number of spatial discretization points has to satisfy $\pi/h_x \geq Q = h_q N_q$, where we have used Equation [6.24]. In principle the wavenumber discretization length h_q used in Equation [6.24] is independent of the one h'_q obtained from the Fourier transform. However, from a numerical point of view it is not very practical to choose different values for h_q and h'_q , and in the present calculations they were assumed to be the same, $h'_q = h_q$. The discretization lengths in coordinate and wave-number space are related by $h_q = 2\pi/Nh_x$, where N is the number of spatial discretization points. If the latter result is used in the inequality $\pi/h_x \geq Q = h_q N_q$, we find that $N \geq 2N_q$. In the present calculations the relation $N = 2N_q$ was assumed for convenience.

To evaluate the integral Equation [6.26] the integrand was expanded in powers of $h(x)$ and the resulting expression was integrated term-by-term. For a moderately rough surface this expansion converges quickly. The most attractive feature of this approach, however, is that for a given realization of the surface profile function $h(x)$ the Fourier transforms of $h^n(x)$ needed to calculate $I(\gamma q)$ have to be calculated once and for all, and do not have to be recalculated for each value of the variable γ , as would be the case if the expression Equation [6.26] were to be calculated directly as a Fourier transform.

The calculations were carried out for the scattering of p- and s-polarized light of wavelength $\lambda = 632.8$ nm from a dielectric film whose dielectric constant at this wavelength is $\epsilon_d = 2.6896 + i0.01$. The mean thickness of the film is $d = 500$ nm, and the rms height of the roughness is $\sigma = 30$ nm. The length of the x axis covered by the rough surface is $L = 160.1\lambda = 101343.3$ nm, the number of spatial discretization points was set to $N = 1604$, so that $N_q = 802$, and ten terms were kept in the expansion for $I(\gamma q)$.

The surface roughness was defined by the West-O'Donnell power spectrum, Equation [6.19], with $k_- = 0.82(\omega/c)$ and $k_+ = 1.97(\omega/c)$. With these values and normal incidence, single-scattering processes do not contribute to $\langle \partial R_p / \partial \theta_s \rangle_{\text{incoh}}$ for scattering angles satisfying $|\theta_s| < 55.1^\circ$. Results obtained for $N_p = 3000$ realizations of the surface profile function were averaged to obtain the contribution to the mean differential reflection coefficient from the light scattered incoherently.

In Fig. 6.4a we present a plot of $\langle \partial R_p / \partial \theta_s \rangle_{\text{incoh}}$ as a function of θ_s when p-polarized light is incident normally ($\theta_0 = 0^\circ$) on the scattering structure. In the absence of roughness and absorption this structure supports



6.4 The contribution to the mean differential reflection coefficient from the incoherent component of the scattered light when a plane wave is incident normally from vacuum on the planar surface of a dielectric film deposited on the one-dimensional randomly rough surface of a perfect conductor. (a) p-polarization; (b) s-polarization.¹¹

three guided waves,¹⁰ which according to their dispersion relation¹⁰ have the wavenumbers $q_1(\omega) = 1.6125(\omega/c)$, $q_2(\omega) = 1.3821(\omega/c)$ and $q_3 = 1.0029(\omega/c)$. Therefore, according to Equation [6.1] there are six possible satellite peaks, and for normal incidence they occur at scattering angles $\theta_s^{(1,2)} = \pm 13.3^\circ$, $\theta_s^{(2,3)} = \pm 22.3^\circ$ and $\theta_s^{(1,3)} = \pm 37.6^\circ$. These angles lie within the angular region within which no single-scattering processes can occur. Therefore if the corresponding peaks are present, they must be multiple-scattering effects. In addition to the well-defined enhanced backscattering peak in the retroreflection direction ($\theta_s = 0^\circ$), the satellite peaks at $\pm 22.3^\circ$ are well defined in Fig. 6.4a. The peaks at $\pm 18.3^\circ$ though weaker, are clearly seen in this figure. The peaks at $\pm 37.6^\circ$ are not visible at all. This may indicate that the coupling of the incident light to the guided mode with wavenumber $q_3(\omega)$ is very weak. This cannot be the complete reason for the absence of these peaks because the peaks at $\pm 22.3^\circ$ which also involve the guided wave with wavenumbers $q_3(\omega)$, are observed, and in fact have the strongest intensities. This result can be explained by noting that the mode $q_1(\omega)$ has the largest wavenumber of the three possible guided waves, and therefore is the one that is the most difficult for the incident wave to excite. Therefore we expect the peaks at $\pm 37.6^\circ$ to have a reduced amplitude compared to those at $\pm 22.3^\circ$. The result that the height of the enhanced backscattering peak (at $\theta_s = 0^\circ$) is twice the height of the background at its position is additional evidence that single-scattering processes have not contributed to it.¹⁴

Turning now to the case of s-polarized incident light, we present in Fig. 6.4b a plot of $\langle \partial R_s / \partial \theta_s \rangle_{\text{incoh}}$ as a function of θ_s when s-polarized light is incident normally on the scattering structure. In the absence of roughness and absorption this structure supports two guided waves with wavenumbers $q_1(\omega) = 1.5466(\omega/c)$ and $q_2(\omega) = 1.2423(\omega/c)$.⁴ According to Equation [6.1] the corresponding satellite peaks are expected to occur at $\theta_s = \pm 17.7^\circ$. These peaks are clearly seen in Fig. 6.4b. They fall within the angular region within which no single-scattering processes are allowed and hence are multiple-scattering effects.

6.3 Reduced Rayleigh equations for the scattering of p- and s-polarized light from, and its transmission through, a film with two one-dimensional rough surfaces

Theoretical and computational studies of the scattering of light from a rough surface are significantly simplified if the electromagnetic field within the scattering medium can be eliminated from consideration, so that only the field in the medium of incidence has to be calculated. The method of

reduced Rayleigh equations affects this elimination. This method was originally developed for the scattering of p- and s-polarized light from a medium bounded by a one-dimensional rough surface¹⁷ and from a medium bounded by a two-dimensional rough surface.¹⁸ In the former case a single one-dimensional integral equation for the scattering amplitude is obtained, instead of the pair of coupled one-dimensional integral equations for the scattering and transmission amplitudes produced by a straightforward application of the Rayleigh method to the scattering problem. In the latter case a 2×2 matrix two-dimensional integral equation is obtained for the amplitudes of the p- and s-polarized components of the scattered field, instead of the set of four coupled integral equations for the amplitudes of the p- and s-polarized components of the scattered and transmitted fields obtained by the application of the Rayleigh method to this scattering problem. The reduction of the number of integral equations that have to be solved in solving a scattering problem by the use of reduced Rayleigh equations is what gives the method its name. Reduced Rayleigh equations have also been derived for the amplitudes of the p- and s-polarized components of the field transmitted through a one-dimensional rough surface,¹⁷ or through a two-dimensional rough surface.¹⁹

Reduced Rayleigh equations have also been used in studies of the scattering of light from, and its transmission through, a film with a rough surface. Reduced Rayleigh equations have been derived for the scattering amplitude in the case of the scattering of p-polarized⁶ or s-polarized⁴ light from a dielectric film deposited on the planar surface of a perfect conductor, when the illuminated surface of the dielectric film is a one-dimensional rough surface. They have also been derived for the scattering amplitude when the illuminated surface of the dielectric film is planar, while the interface between the dielectric film and the perfect conductor is a one-dimensional rough interface.¹¹ Reduced Rayleigh equations have been derived for the scattering and transmission amplitudes for p-polarized light incident on a free-standing metal film whose illuminated surface is a one-dimensional rough surface, while its back surface is planar.⁸ Reduced Rayleigh equations have also been obtained for the scattering and transmission amplitudes for four-layer systems in which one of the three interfaces is a one-dimensional rough interface, while the other two interfaces are planar.²⁰

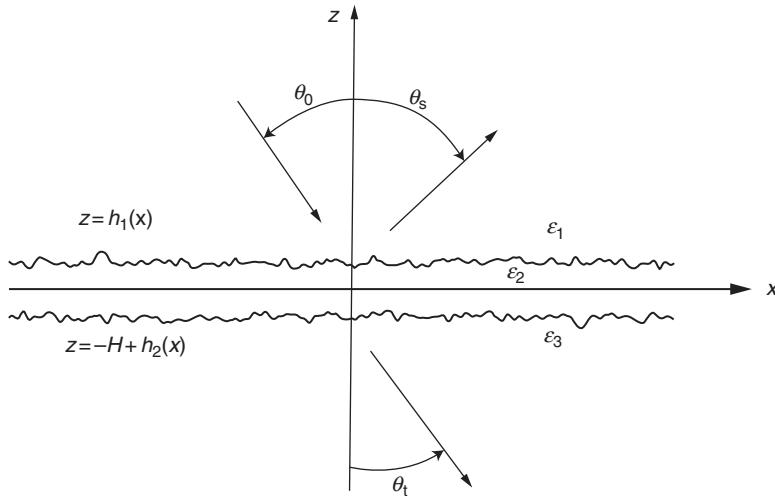
In the preceding examples of reduced Rayleigh equations for the scattering of light from, or its transmission through, a free-standing or supported film, all of the rough interfaces were one-dimensional. A 2×2 matrix reduced Rayleigh equation was derived for the amplitudes of the p- or s-polarized light scattered from, or transmitted through, a dielectric film, one of whose surfaces is a two-dimensional rough surface, while the other is planar.^{21,22}

In all the film systems cited above, for which reduced Rayleigh equations have been derived, only one of the interfaces was assumed to be rough, while the remaining surfaces or interfaces were assumed to be planar. The derivation of reduced Rayleigh equations for the amplitudes of light scattered from, or transmitted through, a film bounded by two rough surfaces is a relatively unexplored problem. Such a derivation has been carried out for the case of a dielectric film bounded by two two-dimensional rough surfaces.²³

Reduced Rayleigh equations for the amplitudes of p- and s-polarized light scattered from, or transmitted through, a film bounded by two one-dimensional rough surfaces have been obtained in two different forms. The first form consists of a pair of coupled one-dimensional integral equations for the scattering and transmission amplitudes.²⁴ This represents a reduction in the number of integral equations that have to be solved from the four that result from a straightforward application of the Rayleigh method to the solution of the scattering or transmission problem. The second form consists of a single two-dimensional integral equation for the scattering amplitude alone or for the transmission amplitude alone. This represents the maximum possible reduction in the number of integral equations that have to be solved. Such maximally reduced Rayleigh equations have been obtained for the case in which the illuminating light is s-polarized²⁵ and for the case in which it is p-polarized.²⁶ It is to a discussion of this form of reduced Rayleigh equations that this section is devoted.

The optical properties of films with two rough surfaces are of interest for several reasons. When both surfaces are periodically corrugated and anti-correlated ($h_2(x) = -h_1(x)$) they have been used in studies of the transmission of light through them that showed that the extraordinary transmission found for a metal film pierced by a parallel array of slits²⁷ can occur without the presence of complete slits.^{24,28,29} When both surfaces are randomly corrugated, multiple-scattering effects such as enhanced backscattering or the occurrence of satellite peaks, can be enhanced or diminished by changing the correlations between the surface profile functions on the two surfaces.^{25,26} The derivation of reduced Rayleigh equations for use in calculations of the scattering of light from, and its transmission through, films with these kinds of surface roughness has as its goal the simplification of such calculations.

The physical system we study in this section is depicted in Fig. 6.5. It consists of a dielectric characterized by a dielectric constant ϵ_2 in the region $z > h_1(x)$, a dielectric characterized by a dielectric constant ϵ_2 in the region $-H + h_2(x) < z < h_1(x)$, and a dielectric characterized by a dielectric constant ϵ_3 in the region $z < -H + h_2(x)$. One or more of these dielectric constants can be frequency dependent. The surface profile functions $h_1(x)$ and $h_2(x)$ are assumed to be single-valued functions of x that are differentiable. The surface $z = h_1(x)$ is illuminated from the region $z > h_1(x)$ by a p-polarized or by an s-polarized plane wave of frequency ω , whose plane of incidence is the xz



6.5 The scattering system studied in Section 6.3.

plane. There is no cross-polarized scattering in this geometry. We consider these two polarizations in turn.

6.3.1 p-Polarization

In the case of p-polarization it is convenient to work with the single nonzero component of the magnetic field in this structure. It is given in the region $z > h_1(x)_{max}$ by

$$H_2(x, z | \omega) = \exp[ikx - i\alpha_1(k)z] + \int_{-\infty}^{\infty} \frac{dq}{2\pi} R(q | k) \exp[iqx + i\alpha_1(q)z]; \quad [6.27]$$

in the region $-H + h_2(x) < z < h_1(x)$ by

$$H_2(x, z | \omega) = \int_{-\infty}^{\infty} \frac{dq}{2\pi} \exp(iqx) \{A_1(q | k) \exp[i\alpha_2(q)z] + A_2(q | k) \exp[-i\alpha_2(q)z]\}; \quad [6.28]$$

and in the region $z < -H + h_2(x)_{min}$ by

$$H_2(x, z | \omega) = \int_{-\infty}^{\infty} \frac{dq}{2\pi} T(q | k) \exp[iqx - i\alpha_3(q)z], \quad [6.29]$$

where

$$\alpha_i(q) = [\varepsilon_i(\omega/c)^2 - q^2]^{\frac{1}{2}}, \operatorname{Re}\alpha_i(q) > 0, \operatorname{Im}\alpha_i(q) > 0, \quad i = 1, 2, 3. \quad [6.30]$$

We have assumed a time dependence $\exp(-i\omega t)$ for the field, but have not indicated this explicitly.

The boundary conditions at the interface $z = h_1(x)$ require the continuity of $H_2(x, z|\omega)$ and $\varepsilon^{-1}\partial H_2(x, z|\omega)/\partial N_1$ across it, where ε is the dielectric constant of the region in which the field is being calculated, and $\partial/\partial N_1 = -h'_1(x)\partial/\partial x + \partial/\partial z$, where the prime denotes differentiation with respect to x . Their satisfaction yields the pair of equations

$$\begin{aligned} & \exp[ikx - i\alpha_1(k)h_1(x)] + \int_{-\infty}^{\infty} \frac{dq}{2\pi} R(q|k) \exp[iqx + i\alpha_1(q)h_1(x)] \\ &= \int_{-\infty}^{\infty} \frac{dq}{2\pi} \{A_1(q|k) \exp[iqx + i\alpha_2(q)h_1(x)] \\ & \quad + A_2(q|k) \exp[iqx - i\alpha_2(q)h_1(x)]\} \end{aligned} \quad [6.31]$$

and

$$\begin{aligned} & \frac{1}{\varepsilon_1} [-h'_1(x)k - \alpha_1(k)] \exp[ikx - i\alpha_1(k)h_1(x)] \\ &+ \frac{1}{\varepsilon_1} \int_{-\infty}^{\infty} \frac{dq}{2\pi} [-h'_1(x)q + \alpha_1(q)] R(q|k) \exp[iqx + i\alpha_1(q)h_1(x)] \\ &= \frac{1}{\varepsilon_2} \int_{-\infty}^{\infty} \frac{dq}{2\pi} \{A_1(q|k)[-h'_1(x)q + \alpha_2(q)] \exp[iqx + i\alpha_2(q)h_1(x)] \\ & \quad + A_2(q|k)[-h'_1(x)q - \alpha_2(q)] \exp[iqx - i\alpha_2(q)h_1(x)]\}. \end{aligned} \quad [6.32]$$

The boundary conditions at the interface $z = -H + h_2(x)$ require the continuity of $H_2(x, z|\omega)$ and $\varepsilon^{-1}\partial H_2(x, z|\omega)/\partial N_2$ across it, where $\partial/\partial N_2 = -h'_2(x)\partial/\partial x + \partial/\partial z$. Their satisfaction yields a second pair of equations

$$\begin{aligned} & \int_{-\infty}^{\infty} \frac{dq}{2\pi} \{A_1(q|k) \exp[iqx + i\alpha_2(q)(-H + h_2(x))] \\ & \quad + A_2(q|k) \exp[iqx - i\alpha_2(q)(-H + h_2(x))]\} \\ &= \int_{-\infty}^{\infty} \frac{dq}{2\pi} T(q|k) \exp[iqx - i\alpha_3(q)(-H + h_2(x))] \end{aligned} \quad [6.33]$$

and

$$\begin{aligned} & \frac{1}{\varepsilon_2} \int_{-\infty}^{\infty} \frac{dq}{2\pi} [A_1(q|k)[-h'_2(x)q + \alpha_2(q)] \exp[iqx + i\alpha_2(q)(-H + h_2(x))] \\ & + A_2(q|k)[-h'_2(x)q - \alpha_2(q)] \exp[iqx - i\alpha_2(q)(-H + h_2(x))]] \\ & = \frac{1}{\varepsilon_3} \int_{-\infty}^{\infty} \frac{dq}{2\pi} T(q|k)[-h'_2(x)q - \alpha_3(q)] \exp[iqx - i\alpha_3(q)(-H + h_2(x))]. \end{aligned} \quad [6.34]$$

To obtain a single integral equation for the scattering amplitude $R(q|k)$ alone, we first multiply Equation [6.31] by $\varepsilon_2^{-1}[-h'_1(x)p + \alpha_2(p)]\exp[-ipx - i\alpha_2(p)h_1(x)]$, multiply Equation [6.32] by $\exp[-ipx + i\alpha_2(p)h_1(x)]$, where p is an arbitrary wavenumber, integrate the resulting equations over x , and add them. The result is

$$\begin{aligned} & \left(\frac{1}{\varepsilon_2} - \frac{1}{\varepsilon_1} \right) \frac{I_1(\alpha_2(p) + \alpha_1(k)|p-k)}{\alpha_2(p) + \alpha_1(k)} [\alpha_2(p)\alpha_1(k) - pk] \\ & - \left(\frac{1}{\varepsilon_2} - \frac{1}{\varepsilon_1} \right) \int_{-\infty}^{\infty} \frac{dq}{2\pi} \frac{I_1(\alpha_2(p) - \alpha_1(q)|p-q)}{\alpha_2(p) - \alpha_1(q)} [\alpha_2(p)\alpha_1(q) + pq] R(q|k) \\ & = \frac{2\alpha_2(p)}{\varepsilon_2} A_1(p|k), \end{aligned} \quad [6.35]$$

where ($j = 1, 2$)

$$I_j(\gamma|Q) = \int_{-\infty}^{\infty} dx \exp[-iQx - i\gamma h_j(x)]. \quad [6.36]$$

We next multiply Equation [6.31] by $\varepsilon_2^{-1}[h'_1(x)p + \alpha_2(p)]\exp[-ipx + i\alpha_2(p)h_1(x)]$, multiply Equation [6.32] by $\exp[-ipx + i\alpha_2(p)h_1(x)]$, integrate the resulting equations over x , and subtract the second from the first. In this way we obtain

$$\begin{aligned} & \left(\frac{1}{\varepsilon_2} - \frac{1}{\varepsilon_1} \right) \frac{I_1(-\alpha_2(p) + \alpha_1(k)|p-k)}{-\alpha_2(p) + \alpha_1(k)} [\alpha_2(p)\alpha_1(k) + pk] \\ & - \left(\frac{1}{\varepsilon_2} - \frac{1}{\varepsilon_1} \right) \int_{-\infty}^{\infty} \frac{dq}{2\pi} \frac{I_1(-\alpha_2(p) - \alpha_1(q)|p-q)}{-\alpha_2(p) - \alpha_1(q)} [\alpha_2(p)\alpha_1(q) - pq] R(q|k) \\ & = \frac{2\alpha_2(p)}{\varepsilon_2} A_2(p|k). \end{aligned} \quad [6.37]$$

We continue by multiplying Equation [6.33] by $\varepsilon_3^{-1}[-h'_2(x)p + \alpha_3(p)\exp[-ipx - i\alpha_3(p)h_2(x)]$, multiplying Equation [6.34] by $\exp[-ipx - i\alpha_3(p)h_2(x)]$, integrating the resulting equations over x , and adding them. The result is

$$\begin{aligned} & \left(\frac{1}{\varepsilon_2} - \frac{1}{\varepsilon_3} \right) \int_{-\infty}^{\infty} \frac{dq}{2\pi} \left\{ \frac{I_2(\alpha_3(p) - \alpha_2(q) | p - q)}{\alpha_3(p) - \alpha_2(q)} [\alpha_3(p)\alpha_2(q) + pq \right. \\ & \quad \times A_1(q | k) \exp[-i\alpha_2(q)H] \\ & \quad \left. - \frac{I_2(\alpha_3(p) + \alpha_2(q) | p - q)}{\alpha_3(p) + \alpha_2(q)} [\alpha_3(p)\alpha_2(q) - pq] \right. \\ & \quad \left. \times A_2(q | k) \exp[i\alpha_2(q)H] \right\} = 0. \end{aligned} \quad [6.38]$$

On substituting the expressions for $A_1(q|k)$ and $A_2(q|k)$ given by Equations [6.35] and [6.37], respectively, into Equation [6.38], we obtain

$$\begin{aligned} & \int_{-\infty}^{\infty} \frac{dq}{2\pi} \left\{ \frac{I_2(\alpha_3(p) - \alpha_2(q) | p - q)}{\alpha_3(p) - \alpha_2(q)} [\alpha_3(p)\alpha_2(q) + pq] \frac{\exp[-i\alpha_2(q)H]}{\alpha_2(q)} \right. \\ & \quad \times \frac{I_1(\alpha_2(q) + \alpha_1(k) | q - k)}{\alpha_2(q) + \alpha_1(k)} [\alpha_2(q)\alpha_1(k) - qk] \\ & \quad \left. - \frac{I_2(\alpha_3(p) + \alpha_2(q) | p - q)}{\alpha_3(p) + \alpha_2(q)} [\alpha_3(p)\alpha_2(q) - pq] \frac{\exp[i\alpha_2(q)H]}{\alpha_2(q)} \right. \\ & \quad \left. \times \frac{I_1(-\alpha_2(q) + \alpha_1(k) | q - k)}{-\alpha_2(q) + \alpha_1(k)} [\alpha_2(q)\alpha_1(k) + qk] \right\} \\ & - \int_{-\infty}^{\infty} \frac{dq}{2\pi} \int_{-\infty}^{\infty} \frac{dr}{2\pi} \left\{ \frac{I_2(\alpha_3(p) - \alpha_2(q) | p - q)}{\alpha_3(p) - \alpha_2(q)} [\alpha_3(p)\alpha_2(q) + pq] \right. \\ & \quad \times \frac{\exp[-i\alpha_2(q)H]}{\alpha_2(q)} \frac{I_1(\alpha_2(q) - \alpha_1(r) | q - r)}{\alpha_2(q) - \alpha_1(r)} [\alpha_2(q)\alpha_1(r) + qr] \\ & \quad \left. - \frac{I_2(\alpha_3(p) + \alpha_2(q) | p - q)}{\alpha_3(p) + \alpha_2(q)} [\alpha_3(p)\alpha_2(q) - pq] \right. \\ & \quad \left. \times \frac{\exp[i\alpha_2(q)H]}{\alpha_2(q)} \frac{I_1(-\alpha_2(q) - \alpha_1(r) | q - r)}{-\alpha_2(q) - \alpha_1(r)} [\alpha_2(q)\alpha_1(r) - qr] \right\} R(r | k) = 0 \end{aligned} \quad [6.39]$$

Equation [6.39] is the reduced Rayleigh equation for the scattering amplitude $R(q|k)$ in p-polarization.

To obtain a single integral equation for the transmission amplitude $T(q|k)$ alone, we first multiply Equation [6.31] by $\varepsilon_1^{-1}[h'_1(x)p + \alpha_1(p)]\exp[-ipx + i\alpha_1(p)h_1(x)]$, multiply Equation [6.32] by $\exp[-ipx + i\alpha_1(p)h_1(x)]$, integrate the resulting equations over x , and subtract the second from the first. The result is

$$\begin{aligned} 2\pi\delta(p-k)\frac{2\alpha_1(k)}{\varepsilon_1} &= \left(\frac{1}{\varepsilon_1} - \frac{1}{\varepsilon_2}\right) \int_{-\infty}^{\infty} \frac{dq}{2\pi} \left\{ \frac{I_1(-\alpha_1(p) - \alpha_2(q)|p-q)}{\alpha_1(p) + \alpha_2(q)} \right. \\ &\quad \times [\alpha_1(p)\alpha_2(q) - pq]A_1(q|k) - \frac{I_1(-\alpha_1(p) + \alpha_2(q)|p-q)}{\alpha_1(p) - \alpha_2(q)} \\ &\quad \left. \times [\alpha_1(p)\alpha_2(q) + pq]A_2(q|k) \right\}. \end{aligned} \quad [6.40]$$

To obtain $A_1(q|k)$ and $A_2(q|k)$ in terms of $T(q|k)$ we begin by multiplying Equation [6.33] by $\varepsilon_2^{-1}[h'_2(x)p + \alpha_2(p)]\exp[-ipx + i\alpha_2(p)h_2(x)]$, multiplying Equation [6.34] by $\exp[-ipx + i\alpha_2(p)h_2(x)]$, integrating the resulting equations over x , and subtracting the second from the first. In this way we obtain

$$\begin{aligned} \frac{2\alpha_2(p)}{\varepsilon_2} \exp[i\alpha_2(p)H]A_2(p|k) &= \left(\frac{1}{\varepsilon_3} - \frac{1}{\varepsilon_2}\right) \int_{-\infty}^{\infty} \frac{dq}{2\pi} \frac{I_2(-\alpha_2(p) + \alpha_3(q)|p-q)}{\alpha_2(p) - \alpha_3(q)} \\ &\quad \times [\alpha_2(p)\alpha_3(q) + pq] \exp[i\alpha_3(q)H]T(q|k). \end{aligned} \quad [6.41]$$

We continue by multiplying Equation [6.33] by $\varepsilon_2^{-1}[-h'_2(x)p + \alpha_2(p)\exp[-ipx - i\alpha_2(p)h_2(x)]]$, multiplying Equation [6.34] by $\exp[-ipx - i\alpha_2(p)h_2(x)]$, integrating the resulting equations over x , and adding them. The result is

$$\begin{aligned} \frac{2\alpha_2(p)}{\varepsilon_2} \exp[-i\alpha_2(p)H]A_1(p|k) &= -\left(\frac{1}{\varepsilon_3} - \frac{1}{\varepsilon_2}\right) \int_{-\infty}^{\infty} \frac{dq}{2\pi} \frac{I_2(\alpha_2(p) + \alpha_3(q)|p-q)}{\alpha_2(p) - \alpha_3(q)} \\ &\quad \times [\alpha_2(p)\alpha_3(q) - pq] \exp[i\alpha_3(q)H]T(q|k). \end{aligned} \quad [6.42]$$

Finally, we substitute the expressions for $A_1(q|k)$ and $A_2(q|k)$ given by Equations [6.42] and [6.41], respectively, into Equation [6.40], and obtain

$$\begin{aligned}
2\pi\delta(p-k)\frac{2\alpha_1(k)}{\varepsilon_1} &= \varepsilon_2\left(\frac{1}{\varepsilon_2}-\frac{1}{\varepsilon_1}\right)\left(\frac{1}{\varepsilon_3}-\frac{1}{\varepsilon_2}\right) \\
&\times \int_{-\infty}^{\infty} \frac{dq}{2\pi} \int_{-\infty}^{\infty} \frac{dr}{2\pi} \left\{ \frac{I_1(-\alpha_1(p) - \alpha_2(q) | p-q)}{\alpha_1(p) + \alpha_2(q)} [pq - \alpha_1(p)\alpha_2(q)] \right. \\
&\times \frac{I_2(\alpha_2(q) + \alpha_3(r) | q-r)}{\alpha_2(q) + \alpha_3(r)} [qr - \alpha_2(q)\alpha_3(r)] \\
&\times \exp\{i[\alpha_2(q) + \alpha_3(r)]H\} + \frac{I_1(-\alpha_1(p) + \alpha_2(q) | p-q)}{\alpha_1(p) - \alpha_2(q)} \\
&\times [pq + \alpha_1(p)\alpha_2(q)] \frac{I_2(-\alpha_2(q) + \alpha_3(r) | q-r)}{\alpha_2(q) - \alpha_3(r)} \\
&\times [qr + \alpha_2(q)\alpha_3(r)] \exp\{-i[\alpha_2(q) - \alpha_3(r)]H\} \frac{T(r | k)}{2\alpha_2(q)}. \tag{6.43}
\end{aligned}$$

Equation [6.43] is the reduced Rayleigh equation for the transmission amplitude $T(q|k)$ in p-polarization.

Thus, the system of four coupled integral Equations [6.31]–[6.34] from which $R(q|k)$ and $T(q|k)$ can be determined has been reduced to a single integral equation for each of these amplitudes. The price we pay for this significant reduction in the number of equations that have to be solved is that the resulting integral equations are two-dimensional integral equations, which makes their numerical solution time consuming.

6.3.2 s-Polarization

In the case of s-polarization we work with the single nonzero component of the electric field in this system. It can be written in the form

$$\begin{aligned}
E_2(x, z | \omega) &= \exp[ikx - i\alpha_1(k, \omega)z] \\
&\times \int_{-\infty}^{\infty} \frac{dq}{2\pi} R(q | k) \exp[iqx + i\alpha_1(q, \omega)z] \tag{6.44}
\end{aligned}$$

in the region $z > h_1(x)_{max}$,

$$\begin{aligned}
E_2(x, z | \omega) &= \int_{-\infty}^{\infty} \frac{dq}{2\pi} \exp(iqx) \{A_1(q | k) \exp[i\alpha_2(q, \omega)z] \\
&+ A_2(q | k) \exp[-i\alpha_2(q, \omega)z]\}, \tag{6.45}
\end{aligned}$$

in the region $-H + h_2(x) < z < h_1(x)$, and

$$E_2(x, z | \omega) = \int_{-\infty}^{\infty} \frac{dq}{2\pi} T(q | k) \exp[iqx - i\alpha_3(q, \omega)z] \quad [6.46]$$

in the region $z < -H + h_2(x)_{min}$.

The boundary conditions at each interface require the continuity of $E_2(x, z | \omega)$ and its normal derivative across it. This leads to the system of Rayleigh equations for the amplitudes $R(q|k)$, $A_1(qk)$, $A_2(q|k)$, and $T(q|k)$:

$$\begin{aligned} & \exp[ikx - i\alpha_1(k, \omega)h_1(x)] + \int_{-\infty}^{\infty} \frac{dq}{2\pi} R(q | k) \exp[iqx + i\alpha_1(q, \omega)h_1(x)] \\ &= \int_{-\infty}^{\infty} \frac{dq}{2\pi} \{A_1(q | k) \exp[iqx + i\alpha_2(q, \omega)h_1(x)] \\ &+ A_2(q | k) \exp[iqx - i\alpha_2(q, \omega)h_1(x)]\} \end{aligned} \quad [6.47]$$

$$\begin{aligned} & -[h'_1(x)k - \alpha_1(k, \omega)] \exp[ikx - i\alpha_1(k, \omega)h_1(x)] \\ &+ \int_{-\infty}^{\infty} \frac{dq}{2\pi} [-h'_1(x)q + \alpha_1(q, \omega)] R(q | k) \exp[iqx + i\alpha_1(q, \omega)h_1(x)] \\ &= \int_{-\infty}^{\infty} \frac{dq}{2\pi} \{A_1(q | k)[-h'_1(x)q + \alpha_2(q, \omega)] \exp[iqx + i\alpha_2(q, \omega)h_1(x)] \\ &+ A_2(q | k)[-h'_1(x)q - \alpha_2(q, \omega)] \exp[iqx - i\alpha_2(q, \omega)h_1(x)]\} \end{aligned} \quad [6.48]$$

$$\begin{aligned} & \int_{-\infty}^{\infty} \frac{dq}{2\pi} \{A_1(q | k) \exp[iqx + i\alpha_2(q, \omega)(-H + h_2(x))] \\ &+ A_2(q | k) \exp[iqx - i\alpha_2(q, \omega)(-H + h_2(x))]\} \\ &= \int_{-\infty}^{\infty} \frac{dq}{2\pi} T(q | k) \exp[iqx - i\alpha_3(q, \omega)(-H + h_2(x))] \end{aligned} \quad [6.49]$$

$$\begin{aligned} & \int_{-\infty}^{\infty} \frac{dq}{2\pi} \{A_1(q | k)[-h'_2(x)q + \alpha_2(q, \omega)] \exp[iqx + i\alpha_2(q, \omega)(-H + h_2(x))] \\ &+ A_2(q | k)[-h'_2(x)q - \alpha_2(q, \omega)] \exp[iqx - i\alpha_2(q, \omega)(-H + h_2(x))]\} \\ &= \int_{-\infty}^{\infty} \frac{dq}{2\pi} T(q | k)[-h'_2(x)q - \alpha_3(q, \omega)] \exp[iqx - i\alpha_3(q, \omega)(-H + h_2(x))]. \end{aligned} \quad [6.50]$$

To obtain a single integral equation for the scattering amplitude $R(q|k)$ and for the transmission amplitude $T(q|k)$ we carry out the same sequence of multiplications of Equations [6.47]–[6.50], integrations over x , and addition or subtraction of the resulting equations, as was done in the case of p-polarization, with one exception. Due to the absence of dielectric constants multiplying the normal derivatives in the boundary conditions expressing the continuity of the tangential component of the magnetic field across each

interface, the factors multiplying Equations [6.47]–[6.50] also contain no explicit dielectric constants. The results are²⁵

$$\begin{aligned}
 & \int_{-\infty}^{\infty} \frac{dq}{2\pi} \left\{ \frac{I_2(\alpha_3(p, \omega) - \alpha_2(q, \omega) | p - q)}{\alpha_3(p, \omega) - \alpha_2(q, \omega)} \frac{\exp[-i\alpha_2(q, \omega)H]}{\alpha_2(q, \omega)} \right. \\
 & \quad \times \frac{I_1(\alpha_2(q, \omega) + \alpha_1(k, \omega) | q - k)}{\alpha_2(q, \omega) + \alpha_1(k, \omega)} \\
 & \quad + \frac{I_2(\alpha_3(p, \omega) + \alpha_2(q, \omega) | p - q)}{\alpha_3(p, \omega) + \alpha_2(q, \omega)} \frac{\exp[i\alpha_2(q, \omega)H]}{\alpha_2(q, \omega)} \\
 & \quad \times \left. \frac{I_1(-\alpha_2(q, \omega) + \alpha_1(k, \omega) | q - k)}{\alpha_2(q, \omega) - \alpha_1(k, \omega)} \right\} \\
 & + \int_{-\infty}^{\infty} \frac{dq}{2\pi} \int_{-\infty}^{\infty} \frac{dr}{2\pi} \left\{ \frac{I_2(\alpha_3(p, \omega) - \alpha_2(q, \omega) | p - q)}{\alpha_3(p, \omega) - \alpha_2(q, \omega)} \frac{\exp[-i\alpha_2(q, \omega)H]}{\alpha_2(q, \omega)} \right. \\
 & \quad \times \frac{I_1(\alpha_2(q, \omega) - \alpha_1(r, \omega) | q - r)}{\alpha_2(q, \omega) - \alpha_1(r, \omega)} \\
 & \quad + \frac{I_2(\alpha_3(p, \omega) + \alpha_2(q, \omega) | p - q)}{\alpha_3(p, \omega) + \alpha_2(q, \omega)} \frac{\exp[i\alpha_2(q, \omega)H]}{\alpha_2(q, \omega)} \\
 & \quad \times \left. \frac{I_1(-\alpha_2(q, \omega) - \alpha_1(r, \omega) | q - r)}{\alpha_2(q, \omega) + \alpha_1(r, \omega)} \right\} R(r | k) = 0,
 \end{aligned} \tag{6.51}$$

and

$$\begin{aligned}
 2\alpha_1(k, \omega)2\pi\delta(p - k) &= (\epsilon_1 - \epsilon_2)(\epsilon_2 - \epsilon_3) \left(\frac{\omega}{c} \right)^4 \int_{-\infty}^{\infty} \frac{dq}{2\pi} \int_{-\infty}^{\infty} \frac{dr}{2\pi} \\
 & \times \left\{ \frac{I_1(-\alpha_1(p, \omega) - \alpha_2(q, \omega) | p - q)}{\alpha_1(p, \omega) + \alpha_2(q, \omega)} \frac{\exp[i[\alpha_2(q, \omega) + \alpha_3(r)]H]}{2\alpha_2(q, \omega)} \right. \\
 & \quad \times \frac{I_2(\alpha_2(q, \omega) + \alpha_3(r, \omega) | q - r)}{\alpha_2(q, \omega) + \alpha_3(r, \omega)} \\
 & \quad + \frac{I_1(-\alpha_1(p, \omega) + \alpha_2(q, \omega) | p - q)}{\alpha_1(p, \omega) - \alpha_2(q, \omega)} \frac{\exp[i[-\alpha_2(q) + \alpha_3(r)]H]}{2\alpha_2(q, \omega)} \\
 & \quad \times \left. \frac{I_2(-\alpha_2(q, \omega) + \alpha_3(r, \omega) | q - r)}{\alpha_2(q, \omega) - \alpha_3(r, \omega)} \right\} T(r | k).
 \end{aligned} \tag{6.52}$$

Equations [6.51] and [6.52] are the reduced Rayleigh equations for the scattering amplitude $R(q|k)$ and the transmission amplitude $T(q|k)$ in s-polarization.

6.3.3 Results

The ability to calculate the scattering and transmission amplitudes $R(q|k)$ and $T(q|k)$ is central to the solution of the scattering and transmission problems. This is because the differential reflection and transmission coefficients, which are measurable quantities, are expressed in terms of these amplitudes, respectively.

The differential reflection coefficient $(\partial R / \partial \theta_s)$ is defined such that $(\partial R / \partial \theta_s) d\theta_s$ is the fraction of the total time-averaged incident flux that is scattered into the angular interval $(\theta_s, \theta_s + d\theta_s)$ in the limit as $d\theta_s \rightarrow 0$. The differential transmission coefficient $(\partial T / \partial \theta_t)$ is defined such that $(\partial T / \partial \theta_t) d\theta_t$ is the fraction of the total time-averaged incident flux that is transmitted into the angular interval $(\theta_t, \theta_t + d\theta_t)$ in the limit as $d\theta_t \rightarrow 0$. For p-polarized light we find that

$$\frac{\partial R_p}{\partial \theta_s} = \frac{\sqrt{\epsilon_1}}{L_1} \left(\frac{\omega}{2\pi c} \right) \frac{\cos^2 \theta_s}{\cos \theta_0} |R_p(q|k)|^2, \quad [6.53]$$

where $k = \sqrt{\epsilon_1}(\omega/c) \sin \theta_0$, $q = \sqrt{\epsilon_1}(\omega/c) \sin \theta_s$, and

$$\frac{\partial T_p}{\partial \theta_t} = \frac{\sqrt{\epsilon_1}}{L_1} \left(\frac{\omega}{2\pi c} \right) \frac{\cos^2 \theta_t}{\cos \theta_0} |T_p(q|k)|^2, \quad [6.54]$$

where $k = \sqrt{\epsilon_1}(\omega/c) \sin \theta_0$, $q = \sqrt{\epsilon_3}(\omega/c) \sin \theta_t$. In Equations [6.53] and [6.54] L_1 is the length of the x axis covered by the rough surface. Here θ_0 is the angle of incidence, measured counterclockwise from the z axis, θ_s is the scattering angle measured clockwise from the z axis and θ_t is the angle of transmission, measured counterclockwise from the negative z axis. For s-polarized light we obtain

$$\frac{\partial R_s}{\partial \theta_s} = \frac{\sqrt{\epsilon_1}}{L_1} \left(\frac{\omega}{2\pi c} \right) \frac{\cos^2 \theta_s}{\cos \theta_0} |R_s(q|k)|^2 \quad [6.55]$$

and

$$\frac{\partial T_s}{\partial \theta_t} = \frac{1}{L_1} \frac{\epsilon_3}{\sqrt{\epsilon_1}} \left(\frac{\omega}{2\pi c} \right) \frac{\cos^2 \theta_t}{\cos \theta_0} |T_s(q|k)|^2. \quad [6.56]$$

In the case that both surfaces are randomly rough it is the average of each of these coefficients over the ensembles of realizations of the surface profile

functions $h_1(x)$ and $h_2(x)$ that we must calculate. The contribution to the mean differential reflection (transmission) coefficient from the incoherent (diffuse) component of the scattered (transmitted) light is then given for p-polarized incident light by

$$\left\langle \frac{\partial R_p}{\partial \theta_s} \right\rangle_{\text{incoh}} = \frac{\sqrt{\epsilon_1}}{L_1} \left(\frac{\omega}{2\pi c} \right) \frac{\cos^2 \theta_s}{\cos \theta_0} [\langle |R_p(q|k)|^2 \rangle - |\langle R_p(q|k) \rangle|^2] \quad [6.57]$$

$$\left\langle \frac{\partial T_p}{\partial \theta_t} \right\rangle_{\text{incoh}} = \frac{\sqrt{\epsilon_1}}{L_1} \left(\frac{\omega}{2\pi c} \right) \frac{\cos^2 \theta_t}{\cos \theta_0} [\langle |T_p(q|k)|^2 \rangle - |\langle T_p(q|k) \rangle|^2], \quad [6.58]$$

and for s-polarized incident light by

$$\left\langle \frac{\partial R_s}{\partial \theta_s} \right\rangle_{\text{incoh}} = \frac{\sqrt{\epsilon_1}}{L_1} \left(\frac{\omega}{2\pi c} \right) \frac{\cos^2 \theta_s}{\cos \theta_0} [\langle |R_s(q|k)|^2 \rangle - |\langle R_s(q|k) \rangle|^2] \quad [6.59]$$

$$\left\langle \frac{\partial T_s}{\partial \theta_t} \right\rangle_{\text{incoh}} = \frac{1}{L_1} \frac{\epsilon_3}{\sqrt{\epsilon_1}} \left(\frac{\omega}{2\pi c} \right) \frac{\cos^2 \theta_t}{\cos \theta_0} [\langle |T_s(q|k)|^2 \rangle - |\langle T_s(q|k) \rangle|^2]. \quad [6.60]$$

Equations [6.39], [6.43] and Equations [6.50] and [6.52] have not yet been solved by nonperturbative, purely numerical means. Equations [6.51] and [6.52] have been solved as expansions in powers of the surface profile functions $h_1(x)$ and $h_2(x)$ of the forms

$$\begin{aligned} R(q|k) &= R_0(k) 2\pi d(q-k) + \sum_i^2 R_i^{(1)}(q|k) \hat{h}_i(q-k) \\ &\quad + \sum_{i,j}^2 \int_{-\infty}^{\infty} \frac{dp}{2\pi} R_{ij}^{(2)}(q|p|k) \hat{h}_i(q-p) \hat{h}_j(p-k) \\ &\quad + \sum_{i,j,m}^2 \int_{-\infty}^{\infty} \frac{dp}{2\pi} \int_{-\infty}^{\infty} \frac{dr}{2\pi} R_{ijm}^{(3)}(q|p|r|k) \hat{h}_i(q-p) \hat{h}_j(p-r) \hat{h}_m(r-k) + \dots \end{aligned} \quad [6.61]$$

and

$$\begin{aligned} T(q|k) &= T_0(k) 2\pi \delta(q-k) + \sum_i^2 T_i^{(1)}(q|k) \hat{h}_i(q-k) \\ &\quad + \sum_{i,j}^2 \int_{-\infty}^{\infty} \frac{dp}{2\pi} T_{ij}^{(2)}(q|p|k) \hat{h}_i(q-p) \hat{h}_j(p-k) \\ &\quad + \sum_{i,j,m}^2 \int_{-\infty}^{\infty} \frac{dp}{2\pi} \int_{-\infty}^{\infty} \frac{dr}{2\pi} T_{ijm}^{(3)}(q|p|r|k) \hat{h}_i(q-p) \hat{h}_j(p-r) \hat{h}_m(r-k) + \dots \end{aligned} \quad [6.62]$$

where the subscripts refer to the surface profile functions $h_1(x)$ or $h_2(x)$, the superscripts denote the order in the expansion, and

$$\hat{h}_j(Q) = \int_{-\infty}^{\infty} dx h_j(x) \exp(-iQx). \quad [6.63]$$

The coefficients in these expansions are lengthy and complicated functions, and will not be presented here. They can be found in Reference [25].

To illustrate the preceding results we assume that each surface profile function constitutes a stationary, zero-mean, Gaussian random process defined by ($j = 1, 2$)

$$\langle h_j(x)h_j(x') \rangle = \sigma_j^2 w_j(|x - x'|), \quad [6.64]$$

where the angle brackets denote an average over the ensemble of realizations of the surface profile function, and $\sigma_j = \langle h_j^2(x) \rangle^{1/2}$ is the rms height of the corresponding surface. The surface height autocorrelation function $w_j(|x|)$ is assumed to have the Gaussian form

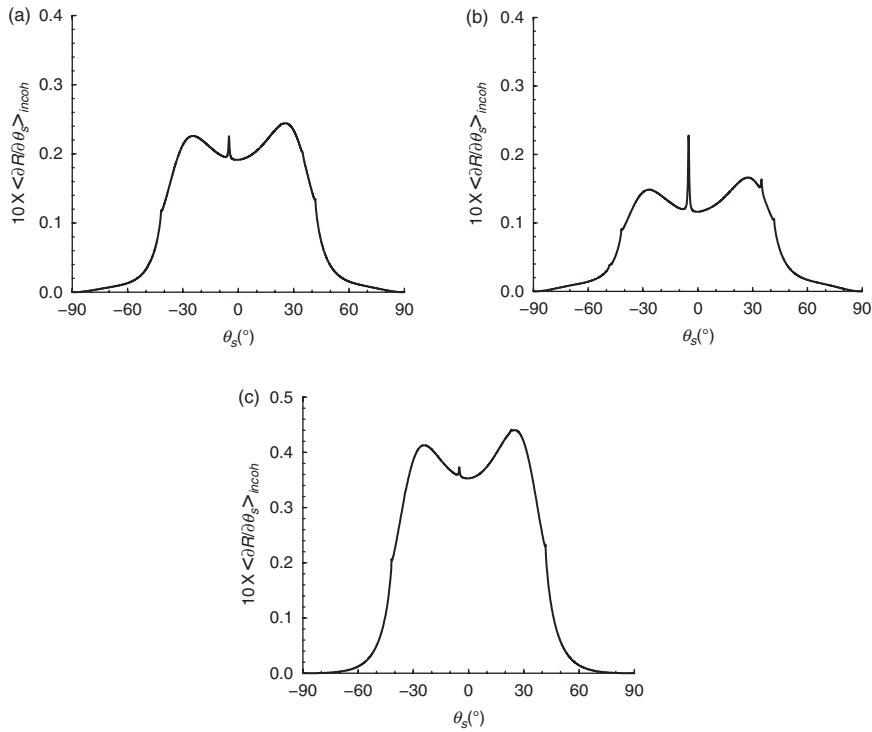
$$w_j(|x|) = \exp\left(-\frac{x^2}{a_j^2}\right), \quad [6.65]$$

where the characteristic length a_j is the transverse correlation length of the surface roughness.

In the calculations three cases were considered: (i) $h_1(x)$ and $h_2(x)$ are uncorrelated, so that $\langle h_1(x)h_2(x') \rangle = \langle h_2(x)h_1(x') \rangle = 0$; (ii) $h_1(x)$ and $h_2(x)$ are correlated, $h_2(x) = h_1(x)$; and (iii) $h_1(x)$ and $h_2(x)$ are anti-correlated, $h_2(x) = -h_1(x)$.

It was assumed that the wavelength of the incident light was $\lambda = 632.8$ nm, the angle of incidence was $\theta_0 = 5^\circ$, the region $z > h_1(x)$ was glass ($\epsilon_1 = 2.25$), the region $-H + h_2(x) < z < h_1(x)$ was silicon ($\epsilon_2 = 11.97+i0.02$), and the region $z < -H + h_2(x)$ was vacuum ($\epsilon_3 = 1$). The mean thickness of the silicon film was $H = 650$ nm. The rms height of each surface was $\sigma = 5$ nm, and the transverse correlation length of the surface roughness was $a = 100$ nm for each surface.

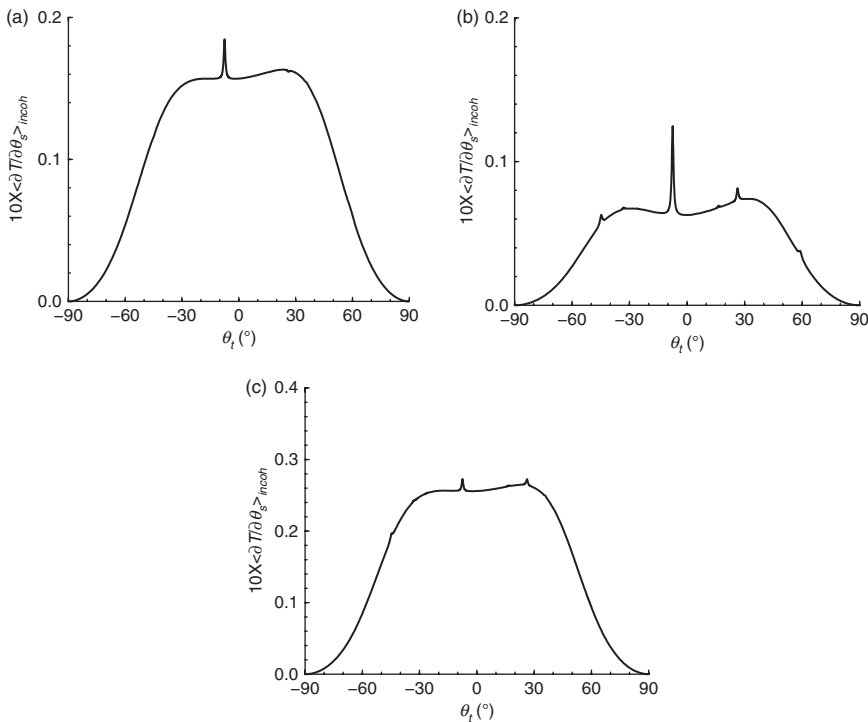
In Fig. 6.6 we present plots of $\langle \partial R_s / \partial \theta_s \rangle$ as functions of the angle of scattering θ_s , in the cases where the film surface profile functions are (a) uncorrelated, (b) correlated, and (c) anti-correlated. In each of these figures an enhanced backscattering peak¹ is observed at the scattering angle $\theta_s = -5^\circ$. In addition satellite peaks³ are present at $\theta_s = -48.15^\circ, -41.8^\circ, 34.9^\circ$ and 41.8° in the case of correlated surface profile functions (Fig. 6.6b). These arise due to the guided waves supported by the scattering structure. Only two of the



6.6 The contribution to the mean differential reflection coefficient from the light scattered incoherently. (a) Uncorrelated surface profile functions; (b) correlated surface profile functions; (c) anti-correlated surface profile functions.²⁵

satellite peaks, at $\theta_s = -41.8^\circ$ and 41.8° , survive in the case where the surface profile functions are anti-correlated (Fig. 6.6c), and three of the satellite peaks, at $\theta_s = -41.8^\circ$, 34.9° and 41.8° , are present in the case of uncorrelated surface profile functions (Fig. 6.6a). The enhanced backscattering peak is most strongly expressed in the result obtained for the case of correlated surface profile functions.

In Fig. 6.7 we present plots of $\langle \partial R_s / \partial \theta_i \rangle$ as functions of the angle of transmission θ_i in the cases where the film surface profile functions are (a) uncorrelated, (b) correlated, and (c) anti-correlated. An enhanced transmission peak⁹ is present in each of these figures. In addition, satellite peaks³ are present at $\theta_i = -44.75^\circ$, -33.05° , 16.54° , 26.33° and 58.84° in the case of correlated surface profile functions (Fig. 6.7b). Only the satellite peaks at $\theta_i = -44.75^\circ$, 16.54° and 26.33° , survive in the case where the surface profile functions are anti-correlated (Fig. 6.7c). No satellite peaks are observed in the case of the uncorrelated surface profile functions, but a weak satellite dip is present at



6.7 The contribution to the mean differential transmission coefficient from the light transmitted incoherently. (a) Uncorrelated surface profile functions; (b) correlated surface profile functions; (c) anti-correlated surface profile functions.²⁵

$\theta_t = 26.33^\circ$ (Fig. 6.7a). The strongest enhanced transmission peak is observed in the case where the surface profile functions are correlated.

Thus, in this section we have shown how the sets of four coupled one-dimensional integral Equations [6.31]–[6.34] and [6.47]–[6.50] from which the scattering amplitudes $R(q|k)$ and transmission amplitude $T(q|k)$ can be obtained for p- and s-polarized light, respectively, incident on a film bounded by two one-dimensional rough surfaces, can be reduced to a single two-dimensional integral equation for each of these amplitudes. The numerical solution of these equations poses challenging computational problems, but they yield to high-order perturbative solutions as expansions in powers of the surface profile functions, as our illustrative solution shows. It has also been demonstrated that changing the degree of correlation between the two surface profile functions can significantly alter the strength of multiple-scattering effects such as enhanced backscattering and enhanced transmission, and the existence of satellite peaks.

6.4 Numerical solution of the reduced Rayleigh equation for the scattering of light from a two-dimensional randomly rough penetrable surface

A rigorous calculation of the electromagnetic field scattered from a two-dimensional randomly rough surface presents a significant computational challenge. For this reason in the past this problem has been addressed primarily by approximate methods, such as the small-amplitude perturbation theory. In the most advanced form of this method, the amplitudes of the p- and s-polarized components of the scattered field were expanded in powers of the surface profile function through terms of third order.^{21,30,31}

However, numerical calculations of the scattering of light from two-dimensional randomly rough, perfectly conducting^{32–39} and penetrable^{37,40–45} surfaces have been carried out in recent years, by a variety of approaches. Nevertheless, such calculations remain computationally intensive, and need improvements in the methods used in carrying them out.

In this section we describe a new approach to the calculation of the angular dependence of the intensity of the light scattered from a two-dimensional randomly rough surface of a penetrable medium in contact with vacuum. It is based on a purely numerical solution of the reduced Rayleigh equations for the scattering of p- and s-polarized light incident from vacuum on a clean, two-dimensional randomly rough penetrable surface.⁴⁶

The physical system we consider here consists of vacuum in the region $z > h(\mathbf{x})$, where $\mathbf{x} = (x, y, 0)$, and the scattering medium, whose dielectric function is $\varepsilon(\omega)$, in the region $z < h(\mathbf{x})$. The surface profile function $h(\mathbf{x})$ is assumed to be a single-valued function of \mathbf{x} that is differentiable with respect to x and y , and constitutes a stationary, zero-mean, Gaussian random process defined by $\langle h(\mathbf{x})h(\mathbf{x}') \rangle = \sigma^2 w(\mathbf{x} - \mathbf{x}')$. The angle brackets here denote an average over the ensemble of realizations of the surface profile function, and $\sigma = \langle h^2(\mathbf{x}) \rangle^{1/2}$ is the rms height of the surface.

The numerical generation of each realization of the surface profile function is carried out by a two-dimensional version³⁹ of the filtering method used in Reference [12]. This method is based on the power spectrum of the surface roughness $g(\mathbf{k})$, where $\mathbf{k} = (k_x, k_y, 0)$, which is defined by

$$g(\mathbf{k}) = \int d^2x w(\mathbf{x}) \exp(-i\mathbf{k} \cdot \mathbf{x}). \quad [6.66]$$

The electromagnetic field in the vacuum region $z > h(\mathbf{x})$ is the sum of an incident and a scattered field $\mathbf{E}(\mathbf{r}; t) = [\mathbf{E}(\mathbf{r}|\omega)_{inc} + \mathbf{E}(\mathbf{r}|\omega)_{sc}] \exp(-i\omega t)$, where $\mathbf{r} = (x, y, z)$,

$$E(r|\omega)_{inc} = \left\{ -\frac{c}{\omega} [\alpha_0(k)\hat{k} + k\hat{\mathbf{e}}_z]B_p(\mathbf{k}) + (\hat{\mathbf{e}}_z \times \hat{\mathbf{k}})B_s(\mathbf{k}) \right\} \exp[i\mathbf{k} \cdot \mathbf{x} - i\alpha_0(k)z] \quad [6.67a]$$

$$E(r|\omega)_{sc} = \int \frac{d^2q}{(2\pi)^2} \left\{ \frac{c}{\omega} [\alpha_0(\mathbf{q})\hat{\mathbf{q}} - \mathbf{q}\hat{\mathbf{e}}_z]A_p(\mathbf{q}) + (\hat{\mathbf{e}}_z \times \hat{\mathbf{q}})A_s(\mathbf{q}) \right\} \exp[i\mathbf{q} \cdot \mathbf{x} + i\alpha_0(q)z], \quad [6.67b]$$

the subscripts p and s denote the p-polarized and s-polarized components of these fields with respect to the local planes of incidence and scattering, respectively, and $\alpha_0(q) = [(\omega/c)^2 - q^2]^{\frac{1}{2}}$, with $\text{Re}\alpha_0(q) > 0$, $\text{Im}\alpha_0(q) > 0$.

Maxwell's equations imply a linear relation between the amplitudes $A_\alpha(\mathbf{q})$ and $B_\beta(\mathbf{k})$ of the form ($\alpha, \beta = p, s$).

$$A_\alpha(\mathbf{q}) = \sum_\beta R_{\alpha\beta}(\mathbf{q}|\mathbf{k}) B_\beta(\mathbf{k}). \quad [6.68]$$

The scattering amplitudes $R_{\alpha\beta}(\mathbf{q}|\mathbf{k})$ play a central role in the present approach, because the contribution to the mean differential reflection coefficient from the incoherent (diffuse) component of the scattered light, when incident light of β polarization, whose wavevector has the projection \mathbf{k} on the mean scattering surface, is scattered into light of α polarization, whose wave vector has the projection \mathbf{q} on the mean scattering surface, is given by

$$\left\langle \frac{\partial R_{\alpha\beta}(\mathbf{q}|\mathbf{k})}{\partial \Omega_S} \right\rangle_{incoh} = \frac{1}{S} \left(\frac{\omega}{2\pi c} \right)^2 \frac{\cos^2 \theta_S}{\cos \theta_0} \left[\left\langle |R_{\alpha\beta}(\mathbf{q}|\mathbf{k})|^2 \right\rangle - \left| \left\langle \mathbf{R}_{\alpha\beta}(\mathbf{q}|\mathbf{k}) \right\rangle \right|^2 \right]. \quad [6.69]$$

Here S is the area of the plane $z = 0$ that is covered by the rough surface, and $\theta_0(\theta_S)$ is the polar angle of incidence (scattering) measured counterclockwise (clockwise) from the z axis.

The scattering amplitudes $R_{\alpha\beta}(\mathbf{q}|\mathbf{k})$ satisfy the 2×2 matrix integral equation¹⁸

$$\int \frac{d^2q}{(2\pi)^2} \frac{I(\alpha(p)) - \alpha_0(q)|\mathbf{p} - \mathbf{q}|}{\alpha(p) - \alpha_0(q)} \mathbf{M}^{(+)}(\mathbf{p}|\mathbf{q}) \mathbf{R}(\mathbf{q}|\mathbf{k}) = - \frac{I(\alpha(p)) + \alpha_0(k)|\mathbf{p} - \mathbf{k}|}{\alpha(p) + \alpha_0(k)} \mathbf{M}^{(-)}(\mathbf{p}|\mathbf{k}), \quad [6.70]$$

where $\alpha(p) = [\varepsilon(\omega)(\omega/c)^2 - p^2]^{1/2}$, with $\text{Re}\alpha(p) > 0$, $\text{Im}\alpha(p) > 0$, and

$$I(\gamma|\mathbf{Q}) = \int d^2x \exp(-i\mathbf{Q} \cdot \mathbf{x}) \exp[-i\gamma h(\mathbf{x})]. \quad [6.71]$$

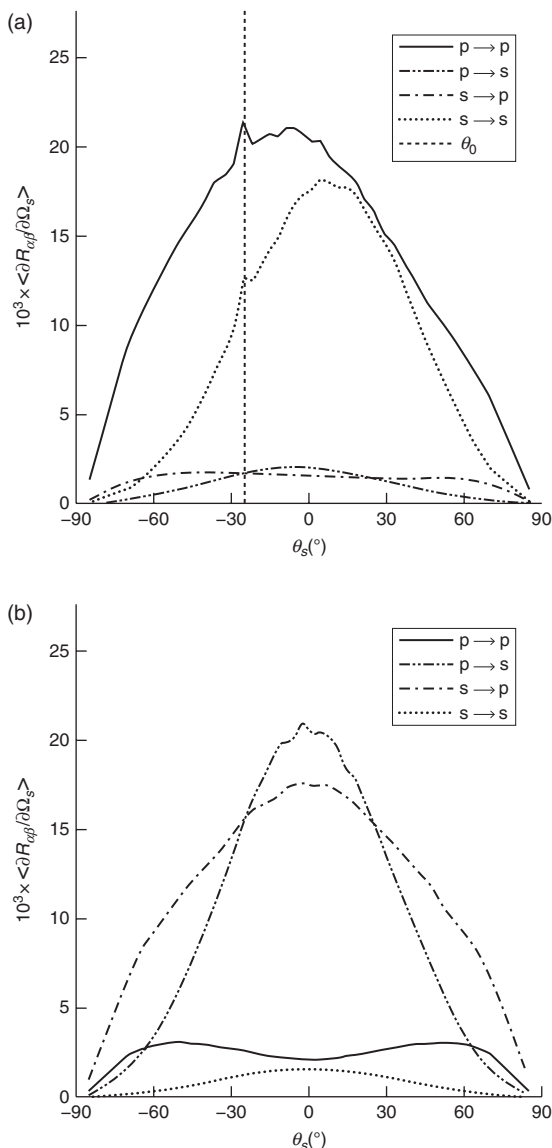
The matrices $\mathbf{M}^{(\pm)}(\mathbf{p}|\mathbf{q})$ are given by

$$\mathbf{M}^{(\pm)}(\mathbf{p}|\mathbf{q}) = \begin{pmatrix} [pq \pm \alpha(p)\hat{\mathbf{p}} \cdot \hat{\mathbf{q}}\alpha_0(q)] - \frac{\omega}{c}\alpha(p)(\hat{\mathbf{p}} \times \hat{\mathbf{q}})_z \\ \pm \frac{\omega}{c}(\hat{\mathbf{p}} \times \hat{\mathbf{q}})_2 \alpha_0(q) & \frac{\omega^2}{c^2} \hat{\mathbf{p}} \cdot \hat{\mathbf{q}} \end{pmatrix}. \quad [6.72]$$

A nonperturbative purely numerical solution of Equations [6.70]–[6.72] was obtained in the following way. A realization of the surface profile function was generated by the method described in Reference 39 on a square grid of N_x^2 points within a square region of the xy plane of edge L . The (linear) sampling interval was therefore $\Delta x = L/N_x$. The function $I(\gamma|\mathbf{Q})$ was then calculated by expanding the integrand in Equation [6.71] in powers of the surface profile function $h(\mathbf{x})$, and calculating the Fourier transform of $h''(\mathbf{x})$ by the Fast Fourier Transform. In evaluating the integral over \mathbf{q} in Equation [6.70] the infinite limits were replaced by finite ones, $|q_x| < Q/2$, $|q_y| < Q/2$. The Nyquist sampling theorem⁴⁷ states that $|q_x|$ and $|q_y|$ cannot be larger than $q_c = \pi/\Delta x = \pi N_x/L$. The components of the vector $\mathbf{Q} = \mathbf{p} - \mathbf{q}$ needed in $I(\gamma|\mathbf{Q})$, are in the interval $[-Q, Q]$, so that Q was chosen to equal q_c . A square grid with a grid constant $\Delta q = 2\pi/L$ was constructed within the square region of the $q_x q_y$ plane where $|q_x| < Q/2$ and $|q_y| < Q/2$. The integral over this region in Equation [6.70] was carried out by a two-dimensional version of the extended midpoint rule.⁴⁸ The values of \mathbf{q} and \mathbf{p} used in calculating $R_{\alpha\beta}(\mathbf{q}|\mathbf{k})$ from Equation [6.70] were given by points on this grid for a given value of \mathbf{k} , which was also a point on this grid. The resulting matrix equations were solved by LU factorization and back substitution. The values of $R_{\alpha\beta}(\mathbf{q}|\mathbf{k})$ and $|R_{\alpha\beta}(\mathbf{q}|\mathbf{k})|^2$ were then calculated for N_p realizations of the surface profile function. An arithmetic average of the N_p results for each of these functions yielded the averages $\langle R_{\alpha\beta}(\mathbf{q}|\mathbf{k}) \rangle$ and $\langle |R_{\alpha\beta}(\mathbf{q}|\mathbf{k})|^2 \rangle$ from which the mean differential reflection coefficients were calculated according to Equation [6.69].

To illustrate this approach to the scattering of light from a penetrable surface, it has been applied to the scattering of p- and s-polarized plane waves, whose wavelength is $\lambda = 632.8$ nm, from a silver surface.⁴⁶ The dielectric function of silver at this wavelength is $\epsilon(\omega) = -16.0 + i1.088$.⁴⁹ The roughness of the surface was characterized by a Gaussian power spectrum $g(\mathbf{k}) = \pi a^2 \exp(-a^2 k^2/4)$, where the transverse correlation length a was given the value $a = \lambda/4$, while the rms height of the surface was $\sigma = \lambda/40$. For the numerical parameters the values $L = 15\lambda$ and $N_x = 319$ were used, which imply that $Q = 6.4(\omega/c)$ and $\Delta x = \pi/Q = 0.0781\lambda$.

In Fig. 6.8 we present contributions to the mean differential reflection coefficients from the light scattered incoherently as functions of the polar scattering angle θ_s for the in-plane ($\phi_s = 0^\circ$) and out-of-plane ($\phi_s = 90^\circ$) co-polarized (p→p, s→s) and cross-polarized (p→s, s→p) scattering when



6.8 The mean differential reflection coefficients, $\langle \partial R_{ab} / \partial \Omega_s \rangle$ ($\beta \rightarrow \alpha$), as functions of the polar scattering angle θ_s . (a) In-plane ($\phi_s = \phi_o$) scattering. At, $\theta_s = 0^\circ$, from top to bottom the curves correspond to ($p \rightarrow p$), ($s \rightarrow s$), ($p \rightarrow s$), ($s \rightarrow p$), scattering. (b) Out-of-plane ($\phi_s = \phi_o + 90^\circ$) scattering. At $\theta_s = 0^\circ$, from top to bottom the curves correspond to ($p \rightarrow s$), ($s \rightarrow p$), ($p \rightarrow p$), ($s \rightarrow s$) scattering. The wavelength of the incident light is $\lambda = 632.8\text{ nm}$. It is incident from vacuum on a two-dimensional randomly rough silver surface ($\varepsilon(\omega) = -16.0 + i1.088$). The roughness of the surface is characterized by a Gaussian power spectrum with a transverse correlation length $a = \lambda/4$ and an rms height $\sigma = \lambda/40$. The angles of incidence are $(\theta_o, \phi_o) = (25^\circ, 0^\circ)$.

p- and s-polarized plane waves are incident on the surface at angles of incidence $(\theta_0, \phi_0) = (25^\circ, 0^\circ)$. An arithmetic average of results obtained for $N_p = 10\,000$ realizations of the surface profile function was carried out to produce Fig. 6.8. There is no single-scattering contribution to the mean differential reflection coefficient in the cases in-plane cross-polarized and out-of-plane co-polarized scattering,³² and the magnitudes of these contributions are seen to be significantly smaller than they are in the cases of in-plane co-polarized and out-of-plane cross-polarized scattering, which contain contributions from single-scattering processes. A weak enhanced backscattering peak at $\theta_s = -25^\circ$ is present in the cases of in-plane scattering, but not in the cases of out-of-plane scattering. It appears as if a rougher surface is needed to produce this peak in results for out-of-plane scattering.

When the imaginary part of the dielectric function of the metal was artificially set equal to zero, it was found that the numerical approach used to solve the reduced Rayleigh equation, Equation [6.70], conserves energy in the scattering process with an error smaller than 0.5% for the values of the parameters assumed in these calculations.

Thus, nonperturbative, purely numerical solutions of reduced Rayleigh equations open the door to theoretical studies of scattering of electromagnetic waves from weakly rough, two-dimensional randomly rough surfaces that would be difficult to solve by other methods. We will see another example of the use of this approach in the following section.

6.5 Scattering of light from a dielectric film with a two-dimensional randomly rough surface deposited on a planar metal substrate

The scattering of p- and s-polarized light from a metal surface coated with a dielectric film that has a two-dimensional randomly rough interface with a vacuum superstrate and/or a two-dimensional randomly rough interface with a metallic substrate has undergone little theoretical study until now. Reduced Rayleigh equations for the scattering amplitudes have been obtained for films with a single two-dimensional randomly rough surface^{50,51} and for a film with two two-dimensional randomly rough surfaces.²³ However, until now they have been solved only by small-amplitude perturbation theory.^{23,50} A perturbative solution of this scattering problem, by means of the stochastic functional approach, has been carried out by Kawanishi *et al.*⁵²

In this section we describe a nonperturbative, purely numerical solution of the reduced Rayleigh equation for the case where the dielectric film has a two-dimensional randomly rough interface with a vacuum superstrate and a planar interface with a metallic substrate.⁵³

The system we consider consists of vacuum (ϵ_1) in the region $z > d + h(\mathbf{x})$; a dielectric film (ϵ_2) in the region $0 < z < d + h(\mathbf{x})$; and a lossy metal (ϵ_3) in the region $z < 0$. The surface profile function $h(\mathbf{x})$ is assumed to be a single-valued function of \mathbf{x} , that is differentiable with respect to x and y , and constitutes a zero-mean, stationary, isotropic, Gaussian random process defined by

$$\langle h(\mathbf{x})h(\mathbf{x}') \rangle = \sigma^2 w(\mathbf{x} - \mathbf{x}') \quad [6.73]$$

The angle brackets here and in all that follows denote an average over the ensemble of realizations of the surface profile function, and $\sigma = \langle \zeta^2(\mathbf{x}) \rangle^{1/2}$ is the rms height of the surface roughness.

The electric field in the vacuum ($z > d + h(\mathbf{x})$) is the sum of an incident and a scattered field, $\mathbf{E}(\mathbf{r}; t) = [\mathbf{E}(\mathbf{r}|\omega)_{inc} + \mathbf{E}(\mathbf{r}|\omega)_{sc}] \exp(-i\omega t)$, where $\mathbf{r} = (x, y, z)$,

$$\mathbf{E}(\mathbf{r} | \omega)_{inc} = \left\{ \frac{c}{\omega} [\hat{\mathbf{k}}\alpha_1(k) + \hat{\mathbf{e}}_z k] B_p(\mathbf{k}) + (\hat{\mathbf{e}}_z \times \hat{\mathbf{k}}) B_s(\mathbf{k}) \right\} \exp[i\mathbf{k} \cdot \mathbf{x} - i\alpha_1(k)z] \quad [6.74a]$$

$$\mathbf{E}(\mathbf{r} | \omega)_{sc} = \int \frac{d^2\mathbf{q}}{(2\pi)^2} \left\{ \frac{c}{\omega} [\hat{\mathbf{q}}\alpha_1(q) - \hat{\mathbf{e}}_z q] A_p(\mathbf{q}) + (\hat{\mathbf{e}}_z \times \hat{\mathbf{q}}) A_s(\mathbf{q}) \right\} \exp[i\mathbf{q} \cdot \mathbf{x} + i\alpha_1(q)z]. \quad [6.74b]$$

and the subscripts p and s denote the p-polarized and s-polarized components of these fields with respect to the local planes of incidence and scattering. A caret over a vector indicates that it is a unit vector. The functions $\alpha_i(q)(i = 1, 2, 3)$ are defined by $\alpha_i(q) = [\epsilon_i(\omega/c)^2 - q^2]^{1/2}$, with $Re\alpha_i(q_1) > 0$, $Im\alpha_i(q) > 0$.

It follows from Maxwell's equations that there is a linear relationship between the amplitudes $A_\alpha(\mathbf{q})$ and $B_\beta(\mathbf{k})$, which we write as ($\alpha, \beta = p, s$)

$$A_\alpha(\mathbf{q}) = \sum_\beta R_{\alpha\beta}(\mathbf{q} | \mathbf{k}) B_\beta(\mathbf{k}). \quad [6.75]$$

It has been shown by Soubret *et al.*⁵⁰ and Leskova⁵¹ that the scattering amplitudes $\{R_{\alpha\beta}(\mathbf{q} | \mathbf{k})\}$ satisfy the matrix integral equation

$$\int \frac{d^2q}{(2\pi)^2} \mathbf{M}(\mathbf{p} | \mathbf{q}) \mathbf{R}(\mathbf{q} | \mathbf{k}) = -\mathbf{N}(\mathbf{p} | \mathbf{k}). \quad [6.76]$$

The elements of the matrices $\mathbf{M}(\mathbf{p}|\mathbf{q})$ and $\mathbf{N}(\mathbf{p}|\mathbf{k})$ in the forms given by Leskova⁵¹ are

$$\begin{aligned} M_{pp}(\mathbf{p}|\mathbf{q}) = & [pq + \alpha_2(p)(\hat{\mathbf{p}} \cdot \hat{\mathbf{q}})\alpha_1(q)]\Gamma_p(p) \exp[-i\{\alpha_2(p) - \alpha_1(q)\}d] \\ & \times \frac{I(\alpha_2(p) - \alpha_1(q))(\mathbf{p} - \mathbf{q})}{\alpha_2(p) - \alpha_1(q)} \\ & + [pq - \alpha_2(p)(\hat{\mathbf{p}} \cdot \hat{\mathbf{q}})\alpha_1(q)]\Delta_p(p) \exp[i\{\alpha_2(p) + \alpha_1(q)\}d] \\ & \times \frac{I(-\{\alpha_2(p) + \alpha_1(q)\})\mathbf{p} - \mathbf{q}}{\alpha_2(p) + \alpha_1(q)} \end{aligned} \quad [6.77a]$$

$$\begin{aligned} M_{ps}(\mathbf{p}|\mathbf{q}) = & -\frac{\omega}{c} \alpha_2(p)[\hat{\mathbf{p}} \times \hat{\mathbf{q}}]_z \{\Gamma_p(p) \exp[-i\{\alpha_2(p) - \alpha_1(q)\}d] \\ & \times \frac{I(\alpha_2(p) - \alpha_1(q))(\mathbf{p} - \mathbf{q})}{\alpha_2(p) - \alpha_1(q)} \\ & - \Delta_p(p) \exp[i\{\alpha_2(p) + \alpha_1(q)\}d] \frac{I(-\{\alpha_2(p) + \alpha_1(q)\})\mathbf{p} - \mathbf{q}}{\alpha_2(p) + \alpha_1(q)}\} \end{aligned} \quad [6.77b]$$

$$\begin{aligned} M_{sp}(\mathbf{p}|\mathbf{q}) = & \frac{\omega}{c} [\hat{\mathbf{p}} \times \hat{\mathbf{q}}]_z \{\Gamma_s(p) \exp[-i\{\alpha_2(p) - \alpha_1(q)\}d] \\ & \times \frac{I(\alpha_2(p) - \alpha_1(q))(\mathbf{p} - \mathbf{q})}{\alpha_2(p) - \alpha_1(q)} \\ & + \Delta_s(p) \exp[i\{\alpha_2(p) + \alpha_1(q)\}d] \frac{I(-\{\alpha_2(p) + \alpha_1(q)\})\mathbf{p} - \mathbf{q}}{\alpha_2(p) + \alpha_1(q)}\} \end{aligned} \quad [6.77c]$$

$$\begin{aligned} M_{ss}(\mathbf{p}|\mathbf{q}) = & \frac{\omega^2}{c^2} (\hat{\mathbf{p}} \cdot \hat{\mathbf{q}}) \{\Gamma_s(p) \exp[-i\{\alpha_2(p) - \alpha_1(q)\}d] \frac{I(\alpha_2(p) - \alpha_1(q))(\mathbf{p} - \mathbf{q})}{\alpha_2(p) - \alpha_1(q)} \\ & + \Delta_s(p) \exp[i\{\alpha_2(p) + \alpha_1(q)\}d] \frac{I(-\{\alpha_2(p) + \alpha_1(q)\})\mathbf{p} - \mathbf{q}}{\alpha_2(p) + \alpha_1(q)}\} \end{aligned} \quad [6.77d]$$

and

$$\begin{aligned} N_{pp}(\mathbf{p}|\mathbf{q}) = & -[pk - \alpha_2(p)(\hat{\mathbf{p}} \cdot \hat{\mathbf{k}})\alpha_1(k)]\Gamma_p(p) \exp[-i\{\alpha_2(p) + \alpha_1(k)\}d] \\ & \times \frac{I(\alpha_2(p) + \alpha_1(k))(\mathbf{p} - \mathbf{k})}{\alpha_2(p) + \alpha_1(k)} \\ & - [pk + \alpha_2(p)(\hat{\mathbf{p}} \cdot \hat{\mathbf{k}})\alpha_1(k)]\Delta_p(p) \exp[i\{\alpha_2(p) - \alpha_1(k)\}d] \\ & \times \frac{I(-\{\alpha_2(p) - \alpha_1(k)\})\mathbf{p} - \mathbf{k}}{\alpha_2(p) - \alpha_1(k)} \end{aligned} \quad [6.78a]$$

$$\begin{aligned} N_{ps}(\mathbf{p}|\mathbf{q}) = & -\frac{\omega}{c} \alpha_2(p)[\hat{\mathbf{p}} \times \hat{\mathbf{k}}]_z \{\Gamma_p(p) \exp[-i\{\alpha_2(p) + \alpha_1(k)\}d] \\ & \times \frac{I(\alpha_2(p) + \alpha_1(k))(\mathbf{p} - \mathbf{k})}{\alpha_2(p) + \alpha_1(k)} \\ & - \Delta_p(p) \exp[i\{\alpha_2(p) - \alpha_1(k)\}d] \frac{I(-\{\alpha_2(p) + \alpha_1(k)\})\mathbf{p} - \mathbf{k}}{\alpha_2(p) - \alpha_1(k)}\} \end{aligned} \quad [6.78b]$$

$$\begin{aligned} N_{sp}(\mathbf{p}|\mathbf{k}) &= \frac{\omega}{c} [\hat{\mathbf{p}} \times \hat{\mathbf{k}}]_z \alpha_1(k) \{ \Gamma_s(\mathbf{p}) \exp[-i(\alpha_2(p) + \alpha_1(k))d] \\ &\quad \times \frac{I(\alpha_2(p) + \alpha_1(k))\mathbf{p} - \mathbf{k}}{\alpha_2(p) + \alpha_1(k)} \\ &\quad + \Delta_s(p) \exp[i\{\alpha_2(p) - \alpha_1(k)\}d] \frac{I(-\{\alpha_2(p) - \alpha_1(k)\}\mathbf{p} - \mathbf{k})}{\alpha_2(p) - \alpha_1(k)} \} \end{aligned} \quad [6.78c]$$

$$\begin{aligned} N_{ss}(\mathbf{p}|\mathbf{k}) &= \frac{\omega^2}{c^2} (\hat{\mathbf{p}} \cdot \hat{\mathbf{k}}) \{ \Gamma_s(\mathbf{p}) \exp[-i(\alpha_2(p) + \alpha_1(k))d] \\ &\quad \times \frac{I(\alpha_2(p) + \alpha_1(k))\mathbf{p} - \mathbf{k}}{\alpha_2(p) + \alpha_1(k)} \\ &\quad + \Delta_s(p) \exp[i\{\alpha_2(p) - \alpha_1(k)\}d] \frac{I(-\{\alpha_2(p) - \alpha_1(k)\}\mathbf{p} - \mathbf{k})}{\alpha_2(p) - \alpha_1(k)} \} \end{aligned} \quad [6.78d]$$

In writing Equations [6.77] and [6.78] we have introduced the functions

$$\Gamma_p(p) = \varepsilon_2 \alpha_3(p) + \varepsilon_3 \alpha_2(p) \quad [6.79a]$$

$$\Delta_p(p) = \varepsilon_2 \alpha_3(p) - \varepsilon_3 \alpha_2(p) \quad [6.79b]$$

$$\Gamma_s(p) = \alpha_3(p) + \alpha_2(p) \quad [6.80a]$$

$$\Delta_s(p) = \alpha_3(p) - \alpha_2(p) \quad [6.80b]$$

and

$$I(\gamma|\mathbf{Q}) = \int d^2x \exp[-i\mathbf{Q} \cdot \mathbf{x}] \exp[-i\gamma h(\mathbf{x})]. \quad [6.81]$$

Realizations of the random surface profile function $h(\mathbf{x})$ were generated numerically by means of a two-dimensional version^{39,54} of the filtering method used by Maradudin *et al.*¹² Equation [6.76] was then solved by the method described in Section 6.4.

The preceding approach to the study of the scattering of light from a planar metal surface coated with a rough dielectric film has been applied⁵³ to the scattering of p- and s-polarized plane waves, whose wavelength is $\lambda = 633$ nm, incident from vacuum ($\varepsilon_1 = 1$) on a dielectric film ($\varepsilon_2 = 2.6896 + i0.01$) coating a silver surface ($\varepsilon_3 = -18.28 + i0.481$).⁴⁹ The mean thickness of the film is $d = 0.756\lambda = 478.5$ nm. The roughness of the vacuum-dielectric interface was characterized by a two-dimensional version of the West-O'Donnell power spectrum¹³ given by³⁰

$$g(\mathbf{k}) = \frac{4\pi}{k_+^2 - k_-^2} \theta(|\mathbf{k}| - k_-) \theta(k_+ - |\mathbf{k}|), \quad [6.82]$$

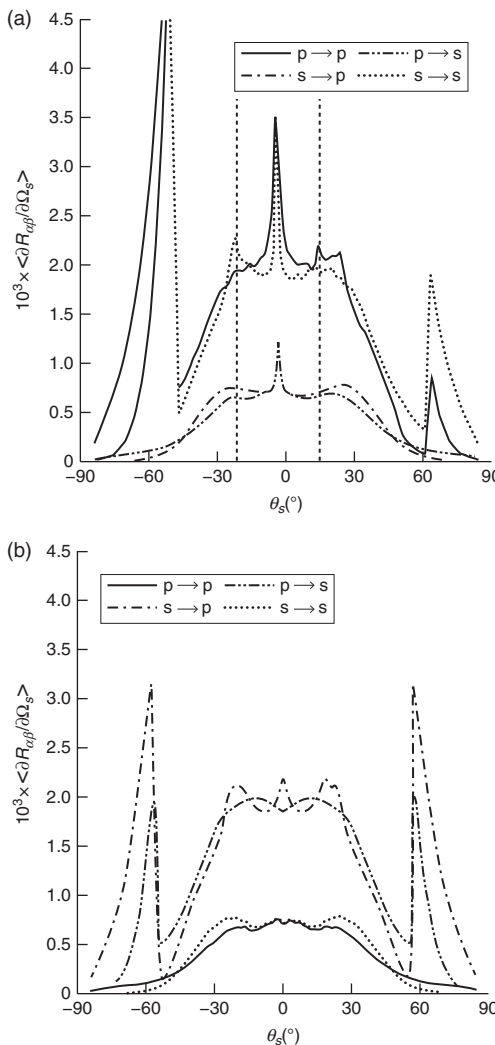
where $\theta(x)$ is the Heaviside unit step function, and $k_- = 0.82(\omega/c)$, $k_+ = 1.97(\omega/c)$. The rms height of the surface roughness was assumed to be $\sigma = \lambda/40 = 15.82$ nm.

We will denote by $\langle \partial R_{\alpha\beta}(\mathbf{q}|\mathbf{k}) / \partial \Omega_s \rangle_{\text{incoh}}$ the contribution to the mean differential reflection coefficient when light of β polarization with a projection \mathbf{k} of its wave vector on the mean scattering surface is scattered incoherently into light of α polarization with a projection \mathbf{q} of its wave vector on the mean scattering surface. The contribution to $\langle \partial R_{\alpha\beta}(\mathbf{q}|\mathbf{k}) / \partial \Omega_s \rangle_{\text{incoh}}$ from light scattered by single scattering processes (second order in $h(\mathbf{x})$) is proportional to $g(|\mathbf{q} - \mathbf{k}|)$, where $\mathbf{q} = (\omega/c) \sin \theta_s (\cos \phi_s, \sin \phi_s, 0)$, $\mathbf{k} = (\omega/c) \sin \theta_0 (\cos \phi_0, \sin \phi_0, 0)$.³⁰ Since the power spectrum Equation [6.82] is identically zero for $|\mathbf{k}| < k_-$, it follows that there is no contribution to the mean differential reflection coefficient from the light scattered incoherently by single-scattering processes when the wave vectors \mathbf{q} and \mathbf{k} satisfy the inequality $|\mathbf{q} - \mathbf{k}| < k_-$.

In Fig. 6.9a we present the contributions to the mean differential reflection coefficients from the light scattered incoherently as functions of the polar scattering angle θ_s for the in-plane ($\phi_s = \phi_0 = 45^\circ$) co-polarized ($p \rightarrow p, s \rightarrow s$) and cross-polarized ($p \rightarrow s, s \rightarrow p$) scattering when a p - or s -polarized plane wave is incident on the dielectric film at angles of incidence (θ_0, ϕ_0) given by $(3.7^\circ, 45^\circ)$. An arithmetic average of results obtained for $N_p = 11,165$ realizations of the surface profile function was carried out to produce these figures. In this case of in-plane scattering there is no contribution to the mean differential reflection coefficients for scattering angles in the interval $-49.06^\circ < \theta_s < 62.20^\circ$. A well-defined enhanced backscattering peak is present in the retroreflection direction in each of the four curves plotted in this figure. The height of this peak in each case is very close to twice that of the background at its position, which supports the conclusion that it occurs in an angular interval within which single-scattering processes make no contribution to the mean differential reflection coefficients.⁵⁵

In addition to the enhanced backscattering peaks in Fig. 6.9a additional peaks are seen on both sides of this peak in the $s \rightarrow s$ co-polarized scattering contribution to the mean differential reflection coefficient. These peaks are identified as satellite peaks.

We saw earlier that in the in-plane co-polarized scattering of light of frequency ω from a one-dimensional randomly rough surface of a film system, when the plane of incidence is perpendicular to the generators of the surface, satellite peaks occur at scattering angles given by Equation [6.1]. The scattering angles defined by this equation are expected to give the angles at which satellite peaks occur in the in-plane co-polarized scattering from the two dimensional randomly rough surfaces of the film system studied here.



6.9 The contributions to the mean differential reflects coefficients as functions of the polar scattering angle θ_s for the scattering of light incident from vacuum on the two-dimensional randomly rough surface of a dielectric film deposited on a planar silver surface. The wavelength of the incident light is $\lambda = 632.8 \text{ nm}$, the dielectric constant of silver at this wavelength is $\epsilon_3 = -18.28 + i0.481$, and the angles of incidence are $(\theta_o, \phi_o) = (3.7^\circ, 45^\circ)$. The dielectric constant of the film is $\epsilon_2 = 2.6896 + i0.01$, and its mean thickness is $d = 478.5 \text{ nm}$. The roughness of the dielectric surface is characterized by the West-O'Donnell power spectrum, Equation [6.82], with $k_- = 0.82(\omega/c)$, $k_+ = 1.97(\omega/c)$, and its rms height is $\sigma = 15.82 \text{ nm}$. (a) In-plane ($\phi_s = \phi_0$) scattering. At $\theta_s = -25^\circ$, from top to bottom the curves correspond to $(s \rightarrow s)$, $(p \rightarrow p)$, $(s \rightarrow p)$, $(p \rightarrow s)$ scattering. (b) Out-of-plane ($\phi_s = \phi_0 + 90^\circ$) scattering. At $\theta_s = -25^\circ$, from top to bottom the curves correspond to $(s \rightarrow p)$, $(p \rightarrow s)$, $(s \rightarrow s)$, $(p \rightarrow p)$, scattering.

It has been found that in the absence of absorption and roughness this film system supports two guided waves in p-polarization, whose wavenumbers are

$$q_1(\omega) = 1.4391(\omega/c), q_2(\omega) = 1.0119(\omega/c),$$

and two guided waves in s-polarization, whose wavenumbers are

$$q_1(\omega) = 1.5467(\omega/c), q_2(\omega) = 1.2432(\omega/c).$$

These results predict satellite peaks at scattering angles $\theta_s = -29.46^\circ$ and $\theta_s = 21.26^\circ$ in p polarization, and at $\theta_s = -21.60^\circ$ and $\theta_s = 13.82^\circ$ in s polarization. These scattering angles are indicated by vertical dotted lines in this figure. The peaks at $\theta_s = -21.60^\circ$ and 13.82° are seen in the s→s co-polarized scattering contribution to the mean differential reflection coefficient. The satellite peaks predicted to occur at $\theta_s = -29.46^\circ$ and 21.26° in the p→p co-polarized contribution to the mean differential reflection coefficient are not visible, presumably because they are too weak to be seen. This result disagrees with those of Soubret *et al.*,⁵⁰ where no satellite peaks were found in the in-plane s→s scattering contribution to the mean differential reflection coefficient when the substrate is a metal, although they are present when the substrate is a perfect conductor. However, the randomly rough surface studied by Soubret *et al.*⁵⁰ was characterized by a Gaussian power spectrum, not by the two-dimensional West-O'Donnell power spectrum given by Equation [6.82]. This result also disagrees with those of Reference [52], where no evidence of satellite peaks was observed in any scattering configuration. In this work the roughness of the vacuum-film interface was characterized by a Gaussian power spectrum, and the substrate was a perfect conductor. It is shown¹⁰ that the use of a Gaussian power spectrum to describe the one-dimensional roughness of a dielectric film on a planar perfectly conducting surface produces weaker satellite peaks than when the roughness is characterized by a West-O'Donnell power spectrum.

Turning now to the results for out-of-plane scattering presented in Fig. 6.9b, we note first that single-scattering processes give no contribution to the mean differential reflection coefficient for $-54.83^\circ < \theta_s < 54.83^\circ$. A weak enhanced backscattering peak is present in the cross-polarized (p→s,s→p) contributions to the mean differential reflection coefficient. The enhanced backscattering peak in the in-plane p→p scattering turns into the peak in the out-of-plane p→s scattering. Hence, the out-of-plane p→s 'enhanced backscattering peak' is simply the shoulder of the in-plane p→p enhanced backscattering peak. From Fig. 6.9a it is seen that the p→p peak is broader than the s→s peak, which means that there is no s→s 'backscattering shoulder' in the out-of-plane scattering.

It is important to note that in out-of-plane scattering the dominant contribution to the differential reflection coefficient is due to cross-polarized scattering. Satellite peaks are now present in the $p \rightarrow s$ scattering contribution, which means that incident p -polarized light excites both of the s -polarized guided waves with wave vectors in the $\phi_s = \phi_0 + 90^\circ$ direction, which then interferes to produce satellite peaks in out-of-plane scattering. Consequently, the satellite peaks found in the in-plane co-polarized scattering of light from one-dimensional randomly rough surfaces turn into a kind of ‘satellite ring’ formation in scattering from two-dimensional randomly rough surfaces, where part of a ring is co-polarized ($s \rightarrow s$, in-plane) and part is cross-polarized ($p \rightarrow s$, out-of-plane). We note that the out-of-plane scattering contributions have not been calculated in the earlier perturbative studies of the current problem.^{50,52}

The main physical result obtained from the calculations described in this section is that satellite peaks can arise in the scattering of light from the film structure studied. This result is in agreement with results of Soubret *et al.*⁵⁰ but not with those of Kawanishi *et al.*⁵² A detailed study of the conditions under which satellite peaks occur in the presence of two-dimensional surface roughness is lacking. Perhaps the computational approach described here will be used to determine them.

6.6 Analytical methods for the scattering from a three-dimensional film with randomly rough surfaces

Theoretical and numerical approaches for wave scattering from rough structures have received wide interest. We can mention the small-perturbation method (SPM),^{31,56–59} the Kirchhoff (or tangent plane) approximation method^{60–62} and the previous sections give an overview of numerical methods. However, some restrictions limit the domain of their applicability: the perturbation method is only valid for surfaces with small roughness, and the Kirchhoff approximation is applicable to surfaces with a long correlation length. Many new approaches have been suggested, such as the full-wave method,⁶³ the surface-field phase-perturbation technique^{64,65} and the quasislope approximation.⁶⁶ Voronovich^{67–71} proposed a new method called the small-slope approximation (SSA), which is valid for arbitrary roughness provided that the slopes of the surface are smaller than the angles of incidence and scattering, irrespective of the wavelength of the incident radiation. The SSA makes a bridge between the Kirchhoff approximation and the small-perturbation method.

In this section we will focus on the SSA method and the SPM with a view to studying different three-dimensional rough structures like slabs or films, considering the effects of higher orders in a perturbative expansion.

The problem of scattering by randomly rough surfaces up to the order 3 is treated in References [73–74]. References [73] and [75] consider the second order of the SSA. Gilbert and Johnson⁷³ proposed simplified forms for the first three SSA terms in the case of penetrable surfaces under the assumption of a Gaussian random process with an isotropic Gaussian correlation function. Berginc⁷⁵ gives results up to the third SSA term for incoherent scattering from dielectric and metallic surfaces with Gaussian and non-Gaussian correlation functions.

Since the higher order SSA corrections involve components of the SPM in the calculations, results of previous works^{59,74} developed under the Rayleigh hypothesis have been used in this section. We numerically develop two cases of the light scattering by a two-dimensional randomly rough surface and a case of light scattering from a random film with randomly rough boundaries. The scattered intensities from a randomly rough surface or a random film can be decomposed into coherent and incoherent components. Coherent components contribute only in the specular reflected or transmitted directions, whereas incoherent components contribute in all directions. In this section we focus on the incoherent components.

6.6.1 Definition of the scattering matrix

The main structure we consider in this section is shown in Fig. 6.10, where the two rough surfaces separate three media. The different media are characterized by isotropic, homogeneous, dielectric constants ϵ_0, ϵ_1 and ϵ_2 , respectively. The two rough surfaces are located at the heights $z = h_1(\mathbf{x})$, $z = -H + h_2(\mathbf{x})$, where $\mathbf{x} = (x, y, 0)$. We assume that the randomly rough surfaces $h_1(\mathbf{x})$ and $h_2(\mathbf{x})$ are stationary, isotropic, uncorrelated Gaussian random processes defined by their moments:

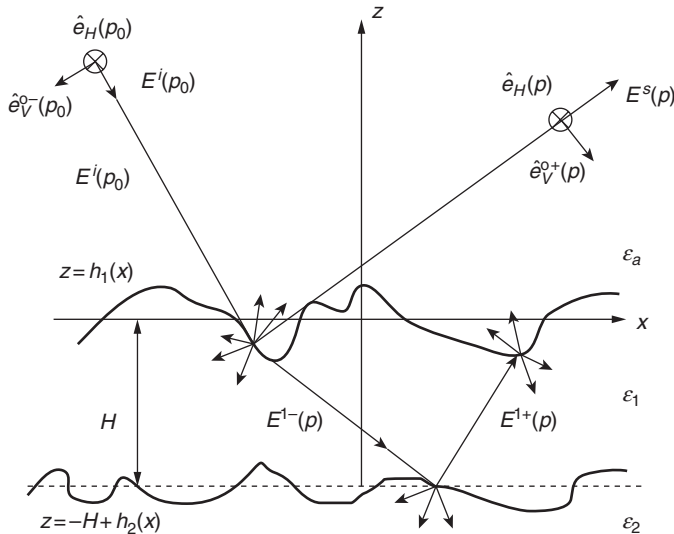
$$\langle h_i(\mathbf{x}) \rangle = 0, \quad [6.83]$$

$$\langle h_i(\mathbf{x}) h_i(\mathbf{x}') \rangle = W_i(\mathbf{x} - \mathbf{x}'), \quad [6.84]$$

$$\langle h_1(\mathbf{x}) h_2(\mathbf{x}') \rangle = 0, \quad [6.85]$$

where $i = 1, 2$, and the angle brackets denote an average over the ensembles of realizations of the functions $h_1(\mathbf{x})$ and $h_2(\mathbf{x})$. A Gaussian form is used for the surface-height correlation functions $W_1(\mathbf{x})$ and $W_2(\mathbf{x})$:

$$W_i(\mathbf{x}) = \sigma_i^2 \exp\left(-\frac{\mathbf{x}^2}{l_i^2}\right), \quad [6.86]$$



6.10 Incident wave from medium 0 scattered by a slab with two rough surfaces.

where σ_i is the rms height of the surface $h_i(\mathbf{x})$, and l_i is the correlation length.

We consider that the different electromagnetic waves propagate with a frequency ω , and the time dependence is assumed to be $\exp(-i\omega t)$. The electric fields \mathbf{E}^i satisfy in the different media a Helmholtz equation.

In the medium 0, \mathbf{E}^0 can be written as a superposition of an incident and a scattered field:

$$\mathbf{E}^0(\mathbf{x}, z) = \mathbf{E}^i(\mathbf{p}_0) \exp(i\mathbf{p}_0 \cdot \mathbf{x} - i\alpha_0(\mathbf{p}_0)z) + \int \frac{d^2 p}{(2\pi)^2} \mathbf{E}^s(\mathbf{p}) \exp(i\mathbf{p} \cdot \mathbf{x} + i\alpha_0(\mathbf{p})z), \quad [6.87]$$

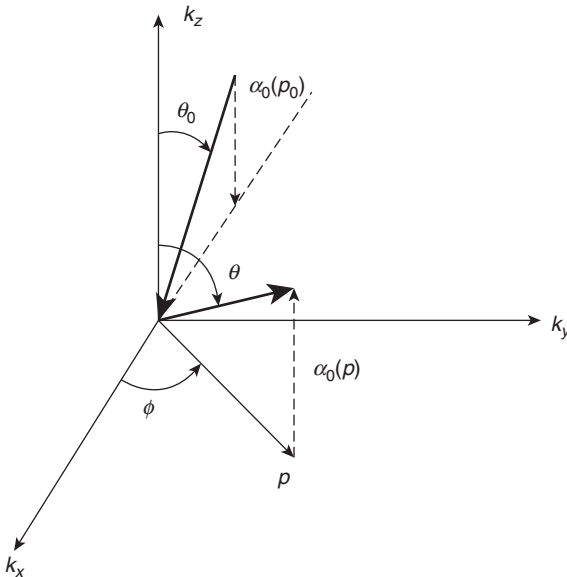
where we define (see Fig. 6.11)

$$\alpha_0(\mathbf{p}) = (\epsilon_0 K_0^2 - \mathbf{p}^2)^{\frac{1}{2}}, \quad [6.88]$$

$$K_0 = \omega/c, \quad [6.89]$$

$$\mathbf{E}^i(\mathbf{p}_0) = E_V^i(\mathbf{p}_0) \hat{\mathbf{e}}_V^{0-}(\mathbf{p}_0) + E_H^i(\mathbf{p}_0) \hat{\mathbf{e}}_H(\mathbf{p}_0), \quad [6.90]$$

$$\mathbf{E}^s(\mathbf{p}) = E_V^s(\mathbf{p}) \hat{\mathbf{e}}_V^{0+}(\mathbf{p}) + E_H^s(\mathbf{p}) \hat{\mathbf{e}}_H(\mathbf{p}). \quad [6.91]$$



6.11 Definition of the scattering vectors.

The subscript H refers to the horizontal polarization (TE), and V to the vertical polarization (TM). They are defined by the following two vectors:

$$\hat{\mathbf{e}}_H(\mathbf{p}) = \hat{\mathbf{e}}_z \times \hat{\mathbf{p}}, \quad [6.92]$$

$$\hat{\mathbf{e}}_V^{0\pm}(\mathbf{p}) = \pm \frac{\alpha_0(\mathbf{p})}{\sqrt{\epsilon_0 K_0}} \hat{\mathbf{p}} - \frac{\|\mathbf{p}\|}{\sqrt{\epsilon_0 K_0}} \hat{\mathbf{e}}_z, \quad [6.93]$$

where the minus sign corresponds to the incident wave and the plus sign to the scattered wave.

It is important to notice that the vectors $\mathbf{E}^s(\mathbf{p})$ and $\mathbf{E}^i(\mathbf{p}_0)$ are expressed in a different basis due the fact that $\hat{\mathbf{e}}_V^{0\pm}(\mathbf{p})$ and $\hat{\mathbf{e}}_V^{1\pm}(\mathbf{p})$ depend on \mathbf{p} . In medium 1, we have a similar expression, namely:

$$\mathbf{E}^1(\mathbf{r}) = \int \frac{d^2 p}{(2\pi)^2} \mathbf{E}^{1-}(\mathbf{p}) \exp(i\mathbf{p} \cdot \mathbf{x} - i\alpha_1(\mathbf{p})z) + \int \frac{d^2 p}{(2\pi)^2} \mathbf{E}^{1+}(\mathbf{p}) \exp(i\mathbf{p} \cdot \mathbf{x} + i\alpha_1(\mathbf{p})z), \quad [6.94]$$

where

$$\alpha_1(\mathbf{p}) \equiv (\epsilon_1 K_0^2 - \mathbf{p}^2)^{\frac{1}{2}}. \quad [6.95]$$

The field \mathbf{E}^{1-} is decomposed in the basis $(\hat{\mathbf{e}}_V^{1-}(\mathbf{p}), \hat{\mathbf{e}}_H(\mathbf{p}))$ and \mathbf{E}^{1+} in the basis $(\hat{\mathbf{e}}_V^{1+}(\mathbf{p}), \hat{\mathbf{e}}_H(\mathbf{p}))$ with

$$\hat{\mathbf{e}}_H(\mathbf{p}) = \hat{\mathbf{e}}_z \times \hat{\mathbf{p}}, \quad [6.96]$$

$$\hat{\mathbf{e}}_V^{1+}(\mathbf{p}) = \pm \frac{\alpha_1(\mathbf{p})}{\sqrt{\epsilon_1 K_0}} \hat{\mathbf{p}} - \frac{\|\mathbf{p}\|}{\sqrt{\epsilon_1 K_0}} \hat{\mathbf{e}}_z. \quad [6.97]$$

We can now define the scattering matrix connecting the incident field to the scattered field by the following expression:

$$\mathbf{E}^s(\mathbf{p}) \equiv \bar{\mathbf{R}}(\mathbf{p} | \mathbf{p}_0) \cdot \mathbf{E}^i(\mathbf{p}_0), \quad [6.98]$$

where $\bar{\mathbf{R}}(\mathbf{p} | \mathbf{p}_0)$ is a two-dimensional matrix where the components depend on the polarizations V and H

$$\bar{\mathbf{R}}(\mathbf{p} | \mathbf{p}_0) = \begin{pmatrix} R_{VV}(\mathbf{p} | \mathbf{p}_0) & R_{VH}(\mathbf{p} | \mathbf{p}_0) \\ R_{HV}(\mathbf{p} | \mathbf{p}_0) & R_{HH}(\mathbf{p} | \mathbf{p}_0) \end{pmatrix}.$$

We will consider a perturbative development of $\bar{\mathbf{R}}$ in powers of the height h of the following form which is given by the SPM

$$\bar{\mathbf{R}}(\mathbf{p} | \mathbf{p}_0) = \bar{\mathbf{R}}^{(0)}(\mathbf{p} | \mathbf{p}_0) + \bar{\mathbf{R}}^{(1)}(\mathbf{p} | \mathbf{p}_0) + \bar{\mathbf{R}}^{(2)}(\mathbf{p} | \mathbf{p}_0) + \bar{\mathbf{R}}^{(3)}(\mathbf{p} | \mathbf{p}_0) + \dots \quad [6.99]$$

The expression for the scattered field represents the general solution of the Maxwell equations that satisfies the radiation condition. For instance, in medium 0, the scattered field reads

$$\mathbf{E}^s(r) = \int \frac{d^2 p}{(2\pi)^2} \bar{\mathbf{R}}(\mathbf{p} | \mathbf{p}_0) \cdot \mathbf{E}^i(\mathbf{p}_0) \exp(i\mathbf{k}_p^{0+} \cdot \mathbf{r}). \quad [6.100]$$

where $\mathbf{k}_p^{0+} \equiv \mathbf{p} \pm \alpha_0(\mathbf{p}) \hat{\mathbf{e}}_z$.

In order to determine the scattering matrix we have to take into account the boundary conditions on the rough surfaces by writing the continuity of the tangential components of the electric and magnetic fields.

6.6.2 The small-slope approximation and the small perturbation method for a two-dimensional rough surface

Formulation

In this section, we will study the expression of the SSA and the SPM for the scattering of light from a two-dimensional randomly rough surface. The expressions obtained in this case will be generalized for the case of a slab. We summarize the procedure to obtain the formulation which can be applied to the scattering from a two-dimensional randomly rough surface. In the first step Voronovich⁶⁹ noticed that the unitary of the scattering matrix implies a reciprocity theorem leading to the following properties:

$$\bar{R}(\mathbf{p} | \mathbf{p}_0) = \bar{R}(\mathbf{p}_0 | -\mathbf{p}); \quad [6.101]$$

for a horizontal translation of the rough boundary $h(\mathbf{r}) \rightarrow h(\mathbf{r} - \mathbf{a})$

$$\bar{R}(\mathbf{p} | \mathbf{p}_0) \rightarrow \bar{R}(\mathbf{p} | \mathbf{p}_0) \exp [-i(\mathbf{p} - \mathbf{p}_0) \cdot \mathbf{a}]; \quad [6.102]$$

and for a vertical translation $h(\mathbf{r}) \rightarrow h(\mathbf{r}) + H$

$$\bar{R}(\mathbf{p} | \mathbf{p}_0) \rightarrow \bar{R}(\mathbf{p} | \mathbf{p}_0) \exp [-i(\alpha(\mathbf{p}) + \alpha(\mathbf{p}_0)) H]. \quad [6.103]$$

Using these results Voronovich⁸⁸ proposes the following expression for the scattering matrix

$$\bar{R}(\mathbf{p} | \mathbf{p}_0) = \int \frac{d^2 r}{(2\pi)^2} \exp [-i(\mathbf{p} - \mathbf{p}_0) \cdot \mathbf{r} - i(\alpha(\mathbf{p}) + \alpha(\mathbf{p}_0)) h(r)] \bar{\Phi}[\mathbf{p} | \mathbf{p}_0; [h]], \quad [6.104]$$

in the case of a rough surface located between media 0 and 1. The functional $\bar{\Phi}$ which depends on h has to be determined. The translation conditions Equations [6.102] and [6.103] lead to some properties of $\bar{\Phi}$. It can be noticed that it is more convenient to work with the Fourier transform $\bar{\Phi}[\mathbf{p}, \mathbf{p}_0, \mathbf{r}; [h]]$ with respect to the variable r .

The first condition Equation [6.102] reads:

$$\bar{R}(\mathbf{p} | \mathbf{p}_0) = \int \frac{d^2 \xi}{(2\pi)^2} d^2 r e^{-i(\mathbf{p} - \mathbf{p}_0 - \xi) \cdot \mathbf{r} - i(\alpha_0(\mathbf{p}) + \alpha_0(\mathbf{p}_0)) h(r)} \bar{\Phi}(\mathbf{p}, \mathbf{p}_0, \xi), \quad [6.105]$$

and the second Equation [6.103]

$$\overline{\Phi}_{x \rightarrow h(x-\alpha)}(\mathbf{p}, \mathbf{p}_0, \xi) = e^{i\xi \cdot \alpha} \overline{\Phi}_{x \rightarrow h(x)}(\mathbf{p}, \mathbf{p}_0, \xi), \quad [6.106]$$

for all vectors α . In the framework of a perturbative development, $\overline{\Phi}$ is expanded as an integral-power series of h namely:

$$\begin{aligned} \overline{\Phi}(\mathbf{p}, \mathbf{p}_0, \xi) &= \delta(\xi) \widetilde{\Phi}^0(\mathbf{p}, \mathbf{p}_0) + \int \frac{d^2 \xi_1}{(2\pi)^2} \delta(\xi - \xi_1) \widetilde{\Phi}^{(1)}(\mathbf{p}, \mathbf{p}_0, \xi_1) h(\xi_1) \\ &+ \int \int \frac{d^2 \xi_1}{(2\pi)^2} \frac{d^2 \xi_2}{(2\pi)^2} \delta(\xi - \xi - \xi_1 - \xi_2) \widetilde{\Phi}^{(2)}(\mathbf{p}, \mathbf{p}_0, \xi_1, \xi_2) h(\xi_1) h(\xi_2) + \dots \end{aligned} \quad [6.107]$$

The condition Equation [6.103] imposes:

$$\overline{\Phi}_{x \rightarrow h(x)+H}(\mathbf{p}, \mathbf{p}_0, \xi) = \overline{\Phi}_{x \rightarrow h(x)}(\mathbf{p}, \mathbf{p}_0, \xi). \quad [6.108]$$

We have:

$$\widetilde{\Phi}^{(n)}(\mathbf{p}, \mathbf{p}_0, \xi_1, \dots, \xi_n) = 0 \quad \forall k \in [1, n]. \quad [6.109]$$

Using a finite expansion with respect to the variables ξ_1, \dots, ξ_n it follows that:

$$\widetilde{\Phi}^{(n)}(\mathbf{p}, \mathbf{p}_0, \xi_1, \dots, \xi_n) = \sum_{\alpha_1, \dots, \alpha_n = x, y} \xi_{1\alpha_1} \dots \xi_{n\alpha_n} \widetilde{\Phi}^{(n)\alpha_1\dots\alpha_n}(\mathbf{p}, \mathbf{p}_0, \xi_1, \dots, \xi_n), \quad [6.110]$$

where $\xi_i = (\xi_{ix}, \xi_{iy}, 0)$. This expansion justifies the name of small-slope approximation when the effects due to the frontiers are neglected in the integration

$$i\xi_\alpha h(\xi) = \int d^2 x \frac{\partial h(x)}{\partial x_\alpha} e^{-i\xi x}. \quad [6.111]$$

Voronovich⁸⁴ showed that $\overline{\Phi}^{(n)}$ can be expanded as:

$$\widetilde{\Phi}^{(n)} = \widetilde{\Phi}^{(n)}|_{\xi_n = p - p_0 - \xi_1 - \dots - \xi_{n-1}} + [\widetilde{\Phi}^{(n)} - \widetilde{\Phi}^{(n)}|_{\xi_n = p - p_0 - \xi_1 - \dots - \xi_{n-1}}]. \quad [6.112]$$

The first term of the right side can be transformed into a term of order $n - 1$ that is analogous to $\tilde{\Phi}^{(n-1)}$, and the term between brackets is transformed into a term of order $n + 1$. This important relation will simplify the formulas in the following.

Taking as an example the first terms in the expansion Equation [6.107], and using Equation [6.112], the computation of the term $\tilde{\Phi}^{(0)}$ should involve $\tilde{\Phi}^{(1)}$ and its coefficient can be related to $\tilde{\Phi}^{(0)}$ and $\tilde{\Phi}^{(2)}$ and then replaced; we thus obtain the formula

$$\begin{aligned}\bar{R}(\mathbf{p} | \mathbf{p}_0) = & \int d^2 r e^{-i(\mathbf{p}-\mathbf{p}_0) \cdot \mathbf{r} - i(\alpha_0(\mathbf{p}) + \alpha_0(\mathbf{p}_0)) h(r)} \tilde{\Phi}^{(0)}(\mathbf{p}, \mathbf{p}_0) \\ & + \int \frac{d^2 \xi}{(2\pi)^2} d^2 r e^{-i(\mathbf{p}-\mathbf{p}_0) \cdot \mathbf{r} - i(\alpha_0(\mathbf{p}) + \alpha_0(\mathbf{p}_0)) h(r)} (2\pi)^2 \delta(\xi - \xi_1 - \xi_2) \tilde{\Phi}^{(2)}(\mathbf{p}, \mathbf{p}_0, \xi_1, \xi_2) h(\xi_1) h(\xi_2).\end{aligned}\quad [6.113]$$

In this expression, if we take the term of order 1 in h , we get

$$\bar{R}(\mathbf{p} | \mathbf{p}_0) = \tilde{\Phi}^{(0)}(\mathbf{p}, \mathbf{p}_0) [(2\pi)^2 \delta(\mathbf{p} - \mathbf{p}_0) - i(\alpha_0(\mathbf{p}) + \alpha_0(\mathbf{p}_0)) h(\mathbf{p} - \mathbf{p}_0)].\quad [6.114]$$

Voronovich^{68,69} proposed to identify the expression Equation [6.113] with the SPM (see Reference [74] Equation [53]). It follows that

$$\begin{aligned}\bar{R}^{10}(\mathbf{p} | \mathbf{p}_0) = & (2\pi)^2 \delta(\mathbf{p} - \mathbf{p}_0) \bar{X}_s^{(0)}(\mathbf{p}_0) + \alpha_0(\mathbf{p}_0) \bar{X}_s^{(1)}(\mathbf{p} | \mathbf{p}_0) h(\mathbf{p} - \mathbf{p}_0) \\ & + \alpha_0(\mathbf{p}_0) \int \frac{d^2 p_1}{(2\pi)^2} \bar{X}_s^{(2)}(\mathbf{p} | \mathbf{p}_1 | \mathbf{p}_0) h(\mathbf{p} - \mathbf{p}_1) h(\mathbf{p}_1 - \mathbf{p}_0).\end{aligned}\quad [6.115]$$

The upper indices 10 in Equation [6.115] must be read from right to left, indicating the order of the successive media. The same notation will be used in the following, and we obtain the identities:

$$\tilde{\Phi}^{(0)}(\mathbf{p}_0, \mathbf{p}_0) = \bar{X}_s^{(0)}(\mathbf{p} | \mathbf{p}_0),\quad [6.116]$$

$$-i(\alpha_0(\mathbf{p}) + \alpha_0(\mathbf{p}_0)) \tilde{\Phi}^{(0)}(\mathbf{p}, \mathbf{p}_0) = \alpha_0(\mathbf{p}_0) \bar{X}_s^{(1)}(\mathbf{p} | \mathbf{p}_0),\quad [6.117]$$

or

$$\tilde{\Phi}^{(0)}(\mathbf{p}_0, \mathbf{p}_0) = \frac{\alpha_0(\mathbf{p}_0)}{-i(\alpha_0(\mathbf{p}) + \alpha_0(\mathbf{p}_0))} \bar{X}_s^{(1)}(\mathbf{p}_0 | \mathbf{p}_0),\quad [6.118]$$

$$-2i\bar{X}^{(0)}(\mathbf{p}_0) = \bar{X}_s^{(1)}(\mathbf{p}_0 | \mathbf{p}_0).\quad [6.119]$$

The first equation gives the coefficient $\tilde{\Phi}^{(0)}(\mathbf{p}_0, \mathbf{p}_0)$ where corresponding scattering matrix becomes

$$\bar{R}^{10}(\mathbf{p}|\mathbf{p}_0) = \frac{i\alpha_0(\mathbf{p}_0)}{(\alpha_0(\mathbf{p}) + \alpha_0(\mathbf{p}_0))} \bar{X}_s^{(1)}(\mathbf{p}|\mathbf{p}_0) \int d^2r e^{-i(\mathbf{p}-\mathbf{p}_0)\cdot\mathbf{r} - i(\alpha_0(\mathbf{p}) + \alpha_0(\mathbf{p}_0))h(r)}, \quad [6.120]$$

where $\bar{X}_s^{(1)}(\mathbf{p}|\mathbf{p}_0)$ is given by Equation [A6.11.2] of Appendix 6.11.1. Following the same procedure, the order 2 approximation $\tilde{\Phi}^{(2)}$ can be written in terms of orders 1 and 3, leading to the expression:

$$\begin{aligned} R^{10}(\mathbf{p}|\mathbf{p}_0) &= \frac{\alpha_0(\mathbf{p}_0)}{-i(\alpha_0(\mathbf{p}) + \alpha_0(\mathbf{p}_0))} \int \frac{d\xi}{(2\pi)^2} d^2r e^{-i(\mathbf{p}-\mathbf{p}_0-\xi)\cdot\mathbf{r} - i(\alpha_0(\mathbf{p}) + \alpha_0(\mathbf{p}_0))h(r)} \\ &\quad \times \{(2\pi)^2 \delta(\xi) \bar{X}_s^{(1)}(\mathbf{p}|\mathbf{p}_0) \\ &+ \frac{1}{2} [\bar{X}_s^{(2)}(\mathbf{p}|\mathbf{p}-\xi|\mathbf{p}_0) + \bar{X}_s^{(2)}(\mathbf{p}|\mathbf{p}+\xi|\mathbf{p}_0) + i(\alpha_0(\mathbf{p}_0) + (\alpha_0(\mathbf{p}_0))\bar{X}_s^{(1)}(\mathbf{p}|\mathbf{p}_0)) h(\xi)]\}, \end{aligned} \quad [6.121]$$

where $\bar{X}_s^{(2)}$ is given by Equation [A6.11.3]. We immediately deduce

$$\begin{aligned} \tilde{\Phi}^{(1)}(\mathbf{p}|\mathbf{p}_0, \xi) &= \frac{i\alpha_0(\mathbf{p}_0)}{(\alpha_0(\mathbf{p}) + \alpha_0(\mathbf{p}_0))} \frac{1}{2} [\bar{X}_s^{(2)}(\mathbf{p}|\mathbf{p}-\xi|\mathbf{p}_0) + \bar{X}_s^{(2)}(\mathbf{p}|\mathbf{p}_0+\xi|\mathbf{p}_0) \\ &\quad + i(\alpha_0(\mathbf{p}) + (\alpha_0(\mathbf{p}_0))\bar{X}_s^{(1)}(\mathbf{p}|\mathbf{p}_0))]. \end{aligned} \quad [6.122]$$

The SSA method contains, following the construction procedure, a perturbative term of order 1: Equation [6.120], and of order 2: Equation [6.122]. It also contains a phase factor coming from the tangent plane approximation. In addition, Voronovich has shown in the scalar case with Dirichlet boundary conditions that the Kirchhoff tangent plane approximation is included in the small-slope method for order 2 (Equation [6.122]).

Computation of the Cross-Section and the Mueller Matrices

In this section, we give the definition of the Mueller matrix. With this derivation, we can now calculate the cross-section of the rough surface. The scattered field is related to the incident field by:

$$\mathbf{E}^s(\mathbf{x}, z) = \frac{\exp(iK_0||\mathbf{r}||)}{||\mathbf{r}||} \bar{\mathbf{f}}(\mathbf{p}|\mathbf{p}_0) \cdot \mathbf{E}^i(\mathbf{p}_0), \quad [6.123]$$

with

$$\bar{\mathbf{f}}(\mathbf{p}|\mathbf{p}_0) \equiv \frac{K_0 \cos \theta}{2\pi i} \bar{\mathbf{R}}(\mathbf{p}|\mathbf{p}_0), \quad [6.124]$$

$$\mathbf{p} = K_0 \frac{\mathbf{x}}{||\mathbf{r}||}, \quad [6.125]$$

where θ is the angle between $\hat{\mathbf{e}}_z$ and the scattering direction. Introducing the Mueller matrix $\bar{\mathbf{M}}(\mathbf{p} | \mathbf{p}_0)$ in the relations, the bistatic matrix is defined by the relations:

$$\bar{\gamma}(\mathbf{p} | \mathbf{p}_0) \equiv \frac{1}{A \cos(\theta_0)} \bar{\mathbf{M}}(\mathbf{p} | \mathbf{p}_0), \quad [6.126]$$

$$= \frac{1}{A \cos(\theta_0)} \bar{\mathbf{f}}(\mathbf{p} | \mathbf{p}_0) \odot \bar{\mathbf{f}}(\mathbf{p} | \mathbf{p}_0), \quad [6.127]$$

$$= \frac{K_0^2 \cos^2(\theta)}{(2\pi)^2 A \cos(\theta_0)} \bar{\mathbf{R}}(\mathbf{p} | \mathbf{p}_0) \odot \bar{\mathbf{R}}(\mathbf{p} | \mathbf{p}_0), \quad [6.128]$$

where the product \odot of two matrices $\bar{\mathbf{f}}$ and $\bar{\mathbf{g}}$ is defined by:

$$\begin{aligned} \bar{\mathbf{f}} \odot \bar{\mathbf{g}} &\equiv \begin{pmatrix} f_{VV} & f_{VH} \\ f_{HV} & f_{HH} \end{pmatrix} \odot \begin{pmatrix} g_{VV} & g_{VH} \\ g_{HV} & g_{HH} \end{pmatrix} \\ &= \begin{pmatrix} f_{VV} g_{VV}^* & f_{VH} g_{VH}^* & Re(f_{VV} g_{VH}^*) & -Im(f_{VV} g_{VH}^*) \\ f_{HV} g_{HV}^* & f_{HH} g_{HH}^* & Re(f_{HV} g_{HH}^*) & -Im(f_{HV} g_{HH}^*) \\ 2Re(f_{VV} g_{HV}^*) & 2Re(f_{VH} g_{HH}^*) & Re(f_{VV} g_{VV}^* + f_{HV} g_{VH}^*) & -Im(f_{VV} g_{HH}^* - f_{VH} g_{VH}^*) \\ 2Im(f_{VV} g_{HV}^*) & 2Im(f_{VH} g_{HH}^*) & Im(f_{VV} g_{VV}^* + f_{HV} g_{VH}^*) & Re(f_{VV} g_{HH}^* - f_{VH} g_{VH}^*) \end{pmatrix}. \end{aligned} \quad [6.129]$$

The scattering from a randomly rough surface is a stochastic process, so the computations of the laser cross-section for the coherent and incoherent parts involve an average over the realizations of the surfaces. The definition of the coherent bistatic matrix reads

$$\begin{aligned} \bar{\gamma}^{coh} &\equiv \frac{1}{A \cos \theta_0} \langle \bar{\mathbf{f}}(\mathbf{p} | \mathbf{p}_0) \rangle \odot \langle \bar{\mathbf{f}}(\mathbf{p} | \mathbf{p}_0) \rangle \\ &= \frac{K_0^2 \cos^2(\theta)}{A(2\pi)^2 \cos(\theta_0)} \langle \bar{\mathbf{R}}(\mathbf{p} | \mathbf{p}_0) \rangle \odot \langle \bar{\mathbf{R}}(\mathbf{p} | \mathbf{p}_0) \rangle, \end{aligned} \quad [6.130]$$

and the definition of the incoherent bistatic matrix is

$$\begin{aligned} \bar{\gamma}^{incoh}(\mathbf{p} | \mathbf{p}_0) &\equiv \frac{1}{A \cos \theta_0} [\langle \bar{\mathbf{f}}(\mathbf{p} | \mathbf{p}_0) \odot \bar{\mathbf{f}}(\mathbf{p} | \mathbf{p}_0) \rangle \langle \bar{\mathbf{f}}(\mathbf{p} | \mathbf{p}_0) \odot \bar{\mathbf{f}}(\mathbf{p} | \mathbf{p}_0) \rangle], \\ &= \frac{K_0^2 \cos^2 \theta}{A (2\pi)^2 \cos \theta_0} [\langle \bar{\mathbf{R}}(\mathbf{p} | \mathbf{p}_0) \odot \bar{\mathbf{R}}(\mathbf{p} | \mathbf{p}_0) \rangle \\ &\quad - \langle \bar{\mathbf{R}}(\mathbf{p} | \mathbf{p}_0) \rangle \odot \langle \bar{\mathbf{R}}(\mathbf{p} | \mathbf{p}_0) \rangle]. \end{aligned} \quad [6.131]$$

These formulas are particularly important because they contain all the information about the scattering process. If we consider the case of a single rough surface, Equation [6.121], where we have

$$\bar{\Sigma}_s^0(\mathbf{p} | \mathbf{p}_0 | \boldsymbol{\xi}) = \bar{X}_s^{(2)}(\mathbf{p} | \mathbf{p} - \boldsymbol{\xi} | \mathbf{p}_0) + \bar{X}_s^{(2)}(\mathbf{p} | \mathbf{p}_0 + \boldsymbol{\xi} | \mathbf{p}_0) + i(\alpha_0(\mathbf{p}) + \alpha_0(\mathbf{p}_0))\bar{X}_s^{(1)}(\mathbf{p} | \mathbf{p}_0), \quad [6.132]$$

we must emphasize an important point: this matrix does not comply with the reciprocity condition, so we will define a reciprocal matrix by the relation:

$$\bar{\Sigma}_s(\mathbf{p} | \mathbf{p}_0 | \boldsymbol{\xi}) = \frac{1}{2}[\bar{\Sigma}_s^0(\mathbf{p} | \mathbf{p}_0 | \boldsymbol{\xi}) + \bar{\Sigma}_s^0(-\mathbf{p}_0 | -\mathbf{p} | -\boldsymbol{\xi})^{aT}], \quad [6.133]$$

where aT means the anti-transpose of a matrix, with the definition:

$$\begin{pmatrix} a & b \\ c & d \end{pmatrix}^{aT} = \begin{pmatrix} a & -c \\ -b & d \end{pmatrix}. \quad [6.134]$$

Taking the statistical average of the matrix $R^{10}(\mathbf{p} | \mathbf{p}_0)$ one obtains for the coherent part:

$$\begin{aligned} < R^{10}(\mathbf{p} | \mathbf{p}_0) > \equiv & \frac{i\alpha_0(\mathbf{p}_0)}{(\alpha_0(\mathbf{p}) + \alpha_0(\mathbf{p}_0))} e^{-(\alpha_0(\mathbf{p}) + \alpha_0(\mathbf{p}_0))^2 \sigma^2 / 2}, \\ & \int d^2 r e^{-i(\mathbf{p} - \mathbf{p}_0) \cdot \mathbf{r}} \left\{ \bar{X}_s^{(1)}(\mathbf{p} | \mathbf{p}_0) + \frac{(\alpha_0(\mathbf{p}) + \alpha_0(\mathbf{p}_0))}{2} \int \frac{d^2 \boldsymbol{\xi}}{(2\pi)^2} W(\boldsymbol{\xi}) \bar{\Sigma}_s(\mathbf{p} | \mathbf{p}_0 | \boldsymbol{\xi}) \right\}, \end{aligned} \quad [6.135]$$

and for the incoherent part the expression:

$$\begin{aligned} \bar{\gamma}^{incoh}(\mathbf{p} | \mathbf{p}_0) \equiv & \frac{K_0^2 \cos^2 \theta}{A(2\pi)^2 \cos \theta_0} [< R^{10}(\mathbf{p} | \mathbf{p}_0) \odot R^{10}(\mathbf{p} | \mathbf{p}_0) > \\ & - < R^{10}(\mathbf{p} | \mathbf{p}_0) > \odot < R^{10}(\mathbf{p} | \mathbf{p}_0) >], \end{aligned} \quad [6.136]$$

where

$$\begin{aligned}
 < R^{10}(\mathbf{p} | \mathbf{p}_0) \odot R^{10}(\mathbf{p} | \mathbf{p}_0) > &= \frac{\alpha_0(\mathbf{p}_0)\alpha_0(\mathbf{p})}{-(\alpha_0(\mathbf{p}) + \alpha(\mathbf{p}_0))^2} e^{-(\alpha_0(\mathbf{p}) + \alpha_0(\mathbf{p}_0))^2 \sigma^2/2} \\
 &\int d^2\mathbf{r} \int d^2\mathbf{r}' e^{(\alpha_0(\mathbf{p}) + \alpha_0(\mathbf{p}_0))^2 W(\mathbf{r} - \mathbf{r}')} e^{-i(\mathbf{p} - \mathbf{p}_0) \cdot (\mathbf{r} - \mathbf{r}')}. \\
 &\left\{ \left[\bar{X}_s^{(1)}(\mathbf{p}, \mathbf{p}_0) - \frac{i(\alpha_0(\mathbf{p}) + \alpha(\mathbf{p}_0))}{2} \int \frac{d^2\boldsymbol{\xi}}{(2\pi)^2} W(\boldsymbol{\xi})(e^{i\boldsymbol{\xi} \cdot (\mathbf{r} - \mathbf{r}')} - 1) \bar{\Sigma}_s(\mathbf{p} | \mathbf{p}_0 | \boldsymbol{\xi}) \right] \odot \right. \\
 &\left[\bar{X}_s^{(1)}(\mathbf{p}, \mathbf{p}_0) - \frac{i(\alpha_0(\mathbf{p}) + \alpha_0(\mathbf{p}_0))}{2} \int \frac{d^2\boldsymbol{\xi}}{(2\pi)^2} W(\boldsymbol{\xi})(e^{i\boldsymbol{\xi} \cdot (\mathbf{r} - \mathbf{r}')} - 1) \bar{\Sigma}_s(\mathbf{p} | \mathbf{p}_0 | \boldsymbol{\xi}) \right]^* \\
 &\left. + \frac{1}{4} \int \frac{d^2\boldsymbol{\xi}}{(2\pi)^2} W(\boldsymbol{\xi}) \bar{\Sigma}_s(\mathbf{p} | \mathbf{p}_0 | \boldsymbol{\xi}) \odot \bar{\Sigma}_s(\mathbf{p} | \mathbf{p}_0 | \boldsymbol{\xi}) \right\}. \quad [6.137]
 \end{aligned}$$

A randomly rough surface between two semi-infinite media

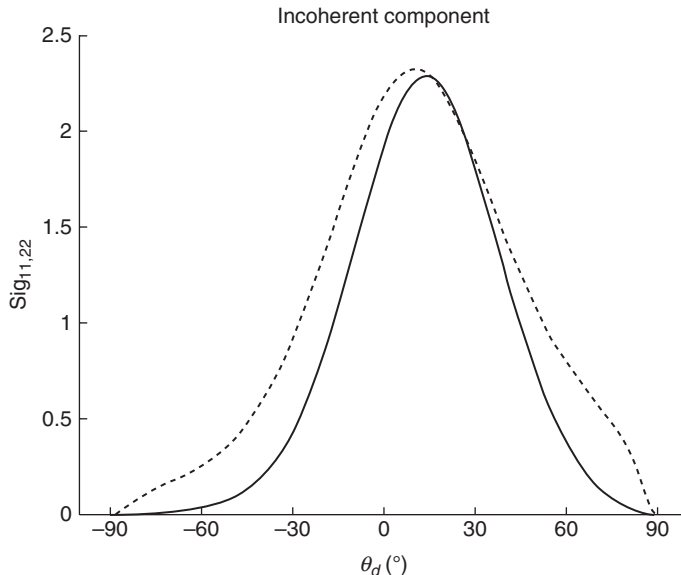
In this section we apply the above derivation to the case of a rough surface between two semi-infinite media. We consider a rough surface made of aluminum with relative permittivity $\varepsilon_1 = -40 - i1.1$. The rough surface is supposed to be homogeneous and isotropic with a rms height ($\sigma = 0.3/K_0$) of Gaussian nature, and with a correlation length ($l = 3/K_0$). The incident wave length is $\lambda = 632.8$ nm, the angle of incidence $\theta_i = 20^\circ$, and the azimuthal plane of incidence $\phi_i = 0$. The incoherent components $\gamma^{\text{incoh}}(\theta_d)$ are plotted in Fig. 6.12 and 6.13 as functions of the scattering angle θ_d , calculated up to the second order in the Small-Slope Approximation.

6.6.3 The small slope approximation and the small perturbation method for slabs with randomly rough boundaries

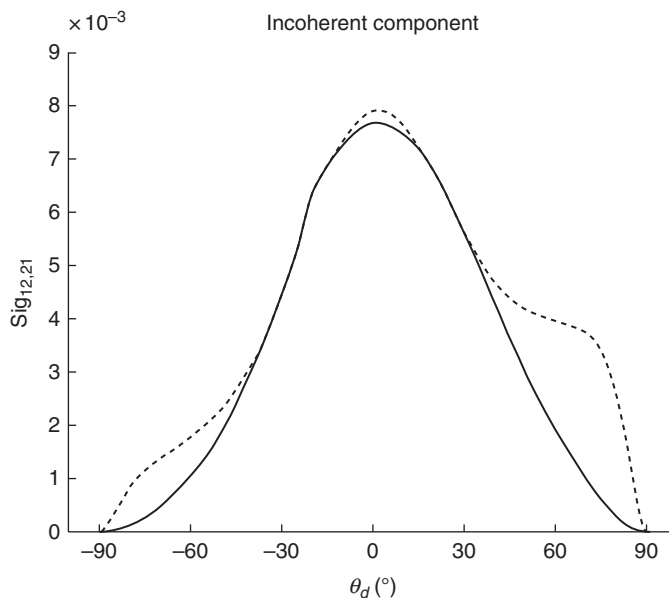
Formulation

In this section, we give some elements of the theory of the SSA and the SPM for the scattering of light from a three-dimensional slab bounded by two randomly rough surfaces. The configuration is shown in Fig. 6.10, where the three regions are characterized by different homogenous and isotropic permittivities, ε_0 , ε_1 and ε_2 . The slab is delimited by two rough surfaces located at $z = h_1(\mathbf{x})$ and $z = -\mathbf{H} + h_2(\mathbf{x})$, $\mathbf{x} = (x, y, 0)$.

The SSA method involves the knowledge of the scattering matrices calculated in the small-perturbation method. We summarize the results already obtained in Reference [23] and needed in the following. For a system with



6.12 Incoherent components $\gamma^{\text{incoh}}(\theta_d)$ as functions of the scattering angle θ_d . VV (dashed line), HH (solid line). Incident wavelength $\lambda = 632.8$ nm, height $\sigma = 0.3/K_0$, correlation length $l = 3/K_0$. Angles: $\theta_i = 20^\circ$, $\phi_i = 0^\circ$, permittivity: $\varepsilon_0 = 1$, $\varepsilon_1 = -40 - i1.1$.



6.13 Same characteristics as for Fig. 6.12 Components VH (dashed line), and HV (solid line).

two rough surfaces the perturbative development of the scattering matrix $\bar{\mathbf{R}}$ can be expanded as:

$$\mathbf{R} = \bar{\mathbf{R}}^{(00)} + \bar{\mathbf{R}}^{(10)} + \bar{\mathbf{R}}^{(01)} + \bar{\mathbf{R}}^{(11)} + \bar{\mathbf{R}}^{(20)} + \bar{\mathbf{R}}^{(21)} + \bar{\mathbf{R}}^{(22)} + \bar{\mathbf{R}}^{(30)} + \bar{\mathbf{R}}^{(03)} + \dots \quad [6.138]$$

where the terms associated with the products of the heights of the two surfaces $h_1^n h_2^m$ are labelled $\bar{\mathbf{R}}^{(nm)}$.

Concerning the bistatic incoherent cross-sections, we decompose their expressions into three terms corresponding to the contributions of the upper and lower surfaces alone plus a contribution due to the interferences between the two rough surfaces,

$$\bar{\gamma}^{incoh}(\mathbf{p} | \mathbf{p}_0) = \bar{\gamma}_u^{incoh}(\mathbf{p} | \mathbf{p}_0) + \bar{\gamma}_d^{incoh}(\mathbf{p} | \mathbf{p}_0) + \bar{\gamma}_{ud}^{incoh}(\mathbf{p} | \mathbf{p}_0), \quad [6.139]$$

where

$$\bar{\gamma}_u^{incoh}(\mathbf{p} | \mathbf{p}_0) = \frac{K_0^2 \cos^2 \theta}{A(2\pi)^2 \cos \theta_0} \left[< \bar{\mathbf{R}}^{(10)} \odot \bar{\mathbf{R}}^{(10)} > + < \bar{\mathbf{R}}^{(20)} \odot \bar{\mathbf{R}}^{(20)} > + < \bar{\mathbf{R}}^{(30)} \odot \bar{\mathbf{R}}^{(10)} > \right] \quad [6.140]$$

corresponds to the contribution of the upper surface ($h_1(\mathbf{x}) = 0$), where the perturbative expansion is limited to the order 3 as a function of the mean height σ_1 . In a similar way the contribution due to the lower surface can be written by permuting the upper indices. The interference term $\bar{\gamma}_{ud}^{incoh}$, contains the contributions of the field interacting with the two rough surfaces, and the dominant parts are given by

$$\begin{aligned} \bar{\gamma}_{ud}^{incoh}(\mathbf{p} | \mathbf{p}_0) = & \frac{K_0^2 \cos^2 \theta}{A(2\pi)^2 \cos \theta_0} \left[< \bar{\mathbf{R}}^{(10)} \odot \bar{\mathbf{R}}^{(12)} > + < \bar{\mathbf{R}}^{(12)} \odot \bar{\mathbf{R}}^{(10)} > \right. \\ & + < \bar{\mathbf{R}}^{(01)} \odot \bar{\mathbf{R}}^{(21)} > + < \bar{\mathbf{R}}^{(21)} \odot \bar{\mathbf{R}}^{(01)} > \\ & \left. + < \bar{\mathbf{R}}^{(11)} \odot \bar{\mathbf{R}}^{(11)} > + \dots \right]. \end{aligned} \quad [6.141]$$

These contributions contain all the terms with the elements $\sigma_1^i \sigma_2^j$ ($1 \leq i+j \leq 4$). If the values σ_1 and σ_2 are close, their contributions will be equivalent to fourth order terms in Equations [6.140] and [6.141]. So we have supposed in Equation [6.141] that the terms corresponding to

$\sigma_1^4\sigma_2^2, \sigma_1^2\sigma_2^4, \sigma_1^4\sigma_2^4$ are negligible compared to the terms kept in Equation [6.141].

In the case of the SSA method we will study a perturbative development of the scattered field which depends on the slopes of the surfaces h_1, h_2 . The scattering matrix we have used in previous sections must be generalized to the case with two randomly rough surfaces. We propose the following generalization with an ‘Ansatz’ similar to the functional form proposed by Voronovich:

$$\bar{R}(\mathbf{p}, \mathbf{p}_0) = \int d^2\mathbf{r} d^2\mathbf{r}' \exp[-i(\mathbf{p} - \mathbf{p}_0) \cdot (\mathbf{r} + \mathbf{r}') - i(\alpha(\mathbf{p}) + \alpha(\mathbf{p}_0))(h_1(\mathbf{r}) + h_2(\mathbf{r}'))] \times \bar{\Phi}[\mathbf{p}, \mathbf{p}_0; \mathbf{r}; \mathbf{r}'; [h_1(\mathbf{r})]; [h_2(\mathbf{r}')]]. \quad [6.142]$$

A natural extension of the scattering amplitude involving two rough surfaces reads in Fourier space:

$$\bar{R}(\mathbf{p}, \mathbf{p}_0) = \int d^2\mathbf{r} d^2\mathbf{r}' \frac{d^2\xi}{(2\pi)^2} \frac{d^2\xi'}{(2\pi)^2} \times \exp[-i(\mathbf{p} - \mathbf{p}_0 - \xi) \cdot \mathbf{r} - i(\mathbf{p} - \mathbf{p}_0 - \xi') \cdot \mathbf{r}' - (\alpha(\mathbf{p}) + \alpha(\mathbf{p}_0))(h_1(\mathbf{r}) + h_2(\mathbf{r}'))] \times \tilde{\Phi}[\mathbf{p}, \mathbf{p}_0; \xi; \xi'; [h_1(\xi)]; [h_2(\xi')]], \quad [6.143]$$

where, $h_1(\xi)$ and $h_2(\xi)$ are the Fourier transforms of the roughnesses of the different surfaces. Following the method proposed by Voronovich we expand the functional $\tilde{\Phi}$ in the form of a Taylor series:

$$\tilde{\Phi}(\mathbf{p}, \mathbf{p}_0, \xi, \xi') = \sum_{nm, i_1 \dots i_p} \int d^2\xi_1 \dots d^2\xi_p \delta(\xi - \xi_1 - \dots - \xi_p) \tilde{\Phi}^{(nm)i_1 \dots i_p}(\xi_1 \dots \xi_p) h_1(\xi_1) \dots h_2(\xi_p), \quad [6.144]$$

where we have truncated the series at the fourth order. $\tilde{\Phi}^{(nm)i_1 \dots i_p}(\xi_1 \dots \xi_p)$ represent the 14 unknown kernel functions we have to determine for this structure. From gauge transformations we can derive an important relation between the orders $n - 1; n; n + 1$, namely:

$$\tilde{\Phi}^{(nm)} = [\tilde{\Phi}^{(nm)} - \tilde{\Phi}^{(nm)}|_{\xi_n=p-p_0-\xi_1-\dots-\xi_{n-1}}] + \tilde{\Phi}^{(nm)}|_{\xi_n=p-p_0-\xi_1-\dots-\xi_{n-1}}. \quad [6.145]$$

As an example of the expression of order 2 in the above series we obtain the complex expression:

$$\begin{aligned}
 & \int \frac{d^2 p_1}{(2\pi)^2} \left[-\frac{(\alpha_0(p) + \alpha_0(p_0))^2}{2} (\tilde{\Phi}_u^{(0)}(p, p_0) + \tilde{\Phi}_d^{(0)}(p, p_0)) \right. \\
 & \quad \left. + \tilde{\Phi}^{(11)12}(p, p_0, p - p_1, p_1 - p_0) \right] h_1(p - p_1) h_2(p - p_0) \\
 & + \int \frac{d^2 p_1}{(2\pi)^2} \left[-\frac{(\alpha_0(p) + \alpha_0(p_0))^2}{2} (\tilde{\Phi}_u^{(0)}(p, p_0) + \tilde{\Phi}_d^{(0)}(p, p_0)) \right. \\
 & \quad \left. + \tilde{\Phi}^{(11)21}(p, p_0, p - p_1, p_1 - p_0) \right] h_2(p - p_1) h_1(p_1 - p_0) \\
 & + \int \frac{d^2 p_1}{(2\pi)^2} \left[-\frac{(\alpha_0(p) + \alpha_0(p_0))^2}{2} \tilde{\Phi}_u^{(0)}(p, p_0) \right. \\
 & \quad \left. + \tilde{\Phi}^{(20)}(p, p_0, p - p_1, p_1 - p_0) \right] h_1(p - p_1) h_1(p - p_0) \\
 & + \int \frac{d^2 p_1}{(2\pi)^2} \left[-\frac{(\alpha_0(p) + \alpha_0(p_0))^2}{2} \tilde{\Phi}_d^{(0)}(p, p_0) \right. \\
 & \quad \left. + \tilde{\Phi}^{(02)}(p, p_0, p - p_1, p_1 - p_0) \right] h_2(p - p_1) h_2(p_1 - p_0). \tag{6.146}
 \end{aligned}$$

We can find the expressions for the different orders in Reference [76]. The kernel functions can be computed. For each order of the small-slope approximation the functions $\tilde{\Phi}^{(nm)}$ are identified with $\bar{X}^{(nm)}$ obtained from the small-amplitude perturbation method described in Reference [59].

For instance, $\tilde{\Phi}^{(12)221}$ describes the interaction of the electromagnetic field once with the upper surface and twice with the lower surface in the order 2-2-1 (see Reference [76] for the expressions for the different contributions).

We have:

$$\begin{aligned}
 \tilde{\Phi}^{(12)221}(p, p_0, \xi_1, \xi_2, \xi_3) = & \frac{i \alpha_0(p_0)}{\alpha_0(p) + \alpha_0(p_0)} \\
 & \left\{ \frac{1}{5} \left[\bar{X}^{(22)1221} + \bar{X}^{(22)2121} + \bar{X}^{(22)2211} + \bar{X}^{(13)2221} + \bar{X}^{(13)2212} \right] \right. \\
 & + i \frac{1}{240} (\alpha_0(p) + \alpha_0(p_0)) \left[72 \bar{X}^{(21)211} + 90 \bar{X}^{(21)121} + 18 \bar{X}^{(21)112} + 138 \bar{X}^{(12)212} \right. \\
 & \left. + 66 \bar{X}^{(12)122} + 216 \bar{X}^{(12)221} + 24 \bar{X}^{(30)} + 120 \bar{X}^{(03)} \right] \\
 & - \frac{1}{240} (\alpha_0(p) + \alpha_0(p_0))^2 \left[312 \bar{X}^{(11)12} + 516 \bar{X}^{(11)21} + 749 \bar{X}^{(02)} + 389 \bar{X}^{(20)} \right] \\
 & \left. - i \frac{1}{480} (\alpha_0(p) + \alpha_0(p_0))^3 (1445 \bar{X}_u^{(1)} + 1837 \bar{X}_d^{(1)}) \right\}. \tag{6.147}
 \end{aligned}$$

When the expressions $\tilde{\Phi}^{(nm)}$ are calculated we can deduce the scattering matrices $\bar{R}^{(nm)}$. With the definition of the following integration operator $J^{(n)}$

$$\begin{aligned} J^{(n)} = & \int d^2\mathbf{r} d^2\mathbf{r}' \frac{d^2\xi}{(2\pi)^2} \frac{d^2\xi'}{(2\pi)^2} \frac{d^2\xi_1}{(2\pi)^2} \dots \frac{d^2\xi_n}{(2\pi)^2} \\ & \times \exp [-i(\mathbf{p} - \mathbf{p}_0 - \xi) \cdot \mathbf{r} - i(\mathbf{p} - \mathbf{p}_0 - \xi') \cdot \mathbf{r}' \\ & - i(\alpha(\mathbf{p}) + \alpha(\mathbf{p}_0))(h_1(\mathbf{r}) + h_2(\mathbf{r}'))], \end{aligned} \quad [6.148]$$

we obtain the expressions:

$$\begin{aligned} \bar{R}^{(10)}(\mathbf{p} | \mathbf{p}_0) &= J^{(1)} \tilde{\Phi}^{(10)}(\mathbf{p}, \mathbf{p}_0, \xi_1) h_1(\xi_1) \\ \bar{R}^{(01)}(\mathbf{p} | \mathbf{p}_0) &= J^{(1)} \tilde{\Phi}^{(01)}(\mathbf{p}, \mathbf{p}_0, \xi_1) h_2(\xi_1) \\ \bar{R}^{(11)}(\mathbf{p} | \mathbf{p}_0) &= J^{(2)} \left[\tilde{\Phi}^{(11)12}(\mathbf{p}, \mathbf{p}_0, \xi_1, \xi_2) h_1(\xi_1) h_2(\xi_2) \right. \\ &\quad \left. + \tilde{\Phi}^{(11)21}(\mathbf{p}, \mathbf{p}_0, \xi_1, \xi_2) h_2(\xi_2) h_1(\xi_1) \right] \\ \bar{R}^{(20)}(\mathbf{p} | \mathbf{p}_0) &= J^{(2)} \tilde{\Phi}^{(20)}(\mathbf{p}, \mathbf{p}_0, \xi_1, \xi_2, \xi) h_1(\xi_1) h_1(\xi_2) \\ \bar{R}^{(02)}(\mathbf{p} | \mathbf{p}_0) &= J^{(2)} \tilde{\Phi}^{(02)}(\mathbf{p}, \mathbf{p}_0, \xi', \xi_1, \xi_2) h_2(\xi_1) h_2(\xi_2) \\ \bar{R}^{(21)}(\mathbf{p} | \mathbf{p}_0) &= J^{(3)} \left[\tilde{\Phi}^{(21)112}(\mathbf{p}, \mathbf{p}_0, \xi_1, \xi_2, \xi_3) h_1(\xi_1) h_1(\xi_2) h_2(\xi_3) \right. \\ &\quad \left. + \tilde{\Phi}^{(21)121}(\mathbf{p}, \mathbf{p}_0, \xi_1, \xi_2, \xi_3) h_1(\xi_1) h_2(\xi_3) h_2(\xi_2) \right. \\ &\quad \left. + \tilde{\Phi}^{(21)211}(\mathbf{p}, \mathbf{p}_0, \xi_1, \xi_2, \xi_3) h_2(\xi_3) h_1(\xi_1) h_1(\xi_2) \right] \\ \bar{R}^{(12)}(\mathbf{p} | \mathbf{p}_0) &= J^{(3)} \left[\tilde{\Phi}^{(12)221}(\mathbf{p}, \mathbf{p}_0, \xi_1, \xi_2, \xi_3) h_2(\xi_1) h_2(\xi_2) h_1(\xi_3) \right. \\ &\quad \left. + \tilde{\Phi}^{(12)212}(\mathbf{p}, \mathbf{p}_0, \xi_1, \xi_2, \xi_3) h_2(\xi_1) h_1(\xi_3) h_2(\xi_2) \right. \\ &\quad \left. + \tilde{\Phi}^{(12)122}(\mathbf{p}, \mathbf{p}_0, \xi_1, \xi_2, \xi_3) h_1(\xi_3) h_2(\xi_1) h_2(\xi_2) \right] \\ \bar{R}^{(30)}(\mathbf{p} | \mathbf{p}_0) &= J^{(3)} \tilde{\Phi}^{(30)}(\mathbf{p}, \mathbf{p}_0, \xi_1, \xi_2, \xi_3) h_1(\xi_1) h_1(\xi_2) h_1(\xi_3) \\ \bar{R}^{(03)}(\mathbf{p} | \mathbf{p}_0) &= J^{(3)} \tilde{\Phi}^{(03)}(\mathbf{p}, \mathbf{p}_0, \xi_1, \xi_2, \xi_3) h_2(\xi_1) h_2(\xi_2) h_2(\xi_3). \end{aligned} \quad [6.149]$$

To calculate the bistatic cross-section, we take the expansion of \bar{R} in terms of the (mn) scattering matrices given by $\bar{R}^{(nm)}$. The incoherent bistatic cross-section is given by:

$$\bar{\gamma}_{ij}^{incoh}(\mathbf{p} | \mathbf{p}_0) = \frac{K_0^2 \cos^2 \theta}{A (2\pi)^2 \cos \theta_0} \left[< \bar{R}(\mathbf{p} | \mathbf{p}_0) \odot \bar{R}(\mathbf{p} | \mathbf{p}_0) > \right. \\ \left. - < \bar{R}(\mathbf{p} | \mathbf{p}_0) > \odot < \bar{R}(\mathbf{p} | \mathbf{p}_0) > \right], \quad [6.150]$$

where the angle brackets denote an average over the ensembles of realizations of the functions $h_i(r)$, and ij are the polarization components.

An example of a contribution coming from $4h_2$ heights reads:⁷⁶

$$\begin{aligned}
 & \langle \bar{\mathbf{R}}^{(03)}(\mathbf{p} | \mathbf{p}_0) \odot \bar{\mathbf{R}}^{(01)}(\mathbf{p} | \mathbf{p}_0) \rangle = \exp [-(\alpha_0(\mathbf{p}) + \alpha_0(\mathbf{p}_0))^2 / 2W_{22}(0)] \\
 & \times \int d^2x_1 d^2x_2 \exp [-i(\mathbf{p} - \mathbf{p}_0)(\mathbf{x}_1 - \mathbf{x}_2)] \exp [(\alpha_0(\mathbf{p}) + \alpha_0(\mathbf{p}_0))^2 W_{22}(\mathbf{x}_1 - \mathbf{x}_2)] \\
 & \times \int \frac{d^2\xi}{(2\pi)^2} \exp [i\xi(\mathbf{x}_1 - \mathbf{x}_2)] W_{22}(\xi) \int \frac{d^2\xi_2}{(2\pi)^2} W_{22}(\xi_2) \left[\widetilde{\Phi}^{(03)}(\mathbf{p}, \mathbf{p}_0, \xi, \xi_2, -\xi_2) \odot \widetilde{\Phi}^{(01)*}(\mathbf{p}, \mathbf{p}_0, \xi) \right. \\
 & + \widetilde{\Phi}^{(03)}(\mathbf{p}, \mathbf{p}_0, \xi_2, \xi, -\xi_2) \odot \widetilde{\Phi}^{(01)*}(\mathbf{p}, \mathbf{p}_0, \xi) \\
 & \left. + \widetilde{\Phi}^{(03)}(\mathbf{p}, \mathbf{p}_0, \xi_2, -\xi_2, \xi) \odot \widetilde{\Phi}^{(01)*}(\mathbf{p}, \mathbf{p}_0, \xi) \right],
 \end{aligned}$$
[6.151]

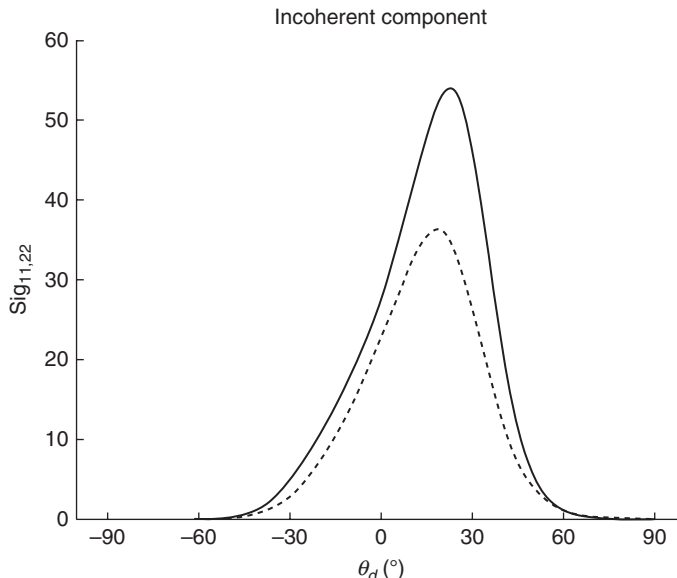
where we have assumed a Gaussian expression for the heights in our applications, and W_{ij} are the correlation functions associated with the surfaces.

Applications of the SSA method

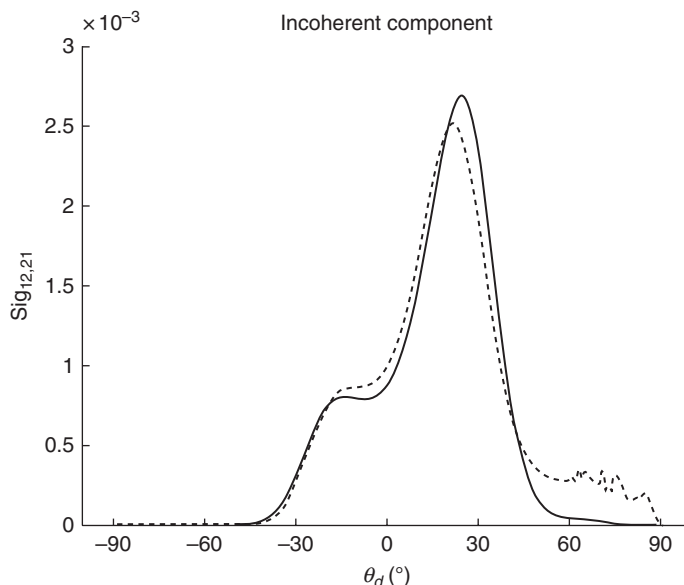
In this section, we give some examples of films with two-dimensional randomly rough surfaces. In the following, the complex pattern of the cross-section is related to the randomly rough surfaces. For the first example, we take as the incident medium a vacuum followed by a dielectric medium ($\epsilon_1 = 1.62 + i0.001$), the boundary being a rough surface with a rms height $\sigma = 0.223 \mu\text{m}$, a correlation length $l = 1.42 \mu\text{m}$, the incident wavelength $\lambda = 632.8 \text{ nm}$, the angle of incidence $\theta_i = 20^\circ$ and the azimuthal angle $\phi_i = 0^\circ$. We introduce a slab of thickness $H = 500 \text{ nm}$ with a perfectly conducting lower planar surface. The results are presented in Figs 6.14 and 6.15. We observe the same maximum around the backscattering direction for the polarizations VV and HH but an increase of the scattered intensity by a factor of 100. We notice for the polarizations HV and VH the presence of small oscillations for $\theta_d > 60^\circ$ due to the numerical integration method.

We take as another example a slab of thickness $H = 500 \text{ nm}$, with an upper rough surface $\sigma = 15 \text{ nm}$, $l = 100 \text{ nm}$, and a lower planar surface made of a perfect conductor. The successive media are defined with the following permittivities: $\epsilon_0 = 1$, $\epsilon_1 = 2.6896 + i0.0075$. The wavelength is $\lambda = 632.8 \text{ nm}$ and the angle of incidence is $\theta_i = 20^\circ$. The results are shown in Figs 6.16 and 6.17. The intensities are concentrated in the backscattering region for the polarizations VV and HH , while for the VH and VH polarizations the intensities reach maxima in a region opposite the incident scattering angle.

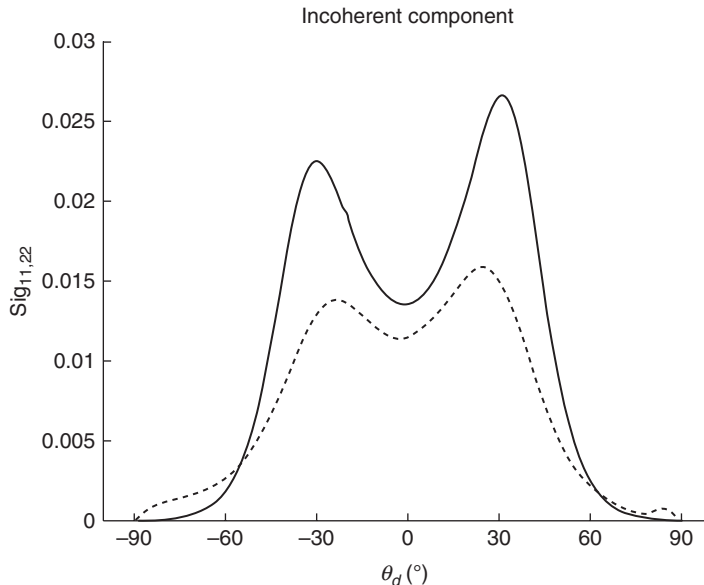
For the last example we take a slab of thickness $H = 500 \text{ nm}$, with an upper rough surface characterized by the parameters: rms height $\sigma_1 = 15 \text{ nm}$, correlation length $l_1 = 100 \text{ nm}$ and a lower rough surface: $\sigma_2 =$



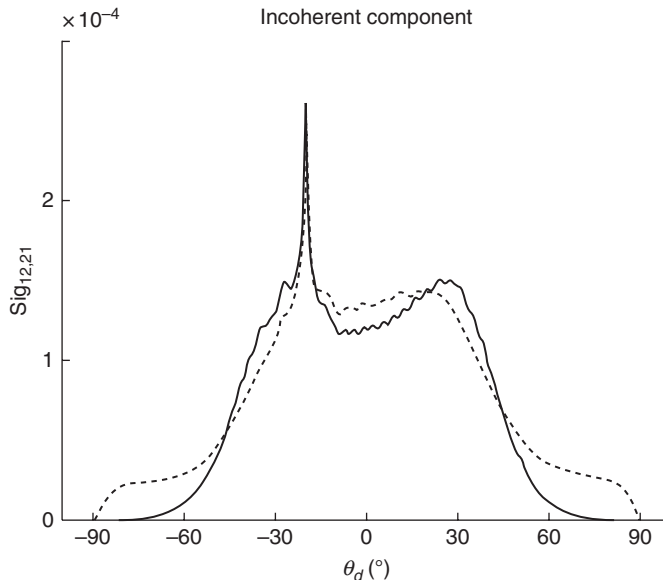
6.14 Incoherent components $\gamma^{\text{incoh}}(\theta_d)$ to the order 2. VV (dashed curve), HH (solid curve), Surface height $\sigma = 0.223 \mu\text{m}$, correlation length $l = 1.42 \mu\text{m}$, slab thickness 500 nm. Permittivities $\varepsilon_0 = 1$, $\varepsilon_1 = 1.62 + i0.001$, $\varepsilon_2 = +i\infty$. Incident angles: $\theta_i = 20^\circ$, $\phi_i = 0^\circ$, wavelength $\lambda = 632.8 \text{ nm}$.



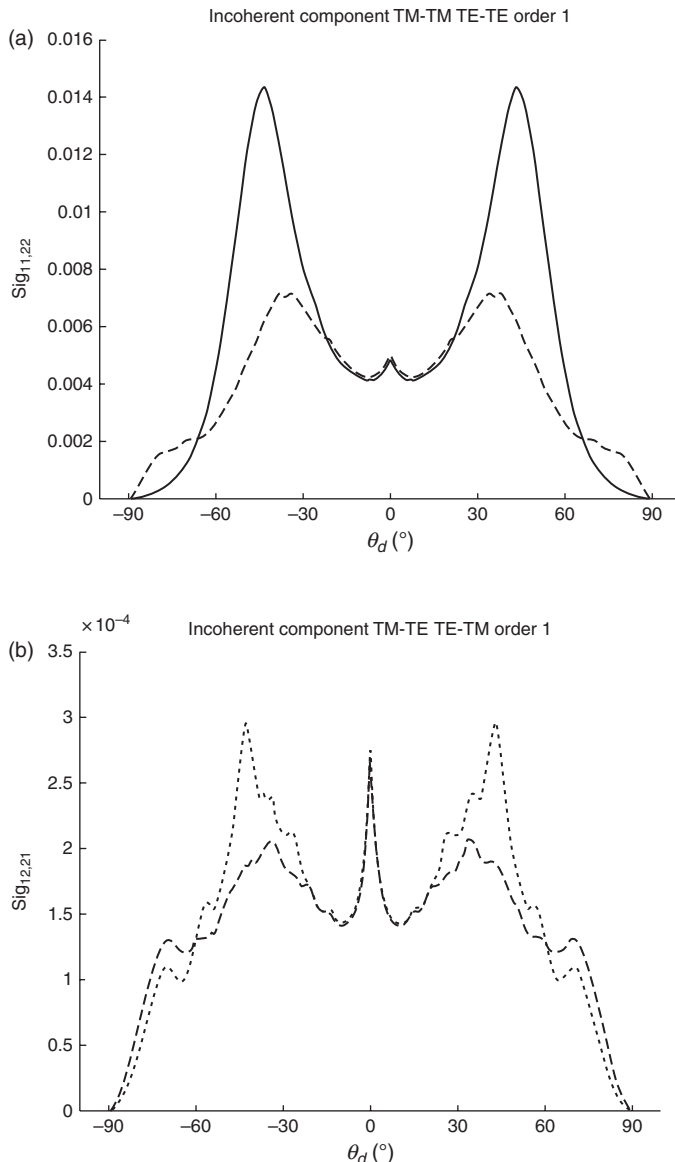
6.15 Same characteristics as for Fig. 6.14. Incoherent components VH (dashed line) and HV (solid line).



6.16 Incoherent components $\gamma^{\text{incoh}}(\theta_d)$ to the order 2, VV (dashed line), HH (solid line), surface height $\sigma = 15 \text{ nm}$, correlation length $l = 100 \text{ nm}$, slab thickness 500 nm. Permittivities $\epsilon_0 = 1$, $\epsilon_1 = 2.6896 + i0.0075$, $\epsilon_2 = +i\infty$. Incident angles: $\theta_i = 20^\circ$, $\phi_i = 0^\circ$, wavelength $\lambda = 632.8 \text{ nm}$.



6.17 Same characteristics as for Fig. 6.16. Incoherent components VH (dashed line) and HV (solid line).



6.18 Incoherent components $\gamma^{\text{incoh}}(\theta_d)$: VV (dashed-dotted line), HH (solid line), HV (dashed line), VH (dotted line).

5 nm, $l_2 = 100$ nm. The permittivities of the successive media are: $\epsilon_0 = 1$, $\epsilon_1 = 2.6896 + i0.0075$ and $\epsilon_2 = -18.3 + i0.55$. The incident angles are $\theta_i = 0^\circ$, $\phi_i = 0^\circ$ and the wavelength is $\lambda = 632.8$ nm. The results to the order 1 are plotted in Fig. 6.18.

6.6.4 Conclusions

In this section, we have presented numerical results for the scattering of light from random rough films with the small-slope approximation and the small-perturbation method. We have shown the development of the SSA series with the third-order SPM kernel. These formulations generalize the SSA to a layer bounded with two randomly rough surfaces. The new terms introduced in the SSA development estimate the coupling between the two rough surfaces. We have given the complete expressions of the scattering matrices and the expressions of the cross-sections needed for the different polarization states by introducing the Mueller matrices. With this formulation of the SSA, we have observed the backscattering enhancement for a rough layer. The calculation of the scattering amplitudes involves a knowledge of the SPM scattering matrices. We have used those obtained in References [74] and [23]. This type of simulation computation can give some experimental conditions and specifications to realize integrated optical devices that use metallic or metallo-dielectric nano-scale structures.

6.7 Theoretical methods for the scattering of polarized light from randomly rough interfaces and random media

Random volume and surface scattering is a topic that has been studied in many domains such as optical wave propagation in turbulent media, plasmonics and surface optics. Random media have attracted much attention, not only in electromagnetic wave propagation, but also in solid-state physics. On the other hand, randomly rough boundary scattering has been investigated to predict the angular distribution of the scattered waves. Useful phenomena in the optical range can be produced by random media with randomly rough surfaces. Designing disordered slabs with rough surfaces can produce new optical components, which can transmit or scatter optical fields with specified angular, spatial or spectral properties. The equations for field moments in random media are known as: the Dyson equation for the first moment, the mean value of the field or the coherent part of the interaction with the random medium; and the Bethe-Salpeter equation for the second moment, the mean value of the intensity or the incoherent part of the interaction with the random medium. They have been widely discussed in the literature.^{58,77–80} As a rule, the complexity of the calculation of the statistical moments increases with their order. In this section, we consider a three-dimensional disordered medium with randomly rough interfaces. We gave in an explicit way^{81,82} the theoretical formulas, which describe the intensity of a wave scattered from a disordered medium with rough surfaces. The

governing equation can be written in the form of a Bethe-Salpeter equation. The problem is then reduced to finding a good approximation to the solution of this equation. For a three-dimensional system composed of a random medium bounded by two randomly rough surfaces, the Bethe-Salpeter equation is constructed in order that the medium and the boundaries are treated on the same footing. This unified Bethe-Salpeter equation enables us to obtain a general expression, whatever the choice of the scattering operators used at the boundaries. We present a theory of transport based on the Bethe-Salpeter equation. We confine our considerations to the necessary background, and quote the final results.

6.7.1 Specific intensity and cross-section

The main characteristic we must study is the specific intensity $I(\mathbf{R}, \mathbf{k})$. If we take into account the polarization of the wave, the specific intensity is defined as a Stokes vector or a tensor which gives the intensity at the point \mathbf{R} in the direction $\hat{\mathbf{k}}$. If particles are inside a slab with a permittivity different from that of the outside medium, boundary conditions must be added to the radiative transfer equation in order to calculate the specific intensity. For rough surfaces, these boundary conditions are expressed in terms of scattering operators, where several approximate analytical expressions exist depending on the roughness of the surface, for example the SPM or the SSA. It can be shown that the specific intensity can be deduced from the Wigner function of the electric field. After having determined the relation between the electromagnetic field and the specific intensity, we can derive the radiative transfer equation from the Maxwell equations. The procedure is to write the Maxwell equations in an integral form with the help of Green functions and to apply the Wigner transform to the equation obtained. The main advantage to starting from wave equations is that we are able to take into account new contributions to the scattered intensity such as the enhanced backscattering and the correlations between the scatterers that cannot be obtained from phenomenological radiometric considerations. Our objective in this section is to derive the radiative transfer equations from the wave equations, taking into account rough boundaries. Several works have investigated this topic.⁸³⁻⁸⁹ In our approach, we use scattering operators, which are a unified way to describe how the electromagnetic waves interact with the boundaries. To use these operators, we have introduced two kinds of Green functions.⁸¹ The first one $\bar{\mathbf{G}}_{sv}$ describes the field scattered by the volume (V), which contains the scatterers, and by the rough surfaces (S). The second type of Green function is $\bar{\mathbf{G}}_s$, which gives the field scattered by a slab with rough boundaries where the scatterers have been replaced by a homogeneous

medium described by an effective permittivity. With these Green functions, we can separate the contributions of the surfaces and the volume. The main advantage of our approach is that the equations obtained are similar to the equations generally used to describe the wave scattered by an infinite random medium. The geometry of the problem and the notations are described in Section 6.6.1. We give the definitions of the incident and scattered wave vectors we use in Figs 6.19 and 6.20. We consider harmonic waves with $e^{-i\omega t}$ time dependence. In order to characterize the intensity of a field scattered by an object, we usually introduce the bistatic cross section, which is the power scattered per solid angle normalized by the incident power. In this section, we will use a generalization of this concept called Mueller bistatic cross section, which enables us to account for every polarization state of the incident and scattered wave. First we define the different geometrical components. We have:

$$K_0^2 = \epsilon_0 \left(\frac{\omega}{c_{vac}} \right)^2, K_1^2 = \epsilon_1 \left(\frac{\omega}{c_{vac}} \right)^2. \quad [6.152]$$

We define the wave vectors $\mathbf{k}_p^{0\pm}$ and $\mathbf{k}_p^{1\pm}$ by:

$$\mathbf{k}_p^{0\pm} \equiv \mathbf{p} \pm \alpha_0(\mathbf{p}) \hat{\mathbf{e}}_z \quad [6.153]$$

$$\mathbf{k}_p^{1\pm} \equiv \mathbf{p} \pm \alpha_1(\mathbf{p}) \hat{\mathbf{e}}_z \quad [6.154]$$

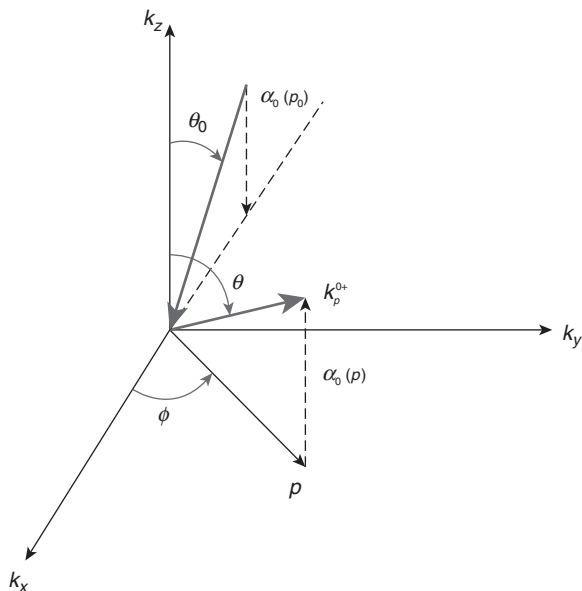
where

$$\alpha_0(\mathbf{p}) = \sqrt{K_0^2 - \mathbf{p}^2}, \alpha_1(\mathbf{p}) = \sqrt{K_1^2 - \mathbf{p}^2}. \quad [6.155]$$

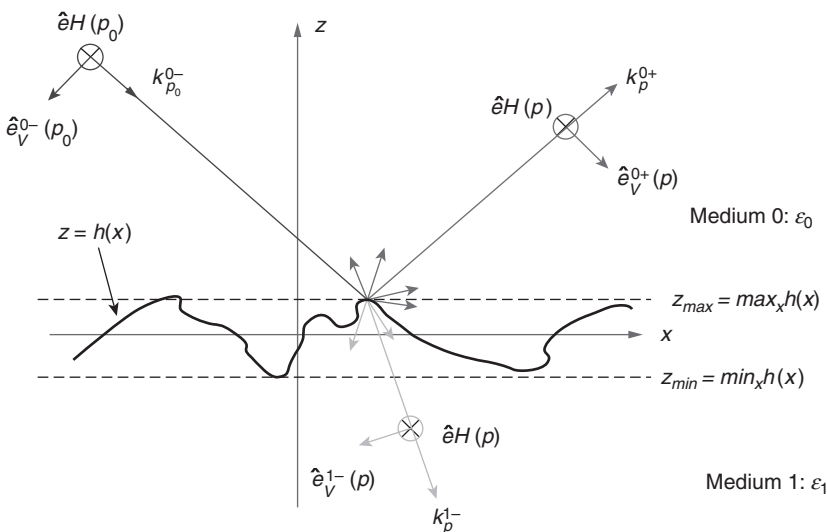
We now define the field $\mathbf{E}_S^{0s}(\mathbf{r})$ scattered by the interfaces without any interaction with the scatterers, and the field $\mathbf{E}_S^{1t}(\mathbf{r})$ transmitted into the layer before an interaction with the scatterers. Their expressions are given by:

$$\mathbf{E}_S^{0s}(\mathbf{r}) = \int \frac{d^2 p}{(2\pi)^2} e^{i p \cdot x + i \alpha_0(p) z} \bar{\mathbf{S}}^{0+,0-}(\mathbf{p} | \mathbf{p}_0) \cdot \mathbf{E}^{0\,i}(\mathbf{p}_0), \quad [6.156]$$

$$\mathbf{E}_S^{1t}(x, z) = \int \frac{d^2 p}{(2\pi)^2} e^{i p \cdot x} \left[e^{i \alpha_1(p) z} \bar{\mathbf{S}}^{1+,0-}(\mathbf{p} | \mathbf{p}_0) + e^{-i \alpha_1(p) z} \bar{\mathbf{S}}^{1-,0-}(\mathbf{p} | \mathbf{p}_0) \right] \cdot \mathbf{E}^{0\,i}(\mathbf{p}_0), \quad [6.157]$$



6.19 Decomposition of the wave vectors with $\theta, \theta_0 \in [-\pi/2, \pi/2]$ and $\phi, \phi_0 \in [0, \pi]$. θ_0 is the incidence angle, θ is the scattering angle.

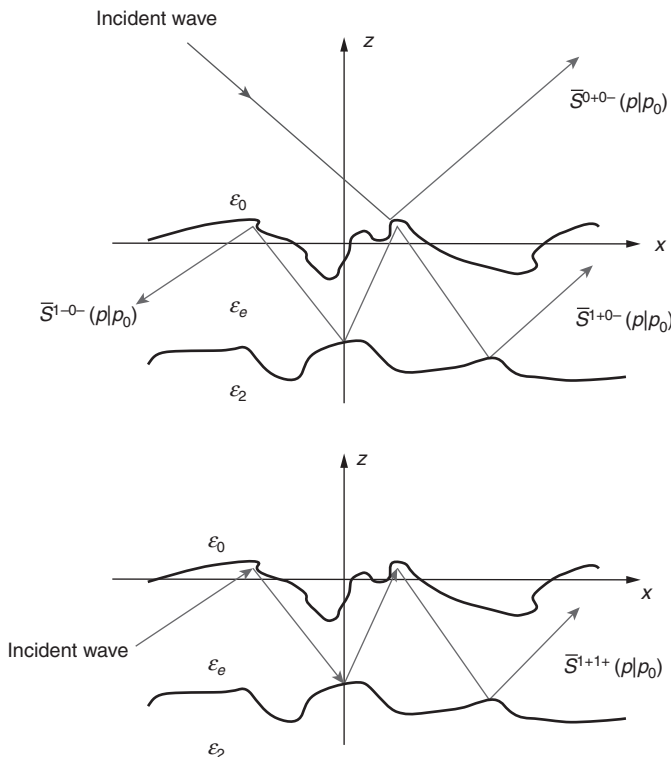


6.20 Scattering of an incident plane wave with a wave vector $k_{p_0}^{0-}$, reflected wave vector k_p^{0+} , transmitted wave vector k_p^{0-} . The polarization bases TE and TM are given for each wave.

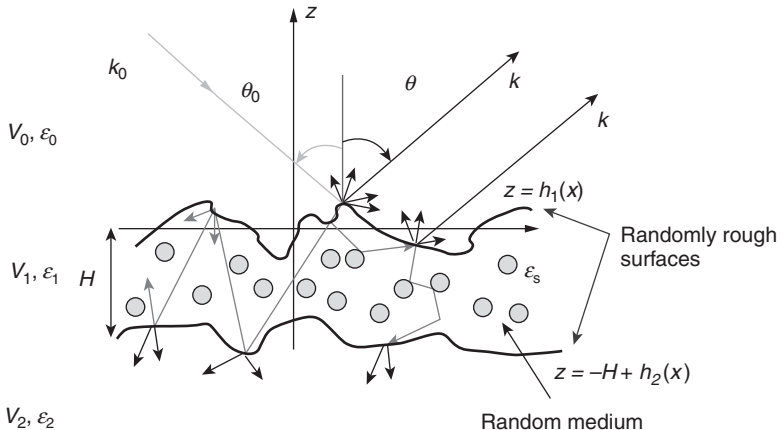
where $\mathbf{E}^{0i}(\mathbf{r})$ represents the incident field. We define an upgoing wave if the wave vector is directed along $z > 0$ ($a = +$), and a downgoing wave if the wave vector is directed along $z < 0$ ($a = -$). For the matrices and the operators, we introduce the following notations.

For example, $\bar{\mathcal{S}}^{1+,0-}(p|p_0)$ describes the scattering operator of an incident downgoing wave from medium 0 which is scattered into an upgoing wave in medium 1, that is, the source in the medium 0 generates in the medium 1 a transmitted downgoing wave, which after a reflection on the second rough surface generates an upgoing wave. In Fig. 6.21, we give the representations of different scattering operators. We notice that we have replaced the permittivity of the medium by an effective permittivity which will be defined in Section 6.7.3. With this effective permittivity we can consider the medium as homogeneous.

First of all, as an intermediate calculation, we have to introduce the scattering operators describing the field scattered by the rough surfaces and the random media. The slab is described in Fig. 6.22. We are going to study a



6.21 Definition of the scattering operators.



6.22 Random volume with rough boundaries.

three-dimensional system (see Fig. 6.22), which is composed of an incident medium of permittivity ϵ_0 , a first randomly rough boundary at $z = 0$, a random medium defined by a permittivity ϵ_1 which contains scatterers, a second randomly rough boundary at $z = -H$ and a semi-infinite homogeneous medium with a permittivity ϵ_2 .

The field scattered by the random medium and the rough boundaries is:

$$\mathbf{E}_{SV}^{0s}(\mathbf{r}) = \int \frac{d^2\mathbf{p}}{(2\pi)^2} e^{i\mathbf{p}\cdot\mathbf{r} + i\alpha_0(\mathbf{p})z} \bar{\mathbf{R}}_{SV}(\mathbf{p} | \mathbf{p}_0) \cdot \mathbf{E}^{0i}(\mathbf{p}_0). \quad [6.158]$$

We can write the scattering operators in the bases defined in Fig. 6.20 with a dyadic notation as follows:

$$\begin{aligned} \bar{\mathbf{R}}_{SV}(\mathbf{p} | \mathbf{p}_0) = & R_{SV}(\mathbf{p} | \mathbf{p}_0)_{VV} \hat{e}_V^{0+}(\mathbf{p}) \hat{e}_V^{0-}(\mathbf{p}_0) + R_{SV}(\mathbf{p} | \mathbf{p}_0)_{HV} \hat{e}_H(\mathbf{p}) \hat{e}_V^{0-}(\mathbf{p}_0) \\ & + R_{SV}(\mathbf{p} | \mathbf{p}_0)_{VH} \hat{e}_V^{0+}(\mathbf{p}) \hat{e}_H(\mathbf{p}_0) + R_{SV}R_{SV}(\mathbf{p} | \mathbf{p}_0)_{HH} \hat{e}_H(\mathbf{p}) \hat{e}_H(\mathbf{p}_0) \end{aligned} \quad [6.159]$$

or with a matrix notation

$$[\bar{\mathbf{R}}_{SV}(\mathbf{p} | \mathbf{p}_0)] = \begin{pmatrix} R_{SV}(\mathbf{p} | \mathbf{p}_0)_{VV} & R_{SV}(\mathbf{p} | \mathbf{p}_0)_{VH} \\ R_{SV}(\mathbf{p} | \mathbf{p}_0)_{HV} & R_{SV}(\mathbf{p} | \mathbf{p}_0)_{HH} \end{pmatrix}. \quad [6.160]$$

As mentioned in the introduction, the fundamental quantity in the radiative transfer equation is the specific intensity. We define $\mathbf{I}(\mathbf{R}, \mathbf{k})$ as the Wigner

transform of the incoherent intensity of the light scattered by the random medium and the surfaces in the medium 0,

$$\begin{aligned} \mathbf{I}^{incoh}(\mathbf{R}, \mathbf{k}) = e_0 \int_{V_0} d^3r \exp(-i \mathbf{k} \cdot \mathbf{r}) & \left[\langle\langle \mathbf{E}_{SV}^{0s}(\mathbf{R} + \frac{\mathbf{r}}{2}) \otimes \mathbf{E}_{SV}^{0s*}(\mathbf{R} - \frac{\mathbf{r}}{2}) \rangle\rangle_{SV} \right. \\ & \left. - \langle\langle \mathbf{E}_{SV}^{0s}(\mathbf{R} + \frac{\mathbf{r}}{2}) \rangle\rangle_{SV} \otimes \langle\langle \mathbf{E}_{SV}^{0s*}(\mathbf{R} - \frac{\mathbf{r}}{2}) \rangle\rangle_{SV} \right] \end{aligned} \quad [6.161]$$

with $e_0 = \epsilon_{vacuum} c_{vacuum} n_0/2$. \otimes defines the tensorial product of two vectors, and the symbol $\langle\langle .. \rangle\rangle_{SV}$ is the average over the surface and the volume disorder. We assume that the properties of the rough surfaces and the random medium are statistically independent. With the quasi-uniform field approximation,⁹⁵ we obtain the relation between the cross-section $\bar{\sigma}^{incoh}(\hat{\mathbf{k}} | \hat{\mathbf{k}}_0)$ and the specific intensity:

$$4\pi \cos \theta \mathbf{I}^{incoh}(\mathbf{R}, \hat{\mathbf{k}}) = \bar{\sigma}^{incoh}(\hat{\mathbf{k}} | \hat{\mathbf{k}}_0) : \mathbf{J}^{0i}(\hat{\mathbf{k}}_0), \quad [6.162]$$

where

$$\mathbf{J}^{0i}(\hat{\mathbf{k}}_0) = e_0 \mathbf{E}^{0i}(\hat{\mathbf{k}}_0) \otimes \mathbf{E}^{0i*}(\hat{\mathbf{k}}_0). \quad [6.163]$$

The tensor $\mathbf{I}(\mathbf{R}, \mathbf{k})$ is not exactly the specific intensity used in the radiometry theory since it is not homogeneous to an energy per unit time and solid angle. The specific intensity $\mathbf{I}^{incoh}(\mathbf{R}, \hat{\mathbf{k}})$ is related to the intensity $\mathbf{I}(\mathbf{R}, \mathbf{k})$ by a Dirac distribution, which ensures that the wave propagation direction $\hat{\mathbf{k}}$ has a fixed norm given by K_0 . The relation between the specific intensity and the cross-section is given by a product of two tensors defined by the symbol “:” (see the definition in Appendix 6.11.2). We have assumed that the medium 0 is non-absorbing and the intensity does not depend on R as can be seen in Equation [6.162]. From Equation [6.162], we can determine the bistatic cross-section in calculating the specific incoherent intensity defined by the Wigner transform Equation [6.161].

6.7.2 Specific intensity and Bethe-Salpeter equations

To obtain the bistatic cross-section, we are now going to calculate the specific intensity by using the Green functions of this problem. Hence, by having the Green functions of this problem, $\bar{\mathbf{G}}_S^{00}, \bar{\mathbf{G}}_S^{01}, \bar{\mathbf{G}}_S^{11}$, we can derive Dyson and Bethe-Salpeter equations for a slab of a random medium with randomly

rough surfaces. We obtain the Lippman-Schwinger equation for the source and the receiver in the medium,

$$\bar{\mathbf{G}}_{SV}^{11} = \bar{\mathbf{G}}_S^{11} + \bar{\mathbf{G}}_S^{11} \cdot \bar{\mathbf{V}}^{11} \cdot \bar{\mathbf{G}}_{SV}^{11}, \quad [6.164]$$

where $\bar{\mathbf{V}}^{11}$ is called the impurity potential operator. The superscripts i, j are, respectively, the receiver location and the source location (0, 1, 2 for the media 0, 1, or 2). We define the transition operator by

$$\bar{\mathbf{G}}_{SV}^{11} = \bar{\mathbf{G}}_S^{11} + \bar{\mathbf{G}}_S^{11} \cdot \bar{\mathbf{T}}_{SV}^{11} \cdot \bar{\mathbf{G}}_S^{11}. \quad [6.165]$$

The operator $\bar{\mathbf{V}}^{11}$ is related to the transition operator $\bar{\mathbf{T}}_{SV}^{11}$ by:

$$\bar{\mathbf{T}}_{SV}^{11} = \bar{\mathbf{V}}^{11} + \bar{\mathbf{V}}^{11} \cdot \bar{\mathbf{G}}_S^{11} \cdot \bar{\mathbf{T}}_{SV}^{11}. \quad [6.166]$$

$\bar{\mathbf{T}}_{SV}^{11}$ satisfies the coherent potential approximation $\langle \bar{\mathbf{T}}_{SV}^{11} \rangle_V = 0$. All the scattering processes in the random medium are contained in the transition operator. If we evaluate this operator, then we calculate the different fields in the different media. For example, we can evaluate the field in the medium scattered by the slab from a source in the medium 0. In a compact form, we have

$$\bar{\mathbf{G}}_{SV}^{00} = \bar{\mathbf{G}}_S^{00} + \bar{\mathbf{G}}_S^{01} \cdot \bar{\mathbf{T}}_{SV}^{11} \cdot \bar{\mathbf{G}}_S^{10}. \quad [6.167]$$

To evaluate the scattered intensity in the medium, we define the tensor

$$\bar{\Gamma}_S^{11} = \langle \bar{\mathbf{T}}_{SV}^{11} \otimes \mathbf{T}_{SV}^{11*} \rangle_V. \quad [6.168]$$

We express the average tensorial product of the Green functions which is given by:

$$\begin{aligned} \langle \langle \bar{\mathbf{G}}_{SV}^{11} \otimes \bar{\mathbf{G}}_{SV}^{11*} \rangle \rangle_{SV} &= \langle \bar{\mathbf{G}}_S^{11} \otimes \bar{\mathbf{G}}_S^{11*} \rangle_S \\ &+ \langle \bar{\mathbf{G}}_S^{11} \otimes \bar{\mathbf{G}}_S^{11*} \rangle_S : \bar{\mathbf{P}}^{11} : \langle \langle \bar{\mathbf{G}}_{SV}^{11} \otimes \bar{\mathbf{G}}_{SV}^{11*} \rangle \rangle_{SV}. \end{aligned} \quad [6.169]$$

Here $\langle \dots \rangle_S$ denotes the average over the ensemble of realizations of the random surfaces. In Equation [6.169], we have introduced the intensity operator $\bar{\mathbf{P}}^{11}$, which is defined by

$$\langle \bar{\Gamma}_S^{11} \rangle_S = \bar{\mathbf{P}}^{11} + \bar{\mathbf{P}}^{11} : \langle \langle \bar{\mathbf{G}}_{SV}^{11} \otimes \bar{\mathbf{G}}_{SV}^{11*} \rangle \rangle_{SV} : \bar{\mathbf{P}}^{11}. \quad [6.170]$$

In the next section we will give an approximate expression for the intensity operator that will not depend on the rough surface profiles but only on the properties of the scatterers. It will appear that the tensor $\bar{\mathbf{P}}^{11}$ describes the intensity of the light scattered by a particle taking into account the correlation with other particles. To simplify the notations, we introduce two new tensors:

$$\bar{\mathcal{G}}_{\ll SV \gg}^{11} = \ll \bar{\mathbf{G}}_{SV}^{11} \otimes \bar{\mathbf{G}}_{SV}^{11*} \gg_{SV}, \quad [6.171]$$

$$\bar{\mathcal{G}}_{\infty S}^{11} = \langle \bar{\mathbf{G}}_S^{11} \otimes \bar{\mathbf{G}}_S^{11*} \rangle_S. \quad [6.172]$$

The Bethe-Salpeter equation can be written as follows:

$$\bar{\mathcal{G}}_{\ll SV \gg}^{11} = \bar{\mathcal{G}}_{\infty S}^{11} + \bar{\mathcal{G}}_{\infty S}^{11} : \bar{\mathbf{P}}^{11} : \bar{\mathcal{G}}_{\ll SV \gg}^{11}, \quad [6.173]$$

where we have introduced the symbol ∞ to emphasize that the propagator $\bar{\mathcal{G}}_{\infty S}^{11}$ between two scattering events by the particles describes either a wave propagating directly between the two scatterers or a wave reflected by the boundaries. We can express the intensity in the medium 0 produced by a source in the medium 0. This intensity is described by the tensor $\bar{\mathcal{G}}_{\ll SV \gg}^{00}$ as a function of the tensor $\bar{\mathcal{G}}_{\ll SV \gg}^{11}$. We use the expression for the Green function $\bar{\mathcal{G}}_{\ll SV \gg}^{11}$,

$$\begin{aligned} \bar{\mathcal{G}}_{\ll SV \gg}^{00} &= \bar{\mathcal{G}}_{\infty S}^{00} + \bar{\mathcal{G}}_{\infty S}^{01} : \bar{\mathbf{P}}^{11} : \bar{\mathcal{G}}_{\infty S}^{10} \\ &\quad + \bar{\mathcal{G}}_{\infty S}^{01} : \bar{\mathbf{P}}^{11} : \bar{\mathcal{G}}_{\ll SV \gg}^{11} : \bar{\mathbf{P}}^{11} : \bar{\mathcal{G}}_{\infty S}^{10}, \end{aligned} \quad [6.174]$$

where:

$$\bar{\mathcal{G}}_{\ll SV \gg}^{00} = \ll \bar{\mathbf{G}}_{SV}^{00} \otimes \bar{\mathbf{G}}_{SV}^{00*} \gg_{SV}, \quad [6.175]$$

$$\bar{\mathcal{G}}_{\infty S}^{00} = \langle \bar{\mathbf{G}}_S^{00} \otimes \bar{\mathbf{G}}_S^{00*} \rangle_S, \quad [6.176]$$

$$\bar{\mathcal{G}}_{\infty S}^{01} = \langle \bar{\mathbf{G}}_S^{01} \otimes \bar{\mathbf{G}}_S^{01*} \rangle_S, \quad [6.177]$$

$$\bar{\mathcal{G}}_{\infty S}^{10} = \langle \bar{\mathbf{G}}_S^{10} \otimes \bar{\mathbf{G}}_S^{10*} \rangle_S. \quad [6.178]$$

As the intensity operator $\bar{\mathbf{P}}^{11}$ represents the intensity due to scattering by one particle, Equation [6.174] decomposes the scattering process into three

terms: the first one where no scattering in the volume occurs (the medium 1 is modeled by an effective permittivity), the second one is the single scattering term, and the third term contains higher scattering contributions by particles. We can now calculate $\mathbf{I}(\mathbf{R}, \mathbf{k})$ in Equation [6.161]. The intensity of the scattered light E_{SV}^{0s} is related to the Green function $\bar{\mathbf{G}}_{SV}^{00}$, and we can develop the tensorial product of the Wigner transform of the specific intensity by using Equation [6.174]. We obtain the four following contributions for the specific intensity defined by Equation [6.161]:

$$\bar{\mathbf{I}}^{incoh} = \bar{\mathbf{I}}_{L=0}^{incoh} + \bar{\mathbf{I}}_{L=1}^{incoh} + \bar{\mathbf{I}}_{Ladder}^{incoh} + \bar{\mathbf{I}}_{Crossed}^{incoh}, \quad [6.179]$$

where the contributions are given by:

$$\begin{aligned} \bar{\mathbf{I}}_{L=0}^{incoh}(\mathbf{R}, \mathbf{k}) &= e_0 \int_{V_0} d^3r \exp(-i\mathbf{k}\cdot\mathbf{r}) \left[<\mathbf{E}_S^{0s} \left(\mathbf{R} + \frac{\mathbf{r}}{2} \right) \otimes \mathbf{E}_S^{0s*} \left(\mathbf{R} - \frac{\mathbf{r}}{2} \right) >_S \right. \\ &\quad \left. - <\mathbf{E}_S^{0s} \left(\mathbf{R} + \frac{\mathbf{r}}{2} \right) >_S \otimes <\mathbf{E}_S^{0s*} \left(\mathbf{R} - \frac{\mathbf{r}}{2} \right) >_S \right], \end{aligned} \quad [6.180]$$

$$\begin{aligned} \bar{\mathbf{I}}_{L=1}^{incoh}(\mathbf{R}, \mathbf{k}) &= e_0 \int_{V_0} d^3r \exp(-i\mathbf{k}\cdot\mathbf{r}) \bar{\mathcal{G}}_{<S>}^{01} : \bar{\mathbf{P}}^{11} \\ &\quad : <\mathbf{E}^{1t} \otimes \mathbf{E}^{1t*} >_S \left(\mathbf{R} + \frac{\mathbf{r}}{2}, \mathbf{R} - \frac{\mathbf{r}}{2} \right), \end{aligned} \quad [6.181]$$

$$\begin{aligned} \bar{\mathbf{I}}_{Ladder}^{incoh}(\mathbf{R}, \mathbf{k}) &= e_0 \int_{V_0} d^3r \exp(-i\mathbf{k}\cdot\mathbf{r}) \bar{\mathcal{G}}_{<S>}^{01} : \bar{\mathbf{P}}^{11} : \bar{\mathcal{G}}_{<>SV>}^{11} \\ &\quad : \bar{\mathbf{P}}^{11} : <\mathbf{E}^{1t} \otimes \mathbf{E}^{1t*} >_S \left(\mathbf{R} + \frac{\mathbf{r}}{2}, \mathbf{R} - \frac{\mathbf{r}}{2} \right), \end{aligned} \quad [6.182]$$

$$\begin{aligned} \bar{\mathbf{I}}_{Crossed}^{incoh}(\mathbf{R}, \mathbf{k}) &= e_0 \int_{V_0} d^3r \exp(-i\mathbf{k}\cdot\mathbf{r}) \left[\bar{\mathcal{G}}_{<S>}^{01} : \bar{\mathbf{P}}^{11} : \bar{\mathcal{G}}_{<>SV>}^{11} \right. \\ &\quad \left. : \bar{\mathbf{P}}^{11} : <\mathbf{E}^{1t} \otimes \mathbf{E}^{1t*} >_S \right]^{T_R} \left(\mathbf{R} + \frac{\mathbf{r}}{2}, \mathbf{R} - \frac{\mathbf{r}}{2} \right). \end{aligned} \quad [6.183]$$

T_R defines the right transpose of a tensor. The superscripts for the operators and the Green functions correspond, respectively, to the receiver location and the source location (0 for the medium 0, 1 for the medium 1, 2 for the medium 2). In the previous formulas we can follow, from right to left, how the scattering process is defined by the combination of the different operators. The introduction of tensor products of matrices is related to the fact that we calculate a cross-section, which depends on the squared modulus of a scattering amplitude. The first term $\bar{\mathbf{I}}_{L=0}^{incoh}$ corresponds to the scattering

by the slab with rough boundaries and defined by an effective permittivity ϵ_e we will study in the next subsection. The second term $I_{L=1}^{incoh}$ corresponds to the first approximation where only one process of scattering by a particle is taken into account. We will examine the expression for the tensor \bar{P}^{11} . The two last terms I_{Ladder}^{incoh} and $I_{Crossed}^{incoh}$ correspond to the higher-order particle scattering contributions. $\bar{\mathcal{G}}_{\ll SV \gg}^{11}$ is the Green tensor which contains the interaction between the scatterers and the surfaces. The lower index $\ll SV \gg$ represents the average over the randomly rough surfaces and the disordered medium. We will study the expression for $\bar{\mathcal{G}}_{\ll SV \gg}^{11}$ in the next subsections.

6.7.3 Effective permittivity

To determine the effective permittivity ϵ_e , we use the fact that when the effective medium is not spatially dispersive, it can be shown, using a diagrammatic technique, that the coherent part of the field $\langle E \rangle_V$ which propagates inside an infinite random medium behaves as a wave in an homogeneous medium with a renormalized effective permittivity. We introduce the Coherent Potential Approximation (CPA), which postulates that:

$$\langle \bar{\mathbf{G}}_{SV}^{11} \rangle_V = \bar{\mathbf{G}}_S^{11}. \quad [6.184]$$

We also use another approximation, which is the Quasi-Crystalline Approximation (QCA). This approximation is strictly valid when the particles have fixed positions, as in a crystal. The quasi-crystalline approximation is equivalent to neglecting the fluctuation of the effective field on a particle located at r_j , due to a deviation of a particle located at r_i from its average position.

Under the quasi-crystalline coherent potential approximation (QC-CPA) for Rayleigh scatterers, an approximate formula for ϵ_e can generalize the usual Maxwell-Garnett formula. We can also obtain an approximate formula for the effective permittivity, which contains the Maxwell-Garnett formula and the Keller approximation.⁹⁰

The equation for ϵ_e is given by the following expression:

$$\epsilon_e = \epsilon_1 + \frac{3(\epsilon_d - \epsilon_1)\epsilon_e f_{vol}}{(\epsilon_d - \epsilon_1)(1 - f_{vol} - \frac{2i}{3}(K_{vac}r_d)^3\epsilon_e^{3/2}w) + 3\epsilon_e}, \quad [6.185]$$

where ϵ_1 is the permittivity of the slab, ϵ_d the permittivity of the scatterers, f_{vol} the volume fraction of the scatterers and r_d the radius of the scatterers. The function w is the Percus-Yevick distribution

$$w = \frac{(1-f_{vol})^4}{(1+2f_{vol})^2}. \quad [6.186]$$

With a development at the first order of Equation [6.185] we obtain:

$$\begin{aligned} \varepsilon_e &= \varepsilon_1 + \frac{\varepsilon_1(\varepsilon_d - \varepsilon_1)(1-f_{vol}) + 3\varepsilon_1\varepsilon_e + 3(\varepsilon_d - \varepsilon_1)\varepsilon_e - f_{vol}}{(\varepsilon_d - \varepsilon_1)(1-f_{vol}) + 3\varepsilon_e} \\ &\quad + 2i \frac{(K_{vac}r_d)^3(\varepsilon_d - \varepsilon_1)^2 w f_{vol} \varepsilon_e^{5/2}}{[(\varepsilon_d - \varepsilon_1)(1-f_{vol}) + 3\varepsilon_e]^2}. \end{aligned} \quad [6.187]$$

If the real part of ε_e is larger than the imaginary part, we obtain an approximate solution of Equation [6.187]:

$$\begin{aligned} Re(\varepsilon_e) &= \frac{1}{6}[-\{(\varepsilon_d - \varepsilon_1)(1-f_{vol}) - 3\varepsilon_1 - 3(\varepsilon_d - \varepsilon_1)f_{vol}\} + \sqrt{\Delta}], \\ Im(\varepsilon_e) &= 2 \frac{(K_{vac}r_d)^3(\varepsilon_d - \varepsilon_1)^2 w f_{vol} Re(\varepsilon_e)^{5/2}}{[(\varepsilon_d - \varepsilon_1)(1-f_{vol}) + 3Re(\varepsilon_e)]^2}, \end{aligned} \quad [6.188]$$

where

$$\Delta = [(\varepsilon_d - \varepsilon_1)(1-f_{vol}) - 3\varepsilon_1 + 3(\varepsilon_d - \varepsilon_1)f_{vol}]^2 + 12\varepsilon_1(\varepsilon_d - \varepsilon_1)(1-f_{vol}).$$

6.7.4 Expression of the intensity operator \bar{P}^{11}

In the preceding subsection, we introduced the intensity operator \bar{P}^{11} to write the Bethe-Salpeter equation. This intensity operator can be determined by using the energy conservation principle. With the Dyson equation and the Bethe-Salpeter Equation [6.170] in the energy conservation equation, we obtain a Ward identity which defines a relation between the intensity operator \bar{P}^{11} and the mass operator \bar{M}^{11} which is a function of the effective permittivity ε_e .⁹³ Under the QC-CPA, the scalar ε_e satisfies a non-linear system of equations. In using these equations in the Ward identity, we obtain an expression, called the modified ladder approximation, for the intensity operator \bar{P}^{11} , which satisfies energy conservation.⁵⁸ We do not reproduce here the derivation of the Ward identity since the demonstration is formally identical

to the infinite random medium case and is well-documented.^{58,77} The expression for $\bar{\mathbf{P}}^{11}$ is given by

$$\begin{aligned} \bar{\mathbf{P}}^{11}(\mathbf{R}, \mathbf{k} | \mathbf{R}_0, \mathbf{k}_0) = & n w(\mathbf{k} - \mathbf{k}_0) \int \frac{d^3 K}{(2\pi)^3} \exp(i \mathbf{K} \cdot (\mathbf{R} - \mathbf{R}_0)) \\ & \times \bar{\mathbf{C}}_{(e)o}^{11}(\frac{\mathbf{K}}{2} + \mathbf{k} | \frac{\mathbf{K}}{2} + \mathbf{k}_0) \otimes \bar{\mathbf{C}}_{(e)o}^{11*}(-\frac{\mathbf{K}}{2} + \mathbf{k} | \frac{\mathbf{K}}{2} + \mathbf{k}_0), \end{aligned} \quad [6.189]$$

where $w(\mathbf{k} - \mathbf{k}_0)$ is the structure factor of the medium, identical to the one defined in the scattering of X-rays, and n is the density of the scatterers. $\bar{\mathbf{C}}_{(e)o}^{11}$ is the transition operator, which should be expressed as

$$\begin{aligned} \bar{\mathbf{C}}_{(e)o}^{11}(\mathbf{k} | \mathbf{k}_0) = & \bar{t}_{(e)o}^{11}(\mathbf{k} | \mathbf{k}_0) + n \int \frac{d^3 k_1}{(2\pi)^3} h(\mathbf{k} - \mathbf{k}_1) \bar{t}_{(e)o}^{11}(\mathbf{k} | \mathbf{k}_0) \cdot \bar{\mathbf{G}}_e^\infty(\mathbf{k}_1) \cdot \bar{\mathbf{C}}_{(e)o}^{11}(\mathbf{k} | \mathbf{k}_0), \end{aligned} \quad [6.190]$$

with

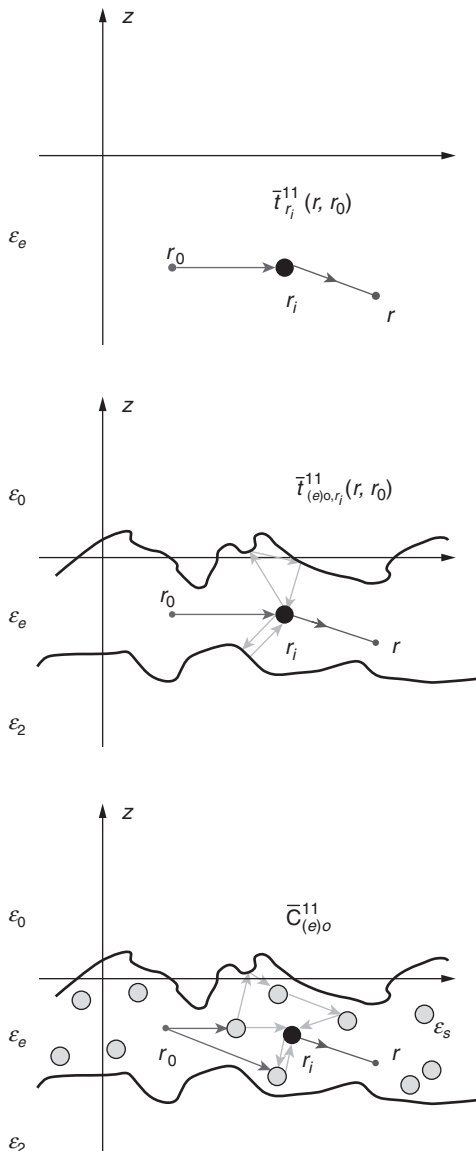
$$h(\mathbf{k} - \mathbf{k}_1) = \int d^3 r \exp(-(\mathbf{k} - \mathbf{k}_1) \cdot \mathbf{r}) [g(\mathbf{r}) - 1]. \quad [6.191]$$

$g(\mathbf{r})$ is the correlation function between two scatterers, and

$$\begin{aligned} \bar{\mathbf{G}}_e^\infty(\mathbf{r}, \mathbf{r}_0) = & \frac{i}{2} \int \frac{d^2 p_0}{(2\pi)^2} \exp(i \mathbf{p}_0 \cdot (\mathbf{x} - \mathbf{x}_0) + i \alpha_e(\mathbf{p}_0)(z - z_0)) (\bar{\mathbf{I}} - \hat{\mathbf{k}}_{p_0}^{1+} \hat{\mathbf{k}}_{p_0}^{1+}) \frac{1}{\alpha_e(p_0)}, \\ \text{for } z > z_0, \end{aligned} \quad [6.192]$$

$$\begin{aligned} \bar{\mathbf{G}}_e^\infty(\mathbf{r}, \mathbf{r}_0) = & \frac{i}{2} \int \frac{d^2 p_0}{(2\pi)^2} \exp(i \mathbf{p}_0 \cdot (\mathbf{x} - \mathbf{x}_0) - i \alpha_e(\mathbf{p}_0)(z - z_0)) (\bar{\mathbf{I}} - \hat{\mathbf{k}}_{p_0}^{1-} \hat{\mathbf{k}}_{p_0}^{1-}) \frac{1}{\alpha_e(p_0)}, \\ \text{for } z < z_0, \end{aligned} \quad [6.193]$$

with $\mathbf{k}_{p_0}^{1\pm} = \mathbf{p}_0 - \alpha_e(\mathbf{p}_0) \hat{\mathbf{e}}_z$ and $\hat{\mathbf{k}}_{p_0}^{1\pm} = \mathbf{k}_{p_0}^{1\pm} / \| \mathbf{k}_{p_0}^{1\pm} \|$. Equation [6.189] is given by a Wigner transform. The expression for $\bar{\mathbf{P}}^{11}$ is complex because the operator is nonlocal. The operator $\bar{t}_{(e)o}^{11}$ may be expressed with \bar{t}_o , for a particle located at the origin, which does not take into account the correlations with the other scatterers, by replacing the permittivity ϵ_d of the scatterer by the permittivity $\tilde{\epsilon}_d \equiv \epsilon_d - \epsilon_1 + \epsilon_e$, and replacing the permittivity ϵ_1 of the medium by the effective medium ϵ_e (see Fig. 6.23). With the CPA, we can express the transition operators $\bar{t}_{(e)o}^{11}$ with the effective medium. The transition operator $\bar{t}_{(e)o}^{11}$ can be written in the Fourier space as



6.23 The operator \bar{t}_i^{11} represents the scattering from one particle in an infinite medium, the operator $\bar{t}_{(e)o,r_i}^{11}$ gives the scattering by one particle in a finite volume, and $\bar{C}_{(e)o}^{11}$ is the field scattered by a particle, taking into account the effects of the other particles and the boundaries.

$$\bar{t}_{(e)o}^{11}(\mathbf{k} \mid \mathbf{k}_0) = \int \int \frac{d^3 r d^3 r_0}{(2\pi)^3 (2\pi)^3} \exp(-i \mathbf{k} \cdot \mathbf{r} + i \mathbf{k}_0 \cdot \mathbf{r}_0) \bar{t}_{(e)o}^{11}(\mathbf{r} \mid \mathbf{r}_0). \quad [6.194]$$

$$= t_{(e)}^1(\omega) \delta(\mathbf{k} - \mathbf{k}_0) \bar{\mathbf{I}}. \quad [6.195]$$

For Rayleigh scatterers, we obtain

$$t_{(e)}^1(\omega) = K_{vac}^2 \alpha_{(e)ray}^1, \quad [6.196]$$

$$\alpha_{(e)ray}^1 \equiv \frac{\alpha_{(e)pol}^1}{1 - K_{vac}^2 \alpha_{(e)pol}^1 \frac{i K_e}{6\pi}}, \quad [6.197]$$

$$\alpha_{(e)pol}^1 = 3 \varepsilon_e v_d \frac{\tilde{\varepsilon}_d - \varepsilon_e}{\tilde{\varepsilon}_d + 2\varepsilon_e}, \quad [6.198]$$

where $\tilde{\varepsilon}_d \equiv \varepsilon_d - \varepsilon_1 + \varepsilon_e$ and v_d is the volume of a scatterer. By substituting Equation [6.195] into Equation [6.190], we obtain:

$$\bar{C}_{(e)o}^{11}(\mathbf{k} \mid \mathbf{k}_0) = \left[\bar{\mathbf{I}} - n t_{(e)}^1(\omega) \int \frac{d^3 k_1}{(2\pi)^3} h(\mathbf{k}_1 - \mathbf{k}_0) \bar{G}_e^\infty(\mathbf{k}_1) \right]^{-1} t_{(e)}^1(\omega) \bar{\mathbf{I}}. \quad [6.199]$$

By using the expression for $\bar{G}_e^\infty(\mathbf{k}_1)$ and the fact that the correlation function of small scatterers has an effect at small range, we have:

$$h(\mathbf{r}_j - \mathbf{r}_i) \approx \delta(\mathbf{r}_j - \mathbf{r}_i) \int d^3 r h(\mathbf{r}). \quad [6.200]$$

We obtain from Equation [6.199] the expression for $\bar{C}_{(e)o}^{11}$. The expression for $h(0)$ comes from the singularity of the Green function $\bar{G}_e^\infty(\mathbf{r}, \mathbf{r}_0)$;

$$\bar{C}_{(e)o}^{11}(\mathbf{k} \mid \mathbf{k}_0) = \frac{t_{(e)}^1(\omega) \delta(\mathbf{k} - \mathbf{k}_0) \bar{\mathbf{I}}}{1 - n \left(\frac{h(0)}{3K_e^2} + \frac{iK_e}{6\pi} \int d^3 r h(\mathbf{r}) \right) t_{(e)}^1(\omega)}, \quad [6.201]$$

where the integral expression $h(\mathbf{r})$ is obtained from the relation

$$w \equiv 1 + n \int d^3 r h(\mathbf{r}) = 1 + n \int d^3 r [g(\mathbf{r}) - 1], \quad [6.202]$$

and w is the Percus-Yevick correlation function Equation [6.186]. We can finally write

$$\bar{C}_{(e)o}^{11}(\mathbf{k} \mid \mathbf{k}_0) = \frac{t_{(e)}^1(\omega)\delta(\mathbf{k} - \mathbf{k}_0) \bar{I}}{1 + \left\{ \frac{n}{K_e^2} + \frac{iK_e}{6\pi}(w-1) \right\} t_{(e)}^1(\omega)}. \quad [6.203]$$

With these approximations, the intensity operator for one particle may be expressed as:

$$\bar{\mathbf{P}}^{11}(\mathbf{k} \mid \mathbf{k}_0) = n w(\mathbf{k} - \mathbf{k}_0) \bar{C}_{(e)o}^{11}(\mathbf{k} \mid \mathbf{k}_0) \otimes \bar{C}_{(e)o}^{11*}(\mathbf{k} \mid \mathbf{k}_0). \quad [6.204]$$

We note that, with the several approximations, the intensity operator $\bar{\mathbf{P}}^{11}$ becomes localized at $\mathbf{R} = \mathbf{R}_0$.

6.7.5 Expression for the incoherent intensity and the Green tensor $\bar{\mathbf{P}}^{11}$

As we have seen, the incoherent intensity is given by:

$$\bar{\mathbf{I}}^{incoh} = \bar{\mathbf{I}}_{L=0}^{incoh} + \bar{\mathbf{I}}_{L=1}^{incoh} + \bar{\mathbf{I}}_{Ladder}^{incoh} + \bar{\mathbf{I}}_{Crossed}^{incoh}. \quad [6.205]$$

From Equation [6.180], we notice that the term $\bar{\mathbf{I}}_{L=0}^{incoh}$ is determined by the scattering matrix $\bar{\mathbf{S}}^{0+,0-}$ because we can write the field \mathbf{E}_S^{0s} scattered by the effective medium bounded by the randomly rough surfaces as

$$\mathbf{E}_S^{0s}(\mathbf{r}) = \int \frac{d^2 p}{(2\pi)^2} e^{i \mathbf{p} \cdot \mathbf{r} + i \alpha_0(\mathbf{p}) z} \bar{\mathbf{S}}^{0+,0-}(\mathbf{p} \mid \mathbf{p}_0) \cdot \mathbf{E}^{0i}(\mathbf{p}_0). \quad [6.206]$$

The term $\bar{\mathbf{I}}_{L=1}^{incoh}$ is evaluated relative to the tensor $\bar{\mathbf{P}}^{11}$ and the scattering operators $\bar{\mathbf{S}}^{0+,1-}$, $\bar{\mathbf{S}}^{0+,1+}$, $\bar{\mathbf{S}}^{0+,0-}$ and $\bar{\mathbf{S}}^{0-,0-}$ because the transmitted field is given by

$$\mathbf{E}_S^{1i}(\mathbf{x}, z) = \int \frac{d^2 p}{(2\pi)^2} e^{i \mathbf{p} \cdot \mathbf{x}} \left[e^{i \alpha_1(\mathbf{p}) z} \bar{\mathbf{S}}^{1+,0-}(\mathbf{p} \mid \mathbf{p}_0) + e^{-i \alpha_1(\mathbf{p}) z} \bar{\mathbf{S}}^{1-,0-}(\mathbf{p} \mid \mathbf{p}_0) \right] \cdot \mathbf{E}^{0i}(\mathbf{p}_0), \quad [6.207]$$

and the Green function $\bar{\mathbf{G}}_S^{01}$ may be decomposed as:

$$\bar{\mathbf{G}}_S^{01} = \bar{\mathbf{G}}_S^{0+1+} + \bar{\mathbf{G}}_S^{0+1-}. \quad [6.208]$$

The symbol – describes a downgoing wave, the symbol + an upgoing wave relative to the direction Oz . These two Green functions may be evaluated as integral functions containing the two scattering operators $\bar{S}_{\text{incoh}}^{0+,0-}$, $\bar{S}_{\text{incoh}}^{0+,1+}$.

For the two terms \bar{I}_{Ladder} and \bar{I}_{Crossed} , we need to evaluate the Green tensor $\bar{\mathcal{G}}_{\ll SV \gg}^{11}$, which satisfies a Bethe-Salpeter Equation [6.173]. It is convenient to write the Bethe-Salpeter Equation [6.173], satisfied by $\bar{\mathcal{G}}_{\ll SV \gg}$ by introducing the Wigner transform of a tensor. Equation [6.173] may be written as an integral

$$\begin{aligned} \bar{\mathcal{G}}_{\ll SV \gg}^{11} (\mathbf{R}, \mathbf{k} | \mathbf{R}_0, \mathbf{k}_0) = & \bar{\mathcal{G}}_{\infty \ll S \gg}^{11} (\mathbf{R}, \mathbf{k} | \mathbf{R}_0, \mathbf{k}_0) + \int V_1 d^3 R_1 d^3 R_2 \int \frac{d^3 k_1}{(2\pi)^3} \frac{d^3 k_2}{(2\pi)^3} \\ & \times \bar{\mathcal{G}}_{\infty \ll S \gg}^{11} (\mathbf{R}, \mathbf{k} | \mathbf{R}_1, \mathbf{k}_1) : \bar{\mathbf{P}}^{11} (\mathbf{R}_1, \mathbf{k}_1 | \mathbf{R}_2, \mathbf{k}_2) : \bar{\mathcal{G}}_{\ll SV \gg}^{11} (\mathbf{R}_2, \mathbf{k}_2 | \mathbf{R}_0, \mathbf{k}_0). \end{aligned} \quad [6.209]$$

Between two scattering processes on the rough surfaces, the wave interacts with the particles, and accordingly, it is reasonable to assume that the scattering events on the rough surfaces are uncorrelated. The propagator $\bar{\mathcal{G}}_{\infty \ll S \gg}^{11} = \langle \bar{\mathbf{G}}_S^{11} \otimes \bar{\mathbf{G}}_S^{11*} \rangle_S$ in Equation [6.209] may be approximated by:

$$\begin{aligned} \langle \bar{\mathbf{G}}_S^{11} \otimes \bar{\mathbf{G}}_S^{11*} \rangle_S = & \bar{\mathbf{G}}_1^\infty \otimes \bar{\mathbf{G}}_1^{\infty*} + \langle \bar{\mathbf{G}}_S^{1+1+} \otimes \bar{\mathbf{G}}_S^{1+1+*} \rangle_S + \langle \bar{\mathbf{G}}_S^{1-1+} \otimes \bar{\mathbf{G}}_S^{1-1+*} \rangle_S \\ & + \langle \bar{\mathbf{G}}_S^{1+1-} \otimes \bar{\mathbf{G}}_S^{1+1-*} \rangle_S + \langle \bar{\mathbf{G}}_S^{1-1-} \otimes \bar{\mathbf{G}}_S^{1-1-*} \rangle_S, \end{aligned} \quad [6.210]$$

which represents the scattering process of a wave propagating directly between two scatterers (the first term of the expansion) or a wave reflected by the randomly rough surfaces (the four following terms). We used the expansion of the Green function $\bar{\mathcal{G}}_S^{11}$. With a condensed notation Equation [6.210] may be written as:

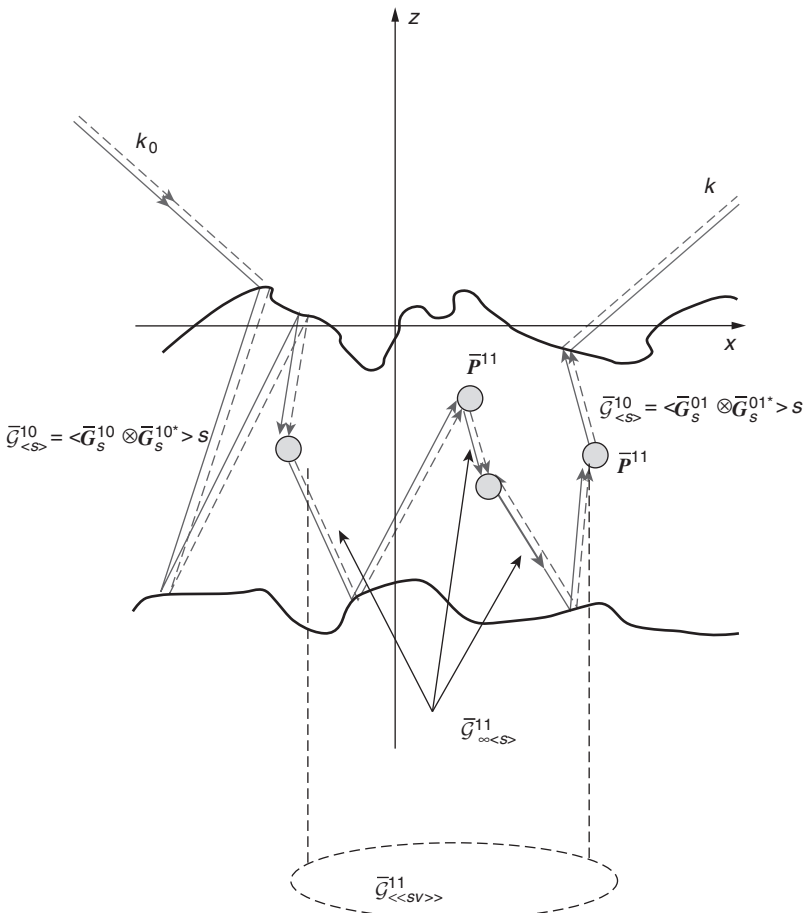
$$\bar{\mathcal{G}}_{\infty \ll S \gg}^{11} = \bar{\mathcal{G}}_\infty^{11} + \sum_{a,a_0=\pm} \bar{\mathcal{G}}_{\ll S \gg}^{1a1a_0}, \quad [6.211]$$

with

$$\bar{\mathcal{G}}_\infty^{11} = \bar{\mathbf{G}}_1^\infty \otimes \bar{\mathbf{G}}_1^{\infty*}, \quad [6.212]$$

$$\bar{\mathcal{G}}_{\ll S \gg}^{1a1a_0} = \langle \bar{\mathbf{G}}_S^{1a1a_0} \otimes \bar{\mathbf{G}}_S^{1a1a_0*} \rangle_S, \quad [6.213]$$

where a, a_0 are the signs + or $-$. The Green functions $\bar{G}_S^{1a_1 a_0}$ are defined with the scattering operators $\bar{S}^{1a_1 a_0}$.⁸¹ Then, the hypothesis of non-correlated diffusion on the rough surfaces must also be applied to each term of the operators $\bar{S}^{1a_1 a_0}$. The Green function \bar{G}_1^∞ is given by Equations [6.192] and [6.193], the permittivity in the expressions is the effective permittivity we have defined in the preceding section. Under these approximations, the Bethe-Salpeter equation [6.209] describes the scattering processes depicted in Fig. 6.24, where the waves on the left and right sides of the tensorial products follow the same path.



6.24 Scattering processes for the ladder approximation. The solid and dashed lines represent, respectively, the propagating waves on the right and left sides of the tensorial products
 $\bar{G}_{\ll SV \gg}^{11} = \ll \bar{G}_{SV}^{11} \otimes \bar{G}_{SV}^{11*} \gg_{SV}$.

We can use Feynman diagrams⁹³ to represent the different terms of $\bar{\mathcal{G}}_{\ll SV \gg}^{11}$ in the ladder approximation obtained by iteration of the Bethe-Salpeter equation:

$$\begin{aligned}\bar{\mathcal{G}}_{\ll SV \gg}^{11} = & \bar{\mathcal{G}}_{\infty \ll S \gg}^{11} + \bar{\mathcal{G}}_{\infty \ll S \gg}^{11} : \bar{\mathbf{P}}^{11} : \bar{\mathcal{G}}_{\infty \ll S \gg}^{11} \\ & + \bar{\mathcal{G}}_{\infty \ll S \gg}^{11} : \bar{\mathbf{P}}^{11} : \bar{\mathcal{G}}_{\infty \ll S \gg}^{11} : \bar{\mathbf{P}}^{11} : \bar{\mathcal{G}}_{\infty \ll S \gg}^{11} + \dots .\end{aligned}\quad [6.214]$$

We have restricted ourselves to an approximate form of the Bethe-Salpeter equation: the ladder approximation. As we can see, the ladder approximation allows a microscopic derivation of the radiative transfer equation. For the transport of energy we must consider the intensity. We have to multiply the Green function by its complex conjugate. In other words, we multiply the retarded Green function by the advanced one before averaging over disorder. This leads to the classical picture of propagation of intensity from one scatterer to another as depicted in Fig. 6.24. The term ‘ladder’ comes from the pattern of the Feynman diagrams. As the Bethe-Salpeter equation sums up the interaction many times, the resulting Feynman graph has the form of a ladder.

By taking into account the fact that the random layer is infinite in the two directions x and y and that the medium and the rough surfaces are statistically homogeneous and independent, the tensors $\bar{\mathcal{G}}(\mathbf{R}, \mathbf{k} | \mathbf{R}_0, \mathbf{k}_0)$ depend on Z and Z_0 and the following difference $\mathbf{X} - \mathbf{X}_0 = (X - X_0, Y - Y_0)$. These functions are given in terms of a Fourier transform along the X, Y axes,

$$\bar{\mathcal{G}}(Z, \mathbf{k} | Z_0, \mathbf{k}_0; \mathbf{P}) = \int d^2(\mathbf{X} - \mathbf{X}_0) e^{-i(\mathbf{X} - \mathbf{X}_0) \cdot \mathbf{P}} \bar{\mathcal{G}}(\mathbf{R}, \mathbf{k} | \mathbf{R}_0, \mathbf{k}_0), \quad [6.215]$$

with

$$\mathbf{R} = X\hat{\mathbf{e}}_x + Y\hat{\mathbf{e}}_y + Z\hat{\mathbf{e}}_z = \mathbf{X} + Z\hat{\mathbf{e}}_z,$$

$$\mathbf{R}_0 = X_0\hat{\mathbf{e}}_x + Y_0\hat{\mathbf{e}}_y + Z_0\hat{\mathbf{e}}_z = \mathbf{X}_0 + Z_0\hat{\mathbf{e}}_z.$$

This transformation may be also applied to the operators $\bar{\mathcal{G}}_{\ll S \gg}^{1a1a_0}$ and $\bar{\mathcal{G}}_{\infty}^{11}$.

We obtain for the terms $\bar{\mathcal{G}}_{\infty \ll S \gg}^{11}$ in Equation [6.209]:

$$\begin{aligned}\bar{\mathcal{G}}_{\infty \ll S \gg}^{11}(Z, \mathbf{k} | Z_0, \mathbf{k}_0; \mathbf{P}) = & \bar{\mathcal{G}}_{\infty}^{11}(Z, \mathbf{k} | Z_0, \mathbf{k}_0; \mathbf{P}) + \sum_{a, a_0 = \pm} \bar{\mathcal{G}}_{\ll S \gg}^{1a1a_0}(Z, \mathbf{k} | Z_0, \mathbf{k}_0; \mathbf{P}),\end{aligned}\quad [6.216]$$

where a, a_0 are related to the propagation directions of the waves. With this expression, we can demonstrate that the Bethe-Salpeter Equation [6.209] can be expressed as:

$$\begin{aligned} \bar{\mathcal{G}}_{\ll SV \gg}^{1a1a_0}(Z, \hat{\mathbf{k}} | Z_0, \hat{\mathbf{k}}_0; \mathbf{P}) &= \bar{\mathcal{G}}_{\infty S}^{1a1a_0}(Z, \mathbf{p} | Z_0, \mathbf{p}_0; \mathbf{P}) + \sum_{a_1 a_2} \int \frac{d^2 p_1}{(2\pi)^2} \frac{d^2 p_2}{(2\pi)^2} \int_{-H}^0 dZ_{21} \\ &\times \bar{\mathcal{G}}_{\infty S}^{1a1a_2}(Z, \mathbf{p} | Z_{21}, \mathbf{p}_2; \mathbf{P}) : \bar{\mathbf{P}}^{1a_2 1a_1}(\mathbf{p}_2 | \mathbf{p}_1; \mathbf{P}) : \bar{\mathcal{G}}_{\ll SV \gg}^{1a1a_0}(Z_{21}, \mathbf{p}_1 | Z_0, \mathbf{p}_0; \mathbf{P}), \end{aligned} \quad [6.217]$$

with

$$\bar{\mathcal{G}}_{\infty S}^{1a1a_0}(Z, \mathbf{p} | Z_0, \mathbf{p}_0; \mathbf{P}) = \bar{\mathcal{G}}_{\infty}^{1a1a_0}(Z, \mathbf{p} | Z_0, \mathbf{p}_0; \mathbf{P}) + \bar{\mathcal{G}}_{S}^{1a1a_0}(Z, \mathbf{p} | Z_0, \mathbf{p}_0; \mathbf{P}). \quad [6.218]$$

The propagator $\bar{\mathbf{P}}^{1a_2 1a_1}$ can be written as:⁸²

$$\bar{\mathbf{P}}^{1a_2 1a_1}(\mathbf{p}_2 | \mathbf{p}_1; \mathbf{P}) = n w(\hat{\mathbf{k}}_{p_2}^{1a_2} - \hat{\mathbf{k}}_{p_1}^{1a_1}) \bar{\mathbf{C}}_o^{11}(\hat{\mathbf{k}}_{p_2}^{1a_2} | \hat{\mathbf{k}}_{p_1}^{1a_1}) \otimes \bar{\mathbf{C}}_o^{11*}(\hat{\mathbf{k}}_{p_2}^{1a_2} | \hat{\mathbf{k}}_{p_1}^{1a_1}), \quad [6.219]$$

$$\mathbf{p}_1^\pm = \mathbf{p}_1 \pm \frac{\mathbf{p}}{2}, \quad \mathbf{p}_2^\pm = \mathbf{p}_2 \pm \frac{\mathbf{p}}{2}, \quad \hat{\mathbf{k}}_p^{1a} = \mathbf{p} + a \alpha'_e(\mathbf{p}) \hat{\mathbf{e}}_z, \quad [6.220]$$

where $\alpha'_e(\mathbf{p})$ is the real part of α_e . Equation [6.217] can give us an iterative development of $\bar{\mathcal{G}}_{\ll SV \gg}^{1a1a_0}$. For example, introducing in Equation [6.209] the first term of the iteration Equation [6.214] is

$$\bar{\mathcal{G}}_{\ll SV \gg}^{1a1a_0}(Z, \mathbf{p} | Z_0, \mathbf{p}_0; \mathbf{P}) = \bar{\mathcal{G}}_{\infty}^{1a1a_0}(Z, \mathbf{p} | Z_0, \mathbf{p}_0; \mathbf{P}) + \bar{\mathcal{G}}_{S}^{1a1a_0}(Z, \mathbf{p} | Z_0, \mathbf{p}_0; \mathbf{P}),$$

we obtain the contributions of the double scattering processes. $\bar{\mathcal{G}}_{\infty}^{1a1a_0}$ describes the direct propagation of the electromagnetic wave between two scatterers, and $\bar{\mathcal{G}}_{S}^{1a1a_0}$ describes the interaction with the layer boundaries between a double scattering process by the particles.

We give the following approximation which consists of retaining the two first terms of the expansion Equation [6.214]:

$$\begin{aligned} \bar{\mathcal{G}}_{\ll SV \gg}^{1a1a_0}(Z, \mathbf{p} | Z_0, \mathbf{p}_0; \mathbf{P}) &= \bar{\mathcal{G}}_{\infty S}^{1a1a_0}(Z, \mathbf{p} | Z_0, \mathbf{p}_0; \mathbf{P}) + \sum_{a_1, a_2} \int \frac{d^2 p_1}{(2\pi)^2} \frac{d^2 p_2}{(2\pi)^2} \int_{-H}^0 dZ_{21} \\ &\times \bar{\mathcal{G}}_{\infty S}^{1a1a_0}(Z, \mathbf{p} | Z_{21}, \mathbf{p}_2; \mathbf{P}) : \bar{\mathbf{P}}^{1a_2 1a_1}(\mathbf{p}_2 | \mathbf{p}_1; \mathbf{P}) : \bar{\mathcal{G}}_{\ll SV \gg}^{1a1a_0}(Z_{21}, \mathbf{p}_1 | Z_0, \mathbf{p}_0; \mathbf{P}). \end{aligned} \quad [6.221]$$

If we introduce the expression Equation [6.218] for $\bar{\mathcal{G}}_{\infty S}^{1a_1 a_0}$ we can write Equation [6.221] as

$$\begin{aligned}\bar{\mathcal{G}}_{\infty SV}^{1a_1 a_0}(Z, p | Z_0, p_0; \mathbf{P}) &= \left[\bar{\mathcal{G}}_{\infty}^{1a_1 a_0} + \bar{\mathcal{G}}_{S}^{1a_1 a_0} \right] (Z, p | Z_0, p_0; \mathbf{P}) + \sum_{a_1, a_2} \int \frac{d^2 p_1}{(2\pi)^2} \frac{d^2 p_2}{(2\pi)^2} \int_{-H}^0 dZ_{21} \\ &\times \left[\bar{\mathcal{G}}_{\infty}^{1a_1 a_2} + \bar{\mathcal{G}}_{S}^{1a_1 a_2} \right] (Z, p | Z_{21}, p_2; \mathbf{P}) : \bar{\mathbf{P}}^{1a_2 1a_1} (p_2 | p_1; \mathbf{P}) \\ &: \left[\bar{\mathcal{G}}_{\infty}^{1a_1 a_0} + \bar{\mathcal{G}}_{S}^{1a_1 a_0} \right] (Z_{21}, p_1 | Z_0, p_0; \mathbf{P}).\end{aligned}\quad [6.222]$$

The numerical solution of the integral equations is a difficult task. Due to the large difference in the orders of magnitude of the computed quantities, special attention must be paid to the precision in the calculation of multiple integrals. The numerical calculation of the incoherent cross-section requires multi-dimensional integration over two-dimensional wave vectors. We adopt the following procedures: the integration domain is decomposed into sub-domains whose size is adapted to the behavior of the functions to be integrated. In each sub-domain a Gauss-Legendre method with N points is used, the number of points varies with the precision required. The integral equation is well suited if we want to obtain an iterative solution of Equation [6.209] as we have seen. We define the Green tensor $\bar{\mathcal{G}}_{\infty SV}$ describing the interactions between the surfaces and the medium with a perturbative development up to the second order. This development contains 6 terms, the physical meaning of which will now be explained. We omit the superscripts of the expressions of the different tensors.

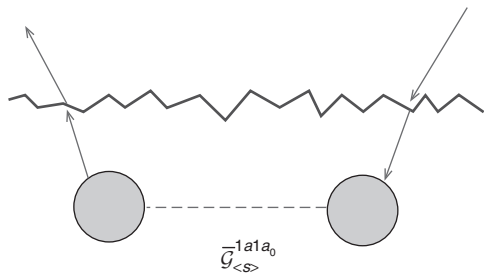
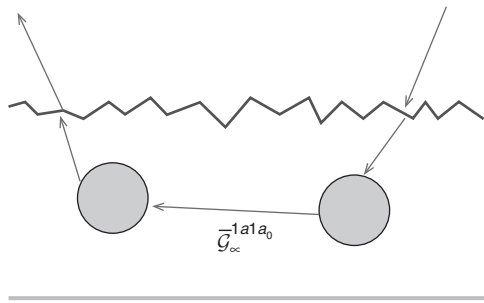
For the first order, the term $\bar{\mathcal{G}}_{\infty}$ describes an incident wave penetrating into the layer, scattered by a first particle, propagating directly toward a second particle, scattered by this particle, and transmitted back into the incident medium. The term $\bar{\mathcal{G}}_{S}$ describes an incident wave penetrating into the layer, scattered by a first particle, interacting with the boundaries, reaching a second particle, scattered by this particle, and transmitted back into the incident medium.

For the second order, the term $\bar{\mathcal{G}}_{\infty} : \bar{\mathbf{P}} : \bar{\mathcal{G}}_{\infty}$ describes a wave penetrating into the layer, scattered by a first particle, propagating directly toward a second particle, scattered by this particle, propagating directly toward a third particle, scattered by this particle and transmitted into the incident medium. The term $\bar{\mathcal{G}}_{S} : \bar{\mathbf{P}} : \bar{\mathcal{G}}_{S}$ describes a wave penetrating into the layer, scattered by a first particle, interacting with the boundaries, reaching a second particle, scattered by this particle and interacting with the boundaries, reaching a third particle, scattered by this particle and transmitted into the incident medium. The term $\bar{\mathcal{G}}_{\infty} : \bar{\mathbf{P}} : \bar{\mathcal{G}}_{S}$ describes a wave penetrating into the layer, scattered by a first particle, interacting with the boundaries, reaching a second particle, scattered by this particle, propagating directly toward a third

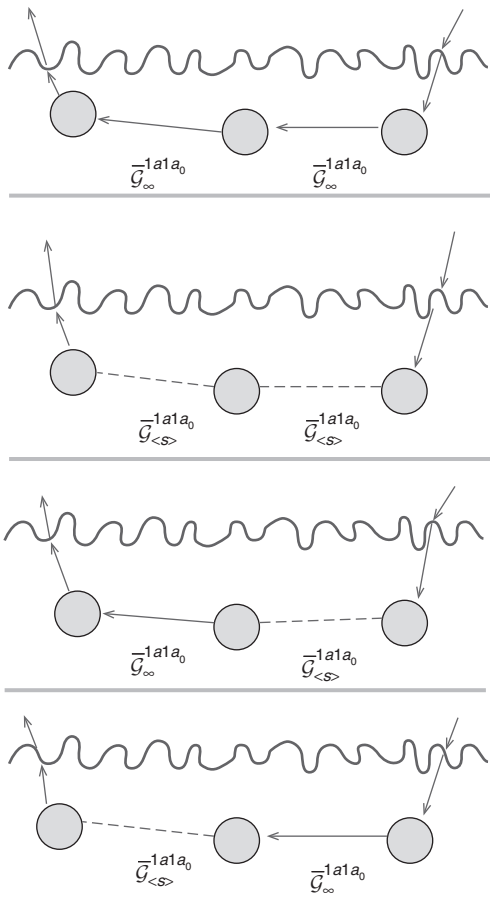
particle, scattered by this particle and transmitted into the incident medium. The term $\bar{\mathcal{G}}_{\langle s \rangle} : \bar{\mathbf{P}} : \bar{\mathcal{G}}_\infty$ describes a wave penetrating into the layer, scattered by a first particle, propagating directly toward a second particle, scattered by this particle, interacting with the boundaries, reaching a third particle, scattered by this particle and transmitted into the incident medium.

In Figs 6.25 and 6.26 we can see the different contributions for a scattering sequence with two particles (second-order scattering) or for a scattering sequence with three particles (third-order scattering).

We now examine the term $\bar{I}_{Crossed}^{incoh}$. Barabanenkov (e.g. References [91–93]) observed a new class of Feynman diagrams (the maximally-crossed diagrams) which contributes to the scattering with the ladder diagrams in the vicinity of the source direction. Far from the source direction, their contributions become negligible. The coherent backscattering enhancement is an interference effect which manifests itself at the level of the averaged mean intensity, it is also known as the weak localization effect. During the two last decades, several studies have been concerned with the enhanced backscattering.^{94–104} This phenomenon produces a peak in the backscattering direction $\hat{\mathbf{k}} = -\hat{\mathbf{k}}_0$ due to the interference of waves following the same path but in opposite directions



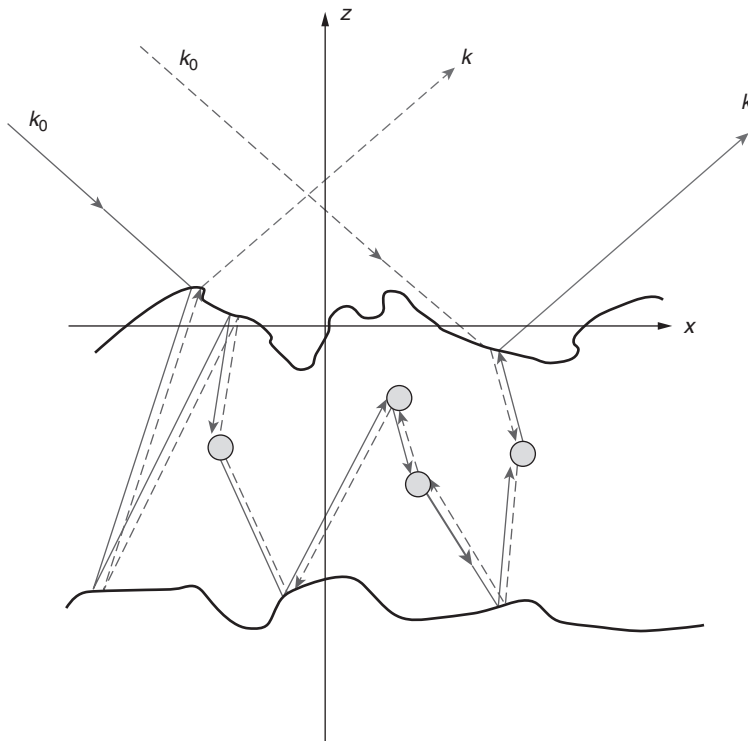
6.25 Contributions of the Green tensor to the first order.



6.26 Contributions of the Green tensor to the second order.

in a scattering medium composed of fixed, randomly placed spherical scatterers as shown in the schematic illustration in Fig. 6.27.

The most elegant way to introduce the enhanced backscattering in the theory is to use the reciprocity principle.¹⁰⁴ Heuristically, it means that when we exchange the source and the detector positions (respectively given by r_0 and r and their polarization), the field measured is the same. This physical property may be expressed with a mathematical operator the right transpose T_R of a tensor, whose definition is given in Appendix 6.11.2. Therefore we can write $\bar{I}_{\text{Crossed}}(\mathbf{R}, \mathbf{k})$ as a function of $\bar{I}_{\text{Ladder}}(\mathbf{R}, \mathbf{k})$. The demonstration is given in Reference [82]. The maximally-crossed terms are added to the expression for the specific intensity to satisfy the reciprocity principle. They



6.27 Process of the backscattering enhancement.

correspond to the maximally-crossed Feynman diagrams which describe the leading interference terms.

We have presented above a general formalism based on rigorous Dyson and Bethe-Salpeter equations which takes into account the scattering by the surface and the volume, the polarization components, the correlation between the scatterers and the expression for the coherent backscattering.

6.7.6 Coherent backscattering

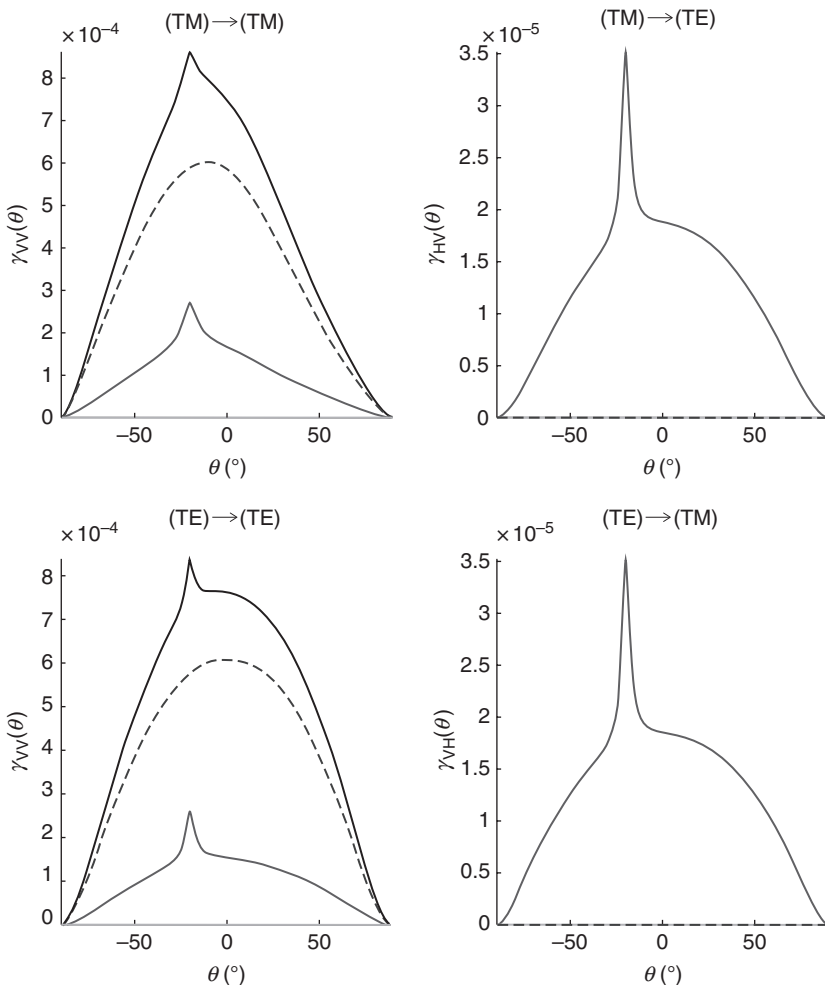
In this section, we study the coherent backscattering and the pattern of the cross-section from slabs illuminated by plane waves. We apply the transport theory based on the Bethe-Salpeter equation and its solution by moments discussed in the previous sections. We have obtained numerically the solutions for the cross-section involving laser light reflection from disordered samples in which coherent backscattering may be directly observed. With these examples, we give direct demonstrations of the effect.

Semi-infinite medium

For the first example, we take a semi-infinite three-dimensional medium with a planar interface. This example is interesting because the mean intensity, that is, the second moment of the Green function, contains only the contribution of the disordered medium. The permittivity of the medium containing the incident source is $\epsilon_0 = 1$, and we can assume that $H / \lambda \gg 1$. With this configuration, we can consider layers with large depth. The permittivity of the medium is $\epsilon_1 = 2 + i0.03$. We consider spherical scatterers with a radius given by $r_d = 0.035\lambda$, permittivity of $\epsilon_d = 5$, and a volume fraction of $f_{vol} = 10\%$. The scatterers are located randomly in the medium. In Fig 6.28, we have plotted the incoherent cross-section of the polarization components $TM-TM$, $TE-TE$, $TE-TM$ and $TM-TE$ for an angle of incidence $\theta_0 = -20^\circ$. The bistatic coefficients are computed in the plane of incidence ($\phi = \phi_0 = 0^\circ$). The total volume contribution is given by the black solid curve, the first order contribution is given by the blue dashed curve, and the higher order contribution (ladder and maximally crossed cross-section) by the solid red curve. The theoretical profile demonstrates the presence of a backscattering enhancement due to the higher-order contributions. Only the ‘ladder + most-crossed’ contributions give a depolarized effect ($TE-TM$ and $TM-TE$ curves). The fact that the peak value of the backscattering enhancement seems to be low is due to the dielectric scatterers for which the permittivity contrast between the medium and the scatterers is not high. As the contrast becomes lower, the higher order contributions are cut-off from the effect. Another phenomenon can eliminate the higher-order contributions given by the perturbative development of the Bethe-Salpeter equation, namely absorption in the medium. Limitation through absorption is a probabilistic process, whereas limitation through sample size is deterministic. We are in a configuration where the coherent backscattering peak is observable in the total scattered intensity, that is, it becomes measurable.^{106–109}

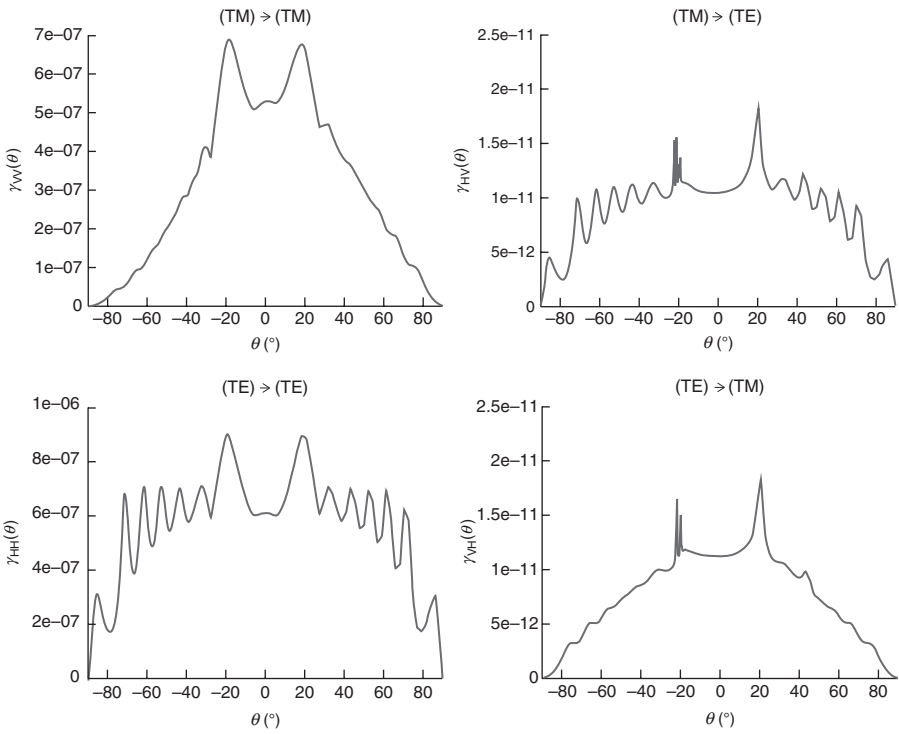
Random medium with two planar interfaces

In this section, we consider a dielectric slab with two planar interfaces. The depth of the layer is $H = 5\lambda$. The permittivity of the medium of the layer is $\epsilon_1 = 1.2$, this layer contains scatterers which are located randomly in the slab. The permittivity of the scatterers is $\epsilon_d = 2$, and they are considered to be spherical particles of radius $r_d = 0.035\lambda$. The fractional volume of the scatterers is $f_{vol} = 0.01\%$. The layer is deposited on a semi-infinite medium of permittivity $\epsilon_2 = 16$. We plot in Fig. 6.29 the polarized cross-section as a function of the scattering angle in the plane of incidence, the angle of incidence is $\theta_i = -20^\circ$. For the four polarization components $TM-TM$, $TE-TE$, $TE-TM$ and $TM-TE$, we observe a backscattering enhancement and a reflective enhancement, although the magnitude of the cross-section



6.28 Incoherent bistatic cross-section for the co-polarized and the cross-polarized scattering in the plane of incidence ($\phi = \phi_0 = 0^\circ$). The parameters of the medium are $\epsilon_1 = 2 + i0.03$, $\epsilon_d = 5$, $r_d = 0.035$, λ , $H/\lambda \gg 1$ and $f_{vol} = 10\%$. Total contribution (solid line); order 1 contribution (dashed line), the third curve (TE-TE and TM-TM components) represents higher-order contributions. We observe that the backscattering enhancement is given by the latter contributions. For the cross-polarized scattering only the higher-order contributions contribute to the total cross-section.

is small. In Fig. 6.30, we have the same parameters as Fig. 6.29 except that the scatterers are now metallic. The bistatic cross-section is larger (almost 15 dB). The theoretical profile of the coherent scattering is the same as in Fig. 6.29. We observe an order of magnitude enhancement of the incoherent

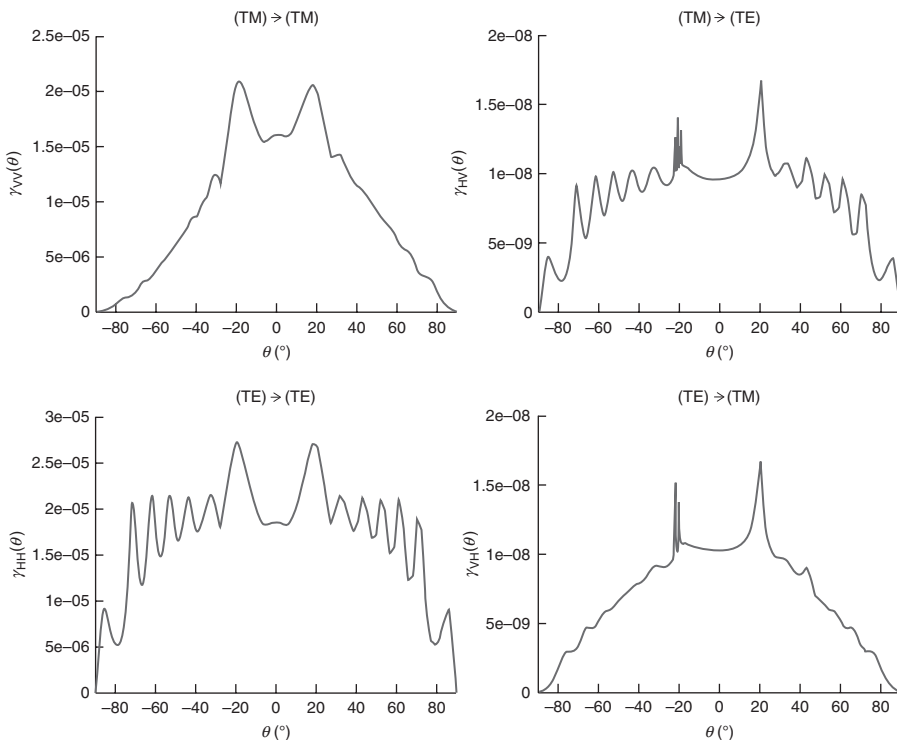


6.29 Total incoherent cross-section of a layer with dielectric scatterers bounded by two plane interfaces. Incident angle $\theta_i = -20^\circ$.

cross-section in the specular and anti-specular directions. We will now study the three-dimensional profile of the coherent backscattering. We have the same parameters as before. The scatterers are dielectric but the depth of the layer is 15λ . In Fig. 6.31, we plot the 3D TM-TM scattering coefficient. The axis represent $x = \sin\vartheta_d \cos\phi_d$, $y = \sin\vartheta_d \sin\phi_d$. Comparison of the results in the two figures indicates that a larger thickness gives a sharper backscattering peak. An important point to be noted is that the three-dimensional profile of the coherent backscattering has a cylindrical pattern.

Random medium with random rough interfaces

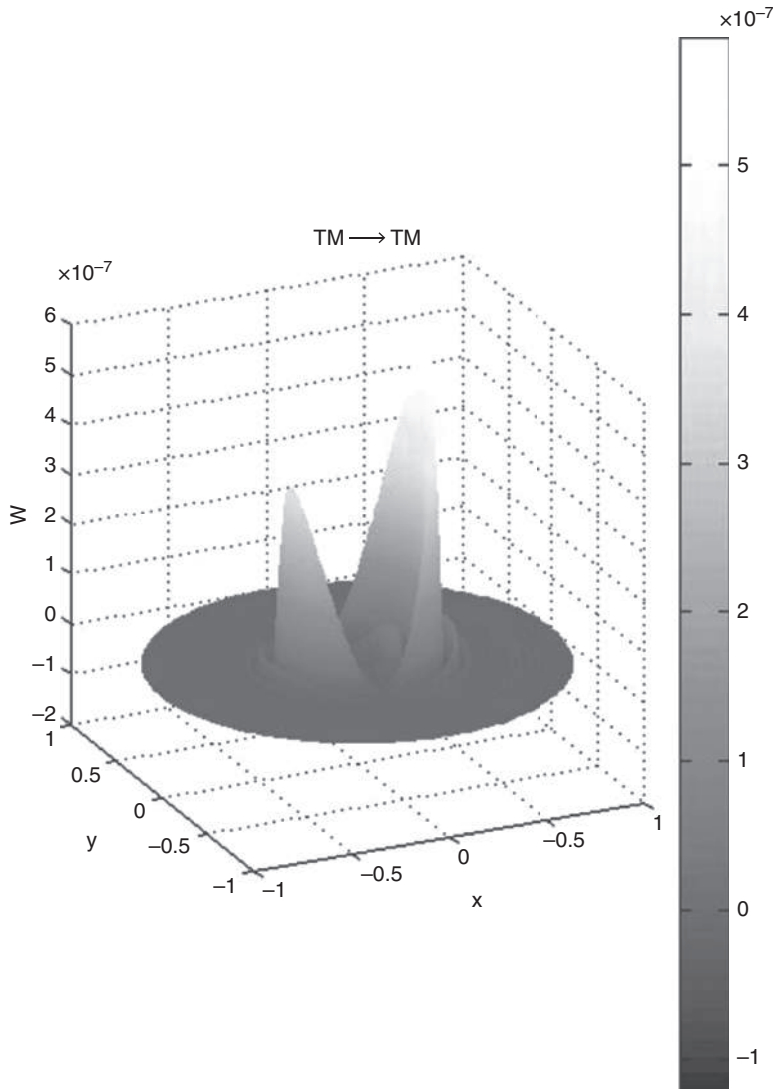
In this section, we consider a three-dimensional layer with randomly located spherical scatterers, that is bounded with a randomly rough upper surface and a planar lower interface. The upper surface is a Gaussian randomly rough surface, whose parameters are $\sigma/\lambda = 0.005$, $l/\lambda = 0.25$. The contribution of the randomly rough surface is computed (Fig. 6.32) with the small-perturbation approximation presented in the Section 6.6, and higher orders



6.30 Total incoherent cross-section of a layer with metallic scatterers bounded by two planar interfaces. Incident angle $\theta_i = -20^\circ$.

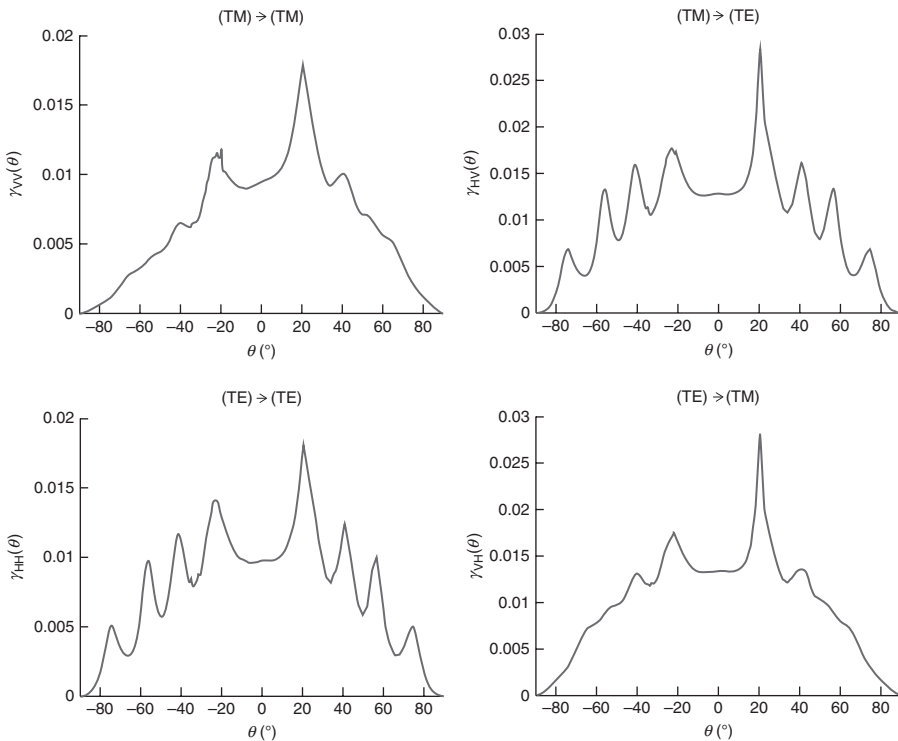
in the perturbative development must be used. The thickness of the layer is $H = 5\lambda$, its permittivity is $\epsilon_1 = 1.2$, The scatterers are spherical with a radius $r_d = 0.035\lambda$ and their permittivity is $\epsilon_d = 2$. The layer is deposited on a semi-infinite medium of permittivity $\epsilon_2 = 16$. The volume fraction of the scatterers is 0.15%. The wavelength is $\lambda = 1.54 \mu\text{m}$. The backscattering in the retroreflection direction is smaller than in the case of two planar interfaces, due to the contribution from the randomly rough surface.

We consider another example with a larger volume fraction of spherical nanoparticles. We compute the incoherent cross-section in the plane of incidence for a slab that is defined as follows. The medium of incidence in vacuum ($\epsilon_0 = 1$). The layer depth is $H = 5 \lambda$, its permittivity is $\epsilon_1 = 2$. The upper layer boundary is defined as a slightly randomly rough surface defined by the rms height of the surface $\sigma/\lambda = 0.01$ and the correlation length is given by $l/\lambda = 0.3$. The lower boundary is a planar interface that separates the layer from a semi-infinite medium of permittivity $\epsilon_2 = 16$. The wavelength is $\lambda = 1.5 \mu\text{m}$. The medium contains two types of spherical metallic particles



6.31 Three-dimensional profile of the TM–TM scattering coefficient. Same parameters as for Fig. 6.30, thickness of the slab is $H = 15\lambda$.

defined as Rayleigh spherical scatterers. The radius of the first type of particles is $r_1 = \lambda/20$. The volume fraction of these particles is $f_{vol1} = 0.0125$. For the second type of particles, the radius is $r_2 = \lambda/200$, the volume fraction is $f_{vol2} = 0.0375$. The total volume fraction is 5%. We obtain (Fig. 6.33) the total incoherent cross-section for an incident angle $\theta = 0^\circ$, for the co- and cross-polarized components and the circular polarization components (right to

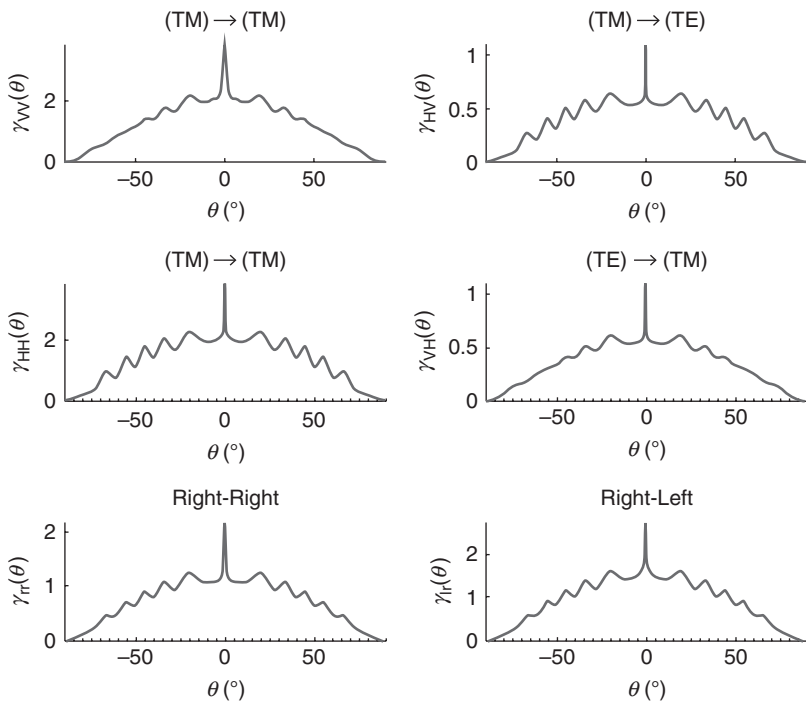


6.32 Incoherent cross-sections for a random slab with an upper rough surface and a plane lower interface in the plane of incidence ($\phi = \phi_0 = 0^\circ$). Angle of incidence $\theta_i = -20^\circ$.

right and right to left). The backscattering enhancement is due to the most-crossed diagram contributions. We notice that the second order contribution in the expansion of the Green tensor is about 5% of the first order contribution.

6.7.7 Conclusion

This section was devoted to a theory of transport based on a Bethe-Salpeter equation. We presented a multiple scattering theory (up to third-order) for a random slab with discrete scatterers and bounded with randomly rough surfaces. There is a smooth transition from the coherent regime, where a random medium appears locally homogeneous to the propagating electromagnetic wave, to the multiple-scattered behavior. Our approach is to treat this transition better by evaluating the Bethe-Salpeter equation. A new expansion of the Green tensor up to second order was developed,



6.33 Cross-section of a slab with an effective permittivity $\epsilon_e = 2.37 + i 1.747 \times 10^{-2}$. The disordered medium contains nanoscale metallic particles, the upper surface of the slab is a randomly rough surface, the angle of incidence is $\theta_0 = 0^\circ$, the wavelength is $\lambda = 1.5 \mu\text{m}$.

and calculations of the incoherent cross-sections were performed taking into account polarization components with the Mueller matrix. With two or three scatterings, we can observe that a fraction of the wave energy becomes incoherent, but there is still a finite fraction of the energy that remains coherent. We treat the behavior of the transport equation as a superposition of coherent and diffusive components. With the computations realized in this section, we explored the effects of the different parameters that characterize the random medium and the rough surfaces. We observed interference effects, backscattering enhancement peaks for the different examples in the case of the maximally-crossed contributions. But it remains an open question as to how many scatterings are required before a complete diffusive transport will be established. What we have demonstrated is that with a few scatterings, and despite the contributions of the rough boundaries, a weak localization of the polarized electromagnetic wave is well-established.

6.8 Applications

In this chapter we dealt with light that has been scattered many times. As we have shown, this is typically the case when light penetrates a medium with many randomly placed scatterers. In this case the light intensity diffuses through the medium. The mean free path gives the length scale defining when a wave is converted into diffuse light. For example, the mean free path exceeds the sample thickness in the ballistic regime and the mean free path is shorter than the sample thickness in the diffuse regime. There are medical applications that use diffusely scattered light, for example to locate and identify cancer cells by reconstructing three-dimensional images. There is another vast range of application of diffuse light scattering: passive or active remote sensing. We can extract information from observation satellite data to investigate, for example, the diffuse reflection from ice in the polar regions. The reflection of laser light in the case of active remote sensing can be used to study the composition of air or to construct laser images of the observed scene. Below, we will give examples of these applications and show that extracting information from the scattered light is a mathematically complex problem.

To illuminate the different applications and examples linked to the computation of rough surface and random volume scattering, we will focus on the problem of active remote sensing. The problem of active remote sensing is governed by the knowledge of the magnitude of the reflectance of the surfaces which compose the objects to be identified. To specify the equipment, it is necessary to compute the scattered intensity from the objects and the scene illuminated by the laser source. The non-conventional imaging systems explore the advantages of laser imagery to form hyperspectral polarimetric two-dimensional or three-dimensional images of the scene. There is considerable interest in the development of these new optical imaging systems that are able to give new information linked to the spectral reflectance of the surfaces of the objects. Potential applications range across the field of defense and security for the recognition of targets. For example, surveillance in land borders implies observation over wide areas and harsh environments like forests. The aim of such systems is to detect, locate, track and recognize persons and vehicles entering territory. This makes it very difficult for common systems like radar or cameras to detect hidden objects. Hyperspectral imagers can provide area surveillance with high resolution and improved capability to detect and identify targets and their traces in a complex background through the detailed analysis of target reflection properties. For these systems, technical challenges include development of software data processing for automatic target detection enabling both fast information and extraction from a large hyperspectral data stream.

Polarimetric analysis can enhance the capabilities of the extracted information to better distinguish man-made objects from a natural background.

The technique of laser imagery is based on the illumination of the scene by a laser and the subsequent collection of the backscattered intensity by a focal plane array to form an intensity image. For laser imaging systems, laser pulse illumination can be used in all lighting conditions, combined with range-gating technology in order to see through vegetation, camouflage and windows. Laser imaging can be applied to detection of persons and vehicles, but because of its high resolution, the technique is particularly suited for eliminating false alarms and for giving information of the target type (person, type of vehicle, etc.). The 1.54 μm laser band is attractive for 2D laser imagery applications where eye-safety is of concern. This band poses little chance for damage to retinal tissue at nominal power levels. Detector technology is critical to enabling 2D laser imagery. Competing focal plane areas in the 1.54 μm band or short wave infrared (SWIR) band are constructed from III-V materials such as InGaAs. Silicon is used for shorter wavelength laser systems that operate in the visible and near infrared band. The technological challenges include better knowledge of natural background clutter and its dependence on environmental conditions, better knowledge of the intensity scattered by the objects and the surfaces, that is, a better analysis of light scattering by random media and rough surfaces. Due to the wavelength of the laser, the surface of the considered objects must be considered as randomly rough surfaces. Broadband lasers allow detailed analysis of the reflection properties of a target and improve recognition capability. Technological challenges include further development of new active imaging concepts like multi-aperture systems, photon counting imaging, reflective tomographic imaging and range profiling for target identification.

High resolution three-dimensional imagery is one of the best candidates to identify objects hidden behind porous occluders like dense canopy. Laser radar (Ladar) technology has enjoyed significant advances over the past decade. Novel focal plane areas, compact laser illuminators and advanced signal processing have enabled the construction of low power 3D laser imagery systems. Synthetic images of three-dimensional objects are based on extraction of laser backscattered signals; the principle of 3D laser radar is based on the use of movable light sources and detectors to collect information on laser scattering, and to reconstruct the 3D object. A 3D reconstruction algorithm is a major component in these optical systems for identification of camouflaged objects. The ladar cameras can be used for measuring absolute distance by the time-of-flight technique. It is based on calculating the travel time of a light pulse to obtain the direct measures of distance. This technique offers outstanding qualities such as the ability to perform 3D measurements at distances from one to tens of kilometers. The

precision of the measurement is around a few centimeters. This 3D ladar system requires a short pulse of laser energy of the order of one nanosecond to separate targets from overlaid camouflage or forest canopy. Resolving closely spaced returns requires a high-bandwidth detector (more than 1GHz) and specific readout electronics. A substantial advantage over similar techniques, such as stereovision, is that the measurement process yields the distance value directly. Also, the devices can work in noisy environments such as dense vegetation spaces, generating three-dimensional images from the measurement of many points forming dense point clouds with a good spatial resolution.

Another alternative approach is based on a reflective tomography concept that takes advantage of the properties of the scattered intensity. This technique uses a set of 2D laser images at different angles of view. These sets contain the data collected by the pixels of the detectors. These data are related to the intensity backscattered by the scene illuminated by a laser pulse. This 3D reconstruction requires a laser system of lower complexity than in the case of the 3D time-of flight concept because we use an ordinary active imagery system. The scattered intensity contains the information for the 3D reconstruction. The robustness of identification of three-dimensional reconstructed images is directly related to the inversion and completion algorithms used in the process of identification. A notable limitation of numerous methods is that inversion algorithms produce blurred and noisy images and incomplete 3D reconstruction regardless of the technology used (3D time-of-flight Laser Radar or Ladar reflective tomography).

We have seen that it is very important to have reliable numerical models and simulations for light scattering cross-sections from random surfaces and media to specify the different 2D and 3D laser systems described above. The physics based model must be designed to provide accurate results but also to include all the electromagnetic interaction mechanisms with the different elements of the scene. The numerical simulation includes the physical structure of the environment, the transfer of radiation through the environment and the interaction of the laser wave with the structure of the different elements of the scene. These models incorporate a detailed understanding of the interaction of the laser electromagnetic wave, which is calculated by the small-slope approximation. The surface of the different vehicles or hard targets is considered as a randomly rough surface, and we compute the laser signature (Laser Cross-Section) of the vehicles.

The total electrical field scattered by a randomly rough surface or a random volume \mathbf{E}^s may be written as:

$$\mathbf{E}^s = \mathbf{E}^{sc} + \mathbf{E}^{si} \quad [6.223]$$

where \mathbf{E}^{sc} and \mathbf{E}^{si} are, respectively, the coherent and incoherent scattered components of the field defined by:

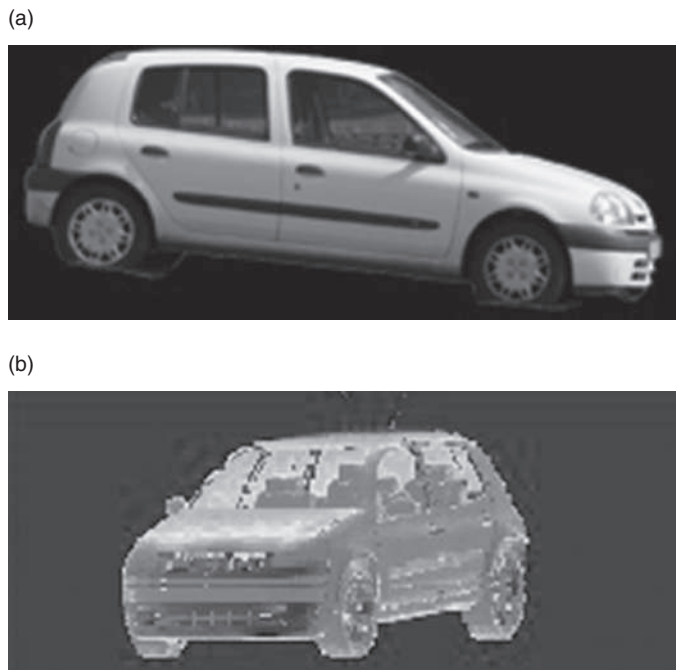
$$\mathbf{E}^{sc} = \langle \mathbf{E}^s \rangle \quad [6.224]$$

with $\langle \mathbf{E}^{si} \rangle = 0$.

The coherent component \mathbf{E}^{sc} is a deterministic component and the incoherent or diffuse component \mathbf{E}^{si} is a stochastic component with a null mean value. The mean value of the intensity of the incoherent scattered field is given by the following relation:

$$\langle |\mathbf{E}^{si}|^2 \rangle = \langle |\mathbf{E}^s - \langle \mathbf{E}^s \rangle|^2 \rangle = \langle |\mathbf{E}^s|^2 \rangle - \langle |\mathbf{E}^{sc}|^2 \rangle. \quad [6.225]$$

The scattering cross-section for a randomly rough surface or a random volume, which is a random variable depending on the stochastic process of the representation of the target surface and the target paint, is given by the first and second moments of the field. With this representation of the field, we can calculate the intensity of the field scattered by the object. All the scattering coefficients (coherent and incoherent components of the electromagnetic field) are functions of the azimuth angles. We define, in this case, the Mueller matrix, which gives all the combinations of the polarization states of the scattered electromagnetic waves as demonstrated in the preceding sections. The randomly rough surfaces of the complex object are characterized by electromagnetic parameters (permittivity) and roughness parameters (standard deviation of rough surface height and autocorrelation function). We take into account an effective permittivity for the paints. Effective medium theory or a homogenization approach is a powerful way to handle the scattering properties of composite materials such as porous media and microstructured materials. We have demonstrated in Section 6.7 that the light scattered from a rough slab with rough boundaries can be decomposed into four terms whose first component corresponds to an effective permittivity modeling the random medium with discrete scatterers. For metamaterials, the other terms can bring interesting contributions in the global laser cross-section in the backscattering direction. For example, small particles made of weakly dissipating materials may exhibit the so-called anomalous scattering (AS) without changes in the frequency of the incident light. Anomalous scattering has very little in common with Rayleigh scattering and results in giant optical resonances. We give examples (Figs 6.34 and 6.35) of 2D laser images for vehicles. We define a CAD model with facets for the different objects. Each facet contains the electromagnetic and roughness parameters. The second step of the numerical computation contains the simulation of the receiver, the transmitter and

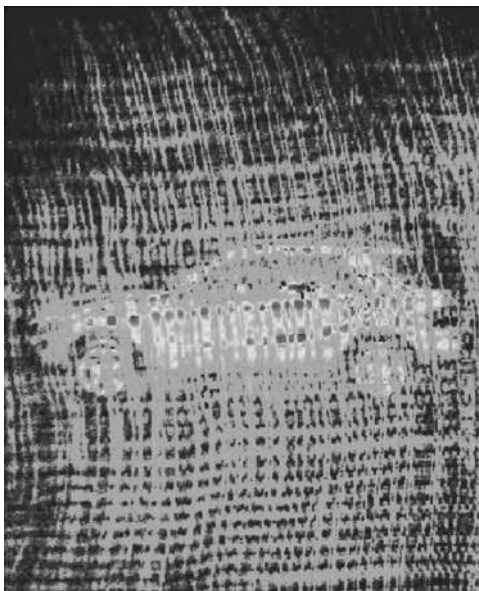


6.34 (a) Visible image of the vehicle. (b) Computation of a 2D laser image of the vehicle; the wavelength of the He-Ne laser is 632 nm. The laser wave is nonpolarized. The shades are related to the magnitude of the backscattered intensity. Our model also addresses transparent structures.

the optics system. The third step is the modeling of the electromagnetic scattering from the different objects of the scene. The fourth step contains the absorption and scattering of the laser wave by the components of the atmosphere, and the simulation of the atmospheric turbulence effects: speckles, scintillation, beam spreading, beam wandering.

We can observe that the simulation results for the 2D laser imaging are highly accurate. The computation of the laser scattering with the SSA is applied to each facet. The Laser Cross-Section of the object may be expressed as a 2×2 matrix in the polarization component basis related to the considered object.

We add now to the computing simulation a last step, which contains the development of a three-dimensional reconstruction algorithm to obtain a high resolved three-dimensional image. This kind of computer model can help to predict 3D Ladar performance, and it is used to develop a 3D reconstruction algorithm. We shall focus on reflective tomography algorithms for reconstructing optical three-dimensional scenes.^{110–112} We develop a cone-



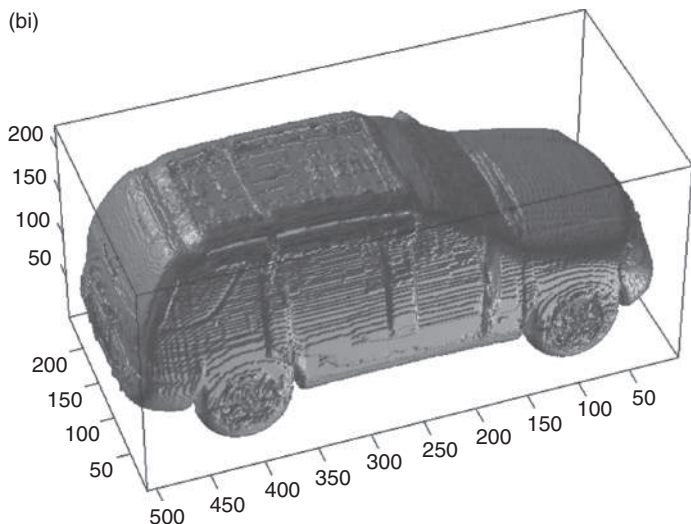
6.35 Computation of a non-polarized 2D laser image of a vehicle hidden behind a camouflage net. Laser wavelength 543 nm. The scattered intensity of the net is computed with measured reflectance data.

beam algorithm, related to the Feldkamp algorithm which is a convolution-backprojection algorithm deduced from the Radon transform.¹¹³ It uses a set of two-dimensional projections. In the case of laser images, these sets contain the data collected by the pixels of the planar detectors or focal plane areas. This backprojection algorithm allows the reconstruction of a 3D scene from a series of images parameterized by an angle of axial rotation. Reflective characteristics of target surfaces can be described by the combination of diffuse and coherent or specular reflection models. This combination is directly linked to the surface roughness and the structure of the volume bounded by the randomly rough surface. In Fig. 6.36, we give a full 3D reconstruction of a vehicle for an air-to-ground scenario. The reconstruction of the object is made of isodensity voxel (volumic pixel). The laser wavelength is 1.54 μm . The range between the scene and the sensor is 500 m. Figure 6.37 describes the scenario used for the 3D reconstruction of concealed vehicles and represents the CAD model of the air-to-ground scenario. Most of the incident laser energy is reflected, scattered, or absorbed by the foliage; a small amount can reach the target and this energy is backscattered by the target towards the focal plane area of the sensor. The sensor collects two-dimensional intensity images and our convolution-backprojection algorithm gives a 3D

(a)



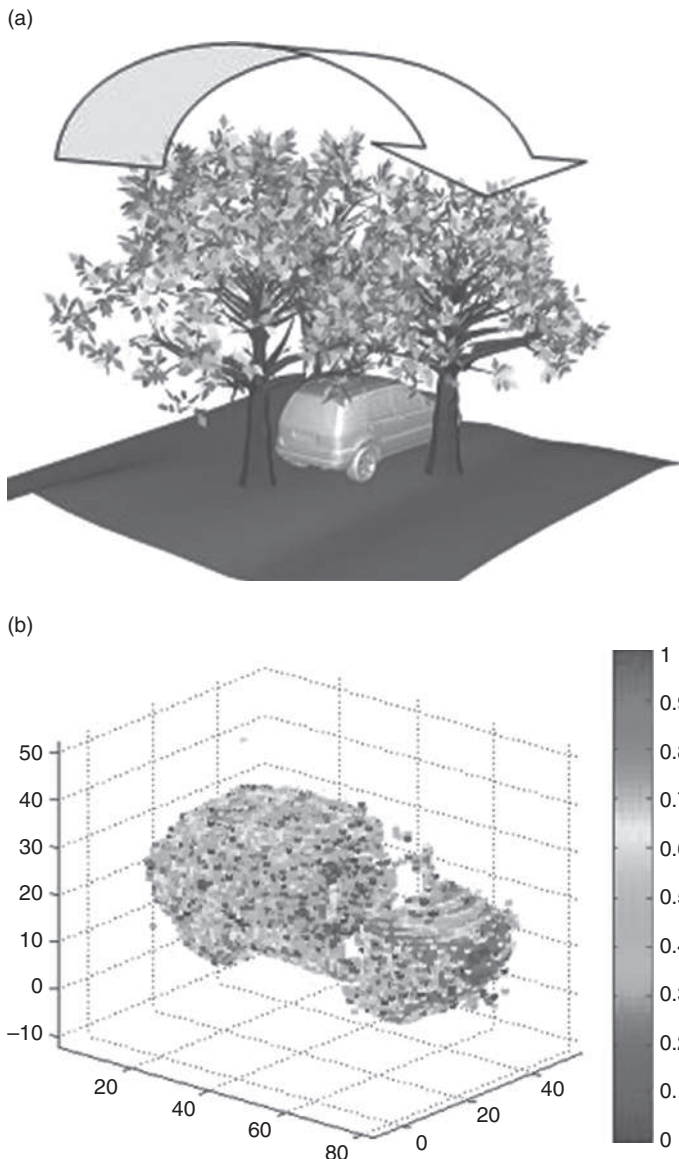
(bi)



(bii)



6.36 (a) Description of the air-to-ground scenario; wavelength $1.54 \mu\text{m}$, range 500 m. (b) Full 3D reconstruction with isodensity voxel (volume pixel), resolution $500 \times 200 \times 200$. (c) Comparison with CAD model.



6.37 (a) Description of the air-to-ground scenario; wavelength $1.54\text{ }\mu\text{m}$, range 500 m , the arrow describes the trajectory of the sensor. (b) Full 3D reconstruction with intensity voxel, the intensity is related to the laser intensity scattered by the different parts of the vehicle for the different angles of view, resolution $50 \times 80 \times 50$.

reconstruction of the vehicle under trees. Trees are modeled by polarized reflectance applied to the different facets generated by the CAD model.

Sparse data availability is due to the structures of the vehicle occluded by the canopy for the different angles of view. In Reference [113], we describe an algorithmic process to complete sparse 3D images at satisfactory levels for reliable identification of concealed objects. We have demonstrated that the reflected light contains sufficient information to recover the 3D objects of the hidden scene. Therefore, computational scattering models for random volumes and surfaces are of considerable importance in numerical simulation of active remote sensing in the visible or infrared band. They must be sufficiently accurate to allow the complete analysis of the reflected information.

6.9 Conclusion

This chapter contains a number of original concepts and new formulations for the scattering of light from random structures. The purposes of this chapter are to delineate a coherent outline of the theory and application of scattering from random structures and to make accessible the relevant theoretical methods of calculation by presenting both the physics and the mathematical framework. The complexity of the random structures considered increases along the different sections. With numerical nonperturbative solutions of reduced Rayleigh equations, we can now analyze extensively coherent phenomena due to multiple scattering for two-dimensional structures or three-dimensional films with one two-dimensional randomly rough surface. The study of the presence of satellite peaks for this kind of structure could be very interesting for the specification of optical films and the analysis of wave energy redistribution, for example the transfer of trapped electromagnetic radiation. The development of the small-slope approximation for three-dimensional rough films can provide new insight into electromagnetic scattering from rougher films. Formulation for rough films with discrete scatterers can give rise to the development of new devices based on metallic nanoparticles embedded in dielectric or insulating media by studying the optical behavior of these layers containing nanostructures and the evaluation of the potential use of these structures for optical applications. These computational tools can specify the exploitation of features of such assemblies as high local scattered intensity enhancement, and resonant behavior inducing absorption in the visible and near infrared spectral ranges. A last important point is the study of singularities in speckle patterns. With these formulations that take into account multiple scattering, we can study statistical properties in the scattering of an electromagnetic wave from rough random structures. For example, the calculation of the fourth moment of the field gives the intensity-intensity correlation function, and contains information about phase interference effects or speckle patterns.

The authors would like to thank Dr. Elena I. Chaikina for preparing Figs 6.1, 6.3 and 6.5; Professor Ingve Simonsen for providing Fig. 6.4; Professor Ingve Simonsen and Messers. Paul Anton Letnes and Tor Nordam for providing Figs 6.8 and 6.9; Dr. Claude Bourrelly for the numerical calculations necessary for many of the figures of Section 6.7 and Dr. Michel Jouffroy for providing figures for Section 6.8.

The research of A.A. Maradudin was supported in part by Air Force Research Laboratory contract FA 9453-08-C-0230.

6.10 References

1. A. R. McGurn, A. A. Maradudin and V. Celli, 'Localization effects in the scattering of light from a randomly rough grating', *Phys. Rev. B* **31**, 4866–4871 (1985).
2. A. A. Maradudin, E. Méndez and T. Michel, 'Backscattering effects in the elastic scattering of p-polarized light from a large amplitude random metallic grating', *Opt. Lett.* **14**, 151–153 (1989).
3. V. Freilikher, M. Pustilnik and I. Yurkevich, 'Wave scattering from a bounded medium with disorder', *Phys. Lett. A* **193**, 467–470 (1994).
4. J. A. Sánchez-Gil, A. A. Maradudin, Jun Q. Lu, V. D. Freilikher, M. Pustilnik and I. Yurkevich, 'Scattering of electromagnetic waves from a bounded medium with a random surface', *Phys. Rev. B* **50**, 15353–15368 (1994).
5. Z. L. Wang, H. Ogura and N. Takahashi, 'Enhanced scattering from a planar waveguide with a slightly rough boundary', *Phys. Rev. B* **52**, 6027–6041 (1995).
6. J. A. Sánchez-Gil, A. A. Maradudin, Jun Q. Lu, V. D. Freilikher, M. Pustilnik and I. Yurkevich, 'Satellite peaks in the scattering of p-polarized light from a randomly rough film on a perfectly conducting substrate', *J. Mod. Opt.* **43**, 435–452 (1996).
7. J. A. Sánchez-Gil, A. A. Maradudin, Jun Q. Lu and V. D. Freilikher, 'New features in the transmission of light through thin metal films with randomly rough surfaces', in IGARSS/IEEE '94 Digest, ed. I. I. Stein (IEEE Publications, Piscataway, NJ, 1994), pp. 273–276.
8. J. A. Sánchez-Gil, A. A. Maradudin, Jun. Q. Lu and V. D. Freilikher, 'Transmission of electromagnetic waves through thin metal films with randomly rough surfaces', *Phys. Rev. B* **51**, 17100–17115 (1995).
9. A. R. McGurn and A. A. Maradudin, 'An analogue of enhanced backscattering in the transmission of light through a thin film with a randomly rough surface', *Opt. Commun.* **72**, 279–285 (1989).
10. A. Madrazo and A. A. Maradudin, 'Numerical solutions of the reduced Rayleigh equation for the scattering of electromagnetic waves from rough dielectric films on perfectly conducting substrates', *Opt. Commun.* **134**, 251–268 (1997).
11. I. Simonsen and A. A. Maradudin, 'Numerical simulation of electromagnetic wave scattering from planar dielectric films deposited on rough perfectly conducting substrates', *Opt. Commun.* **162**, 99–111 (1999).
12. A. A. Maradudin, T. Michel, A.R. McGurn and E. R. Méndez, 'Enhanced backscattering of light from a random grating', *Ann. Phys. (N.Y.)* **203**, 255–307 (1990), Appendix A.

13. C. S. West and K. A. O'Donnell, 'Observation of backscattering enhancement from polaritons on a rough metal surface', *J. Opt. Soc. Am. A* **12**, 390–397 (1995).
14. A. A. Maradudin, A. R. McGurn and E. R. Méndez, 'Surface plasmon polariton mechanism for enhanced backscattering of light from one-dimensional randomly rough metal surfaces', *J. Opt. Soc. Am. A* **12**, 2500–2506 (1995).
15. W. H. Press, S. A. Teukolsky, W. T. Vetterling and B. P. Flannery, *Numerical Recipes*, 3rd ed. (Cambridge University Press, New York, 1992), p. 160.
16. W. H. Press, S. A. Teukolsky, W. T. Vetterling and B. P. Flannery, *Numerical Recipes*, 3rd ed. (Cambridge University Press, New York, 1992), p. 605.
17. F. Toigo, A. Marvin, V. Celli and N. R. Hill, 'Optical properties of rough surfaces: General theory and the small roughness limit', *Phys. Rev. B* **15**, 5618–5626 (1977).
18. G. C. Brown, V. Celli, M. Haller and A. Marvin, 'Vector theory of light scattering from a rough surface: unitary and reciprocal expansions', *Surf. Sci.* **136**, 381–387 (1984).
19. J. J. Greffet, 'Scattering of electromagnetic waves by rough dielectric surfaces', *Phys. Rev.* **37**, 6436–6441 (1988).
20. T. A. Leskova, A. A. Maradudin and W. Zierau, 'Surface plasmon polariton propagation near an index step', *Opt. Commun.* **249**, 23–35 (2005).
21. A. Soubret, G. Berginc and C. Bourrelly, 'Application of reduced Rayleigh equations to electromagnetic wave scattering by two-dimensional rough surfaces', *Phys. Rev. B* **63**, 245411 (1–20) (2001).
22. T. A. Leskova (unpublished work).
23. A. Soubret, G. Berginc and C. Bourrelly, 'Backscattering enhancement of an electromagnetic wave scattered by two-dimensional rough layers', *J. Opt. Soc. Am. A* **18**, 2778–2788 (2001).
24. R. M. Fitzgerald, T. A. Leskova and A. A. Maradudin, 'Transmission of light through a metal film with two corrugated surfaces', *Proc. SPIE* **5878**, 58780Z (1–14) (2005).
25. T. A. Leskova and A. A. Maradudin, 'Reduced Rayleigh equations in the scattering of s-polarized light from, and its transmission through, a film with two one-dimensional rough surfaces', *Proc. SPIE* **7065**, 706505 (1–12) (2008).
26. T. A. Leskova and A. A. Maradudin (unpublished work).
27. J. A. Porto, F. T. Garcia-Vidal and J. B. Pendry, 'Transmission resonances on metallic gratings with very narrow slits', *Phys. Rev. Lett.* **83**, 2845–2848 (1999).
28. I. Avrutsky, Y. Zhao and V. Kochergin, 'Surface-plasmon-assisted resonant tunneling of light through periodically corrugated thin metal film', *Opt. Lett.* **25**, 595–597 (2000).
29. B. Baumeier, T. A. Leskova and A. A. Maradudin, 'Transmission of light through a thin metal film with periodically and randomly corrugated surfaces', *J. Opt. A* **8**, S191S207 (2006).
30. A. R. McGurn and A. A. Maradudin, 'Perturbation theory results for the diffuse scattering of light from two-dimensional randomly rough surfaces', *Waves in Random Media*, **6**, 251–267 (1996).
31. J. T. Johnson, 'Third order small perturbation method for scattering from dielectric rough surfaces', *J. Opt. Soc. Am. A* **16**, 2720–2736 (1999).

32. P. Tran, V. Celli and A. A. Maradudin, ‘Electromagnetic scattering from a two-dimensional, randomly rough, perfectly conducting surface: Iterative methods’, *J. Opt. Soc. Am. A* **11**, 1685–1689 (1994).
33. R. L. Wagner, J. Song and W. C. Chew, ‘Monte Carlo simulation of electromagnetic scattering from two-dimensional randomly rough surfaces’, *IEEE Trans. Antenna Propag.* **45**, 235–245 (1997).
34. K. Pak, L. Tsang, C. H. Chan and J. T. Johnson, ‘Backscattering enhancement of the electromagnetic waves from two-dimensional perfectly conducting random rough surfaces based on Monte Carlo simulations’, *J. Opt. Soc. Am. A* **12**, 2491–2499 (1995).
35. J. T. Johnson, L. Tsang, R. T. Shin, K. Pak, C. H. Chan, A. Ishimaru and Y. Kuga, ‘Backscattering enhancement of electromagnetic waves from two-dimensional perfectly conducting random rough surfaces: a comparison of Monte Carlo simulations with experimental data’, *IEEE Trans. Antenna Propag.* **44**, 748–756 (1996).
36. D. Torrungrueng, H. -T. Chou and J. T. Johnson, ‘A novel acceleration algorithm for the computation of scattering from two-dimensional large-scale perfectly conducting random rough surfaces with the forward-backward method’, *IEEE Trans. Geosci. Remote Sensing* **38**, 1656–1668 (2000).
37. G. Soriano and M. Saillard, ‘Scattering of electromagnetic waves from two-dimensional rough surfaces with an impedance approximation’, *J. Opt. Soc. Am. A* **18**, 124–133 (2001).
38. I. Simonsen, A. A. Maradudin and T. A. Leskova, ‘Scattering of electromagnetic waves from two-dimensional randomly rough perfectly conducting surfaces: The full angular intensity distribution’, *Phys. Rev. A* **81**, 013806 (1–13) (2010).
39. I. Simonsen, J. B. Kryvi, A. A. Maradudin and T. A. Leskova, ‘Light scattering from anisotropic, randomly rough, perfectly conducting surfaces’, *Comp. Phys. Commun.* **182**, 1904–1908 (2011).
40. P. Tran and A. A. Maradudin, ‘Scattering of electromagnetic waves from a randomly rough 2D metallic surface’, *Opt. Commun.* **110**, 269–273 (1994).
41. L. Tsang, C. H. Chan and K. Pak, ‘Backscattering enhancement of a two-dimensional random rough surface (three-dimensional scattering) based on Monte Carlo simulations’, *J. Opt. Soc. Am. A* **11**, 711–715 (1994).
42. K. Pak, L. Tsang and J. T. Johnson, ‘Numerical simulations and backscattering enhancement of electromagnetic waves from two-dimensional dielectric random rough surfaces with the sparse-matrix canonical grid method’, *J. Opt. Soc. Am. A* **14**, 1515–1529 (1997).
43. N. Engheta, W. D. Murphy, V. Rokhlin and M. S. Vassilou, ‘The fast multipole method (FMM) for electromagnetic scattering problems’, *IEEE Trans. Antenna Propag.* **40**, 634–641 (1992).
44. V. Jandhyala, B. Shanker, E. Michielssen and W. C. Chew, ‘Fast algorithm for the analysis of scattering by dielectric rough surfaces’, *J. Opt. Soc. Am. A* **15**, 1877–1885 (1998).
45. I. Simonsen, A. A. Maradudin and T. A. Leskova, ‘Scattering of electromagnetic waves from two-dimensional randomly rough penetrable surfaces’, *Phys. Rev. Lett.* **104**, 223904 (1–4) (2010).

46. T. A. Leskova, P. A. Letnes, A. A. Maradudin, T. Nordam and I. Simonsen, 'The scattering of light from two-dimensional randomly rough surfaces', *Proc. SPIE* **8172**, 817209 (1–20). (2011).
47. W. H. Press, S. A. Teukolsky, W. T. Vetterling and B. P. Flannery, *Numerical Recipes*, 3rd ed. (Cambridge University Press, New York, 2007), p. 605.
48. W. H. Press, S. A. Teukolsky, W. T. Vetterling and B. P. Flannery, *Numerical Recipes*, 3rd ed. (Cambridge University Press, New York, 2007), p. 161.
49. P. B. Johnson and R. W. Christy, 'Optical constants of the noble metals', *Phys. Rev. B* **6**, 4370–4379 (1972).
50. A Soubret, A. Berginc and C. Bourrelly, 'Application of reduced Rayleigh equations to electromagnetic wave scattering by two-dimensional randomly rough surfaces', *Phys. Rev. B* **53**, 245411 (1–20) (2003).
51. T. A. Leskova (unpublished work).
52. T. Kawanishi, H. Ogura and Z. L. Wang, 'Scattering of an electromagnetic wave from a planar waveguide structure with a slightly 2D random surface', *Waves in Random Media*. **7**, 35–64 (1997).
53. T. Nordam, P. A. Letnes, A. A. Maradudin and I. Simonsen, "Satellite peaks in the scattering of light from the two-dimensional surface of a dielectric film on a planar metal surface," *Opt. Express* **20**, 11336–11350 (2012).
54. T. Nordam, P. A. Letnes and I. Simonsen (unpublished work).
55. A. V. Shchegrov, A. A. Maradudin and E. R. Mendez, 'Multiple scattering of light from randomly rough surfaces', in *Progress in Optics*, vol. **46**, ed. E. Wolf (Elsevier, Amsterdam, 2004), Chap. 2.
56. S. O. Rice, 'Reflection of electromagnetic waves from slightly rough surfaces', *Commun. Pure Appl. Math.* **4**, 351–378 (1951).
57. M. Nieto-Vesperinas, 'Depolarisation of electromagnetic waves scattered from slightly rough random surfaces: a study by means of the extinction theorem', *J. Opt. Soc. Am. A* **72**, 539–547 (1982).
58. L. Tsang and J. A. Kong, *Scattering of Electromagnetic Waves, Advanced Topics* (Wiley-Interscience, New York, 2001).
59. G. Berginc, 'Small-amplitude perturbation theory for two-dimensional surfaces' in *Light Scattering and Nanoscale Surface Roughness*, ed. A.A. Maradudin (Springer, Berlin, 2007).
60. A. Beckmann and A. Spizzichino, *The Scattering of Electromagnetic Waves from Rough Surfaces* (Pergamon, Oxford, 1963).
61. J. A. Ogilvy, *Theory of Wave Scattering From Random Rough Surfaces* (Adam Hilger, Bristol, 1991).
62. C. Bourlier, G. Berginc and J. Saillard, 'Theoretical study of the Kirchhoff integral from a two-dimensional randomly rough surface with shadowing effect: application to the backscattering coefficient for a perfectly-conducting surface', *Waves in Random Media*. **11**, 91–118 (2001).
63. E. Bahar, 'Full wave solutions for the depolarization of the scattered radiation fields by rough surfaces of arbitrary slopes', *IEEE Trans. Antennas Propag.* **29**, 443–454 (1981).
64. J. Shen and A. A. Maradudin, 'Multiple scattering of waves from random rough surfaces', *Phys. Rev. B* **22**, 4234–4240 (1980).

65. D. P. Winebrenner and A. Ishimaru, 'Investigation of a surface-field phase-perturbation technique for scattering from rough surfaces', *Radio Sci.* **20**, 161–170 (1985).
66. V. I. Tatarskii, 'The expansion of the solution of the rough-surface scattering problem in powers of quasi-slopes', *Waves in Random Media*. **3**, 127–146 (1993).
67. A. G. Voronovich, 'Small-slope approximation in wave scattering by rough surfaces', *Sov. Phys. JETP*. **62**, 65–70 (1985).
68. A. G. Voronovich, 'Small-slope approximation for electromagnetic wave scattering at a rough interface of two dielectric half-space', *Waves in Random Media*. **4**, 337–367 (1994).
69. A. G. Voronovich, *Wave Scattering from Rough Surfaces* (Springer, Berlin, 1994).
70. A. G. Voronovich, 'A two-scale model from the point of view of small-slope approximation', *Waves in Random Media*. **6**, 73–83 (1996).
71. A. G. Voronovich, 'Non-local small-slope approximation for wave scattering from rough surfaces', *Waves in Random Media*. **6**, 151–167 (1996).
72. I. M. Fuks and A. G. Voronovich, 'Wave diffraction by rough interfaces in an arbitrary plane-layered medium', *Waves in Random Media*. **10**, 253–272 (2000).
73. M.S. Gilbert and J.T. Johnson, 'A study of the higher-order small-slope approximation for scattering from a Gaussian rough surface', *Waves in Random Media*. **13**, 137–149 (2003).
74. A. Soubret, G. Berginc and C. Bourrelly, 'Application of reduced Rayleigh equations to electromagnetic wave scattering by two-dimensional randomly rough surfaces', *Phys. Rev. B* **63**, 245411 (1–20) (2001).
75. G. Berginc, 'Small-slope approximation method: a further study of vector wave scattering from two-dimensional surfaces and comparison with experimental data', *PIER*. **37**, 251–287 (2002).
76. G. Berginc and C. Bourrelly, 'The small-slope approximation method applied to a three-dimensional slab with rough boundaries', *PIER*. **73**, 131–211 (2007).
77. L. Tsang, J.A. Kong and R. Shin, *Theory of Microwave Remote Sensing* (Wiley-Interscience, New York, 1985).
78. L. A. Apresyan and Y. A. Kravtsov, *Radiation Transfer: Statistical and Wave Aspects* (Gordon and Breach, Amsterdam, 1996).
79. P. Sheng, *Introduction to Wave Scattering, Localization, and Mesoscopic Phenomena* (Academic Press, New York, 1995).
80. U. Frisch, 'Wave propagation in random medium', in *Probabilistic Methods in Applied Mathematics* vol 1, ed. A. Bharucha-Reid (Academic Press, New York, 1968).
81. A. Soubret and G. Berginc, 'Electromagnetic wave scattering from a random layer with rough interfaces I: Coherent field', arXiv:physics/0312133 (2003).
82. A. Soubret and G. Berginc, 'Electromagnetic wave scattering from a random layer with rough interfaces II: Diffusive intensity', arXiv:physics/0312136 (2003).
83. K. Pak, L. Tsang, L. Li and C. Chan, 'Combined random rough surface and volume scattering based on Monte-Carlo solutions of Maxwell's equation', *Radio Sci.* **28**, 331–338 (1993).

84. C. M. Lam and A. Ishimaru, 'Mueller matrix calculation for a slab of random medium with both random rough surfaces and discrete particles', *IEEE Trans. Antenna Propag.* **44**, 145–156 (1994).
85. S. Mudaliar, 'Scattering from a rough layer of a random medium', *Waves in Random Media*. **9**, 521–536 (1999).
86. S. Mudaliar, 'Diffuse waves in a random medium layer with rough boundaries', *Waves in Random Media*. **11**, 45–60 (2001).
87. S. Mudaliar, 'Electromagnetic wave scattering from a random medium layer with a random interface', *Waves in Random Media*. **4**, 167–176 (1994).
88. K. Furutsu, 'Random-volume scattering: Boundary effects, and enhanced back-scattering', *Phys. Rev. A* **43**, 2741–2762 (1991).
89. K. Furutsu, *Random Media and Boundaries – Unified Theory, Two-Scale Method, and Applications* (Springer-Verlag, Berlin, 1983).
90. A. Soubret and G. Berginc, 'Effective dielectric constant for random medium', arXiv:physics/0312117 (2003).
91. Y. N. Barabanenkov and V. D. Ozrin, 'Coherent enhancement of backscattered radiation in a randomly inhomogeneous medium: the diffusion approximation', *Sov. Phys. JETP*. **67**, 1117–1121 (1988).
92. Y. N. Barabanenkov, Y. A. Kravtsov, V. D. Ozrin and A.I. Saichev, 'Enhanced backscattering in optics', *Prog. Opt.* **29**, 65–197 (1991).
93. Y.N. Barabanenkov, L.M. Zurk and M. Y. Barabanenkov, 'Single scattering and diffusion approximations for modified radiative transfer theory of wave multiple scattering in dense media near resonance', *Prog. Electromagn. Res.* **15**, 27–61 (1997).
94. M. C. W. van Rossum and T. M. Nieuwenhuizen, 'Multiple scattering of classical waves: Microscopy, mesoscopy and diffusion', *Rev. Modern Phys.* **71**, 313–371 (1999).
95. V. L. Kuz'min and V. P. Romanov, 'Coherent phenomena in light scattering from disordered systems', *Physics Uspekhi* **39**, 231–260 (1996).
96. L. Tsang and A. Ishimaru, 'Backscattering enhancement of random discrete scatterers', *J. Opt. Soc. Am. A* **1**, 836–839 (1984).
97. L. Tsang and A. Ishimaru, 'Theory of backscattering enhancement of random discrete isotropic scatterers based on the summation of all ladder and cyclical terms', *J. Opt. Soc. Am. A* **2**, 1331–1338 (1985).
98. E. E. Gorodnichev, S. L. Dudarev, D. B. Rogozkin and M. I. Ryazanov, 'Coherent effects in backscattering of waves from a medium with random inhomogeneities', *Sov. Phys. JETP*. **66**, 938–944 (1987).
99. E. E. Gorodnichev, S. L. Dudarev and D. B. Rogozkin, 'Coherent backscattering enhancement under conditions of weak wave localization in disordered 3D and 2D systems', *Sov. Phys. JETP*. **69**, 481–490 (1989).
100. B.A. van Tiggelen and R. Maynard, 'Reciprocity and coherent backscattering of light', in *Wave Propagation in Complex Media*, ed. G. Papanicolaou (Springer-Verlag, Berlin, 1997), pp. 247–271.
101. M. B. van der Mark, M. P. van Albada and A. Lagendijk, 'Light scattering in strongly scattering media: multiple scattering and weak localization', *Phys. Rev. B* **37**, 3575–3592 (1988).
102. M. J. Stephen and G. Cwilich, 'Rayleigh scattering and weak localization: effects of polarization', *Phys. Rev. B* **34**, 7564–7572 (1986).

103. E. Akkermans, P. E. Wolf and G. Maret, ‘Theoretical study of the coherent back-scattering of light by disordered media’, *J. Phys. France*, **49**, 77–98 (1988).
104. B. A. van Tiggelen, ‘Localisation of waves’, in *Diffuse Waves in Complex Media*, ed. J. Fouque (Kluwer, Amsterdam, 1999), pp. 1–60.
105. A. Lagendijk and B. A. van Tiggelen, ‘Resonant multiple scattering of light’, *Phys. Rep.* **270**, 143–216 (1996).
106. Y. Kuga and A. Ishimaru, ‘Retroreflectance from a dense distribution of spherical particles’, *J. Opt. Soc. Am. A* **1**, 831–835 (1984).
107. M. P. van Albada and A. Lagendijk, ‘Observation of weak localization of light in a random medium’, *Phys. Rev. Lett.* **55**, 2692–2695 (1985).
108. P. E. Wolf and G. Maret, ‘Weak localization and coherent backscattering of photons in disordered media’, *Phys. Rev. Lett.* **55**, 2696–2699 (1985).
109. S. Etemad, R. Thompson and M. J. Andrejco, ‘Weak localization of photons: universal fluctuations and ensemble averaging’, *Phys. Rev. Lett.* **57**, 575–578 (1986).
110. G. Berginc and M. Jouffroy, ‘Simulation of 3D laser imaging’, *PIERS Online*, **6**(5), 415–419 (2010).
111. G. Berginc and M. Jouffroy, ‘3D laser imaging’, *PIERS Online*, **7**(5), 411–415 (2011).
112. I. Berechet and G. Berginc, ‘Advanced algorithms for identifying targets from a three-dimensional reconstruction of sparse 3D Ladar data’, *Proc SPIE*, **8172**, 81720Z (2011).
113. L. A. Feldkamp, L. C. Davis and J. W. Kress, ‘Practical cone-beam algorithm’, *J. Opt. Soc. Am. A* **6**, 612–619 (1984).

6.11 Appendices

Appendix 6.11.1 Definitions of the Scattering Matrices for a Single Rough Surface

We give here a summary of the formulas derived in Reference [74] in the case of the small-perturbation method.

$$\bar{X}_{s \varepsilon_0, \varepsilon_1}^{(0)}(\mathbf{p}_0) = \bar{\mathbf{D}}_{10}^-(\mathbf{p}_0) \cdot [\bar{\mathbf{D}}_{10}^+(\mathbf{p}_0)]^{-1}, \quad [\text{A6.11.1}]$$

$$\bar{X}_{s \varepsilon_0, \varepsilon_1}^{(1)}(\mathbf{u} | \mathbf{p}_0) = 2i\bar{\mathbf{Q}}^+(\mathbf{u} | \mathbf{p}_0), \quad [\text{A6.11.2}]$$

$$\bar{X}_{s \varepsilon_0, \varepsilon_1}^{(2)}(\mathbf{u} | \mathbf{p}_1 | \mathbf{p}_0) = \alpha_1(\mathbf{u}) \bar{\mathbf{Q}}^+(\mathbf{u} | \mathbf{p}_0) + \alpha_0(\mathbf{p}_0) \bar{\mathbf{Q}}^-(\mathbf{u} | \mathbf{p}_0) - 2 \bar{\mathbf{P}}(\mathbf{u} | \mathbf{p}_1) \cdot \bar{\mathbf{Q}}^+(\mathbf{p}_1 | \mathbf{p}_0), \quad [\text{A6.11.3}]$$

where

$$\bar{Q}^\pm(\mathbf{u} | \mathbf{p}_0) \equiv \frac{\alpha_1(\mathbf{u}) - \alpha_0(\mathbf{u})}{2 \alpha_0(\mathbf{p}_0)} [\bar{M}^{1+,0+}(\mathbf{u} | \mathbf{u})]^{-1} \cdot [\bar{M}^{1+,0-}(\mathbf{u} | \mathbf{p}_0) \pm \bar{M}^{1+,0+}(\mathbf{u} | \mathbf{p}_0) \cdot \bar{X}^{(0)}(\mathbf{p}_0)],$$

[A6.11.4]

or explicitly

$$\begin{aligned} \bar{Q}^+(\mathbf{u} | \mathbf{p}_0) = & (\varepsilon_1 - \varepsilon_0) [\bar{D}_{10}^+(\mathbf{u})]^{-1} \cdot \begin{pmatrix} \varepsilon_1 \| \mathbf{u} \| \| \mathbf{p}_0 \| - \varepsilon_1 \alpha_1(\mathbf{u}) \alpha_1(\mathbf{p}_0) \hat{\mathbf{u}} \cdot \hat{\mathbf{p}}_0 & -\varepsilon_0^{\frac{1}{2}} K_0 \alpha_1(\mathbf{u}) (\hat{\mathbf{u}} \times \hat{\mathbf{p}}_0)_z \\ -\varepsilon_0^{\frac{1}{2}} K_0 \alpha_1(\mathbf{p}_0) (\hat{\mathbf{u}} \times \hat{\mathbf{p}}_0)_z & \varepsilon_0 K_0^2 \hat{\mathbf{u}} \cdot \hat{\mathbf{p}}_0 \end{pmatrix} \\ & \cdot [\bar{D}_{10}^-(\mathbf{p}_0)]^{-1}, \end{aligned}$$

[A6.11.5]

$$\begin{aligned} \bar{Q}^-(\mathbf{u} | \mathbf{p}_0) = & \frac{(\varepsilon_1 - \varepsilon_0)}{\alpha_0(\mathbf{p}_0)} [\bar{D}_{10}^-(\mathbf{u})]^{-1}. \\ & \begin{pmatrix} \varepsilon_0 \alpha_1(\mathbf{p}_0) \| \mathbf{u} \| \| \mathbf{p}_0 \| - \varepsilon_1 \alpha_1(\mathbf{u}) \alpha_0^2(\mathbf{p}_0) \hat{\mathbf{u}} \cdot \hat{\mathbf{p}}_0 & -\varepsilon_0^{\frac{1}{2}} K_0 \alpha_1(\mathbf{u}) \alpha_1(\mathbf{p}_0) (\hat{\mathbf{u}} \times \hat{\mathbf{p}}_0)_z \\ \varepsilon_0^{\frac{1}{2}} K_0 \varepsilon_1 \alpha_0^2(\mathbf{p}_0) (\hat{\mathbf{u}} \times \hat{\mathbf{p}}_0)_z & \varepsilon_0 K_0^2 \alpha_1(\mathbf{p}_0) \hat{\mathbf{u}} \cdot \hat{\mathbf{p}}_0 \end{pmatrix} \\ & \cdot [\bar{D}_{10}^+(\mathbf{p}_0)]^{-1}, \end{aligned}$$

[A6.11.6]

$$\bar{P}(\mathbf{u} | \mathbf{p}_1) \equiv (\alpha_1(\mathbf{u}) - \alpha_0(\mathbf{u})) [\bar{M}^{1+,0+}(\mathbf{u} | \mathbf{u})]^{-1} \bar{M}^{1+,0+}(\mathbf{u} | \mathbf{p}_1)$$

[A6.11.7]

$$= (\varepsilon_1 - \varepsilon_0) [\bar{D}_{10}^+(\mathbf{u})]^{-1} \cdot \begin{pmatrix} \| \mathbf{u} \| \| \mathbf{p} \| + \alpha_1(\mathbf{u}) \alpha_0(\mathbf{p}) \hat{\mathbf{u}} \cdot \hat{\mathbf{p}}_1 & -\varepsilon_0^{\frac{1}{2}} K_0 \alpha_1(\mathbf{u}) (\hat{\mathbf{u}} \times \hat{\mathbf{p}}_1)_z \\ \varepsilon_0^{-\frac{1}{2}} K_0 \alpha_0(\mathbf{p}) (\hat{\mathbf{u}} \times \hat{\mathbf{p}}_1)_z & K_0^2 \hat{\mathbf{u}} \cdot \hat{\mathbf{p}}_1 \end{pmatrix},$$

[A6.11.8]

where

$$\bar{D}_{10}^\pm(\mathbf{p}_0) \equiv \begin{pmatrix} \varepsilon_1 \alpha_0(\mathbf{p}_0) \pm \varepsilon_0 \alpha_1(\mathbf{p}_0) & 0 \\ 0 & \alpha_0(\mathbf{p}_0) \pm \alpha_1(\mathbf{p}_0) \end{pmatrix}.$$

[A6.11.9]

Appendix 6.11.2 Mueller Matrix and Tensor

Tensor product of two matrices

The dimensions of $\bar{A}\{i, j\}$, $\bar{B}\{i, j\}$ are 2×2 , the resulting dimensions are $2 \times 2 \times 2 \times 2$

$$\bar{A} \otimes \bar{B} = \sum_{i,j,i',j'=1}^2 \bar{A}\{i, j\} \bar{B}^*\{i', j'\}, \quad [\text{A6.11.10}]$$

where the asterisk * denotes the complex conjugation of the components.

Product of two tensors defined by the symbol “:”

We define the two tensors $\bar{T}_1\{i, j, i', j'\}$, $\bar{T}_2\{i, j, i', j'\}$.

The product is given by:

$$\bar{T}_3\{i, j, i', j'\} = \sum_{i_1, i'_1} \bar{T}_1\{i, i', i_1, i'_1\} \bar{T}_2^*\{i_1, i', j, j'\}. \quad [\text{A6.11.11}]$$

Mueller Matrix

This matrix gives the intensity of the scattered wave as a function of two scattering matrices.

$$\bar{M}(p | p_0) = \bar{f}(p | p_0) \odot \bar{f}(p | p_0), \quad [\text{A6.11.12}]$$

$$\begin{aligned} \bar{f} \odot \bar{g} &\equiv \begin{pmatrix} f_{VV} & f_{VH} \\ f_{HV} & f_{HH} \end{pmatrix} \odot \begin{pmatrix} g_{VV} & g_{VH} \\ g_{HV} & g_{HH} \end{pmatrix} = \\ &\left\{ \begin{array}{cccc} f_{VV}g_{VH}^* & f_{VH}g_{VH}^* & \operatorname{Re}(f_{VV}g_{VH}^*) & -\operatorname{Im}(f_{VV}g_{VH}^*) \\ f_{HV}g_{HV}^* & f_{HH}g_{HH}^* & \operatorname{Re}(f_{HV}g_{HH}^*) & -\operatorname{Im}(f_{HV}g_{HH}^*) \\ 2\operatorname{Re}(f_{VV}g_{HV}^*) & 2\operatorname{Re}(f_{VH}g_{HH}^*) & \operatorname{Re}(f_{VV}g_{HH}^* + f_{VH}g_{HV}^*) & -\operatorname{Im}(f_{VV}g_{HH}^* - f_{VH}g_{HV}^*) \\ 2\operatorname{Im}(f_{VV}g_{HV}^*) & 2\operatorname{Im}(f_{VH}g_{HH}^*) & \operatorname{Im}(f_{VV}g_{HH}^* + f_{VH}g_{HV}^*) & \operatorname{Re}(f_{VV}g_{HH}^* - f_{VH}g_{HV}^*) \end{array} \right\} \end{aligned} \quad [\text{A6.11.13}]$$

Transformation $Tr^{\otimes \rightarrow \odot}$

This operator transforms a tensor into a Mueller Matrix:

$$Tr^{\otimes \rightarrow \odot} \bar{A}^1 \otimes \bar{A}^2^* = \bar{A}^1 \odot \bar{A}^2, \quad [\text{A6.11.14}]$$

where $\overline{\mathbf{A}}^1$ and $\overline{\mathbf{A}}^2$ are dyadic operators.

Right transpose of a tensor (the demonstration can be found in Ref [103], Equation D)

$$\left[\overline{\mathbf{M}}(\mathbf{p} | \mathbf{p}_0) \right]^{T_R} = \sum_{\beta, \beta', \beta_0, \beta'_0 = H, V} M_{\beta, \beta'; \beta_0, \beta'_0}^{T_R} \left(\hat{\mathbf{e}}_{\beta}^{0+}(\mathbf{p}) \otimes \hat{\mathbf{e}}_{\beta'}^{0+}(\mathbf{p}) \right) \left(\hat{\mathbf{e}}_{\beta_0}^{0-}(\mathbf{p}_0) \otimes \hat{\mathbf{e}}_{\beta'_0}^{0-}(\mathbf{p}_0) \right), \quad [A6.11.15]$$

with

$$M_{\beta\beta'; \beta_0\beta'_0}^{T_R} = M_{\beta\beta'_0; \beta\beta'} \text{ if } \beta' = \beta'_0, \quad [A6.11.16]$$

$$M_{\beta\beta'; \beta_0\beta'_0}^{T_R} = -M_{\beta\beta'_0; \beta\beta'} \text{ if } \beta' \neq \beta'_0, \quad [A6.11.17]$$

for $\beta, \beta', \beta_0, \beta'_0 = H, V$.

Optical properties of thin film materials at short wavelengths

J. LARRUQUERT, Instituto de Óptica-Consejo Superior de Investigaciones Científicas, Spain

DOI: 10.1533/9780857097316.2.290

Abstract: The chapter starts with an overview of the thresholds that are found through short wavelengths, which result in the definition of various ranges over the spectrum. The formulae to calculate reflection on and propagation through absorbing materials are given. The chapter then describes the optical behaviour of materials over the spectrum, going from dielectrics and metals at relatively long wavelengths to independent-atom behaviour and absorption edges at short wavelengths. Finally, the chapter gives the main features of coatings that are specific to short wavelengths, focussing on transmittance filters, high-reflectance coatings and coating-based polarizers and retarders.

Key words: optical properties of materials, far ultraviolet, extreme ultraviolet, soft x-rays, hard x-rays, gamma rays, absorption, thin films, multilayers.

7.1 Introduction

Electromagnetic waves are governed by equations that are common to the whole spectrum. This property displays the power and the beauty of the physics involved. However, materials behave very differently over the spectrum, which destroys this regularity to some extent. The differences in material behaviour are remarkable when one moves from the visible to shorter wavelengths, where dielectric materials start absorbing light somewhere in the ultraviolet (UV), until no material in nature is found to be transparent. When one moves to even shorter wavelengths, this lossy range is left behind and now materials start to interact less and less with radiation. This chapter is devoted to the description of these two regimes of material behaviour at short wavelengths. The optical properties of a material are characterized at each wavelength by the refractive index n , and the extinction coefficient k , usually named the optical constants; n is involved in the refraction introduced by the material, whereas k governs radiation absorption. The first regime encountered at short wavelengths

is characterized by a large value of k , whereas the second regime at even shorter wavelengths shows a continuous trend for a decreasing k , along with n approaching unity.

7.2 Material behaviour over the spectrum

The short-wavelength part of the spectrum can be divided into various ranges. Names for these ranges are not universal; the definitions used here are based on some natural thresholds and some simple wavelength numbers. At wavelengths shorter than the visible, a first strong threshold on material behaviour is found at ≈ 200 nm, where normal air starts to absorb radiation. This feature has important technological implications, since radiation requires vacuum to propagate. For this reason, we call the range below 200 nm the vacuum ultraviolet. However, the range where air absorbs is wide and it is convenient to split it up into several sub-ranges. The first sub-range below 200 nm will be called the far ultraviolet (FUV), as the next in the series is near UV (NUV) and mid UV. In spite of the strong absorption of air and most materials, a few of them are still transparent in the FUV, until a new threshold is reached: at ≈ 100 nm the last transparent material in nature, lithium fluoride (LiF), starts to absorb radiation. We face a significant threshold for optics below 100 nm: the lack of windows and of the possibility of harnessing light through refraction, along with the difficulty to devise efficient multilayer coatings. This threshold marks the entrance to the extreme ultraviolet (EUV), which will refer here to wavelengths shorter than 100 nm. The strong absorption of materials in the long EUV is due to the radiation excitation of outer shell electrons; the energy levels of these less-bound electrons are strongly affected by the chemical bonds of atoms. At short wavelengths, photons are often referred to for their energy in electron-volts:

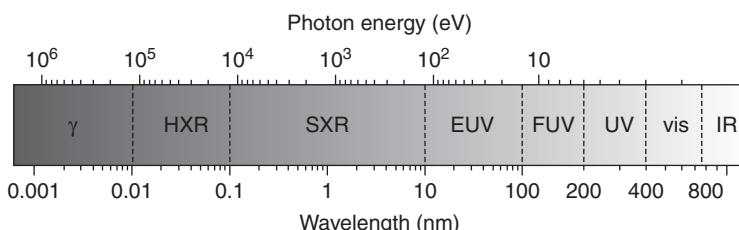
$$E(\text{eV}) = \frac{hc}{\lambda(\text{nm})} = \frac{1239.8}{\lambda(\text{nm})} \quad [7.1]$$

The strong EUV absorption of materials starts to decrease below ≈ 50 nm, that is, above ≈ 25 eV, although the specific wavelength depends on the material. When radiation wavelength keeps decreasing, and hence photon energy increases, the photon energy becomes large enough as to eject an electron from the second outermost shell of the atom; contrary to outer-shell electrons, the energy levels of more tightly bound electrons are much less affected by atomic chemical bonds. We can consider X-rays as the range at which tightly bound electrons are excited. The threshold for tightly bound electron excitation (electrons originating in a shell between the second outer one and

the innermost one) varies with the material and hence the edge between EUV and X-rays is somewhat arbitrary; here we will use 10 nm (124 eV), even though for many materials the excitation of inner electrons starts in the short EUV. The penetration capacity of X-rays through matter increases with photon energy; X-rays are divided into the less penetrating ones, soft X-rays (SXR), and the more penetrating ones, hard X-rays (HXR). The edge between SXR and HXR can be placed at 0.1 nm (12.4 keV), which is in the order of the atomic diameter. We have seen that absorption of materials starts to decrease below \approx 50 nm; the wavelength below which transparent materials are again available could be placed at \approx 1 nm (1.24 keV), where a several micron thick Be window can hold a vacuum over square-centimetre areas (Attwood, 1999). The absorption of air starts to be low enough as to enable optical systems operating in normal air (for a path of one decimetre) at wavelengths below \approx 0.2 nm ($E > 6.2$ keV), at the short-wavelength part of SXR. Hence the wavelength range that requires a vacuum to propagate spans over the \approx 0.2–200 nm (6.2 eV–6.2 keV) range, which involves SXR, EUV and FUV.

The next edge for radiation interaction with materials is gamma rays, with wavelengths shorter than \approx 0.01 nm ($E > 124$ keV), which is a markedly sub-atomic size. The edge between HXR and gamma rays is not abrupt and there is some common wavelength range where radiation will be called X-rays when they are emitted by electrons, but gamma rays when they are emitted by the nucleus. SXR, HXR and gamma rays are ranges of decreasing absorption and refraction, so that optical elements, and particularly coatings, become less and less efficient in manipulating radiation. Figure 7.1 depicts the short-wavelength ranges over the spectrum.

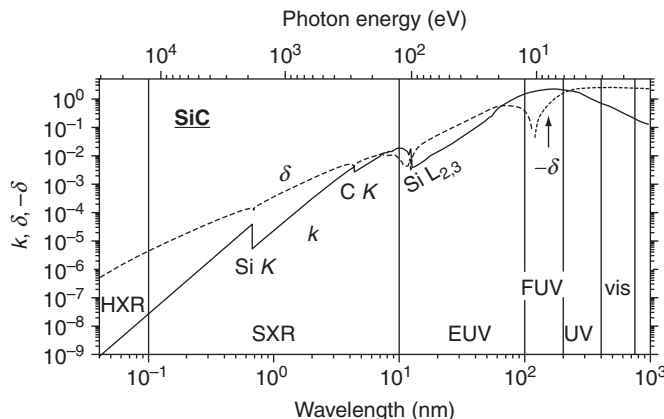
In addition to what was said on absorption, materials show some other specific features at short wavelengths which differ from those exhibited in the visible:



7.1 Names and limits of ranges in the electromagnetic spectrum as used in the chapter.

- Reduced refraction in the SXR and shortwards, with the refractive index approaching unity. This makes light manipulation inefficient.
- Relaxed diffraction limit, which reduces with wavelength. This enables imaging with larger resolution to be performed, useful for fields like microscopy or optical-projection lithography.
- Increased scattering, which depends on the average roughness height normalized to wavelength.
- Total reflection at grazing incidence due to a refractive index slightly lower than unity in the SXR-HXR and the short EUV.
- Information that can be obtained from materials differs from that in the visible; useful for spectroscopy in applications such as astrophysics, hot-plasma diagnostics and also X-ray photoelectron spectroscopy.
- High-energy photons. This results in a large penetration in the HXR and gamma, useful in medicine through radiography and scintigraphy. It also enables short-time pulses, such as attosecond pulses, which require photon energy at least in the short EUV because pulses must spread in a wide energy band.
- Ionizing radiation includes EUV, SXR, HXR and gamma. This results in a health hazard, mainly with the latter two because they can propagate in air.

Figure 7.2 displays $\delta = 1 - n$ and k for SiC in a broad spectrum, where the high absorption in the ultraviolet and the decrease of absorption and refraction at short wavelengths can be observed; δ is used for convenience when n is lower than unity.



7.2 k and $\delta = 1 - n$ of SiC in a broad spectral range (Larrauquert *et al.*, 2011a). At long wavelengths $-\delta = n - 1$ is plotted.

7.3 Reflection and transmission in absorbing materials

The absorption degree of a material is included in the refractive index as an imaginary part, turning the refractive index into a complex number:

$$N = n + ik \quad [7.2]$$

where the imaginary part k is called the extinction coefficient. In Equation [7.2] k is always positive. It is also possible to work with a negative k in Equation [7.2]; both are correct if used properly and the specific sign depends on the choice of the temporal wave term $\exp(\pm i\omega t)$ (Holm, 1998). The complex index N is also usually called the refractive index, like its real part. To avoid confusion, we will use here the upper case for the complex number and the lower case for its real part. The transmission of light through an absorbing medium with thickness x , assuming reflectance is negligible, is given by the Beer-Lambert law:

$$I = I_0 e^{-\mu x} \quad [7.3]$$

where I_0 and I are the radiation irradiance (often called intensity) that enters and exits the medium, respectively. μ (also α is often used) stands for the absorption coefficient, which is related to k through:

$$\mu = \frac{4\pi k}{\lambda} \quad [7.4]$$

where λ is the radiation wavelength in vacuum.

Let us review the formulae for the reflection and transmission at a boundary. Let a plane wave impinge from a non-absorbing medium with refractive index n_0 onto an absorbing medium with refractive index $N_1 = n_1 + ik_1$. Let the incoming wave vector \mathbf{k} (bold face, to avoid confusion with the extinction coefficient) form an angle θ_0 with the normal to the interface, which will be called the incidence angle. Then Snell's law of refraction can be extended to interfaces with absorbing materials through:

$$n_0 \sin \theta_0 = N_1 \sin \Theta_1. \quad [7.5]$$

This is a convenient expression although it must be understood correctly. Since N_1 is complex, so must be Θ_1 . This does not mean that the light propagates with a complex angle; Equation [7.5] and Θ_1 are just convenient tools to calculate radiation propagation through absorbing materials. The fact that Θ_1 is complex arises in that radiation in the absorbing medium propagates as an

inhomogeneous wave, that is, the planes of constant amplitude are not coincident with the planes of constant phase, except at normal incidence (where Θ_1 turns real). The planes of constant amplitude are parallel to the interface, regardless of the incidence angle; the planes of constant phase form a real angle θ_1 (this is the lower case Greek letter, versus the upper case complex Θ_1 in Equation [7.5]) with the normal to the interface given by:

$$\operatorname{tg}\theta_1 = \frac{n_0 \sin \theta_0}{\operatorname{Re}(N_1 \cos \Theta_1)} \quad [7.6]$$

where Re stands for the real part of the complex number. If the material is transparent and hence N_1 is real, then complex Θ_1 of Equation [7.6] simplifies to real θ_1 . The optical response of materials can be also described with other parameters related with the refractive index, such as the dielectric constant ε (i.e., the permittivity of the material normalized to the vacuum permittivity ε_0), the optical conductivity σ (the electrical conductivity in the presence of an electromagnetic wave) and the susceptibility χ (the polarization in response to an electromagnetic wave):

$$\varepsilon = 1 + \frac{i\sigma(\omega)}{\omega\varepsilon_0} = 1 + \chi = N^2 = (n + ik)^2 \quad [7.7]$$

In the above equation, SI units are assumed. All $\varepsilon, \sigma, \chi$ and N are complex for absorbing materials, which means that the specific electrical function will get phase shifted at an interface with an absorbing material with respect to the incoming wave.

Let a plane wave impinge on a plane boundary from medium N_1 to N_2 , both absorbing in general. The electric field of the incident wave at the boundary can be decomposed into two components: one in the incidence plane, which is called p polarization or TM (transversal magnetic), and the other in the perpendicular plane, which is referred to as s polarization or TE (transversal electric). The electric field in the reflected and transmitted waves (both normalized to the incident one) are given by Fresnel coefficients (Hecht, 2002):

$$\begin{aligned} r_s &= \frac{N_1 \cos \Theta_1 - N_2 \cos \Theta_2}{N_1 \cos \Theta_1 + N_2 \cos \Theta_2} \\ t_s &= \frac{2N_1 \cos \Theta_1}{N_1 \cos \Theta_1 + N_2 \cos \Theta_2} \\ r_p &= \frac{N_2 \cos \Theta_1 - N_1 \cos \Theta_2}{N_2 \cos \Theta_1 + N_1 \cos \Theta_2} \\ t_p &= \frac{2N_1 \cos \Theta_1}{N_2 \cos \Theta_1 + N_1 \cos \Theta_2} \end{aligned} \quad [7.8]$$

where r_s , r_p , t_s and t_p are called the reflection and transmission coefficients for the electric fields. When absorbing materials are involved, all these coefficients are complex numbers, which means that at reflection and at transmission, both an amplitude change and also a phase shift are produced, which are given by the coefficient modulus and phase, respectively, of Fresnel coefficients. Depending on the sign convention for the electric field at the reflected wave, r_p can be defined with opposite sign (Holm, 1998).

When we go from one interface to the various interfaces of a multilayer, the accumulated value of the electric field due to interferences among radiation reflected at all interfaces, as with transparent materials, is calculated iteratively starting with the innermost interface (Parratt, 1954), or equivalently with a matrix procedure (Abelès, 1948) which gives a total reflected/transmitted electric field (normalized to the incident one). The calculation procedure when layers absorb radiation is formally identical to the case of transparent layers.

In the most usual case of non-absorbing entrance and exit media, the reflected/transmitted irradiances (intensities) of a multilayer, normalized to the incident one, are given by:

$$\begin{aligned} R_{s,p} &= |r_{s,p}|^2 \\ T_{s,p} &= \frac{n_{\text{out}} \cos \theta_{\text{out}}}{n_{\text{in}} \cos \theta_{\text{in}}} |t_{s,p}|^2 \end{aligned} \quad [7.9]$$

where r and t stand for the accumulated value of the reflected or transmitted electric field of the whole multilayer system. Lower case r , t or upper case R , T are used for reflected/transmitted electric field or irradiance ratio, respectively. (Unfortunately, the previous rule to distinguish real/complex refractive indices with lower/upper case is reversed for reflected and transmitted ratios in order to follow typical notation.) In the following text, the irradiance ratios will simply be named as reflectance and transmittance unless otherwise specified. With absorbing materials, a fraction of the irradiation is lost by absorption A , so that:

$$A + R + T = 1 \quad [7.10]$$

7.3.1 Roughness and scattering

When a wave front interacts with an interface, the presence of roughness distorts the wave front, giving rise to diffusely scattered waves in all directions and to modified (mostly reduced) specular reflectance and direct transmittance (Kretschmann and Kröger, 1975). Roughness-induced effects are

a function of interface roughness normalized to wavelength. When wavelength is long enough, it is technologically feasible to minimize roughness effects, but the shorter the wavelength, the more difficult this minimization, since surface irregularities that are negligible at long wavelengths may be destructive at short ones.

In addition to scattering, the interaction of light with roughness in metals generates absorbing modes called surface plasmons; these modes have a resonant frequency ω_{sp} called the surface plasmon frequency, which for free electron metals is:

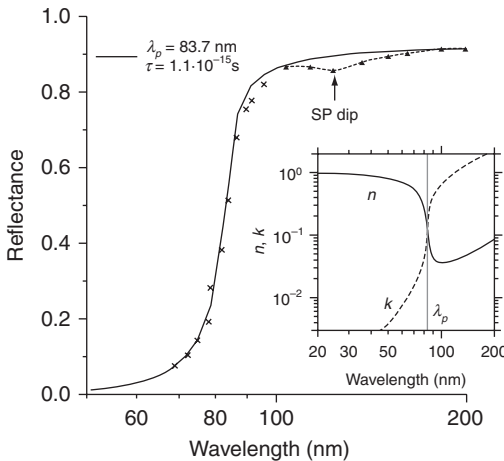
$$\omega_{sp} = \frac{\omega_p}{\sqrt{2}} \quad [7.11]$$

where ω_p is the plasma frequency of the metal that will be defined in Section 7.4.3. In Equation [7.11] light is assumed to impinge on the metal from vacuum. For a metal, the generation of surface plasmons results in a reflectance dip around ω_{sp} . A reflectance dip due to surface-plasmon excitation is displayed in Fig. 7.3. Surface plasmons are generated by the interaction of radiation with micro-irregularities with a width mainly smaller than λ , whereas micro-irregularities wider than λ are responsible for scattered light away from the specular reflection or from the direct transmission.

The exact calculation of roughness effect on optical performance is rather complicated and usually simple approaches are used. For high quality optical surfaces, the deviation of the real surface from the theoretical one in the propagation direction can often be considered to be a small fraction of wavelength. This is usually the case in optics, so that perturbation models can be used.

A theory that gives second-order roughness correction for the reflectance and the transmittance at an interface was obtained by Croce (1977 and 1978), with no further restriction other than the height of irregularities being small; Kretschmann and Kröger (1975) also developed a second-order theory that is limited to the case of normal incidence. These theories incorporate surface roughness by means of its 2-dimension power spectral density, which is obtained through the square modulus of the Fourier transform of the roughness height distribution. Computing the effect of roughness on reflectance and transmittance with the Croce model requires some involved calculations. Therefore, more simple models are usually preferred.

The most common simple roughness-induced scattering model is the one based on the work of Debye (1913) and Waller (1923). In this approach roughness irregularities are assumed to have a width much larger than radiation wavelength; even though this requirement is often not satisfied, the model is used anyway for its simplicity. The model does not describe the generation



7.3 Normal incidence reflectance of Al close to its plasma wavelength. Lines: reflectance calculated with a Drude model with $\lambda_p = 83.7 \text{ nm}$ and $\tau = 1.1 \times 10^{-15} \text{ s}$, as reported by Hunter (1964b). These parameters were calculated using the data of La Villa and Mendlowitz (1962) (crosses) and Madden *et al.* (1963) (triangles), as taken from La Villa (as cited by Hunter 1964b) and from Hunter (1964b). SP stands for surface plasmon. Inset: n, k calculated using the same Drude model.

of surface plasmons; it describes roughness through a single parameter, σ , which stands for the root-mean-square (RMS) height of irregularities with respect to an average plane. In this limit, the Fresnel coefficients of Equation [7.8] can be modified to include surface/interface roughness (Croce, 1977):

$$\begin{aligned} r &= r_0 \exp\left(-\frac{8\pi^2\sigma^2N_1^2\cos\Theta_1^2}{\lambda^2}\right) \\ t &= t_0 \exp\left[-\frac{2\pi^2\sigma^2(N_1\cos\Theta_1 - N_2\cos\Theta_2)^2}{\lambda^2}\right] \end{aligned} \quad [7.12]$$

where r_0 and t_0 stand for the reflection and transmission Fresnel coefficients of an identical interface that is perfectly smooth. N_1 and N_2 stand for the refractive index of the incident and transmission media, respectively. N_1, N_2, Θ_1 and Θ_2 can be complex numbers in general, as described in Section 7.3. A similar result is obtained if the rough interface is approximated by a refractive index continuously progressing from N_1 to N_2 following a Gaussian distribution of width σ (Stearns, 1989 and 1994). At grazing incidence and below the critical angle of total reflection (see Section 7.4.4), Nérot and Croce (1980) found that reflectance measurements are fit better with the following equation:

$$r = r_0 \exp\left(-\frac{8\pi^2\sigma^2N_1\cos\Theta_1N_2\cos\Theta_2}{\lambda^2}\right) \quad [7.13]$$

Additional information can be found in Bennet and Porteus (1961), Kretschmann and Kröger (1975), Croce (1977), Croce (1978), Nérot and Croce (1980), Sinha *et al.* (1988), Stearns (1992) and Spiller (1994). Windt (1998) developed useful software that addresses all relevant calculations on multilayers with absorbing materials, including the effect of rough interfaces.

7.4 The optical constants of materials at short wavelengths

This section gives a simple description of the material–radiation interaction at short wavelengths. More detailed information can be found in the literature (James, 1962; Stern, 1963; Henke *et al.*, 1982, 1993; Spiller, 1994; Chantler *et al.*, 1995; Attwood, 1999; Gullikson, 2000; Kittel, 2005). Other volumes centred on techniques that involve UV radiation also provide valuable information (Samson, 1967b; Samson and Ederer, 2000).

7.4.1 Interaction mechanisms between photons and matter

Absorption at short wavelengths is mostly due to the interaction of an incoming photon with an electron in an atom. The response of atoms (heavier than electrons) to an electric field results in resonance frequencies much smaller than those of electrons; hence the vibrations of atoms are in the IR, whereas those of electrons lie in the visible and shorter wavelengths. Absorption occurs when the incoming photon energy equals the difference between an occupied and a vacant electron energy level of the material; when the photon energy exceeds the binding energy of the electron, the latter is ejected and the atom or molecule is momentarily ionized. When the material is in a condensed state, the outer electron levels extend through a continuum of energies called bands. The excited or ionized atom or molecule will tend to relax by one or more electron transitions from a higher to a lower level, with the emission of one or more photons and sometimes also an electron. The emitted photon or electron brings important information about the atom or molecule energy levels, which is the basis for various spectroscopy techniques, such as Fluorescence Spectroscopy and X-ray Photoelectron Spectroscopy (XPS).

Photons in the visible, NUV, FUV and long EUV have energies able to excite less-bound electrons, as those in a band of a crystalline solid; these

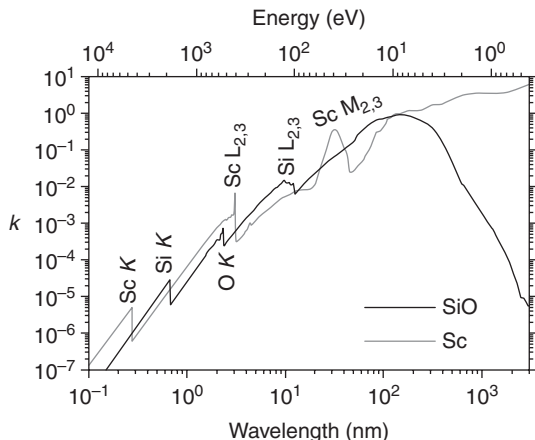
electrons carry information of the molecular bonds. When photon energy is large enough to create a vacancy of a tightly bound electron, such as with HXR, SXR and short EUV, the emitted photon or electron provides information mostly of the energy levels or states of the individual atom involved. Other than photon-electron interaction, absorption of high-energy gamma rays may involve interaction with the nucleus.

This simple approach to understanding the optical properties of materials in the FUV and shorter wavelengths will look at which electrons are involved in the absorption.

- (a) In a dielectric (or semiconductor), there is no essential absorption while the photon energy is smaller than the material bandgap. The bandgap energy marks the edge between the transparent and the absorbing range of the material; this is addressed in Section 7.4.2. The largest bandgaps (and hence the shortest wavelength edge between the transparent and the absorbing range) of materials in nature are in the FUV.
- (b) In a metal, the less-bound (conduction) electrons can be considered as free and their behaviour governs the optical properties of the material, that is, high reflectivity and strong absorption. This is addressed in Section 7.4.3.
- (c) In both metal or dielectric, when the photon energy is large enough to excite the inner electron levels of the atom (HXR, SXR and short EUV) then the difference between metals and dielectrics mostly becomes blurred for optics. This is addressed in Section 7.4.4. An example of this blurring of the difference between metals and dielectrics is displayed in Fig. 7.4, which compares k of metal Sc and dielectric SiO: both show similar trends in the EUV and at shorter wavelengths (except for the specific material absorption edges), and they deviate from each other in the UV and longer wavelengths, where they show their metal or dielectric behaviour.

7.4.2 Transparency cutoff of dielectrics

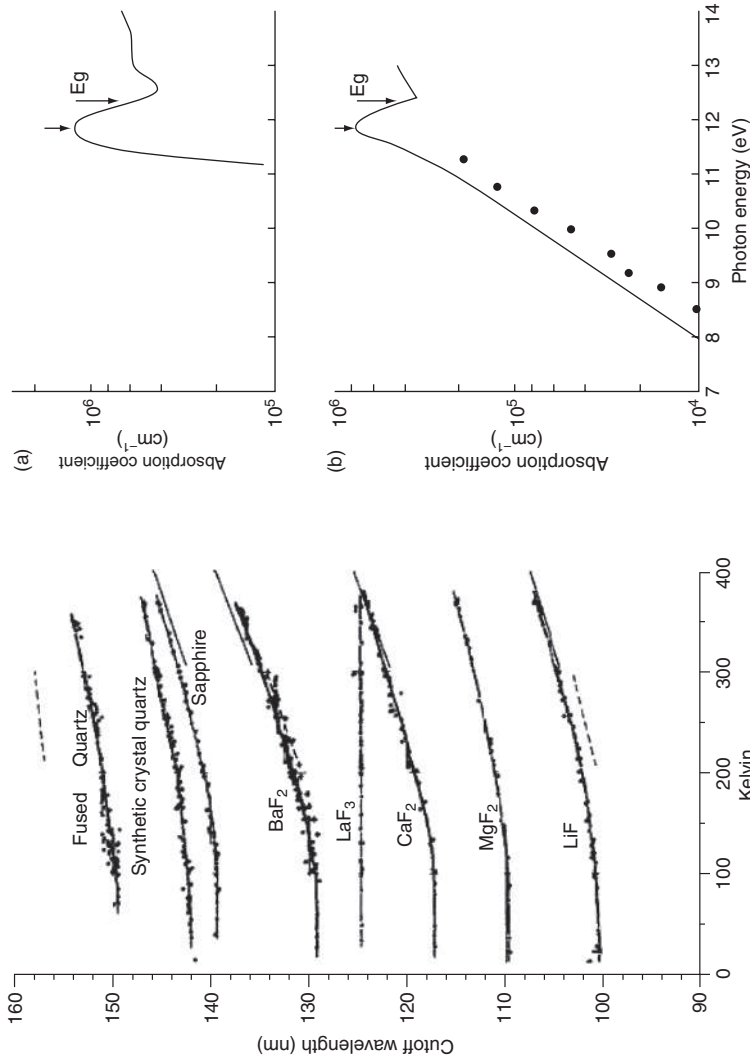
In the visible range we are familiar with dielectrics, that is, materials transparent to radiation, that makes them essential in optics, and particularly in optical coatings. In crystalline dielectrics, their transparency on the short wavelength side arises in that their less-bound electrons fill what is called the valence band, and the next higher allowed level, called the conduction band, is empty; both valence and conduction bands are collective bands of the solid. The less-bound electrons of atoms or molecules do not absorb radiation unless the photon energy equals or exceeds the energy difference between the valence and the conduction band, called the bandgap. The



7.4 k from the infrared to the SXR for metal Sc (Source: Data taken from Fernández-Perea *et al.*, 2006a; Henke *et al.*, 1993; CXRO web) and dielectric SiO (Source: Data taken from Fernández-Perea *et al.*, 2009; Henke *et al.*, 1993; CXRO web). Atom absorption edges are indicated.

material is transparent at wavelengths longer than the bandgap wavelength, which we will refer to as the cutoff, whereas it strongly absorbs at wavelengths shorter than the cutoff. It has been observed that crystals having small ions with strong bonding have a wide spectral range of transparency, such as alkali halides and alkaline earth halides (Li, 1980). The materials that keep transparency to the shortest wavelengths include some oxides, such as SiO_2 and Al_2O_3 , and finally some fluorides, such as BaF_2 and SrF_2 , along with the two materials with the shortest cutoffs in nature: MgF_2 and LiF , which are transparent down to ≈ 115 and 105 nm, respectively. For a material, the cutoff wavelength increases somewhat with temperature due to the thermal broadening of the exciton band and, conversely, the cutoff can be moved to slightly shorter wavelengths by cooling the material (Laufer *et al.*, 1965; Hunter and Malo, 1969); by cooling a pure crystal of LiF , its cutoff can be moved down to ≈ 100 nm, the absolute shortest wavelength of bulk transmission in nature (the window opens again in the HXR and gamma ranges). Figure 7.5 (left) displays the cutoff shift with temperature for a selection of useful materials (Hunter and Malo, 1969).

Coatings are more often either amorphous or nanocrystalline, and hence the energy of the outer electrons does not perfectly follow the bands that are present in single crystals. The presence of defects or impurities in fluorides or oxides results in some blurring of the abrupt cutoffs and the presence of enhanced absorption compared to the crystalline material, such as for a thin film of MgF_2 vs the MgF_2 crystal in Fig. 7.5 (right).



7.5 Left: temperature dependence of the transmittance cutoff of various fluorides and oxides. (Source: Reprinted from *J. Phys. Chem. Solids* **30**, 2739–2745, Hunter W R, Malo SA 'The temperature dependence of the short wavelength transmittance limit of vacuum ultraviolet window materials-I. Experiment' (1969), with permission from Elsevier.) Chemically, quartz is SiO₂ and sapphire is Al₂O₃. Right: absorption coefficient at the cutoff of (a) single crystal MgF₂ plate from Williams *et al.* (1967), (b) thin MgF₂ films deposited onto room temperature substrates from Wood II *et al.* (1984); the solid line represents data by Fabre *et al.* (1964); the bandgap energy Eg is 11.8 eV. (Source: With permission from the Optical Society of America.)

7.4.3 Free electron metals

For metals there is no gap between valence and conduction bands; the less-bound electrons, which are called conduction (also valence) electrons, are shared by all atoms. For photon energies smaller than the threshold for tightly bound electron excitation, the optical properties of many metals can be reasonably approximated by the simple, free-electron Drude model (Drude, 1900a, 1900b), which assumes that the metal conduction electrons behave like a gas. The derivation of the model is presented in many books (Ashcroft and Mermin, 1976; Stenzel, 2005). When free conduction electrons sense a harmonic electric field, they give rise to oscillating dipoles, which determine the metal optical constants. In Drude's assumption, this oscillation is damped due to collisions of electrons with the mostly static positive ions of the solid. The Drude model results in the following dielectric constant:

$$\epsilon = (n + ik)^2 = 1 - \frac{\omega_p^2}{\omega^2 + i\omega/\tau} \quad [7.14]$$

where $\omega_p = (N_{\text{el}}e^2/m\epsilon_0)^{1/2}$ (in SI units) is called the plasma frequency, N_{el} is the free electron density, e and m are the electron charge and mass and ϵ_0 is the vacuum permittivity. τ stands for an electronic relaxation time, and it is related with the dipole-oscillation damping. Wave frequency and photon energy are related through:

$$E = \hbar\omega \quad [7.15]$$

where \hbar is the reduced Planck's constant. At low enough frequencies, free electrons can oscillate following the electric field, which results in a large reflection and absorption in what is a property that we intuitively attribute to metals. ω_p marks a frequency above which electrons cannot follow the electric field any more, which results in a reduced interaction of light with the metal, with a relatively low absorption and both ϵ and n evolving towards unity; hence above ω_p and away from absorption edges, a metal behaves in a way similar to a dielectric. ω_p is the frequency turning point between reflective ($\omega < \omega_p$) and relatively transparent ($\omega > \omega_p$) behaviour. In spite of the simplicity of the free-electron model, it provides a good qualitative and often even quantitative approach to provide the optical and electrical properties of metals away from resonances. Above some frequency/photon energy, tightly bound electrons start to be excited, and the free-electron model cannot explain this situation any more.

Aluminium is a good example of a metal following a Drude model in the EUV, with a plasma wavelength $\lambda_p = 2\pi c/\omega_p \approx 83.5$ nm. Al reflects efficiently

Table 7.1 Plasma wavelength of alkali metals (Srivastava, 1982)

Alkali metal	Plasma energy (eV)	Plasma wavelength (nm)	Melting point (°C)
Li	7.99	155.1	180.5
Na	5.92	209.4	97.7
K	4.27	290.4	63
Rb	3.86	321.2	39

at wavelengths longer than λ_p and has a relatively low absorption below λ_p down to the Al L_{2,3} edge at ≈ 17.2 nm, so that it can be used both as a mirror and as a transmittance filter, depending on the range. Figure 7.3 displays Al experimental reflectance from various sources and their fit to a Drude model in the range close to λ_p . The data of Madden *et al.* (1963) display a modest surface-plasmon reflectance dip (which reveals the presence of short-range irregularities of small amplitude), which according to Equation [7.11] (when expressed in terms of wavelength), is peaked at, or a little longer than, $\lambda_{sp} = \lambda_p \sqrt{2} \approx 120$ nm.

Alkali metals have their λ_p in the FUV to NUV, which makes them attractive materials for their relatively high FUV transmittance below λ_p , where most metal and non-metal materials strongly absorb radiation. However, alkali metals are very reactive, and furthermore, they have a low melting point; this may result in unstable coatings, which complicates their use in practical applications. Transmission filters based on the high FUV-to-visible transmittance of alkali metals are often called Wood filters (Wood, 1933). Table 7.1 displays λ_p for alkali metals. Wood filters based on Na and Li have been used occasionally (Clarke *et al.* 1999).

7.4.4 Tightly bound electrons: atomic scattering factors

In the short EUV ($\lambda < 40$ nm) and shortwards, photon energy is large compared to the energies of the solid-state bands, so that most of the radiation interaction is produced on tightly bound electrons, which are little affected by atom interplay with the surrounding atoms (except at photon energies close to the absorption edges). Due to the small role played by atom bonds at short wavelengths, the optical properties of a material can be obtained to a good approximation by summing the responses of the electrons of all atoms (Gullikson, 2000).

In the classical picture, each bound electron in the atom has a specific resonant frequency; we obtain the interaction of the electromagnetic wave with a multi-electron atom by summing the interaction over all electron resonant frequencies. In a second step, the sum is also extended to all atoms.

As a result of this, matter can be described with its refractive index given by (Attwood, 1999):

$$N(\omega) \approx 1 - \frac{N_{\text{at}} r_e \lambda^2}{2\pi} \sum_s \frac{g_s \omega^2}{\omega^2 - \omega_s^2 + i\gamma\omega} = 1 - \frac{N_{\text{at}} r_e \lambda^2}{2\pi} [f_1^0(\omega) - i f_2^0(\omega)] \quad [7.16]$$

where g_s stands for the oscillator strength associated with the resonant frequency ω_s of s -th electron, and the sum of g_s over all resonant frequencies results in the total number of electrons Z , the atomic number:

$$\sum_s g_s = Z \quad [7.17]$$

in what is known the Thomas-Reiche-Kuhn sum rule. The sum is extended to all atoms through N_{at} , the atom density. In Equation [7.16] $r_e = e^2/4\pi\epsilon_0 m_e c^2 = 2.82 \times 10^{-15}$ m, the classical electron radius. The term in brackets in Equation [7.16] is called the forward atomic scattering factor, which involves the sum of all the resonant terms. The above atomic scattering factors represent the electric field amplitude of the wave scattered by an individual atom in the forward direction relative to that scattered by a free electron (Attwood 1999); Equation [7.16] connects the atomic forward scattering with a collective parameter of the material as it is the refractive index. The approximate, instead of equal sign in Equation [7.16], is there because the original expression is obtained for ϵ and an approximate square root (valid for a refractive index not far from unity) is performed.

The dispersive term connected with the refractive index is contained in f_1^0 ; it represents the amplitude scattered by one atom relative to that of a single free electron, so that for a high enough energy (above all the absorption edges of the atom), f_1^0 approaches Z (the atomic number), that is, at high enough energies the atom scatters radiation as if all electrons were free. In fact Z must be slightly modified to account for a relativistic correction (after the data of Kissel and Pratt (1990) fitted by Henke *et al.* (1993)):

$$Z^* = Z - \left(\frac{Z}{82.5} \right)^{2.37} \quad [7.18]$$

The imaginary part f_2^0 accounts for radiation absorption. Equation [7.16] can be expressed as:

$$N(\omega) = 1 - \delta + i\beta \quad [7.19]$$

where:

$$\delta = \frac{N_{\text{at}} r_e \lambda^2 f_1^0(\omega)}{2\pi} \quad [7.20]$$

$$\beta = \frac{N_{\text{at}} r_e \lambda^2 f_2^0(\omega)}{2\pi}$$

$\delta = 1 - n$ is called the refractive index decrement and β is identical to the extinction coefficient k , but the former notation is often used when data are obtained from the scattering factors. In the short EUV ($\lambda < \approx 40$ nm) and shortwards, δ and β are small compared to unity; they are also positive, except for δ close to some atom absorption edges; this means $n < 1$ mostly at short wavelengths. Far from absorption edges, δ decreases with λ^2 since f_1^0 is relatively independent of λ . β also decreases with λ and it does faster than δ ; its decay rate varies somewhat among materials, and it usually decreases with λ^p , with p of the order of 3; as a comparison, p equals 3 in the high-frequency asymptotic behaviour of the free electron model given by Equation [7.14].

The phase velocity of a wave in a medium of uniform atomic density is given by:

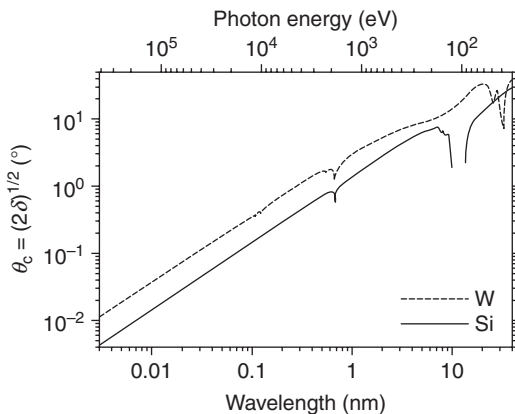
$$v_\varphi = \frac{c}{n} \quad [7.21]$$

At short wavelengths it is larger than the speed of light since $n < 1$; it has to be noted that what can never exceed c is the group velocity of the wave, which is involved in energy flow, and not the phase velocity.

A refractive index n smaller than unity results in that total reflection can be obtained when radiation impinges on the optics from the vacuum side at a grazing enough angle of incidence (Compton 1923). Total reflection is a very useful property since it enables making efficient coatings at short wavelengths when they are not possible at normal incidence. There is a critical angle of incidence θ_c (measured from grazing incidence) below which there is total reflection. When $\beta \ll \delta$, which is usually satisfied in the SXR and shortwards (away from absorption edges), there is a sharp transition in the reflectance-vs-incidence angle at θ_c , which is given by:

$$\theta_c = \sqrt{2\delta} = \sqrt{\frac{N_{\text{at}} r_e \lambda^2}{\pi} f_1^0(\lambda)} \propto \lambda \sqrt{Z} \quad [7.22]$$

where Z is the atomic number of the material. It is desirable for θ_c to be as large as possible in order to increase the optics aperture. Equation [7.22] indicates that θ_c grows with wavelength and, for a fixed wavelength, a



7.6 The total-reflection critical angle θ_c for Si and W calculated with Equation [7.22] using δ from Henke *et al.* (1993) (downloaded from CXRO web) and the atomic factor f_1^0 from Chantler *et al.* (1995) (downloaded from NIST-FFAST web). $\beta \ll \delta \ll 1$ is assumed.

larger θ_c is obtained with the use of high Z materials; proportionality with $Z^{1/2}$ in Equation [7.22] is valid for energies above all electron resonances. Figure 7.6 plots the critical angle vs wavelength for Si and W as calculated with Equation [7.22].

Since atomic scattering factors and also δ and β are calculated by summing the responses of the individual atoms, the optical constants of compounds can be calculated by the addition of the optical constants of all individual elements weighted with their respective atom density, which is a useful simplification. For a material with various possible densities, such as graphite or diamond, the same atomic factors are valid to obtain the optical constants, but the specific atom density must be used. Thus, it is convenient to normalize the optical constants to the material density; when the absorption coefficient is tabulated as μ/ρ , with ρ being the density of the material, it is called the mass attenuation coefficient.

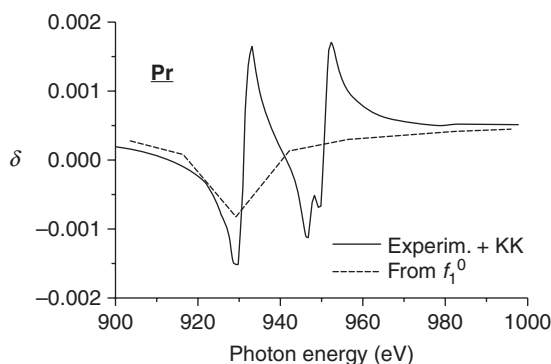
The atomic scattering factors f_1^0 and f_2^0 , along with δ and β , have been calculated and compiled by Henke *et al.* (1982) and Henke *et al.* (1993) for all elements from hydrogen to uranium (Z from 1 to 92) and for energies between 30 and 3×10^4 eV (41–0.041 nm); the data can be conveniently downloaded at CXRO web.

7.4.5 Absorption edges

In the short EUV ($\lambda < \approx 40$ nm) down to HXR, absorption, δ , and the atomic scattering factors steadily decrease with wavelength except for various

abrupt absorption increases that are encountered, which are called absorption edges; an absorption edge occurs when the photon energy reaches the necessary value to eject a tightly bound electron from a specific inner shell. Related to this, a minimum absorption is found slightly longwards of each absorption edge of the atom, that is, minimum absorption is present when the photon energy is slightly insufficient to excite an electron from the next inner shell; this property is used to select the least absorbing material as a spacer in a multilayer coating, which will be addressed in Section 7.7.2. Absorption edges are referred to as K , L , M , etc., in alphabetical order according to the shell from which the electron creates a vacancy, starting with the most tightly bound shell. A shell subscript, such as L_1 , L_2 , L_3 , refers to the specific electron within the shell according to the electron configuration: $K = 1s$, $L_1 = 2s$, $L_2 = 2p_{1/2}$, $L_3 = 2p_{3/2}$, and so on. When the spin-orbit interaction is unresolved one may combine two edges, for example $L_{2,3}$ for a state with a $2p$ vacancy (Inczeďy *et al.*, 1998). Figures 7.2, 7.4 and 7.7 display data of k and/or δ of various materials in which absorption edges can be observed. The energy of absorption edges of the elements can be found in various websites (Schoonjans *et al.*, 2011; NIST-FFAST web).

In Sections 7.4.2 and 7.4.3 it was said that the interaction in a solid largely affects the energy states of the less-bound electrons of individual atoms or molecules in dielectrics and semiconductors. In Section 7.4.4 it was seen that the optical properties of solids in the SXR can be reasonably calculated as the sum of the radiation interaction with the individual atoms. However, the interaction with the other atoms cannot be neglected close to the atom absorption edges; an example of the deviation of calculations with atomic

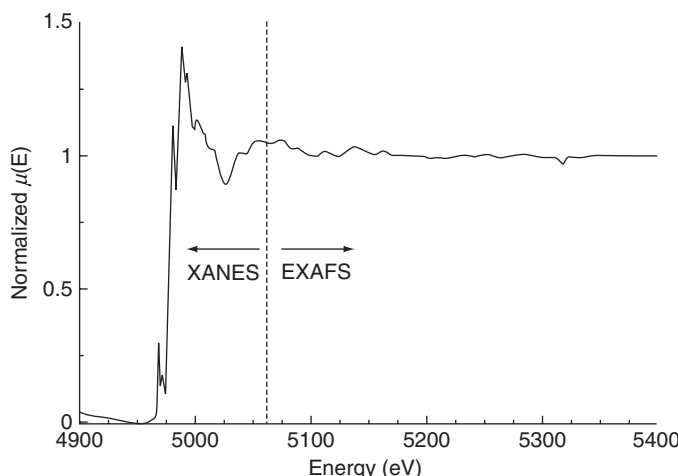


7.7 $\delta = 1 - n$ of Pr obtained from experimental k data using the Kramers-Krönig analysis (Source: Data taken from Fernández-Perea *et al.*, 2008) compared to data calculated with the tabulated atomic scattering factor f_l^0 from Henke *et al.* 1993 (downloaded from CXRO web). The figure displays an important deviation of the data coming from the atomic scattering factor compared to experimental data close to an absorption edge.

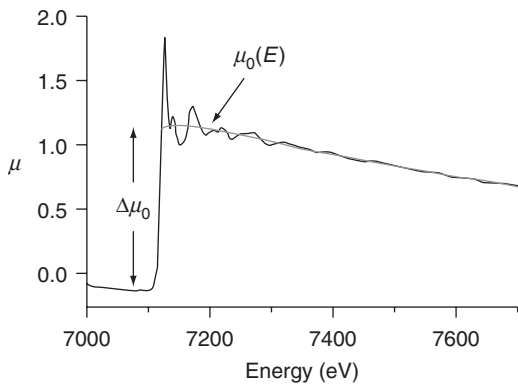
scattering factors compared to experimental data close to an absorption edge is plotted in Fig. 7.7. Solid-state effects have been estimated to result in high-energy optical-constant corrections (compared to data calculated with the independent atom approach) of the order of 10–20%, and they are largest near absorption edges (Rehr and Ankudinov, 2004).

An absorption edge not only displays a sudden absorption increase, but a careful analysis can provide valuable information on the atom surroundings. Hence absorption edges are fingerprints of the material. A consequence of this is that spectroscopy techniques such as X-ray Photoelectron Spectroscopy (XPS) and X-ray Absorption Spectroscopy (XAS) can give information on the chemical bonds of the atoms. When the photoelectron ejected by the X-ray photon leaves the atom, its wave is backscattered by the neighbouring atoms. The constructive and destructive interference between the outgoing photoelectron wave and the backscattered wave gives rise to maxima and minima above the edge in what is called X-ray Absorption Fine Structure (XAFS) (Newville, 2004). In order to analyse XAFS, a tuneable source of X-rays is required, and the availability of synchrotron sources has permitted the important development of XAFS.

The X-ray absorption spectrum at the energy of an absorption edge and above can be divided into two regimes: (1) the structure found right around the absorption edge and up to some ≈ 50 eV above it, which is called X-ray Absorption Near-Edge Spectroscopy (XANES); (2) the structure found at immediately higher energies than XANES up to ≈ 1000 eV above the edge, which is called Extended X-ray Absorption Fine Structure spectroscopy



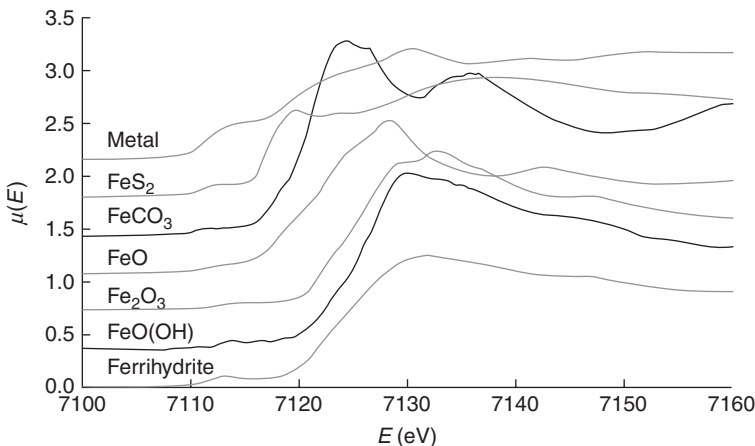
7.8 The XANES and EXAFS regions of a Ti K-edge XAS spectrum of PbTiO_3 . (Source: Reprinted from *J. Alloys Comp.* **401**, 118–126, Ravel B 'A practical introduction to multiple scattering theory' (2005), with permission from Elsevier.)



7.9 Absorption coefficient μ at the Fe K-edge of FeO showing the XAFS spectrum (Newville, 2004). The spectrum oscillates around a smooth background $\mu_0(E)$ and it shows the edge-step $\Delta\mu_0$, which is the absorption jump at the threshold energy E_0 . (Source: Reprinted with permission from Matt Newville.)

(EXAFS). XANES is sensitive to the coordination (such as octahedral, tetrahedral, etc.) and to the oxidation state of the atom, whereas EXAFS gives information on the number of near neighbours and their identity along with the interatomic distances. As an example, Fig. 7.8 displays the XANES range and part of the EXAFS range of a Ti K-edge XAS spectrum of PbTiO₃ (Ravel, 2005). These spectroscopy techniques have experienced significant development in recent decades and they are now in a mature state with an advanced theoretical description of experimental data (Rehr and Albers, 2000; Newville, 2004; Rehr and Ankudinov, 2004; Ravel 2005). Useful websites with XAFS data have been made available (Materlik *et al.*, 1994; UWXAFS project).

Figure 7.9 displays the XAFS spectrum at the Fe K-edge of FeO (Newville, 2004) as an example of how to refer the oscillations to a smooth background function $\mu_0(E)$ representing the absorption of an isolated atom. $\Delta\mu_0$ is the measured absorption jump at the threshold energy E_0 ; it is used as a normalization parameter of the difference $\mu(E) - \mu_0(E)$ in order to define the EXAFS fine-structure function $\chi(E)$; the dependence of χ on $k \propto (E - E_0)^{\frac{1}{2}}$, where k is the wave number of the photoelectron, which can give us information such as the number of neighbouring atoms, the distance to the neighbouring atom and the disorder in the neighbour distance (Newville 2004). Figure 7.10 displays the Fe K-edge XANES spectrum of Fe metal and several Fe compounds (Newville, 2004). In the figure, the edge position and shape are sensitive to formal valence state, ligand type and coordination environment. This figure suggests the potential of these spectroscopy techniques.



7.10 Fe K-edge XANES spectrum of Fe metal and several Fe compounds (Newville, 2004). (Source: Reprinted with permission from Matt Newville.)

7.4.6 Optical properties at higher energies

At wavelengths comparable to the atom dimension, radiation senses the periodical distribution of electronic clouds in a crystal, which results in characteristic diffraction directions (satisfying Bragg's law) that cannot be described with a macroscopic refractive index. Let us see the situation at wavelengths shorter than the atom dimension. Atomic scattering factors are given by Equation [7.16] on the assumption that all electrons in an atom see approximately the same phase and collectively scatter light in phase (Attwood, 1999). This is valid as long as the wavelength is larger than the atom diameter. When radiation wavelength is smaller than the atom diameter (HXR and gamma), the above assumption is still valid for scattering in the forward direction, that is, in the propagation direction of the wave in the material; that is why Equation [7.16] involved forward scattering factors, which remain valid at these larger energies. In fact, it is the interaction of the forward-scattered waves with the incident wave that is responsible for the wave propagation characteristics in the medium that are modified (compared to vacuum) in consistency with what is meant by a refractive index; among these modified characteristics are the phase velocity and the amplitude decay (Attwood, 1999). For wavelengths longer than the atom diameter, the atomic scattering factors are independent of the direction in which the atom scatters and hence the macroscopic interaction of an electromagnetic wave with a uniform medium is fully described with the refractive index. For wavelengths shorter than the atom diameter, the amplitude scattered by an atom decreases when one moves angularly away from the

forward direction (Stanglmeier *et al.*, 1992) due to out-of-phase interferences among the scattered waves at electrons that are separated within the atom at distances comparable to or larger than the wavelength; therefore, scattering away from the forward direction at wavelengths shorter than the atom diameter is not completely described with a macroscopic parameter such as the refractive index. For wavelengths shorter than the spatial distribution of electron density across an atom, radiation–matter interaction turns into a scattering process, which is expressed in terms of a cross section.

Interesting reviews of the behaviour of matter at X-rays or gamma were written by Gålnander (2001) and von Ballmoos (2005). At these high energies, scattering is generated by various interaction mechanisms, which are summarized in Table 7.2. The most important are:

- Photoelectric absorption: photon energy is used in ejecting an electron from an atom and in providing the electron with kinetic energy; dominant below ≈ 100 keV for light atoms, and up to 0.8 MeV for atoms with large Z ;
- Compton (or incoherent) scattering: part of the photon energy ejects an electron and a smaller-energy photon with the remaining energy is scattered; dominant in ≈ 100 keV to ≈ 10 MeV. For atoms with large Z the dominance energy range of Compton scattering is narrowed on both the lower and the upper energy limits;
- Pair production: photon energy is large enough (at least twice the electron rest mass: 1.02 MeV) to generate an electron-positron pair mainly in an interaction in the presence of a nucleus; dominant at energies above ≈ 10 MeV for light atoms, but as low as 4 MeV for atoms with large Z . The positron later annihilates with an electron, which results in the formation of two gamma-ray photons.

The transfer of dominance for the three main HXR/gamma-atom interactions as a function of energy and the atomic number Z were investigated by Evans (1955).

The connection between absorption coefficient and cross section σ is given by:

$$\sigma = \frac{\mu}{N_{\text{at}}} \quad [7.23]$$

where N_{at} stands for the atom density. σ has the units of a surface, and it is measured in barns per atom; 1 barn (b) = 10^{-24} cm 2 . As an example, Fig. 7.11 displays the main cross section components for Carbon (C) (Hubbell *et al.*, 1980). The total absorption coefficient is obtained by summing all the cross-section components for the different interactions.

Table 7.2 Gamma-ray interaction processes

Process	Kind of interaction	Other name	Approximate energy range of maximum importance	Approximate variation with Z
Photoelectric effect	With bound atomic e^-		Dominates at low E (1–500 keV). Decreases as E increases	Z^5
Scattering from electrons; coherent	With bound atomic e^-	Rayleigh scattering Electron resonance scattering	< 1 MeV and greatest at small scattering angles	Z^2 (small angles)
	With free e^-	Thomson scattering	Independent of energy < 1 MeV, least at small scattering angles	Z^3 (large angles)
Scattering from electrons; incoherent	With bound atomic e^-	Compton effect	Dominates in region of 1 MeV. Decreases as energy increases	Z
	With free e^-	(γ, γ) , (γ, n) , (γ, p) , etc., processes Particle production	Above threshold has broad maximum in range of 10–30 MeV	Z
Photonuclear absorption	With nucleus as a whole emits γ or particles	Nuclear photodisintegration	Important only in very narrow resonance range	
Nuclear photoeffect	With material as a whole dependent on nuclear energy levels	Mössbauer effect	Narrow resonance maxima at low energies. Broad maximum in range of 10–30 MeV	Z^2/A^2
Nuclear scattering; coherent	With nucleus as a whole dependent on nuclear energy levels	Nuclear resonance scattering	$\lambda >>$ nuclear radius. Independent of energy	Z^4/A^2
	With nucleus as a whole independent on nuclear energy levels	Nuclear Thomson scattering		

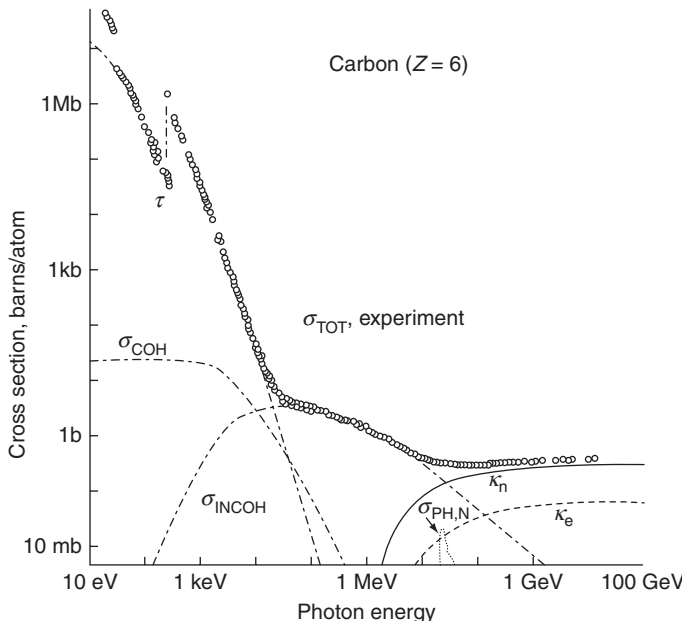
(Continued)

Table 7.2 Continued

Process	Kind of interaction	Other name	Approximate energy range of maximum importance	Approximate variation with Z
Nuclear scattering: incoherent	With individual nucleons	Nuclear Compton scattering	$\lambda \leq$ nuclear radius, i.e. > 100 MeV	
Interaction with a Coulomb field: pair production	In Coulomb field of nucleus	Elastic pair production	Threshold ≈ 1 MeV. Dominates at high E (i.e. > 5 or 10 MeV)	Z^2
	In Coulomb field of electron	Triplet production Inelastic pair production	Increases as E increases Threshold at 2 MeV Increases as E increases	Z
Interaction with a Coulomb field: Delbrück scattering	In Coulomb field of nucleus	Nuclear potential scattering	Real part $>$ imaginary below 3 MeV, $<$ imaginary above 15 MeV Real and imaginary both increase as E increases	Z^4

Source: Reprinted from Davission C M (1965), 'Interaction of γ radiation with matter', chapter II, pages 38–39, in *Alpha-, Beta-, and Gamma-Ray Spectroscopy*, K. Siegbahn, ed., North-Holland, Amsterdam.

Note: Numbers 2, 3, 4, 5 mean powers of Z , the atomic number.



7.11 Contributions to the total measured cross section σ_{TOT} (circles) in carbon over the photon energy range 10 eV–100 GeV of (a) atomic photoelectric effect, τ ; (b) coherent (Rayleigh) scattering, σ_{COH} ; (c) incoherent (Compton) scattering, σ_{INCOH} ; (d) nuclear-field pair production, κ_n ; (e) electron-field pair production, κ_e ; (f) nuclear photoabsorption, $\sigma_{\text{PH},N}$. (Source: Reprinted with permission from Hubbell J H, Gimm H A, Øverbøl (1980), ‘Pair, triplet, and total atomic cross sections (and mass attenuation coefficients) for 1 MeV–100 GeV photons in elements Z = 1 to 100’, *J. Phys. Chem. Ref. Data* **9**, 1023–1147. Copyright 1980, American Institute of Physics.)

The different cross sections in HXR and gamma have mostly been obtained by calculations that make use of the relativistic quantum theory, in which each of the involved interactions requires a specific approach. There is a long literature of calculations of the atomic cross sections of most elements of the periodic table at wide energy ranges (Cromer and Mann, 1968; Scofield, 1973; Hubbell *et al.*, 1980; Chantler *et al.*, 1995). The National Institute for Standards and Technology (NIST) has gathered handy compilations of the mass attenuation coefficient and atomic factors of the elements of the periodic table which cover a large energy range: Photon cross sections database (XCOM) (1 keV–100 GeV) (Berger *et al.*, 2010) and X-ray attenuation and absorption for materials of dosimetric interest database (XAAMDI) (1 keV–100 MeV) (Hubbell and Seltzer, 1995), which were developed for radiological physics and dosimetry, and X-ray form factor, attenuation and scattering tables database (FFAST) (NIST-FFAST web, Chantler 2000) (1 eV–433 keV), which was produced for X-ray diffraction, interferometry and

crystallography, among other areas. A comparison between XCOM and FFAST is also available (XCOM-FFAST comparison website).

7.5 Link between n and k : Kramers-Kronig analysis

The real and imaginary parts of the refractive index $N = n + ik$ are linked as a result of basic principles: linearity and causality; the latter implies that a polarization cannot be induced on a material by an electric field before the field is applied. The links between n and k are referred to as the Kramers-Krönig dispersion relations, which are expressed as:

$$\begin{aligned} n(E) - 1 &= \frac{2}{\pi} P \int_0^{\infty} \frac{E' k(E')}{E'^2 - E^2} dE' \\ k(E) &= -\frac{2E}{\pi} P \int_0^{\infty} \frac{n(E') - 1}{E'^2 - E^2} dE' \end{aligned} \quad [7.24]$$

P stands for the Cauchy principal value, which is an integration variant necessary to deal with the zero in the denominator at $E' = E$. Equation [7.24] enables the calculation of one optical constant if the other is known over the whole spectrum. The latter is never fully possible and interpolations and extrapolations are always required. Nevertheless, the range close to the energy at which the calculation is performed has a higher weight in the integration, which reduces the inaccuracy originating in the use of extrapolations at distant energies. Since it is frequently easier to obtain k from experimental measurements, the first integral is used more often, and thus n is obtained through Kramers-Krönig integration. Similar equations link the real and imaginary parts of the dielectric constant.

The modulus $R^{1/2}$ and phase ϕ of complex reflectance $r = R^{1/2}\exp(i\phi)$ are linked with analogous dispersion relations:

$$\phi(E) = -\frac{E}{\pi} P \int_0^{\infty} \frac{\ln[R(E')/R(E)]}{E'^2 - E^2} dE' \quad [7.25]$$

This is called the Jahoda-Velický (Jahoda, 1957) dispersion relation in the subtractive form (Shiles *et al.*, 1980) and it is a useful relation to calculate the optical constants from reflectance measurements (Section 7.6). There is another formal equation that provides R when ϕ is known over the whole spectrum; however, R and not ϕ is what can usually be measured.

The use of the Kramers-Krönig or Jahoda-Velický dispersion relations is presented here because they are particularly useful in the determination of the optical constants of materials at short wavelengths, which is addressed in the next subsection.

Useful sum-rules are available which enable the evaluation of the global accuracy of optical constants in the whole spectrum. The most common rules for n and k are:

$$\frac{4\epsilon_0 m}{\pi N_{\text{at}} e^2 \hbar^2} \int_0^\infty E' k(E') dE' = Z \quad [7.26]$$

$$\int_0^\infty [n(E) - 1] dE = 0 \quad [7.27]$$

(in SI units), where N_{at} is the atom density, e and m are the electron charge and mass, ϵ_0 is the permittivity of vacuum and \hbar is the reduced Planck's constant. The first sum-rule expresses that the integral of k in the whole spectrum, conveniently normalized, equals the total number of electrons of the atom (a straightforward extension can be obtained for compounds by replacing N_{at} and Z with the compound equivalent parameters); it is another version of the Thomas-Reiche-Kuhn sum-rule given above as Equation [7.17]. The second sum-rule, usually called the inertial sum-rule, expresses that the average of n through the spectrum is unity. The latter means for instance that the refractive index of a dielectric, which is larger than unity in the visible, must be compensated with a refractive index lower than unity in other parts of the spectrum, which occurs in most of the EUV and short-wards. Sum-rules have also been developed for the Jahoda-Velický reflectance dispersion relations (King, 1979).

7.6 Experimental determination of optical constants

We summarize below various techniques that are used for the characterization of the optical constants of materials at short wavelengths. An excellent review on techniques for optical constant determination was published in Palik (1998a and 1998b). Large compilations of experimental optical constants of materials in broad spectral ranges including short wavelengths have been published: Hagemann (1974), Haelbich (1977), Weaver *et al.* (1981) and Palik (1998a, 1998b, 1998c). In the following section the most common techniques are mentioned:

- Reflectance measured at various angles of incidence. Both n and k can be calculated using Fresnel formulae (Equation [7.8]). This technique has been described more extensively by Scott (1988) and Hunter (1998). At short wavelengths, micro-roughness plays an important role in reflectance and it has to be accounted for. Some examples of the use of the

reflectance-vs-angle method are given in Windt *et al.* (1988), Larruquert *et al.* (1995), Soufli and Gullikson (1997), Windt *et al.* (2004b) and Monaco *et al.* (2006).

- Reflectance measured over a large spectrum at near-normal incidence (in a more general case it can be measured at a constant incidence angle, not necessarily near the normal), complemented with the use of the dispersion relations. The measured reflectance in a wide spectral range is used to calculate the complex reflection coefficient r with the Jahoda-Velický dispersion relation given by Equation [7.25]. From the Fresnel reflectance coefficient at normal incidence:

$$r = \frac{1 - N}{1 + N} \quad [7.28]$$

we immediately obtain $N = n + ik$ as:

$$N = \frac{1 - r}{1 + r} \quad [7.29]$$

Examples of the use of this method are in Philipp and Ehrenreich (1963) and Shiles *et al.* (1980).

- Transmittance over a large spectrum for various layers of the investigated material with film thicknesses x_i , k at each wavelength is obtained using the Beer-Lambert law:

$$T_i = T_0 \exp\left(-\frac{4\pi kx_i}{\lambda}\right) \quad [7.30]$$

where k is given by the linear fit of the logarithm of the normalized transmittance vs film thickness. Equation [7.30] is immediately obtained from Equations [7.3] and [7.4], where T_0 and T_i stand for the transmittance of the bare substrate and of the substrate with the x_i film, respectively; Equation [7.30] neglects reflectance. Once k is known, n is obtained with the Kramers-Krönig dispersion relations using Equation [7.24] as described in Section 7.5; this requires knowing k in the whole spectrum. An advantage of this technique versus those involving reflectance measurements is that the effect of any possible contamination can be minimized if it is common to all films regardless of their thicknesses. The dependence on roughness is much smaller for transmittance than for reflectance, as can be seen in Equation [7.12]; this is an important advantage at short wavelengths. Furthermore, transmittance is easier to measure than reflectance. In the EUV and SXR there is a lack of transparent

materials, which impedes the use of solid substrates onto which the target material is deposited; this can be solved by using self-supported thin films that operate as substrates to support the material to be investigated (Hunter, 1973). A variant of this technique has been developed in which the target film is directly deposited on the detector (Uspenskii *et al.*, 2005). A large amount of materials have been characterized with this method. In the pioneering work by Hageman *et al.* (1974) several materials were characterized, mostly metals. Optical constant characterization at large energy ranges has been performed for various materials (Soufli and Gullikson, 1998; Soufli *et al.*, 1999). A full characterization of Sc and lanthanides, except for radioactive Pm, has been performed with this method (Kjornrattanawanich *et al.*, 2010; Fernández-Perea *et al.*, 2011 and references therein).

- Ellipsometry. It is based on the determination of the complex ratio r_p/r_s with the use of linear polarizers and phase retarders. It provides both n and k . There are few available ellipsometers at short wavelengths because of the shortage of efficient wide-band polarizers and retarders. Barth *et al.* (1998) and Hilkiker (2005) discussed the use of ellipsometry to cover the EUV down to 35 nm and the FUV, respectively. Section 7.7.3 addresses the properties of polarizers and phase retarders at short wavelengths.
- Interferometry. The introduction of a layer of the material into one arm of an interferometer produces an optical path difference from which n can be directly measured; it can be combined with transmittance measurements to obtain k (Svatos *et al.*, 1993; Joyeux *et al.*, 1999; Chang *et al.*, 2002). Yet few interferometers are available at short wavelengths. One reason is that beamsplitters are difficult to make in the EUV and SXR since no solid substrates are possible. There is also a lack of wide-band mirrors and beamsplitters. Another difficulty is that this technique requires equalling optical paths to a fraction of a short wavelength.
- Critical angle. When $0 < \delta (= 1 - n) < 1$ and $\beta (= k) \ll \delta$, such as in most of the SXR and HXR, δ can be obtained from the determination of the critical angle (see Section 7.4.4). The presence of a small amount of absorption is circumvented by determining the angle at which the slope of the reflectance vs angle of incidence curve has a maximum (Hunter, 1964a, 1998). The method only provides δ .
- Refraction. When decreasing wavelength towards the HXR, $\beta (= k)$ decreases faster than $\delta (= 1 - n)$ does, so that it becomes possible to obtain n (Compton, 1923; Fontaine *et al.*, 1985; Warburton and Ludwig Jr., 1986; Jark *et al.*, 2011), and even k with supplementary transmittance measurements (Jark *et al.*, 2011), through refraction at grazing incidence on a prism of the material. Recent measurements at gamma energies up to 2 MeV have been reported (Habs *et al.*, 2012).

- Electron energy loss spectroscopy. A beam of high-energy electrons crosses a thin film, and the electrons lose energy; spectra with the number of electrons as a function of energy loss can be used to calculate the film optical constants up to energies mostly in the EUV. Electron mean free paths are small and an electron may undergo more than one scattering event, so that optical constant calculation requires correcting for multiple scattering events. The method is described by Pflüger and Fink (1998).
- Total electron yield. The method is based on the generation of electrons within a film being proportional to radiation absorption, so that electron generation and optical properties are connected. The method is explained in Birken *et al.* (1998) and it is based on the work of Pepper (1970), Gesell and Arakawa (1971) and Arakawa *et al.* (1973). Both n and k can be calculated. The method is applicable at photon energies above the photoemission threshold, so that it is suitable for short wavelengths.

7.7 Specifics of optical coatings at short wavelengths

In the development of efficient multilayer (ML) coatings for short wavelengths specific difficulties are encountered, such as: (1) absorption of materials in the FUV to SXR, (2) very thin films required at short wavelengths, (3) roughness effects strongly increase at short wavelengths and (4) small n contrast over materials, which requires an increase of the number of layers in the ML. Here we summarize the main aspects that are specific for short wavelength MLs. The limited space will allow a short description of three varieties of coatings: transmission filters, high-reflectance coatings, and polarizers and retarders. Various optical devices other than coatings that are used at short wavelengths, such as zone plates, flat and bent crystals, polycapillaries or compound refractive lenses, are out of the scope of this chapter.

7.7.1 Transmission filters

Pass band filters are more efficient at rejecting the out-of-band when they work by transmission compared to reflection. In the FUV, the shortage of transparent materials is an obstacle for these filters. The few transparent materials below 200 nm, mostly fluorides, are still somewhat absorbing, which limits the maximum number of layers in the ML and hence the efficiency of all-dielectric transmission filters. Instead, metal–dielectric transmission

filters are in common use in the FUV with a shortest peak wavelength of ≈ 120 nm. They consist of a ML alternating a fluoride film, such as MgF_2 , with a metal film, usually Al (Malherbe and Guillard, 1970; Fairchild, 1973; Malherbe, 1974a; Fernández-Perea *et al.*, 2006b). Below ≈ 120 nm, interference transmission filters are not available. The situation is even worse in the EUV, since no transparent substrate material with a thickness of the order of ≈ 1 mm can be found below 105 nm.

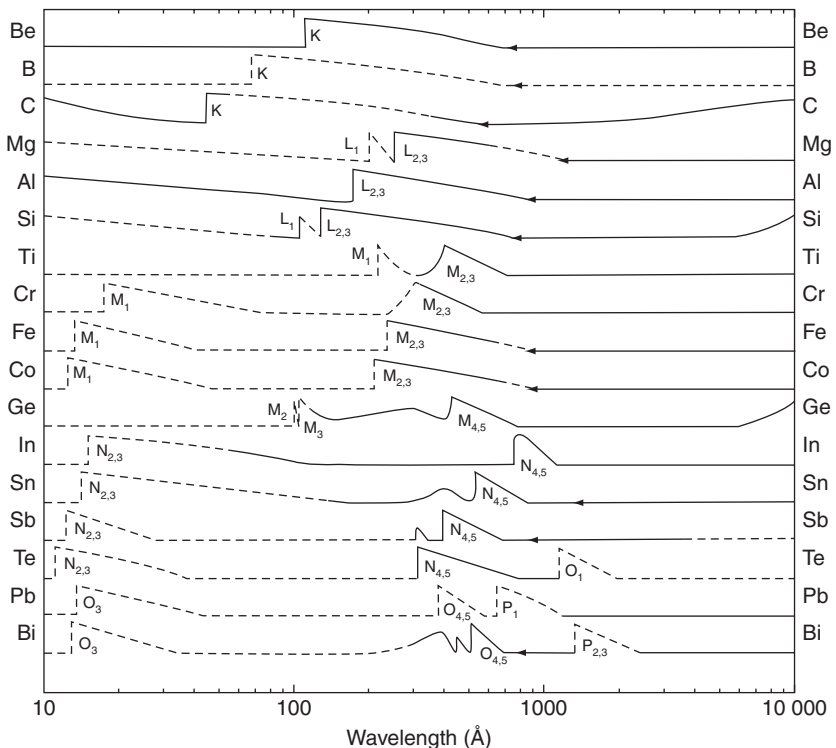
Let us look at filtering with natural bands of materials. In the FUV, few narrowband filters working by natural absorption have been prepared (Carruthers, 1971). The cutoff of various fluorides and oxides, mentioned in Section 7.4.2, provide good edge filters that reject the short wavelengths. Regarding long wavelength rejection, the natural transmittance of alkali metals, with a high FUV-to-long wavelength transmittance ratio, has occasionally been used for FUV transmittance filters. They are called Wood filters, and they are referred to in Section 7.4.3.

Regarding the EUV, the natural low-absorption bands of materials can be used for filtering purposes; these bands are peaked immediately longwards of the material absorption edges. This provides a series of possible bands which are obviously limited by nature (Hunter *et al.*, 1965; Rustgi, 1965; Samson, 1967a; Powell *et al.*, 1990, 1994). Sometimes two or more materials are used in a two-layer coating filter to provide a narrower combined pass-band (Powell *et al.*, 1994). Since no transmitting bulk substrate is available in the EUV, the layers of the filtering materials must be deposited onto a self-supported thin film (the support film can at the same time be a filtering material) (Hunter, 1973). This results in fragile optical elements. In spite of this limitation, EUV filters based on natural low-absorption bands of materials have been largely used particularly in space instruments for astronomy or solar physics. Figures 7.12 and 7.13 summarize the transmission properties of various common materials. Transmittance sharply decreases on the short-wavelength side of each absorption edge.

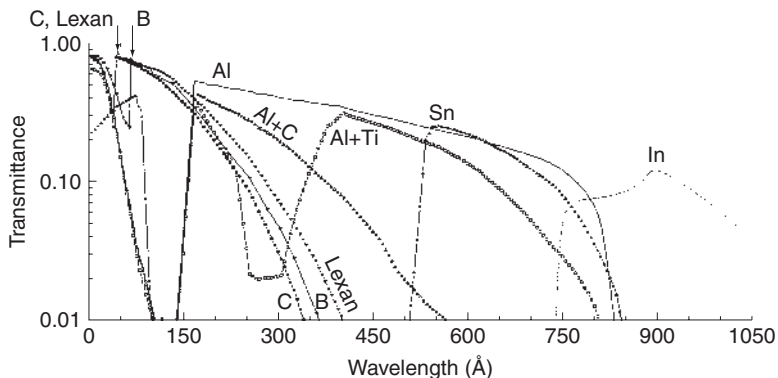
In addition to filters based on the natural bands of materials, some EUV transmittance filters consisting of free-standing interferential MLs have been prepared (Bibishkin *et al.*, 2008; Chkhalo *et al.*, 2010, 2011).

7.7.2 High-reflectance coatings

The presence of relatively transparent materials in the FUV with $\lambda > 120$ nm enables the preparation of high-reflectance (HR) coatings as an extension of the experience in the visible and near UV, with the efficiency decreasing with wavelength. Narrowband, all-dielectric reflective filters have been demonstrated in the FUV (Malherbe, 1974b; Zukic and Torr, 1992; Park *et al.*, 1996) down to a peak wavelength of ≈ 130 nm. A review on FUV coatings



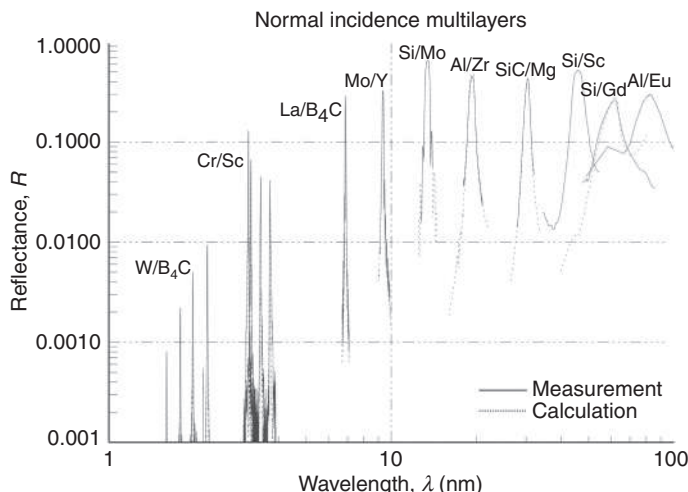
7.12 A summary diagram of the transmission properties of several materials, most of which can be prepared as thin films. Absorption edges are shown as steps (Hunter *et al.*, 1965). Dotted lines suggest probable trends which had not been verified experimentally. The positions of the various X-ray edges are indicated: those observed in absorption by solid lines, and those calculated by broken lines. (Source: With permission from the Optical Society of America.)



7.13 Transmittance expected for commonly used filter materials (Powell *et al.*, 1994). (Source: With permission from V. Drake and from SPIE.)

was performed by Thielsch (2003) and they will not be discussed here. HR coatings in the EUV and shortwards are reviewed below.

In the EUV at $\lambda < 40$ nm, the reflectance of any single material at normal incidence is very low. In order to make an efficient mirror, we require the constructive interference of contributions coming from many interfaces, that is, a ML. The significant absorption of materials in the EUV, and to a lower extent in the SXR, strongly limits the performance of coatings. Reflective ML coatings in the EUV and SXR are based on the selection of at least one material with minimum absorption at the desired wavelength range; as a reminder, the minimum absorption of a material occurs slightly longwards of its absorption edges. Such material is called the spacer of the ML. The second ML component is selected from those with largest n contrast with the spacer material and often also the smallest possible k ; such material is sometimes called the scattering material. A good summary list of useful material pairs for EUV-SXR MLs can be found in Spiller (1994) and Windt *et al.* (2004); a summary of some of the most commonly used material pairs is plotted in Fig. 7.14. Among the plotted ML coatings, the Mo/Si pair at 13.5 nm, slightly above the Si $L_{2,3}$ edge, provides the largest normal reflectance achieved at any wavelength in the EUV or SXR, $\approx 70\%$; its application for the future EUV lithography (EUVL) has resulted in a very thoroughly investigated ML structure. An excellent review on Mo/Si and on other ML coatings for EUVL has been published (Soufli and Bajt, 2009).



7.14 HR coatings spanning the EUV to SXR. (Source: The figure was kindly prepared by D. Windt.)

The reflectance predicted by calculations may be strongly reduced in practice by roughness; the decrease of reflectance with roughness can be calculated with Equations [7.12] and [7.13]. For a given RMS roughness σ , the decrease of reflectance at some long wavelength λ may be negligible, but it may turn deleterious at some shorter one. Reflectance decrease depends on $(\sigma/\lambda)^2$, which makes the turning point sharp. Spiller (1994) marks this turning point as an interface roughness of about 1/10 of the ML period, hence typically $\lambda/20$. If σ is technically difficult to reduce below ≈ 0.2 nm, then the shortest wavelength limit for which efficient normal-incidence MLs can be prepared is roughly 4 nm. A way to overcome this short-wavelength limit is by working away from normal incidence, taking advantage of the inclination factor mentioned in Equations [7.12] and [7.13]. There is a cost for working away from normal incidence, since it results in an optical system with reduced aperture and effective area as well as increased aberrations compared to a normal-incidence system. It was said in Section 7.4.4 that total reflection is obtained with a single material working just more grazing than its critical angle θ_c . Compared to a single material at the critical angle, a ML may be designed to have high reflectance at a much less grazing incidence, which increases the aperture and helps minimize aberrations. ML coatings working at grazing incidence for energies as high as 200 keV have been developed (Windt *et al.*, 2003; Ogasaka *et al.*, 2007). Recently, MLs for an energy as large as 384 keV have been demonstrated (Fernández-Perea *et al.*, 2013a). The physics describing the latter ML extension has been announced (Fernández-Perea *et al.*, 2013b).

The reactivity of some materials impedes their use in MLs in spite of their favourable optical constants. In Section 7.4.4 it was shown that the optical constants of compounds at short wavelengths are obtained as a weighted combination of the compound elements. Therefore, if one focuses only on optical constants, the most useful materials for short-wavelength MLs are always single elements and not compounds, since for instance there will always be a constituent element within a compound with smaller k than the compound, which is important for MLs limited by absorption. But often low-absorption single elements are reactive, and they may give rise to unstable MLs. As an example, reactive Sr has a low-absorption range below its M_5 edge at 133 eV, which makes it attractive as a ML spacer; however, it results in unstable MLs with Mo (Sae-Lao and Montcalm, 2001). To improve ML stability, an element can be replaced with a compound of which it is a constituent, and a reasonable compromise between stability gain and reflectance loss may be found; an example is the replacement of Mo in Mo/Si MLs with Mo_2C to get stable MLs at high temperatures (Feigl *et al.*, 2001).

A useful method to passivate an otherwise unstable interface between two materials is the use of barrier layers. Barrier layers are thin films of a third material that separate layers of the main components in order to minimize the reactivity or interdiffusion between the basic components of the

ML. Typical optical layer thickness in MLs is roughly $\lambda/4$; such thickness is very small for MLs operating in the SXR and short EUV. Therefore, barrier layers must be extremely thin not to degrade significantly ML reflectance. For instance, barrier layers of C, B₄C or SiC with thicknesses of ≈ 0.5 nm and even thinner have been used in Mo/Si MLs to get sharp interfaces and to stabilize them when MLs have to survive at high temperatures (Bajt *et al.*, 2002; Braun *et al.*; 2002; Hecquet *et al.*, 2007). ML reflectance can be optimized with the use of specific barrier layer materials at each of the two interfaces (Larrauquert, 2004). Likewise, reactivity of the outermost layer in contact with air can be avoided with the use of a protective capping layer (Bajt *et al.*, 2002; Yulin *et al.*, 2008).

The period for MLs with maximum reflectance at a desired λ and angle of incidence is given by Bragg's law:

$$2d\bar{n} \cos \theta = m\lambda \quad [7.31]$$

where d is the period thickness, θ is the angle referred to the normal, \bar{n} represents an average refractive index through the period and m stands for the reflection order; in most cases m is set to 1. Bragg's law was formulated to describe X-ray diffraction patterns, but it also governs the optimization of MLs by replacing diffraction planes with layers. For $m = 1$ and transparent materials, the period thickness is shared by the two materials, so that the optimum optical layer thickness (physical thickness times the refractive index) of each material is $\lambda/4$ (the inclination term $\cos \theta$ enables adjusting thickness to the specific angle); such layers are called quarterwave.

The presence of absorption influences the optimum film thicknesses in a ML. For MLs with absorbing materials, a reflectance increase is obtained by reducing the thickness of the scattering material below a quarterwave, in order to increase the wave penetration through the ML (Spiller, 1972a); this thickness reduction is supplemented on the spacer material so that a period consisting of two layers, one of each material, totals an optical thickness of approximately $\lambda/2$. Let us see the film thicknesses that maximize the ML reflectance. Let Γ be the ratio of scattering-to-period layer thicknesses:

$$\Gamma = \frac{x_H}{x_L + x_H} \quad [7.32]$$

where x_H and x_L are the layer thicknesses of the high (scattering) and the low (spacer) absorption material, respectively; strictly speaking, x_H and x_L should refer to optical thickness (the refractive index times the thickness), although often they refer to physical thickness too, since n approaches 1 in the short EUV and shortwards. With absorbing materials, the optimum Γ that maximizes reflectance (Γ_{opt}) is smaller than 0.5. Vinogradov and Zeldovich (1977)

found a transcendental equation to calculate Γ_{opt} that maximizes reflectance at a given λ for a ML with a large number of periods:

$$\tan(\pi\Gamma_{\text{opt}}) = \pi(\Gamma_{\text{opt}} + \rho) \quad [7.33]$$

with $\rho = n_L k_L / (n_H k_H - n_L k_L)$. L and H stand again for the spacer and scattering material, respectively.

When $k_L \ll k_H$, Equation [7.33] can be approximately solved:

$$\Gamma_{\text{opt}}^{(0)} = \frac{1}{\pi} (3\pi\rho)^{1/3} \quad [7.34]$$

The latter approximate solution is correct for small values of Γ_{opt} , but starts deviating from the correct solution when Γ_{opt} is larger than ≈ 0.16 ($\rho > 0.013$). An approximate solution of Equation [7.33] that is valid in a wider range has been derived:

$$\Gamma_{\text{opt}}^{(1)} = \gamma + \frac{1}{2} \left[\sqrt{(\gamma + \rho)^2 - \frac{4}{\pi^2} \left(1 - \frac{\gamma + \rho}{\tan \pi \gamma} \right)} - (\gamma + \rho) \right] \quad [7.35]$$

with:

$$\gamma = \Gamma_{\text{opt}}^{(0)} \left[1 - \frac{2}{15} \frac{\left(\pi \Gamma_{\text{opt}}^{(0)} \right)^2}{1 + \frac{2}{3} \left(\pi \Gamma_{\text{opt}}^{(0)} \right)^2} \right] \quad [7.36]$$

which is valid in the range $0 < \Gamma_{\text{opt}} < 0.42$ ($0 < \rho < 2.6$). For larger values of ρ we can use:

$$\Gamma_{\text{opt}} = \frac{1}{4} + \frac{1}{2} \left(\sqrt{(\rho + 1/2)^2 - 4/\pi^2} - \rho \right) \quad [7.37]$$

which is valid in the range $0.40 < \Gamma_{\text{opt}} < 0.50$ ($\rho > 1.8$).

When material absorption is large, and the maximum number of ML periods contributing to reflectance is limited by absorption, reflectance can be optimized with the use of aperiodic better than periodic MLs. Here Γ is no longer constant through the ML and it decreases from the innermost to the outermost layer to enhance radiation penetration; to design the ML with the largest reflectance, every film thickness must be optimized. MLs with

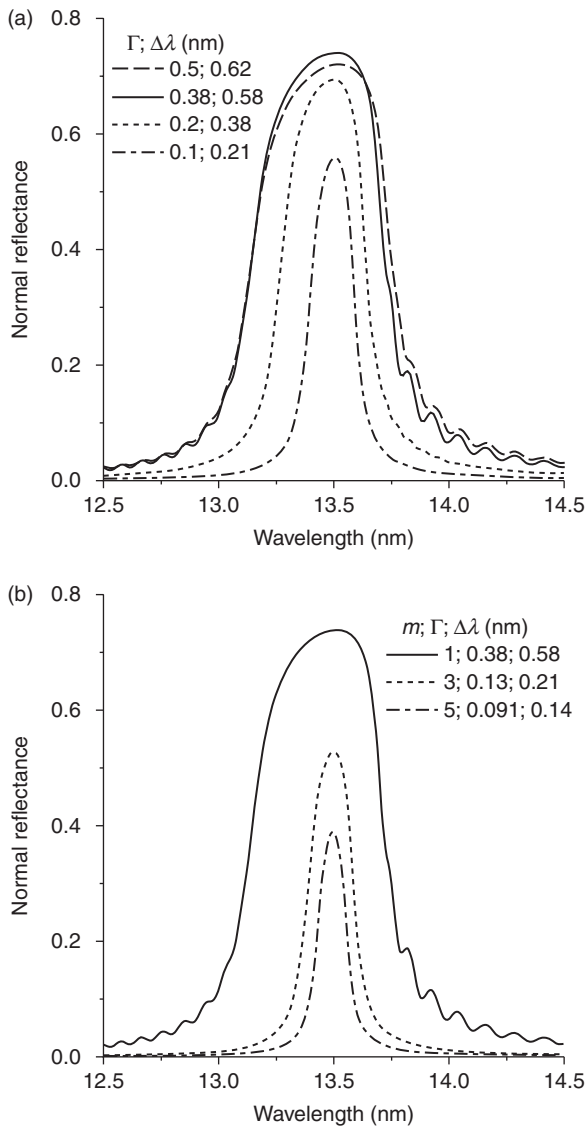
maximum reflectance at a given λ are easy to design step by step: the addition of a new period on top of an already optimized ML does not require the reoptimization of the thickness of the inner periods (actually the outermost layer of the previously optimized ML with one fewer period must be recalculated) (Carniglia and Apfel, 1980). In fact it was found that layer thickness optimization can be done even more easily, in a layer-by-layer process (Yamamoto and Namioka, 1992; Larruquet, 2002b).

The standard ML design results in coatings with a bandwidth that amounts approximately (normal incidence) to:

$$\frac{\Delta\lambda}{\lambda} \geq 1/mN \quad [7.38]$$

where N is the number of periods in the ML and m is the reflection order. Absorption decreases with wavelength, which enhances the penetration and hence it enables the increase of N (which is also necessary due to the decreased reflectance at each interface); as a result, the relative bandwidth ($\Delta\lambda/\lambda$) of the ML decreases with wavelength. There are cases in which modified values of $\Delta\lambda/\lambda$ are required. When a reduced $\Delta\lambda/\lambda$ is needed, one degree of freedom is the reduction of Γ : if we use a Γ lower than the aforementioned optimum value, this enables a larger penetration through the multilayer (with a cost in reflectance), so that more periods contribute to the ML reflectance and this results in a narrower band, according to Equation [7.38]. Figure 7.15a displays the reflectance of Mo/Si MLs optimized at 13.5 nm calculated with decreasing Γ , which results in a decrease of the bandwidth; the thinnest feasible layer thickness limits the lower possible value of Γ . A means of strongly decreasing the ML bandwidth is to increase the reflection order as per Equation [7.38] (Feigl *et al.*, 2005). This results in an important increase of layer thicknesses according to Bragg Equation [7.31]; for absorbing materials, this thickness increase has a cost on peak reflectance due to the larger absorption per reflectance contribution at each interface; in order to minimize the absorption increase of using higher reflection orders, the thickness increase may be performed only at the spacer material (Wu *et al.*, 2011). Figure 7.15b displays the reduced bandwidth calculated for Mo/Si MLs optimized at 13.5 nm designed with the first odd reflection orders (the even orders are also possible), which also results in a decrease of the reflectance peak.

For the opposite requirement of an extended bandwidth, a simple option is the superposition of various MLs, each designed to reflect a specific bandwidth (or angle range); such device is called a supermirror (Christensen *et al.*, 1991). Supermirrors were originally developed for neutron optics (Mezei, 1976). The basics for supermirrors is that a small enough absorption

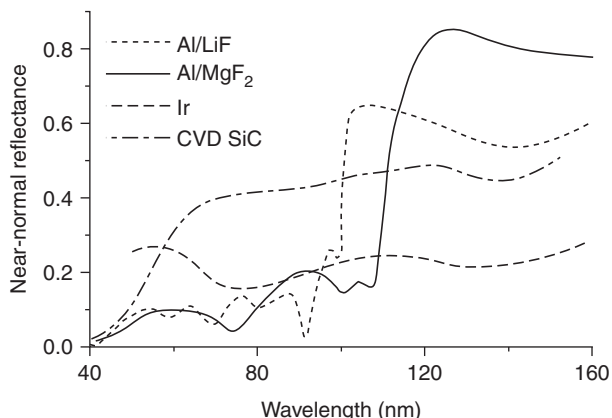


7.15 Calculated reflectance as a function of wavelength of Mo/Si MLs optimized at 13.5 nm for various values of (a) Γ , and (b) Γ and the reflection order m . The bandwidth, as FWHM, is also plotted. The optical constants of Mo (Soufli and Gullikson, 1998) and Si (Soufli and Gullikson, 1997), which were downloaded at CXRO web, were used in the calculations.

permits penetration through more layers than are required to produce a good mirror for a single wavelength, and the extra layers can contribute to reflect at additional wavelengths (Spiller, 1994). A supermirror is feasible for very low absorbing materials, that is, at very short wavelengths such as in the HXR, so that radiation penetrates through many layers. Since the penetration is larger for shorter wavelengths, the ML can be made graded in depth in a way that the period decreases from top to bottom. In practice, an extended bandwidth can be obtained with the optimization of every single layer in a ML. The extended bandwidth always results in some peak-reflectance decrease compared to the ML optimized at a single λ , although the integrated reflectance, either in wavelength, in incidence angle or in both, can be enhanced significantly. MLs with extended bandwidth have been developed by different authors (Joensen *et al.*, 1992; Yamashita *et al.*, 1998; Morawe *et al.*, 2000; Kozhevnikov *et al.*, 2001; Feigl *et al.*, 2005; Aquila *et al.*, 2006; Maury *et al.*, 2010). There are some cases in which, besides an extended bandwidth, a coating is required to reflect more than one individual wavelength and/or to reject secondary wavelengths with a very low reflectance, such as for the simultaneous imaging of various spectral lines while at the same time masking more intense parasitic lines, in applications for astronomical or solar telescopes (Edelstein, 1989; Larruquert and Keski-Kuha, 2001; Hecquet *et al.*, 2009).

At wavelengths in the long EUV ($60 \text{ nm} < \lambda < 105 \text{ nm}$) absorption of all materials in nature is too large to make efficient ML coatings because there is too small a penetration in the ML to get the benefit of constructive interferences. In spite of this, new MLs of moderate efficiency have been developed in the latter range; they are based on the relatively low absorption of lanthanides like Tb (Windt *et al.*, 2005; Kjornrattanawanich *et al.*, 2006), Gd (Kjornrattanawanich *et al.*, 2008), Yb (Vidal-Dasilva *et al.*, 2009) and Eu (Larruquert *et al.*, 2011b); in fact these MLs have few periods: less than two for those based in Yb and Eu. An exception to this is a 10-period, narrow-band AlMg/SiC ML with a large reflectance peaked at 75 nm (Soufli *et al.*, 2012).

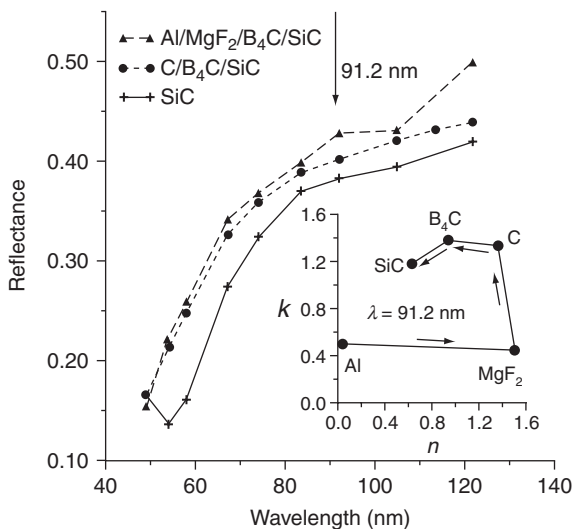
Other than the latter recently developed ML coatings, reflective coatings in the long EUV and longwards are often based on single layers, sometimes overcoated with a protective layer. Figure 7.16 displays the reflectance of various materials used for single layer mirrors in the long EUV and short FUV. Bare Al films have a remarkably high reflectance in a wide range, which extends down to $\approx 83 \text{ nm}$; however, its high reflectance is lost shortwards of $\approx 200 \text{ nm}$ because a thin film of natural aluminum oxide grows on Al in contact with the atmosphere. To avoid this, a protective overcoating layer of MgF_2 on Al can keep high reflectance down to $\approx 115 \text{ nm}$, which can



7.16 Reflectance of materials used for single-layer mirrors in the long EUV: Ir (Hass *et al.*, 1967), chemical-vapour deposited SiC (Keski-Kuha *et al.*, 1988) and Al protected with either LiF or MgF₂ (Hunter *et al.*, 1971). (Source: With permission from the Optical Society of America.)

be extended down to almost 100 nm when MgF₂ is replaced with LiF. Al protected with MgF₂ is a very popular coating which was developed over 50 years ago (Hass and Tousey, 1959); it is stable over time, whereas LiF in Al/LiF is more reactive in the presence of water vapour and hence it is only used when high reflectance is strictly required below ≈ 120 nm. An increase in reflectance for Al/MgF₂ coatings at the hydrogen Lyman α line (121.6 nm) and longwards has been recently reported (Quijada *et al.*, 2012).

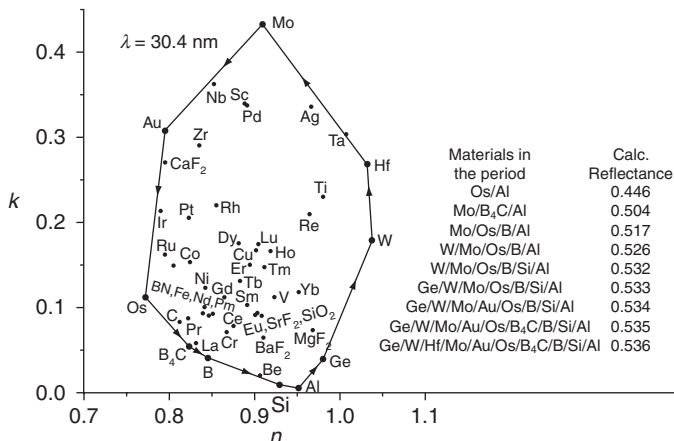
A procedure to make MLs with strongly absorbing materials that are more efficient than single layer coatings has been devised in what has been called sub-quarterwave MLs (SQWMs) (Larraquert, 2001a, 2001b). SQWMs use layers of up to three or more materials with reduced thickness in order to increase the number of interfaces close to the outermost one; this adds extra reflected components close to the outermost interface where radiation has not yet been fully absorbed. For SQWMs, materials must be selected in the correct sequence for the extra reflected components to result in constructive interferences. The procedure starts by plotting in the complex plane the optical constants (n, k) of many materials at the desired target λ . The materials with the most extreme optical constants are the most promising for SQWMs. If all considerations about film thickness and interface stability are obviated, a mere reflectance calculation predicts that maximum ML reflectance is obtained if all the materials with the most extreme optical constants are successively deposited in the SQWM. The condition for the extra reflected components to result in constructive interferences is that the material sequence in the ML is given by counter-clockwise rotation in the $n-k$ plot (in the direction from the innermost to the outermost layer).



7.17 Measured reflectance at near-normal incidence of SQWM with 1–4 layers of as many materials optimized at 91.2 nm. Inset: n, k plot of materials with extreme optical constants at 91.2 nm; arrows indicate the deposition sequence from the innermost to the outermost layer.

Calculated reflectance increases with the number of materials. Figure 7.17 plots n and k of a selection of materials with extreme optical constants at 91.2 nm; arrows indicate the counter-clockwise deposition sequence from the innermost to the outermost layer (Larrauquert and Keski-Kuha, 2002). Figure 7.17 also displays the reflectance increase measured for SQWM when increasing from 1 to 4 materials, one layer per material. The reflectance increase, although modest, extends to a wide range.

SQWMs can be also applied to regions where absorption is not so strong so that there is enough penetration to make standard MLs that alternate layers of two materials. In this case, SQWMs provide a reflectance increase over standard MLs when increasing the number of materials from two to three or more (Larrauquert, 2002a). Figure 7.18 displays the optical constants n, k of many materials at 30.4 nm; the outer polygon connects the materials with the most extreme optical constants, which are the most promising candidates for SQWMs from the optical constants point of view. The figure also gives the calculated reflectance at 30.4 nm when the number of materials is increased for SQWMs with 25 periods. A significant reflectance increase is calculated when the number of materials is increased above the standard of two; the reflectance increase tends to saturation with the number of materials so that the insignificant increase with the addition of the last several materials would be neither worth the complication nor realistic in practice.



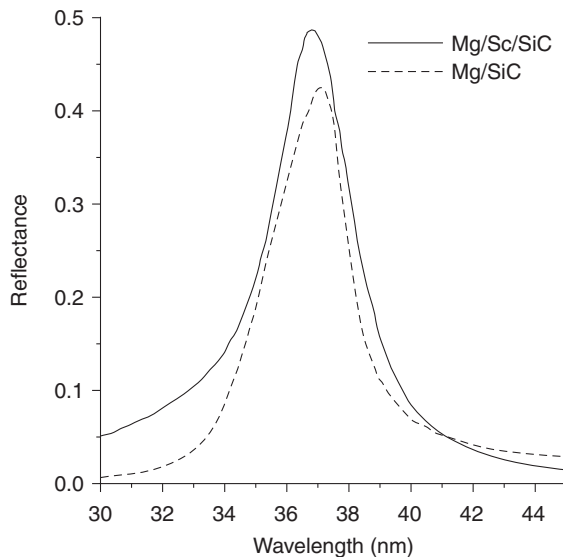
7.18 Optical constants of many materials at 30.4 nm. The outer polygon connects the materials with the most extreme optical constants; arrows indicate the deposition sequence from the innermost to the outermost layer. Inset table: calculated normal reflectance at 30.4 nm of 25-period MLs with increasing number of materials optimized for the largest reflectance at near-normal incidence. For each number of materials, the maximum achievable reflectance among all possible material combinations is given.

Figure 7.19 displays the measured reflectance enhancement for a ML optimized at 37 nm when the number of materials is increased from two (Mg/SiC) to three (Mg/Sc/SiC) (Aquila *et al.*, 2009). Various successful attempts to obtain a reflectance enhancement through multilayers with more than two materials have been reported (Boher *et al.*, 1990; Larruquert and Keski-Kuha, 1999; Gautier *et al.*, 2005; Zhu *et al.*, 2008; Meltchakov *et al.*, 2010; He *et al.*, 2011; Le Guen *et al.*, 2011). A fast SQWM design algorithm that optimizes each layer thickness in the ML has been reported (Larruquert, 2002b), although in many cases periodic multi-material MLs may reach a reflectance close to the optimum aperiodic one.

SQWMs are useful only if reflectance is limited by absorption. If one material existed with negligible absorption, a theoretical reflectance of 100% could be calculated with MLs alternating such material with any secondary absorbing material (Spiller, 1994) so that an SQWM would be unnecessary. Hence the benefit of SQWM is intrinsic to absorption.

7.7.3 Linear polarizers and phase retarders

Linear polarizers and phase retarders, the basic elements for polarimetry, are required for an increasing number of applications at short wavelengths, including ellipsometry, imaging instrumentation for solar physics and



7.19 Reflectance enhancement measured for MLs when the number of materials is increased from two (Mg/SiC) to three (Mg/Sc/SiC) (Aquila *et al.*, 2009). (Source: With permission from the Optical Society of America.)

astrophysics, synchrotron radiation, lasers, solid state physics, atomic and molecular physics, particle-matter interaction, magnetic and chiral material analysis, circular dichroism spectroscopy, spin-polarized photoelectron spectroscopy, magnetic Compton scattering, etc. The polarization state of radiation can be described in terms of the four Stokes parameters S_0 , S_1 , S_2 and S_3 , which represent the total intensity (S_0), the linearly polarized intensity (S_1 , S_2) and the circularly polarized intensity (S_3). In order to make a complete polarization analysis of light, two elements are required: a phase retarder (referred to here simply as retarder), which ideally provides 90° phase retardation between two perpendicular components of the electric field, and a linear polarizer (referred to here simply as polarizer), which provides linearly polarized light. In order to make a polarization measurement we need to have independent rotations of the polarizer and the retarder around the optical axis. Stokes parameters, and hence the polarizing properties of the beam, are obtained from a fit of the recorded intensity upon rotations of the two elements (Schäfers *et al.*, 1999).

For polarizers and retarders operating by reflection, the ratio ρ :

$$\rho = \frac{r_s}{r_p} = \left| \frac{R_s}{R_p} \right|^{\frac{1}{2}} e^{j(\phi_s - \phi_p)} \quad [7.39]$$

contains the information for polarimetry purposes, where p (TM) and s (TE) stand for the electric vector parallel and perpendicular, respectively, to the plane of incidence. A polarizer is required to provide a modulus of ρ as large as possible; a retarder is required to provide a large phase difference between the s and p components, ideally 90° , with the modulus of ρ as close to 1 as possible. For elements working by transmission, reflectance is replaced with transmittance in Equation [7.39] and the roles of p and s are usually inverted.

In the visible range, it is often preferred that polarizers and retarders operate by transmittance, because the optical beam can pass essentially undeviated. This same concept can be extended to short wavelengths, as long as bulk transparent materials are available, that is, down to the LiF cutoff wavelength of ≈ 105 nm; below this wavelength a thin-film substrate can be used. In the transparent range, two mechanisms are used to introduce linear polarization and retardation. Birefringence, that is, the dependence of the refractive index on the direction of the electric field in the medium, which is present for instance in non-cubic crystals, is a useful property to make polarizers and retarders. Rochon prisms are an example of linear polarizers based on birefringence that have been used in the FUV; Rochon prisms deviate the extraordinary ray and keep the ordinary ray undeviated. Birefringence can also provide a phase shift between two waves with perpendicular planes of polarization, which is the basis for retarders. LiF is a cubic crystal and hence it is not a candidate to make retarders; however, its shortest cutoff in nature has made it attractive for inducing piezo-birefringence by compressing the crystal of LiF in one direction (Metcalf and Baird, 1966), which results in a retarder operating at a wavelength as short as 105 nm at room temperature. Other than birefringence, polarization using transparent materials can be produced through the reflection at the Brewster angle, at which the reflectance for p polarization turns zero. The Brewster angle θ_B is connected with the refractive index of the material n by:

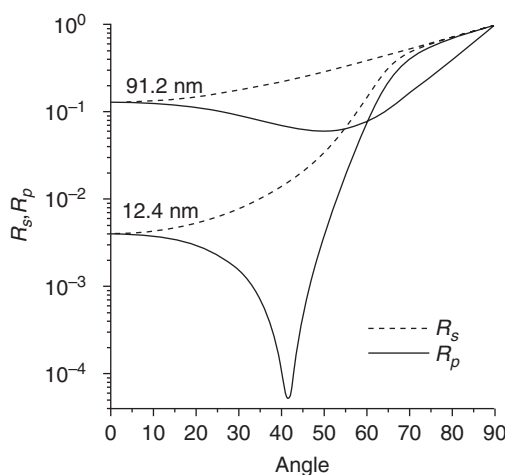
$$\tan \theta_B = n \quad [7.40]$$

This formula is obtained using the r_p expression of Equation [7.8] and Snell's law [7.5]. Hence in order to linearly polarize light by reflection, it is necessary that the material be transparent. A polarizer working by reflection at θ_B results in an undesired deviation of the optical beam (by $2\theta_B$); but the existence of the Brewster angle can be capitalized upon, also working by transmittance due to the increased T_p/T_s ratio of the beam transmitted through a plate. Since a single plate at θ_B provides a modest transmittance polarization ratio, a pile of plates in series at the Brewster angle can be used to increase this ratio (Walker, 1964). A review of the developments based on

all sorts of transparent bulk structures working by transmittance or reflectance and operating in the FUV was written by Hunter (2000) and will not be included here. An older review was reported by Samson (1967c). In the following, only polarizers and retarders based on coatings will be addressed. Interesting reviews on coatings for polarimetry in the EUV and SXR have been reported by Schäfers (2007) and Watanabe *et al.* (2008).

Polarizers or retarders for wavelengths shorter than the LiF cutoff are based on the different reflectance/transmittance modulus or phase for parallel and perpendicular polarization at angles other than normal or grazing incidence.

Let us start with linear polarizers. In contrast to what was said on the Brewster angle for transparent materials, when at least one material at the interface is absorbing, as for every material below the LiF cutoff wavelength, there is no angle at which R_p reaches zero. In spite of this, there is still an angle at which $R_p(\theta)$ reaches a minimum; this angle is often called the pseudo-Brewster angle. The ratio R_s/R_p takes the largest value at an angle in the vicinity of the pseudo-Brewster angle. This property enables polarizers to be made using coatings even when only absorbing materials are available. Figure 7.20 displays the calculated *s* and *p* reflectance vs the incidence angle for a Au layer at two wavelengths; the minimum of R_p vs angle and the enhanced R_s/R_p ratio can be observed. For short enough wavelengths



7.20 The reflectance (log scale) of Au calculated for parallel (R_p) and perpendicular (R_s) polarization versus the angle of incidence (from the normal) at the indicated wavelengths. Data were calculated with optical constants of Canfield *et al.* (1964) (91.2 nm) and downloaded from CXRO web (12.4 nm).

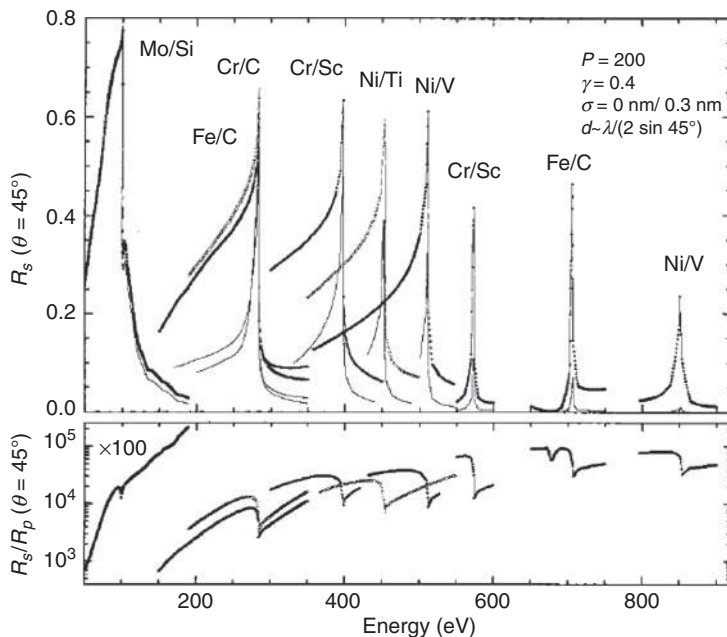
in which the complex refractive index $N = 1 - \delta + i\beta$ satisfies $\delta, \beta \ll 1$, the pseudo-Brewster angle can be approximated by (Attwood, 1999):

$$\theta_{p-B} \approx \frac{\pi}{4} - \frac{\delta}{2} \quad [7.41]$$

Thus at short wavelengths, where δ is mostly positive, the minimum R_p is obtained at an angle slightly smaller than 45° (slightly closer to normal incidence). In the examples of Fig. 7.20, Equation [7.41] is satisfied at 12.4 nm, and less precisely at 91.2 nm (where δ is negative), since in the latter the above condition for β is not met. Yet if we do not restrict ourselves to materials satisfying Equation [7.41], for any wavelength and optical constants and for a single interface it is satisfied that $R_p = R_s^2$ at 45° (Rabinovitch *et al.*, 1965), which results in an enhanced $R_s/R_p = 1/R_s$ ratio at this angle when R_s becomes small; unfortunately a good polarization ratio with a single interface requires a low R_s .

Hence the angle range around 45° is a natural choice to develop reflection polarizers. Unfortunately, at short wavelengths R_s at θ_{p-B} for a single interface, even though larger than R_p , is still small. Since the angle for minimum R_p is close to 45° and this is relatively insensitive to the specific optical constants of the materials at the interface, a multilayer can be optimized for high R_s at angles $\theta \approx 45^\circ$ while keeping a large R_s/R_p ratio (Spiller, 1972b; Gluskin *et al.*, 1986; Dhez, 1987; Kortright, 1993; Bruch *et al.*, 1999; Imazono *et al.*, 2009). Mertins *et al.* (1998) prepared this sort of polarizer for the water window. Schäfers *et al.* (1999) prepared reflective polarizers based on various material pairs for several spectral ranges up to ≈ 570 eV. Figure 7.21 displays R_s and R_s/R_p data calculated at 45° for prospective ML polarizers based on various material pairs covering the range of 50–900 eV, after Schäfers *et al.* (1999). The increasing absorption at long EUV wavelengths causes a decrease in the R_s/R_p ratio (Hunter, 1965). Beyond the long EUV, FUV polarizers (in addition to those based on bulk properties of transparent materials mentioned at the beginning of this section) can also be prepared by means of coatings, such as Al/MgF₂ MLs (Bridou *et al.*, 2011; Larruquert *et al.*, 2013), and such coatings are sometimes preferred over bulk devices when a large R_s is required.

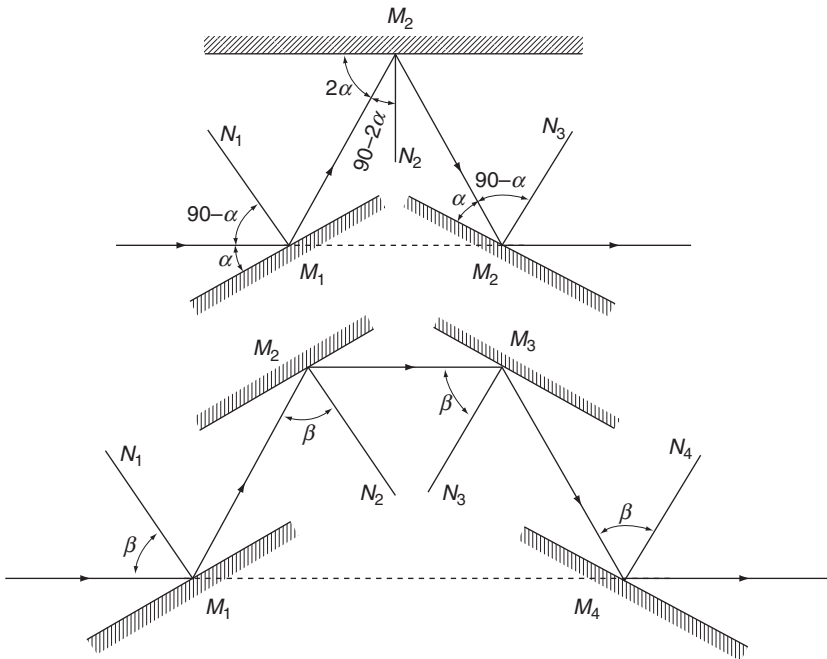
When the coating consists of a ML with many layers, the simple and common approach is the use of a periodic ML. One limitation of a polarizer made using this approach is that it is efficient in a narrow spectral and angular band. By varying the angle of incidence, the band of a ML can be spectrally shifted, which enables covering a larger spectral range with a single ML (Maehara *et al.*, 1991; Yanagihara *et al.*, 1992; Yamamoto, 1993); however, the variation of the angle of incidence results in a deviation of the



7.21 R_s and R_s/R_p calculated at 45° for prospective ML polarizers based on various material pairs covering the range of 50–900 eV (Schäfers *et al.*, 1999). (Source: With permission from the Optical Society of America.)

reflected beam, which complicates the design of a polarimeter. Wideband polarizers have also been developed based on the displacement of a laterally graded multilayer (Kortright *et al.*, 1995). To avoid rotation or travel, wideband polarizers and/or polarizers effective in an enhanced angular range can be designed by optimizing each layer thickness in the ML following a desired figure of merit; experimental demonstration of aperiodic ML polarizers with an increased EUV or SXR spectral band (Wang *et al.*, 2006a, 2006b, 2007b; Tan *et al.*, 2011) and with a wide angular band at 13 nm (Wang *et al.*, 2006c) have been reported.

One disadvantage of reflective polarizers is that they divert the optical beam; this can be avoided by using various mirrors in series. The minimum number of mirrors to avoid beam rotation and shift is three, with the two extreme reflections at a common angle and a central reflection at double the grazing angle of the extreme reflections. If additionally all reflections are desired at a common angle, a minimum of four reflections is required. Figure 7.22 displays the two configurations. The multiple reflections can provide an increased reduction of R_p (Hamm *et al.*, 1965; Rosenbaum *et al.*, 1968; Horton *et al.*, 1969; Hunter, 1978, 2000). These configurations, particularly



7.22 3-mirror (top) and 4-mirror (bottom) polarizer configurations to avoid the deviation of the optical beam. The planes of incidence of all mirrors are coincident and they are on the plane of the sheet. The component of the electric field that is reduced is the one in the plane of incidence.

the 3-mirror one, have been extensively used in the long EUV (and even in the FUV) and they may result in polarizers with a relatively wide band (Horton *et al.*, 1969; Naik and Lodha, 2006). The use of a specific coating for each of the mirrors may provide a polarizer that is operative in a wider band (Hass and Hunter, 1978), with the additional gain of suppressing higher diffraction orders (Yang *et al.*, 2007).

Transmittance polarizers have also been developed with the benefit that they do not deviate the beam. A transmittance polarizer was proposed by Hu *et al.* (1996); it consists of a free-standing (self-supported) transmission multilayer for which a high R_s at an incident angle close to the Bragg angle of the multilayer (angle at which the ML satisfies Equation [7.31]) results in a reduced T_s ; hence T_p/T_s in a transmission polarizer is enhanced vs R_s/R_p for the reflection polarizer. One property of transmission polarizers is that when the layer number increases, the throughput of transmitted light T_p always decreases but the polarization ratio increases (Tan *et al.*, 2009). Transmission polarizers were developed by Haga *et al.* (1998 and 1999). Polarization by

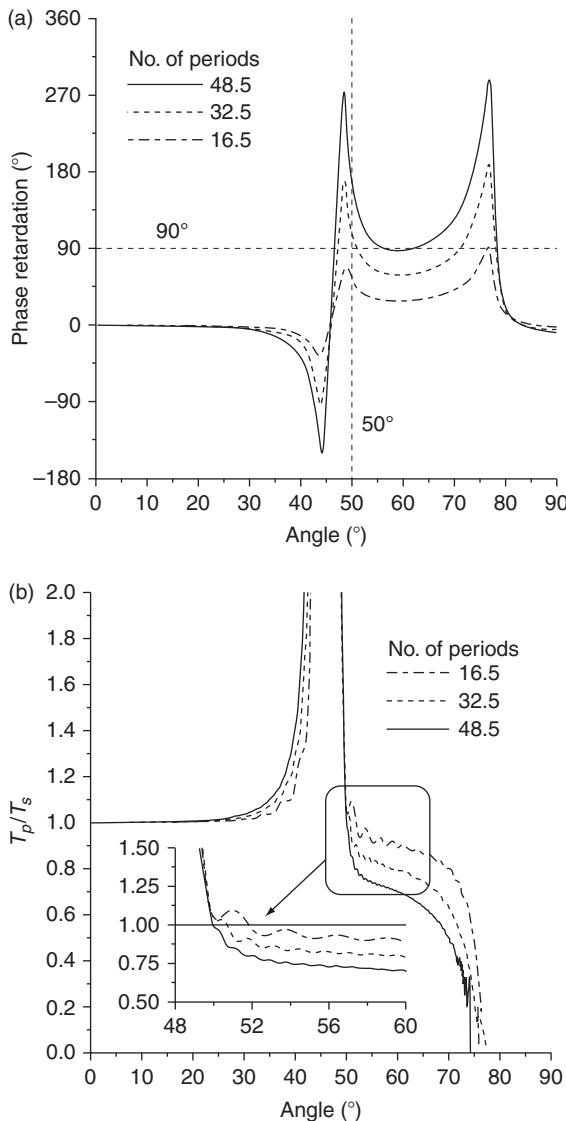
transmission through a ML was developed by Kjornrattanawanich *et al.* (2004) in which the coating was deposited on the detector.

For high energies above ≈ 1 keV, polarizers based on perfect crystals operating close to a Bragg angle can be used and are preferred over MLs (Marx *et al.*, 2011; Wang *et al.*, 2012). Some polarizers are based on the anomalous transmission of X-rays or Borrman effect (Batterman and Cole, 1964; Hart, 1978; Batterman, 1992).

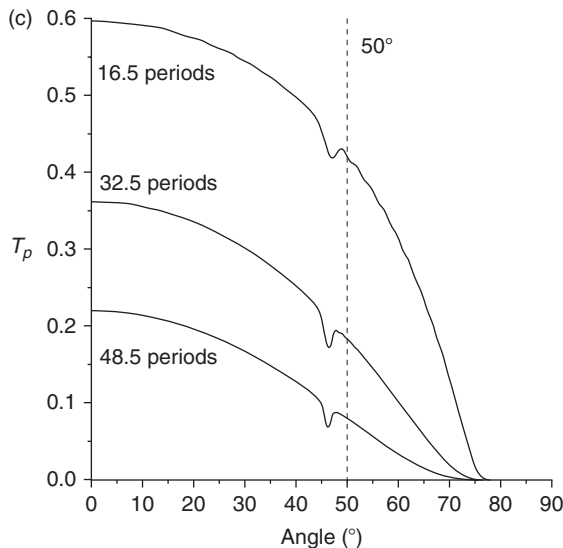
Let us now address phase retarders. They introduce a relative phase change between the *s* and *p* components in either the reflected or the transmitted beam. As with linear polarizers, bulk retarders based on the transparency of materials in the FUV are not reviewed here and the reader is again referred to Hunter (2000). Very useful retarders are those that introduce a phase shift of 90° , called quarter-wave retarders (not to be confused with a quarterwave layer referred to in Section 7.3.3: the latter refers to the optical thickness of a layer, whereas the former refers to phase retardation between the *s* and *p* components), which, in combination with a linear polarizer, enable a complete polarimetric analysis of the incoming beam. As mentioned above, retarders also require that the throughput for *s* and *p* polarization be very similar.

Phase retarders have been developed both based on reflection and on transmission. Wideband retarders based on reflection have been fabricated or at least designed with single (Westerveld *et al.*, 1985; Saito *et al.*, 1990) and multiple (Johnson and Smith, 1983; Höchst *et al.*, 1994; Naik and Lodha, 2006) Au coated mirrors. Multiple reflectors can provide 90° total phase retardation through the addition of the individual phase shifts produced by each single mirror; the configuration for retarders based on multiple mirrors is the same as the one displayed in Fig. 7.22. Höchst *et al.* (1994) could turn linear polarization into circular polarization, that is, could provide 90° phase retardation, by adjusting the common incidence angle of the 4 mirrors and by rotating the quadruple reflector with respect to an axis coincident with the incident beam. Smith and Howells (1994) replaced each of the 4 flat mirrors with a whispering gallery, that is, a cylindrical mirror in which the beam is reflected not one but several times on each mirror, all of them at a more grazing incidence (and hence more efficiently) than when plane mirrors are used. Kim *et al.* (1992) designed 3-layer MgF_2 -Al reflection retarders tuned at 121.6 nm. Imazono *et al.* (2009) prepared reflection Mo/Si ML retarders (and also polarizers) tuned at 13.5 nm.

Similar to polarizers, reflection retarders have the disadvantage that they cause the deviation of the beam, and hence transmission retarders are often preferred. Kortright and Underwood (1990) calculated that an efficient quarter-wave retarder could be made by transmission through an optimized multilayer. The benefit of such a retarder compared to those working by



7.23 The phase retardation on transmission (a), the T_p/T_s ratio (b), and T_p (c) calculated for Mo/Si MLs with various numbers of periods versus the angle of incidence referred to the normal. MLs are designed to satisfy the Bragg condition at 13.5 nm at 45°. The optical constants of Mo (Soufli and Gullikson, 1998) and Si (Soufli and Gullikson, 1997), which were downloaded from CXRO web, were used in the calculations.



7.23 Continued

reflection is that the beam is not essentially deviated; a drawback is that it must be self-supported to avoid full absorption from the substrate, which makes the retarder fragile. Kortright and Underwood (1990) observed how the *s* component of the electric field is subject to larger interference effects than the *p* component, which results in a phase shift between the two components; they found a useful incidence angle range for retardation purposes between the Bragg angle and the critical angle of total reflection.

Figure 7.23 displays the transmission phase retardation, the transmittance ratio and the transmittance for the *p* component calculated for Mo/Si MLs with various numbers of periods at 13.5 nm as a function of the angle of incidence. It can be seen that retardation increases with the number of periods, which is an intuitive result for a transmission coating, although obviously both T_p and T_s decrease with this same number. The request of $T_p \approx T_s$ is satisfied at $\approx 50\text{--}52^\circ$. In this example the ML with 32.5 periods at an angle of $\approx 50^\circ$ is calculated to have a phase retardation of 90° with equal transmittance for the *p* and *s* components of 0.18.

Various quarter-wave retarders working by transmission have been developed for the spectral range around 13 nm (Kortright *et al.*, 1992; Nomura *et al.*, 1992; Yamamoto, 1993; Haga *et al.*, 1998, 1999; the latter developed a polarimeter with no deviation based on a transmissive polarizer and retarder), at the water window (Kimura *et al.*, 2005; Chkhalo *et al.*, 2011) and at energies up to ≈ 1.5 keV (Wang *et al.*, 2012). At high energies it becomes difficult to

achieve large retardation values. The trend of the refractive index towards unity at increasing energies makes it difficult to reach a phase shift as large as 90°. Even though a retardation of 90° is the ideal value to analyze elliptical polarization, a phase-shift angle of a few tens of degrees (Di Fonzo *et al.*, 1994) or even a few degrees at $E > 600$ eV (MacDonald *et al.*, 2008) has been demonstrated to be sufficient in order to obtain the characterization of a beam. Schäfers *et al.* (1999) used Si_3N_4 membranes for retarder substrates to improve robustness; they prepared transmission retarders based on various material pairs to cover several spectral ranges up to ≈ 570 eV.

Similarly to linear polarizers, transmissive retarders based on periodic MLs are often efficient only in a narrow spectral band. As with polarizers, aperiodic-ML transmission retarders that are effective in a wider spectral range can be designed with the optimization of all layer thicknesses in the ML according to a specific figure of merit (Wang *et al.*, 2007a; Wang *et al.*, 2007b); in the latter pieces of research, Si_3N_4 membranes were used as substrates to improve robustness.

At increasing X-ray energies, MLs become increasingly less efficient for making retarders; in this case, perfect crystals can be used instead. When a plane-polarized X-ray beam enters a crystal, the electric field can be separated into a parallel and a perpendicular component with respect to the diffraction planes. The two components propagate with different phase velocities through the crystal, as a sort of birefringence. On recombination at the exit, a phase difference proportional to the optical path length is generated. Two geometries are possible: the diffraction planes are perpendicular (Laue) or parallel (Bragg) to the plate surface, and each of them can operate in transmission or reflection (Hirano *et al.*, 1995; Malgrange *et al.*, 1999). The phase difference is tunable by changing an angle offset away from the Bragg condition (Bouchenoire *et al.*, 2012). A 90° phase retardation can be introduced by a single thin crystal operating in transmission mode (Giles *et al.*, 1995; Hirano *et al.*, 1995; Lang and Strajer, 1995); quarter-wave crystal plates based on multiple reflections have also been developed (Batterman, 1992). Such crystal plates have been used for energies from a few keV to the HXR (Venkataraman *et al.*, 1998).

The present section has given only a partial approach to the field of MLs for short wavelengths and there are coatings for several other applications that have not been covered. Various reviews on MLs for EUV and SXR that may provide supplementary information can be found in the literature (Dhez, 1990; Spiller, 1994; Yulin, 2003).

7.8 Conclusion

The optical properties of materials at short wavelengths are different from those in more familiar ranges, such as the visible, and these differences often

make this spectral range difficult to handle in an efficient way. On the other hand, materials can also provide valuable information at short wavelengths. And coatings at short wavelengths are considered as enabling challenging applications that are becoming possible now that the difficulties inherent in dealing with this radiation are gradually being harnessed. The dramatic development of optics at short wavelengths in recent decades promises a near future full of progress and success.

7.9 Acknowledgements

I am indebted to José Antonio Méndez and Mónica Fernández for reading the draft and giving me many valuable suggestions, and for constant discussions, which were extremely helpful to clarify many points. I gratefully acknowledge David Windt for making Fig. 7.14 for this chapter; he kindly updated older versions with recently developed multilayers. I acknowledge financial support from the National Programme for Space Research, Subdirección General de Proyectos de Investigación, Ministerio de Ciencia y Tecnología, Project No. AYA2010–22032.

7.10 References

- Abelès F (1948), 'Sur la propagation des ondes électromagnétiques dans les milieux stratifiés', *Ann. Phys. (Paris)* **3**, 504–520.
- Aquila A L, Salmassi F, Dollar F, Liu Y, Gullikson E M (2006), 'Developments in realistic design for aperiodic Mo/Si multilayer mirrors', *Opt. Exp.* **14**, 10073–10078.
- Aquila A, Salmassi F, Gullikson E (2008), 'Metrologies for the phase characterization of attosecond extreme ultraviolet optics', *Opt. Lett.* **33**, 455–457.
- Aquila A, Salmassi F, Liu Y, Gullikson E M (2009), 'Tri-material multilayer coatings with high reflectivity and wide bandwidth for 25 to 50 nm extreme ultraviolet light', *Opt. Exp.* **17**, 22102–22107.
- Arakawa E T, Hamm R N, Williams M W (1973), 'Optical properties and electron-attenuation lengths from photoelectric yield measurements', *J. Opt. Soc. Am.* **63**, 1131.
- Ashcroft N W, Mermin N D (1976), *Solid State Physics*, Saunders College Publishing, Philadelphia.
- Attwood D (1999), *Soft X-rays and Extreme Ultraviolet Radiation, Principles and Applications*, Cambridge University Press.
- Bajt S, Alameda J B, Barbee Jr. T W, Folta J A, Kaufmann B, Spiller E A, Clift W M (2002), 'Improved reflectance and stability of Mo-Si multilayers', *Opt. Eng.* **41**, 1797–1804.
- Barth J, Johnson R L, Cardona M (1998), 'Spectroscopic ellipsometry in the 6–35 eV region', in *Handbook of Optical Constants of Solids II*, E. D. Palik, ed., Academic Press, San Diego.
- Batterman B W (1992), 'X-ray phase plate', *Phys. Rev. B* **45**, 12677–12681.
- Batterman B W, Cole H (1964), 'Dynamical diffraction of x rays by perfect crystals', *Rev. Mod. Phys.* **36**, 681–717.

- Bennett H E, Porteus J O (1961), 'Relation between surface roughness and specular reflectance at normal incidence', *J. Opt. Soc. Am.* **51**, 123–129.
- Berger M J, Hubbell J H, Seltzer S M, Chang J, Coursey J S, Sukumar R, Zucker D S, Olsen K (2010), XCOM: Photon Cross Section Database, version 1.5 (2010). [Online] Available: <http://physics.nist.gov/PhysRefData/Xcom/html/xcom1.html> [Wednesday, 20 June 2012 03:27:19 EDT]. National Institute of Standards and Technology, Gaithersburg, MD.
- Bibishkin M S, Chkhalo N I, Gusev S A, Kluenkov E B, Lopatin A Y, Luchin V I, Pestov A E, Salashchenko N N, Shmaenok L A, Tsybin N N, Zuev S Y (2008), 'Multilayer Zr/Si filters for EUV lithography and for radiation source metrology', *Proc. SPIE* **7025**, 702502.
- Birken H-G, Blessing C, Kunz C (1998), 'Determination of optical constants from angular-dependent, photoelectric-yield measurements', in *Handbook of Optical Constants of Solids II*, E. D. Palik, ed., Academic Press, San Diego.
- Boher P, Hennet L, Houdy Ph (1990), 'Three materials soft x-ray mirrors: theory and application', *Proc. SPIE* **1345**, 198–212.
- Bouchenoire L, Morris R J H, Hase T P A (2012), 'A silicon <111> phase retarder for producing circularly polarized x-rays in the 2.1–3 keV energy range', *Appl. Phys. Lett.* **101**, 064107.
- Braun S, Mai H, Moss M, Scholz R, Leson A (2002), 'Mo/Si multilayers with different barrier layers for applications as extreme ultraviolet mirrors', *Jpn. J. Appl. Phys.* **41**, 4074–4081.
- Bridou F, Cuniot-Ponsard M, Desvignes J-M, Gottwald A, Kroth U, Richter M (2011), 'Polarizing and non-polarizing mirrors for the hydrogen Lyman- α radiation at 121.6 nm', *Appl. Phys. A* **102**, 641–649.
- Bruch R, Merabet H, Bailey M, Siems A (1999), 'Characterization of a compact multilayer mirror (MLM) polarimeter for measurements of the degree of linear polarization in the 256 Å to 584 Å wavelength EUV range', *Proc. SPIE* **3764**, 28–39.
- Canfield L R, Hass G, Hunter W R (1964), 'The optical properties of evaporated gold in the vacuum ultraviolet from 300 Å to 2 000 Å', *J. Physique* **25**, 124–129.
- Carniglia C K, Apfel J H (1980), 'Maximum reflectance of multilayer dielectric mirrors in the presence of slight absorption', *J. Opt. Soc. Am.* **70**, 523–534.
- Carruthers G R (1971), 'Narrow-band filter for the Lyman- β wavelength region', *Appl. Opt.* **10**, 1461–1463.
- Chang C, Anderson E, Naulleau P, Gullikson E, Goldberg K, Attwood D (2002), 'Direct measurement of index of refraction in the extreme-ultraviolet wavelength region with a novel interferometer', *Opt. Lett.* **27**, 1028–1030.
- Chantler C T, Olsen K, Dragoset R A, Chang J, Kishore A R, Kotchigova S A, Zucker D S (1995), 'Theoretical form factor, attenuation and scattering tabulation for Z=1–92 from E=1–10 eV to E=0.4–1.0 MeV', *J. Phys. Chem. Ref. Data* **24**, 71–643.
- Chantler C T (2000), 'Detailed tabulation of atomic form factors, photoelectric absorption and scattering cross section, and mass attenuation coefficients in the vicinity of absorption edges in the soft x-ray (Z = 30–36, Z = 60–89, E = 0.1 keV–10 keV), addressing convergence issues of earlier work', *J. Phys. Chem. Ref. Data* **29**, 597–1048.
- Chkhalo N I, Drozdov M N, Gusev S A, Kluenkov E B, Lopatin A Ya, Luchin V I, Salashchenko N N, Shmaenok L A, Tsybin N N, Volodin B A (2011),

- 'Freestanding multilayer films for application as phase retarders and spectral purity filters in the soft X-ray and EUV ranges', *Proc. SPIE* **8076**, 807600.
- Chkhalo N I, Gusev S A, Drozdov M N, Kluenkov E B, Lopatin A Ya, Luchin V I, Pestov A E, Salashchenko N N, Shmaenok L A, Tsybin N N (2010), 'Influence of annealing on the structural and optical properties of thin multilayer EUV filters containing Zr, Mo and silicides of these metals', *Proc. SPIE* **7521**, 752105.
- Christensen F E, Hornstrup A, Westergaard N J, Schnopper H W (1992), 'A graded d-spacing multilayer telescope for high energy x-ray astronomy', *Proc. SPIE* **1546**, 160–167.
- Clarke J T, Skinner W R, Vincent M B, Irgang T, Suratkal V, Grassl H, Trauger J T (1999), 'Laboratory studies of alkali metal filter deposition, ultraviolet transmission, and visible blocking', *Appl. Opt.* **38**, 1803–1813.
- Compton A H (1923), 'The total reflexion of X-rays', *Phil. Mag.* **45**, 1121–1131.
- Croce P (1977), 'Sur l'effet des couches très minces et des rugosités sur la réflexion, la transmission et la diffusion de la lumière par un dioptre', *J. Opt.* **8**, 127–139.
- Croce P (1978), 'Complément à l'étude de l'effet des couches minces sur la réflexion, la transmission et la diffusion de la lumière', *J. Opt.* **9**, 61–63.
- Cromer D T, Mann J B (1968), 'X-ray scattering factors computed from numerical Hartree-Fock wave functions', *Acta Cryst. A* **24**, 321–324.
- CXRO web. URL: http://www-cxro.lbl.gov/optical_constants/
- Davisson C M (1965), 'Interaction of γ radiation with matter', Chapter II in *Alpha-, Beta-, and Gamma-Ray Spectroscopy*, K. Siegbahn, ed., North-Holland, Amsterdam.
- Debye P (1913), 'Über der Intensitätsverteilung in den mit Röntgenstrahlung erzeugten Interferenzbildern', *Verh. d. Deutsch. Phys. Ges.* **15**, 738.
- Dhez P (1987), 'Polarizers and polarimeters in the X-UV range', *Nucl. Instr. Meth. A* **261**, 66–71.
- Dhez P (1990), 'X and X-UV multilayered optics: principles, fabrication methods, tests and applications', *Ann. Phys. Fr.* **15**, 493–527.
- Di Fonzo S, Jark W, Schafers F, Petersen H, Gaupp A, Underwood J H (1994), 'Phase-retardation and full-polarization analysis of soft-x-ray synchrotron radiation close to the carbon K edge by use of a multilayer transmission filter', *Appl. Opt.* **33**, 2624–2632.
- Drude P (1900a), 'Zur Elektronentheorie der metalle', *Ann. Phys.* **306**, 566–613.
- Drude P (1900b), 'Zur Elektronentheorie der Metalle; II. Teil. Galvanomagnetische und thermomagnetische Effecte', *Ann. Phys.* **308**, 369–402.
- Edelstein J (1989), 'Reflection/suppression coatings for the 900–1200 Å radiation', *Proc. SPIE* **1160**, 19–25.
- Evans R D (1955), *The Atomic Nucleus*, McGraw-Hill, New York.
- Fabre D, Romand J, Vodar B (1964), 'Constants optiques et pouvoir réflecteur de couches minces de fluorures dans l'ultraviolet lointain', *J. Phys.* **25**, 55–59.
- Fairchild E T (1973), 'Interference filters for the VUV (1200–1900 Å)', *Appl. Opt.* **12**, 2240–2241.
- Feigl T, Lauth H, Yulin S, Kaiser N (2001), 'Heat resistance of EUV multilayer mirrors for long-time applications', *Microelectron. Eng.* **57–58**, 3–8.
- Feigl T, Yulin S, Benoit N, Kaiser N (2005), 'Multilayer optics for the EUV and soft X-rays', *Opt. Precis. Eng.* **13**, 421–429.

- Fernández-Perea M, Larruquert J I, Aznárez J A, Méndez J A, Poletto L, Malvezzi A M, Giglia A, Nannarone S (2006a), 'Determination of optical constants of scandium films in the 20–1000 eV range', *J. Opt. Soc. Am. A* **23**, 2880–2887.
- Fernández-Perea, M, Méndez, J A, Aznárez, J A, Larruquert, J I (2006b), 'Filters for world space observatory', in *The World Space Observatory Project-Spain*, Gómez de Castro, A.I., Verdugo, E. (eds.). Editorial Complutense, Madrid.
- Fernández-Perea M, Vidal-Dasilva M, Aznárez J A, Larruquert J I, Méndez J A, Poletto L, Garoli D, Malvezzi A M, Giglia A, Nannarone S (2008), 'Transmittance and optical constants of Pr films in the 4–1,600-eV spectral range', *J. Appl. Phys.* **103**, 113515.
- Fernández-Perea M, Vidal-Dasilva M, Larruquert J I, Aznárez J A, Méndez J A, Gullikson E, Aquila A, Soufli R (2009), 'Optical constants of evaporation-deposited silicon monoxide films in the 7.1–800 eV photon energy range', *J. Appl. Phys.* **105**, 113505.
- Fernández-Perea M, Larruquert J I, Aznárez J A, Méndez J A, Poletto L, Frassetto F, Malvezzi A M, Bajoni D, Giglia A, Mahne N, Nannarone S (2011), 'Transmittance and optical constants of Ho films in the 3–1,340 eV spectral range', *J. Appl. Phys.* **109**, 083525.
- Fernández-Perea M, Pivovaroff M J, Soufli R, Alameda J, Mirkarimi P, Descalle M-A, Baker S L, McCarville T, Ziock K, Hornback D, Romaine S, Bruni R, Zhong Z, Honkimäki V, Ziegler E, Christensen F E, Jakobsen A C (2013a), 'Ultra-short-period WC/SiC multilayer coatings for x-ray applications', *Nucl. Instr. Meth. A* **710**, 114–119.
- Fernández-Perea M, Descalle M-A, Soufli R, Ziock K, Alameda J, Baker S L, McCarville T, Honkimäki V, Ziegler E, Jakobsen A C, Christensen F E, Pivovaroff M J (2013b), 'Physics of reflective optics for the soft gamma-ray photon energy range', accepted for publication in *Phys. Rev. Lett.* (Accepted May 29, 2013).
- Fontaine A, Warburton W K, Ludwig Jr. K F (1985), 'Determination of anomalous scattering factors in GaAs using x-ray refraction through a prism', *Phys. Rev. B* **31**, 3599–3605.
- Gålnander B 2001, 'Thin films and deposition processes studied by soft x-ray spectroscopy', Thesis, U. Uppsala, Sweden.
- Gautier J, Delmotte F, Roulliay M, Bridou F, Ravet M-F, Jérôme A (2005), 'Study of normal incidence of three-component multilayer mirrors in the range 20–40 nm', *Appl. Opt.* **44**, 384–390.
- Gesell T F, Arakawa E T (1971), 'Attenuation length for photoelectrons excited in aluminum by 21.2-eV photons', *Phys. Rev. Lett.* **26**, 377–380.
- Giles C, Vettier C, de Bergevin F, Malgrange C, Grübel G, Grossi F (1995), 'X-ray polarimetry with phase plates', *Rev. Sci. Instrum.* **88**, 1518–1521.
- Gluskin E S, Gaponov S V, Dhez P, Ilyinsky PP, Salashchenko N N, Shatunov Yu M, Trakhtenberg E M (1986), 'A polarimeter for soft x-ray and VUV radiation', *Nucl. Instr. Meth. A* **246**, 394–396.
- Gullikson E M (2000), 'Optical properties of materials', in *Vacuum Ultraviolet Spectroscopy I*, J. A. Samson and D. L. Ederer, eds, Academic Press, San Diego, CA.
- Habs D, Günther M M, Jentschel M, Urban W (2012), 'Refractive index of silicon at γ ray energies', *Phys. Rev. Lett.* **108**, 184802.

- Haelbich R-P, Iwan M, Koch E E (1977), 'Optical properties of some insulators in the vacuum ultraviolet region', Physik Daten collection, vol. **8-1** and **18-2**, Zentralstelle für Atomkernenergie-Dokumentation, Eggenstein-Leopoldshafen, Germany.
- Haga T, Utsumi Y, Itabashi S (1998), 'Soft x-ray ellipsometer using transmissive multilayer polarizers', *Proc. SPIE* **3443**, 117–127.
- Haga T, Tinene M C K, Ozawa A, Utsumi Y, Itabashi S, Ohkubo T, Shimada M (1999), 'Fabrication of semitransparent multilayer polarizer and its application to soft x-ray ellipsometer', *Proc. SPIE* **3764**, 13–27.
- Hagemann H -J, Gudat W, Kunz C (1974), 'Optical constants from the far infrared to the X-ray region: Mg, Al, Cu, Ag, Au, Bi, C, and Al₂O₃', DESY report SR-74/7 (Deutsches Elektron-Synchrotron, Hamburg).
- Hamm R N, MacRae R A, Arakawa E T (1965), 'Polarization studies in the vacuum ultraviolet', *J. Opt. Soc. Am.* **55**, 1460–1463.
- Hart M (1978), 'X-ray polarization phenomena', *Phyl. Mag. B* **38**, 41–56.
- Hass G, Tousey R (1959), 'Reflecting coatings for the extreme ultraviolet', *J. Opt. Soc. Am.* **49**, 593–602.
- Hass G, Jacobus G F, Hunter W R (1967), 'Optical properties of evaporated iridium in the vacuum ultraviolet from 500 Å to 2000 Å', *J. Opt. Soc. Am.* **57**, 758–762.
- Hass G, Hunter W R (1978), 'Reflection polarizers for the vacuum ultraviolet using Al + MgF₂ mirrors and an MgF₂ plate', *Appl. Opt.* **17**, 76–82.
- He S, Liu Y, Zhu J, Li H, Huang Q, Zhou H, Huo T, Wang Z, Fu S (2011), 'SiC/W/Ir multilayer-coated grating for enhanced efficiency in 50–100 nm wavelength range in Seya–Namioka mount', *Opt. Lett.* **36**, 163–165.
- Hecht E (2002), *Optics*, Addison-Wesley, San Francisco.
- Hecquet C, Ravet-Krill M-F, Delmotte F, Jérôme A, Hardouin A, Bridou F, Varnière F, Roulliay M (2007), 'Design, conception, and metrology of EUV mirrors for aggressive environments', *Proc. SPIE* **6586**, 65860X.
- Hecquet C, Delmotte F, Ravet-Krill M F, de Rossi S, Jérôme A, Bridou F, Varnière F, Melchakov E, Auchère F, Giglia A, Mahne N, Nanaronne S (2009), 'Design and performance of two-channel EUV multilayer mirrors with enhanced spectral selectivity', *Appl. Phys. A* **95**, 401–408.
- Henke B L, Lee P, Tanaka T J, Shimabukuro R L, Fujikawa B K (1982), At. Data Nucl. Data Tables 1, 27.
- Henke B L, Gullikson E M, Davis J C (1993), At. Data Nucl. Data Tables 54, 181.
- Hilfiker J N (2005), 'VUV ellipsometry', in *Handbook of Ellipsometry*, Tompkins H G, Irene E A, eds., William Andrew, New York.
- Hirano K, Ishikawa T, Kikuta S (1995), 'Development and application of x-ray phase retarders', *Rev. Sci. Instrum.* **66**, 1604–1609.
- Höchst H, Patel R, Middleton F (1994), 'Multiple-reflection $\lambda/4$ phase shifter: a viable alternative to generate circular-polarized synchrotron radiation', *Nucl. Instr. Meth. A* **347**, 107–114.
- Höchst H, Bulicke P, Nelson T, Middleton F (1995), 'Performance evaluation of a soft x-ray quadruple reflection circular polarizer', *Rev. Sci. Instrum.* **66**, 1598–1600.
- Holm R T (1998), 'Convention confusions', in *Handbook of Optical Constants of Solids II*, E. D. Palik, ed., Academic Press, San Diego.
- Horton V G, Arakawa E T, Hamm R N, Williams M W (1969), 'A triple reflection polarizer for use in the vacuum ultraviolet', *Appl. Opt.* **8**, 667–670.

- Hu W, Yamamoto M, Watanabe M (1996), 'Development of EUV free-standing multilayer polarizers', *Proc. SPIE* **2873**, 74–77.
- Hubbell J H, Gimm H A, Øverbø I (1980), 'Pair, triplet, and total atomic cross sections (and mass attenuation coefficients) for 1 MeV–100 GeV photons in elements Z = 1 to 100', *J. Phys. Chem. Ref. Data* **9**, 1023–1147.
- Hubbell J H, Seltzer S M (1995), 'X-ray attenuation and absorption for materials of dosimetric interest' Tables of x-ray mass attenuation coefficients and mass energy-absorption coefficients from 1 keV to 20 MeV for elements Z = 1 to 92 and 48 additional substances of dosimetric interest. NIST Physical Reference Data. Report NISTIR 5632. URL: <http://www.nist.gov/pml/data/xraycoef/index.cfm>
- Hunter W R (1964a), 'Optical constants of metals in the extreme ultraviolet. I. A modified critical-angle technique for measuring the index of refraction of metals in the extreme ultraviolet', *J. Opt. Soc. Am.* **54**, 15–19.
- Hunter W R (1964b), 'On the optical constants of metals at wavelengths shorter than their critical wavelengths', *J. Physique*, **25**, 154–160. URL: <http://dx.doi.org/10.1051/jphys:01964002501-2015400>
- Hunter W R (1965), 'Polarizers for the extreme ultraviolet', *Jpn. J. Appl. Phys.* **4**(1), 520–526.
- Hunter W R (1973), 'The preparation and use of unbacked metal films as filters in the extreme ultraviolet', *Phys. Thin Films* **7**, 43–114 (Academic Press, New York).
- Hunter W R (1978), 'Design criteria for reflection polarizers and analyzers in the vacuum ultraviolet', *Appl. Opt.* **17**, 1259–1270.
- Hunter W R (1998), 'Measurement of Optical Constants in the Vacuum Ultraviolet Spectral Region', in *Handbook of Optical Constants of Solids*, E. D. Palik, ed., Academic Press, San Diego.
- Hunter W R (2000), 'Polarization', in *Vacuum Ultraviolet Spectroscopy I*, J. A. Samson and D. L. Ederer, eds, Academic Press, San Diego, CA.
- Hunter W R, Angel D W, Tousey R (1965), 'Thin films and their uses for the extreme ultraviolet', *Appl. Opt.* **4**, 891–898.
- Hunter W R, Malo S A (1969), 'The temperature dependence of the short wavelength transmittance limit of vacuum ultraviolet window materials-I. Experiment', *J. Phys. Chem. Solids* **30**, 2739–2745.
- Hunter W R, Osantowski J F, Hass G (1971), 'Reflectance of aluminum overcoated with MgF₂ and LiF in the wavelength region from 1600 Å to 300 Å at various angles of incidence', *Appl. Opt.* **10**, 540–544.
- Imazono T, Sano K, Suzuki Y, Kawachi T, Koike M (2009), 'Development and performance test of a soft x-ray polarimeter and ellipsometer for complete polarization analysis', *Rev. Sci. Instrum.* **80**, 085109.
- Inczédy J, Lengyel T, Ure A M (1998), 'Compendium of analytical nomenclature : definitive rules 1997', ed. by International Union of Pure and Applied Chemistry, Osney Mead, Oxford; Malden, MA, Blackwell Science. Chapter 10, Section 3.4.8. URL: http://old.iupac.org/publications/analytical_compendium/Cha10sec348.pdf
- Jahoda F C (1957), 'Fundamental absorption of barium oxide from its reflectivity spectrum', *Phys. Rev.* **107**, 1261–1265.
- James R W (1962), *The Optical Principles of the Diffraction of X-rays*, G. Bell and Sons Ltd, London.

- Jark W, Rigon L, Oliver K (2011), 'Simultaneous determination of the X-ray refractive index and the attenuation length from a single digitally registered radiograph of rectangular prisms', *Opt. Comm.* **284**, 4525–4528.
- Joensen K D, Christensen F E, Schnopper H W, Gorenstein P, Susini J, Høghøj P, Hustache R, Wood J, Parker K (1992), 'Medium-sized grazing incidence high-energy X-ray telescopes employing continuously graded multilayers', *Proc. SPIE* **1736**, 239–248.
- Johnson P D, Smith N V (1983), 'Production of circularly polarized light from synchrotron radiation in the vacuum ultraviolet region', *Nucl. Instr. Meth.* **214**, 505–508.
- Joyeux D, Polack F, Phalippou D (1999), 'An interferometric determination of the refractive part of optical constants for carbon and silver across soft x-ray absorption edges', *Rev. Sci. Instrum.* **70**, 2921–2926.
- Keski-Kuha R A M, Osantowski J F, Herzig H, Gum J S, Toft A R (1988), 'Normal incidence reflectance of ion beam deposited SiC films in the EUV', *Appl. Opt.* **27**, 2815–2816.
- Kim J, Zukic M, Torr D G, Wilson M W (1992), 'Multilayer thin film design as far ultraviolet quarterwave retarders', *Proc. SPIE* **1742**, 403–412.
- Kimura H, Hirono T, Tamenori Y, Saitoh Y, Salashchenko N N, Ishikawa T (2005), 'Transmission type Sc/Cr multilayer as a quarter-wave plate for near 400 eV', *J. Electron Spectrosc. Relat. Phenom.* **144–147**, 1079–1081.
- King F W (1979), 'Dispersion relations and sum rules for the normal reflectance of conductors and insulators', *J. Chem. Phys.* **71**, 4726–4733.
- Kissel L, Pratt R H (1990), 'Corrections to tabulated anomalous-scattering factors', *Acta Crystallogr., Sect. A: Cryst. Phys., Diff., Theor. Gen. Crystallogr.* **46**, 170–175. A fit to the data of Kissel and Pratt was made by Henke *et al.* (1993).
- Kittel C (2005), *Introduction to Solid State Physics*, 8th ed. John Wiley & Sons, New York.
- Kjornrattanawanich B, Bajt S, Seely J F (2004), 'Mo/B4C/Si multilayer-coated photodiode with polarization sensitivity at an extreme-ultraviolet wavelength of 13.5 nm', *Appl. Opt.* **43**, 1082–1090.
- Kjornrattanawanich B, Windt D L, Seely J F, Uspenskii Yu A (2006), 'SiC/Tb and Si/Tb multilayer coatings for extreme ultraviolet solar imaging', *Appl. Opt.* **45**, 1765–1772.
- Kjornrattanawanich B, Windt D L, Seely J F (2008), 'Normal incidence silicon-gadolinium multilayers for imaging at 63 nm wavelength', *Opt. Lett.* **33**, 965–967.
- Kjornrattanawanich B, Windt D L, Seely J F (2010), 'Optical constants determination of samarium, holmium, and erbium in the 1.5–850 eV spectral range using a transmittance method', *Appl. Opt.* **49**, 6006–6013.
- Kortright J B (1993), 'Polarization properties of multilayers in the EUV and soft X-ray', *Proc. SPIE* **2010**, 160–167.
- Kortright J B, Underwood J H (1990), 'Multilayer optical elements for generation and analysis of circularly polarized x-rays', *Nucl. Instr. Meth. A* **291**, 272–277.
- Kortright J B, Kimura H, Nikitin V, Mayama K, Yamamoto M, Yanagihara M (1992), 'Soft x-ray (97-eV) phase retardation using transmission multilayers', *Appl. Phys. Lett.* **60**, 2963–2965.
- Kortright J B, Rice M, Franck K D (1995), 'Tunable multilayer EUV/soft x-ray polarimeter', *Rev. Sci. Instrum.* **66**, 1567–1569.

- Kozhevnikov I V, Bukreeva I N, Ziegler E (2001), 'Design of X-ray supermirrors', *Nucl. Instr. Meth. A* **460**, 424–443.
- Kretschmann E, Kröger E (1975), 'Reflection and transmission of light by a rough surface, including results for surface plasmon effects', *J. Opt. Soc. Am.* **65**, 150–154.
- Lang J C, Srayer G (1995), 'Bragg transmission phase plates for the production of circularly polarized x rays', *Rev. Sci. Instrum.* **66**, 1540–1542.
- Larraquert J I (2001a), 'Reflectance enhancement with sub-quarterwave multilayers of highly absorbing materials', *J. Opt. Soc. Am. A* **18**, 1406–1414.
- Larraquert J I (2001b), 'General theory of sub-quarterwave multilayers with highly absorbing materials', *J. Opt. Soc. Am. A* **18**, 2617–2627.
- Larraquert J I (2002a), 'Reflectance enhancement in the extreme ultraviolet and soft X-rays by means of multilayers with more than two materials', *J. Opt. Soc. Am. A* **19**, 391–397.
- Larraquert J I (2002b), 'New layer-by-layer multilayer design method', *J. Opt. Soc. Am. A* **19**, 385–390.
- Larraquert J I (2004), 'Layer-by-layer design method for multilayers with barrier layers: application to Si/Mo multilayers for EUV lithography', *J. Opt. Soc. Am. A* **21**, 1750–1760.
- Larraquert J I, Méndez J A, Aznárez J A (1995), 'Far UV reflectance measurements and optical constants of unoxidized aluminum films', *Appl. Opt.* **34**, 4892–4899.
- Larraquert J I, Keski-Kuha R A M (1999), 'Multilayer coatings with high reflectance in the EUV spectral region from 50 to 121.6 nm', *Appl. Opt.* **38**, 1231–1236.
- Larraquert J I, Keski-Kuha R A M (2001), 'Multilayer coatings for narrow-band imaging in the extreme ultraviolet', *Appl. Opt.* **40**, 1126–1131.
- Larraquert J I, Keski-Kuha R A M (2002), 'Sub-quarter-wave multilayer coatings with high reflectance in the extreme ultraviolet', *Appl. Opt.* **41**, 5398–5404.
- Larraquert J I, Pérez-Marín A P, García-Cortés S, Rodríguez-de Marcos L, Aznárez J A, Méndez J A (2011a), 'Selfconsistent optical constants of SiC thin films', *J. Opt. Soc. Am. A* **28**, 2340–2345.
- Larraquert J I, Vidal-Dasilva M, García-Cortés S, Rodríguez-de Marcos L, Fernández-Perea M, Aznárez J A, Méndez J A (2011b), 'Multilayer coatings for the far and extreme ultraviolet', *Proc. SPIE* **8076**, 80760D.
- Larraquert J I, Aznárez J A, Rodríguez-de Marcos L, Méndez J A, Malvezzi A M, Giglia A, Miotti P, Frassetto F, Massone G, Nannarone S, Crescenzi G, Capobianco G, Fineschi S (2013), 'Multilayer reflective polarizers for the far ultraviolet', *Proc. SPIE* **8777**, 87771D.
- Laufer A H, Pirog J A, Mcnesby J R (1965), 'Effect of temperature on the vacuum ultraviolet transmittance of lithium fluoride, calcium fluoride, barium fluoride, and sapphire', *J. Opt. Soc. Am.* **55**, 64–66.
- La Villa R, private communication to W. R. Hunter in Hunter, 1964b.
- La Villa R, Mendlowitz H (1962), 'Optical constants of aluminum in vacuum ultraviolet', *Phys. Rev. Lett.* **9**, 149–150.
- Le Guen K, Hu M -H, André J -M, Jonnard P, Zhou S K, Li H C, Zhu J T, Wang Z S, Mahne N, Giglia A, Nannarone S (2011), 'Introduction of Zr in nanometric periodic Mg/Co multilayers', *Appl Phys A* **102**, 69–77.
- Li H H (1980), 'Refractive index of alkaline earth halides and its wavelength and temperature derivatives', *J. Phys. Chem. Ref. Data* **9**, 161–289.

- MacDonald M A, Schaefers F, Pohl R, Poole I B, Gaupp A, Quinn F M (2008), 'A W:B4C multilayer phase retarder for broadband polarization analysis of soft x-ray radiation', *Rev. Sci. Instrum.* **79**, 025108.
- Madden R P, Canfield L R, Hass G (1963), 'On the vacuum-ultraviolet reflectance of evaporated aluminum before and during oxidation', *J. Opt. Soc. Am.* **53**, 620–625.
- Maehara T, Kimura H, Nomura H, Yanagihara M, Namioka T (1991), 'Performance of a wideband soft x-ray polarizer', *Appl. Opt.* **30**, 5018–5020.
- Malgrange C, Varga L, Giles C, Rogalev A, Goulon J (1999), 'Phase plates for x-ray optics', *Proc. SPIE* **3773**, 326–339.
- Malherbe A (1974a), 'Interference filters for the far ultraviolet', *Appl. Opt.* **13**, 1275–1276.
- Malherbe A (1974b), 'Multidielectric components for the far ultraviolet', *Appl. Opt.* **13**, 1276.
- Malherbe A, Guillard M (1970), 'Réalisation industrielle de filtres interférentiels pour l'ultra-violet lointain', *Nouv. Rev. Opt. Appl.* **1**, 401–404.
- Marx B, Uschmann I, Höfer S, Lötzsch R, Wehrhan O, Förster E, Kaluza M, Stöhlker T Gies H, Detlefs C, Roth T, Härtwig J, Paulus G G (2011), 'Determination of high-purity polarization state of X-rays', *Opt. Commun.* **284**, 915–918.
- Materlik G, Sparks C J, and Fischer K (1994), 'Resonant anomalous x-ray scattering: theory and applications', North-Holland, Amsterdam, 389–420. URL: <http://cars9.uchicago.edu/dafs/>
- Maury H, Bridou F, Troussel Ph, Meltchakov E, Delmotte F (2010), 'Design and fabrication of supermirrors for (2–10 keV) high resolution X-ray plasmas diagnostic imaging', *Nucl. Instr. Meth. A* **621**, 242–246.
- Meltchakov E, Hecquet C, Roulliay M, De Rossi S, Menesguen Y, Jérôme A, Bridou F, Varniere F, Ravet-Krill M-F, Delmotte F (2010), 'Development of Al-based multilayer optics for EUV', *Appl. Phys. A* **98**, 111–117.
- Mertins H-C, Schäfers F, Grimmer H, Clemens D, Böni P, Horisberger M (1998), 'W/C, W/Ti, Ni/Ti, and Ni/V multilayers for the soft-x-ray range: experimental investigation with synchrotron radiation', *Appl. Opt.* **37**, 1873–1882.
- Metcalf H, Baird J C (1966), 'Circular polarization of vacuum ultraviolet light by piezobirefringence', *Appl. Opt.* **5**, 1407–1410.
- Mezei F (1976), 'Novel polarized neutron devices: supermirror and spin component amplifier', *Commun. Phys.* **1**, 81–85.
- Monaco G, Garoli D, Frison R, Mattarello V, Nicolosi P, Pelizzo M G, Rigato V, Armelao L, Giglia A, Nannarone S (2006), 'Optical constants in the EUV Soft x-ray (5 ÷ 152 nm) spectral range of B4C thin films deposited by different deposition techniques', *Proc. SPIE* **6317**, 631712.
- Morawe C, Ziegler E, Peffen J-C, Kozhevnikov I V (2002), 'Design and fabrication of depth-graded X-ray multilayers', *Nucl. Instr. Meth. A* **493**, 189–198.
- Naik S R, Lodha G S (2006), 'The effect of misalignment errors in optical elements of VUV polarimeter', *Nucl. Instr. Meth. A* **560**, 211–218.
- Nevot L, Croce P (1980), 'Caractérisation des surfaces par réflexion rasante de rayons X. Application à l'étude du polissage de quelques verres silicates', *Rev. Phys. Appl.* **15**, 761–779.
- Newville M (2004), 'Fundamentals of XAFS', Consortium for Advanced Radiation Sources, University of Chicago, Chicago, IL.

- NIST-FFAST web. URL: <http://physics.nist.gov/PhysRefData/FFast/html/form.html>
- Nomura H, Mayama K, Sasaki T, Yamamoto M, Yanagihara M (1992), 'Design, fabrication, and polarization of soft-x-ray transmission multilayers', *Proc. SPIE* **1720**, 395–401.
- Ogasaka Y, Iwahara T, Miyazawa T, Fukaya Y, Sasaki N, Tamura K, Kanou Y, Kunieda H, Yamashita K (2007), 'Characterization of Pt/C multilayer at 200 keV soft gamma-ray', *Proc. SPIE* **6688**, 66880S.
- Palik E D (1998a), *Handbook of Optical Constants of Solids*, Academic Press, San Diego.
- Palik E D (1998b), *Handbook of Optical Constants of Solids II*, Academic Press, San Diego.
- Palik E D (1998c), *Handbook of Optical Constants of Solids III*, Academic Press, San Diego.
- Park J H, Zukic M, Wilson M, Keffer C E, Torr D G, Hoover R B (1996), 'Design and fabrication of multilayer reflective filters for a Ritchey-Chretien Lyman- α telescope', *Opt. Eng.* **35**, 1479–1482.
- Parratt L G (1954), 'Surface studies of solids by total reflection of X-rays', *Phys. Rev.* **95**, 359–369.
- Pepper S V (1970), 'Optical Analysis of Photoemission', *J. Opt. Soc. Am.* **60**, 805–812.
- Pflüger J, Fink J (1998), 'Determination of optical constants by high-energy, electron-energy-loss spectroscopy (EELS)', in *Handbook of Optical Constants of Solids II*, E. D. Palik, ed., Academic Press, San Diego.
- Philipp H R, Ehrenreich H (1963), 'Optical properties of semiconductors', *Phys. Rev.* **129**, 1550–1560.
- Powell F R, Lindblom J F, Powell S F, Vedder P W (1990), 'Thin film filter performance for extreme ultraviolet and x-ray applications', *Opt. Eng.* **29**, 614–624.
- Powell F R, Drake V A, Sandel B R, Mitchell D G (1994), 'The selection of materials for soft x-ray (SXR) and extreme ultraviolet (EUV) filters for space astronomy and other applications', *Proc. SPIE* **2209**, 480–490.
- Quijada M, Rice S, Mentzell E (2012), 'Enhanced MgF₂ and LiF over-coated Al mirrors for FUV space astronomy', *Proc. SPIE* **84502**, 84502H.
- Rabinovitch K, Canfield L R, Madden R P (1965), 'A method for measuring polarization in the vacuum ultraviolet', *Appl. Opt.* **4**, 1005–1010.
- Ravel B (2005), 'A practical introduction to multiple scattering theory', *J. Alloys Comp.* **401**, 118–126.
- Rehr J J, Albers R C (2000), 'Theoretical approaches to x-ray absorption fine structure', *Rev. Mod. Phys.* **72**, 621–654.
- Rehr J J, Ankudinov A L (2004), 'Solid state effects on X-ray absorption, emission and scattering processes', *Radiat. Phys. Chem.* **70**, 453–463.
- Rosenbaum G, Feuerbacher B, Godwin R P, Skibowski M (1968), 'Measurement of the polarization of extreme ultraviolet synchrotron radiation with a reflecting polarimeter', *Appl. Opt.* **7**, 1917–1919.
- Rustgi Om P (1965), 'Transmittance of thin metallic films in the vacuum-ultraviolet region below 1000 Å', *J. Opt. Soc. Am.* **55**, 630–634.
- Sae-Lao B, Montcalm C (2001), 'Molybdenum-strontium multilayer mirrors for the 8–12-nm extreme-ultraviolet wavelength region', *Opt. Lett.* **26**, 468–470.
- Saito T, Ejiri A, Onuki H (1990), 'Polarization properties of an evaporated aluminum mirror in the VUV region', *Appl. Opt.* **29**, 4538–4540.

- Samson J A R (1967a), 'Filter and window materials', Chapter 6 of *Techniques of Vacuum Ultraviolet Spectroscopy*. John Wiley and Sons Inc., New York.
- Samson J A R (1967b), *Techniques of Vacuum Ultraviolet Spectroscopy*, John Wiley and Sons Inc., New York.
- Samson J A R (1967c), 'Polarization', Chapter 9 of *Techniques of Vacuum Ultraviolet Spectroscopy*. John Wiley and Sons Inc., New York.
- Samson J A, Ederer D L (2000), *Vacuum Ultraviolet Spectroscopy I*, Academic Press, San Diego, CA.
- Schäfers F (2007), 'Multilayer-based soft x-ray polarimetry', *Opt. Prec. Eng.* **15**, 1850–1861.
- Schäfers F, Mertins H-C, Gaupp A, Gudat W, Mertin M, Packe I, Schmolla F, Di Fonzo S, Soullié G, Jark W, Walker R, Le Cann X, Nyholm R, Eriksson M (1999), 'Soft-x-ray polarimeter with multilayer optics: complete analysis of the polarization state of light', *Appl. Opt.* **38**, 4074–4088.
- Schoonjans T, Brunetti A, Golosio B, Sanchez del Rio M, Solé V A, Ferrero C, Vincze L (2011), 'The xraylib library for X-ray–matter interactions. Recent developments', *Spectrochim. Acta B* **66**, 776–784. Web of Biomolecular Structure Center at the University of Washington School of Medicine. URL: <http://ftp.esrf.eu/pub/scisoft/xraylib/readme.html>
- Scofield J H (1973), 'Theoretical photoionization cross sections from 1 to 1500 keV', Lawrence Livermore Laboratory, Report UCRL-51326.
- Scott M L (1998), 'Measurement of n and k in the XUV by the Angle-of-Incidence, Total-External-Reflectance Method', in *Handbook of Optical Constants of Solids II*, E. D. Palik, ed., Academic Press, San Diego.
- Shiles E, Sasaki T, Inokuti M, Smith D Y (1980), 'Self-consistency and sum-rule tests in the Kramers-Kronig analysis of optical data: applications to aluminium', *Phys. Rev. B* **22**, 1612–1628.
- Sinha S K, Sirota E B, Garoff S, Stanley H B (1988), 'X-ray and neutron scattering from rough surfaces', *Phys. Rev. B* **38**, 2297–2311.
- Smith N V, Howells M R (1994), 'Whispering galleries for the production of circularly polarized synchrotron radiation in the XUV region', *Nucl. Instr. Meth. A* **347**, 115–118.
- Soufli R, Gullikson E M (1997), 'Reflectance measurements on clean surfaces for the determination of optical constants of silicon in the extreme ultraviolet–soft-x-ray region', *Appl. Opt.* **36**, 5499–5507.
- Soufli R, Gullikson E M (1998), 'Absolute photoabsorption measurements of molybdenum in the range 60–930 eV for optical constant determination', *Appl. Opt.* **37**, 1713–1719.
- Soufli R, Bajt S, Gullikson E M (1999), 'Optical constants of beryllium from photoabsorption measurements for x-ray optics applications', *Proc. SPIE* **3767**, 251–258.
- Soufli R, Bajt S (2009), 'Multilayer Coatings for EUVL', in *EUV Lithography*, Vivek Bakshi, ed., SPIE, Bellingham and John Wiley & Sons, Inc., Hoboken.
- Soufli R, Fernández-Perea M, Baker S L, Robinson J C, Alameda J, Walton C C (2012), 'Spontaneously intermixed Al-Mg barriers enable corrosion-resistant Mg/SiC multilayer coatings', *Appl. Phys. Lett.* **101**, 043111.
- Spiller E (1972a), 'Low-loss reflection coatings using absorbing materials', *Appl. Phys. Lett.* **20**, 365–367.

- Spiller E (1972b), 'Multilayer interference coatings for the vacuum ultraviolet', *Space Optics, Proc. ICO—IX Santa Monica, 1972*, 581–597.
- Spiller E (1994), *Soft X-ray Optics*, SPIE Optical Engineering Press, Bellingham, Washington.
- Srivastava K (1982), 'Plasmon approach to the band gap of alkali halides', *Phys. Stat. Sol. (b)* **114**, issue 2, 667–671. DOI: 10.1002/pssb.2221140245. Copyright © 1982 WILEY-VCH Verlag GmbH & Co. KGaA (Issue, DOI, and copyright notice required by journal).
- Stanglmeier F, Lengeler B, Weber W, Göbel H, Schuster M (1992), 'Determination of the dispersive correction f'(E) to the atomic form factor from X-ray reflection', *Acta Cryst. A* **48**, 626–639.
- Stearns D G (1989), 'The scattering of x rays from nonideal multilayer structures', *J. Appl. Phys.* **65**, 491–506.
- Stearns D G (1992), 'X-ray scattering from interfacial roughness in multilayer structures', *J. Appl. Phys.* **71**, 4286–4298.
- Stenzel O (2005), 'The physics of thin film optical spectra', *Springer Series in Surface Sciences, Volume 44*, Springer-Verlag, Berlin.
- Stern F (1963), 'Elementary theory of the optical properties of solids', in *Solid State Physic. Advances in Research and Applications, Volume 15*, F. Seitz, D. Turnbull, eds., Academic Press, New York.
- Svatos J, Joyeux D, Phalippou D, Polack F (1993), 'Soft-x-ray interferometer for measuring the refractive index of materials', *Opt. Lett.* **18**, 1367–1369.
- Tan M Y, Zhu J T, Wang H C, Wang Z S, Chen R, Watanabe M (2009), 'Design of transmission multilayer polarizer for soft X-ray using a merit function', *Opt. Exp.* **17**, 2586–2599.
- Tan M Y, Zhu J T, Chen L Y, Wang Z S, Le Guen K, Jonnard P, Giglia A, Mahne N, Nannarone S (2011), 'Molybdenum–silicon aperiodic multilayer broadband polarizer for 13–30 nm wavelength range', *Nucl. Instr. Meth. A* **654**, 588–591.
- Thielsch R (2003), 'Optical coatings for the DUV/VUV', in *Optical Interference Coatings*, N. Kaiser, H. K. Pulker, eds., Springer Series in Optical Sciences (Springer-Verlag,), 255–279.
- Uspenski Y, Seely J, Popov N, Artioukov I, Vinogradov A, Windt D, Kjornrattanawanich B (2005), 'Extreme uv optical constants of rare-earth metals free from effects of air contamination', *Proc. SPIE* **5919**, 59190S.
- UWXAFS project; it involves the development and distribution of high quality analysis software for XAFS. URL: <http://depts.washington.edu/uwxafs/>
- Venkataraman CT, Lang J C, Nelson C S, Srager G, Haeffner D R, Shastri S D (1998), 'A high energy phase retarder for the simultaneous production of right- and left-handed circularly polarized x rays', *Rev. Sci. Instrum.* **69**, 1970–1973.
- Vidal-Dasilva M, Fernández-Perea M, Méndez J A, Aznárez J A, Larruquet J I (2009), 'Narrowband multilayer coatings for the extreme ultraviolet range of 50–92 nm', *Opt. Exp.* **17**, 22773–22784.
- Vinogradov A V, Zeldovich B Ya (1977), 'X-ray and far UV multilayer mirrors: principles and possibilities', *Appl. Opt.* **16**, 89–93.
- von Ballmoos P (2005), 'Instruments for Nuclear Astrophysics', in *High-Energy Spectroscopy Astrophysics*, S. M. Kahn, P. von Ballmoos, R. A. Sunyaev, Saas-Fee Advanced Courses, vol. **30**, 82–197, published by Springer, Berlin.
- Walker W C (1964), 'Pile-of-plates polarizer for the vacuum ultraviolet', *Appl. Opt.* **3**, 1457–1459.

- Waller I (1923), 'Zur Frage der Einwirkung der Wärmebewegung auf die Interferenz von Röntgenstrahlen', *Z. Phys.* **17**, 398–408.
- Wang Z, Wang H, Zhu J, Xu Y, Zhang S, Li C, Wang F, Zhang Z, Wu Y, Cheng X, Chen L, Michette A G, Pfauntsch S J, Powell A K, Schäfers F, Gaupp A, MacDonald M (2006a), 'Extreme ultraviolet broadband Mo/Y multilayer analyzers', *Appl. Phys. Lett.* **89**, 241120.
- Wang Z, Wang H, Zhu J, Wang F, Gu Z, Chen L, Michette A G, Powell A K, Pfauntsch S J, Schäfers F (2006b), 'Broadband multilayer polarizers for the extreme ultraviolet', *J. Appl. Phys.* **99**, 056108.
- Wang Z S, Wang H C, Zhu J T, Wang F L, Gu Z X, Chen L Y, Michette A G, Powell A K, Pfauntsch S J, Schäfers F (2006c), 'Broad angular multilayer analyzer for soft X-rays', *Opt. Exp.* **14**, 2533–2538.
- Wang Z, Wang H, Zhu J, Zhang Z, Xu Y, Zhang S, Wu W, Wang F, Wang B, Liu L, Chen L, Michette A G, Pfauntsch S J, Powell A K, Schäfers F, Gaupp A, MacDonald M (2007a), 'Broadband Mo/Si multilayer transmission phase retarders for the extreme ultraviolet', *Appl. Phys. Lett.* **90**, 031901.
- Wang Z, Wang H, Zhu J, Zhang Z, Wang F, Xu Y, Zhang S, Wu W, Chen L, Michette A G, Pfauntsch S J, Powell A K, Schäfers F, Gaupp A, Cui M, Sun L, MacDonald M (2007b), 'Complete polarization analysis of extreme ultraviolet radiation with a broadband phase retarder and analyzer', *Appl. Phys. Lett.* **90**, 081910.
- Wang H, Dhesi S S, Maccherozzi F, Sawhney K J S (2012), 'Complete polarization analysis of high energy soft x-rays by combining a multilayer phase retarder with crystal analyzer', *J. Appl. Phys.* **111**, 123117.
- Watanabe M, Hatano T, Saito K, Hu W, Ejima T, Tsuru T, Takahashi M, Kimura H, Hirono T, Wang Z, Cui M, Yamamoto M, Yanagihara M (2008), 'Multilayer polarization elements and their applications to polarimetric studies in vacuum ultraviolet and soft X-ray regions', *Nucl. Sci. Tech.* **19**, 193–203.
- Warburton W K, Ludwig Jr. K F (1986), 'Absorption effects in the deter-impanation of anomalous scattering factors using x-ray refraction through a prism', *Phys. Rev. B* **33**, 8424–8432.
- Weaver J H, Kafka C, Lynch D W, Koch E E (1981), 'Optical properties of metals', Physik Daten collection, vols. **18-1** and **18-2**, Fachinformationszentrum Energie-Physik-Mathematik, GmbH, Karlsruhe, Germany.
- Westerveld W B, Becker K, Zetner P W, Corr J J, McConkey J W (1985), 'Production and measurement of circular polarization in the VUV', *Appl. Opt.* **24**, 2256–2262.
- Williams M W, MacRae R A, Arakawa E T (1967), 'Optical properties of magnesium fluoride in the vacuum ultraviolet', *J. Appl. Phys.* **38**, 1701–1705.
- Windt D L (1998), 'IMD—Software for modeling the optical properties of multi-layer films', *Comp. Phys.* **12**, 360–370.
- Windt D L, Cash, Jr. W C, Scott M, Arendt P, Newnam B, Fisher R F, Swartzlander A B (1988), 'Optical constants for thin films of Ti, Zr, Nb, Mo, Ru, Rh, Pd, Ag, Hf, Ta, W, Re, Ir, Os, Pt, and Au from 24 Å to 1216 Å', *Appl. Opt.* **27**, 246–278.
- Windt D L, Donguy S, Hailey C J, Koglin J, Honkimaki V, Ziegler E, Christensen F E, Chen H, Harrison F A, Craig W W (2003), 'W/SiC x-ray multilayers optimized for use above 100 keV', *Appl. Opt.* **42**, 2415–2421.
- Windt D L, Donguy S, Seely J F, Kjornrattanawanich B, Gullikson E M, Walton C C, Golub L, DeLuca E (2004), 'EUV multilayers for solar physics', *Proc. SPIE* **5168**, 1–11.

- Windt D L, Donguy S, Hailey C J, Koglin J, Honkimaki V, Ziegler E, Christensen F E, Harrison F A (2004), ‘Optical constants for hard x-ray multilayers over the energy range $E = 35 - 180$ keV’, *Proc. SPIE* **5168**, 35–40.
- Windt D L, Seely J F, Kjornrattanawanich B, Uspenskii Yu A (2005), ‘Terbium-based extreme ultraviolet multilayers’, *Opt. Lett.* **30**, 3186–3188.
- Wood R W (1933), ‘Remarkable optical properties of the álcali metals’, *Phys. Rev.* **14**, 353–360.
- Wood II O R, Craighead H G, Sweeney J E, Maloney P J (1984), ‘Vacuum ultraviolet loss in magnesium fluoride films’, *Appl. Opt.* **23**, 3644–3649.
- Wu W-J, Wang Z-S, Zhu J-T, Zhang Z, Wang F-L, Chen L-Y, Zhou H-J, Huo T-L (2011), ‘Spectral Resolution Improvement of Mo/Si Multilayers’, *Chin. Opt. Lett.* **28**, 086801.
- XCOM-FFAST comparison web. URL: <http://physics.nist.gov/PhysRefData/XrayNoteB.html>
- Yamamoto M, Namioka T (1992), ‘Layer-by-layer design method for soft-x-ray multilayers’, *Appl. Opt.* **31**, 1622–1630.
- Yamamoto M (1993), ‘Polarimetry with use of soft x-ray multilayers’, *Proc. SPIE* **2010**, 152–159.
- Yamashita K, Akiyama K, Haga K, Kunieda H, Lodha G S, Nakajo N, Nakamura N, Okajima T, Tamura K, Tawara Y (1998), ‘Fabrication and characterization of multilayer supermirrors for hard X-ray optics’, *J. Synchrotron Rad.* **5**, 711–713.
- Yanagihara M, Maehara T, Nomura H, Yamamoto M, Namioka T (1992), ‘Performance of a wideband multilayer polarizer for soft x rays’, *Rev. Sci. Instrum.* **63**, 1516–1518.
- Yang M, Cobet C, Esser N (2007), ‘Tunable thin film polarizer for the vacuum ultraviolet and soft x-ray spectral regions’, *J. Appl. Phys.* **101**, 053114.
- Yulin S (2003), ‘Multilayer coatings for EUV/soft X-ray mirrors’, in *Optical Interference Coatings*, N. Kaiser, H. K. Pulker, eds., Springer Series in Optical Sciences (Springer-Verlag), 281–308.
- Yulin S, Benoit N, Feigl T, Kaiser N, Fang M, Chandhok M (2008), ‘Mo/Si multilayers with enhanced TiO₂- and RuO₂-capping layers’, *Proc. SPIE* **6921**, 692118.
- Zhu J, Wang Z, Zhang Z, Wang F, Wang H, Wu W, Zhang S, Xu D, Chen L, Zhou H, Huo T, Cui M, Zhao Y (2008), ‘High Reflectivity Multilayer for He-II Radiation at 30.4nm’, *Appl. Opt.* **47**, C310–C314.
- Zukic M, Torr D G (1992), ‘Multiple reflectors as narrow-band and broadband vacuum ultraviolet filters’, *Appl. Opt.* **31**, 1588–1596.

Controlling thermal radiation from surfaces

C. G. RIBBING, Uppsala University, Sweden

DOI: 10.1533/9780857097316.2.357

Abstract: Some possibilities for controlling the temperature or the thermal emission from an object are explained and discussed. Following a summary of the basic physical laws, five cases are discussed and references to more detailed reviews are given. These cases are solar selective coatings for thermal collectors and energy saving window coatings, coatings for radiative cooling as well as for prevention of frost formation and suppression of thermal signature.

Key words: optical materials, thermal radiation, blackbody, Planck function, optical selectivity, emissivity, spectral properties.

8.1 Introduction

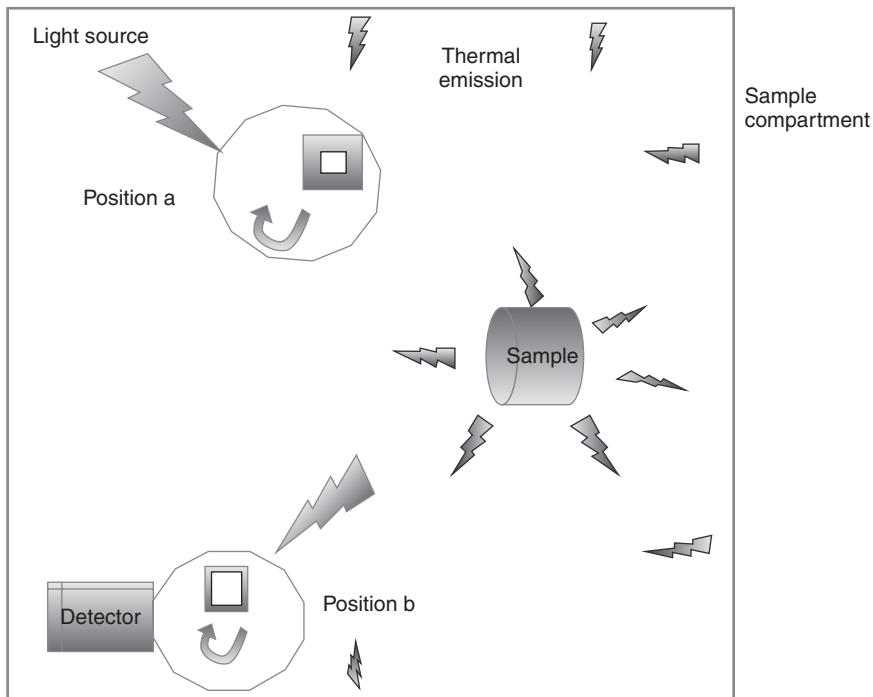
This chapter discusses why and how the heat radiation from solid surfaces can be controlled. Like the other chapters in this book, it is mainly application oriented. However, the first section will present some basic equations that are required for the ensuing description of applications.

The applications will include cases in which either the temperature of the solid, or the thermal radiation emitted by the solid, is to be controlled. In the most general perspective, the purpose may be to radiatively heat an object, to avoid heating it, to avoid cooling it, to cool it, or to reduce the infrared radiation from the object.

Initially, an elementary comment about measuring the heat radiation upon or from a body. The ‘spectrophotometer version’ of the law of energy conservation for an impinging light beam is:

$$R + A + T = 1 \quad [8.1]$$

that is, a sum of fractions of light intensity. Light is either reflected, R , absorbed, A or transmitted, T . This sum is equal to unity. However, when properties in the infrared are studied, care must be taken when measurements are made. If the thermal emission from the sample is registered by



8.1 Sketch illustrating the importance of correct light chopping in a spectrophotometer. The chopper positions a and b are critically different – see text.

the spectrophotometer, *as if it were reflected or transmitted*, errors are introduced. There is a well-known solution to this problem. The instrument light beam should be chopped in the right place such that only true signals, phase locked to the frequency are amplified and registered. The sketch in Fig. 8.1 illustrates the problem and the standard solution.

If the light chopper is placed directly in front of the light source, that is, position a, then the light from the light source will be modulated and amplified by the phase-locked detection system. In position b, the thermal emission from the sample and the surrounding compartment *will also be chopped* and therefore amplified to a signal violating Equation [8.1]. Modern IR spectrophotometers are type a, but there are cases of early publications of IR reflectance spectra that suffer from an error of type b. It should be noted that also in modern instruments, small contributions by thermal emission from the chopper to the surroundings may be registered.

Section 8.2 will present some formalism for thermal emission. The upper limit is that of a *blackbody*, which is the thermodynamic limiting case.

The actual thermal emission from a solid is modified by the emissivity function, $\varepsilon(\lambda, T) \leq 1$. The emissivity as a function of wavelength and temperature will be the subject of Section 8.3 which briefly surveys the formalism and measurement methods for spectral emissivity. In some of the literature on thermal properties and processes, the emissivity is treated as a constant, that is, the material is assumed to be *gray*. In this chapter the ambition is to go beyond that. The fact that emissivity may exhibit variation with wavelength opens possibilities for applications based on spectral selectivity. This will be discussed in Section 8.4.

Section 8.4 describes four different applications of thermal control coatings or surfaces. The first two: thermal solar collectors and, even more so, low-emissivity coatings for energy-conserving windows have been on the market for a long time. Different techniques for large scale manufacturing have been developed and there is an extensive literature discussing these two areas. For this reason the description and discussion will be limited. It is hoped the references given will compensate for the omissions.

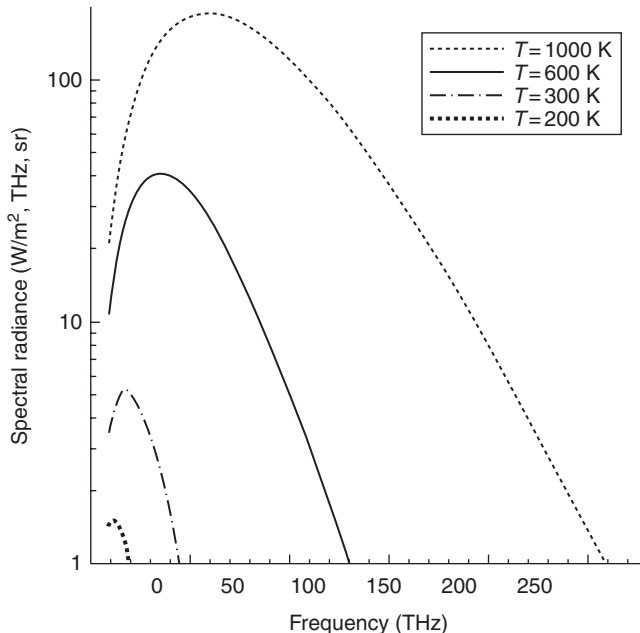
The final three cases are coatings used to increase or prevent radiative cooling. In terms of optical performance the requirements are related. However, they involve different materials being used, which will lead to quite different solutions. None of these potential applications is presently exploited in large scale applications – or at least they are not generally known to be. The scientific literature is not as extensive as for the two first cases. The principles will be explained and some lab scale results will be quoted.

8.2 Blackbody radiation

Blackbody radiation is the upper limit on the thermal emission intensity from a solid surface (Wolfe, 1989; Zalewski, 1995). It is based upon Planck's Law for oscillators, which in turn is derived by using the Bose-Einstein distribution for vibrations in a box (a 'holeraum') of macroscopic dimension. The spectral radiance emitted from a small hole in this 'box' in one unit of space angle is:

$$L_{bb}(v, T) = \frac{2h}{nc^2} \frac{v^3}{\exp(hv/kT) - 1} \quad [8.2]$$

where v is the frequency, c the vacuum velocity for light, h is the Planck constant, k the Boltzmann constant and T the absolute temperature. In most cases the refractive index of the medium, $n = 1$. The SI-dimension of spectral radiance is $\text{W/m}^2\text{Hz,sr}$. The radiance from a blackbody is Lambertian, so the total emission into the half-sphere is given by multiplication with 2π .



8.2 The spectral radiance from a blackbody as a function of frequency in THz at the four temperatures indicated. Notice that the diagram is lin-log.

In Fig. 8.2 we plot this spectral radiance for a few temperatures chosen to show the characteristic behaviour in the infrared where the unit W/m², THz, sr is appropriate.

We notice that the curves never intersect, that is, a curve for a higher temperature, is always above one for a lower temperature. In Fig. 8.2, *frequency* is the independent variable, which is directly linked to the Planck theory. In optics the corresponding expression as function of wavelength is often used. The coordinate transformation, $\lambda = c/v$, is nonlinear which has consequences for the Planck function. The wavelength version is

$$L_{bb}(\lambda, T) = \frac{2hc^2}{n^2\lambda^5} \frac{1}{\exp(hc/kT\lambda) - 1} \quad [8.3]$$

with dimension W/m³, sr. In Fig 8.3 radiance as a function of wavelength for the same temperatures are plotted per μm wavelength as the relevant unit in the infrared.

In this case we also use the diagram to illustrate the well-known Wien's displacement law. The thick dash-dotted curve joins the maxima, λ_m , of the spectral curves. It is given by the expression:

$$\lambda_m = \frac{b_\lambda}{T} \quad [8.4]$$

where the constant $b_\lambda = 2.8978 \times 10^{-3}$ mK.

It shows that the maxima of the blackbody curves move to shorter wavelength when the temperature increases. The corresponding expression for the frequency version of Equation [8.2] is

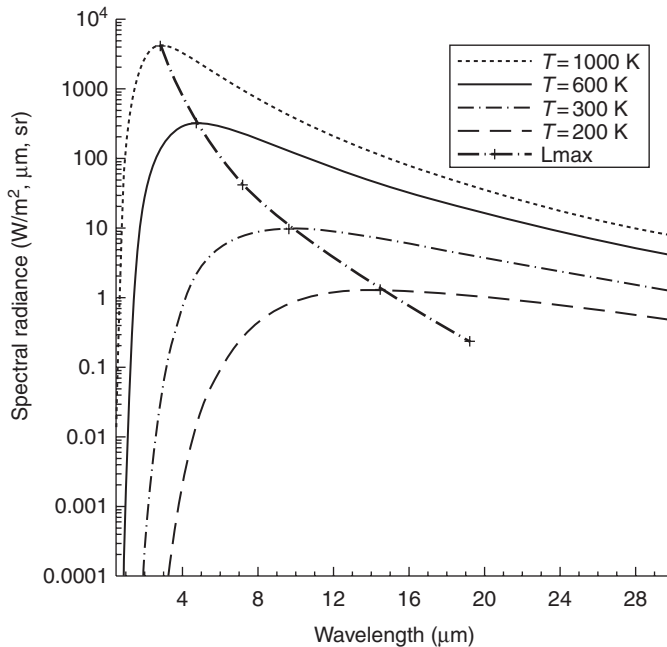
$$\nu_m = b_\nu T \quad [8.5]$$

with the constant $b_\nu = 5.8786 \cdot 10^{10}$ (sK) $^{-1}$

As expected, the maxima move to higher frequencies when the temperature increases. A comparison of Figs 8.2 and 8.3, reveals, however, that *the positions of the maxima are not conserved in the coordinate transformation*. The maximum of the 1000 K curve in Fig. 8.3 is ≈ 2.9 μm . If this wavelength is converted to frequency $\nu = c/\lambda$, we get 103 THz. Looking at Fig. 8.2 the maximum position of the 1000 K curve is considerably lower at ≈ 59 THz. The reason for this shift is the non-linear $\nu \Leftrightarrow \lambda$ coordinate transformation. Physically, it is a consequence of the Planck function being a distribution and having a dimension *per frequency* or *per wavelength unit*. It gives the power density in each infinitesimal frequency or wavelength interval. The non-linear transformation makes the corresponding infinitesimal steps unequal, which influences the shape of the curve. Comparing the diagrams above, we notice that the widths of the peaks increase with temperature in Fig. 8.2, while they decrease in Fig. 8.3.

As an example we choose the solar spectrum, which is on the short wavelength side of Fig. 8.3. It agrees roughly with that for a blackbody at 5800 K. The maximum is at $\lambda = 0.50$ μm (cf. Equation [8.4]). This wavelength almost agrees with the peak of the sensitivity of the human eye – but this agreement is only in the wavelength version. Equation [8.5] gives the corresponding maximum on the frequency axis at 341 THz, which corresponds to 0.88 μm , that is, well beyond 0.50 and actually outside the visible range. The eye sensitivity curve is dimensionless and not affected by the transformation. Consequently, in the wavelength representation the peak of solar radiation is in the middle of the sensitivity of the human eye, but in frequency space the maximum is outside our range of vision. This and a few more consequences of the non-linear transformation of the Planck distribution function have been described in more detail by Soffer and Lynch (1999). Heald (2003) has also discussed the issue of the ‘Wien peak’ position.

The expressions [8.2] and [8.3] tend to 0 in both directions, that is, whether ν or $\lambda \rightarrow 0$ or ∞ . Analyzing the integral of the expression it turns out that they are both finite as long as the temperature is finite (Zalewski, 1995). This



8.3 The spectral radiance from a blackbody as a function of wavelength in μm at the same temperatures as in the previous figure. As in Fig. 8.2 the y-axis is logarithmic. The peaks of the spectral curves for different temperatures are joined by the fat dash-dotted curve which illustrates the Wien's displacement law.

was a strong argument in favour of quantum mechanics when Planck made his derivation, because earlier classical attempts had indicated the opposite. The integral is required to calculate the **total radiance** M from the surface of a blackbody, that is, the Stefan-Boltzmann equation summing the contributions for all wavelengths into the solid angle 2π :

$$M(T) = \sigma T^4 \quad [8.6]$$

with the Stefan-Boltzmann constant $\sigma = 5.6693 \times 10^{-8} \text{ W/m}^2/\text{K}^4$. Equation [8.6] is obtained, whether the variable is v or λ .

This signals that we should recheck are the differences in curve shape noted above. The area under each curve, that is, the total radiance, should be independent of variable. A formal verification requires integration of the two versions [8.2] and [8.3]. The following comment is only a hint: the peak *heights* in the wavelength version increase as T^5 , which is easily shown by inserting Equation [8.4] in Equation [8.3] (Ribbing, 1999). In contrast, the peaks of the

frequency curves only grow as T^3 , which is found by inserting Equation [8.5] in Equation [8.2]. This is compensated for by the changes in peak *widths* noted above. In both versions therefore the Stefan-Boltzmann integrals grow as T^4 .

Emission from a small hole through a large enclosure is virtually non-coherent. This may be the reason for a widespread notion that thermal radiation in general is non-coherent. It is often a reasonable first assumption that radiation from thermal sources has a very short coherence length. Nevertheless, microscopic features on a thermally emitting surface cause spectral and directional interference variations (Carter and Wolf, 1975; Wolf and Carter, 1975). In particular it was proved that Lambertian emission requires a source with some degree of periodicity.

8.3 Emissivity

The previous section considered the special case of thermal emission from a blackbody. This is the theoretical maximum, which a real surface never reaches for all wavelengths. The real emission is obtained by multiplication with the *emissivity* function $\varepsilon(\lambda)$ which is dimensionless and $0 \leq \varepsilon(\lambda) \leq 1$. The emissivity expresses to what extent a real body is a blackbody and modifies Equation [8.3]. A simple illustration is given in Fig. 8.4.

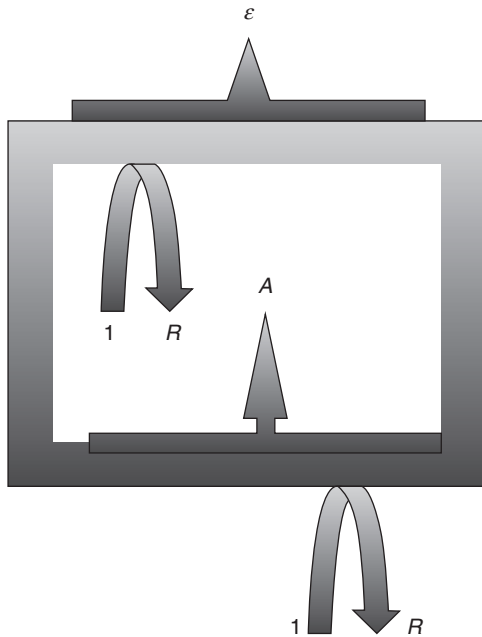
A simple consideration may help to understand the relation between the emissivity and other optical properties. The blackbody radiation from the inside of a real body is partly reflected by the interface towards the outside. This interface cannot store energy. Thus, the fraction that is not reflected is emitted as thermal radiation. The arrow to the left in the diagram gives the result $\varepsilon = 1 - R$, which will be obtained under better defined circumstances as [8.10] below.

The spectral, thermal emission from a general body is

$$L(\lambda, T) = \varepsilon(\lambda) L_{bb}(\lambda, T) \quad [8.7]$$

While the Planck function is an expression from statistical thermodynamics and only a function of temperature, $\varepsilon(\lambda)$ expresses the limits set by *material properties*. We need, for example, the optical functions $n(\lambda)$ and $k(\lambda)$ to obtain the emittance, $\varepsilon(\lambda)$. If the optical constants are temperature dependent this will also make the emissivity temperature dependent. Generally we should therefore write $\varepsilon(\lambda, T)$. This temperature dependence may be important at phase changes. However, in general the temperature dependence in Equation [8.7] is dominated by that of the Planck function, L_{bb} .

There is a general thermodynamic relation concerning the emissivity. According to Kirchhoff's law, the emissivity is equal to the optical absorbtivity, A , the fraction of the total intensity that is absorbed by the solid. This is



8.4 Simplistic illustration of the relationship between the thermal emission from a real body and that from a blackbody. Expressed in the dimensionless fractions for the left arrow in the diagram the obvious result $\varepsilon = 1 - R$ is obtained. The right arrow gives a similar argument for Kirchhoff's law.

understood from a thought experiment. If a body is placed inside the enclosure, it must eventually reach the same temperature as the inner walls of the enclosure. At equilibrium, the radiation intensity emitted by the body is equal to the absorbed, that is,

$$\varepsilon(\lambda) = A(\lambda) \quad [8.8]$$

for all wavelengths and temperatures. Kirchhoff's law has some caveats when we leave the isotropic environment of the *holeraum*. The exceptions are connected to cases when angular dependence and polarization of the radiation have to be considered. In more general cases the impinging radiation may have an angle of incidence different from that where most of the outgoing thermal radiance is leaving. Similarly, the thermal radiation may be more or less polarized depending on the material properties. For the details of these exceptions we refer the reader to more complete sources (Siegel and Howell, 1981; Palmer, 1995).

The intensive research work with photonic crystals during the 1990s evolved around the concept of *photonic bandgaps*, within which electromagnetic waves cannot be transmitted (John, 1984; Yablonovitch, 1987). An incident wave in such a gap is totally reflected and the corresponding thermal emission is suppressed as illustrated in Fig. 8.4. The possibility of controlling, or at least changing part of the thermal emission from a surface with a one-dimensional photonic crystal on the surface of a bulk solid was investigated with model calculations by Cornelius and Dowling (1999). A ‘one-dimensional photonic crystal’ is equivalent to an optical multilayer which is a major component in optical technology. These relatively recent works therefore formulate findings from traditional optical filter technology in a new terminology.

If we combine Kirchhoff’s law [8.8] with [8.1] and assume that polarization and angular effects are negligible, we can express the emissivity in quantities that are measurable in a conventional spectrophotometer. The R - and T -measurements should be made with an integrating sphere if the sample is not highly specular:

$$\varepsilon(\lambda) = 1 - R(\lambda) - T(\lambda) \quad [8.9]$$

Adding the condition that the sample is opaque we arrive at the relation which was hinted to in Fig. 8.4:

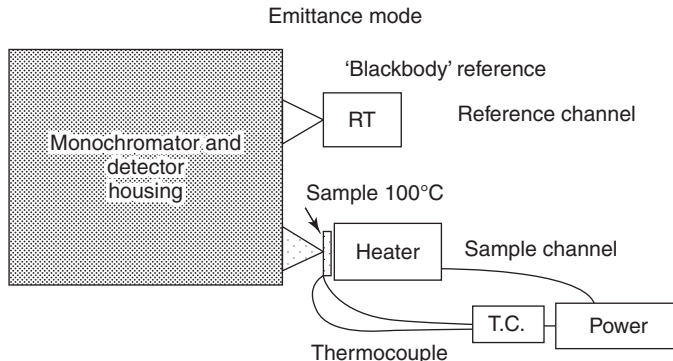
$$\varepsilon(\lambda) = 1 - R(\lambda) \quad [8.10]$$

This points to the simplest method for determining the spectral emissivity, that is, measuring the bulk reflectance of an opaque sample. Provided that the incoming beam is already chopped, as in modern spectrophotometers, this method avoids the problem with eigen-emission mentioned in Section 8.1.

An alternative method is to use a dual-beam spectrophotometer in emission mode, as illustrated in Fig. 8.5.

In emission mode, the instrument does not use the built-in light source but instead normalizes the spectral intensity from the heated sample to that from the sample in the reference channel. This reference should either be an approximate blackbody or a calibrated emissivity standard. The difficulty in this case is to measure at temperatures different from room temperature. Attempts to heat the sample in a double beam spectrophotometer often cause thermal movements of the sample or sample-holder that shift the beam on the detector, which increases the measurement error.

As a third option for emissivity measurement we show an example of radiometer, or heat-camera, measurement in Fig. 8.6. Such instruments do not have a light source and a monochromator, but often have one or several filters



8.5 Schematic showing the use of a conventional infrared spectrophotometer in emittance mode. The spectral intensity of the thermal emission from the heated sample is normalized to that from the reference. The reference sample should either be an approximate blackbody or a calibrated emissivity standard. (Source: The figure is cited from Chibuye *et al.* (1994).)

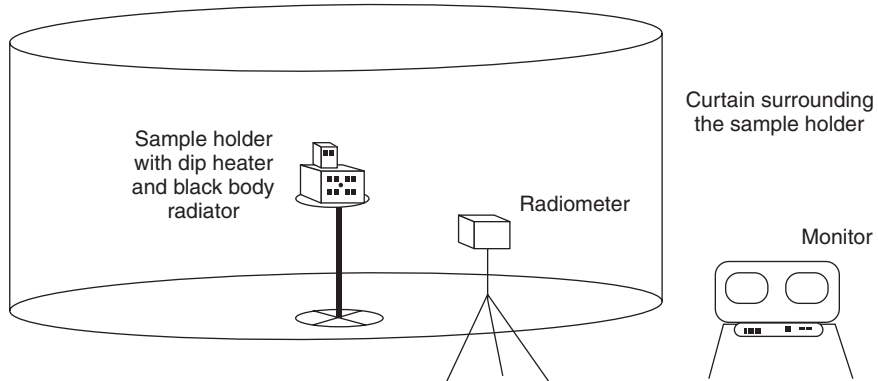
that transmit over a limited wavelength range $\{a,b\}$. The emissivity to be determined is then an average over $\{a,b\}$:

$$\bar{\varepsilon}(T) = \frac{\int_a^b \varepsilon(\lambda) L_{bb}(\lambda, T) d\lambda}{\int_a^b L_{bb}(\lambda, T) d\lambda} \quad [8.11]$$

where the nominator is the total thermal emission from the sample. $\bar{\varepsilon}(T)$ may be named *a,b-band-emittance*. T is the sample temperature, which has to be different from that of the ambient, T_a . The radiometer reads the intensity of the thermal emission from the sample plus the thermal emission from the surroundings that is reflected by the sample. This total intensity of two added components is not sufficient to obtain the sample emissivity. The standard procedure to obtain the sample emissivity is illustrated in Fig. 8.6 and summarized in a few equations. Complete descriptions have been published by, for example, McCluney (1994) and Zhang *et al.* (1986).

Given that the sample is opaque we can use Equation [8.10] and obtain an expression for the radiance reflected by the sample from the surroundings at the ambient temperature, T_a .

$$\begin{aligned} L_r(T_a) &= \int_a^b (1 - \varepsilon(\lambda)) L_{bb}(\lambda, T_a) d\lambda \\ &= (1 - \bar{\varepsilon}(T_a)) \int_a^b L_{bb}(\lambda, T_a) d\lambda \end{aligned} \quad [8.12]$$



8.6 Illustration of a radiometric determination of the band-emittance for the sample in the warm-water tank with samples mounted over holes, and an inside spherical shell as a blackbody reference. (Source: The figure is cited from Ribbing *et al.* (1995).)

In this expression it is assumed that the surroundings radiate as a black-body. This is an approximation which is satisfactory if the surrounding surfaces are sufficiently distant or almost black in $\{a,b\}$. In the arrangement shown in Fig. 8.6 the cylindrical object is a black curtain several metres from the sample. The intensity reading, L_A from the sample can then be written:

$$L_A(T, T_a) = \bar{\epsilon}(T) \int_a^b L_{bb}(\lambda, T) d\lambda + (1 - \bar{\epsilon}(T_a)) \int_a^b L_{bb}(\lambda, T_a) d\lambda \quad [8.13]$$

This sample reading is complemented with two more: L_B , which is from a blackbody spot at temperature T , that is, the opening of an empty sphere mounted in the water container as in Fig. 8.6; and L_C , the measured intensity from a representative spot of the surroundings at temperature T_a . The two quantities are given by the expressions:

$$L_B(T) = \int_a^b L_{bb}(\lambda, T) d\lambda \quad [8.14]$$

and

$$L_C(T_a) = \int_a^b L_{bb}(\lambda, T_a) d\lambda \quad [8.15]$$

using Equations [8.13]–[8.15] we obtain a relationship between the three measured intensities:

$$L_A(T, T_a) = \bar{\varepsilon}(T) L_B(T) + (1 - \bar{\varepsilon}(T_a)) L_C(T_a) \quad [8.16]$$

which, just as expected, shows that the reading A is a sum of two radiances B and C .

If we make the approximation $\bar{\varepsilon}(T) = \bar{\varepsilon}(T_a) = \langle \varepsilon(T) \rangle$ then Equation [8.16] gives

$$\langle \varepsilon(T) \rangle = \frac{L_A - L_B}{L_B - L_C} \quad [8.17]$$

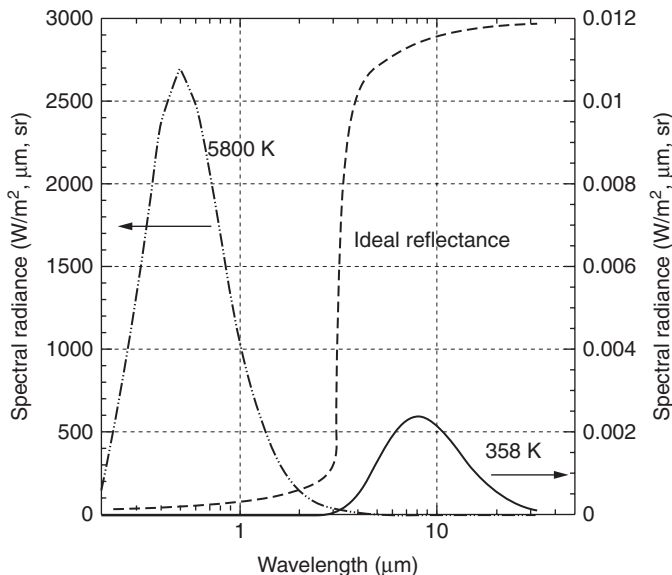
This is a standard expression and under favourable conditions it gives an acceptably accurate approximation of $\bar{\varepsilon}(T)$. In particular, one notices that if the emittance is gray, that is, independent of wavelength = ε' in the a,b -interval, then Equation [8.11] gives $\bar{\varepsilon}(T) = \varepsilon'$ and Equation [8.17] is exact. Since this is not always the case we keep the distinction between $\langle \varepsilon(T) \rangle$ and $\bar{\varepsilon}(T)$. In the opposite case, that is, if $\varepsilon(\lambda)$ has strong variation within $[a,b]$, then $\langle \varepsilon(T) \rangle$ requires corrections to obtain an approximate value for $\bar{\varepsilon}(T)$ (Staaf *et al.*, 1996).

8.4 Optically selective coatings

In this section we review two areas of applications of coatings and surfaces that have been established for several decades. Extensive research has been carried out in the two fields and the scientific literature is vast. Existing products are based on the principles of solar selectivity in the two fields: *Solar thermal absorbers* and *Energy efficient window coatings*. The label ‘solar selective’ refers to the spectral separation between the incoming solar radiation and the thermal emission of moderately hot objects. This separation makes it possible for a surface to have different, or even opposite, optical properties in the two spectral regions. The Section 8.4.2 on window coatings will to some extent overlap with Chapter 20. We hope that some duplications will add depth, rather than cause irritation among readers.

8.4.1 Coatings for thermal solar collectors

In this case the purpose is to heat a medium using solar radiation. The medium, water or air, is in good thermal contact with an absorbing surface. Primarily this surface should be a perfect absorber of incoming solar



8.7 Two blackbody radiance curves on log-lin axes. In principle as Fig. 8.3 but the two different temperatures, display the wavelength gap between the curves. Notice the large difference in radiance values on the y-axes. The high temperature curve, 5520°C is a reasonable approximation for incoming solar radiation, while the 75°C blackbody radiation represent potential losses from a solar collector that is 'black' also in the infrared. The sketched idealized reflectance profile between 0 and 1 on a dimensionless scale illustrates thermal solar selectivity.

radiation. This will raise the surface temperature, which causes thermal losses to the surroundings. Conduction and convective losses can be insulated against, but the radiative losses from the front surface cannot be shielded. To reduce the radiative losses, the surface should exhibit low emittance in the thermal range of the absorber, for a flat plate typically 50–120°C. The high solar absorbance is only required in the wavelength range where the solar radiation is significant (c.f. Section 8.2). The situation is illustrated with two blackbody curves at temperatures 358 K (85°C) and 5800 K (5527°C) in Fig. 8.7.

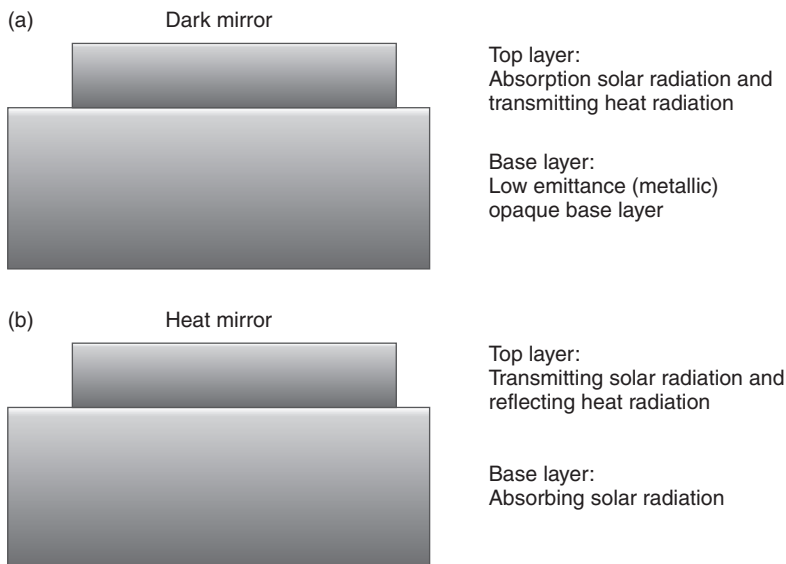
The diagram verifies that high solar absorption, that is, blackbody behaviour, is only essential in the range 0.4–2 μm, while the low emittance is needed in the range 3–30 μm. Using Equations [8.8] and [8.10] we realize that the required optical behaviour is a reflectance that is very low for 0.4–2 μm and as high as possible for 3–30 μm. This ideal reflectance spectrum is sketched in Fig 8.7. This ideal behaviour is unphysical, but it represents a target for developing solar thermal absorbers and *solar selectivity* is a common label for this property. This concept is old, the pioneering work of Tabor (1955)

is often cited as a start for systematic material development. The results of this development have been documented in several monographs (Meinel and Meinel, 1976; Seraphin, 1979; Agnihotri and Gupta, 1981; Duffie and Beckman, 1991; Granqvist, 1991) and review articles on particular aspects, for example, by Craighead *et al.* (1979). An annotated bibliographic listing commenting publications for the period 1955–1981 has been published (Niklasson and Granqvist, 1983). To keep within the framework of this book we shall focus on solar selectivity obtained with optical thin films. The references cited immediately above include other examples like paints and electrochemical treatments.

A natural starting point is a metal substrate. Metals in general have high reflectance that increases with wavelength towards the infrared according to the Hagen-Rubens relation. This corresponds to low thermal emittance, i.e., the second requirement for solar selectivity. Most metals exhibit high reflectance in the visible range, this will impair the first requirement – it will not be effectively heated. If we choose copper, it represents a small step in the right direction. Thanks to interband transitions, copper absorbs some green and blue light, and has low thermal emittance. However, a clean surface of copper does not get hot enough in sunshine to be of any technical use. To summarize a long history of research on single metals as well as compounds, it has been concluded that no single material will provide sufficient and stable solar selectivity for viable heat production. A historical account, including many high stability metal compounds, can be found in Seraphin (1979). The failure in the search for a single material, has led to attempts with double layers. Based on the low thermal emissivity of metals a first choice has been to try oxidized metals. Many metal oxides are black or exhibit colour which indicates absorption bands in the visible range. As an example we again choose copper. It has two oxides, CuO is black and Cu₂O is red, which to some extent grow spontaneously in air depending on the temperature. As early as the 1960s a chemical oxidizing agent ‘Ebanol’ was already on the market for the production of selective solar absorbers. Roos *et al.* (1983) studied the difference between thermal and chemical copper oxide mixtures and concluded that the higher selectivity in the chemical case was due to the roughness of the interface between the growing oxide and the metal.

In a wider perspective we can categorize these tandem absorbers into two different types *the dark mirror* or the *heat mirror* illustrated by Fig. 8.8.

As explained in the caption, the difference between the two cases is in which layer the main absorption of solar radiation and reflection of heat radiation occurs, respectively. In both cases the top layers must have low reflectance for the impinging solar radiation which is a definite loss. This is the reason for sometimes adding a second optical film, that is, a third material, for antireflection of the upper layer.



8.8 (a) The dark mirror primarily absorbs short wave radiation in the top layer which transmits heat radiation. The tandem exhibits low thermal emittance thanks to the substrate. (b) The heat mirror reflects heat radiation from the top layer, which transmits the solar radiation to the absorbing substrate.

With this background we can understand and distinguish the role of optical thin film technology for research, development and production of thermal solar collectors. The transmission required through the top layer indicates that it should be a thin film. The requirements on the base suggest a metal substrate, which would also effectively conduct the collected heat to a transfer medium. In the case of Fig. 8.8a, a dark mirror, one option would be a metal base with a metal oxide coating that ‘antireflects’ the metal in the visible and near infrared (NIR) ranges and also increases the absorption in the metal. This interference approach is the subject of a classical paper by Haas *et al.* (1956) intended for applications in IR instruments. The paper demonstrates the difficulty in making this with high reflectance metals. Apart from the general problem of antireflection over a wide enough wavelength range, the paper identifies the condition to antireflect high metallic reflectance in an expression for the optical constants. If the dielectric coating has refractive index n_1 and the metal substrate $N = n + ik$, the condition for a zero reflectance minimum is:

$$n_1 = \left[n + \frac{k^2}{n-1} \right]^{1/2} \quad [8.18]$$

For high reflectance metals $n < 1$. This gives $n_1 < 1$, which is impossible for a dielectric film. The authors also tested evaporated titanium oxide on an aluminium substrate. In evaporation at normal temperatures, a stoichiometric oxide is grown. This oxide is yellowish and has some visible absorption, that is, $k_1 > 0$. In this case low reflectance over most of the visible range can be obtained.

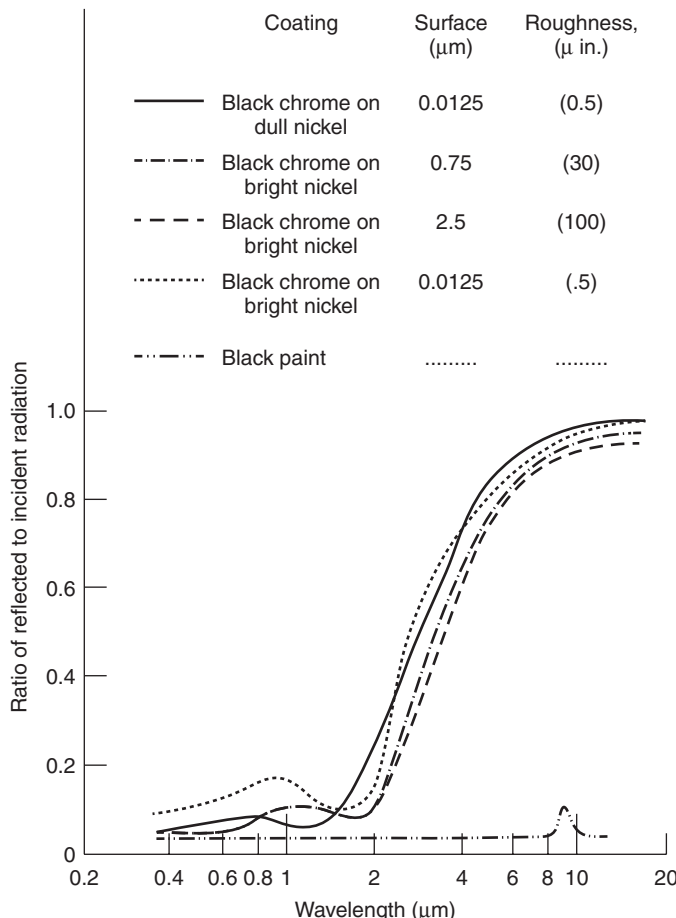
There are limits on the selectivity that can be obtained with a simple tandem concept. The reliance on interference also limits the width on the minimum that can be obtained with just one dielectric film. In this case a low minimum over the entire range 0.3–2.5 μm is not realistic. An additional problem is that interference will also create a *maximum* at some shorter wavelength.

In Fig. 8.9 we cite the example of black chrome tandem reflectance. This coating had already been extensively studied in the early 1970s and marketed for solar thermal collector systems.

Black chrome is applied in a two-step electrochemical process on a nickel or copper base. This application technique does not result in optically smooth interfaces (Lampert and Washburn, 1979) and agreement with straightforward interference behaviour should not be expected. Nevertheless, the different cases in Fig. 8.9 show some interference structure in the region below 2.0 μm . Obviously, the maxima cause losses in collection efficiency. For comparison, the spectrum for ordinary black paint is also given. It has significant IR-absorption and will therefore cause thermal losses.

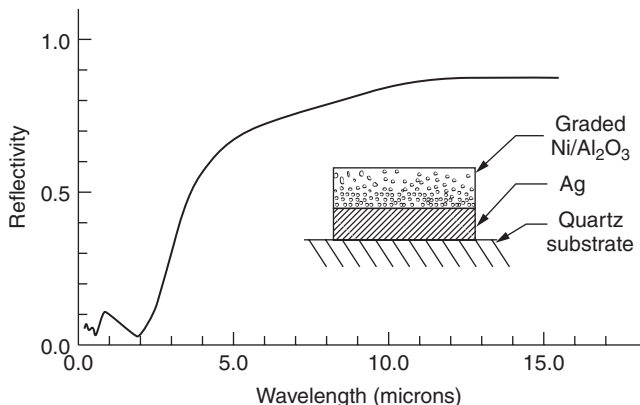
Black chrome is an early example of a more advanced concept of *inhomogeneous* surface coatings for solar heat collection. Typically a metal surface is coated with a *cermet*, that is, a dielectric matrix containing a significant density of small metal particles. Sievers (1979) reviewed the optical properties of small metal particles in which the mean-free-path of the conduction electrons is limited by the particle size. The optical properties of particles + matrix have been modelled with scattering and effective media theories, to determine one dielectric function for the composite medium (Niklasson, 1991).

As already mentioned, it is possible to use a top layer for antireflection in the visible spectral range (VIS)-NIR-region and thereby increase the solar heat collection. An attractive version of this method is to prepare this top layer with a graded index, such that $n(z) \rightarrow 1$ when z approaches the front surface. The literature cited discusses a wide variety of these latter two methods. The advantages gained, however, must balance increased cost for a more complicated production process, and possibly an increased sensitivity for thermal and chemical damage. Figure 8.10 shows high solar selectivity for a graded $\text{Ni}/\text{Al}_2\text{O}_3$ cermet film on silver. In this case (Craighead and Buhrman, 1978), the concentration gradient was achieved by evaporating from two sources that were separately controlled.



8.9 Reflectance spectra for four different samples of black chrome on dull and bright nickel and one for ordinary black paint. (Source: Cited from McDonald (1974).)

Section 8.4.3 treats the deposition techniques used for the large scale fabrication of thermal solar collectors. The Tabor patent mentions electrochemical treatments of a smooth nickel surface. Painting is mentioned and there are special low-emissive black paints containing aluminium flakes which have lower emittance than the example shown in Fig. 8.9. As mentioned above, these kinds of coatings have been analysed and modelled, but they are not typical products of ‘optical technology’. It may be painful for experts in optical technology to find that ‘optical perfection’ often reduces solar selectivity. Evaporation of films normally results in a higher degree of structural perfection and smooth interfaces that fulfill the

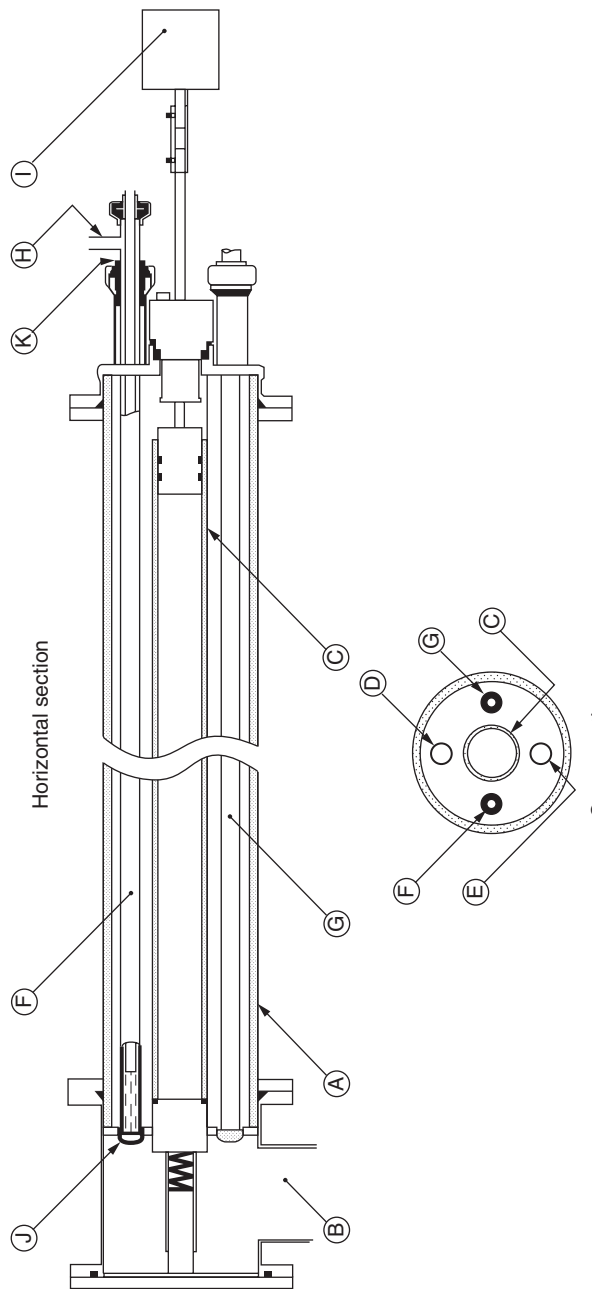


8.10 Reflectance spectrum for a coevaporated graded $\text{Ni}/\text{Al}_2\text{O}_3$ cermet coating on a silver backing. The solar absorption $\alpha = 0.94$ and thermal emissivity $\varepsilon \approx 0.1$ reported. (Source: Cited from Craighead and Buhrman (1978).)

requirements for interference calculations. Lab-scale deposition of evaporated solar absorber coatings has been a valuable method to test new materials and check to what extent interference calculations modified for inhomogeneous composition and/or roughness agree with measurements. However, evaporation is not suited for economic production of m^2 size solar collectors. It has thus been quite important that lab-scale development of *magnetron sputtered* coatings has also been successful, and in a few cases, transferred to full scale production.

A particular advantage with sputtering is that it can be adapted to deposit on curved surfaces. This was required for making tube-shaped collectors for mounting in a moderately concentrating system: a cylindrical solar mirror with the absorber tube along the centre. In Fig 8.11 we cite an early design of a cylindrical sputter unit made by Harding *et al.* (1976).

The particular carbide coating tested in this work was solar selective but not sufficiently so compared with alternatives that have appeared. Through a number of intermediate steps this has been developed to a commercially successful production of solar collectors in China. The coating is a mixed AlN and stainless steel cermet that is created by successive deposition of the two materials in very thin layers. This is obtained by a rotation as fast as 6 rpm of the batch of tubes. The two materials interdiffuse to a semi-homogeneous, high temperature stable cermet. The substrate is a metallic heat reflector as in Fig 8.8a. The resulting collector tubes are reported to have solar absorption as high as 0.95 and the thermal emittance is only 0.05 (Zhang *et al.*, 1998).



8.11 Schematic showing the design of a DC magnetron sputtering unit for deposition of a cermet coating on the exterior of tubes for concentrating solar collectors. (Source: Cited from Harding *et al.* (1976).) A, glass envelope; B, pumping port; C, tubular glass substrate; D, gas inlet tube; E, gas outlet tube; F, stainless steel cathode; G, copper cathode; H, teflon insulator; J, motor; I, cooling water inlet; K, glass insulator; L, teflon insulator and seal.

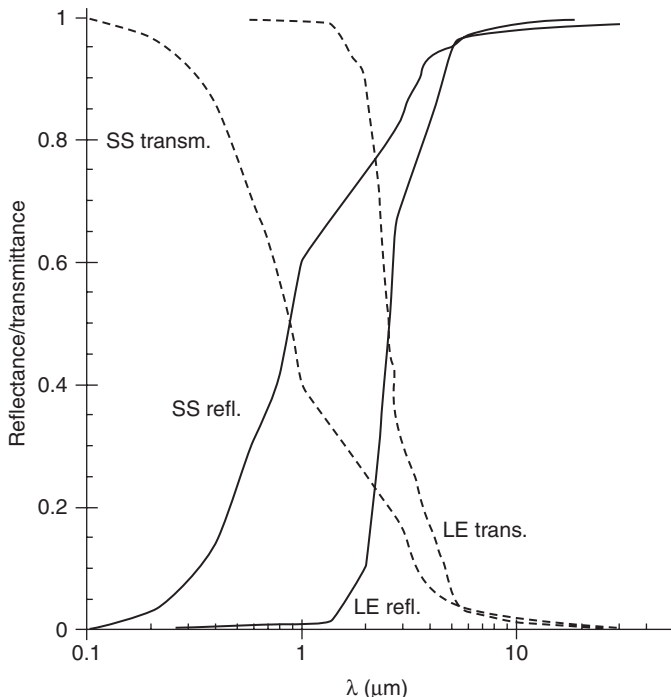
A corresponding development has taken place for the production of flat solar collectors. The collector comprises 20 cm wide, double aluminium fins that embed a flat copper tube. After the coating process the tube was reshaped using pressurized air. In the application it is used for circulating water to be heated. Originally, the coating was made electrochemically in large containers with aggressive chemicals. Today, the corresponding product has similar aluminium fins that are DC sputter-coated with an antireflected Ni-NiO cermet. The sputtering unit is a roll-coater that is charged with up to 1000 m of the rolled fin, which is fed through the deposition zone at a speed that gives the suitable deposition time. The performance is solar absorption 0.96 and thermal emission 0.10 at 100°C (Wäckelgård and Hultmark, 1998).

8.4.2 Energy efficient window coatings

Energy conserving window coatings have been a commercially successful application of advanced and large scale optical coating technology for several decades. The requirements on visual perfection, in transmission as well as reflectance, are very stringent with regard to windows. It is remarkable that they can be satisfied for large areas in different coating processes. The window coatings belong to a larger group named *architectural coatings* (c.f. Chapter 20), which are generally used to improve exterior visual impression. Energy saving, which is the focus of this treatment, is obtained differently depending on the local climate. In warm climate zones the coating should reflect invisible solar heat radiation to save electric power otherwise needed for air conditioning or for improved comfort. It should be noted that more than 40% of the total solar energy appears beyond visible wavelengths, c.f. Fig. 8.7. These coatings are sometimes named *solar screens*. In cold climates the coating should reduce the thermal emission. They are named *low emissive* or *LE-coatings*. In Fig. 8.12 we show the idealized reflectance and transmittance spectra for the two types of coatings.

As shown, the difference between a solar screen and LE-coating is in the wavelength position of the step between transmittance and reflectance. Beyond 4 µm the transmission of the window glass is zero, but the absorption heats the glass, that is, an increase of the heat-load to the inside. The high reflectance in the infrared thus reduces this heating as well as the emission losses in the LE-case as given by Equation [8.10]. As in the case of the seemingly very different application of solar thermal absorbers, the threshold between absorption/transmission and reflectance should ideally be in the 2–3 µm interval.

Integrated parameters can be used to evaluate the performance. T_{SOLAR} is the measured transmittance weighted by the solar spectrum and integrated

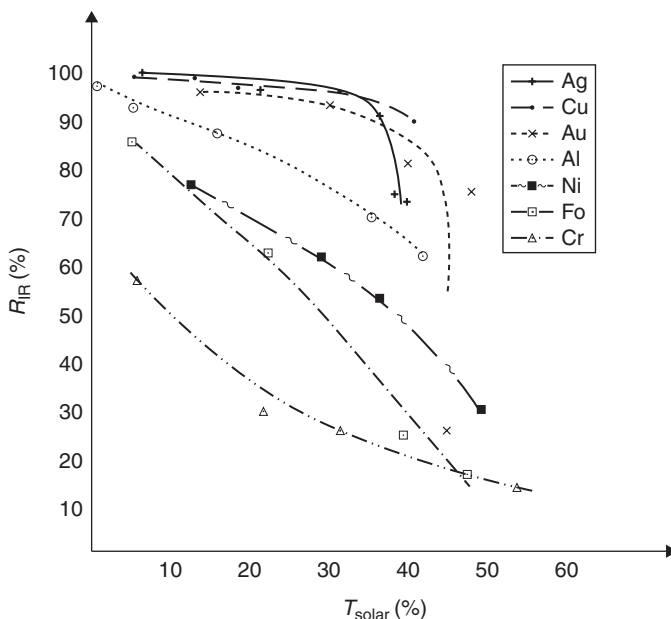


8.12 Idealized reflectance and transmittance spectra for the two types of window coatings mentioned in the text.

over the visible and near infrared ranges. R_{IR} is the measured IR-reflectance weighted by the blackbody function for room temperature integrated over the IR. A LE-window should have both T_{SOLAR} and R_{IR} as close as possible to 100%. In Fig. 8.13 we show examples of the two parameters for thin metal films on a glass substrate. A third parameter, T_{EYE} is an alternative to T_{SOLAR} when solar screen coatings are evaluated. In this case the sensitivity of the human eye is used as a weight function in the integration.

In this subsection we shall first list and comment on the various *coating materials* and combinations thereof that are used to achieve the optical selectivity. Much more extensive treatment of the subject is given in the monographs and reviews by Gläser (2000), Hollands (2001), Jelle *et al.* (2012) and Pulker (1984).

The dominant type of window coating is the *metal-based multilayer*. In typical cases this is a 10–40 nm thick noble metal film sandwiched between two non-absorbing, somewhat thicker metal oxide films. Noble metals, and actually a wider group of free-electron- or Drude-like films, have a small selectivity by themselves. In other words, thin free-electron-like (FE-) films exhibit visual transmission that gradually shifts to high infrared reflectance



8.13 The respective R_{IR} and T_{SOLAR} values as described in the text, for different metal films as indicated. Notice that the noble and FE-metals are closer to the upper right corner than the transition metals. (Source: Cited from Karlsson *et al.* (1981).)

with longer wavelength. This follows from the Drude model and the relation between a typical relaxation time for the conduction electrons and the period of the EM field in the visible and infrared regions. In Fig. 8.13 we show the parameter values T_{SOLAR} and R_{IR} for seven different sets of thin metal films.

Moving from left to right in the diagram, we get values for successively thinner single films on a glass substrate. We notice that a noble metal film alone can give values like $R_{\text{IR}} \approx 90\%$ and $T_{\text{SOLAR}} \approx 40\%$.

In practice a single metal film is not used as an LE-coating for at least two reasons: the parameter values are too low, and the long-term stability is poor if the coating is exposed to the variations of temperature, humidity and acidity in a normal ambient atmosphere. It is fortunate that there are thin film materials that can solve both problems. Typically, these materials are stable metal oxides with optical constants in the visible range suited to antireflect the metal film, and thus increase the T_{SOLAR} value. Typical oxides used are TiO_2 , In_2O_3 and SnO_2 . In some cases 3–7 layers are used to even further improve the optical performance. The long-term stability is still an issue, in particular when a noble metal film is used. The noble metals have the best optical properties, but are easily damaged by humid or acidic atmospheres.

The solution is to use sealed double glazings with the coating facing the sealed space. With this arrangement, lifetimes of up to 10, or even 20, years have been guaranteed.

A higher stability alternative to noble metals, group IVB transition metal nitrides (TiN, ZrN and HfN), have been suggested by Karlsson and Ribbing (1982). These nitrides are well-known hard coatings with high thermal, mechanical and chemical stability. In particular opaque coatings of TiN are used for the protection of tools as well as replacement for gold on exposed surfaces. The colour of gold and TiN originates in both cases from a threshold in the interband optical transitions, but the reasons for the optically FE-like behaviour below this threshold is subtly different (Karlsson, 1981, 1983; Delin, 1996). To date, the thin nitride films have not been introduced in commercial LE-coatings although thicker, TiN-films have been used in solar coatings. Lab-scale investigations have indicated that TiN-base multilayers are optically not quite as effective as silver-based, but they might be stable enough to also be used in unsealed windows (Georgson, 1991).

The second material group in LE-coatings is doped wide-bandgap semiconductors. The bandgaps in SnO_2 , In_2O_3 and ZnO are large enough for films to be transparent over the visible range, that is, more than 3 eV. Such a large bandgap ensures that even a 1 μm thick coating is transparent. Equally important is that the transmission is only weakly thickness dependent, in contrast to the metal multilayer case. This makes large area production easier to control. However, the larger physical thickness of the semiconductor film causes interference variations that impair the visual impression. The main advantage with semiconductor coatings is their higher robustness, such that a sealed atmosphere is not required.

The low emissivity, that is, high IR-reflectance, is obtained by strong doping of the semiconductor. This doping creates an FE-like gas in the conduction band (or a 'hole-gas' in the valence band) that has lower density – but higher mobility, than conduction electrons in metals.

Finally, a few words about the production methods for large area window-coatings. Today, direct magnetron sputtering of the metal layer and reactive of the oxides dominates in deposition of the metal-based multilayers, whether the production is on-line or in batch. The tight control of the sputtering process results in a high degree of visual perfection. Also the group IVB nitrides mentioned above can be reactively magnetron sputtered (Valkonen, 1986). Historically, evaporation has been used and is still used for coating of smaller areas.

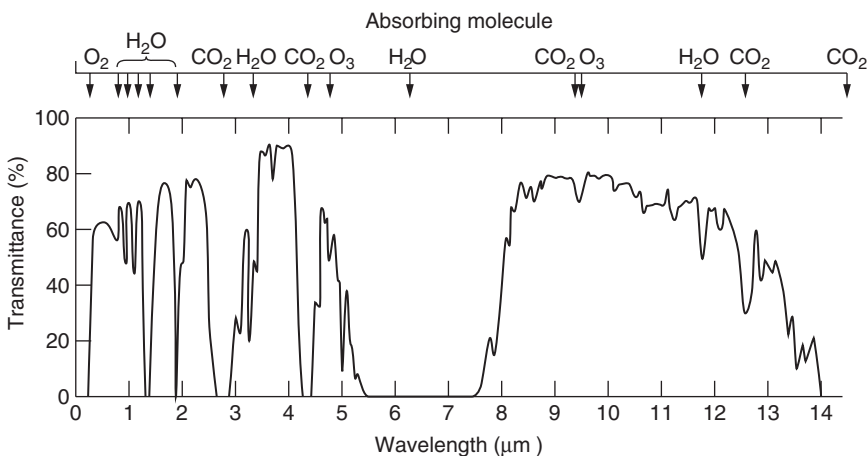
The doped semiconductor coatings, SnO_2 and In_2O_3 can be obtained by pyrolytic spraying at atmospheric pressure (Jarzebski, 1976). A solution of SnCl_4 in alcohol is sprayed as an aerosol against a hot (400°C) glass surface. The chloride decomposes into a SnO_2 layer on the glass, and HCl that is vented off.

8.4.3 Coatings for control of radiative exchange with the atmosphere

In this last subsection we shall consider a few more potential applications of selectivity in the infrared that is based on the non-gray behaviour of the atmosphere. These applications have not found large scale applications or markets as thermal solar absorbers and energy-saving window-coatings. The non-gray property of the atmosphere is manifested by the *atmospheric windows*. In Fig. 8.14 we cite a MODTRAN calculated transmittance spectrum over the distance 1.8 km for a dry, rural atmosphere at an altitude of 1000 m.

We notice that the overall transmittance of the atmosphere is not as high as the transmission of visible radiation 0.36–0.78 μm might lead us to take for granted. Besides this transparent interval, one conventionally talks about the NIR: 0.8–2.5 μm , the medium wave (MW): 3–5 μm and long-wave (LW): 8–13 μm windows. However, in the 8–13 μm window, transmission is sensitive to the water content. It is reduced by rain or high humidity in tropical climates.

Comparing these wavelengths with the blackbody peaks in Fig. 8.3 it is obvious that for ‘normal’ temperatures, 300 K, it is the LW-window that is of interest. Through this window room temperature objects on ground can interact radiatively with much cooler parts of the atmosphere at high altitudes. In thermodynamic jargon, the ‘closed system of object + surroundings’ is not even approximately limited to the nearby air – it must be extended to these higher layers of the atmosphere. As a consequence of this, an object on the ground can cool radiatively to temperatures well below that of the

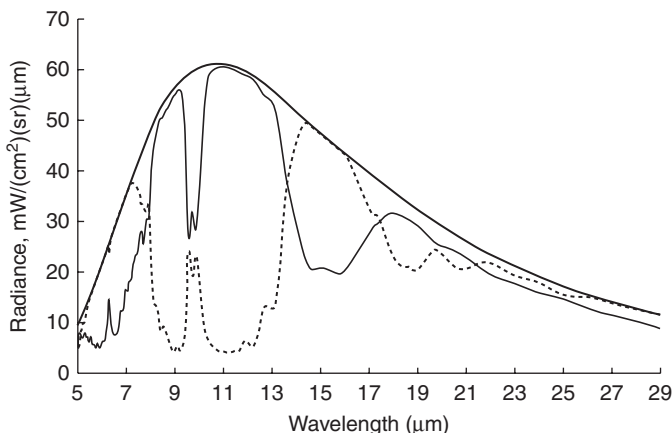


8.14 Atmospheric transmittance over the distance 1.8 km through a rural, dry mid-latitude atmosphere with 23 km visibility at an altitude of 1000 m. (Source: Cited from Bass (1978).)

surrounding air. This explains why water puddles in the desert may freeze during nights, even if the ground temperature is not below zero. Three further factors help to explain this: water has high emittance ≈ 0.8 , the desert sky is indeed dry and often the wind is very weak, that is, the convective contribution to the heat transport is negligible.

This takes us to the subject of radiative cooling. If we want the highest possible radiative cooling power of a hot object – it should simply be as black as possible at the temperature it has. In a more sophisticated application we might wish for the lowest possible equilibrium temperature (during night time). This suggests a different kind of optical selectivity: high emittance in the LW-window, and low at other wavelengths. This possibility has a long history in the scientific literature (Arago, 1858; Heads, 1960; Trombe, 1967). In more recent publications, advanced material combinations by sputtering of mixed films, as well as serial combination of coolers, have been considered (Hamberg *et al.*, 1987). Figure 8.15 shows the reason for optical selectivity in this case and illustrates the potential for radiative cooling.

The three curves are computed spectral radiance functions using the mid-latitude winter model in Fig. 8.14. The topmost curve is the Earth's blackbody curve at 272 K, that is, -1°C . The other full line curve is the *outward* radiation seen from the top of the atmosphere. We notice that in the LW-window it comes close to the blackbody representation of Earth's surface. In other intervals the emission originates from cooler upper layers and is thus reduced



8.15 Radiance functions computed according to mid-latitude winter model. The top curve is a blackbody curve for -1°C , the assumed temperature of the Earth's surface. The lower full line curve is the *outward* radiation. The dashed curve is the *downward* radiation from the atmosphere. The interval, with sign, between the two latter curves represents the potential power of radiative cooling. (Source: Cited from Driscoll and Vaughan (1978).)

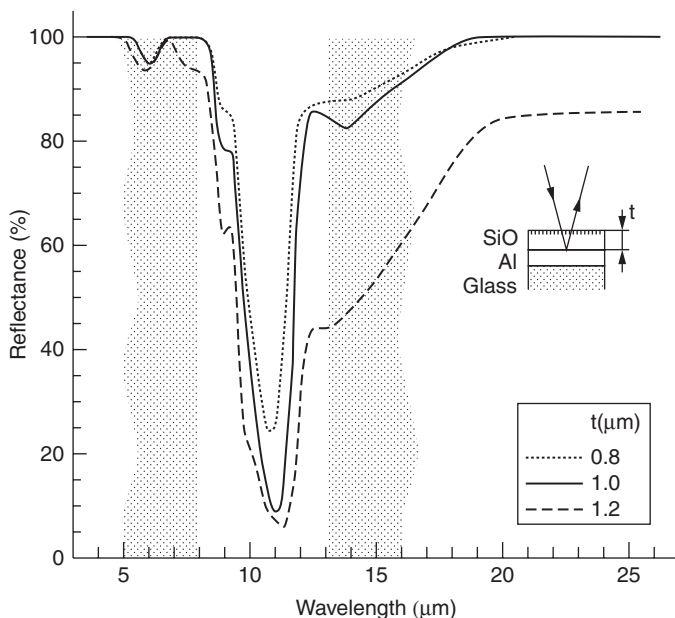
intensity. The dashed curve represents the *downward* radiation from the atmosphere. It is weak in the LW-window since it originates from cold outer space, while it is close to a -1°C blackbody in the 5–8 μm interval, where the humidity in the atmosphere is important. When the outward radiance is above the downward one, the interval represents a potential for cooling. When the dashed curve is above the full line, the interval represents possible radiative heating. The spectral emissivity, or reflectance, of the object to be cooled, determines to what extent the radiative cooling or heating actually occurs. Here, high emittance in the LW-range favours cooling. Depending on their spectral properties, it is feasible for two outdoor objects to show different thermal behaviour. One cools below the temperature of the surrounding air, T_{air} , while the other does not. These considerations of *selective emittance* have taken us to a deeper understanding than the treatment in Section 8.3. Again, the possibility is strongly dependent upon dry air, a clear sky and almost zero wind speed. Even a modest wind could otherwise make convective heat transport take over.

In Fig. 8.16 reflectance spectra for evaporated SiO films on an Al substrate are cited from Granqvist and Hamberg (1981). SiO has an absorption band at 10 μm , that is, in the middle of the LW-window. This will cause strong emission in that interval, while the high transmission for surrounding wavelengths will let the low emittance of the Al substrate dominate (Heads, 1960).

The three recorded spectra in the diagram all show a pronounced reflectance minimum in the LW-range, but otherwise high reflectance, that is, the selectivity required for radiative cooling. The reduced reflectance in the interval 13–20 μm for the 1.2 μm film impairs the cooling capacity and therefore the authors conclude that the 1 μm thick film represents an optimum for radiative cooling.

We shall conclude with some specific applications that require the opposite to radiative cooling, that is, to reduce radiative emission in the LW-window. It is interesting to notice that the conditions introduced by the applications make the solutions different, although they share this one optical feature.

The first two cases concern frost prevention during clear, windless spring or autumn evenings and nights. The frost will preferentially deposit on surfaces that are colder than the surrounding air. In a cold climate one frequently observes car windows facing the sky to be coated with frost in the morning after such nights. A coating on a car window must be visibly transmitting. A low-emissive metallic coating is therefore excluded. Otherwise, it would most probably be efficient as proven by the observation that this kind of frost coating is rarely seen on blank metallic surfaces. It is not surprising that the two Scandinavian car producers SAAB (Adamson, 1976) and Volvo (Hamberg, 1987) have made efforts to prevent frost deposition on



8.16 Reflectance spectra for evaporated SiO films on an Al substrate with thicknesses as indicated. In all cases this reflectance behaviour will result in high outgoing thermal emission through the LW-window, but high reflectance for the incoming thermal radiation from the atmosphere. (Source: Cited from Granqvist and Hamberg (1981).)

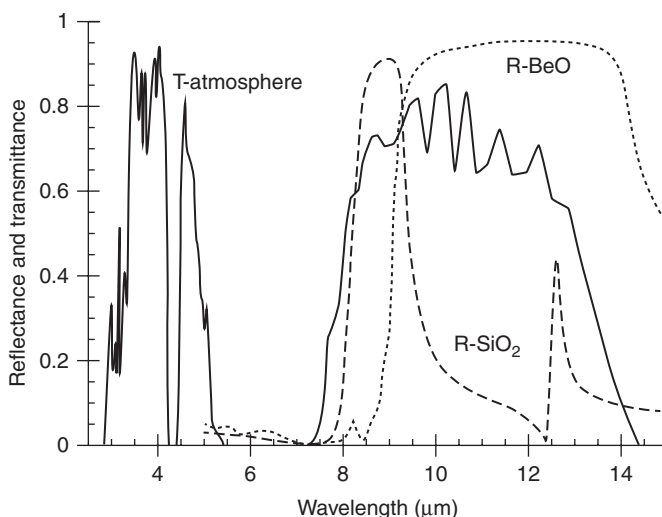
the windscreens using a doped wide bandgap semiconductor coating. As for LE-windows, pyrolytic, doped SnO_2 -coatings have been used. Volvo actually marketed cars with such a coating for frost prevention, but problems with the wiper-cleaning halted this.

A second case of frost prevention by selective emission was for high voltage china insulators. These insulators stick out of the power station at an angle, which exposes the upper surface towards the sky. The insulator is made of china, and as with most silicates (and glass windows), it has high emittance in the LW-window. It may therefore become frost-coated like the sky-facing car windows described above. When the frost melts in the morning the water will create a conducting surface layer that may short-circuit the insulator with serious consequences. A doped SnO_2 -film cannot be used for this case of frost prevention – the electrical conductivity is too high. The requirement in this case is good *electrical insulation*. In summary, we need an electrically insulating material with high average reflectance in the LW-window. In principle there is a dielectric multilayer solution to these requirements – a difficult and probably costly solution for such long and curved objects.

An alternative solution to the materials problem is a compound with ionic bonding. It will be absorbing somewhere in the infrared. Typically, oxides classified as ‘dielectrics’: SiO_2 , TiO_2 , Al_2O_3 , MgO , etc., have at least one strong absorption band in the infrared. The absorption band is caused by lattice excitation of the ionic components and, in that range, the refractive index has strong dispersion combined with high k -values. The textbook cases of this phenomenon are the ionic crystals. Their resonances occurs in the wavelength interval 50–200 μm , that is, far beyond the LW interval. A characteristic feature called the *reststrahlen* band (Eng: residual rays) occurs at wavelengths just below such an absorption band. A group of harder compounds than the ionic crystals: oxides, nitrides, carbides, etc., also feature an ionic contribution to their bonding and exhibit reststrahlen bands at shorter wavelengths (Dobrowolski, 1978; Ribbing and Wäckelgård, 1991).

Instead of a multilayer solution one could therefore hope to identify a compound whose bulk reflectance exhibits a reststrahlen band in the LW-window and thereby reduce the thermal emittance through this window. In such a search BeO (Ribbing, 1989) and SiO_2 (Högström *et al.*, 2005) have been identified as solving at least part of the problem. Figure 8.17 shows the reststrahlen bands of these two compounds and the transmission spectrum for a dry atmosphere with the MW- and LW-windows.

Except for the interval 8–9.5 μm , BeO covers the LW-window reasonably well, while the SiO_2 band only reduces the emittance in that short

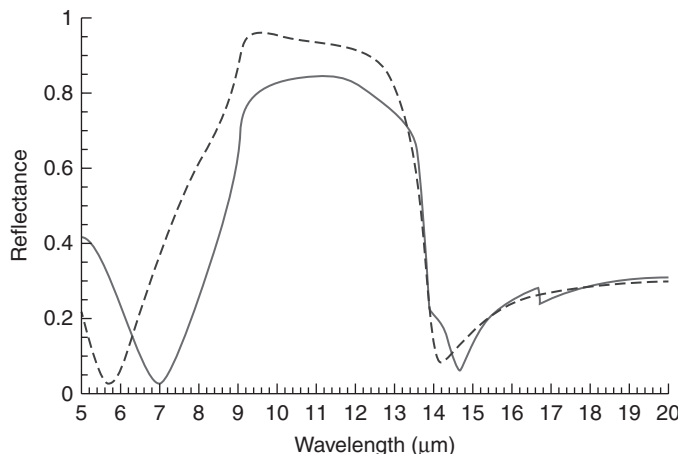


8.17 Spectra showing the reststrahlen bands of BeO (dotted) and SiO_2 (dashed) as well as the transmittance spectrum for 1 km of MODTRAN atmosphere (full line) showing the MW- and LW-windows. (Source: Cited from Högström *et al.* (2005).)

wavelength part of the window. BeO at 50°C was estimated to have the average emittance $e_{\text{LW}} \approx 0.5$ in the LW-window. This is considerably lower than standard silicate ceramics and sufficiently low to avoid growth of frost in most weather situations and environments. Unfortunately, BeO has hygiene problems. Well-controlled green-forming is an accepted process (National Beryllia Div. of General Ceramics Inc., Haskell, NJ), but coating deposition is difficult and not suited for large scale production.

It has been demonstrated in lab-scale that the LW-emittance of BeO can be further reduced by a dielectric coating with suitable refractive index. Again it should be remembered that BeO is not a dielectric at these wavelengths, but the behaviour close to a resonance absorption can be modified with a thin coating. Interference calculations for a double-layer of Si(d)/BeO indicated that maximum average reflectance, that is, minimum thermal emittance in the LW-window, should occur for $d = 0.83 \mu\text{m}$. Figure 8.18 shows a comparison between the calculated reflectance spectrum and the corresponding near-normal measured curve for a BeO substrate with a $0.83 \mu\text{m}$ magnetron sputtered Si-film. The optical constants for BeO were obtained by fitting of the Lorentz oscillator model to the bulk, near-normal reflectance spectrum measured on the polycrystalline BeO used as substrate. Optical constants for Si were taken from the literature, although they may be somewhat different from those of the sputtered films.

Radiometer measurements gave an average emittance for the coated sample $e_{\text{LW}} \approx 0.29$ in the LW-window. Chemical vapour deposition (CVD)

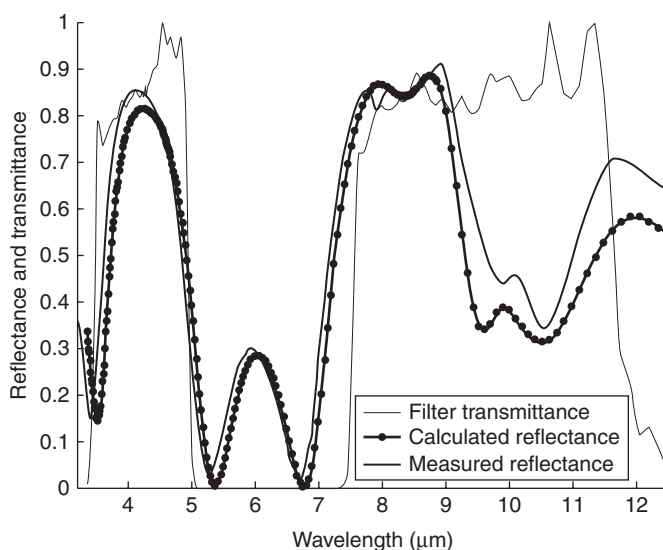


8.18 Measured (line) and calculated (dashed) reflectance spectra for Si($0.83 \mu\text{m}$)/BeO illustrating that the Si coating modifies the short wavelength edge of the BeO restrahlen band to further increase the reflectance within the LW-window. (Source: Cited from Ribbing *et al.* (1995).)

deposition of the Si-film would probably improve the agreement with literature values and further reduce the LW-emittance.

This final part concerns another application of selectively low thermal emittance. In this case, the aim is to reduce the radiance in both the LW- and MW-atmospheric windows. This is relevant for thermal camouflage of objects that are either just above room temperature or as high as 300°C. In the latter case, the blackbody curve has maximum intensity around 4 μm, that is, in the MW-window. The IR-seekers can only discover distant objects using detectors that are filtered for one of the atmospheric windows, and even then, only through a dry atmosphere with few clouds. Under such circumstances it is militarily relevant to suppress the thermal radiation to minimize the chance for detection. An advantage with narrowing the low emittance to the window intervals alone, is that the heated object can then still cool radiatively at other wavelengths. In Fig. 8.19 the result of such an attempt is cited. It proved possible to use the dielectric behaviours in the MW-window, as well as a combination of the reststrahlen band of SiO_2 and Si in the LW-window for a double layer on a Si substrate.

Obviously, the narrow SiO_2 band is not sufficient to cover the long wavelength part of the LW-window. In this case both layers were deposited using



8.19 Calculated (dotted line) and measured (thick line) near-normal reflectance spectra for the double-layer $\text{Si}(0.9 \mu\text{m})/\text{SiO}_2(2.45 \mu\text{m})$ on a Si wafer. The thin, full lines are the transmittance spectra for the IR-filters used in the radiometer. (Source: Cited from Högström *et al.* (2005).)

a high temperature CVD process that is thoroughly documented and used on a large scale in the electronics industry. One notices that the agreement between the calculated and measured spectrum is excellent.

8.5 Conclusion

This chapter has treated various options to control either the temperature of a material or the thermal emission from a surface, using optical materials with a variety of spectral properties. Seemingly very different applications may benefit from a surprisingly simple surface treatment or deposition of a thin film.

The applications considered were: thermal solar collector, energy efficient windows, frost preventing coatings and thermal camouflage coatings, all of which have a particular optical selectivity designed for their purposes.

We conclude with a repeated reminder that radiation is only one mechanism out of three that control the equilibrium temperature. Convection from wind has already been mentioned as a threat for effective radiative cooling applications. Conduction should also be considered and arrangements aimed at this are detailed in some of the references. In the case of frost prevention using BeO, the unusually high thermal conductance of this insulator appears to be beneficial. If the dynamics of the frost growing mechanism are considered (Chibuye *et al.*, 1994), BeO and metals conduct the stored heat to the surface more efficiently than in cases of coated glass. The high thermal conductivity might partly explain why metal surfaces are rarely frost-coated.

8.6 References

- Adamson, B.L. (1976), Fordonsruta av glas Swedish patent no. 7609870–7, *Patent- och registreringsverket*, Stockholm.
- Agnihotri O. P. and Gupta B. K. (1981) *Solar Selective Surfaces* (J. Wiley & Sons).
- Arago, F. (1858) *Oeuvres Complètes de François Arago* (Barral, M. J.-A. Eds, Paris) vol. 8.
- Bass, M. (Ed. OSA, 1995) *Handbook of Optics I* (McGraw-Hill, Inc., NY) Ch. 44, fig. 1.
- Carter, W.H. and Wolf E. (1975) Coherence properties of lambertian and non-lambertian sources, *J. Opt. Soc. Am.* **65**(9), 1067–71.
- Chibuye, T., Ribbing, C. G. and Wäckelgård, E. (1994) Reststrahlen band studies of polycrystalline beryllium oxide, *Appl. Opt.* **33**, 5975–81.
- Cornelius, C. M. and Dowling, J. P. (1999) Modification of Planck blackbody radiation by photonic band-gap structures, *Phys. Rev. A* **59**(6), 4736–46.
- Craighead, H. G. and Buhrman, R. A. (1978) Optical properties of selectively absorbing metal/insulator composite films, *J. Vac. Sci. Technol.* **15**(2), 269–71.
- Craighead, H. G., Bartynski, R., Buhrman, R. A., Wojcik, L. and Sievers, A. J. (1979). Metal/Insulator composite selective absorbers, *Sol. Energy Mat.* **1**, 105–124

- Delin, I., Eriksson, O., Ahuja, R., Johansson, B., Brooks, M., Gasche, T., Auluck, S. and Will, J. M. (1996) Optical properties of the group IVB refractory metal compounds, *Phys. Rev. B* **54**, 1673.
- Dobrowolski, J. (1978) Reststrahlen filters in *Handbook of Optics* (Ed's Driscoll, W. and Vaughan, OSA-McGraw-Hill, New York) Ch. 8, sec. 99.
- Driscoll, W. G. and Vaughan W. (1978) Optical properties of the atmosphere (Eds OSA McGraw-Hill, N. Y.) Ch. 14, Fig. 30.
- Duffie, J. A. and Beckman, W. A. (1991) *Solar Engineering of Thermal Processes* (J. Wiley & Sons, 2nd ed.).
- Georgson, M., Roos, A. and Ribbing, C-G. (1991) Titanium nitride based low emissive coatings – a stability comparison, *Glastechnische Berichte* **64**, 147–54.
- Gläser, H. J. (2000) *Large Area Glass Coatings* (von Ardenne Anlagentachnik GMBH, Dresden).
- Granqvist, C G. and Hjortsberg, A. (1981) Radiative cooling to low temperatures: General considerations and application to selectively emitting SiO films, *J. Appl. Phys.* **52**(6), 4205–20.
- Granqvist, C. G. (Ed. 1991) *Materials Science for Solar energy Conversion Systems* (SPIE, Pergamon Press).
- Hamberg, I., Svensson, J. S. E. M., Eriksson, T. S., Granqvist, C. G., Arrenius, P. and Norin, F. (1987) Radiative cooling and frost formation on surfaces with different thermal emittance: Theoretical analysis and practical experience, *Appl. Opt.* **26**, 2131–36.
- Hollands, K. G. T. ,Wright, J. L. and Granqvist, C. G. (2001) Glazing and coatings in *Solar Energy: The State of the Art ISES Position Papers* (Ed. Gordon J. James & James, London) 29–107.
- Harding, G. L., McKenzie, D. R. and Window, B. (1976) The dc sputter coating of solar selective surfaces onto tubes, *J. Vac. Sci. Technol.* **13**(5), 1073–75.
- Hass, G., Schroeder, H.H. and Turner, A. F. (1956) Mirror coatings for low visible and high infrared reflectance, *J. Opt. Soc. Am.* **40**(1), 31–35.
- Heads, A. K. (1960) (ed.) *Methods and Means for Producing Refrigeration by Selective Radiation* (Gov. of the Commonwealth, Canberra).
- Heald (2003) Where is the ‘Wien Peak’, *Am. J. Phys.* **71**(12), 1322–23.
- Högström, H., Forssell, G. and Ribbing, C. G. (2005) Realization of selective low emittance in both thermal atmospheric windows, *Opt. Eng.* **44**(2), 026001–1–7.
- Jarzebski, Z. M. and Marton, J. P. (1976) Physical properties of SnO₂ materials *J. Electrochem. Soc.* **123**, 1–3, July 199C, Sept. 299C, and Oct. 333C.
- Jelle, B. P., Hynd, A., Gustavsen, A., Arasteh, D., Goudey, H. and Hart, R. (2012) Fenestration of today and tomorrow: A state-of-the-art review and future research opportunities, *Sol. Energy Mat. Solar Cells* **96**, 1–28.
- John, S. (1984) Electromagnetic absorption in a disordered medium near a photon mobility edge, *Phys. Rev. Lett.* **53**, 2169–73.
- Karlsson, B. (1981) Optical properties of solids for solar energy conversion, Thesis, Acta Universitatis Upsaliensis 620, Uppsala, Sweden.
- Karlsson, B., Valkonen, E., Karlsson, T. and Ribbing, C-G. (1981) Materials for solar-transmitting heat-reflecting coatings, *Thin Solid Films* **86**, 91–8.
- Karlsson, B. and Ribbing, C-G. (1982) Optical properties of transparent heat mirrors based on thin films of TiN, ZrN and HfN, *Proc. Soc. Photo-Opt. Instrum. Eng.* **324**, 52.
- Karlsson, B., Shimshock, R. P., Seraphin, B. O. and Haygarth J. C. (1983) Optical properties of CVD-coated TiN, ZrN and HfN, *Sol. Energy Mater.* **7**, 401.

- Lampert, C. M. and Washburn, J. (1979) Microstructure of a black chrome solar selective absorber, *Sol. Energy Mat.* **1**, 81–92.
- Meinel, A. B. and Meinel, M. P. (1976) *Applied Solar Energy: An Introduction* (Addison-Wesley).
- McCluney, R. (1994) *Introduction to Radiometry and Photometry* (Artech House).
- McDonald, G. E. (1974) Refinement in black chrome for use as a solar selective coating, *NASA Report TM X-3136*, Lewis Res. Ctr. Cleveland, Ohio.
- Niklasson, G. A. and Granqvist, C. G. (1983) Surfaces for selective absorption of solar energy: an annotated bibliography 1955–1981, *J. Mat. Sci.* **18**, 3475–534.
- Niklasson, G. A. (1991) Optical properties of of inhomogenous two-component materials, *Granqvist*, 7–43.
- Palmer, J. H. (1995) The measurement of transmission, absorption, emission and reflection in *Handbook of Optics II* (Ed. M. Bass, OSA McGrawHill Inc.) Ch. 25, 25.1–25.25.
- Pulker, H. K. (1984) *Coatings on Glass* in Thin films Sc. and Techn., 6 (Elsevier, Amsterdam).
- Ribbing, C. G. (1990) Beryllium oxide: A frostpreventing insulator, *Opt. Lett.* **15**, 882–4.
- Ribbing, C. G. and Wäckelgård, E. (1991) Reststrahlen bands as property indicator for dielectric coatings, *Thin Solid Films* **206**, 312–17.
- Ribbing, C. G., Staaf, Ö. and Andersson, S. K. (1995) Selective supression of thermal emission from radomes and materials selection therefore, *Opt. Eng.* **34**(11), 3314–22.
- Ribbing, C. G. (1999) Getting the sunshine right, Proc. SPIE vol. **3789**, *Solar Optical Materials XVI* Denver, 22 July, 84–90 (Ed. C. M Lampert).
- Roos, A., Chibuye, T. and Karlsson, B. (1983) Properties of oxidized copper surfaces for solar applications I & II *Sol. En. Mat.* **7**, 453–65 and Roos, and Karlsson, B. (1983) *ibid* II, 467–80.
- Seraphin, B. O. Ed (1979) *Solar Energy Conversion Solid-State Physics Aspects* (Springer-Verlag, Topics in Applied Physica, Vol. 31).
- Siegel, R. and Howell, J. R. (1981) *Thermal Radiation Heat Transfer* (McGrawHill, 2nd ed.) Sections 2.4.4–2.4.10.
- Sievers, A. J. (1979) Spectral selectivity of composite materials in *Solar Energy Conversion Solid-State Physics Aspects* (Ed. B. O. Seraphin, Springer-Verlag, Topics in Applied Physica, Vol. 31), 56–114.
- Soffer, B. H. and Lynch, D. K. (1999) The spectral optimization of human vision: Some paradoxes, errors and resolutions, *Am. J. Phys.* **67**(11), 946–53.
- Staaf, Ö., Ribbing, C. G. and Andersson, S. (1996) Temperature dependence of the band emittance for nongray bodies, *Appl. Opt.* **35**(31), 6120–25.
- Tabor, H. (1955) Solar energy collector design, *Bull. Res. Counc. Isr., Sect. C; Journal Vol.: 5C:1*.
- Trombe, F. (1967) Perspectives sur l'utilisation des Rayonnements Solaires et Terrestres dans Certaines Régions du Monde, *Rev. Gen. Therm.* **6**, 1285.
- Valkonen, E., Ribbing, C. G. and Sundgren, J-E. Optical constants of thin TiN films: thickness and preparation effects, *Appl. Opt.* **25**(20), 3624–30.
- Wäckelgård, E. and Hultmark, G. (1998) Industrially sputtered solar absorber surface, *Solar Energy Mat. Solar Cells* **54**, 165–70.
- Wolf, E. and Carter, W. H. (1975) Angular distribution of radiant intensity from sources of different degrees of spatial coherence, *Opt. Commun.* **13**(3), 205–9.

- Wolfe, W. L. (1989) Radiation theory in *The Infrared Handbook*, Ch 1, 1–38 (Ed. W.L. Wolfe and G. J. Zissis, ERIM, Dept. of the Navy).
- Yablonovitch, E. (1987) Inhibited spontaneous emission in solid state physics and electronics, *Phys. Rev. Lett.* **58**, 2059–62.
- Zalewski, E. F. (1995) Radiometry and photometry in *Handbook of Optics II* (Ed. M. Bass, McGraw-Hill Inc. 1995), Ch. 24, 1–49.
- Zhang, Y.-W., Zhang, C.-G. and Klemas, V. (1986) Quantitative measurements of ambient radiation, emissivity and thermal temperature of a greybody: measurements and experimental results, *Appl. Opt.* **25**, 3683–89.
- Zhang, Q.-C., Zhao, K., Zhang, B.-C., Wang, L.-F., Shen, Z.-L., Lu, D.-Q., Xie, D.-L., Zhou, Z.-J. and Li, B.-F (1998) A cylindrical magnetron sputtering system for depositing metal-aluminium nitride cermet solar coatings onto batches of tubes, *J. Vac. Sci. Technol. A* **16**(2), 628–32.

DOI: 10.1533/9780857097316.2.391

Abstract: Their physical origin distinguishes chemical colors and structural colors, the latter being subdivided into prismatic colors and interference colors. Colors of optical coatings are interference colors. A short history of interference colors is given starting from Isaac Newton, and then continuing with Thomas Young (interference in optics), Leopoldo Nobili (electrochemical ‘metallocromia’), David Brewster, A. Michel-Lévy (interference color chart), J. F. Gabriel Lippmann (interference color photography) and Dobrowolski (anticounterfeiting coatings). A concise review of standard colorimetry (psychophysical and psychometric colorimetry) is given with the aim of introducing the colorimetry of the optical coatings. Gonio-apparent color measurement technique is presented with the updated multi-angle spectrophotometers. As an example, classical computations of colors of optical coatings are shown.

Key words: colorimetry, interference color, structural color, optical coating color.

9.1 Introduction

The color of non-luminous objects in nature is due mainly to absorption, diffusion, refraction and diffraction of light. Traditionally, the colors are called *chemical colors* if caused by pigment absorption and *structural colors* if produced by other fundamental optical processes such as reflection, refraction, interference, diffraction and scattering (Kinoshita *et al.*, 2008). In particular, colors are called *prismatic colors* if caused by refraction of white light through a prism and *interference color* if caused by interference effects.

Interference color effects are produced when a material is scored with fine parallel lines formed of one or more parallel thin layers, or otherwise composed of microstructures on the scale of the color wavelength. In nature structural colors are those of the feathers of many birds, of certain butterfly wings and of beetle shells. These colors depend on the viewing angle and often give rise to an iridescent effect, as in peacock feathers, soap bubbles, films of oil and mother of pearl. The color of the optical coatings is an

interference color and belongs to the *gonio-apparent* or *special-effect* colors. Since 1942, electron microscopy has been used to see the structure of materials and to understand structural colors.

Generally, industrial colorimetry does not deal with interference color and the usual colorimetric instruments are inadequate for measuring it. Only recently, with the new mica-pigment coatings, has colorimetry been considered in the measurement of interference color and new multi-angle spectrophotometers have been produced, mainly for the metallic and mica-pigment finishes applied to automobiles.

Section 9.2 is dedicated to a short historical review of interference color science. Section 9.3 is a general introduction to basic colorimetry, whose standardization is made by Commission Internationale de l'Éclairage (CIE), subdivided in three parts: *psychophysical colorimetry*, *psychometrical colorimetry* and *instrumental color measurement*. Section 9.4 deals with colorimetry of interference colors and generally gonio-apparent colors. For a complete and detailed optical characterization of interference color, the measurement of *bidirectional transmittance* and *reflectance* is needed.

9.2 The development of the understanding of interference color

Interference-color science and color-vision science have parallel, though very different, histories. The understanding of interference colors relates to a physical knowledge, the understanding of human color vision relates to the connection between optical radiations and visual sensations and involves many disciplines: optics, physiology and psychology. Both histories started with Isaac Newton (1642–1727). This section considers, in a very concise way, the history of the color of thin films of transparent materials. Before Newton we had only an intriguing description of the phenomenon, mainly due to Boyle and Hooke:

1. Boyle (1627–1691) seems to have first observed that thin bubbles of the essential oils, spirit of wine, turpentine and soap and water, exhibited beautiful colors and he then succeeded in blowing glass so thin as to show the same hues.
2. Hooke (1635–1703) obtained equally thin films that exhibited the same brilliant color over their whole surface.
3. Brereton (1631–1679) observed the colors of the thin films which the action of the weather produces upon glass (*weathering* phenomenon).

9.2.1 Isaac Newton (1642–1727)

Newton (1704) dedicated the second book of his *Opticks, or a Treatise of the Reflections, refractions, Inflections & Colours of Light*, to the *Observations Concerning the Reflections, Refractions, and Colours of Thin Transparent Bodies*. He made very accurate measurements of the thickness of layers of air, water and glass in relation to the reflected and transmitted colors, and, between these color pairs, he described the *complementary color* correspondence. His ‘figure 3’ is famous, regarding the well known Newton rings, where the sequence of the transmitted and reflected colors are given up to the third order in graphical relation with the air thickness between two glass bodies (Fig. 9.1).

Newton, although described these phenomena well and measured them accurately, was unable to give a complete explanation and suggested the definition of a new quantity, the ‘fits’. Let us recall his definition and the subsequent proposition XIII from the *Opticks* book (Newton, 1704, p. 256):

DEFINITION

*The returns of the disposition of any Ray to be reflected I will call its **Fits of easy Reflexion**, and those of its disposition to be transmitted its **Fits of easy Transmission**, and the space it passes between every return and the next return, the **Interval of its Fits**.*

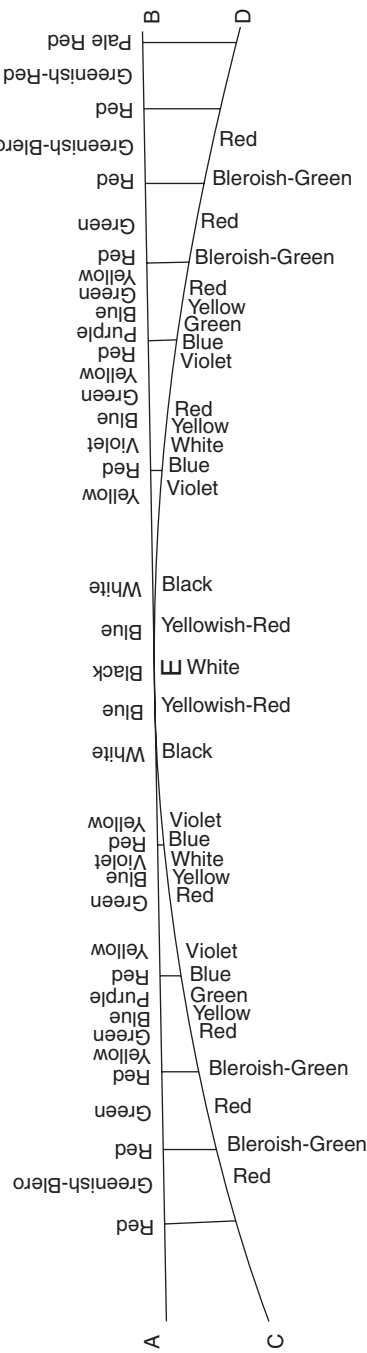
PROP. XIII.

The reason why the Surfaces of all thick transparent Bodies reflect part of the Light incident on them, and refract the rest, is, that some Rays at their Incidence are in Fits of easy Reflexion, and others in Fits of easy Transmission.

Although Newton saw a relationship between colors and thicknesses that to us today appears very accurate and so clear as to lead us to the correct interpretation of these phenomena, Newton gave only a very hypothetical origin of the fits, as a hidden internal degree of freedom of the light (Newton, 1704, p. 257):

... And hence Light is in Fits of easy Reflexion and easy Transmission, before its Incidence on transparent Bodies. And probably it is put into such Fits at its first emission from luminous Bodies, and continues in them during all its progress. ...

A very important item in the Newton analysis is the description of the gonio-dependence of these phenomena. Newton let himself imagine the origin of all the colors of natural bodies, as produced by the same mechanisms present in the thin transparent plates. In Part III of the second book of his *Opticks*, he wrote *Of the Permanent Colours of Natural Bodies and the*



9.1 Newton's representation of the colors of the reflected and transmitted lights when a convex lens is pressed against a glass plate. The illuminating light is constituted by parallel rays of white light coming down from the top. Transmitted colors and reflected colors constitute complementary color pairs. These colors, ordered according to this sequence, are known as 'Newton's color series'. (N.B. This name is not referring to the seven colors of solar spectrum reproduced by Newton through prism dispersion.)

Analogy Between Them and the Colours of Thin Transparent Plates, and considered *How the Phaenomena of Thin Transparent Plates Stand Related to Those of All Other Natural Bodies*. In proposition III (Newton, 1704, p. 223) he described a possible microscopic structure of matter:

Between the parts of opake and colour'd Bodies are many Spaces, either empty or replenish'd, with Mediums of other Densities; as Water between the tinging Corpuscles wherewith any Liquor is impregnated, Air between the aqueous Globules that constitute Clouds or Mists; and for the most part Spaces void of both Air and Water, but yet perhaps not wholly void of all Substance between the parts of hard Bodies.

In proposition IV (Newton, 1704, p.225):

The parts of Bodies and their Interstices must not be less than of some definite bigness, to render them opake arid colour'd.

and in proposition V (Newton, 1704, p.226):

The transparent parts of Bodies according to their several Sizes reflect Rays of one Colour, and transmit those of another, on the same grounds that thin Plates or Bubbles do reflect or transmit those Rays. And this I take to be the ground of all their Colours.

The implausibility of this Newtonian imagination was shown by Thomas Young one century later.

9.2.2 Thomas Young (1773–1829)

A new vision of light was necessary to understand the color phenomena and Young's contribution to color science (physiological hypothesis of three kinds of receptors in the human retina, that Young called 'fibers'), and to optics in general (hypothesis of a wave nature of the light), was very great, similar to that of Newton.

Let us recall the hypotheses and the most interesting propositions of the wave theory of light given by Young in his Bakerian Lecture on the 'Theory of Light and Colors' read November 12, 1801 (Young, 1802a):

HYPOTHESIS I

A luminiferous ether pervades the universe, rare and elastic in a high degree.

HYPOTHESIS II

Undulations are excited in this ether whenever a body becomes luminous.

HYPOTHESIS III

The sensation of different colors depends on the different frequency of vibrations excited by light in the retina.

HYPOTHESIS IV

All material bodies have an attraction for the ethereal medium, by means of which it is accumulated within their substance, and for a small distance around them, in a state of greater density but not of greater elasticity.

PROPOSITION I

All impulses are propagated in a homogeneous elastic medium with an equable velocity.

PROPOSITION II

An undulation conceived to originate from the vibration of a single particle must expand through a homogeneous medium in a spherical form, but with different quantities of motion in different parts.

PROPOSITION III

A portion of a spherical undulation, admitted through an aperture into a quiescent medium, will proceed to be further propagated rectilinearly in concentric superficies, terminated laterally by weak and irregular portions of newly diverging undulations.

PROPOSITION IV

When an undulation arrives at a surface which is the limit of mediums of different densities, a partial reflection takes place proportionate in force to the difference of the densities.

PROPOSITION VIII

When two undulations, from different origins, coincide either perfectly or very nearly in direction, their joint effect is a combination of the motions belonging to each.

Young's interpretation of the colors of thin bodies was based on a wave description of light. These colors are produced by interference of two light waves, one reflected at the first surface and the second reflected at the second surface, and such an interference is constructive or destructive, exactly as happens for the waves on the surface of the water. The very new concept of *optical path* is given. Let us recall the *universal law* written by Young (Young, 1802b, s. 376, p.112):

When two portions of the same light arrive at the eye by different routes, either exactly or very nearly in the same direction, the appearance or disappearance of various colours is determined by the greater or less difference in the lengths of the paths: the same colour recurring, when the intervals are multiples of a length, which, in the same medium, is constant, but in different mediums, varies directly as the sine of refraction.

For Young, the waves were longitudinal. The complete understanding of the nature of light was possible only with Maxwell's electromagnetism theory and Einstein's photon hypothesis. Finally, all the mistakes were corrected: light waves are transversal and today the hidden 'Fits' are considered only as a working hypothesis (N.B. the hidden variables are also considered today in work hypotheses for describing unexplained aspects of quantum mechanics).

Optical interference has been investigated deeply and widely during the entire nineteenth century. The detailed history is too long for a section of a chapter on optical coating colorimetry. However, the contribution of some other scientists merit recognition.

9.2.3 Leopoldo Nobili (1784–1835)

A large part of Nobili's work is related to the color of optical coatings and, in particular, he discovered the *electro-chemical appearances* and began a new artform called *Metallocromia* and presented it at the French Institute in 1828 (Nobili, 1830). The Nobili work describes the production of optical coatings on metals by an electrochemical method and the visual classification of the colors in relation to the thickness of the coatings. He produced a scale, or gamut, of 44 colors of coatings on steel with increasing thickness, carefully controlled by electrochemical deposition with constant current and increasing time. Of course, Nobili had to compare his color scale, shown here as Fig. 9.2, with that given by Newton (Fig. 9.1). Some discrepancies exist, of which Nobili was aware, but gave no reason (he had to consider the superposition of the waves of spectral lights, following the Young hypotheses).

Since these colors are dependent on the incidence angle, Nobili called these colors *iridescent* (in Italian 'cangiante'). These phenomena induced him to enlarge the investigation to the interference colors in insects and the feathers of birds. For Nobili, the polarization of colored light was decisive for the classification of the different mechanisms producing colored light. The analysis of the polarization was made through a birefringence layer of Iceland spar (Nobili, 1830).

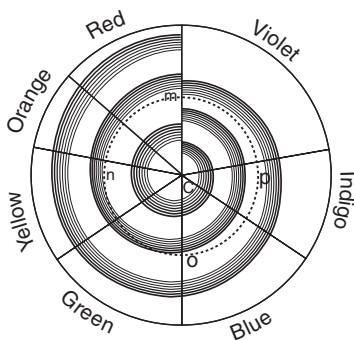
Metallocromia is an art and Nobili dedicated some effort into the production of pieces of this art. One piece is reproduced here (Plate I, see colour section between pages 404 and 405).

9.2.4 David Brewster (1781–1868)

A review of all the effort made towards understanding the nature of light by Grimaldi, Newton, Young and Fresnel was given by Brewster (1853) in his *Treatise on Optics*. Chapter XIII of this book was dedicated to the *Colours of Thin Plates*. With his figure 62 (Brewster, 1853, p. 125), Brewster

44	Pinkish-lacquer
43	Yellow-green
42	Green
41	Violetish-green
40	Violetish-carmine
39	Pinkish-carmine
38	Pinkish-orange
37	Greenish-orange
36	Orange-green
35	Yellow-green
34	Yellowish-green
33	Green
32	Greenish-purple
31	Purplish-carmine
30	Carmine with a hint of turquoise
29	Purplish-carmine
28	Vivid carmine
27	Carmine
26	Orange-carmine
25	Orange-red
24	Red-orange
23	Reddish-orange
22	Orange
21	Orange-yellow
20	Vivid yellow
19	Yellow
18	Very light yellow
17	Sky blue with a hint of yellow
16	Sky blue
15	Light blue
14	Blue
13	Intense blue
12	Indigo
11	Violet
10	Violetish-red
9	Violetish-ochre
8	Ochre
7	Copper red
6	Vivid fulvous
5	Fulvous
4	Vivid blond
3	Gold blond
2	Blond
1	Silver blond

9.2 Nobili's metallocromia color gamut (termed in Italian 'Scala cromatica') of the lights reflected from 44 coatings on steel with increasing thickness, subdivided into four orders (Nobili, 1830). The illuminating light is constituted by parallel rays of white light almost orthogonal to the coatings and seen almost orthogonally.



9.3 Brewster's diagram with the correspondence of the color fringes to the plate thicknesses, and rotating wheel for producing a visual simulation of the color fringes (Brewster, 1853).

summarized in a diagram the relationship between colors and thin plate thicknesses (Fig. 9.3). The interference fringes are drawn on a disk at a distance from the center proportional to the corresponding plate thickness and, by choosing a circle on the disk (represented by a dashed line in Fig. 9.3), it is possible to evaluate the contribution of the different spectral lights to the resulting color for a thickness equal to the radius of the chosen circle. Moreover, the sectors of these wheels are proportional to the amounts of spectral light constituting the white light and the fringes drawn on the wheel have the same spectral color, therefore, ‘if we now suppose all these coloured sectors to revolve rapidly round C as a centre, the effect of them all thus mixed should be the production of the coloured rings as seen by white light’.

9.2.5 Auguste Michel-Lévy (1844–1911)

Pleochroism is the term used to describe the color variation for destructive interference with the polarization direction of the light, which depends on the orientation of the material in the light path and is a characteristic of anisotropic materials only. The view in a microscope of transparent or translucent materials in plane-polarized light is similar to the view in natural light until the specimen is rotated around the microscope optical axis. With the rotation, the brightness and/or color of the specimen under examination change. This effect, termed the *pleochroic effect*, is useful for the identification of a wide variety of materials. An example of a material showing this effect is crocidolite, commonly known as blue asbestos.

Michel-Lévy and Lacroix first gave the *Interference Color Chart* in a book, entitled ‘Les Mineraux des Roches’ (Lévy and Lacroix, 1888). Today, after more than a century, the *Michel-Lévy Interference Color Chart* (Plate II, see colour section between pages 404 and 405), also known as the *Michel-Lévy Table of*

Birefringence, remains in use by analytical microscopists and the most important manufacturers of microscopes also supply this interference color chart.

Polarization colors result from the interference of the two components of light split by the anisotropic specimen and may be regarded as white light minus those colors that are interfering destructively. Interference colors vary in hue with the retardation according to the sequence known as Newton's series (Fig. 9.1). Since the Michel-Lévy chart shows the interrelationships between thickness, birefringence and interference color, the microscopists can determine any one from the chart if they know the other two (Plate II, see colour section). The early applications of the Michel-Lévy Interference Color Chart were in the fields of mineralogy and petrology, for the identification of minerals. Today the chart is used as an aid, not only for the identification of minerals, but also for synthetic textile fibers, chemicals, food ingredients, biological agents, drugs, catalysts, ores, fertilizers, explosives, etc.

9.2.6 J. F. Gabriel Lippmann (1845–1921)

Lippmann was the inventor of *interference color photography* (Connes, 1987) and for this reason was awarded the Nobel Prize in Physics in 1908. He was able to record colors as standing light waves in an emulsion. This technique is very interesting from a scientific point of view, but was not very effective for color photography since the technique for practical use was complicated and the exposure times were too long. Moreover difficulties were encountered in viewing and copying the photographs. He produced four color photographs which, after one century, remain very well preserved.

To understand Lippmann photography, let us consider a monochromatic optical image on a photosensitive emulsion layer that is put on a mirror of mercury. A constructive interference is obtained by the light back-reflected by the mirror and the light reflected by the other side of the emulsion. The standing wave of the interfering light produces a very fine fringe pattern throughout the emulsion with a periodic spacing of $\lambda/(2n)$ that has to be recorded (λ is the wavelength of light in air and n is the refractive index of the emulsion). The color information is stored locally in this way. The larger the separation between the fringes, the longer the wavelength of the recorded part of image information will be. A polychrome recording is more complex, and was first treated mathematically by Lippmann. The developed photograph lit by white light shows different colors in different parts of the recorded image. The light reflected from the recorded fringes creates different colors corresponding to the original ones that produced the recorded interference fringes. The illumination and the view must have normal incidence and if the angle changes, the colors of the image change (iridescence phenomenon).

9.2.7 Soap bubbles

With regard to soap bubbles, history is rich with mathematical attempts to describe their shape. In particular, this problem was called the *Plateau problem*, taken from the name of the mathematician Antoine Ferdinand Plateau, who published two volumes on this topic (Plateau, 1873).

9.2.8 Lens optical coatings

The evolution of lenses for photographic use, and not only, in the last half century, obtained by means of optical coatings is so important in practical terms that it can be considered a historical step in optics. A simple computation of the light reflected in an objective lens and in any complex refractive optical system, made according to Fresnel's laws, shows that the stray light increases significantly with the number of lenses. This was a very important practical problem and was solved by optical coatings conceived to minimize light reflection on the surfaces of the lenses. A single-layer antireflection coating on the air-glass surfaces of a modern objective made of high refractive index glasses, centered at $\lambda = 520$ nm (magenta coating), reduces the average reflection loss to less than 10%, which is acceptable in many practical situations. However, the magenta coloration is distracting and three or more coating layers are necessary for an acceptable achromatization. These problems in antireflection coatings are solved only by a proper application of colorimetry (Dobrowolski *et al.*, 1979).

The colorimetric computation of interference colors is particularly complex and only in the 1950s do we find computations in the literature related to simple coatings, monolayer, bi-layers and tri-layers. These historic works are considered in Section 9.4.

9.2.9 Thin film anti-counterfeiting coatings

The last historical application of interference colors that we will consider is in the anti-counterfeiting of documents and valuable papers, and this was so successful that today we see interference-color figures on banknotes, credit cards, trademarks and many valuable documents. Interference colors are effective against color copying by printers, copiers or cameras, and lithographic reproduction. These kinds of color copying are unable to reproduce optical effects, which include raised intaglio printed line patterns, that reveal special designs or messages when viewed obliquely; special geometric patterns on documents printed at different screen frequencies, that become apparent only when combined with the raster of reproduction

machines; scrambled printed messages, that become intelligible only when a prismatic reader is placed in contact with the document; and holographic devices that present different or changing images when viewed from different angles (Dobrowolski *et al.*, 1989). Colorimetric properties of thin film security devices are very important, because they are easily recognized and reproduced with difficulty. The main constraints in the production of these thin film security devices is imposed by the color detection capability of the human visual system, and are a compromise between the luminance factor and spectral purity: any purity increment decreases the luminance detection (Dobrowolski *et al.*, 1973, 1989).

9.3 Overview of basic colorimetry

Many text books, written by outstanding authors, treat color vision and colorimetry from different points of view: Kaiser and Boynton (1996); Valberg (2005); OSA Committee (1963); Le Grand (1968); Wyszecky and Stiles (1982); Wyszecky and Judd (1975); MacAdam (1986, 1993); McDonald (1987); Sèvre (1996); Kuehni (1997, 2003); Hunt and Pointer (2011); Berns (2000); Shevell (2003); Schanda (2007); Kuehni and Schwarz (2008); Malacara (2002); CIE 15:2004.

Any colorimetric treatment of optical coating colorimetry needs a short introduction to standard basic colorimetry. For practical reasons, this introduction does not follow the historical line and is limited to color vision, called *photopic vision*.

Color is a visual sensation, that is a purely subjective and incommunicable entity. Moreover the human visual system has an adaptation to the visual situation with the consequence that any color judgment is relative to the visual situation itself. We should consider the human visual system to understand this phenomenon. Standard colorimetry proceeds along two different paths, that can be termed *psychophysical* and *psychometric*.

Physiology explains that psychophysical colorimetry is based only on the activation of the three kinds of photosensitive cones, that is, the first step in visual processing, while psychometric colorimetry also involves subsequent stages, not yet completely understood. Moreover the retina is a non-homogeneous tissue that in the central region, termed *macula lutea*, has a yellow inert pigment filtering the light before activating the cones. Therefore, two different kinds of colors exist: one for the macular region (visual field of 2°, and always lower than 4°), and one for the extra macular region (visual field of 10°). By combining these distinctions, four standard colorimetries exist, as shown in Table 9.1.

9.3.1 Psychophysical colorimetry of color stimuli

Psychophysical colorimetry is based on the phenomenon, termed *color matching*, according to which different visible electromagnetic radiation (lights, *color*

Table 9.1 Different colorimetries with reference to the vision zones, visual fields and CIE standard systems

	<i>Psycho-physical system</i>	<i>Psycho-metric system</i>
	1 st visual zone: transduction	2 nd visual zone: illuminant adaptation
Visual field	<i>Basic phenomena: color matching</i>	<i>Basic phenomena: color difference / color scales</i>
	Macular vision (visual field <4°) Standard Observer CIE 1931 (X, Y, Z)	CIELUV system (L^*, u^*, v^*) CIELAB system (L^*, a^*, b^*)
	Extra-macular vision(10° visual field) Supplementary Standard Observer CIE 1964 (X_{10}, Y_{10}, Z_{10})	CIELUV system ($L^*_{10}, u^*_{10}, v^*_{10}$) CIELAB system ($L^*_{10}, a^*_{10}, b^*_{10}$)

Note: Apex '10' is referred to as the 10° visual field.

stimuli) produce the same color sensation. Physiology explains that any color sensation is producible by mixing in a proper ratio three independent lights, and three lights are independent if none of these lights is matched by a mixture of the other two lights. *Trichromacy* means that three is the highest number of independent colors. Color matching is independent of the visual situation, but not the color sensation. The classical visual situation in laboratory is in *aperture mode*, that is, the pair of colors to be matched is viewed in a bipartite field through a hole in a dark room. The color specification in psychophysical colorimetry is given by three numbers, that represent the amounts of the three lights entering the mixture. Grassmann's laws state that these sets of three numbers, termed *tristimulus values*, are the elements of a three-dimensional linear vector space, termed *tristimulus space*. Many different reference frames are possible and therefore many different color specifications with different meanings. Typical specifications are outlined below:

- (L, M, S)

Here L , M and S , termed *cone activations*, are proportional to the (positive) numbers of photons absorbed in the unit of time by the three kinds of photosensitive cells (cones) in the retina; L , M and S refer to Long, Medium and Short wavelength-sensitive cones, respectively. This reference frame is related to the physiology and is used mainly by physiologists.

Light is measured outside the eye and the visible range of wavelength is 360–760 nm. The light entering the eye is named *color stimulus* and is physically represented by a spectral radiance $L_{e,\lambda}$ [W/(sr m² nm)]. Cone activation is based on *Rushton's univariance principle*, that says that the visual effect of a radiation depends only on the number of absorbed photons and is independent of the photon energy, that is, a photon, once absorbed by the pigment

of a cone, triggers a photochemical process, which is independent of the photon energy. Photons with different energy have their own probability of being absorbed and consequently produce different visual effects. In a defined visual situation, the cone activation is in one-to-one correspondence with the color sensation, therefore the cone activations (L, M, S) specify the color sensation.

The *tristimulus values* (L, M, S) are defined by three integrals

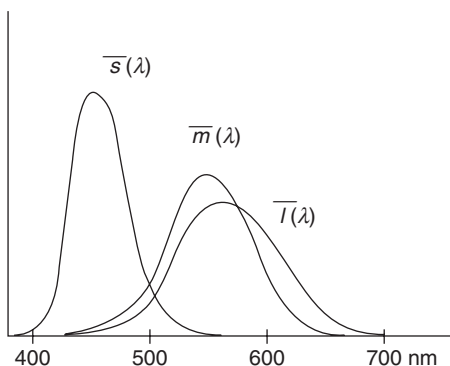
$$\begin{aligned} L &= \int_{380}^{780} L_{e,\lambda} \bar{l}(\lambda) d\lambda \text{ for L cones, } M = \int_{380}^{780} L_{e,\lambda} \bar{m}(\lambda) d\lambda \text{ for M cones,} \\ S &= \int_{380}^{780} L_{e,\lambda} \bar{s}(\lambda) d\lambda \text{ for S cones} \end{aligned} \quad [9.1]$$

where the functions $\bar{l}(\lambda)$, $\bar{m}(\lambda)$ and $\bar{s}(\lambda)$ (Fig. 9.4), named *color-matching functions* (CMFs), are the spectral sensitivities of the cones L, M and S, respectively, and also take into account the light absorption of the lens of the eye and of the macula lutea. The CMFs are normalized to give $S = M = L = 1$ for the *equal-energy radiance* $L_{e,\lambda} = 1$, therefore representing the monochromatic components of the equal-energy stimulus $(\bar{l}(\lambda), \bar{m}(\lambda), \bar{s}(\lambda))$ in the tristimulus space (Figs 9.4 and 9.5), that is, at any given wavelength λ , the CMFs represent the cone activations produced by a monochromatic radiation at equal wavelength and with unitary radiance.

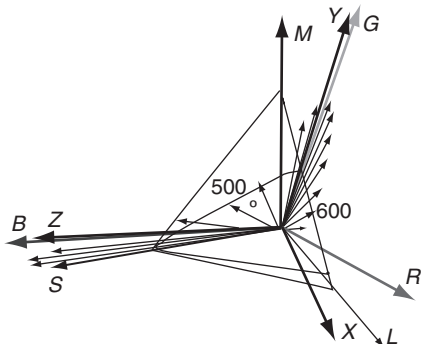
The addition of color stimuli is represented in the tristimulus space by the addition of the corresponding vectors.

The expressions [9.1] that define the (L, M, S) vectors say that the correspondence between color stimuli and tristimulus vectors is many to one, that is, different radiances can produce equal color sensation. This phenomenon is named *metamerism*.

The length of the vectors is related to the intensity of the color stimuli and the direction is related to chromatic sensation. Since the vector directions



9.4 Color-matching functions in the fundamental reference frame for macular vision and CIE 1931 observer.



9.5 Perspective view of the tristimulus space in the fundamental reference frame with tristimulus vectors related to monochromatic color stimuli with unitary radiance, with the plane of the chromaticity diagram, the spectrum locus, the *RGB* and *XYZ* axes of the other reference frames.

are in one-to-one correspondence with the intersection points between the tristimulus vectors and a plane, these points constitute a diagram (Fig. 9.5), termed a *chromaticity diagram*, representing the chromaticity, the practical role of which is very important. The chromaticities of the monochromatic lights are points of a line named the *spectrum locus* and the segment between short wavelength and long wavelength regions relates to the *purple hues*.

- (R, G, B)

Here R , G and B are the intensities of three lights, one red, one green and one blue; very saturated colors require that one of these numbers is negative; this specification is typical for monitors, computers, scanners, photo-cameras, and so on; many different RGB reference frames exist, that must not be confused.

Figure 9.5 shows the tristimulus space in the fundamental reference frame and the vectors \mathbf{X} , \mathbf{Y} , \mathbf{Z} and \mathbf{R} , \mathbf{G} , \mathbf{B} representing the axes of the XYZ and RGB reference frames, respectively. The RGB reference frame is defined by three lights, one red, one green and one blue, and is termed the *instrumental reference frame* because these three lights are used as reference and this choice is proper for the laboratory. The passage between the LMS reference frame and, for example, RGB is made by the matrix that renders mutually orthogonal the \mathbf{R} , \mathbf{G} , \mathbf{B} vectors with the constraint that $\mathbf{R} = \mathbf{G} = \mathbf{B} = 1$ for the *equal-energy radiance* $L_{e,\lambda} = 1$. (In some cases, where the white light has a meaningful role, as in the television standards, the same constraint regards the radiance of the chosen white light.) The same linear transformation is made on the CMFs and $(\bar{l}(\lambda), \bar{m}(\lambda), \bar{s}(\lambda))$ are transformed into $(\bar{r}(\lambda), \bar{g}(\lambda), \bar{b}(\lambda))$. The tristimulus values are defined by the integrals

$$R = \int_{380}^{780} L_{e,\lambda} \bar{r}(\lambda) d\lambda, G = \int_{380}^{780} L_{e,\lambda} \bar{g}(\lambda) d\lambda, B = \int_{380}^{780} L_{e,\lambda} \bar{b}(\lambda) d\lambda \quad [9.2]$$

and the chromaticity coordinates are represented by *baricentric coordinates* (r, g, b)

$$r = \frac{R}{R+G+B}, \quad g = \frac{G}{R+G+B}, \quad b = \frac{B}{R+G+B} = 1 - r - g \quad [9.3]$$

Historically, the CMFs have been measured in an RGB reference frame by a color-matching technique, because in this kind of reference frame it is possible to match a unitary spectral light by a mixture of three reference spectral lights, one red, one green and one blue. The CMFs were first measured by J. C. Maxwell in 1860. Two sets of standard CMFs exist related to the 2° visual field *CIE 1931 standard observer* and denoted by $(\bar{r}(\lambda), \bar{g}(\lambda), \bar{b}(\lambda))$, and to the 10° visual field *CIE 1964 standard observer* and denoted by $(\bar{r}_{10}(\lambda), \bar{g}_{10}(\lambda), \bar{b}_{10}(\lambda))$, respectively (CIE 15:2004). All the quantities related to the standard observer CIE 1931 have no denoting apex while those related to the standard observer CIE 1964 have the apex 10.

A linear transformation exists between the tristimulus values (L, M, S) and (R, G, B).

- (X, Y, Z)

Here X, Y and Z are the tristimulus values (always positive) related to three standard ‘imaginary’ reference vectors $\mathbf{X}, \mathbf{Y}, \mathbf{Z}$, properly defined by the CIE in 1931, where \mathbf{Y} represents the *luminance*.

The CIE 1931 colorimetric system was realized by embedding photometry in colorimetry. The *photometry* relates the luminosity sensation of a light defining the *luminance*, the quantity that would represent the brightness associated the radiance $L_{e,\lambda}$,

$$L_v = k_m \int_{380}^{780} L_{e,\lambda} V(\lambda) d\lambda \text{ cd/m}^2 \quad [9.4]$$

with

- $V(\lambda) = \text{relative photopic luminous efficiency function}$ that defines the *standard photometric observer CIE 24* (Fig. 9.5)
- $K_m = 683 \text{ lumen/watt}$

Abney's law states that the luminance of a color stimulus obtained as a sum of many stimuli is equal to the sum of the corresponding luminances. This law induced scientists to represent luminance as a linear weighted sum of the tristimulus values:

$$L_v = L_L L + L_M M + L_S S = L_R R + L_G G + L_B B \quad [9.5]$$

This equation, is known as Schrödinger's 'Helligkeit' equation (Schrödinger, 1926), where the weights L_L, L_M, L_S, L_R, L_G and L_B are known as Exner's coefficients. Consequently this led scientists to search for a reference frame XYZ such that

- the Y component of the stimulus is proportional to the luminance L_v , that is,

$$L_v = K_m Y \text{ cd/m}^2 \text{ and } \bar{y}(\lambda) = V(\lambda) \quad [9.6]$$

where $\bar{y}(\lambda)$ is the second color-matching function of XYZ system,

- the X, Y and Z axes are mutually orthogonal,
- the X and Z axes belong to the zero luminance plane $Y = 0$,
- the tristimulus vectors with physical meaning have all positive components,
- the planes $X = 0$ and $Z = 0$ are tangent to the spectrum locus in the short and in the long wavelength region, respectively.

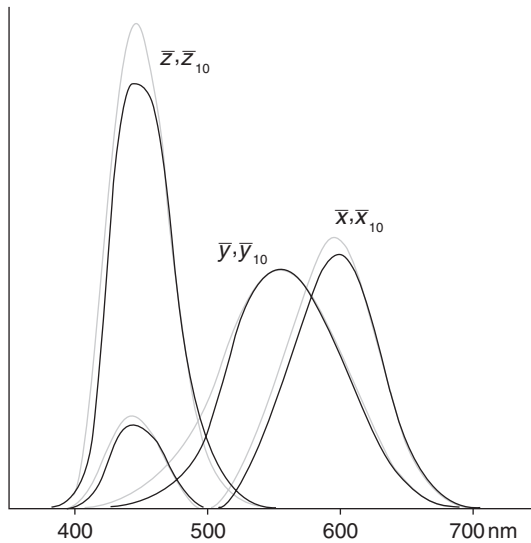
This reference frame is possible and is obtained from the *RGB* one by a linear transformation. This reference frame is the XYZ of the *CIE 1931 standard colorimetric observer* (Figs 9.6 and 9.7). The tristimulus values are

$$X = \int_{380}^{780} L_{e,\lambda} \bar{x}(\lambda) d\lambda, Y = \int_{380}^{780} L_{e,\lambda} \bar{y}(\lambda) d\lambda = \int_{380}^{780} L_{e,\lambda} V(\lambda) d\lambda = \frac{L_v}{K_m}, Z = \int_{380}^{780} L_{e,\lambda} \bar{Z}(\lambda) d\lambda \quad [9.7]$$

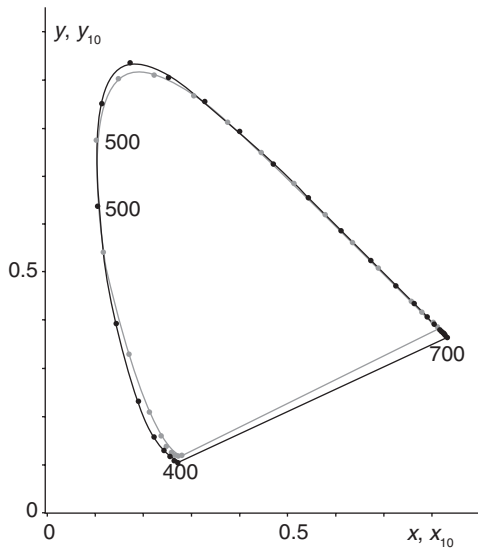
and the chromaticity

$$x = \frac{X}{X+Y+Z}, y = \frac{Y}{X+Y+Z}, z = \frac{Z}{X+Y+Z} = 1 - x - y. \quad [9.8]$$

The usual chromaticity diagram is obtained from the diagram on the plane $X + Y + Z = 1$ by a projection from infinity on the plane $Z = 0$ (Fig. 9.7).



9.6 CIE 1931 (black line) and CIE 1964 (gray line) colour-matching functions. The relative photopic luminous efficiency function of the standard photometric observer CIE 1924 is represented by $V(\lambda) = \bar{y}(\lambda)$.



9.7 CIE 1931 (black line) and CIE 1964 (gray line) chromaticity diagrams.

All the quantities related to the standard observer CIE 1931 have no denoting apex while those related to the standard observer CIE 1964 have the apex 10: as such, the CMFs are $(\bar{x}(\lambda), \bar{y}(\lambda), \bar{z}(\lambda))$ and $(\bar{x}_{10}(\lambda), \bar{y}_{10}(\lambda), \bar{z}_{10}(\lambda))$, the tristimulus values (X, Y, Z) and (X_{10}, Y_{10}, Z_{10}) , and the chromaticities (x, y, z) and (x_{10}, y_{10}, z_{10}) , respectively. Comparison of the CMFs and of the chromaticity diagrams of these two standard observers are shown in Figs 9.6 and 9.7.

9.3.2 Psychophysical colorimetry of light sources and non-self-luminous surfaces

The psychophysical color specification defined in Section 9.3.1 considers the radiance $L_{e,\lambda}$ entering the eye. Conventionally, the color specification of light sources and of non-self-luminous surfaces is made with a normalization: the quantity Y , termed *percentage luminance factor*, is defined on a percentage scale and $Y = 100$ is associated with the radiance reflected by the *perfect reflecting diffuser*, that is non-absorbing and non-transmitting, but it is an isotropic diffuser such that the reflected radiance is the same in all directions and is independent of the irradiation geometry and of the wavelength (the isotropic reflection is called *Lambertian*). This color specification is independent of the exitance value of the light source and of illuminance value of the specimens. The reflected radiance is proportional to the *relative spectral power distribution* of the illuminant $S(\lambda)$ and to the *spectral reflectance factor* $R(\lambda)$, that is, $L_{e,\lambda} \propto S(\lambda)R(\lambda)$ (McCamy, 1966):

$$\begin{aligned} X &= K \int_{380}^{780} S(\lambda)R(\lambda)\bar{x}(\lambda)d\lambda, \quad Y = K \int_{380}^{780} S(\lambda)R(\lambda)\bar{y}(\lambda)d\lambda, \\ Z &= K \int_{380}^{780} S(\lambda)R(\lambda)\bar{z}(\lambda)d\lambda \text{ with } K = 100 / \int_{380}^{780} S(\lambda)\bar{y}(\lambda)d\lambda. \end{aligned} \quad [9.9]$$

where the spectral reflectance factor of the perfect reflecting diffuser is $R(\lambda) = 1$. Here the *XYZ* reference frame is considered, but any other is possible by a linear transformation.

The tristimulus values and the chromaticities related to the standard observer CIE 1931 have no denoting apex while those related to the standard observer CIE 1964 have the apex 10.

The color also depends on the illuminating light. CIE has standardized *illuminants*, that is, files representing the *relative spectral power distributions* $S(\lambda)$ of light sources. The most important CIE standard illuminants are (CIE 15:2004):

- the *illuminant A*, associated with a tungsten lamp with the radiant exitance of the black body at the temperature of ≈ 2856 K;

- the *daylight type* illuminants associated with conventional daylights denoted by D50, D55, D65, D75, ..., corresponding to a temperature of 5000 K, 5500 K, 6500 K, 7500 K, ..., respectively;
- *fluorescent lamps*: F2 coolwhite, F7 daylight fluorescent and F11 white fluorescent.

Spectral reflectance factor is the ratio of the spectral flux reflected by a specimen to the spectral flux reflected by the perfect diffuse reflector under the same geometric and spectral conditions (McCamy, 1966). Since the perfect diffuse reflector does not exist, this is replaced by a physical tile whose spectral reflectance factor is certified by a reference metrological laboratory. The geometries for the reflectance-factor measurement recommended by CIE are (CIE 15:2004):

1. *forty-five degree/normal geometry*, denoted by (45°/0°): the color sample is lit by a parallel light beam with an incidence angle of 45° and the light emerging from the sample with an angle of 0° is analyzed by a spectrometer;
2. *forty-five degree annular/normal geometry*, denoted by (45°a/0°): the color sample is irradiated by light beams uniformly distributed from all directions between two right circular cones with their axes on the normal and with an incidence angle of 45°. The light emerging from the sample with an angle of 0° is analyzed by a spectrometer;
3. *diffuse/eight-degree geometry, specular component excluded*, denoted by (de/8°): the color sample is lit by a diffuse light obtained by integration sphere with specular component excluded and the light emerging from the sample with an angle of 8° is analyzed by a spectrometer;
4. *diffuse/eight-degree geometry, specular component included*, denoted by (di/8°): the color sample is lit by a diffuse light obtained by integration sphere with specular component included and the light emerging from the sample with an angle of 8° is analyzed by a spectrometer.

In the case of a transmitting specimen, the *spectral transmittance factor* $T(\lambda)$ is considered instead of the spectral reflectance factor $R(\lambda)$. $T(\lambda)$ is defined as the *ratio of the spectral flux transmitted by a specimen to the spectral flux through the same optical system with the specimen removed* and the measurement geometries recommended by CIE are (all the following geometries relate to the definition of *transmittance* measurement except the situations with the regular component excluded, which relate to *transmittance factor* measurement) (McCamy, 1966; CIE 15:2004):

1. *normal/normal geometry*, denoted by (0°/0°);
2. *diffuse/normal geometry, regular component included*, denoted by (di/0°);

3. *diffuse/normal geometry, regular component excluded*, denoted by (de/0°);
4. *normal/diffuse geometry, regular component included*, denoted by (0°/di);
5. *normal/diffuse geometry, regular component excluded*, denoted by (0°/de);
6. *diffuse/diffuse geometry*, denoted by (d/d).

For transmission measurements, there is a reference plane for the incident light and a second reference plane, displaced by the sample thickness, for the transmitted light. The measurements are based on the assumption of negligible thickness.

The *spectral reflectance (transmittance) factors* depend on temperature and consequently the color is temperature dependent, too. Therefore, any color specification must be given with the measurement geometry and the temperature; in the case of hygroscopic material, the relative humidity also has to be measured. These standard geometries are meaningful in the vast majority of cases with nearly diffuse reflection or nearly regular transmission.

CIE recommends no particular geometry for optical coatings seen in reflection or seen in transmission. The gonio-dependence of the reflected and transmitted light requires the definition of a new quantity, which is given in Section 9.4.1.

The passage between different reference frames is made by a linear transformation, represented by a 3×3 matrix. The choice of the reference frame is for practical purposes only.

9.3.3 Psychometric colorimetry

Psychometric colorimetry is based on the visual ordering of color samples seen in a defined visual situation (defined illuminant, geometry of illumination, point of view, defined size of color samples and defined background on which the color samples are viewed), and the ordering relates to the perceived color attributes of *lightness*, *hue* and *chroma*. The attributes under consideration are not merely three, but, these are sufficient for our objective. Different and contradictory phenomena exist in relation to the adaptation to a visual situation:

- on one hand is the *color constancy* phenomenon, according to which the perceived color of lit objects seems unchanging with changing illumination;
- on the other hand is the mutability of perceived color related to the proximal field, background, surroundings and illumination level.

These phenomena should be considered in psychometric colorimetry.

In practical terms, psychometric colorimetry is represented by color atlases (not considered here).

The practice of instrumental colorimetry has always used a psychometric system of CIE. CIE defined in 1976 two psychometric systems, termed CIELAB and CIELUV, which are based on the psychophysical color specification (X , Y , Z) of the color sample and of the illuminant (X_n , Y_n , Z_n), for the CIE 1931 standard observer, and on (X_{10} , Y_{10} , Z_{10}) and ($X_{10,n}$, $Y_{10,n}$, $Z_{10,n}$), for the CIE 1964 standard observer (CIE 15:2004). CIELAB is the most widely used system in industry. CIELUV was conceived for monitors, television, etc., but in practice has become obsolete. Here only the widely used CIELAB is considered.

The CIELAB colorimetric system is spanned by the coordinates (L^* , a^* , b^*), that are derived by non-linear transformations from the CIE 1931 or from the CIE 1964 tristimulus space (in this second case the coordinates must be denoted by the subscript '10', i.e. L_{10}^* , a_{10}^* , b_{10}^*). The motivations and the purposes that form the basis of this system are ambitious and not completely satisfied, and the success of this system is due to no more advantageous alternative existing.

Once an illuminant is chosen, whose specification (X_n , $Y_n = 100$, Z_n) is obtained from the spectral measurement of the light reflected by the perfect reflecting diffuser, a color stimulus (X , Y , Z) is specified in the CIELAB system by the coordinates (L^* , a^* , b^*):

1. L^* is the CIE 1976 psychometric lightness
2. a^* and b^* are coordinates recalling the opponent unique hues, according to Hering's hypothesis that synthetically says that color sensation is perceptually organized in two *chromatic opponent processes*, red-green and yellow-blue, and one dark-light process.

The lightness is defined as brightness of an area judged relative to the brightness of a similarly illuminated area that appears to be white. In 1976 CIE proposed the following definition of *psychometric lightness* with range 0–100

$$L^* = \begin{cases} 119(Y/Y_n)^{1/3} - 16 & \text{for } (Y/Y_n) > 0.008856 \\ 903.3(Y/Y_n) & \text{for } (Y/Y_n) \leq 0.008856 \end{cases} \quad [9.10]$$

that is a function of the ratio of the percentage-luminance factor Y of the surface color (X , Y , Z) being considered over Y_n of the color of the perfect diffuser (X_n , $Y_n = 100$, Z_n) illuminated by the chosen illuminant; Equation [9.10] describes the perceived quantity L^* as a function of the relative

luminance Y/Y_n stimulating the visual system, according to *Stevens' power law* (in this case the power is 1/3).

The coordinates a^* and b^* , that should describe the red-green and blue-yellow opponent processes, are defined by differences of suitable quantities:

$$\begin{cases} a^* = 500[f(X/X_n) - f(Y/Y_n)] \\ b^* = 200[f(Y/Y_n) - f(Z/Z_n)] \end{cases} \quad [9.11]$$

where

$$\begin{cases} f(X/X_n) = (X/X_n)^{1/3} & \text{for } (X/X_n) > 0.008856 \\ f(X/X_n) = 7.7867(X/X_n) + 16/116 & \text{for } (X/X_n) \leq 0.008856 \end{cases}$$

and likewise for (Y/Y_n) and (Z/Z_n) .

Often, cylindrical coordinates are used (L^*, h_{ab}, C^*_{ab}) with

$$\begin{cases} h_{ab} = \arctan(b^*/a^*) \quad \text{hue angle measured in degrees} \\ C^*_{ab} = \sqrt{a^{*2} + b^{*2}} \quad \text{chroma} \end{cases} \quad [9.12]$$

All the standard color-difference formulae for industrial practice are defined on the CIELAB system: the original Euclidean formula, the CMC formula, the CIE94 and CIEDE2000.

There is also *Color-Appearance Colorimetry*, that takes into account an almost complete visual adaptation. Over time, CIE proposed two models, CIECAM97s and CIECAM02 (Fairchild, 2004). This chapter considers none of the color appearance models because optical coating color does not need such a sophisticated color specification.

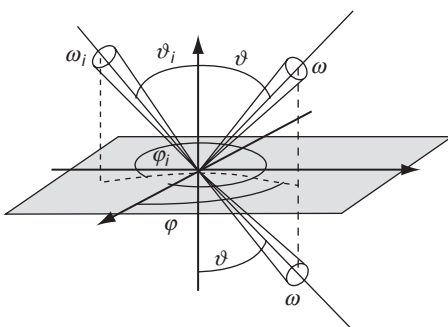
9.4 Optical coating colorimetry

In the sections above, with the definitions of the measurement geometries for spectral reflectance factor and spectral transmittance factor, we have considered non-self-luminous objects, whose appearance has little modification with the directions of illumination and viewing. But it is also common for the appearance of colored samples to vary with the directions of illumination and viewing. A popular example is the often colored, metallic finish applied to many automobiles (McCamy, 1996, 1998; CIE 175: 2006). In this case the pigment of the finish is constituted of micrometric aluminum mirrors and the effect is due to a non-Lambertian diffusion of light. Another popular example is the mica-pigment finish, again applied to automobiles.

In this case the pigment is constituted of micrometric chips of mica coated with a very thin layer of oxide, such as SiO_2 . This coating layer, when illuminated, produces iridescent colored effects. The appearance of this finish changes according to the angles of illumination and viewing. Their color is the so-called *gonio-apparent color* or, more generally, *special-effect color*. The colors of the bodies with optical dishomogeneities constituted of layers with different refractive index and with thicknesses of the same order as the wavelength of the illuminating radiation are produced by interference and are named *interference colors*. Also colors of optical coatings of glasses and lenses are of this kind. In nature we see interference color in butterfly wings, insects, bird feathers and soap bubbles. Because this kind of color is strongly dependent on the illuminating and viewing geometries, it cannot be adequately measured by using the limited conditions of the CIE measuring geometries described above and the color, for a complete characterization, should be measured at more than one illumination/viewing angle combination.

9.4.1 Gonio-apparent color measurement

For a detailed color specification, both the bidirectional transmittance and reflectance have to be measured and *spectro-goniometric measurements* are needed. Here, the term ‘directional’ refers to an infinitesimally small solid angle in a specified direction from the point considered for the measurement and in this case the rays are very close to being parallel. Let us consider an element of incident spectral irradiance $dE_i(\vartheta_i, \varphi_i, \lambda)$ approaching from the direction (ϑ_i, φ_i) of incidence within the solid angle element $d\omega_i$ (Fig. 9.8). In the case of reflected light, Nicodemus *et al.* (1977) defined the *bidirectional reflectance distribution function* (BRDF):



9.8 Geometry for the definition of bidirectional transmittance and reflectance spectral distribution function (BTDF, BRDF).

$$f_r(\vartheta_i, \varphi_i; \vartheta_r, \varphi_r; \lambda) = \frac{dL_r(\vartheta_i, \varphi_i; \vartheta_r, \varphi_r; \lambda; E_i)}{dE_i(\vartheta_i, \varphi_i; \lambda)} [\text{sr}^{-1}] \quad [9.13]$$

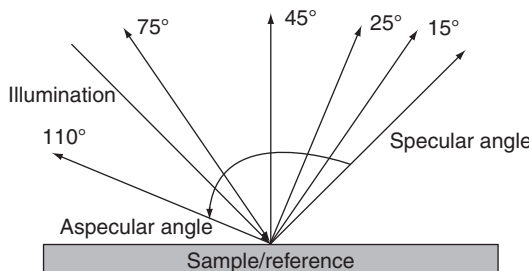
which is the ratio of the spectral radiance $dL_r(\vartheta_i, \varphi_i; \vartheta_r, \varphi_r; \lambda)$ exiting the specimen in the direction ϑ_r, φ_r internal to the solid angle $d\omega$ and the spectral irradiance $dE_i(\vartheta_i, \varphi_i, \lambda)$ irradiating the specimen in the same point. Analogously the *bidirectional transmittance distribution function* (BTDF) is defined.

The instrument for this measurement is the *gonio-spectrophotometer*, which enables the sample to be illuminated from any angle and viewed over a wide range of angles, often by scanning a range from $\pm 80^\circ$ to the normal to the surface. Instruments of this kind are commercially available, but today their use is exceptional due to high cost and the current lack of a standard procedure for making multi-angle measurements (Fig. 9.9).

This limitation is partly overcome by the introduction of so-called *multi-angle spectrophotometers*, which typically measure at four or five angles of reflection. As shown in Fig. 9.9, the illumination angle in these instruments is 45° to the normal to the surface and the measurement angles are designated with respect to the specular angle by introducing the concept of *aspecular angle* (Baba, 1990; Rodrigues, 1990; Rössler, 1990; Carroll, 1997). DIN has published standard defining methods for color measurement using four specular angles: $25^\circ, 45^\circ, 75^\circ$ and 110° (DIN, 2001; Mikula, *et al.*, 2003; Nadal, *et al.*, 2004).

However, for many surfaces, notably some of the pearlescent and interference pigments, that are now being used for product finishes, the limitation to four angles is probably insufficient and the use of a gonio-spectrophotometer becomes necessary. This comment also holds true for optical coatings.

The resulting color specification, made in *XYZ* or *CIELAB* systems, must be given combined with the geometry of measurement and the temperature.



9.9 Multi-angle spectrophotometry: viewing angles are shown measured with respect to the specular angle.

Moreover, because the interference colors are generally seen in macular vision, the preferable observer is the CIE 1931.

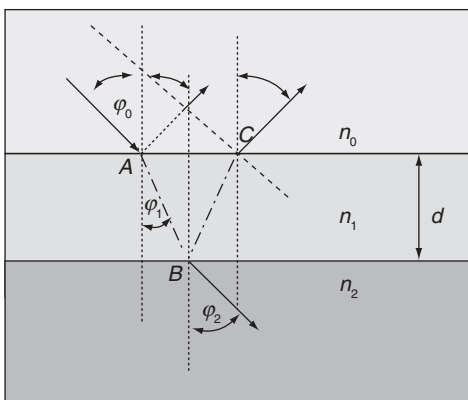
9.4.2 Optical coating color

The colorimetric evaluation of interference color in reflection and transmission of a simple system constituted of three media is considered here from the theoretical point of view. This analysis is based on a few classical papers (Kubota, 1950, 1966; Murray, 1956; Berning, 1963; Heavens, 1964, 1965; MacLeod, 1986).

The interference produced by optical coatings constituted by a set of thin parallel layers of different dielectrics can be described by solutions of Maxwell's equations combined with initial conditions and boundary conditions. In the simplest case of only two isotropic non-absorbing media, the reflection and transmission at the interface is well described by Snell's laws, with regard to the geometry of the phenomenon, and by Fresnel's laws with regard to the polarization and power fluxes, and no interference effect appears (Berning, 1963; Heavens, 1964). The role of the critical and Brewster's angles is important.

If the media are more than two and the thickness of a medium is comparable to the wavelength of the illuminating radiation, interference appears and color changes strongly with the illumination direction, polarization, viewing direction and thickness of the layer (Berning, 1963; Heavens, 1964, 1965; Kubota, 1966; MacLeod, 1986).

Let n_0 , n_1 and n_2 be the refractive indices of the three media, respectively, and d the thickness of the intermediate layer (Fig. 9.10). The spectral



9.10 Representation on the incidence plane of a system of three media, with the intermediate layer of thickness d comparable to the wavelength.

reflectance and transmittance, computed as a superposition of only two waves ignoring multiple reflections within the layer, are

$$\rho(\lambda) = \frac{r_1^2 + 2r_1r_2 \cos(2\delta_1) + r_2^2}{1 + 2r_1r_2 \cos(2\delta_1) + r_1^2r_2^2}, \quad \tau(\lambda) = \frac{n_2}{n_0} \frac{t_1^2 t_2^2}{1 + 2r_1r_2 \cos(2\delta_1) + r_1^2r_2^2} \quad [9.14]$$

where δ_1 is the *phase thickness* of the layer

$$\delta_1 = 2\pi(n_1 d / \lambda) \cos \varphi_1 \quad [9.15]$$

and r_1, r_2, t_1 and t_2 are Fresnel's coefficients, which depend on the polarization and on the refractive indices:

- *p-component* for polarization parallel to the incidence plane

$$\begin{aligned} r_{1p} &= \frac{n_0 \cos \varphi_1 - n_1 \cos \varphi_0}{n_0 \cos \varphi_1 + n_1 \cos \varphi_0}, & r_{2p} &= \frac{n_1 \cos \varphi_2 - n_2 \cos \varphi_1}{n_1 \cos \varphi_2 + n_2 \cos \varphi_1}, \\ t_{1p} &= \frac{2n_0 \cos \varphi_0}{n_0 \cos \varphi_1 + n_1 \cos \varphi_0}, & t_{2p} &= \frac{2n_1 \cos \varphi_1}{n_1 \cos \varphi_2 + n_2 \cos \varphi_1} \end{aligned} \quad [9.16]$$

- *s-component* for polarization orthogonal to the incidence plane

$$\begin{aligned} t_{1s} &= \frac{n_0 \cos \varphi_0 - n_1 \cos \varphi_1}{n_0 \cos \varphi_0 + n_1 \cos \varphi_1}, & r_{2s} &= \frac{n_1 \cos \varphi_1 - n_2 \cos \varphi_2}{n_1 \cos \varphi_1 + n_2 \cos \varphi_2}, \\ t_{1s} &= \frac{2n_0 \cos \varphi_0}{n_0 \cos \varphi_0 + n_1 \cos \varphi_1}, & t_{2s} &= \frac{2n_1 \cos \varphi_1}{n_1 \cos \varphi_1 + n_2 \cos \varphi_2} \end{aligned} \quad [9.17]$$

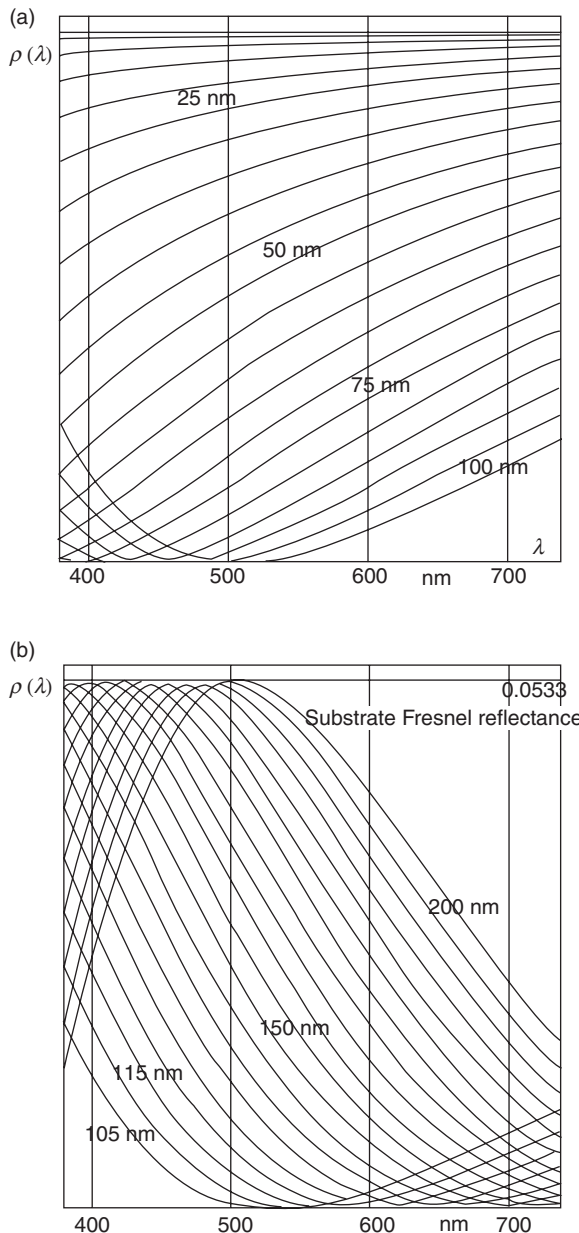
where the angles φ_j are defined by Snell's laws.

Two colorimetric computations are made by applying these formulae with varying layer thickness and varying incidence angle, respectively.

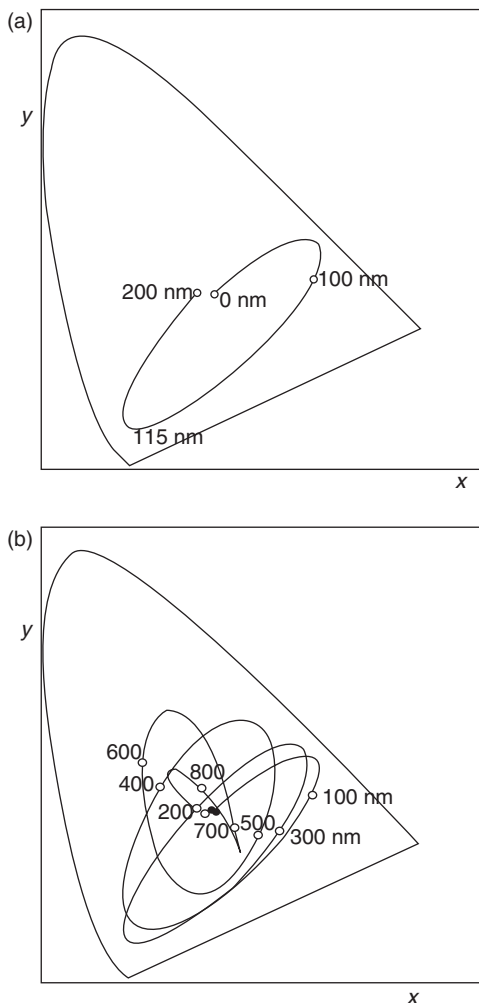
The first computation relates to a coating of an optical glass, like a lens, chosen to obtain the lowest reflection (Kubota, 1950; Murray, 1956). In this case, the normal incidence with $\varphi_0 = \varphi_1 = \varphi_2 = 0$ is close to the practical situation and the coating is achieved satisfying the condition of non-reflection, that is, with the refractive index $n_1 = \sqrt{n_0 n_2}$. The *p* and *s* components of the Fresnel's coefficients become equal and are

$$r_1 = \frac{n_0 - n_1}{n_0 + n_1}, \quad r_2 = \frac{n_1 - n_2}{n_1 + n_2}, \quad t_1 = \frac{2n_0}{n_0 + n_1}, \quad t_2 = \frac{2n_1}{n_1 + n_2} \quad [9.18]$$

The reflectances computed for $n_0 = 1$, $n_2 = 1.6$ and $n_1 = 1.2649$ and for a coating thickness d between 0 and 200 nm are represented in Fig. 9.11. The

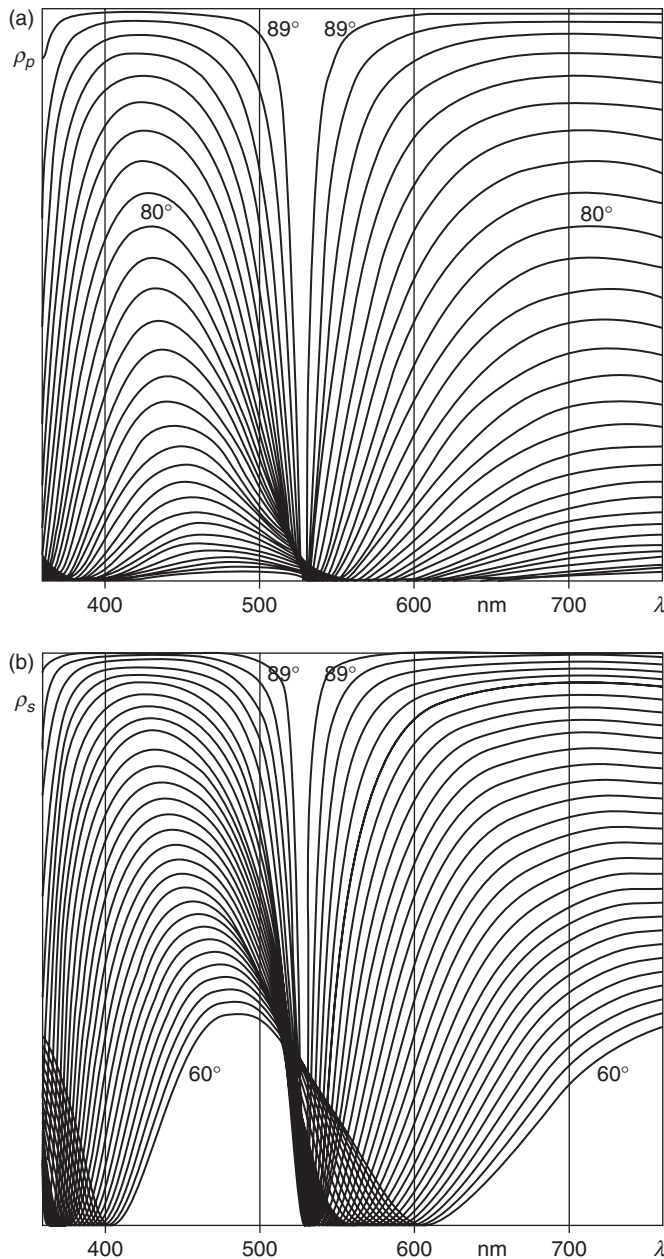


9.11 Spectral reflectances computed by Equation [9.14] for a glass with refractive index $n_2 = 1.6$ in air coated by a layer with $n_1 = 1.2649$ in a condition of non-reflection and for different values of thickness ranging between 0 and 200 nm. The maximum value of the reflectance is equal to the Fresnel's reflectance of the glass and is 0.0533.



9.12 CIE 31 chromaticity coordinates produced by the equal-energy illuminant combined with the reflectances represented in Fig. 9.11. Around a thickness of 115 nm, the reflectance is equal to zero at 555 nm wavelength in correspondence to the maximum of the luminous efficiency $V(\lambda)$ of the visual system. This property of the optical coating is useful for reducing the stray light in the objective lenses. A very small residual reflectance in the short and long wavelength region generates the typical magenta color of the objective lenses.

reflectance is always lower than or equal to the Fresnel's reflectance $\rho_{\text{FRESNEL}} = 0.0533$ of the uncoated substrate. The spectral reflectance has a minimum equal to 0 moving towards a longer wavelength in correspondence to increasing thickness. This minimum, for a thickness equal to 115 nm, is close

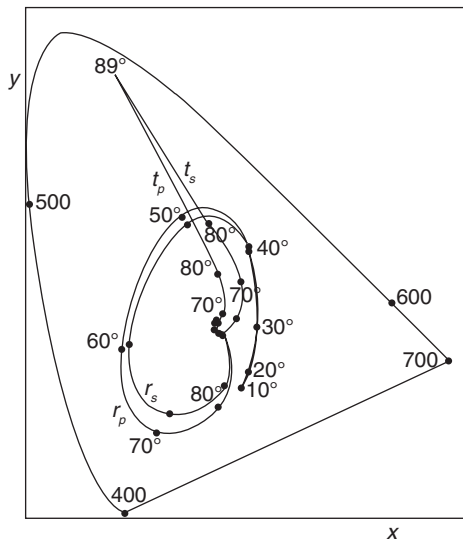


9.13 Spectral reflectances related to the polarization p and s , respectively, of a 600 nm layer of water in air for the incidence angle ranging from 60° to 89°. It is remarkable that the reflectance in the visible range approaches the value one with increasing incidence angle, excluding the wavelengths close to 527 nm, where it is almost equal to zero.

to the wavelength 555 nm, where the spectral luminous sensitivity function $V(\lambda)$ has the maximum value. This situation is very important in practice, in order to minimize the reflected light, that is disturbing.

The chromatic specification of the reflected light is represented in Fig. 9.12 for the CIE 1931 observer and equal-energy illuminant, where it is shown that the reflected light for a thickness of 115 nm assumes the typical color magenta due to the very small reflectance in the short and long wavelength regions.

The second computation relates to a 600 nm water layer in air with light incident at a varying angle. In this case the polarization has an evident role. Figure 9.13 represents the reflectances for p - and s -polarization for incidence angles ranging from 60° to 89° . The reflectances below 60° are low and the transmitted lights are almost achromatic (Fig. 9.14). It is remarkable that the reflectance in the visible range approaches the value one with increasing incidence angle, excluding wavelengths close to 527 nm, where it is almost equal to zero. In this geometrical situation the layer is very selective in wavelength. The selected wavelength depends on the layer thickness. The chromaticities for all incidence angles, between 0° and 89° , are represented in Fig. 9.14 where the wavelength selectivity is well represented by



9.14 CIE 1931 chromaticity diagram with the chromaticities of the lights with p -and s -polarization and with different incidence angles, reflected and transmitted by a 600 nm water layer in air (r_p for reflectance with p -polarization; r_s for reflectance with s -polarization; t_p for transmittance with p -polarization; t_s for transmittance with s -polarization). The corresponding reflectances for incidence angles in the range 60° – 89° are represented in Fig. 9.13. The color specification is made for the equal-energy illuminant.

the chromaticity of the transmitted light, which approaches the spectrum locus with increasing incidence angle. The color specification is made for the CIE 1931 observer and the equal-energy illuminant.

9.5 Conclusion

Colorimetry of the interference color is not yet specifically considered by CIE, although some technical committees have given extensive attention to Color Appearance and technical committee TC2-53 'Multi-geometry color measurement of effect materials' is working in a field close to colorimetry of optical coatings. Today multiangle spectrophotometry is a practical proposal for the measurement of the gonio-apparent colors and the colorimetry of the optical coating is not yet standardized.

9.6 Acknowledgements

The author is very grateful to Pietro Polato, for the introduction to optical coating colorimetry, and to Angela Piegari for the dialog and discussion on this paper.

9.7 References

- Baba, G. (1990). Gonio-spectrophotometric analysis of pearl-mica paint. *Die Farbe*, **37**, pp. 99–110.
- Berning, P. H. (1963). Theory and calculations of optical thin films. In: G. Hass ed. *Physics of Thin Films, Advances in Research and Development, Volume 1*. Riverport Ln: Academic Press, pp. 69–121.
- Berns, R. S. (2000). *Billmeyer and Saltzman's Principles of Color Technology*, 3rd ed. New York: John Wiley & Sons.
- Brewster, D. (1853). *Treatise on Optics*. London: printed for Longman Brown, Green & Longmans, Paternoster Row.
- Carroll, J. (1997). Measuring pearlescent color. *Modern Paint & Coatings*, **87**, pp. 30–34.
- CIE Publication 15:2004 (2004). *Colorimetry*. 3rd ed. Wien, Austria: CIE Central Bureau, Kegelstrasse 27, A-1030.
- CIE Publication 159:2004 (2004). *A Colour Appearance Model for Colour Management Systems: CIECAM02*. Wien, Austria: CIE Central Bureau, Kegelstrasse 27, A-1030.
- CIE Publication 175:2006. (2006). Technical Report, 2005. *A Framework for the Measurement of Visual Appearance*. Wien, Austria: CIE Central Bureau, Kegelstrasse 27, A-1030.
- Connes, P. (1987). Silver salts and standing waves: the history of interference colour photography. *Journal of Optics*, **18**(4), pp. 147–166.
- DIN Standard 6175-2 (2001). *Colour tolerances for Automobile Lacquer Finishes, Part 2: Effect Lacquer Finishes*.

- Dobrowolski, J. A., Baird, K. M., Carman, P. D. and Waldorf, A. (1973). Optical interference coatings for inhibiting of counterfeiting. *Optica Acta*, **20**, pp. 925–937.
- Dobrowolski, J. A., Ho, F. C. and Waldorf, A. (1989). Research on thin film anticounterfeiting coatings at the National Research Council of Canada. *Applied Optics*, **28**, pp. 2702–2717.
- Dobrowolski, J. A. and Mandler, W. (1979). Color correcting coatings for photographic objectives. *Applied Optics*, **18**, pp. 1879–1880.
- Fairchild, M. D. (2004). *Color Appearance Models*, 2nd ed. Wiley-IS&T series. West Sussex England: John Wiley & Sons Ltd.
- Heavens, O. S. (1964). Measurement of optical constants of thin films. In: G. Hass and R. E. Thun, eds. *Physics of Thin Films, Advances in Research and Development, Volume 2*. Riverport, LN: Academic Press, pp. 193–238.
- Hevans, O. S. (1965). *Optical Properties of Thin Solid Films*. New York: Dover Publications, pp. 56–59.
- Hunt, R. W. G. and Pointer, M. R. (2011). *Measuring Color*. 4th ed. Wiley-IS&T series. West Sussex England: John Wiley & Sons Ltd.
- Kaiser, P. K. and Boynton, R. M. (1996). *Human Color Vision*. Washington: Optical Society of America.
- Kinoshita, S., Yoshioka, S. and Miyazaki, J. (2008). Physics of structural colors. *Reports on Progress in Physics*, **71**, pp. 1–30.
- Kubota, H. (1950). On the interference color of thin layers on glass surface. *Journal of the Optical Society of America*, **40**, pp. 146–149.
- Kubota, H. (1966). Interference color. In: H. Kubota and E. Wolf, eds. *Progress in Optics, Volume I*. Amsterdam: North Holland Pub. C., Cap VI, pp. 213–251.
- Kuehni, R. G. (1997). *Color, An Introduction to Practice and Principles*. New York: John Wiley & Sons.
- Kuehni, R. G. (2003). *Color Space, and Its Division*. New York: John Wiley & Sons, Inc.
- Kuehni, R. G. and Schwarz, A. (2008). *Color Ordered, A Survey of Color Order Systems from Antiquity to the Present*. New York: Oxford University Press.
- Le Grand, Y. (1968). *Light, Colour and Vision*, 2nd ed. London: Chapman and Hall.
- MacAdam, D. L. (1985). *Color Measurement*. Berlin: Springer-Verlag.
- MacAdam, D. L. ed. (1993). *Colorimetry-Fundamentals*. SPIE MS 77. Washington DC: SPIE – The International Society for Optical Engineering.
- MacLeod, H. A. (1986). *Thin Film Optical Filters*. New York: MacMillan Publishing Company, pp. 40–43.
- Malacara, D. (2002). *Color Vision and Colorimetry, Theory and Applications*. Bellingham, Washington, USA: SPIE press.
- Maxwell, J. C. (1860). On the theory of compounds colours, and the relations of the colours of the spectrum. *Philosophical Transactions of the Royal Society of London*, **150**, pp. 57–84.
- McCamy, C. S. (1966). Concepts, terminology, and notation for optical modulation. *Photographic Science and Engineering*, **10**, pp. 314–325.
- McCamy, C. S. (1996). Observation and measurement of the appearance of metallic materials. I. Macro appearance. *Color Research and Application*, **21**, pp. 292–304.
- McCamy, C. S. (1998). Observation and measurement of the appearance of metallic materials. II. Micro appearance. *Color Research and Application*, **23**, pp. 362–373.

- McDonald, R. ed. (1987). *Colour Physics for Industry*, Bradford: Society of Dyers and Colourist.
- Michel-Lévy, A. and Lacroix, A. (1888). *Les Minéraux des Roches*. Paris: Librairie Politechnique Baudry et C. Editeurs.
- Mikula, M., Čeppan, M. and Vaško, K. (2003). Gloss and goniocolorimetry of printed materials. *Color Research and Application*, **28**, pp. 335–342.
- Murray, A. E. (1956). Effect of antireflection films on color in optical instruments. *Journal of the Optical Society of America*, **46**, pp. 790–796.
- Nadal, M. and Earley, E. A. (2004). Color measurements for pearlescent coatings. *Color Research and Application*, **29**, pp. 38–42.
- Newton, I. (1704). *Opticks, or a Treatise of the Reflections, Refractions, Inflections & Colours of Light*. Reprinted, New York: Dover, 1952.
- Nicodemus, F. E., Richmond, J. C., Hsia, J. J. and Ginsberg, I. W. (1977 October). *Geometrical considerations on Nomenclature for Reflectance*. Washington, USA: National Bureau of Standards.
- Nobili, L. (1830). Sui colori in generale ed in particolare sopra una nuova scala cromatica dedotta dalla metallocromia ad uso delle sienze e delle arti. *ANTOLOGIA*, September, tomo trigesimonono, N° 117. Firenze: Tipografia di Luigi Pezzati, pp. 1–39.
- Ohta, N. and Robertson, A. R. (2005). *Colorimetry – Fundamentals and Applications*. New York: John Wiley & Sons.
- OSA Committee on Colorimetry (1963). *The Science of Color*. Washington: OSA – The Optical Society of America.
- Plateau, A. F. (1873). *Statique expérimentelle et théorique des liquides aux seules forces moléculaires*. Paris: Gauthier-Villars.
- Rodrigues, A. B. J. (1990). Measurement of metallic and pearlescent colors. *Die Farbe*, **37**, pp. 65–78.
- Rössler, G. (1990). Multigeometry color measurement of effect surfaces. *Die Farbe*, **37**, pp. 111–121.
- Schanda, J. (2007). *Colorimetry: Understanding the CIE System*. New York: John Wiley & Sons.
- Schrödinger, E. (1926). Über das Verhältnis der Vierfarben- zur Dreifarbentheorie. *SbAkad Wien*, **134**, abt. 2a, pp. 471–490.
- Sèvè, R. (1996). *Physique de la couleur*. Paris: Masson.
- Shevell, S. (2003). *The Science of Color*, 2nd ed. Amsterdam: OSA-Elsevier.
- Thomas, Y. (1802a). *A Syllabus of a Course of Lectures on Natural and Experimental Philosophy*. London: from the Press of the Royal Institution, W. Savage, Printer.
- Thomas, Y. (1802b). On the Theory of Light and Colors. Bakerian Lecture read November 12, 1801. *Philosophical Transactions of the Royal Society of London*, **92**, pp 12–48.
- Valberg, A. (2005). *Light Vision Color*. Chichester, UK: Wiley.
- Wyszecky, G. and Judd, D. B. (1975). *Color in Business, Science and Industry*. New York: John Wiley & Sons.
- Wyszecky, G. and Stiles, W. S. (1982). *Color Science*. New York: John Wiley & Sons.

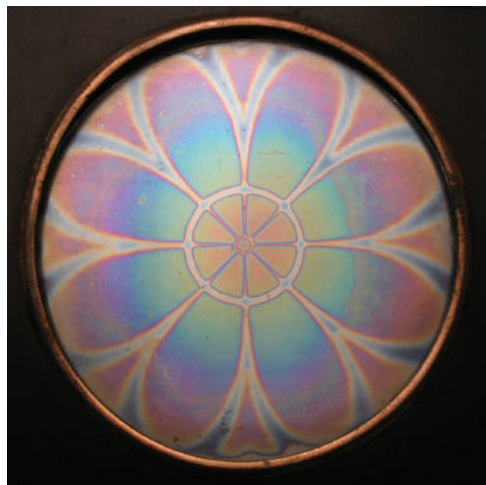


Plate I (Chapter 9) Nobili's metallocromia piece of art, preserved in the Physics Department of the University of Parma.

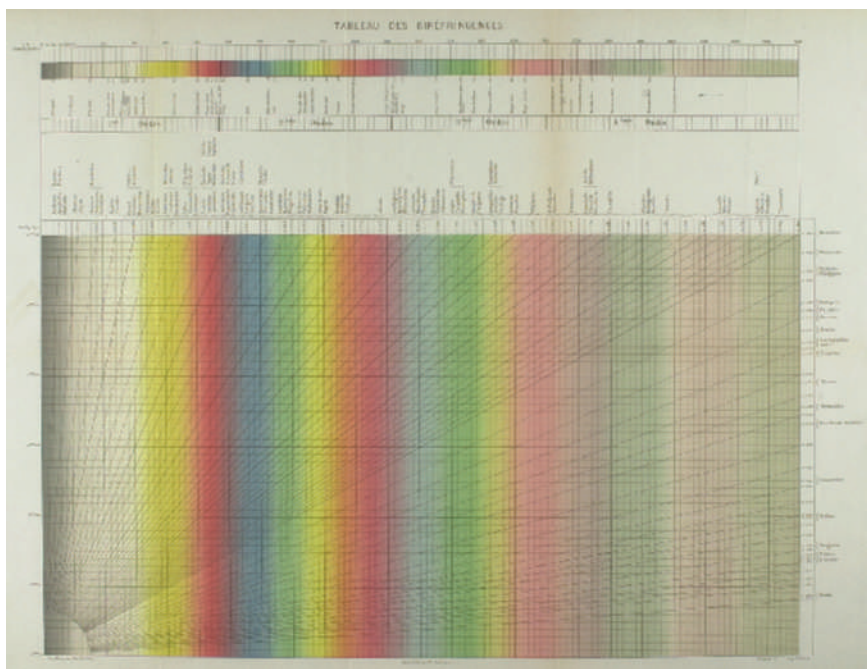


Plate II (Chapter 9) Reproduction of the original Michel-Lévy Interference Color Chart (Lévy and Lacroix, 1888). The different interference color orders are shown in increasing order in the abscissa, while the thickness of the specimen is given in the ordinate. The straight lines radiating from the origin of the coordinates are in correspondence to birefringence refractive index difference ($n_1 - n_2$), written on the right and upper sides of the diagram.

T. NEUBERT and M. VERGÖHL, Fraunhofer Institute for Surface Engineering and Thin Films – IST, Germany

DOI: 10.1533/9780857097316.3.427

Abstract: In this chapter we discuss organic layers for optical layer systems. Thanks to their higher mechanical flexibility, new applications like optical layer systems on deformable substrates or transparent bendable diffusion barriers on polymer foils are becoming possible. Due to properties such as complex molecular structure and higher sensitivity against heat or radiation, the preparation of organic thin films differs from the deposition techniques of oxide thin films. Therefore we describe different vapor deposition techniques for organic thin films such as thermal evaporation, sputter deposition, plasma enhanced chemical vapor deposition and thermal activated chemical vapor deposition. Finally, we discuss the possibility of composite thin films which combine properties of organic and oxide materials like high refractive index and high mechanical flexibility.

Key words: organic optical thin films, physical vapor deposition, chemical vapor deposition, polymer films.

10.1 Introduction

Stacks or single layers of transparent thin films are commonly used to modify the optical behavior of surfaces and to integrate new functions such as scratch resistance or anti-fingerprint. Examples therefore are antireflective coatings for display glass or optical instruments, high reflective mirrors for laser applications or optical filters with practically any kind of spectral characteristic. Very often, dense layers without any spectral shift due to environmental changes (humidity) are required. Therefore, such optical layers are usually made of ceramic materials with a low and high refractive index. A wide number of metal oxides such as silicon oxide (SiO_2), tantalum oxide (Ta_2O_5) or titanium oxide (TiO_2) are used for applications from near ultraviolet to the mid-infrared spectra range. These materials are often deposited by vacuum deposition processes like (ion assisted) evaporation, magnetron or ion beam sputtering or plasma enhanced chemical vapor deposition (PECVD). Besides the excellent optical properties (low absorption, well-defined refraction index, low optical haze), high hardness

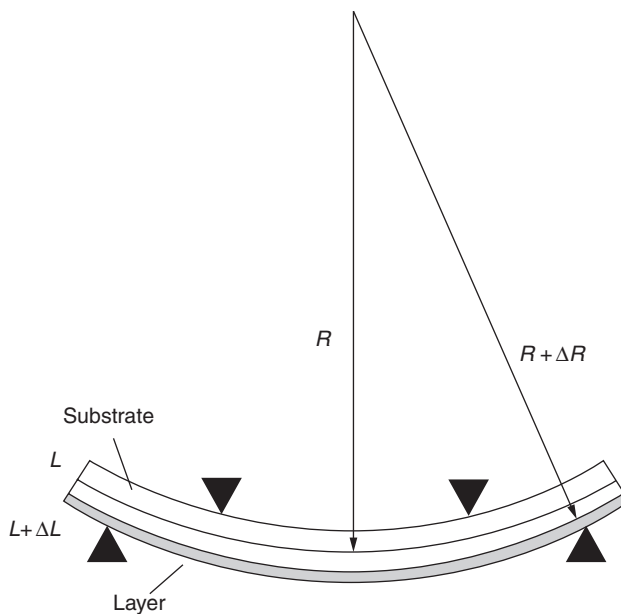
close to the bulk values and low flexibility are typical for these layers whenever plasma technology is applied. However for many applications of optical coatings high hardness and low flexibility, which are normally connected close to each other, are not suited. Especially on polymer substrates (like foils or plates) hard and thus non-flexible layer systems will break and produce stray light and delamination, especially under thermal and mechanical load or after deformation. On the other hand, organic materials have a significantly higher mechanical flexibility. Furthermore some organic materials may offer additional functions such as hydrophobicity, fluorescence, electrical permeability or chemical activity. Last but not least they have a low price. This makes organic materials interesting for optical coatings. However, the mechanical stability of organic layers is too low for many applications. The goal in current research, therefore, is not only to work on deposition processes for pure optical organic layers, but also to improve the mechanical stability of these layers by the use of composites. Therefore, organic layers are also of interest as an additional part of a ceramic layer system.

Organic materials are not only of practical interest just for optical layers. Examples for important applications are organic light emitting diodes (OLED) or organic photo voltaic (OPV) cells.

10.2 Specific properties of organic layers

In organic materials like polymers, the binding energies of the molecules are lower and the structures of the molecules are often more complex than in most metal oxide materials. In vacuum and plasma based deposition processes it is often a difficult task to keep the same polymeric structure in a thin organic layer as in polymer ‘bulk’ materials. This may be one of the reasons that, depending on the organic material, a large variety of deposition techniques have been tried out and some of them have been established in recent years. In this chapter an overview of different vacuum deposition processes is given and some properties of organic materials performed at the Fraunhofer Institute for Surface Engineering and Thin Films (IST) in Braunschweig, Germany and elsewhere are shown.

Organic materials show some special properties compared to ceramic materials. As already mentioned, the mechanical flexibility of organic layers is much higher. The mechanical flexibility or elasticity of films can be determined by measuring the so called crack onset strain' (COS) value. In this method a coated film on a flexible substrate like polycarbonate (PC) of specific thickness is bended in a well-defined way while the film is observed by a microscope. If cracks appear the crack onset strain ε can be calculated



10.1 Set-up for the determination of the crack onset strain.

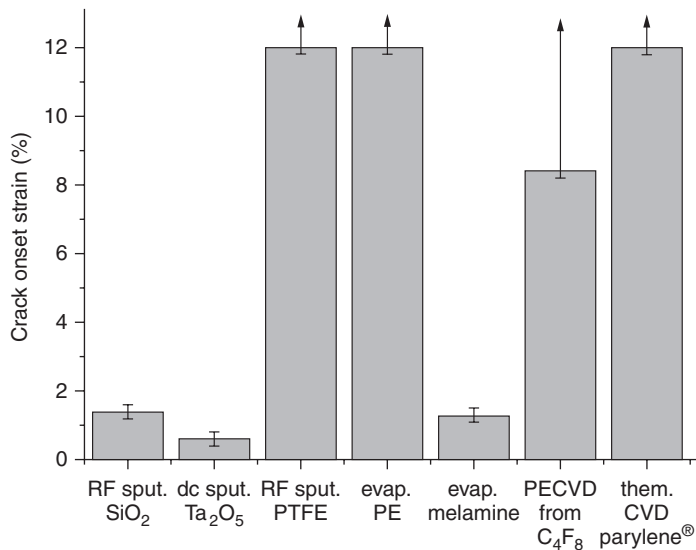
from the bending radius R and the substrate thickness d by Equation [10.1]. Figure 10.1 shows the principle.

$$\varepsilon = \frac{\Delta L}{L} = \frac{\Delta R}{R} = \frac{d}{2 \cdot R} \quad [10.1]$$

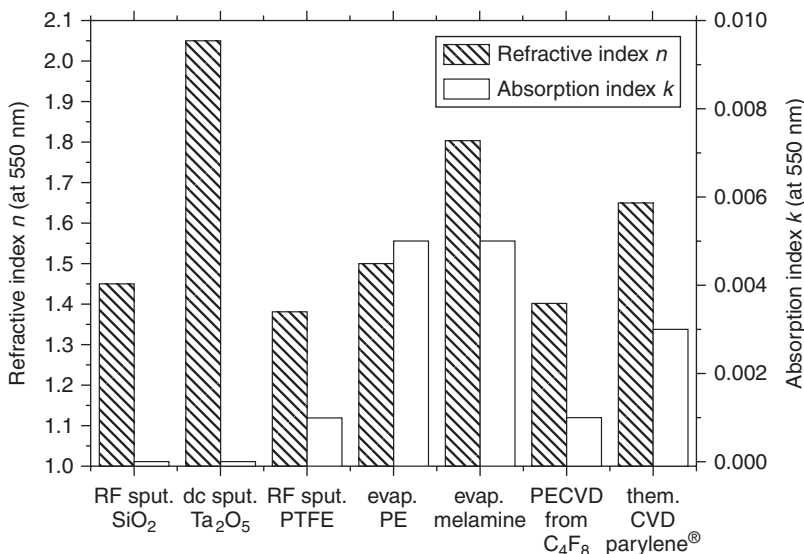
As shown in Fig. 10.2 the crack onset strain value of many organic layer materials is above 12% (this was the maximum value of the experimental set-up). Ceramic layer materials typically show values of about 1% or less. For the coatings on 100 µm thick foils this means a bending radius 12 times lower at 0.4 mm instead of 5 mm until the coating shows cracks.

For the application in optical layer systems a broad range of refraction indices in combination with low absorption and also low haze value is necessary. The refractive indices of organic materials vary from 1.4 (at 550 nm) for RF sputtered fluorocarbon layers to 1.8 for materials like evaporated melamine (Fig. 10.3). This variation is broad enough for simple optical designs like antireflective coatings. Haze values and absorptions of organic thin films are often not as low as in metal oxides used for optical applications. This has to be considered for more complex optical designs.

It is well known that fluorine-containing organic materials (such as parylene® AF-4, PTFE, etc.) show a high water contact angle up to 120°



10.2 Crack onset strain of various layer materials on polycarbonate substrates (Neubert *et al.*, 2011a).



10.3 Refractive and absorption indices of various deposited layer materials (Neubert *et al.*, 2011a).

and a low surface energy (Li *et al.*, 2011). By the use of sputtered PTFE, for example, release layers or easy to clean surfaces of optical systems can be produced. However, care must be taken to avoid delamination of the layers on top of such fluorocarbon layers, since it also reduces the adhesion of subsequent layers. This will be described in more detail in Section 10.4.5.

Organic materials are generally not as stable against heat, radiation and energetic particle bombardment as most oxide materials. This fact limits the tolerable process conditions in the preparation and the operation of these layers. On the other hand it offers a possibility to modify these layers, for example, by plasma treatment for better adhesion of following layers, for better cross linking or to gain special surface structures. A good example therefore is poly-(methyl methacrylate) (PMMA). Deposition on PMMA substrates by sputtering often damages the molecular structure on the surface of the substrate causing typically weak adhesion of the sputtered layers. On the other hand plasma etching of PMMA surfaces can be used to generate fractal moth eye-like surface structures to lower reflectivity of these surfaces (Kaless *et al.*, 2005).

In electronic devices such as OLED on polymer substrates or solar cells, both transparency and diffusion barrier against water and oxygen are required. The permeability of organic materials for water, oxygen and other gases is higher than in most oxides. However, the high crack onset strain of organic layers and some very conform deposition processes which have the tendency to level out the surface roughness like the parylene® deposition process provide useful layers for diffusion barriers, especially in combination with ceramic layers as multilayer systems (Chiang *et al.*, 2006). Creation of diffusion barriers by the use of multilayers and composite materials is a widely studied topic of materials and process research.

10.3 Optical coatings with organic layers

Because of their special properties different applications for organic layers in optical layer systems are possible. Since there is a relatively broad variation of refractive indices from 1.4 to 1.8, pure organic optical interference filters are theoretically possible. Weber showed that these kinds of optical interference layer systems are possible to make with an extruding technique of polymer foils (Weber, 2012). However, pure organic optical interference filters made with vacuum deposition techniques from low and high refractive index materials are hard to find in the literature. Better realizable are combinations of organic layer materials and oxide or metal thin films. Affinito *et al.* showed this for vacuum flash evaporated and radiation cross-linked monomers (hexane diol diacrylate) in combination with sputtered silver for

Fabry-Perot filters (Affinito *et al.*, 1995). Such polymer containing layers are suitable for web coating and coatings for thermo-formable substrates.

Due to its low surface energy in combination with sufficient optical properties (low refraction and absorption indices) of fluorocarbon layers these layers are suited as top coating for optical layer systems with anti-sticking or easy to clean properties (Jaszewski *et al.*, 1999).

An interesting further application is the use of stacks of organic materials and metal oxides as transparent bendable diffusion barriers. These types of barriers are interesting as corrosion protection or diffusion barriers for OLED and organic photovoltaic (OPV) systems react very sensitively to water and oxygen (Singh *et al.*, 2007).

Well defined thin films of organic materials like stearic acid or fluorescent dyes can be used for measurements of photocatalytic surfaces (Neumann and Cerezuela Barreto, 2004; Neubert *et al.*, 2007, 2008). The photocatalytic decomposition processes oxidize the organic layers which can be measured and analyzed by optical measuring methods.

Composites of organic materials with metal oxides can be used to combine different properties of the materials. A good example for this is evaporated color pigments in metal oxides for decorative applications. The composites combine sufficient wear resistance with the intense color of organic dyes (Jäger, 1997).

10.4 Deposition techniques

Organic layers can be deposited by various techniques, such as lacquering, sol-gel and atmospheric plasma deposition processes. Here, the focus is on vacuum deposition methods, which are often used to obtain dense layers with good uniformity, homogeneity and material properties. Thus, for all processes discussed in this chapter, vacuum chambers with suitable pumps (turbo molecular pumps or oil diffusion pumps) were used. Chambers with these pumps typically reach pressures in the range of 10^{-6} mbar.

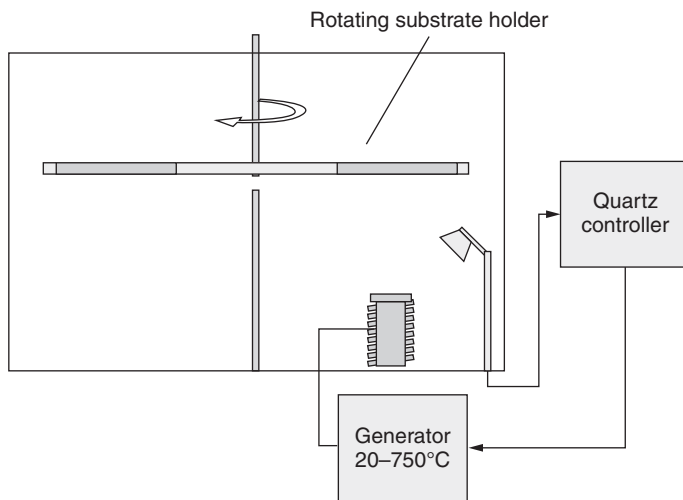
Using organic materials as deposition materials, some factors have to be considered. Organic materials often have lower evaporation temperatures than many inorganic materials. Thus the effort for process equipment can be lower than for the evaporation of metals or oxides. The organic molecules in the gas phase are also often more complex and can act like a precursor in a chemical vapor deposition (CVD) process if a gas discharge is involved in the deposition process. That is why fragments of these molecules can coat pressure gauges or other sensitive parts of the reactor. Organic molecules are also more sensitive against overheating, plasma UV radiation, high energetic particles or chemical active species such as oxygen radicals. Chemical reactions caused by these processes can generate unwanted species in the deposition process and can be harmful. Therefore, the development of

processes suitable for organic coatings has to consider these aspects. In the next section, an overview is given on different processes which were used at the author's facility to deposit organic layers.

10.4.1 Thermal evaporation

Probably the easiest way to deposit organic matter is by thermal evaporation. Many organic materials can be deposited in a classical evaporation set-up with thermal boat evaporators. Because of its lower evaporation temperature (often below 500°C) organic materials can also be evaporated with simpler set-ups, such as using a crucible in a heating cartridge (Figs 10.4 and 10.5). Typical for these types of processes the deposition rate is very sensitive to the heating power. To gain constant deposition rates and defined thicknesses quartz controlling of the heater is recommended.

The choice of evaporable organic materials is mainly limited by thermal degradation processes. In particular, polymers and other large molecules with low vapor pressure will be thermally cracked before being evaporated. Organic materials that can be evaporated are polyethylene (PE) (Bekiarov *et al.*, 1988), polyamide (PA) (Meurisch *et al.*, 2012), polyimide (PI) (Spassova *et al.*, 1996), melamine (Schulz *et al.*, 2011), various color pigments (e.g., Cu-phthalocyanine (Jäger, 1997)) and stearic acid (Neubert *et al.*, 2007), for example. Emission layers in OLEDs like tris-(8-hydroxy-quinolinolato) aluminum (Alq_3) are also known to be deposited with evaporation processes (Lee *et al.*, 2004; Eritt *et al.*, 2010). Evaporated organic



10.4 Evaporation set-up with substrate holder, quartz deposition controller and evaporation source.



10.5 Heating cartridge with quartz crucible as evaporation source for organic material.

materials like TinuvinTM 360 (a commercial UV pigment by BASF) and N,N'-di(1-naphthyl)-N,N'-diphenyl-1,1'-diphenyl-1,4'-diamine (NPD) (a material that can also be used as organic hole transport layer in OLEDs (Iwama *et al.*, 2006)) have been found to be useful as UV protective layers on polymer substrates like polycarbonate (PC) (Präfke *et al.*, 2012). There are also commercial water and oil repellent materials like Patinal® WR5 from Merck, for example, to improve the easy to clean, anti-fingerprint properties and the haptic properties of touch screen surfaces. These materials are typically coated using evaporation, too.

Some materials like polyethylene form a highly viscous melt during the evaporation process. Boiling of a melt like this may cause spitting of droplets that condense on the growing layers with sizes of some 100 µm. This effect is highly undesirable and can be suppressed by higher source-to-substrate distances and heated covers on the crucible.

The addition of energy to the forming layers – by UV radiation or particle bombardment – can induce chemical reactions. Cross-linking of the molecules and the mechanical stability of the layers can be improved by this process (Choukourov *et al.*, 2006). The particle bombardment can be performed with an ion source or by a radio-frequency (RF) gas discharge with the substrate as cathode.

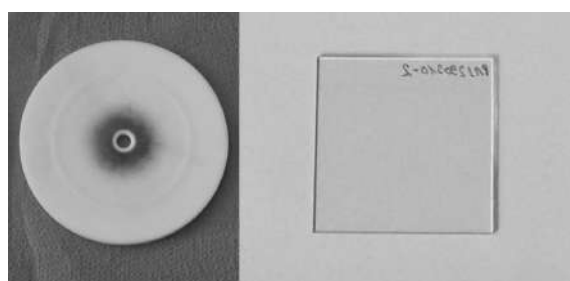
Matrix assisted pulsed laser evaporation (MAPLE) is a special type of evaporation process for organic materials. For this kind of process a pulsed laser beam hits a frozen target (100–200 K) of organic matter in a solvent matrix (Piqué *et al.*, 1999). The laser pulse evaporates the frozen solvent and the solved organic material is released to the gas phase. The solvent concentration has to be high enough that the dissolved molecules are more or less separated from each other. By this technique it is possible to deposit materials with large molecular weights such as polymer chains like PMMA

(Sellinger *et al.*, 2008), polyethylene glycol (PEG) (Paun *et al.*, 2011) or even sugars (Piqué *et al.*, 1999) without damaging the molecules. Although this technique is very promising it seems difficult to scale this deposition process up for large surfaces.

10.4.2 RF sputtering

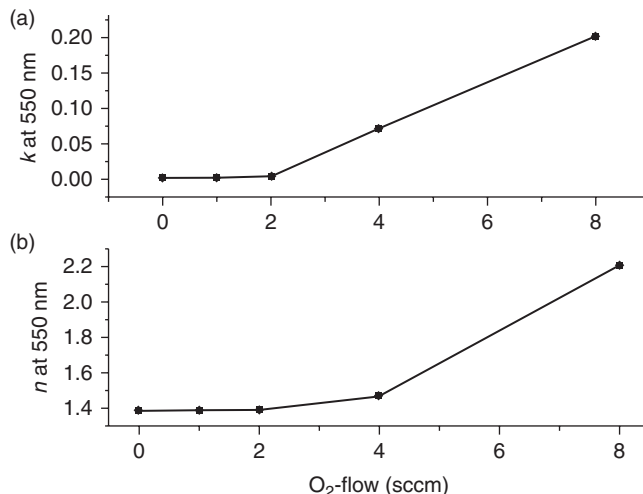
Most organic materials cannot be deposited by direct current (DC) magnetron sputtering. On the one hand, their electrical conductivity is often too low to keep the electric discharge running. On the other hand, the ion bombardment in the sputtering process influences the molecular structure. Normally molecular chains are broken, leading to layers with an amorphous, undefined structure on the substrate. However, there are some reports of sputtered polymer layers like polytetrafluoroethylene (PTFE) (Pratt and Lausman, 1972; Morrison and Robertson, 1973; Biederman *et al.*, 1977; Li *et al.*, 2011), polyimide (PI) (Biederman *et al.*, 2003), polypropylene (PP) (Stelmashuk *et al.*, 2004) and polyethylene (PE) (Kholodkov *et al.*, 2003; Kousal *et al.*, 2005). The deposited layers are structurally not identical to the polymer source materials but they basically consist of shorter fragments of the original material with strong cross linking (Li *et al.*, 2011). Nevertheless some optical, chemical and mechanical properties make these films interesting.

RF sputtering of PTFE has been known since the 1970s. The sputtered fluorocarbon layers typically show a low absorption index ($k \approx 0.001$) (Neubert *et al.*, 2011a), low refractive index ($n = 1.35$ to 1.48 (Biederman *et al.*, 1977)) and high hydrophobicity (water contact angle of about 120° and greater) (Kylián *et al.*, 2011). For the deposition a magnetron sputter deposition chamber with a PTFE plate as sputter target can be used (Fig. 10.6). An RF power supply is needed since PTFE is electrically non-conducting. To avoid chemical reactions, a pure argon atmosphere in the range of 10^{-2} to 10^{-3} mbar should be used. Adding oxygen to the process gas

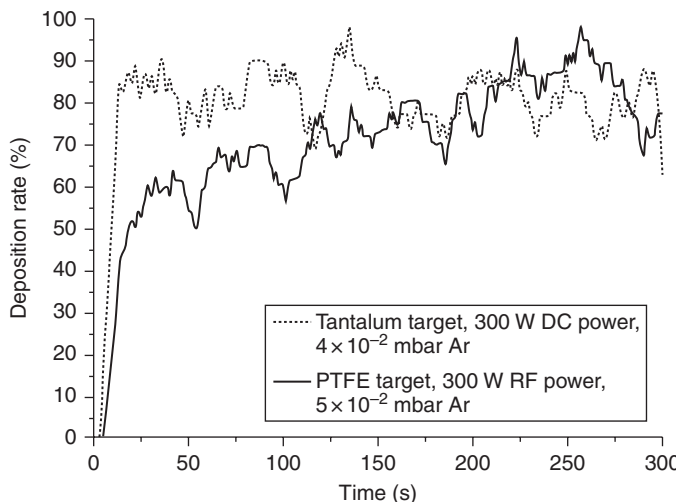


10.6 Pictures of a PTFE sputter target and a sputtered fluorocarbon layer on a glass substrate.

causes decreasing deposition rate and increasing optical absorption of the layers (Fig. 10.7). It can be shown that the deposition rate of sputtered PTFE is not constant during the deposition process compared with ‘standard’ sputtering processes for metal or metal oxide films (Fig. 10.8). Obviously heating of the PTFE target causes an increasing emission of fluorocarbon fragments.



10.7 Influence of oxygen on (a) refractive and (b) absorption index of RF sputtered fluorocarbon layers (Neubert *et al.*, 2010).



10.8 Deposition rate of sputtered PTFE and sputtered tantalum in argon atmosphere as a function of deposition time measured with a quartz monitor.

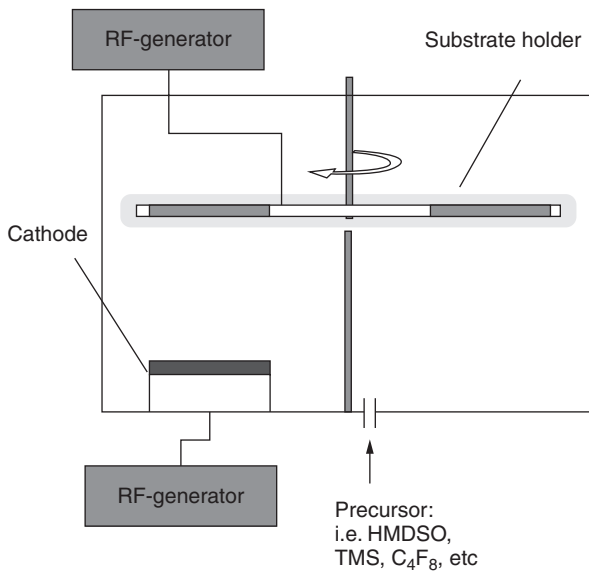
For exact thickness and rate control an optical or quartz crystal monitoring or controlling device can be used.

Pressure and the target-to-substrate distance have an influence on the surface energy and water contact angle of the sputtered fluorocarbon layers. For layers made at relatively high sputter pressures (50 Pa) and at large target-to-substrate distances (25 cm) values of over 170° have been reported (Kylián *et al.*, 2011). The intrinsic hydrophobic effect of the fluorocarbon is amplified by a very porous and rough structure of the layers caused by the lower energy input to the growing layer (Kylián *et al.*, 2011).

10.4.3 Physical enhanced chemical vapor deposition (PECVD)

All chemical vapor deposition processes have in common that gases, vapors or aerosols are delivered to a substrate where they condense to solid layers during controlled process conditions such as energy, temperature or pressure. Plasma enhanced chemical vapor deposition (PECVD) is a widely used technique for the production of coatings. The main advantage of PECVD is that the temperature can be reduced from a range of 400–2000°C down even to room temperature so that temperature sensitive substrates such as polymers can be coated. The plasma can be generated in different ways: electric fields are commonly used, ranging from low frequency (kHz region), high frequency (MHz) or microwaves in the GHz range. To generate the plasma in a practical way, a large variety of process variations have been developed. Plasma sources can be powered from low frequency to microwave and may have a circular or linear shape. Also double linear sources are available. Hollow cathodes or even sputter magnetrons can be used as plasma sources. Often the plasma density is increased by the use of magnetic fields.

To form plasma polymers, an electrical gas discharge is used to crack bonds in organic gaseous precursor molecules to create reactive species that react on surfaces next to the discharge plasma. The gas discharge can be provided by a special ion or plasma source or by a simple glowing cathode. A separate electrode or the substrate itself can be used as cathodes. Since electrical non conducting layers are often produced, the power supply is often by RF, pulsed DC or microwave. Typical working pressures are in the range of 0.01 to 10 torr (ca. 10^{-2} to 10 mbar) (Kinzig and Smardzewski, 1981). However, there are also processes at higher pressures like atmospheric pressure CVD using special dielectric barrier discharge sources. A sketch of a low pressure PECVD set-up using parallel plates is shown in Fig. 10.9. The same set-up can be used for the deposition of ceramic and organic films by PECVD. The type of films is determined by the type of process gases and the deposition conditions.

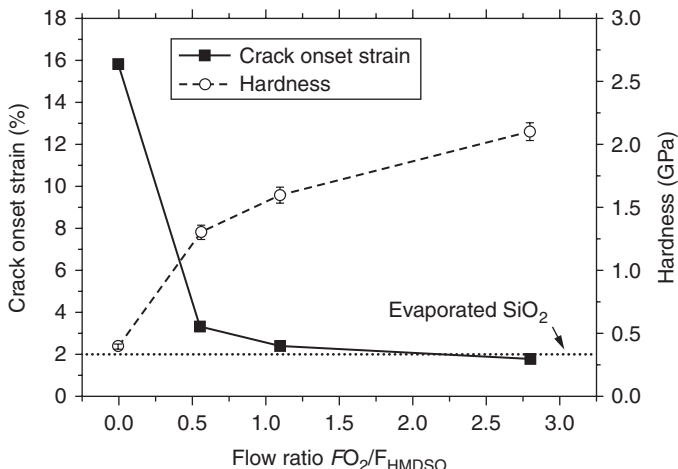


10.9 Sketch of a PECVD coating set-up.

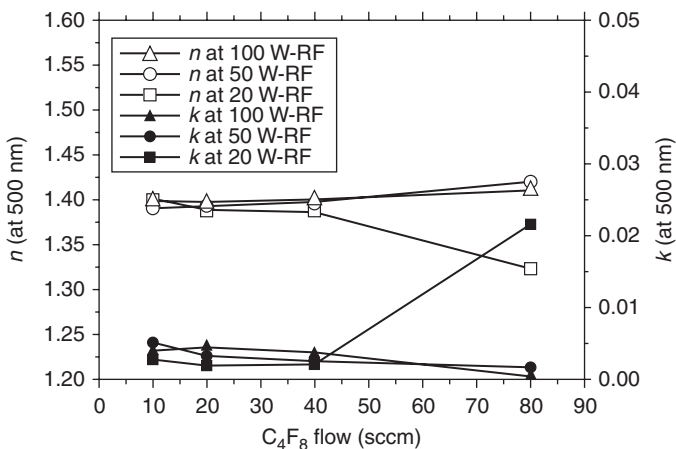
Well known precursors for organic coatings are, for example, silanes like hexamethyldisiloxane (HMDSO) (Schwarz *et al.*, 1998) or tetramethylsilane (TMS) (Noborisaka *et al.*, 2012). While oxygen is present, silicon dioxide-like films can be produced with these compounds. In the absence of oxygen the films gain more organic properties such as higher flexibility and lower hardness (Fig. 10.10). Carbon bindings do not get oxidized by the oxygen and the films get more mechanically flexible. These layers are reported to be transparent in the visible range with a refractive index n between 1.45 to 1.58 and absorption index k below 2.6×10^{-3} (Martin-Palma *et al.*, 2006). Typical applications of these layers are wear resistant coatings to protect sensitive substrates like polymer foils. Non-sticking layers with high water contact angle are also known (SICON®) (Corbella *et al.*, 2008).

Methyl methacrylate (MMA) as precursor can be used to prepare plasma polymerized poly(methyl methacrylate) (pPMMA) thin films (Kinzig and Smardzewski, 1981; Lim and Shin, 2007). These layers have been found to be useful, for example, as buffer layers in OLEDs.

Also different fluorinated precursors such as CF_4 and C_4F_8 can be used (Takahashi *et al.*, 2000). Films prepared with these precursors show very similar properties to RF sputtered thin films from PTFE targets. They are highly transparent. They have high water contact angles of 110° (Matsumoto and Ishida, 2000), a low refraction index of $n = 1.40$ (Fig. 10.11) and the infrared absorption spectra (Fig. 10.12) are almost identical (Neubert *et al.*, 2011a). The deposition rate for these processes depends on power and the

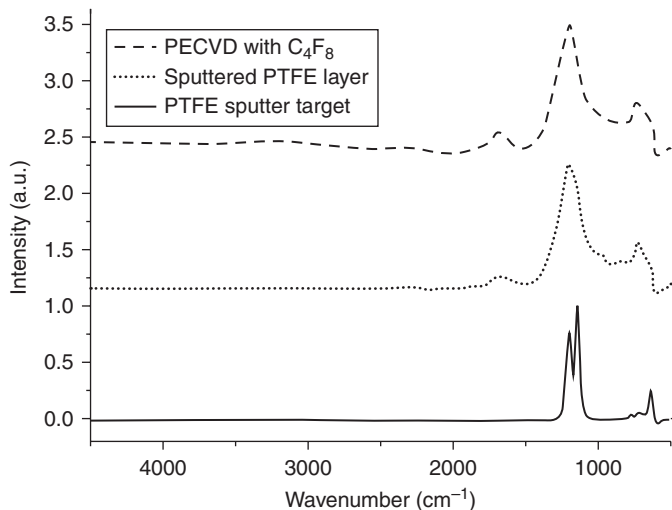


10.10 Crack onset strain and hardness as a function of the ratio of oxygen to HMDSO for PECVD made thin films.

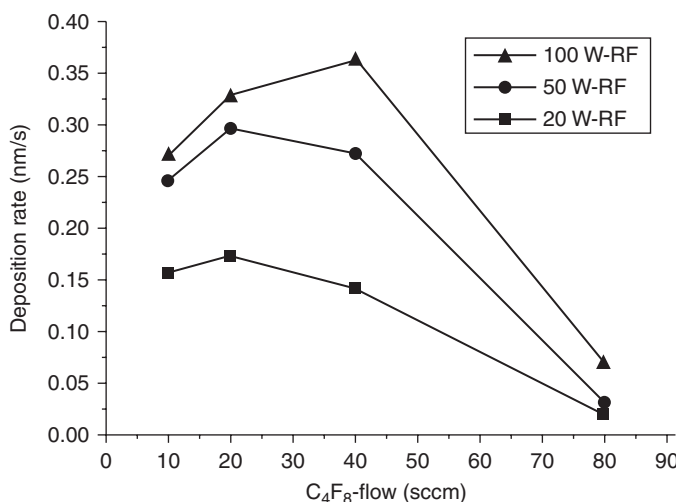


10.11 Refraction and absorption indices at 500 nm for different plasma powers as a function of C₄F₈ precursor flow.

amount of available precursor molecules (Fig. 10.13). Thus, there is an optimal working point: If there are not enough precursor molecules the deposition itself is limited. On the other hand, if there are too many precursor molecules only a part of them can be activated, which limits the deposition process as well. It is reported that a further increase of the deposition rate can be achieved for instance by addition of methane (CH₄) to the process (Matsumoto and Ishida, 2000).



10.12 Infrared attenuated total reflectance (IR-ATR) spectra for PECVD made layers with C_4F_8 as precursor, for RF sputtered fluorocarbon layers and for the used PTFE sputter target.



10.13 Deposition rate for different plasma powers as a function of C_4F_8 precursor flow.

10.4.4 Non-plasma activated chemical vapor deposition

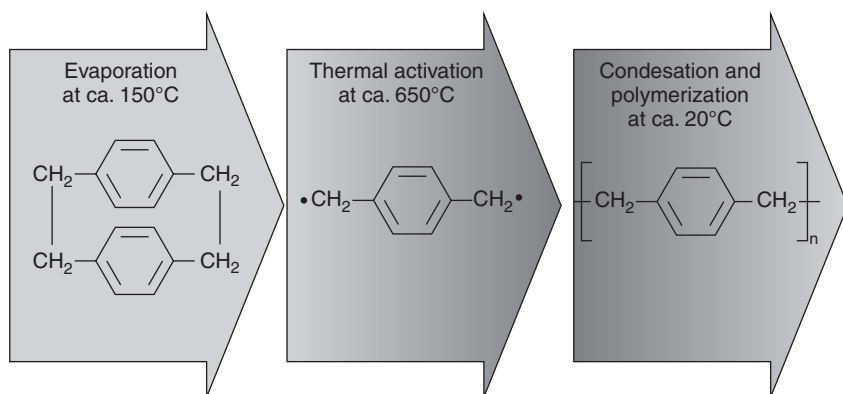
Vacuum deposition processes that use gas discharge plasmas, such as assisted evaporation, sputtering or PECVD, are not suited to obtain organic layers with well-defined chemical structure like polymers. The high energies of

particles in gas discharges of up to some 10 eV (some 100 eV for reflected ions) (Frey, 1995) and UV radiation damage the organic material in the gas phase and in the growing layers. For the preparation of layers with a typical polymer molecular structure (long chains of monomer molecules) using CVD processes, other ways for activating the polymerization reactions have to be used. Possibilities therefore are activations by thermal or chemical processes. Activation by UV light is known too (Ruiz *et al.*, 2010).

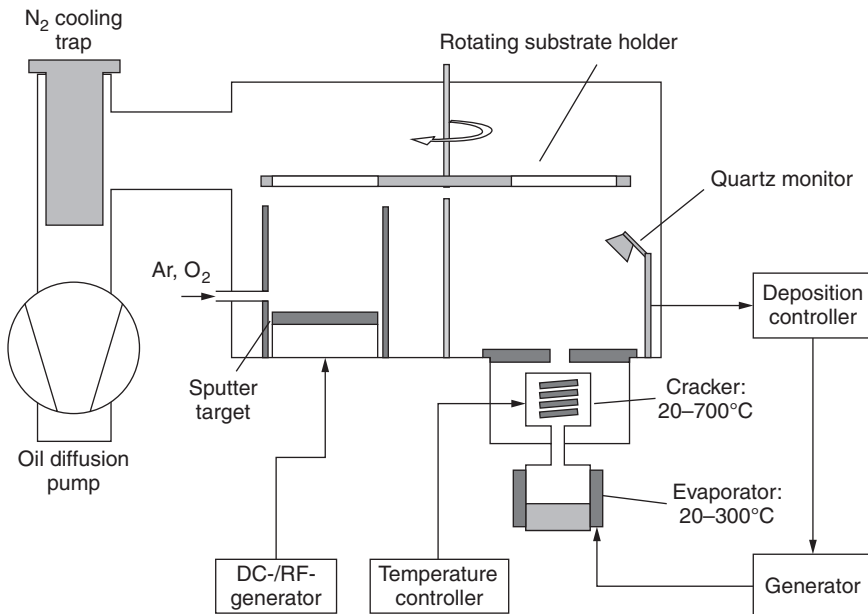
A good example for a CVD process with thermal excitation of the precursor is the deposition of poly-para-xylylene (parylene®). For different applications various derivates of this material are available. Parylene N is the non-modified poly-para-xylylene. Parylene® types C and D are modified with chlorine to gain a more dense coating for applications like diffusion barriers, while parylene® type AF-4 is modified with fluorine and generates hydrophobic surfaces. Typical applications for parylene® layers are diffusion barriers (Ke *et al.*, 2004), biocompatible layers in the medical field (Li *et al.*, 2011b) and corrosion protective layers for electrical devices (Cieslik *et al.*, 2011).

For the parylene® deposition process the dimer molecules (di-para-xylylene) are evaporated in vacuum at temperatures of about 150°C. The vapor is then heated further (up to 650°C) to create radicals. The condensation of these radicals on surfaces at room temperature and low pressures leads to a polymerization process (Fig. 10.14).

Important aspects of these types of deposition process are that the layers are very uniform and dense (Fortin and Lu, 2004). The deposition process takes place in the whole deposition chamber. Thus the backsides and cavities of the substrates and all non-heated parts of the chamber (like vacuum pumps, other deposition sources or pressure gauges) are being coated. The



10.14 Scheme of the polymerization process of poly-para-xylylene (Neubert *et al.*, 2011a).



10.15 Deposition set-up for poly-para-xylylene (Neubert *et al.*, 2011b).

deposition rate strongly correlates with the process pressure and the substrate temperature (Fortin and Lu, 2002). The pressure is a measure for the amount of molecules in the gas phase. Thus a higher pressure causes more monomer molecules to hit the substrate. Substrate temperature influences the sticking coefficient of the monomers. Higher substrate temperatures reduce the resident time of the monomer molecules and lower their possibility to polymerize. There are threshold temperatures above which no deposition takes place.

A possible deposition set-up is sketched in Fig. 10.15. Turbo molecular pumps have water cooled surfaces inside that are being coated by this type of deposition process. This will damage these kinds of pump. Better suited are oil diffusion pumps in combination with nitrogen cooled cooling trap. Similar to evaporation processes the deposition rate can be controlled by a quartz deposition controller.

The refractive index depends slightly on the type of parylene®. For the non-modified poly-para-xylylene values in the range from 1.65 to 1.67 (Fortin and Lu, 2004; Neubert *et al.*, 2011b) are known. Absorption index with $k = 0.001$ and haze values smaller than 1% can be reached for deposition pressures below 10^{-2} mbar (Neubert *et al.*, 2011b).

Another special type of CVD process for the deposition of polymer thin films is the so called initiated CVD (iCVD) for example for PMMA (Chan and Gleason, 2005; Chen and Anthamatten, 2008) or poly(glycidyl

methacrylate) (PGMA) (Spee *et al.*, 2011) thin films. For this process, monomer molecules (i.e. methyl methacrylate (MMA) or glycidyl methacrylate (GMA)) and initiator molecules (i.e. organic peroxides like t-butyl peroxide (TBPO)) are used. At low pressures of a few millibars, the initiator molecules are cracked into radicals at temperatures of about 220°C at a hot zone of the reactor (i.e. a heated tube that the precursor mixtures are conducted through). At low substrate temperatures of about –15°C the gas mixture condenses and the radicals start a polymerization processes. The layers are reported to be very similar to PMMA bulk material. iCVD in combination with ceramic films also turned out to be suitable for barrier layers. It is well known that polymer layers can cover defects which are present in ceramic layers. In addition the spreading of cracks in the ceramic films can be stopped by the organic interlayers. On the other hand ceramic layers have an intrinsically good barrier property, therefore the use of multilayers can be very effective for the realization of ultra-barriers with low water vapor transmission rates.

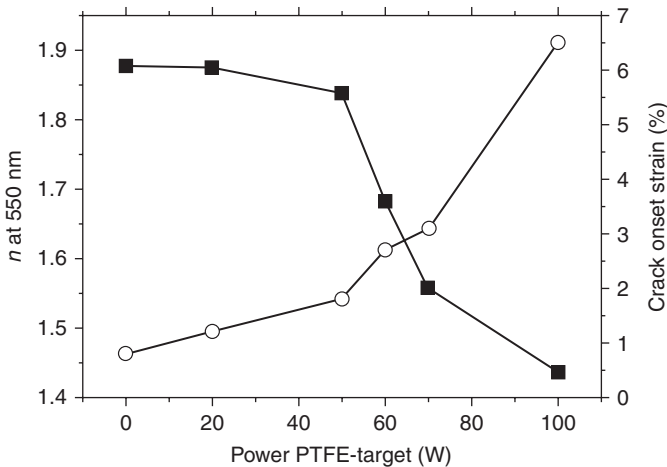
10.4.5 Adhesion improvement by plasma treatment

Adhesion in vacuum deposition processes depends on the substrate material and its surface structure. On organic substrates and surfaces the adhesion can often be improved by special treatments to remove pollutants, to roughen the surface or to create functional groups on the surface. Therefore a plasma treatment in different gas atmospheres (argon, oxygen, nitrogen, etc.) can be used. These treatments can be performed under low pressure conditions by ion sources or under atmospheric conditions by dielectric barrier discharge set-ups.

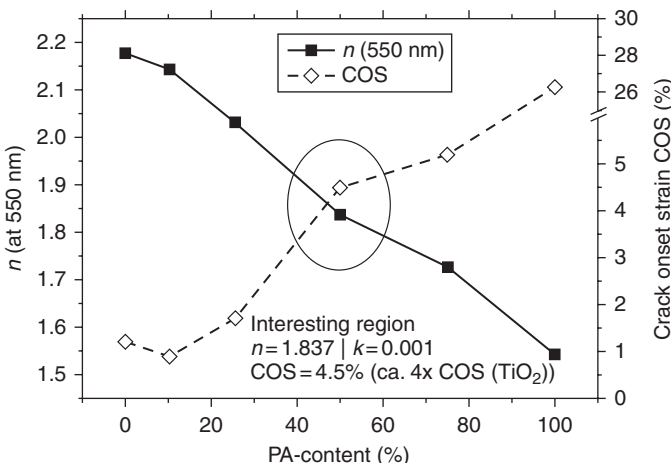
Good examples of adhesion improvement by plasma treatment are fluorocarbon surfaces or PTFE substrates. Due to their low surface energy adhesion of thin films on these surfaces is mostly very poor. A plasma treatment of the surfaces in a hydrogen-containing atmosphere (i.e. argon with 5% hydrogen or ammonia) at low pressures of about 5×10^{-2} mbar can lead to a substitution of fluorine atoms by hydrogen (Badey *et al.*, 1996; Neubert *et al.*, 2012). This effects changes the surface energy and water contact angle of the surfaces and causes better adhesion. This can be used for good adhesion of metal or metal oxide thin films on PTFE substrates as well as for RF sputtered fluorocarbon layers in optical layer stacks.

10.5 Composites

Composite materials offer ways to combine the properties of different materials. The combination of high refractive index oxides with mechanically flexible polymer layers, for example, generates layers with higher



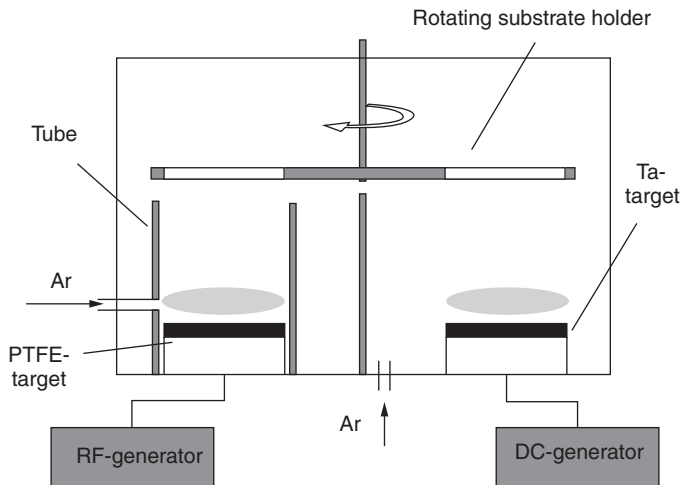
10.16 Refractive index and crack onset strain for co-sputtered Ta_2O_5 -PTFE-composite thin films (Neubert *et al.*, 2010).



10.17 Refractive index and crack onset strain for co-evaporated TiO_2 -polyamide-composite thin films.

refractive index than the original polymer which remain flexible (Figs 10.16 and 10.17). Combinations of evaporated color dyes with hard metal oxides generate decorative layers with higher wear resistance than the dye layers (Jäger, 1997).

A good way to prepare thin film composites is by parallel deposition from two sputter or evaporation deposition sources. The substrate can oscillate between the two sources or the two sources can be focused on one substrate position. Problems occur when the deposition processes influence



10.18 Sketch of a sputtering set-up for organic–inorganic composites (Neubert *et al.*, 2010). Ta-target, Tantalum sputter target.

each other. Activated oxygen and UV radiation from a sputtering process of a metal oxide can chemically attack organic molecules. Gaseous organic substances can be decomposed by the gas discharge of a sputter target and poison the target surface. A good separation of the sources by housing and suitable gas flows can solve problems like this (Fig. 10.18).

10.6 Conclusion

The vacuum deposition of organic thin films is often a difficult task. In particular the complex molecular structure can be influenced by the deposition process. Thus, depending on the coating material, the desired layer properties, the layer applications and the substrate material, different deposition techniques are possible. We presented in this chapter an overview of various vacuum deposition techniques for organic thin films with examples for evaporation, sputter deposition, PECVD and other CVD processes. Nevertheless the organic layer materials offer a broad spectrum of new optical, mechanical, chemical and other properties that make them interesting to extend the usability of ceramic (oxide) layer systems or even to replace them. Besides the deposition of single organic layers, problems like adhesion and the preparation of composites were mentioned, too.

Many questions within this topic remain unanswered. An interesting field for further research would be, for example, better ultra-barriers for OLED and OPV application on flexible substrates, flexible optical thin films for tunable optical filters, switchable wettability, the upscaling of some organic deposition processes for larger substrates and others.

10.7 References

- J. Affinito, P. Martin, M. Gross, C. Coronado, E. Greenwell, 'Vacuum deposited polymer/metal multilayer films for optical application', *Thin Solid Films* **270** (1995) 43–48.
- J. P. Badey, E. Espuchet, D. Sage, B. Chabert, Y. Jugnet, C. Batier, Tran Minh Duc, 'Comparative study of the effects of ammonia and hydrogen plasma downstream treatment on the surface modification of polytetrafluoroethylene', *Polymer* **37** (1996) 1377–1386.
- D. Bekiarov, B. Pashmakov, A. Vateva, 'A study of the adhesion of vacuum evaporated polyethylene films on aluminium', *Thin Solid Films* **157** (1988) 43–48.
- H. Biederman, S. M. Ojha, L. Holland, 'The properties of fluorocarbon films prepared by r.f. sputtering and plasma polymerization in inert and active gas', *Thin Solid Films* **41** (1977) 329–339.
- H. Biederman, V. Stelmashuk, I. Kholodkov, A. Choukourov, D. Slavinska, 'RF sputtering of hydrocarbon polymers and their derivatives', *Surface and Coatings Technology* **174–175** (2003) 27–32.
- K. Chan, K. Gleason, 'Initiated CVD of Poly(methyl methacrylate) thin films', *Chemical Vapor Deposition* **11** (2005) 437–443.
- X. Chen, M. Anthamatten, 'Multicomponent vapor deposition polymerization of poly(methyl methacrylate) in an axisymmetric vacuum reactor', *Polymer* **49** (2008) 1823–1830.
- C.C. Chiang, D.S. Wuu, H.B. Lin, Y.P. Chen, T.N. Chen, Y.C. Lin, C.C. Wu, W.C. Chen, T.H. Jaw, R.H. Horng, 'Deposition and permeation properties of SiN_x/parylene multilayers on polymeric substrates', *Surface & Coatings Technology* **200** (2006) 5843–5848.
- A. Choukourov, J. Hanus, J. Kousal, A. Grinevich, Y. Pihosh, D. Slavinska, H. Biederman, 'Thin polymer films from polyimide vacuum thermal degradation with and without a glow discharge', *Vacuum* **80** (2006) 923–929.
- M. Cieslik, K. Engvall, J. Pan, A. Kotarba, 'Silane–parylene coating for improving corrosion resistance of stainless steel 316L implant material', *Corrosion Science* **53** (2011) 296–301.
- C. Corbella, I. Bialuch, M. Kleinschmidt, K. Bewilogua, 'Modified DLC coatings prepared in a large-scale reactor by dual microwave/pulsed-DC plasma-activated chemical vapour deposition', *Thin Solid Films* **517** (2008) 1125–1130.
- M. Eritt, C. May, K. Leo, M. Toerker, C. Radehaus, 'OLED manufacturing for large area lighting applications', *Thin Solid Films* **518** (2010) 3042–3045.
- J. B. Fortin, T.-M. Lu, 'A model for the chemical vapor deposition of poly(para-xylylene) (parylene) thin films', *Chemical Materials* **14** (2002) 1945–1949.
- J. B. Fortin, T.-M. Lu, *Chemical Vapor Deposition – The Growth and Properties of Parylene Thin Films*, Kluwer Academic Publishers (2004).
- H. Frey, *Vakuumbeschichtung 1 Plasmaphysik – Plasmadiagnostik – Analytik*, VDI Verlag, Düsseldorf (1995).
- Y. Iwama, T. Itoh, T. Mori, T. Mizutani, 'Electroluminescent properties of organic light-emitting diodes using BaAl₂ and Alq₃ co-evaporation layer', *Thin Solid Films* **499** (2006) 364–368.
- S. Jäger, 'Investigation on the optical and mechanical properties of organic dye-metal oxide composite films', *Surface and Coatings Technology* **93** (1997) 58–63.

- R.W. Jaszewski, H. Schift, B. Schnyder, A. Schneuwly, P. Gröning, 'The deposition of anti-adhesive ultra-thin teflon-like films and their interaction with polymers during hot embossing', *Applied Surface Science* **143** (1999) 301–308.
- A. Kaless, U. Schulz, P. Munzert, N. Kaiser, 'NANO-motheye antireflection pattern by plasma treatment of polymers', *Surface & Coatings Technology* **200** (2005) 58–61.
- L. Ke, R. S. Kumar, K. Zhang, S.-J. Chua, A.T.S. Weeb, 'Effect of parylene layer on the performance of OLED', *Microelectronics Journal* **35** (2004) 325–328.
- I. Kholodkov, H. Biederman, D. Slavinska, A. Choukourov, M. Trchova, 'Plasma polymers prepared by RF sputtering of polyethylene', *Vacuum* **70** (2003) 505–509.
- B.J. Kinzig, R.R. Smardzewski, 'Plasma polymerized thin coatings from methyl-methacrylate, styrene and tetrafluoroethylene', *Surface Technology* **14** (1981) 3–16.
- J. Kousal, J. Hanus, A. Choukourov, P. Hlídek, H. Biederman, D. Slavínská, J. Zemek, 'RF magnetron sputtering and evaporation of polyisobutylene and low density polyethylene', *Surface & Coatings Technology* **200** (2005) 472–475.
- O. Kylián, M. Drábik, O. Polonskyi, J. Čechvala, A. Artymenko, I. Gordeev, A. Choukourov, I. Matolínová, D. Slavínská, H. Biederman, 'Deposition of nanostructured fluorocarbon plasma polymer films by RF magnetron sputtering of polytetrafluoroethylene', *Thin Solid Films* **519** (2011) 6426–6431.
- C.B. Lee, A. Uddin, X. Hu, T.G. Andersson, 'Study of Alq₃ thermal evaporation rate effects on the OLED', *Materials Science & Engineering B* **112** (2004) 14–18.
- L. Li, P. M. Jones, Y.-T. Hisa, 'Characterization of a nanometer-thick sputtered polytetrafluoroethylene film', *Applied Surface Science* **257** (2011) 4478–4485.
- W. Li, D. C. Rodger, A. Pinto, E. Meng, J. D. Weiland, M. S. Humayun, Y.-C. Tai, 'Parylene-based integrated wireless single-channel neurostimulator', *Sensors and Actuators A* **166** (2011) 193–200.
- J.-S. Lim, P.-K. Shin, 'Improved performance of organic light-emitting devices with plasma treated ITO surface and plasma polymerized methyl methacrylate buffer layer', *Applied Surface Science* **253** (2007) 3828–3833.
- R.J. Martin-Palma, R. Gago, V. Torres-Costa, P. Fernández-Hidalgo, U. Kreissig, J.M. Martínez Duart, 'Optical and compositional analysis of functional SiOxCy:H coatings on polymers', *Thin Solid Films* **515** (2006) 2493–2496.
- Y. Matsumoto, M. Ishida, 'The property of plasma-polymerized fluorocarbon film in relation to CH₄/C₄F₈ ratio and substrate temperature', *Sensors and Actuators* **83** (2000) 179–185.
- K. Meurisch, B. Gojdka, T. Strunskus, V. Zaporotchenko, and F. Faupel 'Vapour phase deposition of highly crystalline self-poled piezoelectric nylon-11', *Journal of Physics D: Applied Physics* **45** (2012) 055304 (+6pp).
- D.T. Morrison, T. Robertson, 'RF sputtering of plastics', *Thin Solid Films* **15** (1973) 87–101.
- T. Neubert, W. Sun, F. Neumann, M. Vergöhl, 'Characterization of photocatalytic activity of TiO₂ thin films for optical applications', *Conference Optical Interference Coatings* (2007) ThA10.
- T. Neubert, F. Neumann, M. Vergöhl, 'Method for quantifying the photocatalytic activity of surfaces and use thereof', Patent WO 2008/046588 A1.

- T. Neubert, S. Drost, K. Nagel, M. Vergöhl, 'Polymer metal oxide composite layers for optical functional coatings', Conference Proceedings Society of Vacuum Coaters, April 17–22, 2010, Orlando, USA (2010) 308–312.
- T. Neubert, A. Gaida, W. Huwer, M. Vergöhl, 'Organic materials for the use in optical layer systems', Conference Proceedings Optical Systems Design, September 5–8, 2011, Marseille, France (2011a).
- T. Neubert, A. Gaida, W. Huwer, K. Nagel, M. Vergöhl, 'Deposition of optical coatings on plastics using poly-para-xylylene', Conference Proceedings Society of Vacuum Coaters, April 16–21, Chicago, USA (2011b) 265–269.
- T. Neubert, M. Vergöhl, T. Strunkus, F. Faupel, 'Investigations on adhesion of sputtered layers on polytetrafluoroethylene surfaces', Conference Proceedings Society of Vacuum Coaters, April 28–May 3, 2012, Santa Clara, USA (2012).
- F. Neumann, M. Cerezuela Barreto, 'Verfahren zum Nachweis des photokatalytischen Abbaus organischer Farbstoffe mittels Fluoreszenzanalyse', Patent DE102004027118B4 (2004).
- M. Noborisaka, H. Kodama, S. Nagashima, A. Shirakura, T. Horiuchi, T. Suzuki, 'Synthesis of transparent and hard SiOC(–H) thin films on polycarbonate substrates by PECVD method', *Surface & Coatings Technology* **206** (2012) 2581–2584.
- I. A. Paun, V. Ion, A. Moldovan, M. Dinescu, 'Thin films of polymer blends deposited by matrix-assisted pulsed laser evaporation: Effects of blending ratios', *Applied Surface Science* **257** (2011) 5259–5264.
- A. Piqué, R.A. McGill, D.B. Chrisey, D. Leonhardt, T.E. Mslna, B.J. Spargo, J.H. Callahan, R.W. Vachet, R. Chung, M.A. Bucaro, 'Growth of organic thin films by the matrix assisted pulsed laser evaporation (MAPLE) technique', *Thin Solid Films* **355–356** (1999) 536–541.
- I. H. Pratt, T. C. Lausman, 'Some characteristics of sputtered polytetrafluoroethylene films', *Thin Solid Films* **10** (1972) 151–154.
- C. Präfke, U. Schulz, N. Kaiser, 'Preparation and characterization of organic layers for UV protection of polycarbonate', *Thin Solid Films* **520** (2012) 4180–4183.
- J.-C. Ruiz, P.-L. Girard-Lauriault, F. Truica-Marasescu, M.R. Wertheimer, 'Plasma- and vacuum-ultraviolet (VUV) photo-polymerisation of N- and O-rich thin films', *Radiation Physics and Chemistry* **79** (2010) 310–314.
- U. Schulz, C. Präfke, P. Munzert, C. Gödeker, N. Kaiser, 'Formation of antireflective nanostructures on melamine and N,N'-di (1-naphthyl)-N,N'-diphenyl benzidine (NPB)', *Optical Materials Express* **1** (2011) 101–107.
- J. Schwarz, M. Schmidt, A. Ohl, 'Synthesis of plasma-polymerized hexamethyldisiloxane (HMDSO) films by microwave discharge', *Surface and Coatings Technology* **98** (1998) 859–864.
- A.T. Sellinger, A.H. Martin, J.M. Fitz-Gerald, 'Effect of substrate temperature on poly(methyl methacrylate) nanocomposite thin films deposited by matrix assisted pulsed laser evaporation', *Thin Solid Films* **516** (2008) 6033–6040.
- B. Singh, J. Bouchet, G. Rochat, Y. Leterrier, J.-A.E. Månson, P. Fayet, 'Ultra-thin hybrid organic/inorganic gas barrier coatings on polymers', *Surface & Coatings Technology* **201** (2007) 7107–7114.
- E. Spassova, I. Jivkov, G. Danev, T. Dimitrova, J. Koprinarova, A. Paskaleva, 'Low-permittivity evaporated polymer-polyimide', *Vacuum* **47** (1996) 1345–1346.

- D.A. Spee, R. Bakker, C.H.M. van der Werf, M.J. van Steenbergen, J.K. Rath, R.E.I. Schropp, 'Polymer layers by initiated chemical vapor deposition for thin film gas barrier encapsulation', *Thin Solid Films* **519** (2011) 4479–4482.
- V. Stelmashuk, H. Biederman, D. Slavinska, M. Trchova, P. Hlidek, 'Rf magnetron sputtering of polypropylene', *Vacuum* **75** (2004) 207–215.
- K. Takahashi, A. Itoh, T. Nakamura, K. Tachibana, 'Radical kinetics for polymer film deposition in fluorocarbon (C_4F_8 , C_3F_6 and C_5F_8) plasmas', *Thin Solid Films* **374** (2000) 303–310.
- M.F. Weber, 'Recent advances in multilayer polymeric interference reflectors', Conference Proceedings Society of Vacuum Coaters (2012).

Surface multiplasmonics with periodically non-homogeneous thin films

M. FARYAD and A. LAKHTAKIA, Department of Engineering Science and Mechanics, Pennsylvania State University, USA

DOI: 10.1533/9780857097316.3.450

Abstract: Multiple surface-plasmon-polariton (SPP) waves – all of the same frequency but with different phase speeds, attenuation rates, degrees of localization to the SPP wave-guiding interface, and spatial profiles – can be guided in a specific direction by an interface of a metal and a dielectric material that is periodically non-homogeneous along the normal to the interface. The partnering dielectric material can be isotropic or anisotropic. Whereas the solution of the canonical boundary-value problem is the best way to characterize these SPP waves, solutions of the Turbadar–Kretschmann–Raether and the grating-coupled configurations – involving periodically non-homogeneous thin films – assist in the practical launching of multiple SPP waves. The possibility of exciting multiple SPP waves promises multianalyte chemical sensors, multichannel communication, and enhanced efficiency of thin-film solar cells.

Key words: chiral sculptured thin film, grating-coupled configuration, plasmonics, prism-coupled configuration, rugate filter, sculptured thin film, sculptured nematic thin film, surface multiplasmonics, surface plasmon polariton.

11.1 Introduction

The emerging area of *surface multiplasmonics* deals with the excitation and the propagation of multiple surface-plasmon-polariton (SPP) waves – all of the same frequency, but different phase speeds, attenuation rates, and spatial profiles of fields – guided by the planar interface of a metal and a periodically non-homogeneous dielectric material (Lakhtakia, 2011).

This chapter contains an overview of boundary-value problems relevant to the propagation and excitation of multiple SPP waves guided by the interface of a metal and a periodically non-homogeneous dielectric material that is either a rugate filter or a sculptured nematic thin film (SNTF). Rugate filters are isotropic, but SNTFs are anisotropic. A brief history of surface multiplasmonics is presented in Section 11.2. In Section 11.3, the

fabrication techniques and the permittivity profiles of rugate filters and SNTFs are presented. The theoretical formulation of a general canonical boundary-value problem of SPP wave propagation guided by the planar interface of (i) a semi-infinite, periodically non-homogeneous, anisotropic, dielectric material and (ii) a semi-infinite metal is presented in Section 11.4.1. Representative numerical results are presented in Sections 11.4.2 and 11.4.3, respectively, for the metal/rugate filter interface and the metal/SNTF interface. Illustrative numerical results showing the excitation of multiple SPP waves in the grating-coupled configuration and a prism-coupled configuration called the Turbadar–Kretschmann–Raether (TKR) configuration are discussed, respectively, in Sections 11.5 and 11.6 for both the metal/rugate filter and the metal/SNTF interfaces. The numerical results presented here are a representative subset of those presented in journal publications. Significant conclusions drawn from the numerical results are provided in Section 11.7. Finally, a few suggestions for future work and resources are presented in Sections 11.8 and 11.9, respectively.

An $\exp(-i\omega t)$ time-dependence is implicit, with ω denoting the angular frequency, t as time and $i = \sqrt{-1}$. Explicit dependences of various quantities on ω are suppressed throughout the chapter. The free-space wavenumber, the free-space wavelength, and the intrinsic impedance of free space are denoted by $k_0 = \omega\sqrt{\epsilon_0\mu_0}$, $\lambda_0 = 2\pi/k_0$, and $\eta_0 = \sqrt{\mu_0/\epsilon_0}$, respectively, with μ_0 and ϵ_0 being the permeability and permittivity of free space. For all the numerical results reported in this chapter, $\lambda_0 = 633$ nm was fixed. Vectors are in boldface, dyadics are underlined twice, column four-vectors are in boldface and enclosed within square brackets, and 4×4 matrixes are underlined twice and enclosed within square brackets. The 4×4 identity matrix is denoted by $[\mathcal{I}]$. Cartesian unit vectors are identified as $\hat{\mathbf{u}}_x$, $\hat{\mathbf{u}}_y$, and $\hat{\mathbf{u}}_z$.

11.2 Historical development

Until 2008 – barring a few scattered reports on the evidence of *s*-polarized SPP waves (Gaspar-Armenta and Villa, 2003; Salamon *et al.*, 1997; Salamon and Tollin, 2001) – it was conventional wisdom that, at a specific frequency, only one SPP wave, that too of the *p*-polarization state, could be guided by an interface of a metal and a dielectric material. This belief was held because the solution of a canonical boundary-value problem (Dragoman and Dragoman, 2008; Maier, 2007) shows that only one SPP wave can propagate guided by the interface if the partnering dielectric material is isotropic and homogeneous. The same conclusion holds true even if that material is anisotropic (Abdulhalim, 2009; Borstel and Falge, 1982; Elston and Sambles, 1990; Wallis, 1982; Wang, 1995; Yan *et al.*, 2007). However, SPP waves guided by the interface of a metal and a periodically non-homogeneous dielectric material exhibit remarkable characteristics (Polo and Lakhtakia, 2011).

In 2008, it was predicted theoretically (Motyka and Lakhtakia, 2008, 2009) that multiple SPP waves – with different phase speeds, attenuation rates, and field distributions, but all of the same frequency – can propagate in a specific direction, guided by the interface of a metal and a periodically non-homogeneous SNTF. An SNTF is a dielectric material that is anisotropic and periodically non-homogeneous in the thickness direction (which is normal to the waveguiding interface) (Lakhtakia and Messier, 2005). This theoretical prediction was later verified experimentally (Lakhtakia *et al.*, 2009). Shortly afterwards, it was also found, both theoretically (Lakhtakia, 2007; Polo and Lakhtakia, 2009a, 2009b) and experimentally (Devender *et al.*, 2009; Erten, 2011; Gilani *et al.*, 2010), that multiple SPP waves can also be guided in a specific direction by an interface of a metal and a chiral sculptured thin film (STF). A chiral STF is also a dielectric material that is anisotropic and periodically non-homogeneous in the thickness direction (Lakhtakia and Messier, 2005). In all of these studies, the partnering dielectric materials were anisotropic in addition to being periodically non-homogeneous in the direction normal to the waveguiding interface. However, it has been shown by the solution of the canonical boundary-value problem that multiple SPP waves can still be guided if the partnering (periodically non-homogenous) dielectric material is isotropic (Faryad and Lakhtakia, 2010a).

Furthermore, multiple SPP waves can be excited in the TKR (Kretschmann and Raether, 1968; Otto, 1968; Turbadar, 1959) and the grating-coupled configurations with the partnering periodically non-homogeneous dielectric material being either isotropic (Faryad and Lakhtakia, 2011a, 2011b) or anisotropic (Faryad and Lakhtakia, 2011c). Moreover, the coupling of two interfaces of a metal and a periodically non-homogeneous dielectric material – the Sarid configuration (Sarid, 1981) – has also been shown to increase the number of SPP waves (Faryad and Lakhtakia, 2010a, 2010b, 2010c; Faryad, 2012; Jen and Yu, 2011; Jen *et al.*, 2009). Parenthetically, let us note that not all the SPP waves predicted by the theoretical investigations on the canonical boundary-value problem can be excited with a finitely thick partnering dielectric material (Polo *et al.*, 2011); the thickness of the partnering dielectric material could be impractically large for some SPP waves to be excited.

SPP waves are widely used for sensing chemicals and biochemicals (Abdulhalim *et al.*, 2008; Homola, 2006). Furthermore, SPP imaging systems are used for high-throughput analysis of biomolecular interactions – for proteomics, drug discovery, and pathway elucidation (Abdulhalim *et al.*, 2007; Usui-Aoki *et al.*, 2005). SPP-based imaging technology has been successfully applied to the screening of bioaffinity interactions with DNA, carbohydrates, peptides, phage display libraries, and proteins (Kanda *et al.*, 2005). SPP-based imaging techniques are also going to be useful for lithography

(Kiki *et al.*, 2002; Maier, 2007). Finally, as SPP waves can be excited in the terahertz and optical regimes, they may be useful for high-speed communication of information on computer chips (Maier *et al.*, 2001). Whereas conventional wires are very attenuative at frequencies beyond a few tens of gigahertz, ohmic losses are minimal for plasmonic transmission (Dragoman and Dragoman, 2008) which enables long-range communications (Berini, 2009). Recently, SPP waves have been found to be useful for light-harvesting applications in thin-film solar cells due to the coupling of a part of the incident light with the SPP waves (Ferry *et al.*, 2008).

That multiple SPP waves can be launched and provides exciting prospects for enhancing the scope of the applications of SPP waves. For sensing applications, the use of more than one distinct SPP wave would increase confidence in a reported measurement; also, more than one analyte could be sensed at the same time, thereby increasing the capabilities of multi-analyte sensors (Mackay and Lakhtakia, 2010a, 2012). For imaging applications, the simultaneous creation of two images may become possible. For plasmonic communications, the availability of multiple channels would make information transmission more reliable as well as enhance capacity. Moreover, light absorption can be enhanced further in thin-film solar cells by the use of multiple SPP waves (Faryad and Lakhtakia, 2011d).

11.3 Periodically non-homogeneous dielectric materials

Multiple SPP waves have been found to be guided by an interface of a metal and a dielectric material that is periodically non-homogeneous normal to the SPP-wave-guiding interface (Faryad, 2012). One type of each of these isotropic and anisotropic dielectric materials is described in brief in the following subsections.

11.3.1 Rugate filters

Rugate filters are isotropic dielectric thin films that have a continuously varying and periodic refractive index along the thickness direction (Bovard, 1993). A multi-layered structure with a large number of sufficiently thin layers made of isotropic dielectric materials of different refractive indexes may also be classified as a rugate filter (Bovard, 1993). Rugate filters find applications as optical filters (Baumeister, 2004) and light-trapping layers in thin-film solar cells (Fahr *et al.*, 2008).

Rugate filters can be fabricated with various physical- and chemical-deposition techniques. Physical-deposition techniques include cluster-beam deposition (Overland *et al.*, 1992), magnetron sputtering (Zhang *et al.*, 2011),

and ion-beam sputtering (Lee *et al.*, 2006), whereas chemical-deposition techniques include molecular assembly (Nolte *et al.*, 2004) and electrolysis (Lorenzo *et al.*, 2005). Rugate-filter technology is very sophisticated nowadays in suppressing sidebands and reducing the impact of impedance mismatch on either pupil of a rugate filter (Lorenzo *et al.*, 2005; Perilloux, 2002), but these issues are not of direct relevance in this chapter.

The relative permittivity of a rugate filter with sinusoidally changing permittivity along the z axis – designated as parallel to the thickness direction – is given by

$$\epsilon_{\text{rug}}(z) = \left[\left(\frac{n_b + n_a}{2} \right) + \left(\frac{n_b - n_a}{2} \right) \sin\left(\pi \frac{z}{\Omega}\right) \right]^2, \quad [11.1]$$

where n_a and n_b are the lowest and the highest indexes of refraction, respectively, and 2Ω is the period. For the numerical results presented in this chapter, the minimum and maximum indexes of refraction of the rugate filter were fixed as follows (Baumeister, 2004): $n_a = 1.45$ and $n_b = 2.32$.

11.3.2 Sculptured nematic thin films

A sculptured thin film is an assembly of parallel columns of nanoscale cross-sectional diameter, all columns being of the same shape. Shortly after the conceptualization of helicoidal bianisotropic mediums in 1993 (Lakhtakia and Weiglhofer, 1993), the basis of realizing these materials using thin-film technology was articulated (Lakhtakia and Messier, 1994). The general concept of STFs was presented in August 1995 by Lakhtakia and Messier to a group of thin-film researchers assembled at Penn State (Lakhtakia *et al.*, 1996). The topic has enjoyed considerable growth in the ensuing years, chiefly in theory initially, but now in experiments and applications as well (Lakhtakia and Geddes, 2010; Lakhtakia and Messier, 2005).

STFs are commonly grown using physical vapor deposition (PVD), where a directional vapor flux is incident on a substrate, which could be fixed, rotating, and/or rocking. Under the right temperature and pressure, a film grows with columns whose shape is determined by the motion of the substrate. PVD methods adapted to grow STFs include thermal evaporation (Robbie *et al.*, 1995; Young and Kowal, 1959), electron-beam evaporation (Messier *et al.*, 1997), sputtering (Messier *et al.*, 2000; Sit *et al.*, 1999), pulsed laser deposition (Vick *et al.*, 1999), and physicochemical vapor deposition (Pursel *et al.*, 2005; Wei *et al.*, 2010). The interested reader is referred to Martin-Palma and Lakhtakia (2010) for a crash course on PVD techniques and to Martin (2010) for detailed treatments.

Macroscopically, for optical purposes, an STF is a material continuum that is periodically non-homogeneous in a fixed direction. STFs of three types have been considered thus far in the literature on surface multiplasmonics:

1. columnar thin film (CTF), in which all columns are parallel to a straight line;
2. SNTF, for which the shape of each column is described by the same two-dimensional curve in space; and
3. chiral STF, for which each column is described by the same helix.

For the illustrative numerical results presented in this chapter, only periodically non-homogeneous SNTFs were considered.

While an SNTF is grown, the substrate is only rocked about a tangential axis (Messier *et al.*, 1997). The nature of the rocking defines the shape of the columns of the film and hence its macroscopic electromagnetic properties. The plane in which the columnar shape lies is the morphologically significant plane of the SNTF.

As the z axis is parallel to the thickness direction, the permittivity dyadic of a periodically non-homogeneous SNTF is of the form (Lakhtakia *et al.*, 2009; Motyka and Lakhtakia, 2008, 2009)

$$\underline{\underline{\varepsilon}}_{\text{SNTF}}(z) = \varepsilon_0 \underline{\underline{S}}_y(z) \cdot \underline{\underline{\varepsilon}}_{\text{ref}}^o(z) \cdot \underline{\underline{S}}_y^{-1}(z), \quad [11.2]$$

where the dyadics

$$\begin{aligned} \underline{\underline{S}}_y(z) &= (\hat{\mathbf{u}}_x \hat{\mathbf{u}}_x + \hat{\mathbf{u}}_z \hat{\mathbf{u}}_z) \cos[\chi(z)] + (\hat{\mathbf{u}}_z \hat{\mathbf{u}}_x - \hat{\mathbf{u}}_x \hat{\mathbf{u}}_z) \sin[\chi(z)] + \hat{\mathbf{u}}_y \hat{\mathbf{u}}_y \\ \underline{\underline{\varepsilon}}_{\text{ref}}^o(z) &= \varepsilon_a(z) \hat{\mathbf{u}}_z \hat{\mathbf{u}}_z + \varepsilon_b(z) \hat{\mathbf{u}}_x \hat{\mathbf{u}}_x + \varepsilon_c(z) \hat{\mathbf{u}}_y \hat{\mathbf{u}}_y \end{aligned} \quad [11.3]$$

depend on the vapor flux angle $\chi_v(z) = \chi_v(z \pm 2\Omega)$ with respect to the substrate (xy) plane, and 2Ω is the period. In this chapter, $\chi_v(z) = \tilde{\chi}_v + \delta_v \sin(\pi z/\Omega)$ varies sinusoidally about the mean value $\tilde{\chi}_v$ with period 2Ω . The dyadic $\underline{\underline{S}}_y(z)$ is a rotation dyadic that describes the tilt of the columns of the SNTF at a given value of z . The tilt angle $\chi(z)$ with respect to the substrate plane depends upon the vapor flux angle $\chi_v(z)$. The quantities $\varepsilon_a(z')$, $\varepsilon_b(z')$, and $\varepsilon_c(z')$ are the eigenvalues of $\underline{\underline{\varepsilon}}_{\text{ref}}^o(z')$ – and hence of $\underline{\underline{\varepsilon}}_{\text{SNTF}}(z')$ – and should be interpreted as the principal relative permittivity scalars in the plane $z = z'$ (Mackay and Lakhtakia, 2010b). These three quantities and $\chi(z')$ depend on $\chi_v(z')$, the conditions for the fabrication of the SNTF, and the material(s) evaporated to fabricate the SNTF – and therefore need to be found experimentally.

For all the numerical results presented in this chapter, an SNTF made of titanium oxide was considered. The parameters of a CTF of titanium oxide were found experimentally by Hodgkinson *et al.* (1998), but the same have been used for an SNTF in surface multiplasmonics in the absence of more realistic data. These parameters for $\lambda_0 = 633$ nm are (Motyka and Lakhtakia, 2008)

$$\left. \begin{aligned} \varepsilon_a(z) &= [1.0443 + 2.7394v(z) - 1.3697v^2(z)]^2 \\ \varepsilon_b(z) &= [1.6765 + 1.5649v(z) - 0.7825v^2(z)]^2 \\ \varepsilon_c(z) &= [1.3586 + 2.1109v(z) - 1.0554v^2(z)]^2 \\ \chi(z) &= \tan^{-1}[2.8818 \tan \chi_v(z)] \end{aligned} \right\}, \quad [11.4]$$

where $v(z) = 2\chi_v(z)/\pi$. Recent evidence indicates that the relationships are likely to be more complicated for SNTFs (Swiontek, 2012), but those used so far should suffice for illustration.

11.4 Canonical boundary-value problem

The canonical boundary-value problem when both partnering materials are isotropic is straightforward because field representations on both sides of the planar interface are of the textbook kind (Simon *et al.*, 1975; Zenneck, 1907). Field representation is not simple in a periodically non-homogeneous half-space (Lakhtakia, 2010). A matrix procedure devised by Martorell *et al.* (2006) for a periodically piecewise homogeneous half-space was adapted by Lakhtakia and Polo (2007) to formulate the canonical problem, first, for surface waves called Dyakonov–Tamm waves and, then, for surface multiplasmonics (Faryad and Lakhtakia, 2010a; Faryad *et al.*, 2010; Polo and Lakhtakia, 2009a).

11.4.1 Theoretical formulation

Suppose the half-space $z < 0$ is occupied by a homogeneous metal of relative permittivity ε_{met} , while the half-space $z > 0$ is occupied by a linear anisotropic dielectric material (Mackay and Lakhtakia, 2008; Weiglhofer and Lakhtakia, 2003) that is periodically non-homogeneous along the z axis. The frequency-domain constitutive relations of the periodically non-homogeneous partnering material are written in vector-dyadic notation as

$$\mathbf{D}(\mathbf{r}) = \underline{\underline{\varepsilon}}(z) \cdot \mathbf{E}(\mathbf{r}), \quad [11.5]$$

$$\mathbf{B}(\mathbf{r}) = \mu_0 \mathbf{H}(\mathbf{r}), \quad [11.6]$$

where

$$\underline{\underline{\varepsilon}}(z \pm 2\Omega) = \underline{\underline{\varepsilon}}(z), \quad [11.7]$$

and 2Ω is the period.

Let the SPP wave propagate in the xy plane along the direction which makes an angle $\psi \in (0, 2\pi)$ with respect to the x axis, and attenuate as $z \rightarrow \pm\infty$. The electromagnetic field phasors in the metal may be written as

$$\mathbf{E}(\mathbf{r}) = \left[a_p \left(\frac{\alpha_{\text{met}}}{k_0} \hat{\mathbf{u}}_1 + \frac{\kappa}{k_0} \hat{\mathbf{u}}_z \right) + a_s \hat{\mathbf{u}}_2 \right] \exp(i\mathbf{k}_{\text{met}} \cdot \mathbf{r}), \quad z \leq 0, \quad [11.8]$$

and

$$\mathbf{H}(\mathbf{r}) = \eta_0^{-1} \left[-a_p \epsilon_{\text{met}} \hat{\mathbf{u}}_2 + a_s \left(\frac{\alpha_{\text{met}}}{k_0} \hat{\mathbf{u}}_1 + \frac{\kappa}{k_0} \hat{\mathbf{u}}_z \right) \right] \exp(i\mathbf{k}_{\text{met}} \cdot \mathbf{r}), \quad z \leq 0, \quad [11.9]$$

where

$$\mathbf{k}_{\text{met}} = \kappa \hat{\mathbf{u}}_1 - \alpha_{\text{met}} \hat{\mathbf{u}}_z, \quad [11.10]$$

$$\kappa^2 + \alpha_{\text{met}}^2 = k_0^2 \epsilon_{\text{met}}, \quad [11.11]$$

$$\hat{\mathbf{u}}_1 = \hat{\mathbf{u}}_x \cos \psi + \hat{\mathbf{u}}_y \sin \psi, \quad [11.12]$$

$$\hat{\mathbf{u}}_2 = -\hat{\mathbf{u}}_x \sin \psi + \hat{\mathbf{u}}_y \cos \psi, \quad [11.13]$$

κ is a complex-valued scalar such that $\omega/\text{Re}(\kappa)$ is the phase speed, and $\text{Im}(\alpha_{\text{met}}) > 0$ for attenuation as $z \rightarrow -\infty$. Furthermore, a_p and a_s are unknown scalars with the subscripts p and s , respectively, denoting the parallel and perpendicular polarization states with respect to the plane formed by $\hat{\mathbf{u}}_1$ and $\hat{\mathbf{u}}_z$. The field representation (Equations [11.8]–[11.13]) is of the textbook kind.

The field representation in the half-space $z \geq 0$ is more complicated. For all $z \in (-\infty, \infty)$, let us define the fields $\mathbf{e}(z)$ and $\mathbf{h}(z)$ via

$$\begin{aligned} \mathbf{E}(\mathbf{r}) &= \mathbf{e}(z) \exp[i\kappa(x \cos \psi + y \sin \psi)] \\ \mathbf{H}(\mathbf{r}) &= \mathbf{h}(z) \exp[i\kappa(x \cos \psi + y \sin \psi)] \end{aligned} \quad [11.14]$$

Substitution of this representation in the frequency-domain Faraday and Ampère–Maxwell equations and the subsequent use of the constitutive relations (Equations [11.5] and [11.6]) yields two algebraic and four differential equations. The algebraic equations allow the components $e_z(z)$ and $h_z(z)$ to be expressed in terms of the column 4-vector

$$[\mathbf{f}(z)] = [e_x(z) \ e_y(z) \ h_x(z) \ h_y(z)]^T \quad [11.15]$$

which satisfies the matrix ordinary differential equation

$$\frac{d}{dz} [\mathbf{f}(z)] = i [\underline{\underline{P}}(z)] \cdot [\mathbf{f}(z)], \quad z > 0, \quad [11.16]$$

where the 4×4 matrix $[\underline{\underline{P}}(z)]$ is a periodic function of z such that

$$[\underline{\underline{P}}(z \pm 2\Omega)] = [\underline{\underline{P}}(z)]. \quad [11.17]$$

By virtue of the Floquet–Lyapunov theorem (Yakubovich and Starzhinskii, 1975), the solution of the matrix ordinary differential equation (Equation [11.16]) has to be of the form

$$[\mathbf{f}(z)] = [\underline{\underline{F}}(z)] \cdot \exp\left\{iz[\tilde{\underline{\underline{Q}}}\right\} \cdot [\mathbf{f}(0+)], \quad [11.18]$$

where

$$[\underline{\underline{F}}(z \pm 2\Omega)] = [\underline{\underline{F}}(z)] \quad [11.19]$$

is a periodic 4×4 matrix with $[\underline{\underline{F}}(0)] = [\underline{\underline{I}}]$, and $[\tilde{\underline{\underline{Q}}}]$ is a 4×4 matrix independent of z .

Without resorting to the Floquet–Lyapunov theorem, the solution of Equation [11.16] must lead to the relation

$$[\mathbf{f}(2\Omega)] = [\underline{\underline{Q}}] \cdot [\mathbf{f}(0+)], \quad [11.20]$$

where the 4×4 matrix $[\underline{\underline{Q}}]$ can be computed by the piecewise-uniform-approximation method (Lakhtakia and Messier, 2005) as follows. After choosing a sufficiently large number N , the following quantities are defined:

$$\left. \begin{aligned} z_n &= 2\Omega \frac{n}{N} \\ \left[\underline{\underline{W}}_n \right] &= \exp \left\{ i \frac{2\Omega}{N} \left[P \left(\frac{z_{n-1} + z_n}{2} \right) \right] \right\}, \quad n \in [1, \infty). \end{aligned} \right\} \quad [11.21]$$

Then, the approximation

$$\left[\underline{\underline{Q}} \right] \approx \left[\underline{\underline{W}}_N \right] \cdot \left[\underline{\underline{W}}_{N-1} \right] \cdot \dots \cdot \left[\underline{\underline{W}}_2 \right] \cdot \left[\underline{\underline{W}}_1 \right] \quad [11.22]$$

should be adequate, provided that the thickness $2\Omega/N$ is sufficiently small.

Comparison of Equations [11.18] and [11.20] yields the identity

$$\left[\underline{\underline{Q}} \right] = \exp \left\{ i 2\Omega \left[\underline{\underline{\tilde{Q}}} \right] \right\}. \quad [11.23]$$

Both $\left[\underline{\underline{Q}} \right]$ and $\left[\underline{\underline{\tilde{Q}}} \right]$ share the same eigenvectors, and their eigenvalues are also related as follows. Let $[\mathbf{t}^{(m)}]$, $m \in [1, 4]$, be the eigenvector corresponding to the m th eigenvalue σ_m of $\left[\underline{\underline{Q}} \right]$; then, the corresponding eigenvalue α_m of $\left[\underline{\underline{\tilde{Q}}} \right]$ is given by

$$\alpha_m = -i \frac{\ln(\sigma_m)}{2\Omega}, \quad m \in [1, 4]. \quad [11.24]$$

The admissible values of κ for SPP wave propagation are such that all four eigenvalues of $\left[\underline{\underline{\tilde{Q}}} \right]$ have non-zero imaginary parts. These four eigenvalues are labeled such that $\text{Im } [\alpha_1] > 0$, $\text{Im } [\alpha_2] > 0$, $\text{Im } [\alpha_3] < 0$, and $\text{Im } [\alpha_4] < 0$. As the third and the fourth eigenvalues of $\left[\underline{\underline{\tilde{Q}}} \right]$ describe fields that amplify as $z \rightarrow \infty$, it follows that

$$\left[\mathbf{f}(0+) \right] = \sum_{m=1}^2 \tau_m \left[\mathbf{t}^{(m)} \right], \quad [11.25]$$

with τ_1 and τ_2 as unknown scalars (Lakhtakia, 2010).

Satisfaction of the usual boundary conditions across the interface $z = 0$ demands that

$$\left[\mathbf{f}(0+) \right] = \left[\mathbf{f}(0-) \right], \quad [11.26]$$

where the boundary values [$\mathbf{f}(0\pm)$] can be obtained using Equations [11.8], [11.9], and [11.14]. Equation [11.26] may be rearranged as

$$\begin{bmatrix} \underline{\underline{M}}(\kappa) \end{bmatrix} \cdot \begin{bmatrix} \tau_1 \\ \tau_2 \\ a_s \\ a_p \end{bmatrix} = \begin{bmatrix} 0 \\ 0 \\ 0 \\ 0 \end{bmatrix}. \quad [11.27]$$

The dispersion equation for SPP wave propagation is then as follows

$$\det[\underline{\underline{M}}(\kappa)] = 0. \quad [11.28]$$

The solution of the dispersion Equation [11.28] is independent of the value of ψ when the partnering dielectric material is isotropic.

11.4.2 Metal/rugate-filter interfaces

For illustrative numerical results, let us begin with the simpler of the two cases chosen for the dielectric partnering material, that is, a rugate filter with relative permittivity given by Equation [11.1]. Then the 4×4 matrix $[\underline{\underline{P}}(z)]$ of Equation [11.16] is

$$\begin{aligned} [\underline{\underline{P}}(z)] &= \omega \begin{bmatrix} 0 & 0 & 0 & \mu_0 \\ 0 & 0 & -\mu_0 & 0 \\ 0 & -\varepsilon_0 \varepsilon_{rug}(z) & 0 & 0 \\ \varepsilon_0 \varepsilon_{rug}(z) & 0 & 0 & 0 \end{bmatrix} \\ &\quad + \frac{\kappa^2}{\omega \varepsilon_0 \varepsilon_{rug}(z) \mu_0} \begin{bmatrix} 0 & 0 & 0 & -\mu_0 \\ 0 & 0 & 0 & 0 \\ 0 & \varepsilon_0 \varepsilon_{rug}(z) & 0 & 0 \\ 0 & 0 & 0 & 0 \end{bmatrix}. \end{aligned} \quad [11.29]$$

Faryad and Lakhtakia (2010a) fixed $\varepsilon_{met} = -56 + 21i$ (bulk aluminum) and $\underline{\underline{\varepsilon}}(z) = \varepsilon_{rug}(z) \underline{\underline{I}}$, but kept Ω variable. The solutions of the dispersion equation, computed using the Newton–Raphson method (Jaluria, 1996) for $0.005 \leq \Omega/\lambda_0 \leq 2$ and $\kappa/k_0 > 1.0$, are shown in Fig. 11.1. These solutions are organized in 16 branches: eight branches labeled as $s1$ – $s8$ represent SPP waves of the s -polarization state, and eight branches labeled as $p1$ – $p8$ represent SPP waves of the p -polarization state. The gaps in branches $p7$, $s4$, and $s8$ are not numerical artifacts, each gap being accompanied by a discontinuity in $\text{Im}(\kappa/k_0)$.

Clearly from Fig. 11.1, more than one SPP wave can propagate in a specific direction in the xy plane for $\Omega \geq 0.145\lambda_0$. These SPP waves have different phase

speeds $\omega/\text{Re}(\kappa)$ and attenuation rates $1/\text{Im}(\kappa)$. As both partnering materials are isotropic, this multiplicity is due to the periodic non-homogeneity of the dielectric partnering material (i.e., the rugate filter). Although the observability of two SPP waves – one of either linear polarization state – when the partnering dielectric material is periodically non-homogeneous in a piecewise uniform fashion has recently been established numerically for the Sarid and TKR configurations (Jen *et al.*, 2009), the solution of the canonical boundary-value problem not only provides necessary mathematical rigor but also shows that the number of simultaneously excitable SPP waves can exceed two. Moreover, the possibility of solutions of the dispersion equation with $\text{Re}(\kappa/k_0) \in (1, n_a)$ shows that the SPP waves with high phase speed can also be guided by the metal/rugate-filter interface. Very recently, solutions with $\text{Re}(\kappa/k_0) < 1$ have also been found, but their fields are very weakly localized in the rugate filter to the interface (Atalla *et al.*, 2012).

Representative plots of the Cartesian components of the time-averaged Poynting vector

$$\mathbf{P}(x, z) = \frac{1}{2} \text{Re} [\mathbf{E}(x, z) \times \mathbf{H}^*(x, z)] \quad [11.30]$$

along the line $\{x = 0, y = 0\}$, are given in Fig. 11.2 as functions of z for one solution on the branch $s2$: $\Omega = \lambda_0$. The data were computed by setting $a_s = 1 \text{ V m}^{-1}$. The plots show quite strong localization of the SPP wave to the interface. Moreover, the SPP wave is carrying energy along the x axis because the y - and z -components of \mathbf{P} are negligible as compared to its x component. The power density resides in the rugate filter almost wholly within a distance equal to the period 2Ω for the case shown; however, Faryad and Lakhtakia (2010a) have shown that different SPP waves have different degrees of localization to the interface.

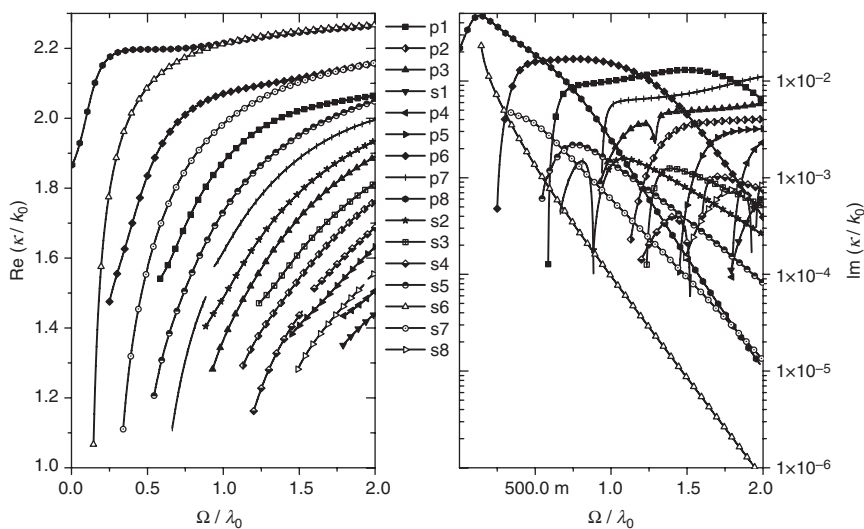
As the period 2Ω of the rugate filter increases in relation to λ_0 , the branches in Fig. 11.1 come closer to each other. At some very high value of Ω/λ_0 , only one solution – indicating a p -polarized SPP wave – should survive, because the rugate filter would be virtually homogeneous over the region of width $\sim 1.5\lambda_0$ next to the interface. Although this possibility could be tested by setting a very large value of Ω/λ_0 , the correct identification of $\alpha_{1,2}$ became problematic for $\Omega/\lambda_0 > 2$, owing to numerical errors in computing $\underline{\underline{\Omega}}$.

In order to overcome this difficulty, Faryad and Lakhtakia (2010a) modified the relative permittivity of the rugate filter from Equation [11.1] to

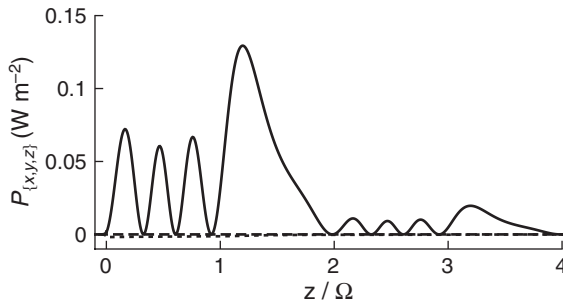
$$\epsilon_{\text{rug}}^{\text{mod}}(z) = \left[\left(\frac{n_b + n_a}{2} \right) + \Gamma \left(\frac{n_b - n_a}{2} \right) \sin \left(\pi \frac{z}{\Omega} \right) \right]^2, \quad \Gamma \in [0, 1], \quad [11.31]$$

fixed $\Omega = 2\lambda_0$, and decreased the parameter Γ from 1 to 0.001. Close to the interface, a decrease in Γ is tantamount to an increase in Ω . It was then shown that all the solution branches in Fig. 11.1 die out when the value of Γ decreases from unity because the imaginary part of κ decreases to zero, except one branch representing *p*-polarized SPP waves. This branch extends to $\Gamma = 0.001$. As Γ decreases even further, the branch approaches the solution for a metal/dielectric interface with the relative permittivity of the dielectric partnering material uniform at $(1/4)(n_a + n_b)^2$. For instance, at $\Gamma = 0.001$, the solution of the dispersion equation gives a *p*-polarized SPP wave with wavenumber $\kappa = (1.9395 + 0.02140i)k_0$, while the *p*-polarized wave guided by the interface of aluminum and a homogeneous isotropic dielectric material with relative permittivity $(1/4)(n_a + n_b)^2 = 3.5532$ has wavenumber $\kappa = (1.9394 + 0.02141i)k_0$ (Abdulhalim *et al.*, 2008; Homola, 2006).

The spatial profiles (such as given in Fig. 11.2) can act as a guide if one wishes to design an experiment to test the foregoing theoretical results. In the conventional TKR configuration, SPP waves are excited at the interface of a metallic thin film and a dielectric thin film. Faryad and Lakhtakia (2010a) have shown that most of the SPP waves guided by the interface of the rugate filter and aluminum are confined within three structural periods of the rugate filter when the real part of κ exceeds k_0 . So a four-period-thick



11.1 Real (left) and imaginary (right) parts of κ/k_0 as functions of Ω/λ_0 for SPP-wave propagation guided by the planar interface of bulk aluminum and a rugate filter in the canonical boundary-value problem. The rugate filter is described by Equation [11.1] with $n_a = 1.45$ and $n_b = 2.32$ (After Faryad and Lakhtakia, 2010a). Most but not all solutions have been captured in this figure.



11.2 Variations with z of the Cartesian components of $\mathbf{P}(x, z)$ along the line $\{x = 0, y = 0\}$ for an s -polarized SPP wave guided by the planar interface of aluminum and the rugate filter in the canonical boundary-value problem, when $\Omega/\lambda_0 = 1$ and $\kappa/k_0 = 1.4864 + 0.0013203i$. The components parallel to $\hat{\mathbf{u}}_x$, $\hat{\mathbf{u}}_y$, and $\hat{\mathbf{u}}_z$, are represented by solid, dashed, and chain-dashed lines, respectively. The data were computed by setting $a_s = 1 \text{ V m}^{-1}$, with a_p , τ_1 , and τ_2 then obtained using Equation [11.27] (Faryad and Lakhtakia, 2010a).

rugate filter deposited upon a metallic thin film, which is thicker than the penetration depth of the metal, can be used in the TKR configuration to excite SPP waves.

11.4.3 Metal/SNTF interface

Let the partnering dielectric material now be an SNTF. The 4×4 matrix $\begin{bmatrix} \underline{\underline{P}}(z) \end{bmatrix}$ for this case is

$$\begin{aligned} \begin{bmatrix} \underline{\underline{P}}(z) \end{bmatrix} = & \omega \begin{bmatrix} 0 & 0 & 0 & \mu_0 \\ 0 & 0 & -\mu_0 & 0 \\ 0 & -\epsilon_0 \epsilon_c(z) & 0 & 0 \\ \epsilon_0 \epsilon_d(z) & 0 & 0 & 0 \end{bmatrix} \\ & + \frac{\kappa^2}{\omega \epsilon_0 \epsilon_a(z) \epsilon_b(z)} \begin{bmatrix} 0 & 0 & \cos \psi \sin \psi & -\cos^2 \psi \\ 0 & 0 & \sin^2 \psi & -\cos \psi \sin \psi \\ 0 & 0 & 0 & 0 \\ 0 & 0 & 0 & 0 \end{bmatrix} \\ & + \kappa \frac{\epsilon_d(z)[\epsilon_a(z) - \epsilon_b(z)]}{\epsilon_a(z) \epsilon_b(z)} \sin[\chi(z)] \cos[\chi(z)] \begin{bmatrix} \cos \psi & 0 & 0 & 0 \\ \sin \psi & 0 & 0 & 0 \\ 0 & 0 & 0 & 0 \\ 0 & 0 & -\sin \psi & \cos \psi \end{bmatrix} \\ & + \frac{\kappa^2}{\omega \mu_0} \begin{bmatrix} 0 & 0 & 0 & 0 \\ 0 & 0 & 0 & 0 \\ -\cos \psi \sin \psi & \cos^2 \psi & 0 & 0 \\ -\sin^2 \psi & \cos \psi \sin \psi & 0 & 0 \end{bmatrix}, \end{aligned} \quad [11.32]$$

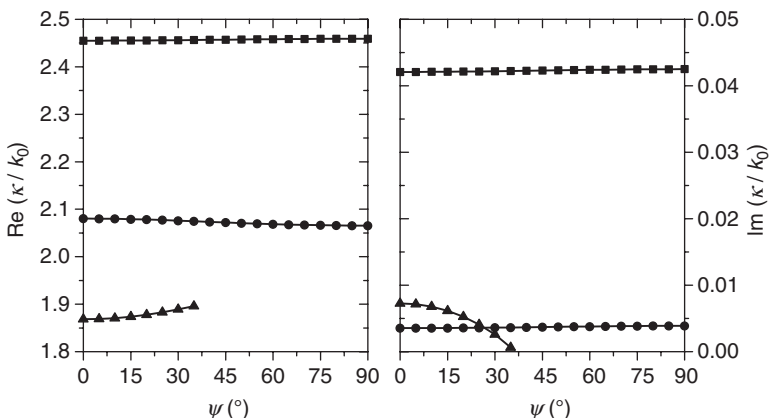
where

$$\varepsilon_d(z) = \frac{\varepsilon_a(z)\varepsilon_b(z)}{\varepsilon_a(z)\cos^2[\chi(z)] + \varepsilon_b(z)\sin^2[\chi(z)]}. \quad [11.33]$$

Faryad *et al.* (2010) fixed $\varepsilon_{\text{met}} = -56 + 21i$ (bulk aluminum) and $\underline{\varepsilon}(z) = \underline{\varepsilon}_{\text{SNTF}}(z)$. The chosen SNTF was made of titanium oxide, and the angles $\tilde{\chi}_v$ and δ_v were taken to be 45° and 30° , respectively, and $\Omega = 200$ nm for the results presented in this subsection.

Computed values of the real and imaginary parts of κ for the canonical problem are shown in Fig. 11.3. These solutions are organized into three branches. For $0^\circ \leq \psi \leq 36^\circ$, three values of κ satisfy Equation [11.28] and therefore represent SPP waves. For $36^\circ \leq \psi \leq 90^\circ$, two values of κ satisfy Equation [11.28]. The different solutions of Equation [11.28] for any specific value of ψ indicate that the SPP waves have different phase speeds $\omega/\text{Re}(\kappa)$ and different e-folding distances $1/\text{Im}(\kappa)$ along the direction of propagation. These results are consistent with theoretical (Motyka and Lakhtakia, 2008, 2009) and experimental (Lakhtakia *et al.*, 2009) results obtained for the TKR configuration.

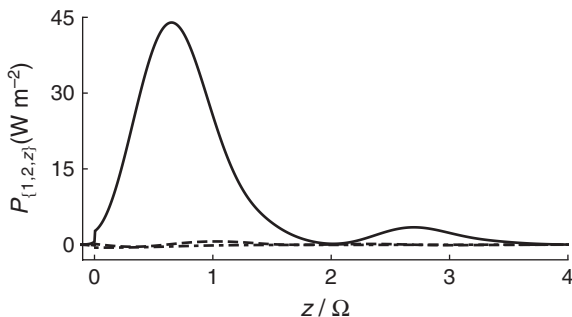
Specifically, for $\psi = 0^\circ$ the values of κ which satisfy Equation [11.28] are $\kappa_1 = (2.455 + 0.04208i) k_0$, $\kappa_2 = (2.080 + 0.003538i) k_0$, and $\kappa_3 = (1.868 + 0.007267i) k_0$.



11.3 (left) Real and (right) imaginary parts of κ as functions of ψ , for SPP-wave propagation guided by the planar interface of bulk aluminum and a periodically non-homogeneous SNTF in the canonical boundary-value problem. See Section 11.3.2 for the constitutive parameters of the SNTF. Either two or three modes are possible, depending on ψ (Faryad *et al.*, 2010).

k_0 . These solutions represent SPP waves with wave vectors lying wholly in the morphologically significant plane of the SNTF. Faryad *et al.* (2010) have shown that the SPP waves with the wavenumbers κ_1 and κ_3 are *p*-polarized, and the SPP wave with κ_2 is *s*-polarized. The localization of these SPP waves around the interface $z = 0$ is evident from the spatial profiles provided by Faryad *et al.* (2010). Moreover, the examination of these profiles shows that, after spatial averaging over an appropriate z -range, the component of the time-averaged Poynting vector along the direction of propagation is higher in magnitude in the SNTF than in the metal, regardless of the polarization state of the SPP wave. This means that the energy of the SPP wave primarily resides in the SNTF.

Only two values of κ were found to satisfy Equation [11.28] for $\psi = 75^\circ$: $\kappa_1 = (2.459 + 0.04247i) k_0$ and $\kappa_2 = (2.066 + 0.003861i) k_0$. The phase speed of the SPP wave with $\kappa = \kappa_2$ exceeds the phase speed of the other SPP wave ($\kappa = \kappa_1$), and the former SPP wave will propagate a longer distance along the interface than the latter SPP wave. The variations of the Cartesian components of \mathbf{P} along the z axis are shown in Fig. 11.4 for κ_2 . This SPP wave cannot be rigorously classified as either *p*- or *s*-polarized. However, the electric field of this SPP wave is predominantly oriented parallel to $\hat{\mathbf{u}}_2$ (Faryad *et al.* 2010), thereby suggesting that the SPP wave for κ_2 could be classified as quasi-*s*-polarized on both sides of the interface. In contrast, the electric field in the spatial plots for κ_1 is predominantly oriented in the plane formed by $\hat{\mathbf{u}}_1$ and $\hat{\mathbf{u}}_z$, which implies that the SPP wave for κ_1 is quasi-*p*-polarized on both sides of the interface.



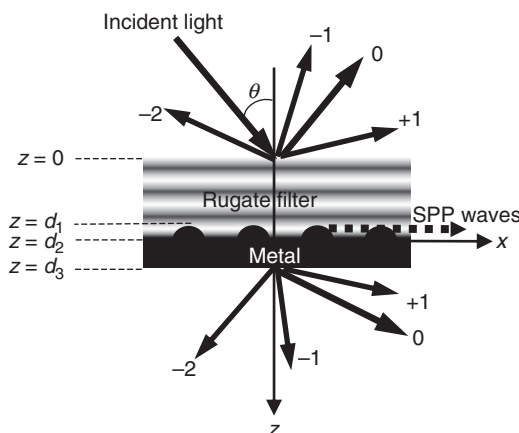
11.4 Variations of components of $\mathbf{P}(x, z)$ with z along the line $\{x = 0, y = 0\}$ for the SPP waves guided by a planar interface of bulk aluminum and the SNTF in the canonical boundary-value problem, for $\kappa = (2.066 + 0.003861i) k_0$ and $\psi = 75^\circ$. The components parallel to $\hat{\mathbf{u}}_1$, $\hat{\mathbf{u}}_2$, and $\hat{\mathbf{u}}_z$, are represented by solid, dashed, and chain-dashed lines, respectively. The data were computed by setting $a_p = 1 \text{ V m}^{-1}$, with a_s , τ_1 , and τ_2 then obtained using Equation [11.27] (Faryad *et al.*, 2010).

11.5 Grating-coupled configuration

Solutions of the canonical boundary-value problem discussed in Section 11.4 provide the number, wavenumbers, and e-folding distances along the direction of propagation and into the partnering materials, of possible SPP waves. However, the canonical boundary-value problem cannot be implemented in a laboratory because it involves semi-infinite expanses of both partnering materials. Therefore, the grating-coupled configuration in this section and the TKR configuration in Section 11.6, with finitely thick partnering materials, are discussed for the practical excitation of multiple SPP waves.

11.5.1 Metal/rugate-filter interface

Let us consider the boundary-value problem shown schematically in Fig. 11.5 for the grating-coupled configuration. The regions $z < 0$ and $z > d_3$ are vacuous, the region $0 \leq z \leq d_1$ is occupied by the dielectric partnering material with relative permittivity $\epsilon_{\text{rug}}(z)$, and the region $d_2 \leq z \leq d_3$ by the metallic partnering material with spatially uniform relative permittivity ϵ_{met} . The region $d_1 < z < d_2$ contains a surface-relief grating of period L along the x axis. The relative permittivity $\epsilon_g(x, z) = \epsilon_g(x \pm L, z)$ in this region is specified as



11.5 Schematic of the grating-coupled configuration used for the excitation of multiple SPP waves by an incident plane wave. Specular reflection and transmission are denoted by order $n = 0$, whereas nonspecular modes are denoted by orders $n \neq 0$. The SPP waves are guided by the periodically corrugated metal/rugate-filter interface. The rugate filter has to be replaced by a periodically non-homogeneous SNTF for the problem addressed in Section 11.5.2.

$$\varepsilon_g(x, z) = \begin{cases} \varepsilon_{\text{met}} - [\varepsilon_{\text{met}} - \varepsilon_{\text{rug}}(d_2 - z)]U[d_2 - z - g(x)], & x \in (0, L_1), \\ \varepsilon_{\text{rug}}(d_2 - z), & x \in (L_1, L), \end{cases} \quad [11.34]$$

for $z \in (d_1, d_2)$, with

$$g(x) = (d_2 - d_1)\sin\left(\frac{\pi x}{L_1}\right), \quad L_1 \in (0, L), \quad [11.35]$$

and

$$U(\zeta) = \begin{cases} 1, & \zeta \geq 0 \\ 0, & \zeta < 0. \end{cases} \quad [11.36]$$

The depth of the surface-relief grating defined by Equation [11.35] is $L_g = d_2 - d_1$.

In the vacuous half-space $z \leq 0$, let a plane wave propagating in the xz plane at an angle θ to the z axis, be incident on the structure. Hence, the incident, reflected, and transmitted electric field phasors may be written in terms of Floquet harmonics as follows:

$$\mathbf{E}_{\text{inc}}(\mathbf{r}) = \sum_{n=-N_t}^{n=N_t} \left(a_s^{(n)} \mathbf{s}_n + a_p^{(n)} \mathbf{p}_n^+ \right) \exp\left[i\left(k_x^{(n)}x + k_z^{(n)}z\right)\right], \quad z \leq 0, \quad [11.37]$$

$$\mathbf{E}_{\text{refl}}(\mathbf{r}) = \sum_{n=-N_t}^{n=N_t} \left(r_s^{(n)} \mathbf{s}_n + r_p^{(n)} \mathbf{p}_n^- \right) \exp\left[i\left(k_x^{(n)}x - k_z^{(n)}z\right)\right], \quad z \leq 0, \quad [11.38]$$

$$\mathbf{E}_{\text{tr}}(\mathbf{r}) = \sum_{n=-N_t}^{n=N_t} \left(t_s^{(n)} \mathbf{s}_n + t_p^{(n)} \mathbf{p}_n^+ \right) \exp\left\{i\left[k_x^{(n)}x + k_z^{(n)}(z - d_3)\right]\right\}, \quad z \leq d_3, \quad [11.39]$$

where $k_x^{(n)} = k_0 \sin \theta + n\kappa_x$, $\kappa_x = 2\pi/L$, and

$$k_z^{(n)} = \begin{cases} +\sqrt{k_0^2 - (k_x^{(n)})^2}, & k_0^2 > (k_x^{(n)})^2 \\ +i\sqrt{(k_x^{(n)})^2 - k_0^2}, & k_0^2 < (k_x^{(n)})^2 \end{cases}. \quad [11.40]$$

The s - and p -polarization states are represented, respectively, by

$$\mathbf{s}_n = \hat{\mathbf{u}}_y \quad [11.41]$$

and

$$\mathbf{p}_n^{\pm} = \mp \frac{k_z^{(n)}}{k_0} \hat{\mathbf{u}}_x + \frac{k_x^{(n)}}{k_0} \hat{\mathbf{u}}_z. \quad [11.42]$$

The boundary-value problem was formulated using the rigorous coupled-wave approach (RCWA) (Li, 1993; Moharam and Gaylord, 1982) and was implemented using a stable algorithm (Chateau and Hugonin, 1994; Moharam *et al.*, 1995; Wang *et al.*, 2004). The accuracy of the solution using RCWA depends on the value of N_t , the number of terms of Floquet harmonics in the representation of field phasors being $2N_t + 1$. The formulation of the boundary-value problem and the numerical algorithm have been explained elsewhere in detail (Faryad and Lakhtakia, 2011b, 2011c) and we skip both to go directly to present some representative numerical results.

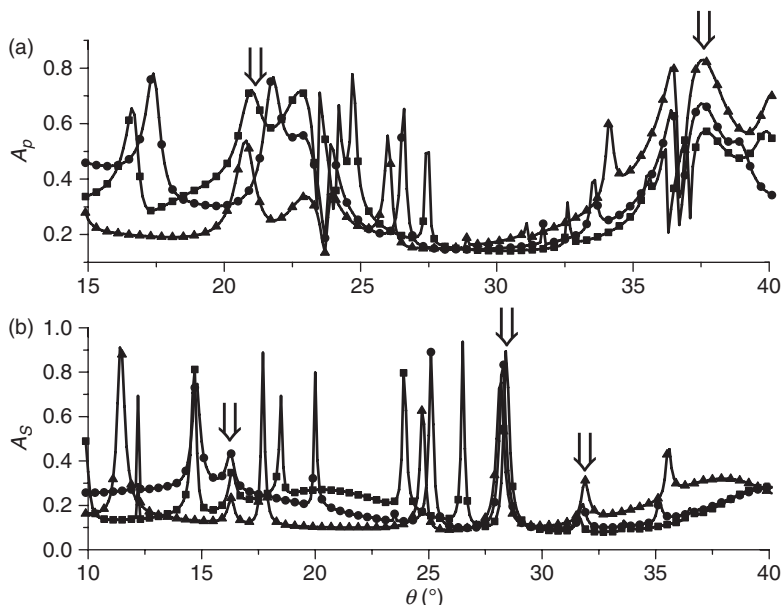
The planewave absorptance was computed as

$$A = 1 - \sum_{n=-N_t}^{N_t} \frac{\left| r_s^{(n)} \right|^2 + \left| r_p^{(n)} \right|^2 + \left| t_s^{(n)} \right|^2 + \left| t_p^{(n)} \right|^2}{\left| a_s^{(0)} \right|^2 + \left| a_p^{(0)} \right|^2} \operatorname{Re}\left(\frac{k_z^{(n)}}{k_z^{(0)}}\right) \quad [11.43]$$

The absorptance for p -polarized incidence is denoted by $A_p = A(a_s^{(0)} = 0, a_p^{(0)} \neq 0)$, and that for s -polarized incidence by $A_s = A(a_s^{(0)} \neq 0, a_p^{(0)} = 0)$. Let us note that $r_s^{(n)} = 0$ and $t_s^{(n)} = 0 \forall n \in \mathbb{Z}$ for p -polarized incident planewaves, and vice versa for the s -polarized case, when the dielectric partnering material is isotropic.

For all calculations reported in the remainder of this subsection, $\varepsilon_{\text{met}} = -56 + 21i$ (bulk aluminum) and $\Omega = \lambda_0$. The surface-relief grating is defined by Equation [11.35] with $L_1 = 0.5L$. The grating depth $L_g = 50$ nm and the thickness of the metal layer $d_3 - d_2 = 30$ nm were also fixed, as their variations would not qualitatively affect the excitation of multiple SPP waves. The rugate filter ($0 < z < d_1$) and the grating region ($d_1 < z < d_2$) were divided into 2- and 1-nm-thick slices, respectively, to use the piecewise-uniform-approximation method. Both A_p and A_s were calculated as functions of θ for $d_1 \in \{4\Omega, 5\Omega, 6\Omega\}$. Absorptances calculated for $N_t = 8$ lay within $\pm 1\%$ of the absorptances calculated with $N_t = 9$.

The solution of the corresponding canonical boundary-value problem formulated in Section 11.4.1 (when both the rugate filter and the metal are semi-infinite in thickness and their interface is planar) results in five p -polarized and four s -polarized SPP waves, the relative wavenumbers κ/k_0 being provided in Table 11.1.



11.6 Absorptances (a) A_p and (b) A_s as functions of the incidence angle θ in the grating-coupled configuration. The surface-relief grating formed by bulk aluminum and a rugate filter defined by Equation [11.35] with $L_1 = 0.5L$, $\lambda_0 = 633$ nm, $\Omega = \lambda_0$, and $L = \lambda_0$. Squares are for $d_1 = 6\Omega$, circles for $d_1 = 5\Omega$, and triangles for $d_1 = 4\Omega$. The grating depth ($d_2 - d_1 = 50$ nm) and the thickness of the metallic layer ($d_3 - d_2 = 30$ nm) are the same for all plots. Each vertical arrow identifies an SPP wave (Faryad and Lakhtakia, 2011b).

For all three values of d_1 , a peak is present at $\theta = 37.7^\circ$ in the plots of A_p vs. θ in Fig. 11.6a. The relative wavenumbers $k_x^{(n)}/k_0$ of several Floquet harmonics at this incidence angle are given in Table 11.2. At $\theta = 37.7^\circ$, $k_x^{(1)}/k_0 = 1.6115$ is close to $\text{Re}(\kappa/k_0) = 1.61782$, where κ/k_0 is the relative wavenumber of a p -polarized SPP wave in the canonical boundary-value problem as provided in Table 11.1. Thus, this A_p -peak represents the excitation of a p -polarized SPP wave as a Floquet harmonic of order $n = 1$. This conclusion is also confirmed from an examination of the spatial profile of $P_x(0.75L, z)$ provided by Faryad and Lakhtakia (2010b) for $\theta = 37.7^\circ$. Indeed, P_x decays quickly away from the plane $z = d_1$ in the region containing metal, and it also decays periodically (Yakubovich and Starzhinskii, 1975) inside the rugate filter away from the same interface.

For the A_p -peak at $\theta \approx 21^\circ$, the angular location changes slightly with the change in the value of d_1 . However, this peak also represents the excitation of a p -polarized SPP wave because (i) $k_x^{(1)}/k_0 = 1.3584$ (Table 11.2) is close to $\text{Re}(\kappa/k_0) = 1.36479$ (Table 11.1) and (ii) the spatial profile of $P_x(0.75L, z)$

Table 11.1 Relative wavenumbers κ/k_0 of possible SPP waves obtained by the solution of the canonical boundary-value problem involving bulk aluminum and a rugate filter (Section 11.4.2) for $\Omega = \lambda_0$. If κ represents an SPP wave propagating in the $\hat{\mathbf{u}}_x$ direction, $-\kappa$ represents an SPP wave propagating in the $-\hat{\mathbf{u}}_x$ direction

p-polarization	$1.36479 + 0.00169i$	$1.61782 + 0.00548i$	$1.87437 + 0.00998i$
	$2.06995 + 0.01526i$	$2.21456 + 0.00246i$	
s-polarization	$1.48639 + 0.00132i$	$1.7324 + 0.0014i$	$1.9836 + 0.0006i$
	$2.2128 + 9.6 \times 10^{-5}i$		

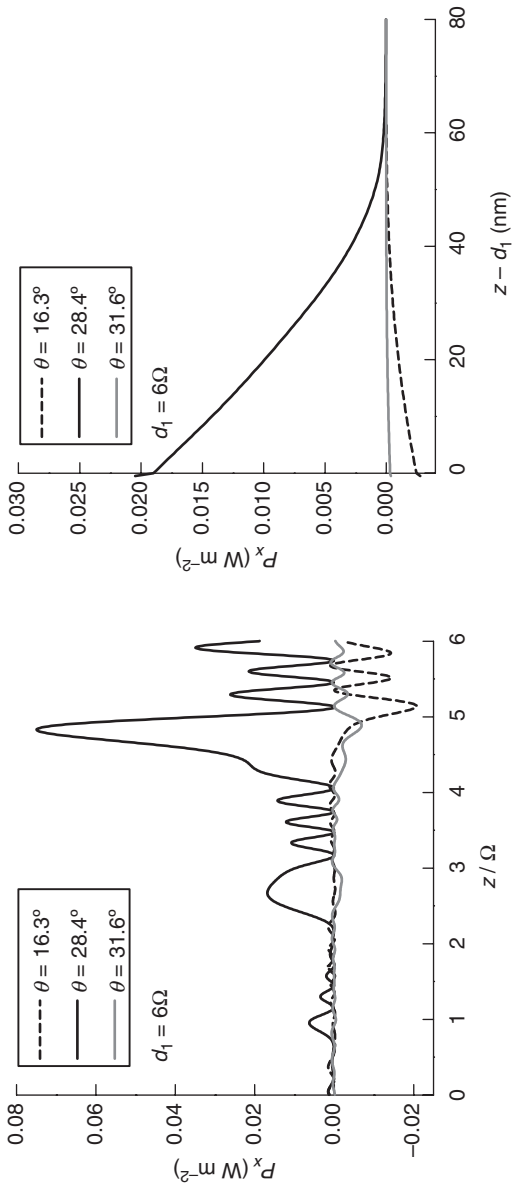
Table 11.2 Relative wavenumbers $k_x^{(n)}/k_0$ of Floquet harmonics at the θ -values of the peaks identified in Fig. 11.6 by vertical arrows when the half-period Ω of the rugate filter is λ_0 and the period L of the surface-relief grating is λ_0 . Boldface entries signify SPP waves

θ	$n = -2$	$n = -1$	$n = 0$	$n = 1$	$n = 2$
16.3°	-1.7210	-0.7210	0.2790	1.2790	2.2790
21.0°	-1.6416	-0.6416	0.3584	1.3584	2.3584
28.4°	-1.5244	-0.5244	0.4756	1.4756	2.4756
31.6°	-1.4760	-0.4760	0.5240	1.5240	2.5240
37.7°	-1.3885	-0.3885	0.6115	1.6115	2.6115

provided by Faryad and Lakhtakia (2011b) is also indicative of a surface wave guided by the metal/rugate-filter interface. The reason for the change in the θ -value of the A_p -peak is the weak localization of this SPP wave in the region $z < d_1$. However, for a sufficiently large value of d_1 , the peak should be independent of the value of d_1 .

Three A_s -peaks are present at $\theta = 16.3^\circ$, 28.4° , and 31.6° in the plots of A_s vs. θ , for all three values of d_1 in Fig. 11.6b. The relative wavenumbers of the Floquet harmonics at these values of the incidence angle are also provided in Table 11.2. At $\theta = 16.3^\circ$, an *s*-polarized SPP wave is excited as a Floquet harmonic of order $n = -2$ because $k_x^{(-2)}/k_0 = -1.7210$ (Table 11.2) is close to $\text{Re}(\kappa/k_0) = -1.7324$ (Table 11.1). The spatial profile of $P_x(0.75L, z)$ given in Fig. 11.7 for $\theta = 16.3^\circ$ also confirms this conclusion. The *s*-polarized SPP wave is propagating in the $-\hat{\mathbf{u}}_x$ direction because it is excited as a Floquet harmonic of a negative order.

The A_s -peak at $\theta = 28.4^\circ$ represents the excitation of an *s*-polarized SPP wave, as a Floquet harmonic of order $n = 1$, because (i) $k_x^{(1)}/k_0 = 1.4756$ (Table 11.2) is close to $\text{Re}(\kappa/k_0) = 1.48639$ (Table 11.1), and (ii) the spatial profile of $P_x(0.75L, z)$ provided in Fig. 11.7 shows that an *s*-polarized SPP wave is guided by the interface $z = d_1$ in the $+\hat{\mathbf{u}}_x$ direction. Coincidentally, the A_s -peak at $\theta = 31.6^\circ$ represents the excitation of the same *s*-polarized SPP wave but as a Floquet harmonic of order $n = -2$ because $k_x^{(-2)}/k_0 = 1.4760$



11.7 Variation of the x -component of the time-averaged Poynting vector \mathbf{P} (x, z) in the grating-coupled configuration along the z axis in the regions (left) $0 < z < d_1$ and (right) $d_1 < z < d_3$ at $x = 0.75 L$, when the surface-relief grating is defined by Equation [11.35] and the partnering dielectric material is a rugate filter. The grating period $L = \lambda_0$ and the incident plane wave is s-polarized (After Faryad and Lakhtakia, 2011b).

(Table 11.2) is close to $\text{Re}(\kappa/k_0) = -1.48639$ (Table 11.1). This is also evident from the comparison of the spatial profiles given in Fig. 11.7 for $\theta = 28.4^\circ$ and $\theta = 31.6^\circ$. Although the two spatial profiles are mirror images of each other, the excitation of the s -polarized SPP wave at $\theta = 31.6^\circ$ is not very efficient because it is excited as a Floquet harmonic of a higher order ($|n| = 2$).

Since not all possible SPP waves (predicted from the solution of the canonical boundary-value problem) can be excited with period $L = \lambda_0$ of the surface-relief grating, the grating period needs to be changed in order to excite the remaining SPP waves (Faryad, 2012). Moreover, a comparison of A_p - and A_s -peaks in Figs. 11.6a and 11.6b shows that A_s -peaks are generally narrower than A_p -peaks.

11.5.2 Metal/SNTF interface

Let us now consider the same boundary-value problem as in the foregoing subsection with the rugate filter in the region $0 \leq z \leq d_1$ replaced by an SNTF with a periodically non-homogeneous permittivity dyadic (Lakhtakia *et al.*, 2009; Motyka and Lakhtakia, 2008, 2009)

$$\underline{\underline{\varepsilon}}_{\text{SNTF}}^{\text{rot}}(z) = \underline{\underline{S}}_z(\gamma) \cdot \underline{\underline{\varepsilon}}_{\text{SNTF}}(z) \cdot \underline{\underline{S}}_z^{-1}(\gamma). \quad [11.44]$$

where

$$\underline{\underline{S}}_z(\gamma) = (\hat{\mathbf{u}}_x \hat{\mathbf{u}}_x + \hat{\mathbf{u}}_y \hat{\mathbf{u}}_y) \cos \gamma + (\hat{\mathbf{u}}_y \hat{\mathbf{u}}_x - \hat{\mathbf{u}}_x \hat{\mathbf{u}}_y) \sin \gamma + \hat{\mathbf{u}}_z \hat{\mathbf{u}}_z. \quad [11.45]$$

Here, $\underline{\underline{\varepsilon}}_{\text{SNTF}}^{\text{rot}}(z)$ is a rotated version of $\underline{\underline{\varepsilon}}_{\text{SNTF}}(z)$ so that the plane formed by the unit vectors $\hat{\mathbf{u}}_z$ and $\hat{\mathbf{u}}_x \cos \gamma + \hat{\mathbf{u}}_y \sin \gamma$ is the morphologically significant plane of the SNTF.

The relative permittivity dyadic $\underline{\underline{\varepsilon}}_g(x, z) = \underline{\underline{\varepsilon}}_g(x \pm L, z)$ in the region $d_1 < z < d_2$ is taken to be

$$\underline{\underline{\varepsilon}}_g(x, z) = \begin{cases} \underline{\underline{\varepsilon}}_{\text{met}} \underline{\underline{I}} - [\underline{\underline{\varepsilon}}_{\text{met}} \underline{\underline{I}} + \underline{\underline{\varepsilon}}_{\text{SNTF}}^{\text{rot}}(d_2 - z)] U [d_2 - z - g(x)], & x \in (0, L_1) \\ \underline{\underline{\varepsilon}}_{\text{SNTF}}^{\text{rot}}(d_2 - z), & x \in (L_1, L), \end{cases} \quad [11.46]$$

for $z \in (d_1, d_2)$, with $\underline{\underline{I}} = \hat{\mathbf{u}}_x \hat{\mathbf{u}}_x + \hat{\mathbf{u}}_y \hat{\mathbf{u}}_y + \hat{\mathbf{u}}_z \hat{\mathbf{u}}_z$. Let us note that the permittivity dyadic defined by Equation [11.46] is a simplistic description of the region $d_1 < z < d_2$ and the actual morphology of the region is very hard to model for the fabricated device (Fiumara *et al.*, 2006).

Faryad and Lakhtakia (2011c) have provided the formulation of this problem in detail where the incidence plane, the grating plane, and the morphologically significant plane of the SNTF can be rotated with respect to each other. Both *p*- and *s*-polarized SPP waves are excited by *p*- and *s*-polarized incident planewaves, respectively, when the morphologically significant plane, the grating plane, and the incidence plane are the same, that is, $\gamma = 0^\circ$.

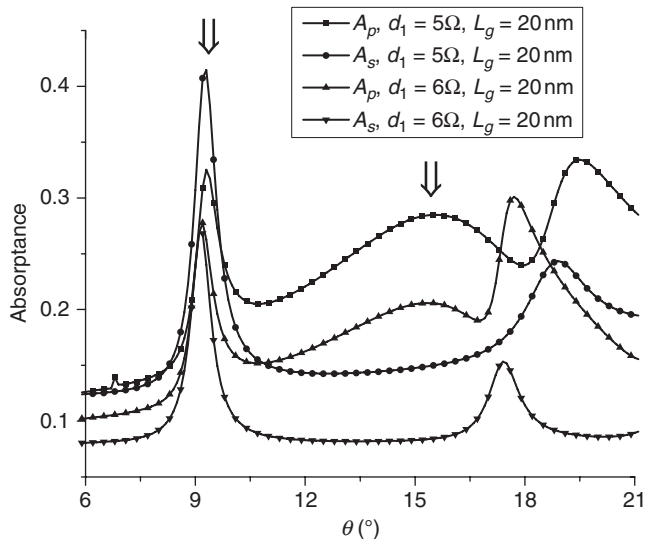
Let us discuss the special case of $\gamma = 75^\circ$, that is, when the morphologically significant plane makes an angle of 75° with the *xz* plane – the incidence plane and the grating plane. Relative wavenumbers κ/k_0 , obtained from the solution of the canonical boundary-value problem for SPP waves propagating at an angle of 75° with respect to the morphologically significant plane, are $\kappa/k_0 = 2.0664 + 0.0039i$ and $\kappa/k_0 = 2.4588 + 0.0425i$. As was discussed in Section 11.4.3, both of these SPP waves are neither purely *p*- nor *s*-polarized because of the anisotropy of the SNTF.

The absorptances A_p and A_s for $L = 286$ nm and $\gamma = 75^\circ$ are presented in Fig. 11.8 as functions of the angle of incidence θ . Independent of the value of d_1 and the polarization state of the incident plane wave, an absorptance peak is present at $\theta \approx 9.2^\circ$. This peak represents the excitation of an SPP wave as a Floquet harmonic of order $n = -1$ because $k_x^{(-1)}/k_0 = -2.0534$ is very close to $\text{Re}(-2.0664 - 0.0039i)$.

The spatial profiles of the *x*- and *y*-components of $\mathbf{P}(0.75L, z)$, given in Fig. 11.9, for $\theta = 9.2^\circ$ indicate that the SPP wave is localized to the metal/SNTF interface. As the magnitude of P_y is approximately ten times smaller than that of P_x , the SPP wave transports energy mainly along the $-\hat{\mathbf{u}}_x$ direction. This is reasonable because the SPP wave is excited in the grating-coupled configuration as a Floquet harmonic of negative order. The notable characteristic of this SPP wave is that it can be excited by a plane wave of either polarization state; however, the excitation is more efficient if the incident plane wave is *s*-polarized. This is due to the fact that this SPP wave is quasi-*s*-polarized, as was seen in Section 11.4.3.

At $\theta \approx 15.5^\circ$ in Fig. 11.8, a peak is present independent of the value of d_1 in the plots of A_p but not of A_s . This A_p -peak represents the excitation of an SPP wave as a Floquet harmonic of order $n = 1$ because $k_x^{(1)}/k_0 = 2.4805$ is very close to $\text{Re}(2.4588 + 0.0425i)$. Contrary to the SPP wave excited at $\theta = 9.2^\circ$, the absence of the peak in the curves of A_s shows that this SPP wave is excited only by a *p*-polarized incident plane wave. The spatial profiles of $\mathbf{P}(0.75L, z)$ at $\theta = 15.5^\circ$ for *s*- and *p*-polarized incident plane waves, provided by Faryad and Lakhtakia (2011c), also support this conclusion; furthermore, the SPP wave is strongly localized in the SNTF to the plane $z = d_1$.

The A_p - and A_s -peaks at $\theta = 9.2^\circ$ are narrower than the A_p -peak at $\theta = 15.5^\circ$, thereby supporting the conclusion that the absorptance peak representing the excitation of an SPP wave with smaller phase speed is broader. The spatial profile in the SNTF ($0 < z < d_1$) of the SPP wave presented in Fig. 11.9 is



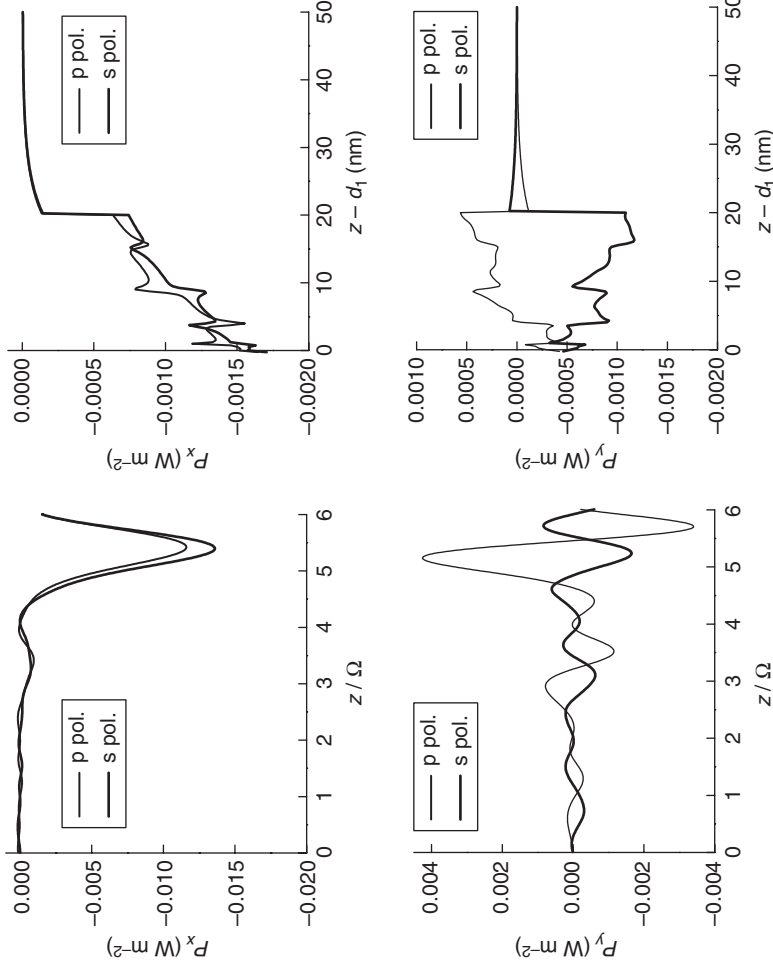
11.8 Absorptances A_p and A_s vs. θ in the grating-coupled configuration when $L = 286\text{ nm}$, $\psi = 0^\circ$, $\gamma = 75^\circ$, and $d_3 - d_2 = 30\text{ nm}$. The metal is bulk aluminum and the partnering dielectric material is a periodically non-homogeneous SNTF with relative permittivity defined by Equation [11.2]. The vertical arrows identify the peaks that represent the excitation of SPP waves (Faryad and Lakhtakia, 2011c).

similar to the profile for the corresponding SPP waves guided by the planar metal/SNTF interface in the canonical boundary-value problem (Fig. 11.4).

To analyze the effect of the direction of the electric field of the incident linearly polarized plane wave on the efficiency of the excitation of SPP waves when $\gamma = 75^\circ$, Faryad and Lakhtakia (2011c) also calculated the absorptance A for an incident plane wave with electric field phasor:

$$\mathbf{E}_{\text{inc}}(\mathbf{r}) = (\cos \alpha \mathbf{s}_0 + \sin \alpha \mathbf{p}_0^+) \exp[i(k_x^{(0)}x + k_z^{(0)}z)], \quad z \leq 0, \quad [11.47]$$

where $\alpha \in [0^\circ, 360^\circ]$. This plane wave is *s*-polarized when $\alpha \in \{0^\circ, 180^\circ\}$ and *p*-polarized when $\alpha \in \{90^\circ, 270^\circ\}$. Efficient excitation of an SPP wave was found to depend not only on the direction of the incident electric field but also on the thickness of the SNTF. This is because A depends on α , and more generally, on the vibration ellipse of the incident plane wave. In addition, as depolarization affects the absorptance, and depolarization must depend on d_1 , the absorptance must also depend on the thickness of the SNTF. The higher the absorptance at the peak representing the excitation of an SPP wave, the more efficient is the excitation of the SPP wave.



11.9 Variation of the x- and y-components of the time-averaged Poynting vector $\mathbf{P}(0.75L, z)$ in the grating-coupled configuration (metal/SNTF interface) along the z axis in the regions (left) $0 < z < d_1$ and (right) $d_1 < z < d_3$ for p- and s-polarized incident plane waves when $\theta = 9.2^\circ$, $L = 286 \text{ nm}$, $\gamma = 75^\circ$, $d_1 = 6\Omega$, $L_g = 20 \text{ nm}$, and $d_3 - d_2 = 30 \text{ nm}$ (After Faryad and Lakhtakia, 2011c).

11.6 Turbadar–Kretschmann–Raether (TKR) configuration

The TKR configuration is an alternative to the grating-coupled configuration for exciting SPP waves, and is widely used for optical-sensing applications (Abdulhalim *et al.*, 2007, 2008; Homola, 2006). It should be noted that, while this configuration is often called the Kretschmann configuration, and sometimes the Kretschmann–Raether configuration after the authors of a 1968 paper (Kretschmann and Raether, 1968), Turbadar (1959) had anticipated that paper by a decade, although he had not used the word ‘plasmon’. Propriety demands that Turbadar’s contribution be adequately acknowledged.

This configuration is now briefly discussed for both the metal/rugate-filter and the metal/SNTF interfaces.

11.6.1 Metal/rugate-filter interface

The boundary-value problem of the TKR configuration is shown schematically in Fig. 11.10. Let the half-spaces $z < 0$ and $z > L$ be occupied by a dielectric material with relative permittivity $\varepsilon_\ell = n_\ell^2$, the region $0 < z < L_m$ by a metal with relative permittivity ε_{met} , and the region $L_m < z < L_m + L_d = L_\Sigma$ by a rugate filter with relative permittivity $\varepsilon_{\text{rug}}(z - L_m)$. The rugate filter was chosen to have integral number of periods: $L_d = 2\Omega N_p$, $N_p \in \{1, 2, 3, \dots\}$; furthermore, $n_\ell > n_b$ is required for the TKR configuration. The half-space $z < 0$ represents a prism.

Let a linearly polarized plane wave, propagating in the half-space $z < 0$ and with its wave vector making an angle θ with the z axis, be incident on the metal-capped rugate filter. The incident, reflected and transmitted electric field phasors may be represented as (Motyka and Lakhtakia, 2008)

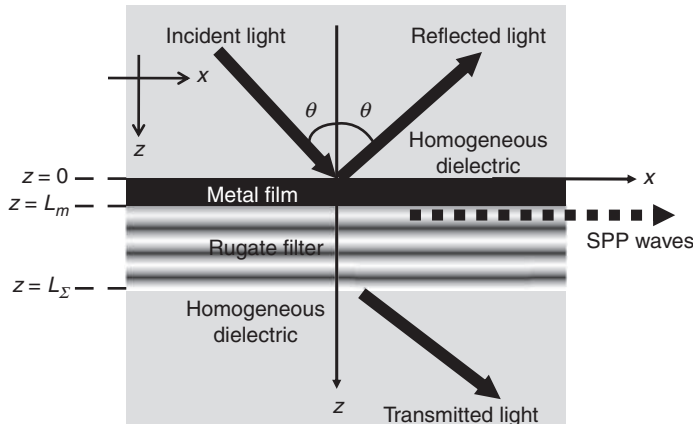
$$\mathbf{E}_{\text{inc}}(\mathbf{r}) = (a_s \mathbf{s} + a_p \mathbf{p}^+) \exp(ik_x x + ik_0 n_\ell z \cos \theta), \quad z \leq 0, \quad [11.48]$$

$$\mathbf{E}_{\text{refl}}(\mathbf{r}) = (r_s \mathbf{s} + r_p \mathbf{p}^-) \exp(ik_x x - ik_0 n_\ell z \cos \theta), \quad z \leq 0, \quad [11.49]$$

$$\mathbf{E}_{\text{tr}}(\mathbf{r}) = (t_s \mathbf{s} + t_p \mathbf{p}^+) \exp[ik_x x + ik_0 n_\ell (z - L_\Sigma) \cos \theta], \quad z \leq L_\Sigma, \quad [11.50]$$

where the unit vectors $\mathbf{s} = \hat{\mathbf{u}}_y$ and $\mathbf{p}^\pm = \mp \hat{\mathbf{u}}_x \cos \theta + \hat{\mathbf{u}}_z \sin \theta$ represent s - and p -polarization states, respectively, and $k_x = k_0 n_\ell \sin \theta \in \mathbb{R}$.

The reflection amplitudes $r_{p,s}$ and the transmission amplitudes $t_{p,s}$ have to be determined in terms of known amplitudes $a_{p,s}$ of the incident plane



11.10 Schematic of the TKR configuration. Incident light inside an optically dense material excites a metal-capped rugate filter. The SPP waves are guided by the metal/rugate-filter interface. The rugate filter has to be replaced by a periodically non-homogeneous SNTF for the problem addressed in Section 11.6.2.

wave. The numerical method of finding unknown transmission and reflection amplitudes r_p , r_s , t_p , and t_s in terms of a_p and a_s is provided in detail by Faryad and Lakhtakia (2010a). For the numerical solution, the region $L_m < z < L_\Sigma$ has to be divided into N_d slices, each a couple of nanometers in thickness.

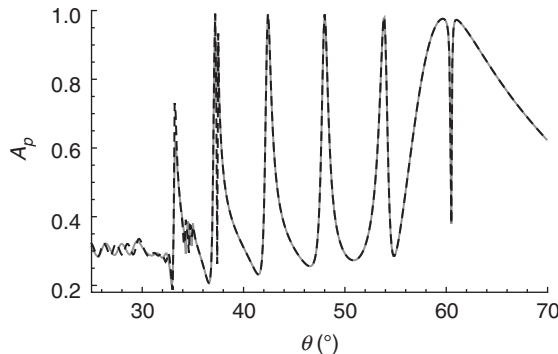
For all the calculations reported in the remainder of this subsection, the half-spaces $z < 0$ and $z > L_\Sigma$ are occupied by zinc selenide ($n_\ell = 2.58$), and the metal film is thin-film aluminum for which $\epsilon_{\text{met}} = (0.75 + 3.9i)^2$ (Lakhtakia *et al.*, 2009). The half-period of the rugate filter is $\Omega = 1.5\lambda_0$ so that the interface of a semi-infinite metal and rugate filter can guide multiple *p*- and multiple *s*-polarized SPP waves according to Section 11.4.2. No depolarization can occur because the partnering dielectric material is isotropic, and absorptances for *p*- and *s*-polarization states can be defined as

$$A_p = 1 - \frac{|r_p|^2 + |t_p|^2}{|a_p|^2}, \quad A_s = 1 - \frac{|r_s|^2 + |t_s|^2}{|a_s|^2}. \quad [11.51]$$

The variation of absorptance A_p vs. the angle of incidence θ is given in Fig. 11.11 for $N_p \in \{3, 4\}$ and $L_m = 30$ nm. The absorptances were calculated for two values of N_p in order to identify and eliminate waveguide modes (Kapany and Burke, 1972; Marcuse, 1991), which must depend on L_d (Motyka and Lakhtakia, 2008; Otto and Sohler, 1971). At seven values of the incidence angle θ , given in Table 11.3, a peak is present independent

Table 11.3 Values of the incidence angle θ and the relative wavenumber k_x/k_0 , where a peak is present in Fig. 11.11 independent of the value of N_p in the TKR configuration. Each peak represents a *p*-polarized SPP wave, not a waveguide mode

θ	$k_x/k_0 = n_\ell \sin \theta$
33.23°	1.4138
37.20°	1.5599
42.41°	1.7400
48.01°	1.9176
53.86°	2.0836
59.66°	2.2266
61.01°	2.2567



11.11 Absorptance A_p as function of the incidence angle θ in the TKR configuration, when $\epsilon_{\text{met}} = (0.75 + 3.9i)^2$, $n_\ell = 2.58$, $L_m = 30$ nm, and the partnering dielectric material is a rugate filter with $\Omega = 1.5\lambda_0$. Solid gray line is for $N_p = 3$ and dashed black line is for $N_p = 4$ (Faryad and Lakhtakia, 2011a).

of the value of N_p . The relative wavenumbers k_x/k_0 at these values of θ are also given in Table 11.3. The seven A_p -peaks in Fig. 11.11 represent the excitation of *p*-polarized SPP waves because of the independence of their θ -value from the value of N_p . Furthermore, any peak identified in Table 11.3 represents either an SPP wave guided by the metal/rugate-filter interface or a coupled SPP wave guided by the metal film (Faryad and Lakhtakia, 2011a).

Further evidence in support of the conclusion that the peaks identified in Table 11.3 represent the excitation of *p*-polarized SPP waves was provided by the solution of the canonical boundary-value problem formulated

Table 11.4 Relative wavenumbers κ/k_0 of SPP waves guided by the interface between semi-infinite metal and semi-infinite rugate filter, when $\Omega = 1.5\lambda_0$ and the metal is thin-film aluminum

<i>p</i> -polarization	1.4109 + 0.0019 <i>i</i>	1.5579 + 0.0053 <i>i</i>	1.7374 + 0.0072 <i>i</i>
	1.9163 + 0.0077 <i>i</i>	2.0856 + 0.0081 <i>i</i>	2.2060 + 0.0987 <i>i</i>
	2.2447 + 0.0022 <i>i</i>		
<i>s</i> -polarization	1.6205 + 0.0018 <i>i</i>	1.7910 + 0.0012 <i>i</i>	1.9528 + 0.0006 <i>i</i>
	2.1037 + 0.0001 <i>i</i>	2.2490 + 1.1021×10 ⁻⁵ <i>i</i>	

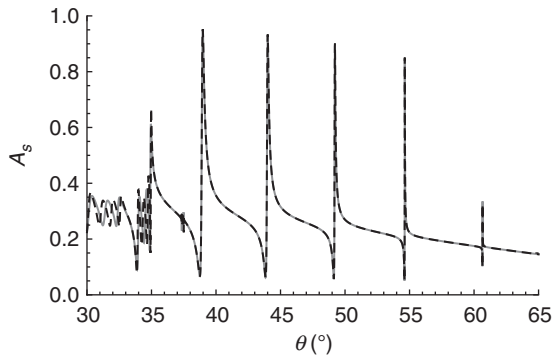
Table 11.5 Values of the incidence angles θ , and the relative wavenumbers k_x/k_0 , where a peak is present in Fig. 11.12 independent of the value of N_p

θ	$k_x/k_0 = n_\ell \sin \theta$
38.97°	1.6226
44.01°	1.7925
49.22°	1.9536
54.63°	2.1038
60.66°	2.2491

in Section 11.4. The solutions of the dispersion equation [11.28] for the chosen metal and the rugate filter are given in Table 11.4. All solutions of the canonical boundary-value problem represent SPP waves. A comparison of Tables 11.3 and 11.4 shows that $\text{Re}(\kappa/k_0)$ of each item in Table 11.4 for *p*-polarized SPP waves is close to the relative wavenumber k_x/k_0 at one of the A_p -peaks, showing that the seven peaks identified in Table 11.3 represent the excitation of *p*-polarized SPP waves.

The absorptance A_s for an *s*-polarized incident plane wave is given in Fig. 11.12 as a function of the incidence angle θ for the TKR configuration with a 30-nm-thick metal film for $N_p \in \{3, 4\}$. For five values of the incidence angle θ , an absorptance peak is present, independent of the value of N_p . The θ values of these peaks along with the relative wavenumbers $k_x/k_0 = n_\ell \sin \theta$ are given in Table 11.5. All of the A_s -peaks represent the excitation of *s*-polarized SPP waves because (i) the peaks are independent of the value of N_p and (ii) the value of $\text{Re}(\kappa/k_0)$ of each item in Table 11.4 for *s*-polarized SPP waves is close to the relative wavenumber k_x/k_0 at one of the A_s -peaks given in Table 11.5. The peak at $\theta \approx 35^\circ$ does not represent the excitation of an *s*-polarized SPP wave (Faryad and Lakhtakia, 2011a).

In Fig. 11.12, the value of A_s at all the peaks that represent the excitation of *s*-polarized SPP waves is greater than 0.8 except for the peak at $\theta = 60.66^\circ$. So the excitation of the *s*-polarized SPP wave at $\theta = 60.66^\circ$ is not as efficient



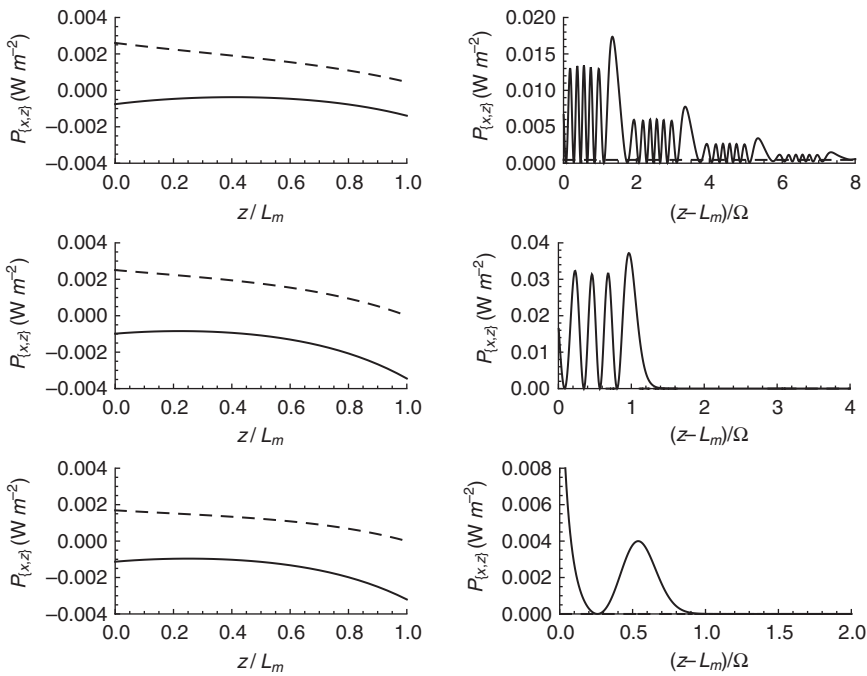
11.12 As Fig. 11.11 except that A_s is plotted instead of A_p (Faryad and Lakhtakia, 2011a).

as those of the rest of the s -polarized SPP waves. Moreover, a comparison of Figs 11.11 and 11.12 shows that the peaks representing the excitation of s -polarized SPP waves are narrower than those representing the excitation of p -polarized SPP waves.

Faryad and Lakhtakia (2011a) have shown that the efficiency of excitation of all p -polarized SPP waves in the TKR configuration is at a maximum when L_m is close to the penetration depth $\Delta_{\text{met}} = [\text{Im}(k_0 \sqrt{\epsilon_{\text{met}}})]^{-1} = 24.91$ nm of the aluminum thin film at the chosen wavelength. The same holds true for all s -polarized SPP waves except for the SPP wave excited at $\theta = 60.66^\circ$. The excitation of the s -polarized SPP wave at $\theta = 60.66^\circ$ is most efficient when $L_m \approx 12$ nm. Therefore, to excite the maximum number of s -polarized SPP waves efficiently, a value of L_m close to Δ_{met} should be used.

Representative plots of the variations of the Cartesian components of time-averaged Poynting vector $\mathbf{P}(x,z)$ are presented in Fig. 11.13 – when the incident plane wave is p -polarized and $\theta \in \{33.21^\circ, 42.41^\circ, 59.66^\circ\}$ – along a line normal to the plane $z = L_m$; $\mathbf{P}(x,z) \equiv \mathbf{P}(z)$ as $k_x \in \mathbb{R}$. The figure shows that P_z decays in the metal film as $z \rightarrow L_m$ and is negligible in the rugate filter ($z > L_m$). This should be expected because a metal is dissipative. However, P_x is localized to the metal/rugate-filter interface and decays away from that interface on both sides. The localization of the P_x to the interface plane $z = L_m$ is a clear indication of an SPP wave. While the variation of P_x is similar in the metal for the three SPP waves, the spatial profiles of P_x in the rugate filter are different for all three, indicating the different degree of localization of the SPP wave excited with a different value of θ .

In all of the plots in Fig. 11.13, $P_x(z=0) \neq 0$, whereas $P_x(z=L_\Sigma) \approx 0$. Because the thickness of the metal film is almost equal to the penetration depth of the metal, P_x does not decay to zero in the thin metal film. If the metal film is sufficiently thick, the energy may reside completely in



11.13 Variations of the x - and z -components of the time-averaged Poynting vector $\mathbf{P}(z)$ in the TKR configuration (left) the metal film and (right) the rugate filter when $L_m = 30$ nm and the incident plane wave is p -polarized ($a_p = 1 \text{ V m}^{-1}$, $a_s = 0$); (top) $\theta = 33.23^\circ$, (middle) $\theta = 42.41^\circ$, and (bottom) $\theta = 59.66^\circ$. Solid lines represent P_x and dashed lines represent P_z , while P_y is identically zero (Faryad and Lakhtakia, 2011a).

the rugate filter and the metal film; however, no SPP waves may be excited in the TKR configuration if the metal film is made too thick. Faryad and Lakhtakia (2011a) noted the same behavior of P_x and P_z for all SPP waves excited by p - and s -polarized incident plane waves.

Faryad and Lakhtakia (2011a) have also shown that the SPP waves excited in the TKR configuration may be coupled to both zinc selenide/metal and metal/rugate-filter interfaces because of the thin metal film; however, the coupling does not result in new SPP waves. Moreover, the coupling is stronger for p -polarized SPP waves than s -polarized SPP waves.

11.6.2 Metal/SNTF interface

The excitation of multiple SPP waves guided by a planar metal/SNTF interface in the TKR configuration is briefly discussed now. In this configuration, a plane wave propagating in a half space occupied by a homogeneous

dielectric material of real refractive index n_ℓ is taken to be incident on a metal-capped SNTF at an angle θ with respect to the thickness direction of the SNTF. The SNTF is of finite but sufficiently large thickness and is terminated by a half space that is occupied by a homogeneous material, whereas the metal film is very thin.

Faryad and Lakhtakia (2011a) implemented the formulation provided by Motyka and Lakhtakia (2008) – when the morphologically significant plane of the SNTF and the incidence plane are the same, with $n_\ell = 2.58$ (zinc selenide), $\varepsilon_{\text{met}} = -56 + 21i$ (bulk aluminum), and the same SNTF as described in Section 11.3.2 – and determined the θ -values of the absorptance peaks that are independent of the thickness of the SNTF and the relative wavenumbers $k_x/k_0 = n_\ell \sin \theta$ at these values of θ . The θ -values for p -polarized incident plane waves are 46.3° and 53.0° , and the corresponding values of k_x/k_0 are 1.8653 and 2.0605. For s -polarized incidence, $\theta = 75.0^\circ$ and $k_x/k_0 = 2.4921$. These values are in excellent agreement with the solutions provided in Fig. 11.3 for the canonical boundary-value problem and the grating-coupled configuration (Faryad and Lakhtakia, 2011c), indicating the excitation of two p - and one s -polarized SPP waves.

Similarly, the relative wavenumbers $k_x/k_0 = n_\ell \sin \theta$ at the θ values of the absorptance peaks independent of the thickness of the SNTF were determined when the morphologically significant plane of the SNTF makes an angle of 75° with the incidence plane (Motyka and Lakhtakia, 2009). These relative wavenumbers (2.0796 and 2.4782) were found to be in agreement with the solutions of the canonical boundary-value problem provided in Fig. 11.3 for $\psi = 75^\circ$, and with the grating-coupled configuration described in Section 11.5.2.

11.7 Conclusions

The solution of the canonical boundary-value problem showed that multiple SPP waves of both p - and s -polarization states can be guided by the planar interface of a metal and a periodically non-homogeneous, isotropic dielectric material. The partnering dielectric material must be non-homogeneous in the direction normal to the waveguiding interface. Furthermore, some SPP waves that are neither p - nor s -polarized can be guided when the partnering dielectric material is anisotropic, although other SPP waves may be linearly polarized. The solution of the canonical boundary-value problem unequivocally proved the existence of multiple SPP waves because the possibility of waveguide modes is not present in a canonical boundary-value problem as is the case with the TKR and the grating-coupled configurations. The possibility of guiding multiple SPP waves by the metal/rugate-filter interface showed that it is the periodic non-homogeneity – and not the anisotropy – of the partnering dielectric

material that is responsible for the multiplicity of SPP waves, provided that the period lies within a certain range.

The excitation of multiple SPP waves by a surface-relief grating formed by a metal and a dielectric material, both of finite thickness, was studied theoretically using the rigorous coupled-wave approach (RCWA) for a practically implementable set-up. The presence of an SPP wave is inferred by a peak in the plot of absorptance vs. the angle of incidence θ , provided that the θ -location of the peak is independent of the thickness of the dielectric partnering material. If that material is homogeneous, only one SPP wave, that too of *p*-polarization state, is excited. When the partnering dielectric material is anisotropic, the efficient excitation of SPP waves not only depends on the direction of the electric field of the incident linearly polarized plane wave but also on the thickness of the SNTF. So, optimization of the grating profile and the thickness of the dielectric partnering material may be necessary for efficient simultaneous excitation of many SPP waves as well as for broadband performance. The excitation of different SPP waves in the grating-coupled configuration sometimes requires different periods of the surface-relief grating. Therefore, the simultaneous excitation of all possible SPP waves may be achieved by using a quasi-periodic grating (Dolev *et al.*, 2011).

In the TKR configuration, a plane wave of either *p*- or *s*-polarization state, propagating in an optically denser dielectric material, was taken to be incident on a metal-capped rugate filter or a metal-capped SNTF. The absorptances were calculated using a stable numerical algorithm as functions of the incidence angle. The excitation of SPP waves was inferred from the presence of those peaks in the absorptance plot that were independent of the thickness of the rugate filter. The results of the canonical boundary-value problem, the grating-coupled configuration, and the TKR configuration were successfully correlated with each other. Besides the agreement of relative wavenumbers of SPP waves in the grating-coupled and the TKR configurations, it turns out that the higher the phase speed of an SPP wave, the narrower is the absorptance peak representing the excitation of that SPP wave. Furthermore, the spatial profiles of SPP waves are similar in both configurations.

In general, the absorptance peak is narrower for an *s*-polarized SPP wave than for a *p*-polarized SPP wave, and the absorptance peak is narrower for an SPP wave of higher phase speed in both the grating-coupled and the TKR configurations. The fact that only *p*-polarized SPP waves can be excited when the partnering dielectric material is homogeneous indicates the difficulty of exciting *s*-polarized SPP waves – which is reflected both in the narrower peaks for A_s than for A_p in the results for the grating-coupled and the TKR configurations, as well as in the greater number of solutions of a relevant canonical boundary-value problem for *p*- than for *s*-polarized SPP waves. Underlying all of these observations is the great mismatch in

optical admittance (Jen *et al.*, 2009) across metal/dielectric interfaces that usually prevails for *s*-polarized fields (Salamon and Tollin, 2001).

The choice of using the TKR or the grating-coupled configuration comes with several trade-offs. On one hand, the TKR configuration is popular because all interfaces involved are planar and, therefore, easy to fabricate. It is also advantageous because the absorptance peaks associated with the excitation of SPP waves are easy to identify because only one SPP wave can be excited at one value of incidence angle with a prism of a specific shape and made of a specific material. On the other hand, the grating-coupled configuration does not require a prism, and therefore does not require an index-matching oil between the prism and the substrate on which the metal film and the partnering dielectric material are deposited. Consequently, the grating-coupled configuration offers greater flexibility in the selection of materials for the periodically non-homogeneous dielectric partner (Rosenblatt *et al.*, 1997). However, these advantages of the grating-coupled configuration come with the requirement of fabricating a periodically undulating interface. Even though it is not as straightforward as fabricating a planar interface, the fabrication of a periodically undulating surface with features on the scale of a few hundreds of nanometers is a routine matter nowadays (Gates *et al.*, 2005).

Whereas the TKR configuration is popular for sensing applications (Homola, 2006), the grating-coupled configuration is becoming popular in enhancing the efficiency of thin-film solar cells (Green and Pillai, 2012; Xiao *et al.*, 2012). Furthermore, the grating-coupled configuration allows the reverse process: the efficient coupling of SPP waves, which are otherwise non-radiative, with light (Moreland *et al.*, 1982; Worthing and Barnes, 2001). This is an important advantage over the TKR configuration because it allows for better incorporation of chemical sensors based on SPP waves (Barnes *et al.*, 2003) in integrated optical circuits (Lambeck, 2006).

The numerical results discussed in this chapter were all computed for one value of λ_0 ; however, multiple SPP waves for other values of λ_0 must also be expected. The numbers of *p*- and *s*-polarized SPP waves and their wave-numbers in any related canonical boundary-value problem must depend on λ_0 . This is because all constitutive parameters of causal materials are frequency-dependent, not to mention that the effects of the spatial dimensions of the materials require interpretation in terms of λ_0 . Experimental confirmation has been obtained recently (Hall *et al.*, 2013).

Let us also note that the periodic non-homogeneity of a partnering dielectric material leads to the multiplicity of Fano waves (Faryad *et al.*, 2011). The same attribute is responsible for engendering surface waves recently named Tamm waves (Maab *et al.*, 2011) although known for quite a while (Martorell *et al.*, 2006; Robertson and May, 1999; Yeh *et al.*, 1977), as well as the recently predicted Dyakonov–Tamm waves (Agarwal *et al.*, 2009;

Faryad, 2012; Faryad and Lakhtakia, 2011e, 2011f; Gao *et al.*, 2009a, 2009b, 2009c, 2010). Moreover, the coupling of two interfaces have also been found to increase the number of surface waves (both SPP and Dyakonov–Tamm waves) when the homogeneous material separating the two interfaces is thinner than twice the e-folding distance of the surface wave into that homogeneous material (Faryad, 2012; Faryad and Lakhtakia, 2010b, 2010c, 2011f), besides the periodic non-homogeneity of the partnering dielectric materials.

11.8 Future research

The field of surface multiplasmonics is still in its infancy, and there is considerable room available to work both theoretically and experimentally to gain understanding of the phenomenon and its exploitation for practical devices. A few suggestions for theoretical work follow.

11.8.1 Excitation of multiple SPP waves with finite sources

The study of excitation of multiple surface waves with a finite source, such as a line source, in either the TKR or the grating-coupled configuration will not only increase the scope of applications of SPP waves, but can also provide a route towards exciting multiple SPP waves without the inconvenience of changing the angle of incidence. This can lead to the possibility of exciting multiple surface waves in nano-devices with embedded light sources. This problem can be analyzed easily by expressing the electromagnetic field of the finite source as a spectrum of planewaves (Chew, 1990).

11.8.2 Compound surface-relief gratings

As was seen in Section 11.5, the excitation of all possible SPP waves requires that the period of the surface-relief grating be changed. In a practical situation, this amounts to the fabrication of many different gratings. This problem can be overcome by having a new surface-relief grating such that each period of it contains, say, two or three periods of two (or as many as one likes) different surface-relief gratings. This new structure may allow the simultaneous excitation of all possible SPP waves. Theoretical analysis then requires a new grating shape-function $g(x)$ in the formulations provided by Faryad and Lakhtakia (2011a, 2011b, 2011c), but the number of terms in the Fourier expansion of the grating shape-function $g(x)$ is much higher. Research in this direction has recently commenced (Faryad and Lakhtakia, 2012).

11.8.3 Effects of multiple SPP waves on the efficiency of thin-film solar cells

Faryad and Lakhtakia (2011d) have shown that light absorption can be enhanced if the partnering dielectric material in the grating-coupled configuration is taken to be a periodically non-homogeneous semiconductor. However, the boundary-value problem in their paper cannot be used for actual solar cells because it does not have any *p-n* junctions and no antireflective coatings or transparent-conducting-oxide layers for electrical connection. Moreover, the problem solved in that paper was limited only to the enhancement of light absorption and not the electrical power output. We believe that a complete problem that includes the geometry of an actual solar cell with the aim of optimizing the output power is worth investigating. For this purpose, the formulation provided by Faryad and Lakhtakia (2011b) has recently been modified by Faryad *et al.* (2012) in order to incorporate the layered structure of the solar cell.

11.9 Sources of further information and advice

As has been stated in the foregoing section, surface multiplasmonics is an emerging area of research; therefore, few resources are available for (potential) entrants to this area. To date, three theses (Erten, 2011; Faryad, 2012; Motyka, 2009) and a review article (Polo and Lakhtakia, 2011) are available for consultation. A recent book also provides necessary information (Polo *et al.*, 2013). In addition, anyone interested in finding the latest articles on this field should keep an eye on the journals published by Society of Photo-Optical Instrumentation Engineers (SPIE), Optical Society of America (OSA), American Physical Society (APS), and Institute of Physics (United Kingdom).

11.10 References

- Abdulhalim, I. (2009) ‘Surface plasmon TE and TM waves at the anisotropic film-metal interface’, *J. Opt. A: Pure Appl. Opt.*, **11**, 015002.
- Abdulhalim, I., Zourob, M. and Lakhtakia, A. (2007) ‘Overview of optical biosensing techniques’, in: *Handbook of Biosensors and Biochips* Eds. Marks, R., Cullen, D., Karube, I., Lowe, C. R. and Weetall, H. H., Chichester, United Kingdom, Wiley, 413–446.
- Abdulhalim, I., Zourob, M. and Lakhtakia, A. (2008) ‘Surface plasmon resonance for biosensing: A mini-review’, *Electromagnetics*, **28**, 214–242.
- Agarwal, K., Polo Jr., J. A. and Lakhtakia, A. (2009) ‘Theory of Dyakonov–Tamm waves at the planar interface of a sculptured nematic thin film and an isotropic dielectric material’, *J. Opt. A: Pure Appl. Opt.*, **11**, 074003.
- Atalla, M. R. M., Faryad, M. and Lakhtakia A. (2012) ‘On surface plasmon-polariton waves guided by the interface of a metal and a rugate filter with a sinusoidal

- refractive-index profile. Part II: High-phase-speed solutions'; *J. Opt. Soc. Am. B*, **29**, 3078–3086.
- Barnes, W. L., Dereux, A. and Ebbesen, T. W. (2003) 'Surface plasmon subwavelength optics', *Nature*, **424**, 824–830.
- Baumeister, P. W. (2004) *Optical Coating Technology*, Bellingham, WA, USA, SPIE Press, Sec. 5.3.3.2.
- Berini, P. (2009) 'Long-range surface plasmon polaritons', *Adv. Opt. Photon.*, **1**, 484–588.
- Borstel, G. and Falge, H. J. (1982) 'Surface phonon-polaritons', in: *Electromagnetic Surface Modes*, Ed. Boardman, A. D., New York, NY, USA, Wiley, Chap. 6.
- Bovard, B. G. (1993) 'Rugate filter theory: an overview', *Appl. Opt.*, **32**, 5427–5442.
- Chateau N. and Hugonin, J.-P. (1994) 'Algorithm for the rigorous coupled-wave analysis of grating diffraction', *J. Opt. Soc. Am. A*, **11**, 1321–1331.
- Chew, W. C. (1990) *Waves and Fields in Inhomogeneous Media*, Piscataway, NJ, USA, IEEE Press, Sec. 2.2.
- Devender, Pulsifer, D. P. and Lakhtakia, A. (2009) 'Multiple surface plasmon polariton waves', *Electron. Lett.*, **45**, 1137–1138.
- Dolev, I., Volodarsky, M., Porat, G. and Arie, A. (2011) 'Multiple coupling of surface plasmons in quasiperiodic gratings', *Opt. Lett.*, **36**, 1584–1586.
- Dragoman, M. and Dragoman, D. (2008) 'Plasmonics: Applications to nanoscale terahertz and optical devices', *Prog. Quantum Electron.*, **32**, 1–41.
- Elston, S. J. and Sambles, J. R. (1990) 'Surface plasmon-polaritons on an anisotropic substrate', *J. Mod. Opt.*, **37**, 1895–1902.
- Erten, S. (2011), *Excitation of Multiple Surface-Plasmon-Polariton Waves at Metal/Chiral-Sculptured-Thin-Film Interfaces*, Pennsylvania State University, M.S. thesis (Engineering Science).
- Fahr, S., Ulbrich, C., Kirchartz, T., Rau, U., Rockstuhl, C. and Lederer, F. (2008) 'Rugate filter for light-trapping in solar cells', *Opt. Express*, **16**, 9332–9343.
- Faryad, M. and Lakhtakia, A. (2010a) 'On surface plasmon-polariton waves guided by the interface of a metal and a rugate filter with sinusoidal refractive-index profile', *J. Opt. Soc. Am. B*, **27**, 2218–2223.
- Faryad, M. and Lakhtakia, A. (2010b) 'Multiple surface-plasmon-polariton waves localized to a metallic defect layer in a sculptured nematic thin film', *Phys. Status Solidi RRL*, **4**, 265–267.
- Faryad, M. and Lakhtakia, A. (2010c) 'Surface plasmon-polariton wave propagation guided by a metal slab in a sculptured nematic thin film', *J. Opt. (United Kingdom)*, **12**, 085102.
- Faryad, M. and Lakhtakia, A. (2011a) 'On multiple surface-plasmon-polariton waves guided by the interface of a metal film and a rugate filter in the Kretschmann configuration', *Opt. Commun.*, **284**, 5678–5687.
- Faryad, M. and Lakhtakia, A. (2011b) 'Grating-coupled excitation of multiple surface-plasmon-polariton waves', *Phys. Rev. A*, **84**, 033852.
- Faryad, M. and Lakhtakia, A. (2011c) 'Multiple trains of same-color surface plasmon-polaritons guided by the planar interface of a metal and a sculptured nematic thin film. Part V: Grating-coupled excitation', *J. Nanophoton.*, **5**, 053527.
- Faryad, M. and Lakhtakia, A. (2011d) 'Enhanced absorption of light due to multiple surface-plasmon-polariton waves', *Proc. SPIE*, **8110**, 81100F.

- Faryad, M. and Lakhtakia, A. (2011e) 'Dyakonov–Tamm waves guided by a phase-twist combination defect in a sculptured nematic thin film', *Opt. Commun.*, **284**, 160–168.
- Faryad, M. and Lakhtakia, A. (2011f) 'Propagation of surface waves and waveguide modes guided by a dielectric slab inserted in a sculptured nematic thin film', *Phys. Rev. A*, **83**, 013814.
- Faryad, M. and Lakhtakia, A. (2012) 'Excitation of multiple surface-plasmon-polariton waves using a compound surface-relief grating', *J. Nanophoton.*, **6**, 061701.
- Faryad, M., Polo Jr., J. A. and Lakhtakia, A. (2010) 'Multiple trains of same-color surface plasmon-polaritons guided by the planar interface of a metal and a sculptured nematic thin film. Part IV: Canonical problem', *J. Nanophoton.*, **4**, 043505.
- Faryad, M., Maab, H. and Lakhtakia, A. (2011) 'Rugate-filter-guided propagation of multiple Fano waves', *J. Opt. (United Kingdom)*, **13**, 075101.
- Faryad, M., Hall, A. S., Barber, G. D., Mallouk, T. E. and Lakhtakia, A. (2012) 'Excitation of multiple surface-plasmon-polariton waves guided by the periodically corrugated interface of a metal and a periodic multilayered isotropic dielectric material', *J. Opt. Soc. Am. B*, **29**, 704–713.
- Faryad, M. (2012) *Propagation and Excitation of Multiple Surface Waves*, Pennsylvania State University, Ph. D. dissertation (Engineering Science and Mechanics).
- Ferry, V. E., Sweatlock, A., Pacifici, D. and Atwater, H. A. (2008) 'Plasmonic nanostructure design for efficient light coupling into solar cells', *Nano Lett.*, **8**, 4391–4397.
- Fiumara, V., Chiadini, F., Scaglione, A. and Lakhtakia, A. (2006) 'Theory of thin-film, narrowband, linear-polarization rejection filters with superlattice structure', *Opt. Commun.*, **268**, 182–188.
- Gao, J., Lakhtakia, A., Polo Jr., J. A. and Lei, M. (2009a) 'Dyakonov–Tamm waves guided by a twist defect in a structurally chiral material', *J. Opt. Soc. Am. A*, **26**, 1615–1621.
- Gao, J., Lakhtakia, A., Polo Jr., J. A. and Lei, M. (2009b) 'Dyakonov–Tamm waves guided by a twist defect in a structurally chiral material: erratum', *J. Opt. Soc. Am. A*, **26**, 2399.
- Gao, J., Lakhtakia, A. and Lei, M. (2009c) 'On Dyakonov–Tamm waves localized to a central twist defect in a structurally chiral material', *J. Opt. Soc. Am. B*, **26**, B74–B82.
- Gao, J., Lakhtakia, A. and Lei, M. (2010) 'Dyakonov–Tamm waves guided by the interface between two structurally chiral materials that differ only in handedness', *Phys. Rev. A*, **81**, 013801.
- Gaspar-Armenta, J. A. and Villa, F. (2003) 'Photonic surface-wave excitation: photonic crystal-metal interface', *J. Opt. Soc. Am. B*, **20**, 2349–2354.
- Gates, B. D., Xu, Q., Stewart, M., Ryan, D., Wilson, C. G. and Whitesides, G. M. (2005) 'New approaches to nanofabrication: Molding, printing and other techniques', *Chem. Rev.*, **105**, 1171–1196.
- Gilani, T. H., Dushkina, N., Freeman, W. L., Numan, M. Z., Talwar, D. N. and Pulsifer, D. P. (2010), 'Surface plasmon resonance due to the interface of a metal and a chiral sculptured thin film', *Opt. Eng.*, **49**, 120503.
- Green M. A. and Pillai, S. (2012) 'Harnessing plasmonics for solar cells', *Nature Photon.*, **6**, 130–132.

- Hall, A. S., Faryad, M., Barber, G. D., Liu, L., Erten, S., Mayer, T. S., Lakhtakia, A. and Mallouk, T. E. (2013) 'Broadband light absorption with multiple surface plasmon polariton waves excited at the interface of a metallic grating and photonic crystal', *ACS Nano*, **7**, 4995–5007.
- Hodgkinson, I. J., Wu, Q. h. and Hazel, J. (1998) 'Empirical equations for the principal refractive indices and column angle of obliquely deposited films of tantalum oxide, titanium oxide, and zirconium oxide', *Appl. Opt.*, **37**, 2653–2659.
- Homola, J. (Ed.) (2006) *Surface Plasmon Resonance Based Sensors*, Heidelberg, Germany, Springer.
- Jaluria, Y. (1996) *Computer Methods for Engineering*, Washington, DC, USA, Taylor & Francis.
- Jen, Y.-J. and Yu, C.-W. (2011) 'Optical configuration for unpolarized ultra-long-range surface-plasmon-polariton waves', *Appl. Opt.*, **50**, C154–C158.
- Jen, Y.-J., Lakhtakia, A., Yu, C.-W. and Chan, T.-Y. (2009) 'Multilayered structures for *p*- and *s*-polarized long-range surface-plasmon-polariton propagation', *J. Opt. Soc. Am. A*, **26**, 2600–2606.
- Kanda, V., Kitov, P., Budle, D. R. and McDermott, M. T. (2005) 'Surface plasmon resonance imaging measurements of the inhibition of Shiga-like toxin by synthetic multivalent inhibitors', *Anal. Chem.*, **77**, 7497–7504.
- Kapany, N. S. and Burke, J. J. (1972) *Optical Waveguides*, New York, NY, USA, Academic Press.
- Kik, P. G., Maier, S. A. and Atwater, H. A. (2002) 'Plasmon printing – a new approach to near-field lithography', *MRS Symp. Proc.*, **705**, Y3.6.
- Kretschmann, E. and Raether, H. (1968) 'Radiative decay of non radiative surface plasmons excited by light', *Z. Naturforsch. A*, **23**, 2135–2136.
- Lakhtakia, A. (2007) 'Surface-plasmon wave at the planar interface of a metal film and a structurally chiral medium', *Opt. Commun.*, **279**, 291–297.
- Lakhtakia A. (2010) 'Reflection of an obliquely incident plane wave by a half space filled by a helicoidal bianisotropic medium', *Phys. Lett. A*, **374**, 3887–3894.
- Lakhtakia A. (2011) 'Surface multiplasmonics', *Proc. SPIE*, **8104**, 810403.
- Lakhtakia, A., Messier, R., Brett, M. J. and Robbie, K. (1996) 'Sculptured thin films (STFs) for optical, chemical and biological applications', *Innovations Mater. Res.*, **1**, 165–176.
- Lakhtakia, A., Jen, Y.-J. and Lin, C.-F. (2009) 'Multiple trains of same-color surface plasmon-polaritons guided by the planar interface of a metal and a sculptured nematic thin film. Part III: Experimental evidence', *J. Nanophoton.*, **3**, 033506.
- Lakhtakia, A. and Geddes III, J. B. (2010) 'Thin-film metamaterials called sculptured thin films', in: *Trends in Nanophysics* Eds. Aldea, A. and Bârsan, V., Springer, Heidelberg, Germany, 59–71.
- Lakhtakia, A. and Messier, R. (1994) 'The key to a thin film HBM: the Motohiro-Taga interface', in: *Proceedings of Chiral 94 (Périgueux, France, May 18–20)* Eds. Mariotte, F. and Parneix, J.-P., French Atomic Energy Commission, Le Barp, France, 125–130.
- Lakhtakia, A. and Messier, R. (2005) *Sculptured Thin Films: Nano-engineered Morphology and Optics*, Bellingham, WA, USA, SPIE Press.
- Lakhtakia, A. and Polo Jr., J. A. (2007) 'Dyakonov–Tamm wave at the planar interface of a chiral sculptured thin film and an isotropic dielectric material', *J. Eur. Opt. Soc.–Rapid Pubs.*, **2**, 07021.

- Lakhtakia, A. and Weiglhofer, W. S. (1993) 'Axial propagation in general helicoidal bianisotropic media', *Microw. Opt. Technol. Lett.*, **6**, 804–806.
- Lambeck, P. V. (2006) 'Integrated optical sensors for the chemical domain', *Meas. Sci. Technol.*, **17**, R93–R116.
- Li, L. (1993) 'Multilayer modal method for diffraction gratings of arbitrary profile, depth, and permittivity', *J. Opt. Soc. Am. A*, **12**, 2581–2591.
- Lorenzo, E., Oton, C. J., Capuj, N. E., Ghulinyan, M., Navarro-Urrios, D., Gaburro, Z. and Pavese, L. (2005) 'Fabrication and optimization of rugate filters based on porous silicon', *Phys. Status Solidi C*, **2**, 3227–3231.
- Lee, C. C., Tang, C. J. and Wu, J. Y. (2006) 'Rugate filter made with composite thin films by ion-beam sputtering', *Appl. Opt.*, **45**, 1333–1337.
- Maab, H., Faryad, M. and Lakhtakia, A. (2011) 'Surface electromagnetic waves supported by the interface of two semi-infinite rugate filters with sinusoidal refractive index profiles', *J. Opt. Soc. Am. A*, **28**, 1204–1212.
- Mackay, T. G. and Lakhtakia, A. (2008) 'Electromagnetic fields in linear bianisotropic mediums', *Prog. Opt.*, **51**, 121–209.
- Mackay, T. G. and Lakhtakia, A. (2010a) 'Modeling columnar thin films as platforms for surface-plasmonic-polaritonic optical sensing', *Photon. Nanostruct. Fund. Appl.*, **8**, 140–149.
- Mackay, T. G. and Lakhtakia, A. (2010b) *Electromagnetic Anisotropy and Bianisotropy: A Field Guide*, Singapore, World Scientific.
- Mackay, T. G. and Lakhtakia, A. (2012) 'Modeling chiral sculptured thin films as platforms for surface-plasmonic-polaritonic optical sensing', *IEEE Sens. J.*, **12**, 273–280.
- Maier, S. A. (2007) *Plasmonics: Fundamentals and Applications*, New York, NY, USA, Springer.
- Maier, S. A., Brongersma, M. L., Kik, P. G., Meltzer, S., Requicha, A. A. G. and Atwater, H. A. (2001) 'Plasmonics — A route to nanoscale optical devices', *Adv. Mater.*, **13**, 1501–1505.
- Marcuse, D. (1991) *Theory of Dielectric Optical Waveguides*, San Diego, CA, USA, Academic Press.
- Martin, P. M. (Ed.) (2010) *Handbook of Deposition Technologies for Films and Coatings: Science, Applications and Technology*, 3rd ed., Oxford, United Kingdom, Elsevier.
- Martín-Palma, R. J. and Lakhtakia, A. (2010) *Nanotechnology: A Crash Course*, Bellingham, WA, USA, SPIE Press.
- Martorell, J., Sprung, D. W. L. and Morozov, G. V. (2006) 'Surface TE waves on 1D photonic crystals', *J. Opt. A: Pure Appl. Opt.*, **8**, 630–638.
- Messier, R., Gehrke, T., Frankel, C., Venugopal, V. C., Otaño, W. and Lakhtakia, A. (1997) 'Engineered sculptured nematic thin films', *J. Vac. Sci. Technol. A*, **15**, 2148–2152.
- Messier, R., Venugopal, V. C. and Sunal, P. D. (2000) 'Origin and evolution of sculptured thin films', *J. Vac. Sci. Technol. A*, **18**, 1538–1545.
- Moharam M. G. and Gaylord, T. K. (1982) 'Diffraction analysis of dielectric surface-relief gratings', *J. Opt. Soc. Am.*, **72**, 1385–1392.
- Moharam, M. G., Grann, E. B. and Pommel, D. A. (1995) 'Formulation for stable and efficient implementation of the rigorous coupled-wave analysis of binary gratings', *J. Opt. Soc. Am. A*, **12**, 1068–1076.
- Moreland, J., Adams, A. and Hansma, P. K. (1982) 'Efficiency of light emission from surface plasmons', *Phys. Rev. B*, **25**, 2297–2300.

- Motyka, M. A. (2009), *Multiple Trains of Same-Color Surface Plasmon-Polaritons Guided by the Planar Interface of a Metal Film and a Sculptured Nematic Thin Film*, Pennsylvania State University, M.S. thesis (Engineering Science).
- Motyka, M. A. and Lakhtakia, A. (2008) 'Multiple trains of same-color surface plasmon-polaritons guided by the planar interface of a metal and a sculptured nematic thin film', *J. Nanophoton.*, **2**, 021910.
- Motyka, M. A. and Lakhtakia, A. (2009) 'Multiple trains of same-color surface plasmon-polaritons guided by the planar interface of a metal and a sculptured nematic thin film. Part II: Arbitrary incidence', *J. Nanophoton.*, **3**, 033502.
- Nolte, A. J., Rubner, M. F. and Cohen, R. E. (2004) 'Creative effective refractive index gradients within polyelectrolyte multilayer films: molecularly assembled rugate filters', *Langmuir*, **20**, 3304–3310.
- Otto, A. (1968) 'Excitation of nonradiative surface plasma waves in silver by the method of frustrated total reflection', *Z. Phys.*, **216**, 398–410.
- Otto, A. and Sohler, W. (1971) 'Modification of the total reflection modes in a dielectric film by one metal boundary', *Opt. Commun.*, **3**, 254–258.
- Overend, R., Gibson, D. R., Marshall, R. and Lewis, K. (1992) 'Rugate filter fabrication using neutral cluster beam deposition', *Vacuum*, **43**, 51–54.
- Perilloux, B. E. (2002) *Thin-Film Design: Modulated Thickness and Other Stopband Design Methods*, Bellingham, WA, USA, SPIE Press.
- Polo Jr., J. A. and Lakhtakia, A. (2009a) 'On the surface plasmon polariton wave at the planar interface of a metal and a chiral sculptured thin film', *Proc. R. Soc. Lond. A*, **465**, 87–107.
- Polo Jr., J. A. and Lakhtakia, A. (2009b) 'Energy flux in a surface-plasmon-polariton wave bound to the planar interface of a metal and a structurally chiral material', *J. Opt. Soc. Am. A*, **26**, 1696–1703.
- Polo Jr., J. A. and Lakhtakia, A. (2011) 'Surface electromagnetic waves: A review', *Laser Photon. Rev.*, **5**, 234–246.
- Polo Jr., J. A., Mackay, T. G. and Lakhtakia, A. (2011) 'Mapping multiple surface-plasmon-polariton-wave modes at the interface of a metal and a chiral sculptured thin film', *J. Opt. Soc. Am. B*, **28**, 2656–2666.
- Polo Jr., J. A., Mackay, T. G. and Lakhtakia, A. (2013) *Electromagnetic Surface Waves: A Modern Perspective*, Waltham, MA, USA, Elsevier.
- Pursel, S., Horn, M. W., Demirel, M. C. and Lakhtakia, A. (2005), 'Growth of sculptured polymer submicronwire assemblies by vapor deposition', *Polymer*, **46**, 9544–9548.
- Robbie, K., Brett, M. J. and Lakhtakia, A. (1995) 'First thin film realization of a helicoidal bianisotropic medium', *J. Vac. Sci. Technol. A*, **13**, 2991–2993.
- Robertson, W. M. and May, M. S. (1999) 'Surface electromagnetic wave excitation on one-dimensional photonic band-gap arrays', *Appl. Phys. Lett.*, **74**, 1800–1802.
- Rosenblatt, D., Sharon, A. and Friesem, A. A. (1997) 'Resonant grating waveguide structures', *IEEE J. Quantum Electron.*, **33**, 2038–2059.
- Salamon, Z., Macleod, H. A. and Tollin, G. (1997) 'Coupled plasmon-waveguide resonators: A new spectroscopic tool for probing proteolipid film structure and properties', *Biophys. J.*, **73**, 2791–2797.
- Salamon, Z. and Tollin, G. (2001) 'Optical anisotropy in lipid bilayer membrane: Coupled plasmon-waveguide resonance measurements of molecular orientation, polarizability, and shape', *Biophys. J.*, **80**, 1557–1567.
- Sarid, D. (1981) 'Long-range surface-plasma waves on very thin metal films', *Phys. Rev. Lett.*, **47**, 1927–1930.

- Simon, H. J., Mitchell, D. E. and Watson, J. G. (1975) 'Surface plasmons in silver films – a novel undergraduate experiment', *Am. J. Phys.*, **43**, 630–636.
- Sit, J. C., Vick, D., Robbie, K. and Brett, M. J. (1999) 'Thin film microstructure control using glancing angle deposition by sputtering', *J. Mater. Res.*, **14**, 1197–1199.
- Swiontek, S. E. (2012), *Suppression of Circular Bragg Phenomenon in Chiral Sculptured Thin Films Produced with Simultaneous Rocking and Rotation of Substrate During Serial Bideposition*, Pennsylvania State University, M.S. thesis (Engineering Science).
- Turbadar, T. (1959) 'Complete absorption of light by thin metal films', *Proc. Phys. Soc.*, **73**, 40–44.
- Usui-Aoki, K., Shimada, K., Nagano, M., Kawai, M. and Koga, H. (2005) 'A novel approach to protein expression profiling using antibody microarrays combined with surface plasmon resonance technology', *Proteomics*, **5**, 2396–2401.
- Vick, D., Tsui, Y. Y., Brett, M. J. and Fedosejevs, R. (1999), 'Production of porous carbon thin films by pulsed laser deposition', *Thin Solid Films*, **350**, 49–52.
- Wallis, R. F. (1982) 'Surface magnetoplasmons on semiconductors', in: *Electromagnetic Surface Modes* Ed. Boardman, A. D., New York, NY, USA, Wiley, Chap. 15.
- Wang, H. (1995) 'Excitation of surface plasmon oscillations at an interface between anisotropic dielectric and metallic media', *Opt. Mater.*, **4**, 651–656.
- Wang, F., Horn, M. W. and Lakhtakia, A. (2004) 'Rigorous electromagnetic modeling of near-field phase-shifting contact lithography', *Microelectron. Eng.*, **71**, 34–53.
- Wei, L., Lakhtakia, A., Roopnariane, A. P. and Ritty, T. M. (2010) 'Human fibroblast attachment on fibrous polyimide-C thin-film substrates', *Mater. Sci. Eng. C*, **30**, 1252–1259.
- Weiglhofer, W. S. and Lakhtakia A. (Eds.) (2003) *Introduction to Complex Mediums for Optics and Electromagnetics*, Bellingham, WA, USA, SPIE Press.
- Worthing, P. T. and Barnes, W. L. (2001) 'Efficient coupling of surface plasmon polaritons to radiation using a bi-grating', *Appl. Phys. Lett.*, **79**, 3035–3037.
- Xiao, S., Stassen, E. and Mortensen, N. A. (2012) 'Ultrathin silicon solar cells with enhanced photocurrents assisted by plasmonic nanostructures', *J. Nanophoton.*, **6**, 061503.
- Yakubovich, V. A. and Starzhinskii, V. M. (1975) *Linear Differential Equations with Periodic Coefficients*, New York, NY, USA, Wiley.
- Yan, W., Shen, L., Ran, L. and Kong, J. A. (2007) 'Surface modes at the interfaces between isotropic media and indefinite media', *J. Opt. Soc. Am. A*, **24**, 530–535.
- Yeh, P., Yariv, A. and Hong, C.-S. (1977) 'Electromagnetic propagation in periodic stratified media. I. General theory', *J. Opt. Soc. Am.*, **67**, 423–438.
- Young, N. O. and Kowal, J. (1959) 'Optically active fluorite films', *Nature*, **183**, 104–105.
- Zenneck, J. (1907) 'Über die Fortpflanzung ebener elektromagnetischer Wellen längs einer ebenen Leiterfläche und ihre Beziehung zur drahtlosen Telegraphie', *Ann. Phys. Lpz.*, **23**, 846–866.
- Zhang, J.-C., Fang, M., Shao, Y.-C., Jin, Y.-X. and He, H.-B. (2011) 'Rugate filters prepared by rapidly alternating deposition', *Chin. Phys. B*, **20**, 094212.

Optical thin films containing quantum dots

F. FLORY, Y.-J. CHEN and H.-J. LIN, Ecole
Centrale Marseille, France

DOI: 10.1533/9780857097316.3.493

Abstract: For a few years semiconductor quantum dots have attracted a lot of interest. To be part of photonic structures quantum dots are generally embedded in thin films. After briefly reviewing the application fields, a simple model for 2D structured is presented. Examples of recent results concerning optical properties of poly(methyl methacrylate) (PMMA) thin films containing CdSe/ZnS and TiO₂ quantum dots are given describing their reflection, transmission, absorption and photoluminescence. The problem of the refractive index of thin films containing quantum dots and of quantum dots alone is also addressed.

Key words: quantum dots, thin films, PMMA, CdSe, TiO₂, optical properties, refractive index, luminescence, photovoltaic.

12.1 Introduction

Photodetectors including solar cells, environment sensors, and wide spectra-wide aperture antireflection coatings are important applications in photonics.

Nanostructured materials are extensively studied to reduce the loose of energy coming from reflection, inefficient absorption or inefficient wavelengths : photonic crystals to increase the life time of the light in the active material, structured antireflection coatings to increase the transmission of light through the surface, nano velour structure like black silicon to increase useful light absorption, reticulated materials for organic solar cells, semiconductor nanoparticles, metallic nano-particles to benefit from plasmonic effect, Grätzel cells, carbon nanotubes, silicon nanowires are all under study.

It is mandatory to understand carrier generation, carrier behaviour and more generally the interaction of light with such nanostructures to develop new applications. Most of the models used to study the optical properties of nanophotonics components are based on the electromagnetic theory. They all need the value of the complex refractive index or permittivity as an input. However, the bulk value of the refractive index is

not fitted when the materials are structured in very small dimensions. It is then necessary to take into account the packing density of the material, the crystalline state, or to consider the homogenization theory and to use an effective index.

More than that, when the critical dimension becomes in the order of a few nanometers, the model needs to be revisited further because quantum phenomena must be considered. A quantum dot (QD) is made of a semiconductor nanocrystal of a size smaller than the de Broglie wavelength, in the order of a few nanometers in the three spatial dimensions, surrounded by a material of a larger band gap. QDs were discovered at the beginning of the 1980s by Ekimov *et al.* (1985) in a glass matrix and by Brus *et al.* (1983) in colloidal solutions. The term ‘quantum dot’ was coined by Mark Reed (1988). In these nanoparticles the carriers, electrons and holes, are confined and they can have only discrete energy levels which depend on the QD size. Because of their very attractive properties they are studied by many research laboratories since a dozen of years. The atom like behaviour of the QDs gives absorption and luminescent spectra which depend both on the properties of the semiconductor used and on the size of the QDs. In photonic structures QDs can be embedded in another material or deposited as a QDs layer or coupled to some other structures. The complex refractive index of these materials, generally in thin film form, must be known to model the propagation of optical electromagnetic fields. We will try to bring here some elements of a response.

We will first briefly review some actual applications of QDs. Then we will present a simple model to describe the electron and hole distributions in not coupled and coupled quantum wells (QWs) and in single QDs. This model gives results which will be discussed in particular for coupled QWs. The limits of these models are also addressed. In the third part we will present the realization technique of PMMA layers containing different concentrations of core/shell CdSe/ZnS and TiO₂ QDs. The reflection, transmission and absorption of these layers are presented and discussed. Ellipsometry and m-lines are used to measure the effective index of the layers. A conclusion and some perspectives are also given.

12.2 Applications of quantum dots

The discrete energy levels of carriers, the bandgap and the luminescence wavelength of QDs can be chosen by controlling their size. As an example CdSe QDs can emit light at different wavelengths covering a large part of the visible spectrum. The emitted wavelength changes from 470 to 630 nm, when the QDs size is tuned from 1.5 to 6 nm. The Quantum yield (QY) can be very high. As an example luminescence QY of CdSe/ZnSe core/shell QDs has been reported in the range of 60–85% (Reiss *et al.*, 2002).

QDs made of semiconductor materials concerning different wavelength ranges are now commercially available. This strongly helps the development of applications (Bera *et al.*, 2010). Researchers and companies study the interest of QDs for solar cells (Nozik, 2002), for light emitting diodes (LEDs) (Pagan *et al.*, 2006), for displays (Kim *et al.*, 2011) and for laser diodes (Jang *et al.*, 2004). QDs can also be used as single photon or entangled photons sources of a great interest for secure optical telecommunications (Fattal *et al.*, 2004).

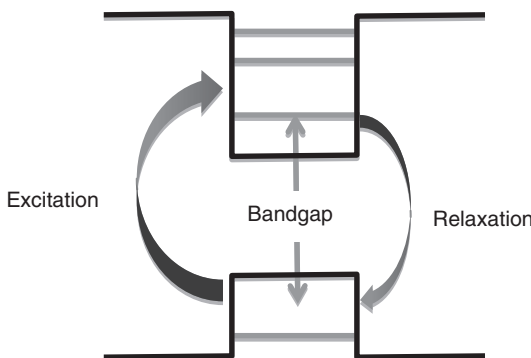
Quite a lot of work has also been performed to use quantum dots as luminescent tags for biology and medical imaging (Larson *et al.*, 2003). QDs help cancer researchers to observe the fundamental molecular events occurring in the tumor cells. They used fluorescent microscopy with QDs of different sizes and thus different colors, linked to multiple different biomolecules. However the heavy metals used like Cd are highly toxic and extensive research is required to determine the long-term effects of administering QDs. They can be encapsulated in non-toxic shell like silica or other materials considered.

Quantum structures can also be used to increase the photovoltaic solar cell efficiency (Kamat, 2008) and to go beyond the Shockley-Queisser limit of 32% for Si based solar cells (Shockley *et al.*, 1961) (see Chapter 16).

At first, thanks to their luminescent properties, QDs can be used to change the UV part of the solar spectrum into longer wavelengths (Fig. 12.1). The material is luminescent if the radiative recombination rate of electrons generated by energetic photons is faster than non-radiative recombination. This has two advantages which are to convert inefficient UV wavelength into more efficient wavelengths and to protect the solar cell from UV to increase its lifetime. However this down-conversion process is only partially efficient as the absorption spectrum can overlap the spectrum efficiently absorbed by the active material. The stokes shift, which is the difference between the first maximum in the absorption band corresponding to the fundamental exciton and the maximum of the luminescent band, depends on the material and is increasing when decreasing the QDs size (Chen *et al.*, 2011). As an example, for 3 nm CdSe/ZnS core/shell QDs, the stokes shift is only of ~10 nm.

Another example is with ZnO quantum dots which can exhibit 2 luminescent bands. One is centered in the green, the other in the near UV. The luminescence in the green can enhance the performance of Solar cells but is not completely explained. It may be due to oxygen vacancies (Studenikin *et al.*, 1998). The luminescence in the UV is coming from quantum confinement with an energy level close to the edge of the bandgap. This UV wavelength is not sufficiently large to be useful for solar cells. Other nanocrystals made with semiconductor materials such as CdS, PbS, TiO₂, etc., are now under study for up and down conversion.

QDs can also be used to create charge carriers. Depending on their size CdSe nanoparticles produce electrons and holes by absorbing photons



12.1 Discrete energy levels, excitation and relaxation processes.

with different energies across the visible spectrum. These nanoparticles can also replace dye molecules in TiO_2 sensitized dye solar cells (Robel *et al.*, 2006), the charges being transferred to the TiO_2 by resonant transfer. It is interesting to notice that, thanks to the relative band offset, CdSe quantum dots have an electron energy level resonant with the conduction band of TiO_2 . ‘Rainbow’ solar cells using CdSe quantum structures of different-sized quantum dots assembled in an orderly fashion are also under study (Kongkanand *et al.*, 2008).

Hybrid organic/inorganic cells can also be made with poly(3-hexylthiophene-2,5-diyl) (P3HT) and CdSe nanorods or P3HT and PbS nanoparticles. With size-quantized PbS nanoparticles, close to 3% incident photon to current efficiencies (IPCE) under 550-nm monochromatic irradiation is obtained (Günes *et al.*, 2007). The cell was made of a 120 nm thick Indium Tin Oxide (ITO) layer, a spin coated PbS film and 1 wt. % of P3HT in chlorobenzene drop cast onto the PbS film. Then 160 nm of gold was thermally evaporated onto the stack and the film was annealed at 200°C for 1 h.

A photovoltaic (PV) cell based on 7×60 nm CdSe nanorods produced 6.9% IPCE under 0.1 mWcm^{-2} illumination at 515 nm (Huynh *et al.*, 2002; Jiu *et al.*, 2010).

To increase the photovoltage, hot carriers created by high energy photons must be extracted from the photoconverter before they cool down by collisions with the atoms or phonons. Carriers either have to go through the cell very quickly, i.e. during the time it takes a photogenerated carrier to cross the material, or cooling rates have to be slowed in some way. The discretization of energy states in QDs increases the lifetime in the excited states and could leave enough time to collect the electrons.

To increase the photocurrent, energetic hot carriers must produce two or more electron–hole pairs through impact ionization (Multiple Exciton Generation: MEG) (Jiu *et al.*, 2005; Nozik, 2008). This can occur in QD nanoparticles. In principle it can give up to 75% efficient conversion.

A large amount of articles and books concerning QDs and their uses are published. We will focus our attention to some results concerning QDs embedded in thin films.

12.3 Modelling the electronic properties of multiple quantum wells

As for spherical quantum dots the possible electron and hole energies (Gaponenko, 1998) are the same than for a quantum well in the direction of confinement, a first modelling can be implemented for quantum wells.

In the approximation of the effective mass, the allowed energies of electrons are the eigenvalues of the stationary Schrödinger equation (Cohen-Tannoudji *et al.*, 1997):

$$\frac{-(\hbar^2/4\pi^2)}{2m} [\nabla^2 + V(r)] \psi(r) = E \psi(r) \quad [12.1]$$

where \hbar is the Planck's constant, V is the local potential and m is the electron effective mass. For the 2D problem of quantum wells, the equation giving the energy levels is very similar to that used for planar waveguides, the electron wave function ψ taking place of the electric field. For quantum wells in the x direction, the wavefunction can be written as:

$$\psi(x) = A e^{ix\chi} + A' e^{-ix\chi} \quad \text{for } E > V \quad [12.2]$$

and

$$\psi(x) = A e^{\rho x} + A e^{-\rho x} \quad \text{for } E < V \quad [12.3]$$

with

$$\chi^2 = \frac{2m}{\hbar^2} (E - V) \quad [12.4]$$

and

$$\rho^2 = \frac{2m}{\hbar^2} (V - E) \quad [12.5]$$

and m is the effective mass of electron, A is an integrating constant and $\hbar = h/2p$. Depending on the material, the effective mass of the electron can take different values.

As for multilayer planar waveguides, this formalism can be extended to multiple quantum wells (Flory *et al.*, 2011). Thanks to the continuity of ψ and its derivative with the direction x perpendicular to the well boundaries, a recurrent relation can be found for the function $Q = (\mathrm{d}\psi/\mathrm{d}x)/\psi$, which is similar to the recurrent relation obtained for the optical admittance in multilayer waveguides:

$$Q_j = k_j \frac{Q_{j-1} - k_j \tan(k_j a_j)}{Q_{j-1} \tan(k_j a_j) + k_j} \quad [12.6]$$

with j referring to a well boundary in the structure. So, the value of Q on one limit of a structure can be obtained as a function of Q on its other limit.

If the electron is confined in a structure, ψ is evanescent in the surrounding media like the electric field is evanescent in the media surrounding a waveguide. The values of Q is then known on both sides of the structure. The equation describing the possible discrete energy levels is then derived from these considerations. The wavefunction and its square giving the electron density probability distribution can be then calculated in the whole structure:

$$\psi_j = C_j^+ \left[e^{ik_j x} + \frac{ik_j - Q_{j-1}}{Q_{j-1} + ik_j} e^{ik_j (2x_{j-1} - x)} \right] \quad [12.7]$$

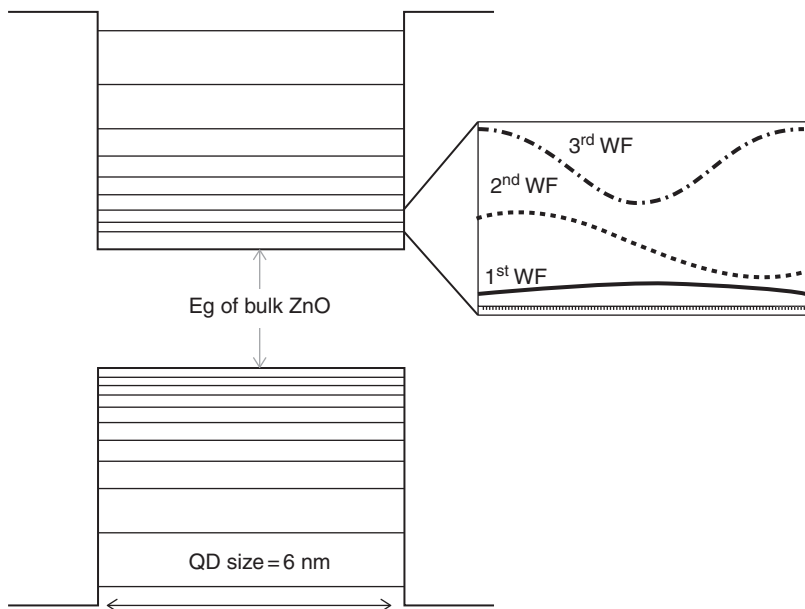
12.4 Numerical results

For a single quantum well, analytic values can be obtained (Eisberg and Resnick, 1985). The results obtained from the presented formalism are in good agreement with them. An example of a comparison between the analytical values and the values obtained with our calculation is given on Fig. 12.2, together with the wavefunctions.

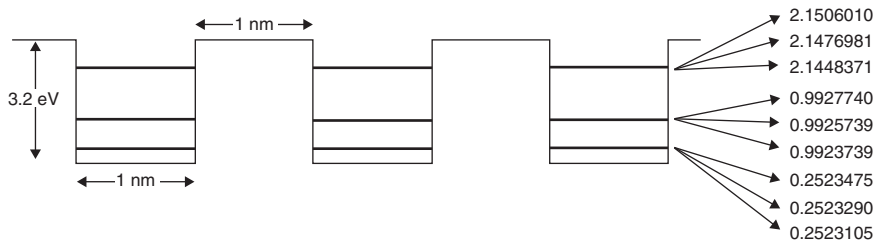
An example of agreement between the bandgap calculated with this model and the measured bandgap is shown for 6 nm ZnO QDS dispersed in a liquid, in Flory *et al.* (2011).

When N identical quantum wells are coupled, each energy level is split in N sub-levels. Figure 12.3 gives an example of the energy levels of electrons for three coupled identical wells of 1 nm width and 1 nm spacing and a depth of 3.2 eV. Similarly in a molecule, the electron energies of an atom are split into sub-levels when the atom is coupled to others because of vibrational and rotational modes.

Figure 12.4 shows how the highest energy level of the electrons in a single well is split when considering 2, 3, 4 and 5 identical coupled wells. Each well



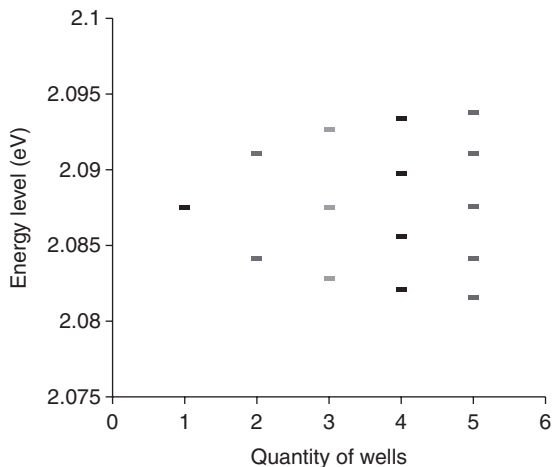
12.2 Distribution of the discrete energy levels of ZnO QDs with a size of 6 nm. The first energy level can be selected by considering the spatial distributions of the electrons/holes wave function (WF) as shown on the right.



12.3 Energy levels of electrons for three coupled identical quantum wells of 1 nm width, 1 nm spacing and of 3.2 eV depth.

has a depth of 2.9 eV, a width of 1 nm and the distance between the wells is also 1 nm. When the number of coupled wells increases, the different sub levels fill a band.

The Krönig-Penney model applies when the structure is periodic and infinite (Carpena *et al.*, 1999). The different energy bands found with this model are in agreement with the solutions obtained with the previous formalism for a periodic structure. So, for a large number of identical coupled quantum wells, each energy level of a single well is split into a large number of sub



12.4 Highest energy level of the electrons in a single well is split when considering 2, 3, 4 and 5 identical coupled wells (Flory *et al.*, 2011).

levels filling an energy band. It is a homogeneous band broadening. When the coupling is strong, the different bands are widened and can join to make a continuous band, and the material behaves like bulk. The coupling distance must not be larger than a few nanometers.

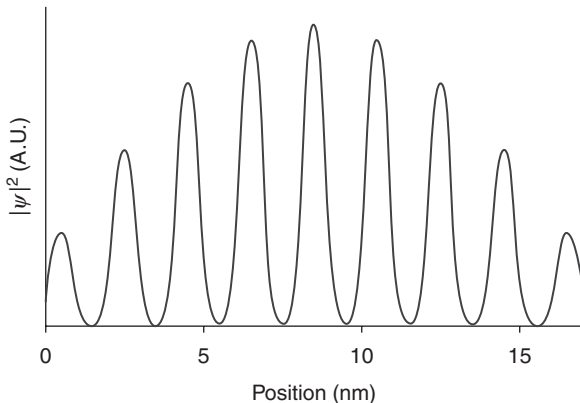
Figure 12.5 gives the electron probability density of the lowest energy in the structure composed of nine identical wells of 2.9 eV depth, of 1 nm width and the distance between the wells is 1 nm. As can be seen the electrons are delocalized in the whole structure.

When the coupled wells are not identical the electron density of probability can be confined into one well or distributed into several wells depending on the considered structure and the considered energy level. The electron density of probability is presented on Fig. 12.6 for a non-periodic structure composed of five coupled wells, the well in the center of the structure being of 2 nm width, twice larger than the others.

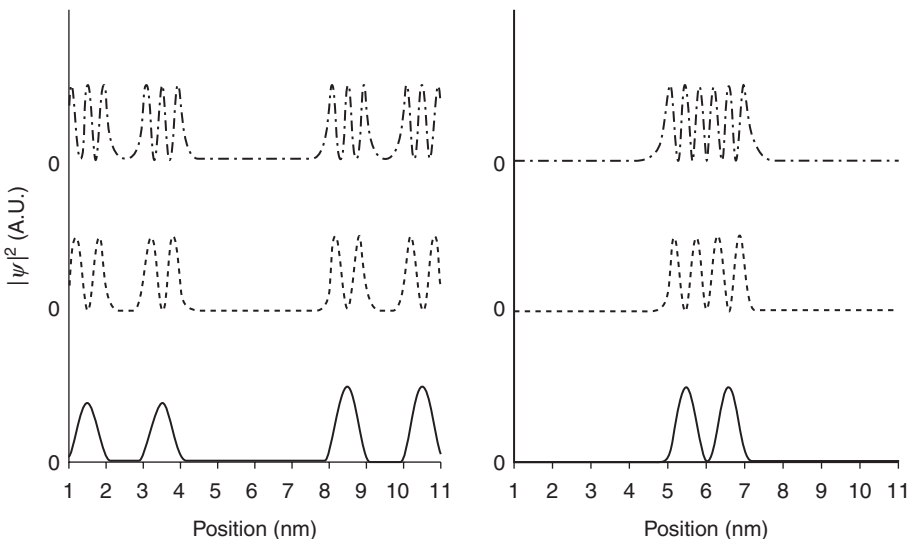
The electrons can be localized in the largest well or delocalized in the other wells depending on the energy level considered. The electrons behave in a similar way than in molecules for which the electrons can be linked to a particular atom or delocalized in the whole molecule.

In practice, in a set of QDs there is some size dispersion. The size dispersion induces a band broadening which is an inhomogeneous band broadening instead of a homogenous band broadening induced by QDs coupling.

There could be other band broadening phenomena like natural broadening link to the excited state lifetime or the temperature which can



12.5 Electron probability density of the lowest energy in the structure composed of nine identical wells of 2.9 eV depth, of 1 nm width, and the distance between the wells is 1 nm (Flory *et al.*, 2011).



12.6 Density of probability of electrons in a non-periodic structure composed of five coupled wells of depth 2.9 eV, of width 1, 1, 2, 1 and 1 nm, respectively. The distance between each well is 1 nm (Flory *et al.*, 2011).

induce coupling to phonons or trap states. So it is very difficult to model these effects.

The resulting absorption spectra exhibit a strong modulation with maxima corresponding to excitonic states to which oscillators can be associated with band broadening.

The oscillator strengths associated with the excitonic states and possible transitions are not yet well modeled and only measurements can give valuable information on the optical properties. A review of theory can be found in Woggon (1997).

The extinction coefficient dispersion with wavelength is then a complex function and the real part of the refractive index dispersion is then also different from the bulk one.

12.5 Realization of thin films containing quantum dots

Si QDs can be obtained in a silica film when the silica film is sub stoichiometric (Conibeer *et al.*, 2012). After annealing Si nanocrystals appear in the silica matrix. But generally thin films containing quantum dots are made by spin coating. In particular it is interesting to use PMMA as a host material because it is easy to spin coat a thin films and it is a highly transparent material in the visible with a wavelength bandgap below 260 nm (Plate III, see colour section between pages 404 and 405).

PMMA is soluble in chloroform. So, by choosing hydrophobic QDs which are also soluble in chloroform, one can use solutions with different concentrations of QDs to add to the PMMA solution before depositing the layer by spin coating. As an important part of the atoms are on the surface of nanocrystals of a few nanometers, a shell is required to have a good charge confinement and large photoluminescence efficiency. For example, roughly 15% of the atoms in a 5 nm CdS QDs are at the surface (Wang *et al.*, 1991).

CdSe/ZnS QDs of ~3 nm have been bought to the company PlasmaChem GmbH. The TiO₂ nanocrystals were prepared through hydrothermal method, described in greater detail by Reyes-Coronado *et al.* (2008). Amorphous titania was prepared by drop wise addition of a solution of 1.14 mL of water in 105 mL of 2-propanol to a solution of 5 mL of titanium (IV) isopropoxide (Aldrich 97%) in 105 mL of 2-propanol. The solution was stirred for 24 h at room temperature, and filtered to yield a white paste of amorphous Titania. Then, the amorphous Titania paste was diluted to 0.3 M in aqueous solutions of acetic acid and subjected to hydrothermal treatment at 200°C during 2 h. The as-obtained samples were characterized by X-Ray diffraction (XRD) and transmission electron microscopy (TEM). The XRD patterns of the as-synthesized samples

presents diffraction peaks that could be indexed as the TiO₂ anatase phase. TEM images shows that the as-obtained samples were composed by nanoparticles of around 5 nm.

12.5.1 Realization process of PMMA layers including different QDs concentrations

The samples were all prepared on silica substrate. The substrates were cleaned at first in an ultrasonic bath of deionized (DI) water. Then they were immersed in DI water three more times and in acetone also three times before being kept in an oven at 200°C for 20 min.

Two types of QDs have been considered: core/shell CdSe/ZnS of ~ 2.7 nm and TiO₂ of ~ 5 nm. Different QDs concentrations have been used.

These quantum dots are hydrophobic and then can be well dispersed in chloroform. 2.5, 5 and 10 mg of QDs corresponding to weight ratio of approximately 4.2%, 8.3% and 16.6%, respectively, have been separately dispersed in 0.4 mL of chloroform. Each QD solution has been mixed to a solution of 60 mg of PMMA in 0.6 mL so as to obtain 1 mL of mixture. An ultrasonic bath was used for 15 min after several hours with mechanical stirring for the mixed solutions. These solutions have then been spin coated on fused silica substrates at 2000 rpm in a glove box in a neutral atmosphere and baked at 80°C for a few minutes for evaporating the rest of chloroform. The layers have a thickness close to 2 μm.

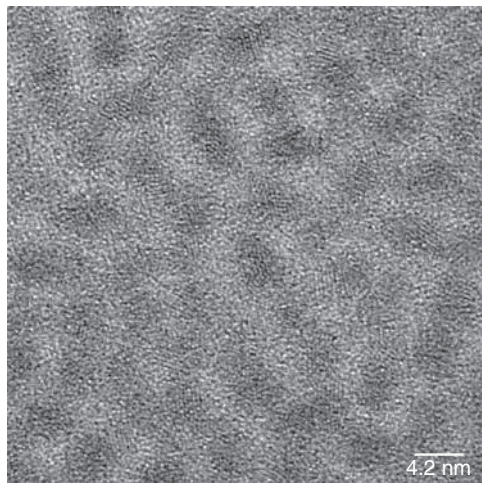
12.6 Characterization of thin films containing quantum dots

TEM can be used to measure the quantum dot size and spectroscopy to measure reflection, transmission and absorption of PMMA thin films containing quantum dots. Photoluminescence brings also information related to quantum confinement.

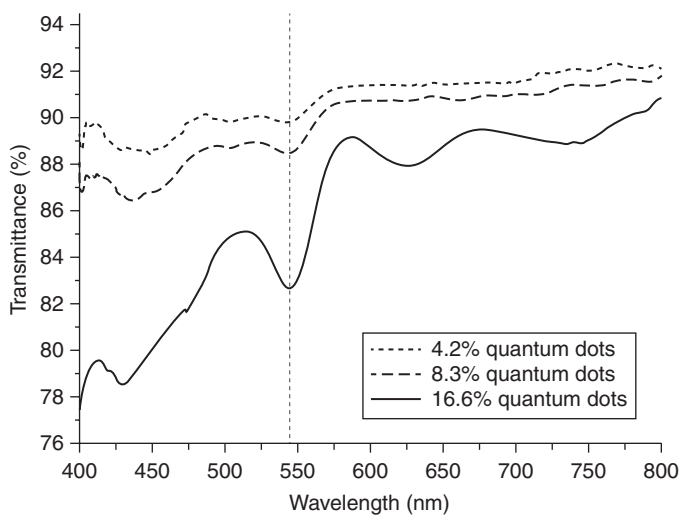
12.6.1 Transmission electronic microscopy

CdSe/ZnS QDs has been examined by transmission electronic microscopy (TEM) in order to study their size distribution as shown in Fig. 12.7. We can notice that the QDs are well-dispersed. The crystallized QDs appear to be approximately 3 nm with weak size dispersion, as expected.

Due to the structure of core-shell CdSe/ZnS QDs, the electrons are well confined in the structure. Therefore, the layers including this type of QD exhibit strong excitonic absorption peaks.



12.7 TEM images of CdSe/ZnS QDs.



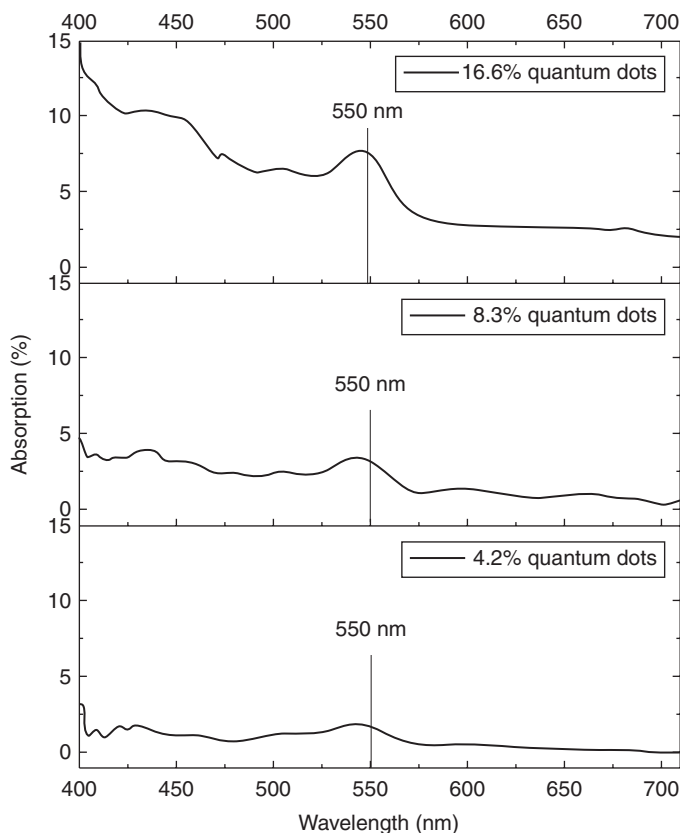
12.8 Transmittance spectrum of CdSe/ZnS QDs with weight ratio percentage of 4.2%, 8.3% and 16.6%.

12.6.2 Transmittance, reflectance and absorption

The transmittance spectra of the different samples measured with an integrating sphere spectrometer are shown on Fig. 12.8. It can be noticed that the transmittance is decreasing when the QD weight ratio percentage is increasing. On the other hand, the transmittance spectrum of the layer with

wt. 16.6% QDs revealed interference ripples in the range of 575–800 nm more pronounced than for the two other samples. This is due to an increase of effective refractive index leading to stronger interference effects in the film thickness, in its transparency range. After measuring the transmittance and reflectance spectrum, the absorption could be determined as shown in Fig. 12.9.

All samples exhibit the same absorption shape with an absorption peak close to 550 nm. As expected, the absorption increases while the weight ratio increases. Other absorption peaks at 500 and 450 nm clearly appear when increasing the percentage of QDs. They should be induced by transitions between other discrete energy levels in the QDs. As PMMA material has wide bandgap at around 4.9 eV, it does not affect the absorption in the near UV and visible spectral range. This allows us to attribute the optical absorption in the spectral range of 400–560 nm to the QDs.



12.9 Absorption spectrum of PMMA layers including CdSe/ZnS QDs with a weight ratio of 4.2%, 8.3% and 16.6%.

PMMA layers including TiO_2 nanoparticles are also interesting to consider. Absorbances of such layers including TiO_2 anatase nanocrystals with different weight ratios are shown on Plate IV (see colour section between pages 404 and 405). The absorbance is increasing with the weight ratio and their wavelength bandgap is nearly the same than bulk anatase, that is, 387 nm, for all the samples. So no bandgap shift is observed. No evidence of quantum confinement is shown. The absorption also increases with the concentration in the visible range. This is certainly due to a lack of oxygen and clustering effects.

12.6.3 Luminescence of quantum dot layers

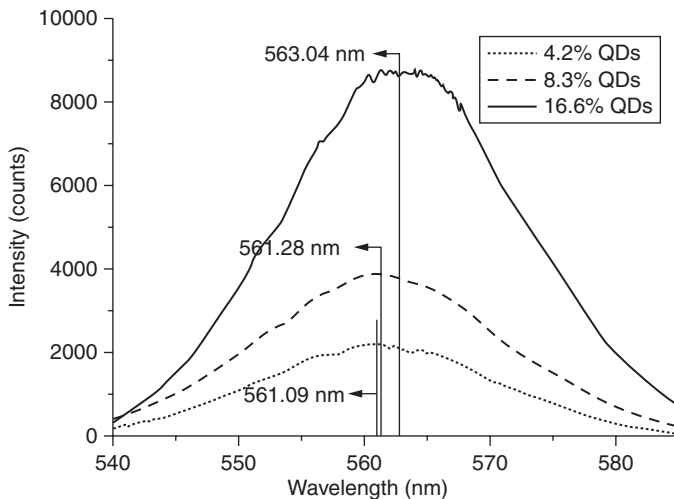
In QDs radiative decays occur between the lowest energy level in the conduction band and the highest level in the valence band. A 1 s electron is then recombined with a 1 s hole.

The PMMA layers including CdSe/ZnS QDs considered before exhibit strong luminescence around 560 nm, as expected from the QDs size. The luminescence is strong because of the ZnS core which reduces electron trapping on the core surface or electron coupling in the surrounding medium. It is also interesting to notice that the luminescent spectrum fits well with that provided by the company, which is obtained for QDs in a solution. So, the luminescent spectrum appears not to depend on the host PMMA medium.

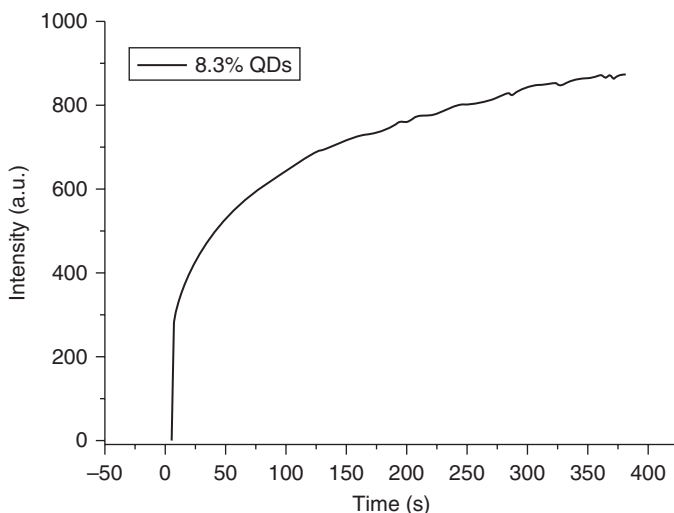
The luminescence of these layers has been measured with a continuous Ar laser excitation at the wavelength of 514 nm. As it can be seen on Fig. 12.10 the luminescence increases with the QDs concentration. The luminescent bands can be well fitted with Gaussian curves indicating an inhomogeneous band broadening. The band broadening is certainly induced by the QDs size dispersion. Luminescence measurement performed with a pump line at 488 nm shows the same spectrum.

The evolution of the average value of the luminescence as a function of pumping time at 514 nm with a 0.3 μW pump power is shown on Fig. 12.11. It can be seen that under several minutes of illumination a strong increase appears, with a saturation behaviour.

Similar results have been obtained by Korsunska *et al.* (2005) showing also an increase but also a possible decrease in luminescence depending on the pump power density for the same CdSe/ZnS QDs of ~ 3 nm, diluted with phosphate buffer (PBS) in a 1:50 volume ratio (Fig. 12.12). The reversible and non-reversible parts of the effects are also described. The increase of the photoluminescence intensity is mainly attributed to an increase in the potential barrier around the QDs because of charge trapping, inducing an increase in the recombination rate of the carriers. The increase of the potential barrier could be due to charge trapping in the QDs surface or in the ZnS shell.



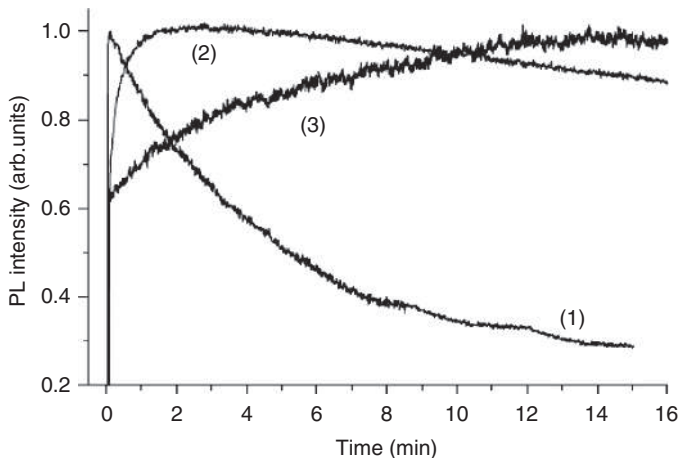
12.10 Luminescence spectra of PMMA layers containing different QDs concentrations.



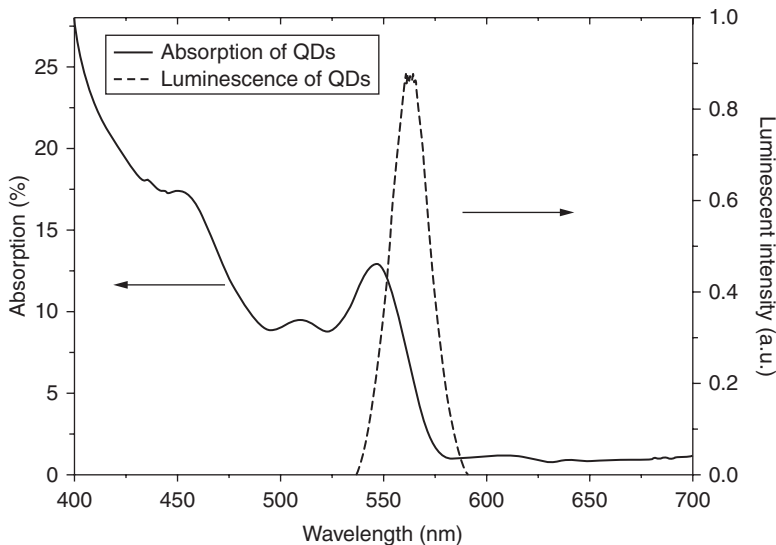
12.11 Evolution of the average value of the luminescence in function of the time with a pump power of $0.3 \mu\text{W}$ at 514 nm.

The photoluminescence wavelength band is centered at a smaller wavelength than the maximum of the absorbed wavelength band (Fig. 12.13). So it is a down-conversion process.

The frequency down-conversion could be induced by phonon coupling or could involve some forbidden transition sometime called ‘dark exciton’ (Demchenko *et al.*, 2009).



12.12 Photoluminescence intensity variations of the 550 nm luminescence band at room temperature and different laser power density (W cm^{-2}): (1) 500; (2) 20; (3) 0.2. The photoluminescence intensity is normalized using a multiplication factor of 25 in curve (2), 2500 in curve (3) (Korsunskaya *et al.*, 2005).



12.13 Absorption and luminescent spectra of a PMMA layer with a weight ratio of 16.6% of CdSe/ZnS QDs.

This down conversion effect can be used to collect the UV of the solar spectrum and to change it in visible that is more efficiently converted into charges in the solar cells. An evidence of an effective down-conversion process is shown on Fig. 12.13. The External Quantum Efficiency (EQE) of Si solar cell has been measured with a substrate coated with a pure PMMA

layer put in front and with a substrate coated with a PMMA including wt. 5.4% of CdSe/ZnS QDs of 3 nm size. As expected it can be seen that the response is reduced in the absorption band of the layer with QDs and increased in the region of its luminescence.

An interesting perspective is to consider including both QDs and metallic nanoparticles to enhance the luminescence by plasmon resonance (Song *et al.*, 2005).

12.7 Refractive index of layers containing quantum dots and of quantum dots alone

As mentioned in the introduction, the knowledge of the refractive index is necessary to design photonics components by using Maxwell equations. It is then necessary to study the refractive index of QDs to study different structures including QDs. With dimension very small in front of the wavelength of light, the quantum confinement which governs the electrons and holes behaviour changes drastically the optical properties. As seen in Section 12.2 it is impossible up to now to model the properties of a set of QDs, in particular band widening phenomena, oscillator strengths, QDs coupling, phonon coupling, heavy and light electron and hole behaviour, etc. So it is necessary to find the complex refractive index from measurement. The absorption spectrum of QDs in solution or in a thin film can be easily measured on a large wavelength range. As proposed by Moreels *et al.* (2010), and implemented by him in 2012 for different PbS QDs concentrations below 2%, the extinction coefficient dispersion with wavelength of a thin film can be obtained from the absorption spectrum. The dispersion with wavelength of the real part of the refractive index can then be deduced from the Kramers–Krönig relations.

$$n(E) - 1 = \frac{2}{\pi} P \int_0^{\infty} \frac{E' k(E)}{E'^2 - E^2} dE' \quad [12.8]$$

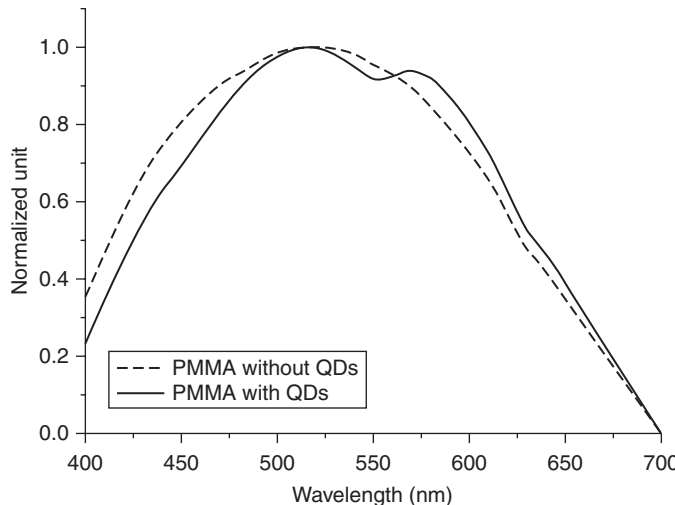
and

$$k(E) = -\frac{2E}{\pi} P \int_0^{\infty} \frac{n(E')}{E'^2 - E^2} dE' \quad [12.9]$$

Knowing the refractive index of the host material one can determine a value for the refractive index of QDs alone from an inverse effective index medium theory like Maxwell–Garnett or the homogenization theory.

The refractive index of the films can also be obtained with conventional methods like ellipsometry or m-lines technique (Flory, 1995). As examples

we can consider again the samples which absorption spectra are given on Fig. 12.14. Tables 12.1, 12.2, 12.3 and Fig. 12.15 give, for different wavelengths, the refractive index of these PMMA films including 4.2, 8.3 and 16.6 wt.% of CdSe/ZnS QDs of 3 nm size deposited on silica substrates.



12.14 Normalized EQE for a Si solar cell with a silica substrate coated with a pure PMMA layer and the same solar cell with a silica coated with a PMMA layer including CdSe/ZnS QDs.

Table 12.1 Refractive index measured by m-line technique for different wavelengths of a PMMA layer with 16.6 wt. % of CdSe/ZnS QDs

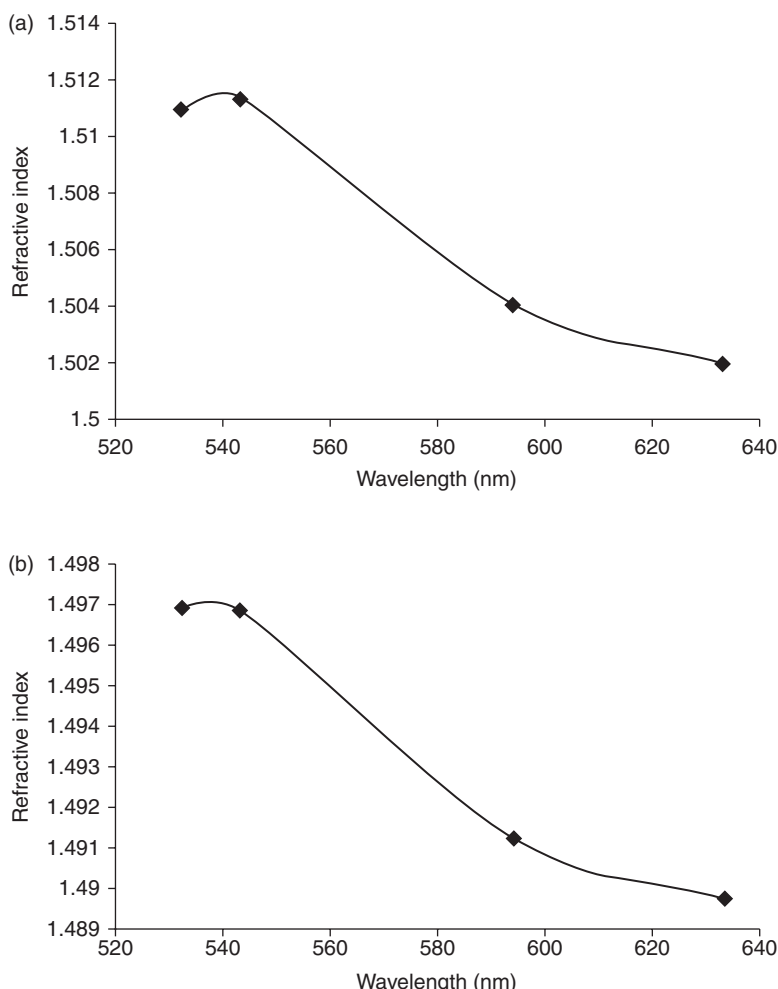
Wavelength (nm)	Refractive index
532	1.5110
543	1.5114
594	1.5041
633	1.5020

Table 12.2 Refractive index measured by m-line technique for different wavelengths of a PMMA layer with 8.3 wt. % of CdSe/ZnS QDs

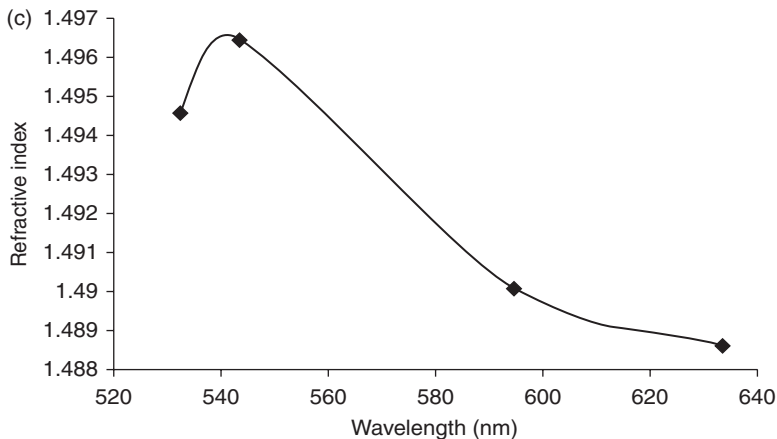
Wavelength (nm)	Refractive index
532	1.49692
543	1.49635
594	1.49126
633	1.48979

Table 12.3 Refractive index measured by m-line technique for different wavelengths of a PMMA layer with 4.2 wt. % of CdSe/ZnS QDs

Wavelength (nm)	Refractive index
532	1.4946
543	1.4965
594	1.4901
633	1.4886



12.15 Refractive index dispersion of PMMA layers including QDs with (a) 16.6 wt. %, (b) 8.3 wt. % and (c) 4.2 wt. %. Uncertainty 1×10^{-3} .



12.15 Continued

These results are obtained from guided mode measurements with the m-lines technique at 633, 594, 543 and 532 nm. The thicknesses of the films are 1964, 1969 and 1268 nm (uncertainty 2 nm), respectively. The refractive index is modulated in the wavelength range close to 550 nm where a resonant electronic transition occurs (uncertainty 1×10^{-3}).

12.8 Conclusion

In quantum dots the energy and wave function of electrons and holes can be controlled by the QDs size and coupling. As the optical properties are strongly depending on the electronic properties it appears possible to tune the dielectric function by controlling the QDs geometry. The dispersion of QDs in thin films gives materials with new properties. The complex refractive index is modified and photoluminescence is observed. Thanks to simple models and experiments the optical properties of thin films including quantum dots starts to be understood but it still remains a lot of work to be performed. Models for 1D and 0D structures, charge transfer, band broadening, phonon coupling, forbidden states, oscillator strength, life time of excited states, charges trapping, etc., are all subjects under investigations.

Thin film is part of nanophotonics and, when they include QDs, the knowledge of their basic properties like their complex refractive index paves the way to complex nanophotonics components like multilayers, diffracting structures, photonics crystals, waveguides, etc., with both a control of charge properties, spectral and spatial responses to optical waves, spectral and spatial light emission, materials with optical gain, etc. The application potential is very large. In thin film solar cells the use of QDs is a way to enhance their

efficiency by frequency conversion, hot electron collection or multiple electron generation.

QDs made of different materials can certainly be associated and adjusting their energy band diagram can allow better exciton generation and better charge transport.

Plasmonic effect and field enhancement obtained with metallic nanoparticles are used to enhance light trapping by an increase of the local field around the particles and by extending the path of light because of scattering (Duche *et al.*, 2009). The association of metallic nanoparticles and QDs is also worthy to be studied (Pillai *et al.*, 2011).

Thin films containing QDs can also be part of multilayer structures to design absorbing or luminescent coatings.

12.9 Acknowledgements

We thank the French Institute in Taipei and National Central University in Taiwan for their support. We also thank Alexandre Merlen and Claude Alfonso from the Institut Matériaux, Microélectronique et Nanosciences de Provence for the photoluminescence measurement and TEM measurement, respectively.

12.10 References

- Bera, D., Qian, L., Tseng T-K. and Holloway, P. H. (2010), ‘Quantum dots and their multimodal applications: a review’, *Materials*, vol. **3**, pp 2260–2345.
- Carpena, P., Gasparian, V. and Ortúño, M. (1999), ‘Number of bound states of a Krönig-Penney finite-periodic Superlattice’, *Eur. Phys. J. B*, vol **8**, pp 635–641.
- Chen, Z.-H., Hellstrom, S. Ning, Z.-J., Yu, Z.-Y. and Fu, Y. (2011), ‘Exciton polariton contribution to the stokes shift in colloidal quantum dots’, *J. Phys. Chem. C*, vol **115** (13), pp 5286–5293.
- Cohen-Tannoudji, C., Diu, B. and Laloë, F. (1997), *Mécanique quantique*, vol. **1**, Hermann.
- Conibeer, G., Perez-Wurfl, I., Hao, X., Di, D. and Lin, D. (2012), ‘Si solid state quantum dot based materials for tandem solar cells’, *Nanoscale Res. Lett.*, vol **7**, p 193, doi:10.1186/1556-276X-7-193
- Demchenko, D.O. and Wang, L.W. (2009), ‘Optical transitions and nature of Stokes shift in spherical CdS quantum dots’, Lawrence Berkeley National Laboratory. Retrieved from: <http://escholarship.org/uc/item/20v0s9td>
- Duche, D., Torchio, Ph., Escoubas, L., Monestier, F., Simon, J.J., Flory, F. and Mathian, G. (2009), ‘Improving light absorption in organic solar cells by plasmonic contribution’, *Sol. Energy Mater. Sol. Cells*, vol. **93**, pp. 1377–1382.
- Eisberg, R. and Resnick, R. (1985), *Quantum Physics of Atoms, Molecules, Solids, Nuclei and Particles*, 2nd edition, John Wiley and Sons, Appendix H.
- Ekimov, A.I., Efros, A.L. and Onushchenko, A.A. (1985), ‘Quantum size effect in semiconductor microcrystals’, *Solid State Commun.*, vol **56**, pp 921–924.

- Ellingson, R.J., Beard, M.C., Johnson, J.C., Yu, P., Micic, O.I., Nozik, A.J., Shabaev, A. and Efros, A.L. (2005), 'Highly efficient multiple exciton generation in colloidal PbSe and PbS quantum dots', *Nano Lett.*, vol **5** (5), pp 865–871.
- Fattal, D., Diamanti, E., Inoue, K. and Yamamoto, Y. (2004), 'Quantum teleportation with a quantum dot single-photon source', *Phys. Rev. Lett.*, vol **92**, pp 037904.
- Flory, F., Chen, Y.-J., Lee, C.-C., Escoubas, L., Simon, J.-J., Torchio, P., Le-Rouzo, J., Vedraine, S., Derbal-Habak, H., Shupyk, I., Didane, Y. and Ackermann, J. (2011), 'Optical properties of dielectric thin films including quantum dots', *Appl. Optics*, vol **50** (9), pp 129–134.
- Flory, F. (1995), 'Characterization: guided wave techniques', in Flory F. (ed.), *Thin Films for Optical Systems*, Marcel Dekker Inc. USA, Optical Engineering Series n°49.
- Gaponenko, S.V. (1998), *Optical Properties of Semiconductor Nanocrystals*, Cambridge University Press, Cambridge.
- Günes, S., Fritz, K.P., Neugebauer, H., Sariciftci, N.S., Kumarb, S. and Scholes, G.D. (2007), 'Hybrid solar cells using PbS nanoparticles', *Sol. Energy Mater. Sol. Cells*, vol **91** (5), pp 420–423.
- Huynh, W.U., Dittmer, J.J. and Alivisatos, A.P. (2002), 'Hybrid nanorod-polymer solar cells', *Science*, vol **295** (5564), pp 2425–2427.
- Jang, J.W., Ryun, S.H., Lee, S.H., Lee I.C., Jeong W.G. and Stevenson, R. (2004), 'Room temperature operation InGaAs/InGaAsP/InP quantum dots laser', *Appl. Phys. Lett.*, vol **85**, pp 3674.
- Jiu, T., Reiss, P., Guillerez, S., de Bettignies, R., Bailly S. and Chandezon, (2010), 'F hybrid solar cells based on blends of CdSe nanorods and poly(3-alkylthiophene) nanofibers', *IEEE J. Sel. Top. Quantum Electron.*, vol **16** (6), pp 1619–1626.
- Kamat, P.V. (2008), 'Quantum dot solar cells. Semiconductor nanocrystals as light harvesters', *J. Phys. Chem. C*, vol **112**, pp 18737–18753.
- Kim, T.H., Cho, K.S., Lee, E.K., Lee, S.J., Chae, J., Kim, J.W., Kim, D. H., Kwon, J.Y., Amaralunga, G., Lee, S.Y., Choi, B.L., Kuk, Y., Kim, J.M. and Kim, K. (2011), 'Full-colour quantum dot displays fabricated by transfer printing', *Nat. Photon.*, vol **5**, pp 176–182.
- Kongkanand, A., Tvrdy, K., Takechi, K., Kuno, M. and Kamat, P.V. (2008), 'Quantum dot solar cells. Tuning photoresponse through size and shape control of CdSe-TiO₂ architecture', *J. Am. Chem. Soc.*, vol **130**, pp 4007–4015.
- Korsunskaya, N.E., Dybiec, M., Zhukov, L., Ostapenko S. and Zhukov, T. (2005), 'Reversible and non-reversible photo-enhanced luminescence in CdSe/ZnS quantum dots', *Semicond. Sci. Technol.*, vol **20**, pp 876–881, doi:10.1088/0268-1242/20/8/044
- Larson, D.R., Zipfel, W.R., Williams, R.M., Clark, S.W., Bruchez, M.P. and Wise, F.W. (30 May 2003), 'Water-soluble quantum dots for multiphoton fluorescence imaging in vivo', *Science*, vol **300** (5624), pp. 1434–1436, doi: 10.1126/science.1083780
- Moreels, I., Kruschke, D., Glas, P. and Tomm, J.W. (2012), 'The dielectric function of PbS quantum dots in a glass matrix', *Opt. Mat. Express*, vol. **2** (5), pp 496–500.
- Moreels, I., Allan, G., De Geyter, B., Wirtz, L., Delerue, C. and Hens, Z. (2010), 'Dielectric function of colloidal lead chalcogenide quantum dots obtained by a Kramers-Kronig analysis of the absorbance spectrum', *Phys. Rev. B*, vol **81** (23), pp 235319–235325.
- Nozik, A.J. (2008), 'Multiple exciton generation in semiconductor quantum dots', *Chem. Phys. Lett.*, vol **457** (1–3), pp 3–11.

- Nozik, A.J. (2002), 'Quantum dot solar cells', *Physica E*, vol **14** (1–2), pp 115–120.
- Pagan, J.G., Stokes, E.B., Patel, K., Burkhardt, C.C., Ahrens, M.T., Barletta, P.T. and O'Steen, M. (2006), 'Colloidal quantum dot active layers for light emitting diodes', *Solid-State Electron.*, vol **50** (7–8), pp 1461–1465.
- Pillai, S., Perez-Wurfl, I., Conibeer, G.J. and Green, M.A. (2011), 'Surface plasmons for improving the performance of quantum dot structures for third generation solar cell applications', *Phys. Status Solidi C*, **8** (1), pp 181–184, doi: 10.1002/pssc.201000644
- Reed, M.A., Randall, J.N., Aggarwal, R.J., Matyi, R.J., Moore, T.M. and Wetsel, A.E. (1988), 'Observation of discrete electronic states in a zero-dimensional semiconductor nanostructure', *Phys. Rev. Lett.*, vol **60**, pp 535–537.
- Reiss, P., Bleuse, J. and Pron, A. (2002), 'Highly luminescent CdSe/ZnSe core/shell nanocrystals of low size dispersion', *Nano Lett.*, vol **2**, pp 781–784.
- Reyes-Coronado, D., Rodriguez-Gattorno, G., Espinosa-Pesqueira, M.E., Cab, C., de Coss, R. and Oskam, G. (2008), 'Phase-pure TiO₂ nanoparticles: anatase, brookite and rutile', *Nanotechnology*, vol **19**, pp 45605–145604.
- Robel, I., Subramanian, V., Kuno, M. and Kamat, P.V. (2006), 'Quantum dot solar cells. Harvesting light energy with CdSe nanocrystals molecularly linked to mesoscopic TiO₂ films', *J. Am. Chem. Soc.*, vol **128**, pp 2385–2393.
- Rossetti, R., Nakahara, S. and Brus, L.E. (1983), 'A simple model for the ionization potential, electron affinity, and aqueous redox potentials of small semiconductor crystallites', *J. Chem. Phys.*, vol **79**, pp 5566–5571.
- Shockley, W. and Queisser, H.J. (1961), 'Efficiency loss mechanisms: theory and characterization', *Appl. Phys.*, vol **32**, pp 510–519.
- Song, J.H., Atay, T., Shi, S., Urabe, H. and Nurmikko, A.V. (2005), 'Large enhancement of fluorescence efficiency from CdSe/ZnS quantum dots induced by resonant coupling to spatially controlled surface plasmons', *Nano Lett.*, vol **5** (8), pp 1557–1561.
- Studenikin, S.A., Golego, N. and Cocivera, M. (1998), 'Fabrication of green and orange photoluminescent, undoped ZnO films using spray pyrolysis', *J. Appl. Phys.*, vol **84** (4), pp 2287–2294.
- Wang, Y. and Herron, N. (1991), 'Nanometer-sized semiconductor clusters—materials synthesis, quantum size effects, and photophysical properties', *J. Phys. Chem.*, vol **95**, pp 525–532.
- Woggon, U. (1997), *Optical Properties of Semiconductor Quantum Dots*, Springer Tracts in Modern Physics, Volume **136**, Springer Verlag, doi: 10.1007/BFb0119351

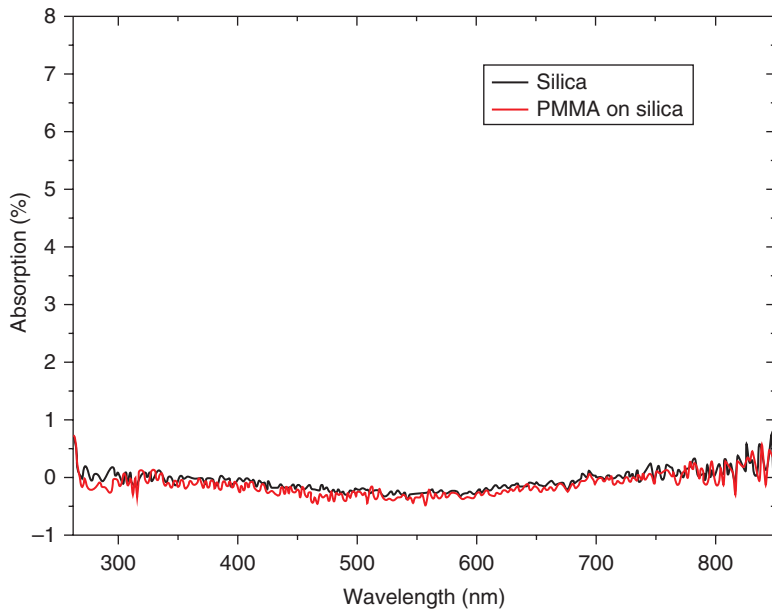


Plate III (Chapter 12) Measured absorption spectra of a pure silica glass and a silica glass coated with a PMMA layer.

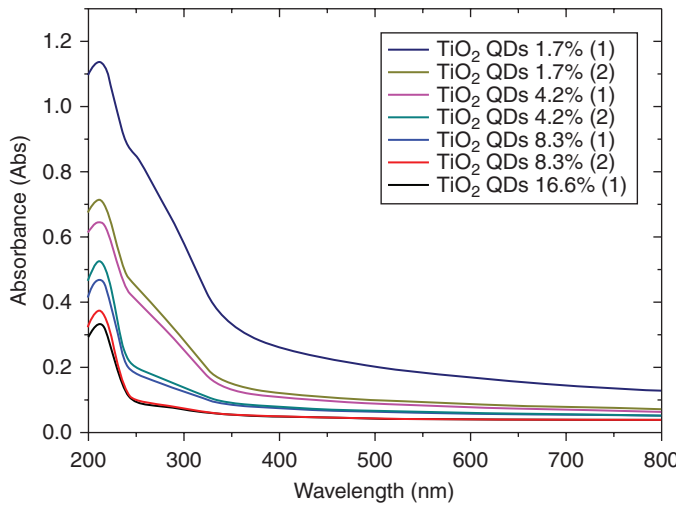


Plate IV (Chapter 12) Absorbances of PMMA layers including TiO_2 anatase nanocrystal on pure silica (1) and on BK7 glass (2) with different weight ratios.

Optical coatings on plastic for antireflection purposes

U. SCHULZ, Fraunhofer Institute of Applied Optics
and Precision Engineering, IOF, Germany and
R. W. SCHAFFER, Evaporated Coatings Inc., USA

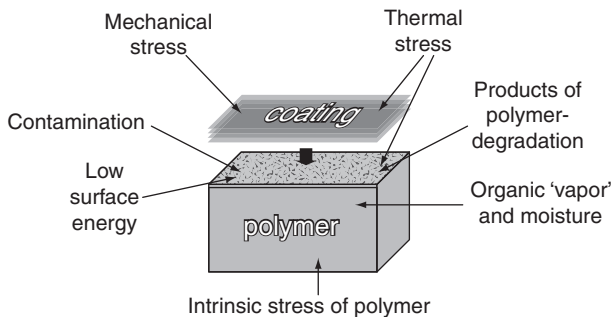
DOI: 10.1533/9780857097316.4.519

Abstract: This chapter first reviews the properties of various thermoplastic polymers and how these polymers react in vacuum. The chapter then discusses critical process considerations including interaction with emission from plasma, thermal stress, water adsorption and desorption, and other general concerns for vacuum coating polymers. State-of-the-art vacuum processes for coating, as well as new results of research and development in the fields of wet chemical coatings and antireflective structures, will be introduced and described.

Key words: antireflection, plastic optics, plasma treatment, adhesion, nanostructures.

13.1 Introduction

Plastic materials are replacing glass optics whenever advantageous physical properties or cost reduction can be achieved. Plastic materials benefit from properties like low weight and low breakage. They can be shaped in cost effective mass production by injection molding or embossing. The requirement for optical coating has to be considered in a very early stage of development. Antireflection (AR) is the most important optical function. The requirements to achieve antireflection properties are increasing continuously. AR coatings have been tried and tested on lacquered eyeglasses for about 50 years. AR coatings on precision plastic optics have been in existence for about 40 years. However, AR coatings for camera lenses and display covers consisting of thermoplastic polymers like acrylic (poly(methyl methacrylate) (PMMA)) or polycarbonate (PC) are still challenging. New applications create increasingly stringent environmental requirements. The basic problems involved with vacuum coating of plastics are illustrated in Fig. 13.1. The effort to achieve coatings with high adhesion and extended environmental stability is different for each type of polymer and in some



13.1 Basic problems for vacuum coating of plastics.

cases it is difficult or impossible to obtain good results. Complex chemical reactions may occur, especially in the common plasma-assisted deposition processes. The following sections may help to understand the special behavior of polymer materials for coating, especially in vacuum coating processes. The state-of-the-art processes for vacuum coating, as well as new results of research and development in the fields of wet-chemical coatings and antireflective structures, will be introduced and discussed.

13.2 Transparent polymer materials for optics

Plastic optics include spherical and aspherical as well as free form, diffractive, Fresnel and mirror surfaces. A manifold of materials is available which allow the integration of different optical functions as well as elements for sticking and assembling into one injection molded part. At the prototyping stage single-point diamond turning manufacturing processes are commonly used. The progress in material grades is continuing; for example, advances in polycarbonate and polycycloolefine materials have resulted in higher heat resistance, improved stability and lower birefringence properties. The optical properties of the polymers and also properties such as specific gravity, as well as chemical and environmental stability must be considered in developing applications (Bäumer, 2010). Table 13.1 shows an extract of materials and their most important properties to be taken into account for coating.

Plastics are mainly used for eyeglasses and numerous precision optical lens systems used in cameras, medical devices, projectors, displays, fiber optics and automotive devices, to name a few. Eyeglasses are special because thermosetting materials are used rather than the thermoforming materials listed in Table 13.1. Developments for eyeglasses include especially high index polymers based on thiourethanes and lightweight materials with high impact resistance, such as, Trivex® and Tribrid® (PPG Optical

Table 13.1 Properties of important thermoplastics for optics

Polymer name	Brand name	n_D (587.6 nm)	Abbe number	Trans- mittance 3 mm (%)	Density (g/cm ³)	Water absorption (%) ISO 62	Tensile modulus (MPa)	Pencil hard- ness	Defect. temperature ISO75-2 (°C)	Coating adhesion*
Poly(methyl methacrylate)	Plexiglas 7N	1.491	58	92	1.19	2.2	3200	3H	85	+
Methyl methacrylate copolymer	Plexiglas HW55	1.51	49	90	1.19	2.2	3600	3H	106	++
Poly(n-methyl methacryl imide)	Pleximid TT70	1.54	43	91	1.21	6	4000	4H	158	++
Polycarbonate	Makrolon LQ2647	1.585	30	89	1.2	0.4	2400	B	120	++
Polycarbonate copolymer	Apec HT9351	1.572	30	88	1.15	0.3	2400	B	159	+
Cycloolefin copolymer	Topas 5013	1.533	58	92	1.02	<0.01	3100	H	123	+++
Cycloolefin polymer	Zeonex E48R	1.53	56	92	1.01	<0.01	2500	H	122	+++
Cycloolefin polymer	Zeonex 480R	1.525	56	92	1.01	<0.01	2200	H	123	+++
Cycloolefin polymer	Zeonor 1020R	1.53	56	92	1.01	<0.01	2100	HB	101	+++
Cycloolefin polymer	Zeonex 330R	1.509	56	92	0.95	<0.01	1770	2H	110	+
Polyether sulfone	Ultraslon E2010	1.65	20	83	1.37	2.2	2700	H	212	+++
Polyamide	Trogamid CX7323	1.516	45	89	1.02	3.5	1400	B	122	+++
Polyester	OKP4	1.607	27	88	1.22	0.15	2000	2H	105	+++

* Own experiences, AR coatings deposited by plasma-ion assisted deposition; +++ very good; ++ good with some limitations; + good only by applying special conditions.

Products, 2012). Some of the eyeglass materials would also be attractive for other optical parts. But shaping to lenses can only be carried out by casting the monomer and during polymerizations a considerable shrinkage occurs which makes the technology impractical for precision optics. Substrates for optical coating nowadays also include biobased and biodegradable materials (Narayan, 2008).

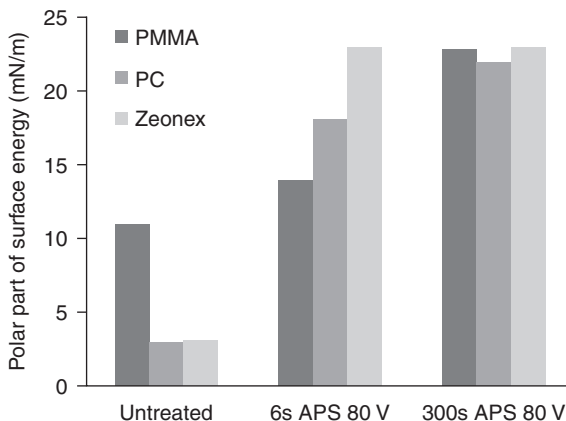
13.3 Plastics in vacuum coating processes

Vacuum evaporation and sputtering processes are commonly used for depositing antireflection coatings. Therefore, the unique behavior of polymer materials in vacuum processes will be discussed here.

13.3.1 Interaction with emissions from plasma

Polymers differ from each other in regard to their chemical composition. In contrast to optical glass, a variety of different surface compositions and surface states are characteristic for the polymers used in optics. The surface regions can additionally be affected by the shaping process and the environmental conditions. Boat-evaporated oxide layers deposited without the influence of plasma emissions exhibit excellent layer adhesion on most plastic substrates. However such cold deposited coatings may suffer from the low energy level. The films are porous and cannot pass all environmental tests. A common method to deposit coatings on temperature-sensitive substrates is plasma-ion assisted deposition (PIAD) (Pongratz and Zöller, 1992). However, special magnetron sputtering methods have also been described for coating plastics, among them are closed field magnetron sputtering (Gibson *et al.*, 2004) and reactive pulse magnetron sputtering in an unipolar mode (Lau *et al.*, 2009). In these modern vacuum coating processes plasma, and therefore short wavelength radiation, is produced by electron beam evaporators, ion source, glow-discharge cathodes and other enhancements.

For most plastic materials, their special interaction with plasma emissions is the essential factor for good or bad coating adhesion. Plasma treatments typically produce polar groups on polymer surfaces. Wettability is therefore always increased. Improvement in adhesion by plasma treatments has been variously attributed to this improved wettability or to surface cross-linking (Liston *et al.*, 1993; Fozza *et al.*, 1997; Sarto *et al.*, 1999; Rank *et al.*, 2005). However ions emitted by ion sources and short wavelength radiation often break chemical bonds in polymers and thereby chemical modifications are initiated. Normally a weakly bonded coating can be removed from the substrate using a tape. It is important to identify the locus of failure by investigating both the tape with the removed coating and the substrate. If the break has occurred cohesively inside the substrate, parts of the destroyed polymer are detectable by X-ray photoelectron

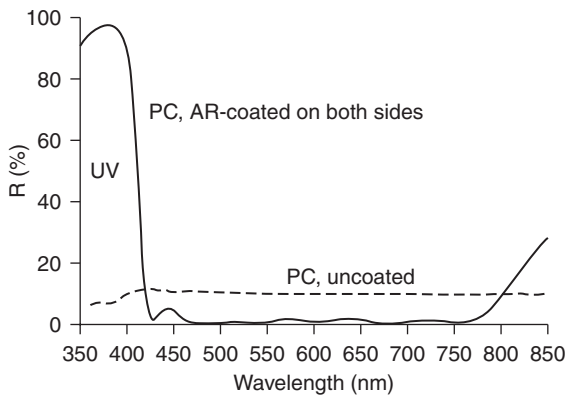


13.2 Polar component of surface energy of PMMA, Makrolon and Zeonex depending on the treatment time (ion source APS (Leybold), 80 V Bias, Ar, 2×10^{-4} mbar).

spectroscopy (XPS) or Fourier transform infrared spectroscopy (FTIR) on the removed tape and efforts should be directed to avoid the formation of a weak boundary layer. Taking into account the very short treatment times sufficient for the activation of most polymer surfaces and the danger of forming weakly bonded layers, all plasma or ion treatments should be as short as possible. Figure 13.2 shows the increase of the polar component of surface energy dependent on the plasma treatment time for different polymers. In particular, polycycloolefines like Zeonex can be activated within seconds.

In the case of acrylic, the adhesion is typically decreased after contact with plasma (Lian *et al.*, 1995; Licciardello *et al.*, 1996). To switch on the e-beam evaporator for a short time can always be critical. It is proven that the inadequate adhesion is caused by the formation of weak boundary layers of degradation products (Hook *et al.*, 1987). For PMMA we suggest as a first step to deposit a protection layer without the use of plasma. The layer has to effect blocking ultraviolet radiation at wavelengths shorter than about 350 nm. After that, optical interference coatings can be deposited on this base layer by applying plasma assistance and taking into account some limitations for the coating design (Munzert *et al.*, 2007).

As shown in Table 13.1, electron-beam-evaporated oxide layers deposited with plasma ion assistance show best adhesion on certain types of polycycloolefines, polycarbonates, polyamides and polyether sulfones (Munzert *et al.*, 2004). However, poly-bisphenol-A-carbonate (Makrolon®, Lexan®), not only provides adhesion problems caused by plasma but also by ultraviolet radiation at a later time. Some plasma conditions are described to assist in improving the adhesion properties (Vallon *et al.*, 1996; Hofrichter *et al.*,

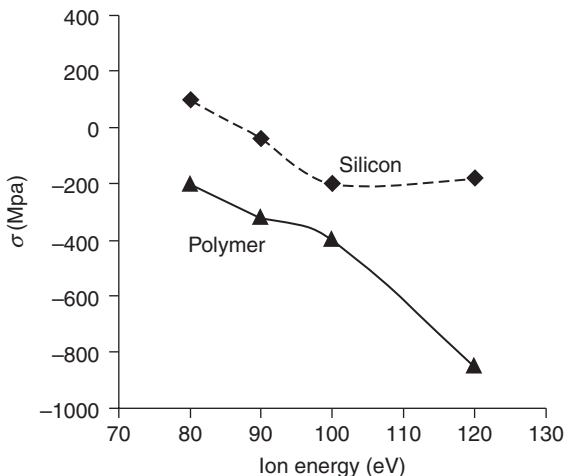


13.3 Antireflection coating (17 layers, 1.5 μm total thickness) providing UV-protection to the polycarbonate substrate.

2002; Muir *et al.*, 2006). But unfavorable results are also possible if longer or more intensive treatments are applied. UV-protective coatings are necessary for outdoor uses of polycarbonate to prevent coating ablation later (Schulz *et al.*, 2008). This is a special challenge for optical coatings because the absorption characteristics of the typical evaporation materials are not sufficient to block the critical wavelength range between 350 and 400 nm by absorption (Rivaton, 1995). An antireflective coating with improved sunlight resistance was achieved with a high reflecting band as part of a non-absorbing interference multilayer (Fig. 13.3).

13.3.2 Thermal and stress related effects

Further material-specific properties with more or less influence on vacuum processes are thermal characteristics and degassing behavior. Stress can adversely affect the interface between coating and polymer and initiate cracking or ablation of thin films. The mechanical stress of coatings mainly depends on the deposition parameters, especially on ion bombardment energy and deposition rate (Doerner and Nix, 1988). If deposited cold and without ion assistance, most high index coating materials would exhibit tensile stress. With the application of ion bombardment at a low level the growth stress of nearly all materials can be shifted in the compressive range. However, on polymers, a thermal stress component must always be considered if the substrate temperature is slowly increasing during layer deposition. This is caused by the typically high thermal expansion coefficient of plastic substrates. Therefore thermal stress during film deposition may cause tensile stress cracking despite the compressive growth stress of the film. The residual stress of TiO_2 -coatings deposited by PIAD on silicon and a plastic

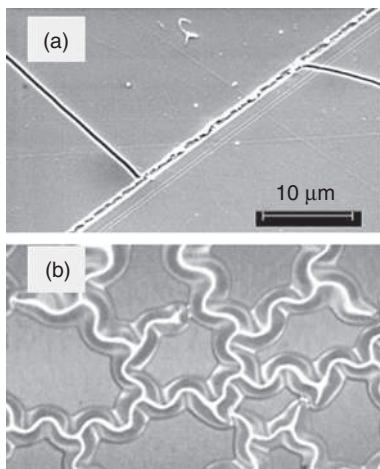


13.4 Residual stress of TiO_2 -coatings on silicon and plastic depending on the ion assistance energy applied during PIAD-process. Higher ion energy yields to increased layer densification but also to an increased substrate temperature. The stronger increase of compressive stress on plastic compared to silicon is caused by the thermal stress.

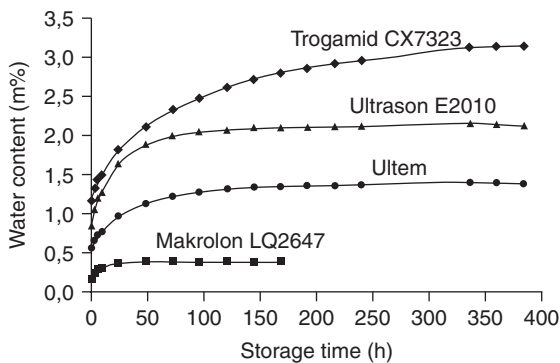
substrate are compared in Fig. 13.4 (Schulz and Kaiser, 2003). The growth stress of the layers is increasing with higher ion assistance energy because of the higher densification. In addition, the substrate temperature rises if higher ion energy is applied. Because of the higher thermal expansion the plastic sample will receive much higher compressive stress than the silicon substrate. One possibility for avoiding tensile stress during film deposition is to heat the substrates carefully to a value below their heat distortion temperature. The coating design and temperature management during film deposition are essential factors to avoid cracking. The deposition rate and ion energy in ion-assisted processes have to be carefully optimized for the respective coating material and coating thickness. In choosing the optimal deposition parameters the later application conditions (temperature range, outdoor or indoor conditions) have to be taken into account. From our experience the best results on polymers can be achieved if all deposited layers have a moderate compressive stress in a range of -150 to -250 MPa (Schulz and Kaiser, 2003). Figure 13.5 shows typical pictures of tensile stress cracking and of a 'buckling' defect caused by high compressive stress in combination with insufficient adhesion.

13.3.3 Water absorption and desorption

Most polymers absorb water and exhibit a certain water content dependent on the environment. Some examples are shown in Fig. 13.6. Contrary

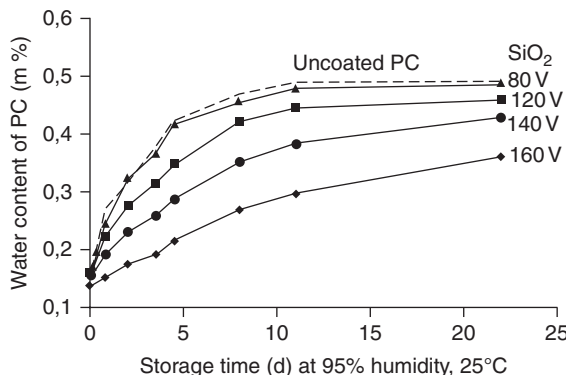


13.5 Typical defects in coatings on plastic: (a) tensile stress cracking and (b) 'buckling' caused by high compressive stress in combination with insufficient adhesion.



13.6 Water content of polymers depending on storage time at 25°C, 95% humidity.

to popular opinion, there is no obvious relationship between the coating ability of a material and its water content. Certainly a high outgassing may increase the time to achieve a good vacuum. A warming of the substrate during deposition can increase the rate of desorption and these gases can react with the arriving atoms affecting both the refractive index and the condensation rate of the arriving film. Storage at moderate temperature before coating may help. However an intense reduction to a water content below the equilibrium value would trigger stronger water diffusion through the deposited coating and promote cracking and delamination. If the materials have higher water content than about 0.2 wt.% the barrier properties



13.7 Water absorption of polycarbonate (PC) without coating (dashed line) and coated with 1 μm silica applying PIAD with APS ion source. Different levels of ion assistance energy (corresponding to the Bias Voltage value) cause the different barrier behavior.

of the thin film material have to be taken into account. Figure 13.7, shows the water absorption of PC samples without coating and when covered with 1 μm thick silica layers. The ion assistance energy was varied obtaining layers with different density and barrier effect. In principle the deposition parameters (deposition rate, temperature, ion energy) have to be adjusted so that water vapor is able to penetrate through the coating. Otherwise crinkling and delamination can occur. For the same reason, metallic layers, which always inhibit the penetration of water, should not be applied on polymers with higher water content.

13.3.4 General considerations for plasma-assisted vacuum coating processes

Concluding from the section above, some rules can be derived for vacuum deposition of interference coatings on plastics:

- The materials and thicknesses of the layers have to be adjusted taking into consideration the stress of the thin film materials. Fluorides are in any case less favorable than oxides.
- The total amount of heat dissipated in the film during the deposition process has to be taken into account. The composition of coatings may be displaced in favor of the low-index ratio because the evaporation of silica occurs at a lower temperature than of higher index oxides.
- Evaporation and plasma-assist parameters have to be chosen carefully to reduce the danger of damage to the polymer. Effects in the bulk (yellowing) and interface (delamination) may occur immediately. But they can also begin to appear after a longer period of time.

- High-index materials have to be considered in order to achieve protection of the interfaces or the bulk polymer from UV radiation, depending on the type of polymer substrate.
- Outgassing of some polymers can affect the condensation rate and the refractive index of arriving materials and must be taken into account in the calculation of the design.
- In some cases interfacial zones with changed optical properties due to plasma treatment have to be taken into account in the calculation of the design.
- Designs have to be tolerant to changes of the optical constants because the layer materials cannot be densified completely.

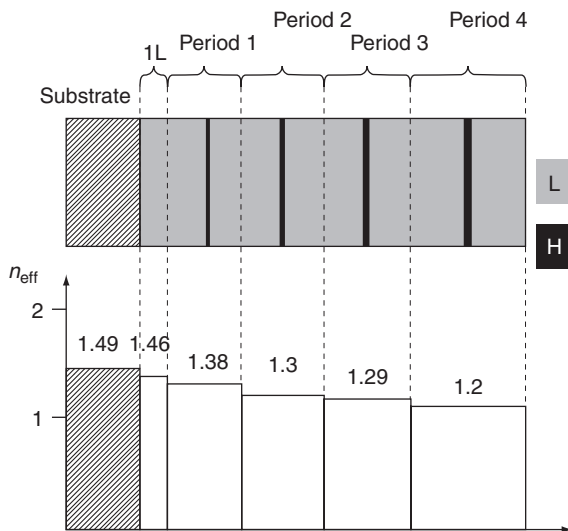
13.4 Antireflection methods

Due to the physical properties of polymers, special techniques and requirements must be applied. This section will discuss unique techniques to achieve good AR results and other physical enhancements. Vacuum deposited coatings which are the most common method used, as well as AR structures and wet chemical processes, will be covered.

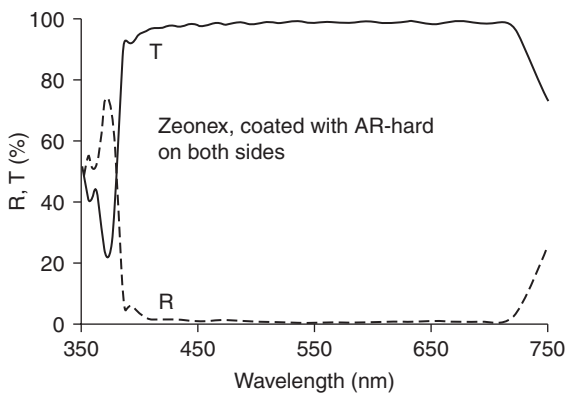
13.4.1 Vacuum deposited antireflective-coatings

The most frequently used broad-band AR coatings for the visible spectral range are adapted from the ‘quarter–half–quarter’ design, where the first quarter-wave layer, of medium refractive index, is replaced by parts of high-index and low-index layers followed by a half-wave high-index layer and a low-index quarter-wave layer (Macleod, 2001). The commonly used low-index material for coating plastics is silica ($n = 1.5$) because magnesium fluoride is hard to densify without heating the substrate and would exhibit unfavorable tensile stress. The higher index materials can be selected from a variety of oxide materials with refractive indices in the range between 1.67 (alumina) and 2.4 (titanium dioxide). The selection of the material is important for coating plastics because of effects such as heat emission during evaporation and the absorption of ultraviolet light as mentioned before.

Modern software tools allow the generation of specific antireflective designs. An increased total coating thickness is sometimes desirable because of the hardening effect obtained together with the optical effect. By applying the design called ‘AR-hard’ developed for plastics it is possible to adjust the total thickness on the AR stack by introducing a large amount of low-index material (Schulz *et al.*, 2002). The basic construction scheme of AR-hard is shown in Fig. 13.8. For example, a three micron thick AR-hard coating on Zeonex shown in Fig. 13.9 is withstanding an abrasion test with steel wool. The much softer polycarbonate surfaces would require a coating thickness of about 5 μm to achieve similar results.



13.8 Principle of design AR-hard: equivalent layers with low effective refractive index n_{eff} are formed by periods of conventional low (L) and high (H)-index layers.



13.9 Reflection R and Transmission T of scratch resistant AR-hard layer (thickness 3 μm) on Zeonex E48R (coating on both sides).

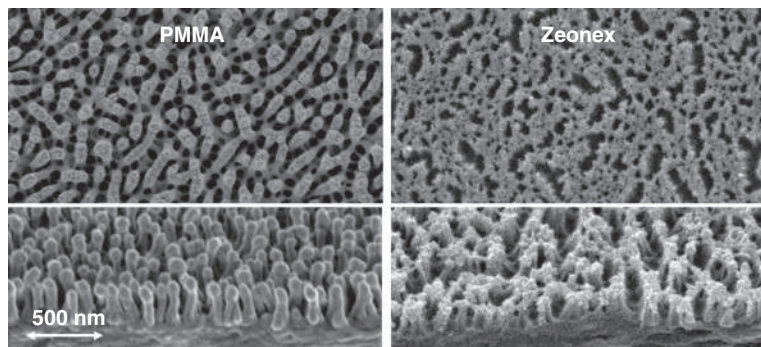
AR-hard design was developed for thermoplastic optics where lacquering is unfavorable or cost intensive. On eyeglasses, combinations of a hard-coating lacquer (i.e., a wet-chemical applied polysiloxane compound) with an interference antireflective layer on top are commonly used (Blacker *et al.*, 2000). Sony has developed a broad-band three-layer antireflective coating on plastic film. The structure is plastic film/SiO_x/TiN/SiO₂. This AR coating has a high wear resistance and high AR quality. The residual reflectance is about 0.2% and the bandwidth is 1.65 (Ishikawa *et al.*, 1999).

13.4.2 Antireflective structures (ARS)

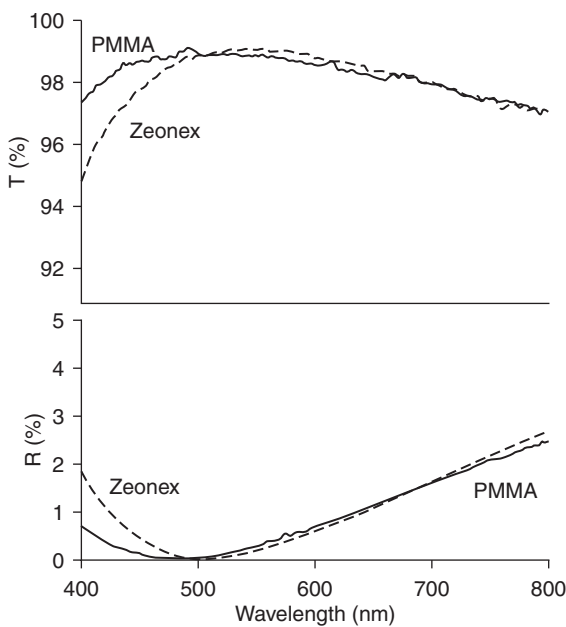
Investigations of antireflective structures (ARS) have been pursued for almost four decades since they were discovered and explained on the eye of a night-active moth (Clapham and Hutley, 1973). The periodically structured moth eye acts as an effective antireflective medium featuring a decreasing refractive index from the substrate side to the surrounding air. Sub-wavelength surface structures are typically less sensitive to the angle of incidence of light than homogeneous multilayer stacks (Minot, 1977; Dobrowolski *et al.*, 2002). Most theoretical analysis of reflection characteristics is done by using a rigorous coupled-wave analysis (RCWA) (Gaylord and Moharam, 1985) or effective medium theory (EMT) (Raguin and Morris, 1993).

A number of bottom-up (coating) and top-down (etching, embossing) techniques have been developed in order to create ARS. In the case of plastics, top-down procedures are preferred because of the removal of material as well as the deformation by thermal embossing being much easier than on glass and other inorganic substrates. The first technical implementation of ARS into a polymer was achieved using a holographic superposition of a light-exposed photoresist (Gombert *et al.*, 1999). Currently, master structures with a pitch of 250 nm and an average depth of 200 nm are commercially available (Holotools, 2012). Another method for producing a master tool for embossing into plastics is the use of anodic oxidation of aluminum (Yanagishita *et al.*, 2008). The structure is generated directly on the tool for hot embossing by depositing the metal layer followed by the wet-chemical oxidation procedure. Modern development of embossing comprises the use of nanoimprinting (Chen *et al.*, 2009). To overcome deformation problems, the structures are introduced into an acrylic resist material that is typically cross-linked by UV radiation before the deforming step. Embossing processes are mostly restricted to flat or slightly curved substrates. Embossing of ARS with an aspect ratio (depth to period ratio) higher than about one seems to be difficult to achieve because of deforming problems.

ARS can also be achieved directly from the top-down by applying plasma etching on polymers (Kaless *et al.*, 2005). Optimized plasma-etched structures on poly(methyl methacrylate) (PMMA) and in Zeonex are shown in Fig. 13.10. For the PMMA structure the aspect ratio is about two and the residual reflectance is below 0.5% from 420 to 750 nm and incidence angles from 0° to 45°. The ‘sponge’-like structure of Zeonex exhibits lower gradient characteristics. Reflectance and transmission for both samples are shown in Fig. 13.11. However, the Zeonex surface structure shown in Fig. 13.10 can be preserved during cleaning and handling because the surface holes were closed almost completely by a protective silica top-layer (Schulz *et al.*, 2007; Wendling *et al.*, 2009). The optical advantages of plasma etched ARS can be



13.10 Scanning electron micrographs showing PMMA and Zeonex surfaces with optimized antireflective nanostructures (top view and 45° inclined view below).



13.11 Reflectance and transmission spectra of plasma-etched plastic sheets (both sides) caused by the nanostructures shown in Fig. 13.10.

revealed especially with sharp curved plastic lenses and Fresnel lenses. Such lenses are protected from mechanical damage if they are mounted inside of an objective.

During recent years a number of additional single layers with a nanoporous structure have been described. In particular, the aqueous-based layer-by-layer assembly process is harmless to plastics (Hiller *et al.*, 2002). A basic

procedure is based on the sequential adsorption of poly(acrylic acid) and poly(allylamine) (Mendelsohn *et al.*, 2000). Porous acrylic (PMMA) films were produced by spin-coating of a polystyrene (PS)/PMMA-blend followed by selectively etching the PS phase (Walheim *et al.*, 1999), by selectively solving the PS phase (Zhao *et al.*, 2005) or by spin-coating and microphase separation between two PMMA blocks (Park *et al.*, 2005). Another spin-casted PMMA/PS latex with antireflective properties was synthesized by emulsion polymerization (Jiang *et al.*, 2011). The PMMA nanoparticles were used to form a porous skeleton structure, while the PS particles were used to control the porosity. Al_2O_3 gel films (flower-like Al_2O_3) were prepared on PMMA substrates through immersion of the films in hot water. The reflectance of PMMA substrates coated with the flower-like Al_2O_3 was less than 0.8% in the visible light region and exhibited very small incident-angle dependence in transmittance up to 60° (Tadanaga *et al.*, 2008).

A special property of ARS is the opportunity to manage the wettability over a wide range. In combination with a hydrophobic layer, nanostructured surfaces can exhibit the Lotus effect whereas a hydrophilic surface chemistry may cause antifogging properties (Cebeci *et al.*, 2006). On the other hand, the weak mechanical strength caused by porosity of the surfaces is the main disadvantage of AR structures. To the knowledge of the authors not a single one of the AR structured surfaces described in the literature is able to pass the mechanical tests defined by ISO standards. Most of the surfaces may not be touched; some can be touched and cleaned carefully.

13.4.3 Wet-chemical AR coatings on plastics

Wet-chemical coatings for antireflective applications on glass have been commercially produced since the 1960s. The Sol-gel process classically involves the use of inorganic salts or metal alkoxides as precursors. Typically an elevated temperature up to 400°C is needed for hydrolysis and polycondensation to accomplish an inorganic oxide network (Dislich, 1983). An alternative way was opened by the use of organic–inorganic composite materials. Typical examples are organically modified silanes (Chen, 2001). The final polymerization can either be performed photochemically or thermally, or by a combination of both. The principles of varying the composition and the properties of hybrid sol-gel derived materials are reviewed by Schottner *et al.* (2003). Scratch-resistant coatings are often modified with cross-linking agents and colloidal silica. On polycarbonate substrates the pencil hardness was increased from grade 2B to 5H by adjusting the composition and the total layer thickness (Wu *et al.*, 2008). Wet-chemical coatings are usually deposited by dip coating or spin coating on flat or slightly curved substrates. Injection-molded parts with complicated shapes are not suitable

for this deposition method. Moreover, the preparation of multilayers is complex because the depositing and hardening steps have to be repeated several times.

Wet-chemical antireflective coatings may exhibit some advantages compared to vacuum deposited coatings. The mechanical properties of the coatings can be easily adapted to suit plastic substrates and the stability during temperature change should therefore be better. In addition, the variety of materials allows formulations with defined middle refractive indices for two-layer AR coatings or to match the index of a protective layer index perfectly to that of the substrate.

Antireflective coatings for plastics comprise mainly single layers and two-layer systems. An early described porous single layer coating for PMMA was produced from a reliquefied gel containing long polymer chains and exhibited low-index layers ($n = 1.22$) (Ashley, 1990). Many of the single composite layers contain fluorine, among them is an organic fluoropolymer for curing at 120°C (Sakai *et al.*, 2001), a fluorine-containing binder-aided colloidal silica (Floch and Belleville, 1994) and UV-curable fluorine containing polymers (Araki *et al.*, 2003). Patented systems especially for eyeglasses typically start with a hard coating formulation followed by a high-index and a low-index layer. A thermal hardening sol-gel coating made from metal alkoxides for eyeglasses was developed by Vision Ease Lens Inc. (Moravec *et al.*, 2004). The formulations for the interference layers can be filled with nanoparticles and are mostly cured by UV-radiation (Yoshikawa and Yamaya, 2004). The high index nanoparticles may comprise TiO_2 but also indium tin oxide to achieve antistatic properties (Nishida *et al.*, 2002). Another two-layer coating on a protective acrylate layer consists of metal oxide sol with $n = 1.6$ followed by a cured fluorinated organic-group bearing silicone (Yamaya and Sato, 2003). Seiko has developed a similar system for eyeglasses consisting of a high-index layer filled with TiO_2 -nanoparticles followed by an organo-silicone layer containing silica fine particles with index 1.16–1.39 (Naito *et al.*, 2006). This first organic antireflection layer for eyeglasses was introduced to the market by Seiko (2007). Wet-chemical antireflective coatings are nowadays on the market especially for acrylic or polycarbonate sheets for display application (Eyesaver International, 2012). Other commercially available formulations contain nanoparticles immobilized into binders depending on the substrate material (i.e., PC, CR39 and triacetyl cellulose) (Oxford Advanced Surfaces, 2012). The products are not recommended for outdoor use. The optical performance of all wet-chemical compositions do not seem to accomplish the quality of high-performance vapor deposited AR-coatings. However, the number of single layer solutions has been steadily increasing during the recent years, especially in achieving good layers on glass for solar applications. It is apparent that coatings on plastics will follow this trend, especially for achieving antireflection properties on larger and slightly curved screens.

13.5 Conclusion

Optics increasingly appear in all aspects of our everyday lives. We see plastic optics used in eyeglasses, scanners, CD players, cameras for phones, automobiles, security, ink jet printers, image scanners, laparoscopic devices, diagnostic medical devices, fiber optics, identification and tracking systems, laser guided systems, displays, lighting systems and more.

New applications are being developed daily, particularly in medical and bio-photonic devices, smart phones and displays of all types. Precision plastic optics are at the forefront of these applications because of cost, ease of manufacture and the ability to make complex and multifunctional configurations in one part. Without the benefits of plastic optics many of these applications would not be feasible. As new ideas and applications expand, so do the demands for increased durability, environmental stability and stringent spectral output. The farther we stretch these physical limits, the more new innovative products will become feasible.

The challenge for AR coatings is to improve physical characteristics and achieve uniformity on complex surfaces ranging from micro to large parts with minimal angular effects. This needs to be accomplished with minimum cost and handling. Vacuum deposited coatings with appropriate plasma treatment have been successful in producing efficient, high quality antireflection coatings on plastics. At present it is the most widely used and practical method in the industry. The type of polymer selected has an impact on the adherence and environmental stability of the films and is an integral part of the finished result. Work continues in the development of organic coatings and nanostructures, both of which offer their own unique benefits depending on the application. An optimum solution for AR coatings may come from integrating multiple technologies combined in a unique way. Research has been directed in this area and continues with the goal to push the state of the art to the next level.

13.6 Sources of further information and advice

More information about plastic optics in general is available from the book 'Handbook of plastic optics' including one chapter about coatings (Bäumer, 2010). An online database for plastic materials is available which includes more than 55 000 data sheets (Kipp, 2010). Important review articles (Liston *et al.*, 1993; Gerenser, 2002; Weikart and Yasuda, 2000) and books (Agostino, 1990; Sabatini and Zambonin, 1993) deal with the surface chemistry of plasma-treated polymers. The special problems connected with vacuum coating of plastics are already covered in early review articles by Schaffer (1988) and Günther (1988). Other review articles are focused especially on plasma enhanced chemical vapor deposition (PECVD) processes (Martinu

and Klemburg-Sapieha, 2003) and on antireflection coatings (Schulz, 2006). Recently published review articles describe the state-of-the-art of ARS including several substrate materials (Chattopadhyay *et al.*, 2010) and give guidelines for the design of one-dimensional periodic surface microstructures for antireflective polymer lenses (Søndergaard *et al.*, 2010).

13.7 References

- Agostino, R. (1990) *Plasma Deposition, Treatment, and Etching of Polymers*, Burlington, Academic Press Inc.
- Araki, T., Ohashi, M., Tanaka, Y. and Shimizu, T. (Daikin Industries, Ltd.) (2003) *Curable fluoropolymer, curable resin composition containing the same, and anti-reflection film*. EP 1347001 A1. 24 September 2003.
- Ashley, C. S. and Reed, S. T. (US Department of Energy) (1990) Sol-gel antireflective coating on plastics. US patent 4,966,812, 30 October 1990.
- Bäumer, S. (2010) *Handbook of Plastic Optics*, Berlin, Wiley-VCH.
- Blacker, R., Bohling, D., Coda, M., Kolosey, M. and Marechal, N. (2000) ‘Development of intrinsically conductive antireflection coatings for the ophthalmic industry’, *Society of Vacuum Coaters: 43rd Annual Technical Conference Proceedings*, 212–216.
- Cebeci, F., Wu, Z., Zhai, L., Cohen, R. E. and Rubner, M. F. (2006) ‘Nanoporosity-driven superhydrophilicity’, *A Means to Create Multifunctional Antifogging Coatings*, **22**, 2856–2862.
- Chattopadhyay, S., Huang, Y. F., Jen, Y. J., Ganguly, A., Chen, K. H. and Chen L. C. (2010) ‘Anti-reflecting and photonic nanostructures’, *Materials Science and Engineering Reports*, **69**, 1–35.
- Chen, D. (2001) ‘Anti-reflection (AR) coatings made by sol-gel processes: A review’, *Solar Energy Materials & Solar Cells*, **68**, 313–336.
- Chen, Q., Hubbard, G., Shields, P.A., Liu, C., Allsopp, D. W. L., Wang, W. N. and Abbott, S. (2009) ‘Broadband moth-eye antireflection coatings fabricated by low-cost nanoimprinting’, *Applied Physics Letters*, **94**, 263118.
- Clapham, P. B. and Hutley, M. C. (1973) ‘Reduction of lens reflexion by the “moth eye” principle’, *Nature*, **244**, 281–282.
- Dislich, H. (1983) ‘Glassy and crystalline systems from gels: chemical basis and technical application’, *Journal of Non-crystalline Solids*, **57**, 371–388.
- Doerner, M.F. and Nix, W. D. (1988) ‘Stresses and deformation processes in thin films on substrates’, *CRC Critical Reviews in Solid State and Materials Science*, **14**, 225–268.
- Dobrowolski, J. A., Poitras, D., Ma, P., Vakil, H. and Acree, M. (2002) ‘Toward perfect antireflection coatings: numerical investigation’, *Applied Optics*, **41**(16), 3075–3083.
- Eyesaver International (2012), ‘Viewmax’ Premium Reflection and Glare Protection, Hanover (MA), Eyesaver International. Available from: http://www.eyesaver-international.com/viewmax_anti_glare.htm [Accessed 20 February 2012].
- Floch, H. G. and Belleville, P. F. (1994) ‘A scratch-resistant single-layer antireflective coating by a low temperature sol-gel route’, *Journal of Sol-Gel Science and Technology*, **1**, 293–304.
- Fozza, A. C., Roch, J., Klemburg-Sapieha, J. E., Kruse, A., Holländer, A. and Wertheimer, M. R. (1997) ‘Oxidation and ablation of polymers by vacuum-UV

- radiation from low pressure plasmas', *Nuclear Instruments and Methods in Physics Research B*, **131**, 205–210.
- Gaylord, T.K. and Moharam, M. G. (1985) 'Analysis and applications of optic diffraction by gratings', *Proceedings of the IEEE*, **73**, 894–937.
- Gerenser, L. J. (2002), 'Surface chemistry for plasma-treated polymers', in Glocke D. and Ismat Shah S., *Handbook of Thin Film Process Technology*, Taylor Francis, Sec E.3.1, vol. 2.
- Gibson, D. R., Walls, J. M., Brinkley, I., Teer, D. G., Teer, P. and Hampshire, J. (2004) 'Flexible and high throughput deposition of multilayer optical coatings using closed field magnetron sputtering', *Society of Vacuum Coaters: 47th Annual Technical Conference Proceedings*, 1–6.
- Gombert, A., Glaubitt, W., Rose, K., Dreibholz, J., Blasi, B., Heinzel, A., Sporn, D., Doll, W. and Wittwer, V. (1999) 'Subwavelength-structured antireflective surfaces on glass', *Thin Solid Films*, **351**, 73–78.
- Günther, K. H. (1988) 'Coating of plastics – coatings on plastic', *Proceedings of the SPIE*, **896**, 134–139.
- Hiller, J., Mendelsohn, J. D. and Rubner, M. F. (2002) 'Reversibly erasable nanoporous anti-reflection coatings from polyelectrolyte multilayers', *Nature Materials*, **1**, 59–63.
- Hofrichter, A., Bulkin, P. and Dréillon, B. (2002) 'Plasma treatment of polycarbonate for improved adhesion', *Journal of Vacuum Science and Technology A*, **20**, 245–250.
- Hook, T. J., Gardella, J. A. and Salvati, L. (1987) 'Multitechnique surface spectroscopic studies of plasma-modified polymers I: H₂O/AR plasma-modified polymethylmethacrylates', *Journal of Materials Research*, **2**, 117–131.
- Ishikawa, H., Honjo, Y. and Watanabe, K. (1999) 'Three-layer broad-band antireflective coating on web', *Thin Solid Films*, **351**, 212–215.
- Jiang, H., Zhao, W., Li, C. and Wang, Y. C. (2011) 'Polymer nanoparticle-based porous antireflective coating on flexible plastic substrate', *Polymer*, **52**, 778–785.
- Kaless, A., Schulz, U., Munzert, P. and Kaiser, N. (2005) 'NANO moth eye antireflection pattern by plasma treatment of polymers', *Surface and Coatings Technology*, **200**, 58–61.
- Kipp, D. O. (2010), Plastic Material Data Sheets, MatWeb – Division of Automation Creation, Inc. Available from: http://www.knovel.com/web/portal/browse/display?_EXT_KNOVEL_DISPLAY_bookid=1023&VerticalID=0 [Accessed 04 March 2012].
- Lau, K., Weber, J., Bartzsch, H. and Frach, P. (2009) 'Reactive pulse magnetron sputtered SiOxNy coatings on polymers', *Thin Solid Films*, **517**, 3110–3114.
- Lian, Y. M., Leu, K. W., Liau, S.L. and Tsai, W. H. (1995) 'Effects of surface treatments and deposition conditions on the adhesion of silicon dioxide thin film on polymethylmethacrylate', *Surface and Coatings Technology*, **71**, 142–150.
- Licciardello, A., Fragala, M. E., Foti, G., Compagnini, G. and Puglisi, O. (1996) 'Ion beam effects on the surface and on the bulk of thin films of polymethylmethacrylate', *Nuclear Instruments and Methods in Physics Research B*, **116**, 168–172.
- Liston, E. M., Martinu, L. and Wertheimer, M. R. (1993) 'Plasma surface modification of polymers for improved adhesion: A critical view', *Journal of Adhesion Science and Technology*, **7**(10), 1091–1127.

- Martinu, L. and Klemburg-Sapieha, E. J. (2003) 'Optical coatings on plastics', in *Optical Interference Coatings*, N. Kaiser and H. Pulker, eds., Springer-Verlag, Berlin, Heidelberg.
- Mendelsohn, J. D., Barrett, C. J., Chan, V. V., Pal, A. J. A., Mayes, M. and Rubner, M. F. (2000) 'Fabrication of microporous thin films from polyelectrolyte multilayers', *Langmuir*, **16**, 5017–5023.
- Minot, M. (1977) 'The angular reflectance of single-layer gradient refractive-index films', *Journal of Optical Society of America*, **67**, 1046–1050.
- Moravec, T. J., Hage, M. L. and Boulineau, M. S. (Vision-Ease Lens, Inc.) (2004) Rapid, thermally cured, back side mar resistant and antireflective coating for ophthalmic lenses. WO/2004/056495. 08 July 2004.
- Muir, B. W., Thissen, H., Simon, G. P., Murphy, P. J. and Griesser, H. J. (2006) 'Factors affecting the adhesion of microwave plasma deposited siloxane films on polycarbonate', *Thin Solid Films*, **500**, 34–40.
- Munzert, P., Schulz, U. and Kaiser, N. (2004) 'Transparent thermoplastic polymers in plasma-assisted coating processes', *Surface and Coatings Technology*, **173–174**, 1048–1052.
- Munzert, P., Schulz, U. and Kaiser, N. (2007) 'Method for the vacuum deposition of optical coatings on polymethyl methacrylate', *Plasma Processes and Polymers*, **4**, 1036–1040.
- Naito, S., Kinoshita, J., Kutsukake, Y., Mizuno, H. and Tanaka, H. (Seiko Epson Corporation) (2006) Plastic lens and method for producing plastic lens. WO/2006/095469. 14 September 2006.
- Narayan, R. (2008) 'Tutorial on biobased and biodegradable plastic films – new substrates for vacuum coating and related technologies', *Society of Vacuum Coaters: 51st Annual Technical Conference Proceedings*, 229–234.
- Nishida, M., Ohno, S., Yoshikawa, M. and Kato, N. (Bridgestone Corporation) (2002) Antireflection film. US patent 2002/0127408 A1, 12 September 2002.
- Oxford Advanced Surfaces (2012), VISARC™ Anti-Reflective Coatings, Oxford Advanced Surfaces. Available from: <http://www.oxfordsurfaces.com/content/visarc/visarc.asp> [Accessed 05 March 2012].
- Park, M. S., Lee, Y. and Kim, J. K. (2005) 'One-step preparation of antireflection film by spin-coating of polymer/solvent/nonsolvent ternary system', *Chemistry of Materials*, **17**, 3944–3950.
- Pongratz, S. and Zöller, A. (1992) 'Plasma ion-assisted deposition: A promising technique for optical coatings', *Journal of Vacuum Science and Technology A*, **10**, 1897–1904.
- PPG Optical Products (2012), Trivex® Lens Material. Available from: <http://www.ppg.com/optical/opticalproducts/opticalmaterials/Pages/Trivex.aspx> [Accessed 05 March 2012].
- Raguin, D. H. and Morris, G.M. (1993) 'Analysis of antireflection-structured surfaces with continuous one-dimensional surface profiles', *Applied Optics*, **32**, 2582–2598.
- Rank, R., Wuensche, T., Fahland, M., Charlton, C. and Schiller, N. (2005) 'Adhesion promotion techniques for coating of polymer films', *SVC Winter News Bulletin*, 34–42.
- Rivaton, A. (1995) 'Recent advances in bisphenol-A polycarbonate photodegradation', *Polymer Degradation and Stability*, **49** (1), 163–179.

- Sabatini, L. and Zambonin, P. G. (1993) *Surface Characterization of Advanced Polymers*, Cambridge, VCH publishers.
- Sakai, Y., Norimatsu, H., Saito, Y., Inomata, H. and Misuno, T. (2001) 'Silica coating on plastics by liquid phase deposition (LPD) method', *Thin Solid Films*, **392**, 294–298.
- Sarto, F., Alvisi, M., Melissano, E., Rizzo, A., Scaglione, S. and Vasanelli, L. (1999) 'Adhesion enhancement of optical coatings on plastic substrate via ion treatment', *Thin Solid Films*, **346**, 196–201.
- Schaffer, R. W. (1988) 'Problems and solutions for coating plastic optics', *Proceedings of the SPIE*, **896**, 140–144.
- Schottner, G., Rose, K. and Posset, U. (2003) 'Scratch and abrasion resistant coatings on plastic lenses – state of the art, current developments and perspectives', *Journal of Sol-Gel Science and Technology*, **27**, 71–79.
- Schulz, U. (2006) 'Review of modern techniques to generate antireflective properties on thermoplastic polymers', *Applied Optics*, **45**, 1608–1618.
- Schulz, U. (2010) 'Coating on plastics', in Bäumer, S., ed., *Handbook of Plastic Optics*, 2nd ed., Berlin, Wiley-VCH, 161–195.
- Schulz, U. and Kaiser, N. (2003) 'Thermal stress in antireflective coatings on polymer substrates', *Society of Vacuum Coaters: 46th Annual Technical Conference Proceedings*, 419–424.
- Schulz, U., Lau, K. and Kaiser, N. (2008) 'Antireflection coating with UV-protective properties for polycarbonate', *Applied Optics*, **47**, C83–C87.
- Schulz, U., Munzert, P., Leitel, R., Wendling, I., Kaiser, N. and Tünnermann, A. (2007) 'Antireflection of transparent polymers by advanced plasma etching procedures', *Optics Express*, **15**, 13108–13113.
- Schulz, U., Schallenberg, U. B. and Kaiser, N. (2002) 'Antireflection coating design for plastic optics', *Applied Optics*, **41**(16), 3107–3110.
- Seiko Optical Europe GmbH (2007) Orgatech-Press Release, Willich, Seiko Optical Europe GmbH. Available from: http://www.seiko_optical.com/fileadmin/media/de_sonstiges/startseite/SEIKO_Orgatech_pressrelease_consumer.pdf [Accessed 07 February 2012].
- Søndergaard, T., Gadegaard, J., Kristensen, P. K., Jensen, T. K., Pedersen, P. K. and Pedersen, K. (2010) 'Guidelines for 1D-periodic surface microstructures for antireflective lenses', *Optics Express*, **18**, 26245–26258.
- Tadanaga, K., Yamaguchi, N., Uraoka, Y., Matsuda, A., Minami, T. and Tatsumisago, M. (2008) 'Anti-reflective properties of nano-structured alumina thin films on poly(methyl methacrylate) substrates by the sol-gel process with hot water treatment', *Thin Solid Films*, **516**, 4526–4529.
- Vallon, S., Hofrichter, A., Dréville, B., Klemburg-Sapieha, J., Martinu, L., Poncin-Epaillard, F., Schalchli, A. and Benattar, J. (1996) 'Adhesion improvement of silica layers on polypropylene and polycarbonate induced by plasma treatments', *23rd International Conference on Metallurgical Coatings and Thin Films*, 325–330.
- Walheim, S., Schäffer, E., Mlynek, J. and Steiner, U. (1999) 'Nanophase-separated polymer films as high-performance antireflection coatings', *Science*, **283**, 520–522.
- Weikart, C. M. and Yasuda, H. K. (2000) 'Modification, degradation, and stability of polymeric surfaces treated with reactive plasmas', *Journal of Polymer Science Part A: Chemistry*, **38**, 3028–3042.

- Wendling, I., Munzert, P., Schulz, U., Kaiser, N. and Tünnermann, A. (2009) 'Creating anti-reflective nanostructures on polymers by initial layer deposition before plasma etching', *Plasma Processes and Polymers*, **6**, 716–721.
- Wu, L. Y. L., Chwa, E., Chen, Z. and Zeng, X. T. (2008) 'A study towards improving mechanical properties of sol-gel coatings for polycarbonate', *Thin Solid Films*, **516**, 1056–1062.
- Yamaya, M. and Sato, K. (Shin-Etsu Chemical Co., Ltd.) (2003) Antireflective, mar-resistant multilayer laminate. US patent 2003/0087102 A1, 8 May 2003.
- Yanagishita, T., Kondo, T., Nishio, K. and, Masuda, H. (2008) 'Optimization of anti-reflection structures of polymer based on nanoimprinting using anodic porous alumina', *Journal of Vacuum Science & Technology B*, **26**, 1856–1860.
- Yoshikawa, Y. and Yamaya, M. (Shin-Etsu Chemical Co., Ltd.) (2004) Antireflection films and their manufacture. EP 1403665 A2, 31 March 2004.
- Zhao, M., Yang, Z., Zhu, D. and Huang, D. (2005) 'Influence of the fabrication technique on the porous size of the polymer nanoporous antireflection coatings', *Journal of the Optical Society of America B*, **22**, 1330–1334.

Protective coatings for optical surfaces

T. W. BOENTORO, Fraunhofer Institute for Surface Engineering and Thin Films-IST, Germany and B. SZYSZKA, Institute for High-Frequency and Semiconductor System Technologies, Berlin, Germany

DOI: 10.1533/9780857097316.4.540

Abstract: Thin films and coatings are a backbone for optical applications in industry, medical equipment, automotive construction, building sector, even in household. Thin films applied on the substrate such as on glass or polymers, for example, polycarbonate, enable the substrate to gain beneficial functions which can improve its energy saving properties, optical transparency and operational life span. This chapter will focus on the application of protective coatings and some evaluation methods for characterizing and optimizing the coating quality.

Key words: protective coatings, scratch resistance, ITO, polycarbonate, finite element.

14.1 Introduction

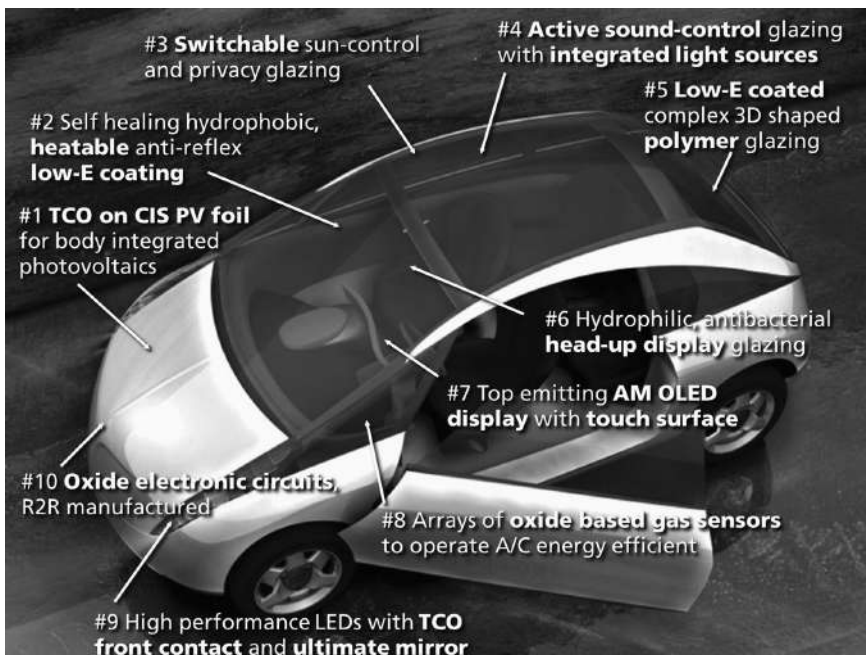
The continuous growth of thin film coating technologies is driven by industrial needs, that is, new coating functionalities, improvement of coating quality, production cost-efficiency and environmental aspects. Technological development of thin film coatings allows these useful functions to be applied elegantly on the optical surfaces as can be seen in Figs 14.1 and 14.2.^{1,2}

The protective coating on a polycarbonate (PC) substrate is an example of such a functional coating. Polycarbonate is an excellent alternative material for glass.³ It is transparent but it is also lighter, more impact resistant and can be produced in more complex shapes; however, polycarbonate can easily be scratched and degraded by UV-radiation. By applying functional coatings of some few micrometres thick,⁴ the mechanical and chemical properties of polycarbonate can be improved. The most common polycarbonate coating is made of heat cured, wet-chemical based lacquers.⁵ The UV-protection is provided by the organic UV-blocking molecules, which are dissolved in the wet chemical lacquer. This coating has very good adhesion but its hardness is relatively low for protecting the underneath coatings and substrate. Furthermore, the UV stability is limited due to the degradation of the UV-blocking molecules.⁶



14.1 Thin film application in architectural glazing can provide further functions such as low-emittance (low-E), sun control, antireflection, hydrophobicity and hydrophilicity. Even switchable optical properties can be achieved for example, by electrochromic coatings (left dark state, right transparent state).

Both issues, the mechanical properties and the UV stability, can be improved by dry, vacuum-based coating technologies^{5,7} which have been intensively developed for precision optics and ophthalmology.⁸ Thus, the coating of polycarbonate using a plasma coating technique has been a major theme over the last 15 years. However, coating techniques such as Physical Vapor Deposition (PVD) have to cope with the plasma and thermal load during deposition which may lead to micro-cracking and adhesion problems. The technology of plasma Ion Assisted Deposition (plasma IAD) offers coating processes at lower substrate temperature.⁹ This technique is



14.2 Potential application of functional thin film coatings in the automotive sector.^{1,2}

well suited for plastic coating and was basically developed for coating of injection-molded precision lenses under vacuum.

Plasma Enhanced Chemical Vapour Deposition (PECVD) technology offers the possibility of depositing coating on a larger geometry.⁵ This technique can also be divided into some competing technologies. One of them is the application of PECVD with RF-excited plasma polymerization technique. This technique was used in the early 1990s for applying the first hard coating system on CR39 plastic substrate. Primarily, this coating technique was aimed at competing with the already developed lacquer process technique.¹⁰ Another coating technology is the Plasma Impulse Chemical Vapor Deposition (PICVD). Here, plasma excitation is gained by coupling microwave power in a pulsed process. This technology is acceptable for optical lenses. However it is not scalable, therefore it is not suitable for automotive glass coating.¹¹

Generally, coatings on plastics applied with PECVD show good adhesion and scratch resistance, but the deposition rate is still low and must be improved. Further development has shown that employing microwave power can increase the deposition rates.¹² Moreover, the coating composition can be adjusted by regulating the reactive gas and precursors during

the deposition process. Such adjustment of the chemical composition is necessary to achieve soft, substrate-like mechanical properties near the substrate and hard, glass-like properties near the surface. This concept of gradient layers¹² is crucial in order to achieve highly adherent and scratch resistant layers.

Further, in mineral glass based architectural and automotive glazing (windshield, side window, quarter glass, sunroof, back window, etc.) the use of surface coating has increased tremendously.¹³ A glazing can be transformed into a multifunctional device by means of coating technology. For example, spectral selectivity allows for tailored optical properties, such as low-emissive (low-E) coatings which minimize the infrared (IR) radiation and thus heat losses.¹⁴ The same concept can also be used for near infrared light blocking to achieve sun protection. In general, such low-E or sun-control layers consist of complex insulator–metal–insulator stacks which must be encapsulated to hinder environmental degradation.

The deposition of more durable coatings on the outer or inner surface of the glazing allows for further functionalities: transparent and conductive oxide layers can be used as heatable electrodes and even as low-E coatings on the outer pane of the window to minimize thermal losses. The ice-free window¹ takes advantage of such a low-E coating on the outer surface.

Further functions can be achieved by coating technologies, such as hydrophobicity¹⁵ or hydrophilicity.¹⁶ Hydrophobic coatings serve as non-stick surfaces and thus as easy-to-clean coating.

They can be produced either by wet chemical deposition¹⁵ or by low pressure plasma processes such as sputtering¹⁷ and PECVD.¹⁸ Hydrophobic layers on automotive windshields may substitute the use of wipers.

Hydrophilic layers on the other hand increase the surface energy of the glass. The formation of stray light and unwanted reflections due to water droplets is suppressed.¹⁹ Such hydrophilicity can be achieved, for example, by short wavelength illumination of photocatalytic materials such as TiO₂, where the photocatalyst is also used for the decomposition of organic contaminations²⁰ such as fingerprints.

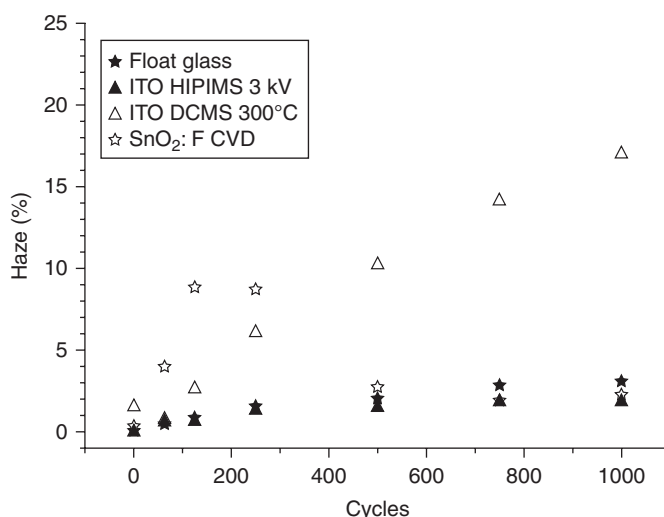
Another advantage of coating technology is the increase of material lifespan. For example, corundum (α -Al₂O₃) coating, which is harder than quartz, was studied to increase the abrasive resistance of windshields. A coating of 100 nm was deposited by sol gel technique in combination with thermal heating (1200°C) to form optimal corundum properties with 10 nm grain.²¹

The next interesting development on surface coating is adapted from aeronautical application. De-icing of aircraft windows by transparent and conductive layers serving as ohmic resistors have been used since 1940s.²² Fluorine doped tin oxide (SnO₂:F, FTO) deposited by spray pyrolysis on large area glasses has been utilized. Furthermore, a low emittance (low-E) coating on the outside of the window pane (position 1) allows also for

an ice-free window even without heating.²³ In the 1980s, researchers at the University of Uppsala and Volvo had applied these airplane window coatings to automotive winds. $\text{SnO}_2:\text{F}$ coating which was deposited by pyrolysis, had reconfirmed this concept. They showed that part of the windshield which was treated with this coating stayed ice-free while the uncoated part was fully covered with ice film.²⁴ However, the pyrolysis technology resulted in the formation of rough layers which caused substantial wear of the windshield when mechanical load was applied. Therefore, the coating could not fulfill the automotive glazing standard requirements.²⁵ After the initial work by Laffay²³ and Hamberg,²⁴ the subject of FTO coatings for windshields was not followed up. Further oxide material which has beneficial properties for durable low-E coatings is tin doped indium oxide ($\text{In}_2\text{O}_3:\text{Sn}$) (Indium tin oxide, ITO). It has been an important subject of many studies since it also allows application on bendable layers on glass, thus improving its scratch resistance compared to uncoated glass surface (Fig. 14.3).

For use in fine optics like ophthalmic lenses, camera filters, watches, etc., thin film coatings play an essential role because the coating system has to satisfy a complex set of requirements such as reduction of the reflection in external view with high mechanical stability.

In general, most of the aforementioned coating applications are dealing with the external environment such as impact and abrasive processes from dust or sand particles, UV-radiation and chemical attack. In automotive applications, the coatings have to additionally face mechanical loads due to car washing, wipers, ice scraping, etc.



14.3 Abrasive performance of float glass, ITO HIPIMS, ITO dc and $\text{SnO}_2:\text{F}$ coatings.²⁵ DCMS, direct current magnetron sputtering.

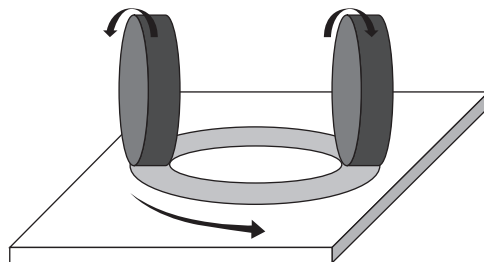
Therefore, the application of protective coatings needs careful selection of material and technique which can provide high mechanical toughness, as well as chemical and UV resistance, in order to perform the required functions with long-term stability.

14.2 Testing methods

Owing to the exposure to abrasive processes at the outside of the window pane, coatings in these positions require high mechanical stability. Therefore, the evaluation of coating durability is essential. There are diverse methods and coating property measurements for quantifying coating mechanical durability and some of the tests have been standardized according to their field of application. The methods for evaluating the coating quality in automotive glazing are covered in the international regulation for vehicle glazing ECE R43²⁶ and the test methods in architectural glazing mostly referred to are DIN ISO 9211–3²⁷ and DIN ISO 9211–4,²⁸ which can be combined with test methods from automotive applications. Some of these principal test methods are specified in this section.

14.2.1 Taber abrasion test

To evaluate the mechanical stability of coatings, various abrasion tests have been developed, for example, Taber test, sand drop, oscillating sand abrasion (Bayer Test), steel wool abrasion, eraser rub test, etc. Taber abrasion is one of the commonly used methods for evaluating the coating resistivity against wear, which corresponds to DIN standard 52347.²⁹ In this test, the planar samples with upside surface coating are placed against a pair of abrading wheels and each wheel is weighted by 500 g load. The sample rotates and consequently the abrading wheels rotate in the opposite direction. Figure 14.4 shows the schematic of the taber abrasion test. The abrasion resistance of the sample can be quantitatively evaluated by measuring



14.4 Schematic of taber abrasive test.

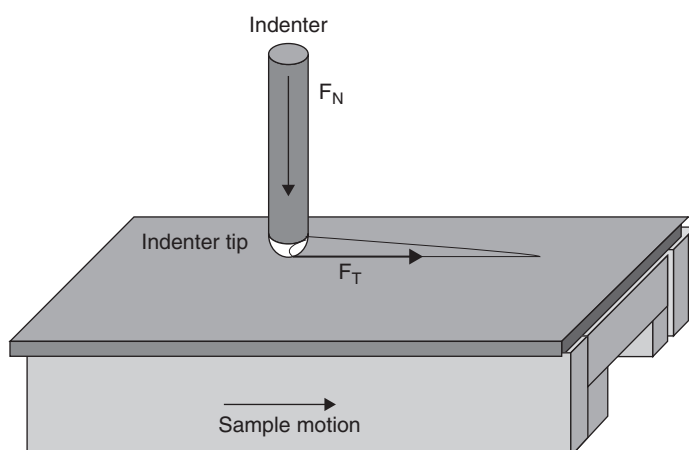
the increase of the haze (refer to Section 14.2.9) before and after the test in the four positions of the abraded area. The abraded area of an uncoated glass has haze increase of about 2% after 1000 cycles. Functional coating on glass substrate should have at least a comparable abrasive resistance to uncoated glass or even better.

14.2.2 Sand trickling

The sand trickling test is used for characterizing the coating abrasion due to impact. According to DIN standard 52348,³⁰ 3 kg of sand with defined grain size should be dropped over the rotating coating sample from a 1.5 m elevation. The surface damage can be quantified by comparing the haze before and after the sand trickling test (see Section 14.2.9).

14.2.3 Scratch test

The scratch test is one method for evaluating the coating adhesion and scratch resistivity. The scratches can be produced by loading the diamond indenter or other specified tip on the coated surface with increasing load, specific velocity and length. Figure 14.5 presents the schematic of the scratch test. Sliding, pulling and ploughing occurred simultaneously³¹ during the scratch test. Many different failures are observed afterwards, which include coating detachment, through-thickness cracking and plastic deformation or cracking in the coating or substrate.³² Based on the interest of the failure type that occurs at a load, the critical load can be determined. However, the



14.5 Schematic of the scratch test.

scratch lengths can also be used as a criterion. The loads causing the visible scratch determine the critical load that can be carried by the coating.

14.2.4 Hardness and indentation elasticity

One method used to characterize mechanical properties of the coating is measuring the hardness and indentation elasticity of the coating. The hardness and indentation elasticity are determined by extracting the indentation load–displacement curve which is obtained during loading and unloading. However, to get a reliable result without substrate influence, the indentation depth should be at least 10% of the coating thickness. Nano-indentation is used in the case of indentation depths smaller than 100 nm and micro-indentation is used for indentation depths larger than 100 nm.³³

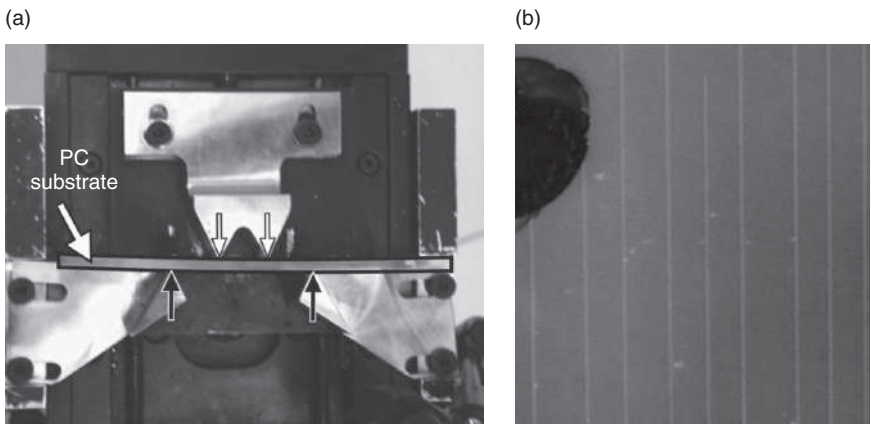
For sensing the substrate influence, the indentation can be started at very low indentation loading at some statistical measurement points, where the coating properties dominate the measurement (for examples indentation series of 1, 2, 5 10 and 30 mN).

14.2.5 Crack onset strain

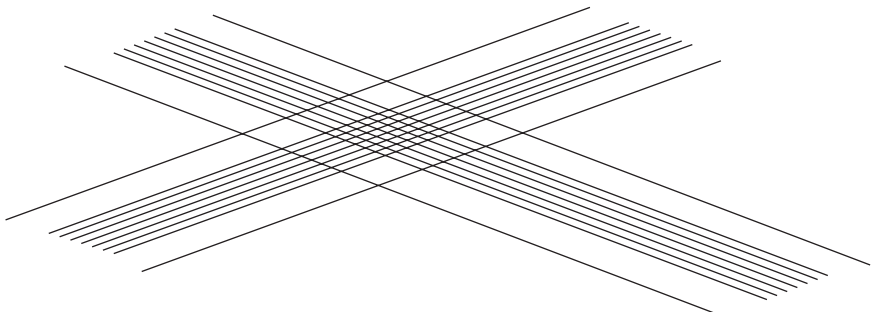
Polycarbonate as substrate is softer and much more elastic in comparison to glass substrate. The coating applied on such a substrate, needs toughness in order to follow the flexibility of the substrate. One method to observe the coating toughness is by using Crack onset strain (COS).³⁴ This method is essentially based on a four-point bending loading system. The coated polycarbonate will be stretched and bent with the help of micrometer screw. By using a binocular loupe, first crack occurrence can be observed. Then, based on the measured displacement at the first cracks, the maximum strain at failure will be obtained (Fig. 14.6).

14.2.6 Adhesion

Coating adhesion of polycarbonate is known to be critical and many studies have been carried out to improve the coating adhesion on polycarbonate.^{35–37} Therefore, the methods for evaluating adhesion are expanded as well. However, in the optical industry, crosshatch and peel test is one of the common methods for evaluating the coating adhesion.^{38,39} The cutter contains multiple and equally spaced blades. When the cutter is applied carefully with steady pressure, the blades will generate parallel cuts. The second cut performed at a 90° angle to the first cut will form a square pattern (Fig. 14.7). Here, the primary adhesion, which is unaffected from the adhesive tape, can be observed. Based on the amount of delamination in



14.6 Four point bending test for measuring the strain at failure Crack Onset Set (COS), where the coated samples will be stretched and bent (a). The occurrence of the first cracks in the deflection of the substrate was observed with a binocular microscope (b). Based on the substrate deflection at failure, the maximum strain will be calculated.



14.7 Surface damage by crosshatch cutter for evaluating the coating adhesion on plastic substrate.

the square area, the coating adhesion can be classified visually from 0 to 5. The 0 value refers to no delamination and the increased detachment area of the cross cut of less than 5% (grade 1), 5–15% (grade 2), 15–35% (grade 3), 35–65% (grade 4) and value of 5 corresponds to larger delamination than grade 4 at the observed cross cut area. Afterwards, the tape test is carried out over this pattern. The type of adhesive tape and its removal, as well as the detailed grading of the detached cross cut area, are described in DIN EN ISO 2409.⁴⁰

Coatings with excellent adhesion can be further evaluated at the intensified test level. This evaluation involves the crosshatch test, tape test and additionally the boiling test. The boiling test simulates the temperature and

humidity load to the coating which is critical due to the major difference from the thermal expansion coefficient of polycarbonate $70 \times 10^{-6}/\text{K}$ and general like glass coating $0.56 \times 10^{-6}/\text{K}$. This difference may induce significant stress at the interface. The boiling test at the early test phase can be combined by switching from boiled deionized water to room temperature at settled time for several cycles, and at the next level, it can be extended periodically.

14.2.7 Weathering

The weatherability of coatings on optical surfaces is dependent upon complex interactions of environmental aspects – mainly solar radiation – temperature and humidity which are also related to the geographical area.⁴¹ For outdoor uses, these aspects negatively influence the service life of polycarbonate because, when exposed to UV-radiation, photolysis reactions can occur and induce degradation such as discoloration and loss of mechanical properties.⁴² A similar behavior is also observed in siloxane-based hardcoats on polycarbonate where the coating becomes brittle in outdoor exposure. Moreover, during the service life for automotive application, the damage may occur due to car washing or dusty environments. Coating degradation caused by mechanical loadings may result in damage in the micrometer scale (mar) or even larger damage such as scratches, which could be further enhanced by additional outdoor exposure. As a result, the catastrophic cracking of polycarbonate may be induced and followed by delamination of the hardcoats.^{43,44} Polycarbonate requires not only a proper scratch resistance coating, but also a UV absorbing layer. To evaluate the lifetime of the coating system, it is necessary to study the stability of the coating in general weather. For this application, the critical weathering environments are represented in the following example of test environments:

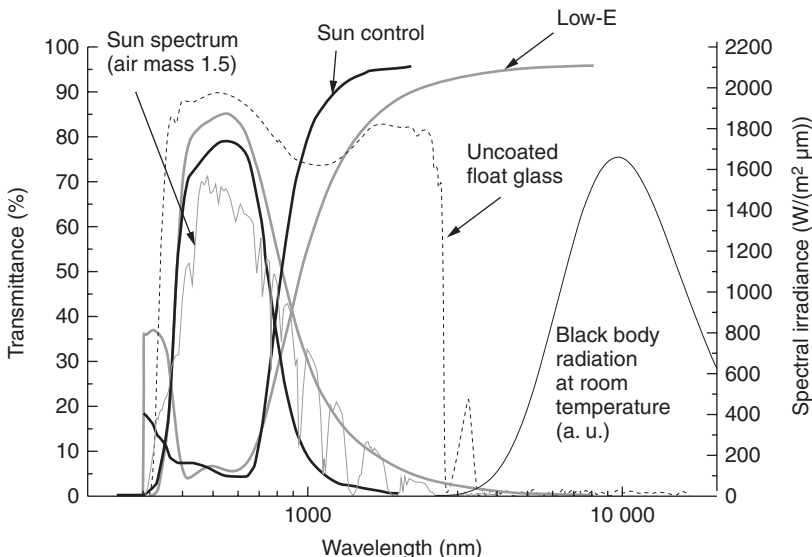
- South Florida: high intensity and duration of solar radiation, high average temperature, high humidity and rainfall.
- Arizona desert or Kalahari, South Africa: high intensity and long duration of solar radiation, high annual average temperature, low humidity and almost no rainfall.

For accelerated weathering testing, there are some industrial climatic tests,⁴⁵ which simulate climates such as Florida or Arizona and can be combined with varying temperature, humidity, etc. Polycarbonate coatings would need to show sufficient mechanical and chemical stability for at least 3000 h of an accelerated Florida weathering test,⁵ which is equivalent to 3 years of outdoor exposure.

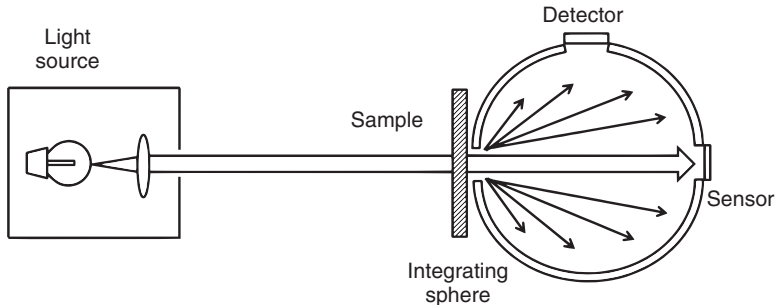
14.2.8 Characterization of optical properties

Optical spectroscopy is the general method for characterizing the optical properties of the coatings such as reflectance and transmittance in the region of the electromagnetic spectra. The range of spectrometer measurement depends on the field of application. For polycarbonate coating, the optical properties of the coating from the UV to visible wavelength range are essential, and according to the experiments by Lau,⁴⁶ the coating with UV-protection function should have an absorption edge in the range 380–400 nm.

The analysis of transparent conductive coatings needs broader electromagnetic spectra. Figure 14.8 shows a solar control coating which allows the transmittance of light in the visible wavelength range, but reflects the heat from the near infrared wavelength region to reduce the cooling costs. On the other hand, low-E coating properties have shown to be able to transmit light in the visible and near infrared wavelength regions, which is important in order to allow the visible light and near infrared energy from the sun to enter the room. Moreover, the black body radiation which has its maximum in the far infrared region can be reflected back into the room.¹⁴ Szczyrbowski *et al.*⁴⁷ showed that the electrical conductivity of the coating is directly related with the emissivity where emissivity is $(1-R)$. Therefore, the amount of heat transfer can be determined by measuring the electrical conductivity of the coating and its spectral reflection in the far infrared range. This ability to reduce heat transfer (U_g -value) is described by the mathematical method in the European Standard EN 673.⁴⁸ Due to the spectral



14.8 The transmission and reflection of low-E, solar control coating and uncoated glass in comparison to the sun spectrum and the radiation of black body at room temperature.¹⁴



14.9 Schematic of haze meter measurement principle. Incidence of light directed through the sample. A detector captures the difference of the diffused and transmitted light.

selective properties, the coatings can be optimized for reducing the energy used to heat or to cool buildings.

14.2.9 Haze

The mechanical wear on a coating results in surface defects, which become critical in the visible wavelength range. To evaluate the performance of the coatings, the defects can be inspected visually and also determined quantitatively by measurement of haze (ASTM D1003).⁴⁹ Haze is defined as percentage of the transmitted light which is diffusely scattered due to surface defects, compared with the total transmitted light (Fig. 14.9).

14.3 Coating design

In order to achieve the optimum coating performance, it is necessary to consider the material selection, the coating process and their influence to the production costs. Additionally, computer based simulation enable the observation of coating behavior for example due to mechanical and thermal loading, which may improve the coating system functionality.

14.3.1 Coating system on glass substrate

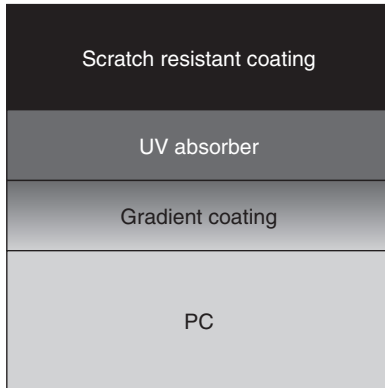
The current development of the magnetron sputtering technique allows low-cost industrialization of large scale and large area ITO with better mechanical stability. In one reported example, in the field of large area flat panel displays,⁵⁰ ITO with an average thickness of 100 nm and a substrate area of about 0.6 m² has fulfilled the necessary properties for flat panel displays. The specific resistivity is about 150 $\mu\Omega$ cm and transmittance value is above 92% at 550 nm wavelengths. These properties can be achieved by polycrystalline ITO films which are induced by elevating the substrate temperature

(200°C) during the deposition. However, heating the substrate during the coating step is less economically effective for industrialization. As an alternative, post annealing is mostly preferred to attain polycrystalline coatings with excellent properties. Previous work had been done to improve the quality of the coating during the magnetron sputtering process. Kouznetsov *et al.* have shown the sputtering technique of high power pulse magnetron sputtering (HPPMS) which is also known as HIPIMS (high power impulse magnetron sputtering). This technique improves the plasma densities and the sputtered material ionization, which allows depositing the coating with enhanced adhesion and film structure, and with consistent manufacturing properties.⁵¹ In comparison to HIPIMS application on architectural glazing and flat panel displays, the form of windshields is typically curved according to their design and styling. For this demand, coatings for windshields challenge this technique even further because the homogeneity of the magnetron sputtering technique on 3-dimensional substrate is insufficient. Therefore, annealing and bending should be carried out after ITO deposition, which is economically more efficient. To protect ITO from oxidation during the annealing process, the ITO needs a top coating to encapsulate the system.²⁵ Based on the previous study of SnO₂:F, which has premature wear in the abrasive test due to the high surface roughness, the complete stack of the encapsulated ITO system has a smoother surface in comparison to the SnO₂:F coating.

14.3.2 Coating system on polycarbonate

The beneficial properties of polycarbonate may be exploited for replacing mineral glasses by improving its mechanical stability through coating techniques. Hard material for coating on soft polycarbonate is expected to protect the substrate.⁵ However, a coating with high hardness applied on soft polycarbonate, will induce the so-called ‘eggshell’ effect. When an impact load is applied, the soft substrate is plastically deformed prior to the harder coatings, and the hard coatings induce high stress difference at the interface. This condition may lead to abrupt delamination. Therefore, the coating system on polycarbonate needs a proper gradual adjustment of mechanical properties to improve the coating adhesion between the substrate (extremely low hardness, low elasticity) and the harder coating (higher hardness, higher elasticity), in addition to integrating the UV protective coating (Fig. 14.10).

The gradient coatings can be obtained by varying the coating properties (from organic to inorganic), the coating composition (hydrocarbons to oxides) or the coating microstructure (columnar to amorphous). PECVD allows the deposition of gradient coatings which involves the silicon-containing monomers such as tetramethylsilane (TMS), hexamethyl-disiloxane (HMDSO), etc. The material properties of the deposited coatings can be



14.10 Schematic design of coating stack with gradient adjustment coating from soft to hard properties to bridge the UV absorber and scratch resistant coatings.

controlled by varying the process parameters such as plasma power, activation and oxygen flow.

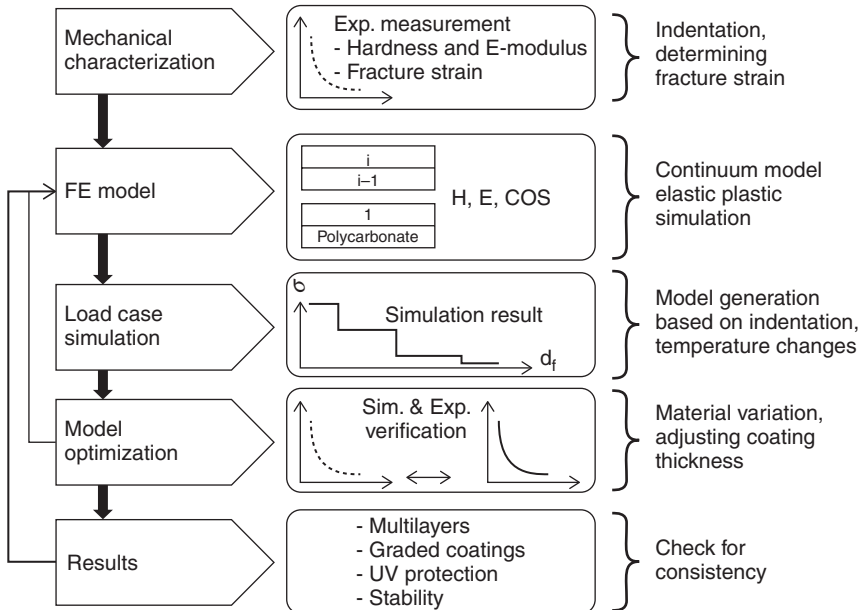
14.3.3 Numerical simulation

To optimize the efficiency of the coating stacks, it is important to study the mechanical behavior of the coating under loading in terms of numerical methods. The finite elements method serves an effective tool to analyze and optimize the mechanical and thermal behaviors of various coating systems. Figure 14.11 showed the development of numerical simulations based on experimental setup. From experiments such as indentation elasticity and COS, the material parameter can be extracted and used in the simulation models (Fig. 14.12).

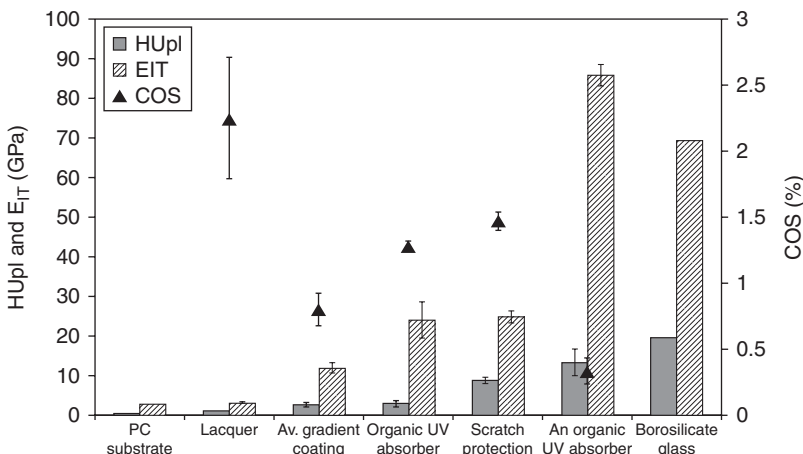
As an example, simulation of the cooling down of PC/SiO_x, had shown that the major compressive stress is located between the glass-like coating and the substrate. By modeling the gradation layer between the coating and the substrate, the stress could be distributed into these gradation layers, and the stress mismatch at the interface reduced. (Fig. 14.13). Such a result will be helpful in lowering the experimental expenses and overestimation of the coating material selection, which will optimize the material cost in production.

14.3.4 Multi-functional coatings

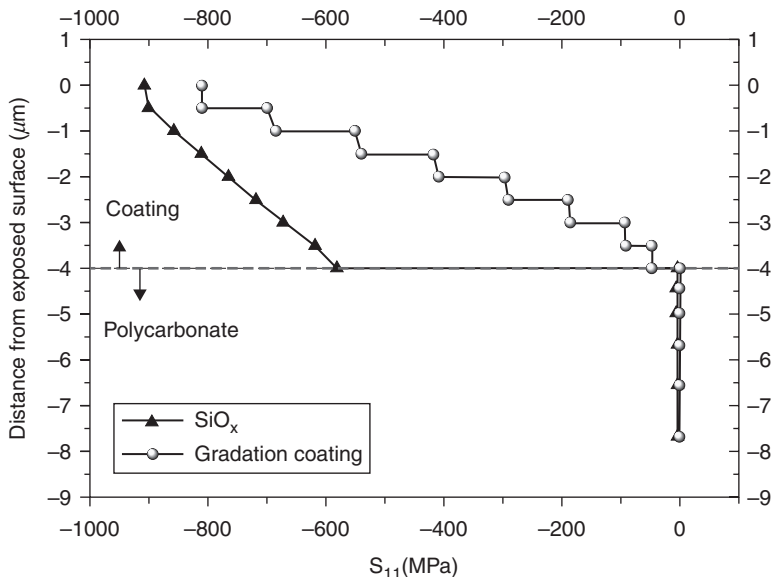
It is a very attractive proposition to combine in PC coatings the functions such as UV protection, scratch resistance, photo catalysis and anti-reflection. However, the obstacle of coating on PC is its adhesion. This is caused by the major difference in thermal expansion coefficient of the coatings and the PC. Therefore, it is essential to improve the adhesion of



14.11 Overview of simulation and experimental result for understanding the critical condition under diverse load cases and optimizing the coating system.



14.12 Experimental results of indentation and bending tests from diverse coatings in comparison with polycarbonate and glass substrate. H_{Upf}, plastic hardness.



14.13 The stress distribution of a simulation example two coatings system with and without gradient after 100°C cooling. The stress jump in substrate/coating interface is minimized by applying starter coating which has properties close to the substrate.

the PC/coating interface. Most functional coatings have specific material properties which are different from PC. The best approach to improving adhesion at the interface is by applying a coating which can follow the deformation of PC in case of loading. This can be achieved by depositing a coating which has similar mechanical properties to PC. To combine these functional coatings, some micrometer coatings can be inserted to adjust the material properties. A proper coating technique allows deposition with controlled hardness and elasticity. By depositing a PC-like coating next to the substrate, followed gradually by coatings with harder and stiffer properties, further functional coatings can be combined consecutively. As a result, a long-term stable PC with diverse functional coatings and sufficient adhesion can be obtained.

14.4 Application examples

Protective coating especially for outside application is substantial against environmental influences. As examples, transparent and conductive oxides are useful as low emissivity (low-e) coating to prevent moisture formation on the outer glass surface. For the emerging field of polycarbonate (PC) glazing, scratch protecting films are necessary to achieve mechanical properties similar to glass on soft substrates.

14.4.1 Low-E coatings on windshield

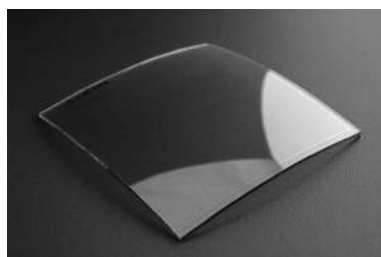
By adapting high power pulse magnetron sputtering, ITO coatings have been developed for windshield application without substrate heating.²⁵ The ITO film on the glass substrate has a thickness of about 140 nm. To avoid oxidation of the ITO during annealing, a 40 nm silicon oxynitride (SiO_xN_y) film is always deposited on top of the ITO. The ITO coating, which is deposited by an optimized process and annealed, has a transmittance of more than 80% and a resistivity lower than 300 $\mu\Omega \text{ cm}$. The coating structure without heating is polycrystalline, and this structure remains unaffected after annealing. The optimized coating process has been performed by 3 kV charging voltage and this coating has shown better performance in mechanical stability in comparison with the $\text{SnO}_2:\text{F}$ ITO from DC processing coating and uncoated glass.

In a taber abrasive test, the conventional ITO DCMS coating with 300°C substrate heating showed an increased haze of 17% after 1000 cycles. The uncoated glass reached about 2% haze after 1000 abrasive cycles. The pyrolysis $\text{SnO}_2:\text{F}$ coating showed haze of 10% after 200 taber rotations and then the haze decreased to the haze of uncoated glass. The ITO HIPIMS performed likewise and ended up even lower than the haze of uncoated glass. According to the atomic force microscopy (AFM) surface roughness analysis, the root-mean-squared (rms) roughness of ITO HIPIMS coating is about 2 nm in comparison with the pyrolysis $\text{SnO}_2:\text{F}$ coating with rms roughness of 18 nm which could be one reason for the wear instability of $\text{SnO}_2:\text{F}$ coating.⁵²

The sand trickling test confirmed the result of the abrasive test. After 3 kg sand fell over the coating, the haze of the ITO HIPIMS coating was about 0.6%, followed by float glass with 0.8%, and ITO DCMS with 1% haze.

The scratch test using a Rockwell indenter with linearly increasing load 1–30 N and 5 mm/min velocity has shown that the optimized ITO HIPIMS (3 kV) has higher average critical load (14 N) in comparison to the uncoated glass (8–13 N (annealed)) and other variants of ITO HIPIMS (2 kV) for 12.5 N.

Figure 14.14 gives an example for an annealed and bent glass pane which shows the stability of the coating. In Fig. 14.15, the thin metal layer on the glass substrate demonstrates its functions for outer application.



14.14 ITO coating on glass after annealing and bending.



14.15 Two glass panes are set side by side under the same weathering conditions for comparison: uncoated glass (left); ITO coating on the glass pane (right) remains ice-free.¹

14.4.2 Polycarbonate in automotive glazing

Thus, polycarbonate has exciting opportunities in the automotive industry especially for weight reduction which could increase fuel efficiency. The replacement of traditional glass with polycarbonate is mainly used for the panoramic roof, lighting system and fix side car windows. These applications demand a high environmental stability since the exposed surfaces are subject to weathering, UV-radiation and mechanical wear. Therefore, the coating technology is challenged to answer these needs.⁶ For automotive polycarbonate glazing, there are some works for depositing SiO₂ protective coating. The plasma enhanced chemical vapor deposition (PECVD) technique has shown that the coatings are able to fulfill the automotive criteria, but the deposition rates of this technique are low. To improve the deposition rates with almost similar coating quality, hollow cathode activated deposition (HAD) has been further developed.⁴ However, for industrial implementation, the HAD technology has met difficulties in depositing the UV protective coating. As an alternative to those techniques, a promising concept combines the available UV-protective coating from a lacquer process and scratch protective coating from PECVD technique. The major constraint of this concept lies in its particular two-stage process (i.e., coating of primer and UV protection, followed by vacuum coating), which increases the cost

structure significantly. PECVD seems to be very promising for depositing the SiO_2 coating with good adhesion and scratch resistance. To increase the rate, Schmauder and team⁵ have worked with microwave power during the PECVD process and shown that this technique can compete economically with the lacquer technique. However, the next demanding criteria, that is, the UV-stability of the whole system, remains a major topic for research.

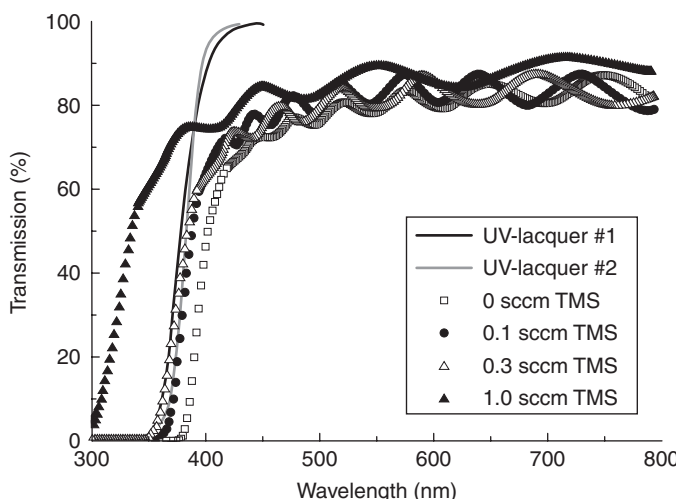
Sputtered UV-protective coating on polycarbonate

Coating on polycarbonate for exterior applications needs to be protected at the solar wavelength in the wavelength range of 350–400 nm. To answer this need, classical materials such as titanium oxide and zinc oxide are potential candidates to be applied as UV-protective coating. By using a specific sputtering technique, that is, Gas Flow Sputtering (GFS), such coating can be deposited. This development of zinc oxide coating has been shown in Figs 14.16 and 14.17 by Luebke.⁵³

Although the prepared coatings are whole, the adhesion of zinc oxide failed in the boiling test. This happened due to the great difference in thermal expansion between polycarbonate ($65 \times 10^{-6}/\text{K}$) and the zinc oxide coating ($4 \times 10^{-6}/\text{K}$).⁵⁴

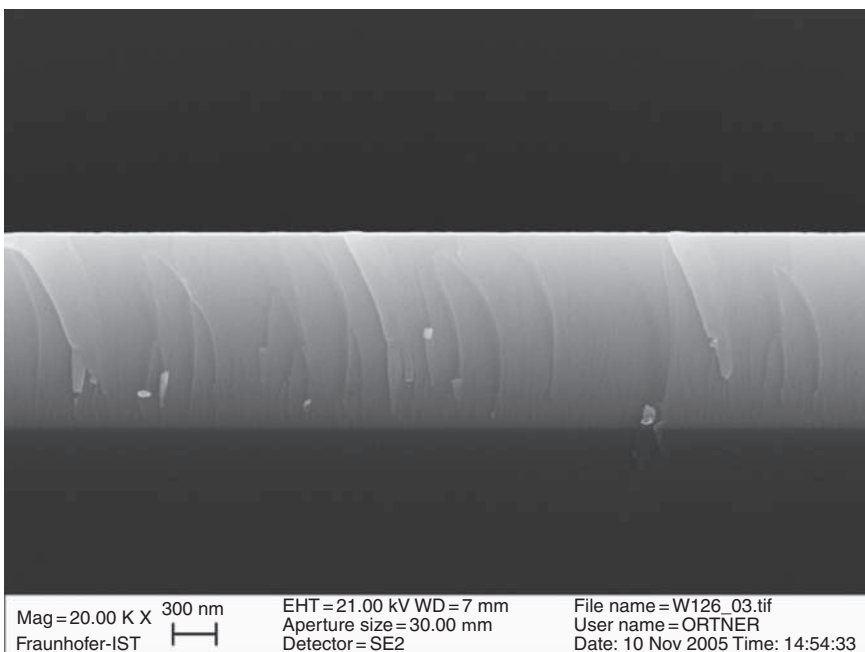
Optimized adhesion of functional coating on polycarbonate

A graded transition coating is needed to bridge the soft polycarbonate and the harder zinc oxide coating. After the boiling test, to date, no zinc oxide coatings survived when they were directly deposited on the polycarbonate.⁵³ With the graded coating in between, the system has showed much better

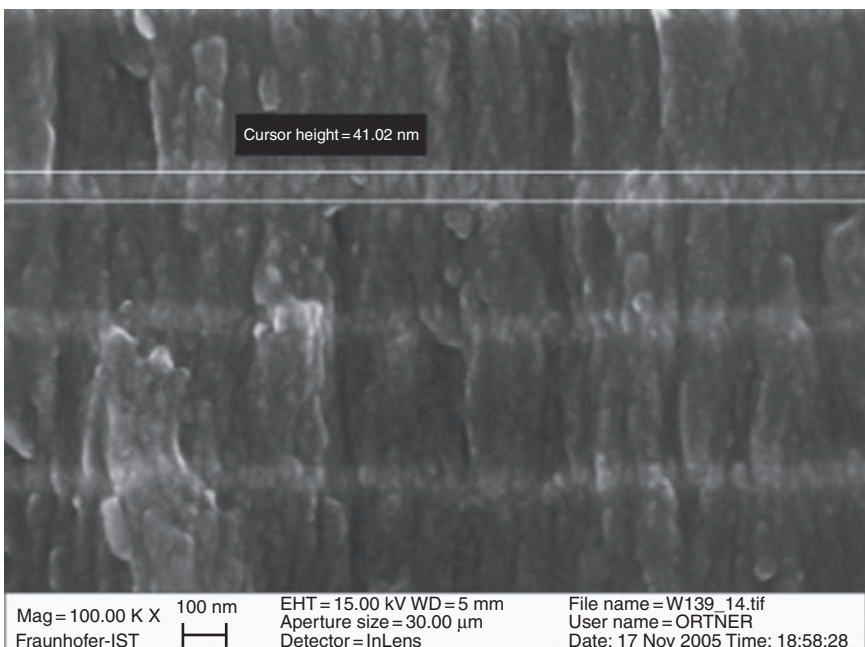


14.16 UV absorption edge of lacquers, ZnO and ZnO:TMS samples.⁵³

(a)



(b)



14.17 Breaking edge of ZnO:TMS on silicon wafer with dense morphology (a). Multi-layer coating of ZnO and ZnO:TMS (b).⁵³

adhesion stability in the boiling test. The stress in the coating caused by thermal loading of boiling water can be distributed in the graded coating, thus reducing the stress jump at the polycarbonate interface.

14.5 Conclusion

The continuous development of coating material and process techniques enables the expansion of the coating application and functionalities. The ITO coating enhances the range of its functionalities. For windshield application in particular, the ITO coating has shown its excellent transmittance, low resistivity and consistence after annealing and bending. In mechanical tests, this coating provides better scratch resistance in comparison to uncoated glass and prevents the windshield from freezing. These characteristics confirm the great potential of this coating on weather exposed windshields. Additionally, application of such coating properties could further be used as triple glazing in buildings, which can improve the insulation from condensation on the outside of the glass panes. Furthermore, the coating can also be used as a heat conductor. In chemical process engineering, for example, reactor vessels can be equipped with a transparent heating system.

The functionalities such as scratch and UV-resistance with good adhesion may sustain the lightweight properties of polycarbonate. With the assistance of numerical simulations, the critical conditions of the coating can be studied and optimized. Large area coating with plasma technology is addressing the challenge for improving the deposition rate. However, some progressive studies in optimizing process parameters and combining microwave activation have shown promising results. The development of realistic multi-scale models bridging the gap from material properties to layer designs and coating processes appears as a new and very powerful approach to fulfill these urgent demands on low cost deposition of high performance coatings.

14.6 References

1. Szyszka, B., Dewald, W., Gurram, S.K., Pflug, A., Schulz, C., Siemers, M., Sittinger, V. and Ulrich, S. (2012), 'Recent developments in the field of transparent conductive oxide films for spectral selective coatings, electronics and photovoltaics', *Current Applied Physics*, **12**, S2–S11.
2. Bewilogua, K., Bräuer, G., Dietz, A., Gäbler, J., Goch, G., Karpuschewski, B. and Szyszka, B. (2009), 'Surface technology for automotive engineering', *CIRP Annals – Manufacturing Technology*, **58**, 608–27.
3. Staudigl, G., Benien, H. and Suchentrunk, R. (2000), 'Transparente Kratzschutzbeschichtungen für Kunststoff', *Mat.-wiss. u. Werkstofftech.*, **31**, 360–4.
4. Katsamberis, D., Browall, K., Iacovangelo, C., Neumann, M. and Morgner, H. (1998), 'Highly durable coatings for automotive polycarbonate glazing', *Progress in Organic Coatings*, **34**, 130–4.

5. Schmauder, T., Nauenburg, K.-D., Kruse, K. and Ickes, G. (2006), 'Hard coatings by plasma CVD on polycarbonate for automotive and optical applications', *Thin Solid Films*, **502**, 270–4.
6. Sargent, J. R. and Pickett, J. E. (2006), 'Accelerated weathering using xenon arc with boro/boro filters, important factors for testing and translation to standard 5° FL outdoor test protocols', *Proceedings ICCG*, Dresden, 18–22 June 2006, 215–9.
7. Suchentrunk, R., Fuesser, H. J., Staudigl, G., Jonke, D. and Meyer, M. (1999), 'Plasma surface engineering – innovative processes and coating systems for high-quality products', *Surface and Coatings Technology*, **112**, 351–7.
8. Beckmann, R., Deppisch, G., Hagedorn, H., Hermann, H.-U., Naumann, T. and Pistner, J. (2002), 'Beschichten transparenter Kunststoffe mit Kratzschutz und AR in einer kombinierten InLine-Anlage', *Vakuum in Forschung und Praxis*, **1**, 9–15.
9. Schulz, U., Jakobs, S. and Kaiser, N. (1996), 'SiO₂ protective coatings on plastic optics deposited with plasma-IAD', *In SPIE*, **2776**, 169–74.
10. Wohlrab, C. and Hofer, M. (1995), 'Application of plasma polymerization on ophthalmic lenses: equipment and processes', *Optical Engineering*, **34**, 2712–8.
11. Kuhr, M., Bauer, S., Rothhaar, U. and Wolff, D. (2003), 'Coatings on plastics with the PICVD technology', *Thin Solid Films*, **442**, 107–16.
12. Beckmann, R., Nauenburg, K.-D., Naumann, T., Patz, U., Ickes, G., Hagedorn, H. and Snyder, J. (2001), 'A new high-rate deposition process for scratch- and wipe-resistant coatings for optical and decorative plastic parts', *Society of Vacuum Coaters*, 44th Annual Technical Conference Proceedings-Philadelphia, 21–26 April 2001, 288–94.
13. Gläser, H. J. (2007), 'The European history of coatings on architectural glazing', glassfiles.com. Article March 22nd, 2007.
14. Arbab, M. and Finley, J. J. (2010), 'Glass in architecture', *International Journal of Applied Glass Science*, **1**, 118–29.
15. Gunji, F. (2001), 'Present status and future trends of coatings on glass for automobiles', *Proceedings Glass Processing Days*, Tampere, 15–18 June 2001, 502–4.
16. Takagi, K., Makimoto, T., Hiraiwa, H. and Negishi, T. (2001), 'Photocatalytic, antifogging mirror', *Journal of Vacuum Science and Technology*, **19**, 2931–6.
17. Taga, Y. (1999), 'Review of plasma thin-film technology in automobile industry', *Surface and Coatings Technology*, **112**, 339–46.
18. Takai, O., Hozumi, A. and Sugimoto, N. (1997), 'Coating of transparent water-repellent thin films by plasma-enhanced CVD', *Journal of Non-Crystalline Solids*, **218**, 280–5.
19. Nakamura, M., Kobayashi, M., Kuzuya, N., Komatsu, T. and Mochizuka, T. (2006), 'Hydrophilic property of SiO₂/TiO₂ double layer films', *Thin Solid Films*, **502**, 121–4.
20. Mills, A., Lepre, A., Elliott, N., Bhopal, S., Parkin, I. P. and O'Neill, S. A. (2003), 'Characterisation of the photocatalyst Pilkington Activ™: a reference film photocatalyst?', *Journal of Photochemistry and Photobiology A: Chemistry*, **160**, 213–24.
21. Hauk, R., Frischat, G. H. and Ruppert, K. (1999), 'Sol-gel preparation of scratch-resistant Al₂O₃ coatings on float glass', *Glastech. Ber. Glass Science and Technology*, **12**, 386–92.
22. Greenall, M. R. (2003), 'Heated glazing for vehicles', in *Proceedings Glass Processing Days*, Tampere, 15–18 June 2003, 519–24.

23. Laffay, G., Fadeuilhe, G., Schambourg, F. and Keita, K., Patent DE2833234C2, filed 28 June 1978.
24. Hamberg, I., Svensson, J. S. E. M., Eriksson, T. S., Granqvist, C. G., Arrenius, P. and Norin, F. (1987), 'Radiative cooling and frost formation on surfaces with different thermal emittance: theoretical analysis and practical experience', *Applied Optics*, **26**(11), 2131–6.
25. Horstmann, F., Sittinger, V. and Szyszka, B. (2009), 'Heat treatable indium tin oxide films deposited with high power pulse magnetron sputtering', *Thin Solid Films*, **517**, 3178–82.
26. UN Economic Commission for Europe, ECE R43 (2003): Uniform provisions concerning the approval of safety glazing materials and their installation on vehicles, Rev. 2.
27. Deutsches Institut für Normung, DIN ISO 9211–3 (2010) Optics and photonics – Optical coatings – Part 3: Environmental durability, Berlin, Beuth.
28. Deutsches Institut für Normung, DIN ISO 9211–4 (2006) Optics and optical instruments – Optical coatings – Part 4: Specific test methods, Berlin, Beuth.
29. British Standards Institution, DIN 52347 (1987) Testing of glass and plastics, abrasion test; method using abrasion wheels and scattered light measurement, Milton Keynes: Technical Help to Exporters.
30. British Standards Institution, DIN 52348 (1985) Testing of glass and plastics: abrasion test; sand trickling method, Milton Keynes: Technical Help to Exporters.
31. Holmberg, K., Laukkanen, A., Ronkainen, H., Wallin, K. and Varjus, S. (2003), 'A model for stresses, crack generation and fracture toughness calculation in scratched TiN-coated steel surfaces', *Wear*, **254**, 278–91.
32. Bull, S. J. and Berasategui, E. G. (2006), 'An overview of the potential of quantitative coating adhesion measurement by scratch testing', *Tribology International*, **39**, 99–114.
33. Yang, F. and Li, J. C. M.; (2008), *Micro and Nano Mechanical Testing of Material and Devices*, New York, Springer, 49.
34. Leterrier, Y., Medico, L., Demarco, F., Manson, J.-A. E., Betz, U., Escola, M.F., Kharrazi Olsson, M. and Atamny, F. (2004), 'Mechanical integrity of transparent conductive oxide films for flexible polymer-based displays', *Thin Solid Films*, **460**, 156–66.
35. Vallon, S., Hofrichter, A., Guyot, L., Drevillon, B., Klemburg-Saphieha, J. E., Martinu, L. and Poncin-Epaillard, F. (1996), 'Adhesion mechanisms of silica layers on plasma-treated polymers. Part I. Polycarbonate', *Journal of Adhesion Science and Technology*, **10**, 1287–311.
36. Leterrier, Y. (2003), 'Durability of nanosized oxygen-barrier coatings on polymers', *Progress in Materials Science*, **48**, 1–55.
37. Muir, B. W., Thissen, H., Simon, G. P., Murphy, P. J. and Griesser, H. J. (2006), 'Factors affecting the adhesion of microwave plasma deposited siloxane films on polycarbonate', *Thin Solid Films*, **500**, 34–40.
38. Chalker, P. R., Bull, S. J. and Rickerby, D. S. (1991), 'A review of the methods for the evaluation of coating – substrate adhesion', *Materials Science and Engineering*, **A140**, 583–92.
39. Awaja, F., Gilbert, M., Kelly, G., Fox, B. and Pigram, P. J. (2009), 'Adhesion of polymers', *Progress in Polymer Science*, **34**, 948–68.

40. Deutsches Institut für Normung, DIN EN ISO 2409 (2010) Paints and varnishes – Cross-cut test, Berlin, Beuth.
41. Wypyck, G. (2003), *Handbook of Material Weathering*, 3rd Edition, Canada, ChemTec Publishing.
42. Diepens, M. (2009), ‘Photodegradation and stability of bisphenol A polycarbonate in weathering conditions’, PhD thesis.
43. Nichols, M. E. and Peters, C. A. (2002), ‘The effect of weathering on the fracture energy of hardcoats over polycarbonate’, *Polymer Degradation and Stability*, **75**, 439–46.
44. Schulz, U., Wachtendorf, V., Klimmasch, T. and Alers, P. (2001), ‘The influence of weathering on scratches and on scratch and mar resistance of automotive coatings’, *Progress in Organic Coatings*, **42**, 38–48.
45. Pickett, J. E., Sargent, J. R., Blaydes, H. A. and Babbie, N. (2009), ‘Effects of temperature on the weathering lifetime of coated polycarbonate’, *Polymer Degradation and Stability*, **94**, 1085–91.
46. Lau, K. (2006), ‘Plasmagestützte Aufdampsprozesse für die Herstellung haftfester optischer Beschichtungen auf Bisphenol-A Polycarbonat’, PhD thesis, Fraunhofer IOF.
47. Szczyrbowski, J., Bräuer, G., Ruske, M., Schilling, H. and Zmely, A. (1999), ‘New low emissivity coating based on TwinMag sputtered TiO₂ and Si₃N₄ layers’, *Thin Solid Films*, **351**, 254–9.
48. Deutsches Institut für Normung, für Normung, DIN EN 673 (2003), ‘Glass in building – Determination of thermal transmittance (U value) – Calculation method’, Beuth, Berlin.
49. American Society for Testing and Materials, ASTM D1003 (2000) Standard test method for haze and luminous transmittance of transparent plastics, Philadelphia.
50. Betz, U., Kharrazi Olsson, M., Marthy, J., Escolá, M. F. and Atamny, F. (2006), ‘Thin films engineering of indium tin oxide: Large area flat panel displays application’, *Surface and Coatings Technology*, **200**, 5751–9.
51. Sarakinos, K., Alami, J. and Konstantinidis, S. (2009), ‘High power pulsed magnetron sputtering: A review on scientific and engineering state of the art’, *Surface and Coatings Technology*, **204**, 1661–84.
52. Szyszka, B. (1999), ‘Reaktives Magnetronspattern von transparenten und leitfähigen Oxidschichten’, PhD thesis, Fraunhofer IST.
53. Lübke, M. (2009), ‘Abscheidung einer PVD-PECVD Hybridschicht als UV-Schutz auf Polycarbonat’, Master’s thesis in Fraunhofer IST und IOT TU Braunschweig.
54. Prasada Rao, T., Santosh Kumar, M. C., Anbumozhi Angayarkanni, S. and Ashok, M (2009), ‘Effect of stress on optical band gap of ZnO thin films with substrate temperature by spray pyrolysis’, *Journal of Alloys and Compounds*, **485**, Issues 1–2, 413–417.

C.-C. LEE and C.-C. KUO,
National Central University, Taiwan

DOI: 10.1533/9780857097316.4.564

Abstract: Flat panel displays, projection televisions and light-emitting diodes are typical systems that require optical coatings that not only enable them to function, but also improve their efficiency, quality, and visual comfort.

Key words: angular selection, wavelength shift, chromaticity.

15.1 Introduction

The invention of the liquid crystal display¹ opened the way to a thin and light flat panel display (FPD),² that could take the place of the cathode ray tube (CRT). The FPD then became generally used in notebooks,³ cell phones,⁴ video games,⁵ personal digital assistants,⁶ and many other displays used in daily life, even extending to global positioning systems (GPS), etc. There are several types of FPD such as plasma display panel (PDP), field emission display (FED), electroluminescence display (ELD), vacuum fluorescent display (VFD) and thin film transistor liquid crystal display (TFT LCD). The front surfaces of all these FPDs need antireflection coatings and/or antiglare coatings. A different type of display popularly used in conference rooms, public places, and home theaters is projection television (PTV).⁷ It needs not only antireflection coating, but also other kinds of optical coatings, such as cold light high reflection coating, UV-IR cut coating, color separation coating, polarization splitting coating, etc. Thanks to the optical coatings the PTV can be made very small so that it can be installed easily while having a large display area. Therefore nowadays most meeting rooms and classrooms are equipped with different types of PTV. Further, technologies such as micro electro mechanical system (MEMS),⁸ Liquid Crystal on Silicon (LCoS),⁹ digital light processing (DLP),¹⁰ digital micromirror device (DMD),¹¹ and so on, help us make the FPD and PTV still more compact with larger display screens and higher image resolution.

At the same time, energy saving, lifetime, and environmental benefit requirements have encouraged a new type of light source, the light emitting

diode (LED).¹² This is a possible replacement for halogen lamps or fluorescent tubes in lighting applications.¹³ Some types of FPDs and PTVs already use LED light sources.¹⁴ Nowadays, there are many types of FPDs, PTVs, and LEDs, but all of them need several different kinds of coatings. These assure their function but will also improve their quality, make them visually comfortable to the eyes and increase their output efficiency.

15.2 Optical coatings for flat panel display (FPD)

To avoid blurred images and to eliminate unwanted reflected light, the screen surface of an FPD must carry an antireflection (AR) coating. To reduce the annoying disturbance from external sources like bright ambient lights, and to enhance the contrast of the images, an antiglare (AG) coating is necessary. In some cases, the coating can combine the AR and AG attributes. In addition, a hydrophobic coating to keep the screen surface free of contamination from fingerprints and dirt, as well as making the surface easier to clean with a soft cloth or tissue, is a general requirement for a daily used FPD.

The AR coating must make the FPD screen surface present low reflectance throughout the visible range within certain view angles. If the screen is constructed from glass, non-absorbing oxides are usually the coating materials of choice for AR coatings. The high-index material is usually chosen from TiO_2 , Nb_2O_5 , Ta_2O_5 , and ZrO_2 , while SiO_2 is the general choice for low-index material, although MgF_2 can occasionally be employed. For an intermediate index Al_2O_3 is a good material. Coatings of up to five layers of coating are normally good enough to meet the specification for general purpose AR coatings.¹⁵ However, very high pixelated cameras embedded in cell phones require coatings of up to eight layers.

Since glare is caused by the reflection of bright, ambient light from the surface of the screen, antiglare quality and contrast enhancement can be achieved with a matte finish. Alternatively adding microparticles to the screen or attaching a thin sheet embedded with microparticles will increase the diffusive properties so that unwanted light is scattered. However, a disadvantage of those methods is possible reduction in the clarity and resolution of the image. To retain good clarity, coatings depending on optical interference are better. Then, one may use absorbing material as one of the coating layers to provide an AG property, although it will certainly decrease the transmittance by a few percent.¹⁶ In fact, the coating can combine both antireflection and antiglare properties if the correct materials are used. For example, Cr/CrO_x , Fe/FO_x , ITO/SiO_2 , $\text{TiNO}_x/\text{SiO}_2$,¹⁷ and $\text{TiN}_x\text{W}_y/\text{SiO}_2$ ¹⁸ have been tried as AR and AG coating materials. Recently a new type of FPD has been developed using ambient light instead of back light as a light source; in this case AR and AG coatings with better performance are required.

Since the screen of an FPD is exposed to the outside world, it will normally accumulate contamination by dirt and fingerprints, unpopular with customers. To help keep it free from such contamination, as well as making the surface easier to clean with a soft cloth or tissue, a hydrophobic coating can be added. The key technology of a hydrophobic coating is the addition of a coating of low surface energy over the final layer of the existing coating. Usually, the water contact angle should be greater than 110° .¹⁹ Although physical vapor deposition is usually more convenient for multilayer coatings, a silica sol–gel dip coating has been found to be good for a large flat panel displays that has hydrophobic and AR properties coupled with high scratch resistance. Sol–gel coatings produced by dipping or spinning processes are also suitable for plastic substrates, such as polymer molded optics (including eye glasses and camera lenses), of materials such as polycarbonate, acrylic, poly(methyl methacrylate) (PMMA), Zeonex, polyethylene terephthalate (PET), polyethylene naphthalate (PEN), polyimide (PI), etc.²⁰ Alternatively, perfluoropolyether polymers modified with organofunctional silanes have been developed to present a hydrophobic surface.²¹ In all circumstances, keeping surfaces dry and clean is very important for good coatings no matter whether by vacuum processes or by non-vacuum sol–gel techniques. Ion sources also improve adhesion for coatings on plastic substrates in vacuum coating. For glass substrates, the use of an ion source in assisted ion deposition can reduce the need for substrate heating and thus reduce the coating process time.

Color filters used in FPDs are absorption filters in most cases. A red color filter absorbs green and blue light, green absorbs red and blue, and blue absorbs green and red. This absorption costs us at least two thirds of the available light. Although mosaics with coated blue, green and red high transmission color filters, based on interference rather than absorption, have been proposed, commercial FPDs do not use them for economic reasons. However, with a new lithographic technology and a new design of using mosaics with coated blue, green and red high transmission color filters, based on interference rather than absorption, have been proposed again. Then the reflected complementary colors can be reused through the process of bounces back and forth. The light will be fully used, since no light is wasted. For instance, when white light is incident on the blue filter, blue light is transmitted, while its complementary color, yellow, containing green and red light will be reflected and bounced back and then transmit to the green and red filters, respectively. Similarly, when the white light is incident on the green or red filter, their complementary colors will be reflected and reused.

Another important coating for FPDs is a transparent conductive coating. It is used as an electrode for thin film transistor liquid crystal displays, TFT LCD,²² touch panels,²³ E-paper,²⁴ low emissivity glass,²⁵ electrochromic windows,²⁶ LEDs,²⁷ etc. Nowadays, most transparent conductive coatings are oxides because of their chemical stability, and the term used to describe them is transparent conductive oxide (TCO). TCO was pioneered in the

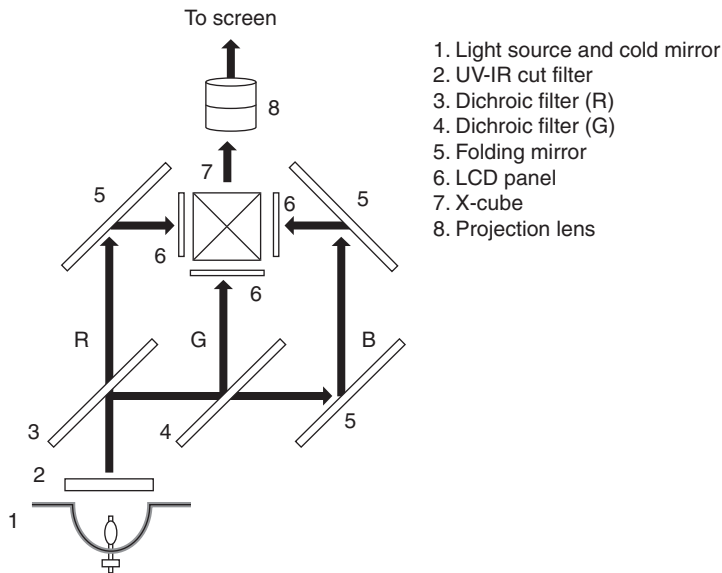
early twentieth century by Streintz.²⁸ Later, magnetron sputtering brought fabrication to lower temperatures.²⁹ Then indium tin oxide (ITO) became the main TCO for most applications.³⁰ Several types of doped TCO, such as F:SnO₂, Al:ZnO, Ga:ZnO, Nb:TiO₂, Sb:SnO₂, etc., are under development with the objective of taking over from ITO, since indium is a rare material in short supply.^{31–37} All TCO films are required to have high transmittance, higher than 85%, and low sheet resistance ranging from a few tens to several hundreds of Ω/□, according to the application.

The traditional back light used in FPDs is either the cold-cathode fluorescent lamp (CCFL), the external electrode fluorescent lamp (EEFL), the hot cathode fluorescent lamp (HCFL), or the flat fluorescent lamp (FFL). Nowadays these lamps are gradually being replaced by LEDs because of energy saving and lifetime issues and because of environmental factors. Thin film coatings are necessary in backlighting units so that full use can be made of the light source. Besides AR coatings, high reflectance behind the light source is required. The reflector is coated with a silver thin film (about 100 nm) and a protective film, like thin nickel or nickel-chromium nitride (a few nanometers) or with dielectric films (SiO₂/TiO₂) to achieve a reflectance greater than 98%.

15.3 Optical coatings for projectors

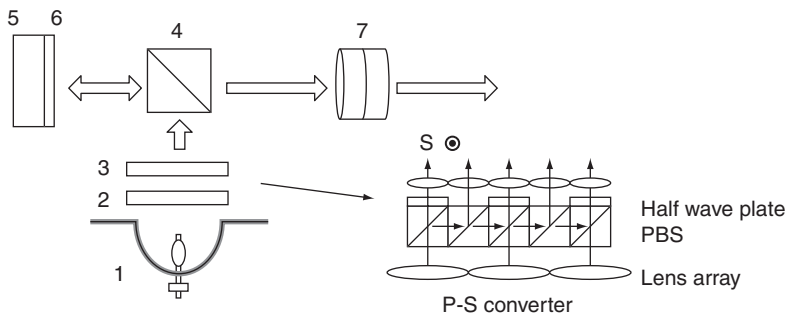
As well as the AR coatings on each surface of its optical components, projectors need several other types of coatings, such as cold mirrors, UV-IR cut filters, three primary color filters (dichroic filters), beam splitters, polarizers, and so on, as indicated in Figs 15.1 and 15.2. Figure 15.1 is a transmission type projector with liquid crystal display, where the three primary colors are separated spatially by red (R) and green (G) dichroic filters and folding mirrors.³⁸ The X-cube prism is constructed from crossed dichroic filters. These recombine the light that has passed through the three LCD light valves, located at the three faces of the cube.³⁹ After their combination the images are projected onto the screen by the projection lens.

Light generated by an ultrahigh pressure (UHP) mercury lamp or halogen lamp is collected by an elliptical reflector carrying a cold mirror. The cold mirror reflects only the visible light letting the UV and IR radiation be transmitted. The reflection cup is a very deep elliptical reflector and the coating, based on quarter-wave stacks, on such a deep cup must be very uniform, so that the reflectance can be high enough to achieve flux greater than 8000 lx from a 120 W halogen lamp. A UV-IR cut filter is also placed in front to filter direct light from the source. UV and IR radiation are eliminated to prevent damage to the liquid crystal, the optical components and charge-coupled device (CCD)/complementary metal-oxide-semiconductor (CMOS) and to keep the right color temperature. Figure 15.3 shows



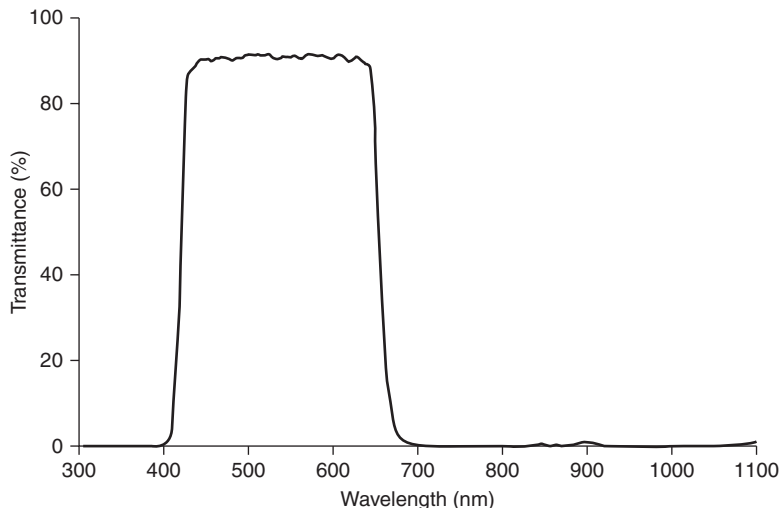
15.1 Transmission type projector with liquid crystal panel. R, G, and B stand for red, green, and blue light, respectively.

1. Light source and cold mirror
2. UV-IR cut filter
3. P-S converter
4. PBS
5. LCoS
6. Quarter wave plate
7. Projection lens



15.2 Reflection type projector using LCoS.

the spectrum of UV-IR cut filter coated with a multilayer of TiO_2 and SiO_2 , based on the design: Sub/(0.6L 1.2H.6L) 10 (0.5L H.5L) 10 /air, with central wavelength at 780 nm, where Sub indicates the substrate, and H and



15.3 Spectrum of UV-IR cut filter.

L are quarter wave layers of high (TiO_2) and low (SiO_2) refractive index, respectively.

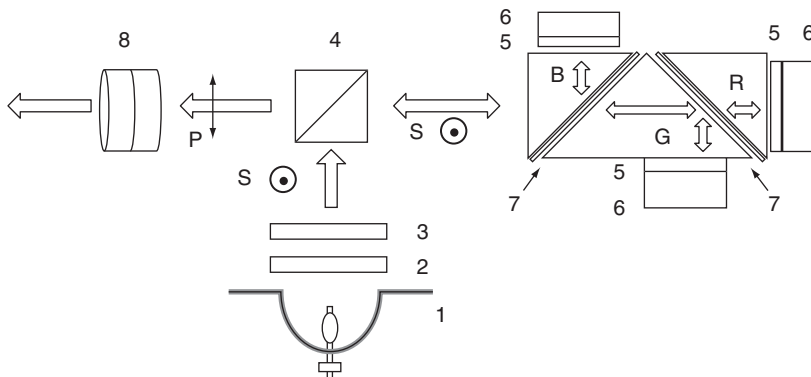
Figure 15.2 shows a reflection type projector using Liquid Crystal on Silicon⁴⁰ technology. In an LCoS device, the CMOS transistors and pixel mirrors, designed to modulate the light with the image data, are built on a silicon chip by semiconductor techniques. The liquid crystal filled a gap between the silicon chip and an overlaid glass plate. The p-s converter in front of the lamp converts all the output light to pure s-polarized. A schematic of a p-s converter is included at the foot of Fig. 15.2 on the right. It is a combination of an array of lenses and polarization beam splitters (PBSs). There are half wave plates on the output surfaces of the odd numbered PBSs to convert p-polarized light to s-polarized light. The s-polarized light is then reflected by a PBS (#4) and modulated by an LCoS light valve. The phase retarder in front of the LCoS is a quarter wave plate that acts as an s-p converter. The modulated light (that is light impressed with the image data) then passes through the PBS and the projection lens and then to the screen.

For high throughput we use three LCoS light valves as shown in Fig. 15.4. Here we need two dichroic beam splitters to extract three primary colors, modulated by three LCoS light valves. The dichroic beam splitters must be insensitive to polarization.

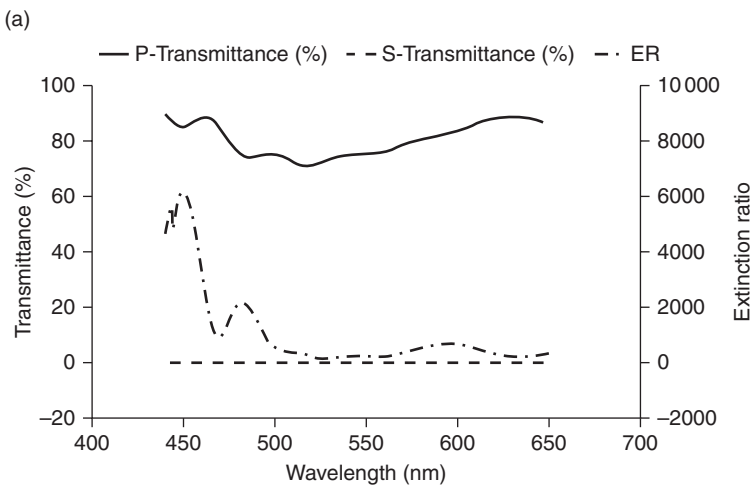
Reflection type projectors using LCoS technology need a high extinction ratio (ER) of PBS. The coating for such a PBS is based on the principle of the Brewster angle to have high transmission for p-polarized and high reflection for s-polarized light. The ER should be greater than 1000 and the

transmittance of p-polarized light higher than 80% for wavelengths from 440 to 650 nm within incident angles of $45^\circ \pm 14^\circ$. Two stacks and three coating materials coated on a high-index substrate will usually meet this requirement. The design can be based on Sub/0.7(MHML)⁷ 0.95(MHML)⁷/

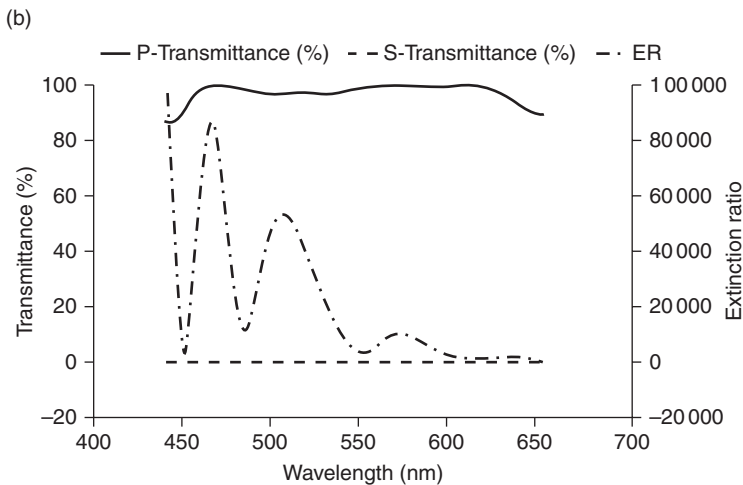
1. Light source and cold mirror
2. UV-IR cut filter
3. P-S converter
4. PBS
5. Quarter wave plate
6. LCoS
7. Dichroic beam splitters
8. Projection lens



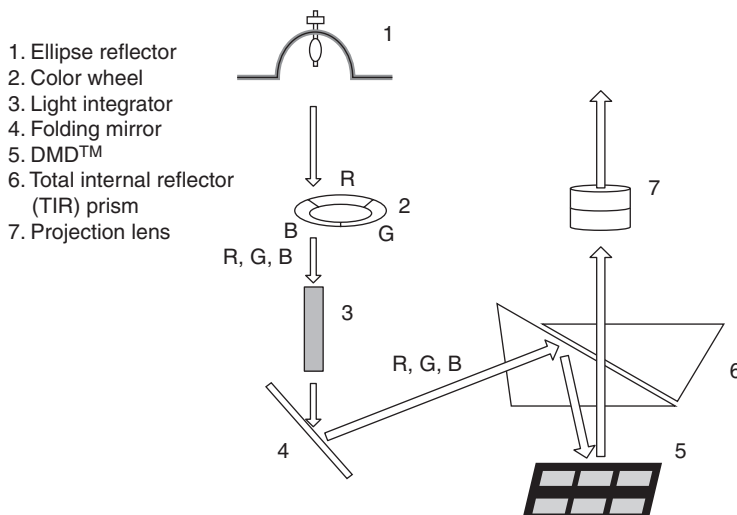
15.4 Reflection type projector using three LCoSs.



15.5 Spectrum and ER of PBS at (a) 31° and (b) 45°.



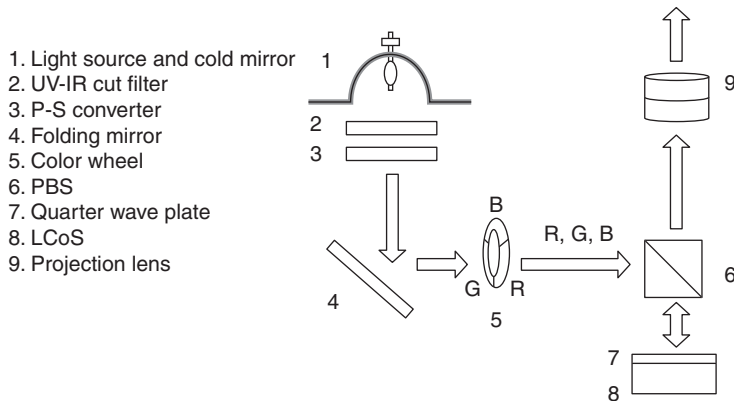
15.5 Continued



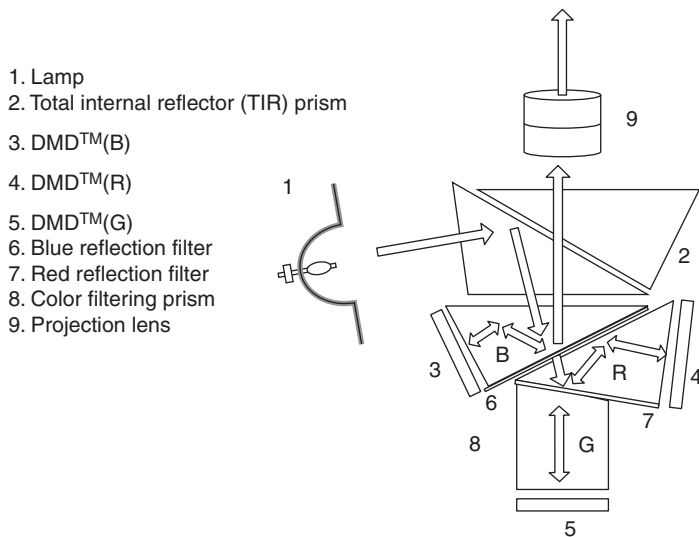
15.6 Schematic drawing of DLP project system.

Sub, where typically, the substrate can be Schott glass SF57HHT having refractive index 1.847 at 550 nm, and H, L, and M quarter wave layers with refractive indices 2.3 (TiO_2), 1.46 (SiO_2), and 1.9 (Mixed Ta_2O_5 with Al_2O_3), respectively. Figure 15.5 shows the spectra and ERs of the PBSs at 31° and 45° based on the above design (Fig. 15.6).

An alternative way to separate the three primary colors is to use a multi-segment color wheel composed of three primary color filters. Here the different colors pass through the color wheel in sequence as shown in Fig. 15.6.



15.7 Schematic drawing of LCoS projector using color wheel.



15.8 Schematic drawing of DLP project system with three DMDs.

Such a projector system is known by the term digital light processing (DLP). The light is collected by an elliptical reflector and focused on an end face of a mixing rod, a type of light integrator. After the light passes through the light integrator and relay lens, the collimated colored light is then reflected by a digital micromirror device (DMD) chip. The DMD chip is an optical semiconductor that is at the core of DLP projection technology. It was invented by Dr Larry Hornbeck and Dr William E. 'Ed' Nelson of Texas Instruments (TI) in 1987. With a DMD, the image can be digitally processed. The light

integrator is a rectangular tunnel with a highly reflecting internal surface. It is usually silver coated with a protective overcoat or carries a broad band quarter-wave stack. The average reflectance must be greater than 98% for 70° incident angle from 420 to 680 nm.

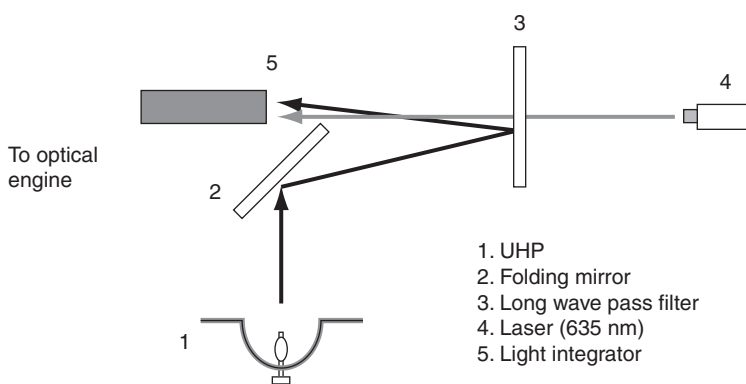
Separation of the three primary colors using a multi-segment color wheel can also be applied to the LCoS projector, as shown in Fig. 15.7. In that case we need only one LCoS panel, but we do also need a broad band p-s converter.

To achieve high throughput in a DLP projection system (Fig.15.6) we can use three DMDs for the three primary colors, blue (B), green (G), and red (R) as shown in Fig. 15.8, where #6 and #7 indicate blue and red reflective coatings, respectively.

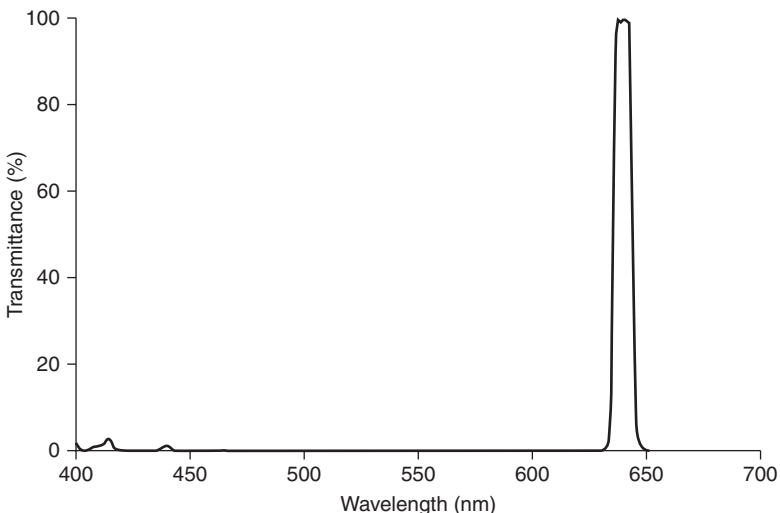
15.4 Optical coatings for projectors using light emitting diode (LED) light source

The increase of the efficiency of blue LEDs makes white light LEDs possible and could be a new lighting source, particularly when the energy saving, lifetime of the light source and environmental benefits are considered. Therefore, traditional high pressure halogen lamps could be replaced by LEDs and laser diodes (LDs)⁴¹ as the light source of projectors. Careful choice of LEDs with the correct three primary colors could make PTVs with a better color gamut.

The color gamut can also be increased by adding a red LD with wavelength 635 nm combined with a long wavepass filter (LPF), in a regular DLP as shown in Fig. 15.9. The long wave pass filter passes red and reflects most of the white light coming from the ultra high pressure (UHP) halogen lamp. The elliptical



15.9 Increasing the color gamut by adding a red LD in a regular DLP.

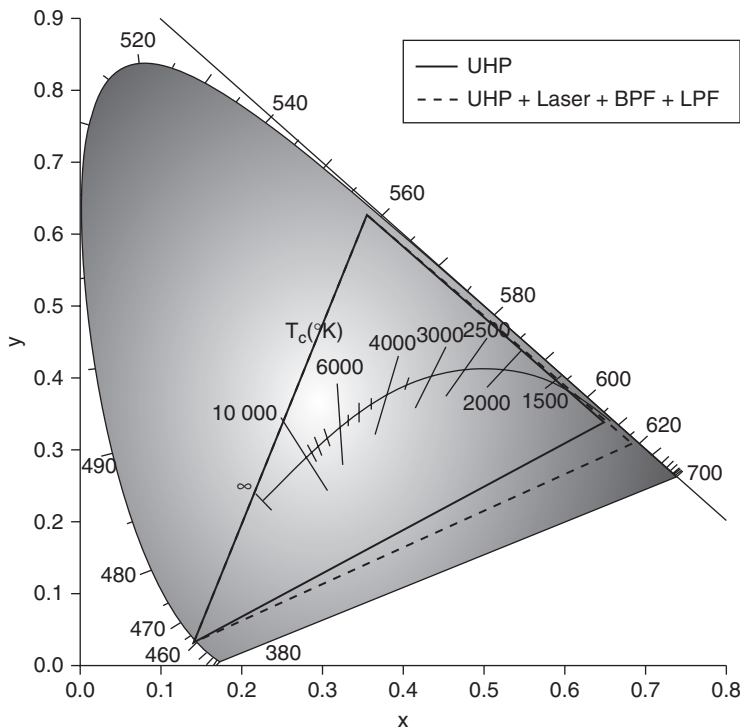


15.10 Spectrum of a band pass filter used in color gamut-enhanced DLP.

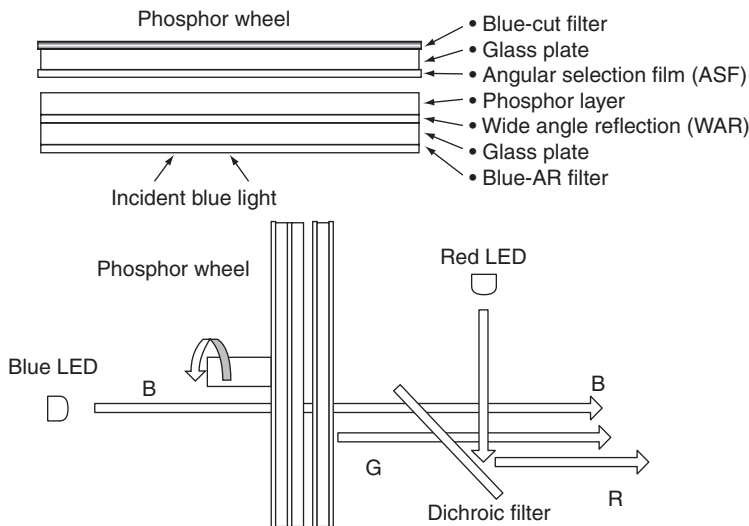
reflector collects the white light and focuses it on the end face of the light integrator. We can further increase the color gamut by replacing the long wave pass filter with a band pass filter as shown in Fig. 15.10. This is a three-cavity narrowband pass filter (BPF) using TiO_2 and SiO_2 , combed with a long wave pass filter. The half maximum bandwidth is 8 nm and there is no influence on the transmission at 639 nm within $\pm 8^\circ$ such that light intensity is increased by 9% resulting in a better color gamut. The increase of color gamut is shown by the CIE (Commission Internationale de L'Eclairage or International Commission on Illumination) 1931 chromaticity diagram in Fig. 15.11.

Using LEDs, we can save energy still further by using a phosphor color wheel as shown in Fig. 15.12. The green phosphor is excited by a blue LED to emit green light. The angular selection filter (ASF)⁴² allows only light with an incident angle less than 35° to pass through. Light with an incident angle larger than 40° is reflected and reused to excite the phosphor, as shown in Fig. 15.13. The design principle of this ASF is as follows.

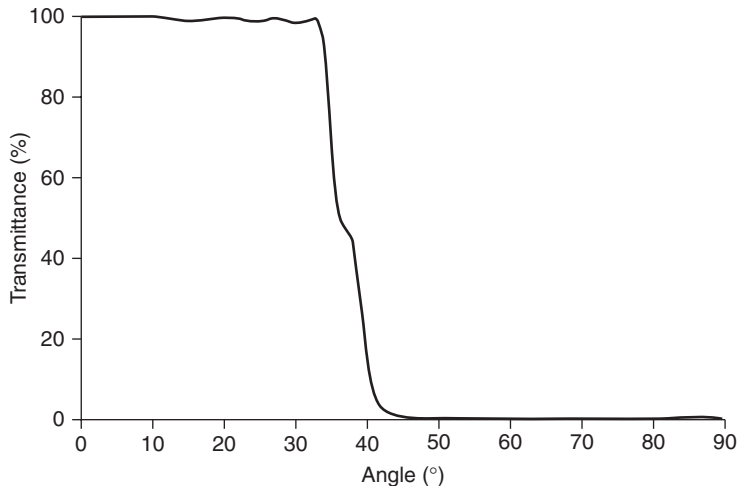
An ASF is a kind of edge filter in which the main property is a rapid change between the regions of rejection and transmission. Its basic design is a symmetrical stack or a quarter-wave stack from two or more alternating dielectric thin films with a large contrast of refractive indices.¹⁵ Most of the thin-film interference filters are angle-sensitive, which means that the pass band and cut-off region shifts toward shorter wavelengths with the increase of incident angle from normal incidence to a higher angle. In addition, the polarizing effect of optical filters at oblique angles of incidence makes the s- and p-polarized lights shift differently. ASFs can control the amount of



15.11 The CIE 1931 chromaticity diagram shows the increase of color gamut when LD is added to the UHP light source.



15.12 Phosphor color wheel and red LED to produce red, green, and blue colors.



15.13 Transmittance of green light 525 nm by ASF at different incident angles – a design.

spectrum shift at the oblique incidence. Therefore the ASF design can be used to control emission direction and feed back the large-angle light for recycling of light. Previous investigations^{43–45} have led to the development of dielectric layer filters with angle-selective properties.

Let the design of angular selection filter be as follows,

$$\text{Substrate} | (aHbL)^p aH | \text{Air} \quad [15.1]$$

where H and L represent the quarter wave optical thickness of the high and low refractive indices layer, respectively, p is the number of periods, and a and b are the ratio of thickness of the corresponding high and low refractive index layers. The width of the high reflectance zone can be derived from the characteristic matrix of thin film,¹⁵

$$[M] = [m]^p, \quad [m] = \begin{bmatrix} m_{11} & m_{12} \\ m_{21} & m_{22} \end{bmatrix} \quad [15.2]$$

where $[m]$ is the matrix of fundamental period. Then, the high reflectivity is dependent on the condition whether

$$\left| \frac{m_{11} + m_{22}}{2} \right| \geq 1 \quad [15.3]$$

The reflectance increases steadily with increasing periodic number. A high reflectance zone should exist and obtain the full width at half maximum (FWHM) of the stop band. This boundary is expressed by:^{46,47}

$$\left| \frac{m_{11} + m_{22}}{2} \right| = 1 \quad [15.4]$$

The quarter-wave stack consists of a number of two layer periods with one extra high-index layer. Each period has a characteristic matrix given by,

$$[m] = \begin{bmatrix} \cos \delta_H \cos \delta_L - \frac{n_L}{n_H} \sin \delta_H \sin \delta_L & i \left(\frac{1}{n_L} \cos \delta_H \sin \delta_L + \frac{1}{n_H} \sin \delta_H \cos \delta_L \right) \\ i(n_H \sin \delta_H \cos \delta_L + n_L \cos \delta_H \sin \delta_L) & \cos \delta_H \cos \delta_L - \frac{n_L}{n_H} \sin \delta_H \sin \delta_L \end{bmatrix} \quad [15.5]$$

so that

$$\left| \frac{m_{11} + m_{22}}{2} \right| = \left| \cos \delta_H \cos \delta_L - \frac{1}{2} \left(\frac{n_L}{n_H} + \frac{n_H}{n_L} \right) \sin \delta_H \sin \delta_L \right| \quad [15.6]$$

The right-hand side cannot be greater than +1, therefore the boundary of the high reflectance zone can be set as follows,

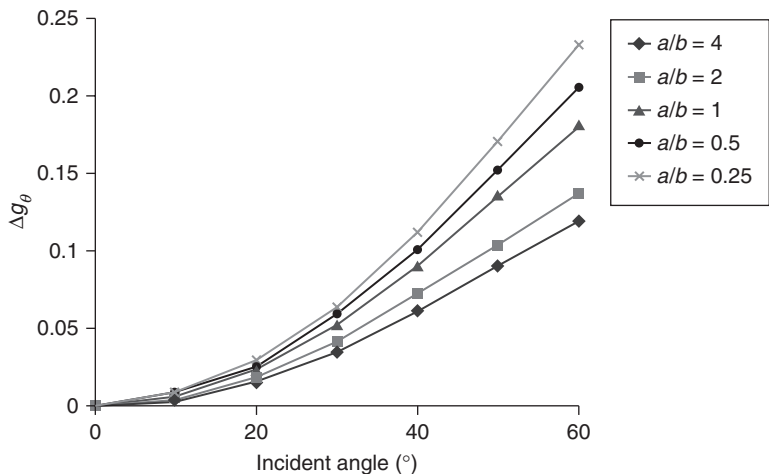
$$\cos \delta_H \cos \delta_L - \frac{1}{2} \left(\frac{n_L}{n_H} + \frac{n_H}{n_L} \right) \sin \delta_H \sin \delta_L = -1 \quad [15.7]$$

Since the phase thickness of high and low indices layer are the same, that is $\delta_H = \delta_L$, which can be set equal to δ_e such that

$$\cos \delta_e = \left(\frac{n_H - n_L}{n_H + n_L} \right)^2 \quad [15.8]$$

Let the edge of the high reflectance zone be $g = 1 \pm \Delta g$, then

$$\delta_e = \frac{\pi}{2} g = \frac{\pi}{2} (1 \pm \Delta g) \quad [15.9]$$



15.14 Simulation of spectrum shift at incident angle from 0° to 60°.

where $g = \lambda_0/\lambda$, the relative wave number, and λ_0 is the central wavelength for which the layers have quarter-wave optical thickness.

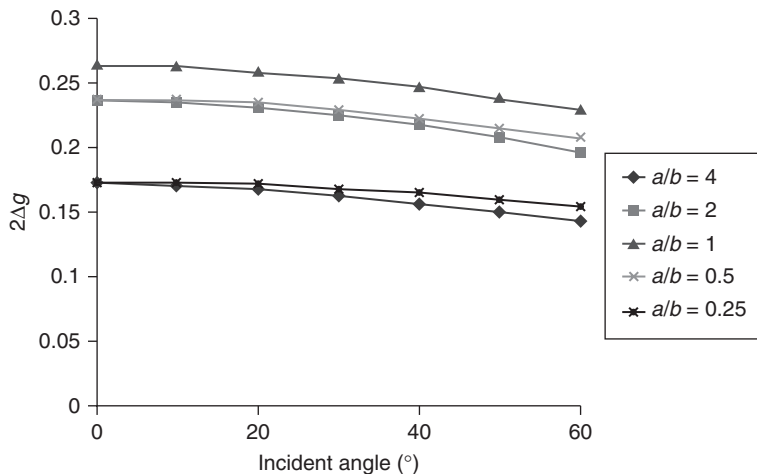
The FWHM of the high reflectance zone is $2\Delta g$. With some rearrangement, we can write this as

$$2\Delta g = \frac{4}{\pi} \sin^{-1} \left(\frac{n_H - n_L}{n_H + n_L} \right) \quad [15.10]$$

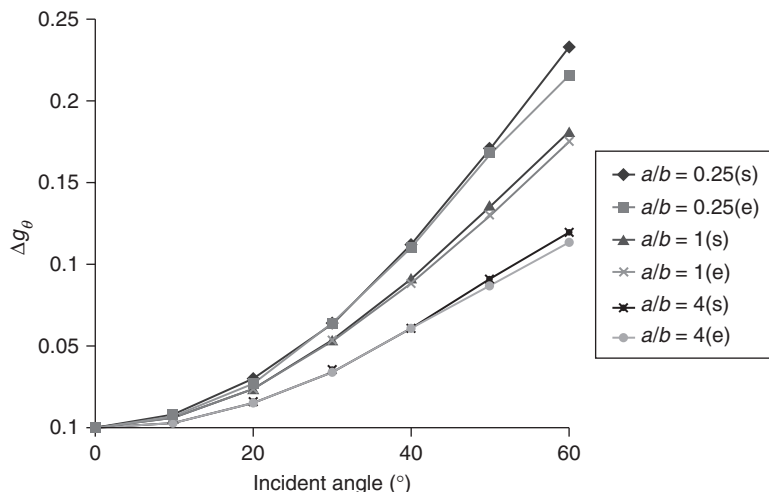
The spectrum shift at oblique incidence Δg_θ is given by the expression

$$\Delta g_\theta = \Delta g_{\theta=0} - \Delta g_{\theta=0} \cos \theta_i \quad [15.11]$$

where $\Delta g_{\theta=0}$ is half of FWHM at angle θ_i . In this case, δ_H is not equal to δ_L . This is a complex expression, and we need a computer to do the calculation to understand the spectrum shift at oblique incidence. We choose the periodic number of 12, and the high and low refractive index materials are Ta_2O_5 and SiO_2 , respectively, in the ASF design. Figure 15.14 shows the spectrum shift at different ratios of a to b as a function of incident angle. This shows the interesting result that the spectrum shift with incident angle can be controlled by adjusting the ratio of a to b . The spectrum shift is larger than quarter-wave stacks when a/b is less than one, and smaller when a/b is greater than one. Nevertheless, the FWHM becomes narrower as a/b tends away from one as shown in Fig. 15.15. Therefore a good ASF should choose a correct value of a/b so that the ASF can have a suitable spectrum shift while keeping a larger FWHM.

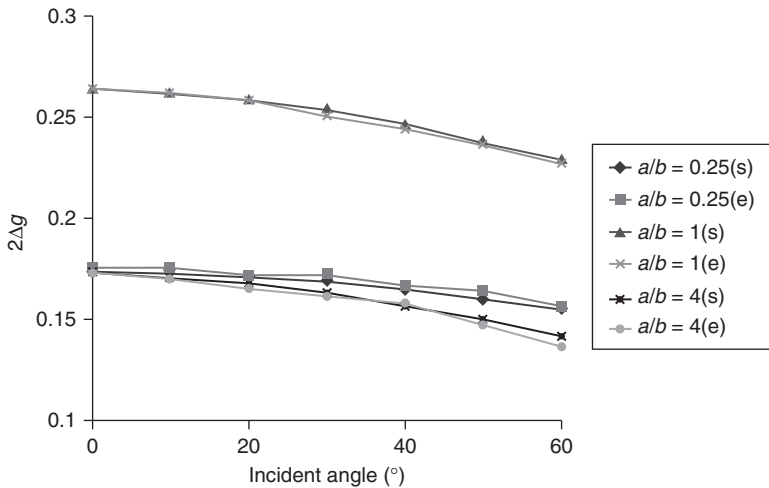


15.15 Simulation of FWHM at incident angle from 0° to 60°.

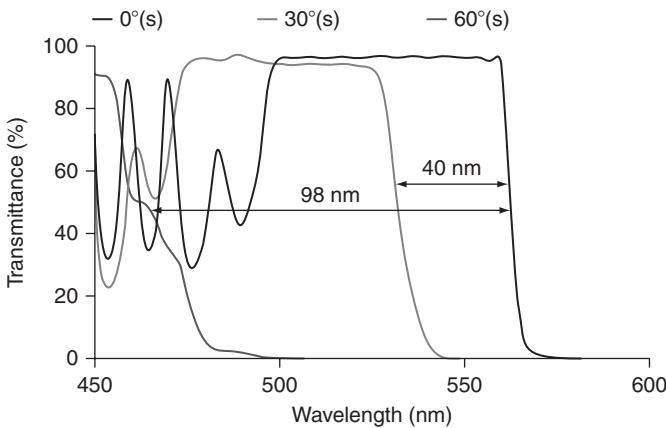


15.16 Simulation(s) and experiment (e) of the spectrum shift at incident angle from 0° to 60°.

Figures 15.16 and 15.17 show the simulation and experiment spectrum shift and the FWHM vs. incident angle. The experimental result is similar to the simulation. The ASF is a 61-layer coating with $a/b = 0.25$ using Ta_2O_5/SiO_2 , based on the design Sub/(0.5H2L)¹⁵ 0.525H 2.2L (0.55H2.2L)¹⁴ 0.55H/Air, with central wavelength at 500 nm. The simulated and experimental spectra of the ASF at different incident angles are shown in Figs 15.18 and 15.19. The wavelength shift from 0° to 30° is 40 nm, and from 0° to 60° is near 100 nm. As we expected that the wavelength shift to angle of the new design is more sensitive than the conventional design.



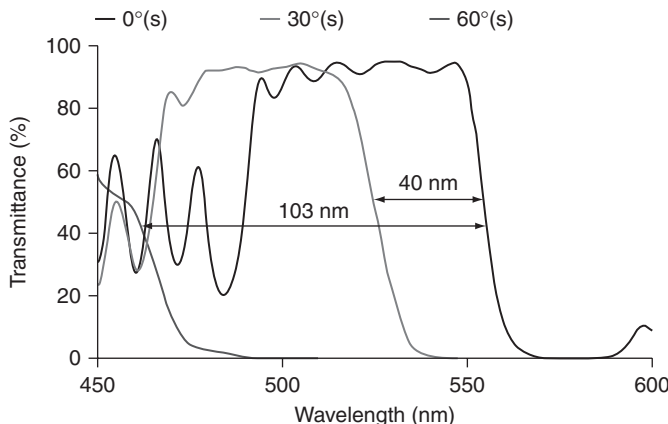
15.17 Simulation (s) and experiment (e) of FWHM at incident angle from 0° to 60°.



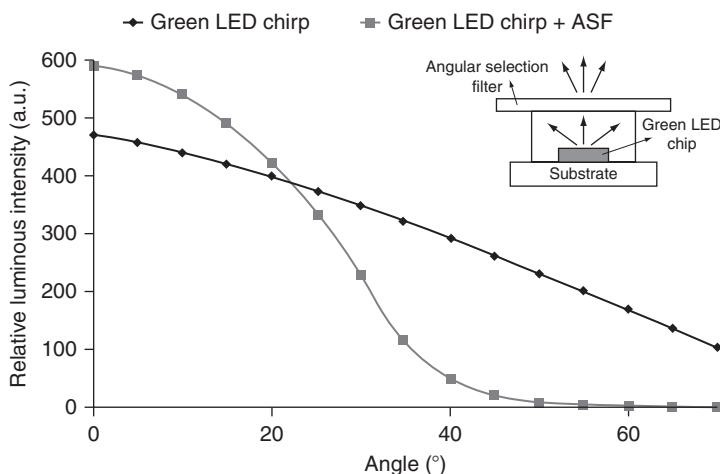
15.18 Simulated spectrum of ASF at different incident angles.

Without the ASF, the green LED chip output light angle is from 0° to 70°. The output light angle is limited to 40° when an ASF is applied on the green LED chip as shown in Fig. 15.20. The ASF recycles the light at the output light from 40° to 70° and increases the output light from 0° to 30° of green LED light source system.

To keep the purity of green color and increase the output, a blue-cut filter was installed after the ASF. The blue-cut filter reflects the blue light to excite the green phosphor again. In the phosphor color wheel, there is a section not coated with phosphor but with an AR for blue light.



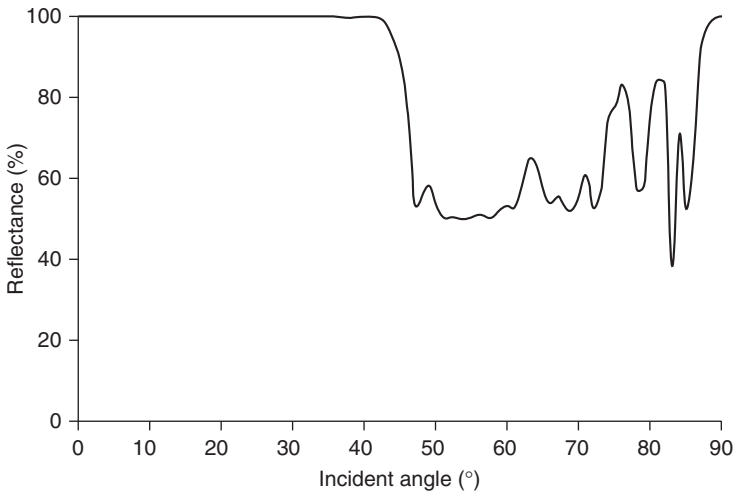
15.19 Experimental spectrum of ASF at different incident angles.



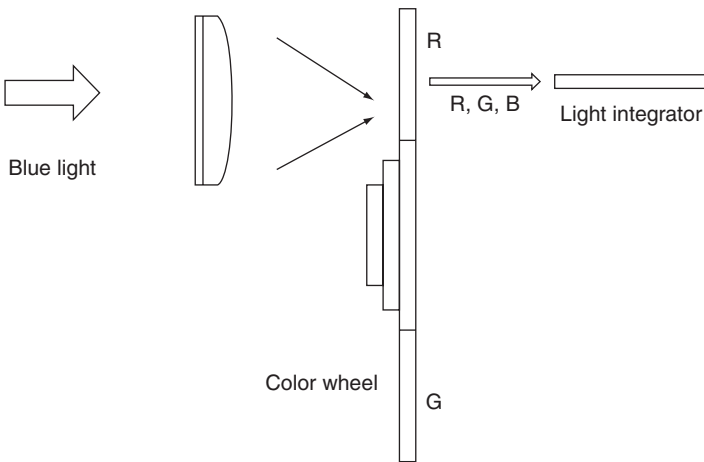
15.20 Luminance with and without ASF measured at different output angles. The inset shows green LED with angular selection filter.

Therefore, that section allows blue light to pass through, so that we have blue, green, and red colors, as shown in Fig. 15.12. The wide angle reflection filter (WAR) shown in Fig. 15.21, reflects all the green light from 0° to 45° to recycle it. The WAR filter is a 43-layer coating made from Ta_2O_5/SiO_2 , based on the design Sub/(1.2H1.2L) 10 (HL) 12 H/Air, with central wavelength 550 nm.

A phosphor color wheel can be coated with a green phosphor on one part and with red phosphor on another. In that case we employ only a blue LED or LD as shown in Fig. 15.22.



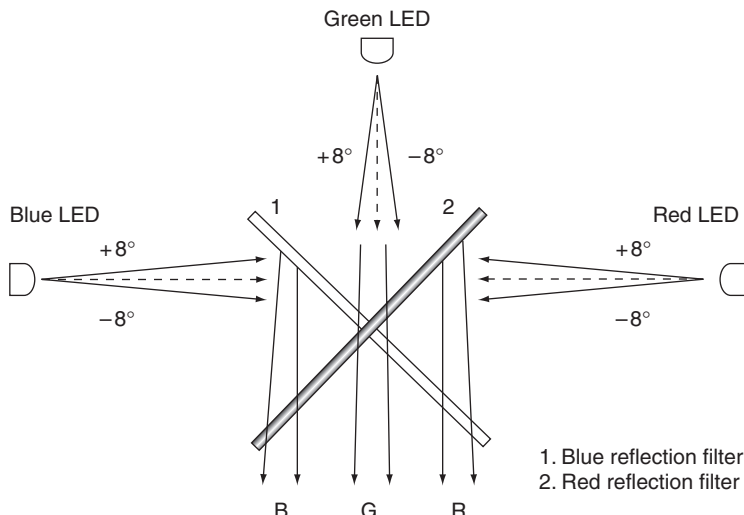
15.21 Reflectance of green light 525 nm by WAR filter at different incident angles.



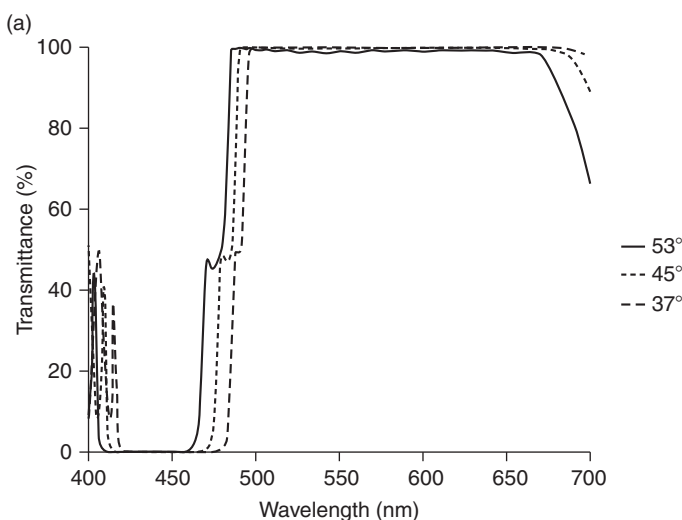
15.22 Phosphor color wheel to produce red, green and blue colors.

By utilizing LEDs and a specially designed X-plate, we can also increase the color gamut. Figure 15.23 shows three LEDs (red, green, and blue) combined with an X-plate in a projector to increase the color gamut. Since the divergence angle of the LEDs is confined to $\pm 8^\circ$ to maintain high brightness, the coatings on the X-plate must have properties insensitive to angle. The spectra of typical coatings for an X-plate,⁴⁸ the blue and red reflection filters shown in Fig. 15.24, indicate a shift of less than 15 nm in their spectrum with

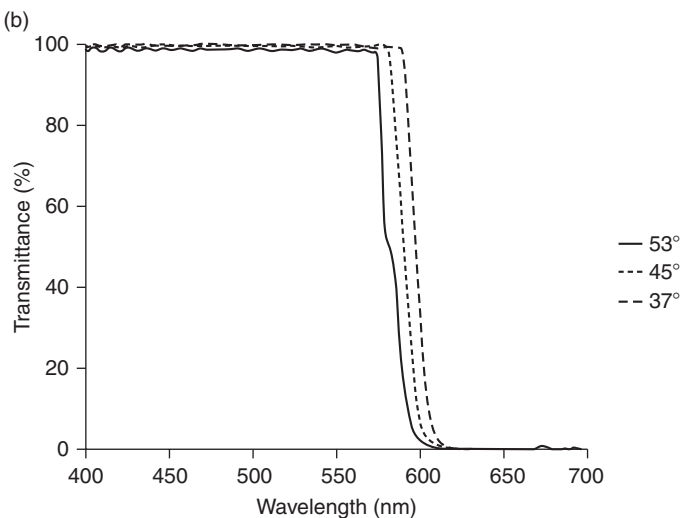
incidence in the range $45^\circ \pm 8^\circ$. The blue and red reflection filters are angle insensitive filters with $a/b = 4$ having coatings with 40 layers (based on the design Sub/(2H 0.5L)²⁰/Air, central wavelength at 550 nm) and 47 layers (based on the design Sub/(3H 0.5L)¹⁷ (1.07L 2.14H 1.07L)⁶/Air, central wavelength at 390 nm) of TiO₂/SiO₂, respectively.



15.23 LEDs and X-plate used in a projector.



15.24 Spectra of (a) blue reflection filter and (b) red reflection filter of X-plate at $45^\circ \pm 8^\circ$.



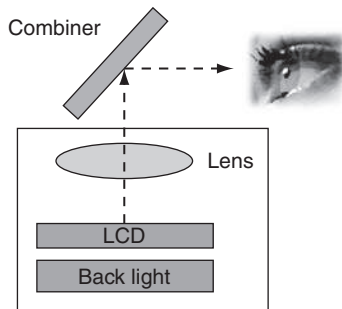
15.24 Continued

15.5 Optical coating for automobiles head up display (HUD)

A head up display (HUD) is a display that allows the user to see displayed data without looking away from the outside world. It was initially developed for military aircraft pilots but now has many other applications. In this chapter we will talk only about the displays for automobiles. The displayed data can be the speed of the car, navigational information, warning signals, and so forth.

Normally, the projected image from a HUD is fuzzy because of the double reflection from the two surfaces of the thick windshield of the car. This is known as a double image or ghost image. A possible solution for automotive head-up displays is the attachment of a dark film over the windshield to decrease the reflective lightness of the second image. However, although improving the contrast of the image, this might decrease the transparency of the windshield. Another popular solution is using wedge or doublet glasses to separate the second reflection image sufficiently far from the first one or to superimpose the two images.^{49,50} However, there are two main disadvantages of wedge or doublet glasses. They need very precise design and their manufacture would be very expensive.

The other way of combining the outside view with the data is to use a beam splitter using optical thin film technology.⁵¹ This approach has many advantages such as multicolor reflectance, decreasing the influence of double images and achieving a transmittance of 70% or more.



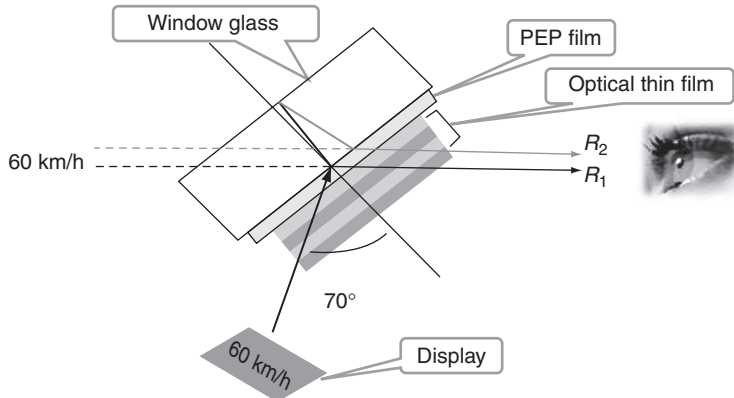
15.25 Schematic architecture of HUD system.

In general, an automotive HUD system includes four parts, an LED array, a thin film transistor (TFT) projection display, a lens system, and the beam splitter. Figure 15.25 shows the schematic architecture of such an HUD system. The light source of the HUD is a white LED. An aspheric lens is positioned in front of the LCD panel to magnify the image to the desired display size, correcting aberration introduced by optical system and placing the virtual image at a desired viewing distance in front of the driver. This HUD unit also has an ambient light sensor, so that the brightness of the display can be controlled with feedback from the sensor. In this way the power consumption can be reduced according to the brightness of surroundings, and this also helps to improve the visual comfort of the driver.

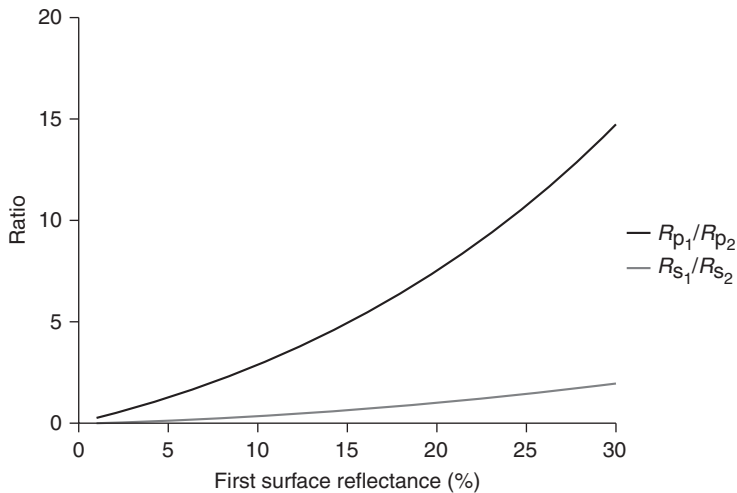
The optical design of a beam splitter consisting of a coated multilayer on a poly ethylene propylene (PEP) substrate is shown as Fig. 15.26. The angle between windshield and dashboard is $70^\circ \pm 5^\circ$. We can eliminate double images by increasing the contrast ratio of the first reflection (R_1) to the second one (R_2). Typically, the viewing distance from the windshield is 50 cm, and the eye box on the viewer side is about 135 mm (W) \times 50 mm (H), which is the spatial range within which the entire HUD image can be seen without vignetting.⁵² The eye box size determines the required aperture of the optical system and consequently the required space for mounting the HUD in a vehicle.

The light includes both s- and p-polarizations. Let the reflectance of the first surface of the PEP substrate be R_1 and of the second surface R' . Let R_2 be the reflectance for light passing through the first surface, reflecting off the second surface then finally emerging from the first surface. R_2 is equal to $(1 - R_1) \times R' \times (1 - R_1)$. The contrast ratio R_1/R_2 for p-polarization is better than that for s-polarization as shown in Fig. 15.27. For that reason, p-polarized light was chosen for the optical film design in this study.

In order to see both the outside scene and the projected information clearly, it is necessary to arrange a high transmittance beam splitter. Figure 15.27 demonstrates that it is only where R_1 is less than 30%

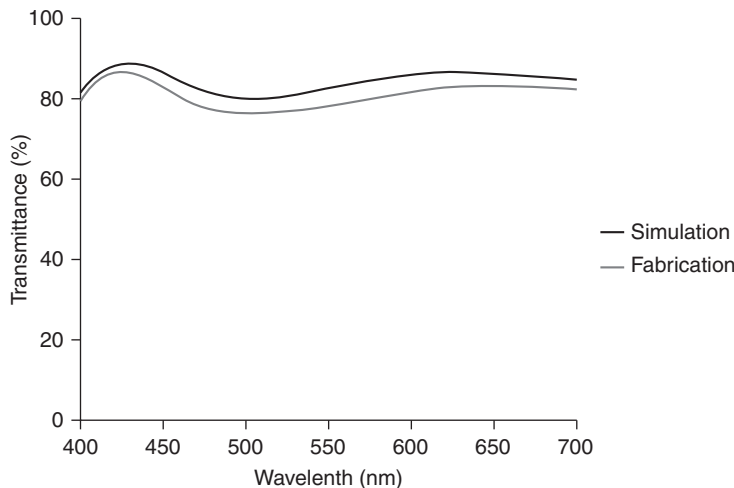


15.26 The optical design of a beam splitter for HUD.

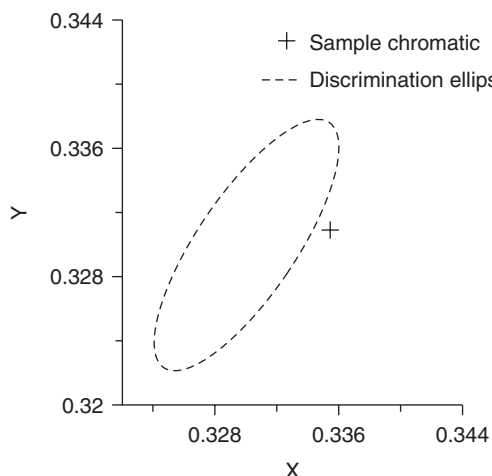
15.27 R_1/R_2 for s- and p-polarization in $R_1 < 30\%$ region.

that we need to enhance total reflecting contrast. Transmittance of the simulated coating together with that of an actual fabricated one are shown as Fig. 15.28. The average transmittance is 74.5% and the contrast R_1/R_2 is 6.6.

The color in CIE 1931 x-y chromaticity coordinates was calculated from the transmittance spectra of the sample beam splitter and clearly it is located almost at the white point, implying that the color of the beam splitter is almost neutral. Precise calculation shows that the color of the beam splitter is sited near the chromatic discrimination ellipse of white light as shown in Fig. 15.29.



15.28 Transmittance spectra with different wavelengths for simulation and fabricated films.



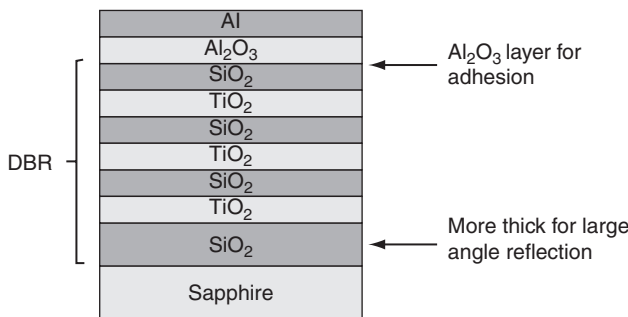
15.29 The relationship between the chromatic discrimination ellipse of white light and beam splitter.

15.6 Optical coatings for LEDs

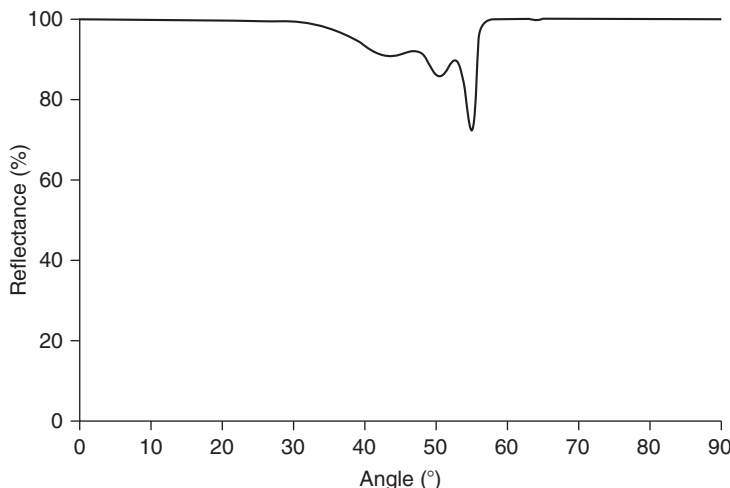
Energy saving, lifetime and environmental considerations make the light-emitting diode (LED) an attractive new light source that could possibly replace halogen lamps or fluorescent tubes for lighting applications.⁵³ To increase light extraction, an AR coating on the output side of an LED chip

and a high reflection (HR) coating on the rear side are necessary.^{54–58} The HR coating can be a multilayer quarter-wave stack, sometimes called a diffraction Bragg reflector (DBR) or it can be a single layer of high reflectance silver, or aluminum with enhancing dielectric layers, or a so-called omnidirectional reflecting coating (ODR). Figure 15.30 shows the structure of an example ODR where the first SiO_2 layer must be more than 500 nm to give high reflectance at large angles as shown in Fig. 15.31. A structural photonic crystal ODR has also been proposed.⁵⁹ The AR can be achieved by texturing the outside surface of the LED,⁶⁰ adding a multilayer coating, or a coating with graded refractive-index layer.

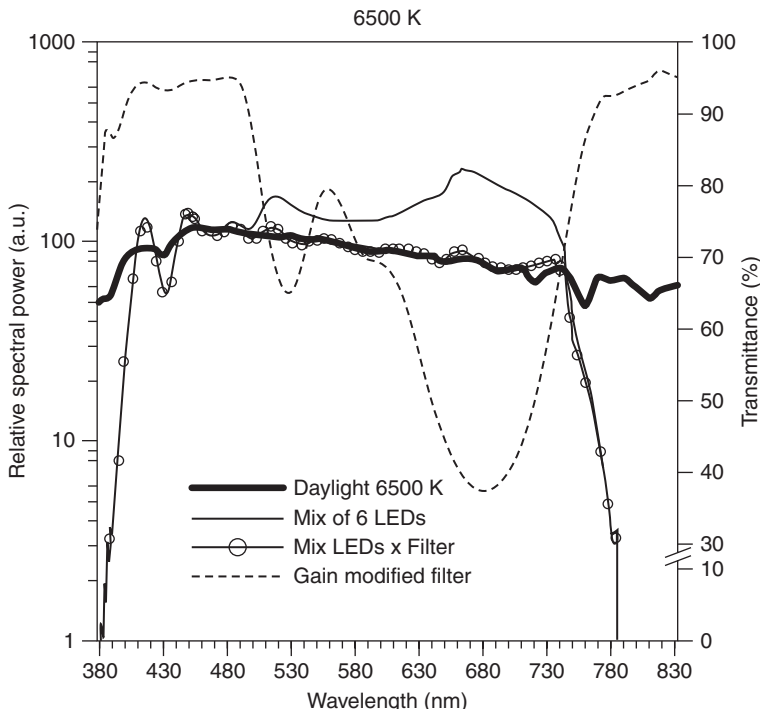
In general LEDs cannot be true white light sources similar to sunlight or, say, the D_{65} illuminant. Such a deficiency can be overcome by using a gain modified filter (GMF) the so-called daylight simulation coating.^{61,62}



15.30 Structure of an ODR coating, where the thickness of the first SiO_2 layer is larger than 500 nm to give high reflectance at large angles.



15.31 Reflectance at 460 nm vs angle of ODR reflector.

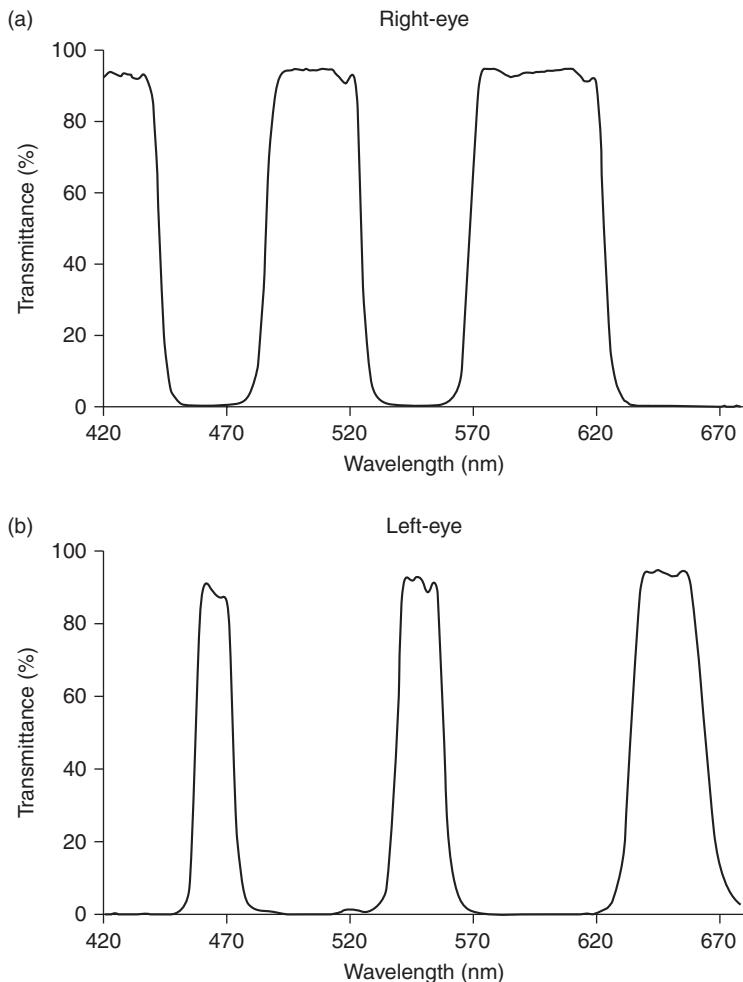


15.32 Daylight simulation coating of LEDs by adding GDF.

Figure 15.32 shows a spectrum of white light from a combination of six LEDs, as well as the spectra of the GMF and the D₆₅ illuminant. The addition of the GMF gives us a spectrum equivalent to the D₆₅. The GMF shown in Fig. 15.32 is a 19-layer TiO₂/SiO₂ multilayer coating. Based on the same principle we can enhance the color gamut by adding a GMF to LEDs of any color when they are used as the light source in projectors or for other applications.

15.7 Conclusion

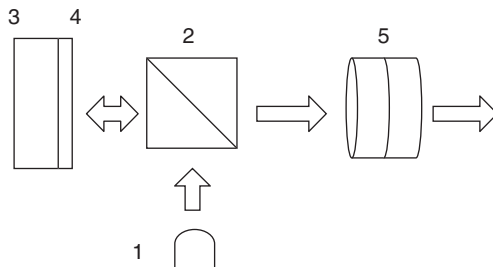
Display and LED lighting have been developed to the stage where they play an important part in our daily life. Most people, however, would not accept them without their optical coatings. Several types of optical coatings are required. These include antireflective coatings, antiglare coatings, high reflectance coatings, color selection coatings (band pass filters, long wave pass filters, short pass filters), polarizers, polarization insensitive coatings, angle insensitive coatings, angular selection filter, wide angle reflection filter, view angle limited coatings (for privacy), and even hydrophobic repelling (repelling water, dirt, dust, fingerprints, stains) coatings



15.33 High resolution multi-band coating technology without cross-talk of the R/L signal, (a) R signal (b) L signal. (Courtesy of Orange Bright Optics; <http://www.ob-optics.com>).

and hard coating. These make displays and LEDs function properly, improve their quality and make them visually comfortable to the human eye, increase their output efficiency, and improve their durability with consequently long life. Some of the coatings are quite simple and others are very challenging. Examples are coatings for high incident angle in short throw PTV⁶³ and multi-band pass filters (MBPF) for 3D projectors (<http://www.ob-optics.com>).

1. White LED
2. PBS
3. LCoS
4. Quarter wave plate
5. Projection lens



15.34 Schematic drawing of a micro-projector.

For 3D cinema applications, optical coatings are simpler with better color saturation and brightness compared with other methods. 3D cinema usually employs a polarization methodology. To have a solution which does not involve polarization, a MBPF is utilized. Figure 15.33 shows the spectra of two three-primary-color filters for glasses of the right eye (a) and the left eye (b), which are also the two halves of the color wheel. That means there are six colors composed in the color wheel. With a high color wheel rotation rate, the right eye and left eye receive three different primary colors sequentially and thus see the 3D images.

A handy projector with minimal size is a dream of many people. This has been realized by utilizing a micro-LCoS technique. Figure 15.34 shows the schematic drawing of a micro-projector. Its size is small enough to put in the palm of the hand or carry in a pocket or be installed in a cell phone. However, the output flux is still not high enough to make it widely popular.

15.8 Acknowledgements

The authors would like to thank Prof. Angus H. Macleod and Prof. Francois Flory for their valuable suggestions.

15.9 References

1. Brody T. P., Asars J. A. and Dixon, G. D. (1973) 'A 6 × 6 inch 20 lines-per-inch liquid-crystal display panel', *IEEE Transactions on Electron Devices*, **20**(11), 995–1001.
2. Tannas L. E. (1989) 'Flat-panel displays displace large, heavy, power-hungry CRTs', *Spectrum, IEEE*, **26**, 34–35.

3. Mentley D. E. (2002) 'State of flat-panel display technology and future trends', *Proc. IEEE*, **90**, 453–459.
4. Allen K. J. (2005) 'Reel to real: prospects for flexible displays', *Proc IEEE*, **93**, 1394–1399.
5. Tannas L. E. (1994) 'Evolution of flat-panel displays', *Proc. IEEE*, **82**, 499–509.
6. Kimmel J., Hautanen J. and Levola T. (2002) 'Display technologies for portable communications devices', *Proc. IEEE*, **90**, 581–590.
7. Epstein D. W. and Maloff I. G. (1945) 'Projection Television', *SMPTE Mot. Imag. J.*, **44**, 443–455.
8. Van Kessel P. F., Hornbeck L. J., Meier R. E. and Douglass M. R. (1998) 'A MEMS-based projection display', *Proc. IEEE*, **86**, 1687–1704.
9. Shimizu J. A. (2001) 'Scrolling Color LCOS for HDTV Rear Projection', *SID Symposium Digest*, **32**, 1072–1075.
10. Hornbeck L. J. (1997) 'Digital light processing for high-brightness, high-resolution applications', *Proc. SPIE*, **3013**, 27–40.
11. Hornbeck L. J. (1993) 'Current status of the digital micromirror device (DMD) for projection television applications', *IEDM*, **93**, 381–384.
12. Ponce F. A. and Bour D. P. (1997) 'Nitride-based semiconductors for blue and green light-emitting devices', *Nature*, **386**, 351–359.
13. Arik M., Petroski J. and Weaver S. (2002) 'Thermal challenges in the future generation solid state lighting applications: light emitting diode', *ITHERM 2002*, 113–120.
14. Harbers G. and Hoelen C. (2001) 'High performance LCD backlight using high intensity red, green and blue light emitting diodes', *SID Tech. Dig.*, **32**, 702–705.
15. Macleod H. A. (2001), *Thin-Film Optical Filters*, 3rd ed., Institute of Physics Publishing, Bristol, Philadelphia.
16. Al-Dahoudi N., Bisht H., Gobbert C., Krajewski T. and Aegeerter A. M. (2001) 'Transparent conducting, anti-static and anti-static–anti-glare coatings on plastic substrates', *Thin Solid Films*, **392**, 299–304.
17. Zheng Y., Kikuchi K., Yamasaki M., Sonoi K. and Uehara K. (1997) 'Two-layer wideband antireflection coatings with an absorbing layer', *Appl. Opt.*, **36**, 6335–6338.
18. Ishikawa H. and Lippey B. (1996) 'Two Layer Broad Band AR Coating', *Proceedings of Tenth International Conference on Vacuum Web Coating*; 12 November, 221–233.
19. McHale G., Shirtcliffe N. J. and Newton M. I. (2004) 'Contact-angle hysteresis on super-hydrophobic surfaces', *Langmuir*, **20**, 10146–10149.
20. Chen D., Yan Y., Westenberg E., Niebauer D., Sakaitani N. and Chaudhuri, S. R. (2000) 'Development of anti-reflection (AR) coating on plastic panels for display applications', *J. Sol-Gel Sci. Tech.*, **19**, 77–82.
21. Mascia L. and Tang T. (1998) 'Polyperfluoroether-silica hybrids', *Polymer*, **39**, 3045–3057.
22. Katayama M. (1999) 'TFT-LCD technology', *Thin Solid Films*, **341**, 140–147.
23. Exarhos Gregory J. and Zhou X. D. (2007) 'Discovery-based design of transparent conducting oxide films', *Thin Solid Films*, **515**, 7025–7052.
24. Rogers J. A., Bao Z., Baldwin K., Dodabalapur A., Crone B., Raju V. R., Kuck V., Katz H., Amundson K., Ewing J. and Drzaic P. (2001) 'Paper-like electronic displays: Large-area rubber-stamped plastic sheets of electronics

- and microencapsulated electrophoretic inks'; *Proc. Natl. Acad. Sci. USA*, **98**, 4835–4840.
- 25. Szczyrbowski J., Dietrich A. and Hartig K. (1989) 'Bendable silver-based low emissivity coating on glass'; *Solar Energy Mater.*, **19**, 43–53.
 - 26. Rauh R. D. (1999) 'Electrochromic windows: an overview'; *Electrochim. Acta*, **44**, 3165–3176.
 - 27. Hosono H., Ohta H., Orita M., Ueda K. and Hirano M. (2002) 'Frontier of transparent conductive oxide thin films'; *Vacuum*, **66**, 419–425.
 - 28. Streintz F. (1902) 'On the electrical conductivity of pressed powders'; *Ann. Phys. (Leipzig)*, **9**, 854.
 - 29. Minami T. (1999) 'Transparent and conductive multicomponent oxide films prepared by magnetron sputtering'; *J. Vac. Sci. Technol. A*, **17**, 1765–1772.
 - 30. Zhang K., Zhu F., Huan C. H. A. and Wee A. T. S. (2000) 'Indium tin oxide films prepared by radio frequency magnetron sputtering method at a low processing temperature'; *Thin Solid Films*, **376**, 255–263.
 - 31. Manifacier J. C., Szepessy L., Bresse J. F., Perotin M. and Stuck R. (1979) 'In₂O₃; (Sn) and SnO₂ : (F) films – application to solar energy conversion part II – Electrical and optical properties'; *Mater. Res. Bull.*, **14**, 163–175.
 - 32. Tominaga K., Umezu N., Mori I., Ushiro T., Morifa T. and Nakabaayashi I. (1998) 'Transparent conductive ZnO film preparation by alternating sputtering of ZnO:Al and Zn or Al targets'; *Thin Solid Films*, **334**, 35–39.
 - 33. Bhosle V., Tiwari A. and Narayan J. (2006) 'Electrical properties of transparent and conducting Ga doped ZnO'; *J. Appl. Phys.*, **100**, 033713–033718.
 - 34. Dabney M. S., van Hest M. F. A. M., Teplin C. W., Arenkiel S. P., Perkins J. D. and Ginley D. S. (2008) 'Pulsed laser deposited Nb doped TiO₂ as a transparent conducting oxide'; *Thin Solid Films*, **516**, 4133–4138.
 - 35. He Y. S., Campbell J. C. and Murphy R. C. (1993) 'Electrical and optical characterization of Sb: SnO₂'; *J. Mater. Res.*, **8**, 3131–3134.
 - 36. Li M. C., Kuo C. C., Peng S. H., Chen S. H. and Lee C. C. (2011) 'Influence of hydrogen on the properties of Al and Ga-doped ZnO films at room temperature'; *Applied Optics*, **50**, C197–C200.
 - 37. Liao B. H., Kuo C. C., Chen P. J. and Lee C. C. (2011) 'Fluorine-doped tin oxide films grown by pulsed direct current magnetron sputtering with an Sn target'; *Applied Optics*, **50**, C106–C110.
 - 38. Takeda M. and Miyatake Y. (1992) 'Three-LCD projector having specified scanning directions'; *US Patent 5122870*.
 - 39. Shikama S., Kida H., Daijogo A., Maemura Y. and Kondo M. (1993) 'A compact LCD rear projector using a new bent-lens optical system'; *SID Symp. Digest*, **24**, 295–298.
 - 40. Jepsen M. L. (2003) 'Rear projection TV: Single panel LCOS lumen throughput'; *SID Symp. Digest*, **34**, 112–125.
 - 41. Yu X. J., Ho Y. L., Tan L., Huang H. C. and Kwok H. S. (2007) 'LED based projection systems'; *J. Disp. Technol.*, **3**, 295–303.
 - 42. Wei Z. C., Kuo C. C., Huang J. J. and Lee C. C. (2010) 'Research on angle-selective filters of phosphors color wheel for LED projector'; *Proc. SPIE*, **7786**, 778604.
 - 43. Mailloux R. J. (1976) 'Synthesis of spatial filters with Chebyshev characteristics'; *IEEE Trans. Antennas Propagat.*, **24**, 79–85.

44. Fink Y., Winn J., Fan S., Chen C., Michel J., Joannopoulos J. D. and Thomas E. L. (1998) 'A dielectric omnidirectional reflector', *Science*, **282**, 1679–1682.
45. Hsueh W. J., Wun S. J. and Yu T. H. (2010) 'Characterization of omnidirectional bandgaps in multiple frequency ranges of one-dimensional photonic crystals', *J. Opt. Soc. Am. B*, **27**, 1092–1098.
46. Epstein L. I. (1955) 'Low loss multilayer dielectric mirrors', *J. Opt. Soc. Am.*, **45**, 360–362.
47. Born M. and Wolf E. (1965) *Principles of Optics*, 3rd ed., Pergamon Press Ltd., 66.
48. Chen H. C., Lee C. C. and Huang J. J. (2006) 'Improving the illumination efficiency and color temperature for a projection system by depositing thin-film coatings on an x-cube prism', *Opt. Eng.*, **45**, 113801–113805.
49. Peng G., Rapids C., Steffensmeier M. J. and Rapids C. (2009) 'Head up display having a combiner with wedge lenses', *United States Patent*, Patent No. US 7,570,430 Bl.
50. Sauer G. and Stolberg (2005) 'Laminated glass windscreen intended to be used at the same time as a HUD system reflector', *United States Patent*, Patent No.: US 6,866,918 B2.
51. Caudell T. P. and Mizell D. W. (1992) 'Augmented reality: an application of heads-up display technology to manual manufacturing processes', *Proc. Hawaii International Conf. Systems Science*, **2**, 659–669.
52. Lee C. C., Tsai S. H., Kuo C. C., Chen C. H., Teng L. M. and Luo K. T. (2011) 'Free ghost image and high transmittance optical thin film beam splitter for head-up display', *SID Symp. Digest*, **42**, 1451–1453.
53. Muthu S. and Gaines J. (2003) 'Red, green and blue LED-based white light source: implementation challenges and control design', *Proc. IEEE IAS Annu. Meeting*, **1**, 515–522.
54. Gessmann T., Schubert E. F., Graff J W., Streubel K. and Karnutsch C. (2003) 'Omnidirectional reflective contacts for light-emitting diodes', *Electron Dev. Lett.*, **24**, 683–685.
55. Kim J. K., Gessmann, T., Schubert E. F., Xi J. Q., Hong L., Cho, J., Sone C. and Park Y. (2006) 'GaN light-emitting diode with conductive omnidirectional reflector having a low-refractive-index indium-tin oxide layer', *Appl. Phys. Lett.*, **88**, 013501–013503.
56. Kim J. K., Luo H., Xi Y., Shah J. M., Gessmann T. and Schubert E. F. (2006) 'Light extraction in GaInN light-emitting diodes using diffuse omnidirectional reflectors', *J. Electrochem. Soc.*, **153**, G105–G107.
57. Gessmann T., Luo H., Xi J.-Q., Streubel K. P. and Schubert E. F. (2004) 'Light-emitting diodes with integrated omnidirectionally reflective contacts', *Proc. SPIE*, **5366**, 53–61.
58. Huang H. W., Kuo H. C., Lai C. F., Lee C. E., Chiu C. W., Lu T. C., Wang S. C., Lin C. H. and Leung K. M. (2007) 'High-performance GaN-based vertical-injection light-emitting diodes with TiO₂–SiO₂ omnidirectional reflector and n-GaN roughness', *Photon. Tech. Lett.*, **19**, 565–567.
59. Dong J. W., Han P. and Wang H. Z. (2003) 'Broad omnidirectional reflection band forming using the combination of Fibonacci quasiperiodic and periodic one-dimensional photonic crystals', *Chin. Phys. Lett.*, **20**, 1963–1965.

60. Cho J. Y., Byeon K. J. and Lee H. (2011) 'Forming the graded-refractive-index antireflection layers on light-emitting diodes to enhance the light extraction', *Opt. Lett.*, **36**, 3203–3205.
61. Lo M. L., Yang T. H. and Lee C. C. (2011) 'Fabrication of a tunable daylight simulator', *Appl. Opt.*, **50**, C95–C99.
62. Lee C. C., Yang T. H., Liao S. F. and Chang K. (2009) 'LED-spectrum shaping by optical filter achieves tunable daylight simulator', *SPIE Newsroom*, 17 June.
63. Jorke, H., Simon A. and Fritz M. (2009) 'Advanced stereo projection using interference filters', *J. Soc. Inf. Display*, **17**, 407–410.

L. ESCOUBAS, J. J. SIMON and J. LE ROUZO (IM2NP),
Aix-Marseille Université, IM2NP, France and
V. BERMUDEZ, Nexcis, France

DOI: 10.1533/9780857097316.4.596

Abstract: This chapter discusses the use of new approaches in thin film photovoltaic solar cells. The chapter first reviews devices which use nanowires and quantum dots in inorganic thin film solar cells. The second part is devoted to organic solar cells, explaining their working principles and strategies for light trapping and efficiency enhancement. The last part describes new chalcopyrite materials deposited by state-of-the-art technologies at the industrial level such as spray, electrodeposition, or doctor blading. Such technologies allow low-cost deposition of advanced materials on large surfaces for harvesting sun energy.

Key words: photovoltaic, solar cells, chalcopyrite, nanowires, quantum dots, organic.

16.1 Introduction

The production of a considerable amount of CO₂ is the consequence of the generation of the largest part of the energy requirements which come from fossil fuel. In our society, sustainable development is a priority and we must develop renewable energies allowing innovative solutions to the problem of CO₂ gas emission. In 2012, only 5% of energy production worldwide corresponded to renewable energy. Thus, huge efforts have gone into harvesting renewable energy, such as solar, hydroelectric, wind and hydrothermal energy.

As regards to solar energy, and more precisely photovoltaics, solar modules based on the use of bulk silicon wafers have dominated the market over recent years. But wafer costs account for over 50% of the total module cost and replacing wafers by thin films of semiconductors deposited onto a substrate (Green, 2007) is one reliable option for eliminating this major cost component.

In the photovoltaic market, thin film photovoltaic modules show great promise for producing sustainable, low-cost, clean electricity from sunlight (Topič, 2011): the global market share of inorganic thin film photovoltaic materials and their solar cell structures in 2010 was around 15% (3.2 GW of 21 GW) and is predicted to increase to 21% in 2012 (Jäger-Waldau, 2011).

The two main advantages among others of thin film solar cells are:

1. lower consumption of materials and energy during their fabrication processes and
2. low-cost production because process are applicable to large areas in either batch or roll-to-roll production lines.

But solar cell thin film technologies also face some drawbacks:

- lower module conversion efficiencies and
- in some cases, light-induced degradation of the materials.

However, inorganic thin film solar cells and modules are competitive with crystalline silicon solar cells, regarding total cost and state-of-the-art performance (Jäger-Waldau, 2011).

Two main classes of thin film solar cells have been developed at an industrial level: one based on silicon in amorphous, nanocrystalline and polycrystalline phases and the other on polycrystalline chalcogenide semiconducting compounds. A third class, based on organic materials coming from chemical synthesis, has developed very quickly over recent years thanks to the efforts of companies such as Mitsubishi, Sumitomo Chemical, Heliatek, Konarka and Solarmer.

Even if thin film solar cells share a common device structure – typically consisting of a front contact, a p–n junction comprising an absorber layer and a back contact – various fabrication processes depending on thin film materials need to be used to reach the best conversion efficiency (Yan, 2011). Indeed, thin film silicon-based solar cells include hydrogenized amorphous, nanocrystalline or microcrystalline silicon (a-Si:H, nc-Si:H, μc-Si:H). To achieve high efficiencies, Si thin film solar cells require hydrogen (H) passivation. The record efficiency of an a-Si:H solar cell, from United Solar, is 12.5% (Table 16.1).

As regards chalcopyrite solar cells, the main representative is polycrystalline Cu(In, Ga)(Se,S)₂ (CIGS), while for II–VI semiconductors it is polycrystalline cadmium telluride (CdTe). CdTe cells require heat treatment in CdCl₂, whereas for CIGS solar cells a heat post-treatment is necessary to activate Na coming from the glass substrate to passivate defects in the CIGS absorber. In CIGS and CdTe, a very efficient absorption of

Table 16.1 Record conversion efficiencies of thin film solar cells (June 2012)

	a-Si:H	CIGS	CdTe	CZTSSe	DSSC	Organic	Organic tandem	Quantum dot
Conversion efficiency	12.5%	20.3%	17.3%	11.1%	11.4%	10.0%	10.7%	5.1%

Lab or company United Solar ZSW First Solar IBM NIMS Mitsubishi Chemical Heliatek Univ Toronto (PbS quantum dots)

solar spectrum occurs as they exhibit higher absorption coefficient than crystalline silicon (c-Si).

The use of various rigid or flexible substrates such as glass, plastic or metal foils, is possible as thin layers of the materials may be deposited at low temperatures (200–500°C for a-Si:H) or even at room temperature.

When considering the efficiency performances of thin film solar cells, to date, the record conversion efficiencies for CIGS and CdTe based solar cells have reached 20.3% and 17.3%, respectively (Table 16.1). These thin film absorber materials share the same basic structural feature – diamond-based.

Defects, including point defects, extended defects and interfaces, make a major contribution to the performance of thin film solar cells. A good review of defects physics in thin film solar cell materials including Si, CdTe, copper indium selenium (CIS), and CIGS by the combination of transmission electron microscopy (TEM) technique and density-functional theory (DFT) is given by Yan (2011). It is shown that some defects, such as stacking faults and special twins, have similar electronic properties in these thin film materials but some other defects, such as grain boundaries and interfaces, exhibit very different electronic properties. As an example, whereas grain boundaries produce deep levels in CdTe, it is generally not the case in CIGS with Na in diffusion treatments.

With the exception of silicon thin film solar cells, CdTe and CIGS absorbing materials have dominated the research in thin film solar cells in the last decade. But, one important issue concerns the environmental impact of cadmium and a second is linked to the limited availability of indium. Indeed, viable solar cell should be made from cheap and simple materials for terawatt scale production of energy. Abundance of the elements comprising the solar cell is a prerequisite. And it is very important to consider materials exhibiting extraction costs which are lower than for silicon as well as electricity production potential which is greater than silicon. Thus, new substitute light absorbers made from earth-abundant, environmentally benign materials, and showing good stability and long life, are highly desirable. Unconventional solar cell candidates including FeS_2 , CuO and Zn_3P_2 have

been proposed by Wadia *et al.* (2009). But Cu₂ZnSnS₄ (CZTS) semiconductor material has emerged as one of the most promising candidates for this application and has attracted considerable interest recently (Wang, 2011). All the constituent elements in CZTS are earth abundant and environmentally benign. It is found that the abundance of Zn and Sn in the Earth's crust is 1500 times and 45 times greater than that of In, respectively, and the price of In is almost two orders of magnitude higher than those of Zn and Sn. The record conversion efficiency for a CZTS solar cell has been pushed up to 11.1% by IBM (Table 16.1) using wet chemical methods.

A third class of emerging technologies is based on organometallic dyes and polymers. Organic (or plastic) solar cell (OPV) and dye-sensitized solar cells (DSSC) are promising emerging PV technologies based on organic semiconductor materials. Organic solar cells consist of conductive organic polymers (deposited from spin coated solutions of molecules in solvents) or small organic molecules (evaporated under vacuum) for light absorption, charge separation and transport. Such active organic materials are sandwiched between the contact layers: a transparent conductive oxide layer such as indium tin oxide (ITO) is used as the front contact and usually aluminum as the back contact. Record conversion efficiencies for OPV single junction, OPV multijunction solar cells and DSSC have reached 10.0%, 10.7% and 11.4%, respectively (Table 16.1).

In the following sections we will present a few innovative approaches in thin film solar cells. We begin with the use of nanostructures, such as nanowires or quantum dots, to improve the performances of thin film solar cells. Indeed, a thin film solar cell can be considered as a multilayer interference optical coating to calculate the solar optical field distribution. Furthermore, photonic crystals, nanoplasmonics and other light trapping strategies concern nanostructured thin films. A state-of-the-art review of organic solar cells is then presented along with light trapping strategies which are also a major concern for organic solar cells. However, material and electrical considerations also have to be taken into account. The last part of this chapter is devoted to CIGS coatings, at industrial level, with novel vacuum free deposition technologies.

16.2 Inorganic nanostructures for photovoltaic solar cells

As mentioned in the introduction of this chapter, the costs of photovoltaic energy are still too large in comparison with those of conventional energies. Cost reduction can be obtained by an increase of cell performance. Antonio Luque (2011) in one of his last articles asked whether it is possible to achieve solar cell efficiencies above 50% and thus overcome the

current record, obtained by a multijunction solar cell under concentrated sunlight (Green, 2011). To do this, the photovoltaic research and industry must answer two fundamental questions. Firstly, how to succeed in lowering the expenses of manufacture? And secondly, how to enhance the efficiency of solar cells? One route of investigation is the development of nanostructures in thin film layers.

As described previously, the use of thin films for solar cells is one of the keys of success for photovoltaics. The direct bandgap materials like CIGS, CdTe or GaAs can directly address this issue. And if we go further, some thin film solar cells, including nanostructures, have both improved light trapping and photo-carrier collection thus improving the efficiency of solar cells.

16.2.1 New concepts of solar cells

The fast development of nanotechnology allows the realization of objects with very small dimensions such as nanowires (Lu, 2006) or quantum dots (see Chapter 12). Two nanostructures will be detailed in this part. These nanostructures have the distinction of having different physical properties from those of macroscopic structures. Of these, one can notice changes in the bandgap, the refractive index, the rate of recombination of carriers and a large surface-to-volume ratio. For example, because of quantum confinement effects, alteration of their physical and electronic properties is observed when the size of these structures is as small as or smaller than the Bohr exciton radius of the material providing some new concepts of solar cells. Quantum structures can reach the Shockley-Queisser limit of 32% for Si-based solar cells (Shockley, 1961).

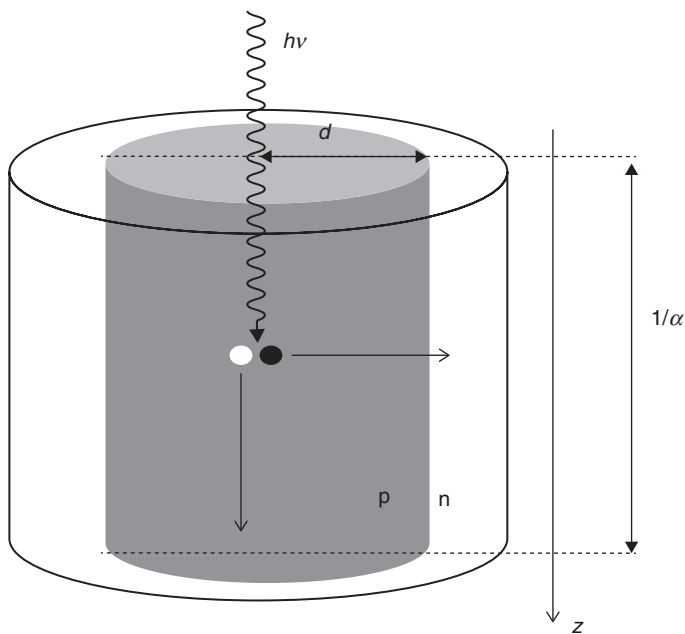
Different materials and solar cell structures based on nanostructures have been studied. Both new photovoltaic mechanisms and new concepts for solar cells are thus expected such as multijunction solar cells (Kandala, 2008), hot carrier solar cells (Tisdale, 2010), intermediate band solar cells (Luque, 2012), hybrid solar cells (Skompska, 2010), frequency conversion (Meijer, 2010) and multiple-exciton generation (Nozik, 2008), which belongs to a new generation of photovoltaic technology (Brown, 2009). These cells are very interesting in terms of theoretical research and very promising for the future of photovoltaic devices and more generally for optoelectronics. More than that, different photonic structures can be studied to enhance either the absorption or the antireflective effect in these solar cells such as photonic crystals or plasmonics, two innovative concepts widely studied nowadays (El Daif, 2010; Pillai, 2011). Although most of these technologies are still under research, the many advances made in recent years make it possible to foresee a rapid evolution of these cells toward their commercial manufacture (Lunt, 2011).

16.2.2 Light trapping and photo-carrier collection

Now that we know the current possibilities of ‘nanostructured solar cells’, we will get into more detail on the benefits of these thin films including nanostructures. As previously written, in order to enhance the performance of solar cells, we need both to improve the light trapping and the photo-carrier collection. Indeed, in a ‘classical’ silicon solar cell, because of its indirect bandgap, we need a sufficiently thick layer to optimize the absorption of sunlight. This large thickness results in a decrease of the collection of photo-generated carriers, due to a higher probability of recombination. Similarly, in thin film solar cells, the collection of carriers is increased at the expense of the absorption of photons, even in high absorbing materials.

The use of different mechanisms of light trapping in solar cells is a prerequisite in order to improve the absorption. Several nanostructures such as nanowires, nanopillars or nanocones, have already shown their ability to absorb light very efficiently. For example, a strong increase in path length enhancement factor with nanowire length has been demonstrated in silicon nanowire solar cells (Garnett, 2010). The path length enhancement factor is defined as the apparent optical thickness of the structure divided by its actual thickness. The best nanowire arrays showed path length enhancement factors of up to 73, exceeding the randomized scattering limit ($2n^2 \approx 25$ because there was no back reflector) (Yablonovitch, 1982). Zhu *et al.* (2009) have also shown that for a-Si:H nanocone arrays, more than 90% of light is absorbed at angles of incidence up to 60° , which is better than thin films (45%). A highly efficient antireflective coating for photovoltaic solar cells can also be developed thanks to silicon nanowires. These structures, known as ‘Black Silicon’, exhibit an average reflection value around 2% in the wavelength range of 300–1000 nm (Jung, 2010). The optical properties (reflection, transmission, absorption, scattering) of InP, GaP nanowires (Muskens, 2008), Ge nanowires (Cao, 2009) and CdS nanopillars (Fan, 2009) have also been studied showing a great interest in these materials for photovoltaic applications. Instead of structuring direct semiconductors at the nanoscale, Yu *et al.* (2011) have developed a simple and inexpensive method to fabricate Al nanospikes (NSP) arrays on which they deposit thin film photovoltaic materials, such as a-Si or CdTe to form 3D conformal coating. With these kinds of structures they achieve up to 94% day-integrated sunlight, in the 300–900 nm wavelength range.

In order to optimize the ratio of collected and photogenerated carriers, the nanostructures must be well defined. It means that the diffusion length of the minority carriers must fit with the dimensions of the structure. Since we need a p–n junction to collect carriers, one solution consists of making a nanostructure that offers a p–n junction orthogonal to the absorption of light. In this configuration, the decoupling of light absorption and carrier extraction



16.1 Design of a radial p–n junction in a nanorod. The decoupling of light absorption and carrier extraction is clearly shown.

might provide a way to improve carrier-collection efficiency (Kayes, 2005; Spurgeon, 2008), which is clearly identified in Fig. 16.1. Indeed, the absorption of photons occurs along the nanowire measuring a few micrometers, while the depletion region of the p–n junction is in the radial direction with dimensions of few nanometers.

16.2.3 Quantum dots and nanowires included in thin film solar cells

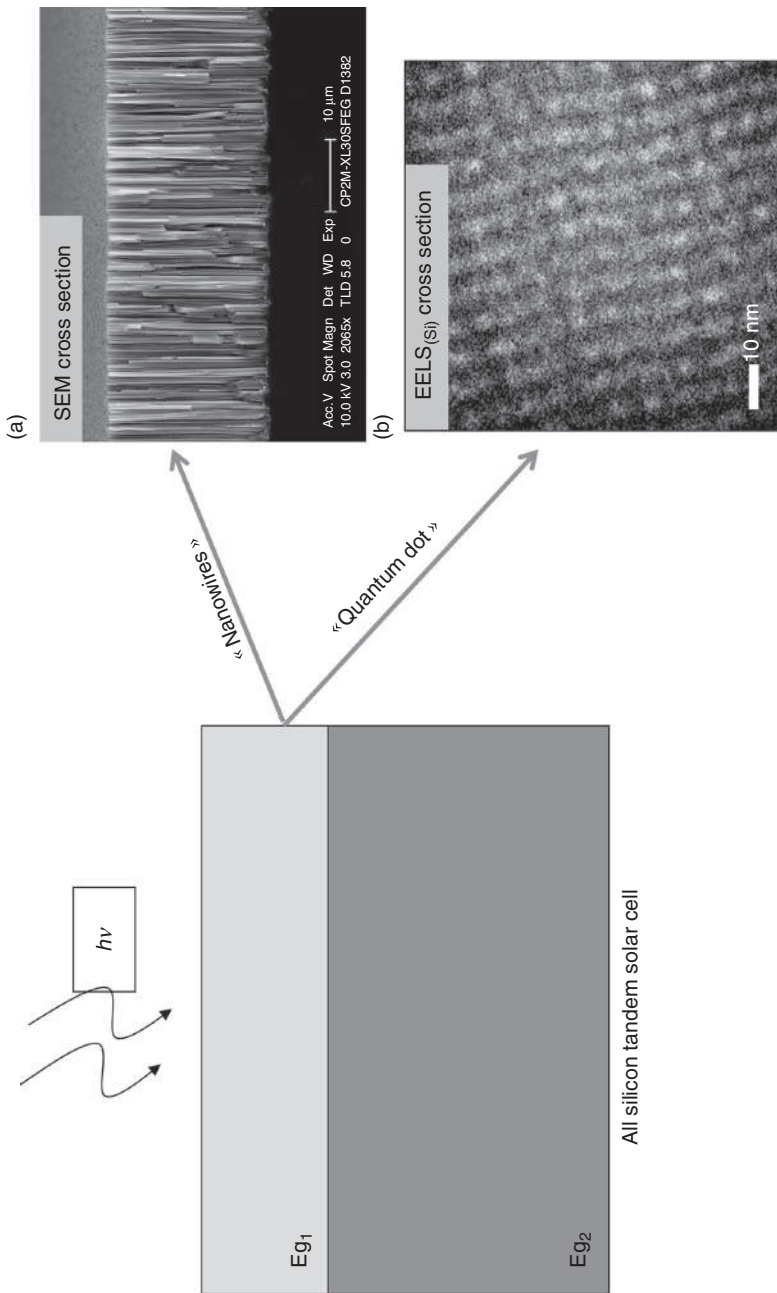
Among all the nanostructures used in photovoltaic solar cells, we are particularly interested in nanowires and quantum dots, which are the most studied and most promising for solar cells for all the reasons described previously. We thus present some examples of new architectures of photovoltaic solar cells including these nanostructures which exhibit many advantages to increase solar cell efficiencies.

First, quantum dots and nanowires can be inserted into multijunction solar cells and particularly in tandem solar cells. This architecture allows considerable increases in the absorption of light over a larger spectral range than a conventional solar cell made with a single junction. To go into further

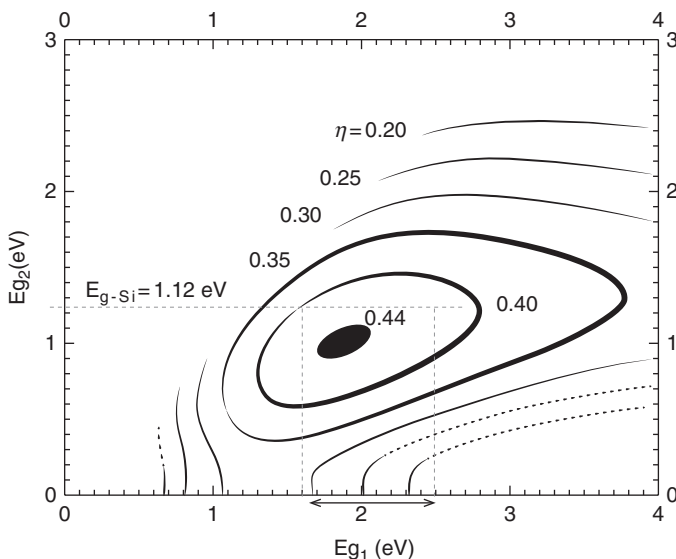
detail on this device, we take silicon material as an example. The principle is as follows: the upper cell is a nanostructured layer in silicon and the cell below is made of bulk silicon. The first solar cell presents a gap (Eg_1) higher than the second one (Eg_2) in order to avoid losses in absorption. This difference in the bandgap of the two layers is obtained thanks to quantum confinement. Indeed, Fig. 16.2 presents a tandem silicon solar cell (2 junctions) with the first layer which can be either an array of nanowires or a layer comprising quantum dots. Alexis De Vos (1980) proposed a model to calculate the limit efficiency of a tandem solar cell, taking into account the fact that a particular cell is not only illuminated by part of the solar irradiance but also by the electroluminescence of other cells of the set. He showed that a maximum of 42.3% occurs for $Eg_1 = 1.9$ eV and $Eg_2 = 1.0$ eV (above the Shockley-Queisser limit for a single junction). If the value $Eg_2 = 1.12$ eV is taken for bulk silicon, several bandgaps Eg_1 , between 1.6 and 2.2 eV, are available to reach an efficiency around 40% as shown in Fig. 16.3. Higher bandgap for silicon (e.g., 1.7 eV) can be obtained by reducing the size until a few nanometers (less than 3 nm for nanowires and quantum dots) (Takagi, 1990). These experimental constraints are an impediment to the development of inorganic tandem solar cells using nanostructures. However, we can note that multijunctions solar cells using inorganic materials, are manufactured and work well providing the record photovoltaic efficiency of 42.3% with GaInP/GaInAs/Ge two terminal, triple junction cells (Green, 2011).

Several teams have recently obtained promising results on nanowires solar cells combining low-cost and high efficiency. The most recent study is proposed by Huang *et al.* (2012). Nanowire arrays were synthesized by using the wet electroless etching technique. This study proposes a low-cost, silicon nanowire (SiNW) arrays fabrication process using a new solution as the doping source, with a screen-printing method to coat electrodes to create SiNW array-based solar cells. This latter exhibits a conversion efficiency of 10.15% with a short-circuit current J_{sc} of 30.65 mA cm^{-2} and an open circuit voltage V_{oc} of 520 mV. This is very promising for low-cost fabrication of solar cells with high efficiency.

Another research method for increasing solar cell efficiency with nanostructures is the modulation of the solar spectrum. The two main losses in a single junction solar cell are firstly the inability of the bulk semiconductor to absorb photons of lower energy than their energy bandgap and secondly the thermalization of photogenerated carriers. The idea is to change the whole solar spectrum to accommodate the absorption of the solar cell (directly connected to the gap); it requires some frequency conversion. This can be done by the up- and down-converter structures placed, respectively, in the back and in the front side of a solar cell (Conibeer, 2007). Recently, Chun-Ying Huang *et al.* (2010) have demonstrated that a hybrid colloidal ZnS nanoparticles/Si nanotips p–n active layer in crystalline silicon-based



16.2 An all silicon tandem solar cell. The upper cell is a nanostructured layer in silicon (Eg₁) and the cell below is made of bulk silicon (Eg₂). The first cell is made by either: (a) an array of nanowires (SEM cross section, Le Rouzo, 2009), or (b) an array of quantum dots (EELS cross section, Rezgui, 2010).



16.3 Theoretical calculation of the conversion efficiency of a tandem solar cell. The silicon material has been taken as an example for the cell. (Source: Reproduced with the permission of IOPP publications (in progress).)

solar cells presents an enhancement of 20% in the short-circuit current and approximately 10% in power conversion efficiency compared to its counterpart without integrating ZnS nanoparticles. ZnS nanoparticles not only act as frequency down-conversion centers in the ultraviolet region but also serve as an antireflective coating for light trapping in the measured spectral regime.

The multiple exciton generation (MEG) is another mechanism which will increase the photocurrent. The energetic hot carriers (with energy higher than the bandgap of the material) must produce two or more electron–hole pairs through impact ionization (Conibeer, 2007). Semonin *et al.* (2011) reported on photocurrent enhancement arising from MEG in lead selenide (PbSe) QD-based solar cells, as manifested by an external quantum efficiency (the spectrally resolved ratio of collected charge carriers to incident photons) that peaked at $114 \pm 1\%$ in the best device measured. The associated internal quantum efficiency (corrected for reflection and absorption losses) was 130%.

To conclude for these new concepts of solar cells, we will finish with hybrid nanostructure solar cells which combine both organic and inorganic semiconductors (Skompska, 2010). Different inorganic semiconductor materials are used either like quantum dots or nanowires. Ren *et al.* (2011) demonstrated quantum dot-based hybrid solar cells. The CdS quantum dots

were bound onto crystalline poly(3-hexylthiophene) (P3HT) nanowires through solvent-assisted grafting and ligand exchange, leading to controlled organic–inorganic phase separation and an improved maximum power conversion efficiency of 4.1% under AM 1.5 solar illumination.

Organic solar cells will be described in more detail in the following part of this chapter.

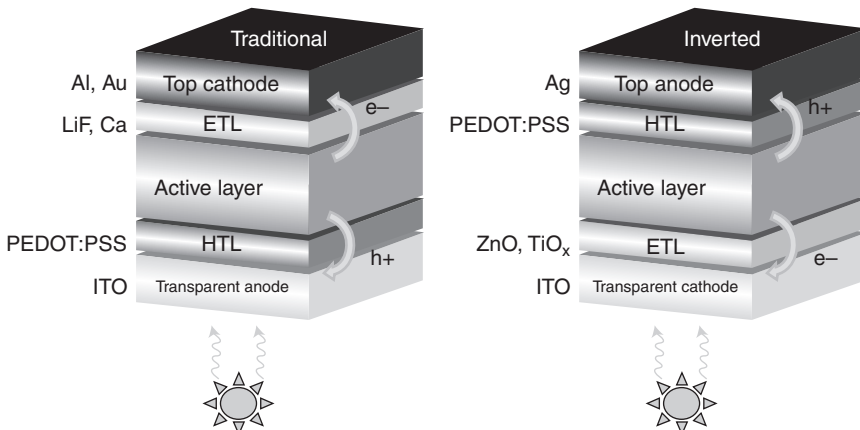
16.3 Organic thin film solar cells

Organic solar cells (OSC) have received increasing attention over the last few years. Indeed, the materials used in the photovoltaic polymer domain offer many practical advantages over conventional photovoltaic materials such as silicon thanks to the solution processing techniques used to fabricate the cells (low-cost, flexible and large-scale applications). Moreover, OSC performance has significantly increased in the last few years through the design and synthesis of novel new active materials (Boudreault, 2011; Zhang, 2012), modified interfacial layers (Motiei, 2010; Yip, 2012), optimized film morphologies (Ma, 2005; Peet, 2009) and engineered device architectures (Sun, 2011; Zhang, 2011). The power conversion efficiency of polymer-based solar cells has been significantly increased from 1% in 1986 (Tang, 1986) to 5% in 2005 (Xue, 2005) and, more recently, higher than 12% in 2013 by Heliatek (2012). With such efficiencies, OSC could become a competitive alternative to inorganic solar cells in the near future. The revolutionary development in OSC came in the mid-1990s with the introduction of the bulk heterojunction (BHJ) devices (Yu, 1995), where the donor and acceptor material are blended together. In such a nanoscale interpenetrated network, each exciton created could reach a dissociating site (interface D/A) within a distance smaller than the exciton diffusion length. Nowadays, the bulk heterojunction is still the most promising concept for all-organic PV cells. While various combinations of donor and acceptor materials have been studied, the most reported material system in BHJs, from 2002 to 2010, is the mixture of regioregular poly(3-hexylthiophene) (RR-P3HT) as donor and 6,6-phenyl C₆₁-butyric acid methyl ester (PCBM) as acceptor (Dang, 2011). Many more high-performance polymers have been developed in recent years. The most impressive high-performance polymers are those designed by Liang (2009), which are composed of thieno[3,4-b]-thiophene (TT) and benzodithiophene (BDT) alternating units. This was the first polymer donor system capable of reaching a power conversion efficiency of 7–8%. Generally, the different organic solar cells are distinguished by the production technique (roll-to-roll or vacuum deposition techniques), by the photoactive materials used (polymer or small molecules), and by the device architecture (single or tandem, bilayer heterojunction or bulk heterojunction, normal or inverted structure).

16.3.1 Working principles of an organic solar cell

Today, two main device geometries exist: the traditional and the inverted structure schematically represented in Fig. 16.4.

As observed, the cells are illuminated through a transparent substrate. A conductive and semitransparent electrode (usually indium tin oxide, ITO) is deposited on the substrate and usually five layers are then deposited on top of this electrode. In the normal geometry the first layer stack is an interfacial hole transport layer (HTL) of poly(3,4-ethylenedioxythiophene):poly(styrene sulfonate) (PEDOT:PSS), followed by the active layer, an electron transport layer (ETL, LiF or Ca) and a low work function metal thick top layer (Al or Au). In the inverted type geometry the order of the layers are reversed with the high work function top metal electrode now being the hole collecting anode (Ag). The PEDOT:PSS usually remains as the HTL while the ETL can be made of ZnO or TiO_x. The main advantage of the inverted structure is the improvement of the device stability which can be related to the chemical properties of the interfaces (Norman, 2010). The organic materials composing the photoactive layers are generally split into two groups: small molecules and conjugated polymers. These two classes of materials are rather different in terms of their synthesis, purification and device fabrication processes. Small molecules, which have a well-defined molecular weight, are usually deposited by low or high pressure vapor methods. To create interpenetrating donor–acceptor networks co-evaporation techniques can be applied. We should notice that the group of Heeger has recently reported a power conversion efficiency of 6.7% for a BHJ OSC



16.4 The traditional structure (left) and the inverted structure (right) of an organic solar cell. HTL: hole transport layer; ETL: electron transport layer.

based on solution-processed small donor molecules (Sun, 2011). Polymers are usually processed from solution in organic solvents (spin-coating and doctor blading in laboratories, screen-printing or roll-to-roll techniques in companies (Sondergaard, 2012)).

There is a fundamental difference between solar cells based on inorganic or on organic semiconductors. In solar cells made from inorganic semiconductors, photons are directly converted at room temperature into free charge carriers. In OSC, a photon absorption leads to the creation of a bound electron–hole pair called exciton, for which binding energies range from 50 meV up to >1 eV (Gregg, 2003). Excitons then have to diffuse to be dissociated into free charges. This additional stage of exciton diffusion completely changes the scale of the physical phenomenon involved in OSC. Indeed in organic materials, both the exciton diffusion length and the charge carrier diffusion lengths are in the submicronic range (10–20 nm for excitons and 100–200 nm for charge carriers). The most visible consequence of such low values is the design of the organic photovoltaic devices where the active layer thicknesses do not exceed 200 nm. In addition, the control of the morphology of each layer at the nanometer scale strongly impacts the performance of OSC.

Before going into more detail, we recall here the four steps of the photovoltaic conversion process in OSC.

Photon absorption

Upon absorption of a photon having an energy larger than the gap, an electron is promoted from the HOMO band (Highest Occupied Molecular Orbital) to the LUMO band (Lowest Unoccupied Molecular Orbital) of the donor material. The majority of organic materials have bandgaps higher than 2 eV which limits to less than 30% of the possible harvesting of solar photons. Moreover, due to low charge carrier mobilities, the active layer thickness should be restricted to around 150 nm to avoid series resistances. Fortunately, absorption coefficients are high in organic materials (exceeding 10^5 cm^{-1}) and make absorbing the main part of the incident light possible, even with thicknesses of around 100 nm. Thicknesses of the films are not the bottleneck.

Exciton diffusion

The strong local electrical field at a donor–acceptor material interface will be used to dissociate excitons. For efficient dissociation of excitons, the distance between the photon absorption and the first interface should be lower than the exciton diffusion length (between 10 and 30 nm).

Exciton dissociation or charge separation

When an exciton reaches the interface between donor and acceptor materials, the charge separation takes place in an ultrafast timescale of about 45 femtoseconds (Brabec, 2001). However, a necessary condition for efficient dissociation of the created excitons is that the difference between the LUMO of the donor and the acceptor is higher than the exciton binding energy. If this is the case, electrons are transferred to the acceptor. Up to now, in conjugated polymer based organic solar cells the most efficient electron acceptors found are C_{60} based fullerenes. Because the separation is faster than any other competing process, its efficiency is about 100%.

Charge transport

The separated charges then need to diffuse to the respective device electrodes, holes to the anode and electrons to the cathode to provide voltage. In conjugated polymers, the transport of charge carriers is done by successive jumps (hopping) from a localized state to another. Mobilities in organic materials are low and could also be reduced by traps. Values are typically in the 10^{-4} – 10^{-2} cm 2 V $^{-1}$ s $^{-1}$ range.

16.3.2 Light trapping strategies for organic solar cells (OSCs)

The basic idea developed in this section is to increase the part of the incident light which is absorbed in the photoactive layer. If we consider the spectral redistribution of the incoming light in the traditional structure of Fig. 16.4, most of the incoming light is absorbed in the blend in the 400–700 nm range, average reflection is about 10%, ITO absorption is about 15% while PEDOT absorbs mainly in the blue range (4%). The first approach to improving the performance of the cell is to increase the thickness of the absorbing layer. However, this thickness is generally restricted (<150 nm) by the limited charge carrier mobility in conjugated polymers (highly efficient devices with thickness around 200–250 nm have been demonstrated (Irwin, 2008)). Thus, to overcome this problem, and from the optical point of view, the following solutions can be considered:

- optimization of the electromagnetic field distribution inside an organic solar cell;
- implementation of periodic structures (such as gratings or photonic crystals) in the thin layer stacking;
- investigation of plasmon effects for increasing absorption in OSC.

Optimization of the electromagnetic field distribution

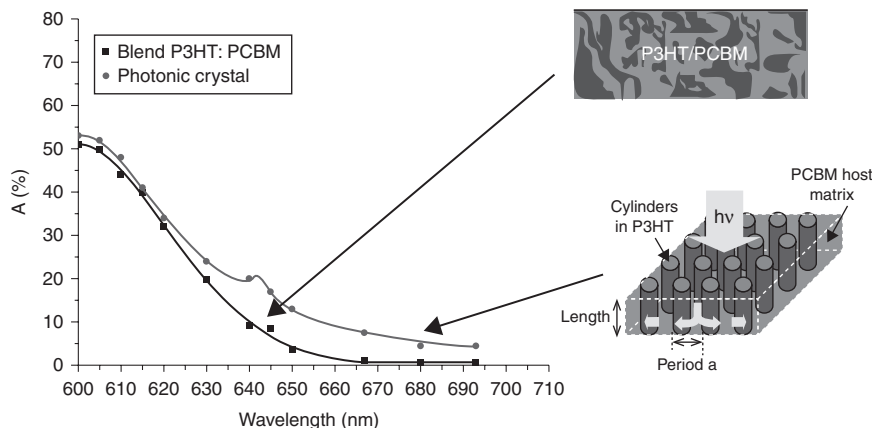
An organic solar cell is modeled as stacked thin films surrounded by a semi-infinite substrate and a semi-infinite transparent medium. Each layer ' i ' is defined by its thickness d_i , its refractive index n_i and its extinction coefficient k_i as a function of wavelength, λ . This model assumes layers to be smooth and homogeneous, interfaces to be parallel, and does not take scattering into account. To go further into detail and to link the optical properties to the electrical properties in OSC, the key equation is:

$$Q_i(z, \lambda) = \frac{1}{2} \sqrt{\frac{\epsilon_0}{\mu_0}} n_i \alpha_i |E(z)|^2 = \frac{n_i}{n_0} \alpha_i I_{\text{solarlight}} \left| \frac{E(z)}{E_0} \right|^2 \quad [16.1]$$

where $|E|^2$ is the squared modulus of the electromagnetic field, Q_i is the local energy dissipated in the material, ϵ_0 is the permittivity of vacuum, μ_0 is the permeability of vacuum, α_i is the absorption coefficient, n_0 is the real part of the complex refractive index of the glass substrate and $I_{\text{solarlight}}$ is the polychromatic incoming light with standard AM 1.5 spectrum. Indeed, the generation rate of excitons and then the short circuit current density J_{sc} can be computed from Equation [16.1] and used to predict the organic solar cell efficiency (Pettersson, 1999). It has also been shown that for organic solar cells based on blended heterojunctions the dependence of the short circuit current density (J_{sc}) on the active layer thickness follows a rather complicated behavior (Hoppe, 2003; Monestier, 2007). More generally, to optimize an OSC, interference effects should be taken into account inside the multilayer thin film structure. The optimal thicknesses of each layer are determined to maximize the square modulus of the normalized electromagnetic field in the photoactive layer and as a consequence the short circuit current of the solar cells. To achieve such multi layer optimization by varying all layer thicknesses independently of each other, a numerical software package, based on a simple optimization matrix method, can be used (Monestier, 2007).

Implementation of periodic structures in the multilayer stack

The challenge in OSC is to implement periodic structures inside the multilayer stack to confine the incident light in the active layer. Although there were some difficulties in correlating computations and initial experimental results, the potential of diffractive optical structures for OSC has been evaluated for the first time by Niggemann (2004) with the simulation and realization of diffraction gratings and buried nano-electrodes. In 2006, nanometric periodic patterning in OSC was reported by Cocoyer (2006). More recently, the concept of 2D and 3D photonic crystals in OSC has



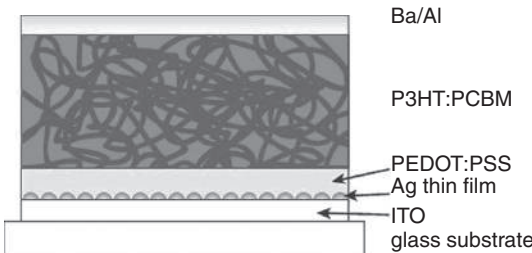
16.5 Absorption of a P3HT/PCBM blend active layer compared to P3HT/PCBM photonic crystal ordered heterostructure absorption. The thickness of the two layers is the same: 150 nm.

been investigated in order to improve light trapping. For example, Duche *et al.* (2008) are the first to theoretically demonstrate that an improved absorption, close to the band edge of the material ($\lambda > 600$ nm), can be obtained in nanostructured P3HT/PCBM thin films by coupling slow Bloch modes in the photonic crystal (Fig. 16.5). This concept was experimentally demonstrated in 2011 by the group of Richard Friend who realized a double nanoimprinting process that allows the formation of nanostructured polymer:PCBM heterojunctions of composition and morphology that can be selected independently (He, 2011).

Plasmons for increasing absorption in OSCs

An optically generated oscillation of free electrons that takes place along a metal/dielectric interface is a surface plasmon. By tuning the excitation light, a resonance occurs when the incident photon frequencies match the collective oscillations of the conduction electrons of the metallic particles. In photonics, this field of interest is known as plasmonics. Among a wide range of applications, these surface plasmon properties can be used in the organic photovoltaic domain in order to improve performances of solar cells. Noble metal particles such as gold or silver can exhibit an enhanced absorption in the visible range.

In the systems ITO/metal-clusters/CuPc/In, it was shown by Stenzel (1995) that the incorporation of copper or gold increases the photocurrent by a factor of more than two. This work was also performed with ITO/silver-clusters/ZnPc/Ag components by Westphalen (2000). More recently, Morfa (2008) at the National Renewable Energy Laboratory (Golden, Colorado)



16.6 Device fabricated with a thin silver film deposited onto ITO on a glass substrate. PEDOT:PSS was spun onto the silver layer followed by P3HT:PCBM and a barium/aluminum back electrode. (Source: Reproduced with permission from the American Institute of Physics (in progress).)

included plasmon-active silver nanoparticle layers in solution-processed bulk heterojunction solar cells, as shown in Fig. 16.6. A strong increase in EQE (external quantum efficiency) is observed for all samples with silver nanoparticles. The optimized thickness of the silver layer is 1 nm and the resulting solar energy conversion efficiency for a bulk heterojunction photovoltaic device of P3HT:PCBM was found to increase from 1.3% to 2.2% for devices employing thin plasmon active layers.

16.4 Copper indium gallium diselenide thin film solar cells

In the last decade, the polysilicon shortage led to an incredible amount of resources being focused in low-cost, high efficiency thin film based devices. These efforts lead to the creation of many companies trying to develop and industrialize thin film based modules (including First Solar, Unisolar, Würth Solar, Solar Frontier (formerly Shell Solar), Solopower, Nanosolar, Heliovolt, Solyndra, Solecture (formerly Sulfurcell)). Among the materials chosen by these companies, the most intriguing is copper indium gallium diselenide (CIGS), which has great potential to reset the market and make new applications cost-effective and viable. CIGS technologies are differentiated from competing thin film materials by a combination of factors, such as high demonstrated efficiency, which stands today at 20.3% at cell level (Jackson *et al.*, 2011), 17.8% at submodule level and 15.7% for commercial modules (aperture area) (Dimmler, 2012). However, despite the low-cost, high efficiency and radical form factor promise of many thin film photovoltaic technologies, scaling CIGS to large-volume production currently presents a wide range of challenges. In particular, besides the big efforts made in technology transfer, a big gap between previously cited efficiencies and

medium commercial modules (11–13% efficiency) still exists, mainly related to the specific characteristics of CIGS material.

CIGS is a direct bandgap semiconductor with good light absorption properties and a bandgap energy well-matched to the solar spectrum. It belongs to the multinary Cu-chalcopyrite system, where the bandgap can be modified by varying the group III cations among In, Ga and Al and the anions between Se and S (Dimmler *et al.*, 1987; Goushi *et al.*, 2009). This p-type semiconductor material has excellent long term stability and has been called a ‘smart’ or ‘self-healing’ material because of its copper related properties. A wide range of bandgaps can be obtained by mixing Ga and the bandgap range of interest for this technology is between 1 and 1.7 eV (Dimmler *et al.*, 1987).

CIGS devices are usually grown in what is known as substrate configuration, which means that the substrate is the first step in the fabrication process, but the back layer to illumination. The preferred substrate for CIGS devices is soda-lime glass as it is rigid, stable, and allows for Na doping of the CIGS absorber during growth. Other substrates, such as stainless steel foils, modified aluminum foils, or polyimides have been chosen because significant competitive advantages are possible compared with other thin film technologies and processes. The foil is relatively lightweight and flexible—valuable characteristics for emerging building integrated photovoltaic (BIPV) applications. At present polyimide based CIGS devices provide the largest efficiency in terms of CIGS devices (Press communication, 2011), while commercial modules on stainless steel or aluminum based foils can be found in industry with efficiencies of about 10%.

CIGS device preparation is not simple. It starts with the deposition of the back electrode on the chosen substrate. The back electrode material is deposited by sputtering. The preferred metal is molybdenum, due to its insignificant diffusion into the absorber during cell processing (Granath *et al.*, 1995). The thickness of the Mo layer has to be optimized for adhesion, sheet resistance, morphology, and maximum performance and minimal costs (Contreras *et al.*, 1996). Yoon *et al.* (2010) has found that the growth parameters, such as argon flow rate, RF power, bi-layer Mo thin film and substrate temperature, have significant influence on the properties of Mo films. The presence of sodium supports the grain growth with a higher degree of <112> texturing for CIGS films, and increases the carrier concentration. All the highest performance devices have used soda-lime glass as the substrate material. Growth on substrates with no Na content requires dosing of the CIGS film usually by laying a 60–120 Å NaF layer on the Mo back contact, or introducing NaF during CIGS deposition (Kronik *et al.*, 1998). Rudman *et al.* (2003) have developed a Na-after-CIGS deposition process for their low temperature process on polyimide substrates. Na content is more

important for high efficiency than variations in In/(Cu+In) ratio allowing variations between 52% and 64% (Abu Ras, 2002).

Once the back contact is ready the CIGS absorber is deposited using any of the methods of flux delivery:

- Evaporation of elements simultaneously or in a prescribed sequence;
- Sputtering or electrodeposition of metals followed by:
 - Selenization and/or sulfurization with H₂Se and/or H₂S;
 - Selenization and/or sulfurization from Se powder sources;
- Reactive sputtering of metals with Se vapor;
- Printing of metals from ink precursors followed by selenization.

Coating uniformity of the copper, gallium and indium films is critical to achieving optimal CIGS device performance and high yields.

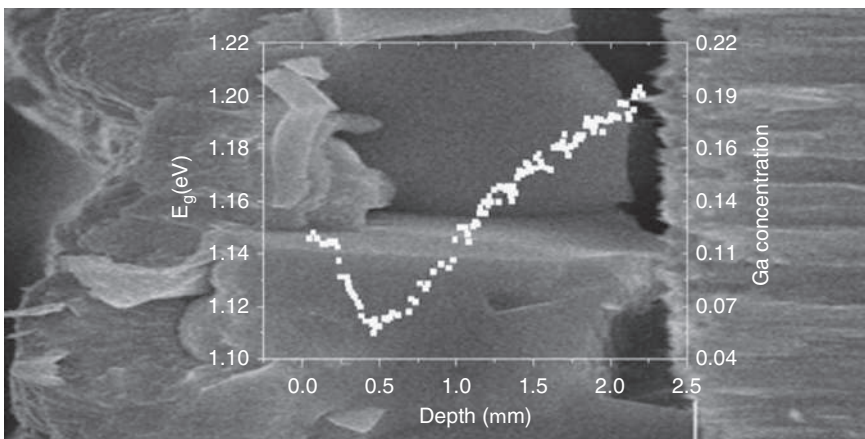
From the point of view of crystal growth, Cu-rich compositions are necessary although this Cu excess should be removed because of the formation of Cu_{2-y}(S,Se) phases, which have a metallic nature and do not allow the formation of efficient heterojunctions. Etching may involve some damage to the absorber surface as well as introduction of shunt paths between electrodes.

It is important to mention that selenization and (eventually) sulfurization processes under H₂Se and H₂S are performed on metal stacked layer precursors of Cu, Ga and In layers (or binaries of this elemental metals). A variation of this method avoiding the use of highly toxic H₂Se during selenization is the rapid thermal process of stacked elemental layers. Na control is again crucial.

The major difference between Cu(In,Ga)S₂ and Cu(In,Ga)(S,Se)₂ is that for the former one of the main limitation of efficiency at about 12% comes from an open voltage that is too low as compared with the bandgap. Even when Zn or Ga has been added efficiencies are still limited by reduced fill factors or short-circuit current densities.

An interesting property of the CuIn_{1-x}Ga_x(S_{1-y},Se_y)₂ alloy system is the possibility of designing graded gap structures that optimize the electronic properties of the final device. This is done by varying the composition depth profile of Ga and/or S. Figure 16.7 illustrates how the composition depth profile modifies the bandgap profile of the absorber and thus the optoelectronic properties of the device.

The art of designing optimum bandgap grading is to push back charge carriers from critical regions, that is, regions with high recombination probability within the device. Such critical regions are: (1) interfaces between back contacts and absorber layers; (2) the heterojunction, including the absorber/buffer interface. We can imagine an optimal band diagram of a grading structure fulfilling requirements for minimizing recombination losses. This band diagram is very similar to one of the current record cells of NREL and ZSW devices (Repins *et al.*, 2008 and Jackson *et al.*, 2011, respectively).



16.7 Ga composition depth profile and associated modification of the bandgap profile for a CIGS absorber with 'notch' Ga composition as distributed in the thickness of absorber.

The cadmium sulfide (CdS) layer is then applied. This layer acts as the 'n' part of the p-n junction that forms the PV cell, and is usually deposited in a wet chemical bath, although vacuum methods such as sputtering are also starting to be used (as in the case of manufacturer Miasole). CdS and the deposition method used have diverse beneficial properties and are important factors in the manufacturing of a robust PV material. Targeted CdS thickness is approximately 80 nm. If the CdS coating thickness is less than optimal, open circuit voltage (V_{oc}) and field factor (FF) are reduced; in much the same way, if the CdS thickness exceed the optimal value, short circuit current density (J_{sc}) is decreased because of increased absorption of light within the CdS coating.

Alternative Cd-free buffer layers are being developed due to the concerns over toxicity of Cd. In₂S₃, ZnS and ZnS(O,OH) buffers are of the most promising candidates for high-efficiency Cd-free CIGS solar cells in near future (Naghavi *et al.*, 2010). Solar Frontier (with 1 GW of capacity production) is already using in mass exploitation CIGS modules with ZnS(O,OH) buffer layer.

To finish the photovoltaic cell a transparent conducting oxide is deposited on the buffer layer. Transparent conducting oxides (TCOs) are a major component of all non-wafer based solar cells using thin film compound semiconductors, thin film silicon, dye sensitized titanium dioxide and organic absorbers to generate electricity from light. The main requirements for TCOs for use as contacts in a solar cell are: (i) a high enough conductivity to minimize resistive losses and (ii) minimal optical absorption over the wavelength range in which the solar cell absorber is responsive. Typically,

as conductivity of a TCO is increased, the NIR wavelength range transparency is reduced as a result of enhanced free charge carrier absorption. Thus, in the design of TCO materials, a trade-off is sought between these two properties. However, the conductivity also depends on the carrier mobility which has no influence on the TCO transparency. Therefore, high carrier mobility is a prerequisite for developing transparent conducting materials with coexisting high electrical conductivity and high transparency over the wavelength range from 300 to at least 1200 nm.

In particular in CIGS technology a bilayer consisting of intrinsic zinc oxide (IZO) and conducting ZnO (typically ZnO:Al, aluminium doped zinc oxide AZO) is deposited by sputtering. These layers can also be deposited by chemical-vapor deposition processes and other non atmospheric techniques are under development (Rousset *et al.*, 2010). The AZO layer acts as the front electrode for the device, allowing electrical contact with the device, acting as the current collection layer and protecting the semiconductor layer below. The TCO is an n-material that complements the underlying CdS n-type buffer coat. Highly conductive AZO films exhibit significant homogeneity in the spatial distribution of resistivity and transparency values. The origin of this spatial distribution is usually related to the use of ceramic targets instead of metallic ones (Byeong-Yun *et al.*, 2005). This pattern is identified to correspond with the erosion pattern in the target where a direct correlation between the increasing erosion areas with the increasing resistivity in the layer can be stated. Rather poor electrical properties of AZO films are mainly due to depletion regions formed by the absorption of negatively charged species on grain boundary surfaces. It has been stated that hydrogen plays a significant and beneficial role in removing depletion impurities regions (Theyv *et al.*, 1997; Zhong *et al.*, 1999; Zhuo *et al.*, 2004), minimizing resistivity. As an example the typical deposition process of an AZO layer (from ceramic targets) and grown under a typical RF magnetron sputtering consist of (Liu *et al.*, 2007): cleaning of the substrate in acetone, rinsing in deionised water, and drying in flowing nitrogen gas. Evacuation of the growth chamber to less than 4×10^{-4} Pa background pressure is necessary. The working gas is usually an Ar and H₂ mix, independently fed into the reaction chamber with mass flow controllers. Typical working pressure is 0.5 Pa. The RF power is fixed to about 200 W. Time conditions and scans are fixed to obtain a 500 nm AZO layer usually. Typical electrical parameters for a layer deposited under these conditions are:

Without H₂ flux:

Electrical resistivity	$23 \times 10^{-4} \Omega\text{cm}$
Carrier concentration.....	$0.36 \times 10^{21} \text{ cm}^{-3}$
Carrier mobility	$7.4 \text{ cm}^2\text{V}^{-1}\text{s}^{-1}$

With H₂ flux of 1.0 sccm,

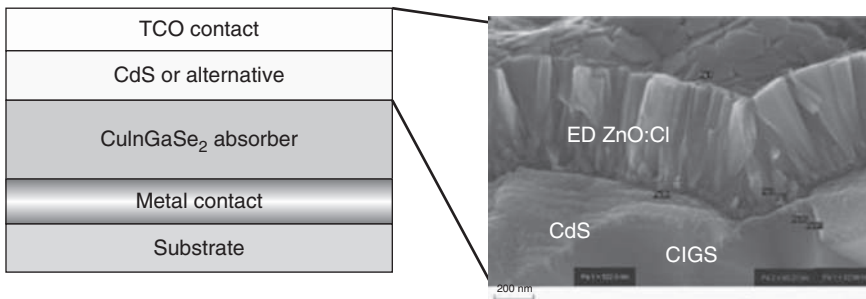
Electrical resistivity	$4.1 \times 10^{-4} \Omega\text{cm}$
Carrier concentration.....	$3 \times 10^{21} \text{ cm}^{-3}$
Carrier mobility	$6 \text{ cm}^2\text{V}^{-1}\text{s}^{-1}$

TCO films useful for most applications must have a wide bandgap (> 3.0 eV, to assure a high number of photons being absorbed by CIGS layer) which requires a degenerate carrier density $\geq 10^{20} \text{ cm}^{-3}$ and ideally a resistivity of $\rho < 10^{-3} \Omega\text{cm}$, so the corresponding Hall mobility should be $\mu \geq 62.5 \text{ cm}^2\text{V}^{-1}\text{s}^{-1}$ (Coutts *et al.*, 2000). Resistivity values of the films are mainly affected by carrier concentration (N) and mobility. Though the NIR optical losses may be further reduced by reducing carrier concentration, doing so indiscriminately can decrease the conductivity and/or the optical bandgap of the TCO layer and adversely affect the electrical properties and transparency in the visible wavelength region. Therefore, TCO materials with sufficiently high N ($\geq 10^{20} \text{ cm}^{-3}$) while maintaining a high mobility and transparency are desirable. High mobility TCO materials have been prepared in the past but the resistivity has been greater than $10^{-3} \Omega\text{cm}$ because of a relatively low $N < 10^{19} \text{ cm}^{-3}$ (Nozik *et al.*, 1972; Toukazaki *et al.*, 2006). Such low carrier density levels would require a Hall mobility in excess of $400 \text{ cm}^2\text{V}^{-1}\text{s}^{-1}$ to achieve $\rho < 10^{-4} \Omega\text{cm}$.

The increase in carrier concentration might be attributed to the formation of oxygen vacancies (Naghavi *et al.*, 2000) and a small quantity of hydrogen atoms situated in the Zn-O bond center (Minami *et al.*, 2000). It is important to note that these films changed from Zn-rich to Zn-deficient when the films were deposited in H₂ ambient (Liu *et al.*, 2006), indicating that H₂ has a very important role in the stoichiometry of the layer as a result of extraction of oxygen from AZO films by hydrogen atoms. Moderate Ar + H₂ ambient can markedly optimize the properties of AZO films prepared at low temperature.

In the case of AZO films grown without a H₂ atmosphere, a post-annealing treatment has also been demonstrated to be beneficial to increasing conductivity of the layer (Zhuo *et al.*, 2004). An explanation of this effect can be attributed to desorption of negatively charged oxygen species from the grain boundaries which can act as trapping sites and form the potential barriers during the hydrogen treatment. It means that hydrogen treatment acts as passivation mechanisms on the grain boundary surfaces. This passivation is stable over time.

The conduction mechanism for TCOs can be classified into two large categories: (i) occurrence of intrinsic carrier by oxygen vacancies and (ii) introduction of extrinsic carrier by impurity doping.



16.8 Schematics of CIGS devices and SEM cross section of an efficient CIGS solar cell with an electrodeposited ZnOTCO layer. The hexagonal shape of the grains demonstrates the high structural quality of the electrodeposited ZnO.

Jeong *et al.* (2006) showed that impurity doping is a determinant for the occurrence of the carrier caused by the development of resistivity. In this work they perform different experiments with metallic and ceramic targets to identify the possible influence on target nature in the resistivity of the AZO film. In this case, films deposited by the undoped target did not show a great increase in resistivity as they do in the case of an Al target.

Figure 16.8 shows the final scheme and scanning electron microscope picture of a CIGS device.

16.4.1 State-of-the-art technologies at industry level

In December 2011, Manz bought the first European company producing CIS modules, Würth Solar, and they no longer sell modules but process solutions. Würth was, for a long time, an example of fully integrated production and continuous line operation with a high level of automation. The modules produced by Würth Solar had proven long-term stability and less energy payback time than counterpart Si based modules. These modules were installed in several countries.

At present Solar Frontier is leading the market with their CIGSSe modules and a 1 GW production capacity. Solar Frontier produces modules using thin film synthesis by selenization/sulfurization of metal precursors and chemical bath deposited ZnS as an alternative buffer layer.

Nanosolar Inc., Solarion AG, Heliovolt Corporation, NEXCIS, Honda Soltech Co. Ltd, Solartechnich GmbH, Solibro GmbH and Global Solar Energy Inc. among others, are prominent manufacturers of CIGS thin film modules employing different technologies (Dimmler, 2012). During 2011 and early 2012 many of the leading companies filed for bankruptcy including Solyndra, Q-cells, Solecture and Odersun; this exemplifies the

challenges this technology is affording in their competition with costs, time and Si module producers.

16.4.2 Novel absorbers

The thin film PV technology offers in principle the opportunity to lower the cost of materials and processing compared to its crystalline silicon counterpart. The most efficient compound demonstrated today is based on the chalcopyrite system Cu(In,Ga)(Se,S). To develop a lasting and credible photovoltaic technology capable of playing an important role in the energy production of tomorrow it is however crucial to base it on inexpensive and abundant materials. Therefore, in the long run, the increasing price and accelerating rarity of indium and to a lesser extent gallium imposes a necessity to find alternative earth abundant and non-toxic materials. Indium scarcity is considered an economical and geo-economical political issue in the mass expansion of CIGS technologies. To comply with this objective, a new CuZnSnS(Se) (CZTS) kesterite compound where In and Ga are replaced by Sn and Zn has been put forward and extensively studied in recent years. The best reported efficiency for kesterite cells today is 11.1% (Todorov *et al.*, 2012), obtained from cells fabricated using liquid approaches based on the toxic hydrazine solution. Vacuum based techniques that have been successful for the CIGS technology, have so far demonstrated poor efficiencies in comparison. The second major limitation in this field of research is the excessive emphasis on fabrication approaches, to the detriment of characterization and a deeper understanding of these materials and their intrinsic optic and optoelectronic properties.

16.4.3 Vacuum free deposition

In spite of the considerable promise of CIGS photovoltaic technology, commercialization is progressing slowly, in large part due to the high cost and complexity of the processes used to deposit photovoltaic thin films. Photovoltaic thin films, typically deposited by using co-evaporation or sputtering methods, capture only a portion of the materials cost savings inherent in thin film concepts. The complexity of the process and cost of the capital equipment needed for vacuum based deposition further complicate high yield manufacturing and limit the overall cost savings.

In order to increase the use of photovoltaic energy, high efficiency solar cells are being developed using low-cost, simple deposition processes. The approach being used is to form semiconductor films by densifying porous layers of sub-micron precursors deposited by simple, non-vacuum methods

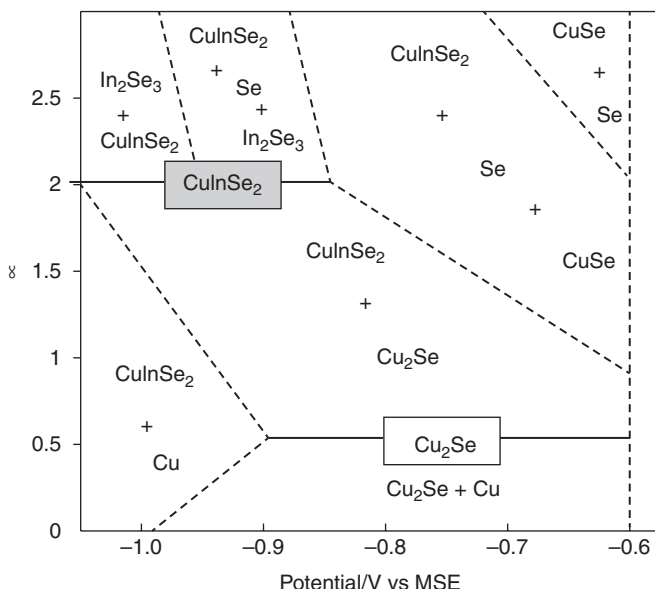
like printing, doctor blade, spraying or electrodeposition and chemical bath deposition using aqueous/non-aqueous solutions.

Most of the proposed low-cost methods for the deposition of chalcogenide based solar cells were developed many years ago. However, the efficiencies achieved have remained rather low largely due to a lack of knowledge and understanding of the layer and interface formation. As a result, the development of these methods was substantially diminished. Over the last few years, much progress was made on this fundamental understanding by groups working on vacuum based chalcogenide deposition. With this improved knowledge, low-cost deposition processes have been revisited and allowed for the development of highly efficient and cost effective chalcogenide solar cells (Heather, 2010). Some of the most common and well known techniques are described on the following pages.

Electrodeposition

Electrodeposition (ED) of the absorber layer is a high potential path to low-cost manufacturing. ED is a versatile deposition method with the ability to yield thin films of metals, metallic alloys and compounds, which can be utilized in the preparation of precursor layer structures. ED equipment is low-cost and the process is energy efficient since it is typically carried out near room temperature. Materials utilization in electrodeposition processes can be close to 100% if stable electrolytes with long lifetimes are employed. Conformal coverage, control of grain size, crystallinity (or lack thereof) and mixing (alloys) are easily afforded in electroplating. ED is already a major technology for mass production of large-area metallic protective coatings in industry, with impressive figures as, for instance, in the case of zinc coatings by roll-to-roll processes (several meters per minute, deposition rates of tens of microns per hour, several meter large plates, etc.). The application of this technique is extremely well adapted for the large area photovoltaic industry and can contribute to the successful mass production of CIGS solar modules.

A wide range of processing approaches employing electrodeposition have been explored for CIGS film formation during the last two decades (Lincot *et al.*, 2004). These approaches include: (i) electrodeposition of thin Cu and In layers forming a Cu/In precursor stack and reacting this metallic stack with gaseous Se species to form the compound (Tarrant *et al.*, 2010); (ii) electrodeposition of a Cu/In/Se stack on a substrate and rapid thermal annealing of the stack to form Copper Indium Selenium (CIS) (Kapur *et al.*, 1987); (iii) electrodeposition of In-Ga (Frizt *et al.*, 1994), Cu-Ga (Zauk *et al.*, 1996) or Cu-In-Ga (Friedfeld *et al.*, 1999) metal alloys to form precursor layers and reacting these precursor layers to form the compound;



16.9 Electrochemical phase diagram showing the composition of one step electrodeposited films in the Cu-In-Se system from acidic solutions as a function of the ED potential and the flux ratio between selenium (IV) and copper (II) ionic species in solution.

(iv) electrodeposition of In-Se and Cu-Se on a substrate forming a stacked precursor such as a Cu/In-Se/Cu-Se structure and annealing the structure in inert atmosphere to form CIS (Gauchev *et al.*, 2006); and (v) one-step electrodeposition of CIS or CIGS compound films then subjecting them to a high temperature crystallization step to improve their photovoltaic properties (Bhattachayra *et al.*, 1998). The direct electrodeposition of a CuInSe precursor films by using a single bath containing the four elements, called ‘one step electrodeposition’, involving only one electrochemical step for deposition of all components implies more complex electrochemical aspects, with the possibility of forming either the elements in their elemental form, or as binary compounds in addition to the desired CIS phase (see Fig. 16.9).

The insertion of gallium in the standard ED potential domain appears difficult. This is a direct consequence of the negative shift of the redox potential for gallium deposition. Several groups have now reported the successful insertion of gallium in the films up to amounts corresponding to the optimal values for the preparation of high efficiency cells. In particular, Solopower is already in the market with flexible modules based on ED-CIGS at 10%. Their record efficiency for a 1.5 m long flexible panel is 13.4% efficiency (Aksu *et al.*, 2012).

Ultrasonic spray

Chemical spray pyrolysis and ink-jet printing are versatile deposition methods that are simple, cost effective and can be adapted to large area deposition. Up to 1000 times higher throughput can be achieved by implementing these techniques on flexible substrates compared to standard evaporation deposition. Being non-contact processes they allow the deposition of multiple layers without destroying those underlying. In the concept of ink jet printing, precursor-containing slurries are driven through small nozzles by means of piezoelectric materials, micro heaters or pressure pumps to be dispersed on the substrate. Ultrasonic spray pyrolysis (USP) disperses the slurry to fine droplets that are then led to the substrate by a carrier gas. The thickness of the layer can be simply adjusted by variable spraying/printing time. In contrast to the doctor blade technique, the transition vehicle is not required to be viscous which opens the route for binder-free solutions. Two types of slurries can be distinguished being based on nanoparticles or metal salts. Most research activities followed the route of forming the chalcopyrite phase directly during deposition by including the respective anion for CIGS formation rather than creating a preliminary precursor layer that is converted by subsequent selenization. 5% conversion efficiency was obtained for a gallium free device by Duchemin *et al.* (1989) which was the highest reported value for a fully non-vacuum produced solar cell at that time. Nanosolar hold the record for highest conversion efficiency (17.3%) for printed core-shell nanoparticles from liquid solutions.

Printing/doctor blade

Coating a substrate with particulate ink or slurry offers an extremely material-efficient method of depositing a thin film precursor layer. Doctor blade deposition is a simple method to apply films with controlled thicknesses down to the micrometer range. The requirements consists only of a blade and a mechanism that controls the distance between substrate and blade to level the paste into a layer of desired thickness and width. A paste mostly comprises a mixture of suitable precursor materials, solvents, plasticizers, deflocculants, wetting agents and binders. The formation of this liquid application vehicle is of paramount importance to control uniformity and stoichiometry of the obtained film. Inorganic precursors might be provided either in the form of inorganic salts or nanoparticles. North American organizations ISET and Unisun have both reported doctor bladed CIGS solar cells with 13.6% and 11.7% efficiency, respectively. Nanoparticles in the form of In-, Ga- and Cu-oxides were used in both cases as metal precursors that were converted to CIGS with the help of the highly toxic, gaseous reducing agent H₂Se. Nanosolar use an approach that is based on Unisun technology and which has presented record efficiencies of 17.3% showing the potential

of doctor bladed CIGS. Another approach to prevent the formation of metal oxides in the first place stems from IBM who again make use of highly toxic hydrazine as a solvent. Omitting toxic agents, ETH Zürich (now EMPA) successfully demonstrated this technique in 2004 to reach 6.7% conversion efficiency solar cells. Although a remarkable accomplishment, layers still suffered from insufficient thickness, rough morphology, Ga-rich composition at the Mo/CIGS interface and a parasitic carbon layer stemming from the use of a non-volatile binder material.

Another problem of compositional gradients can be approached by advanced heat and selenization processes. Gallium and indium secondary precursors are known to exhibit low evaporation temperatures that lead to material losses during CIGS formation. Rapid thermal annealing (RTP) providing substrate heating speeds of 50°Cs^{-1} will increase material utilization and compositional control of quaternary absorber layers due to minimum elemental diffusion.

16.5 Conclusion

The use of thin films in the design of solar cells is of high interest in decreasing the quantity of material required which accounts for a large part of the cost of the devices. Yet, when using thin films, new strategies have to be developed to minimize or avoid difficulties lowering the efficiency of devices such as inefficient absorption of solar photons, low mobilities of charge carriers and poor electronic transport properties, high density of defects, resistivity of transparent conductive oxides, reliability of materials and devices and so on. Furthermore, thin film non-pollutant deposition processes on large surfaces, with high throughput, and at low energy expense, such as roll-to-roll or batch processing, are highly in demand for solar cell fabrication. Last but not least, cheap and simple materials are required for terawatt scale production of energy via solar cells. It is thus mandatory to consider abundant elements in the Earth's crust and their associated extraction costs. The merit figure to be maximized corresponds to the efficiency/cost ratio aimed at decreasing the kW per hour electricity cost produced from the Sun.

This chapter summarizes new insights in the use of nanotechnologies and nanostructures, such as nanowires, quantum dots and photonic crystals, to tune or optimize the physical properties of materials in terms of photon absorption and photon-to-electron conversion and charge transport. Organic solar cells which present the main advantage to allow fine tuning of materials by chemical synthesis are also described. Indeed, we have faced in the last few years a very sharp increase of organic solar cell efficiencies (about 1% per year). This efficiency increase is mainly due to the discovery of new polymer materials the properties of which (absorption band, electronic properties, etc.) are shaped by the chemists. Finally, the last part of

this chapter is devoted to new efficient processes developed at the industrial level to produce solar cells from CIGS and from earth abundant materials composing CZTS.

To conclude, studying and understanding physical phenomena at the nanoscale, in the laboratories, will open many research directions in the future to reach high efficiency, low-cost, non pollutant and reliable solar cells. Furthermore, many challenges mainly related to closing the gap between cell efficiencies and commercial modules, assuring low-cost through increasing efficiency and securing source materials need to be addressed. All these challenges (plus those related to quality, reliability and energy production) will need from strong implication of R&D and development actors to lead the emerging technologies towards market.

16.6 References

- Bhattacharya, R.N., Batchelor, W., Granata, J.E., Hasoon, F., Wiesner, H., Ramanathan, K., Keane, J. and Noufi, R.N. (1998) ‘CuIn_{1-x}Ga_xSe₂-based photovoltaic cells from electrodeposited and chemical bath deposited precursors’, *Solar Energy Materials and Solar Cells*, **55**, 83.
- Boudreault, P-L.T., Najari, A. and Leclerc, M. (2011) ‘Processable low-bandgap polymers for photovoltaic applications’, *Chemistry of Materials*, **23**(3), 456–469.
- Brabec, C.J., Zerza, G., Cerullo, G., De Silvestri, S., Luzzati, S., Hummelen, J.C. and Sariciftci, N.S. (2001) ‘Tracing photoinduced electron transfer process in conjugated polymer/fullerene bulk heterojunctions in real time’, *Chemical Physics Letters*, **340**, 232.
- Brown, G.F. and Wu, J. (2009) ‘Third generation photovoltaics’, *Laser & Photon Rev.*, **3**, 394–405.
- Cao, L., White, J.S., Park, J-S., Schuller, J.A., Clemens, B.M. and Brongersma, M.L. (2009) ‘Engineering light absorption in semiconductor nanowire devices’, *Nature Materials*, **8**, 643–647.
- Cocoyer, C., Rocha, L., Sicot, L., Geffroy, B., de Bettignies, R., Sentein, C., Fiorini-Debuisschert, C. and Raimond, P. (2006) ‘Implementation of submicrometric periodic surface structures toward improvement of organic-solar-cell performances’, *Applied Physics Letters*, **88**, 133808/1–3.
- Conibeer, G. (2007) ‘Third-generation photovoltaics’, *Materials Today*, **10**, 11, 42–50.
- Contreras, M.A., Tuttle, J., Gabor, A., Tenant, A., Ramanathan, K., Asher, S., Franz, A., Keane, J., Wang, L. and Noufi, R. (1996) ‘High efficiency graded bandgap thin-film polycrystalline Cu(In,Ga)Se₂-based solar cells’, *Solar Energy Materials and Solar Cells*, **41–42**, 231–246.
- Coutts, T.J., Young, D.L. and Li, X. (2000) ‘Characterization of transparent conducting oxides’, *MRS Bulletin*, **25**, 58.
- Dang, M.T., Hirsch, L. and Wantz, G. (2011) ‘P3HT:PCBM, Best Seller in Polymer Photovoltaic Research’, *Advanced Materials*, **23**, 3597–3602.
- De Vos, A. (1980) ‘Detailed balance limit of the efficiency of tandem solar cells’, *Journal of Physics D: Applied Physics*, **13**, 839.
- Dimmler, B., Dittrich, H., Menner, R. and Schock, H.W. (1987) ‘Performance and optimization of heterojunctions based on Cu(Ga,In)Se₂’, in *19th IEEE Photovoltaic Specialists Conference*, New Orleans, Louisiana, May 1987, 1454–1460.

- Duché, D., Escoubas, L., Simon, J.-J., Torchio, P., Vervisch, W. and Flory, F. (2008) 'Slow Bloch modes for enhancing the absorption of light in thin films for photovoltaic cells', *Applied Physics Letters*, **92**, 193310.
- Duchemin, S., Bougnat, J., El Ghzizal, A. and Belghit, K. (1989) 'Studies on the improvement of sprayed CdS–CuInSe₂ solar'. *Conference Record of the Ninth European Photovoltaic Solar Energy Conference*, Freiburg, Germany, 476–479.
- El Daif, O., Drouard, E., Gomard, G., Kaminski, A., Fave, A., Lemiti, M., Ahn, S., Kim, S., Roca i Cabarrocas, P., Jeon, H. and Seassal, C. (2010) 'Absorbing one-dimensional planar photonic crystal for amorphous silicon solar cell', *Optics Express*, **18**(S3), A293–A299.
- Fan, Z., Razavi, H., Do, J.-W., Moriwaki, A., Ergen, O., Chueh, Y.-L., Leu, P.W., Ho, J.C., Takahashi, T., Reichertz, L.A., Neale, S., Yu, K., Wu, M., Ager, J.W. and Javey, A. (2009) 'Three-dimensional nanopillar-array photovoltaics on low-cost and flexible substrates', *Nature Materials*, **8**, 648–653.
- Fernandez, A.M., Calixto, M.E., Sebastian, P.J., Gamboa, S.A., Hermann, A.M. and Noufi, R.N. (1998) 'Electrodeposited and selenized (CuInSe₂) (CIS) thin films for photovoltaic applications', *Solar Energy Materials and Solar Cells*, **52**, 423.
- Friedfeld, R., Raffaelle, R.P. and Mantovani, J.G. (1999) 'Electrodeposition of CuIn_xGa_{1-x}Se₂ thin films', *Solar Energy Materials and Solar Cells*, **31**, 163.
- Fritz, H.P. and Chatziagorastou, P. (1994) 'A new electrochemical method for selenization of stacked CuIn layers and preparation of CuInSe₂ by thermal annealing', *Thin Solid Films*, **247**, 129.
- Ganchev, M., Kois, J., Kaelin, M., Bereznev, S., Tzvetkova, E., Volobujeva, O., Stratieva, N. and Tiwari, A. (2006) 'Preparation of Cu(In,Ga)Se₂ layers by selenization of electrodeposited Cu-In-Ga precursors', *Thin Solid Films*, **511–512**, 325.
- Garnett, E. and Yang, P.D. (2010) 'Light trapping in silicon nanowire solar cells', *Nano Letters*, **10**(3), 1082–1087.
- Goushi, Y., Hakuma, H., Tabuchi, K., Kijima, S. and Kushiya, K. (2009) 'Fabrication of pentanary Cu(InGa)(SeS)₂ absorbers by selenization and sulfurization', *Solar Energy Materials and Solar Cells*, **93**, 1318–1320.
- Granath, K., Rockett, A., Bodegard, M., Nender, C. and Stolt, L. (1995) 'Mechanical issues of Mo back contacts for Cu(In,Ga)Se₂ devices', in *13th European Photovoltaic Solar Energy Conference*, Nice, France, October 1995.
- Green, M.A. (2007) 'Thin film solar cells: review of materials, technologies and commercial status', *Journal of Materials Science: Materials in Electronics*, **18**, S15–S19.
- Green, M.A., Emery, K., Hishikawa, Y. and Warta, W. (2011), 'Solar cell efficiency tables (version 37)', *Progress in Photovoltaics: Research and Applications*, **19**, 84.
- Gregg, B.A. (2003) 'Excitonic solar cells', *Journal of Physical Chemistry B*, **107**(20), 4688–4698.
- Hava, S. and Auslender, M. (2000) 'Design and analysis of low-reflection grating microstructures for a solar energy absorber', *Solar Energy Materials & Solar Cells*, **61**, 143–151.
- Heather, A.S., Platt, H.A.S., Li, Y., Nowak, J.P. and Van Hest, M.F.A.M. (2012) 'Atmospheric deposition techniques for photovoltaics', *Photovoltaic Technologies*, **19**, 121–127.
- Heliatek (2012), <http://www.heliatek.com/>
- He, X., Gao, F., Tu, G., Hasko, D.G., Hüttner, S., Greenham, N.C., Steiner, U., Friend, R.H. and Huck, W.T.S. (2011) 'Formation of well-ordered heterojunctions in

- polymer:PCBM photovoltaic devices', *Advanced Functional Materials*, **21**, 139–146.
- Hin-Lap, Y. and Jen Alex, K.-Y. (2012) 'Recent advances in solution-processed interfacial materials for efficient and stable polymer solar cells', *Energy & Environmental Science*, **5**, 5994–6011.
- Hoppe, H., Arnold, N., Sariciftci, N.S. and Meissner, D. (2003) 'Modeling the optical absorption within conjugated polymer/fullerene-based bulk-heterojunction organic solar cells', *Solar Energy Materials and Solar Cells*, **80**, 105–113.
- Huang, C.-Y., Wang, D-Y., Wang, C-H., Chen, Y-T., Wang, Y-T., Jiang, Y-T., Yang, Y-J., Chen, C-C. and Chen, Y-F. (2010) 'Efficient light harvesting by photon down-conversion and light trapping in hybrid ZnS nanoparticles/Si nanotips solar cells', *ACS Nano*, **4**(10), 5849–5854.
- Huang, B-R., Yang, Y-K., Lin, T-C. and Yang, W-L. (2012), 'A simple and low-cost technique for silicon nanowire arrays based solar cells', *Solar Energy Materials and Solar Cells*, **98**, 357–362.
- Hüpkes, J., Rech, B., Kluth, O., Repmann, T., Zwaygardt, B., Müller, J., Drese, R. and Wuttig, M. (2006) 'Surface textured MF-sputtered ZnO films for microcrystalline silicon-based thin-film solar cells', *Solar Energy Materials and Solar Cells*, **90**, 3054–3060.
- Irwin, M.D., Buchholz, D.B., Hains, A.W., Chang, R.P.H. and Marks, T.J. (2008) 'p-Type semiconducting nickel oxide as an efficiency-enhancing anode interfacial layer in polymer bulk-heterojunction solar cells', *PNAS*, **105**(8), 2783–2787.
- Jackson, P., Hariskos, D., Lotter, E., Paetel, S., Wuerz, R., Menner, R., Wischmann, W. and Powalla, M. (2011) 'New world record efficiency for Cu(In,Ga)Se₂ thin film solar cells beyond 20%', *Progress in Photovoltaics: Research and Applications*, **19**, 894–897.
- Jäger-Waldau, A. (2011) 'PV Status Report 2011', Luxembourg: Office for Official Publications of the European Union, Brussels. Available: <http://re.jrc.ec.europa.eu/refsys/>.
- Jeong, W.J., Kim, S.K. and Park, G.C. (2006) 'Preparation and characteristic of ZnO thin film with high and low resistivity for an application of solar cell', *Thin Solid Films*, **506–507**, 180–183.
- Jung, J-Y., Guo, Z., Jee, S-W., Um, H-D., Park, K-T. and Lee, J-H. (2010) 'A strong antireflective solar cell prepared by tapering silicon nanowires', *Optics Express*, **18**, S3, A286–A292.
- Kapur, V.K., Basol, B.M. and Tseng, E.S. (1987) 'Low-cost methods for the production of semiconductor-films for CuInSe₂/CdS solarcells', *Solar Cells*, **21**, 65.
- Kandala, A., Betti, T. and Fontcuberta i Morral, A. (2008) 'General theoretical considerations on nanowire solar cell designs', *Physica Status Solidi (A)*, **206** (1), 1–6.
- Kayes, B.M., Atwater, H.A. and Lewis, N.S. (2005), 'Comparison of the device physics principles of planar and radial p-n junction nanorod solar cells', *Journal of Applied Physics*, **97**, 114302.
- King, R.R., Law, D.C., Edmondson, K.M., Fetzer, C.M., Kinsey, G.S., Yoon, H., Sherif, R.A. and Karam, N.H. (2007) '40% efficient metamorphic GaInP/GaInAs/Ge multijunction solar cells', *Applied Physics Letters*, **90**(18), 183516–183516–3.
- Kronik, L., Cahen, D. and Schock, H.W. (1998) 'Effects of sodium on polycrystalline Cu(In,Ga)Se₂ and its solar cell performance', *Advanced Materials*, **10**, 31–36.
- Le Rouzo, J., Maestre, D., Barakel, D., Palais, O., Escoubas, L., Alfonso, C., Charrin, L. and Gailhanou, M. (2009) 'Growth and characterization of Si nanowires by an electroless etching process', *EU PVSEC Proceedings*, 408–410.

- Liang, Y.W., Yue, F.D., Tsai, S-T., Son, H-J., Li, G. and Yu, L. (2009) 'Development of new semiconducting polymers for high performance solar cells', *Journal of American Chemical Society*, **131**(1), 56–57.
- Lincot, D., Guillemoles, J.F., Taunier, S., Guimard, D., Sicx-Kurdi, J., Chaumont, A., Roussel, O., Ramdani, O., Hubert, C., Fauvarque, J.P., Bodereau, N., Parissi, L., Panheleux, P., Fanouillere, P., Naghavi, N., Grand, P.P., Benfarah, M., Mogensen, P. and Kerrec, O. (2004) 'Chalcopyrite thin film solar cells by electrodeposition', *Solar Energy*, **77**, 725.
- Liu, W.F., Du, G.T., Sun, Y.F., Bian, J.M., Cheng, Y., Yang, T.P., Yang, Y.C. and Xu, Y.B. (2007) 'Effects of hydrogen flux on the properties of Al-doped ZnO films sputtered in Ar + H₂ ambient at low temperature', *Applied Surface Science*, **253**(6), 2999–3003.
- Lu, W. and Lieber, C.M. (2006) 'Semiconductor nanowires', *Journal of Physics D: Applied Physics*, **39**, R387.
- Lunt, R.R., OSEDACH, T.P., Brown, P.R., Rowehl, J.A. and Bulovic, V. (2011) 'Practical roadmap and limits to nanostructured photovoltaics', *Advanced Materials*, **23**, 5712–5727.
- Luque, A. (2011) 'Will we exceed 50% efficiency in photovoltaics?', *Journal of Applied Physics*, **110**, 031301.
- Luque, A., Martí, A. and Stanley, C. (2012) 'Understanding intermediate-band solar cells', *Nature Photonics*, **6**, 146–152.
- Ma, W., Yang, C., Gong, X., Lee, K. and Heeger, A.J. (2005), 'Thermally stable, efficient polymer solar cells with nanoscale control of the interpenetrating network morphology', *Advanced Functional Materials*, **15**(10), 1617–1622.
- Meijer, J.-M., Aarts, L., Van der Ende, B.M., Vlugt, T.J.H. and Meijerink, A. (2010) 'Downconversion for solar cells in YF₃:Nd³⁺, Yb³⁺', *Physical Review B*, **81**, 035107.
- Minami, T., Sonohara, H., Kakumu, T. and Takata, S. (1995) 'Highly transparent and conductive Zn₂In₂O₅ thin films prepared by RF magnetron sputtering', *Japanese Journal of Applied Physics*, **34**, L971–L974.
- Monestier, F., Simon, J.J., Torchio, P., Escoubas, L., Flory, F., Bailly, S., De Bettignies R., Guillerez, S. and Defranoux, C. (2007) 'Modeling the short-circuit current density of polymer solar cells based on P3HT:PCBM blend', *Solar Energy Materials and Solar Cells*, **91**, 405–410.
- Monestier, F., Torchio, P., Simon, J.J., Escoubas, L. and Cathelinaud, M. (2007) 'Software for automatic optimization of the electromagnetic field in organic solar cells', *Nonlinear Optics and Quantum Optics*, **37**, 159–168.
- Morfa, A.J., Rowlen, K.L., Reilly, T.H., Romero, M.J. and Van De Lagemaat, J. (2008) 'Plasmon-enhanced solar energy conversion in organic bulk heterojunction photovoltaics', *Applied Physics Letters*, **92**, 013504.
- Motiee, L., Yao, Y., Choudhury, J., Marks, T.J., van der Boom, M.E. and Facchetti, A. (2010) 'Self-propagating molecular assemblies as interlayers for efficient inverted bulk-heterojunction solar cells', *Journal of the American Chemical Society*, **132**(36), 12528–12530.
- Muskens, O.L., Gómez Rivas, J., Algra, R.E., Bakkers, E.P.A.M. and Lagendijk, A. (2008) 'Design of light scattering in nanowire materials for photovoltaic applications', *Nano Letters*, **8**(9), 2638.
- Naghavi, N., Abou-Ras, D., Allsop, N., Barreau, N., Bücheler, S., Ennaoui, A., Fischer, C-H., Guillen, C., Hariskos, D., Herrero, J., Klenk, R., Kushiya, K., Lincot, D., Menner, R., Nakada, T., Platzer-Björkman, C., Spiering, S., Tiwari, A.N.

- and Törndahl, T. (2010) ‘Buffer layers and transparent conducting oxides for chalcopyrite Cu(In,Ga)(S,Se)₂ based thin film photovoltaics: present status and current developments’, *Progress in Photovoltaics: Research and Applications*, **18**, 411–433.
- Naghavi, N., Rougier, A., Marcel, C., Guery, C., Leriche, J.B. and Tarascon, J.M. (2000) ‘Characterization of indium zinc oxide thin films prepared by pulsed laser deposition using a Zn₃In₂O₆ target’, *Thin Solid Films*, **360**, 233.
- Niggemann, M., Glatthaar, M., Gombert, A., Hinsch, A. and Wittwer, V. (2004) ‘Diffraction gratings and buried nano-electrodes – architectures for organic solar cells’, *Thin Solid Films*, **451–452**, 619–623.
- Norrmann, K., Madsen, M.V., Gevorgyan, S.A. and Krebs, F.C. (2012) ‘Degradation patterns in water and oxygen of an inverted polymer solar cell’, *Journal of the American Chemical Society*, **132**, 16883–16892.
- Nozik, A.J. (1972) ‘Optical and electrical properties of Cd₂SnO₄: a defect semiconductor’, *Phys. Rev.*, **B 6**, 453.
- Nozik, A.J. (2008) ‘Multiple exciton generation in semiconductor quantum dots’, *Chemical Physics Letters*, **457**(1–3), 3–11.
- Oh, B.-Y., Jeong, M.-C., Kim, D.-S., Lee, W. and Myoung, J.-M. (2005) ‘Post-annealing of Al-doped ZnO films in hydrogen atmosphere’, *Journal of Crystal Growth*, **281**, 475–480.
- Peet, J., Heeger, A.J. and Bazan, G.C. (2009) “Plastic” solar cells: Self-assembly of bulk heterojunction nanomaterials by spontaneous phase separation’, *Accounts of Chemical Research*, **42**, 1700–1708.
- Pettersson, L.A.A., Roman, L.S. and Inganäs, O. (1999) ‘Modeling photocurrent action spectra of photovoltaic devices based on organic thin films’, *Journal of Applied Physics*, **86–1**, 487–496.
- Pillai, S., Perez-Wurfl, I., Conibeer, G.J. and Green, M.A. (2011) ‘Surface plasmons for improving the performance of quantum dot structures for third generation solar cell applications’, *Physica Status Solidi C*, **8**(1), 181–184.
- Press Communication Media release of Swiss Federal Laboratories for Material Science and Technology (19 May 2011) ‘Record efficiency of 18.7% for flexible CIGS solar cells on plastics’, Dubendorf, Switzerland.
- Ren, S., Chang, L-Y., Lim, S-K., Zhao, J., Smith, M., Zhao, N., Bulović, V., Bawendi, M. and Gradečák, S. (2011) ‘Inorganic–organic hybrid solar cell: Bridging quantum dots to conjugated polymer nanowires’, *Nano Letters*, **11**(9), 3998–4002.
- Repins, I., Contreras, M.A., Miguel, A., Egaas, B., DeHart, C., Scharf, J., Perkins, C.L., To, B. and Noufi, R. (2008) ‘19.9%-efficient ZnO/CdS/CuInGaSe₂ solar cells with 81.2% fill factor’, *Progress in Photovoltaics: Research and Applications*, **16**, 235–239.
- Rezgui, B., Sibai, A., Nychyporuk, T., Lemiti, M., Bremond, G., Maestre, D. and Palais, O. (2010), ‘Effect of total pressure on the formation and size evolution of silicon quantum dots in silicon nitride films’, *Applied Physics Letters*, **96**(18), 183105–183105–3.
- Rousset, J., Donsanti, F., Geneve, P., Renou, G. and Lincot, D. (2011) ‘High efficiency cadmium free Cu(In,Ga)Se₂ thin film solar cells terminated by an electrodeposited front contact’, *Solar Energy Materials & Solar Cells*, **95**, 1544–1549.
- Rudmann, D., Bilger, G., Kaelin, M., Haug, F.J., Zogg, H. and Tiwari, A.N. (2003) ‘Effects of NaF coevaporation on structural properties of Cu(In,Ga)Se₂ thin films’, *Thin Solid Films*, **431–432**, 37–40.

- Semonin, O.E., Luther, J.M., Choi, S., Chen, H-Y., Gao, J., Nozik, A.J. and Beard, M.C. (2011) 'Peak external photocurrent quantum efficiency exceeding 100% via MEG in a quantum dot solar cell', *Science*, **334**(6062), 1530–1533.
- Shockley, W. and Queisser, H.J.J. (1961) 'Efficiency loss mechanisms: Theory and characterization', *Applied Physics*, **32**, 510–519.
- Skompska, M. (2010) 'Hybrid conjugated polymer/semiconductor photovoltaic cells', *Synthetic Metals*, **160**, 1–15.
- Søndergaard, R., Hösel, M., Angmo, D., Larsen-Olsen, T.T. and Krebs, F.C. (2012) 'Roll-to-roll fabrication of polymer solar cells', *Materials Today*, **15**(1–2), 36–49.
- Spurgeon, J.M., Atwater, H.A. and Lewis, N.S. (2008) 'A comparison between the behavior of nanorod array and planar Cd(Se, Te) photoelectrodes', *Journal of Physical Chemistry C*, **112**, 6186–6193.
- Stenzel, O., Stendhal, A., Voigtsberger, K. and von Borczyskowski, C. (1995) 'Enhancement of the photovoltaic conversion efficiency of copper phthalocyanine thin film devices by incorporation of metal clusters', *Solar Energy Materials and Solar Cells*, **37**, 337–348.
- Sun, Y., Seo, J.H., Takacs, C.J., Seifter, J. and Heeger, A.J. (2011) 'Inverted polymer solar cells integrated with a low-temperature-annealed sol-gel-derived ZnO film as an electron transport layer', *Advanced Materials*, **23**, 1679–1683.
- Takagi, H., Ogawa, H., Yamazaki, Y., Ishizaki, A. and Nakagiri, T. (1990) 'Quantum size effects on photoluminescence in ultrafine Si particles', *Applied Physics Letters*, **56**, 2379.
- Tang, C.W. (1986) '2-layer organic photovoltaic cell', *Applied Physics Letters*, **48**, 183.
- Tarrant, D.E. (2006) 'CIS Module Process R&D', Final Technical Report to NREL, October 2005–June 2006.
- Theyv, B., Sallet, V., Jomard, F., Lusson, A., Rommeluer, J.F. and Teukam, Z. (1997) 'Effects of intentionally introduced hydrogen on the electrical properties of ZnO layers grown by metalorganic chemical vapor deposition', *Journal of Applied Physics*, **91**, 3922.
- Tisdale, W.A., Williams, K.J., Timp, B.A., Norris, D.J., Aydil, E.S. and Zhu, X.-Y. (2010) 'Hot-electron transfer from semiconductor nanocrystals', *Science*, **328**, 1543.
- Todorov, T.K., Tang, J., Bag, S., Gunawan, O., Gokmen, T., Zhu, Y., Mitzi, D.B. (2013) 'Beyond 11% Efficiency: Characteristics of state-of-the-art Cu₂ZnSn(S,Se)₄ Solar Cells', *Advanced Energy Materials*, **3**(1), 34–38.
- Topič, M. (2011) 'Contemporary inorganic thin film photovoltaic materials and technologies', *Contemporary Materials (Renewable Energy Sources)*, **II-2**, 94–102.
- Tsukazaki, A., Ohtomo, A. and Kawasaki, M. (2006) 'High-mobility electronic transport in ZnO thin films', *Applied Physics Letters*, **88**, 152106:1.
- Wadia, C., Alivisatos, P.A. and Kammen, D.M. (2009) 'Materials availability expands the opportunity for large-scale photovoltaics deployment', *Environmental Science & Technology*, **43**(6), 2072–2077, DOI: 10.1021/es8019534.
- Wang, H. (2011) 'Progress in thin film solar cells based on Cu₂ZnSnS₄', Hindawi Publishing Corporation, *International Journal of Photoenergy*, **2011**, Article ID 801292, 10 pages, doi:10.1155/2011/801292. Available online: <http://www.hindawi.com/journals/ijp/2011/801292/>
- Westphalen, W., Kreibig, U., Rostalski, J., Lüth, H. and Meissner, D. (2000) 'Metal cluster enhanced organic solar cells', *Solar Energy Materials and Solar Cells*, **61**, 97–105.

- Xue, J., Rand, B.P., Uchida, S. and Forrest, S.R. (2005) 'Mixed donor-acceptor molecular heterojunctions for photovoltaic applications', II. Device performance, *Journal of Applied Physics*, **98**, 124903.
- Yablonovitch, E. and Cody, G.D. (1982) 'Intensity enhancement in textured optical sheets for solar cells', *IEEE Transactions on Electron Devices*, **29**, 300–305.
- Yan, Y. (2011) 'Understanding of defect physics in polycrystalline photovoltaic materials', Presented at the 37th IEEE Photovoltaic Specialists Conference (PVSC 37) Seattle, Washington June 19–24, 2011, Conference Paper NREL/CP-5200-50650, Available: <http://www.nrel.gov/docs/fy11osti/50650.pdf>
- Yang, L-G., Chen, L., Bai, R., Yang, F., Wang, M. and Chen, H-Z. (2007) 'Modelling of organic nanograting heterojunctions for photoelectric conversion', *Solar Energy Materials & Solar Cells*, **91**, 1110–1119.
- Yoon, J.-H., Yoon, K.-H., Kim, J.-K., Kim, W.-M., Park, J.-K., Lee, T.S., Baik, Y.-J., Seong, T.-Y. and Jeong, J.-H. (2010) 'Effect of the Mo back contact microstructure on the preferred orientation of CIGS thin films', in *35th IEEE Photovoltaic Specialists Conference*, Hawaii Convention Center (USA), 20–25 June 2010, 2443.
- Yu, R., Ching, K-L., Lin, Q., Leung, S-F., Arcrossito, D. and Fan, Z. (2011) 'Strong light absorption of self-organized 3-D nanospike arrays for photovoltaic applications', *ACS Nano*, **5**(11), 9291–9298.
- Yu, G. and Heeger, A.J. (1995) 'Charge separation and photovoltaic conversion in polymer composites with internal donor/acceptor heterojunctions', *Journal of Applied Physics*, **78**, 4510.
- Zank, J., Mehilin, M. and Fritz, H.P. (1996) 'Electrochemical codeposition of indium and gallium for chalcopyrite solar cells', *Thin Solid Films*, **286**, 259.
- Zhang, F., Xua, X., Tang, W., Zhang, J., Zhuo, Z., Wang, J., Wang, J., Xu, Z. and Wang, Y. (2011) 'Recent development of the inverted configuration organic solar cells', *Solar Energy Materials and Solar Cells*, **95**(7), 1785–1799.
- Zhang, K., Zhu, F., Huan, C.H.A. and Wee, A.T.S. (1999) 'Effect of hydrogen partial pressure on optoelectronic properties of indium tin oxide thin films deposited by radio frequency magnetron sputtering method', *Journal of Applied Physics*, **86**, 974.
- Zhang, Z.-G. and Wang, J. (2012) 'Structures and properties of conjugated Donor-Acceptor copolymers for solar cell applications', *Journal of Materials Chemistry*, **22**, 4178–4187.
- Zhou, Z., Kato, K., Komaki, T., Yoshino, M., Yukawa, H., Morinaga, M. and Morita, K. (2004) 'Effects of dopants and hydrogen on the electrical conductivity of ZnO', *Journal of the European Ceramic Society*, **24**, 139.
- Zhu, J., Yu, Z., Burkhard, G.F., Hsu, C.-M., Connor, S.T., Xu, Y., Wang, Q., McGehee, M., Fan, S. and Cui, Y. (2009) 'Optical absorption enhancement in amorphous silicon nanowire and nanocone arrays', *Nano Letters*, **9**(1), 279–282. DOI: 10.1021/nl802886y.

Optical coatings for security and authentication devices

B. BALOUKAS and L. MARTINU, Department of Engineering Physics, École Polytechnique de Montréal, Canada

DOI: 10.1533/9780857097316.4.631

Abstract: This chapter aims to describe the advances in security devices despite that it may seem counterproductive in an anti-counterfeiting context. After a brief overview of the importance of optical security devices in today's technology-driven world we provide an historical overview of their evolution. Even if a vast literature exists on the subject, it is not our goal to be exhaustive; we rather present the basic principles behind interference-based security devices and underline the various possibilities they offer. In particular, we describe recently added features which increase simplicity of use and enhance efficiency of interference security image structures (ISISs): these include metamerism, magnetic materials, diffraction and interference combination, and use of photonic color technology and active materials.

Key words: anti-counterfeiting, optical security device, interference, optical filters, ISIS, color shifting, metamerism, electrochromic interference filters.

17.1 Introduction

Counterfeiting is unfortunately here to stay. Besides the most frequently considered security documents such as passports and identity cards, as well as valuable documents such as banknotes and credit cards, counterfeiting also affects everyday consumer products from golf clubs to airplane parts. In fact, the Federal Aviation Administration (FAA) estimates that some 520 000 counterfeit parts are installed in planes each year.¹ Other than significant financial consequences – economic losses are estimated to reach up to 1.8 trillion dollars in 2015² – it is public safety that is most at risk. Indeed, copied products made without any regulation and supervision rarely fulfill quality and safety requirements. A perfect example of this is counterfeit pharmaceutical products that, according to the World Health Organization (WHO), may represent up to 25% of the available medicine in developing countries.³ It is therefore no surprise that governments and institutions

have always wielded technology to their advantage in order to protect their documents and products.

Historically, currency has always benefited from the most advanced security devices. Before the advent of such devices, one of the most popular methods of anti-counterfeiting was the death penalty.⁴ Although this may have been an effective means of discouragement it was abandoned as human right issues made headway. As a result, emphasis was put on printing bank notes with intricate and complex images, distinctive typefaces, exclusive colored inks, watermarks, microprinting, and unique serial numbers. These features were sufficient until the arrival of accurate color copiers and, more recently, scanners and high-resolution printers (so-called digifeiting). Incidentally, color was introduced on banknotes in part due to the appearance of black and white photography. To counteract these potentially serious threats, optically variable devices (OVDs) based on diffraction (diffractive optical variable image devices (DOVIDs): holograms, stereograms, kinograms, etc.) and interference (ISIIs) were introduced; the iridescence presented by these devices inhibits the use of standard reprographic technologies. It is important to note that no device is infallible and for this reason modern banknotes benefit from the use of multiple features, each with their specific purpose.⁵

Although all of these features have contributed in some way to the fight against counterfeiting, one must never forget that even the best features are rendered useless without the participation of the general public. It is now recognized that public awareness and understanding, provided through education, is crucial in increasing counterfeit detection.⁶ As a result, security features should always remain simple to use and the effects they present are easy to remember. Indeed, despite the presence of multiple devices, studies have shown that, on average, the public remembers a fairly low number of them (1.7 currency features in The Netherlands in 19997). In another remarkable example, it was shown that the awareness level in the US for the black to green color shifting feature on American banknotes was only 17% in 2004.⁸

In 1968, the Bank of Canada approached the National Research Council (NRC) for ideas on novel security devices. The NRC, spearheaded by J.A. Dobrowolski, proposed optical interference coatings as potential candidates.^{9,10} Although a feature often considered as undesirable in the field of optical filters, the observed angular color change was not only judged as an excellent counterfeiting deterrent, but also an efficient and simple means of authentication for the general public. These structures also had the added advantage of being machine readable.^{11,12}

In December 1987, the Bank of Thailand introduced a commemorative banknote protected with optically variable ink (OVI) produced by Optical Coating Laboratory, Inc. (OCLI). A few months later, in April 1988, British

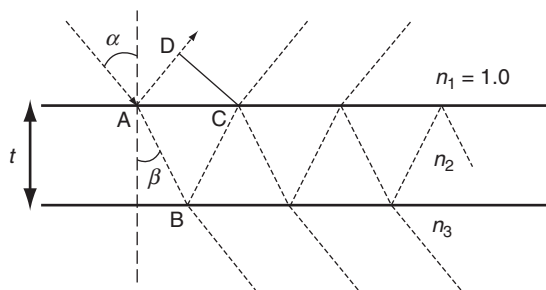
Columbia introduced driver's licenses displaying a transparent to red color shifting five-layer ISIS (made by Identicard and NRC). In December 1989, following extensive work at the NRC in collaboration with Vadeko International, an engineering firm, the Bank of Canada introduced its first 50 dollar bill with a gold to green color shifting ISIS. Since then, ISISs have demonstrated excellent efficiency¹³ and are highly appreciated by the general public;⁸ for example, more than 40 metric tons of optically variable pigments (OVPs) are produced yearly¹⁴ and OVI is used on the currencies of more than 100 countries.¹⁵

17.2 Basic principles and structures currently applied

Let us now consider the basic principles behind the use of optical coatings for security purposes. As previously mentioned, it is the intrinsic color shift observed as a function of the observation angle which is the key feature of ISISs. The color change is due to a shift in the spectral characteristics of the filter towards shorter wavelengths at higher angles of incidence. This can be demonstrated by considering the case of a single thin film of index n_2 and thickness t (see Fig. 17.1). The difference in optical paths Δ between the beam which travels inside the film (ABC) and the incident beam which was simply reflected at point A (AD) is given by $(ABC)n_2 - (AD)n_1$ (in the case where absorption is negligible). One can show following simple trigonometry that:

$$\Delta = 2t\sqrt{n_2^2 - \sin \alpha^2} \text{ if } n_1 = 1 \quad [17.1]$$

where α is the angle of incidence of the beam. As α is increased, Δ is seen to decrease and therefore, if one has constructive interference at λ_0 at normal incidence (i.e., Δ contains an integer number of wavelengths λ_0), this



17.1 Multiple reflections in a thin film of index n_2 and thickness t . The incident medium is air and therefore $n_1 = 1$.

same constructive interference will occur at a $\lambda < \lambda_0$ at higher α values. Consequently, all interference-based devices will shift towards shorter wavelengths as a function of the observation angle. A device having a gold color at normal incidence will thus shift towards the green and eventually blue when observed at a more inclined angle.

Note that the final optical path difference also depends on the presence of soft (when going from a high to low refractive index) and/or hard (when going from a low to high refractive index) reflections at points A and B. In the case where the incident medium is air, point A will typically present a hard reflection and thus a $\lambda/2$ phase shift. For example, if the thickness of a film is equal to a quarter-wave ($t = \lambda/4n$) then Equation [17.1] results in a path difference of $\lambda/2$ at normal incidence. Now, if the index of this quarter-wave film is higher than that of the substrate, a hard reflection will only be present at point A. The total path difference will thus be equal to zero and constructive interference will take place between both beams (increased reflectance).

On the contrary, if the index of the film is lower than that of the substrate, hard reflections will be present at both points A and B. As a result the final path difference will be $\lambda/2$, therefore destructive interference will ensue (decreased reflectance, i.e., antireflection). Correspondingly, the constructive and destructive interference conditions will be inverted for a film of half-wave ($t = \lambda/2n$) thickness. Both these specific thicknesses are very often the basis of many classic filter designs. For example, one can construct a reflector by alternating high (H) and low (L) index of refraction quarter-wave thick materials ($[HL]^xH$ where x is an integer) or fabricate a Fabry-Perot filter by separating two reflectors by a half-wave ($[HL]^xHH[LH]^x$).

It is worth mentioning that single dielectric layer structures (for example, pearl luster or nacreous pigments) benefiting from interference effects have been used for their high luster and brilliance in many applications such as plastics, cosmetics, paints, etc.;¹⁶ one such example is TiO₂-covered mica flakes. However, the fact that these pigments offer practically no color change as a function of the observation angle limits their use for security applications.

Two main categories of optical filters exist: those based on all-dielectric materials and those based on metallic and dielectric materials (metal-dielectric filters). Using dielectric materials with negligible absorption in the visible offers the possibility of a device which can be used both in reflection and/or in transmission (e.g., through the use of a window or when placed over printed information). On the other hand, a high number of layers is often required in order to obtain a sufficiently high color saturation which will inevitably increase fabrication costs. Addition of metallic layers offers the opportunity of rapidly increasing the reflectance and thus decreases the number of layers required as well as the total cost. On the other hand, the

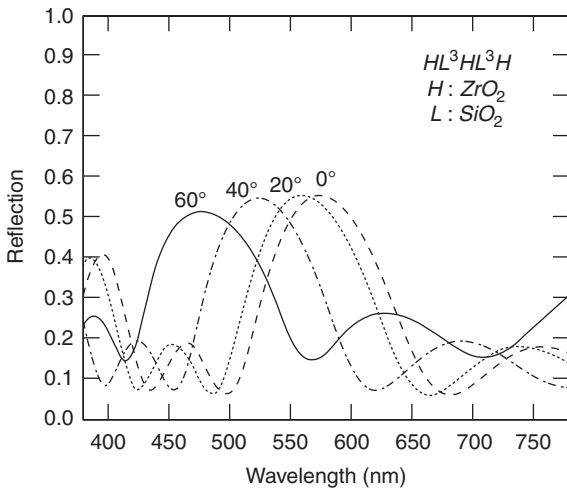
high absorption of metallic films drastically decreases the transmission as well as the maximum attainable reflection, and it can thus limit their use in particular applications. Although more expensive, it has also been shown that all-dielectric filters possess a much higher chemical and mechanical stability over time when compared to metallic layers which have a tendency to age in an unpredictable manner.^{17,18} As a result, metal-dielectric structures must typically be laminated for protection. Note that lamination decreases the saturation of colors due to the added surface reflection and, considering Snell's refraction law, can also limit the maximum incidence angle and thus the color shift.¹⁷

17.2.1 All-dielectric filters

Over the years, there have been a multitude of devices proposed. In his paper published in 1973,⁹ Dobrowolski proposed numerous all-dielectric filters with interesting properties, mainly, a red to blue color shifting filter, a broad-band reflector which would hide underlying information at normal incidence and become transparent at higher angles, as well as a transparent to red filter (reflection peak in the near-infrared would shift into the visible). Note that the latter two effects are more difficult to obtain convincingly with metal-dielectric filters.

As previously mentioned, for physical reasons one typically observes color changes towards shorter wavelengths. In this regard another interesting filter design exists, known for its reverse color shift from blue to red. This effect is obtained by carefully positioning two reflectance bands, one in the blue wavelength region and one in the near-infrared. Thus, when the filter is tilted, the blue band shifts into the ultraviolet (UV), whereas the band in the near-infrared falls into the visible (red).

One example of an all-dielectric filter applied for security is the gold to green color shifting filter present on the 1986 Birds of Canada banknote series. More precisely, this filter was based on five layers of SiO_2 and ZrO_2 (HL^3HL^3H at 585 nm)¹⁹ (see Fig. 17.2 for simulated spectra of the gold to green color shift of this particular device). The filter was transferred from a polyethylene terephthalate (PET) substrate covered by a release layer of organic or synthetic wax²⁰ using a UV curable black adhesive developed by 3M.¹⁷ Indeed, when using all-dielectric filters, the background onto which the filter is apposed is very important. When using a white background, the light which is transmitted through the filter will be reflected back towards the observer, thus adding itself to the reflected beam and resulting in a decreased saturation (reflection and transmission are complementary in the absence of absorption). Obviously, the amount of light which is reflected back specularly will greatly depend on the surface roughness of the background. As a result,



17.2 Reflection spectra at various angles (unpolarized light) of an all-dielectric interference filter simulating the five-layer optical security device initially developed for the Bank of Canada. The high index of refraction material is ZrO_2 ($n_{550\text{ nm}} = 1.88$ – taken from the J.A. Woollam material library) and the low index material SiO_2 ($n_{550\text{ nm}} = 1.46$).²⁴ The structure of the device is indicated in the upper right corner.

a black background is often used to eliminate the transmitted component of the light. Since optical filters reflect light specularly, it can be difficult to observe the color shift when using a single light source; artificially roughening the surface has been shown to help. This is not the case for filters used in transmission, since authentication can simply be made by positioning the filter towards a light source and looking through it.

Placing a filter over sensitive information can also limit forgery while still allowing the information to be read. In fact, tamper evident filters have been developed which exhibit an irreversible color change when tampered with; for example, when an individual tries to remove a filter in order to transfer it onto another document. This effect can be obtained by modifying the adherence between two layers of a thin-film stack.^{21–23}

17.2.2 Metal-dielectric filters

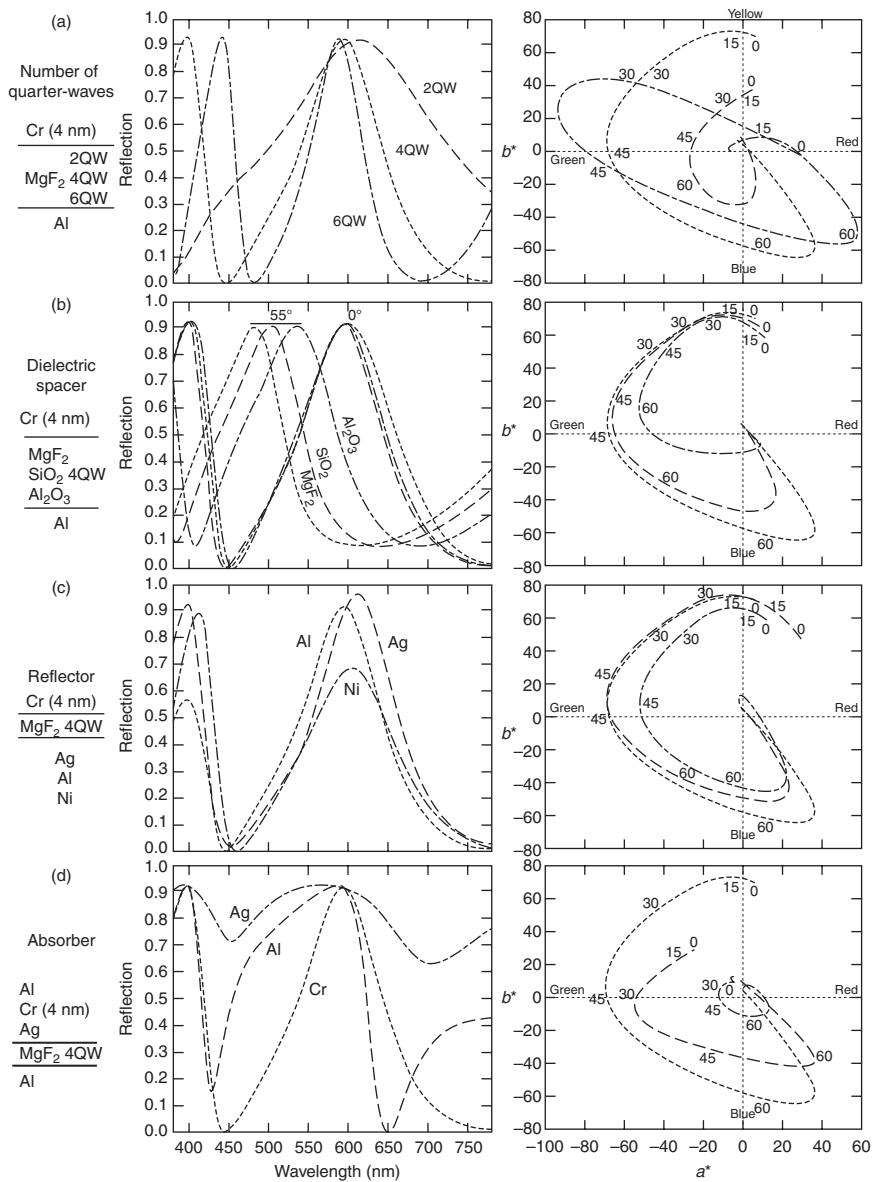
The most popular metal-dielectric structure currently in use is generally based on the following three-layer system: a metallic reflector, followed by a dielectric spacer and completed by a thin, partially absorbing film. Often described as Fabry-Perot-like, this structure allows one to obtain a very high color saturation with a minimum of layers due to a combination of interference and of selective absorption (at specific wavelengths the electric

field reaches a maximum at the absorber).²⁵ This absorption also results in a lower brightness when compared with absorption-free all-dielectric filters.

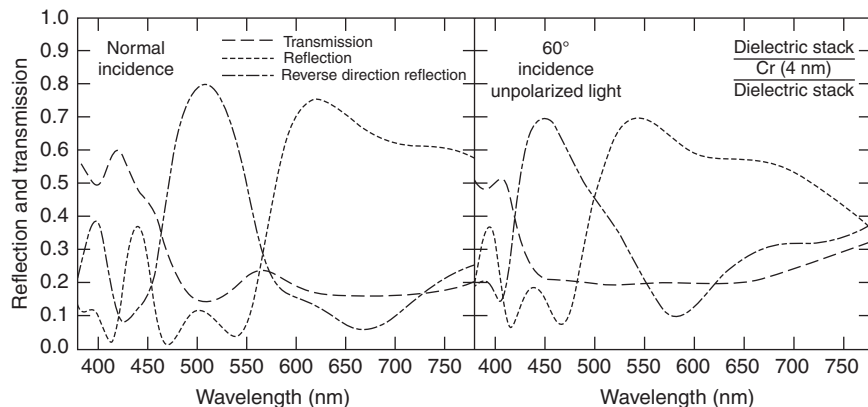
The choice of material for each of the individual layers as well as their thickness is made in order to increase performance and obtain the desired color shifting properties. Modifying the thickness of the spacer allows one to adjust the position of the reflection peaks (see Fig. 17.3). In the example presented in Fig. 17.3a, the reflection of a Fabry-Perot-like structure based on Al|MgF₂|Cr is shown for various thicknesses of MgF₂: two quarter-waves (QWs), four QWs and six QWs at 575 nm (knowing that one QW = $\lambda/4n$ and two QWs is one half-wave). One can see how the width of the main peak decreases as the thickness is increased; this correspondingly increases the saturation in color (curve shown is farther away from the origin in the $L^*a^*b^*$ color space in Fig. 17.3a). Thicknesses are therefore typically chosen between 2 and 8 QWs. On the other hand, the use of too many QWs results in multiple peaks in the visible and can thus lead to desaturated colors.²⁶ One can also see, in the present example, that the color varies from gold to green and eventually to blue. To obtain a simplified two color shift, considered more obvious for lay viewers,²⁷ it has been shown that an overlying colored dye can filter colors at high angles of incidence (e.g., yellow dye to block blue).²⁸

As for the spacer material, it can be shown that choosing a low index of refraction dielectric material increases the color variation (from Snell's law $n_1 \sin\alpha = n_2 \sin\beta$; β will be larger for lower values of n_2) so that SiO₂ or MgF₂ are most often the materials of choice. This is clearly demonstrated in Fig. 17.3b for three spacer materials of a thickness of 4QW: Al₂O₃ ($n_{550\text{ nm}} = 1.77$), SiO₂ ($n_{550\text{ nm}} = 1.49$) and MgF₂ ($n_{550\text{ nm}} = 1.38$).

In order to increase the brightness of the filter, metals possessing a high reflectance and neutral color such as Ag and Al are typically chosen as the bottom reflector. Figure 17.3c shows the effect of different metals when choosing from Ag, Al and Ni ($R_{\text{Ag}} = 96\%$, $R_{\text{Al}} = 92\%$ and $R_{\text{Ni}} = 61\%$ at 550 nm). As predicted, the only significant effect one notices is the decrease in the maximum amplitude of the reflectance peaks as the reflectance of the mirror decreases. In terms of color variation, Ag and Al offer a very similar performance. Although most devices are reflection based, some transmission based metal-dielectric structures have also been proposed.^{25,29} A new, until now unexploited effect has been recently demonstrated when using a semi-transparent mirror: fabricating an asymmetric stack allows one to obtain a device whose color in reflection is dependent on the side of observation, as well as being semi-transparent.³⁰ Figure 17.4 shows an example of such a filter which presents a purple to black color shift in transmission, a red to greenish yellow shift in reflection and a green to blue shift in reverse reflection.



17.3 Various configurations of Fabry-Perot-like metal-dielectric filters and their effect on the reflectance and the color variation performance (calculated under illuminant D65). From top to bottom, we present the effect of changing: (a) the thickness in quarter-waves of the dielectric spacer (at 575 nm), (b) the dielectric spacer material, (c) the metallic reflector material, (d) the absorber material.



17.4 Reflection and transmission spectra at normal incidence of a filter with three different color shifts, one in transmission (purple (RGB = 55, 42, 109) to black (52, 48, 61)) and two in reflection (forward direction from red (229, 32, 40) to greenish yellow (151, 169, 24) and reverse direction from green (0, 156, 68) to blue (20, 62, 169) – calculated under illuminant D65). Note that the structure of the filter is shown in the upper right corner.

Finally, it has also been demonstrated that the top semi-absorbing film must present a ratio of $n/k \approx 1$.³¹ In Fig. 17.3d, we show three examples where the absorber is either Ag ($n/k = 0.04$), Al ($n/k = 0.14$ at 550 nm) or Cr ($n/k = 0.70$) all with a thickness of 4 nm; note that all these metals possess a fairly neutral color. Clearly, the closer the n/k ratio is to 1 (in this case Cr), the higher is the color saturation obtained at normal incidence, and the higher the color travel. Despite this finding, simple structures based purely on the use of aluminium (Al|Al₂O₃|Al) have recently been proposed as potential candidates for security and decorative purposes.³² Obviously, the thickness of the absorber must also be optimized.

The fact that metal-dielectric filters require fewer layers has made them the structure of choice to protect most banknotes. Indeed, the sheer number of banknotes which required protection, often reaching the billions, makes the cost of fabrication a critical parameter. For example, the Bank of Canada converted its five-layer all-dielectric filter to a three-layer metal-dielectric filter with a similar performance. Cost is also the reason why fabrication of OVDs is mostly done by roll-to-roll coating using e-beam evaporation, known for its high deposition rate. Systems must also be equipped with an optical monitoring system to control the thickness of the layers *in situ* and, consequently, the resulting color.³³ A precision as high as 1.5% on thickness is typical and can be required to maintain color consistency.³⁴ Very high uniformity is required in order to ensure a steadfast color across the whole web. Due to the porous nature of e-beam evaporated films, the design may

need to be adjusted to account for the absorption of water once exposed to the ambient environment.³⁵

More recently, there have been proposals to replace the top semi-absorbing film with a metal film presenting nanoclusters (Brandsealing®).^{36,37} By carefully controlling the size and shape of the clusters, the plasmon resonance excitation can be finely tuned and serve as an optical code which is machine readable.³⁸ Others have also integrated an anisotropically scattering layer over the dielectric spacer which is then coated with a semi-absorbing metal film (anisotropically scattering Fabry-Perot). Although these structures show a limited change in color when tilted, due to their highly diffuse character, they still retain good color saturation. Their anisotropic nature also allows for the generation of rotation-dependent optical effects.³⁹

17.2.3 Optically variable pigments

Patterning an interference filter into a specific shape is not a simple task. Although it has been done by using masking during deposition, laser etching,⁴⁰ hot stamping, using soluble materials,⁴¹ embossing,⁴² etc., one method which allows highly complex images to be created is based on using optically variable pigments (OVPs). In this particular case, the desired filter is first deposited onto a release-coated web, it is then delaminated, milled into a powder and incorporated into a printing vehicle, thus forming what is known as optically variable ink (OVI)^{31,43} (OVP is produced by Flex Products as base material for OVI by Société Industrielle et Commerciale de Produits Alimentaires (SICPA)^{44–46}). These pigments are based on Fabry-Perot-like structures, but consist of five layers (absorber|spacer|mirror|spacer|absorber) because they are symmetric around the opaque mirror. This symmetry is essential since, during the printing process, one cannot control on which side the pigment will fall. To ensure the pigments lie flat, the aspect ratio of the thickness versus size of the pigments is kept at approximately 10:1.²⁶ Obviously, all the pigments do not lie perfectly flat ($\approx 10^\circ$ angle on average); therefore, all the diffuse reflection is increased (10% specular and 90% diffuse) giving rise to lower color saturation (average of colors from slightly different angles).^{34,47}

Another advantage procured by the incorporation of OVPs into an ink is that the whole structure is essentially laminated and, as a result, oxidation and damaging of the sensitive metallic layers are no longer an issue. Additionally, OVI is more flexible when compared to a foil-type device where the mechanical properties can be limiting once apposed onto a flexible substrate.³¹

Lately, in an effort to increase the covert security offered by OVPs, it has been demonstrated that the pigments can be made into various shapes (diamonds, squares, etc.) by using an embossed foil as the substrate during



17.5 Example of a micro-structured, square shaped optically variable pigment displaying a Euro symbol. Figure modified from Reference 50.

deposition (see Fig. 17.5).⁴⁸ When viewed under a microscope, one can easily observe these shaped pigments and therefore rapidly validate the authenticity of the device. Furthermore, additional effects can also be generated by patterning one or more of the layers of the filter (laser ablation, flexographic printed oil which vaporizes during deposition,^{48,49} chemical etching, etc.).

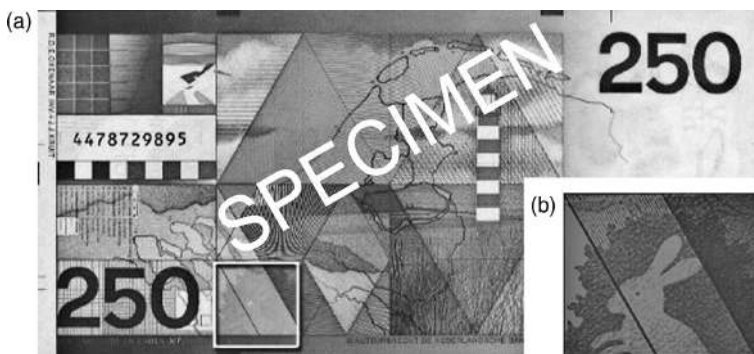
Lastly, note that there are commercial products currently on the market which display iridescent effects (wrapping paper based on co-extruded polymer films, ChromaFlaire by Flex Products,⁵¹ etc.). Although the color shifts offered by such products may not be of the same quality as current security devices, their potential use for counterfeiting must be seriously considered.

17.3 Specific optical effects suitable for security devices

Realizing that a simple color shift may not be sufficient to protect against future counterfeiters, most of the current research has focused on implementing additional features to the classic ISIS. The main goal is to increase fabrication complexity while still maintaining or even simplifying the authenticity validation phase for the general public. In the following subsections, we give a survey of these augmented interference-based devices.

17.3.1 Metamerism

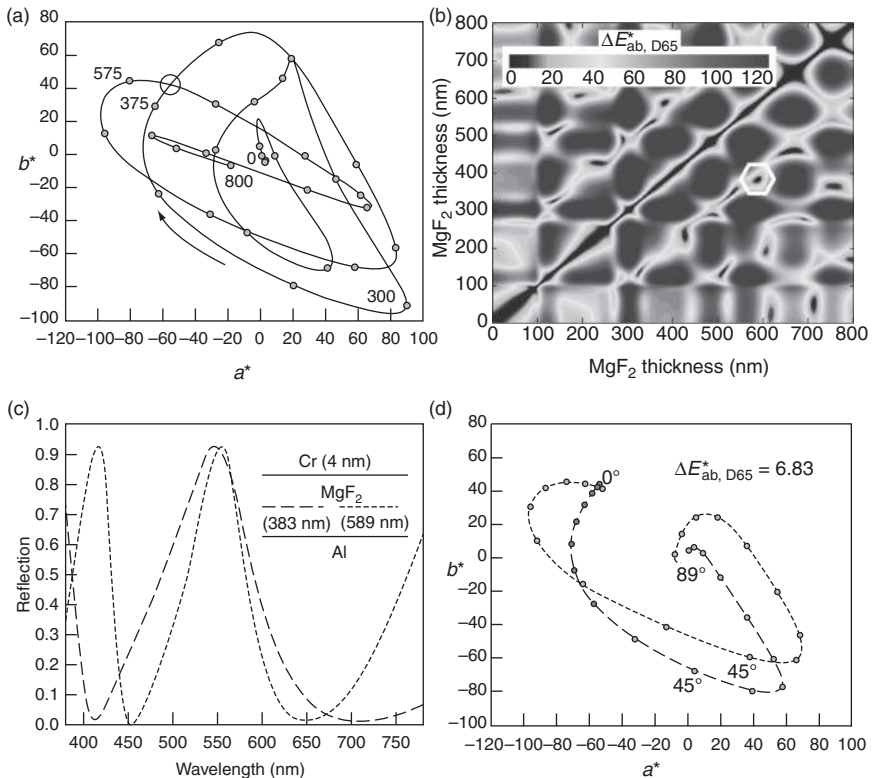
Metamerism is a phenomenon where two objects with different reflection or transmission spectra appear to possess the same color under a specific light



17.6 The 1985 Dutch 250 guilder banknote sporting a feature based on metameric inks (inside white square in (a)). Notice that the rabbit is still slightly visible on the image even under normal lighting. In (b) the inks are viewed through a red filter. Figure modified from Reference 52.

source. Juxtaposing two such elements therefore allows for the creation of a hidden image effect. For example, the 1985 Dutch 250 guilder banknote sported a metameric feature based on green metameric inks. Under normal lighting the feature was fairly uniform in color, but when observed through a red filter, a rabbit would appear (see Fig. 17.6). This effect was possible since the inks had almost identical spectra in the green-wavelength region, whereas they differed in the red.⁵² Hence, the use of a red filter accentuated these differences. In 1999, the polymer Romanian 2000 Lei, went one step further by incorporating a magenta filter onto the banknote itself hence resulting in a self-authenticating banknote. In the previous examples, the metameric devices were based on classical non-iridescent inks. However, there have also been some examples of interference-based metameric features. To our knowledge, the first metameric feature to be proposed⁹ consisted of two filters with identical colors, which when superposed would transmit no light. Perhaps due to its relative complexity and potential cost, this feature was never implemented but, nonetheless, it proposed an innovative concept.

About two decades later, metamerism was once again suggested after it was noticed that Fabry-Perot-like metal-dielectric filters with different spacer thicknesses resulted in similar colors.⁴⁷ Figure 17.7a presents the variation of color in the $L^*a^*b^*$ color space as a function of increasing MgF_2 thickness for a $Al|MgF_2|Cr$ structure (from 0 to 800 nm). As can be seen, there are multiple points where the color trajectories intersect. These points correspond to different MgF_2 thicknesses which generate identical a^* and b^* coordinates. Keep in mind that in order to ensure an adequate color match, one must also consider the luminance value L^* of both configurations (presented in Fig. 17.7b).



17.7 Metameric pairs based on metal-dielectric Fabry-Perot-like filters.
 Part (a) shows the variation in color in the $L^*a^*b^*$ color space when the thickness of the MgF_2 layer is varied between 0 and 800 nm. Each dot represents a 25 nm increment in thickness. Interestingly, the outer boundary formed by the present curve represents the gamut of all possible colors attainable by the present structure. Part (b) presents the $\Delta E_{ab, D65}^*$ for all thickness combinations. This figure is symmetric (line of symmetry $x = y$) and shows that there are 13 combinations resulting in a low color difference. In part (c) we show the reflection spectra of the chosen metamer pair (circle in (a) and hexagon in (b)). Note that the structure of the simulated filters is also shown in the upper right corner. Finally, (d) shows the color variation of both filters as a function of the observation angle. Notice how at 0° the colors coincide (the color difference is also indicated). Each dot represents a 5° increment in angle. This data generated using a combination of *OpenFilters*⁵³ and *Matlab*.

In Fig. 17.7b we present the difference in color $\Delta E_{ab, D65}^*$ between all possible thickness combinations of MgF_2 between 0 and 800 nm. We first notice that this figure is symmetric (line of symmetry $x = y$). We can also see that the lowest $\Delta E_{ab, D65}^*$ is obtained along the diagonal since this region corresponds to two samples with identical MgF_2 thicknesses. In total, there are

13 regions with a fairly low $\Delta E^*_{ab,D65}$. Let us now choose one of these intersections (see circle in Fig. 17.7a and hexagon in Fig. 17.7b); the lowest color difference in this particular case is obtained when comparing samples with MgF₂ thicknesses equal to 383 and 589 nm. The resulting reflection spectra of both these samples are shown in Fig. 17.7c. It is fairly straightforward to understand why these two samples are metameristic. Indeed, the spectra match fairly well in the region of sensitivity of the human eye (between 400 and 700 nm; see Fig. 17.8b), whereas they differ in regions where the eye is less sensitive (near-UV and near-IR). The fact that both filters possess different spectra results in their having different color trajectories as a function of the observation angle (see Fig. 17.7d). Therefore, at normal incidence both samples are green and at an angle of 45° the 383 nm MgF₂ filter displays a bluish tint, whereas the 589 nm MgF₂ filter is more purplish. As a result, printing both these filters side-by-side allows the creation of hidden images. In fact, a product has been developed using this principle and adopted by the pharmaceutical industry (MetaSwitch).^{48,54} In addition, a similar effect is also possible by replacing one of the variable inks with a non-iridescent material (NIM) (e.g., metallic inks).

In the example presented above, $\Delta E^*_{ab,D65} = 6.83$, a value which is fairly high and which may result in a slightly different color appear even at normal incidence. When changing the illuminant to incandescent or fluorescent lighting, the color differences are even higher ($\Delta E^*_{ab,A} = 11.79$ and $\Delta E^*_{ab,F1} = 9.40$). As a result, the present device is highly sensitive to changes in light sources and, therefore, to changes in observer. Consequently, these metameristic features are often optimized for specific lighting conditions (usually fluorescent lighting due to its popularity). Other variations of more complex metal-dielectric metameristic structures have also been proposed, such as a nine layer design (additional absorber|dielectric pairs) which allows fabrication of a filter that presents the same color at normal incidence as well as the same color shift as a typical five-layer OVP but with the absence of reflection peaks in the near-UV and near-infrared.^{31,55} As a result, this type of feature could only be identified via a machine.

Recently, it has been shown that using a slightly higher number of layers allows one to surpass the previous shortcomings, that is, design and fabricate metameristic pairs with a good performance (low ΔE^*_{ab}) and lower sensitivity to changes in light sources and observers.^{30,56–58} By using all-dielectric filters, these devices could also be used in a transmission mode. Figure 17.8 shows two examples of filters which were designed to match the color of a transparent (non-iridescent) colored ink. In Fig. 17.8a, one can clearly see that the designed filter (13 layers of SiO₂ and Ta₂O₅) matches the whole transmission spectrum of the NIM and, consequently, the color difference ΔE^*_{ab} remains low under all three illuminants (decreased metamerism leading towards isomerism). In this same example, the NIM

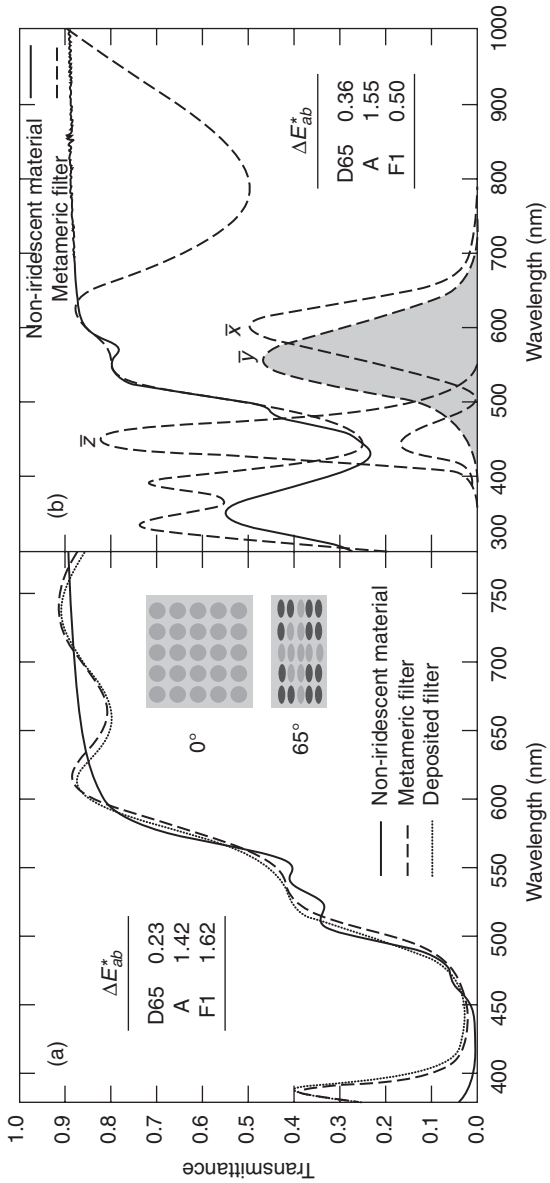
and the filter were patterned in order to create a hidden image effect: an arrow appears at high angles of incidence due to the orange to light yellow color shift of the filter.

In an attempt to reduce the number of layers of the filters, a design methodology based on the use of the luminous efficiency curve of the human eye was developed. Figure 17.8b shows the International Commission on Illumination (CIE) 1931 color matching functions used in color calculations, $\bar{x}\bar{y}\bar{z}$, \bar{y} having the same distribution as the luminous efficiency curve of the human eye. By using transmission targets with tolerances which are inversely proportional to \bar{y} (maximum weight in regions of highest sensitivity), the authors show that filters with a smaller number of layers can be designed without compromising their performance.^{59,60} An example of this is shown in Fig. 17.8b, where the designed filter is allowed to diverge from the NIM spectrum in the low and high wavelength regions where the eye is less sensitive. Obviously, \bar{y} is only one of the three components used in color calculations so that this design methodology cannot be used alone, but must be combined with color target coordinates under at least one illuminant. On the other hand, it does guide the optimization process in the right direction by reducing the amount of possible solutions; indeed, an infinity of metameric spectra exists resulting in color matches.

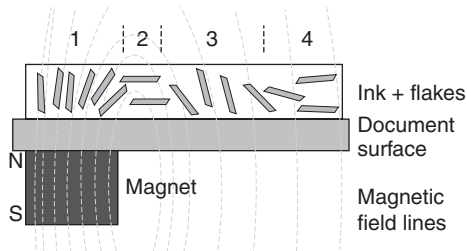
17.3.2 Magnetic films

The presence of magnetic materials (Fe_2O_3 , Fe_3O_4 , barium or strontium ferrite, soft iron or nickel particles, etc.) in security has typically been used to include covert information in documents;⁶¹ obviously, a high coercivity (resistance to demagnetization) is necessary to ensure protection against erasure. They are also commonly used for anti-theft security labels.⁶² It follows that by combining regular inks with magnetic inks of identical color one can encrypt information which is readable using various types of detectors and sensors (see the Canadian 5 dollar bird series banknote from Reference 61, for example).

More recently, optically variable pigments combining both interference effects and a magnetic signature have been demonstrated. Although mixing color shifting pigments with magnetic inks may seem the simplest solution, the colorless nature of the latter renders these mixtures unattractive. A better solution can be obtained by integrating the magnetic material into the structure of the interference filter. For example, one can replace the metallic reflector or absorber by a specific magnetic material (e.g., Co-Ni alloy reflector|MgF₂ spacer|Cr absorber⁶³). Although a slightly more expensive solution, incorporating the magnetic film below the reflector allows one to preserve the optimized optical performance of the filter.



17.8 Two examples of all-dielectric metameristic filters designed to match the transmission spectra of transparent colored inks. In (a), one can see how the filter ('3 layers) matches the whole visible transmission spectrum of the NIM. This automatically results in a low color difference ΔE_{ab}^* under all three illuminants. A hidden image effect is also possible by patterning both elements. In (b), the filter's (9 layers) spectrum is allowed to diverge in regions where the eye is less sensitive as a means to decrease the number of layers without compromising performance. The CIE 1931 color matching functions $\overline{x}\overline{y}\overline{z}$ are also shown as reference.

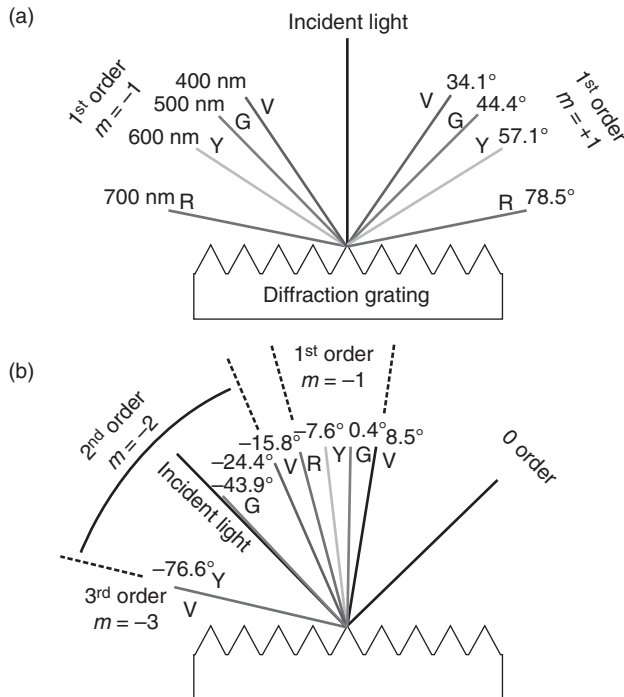


17.9 Magnetic color shifting pigments exposed to the magnetic field of a cylindrical magnet. Notice how the pigments align with the magnetic field lines. This alignment allows for the creation of interesting optical effects. Figure inspired by Reference 63.

The presence of a magnetic material also offers another interesting possibility. When in the presence of a magnetic field, each individual pigment will align itself with the field lines. As a result, when an ink comprising such pigments is cured in the presence of a magnet, specific optical effects can be created (see Fig. 17.9).⁶⁴ In the present example, the reflection will be at its lowest in region 1 since light is essentially lost due to multiple reflections between pigments and absorbed by the substrate, whereas it will be at its highest in region 2. The pigments in region 3 having a fairly acute angle will also present a fairly low reflectivity. Finally, the magnetic field intensity decreases as a function of distance so pigments in region 4 will only be subjected to low magnetic forces and will naturally lay flat (as non-magnetic pigments). For a complete survey of the optical effects which can be generated using this technology, consult the article by Raksha *et al.*⁶⁵ Commercial applications of this concept have been proposed^{66,67} and implemented in high-speed printing.⁶⁸

17.3.3 Combining interference and diffraction

Although DOVIDs are outside the scope of this chapter, it is important to note that there are significant efforts to combine them with ISISs in the hopes of generating stronger features benefiting from the advantages of both technologies. Indeed, holograms do present interesting optical effects, but the security they procure has lately been questioned due to the relative ease with which they can be counterfeited.⁶⁹ Another key feature resides in the fact that interference-based devices can still be viewed under diffused lighting whereas diffractive devices perform best under direct lighting. Their combination therefore results in an increased versatility making authentication possible under various types of lighting situations.⁶⁴ For a complete review of diffraction-based devices, see Reference 52.



17.10 Diffraction of light at (a) normal and (b) 45° of incidence for four different wavelengths on a 1400 lines per mm grating. Letters indicating the color of the wavelength are indicated next to each beam of light (R = red, Y = yellow, G = green, and V = violet). Note that in (b), the 2nd order yellow coincides with the 3rd order violet which can result in a decrease in saturation. Figure inspired by Reference 48.

It is well known that diffraction arises when light arrives upon a surface possessing a periodic structure whose period is near the wavelength of the incident light. Following the Huygens-Fresnel principle, each point on the diffractive grating becomes a secondary source of spherical light emission. These spherical waves then interfere constructively and destructively, and result in each wavelength being diffracted at a specific angle. The following equation allows for the calculation of these angles:

$$m\lambda = d(\sin\alpha + \sin\beta), \quad [17.2]$$

where m is the diffraction order, λ is the wavelength, d is the distance between two grooves, and α and β are the incident and diffracted angles, respectively (relative to the normal of the surface).⁴⁸ When light arrives at normal incidence ($m\lambda = ds\sin\beta$), Equation [17.2] dictates that higher wavelengths will be

diffracted at higher angles (see Fig. 17.10a). Also note that, in the present case of a grating with 1400 lines/mm as presented in Fig. 17.10, only the first diffraction order is visible.

When light arrives obliquely, for example at 45° (see Fig. 17.10b), the zero order ($m = 0$) will be specularly reflected at the same opposite equivalent angle. We can also see that the -1 order has been rotated clockwise, so that contrary to ISIS the observed color change as a function of the observation angle is from shorter to longer wavelengths when observing a diffraction grating. Also note that higher orders are now also visible. Changing the shape (triangular, sinusoidal, etc.), depth, and orientation (blazed) of the grooves of a grating allows one to modify the relative intensities of the various orders.⁷⁰ Interesting color effects can also be obtained by using combination gratings benefiting from the superposition of two diffractive grating profiles or more.⁷¹

Recently, the concept of printable holograms through the use of diffractive pigments has been demonstrated.^{72,73} The fact that these pigments contain ferromagnetic materials allows for their alignment using electromagnetic fields and thus the creation of interesting three dimensional (3D) effects, but also rotation-dependent color effects by printing flakes with a 90° difference in orientation.⁵⁰ Indeed, in order to observe diffraction the grooves must be perpendicular to the observation direction. Finally, metameric diffractive pigments have also been proposed.^{74,75}

Deposition of an interference filter on an embossed substrate results in a highly complex interaction of diffraction and interference.^{48,76,77} Generally speaking, the effect of the interference filter is to block specific wavelengths so that the rainbow effect of diffraction is attenuated and only specific colors are enforced. Various configurations of these two effects are presented in Reference 78. Once again, using an all-dielectric filter allows for transmission-based devices to be created.⁷⁹ The simplest configuration is the use of a high refractive index material (e.g., ZnS) on an embossed polymer substrate for see-through holograms.⁸⁰ Another possibility is to simply laminate a hologram with an interference filter.^{81,82}

From Equation [17.2], it can be seen that when the grating spacing is equivalent to half the wavelength of light (200 nm for a 400 nm violet light, more than 5000 lines/mm), no order other than the zero order will be present ($2m - \sin\alpha = \sin\beta$). Note that for spacings between 200 and 400 nm diffraction will occur, but at very high angles of incidence. These structures are known as zero-order diffraction gratings (ZODs).⁸³ Although ZODs do not present any diffraction, they do present a surprising in-plane color variation (rotation-induced color shift) if viewed parallel or perpendicular to the grooves, typically from red to green.⁸⁴ For obvious reasons, ZODs are harder to replicate since they require very high embossing precision.⁵²

17.3.4 Other color shifting technologies

There are other technologies displaying color shifting properties. This is the case of coextruded polymer films first developed by Dow Chemical in the late 1960s.⁸⁵ Essentially used for decorative and packaging purposes, due to a fairly low color uniformity, the technology has matured, and coextruded polymer films have now made their way into the optical security field. Indeed, 3M has recently proposed filters based on PET and acrylic polymer layers (coPMMA) as well as polyethylene naphtalate (PEN) and coPEN. The low index contrast (1.67 vs. 1.50 in the case of PET and PMMA, respectively) requires a very high number of layers. For example, an orange to yellow color shifting film consisting of 275 layers of PEN and coPEN has been demonstrated with a total thickness of 33 µm. Interestingly, due to the stretching which occurs during extrusion, both the PET and PEN layers display birefringence. This birefringence allows for the creation of interesting polarization effects (in-plane rotation-dependent color shifts when viewed under polarized light parallel or perpendicular to the stretch direction).⁸⁵

There are obviously other technologies which display angle-dependent color variations, which for reasons of conciseness, have not been covered in the present chapter; these include liquid crystals,^{86–88} Lippmann photography, volume-reflection holography, and even nanocrystalline cellulose.⁸⁹ For those interested, a detailed coverage of these technologies in the context of security is given in the book by van Renesse.⁵²

17.4 Active devices

Lately, it has become clear that an ongoing trend in security is the integration of active features in future anticounterfeiting devices.⁹⁰ For example, De La Rue, in one of their 2010 patents⁹¹ clearly mentions that inks may contain ‘functional components that react to an external stimulus’ such as ‘fluorescent, phosphorescent, infrared absorbing, thermochromic, photochromic, magnetic, electrochromic, conductive and piezochromic’ materials. In this section we will describe structures which not only present an active optical change, but which also endeavor to preserve the passive optical change of ISIs.

17.4.1 Application of active materials

In the context of active materials, one particular example is a Fabry-Perot-like structure incorporating a luminescent material which offers an overt color shift as well as a covert feature, in this case the emission of light under the influence of an external stimulus (ultraviolet, visible or infrared radiation,

electric⁹² or magnetic fields, chemicals or even pressure).⁹³ Incorporating the luminescent material inside an interference filter also renders the light emission angle-dependent; this feature can thus provide an added level of security.^{94,95} Others have replaced the dielectric spacer (see Section 17.2.2) by a piezoelectric material which, under the application of fairly high voltages (100–1000 V), sees its thickness change, and as a result, changes the color of the device.⁹⁶ Such high voltages would obviously require extreme caution when authenticating the device and could potentially limit their applicability.

Recently, photonic crystals have been proposed as possible innovative structures for optical security devices.⁹⁷ By using colloidal self-assembly, low-cost 3D photonic crystals were fabricated. In this particular case, self-organized monodisperse silica microspheres were deposited onto a periodic lattice. The space in between the spheres was then filled with a desired material. The spheres were then dissolved resulting in what is typically called an inverse opal structure displaying an angle-dependent color variation. If the matrix material is elastomeric, devices which show a color change under an applied pressure are possible. This change in color due to compression results from a decrease in the distance between the spherical cavities and hence a lower total optical thickness. A similar effect has been demonstrated in Fabry-Perot-like structures using a pressure-deformable spacer layer.⁹⁸ However, acceptance of the pressure sensitive devices may be surpassed by their thermochromic counterparts that can mimic their characteristics since a finger not only applies pressure but also heat.

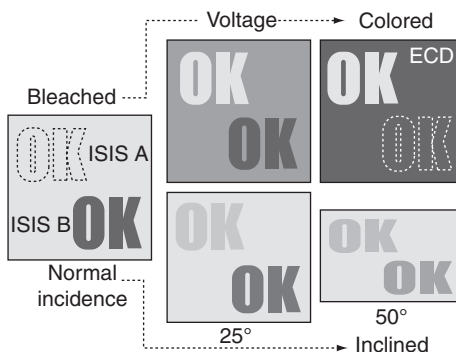
In addition to pressure actuated systems, using an electrically active matrix can result in a structure whose color changes by applying an electric field.⁹⁹ Similarly, an electrochromic WO_3 based inverted opal structure has been proposed as a tunable photonic band gap.¹⁰⁰ Such a structure possessing iridescence as well as a change in color following the application of voltage (to allow ion intercalation) could be of interest for security as a two level authentication device.

17.4.2 Electrochromic devices

The rapid evolution of printed electronics has also led to various proposed optical security devices where the features are optically variable when a voltage is applied. Here too, electrochromic materials are very often the materials of choice due to the low potential required to switch them, as well as their memory effect (colored state is maintained once voltage is removed). For example, Hewlett-Packard has recently suggested an electrochromic device for security tags.¹⁰¹ Another example based on electrochromics has been suggested for security documents such as passports and smart cards.¹⁰² In this particular case, the electronic components of the passport (radio

frequency identification (RFID) technology) can also be used to power the feature via a radio frequency (RF) signal. Based on a five to seven layer structure the total thickness is approximately 30 µm. Such a high thickness may limit their use for banknotes (a pile of 1000 banknotes would result in 3 cm of added thickness). This technology is based on an electrochromic viologen containing TiO₂ matrix apposed onto a white reflector (reflection based device).¹⁰³ Others have also suggested the use of electrochromic paper as a potential candidate for vouchers, tokens and banknotes.¹⁰⁴ Although all of these examples offer an innovative means of authentication, they are mostly aimed as a second level authentication feature for experienced personnel and not for the general public.

To combine both the voltage-driven color shift of an electrochromic device (ECD) and the angle-dependent color shift of an ISIS, Baloukas *et al.* have demonstrated a device linking both of these effects through metamericism.^{59,105} More precisely, an all-dielectric metameristic filter was designed and fabricated which matched an intermediate colored state of the ECD. Figure 17.11 presents a schematic which outlines the basic concept of this system. One can see that at normal incidence, ISIS B is visible, but upon application of a voltage, it disappears following the dark and opaque blue coloration of the ECD (disappearing image effect). The authors mention that a metameristic filter could also be designed with the bleached state (ISIS A in Fig. 17.11). On the other hand, long term cycling of the ECD may affect the bleached state transmission and thus the color match; an intermediate colored state would not suffer from this issue. Although the pre-



17.11 Active metameristic interference security image structure based on the combination of ISISs and an ECD. ISIS A matches the bleached state transmission of the ECD, while ISIS B matches an intermediate colored state. Such a device possesses two levels of authentication: an angular color shift and a voltage-driven color shift.

sent concept is based on the use of an ECD, any other active technology could be used.

In an attempt to lower fabrication costs, the same authors have also shown that it is possible to combine both of the previously presented effects into a single structure. This was made possible by fabricating single-material electrochromic interference filters based on porous and dense WO_3 films (low and high index of refraction, respectively).¹⁰⁶ In order to increase the index contrast, $\text{SiO}_2\text{-WO}_3$ composite films have also been used to replace the porous WO_3 .^{107,108} The resulting filters possessed an angular color shift as well as demonstrating electrochromic properties. However, there are still some issues to solve: for example, the creation of multiple interfaces impacts the coloration and bleaching dynamics of the filters. One proposed solution is to use simpler structures such the one based on a Deb-type ECD which typically presents the following architecture:¹⁰⁸

Substrate|Electrode (Al, Au, ITO, etc.)| WO_3 |Electrolyte (SiO_2 , MgF_2 , etc.)|Electrode (Au, ITO, etc.).

Both electrodes are obviously required to apply the potential and activate the device. The bottom electrode will supply electrons to the WO_3 layer during coloration, while the electrolyte will supply neutralizing hydrogen ions (from electrolysis of the absorbed ambient water). By inverting the potential the electrons and ions are extracted and the device is bleached. One will notice that with the exception of the additional WO_3 film, this structure is very similar to OVI and therefore interesting from the fabrication point of view. Initial tests have indicated that such structures display an angular color shift in reflection, when using an aluminium mirror bottom electrode, as well as a voltage-driven color shift. While this solution works well in reflection, more layers are required when replacing the aluminium with ITO, in order to obtain an interesting color shift in transmission. Although more work is required to demonstrate the feasibility of such devices, if achieved, they will possess two levels of authentication.

17.5 Film functionality and structurally controlled optical coatings

Besides the basic optical function of an ISIS, other characteristics are also required in order for a device to be commercially viable.^{20,31} First and foremost, the system must offer good protection against counterfeiters (hard to duplicate, simulate, and originate). To increase the efficiency of use, the color shift must be easy to detect. This implies choosing the right color shift and a minimum device size to view it adequately ($\sim 1 \text{ cm}^2$). For example,

choosing a red to green color shift might not be ideal considering that most colorblind individuals (between seven to ten per cent of the male population) have difficulty distinguishing red from green. The color of the filter must also be stable as a function of time when exposed to the everyday wear and tear of the protected product, but must also be stable from one production series to another to ensure color consistency (thickness control during deposition). Calculating the effect of deposition errors on the color of a filter is possible and color tolerances can be defined;⁵⁶ however, the best method to tackle this issue is always to proceed with real-life testing. For obvious reasons, the materials used must also meet environmental, safety and health regulations. In the particular case of banknotes, all OVDs must resist very stringent durability tests such as crumpling, abrasion, laundering in washing machines, immersion in chemical solvents, etc., so as not to shorten the lifetime of the banknote.^{18,19} Finally, generally speaking, the fabrication costs must be kept low, although some higher-end products, such as passports, may allow for more expenditure.

We have seen above that nanostructured optical coatings have made their headway to the field of optical security devices. One particular category is nanoporous materials whose application also illustrates progress and added coating functionalities in related fields, specifically in optical gas sensors.¹⁰⁹ Such sensors are of particular interest since the use of light to probe the analytes and to carry the information offers numerous advantages, in particular (i) the ability to operate in conductive or spark-sensitive environments at no contact with the probed medium; (ii) the immunity to electromagnetic interference, cosmic rays or radioactivity and (iii) the possibility to combine the sensors with optical fibers in order to create a sensor network and/or minimize invasion.

Porous films benefit from large surface areas in small volumes, hence considerably increasing the sensitivity of the devices. Several technologies for forming optical sensors based on multilayer interference filters have been considered:

- Formation of porous silicon by electrochemical etching.^{110,111} In general, this process is difficult to control and monitor and the chemical instability of porous silicon over time as well as its strong absorption in the visible spectrum are all important factors that restrict its use in high-quality optical filters.
- Optical films prepared by glancing-angle deposition (GLAD), for example those based on porous TiO₂ rugate filters.^{112,113} This deposition technique depends on the complex rotation of the substrate relative to the vapor flux, an approach that may render scale-up rather complicated.

- Control of the porosity by adjusting the energy of the bombarding ions during the film growth as stipulated by the structure zone model.¹¹⁴ Recently, Vernhes *et al.* have designed and fabricated an all-optical gas sensor based on multilayer porous/dense Si₃N₄ Fabry-Perot stacks^{115–117} using plasma enhanced chemical vapor deposition.^{118,119} The effective refractive index variations caused by the gas (analyte) sorption inside the porous Si₃N₄ material give rise to a shift of the transmission spectrum of the optical filter, which can be easily measured by using a laser diode and a photo detector. In fact, it was this approach which inspired the development of the porous/dense WO₃ and WO₃/SiO₂ ISIS devices described in Section 17.4.2.¹⁰⁶

17.6 Conclusion

This chapter has covered the main concepts and trends in optical coating security devices and cited examples of recent innovations in this field. In addition, interested readers can learn further details in the excellent work by J.A. Dobrowolski,³⁵ the inventor of the first ISIS, as well as in a complementary work by R.L. van Renesse.⁵² For the latest developments, the biennial conference on Optical Document Security is highly recommended.

Although interference-based optical security devices have now been in circulation for more than 25 years, they are still going strong. We have seen through this chapter that in order to achieve such a long-term performance, these features have constantly been refined and additional levels of complexity have been added, mainly through the use of metamerism, magnetic materials, hybrid interference/diffractive elements, etc. It is also important to note, that polymer banknotes as well as recent hybrid paper/polymer banknotes allow for the presence of windows which, therefore, open-up an abundance of possibilities when it comes to transmission-based security features. Clearly, passive ISISs will play an important role in this context.

In an attempt to go even further, we have also shown that passive ISISs have been combined with active materials which can react to various energy sources such as heat, pressure, current, light, etc. Many of the designers of such features have gone to great lengths to incorporate these materials inside classic interference structures in order to preserve their well known angle-dependent color shift. Thus, these devices offer two levels of authentication making them even harder to counterfeit. Some examples presented are already in use, while others still require further research and development. Nevertheless, these devices will provide original means of authentication which hopefully will capture public attention by their innovation and result in stronger and more efficient anti-counterfeiting features.

Finally, we have seen throughout this chapter that much of the progress has been achieved by implementing new and novel, frequently nanostructured and active materials and thin film structures. Although this has had a significant impact on the advancement of security devices themselves, it is important to note that similar advancements can also be noted in optical sensors, architectural and automobile glazing, and other areas of optical coating technology.

17.7 References

1. ‘Danger in the repair shop’, 2007, [Online]. Available at: <http://www.businessweek.com/stories/2007-07-29/danger-in-the-repair-shop> [Consulted on 10/09/2012].
2. *Estimating the global economic and social impacts of counterfeiting and piracy, A REPORT COMMISSIONED BY BASCAP*. Business Action to Stop Counterfeiting and Piracy, 2011.
3. ‘Counterfeit Medicines: Some Frequently Asked Questions?’ *World Health Organization*, [Online]. Available at: http://www.wpro.who.int/mediacentre/factsheets/fs_20050506/en/index.html [Consulted on 10/09/2012].
4. R.L. van Renesse, *Protection of High Security Documents*. Renesse Consulting, 2006.
5. S.E. Church, ‘The technology and practice of currency printing’, in *38th Annual Technical Conference of the Society of Vacuum Coaters*, Chicago, Illinois, USA. Society of Vacuum Coaters, 2001, pp. 425–430.
6. L.A. DiNunzio and S.E. Church, ‘Evaluating public awareness of new currency design features’, in *Optical Security and Counterfeit Deterrence Techniques IV*, San Jose, California, USA, vol. **4677**. SPIE, 2002, pp. 1–14.
7. H.A.M. de Heij, ‘A method for measuring the public’s appreciation and knowledge of banknotes’, in *Optical Security and Counterfeit Deterrence Techniques IV*, San Jose, California, USA, vol. **4677**. SPIE, 2002, pp. 15–55.
8. L. Setlakwe and L.A. DiNunzio, ‘Comparative analysis of public opinion research in the U.S. and Canada’, in *Optical Security and Counterfeit Deterrence Techniques V*, vol. **5310**. SPIE, 2004, pp. 13–24.
9. J.A. Dobrowolski, K.M. Baird, P.D. Carman and A. Waldorf, ‘Optical interference coatings for inhibiting of counterfeiting’, *Optica Acta*, vol. **20**, no. 12, pp. 925–937, 1973.
10. K.M. Baird, J.A. Dobrowolski, A.J. Waldorf and P.D. Carman, ‘Optical interference authenticating means’, U.S. Patent, no. US 3 858 977, 1975.
11. M. Davies and J.A. Dobrowolski, ‘Authenticating system’, U.S. Patent, no. US 5 568 251, 1996.
12. P.G. Coombs, S.F. McCaffery and T. Markantes, ‘Advanced verification methods for OVI® security ink’, in *Optical Security and Counterfeit Deterrence Techniques VI*, San Jose, California, USA, vol. **6075**. SPIE, 2006, pp. I1–I8.
13. R.M. Klein, S. Gadbois and J.J. Christie, ‘Perception and detection of counterfeit currency in Canada: Note quality, training and security features’, in *Optical Security and Counterfeit Deterrence Techniques V*, San Jose, California, USA, vol. **5310**. SPIE, 2004, pp. 1–12.

14. H.H. Weinert, 'New developments for the continuous high rate production of physical vapor deposition (PVD) flake pigments without the use of consumable substrates', in *49th Annual Technical Conference of the Society of Vacuum Coaters*, San Francisco, California, USA, Society of Vacuum Coaters, 2006, pp. 642–647.
15. C.-A. Despland, M. Schmid and P. Degott, 'Creation of novel security features using optically variable magnetic inks', in *Optical Document Security I*, San Francisco, California, USA, R.L. van Renesse, Ed., Reconnaissance International, 2008, pp. 1–10.
16. G. Pfaff, 'Optical coatings for special effect pigments', in *47th Annual Technical Conference of the Society of Vacuum Coaters*, Dallas, Texas, USA, Society of Vacuum Coaters, 2004, pp. 79–85.
17. J.A. Dobrowolski, F.C. Ho and A. Waldorf, 'Research on thin film anticounterfeiting coatings at the National Research Council of Canada', *Applied Optics*, vol. **28**, no. 14, pp. 2702–2717, 1989.
18. E. Çetinörgü-Goldenberg, B. Baloukas, O. Zabeida, J. Klemburg-Sapieha and L. Martinu, 'Optical and tribomechanical stability of optically variable interference security devices prepared by dual ion beam sputtering', *Applied Optics*, vol. **50**, no. 19, pp. 3351–3359, 2011.
19. J. Rolfe, 'Optically variable devices for use on bank notes', in *Optical Security and Anticounterfeiting Systems*, Los Angeles, California, USA, vol. **1210**. SPIE, 1990, pp. 14–19.
20. I. Glick, D.F. Grigg and R.L. Wilkinson, 'Manufacturing of optical security devices by sputtering techniques', in *37th Annual Technical Conference of the Society of Vacuum Coaters*, Boston, Massachusetts, USA, Society of Vacuum Coaters, 1994, pp. 85–96.
21. P. Smits, A.M. Rosenfeld and H.F. DeFerrari, 'Tamper-evident structures', U.S. Patent, no. US 4 837 061, 1989.
22. C.A. Bishop, 'The use of vacuum deposited coatings for security applications', in *44th Annual Technical Conference of the Society of Vacuum Coaters*, Philadelphia, Pennsylvania, USA, Society of Vacuum Coaters, 2001, pp. 425–430.
23. R.W. Phillips, V.C. Spellman, W.L. Gossett and M.A. Kamerling, 'Tamper evident optically variable device and article utilizing the same', U.S. Patent, no. US 4 721 217, 1988.
24. E.D. Palik, *Handbook of Optical Constants of Solids*. Academic Press Inc., 1985.
25. R.W. Phillips, 'Color effects from thin film designs', in *8th International Conference on Vacuum Web Coating*, Las Vegas, Nevada, USA, 1994, pp. 270–284.
26. R.W. Phillips, 'Optically variable films, pigments and inks', in *Optical Thin Films III: New Developments*, San Diego, California, USA, vol. **1323**. SPIE, 1990, pp. 98–109.
27. I.M. Lancaster and A. Mitchell, 'The growth of optically variable features on banknotes', in *Optical Security and Counterfeit Deterrence Techniques V*, San Jose, California, USA, vol. **5310**. SPIE, 2004, pp. 34–45.
28. P.H. Berning and R.W. Phillips, 'Thin film optically variable article and method having gold to green color shift for currency authentication', U.S. Patent, no. US 4 705 300, 1987.

29. R.W. Phillips and P.G. Coombs, 'Transparent optically variable device', U.S. Patent, no. US 5 278 590, 1994.
30. B. Baloukas, S. Larouche and L. Martinu, 'Playing with light – The quest for new optically variable devices', in *48th Annual Technical Conference of the Society of Vacuum Coaters*, Denver, Colorado, USA, Society of Vacuum Coaters, 2005, pp. 381–386.
31. R.W. Phillips and A.F. Bleikolm, 'Optical coatings for document security', *Applied Optics*, vol. **35**, no. 28, pp. 5529–5534, 1996.
32. H.G. Lotz and G. Steiniger, 'Production of color shift layers with electron beam technology for identification and decorative applications', in *50th Annual Technical Conference of the Society of Vacuum Coaters*, Louisville, Kentucky, USA, Society of Vacuum Coaters, 2007, pp. 742–744.
33. M. Nofi and J. Matteucci, 'On-line evaluation of web coatings for color applications', in *41st Annual Technical Conference of the Society of Vacuum Coaters*, Boston, Massachusetts, USA, Society of Vacuum Coaters, 1998, pp. 392–396.
34. J. Rolfe, 'Vacuum coatings for document security', in *34th Annual Technical Conference of the Society of Vacuum Coaters*, Washington, D.C., USA, Society of Vacuum Coaters, 1991, pp. 20–25.
35. J.A. Dobrowolski, *Optical Thin-Film Security Devices*, 2nd ed., Artech House, 1998, ch. 13, pp. 289–328.
36. J. Haglmüller, Y. Alguer, Ch. Mayer, V. Matyushin, G. Bauer, F. Pittner, A. Leitner, F. Ausseneck and T. Schalkhammer, 'Cluster optical coding – from biochips to counterfeit security', in *Photon Processing in Microelectronics and Photonics III*, vol. **5339**. SPIE, 2004, pp. 652–663.
37. M. Bergsmann, F. Kastner, G. Bauer, R. Domnick and H. Walter, 'Novel security feature made by thin film coating technique', in *46th Annual Technical Conference of the Society of Vacuum Coaters*, San Francisco, California, USA, Society of Vacuum Coaters, 2003, pp. 566–569.
38. G. Bauer, J. Hassmann, H. Walter, J. Haglmüller, C. Mayer and T. Schalkhammer, 'Resonant nanocluster technology – from optical coding and high quality security features to biochips', *Nanotechnology*, vol. **14**, no. 12, pp. 1289–1311, 2003.
39. M. Stalder and F. Seils, 'Novel optically variable color devices', in *Optical Security and Counterfeit Deterrence Techniques VI*, San Jose, California, USA, vol. **6075**. SPIE, 2006, pp. U1–U10.
40. J.A. Dobrowolski and A.J. Waldorf, 'Method of manufacturing an optical interference authenticating device', U.S. Patent, no. US 4 626 445, 1986.
41. V.P. Raksha, C.J. Delst, P.G. Coombs, C.T. Markantes and A. Argoitia, 'Patterning of a spacer layer in an interference filter', U.S. Patent, no. US 20100 239 753, 2010.
42. R.W. Phillips and R. Bie, 'Covert security coating', U.S. Patent, no. US 7 630 109, 2009.
43. R.W. Phillips, T. Mayer and G.S. Ash, 'Optically variable thin film flake and collection of the same', U.S. Patent, no. US 5 135 812, 1992.
44. R.W. Phillips, T. Mayer and G.S. Ash, 'Ink incorporating optically variable thin film flakes', U.S. Patent, no. US 5 059 245, 1991.
45. R.W. Phillips, T. Mayer and G.S. Ash, 'Optically variable printing inks', U.S. Patent, no. US 5 279 657, 1994.
46. R.W. Phillips, T. Mayer and G.S. Ash, 'Method of making optical thin flakes and inks incorporating the same', U.S. Patent, no. US 5 383 995, 1995.

47. R.W. Phillips, R. Slusser and B. Holton, 'Angle dependent metamerism in multi-layer thin films', in *Proceedings of the 9th International Conference on Vacuum Web Coating*, 1995, pp. 127–138.
48. R.W. Phillips and A. Argoitia, 'Using vacuum roll coaters to produce anti-counterfeiting devices', in *48th Annual Technical Conference of the Society of Vacuum Coaters*, Louisville, Kentucky, USA, Society of Vacuum Coaters, 2005, pp. 145–152.
49. M. Schmid, 'Optical security in ink: an industry standard that continues to evolve', in *Optical Security and Counterfeit Deterrence Techniques VI*, San Jose, California, USA, vol. **6075**. SPIE, 2006, pp. N1–N6.
50. A. Argoitia and K.-J. Delst, 'Micro structured taggants in security pigments and inks', in *Optical Document Security I*, R.L. van Renesse, Ed., Reconnaissance International, 2008, pp. 1–16.
51. R.W. Phillips and M. Nofi, 'Colors by chemistry or by physics?' in *42nd Annual Technical Conference of the Society of Vacuum Coaters*, Chicago, Illinois, USA, Society of Vacuum Coaters, 1999, pp. 494–499.
52. R.L. van Renesse, *Optical Document Security*, 3rd ed., Artech House, 2005.
53. S. Larouche and L. Martinu, 'OpenFilters: open-source software for the design, optimization, and synthesis of optical filters', *Applied Optics*, vol. **47**, no. 13, pp. C219–C230, 2008.
54. R.W. Phillips, C.T. Markantes, S.P. Fisher, R.G. Slusser, P.K. Higgins and A.F. Bleikolm, 'Paired optically variable article with paired optical structures and ink, paint and foil incorporating the same and method', U.S. Patent, no. US 6 114 018, 2000.
55. P.G. Coombs and R.W. Phillips, 'Optically variable interference device with peak suppression and method', U.S. Patent, no. US 5 214 530, 1993.
56. B. Baloukas and L. Martinu, 'Metameric interference security image structures', *Applied Optics*, vol. **47**, no. 10, pp. 1585–1593, 2008.
57. B. Baloukas, S. Larouche and L. Martinu, 'Use of metameric filters for future interference security image structures', in *Optical Security and Counterfeit Deterrence Techniques VI*, San Jose, California, USA, vol. **6075**. SPIE, 2006, pp. T1–T9.
58. B. Baloukas and L. Martinu, 'Interference security image structure', U.S. Patent no. US 8 064 632, 2011.
59. B. Baloukas, J.-M. Lamarre and L. Martinu, 'Active metameric security devices using an electrochromic material', *Applied Optics*, vol. **50**, no. 9, pp. C41–C49, 2011.
60. B. Baloukas and L. Martinu, 'Advances in metameric security image structures', in *Optical Document Security I*, San Francisco, California, USA, Reconnaissance International, 2008.
61. T. Jagielinski and F. Chamberlain, 'Magnetic imaging of currencies and secure documents', in *Optical Security and Counterfeit Deterrence Techniques IV*, San Jose, California, USA, vol. **4677**. SPIE, 2002, pp. 159–168.
62. H. Lienvens, 'Soft magnetic films for security devices', in *38th Annual Technical Conference of the Society of Vacuum Coaters*, Chicago, Illinois, USA, Society of Vacuum Coaters, 1995, pp. 147–151.
63. P.G. Coombs, V.P. Raksha and T. Markantes, 'Overt and covert verification via magnetic optical security devices', in *Optical Security and Counterfeit Deterrence Techniques IV*, San Jose, California, USA, vol. **4677**. SPIE, 2002, pp. 182–193.

64. P.G. Coombs, A. Argoitia, V.P. Raksha and R.W. Phillips, 'Integration of contrasting technologies into advanced optical security devices', in *Optical Security and Counterfeit Deterrence Techniques V*, San Jose, California, USA, vol. **5310**. SPIE, 2004, pp. 299–311.
65. V.P. Raksha, C.T. Markantes, P.G. Coombs, R.W. Phillips, M. Nofi and K.-J. Delst, 'Printable appearance-changing graphical security devices', in *Optical Document Security I*, San Francisco, California, USA, R.L. van Renesse, Ed., Reconnaissance International, 2008, pp. 1–15.
66. C.-A. Despland, M. Schmid and P. Degott, 'Creation of novel security features using optically variable magnetic inks', in *Optical Document Security I*, San Francisco, California, USA, R.L. van Renesse, Ed., Reconnaissance International, 2008, pp. 1–10.
67. V.P. Raksha, C.J. Delst, P.G. Coombs, C.T. Markantes and A. Argoitia, 'Printed magnetic ink overt security image', U.S. Patent, no. US 8 025 952, 2011.
68. V.P. Raksha, J.M. Holman, P.G. Coombs, C.T. Markantes and R.W. Phillips, 'Apparatus for orienting magnetic flakes', U.S. Patent, no. US 7 934 451, 2011.
69. S.P. McGrew, 'Hologram counterfeiting: Problems and solutions', in *Optical Security and Anticounterfeiting Systems*, Los Angeles, California, USA, vol. **1210**. SPIE, 1990, pp. 66–76.
70. A. Argoitia and M. Whitzman, 'Pigments exhibiting diffractive effects', in *45th Annual Technical Conference of the Society of Vacuum Coaters*, Lake Buena Vista, Florida, USA, Society of Vacuum Coaters, 2002, pp. 539–545.
71. W.R. Tompkin, A. Schilling and R. Staub, 'Color-shifting features for optically variable devices', in *Optical Security and Counterfeit Deterrence Techniques VI*, San Jose, California, USA, vol. **5310**. SPIE, 2004, pp. 244–255.
72. A. Argoitia and S. Chu, 'The concept of printable holograms through the alignment of diffractive pigments', in *Optical Security and Counterfeit Deterrence Techniques IV*, San Jose, California, USA, vol. **5310**. SPIE, 2004, pp. 275–288.
73. A. Argoitia and S. Chu, 'The concept of printable holograms through the alignment of diffractive pigments', in *47th Annual Technical Conference of the Society of Vacuum Coaters*, Dallas, Texas, USA, Society of Vacuum Coaters, 2004, p. 677.
74. J. Orava, N. Heikkila, T. Jaaskelainen and J. Parkkinen, 'Diffractive parameric colors', *Journal of the Optical Society of America A*, vol. **25**, no. 12, pp. 2901–2907, 2008.
75. A. Argoitia, D. Chu and N. Teitelbaum, 'Security device with metameric features using diffractive pigment flakes', U.S. Patent, no. US 7 729 026, 2010.
76. R.W. Phillips, 'Graphic images in optical thin film stacks', in *44th Annual Technical Conference of the Society of Vacuum Coaters*, Philadelphia, Pennsylvania, USA. Society of Vacuum Coaters, 2001, pp. 93–98.
77. W.C. Kittler Jr., V.P. Raksha, R.W. Phillips and G. Zambory, 'Patterned optical structures with enhanced security feature', U.S. Patent, no. US 7 880 943, 2010.
78. A. Argoitia and R.W. Phillips, 'The security enhancement of diffractive optically variable image devices', in *Optical Security and Counterfeit Deterrence Techniques VI*, San Jose, California, USA, vol. **6075**. SPIE, 2006, pp. P1–P18.
79. A. Argoitia, V.P. Raksha and P.T. Kohlmann, 'All-dielectric optical diffractive pigments', U.S. Patent, no. US 6 815 065, 2004.
80. N.A.G. Ahmed and M. Whitnall, 'Semi-transparent optical coating for security holograms', in *44th Annual Technical Conference of the Society of Vacuum*

- Coaters*, Philadelphia, Pennsylvania, USA. Society of Vacuum Coaters, 2001, pp. 444–447.
81. R.W. Phillips and R. Bonkowski, ‘Security enhancement of holograms with interference coatings’, in *Optical Security and Counterfeit Deterrence Techniques III*, San Jose, California, USA, vol. **3973**. SPIE, 2000, pp. 304–315.
 82. R. Bonkowski, P.K. Higgins, C.T. Markantes and R.W. Phillips, ‘Methods for forming security articles having diffractive surfaces and color shifting backgrounds’, U.S. Patent, no. US 7 754 112, 2010.
 83. W.R. Tompkin, A. Schilling and C. Weiteneder, ‘Zero-order gratings for optically variable devices’, in *Optical Security and Counterfeit Deterrence Techniques IV*, San Jose, California, USA, vol. **4677**. SPIE, 2002, pp. 227–237.
 84. Y. Chen and W. Liu, ‘Short period resonant dual-grating structures for applications to anisotropic color change securities’, *Optical Engineering*, vol. **50**, no. 4, p. 048001, 2011.
 85. J.M. Jonza and A.D. Dubner, ‘Multilayer polymeric color-shifting polarizer films’, in *Optical Security and Counterfeit Deterrence Techniques IV*, San Jose, California, USA, vol. **5310**. SPIE, 2004, pp. 256–263.
 86. F. Moia, ‘New coloured security elements using Rolic’s LPP/LCP technology: devices for 1st to 3rd level inspection’, in *Optical Security and Counterfeit Deterrence Techniques IV*, San Jose, California, USA, vol. **4677**. SPIE, 2002, pp. 194–202.
 87. F. Moia, ‘New colour shifting security devices’, in *Optical Security and Counterfeit Deterrence Techniques IV*, San Jose, California, USA, vol. **5310**. SPIE, 2004, pp. 312–320.
 88. Y. Jiang, B. Wilson, A. Hochbaum and J. Carter, ‘Novel pigment approaches in optically variable security inks including polarizing cholesteric liquid crystal (clc) polymers’, in *Optical Security and Counterfeit Deterrence Techniques IV*, San Jose, California, USA, vol. **4677**. SPIE, 2002, pp. 247–254.
 89. Y.P. Zhang, V.P. Chodavarapu, A.G. Kirk and M.P. Andrews, ‘Nanocrystalline cellulose for covert optical encryption’, in *Organic Photonic Materials and Devices XIV*, vol. **8258**. SPIE, 2012, pp. 825 808–1.
 90. D.J. Trevor, ‘A path to the next generation of U.S. banknotes’, in *Optical Document Security I*, San Francisco, California, USA, R.L. van Renesse, Ed., Reconnaissance International, 2008, pp. 1–8.
 91. A. Jeacock and R. Whiteman, ‘Security device and method’, U.S. Patent, no. US 20100164219, 2010.
 92. J.A. Dobrowolski, B.T. Sullivan and R.C. Bajcar, ‘Optical interference electroluminescent device having low reflectance’, U.S. Patent, no. US 5 049 780, 1991.
 93. P.G. Coombs, J. Zieba, R.A. Bradley Jr., C.W. Lantman, T. Mayer, R.W. Phillips and S.A. Yamanaka, ‘Luminescent pigments and foils with color-shifting properties’, U.S. Patent, no. US 6 572 784, 2003.
 94. C.D. MacPherson, D.G. Vendette, G. Girouard and A.O. Stone, ‘Security device’, *World International Property Organization*, no. WO2010096914, 2011.
 95. O. Rozumek and E. Müller, ‘Pigments having a viewing angle dependent shift of color, method of making, use and coating composition comprising of said pigments and detecting device’, *World International Property Organization*, no. WO200160924, 2001.
 96. C.D. MacPherson, ‘Optically variable devices, their production and use’, *World International Property Organization*, no. WO2011130843, 2011.

97. A.C. Arsenault, U. Kamp, A. Cheng and G.A. Ozin, 'Interactive elastic photonic crystals', in *Optical Document Security I*, San Francisco, California, USA, R.L. van Renesse, Ed. Reconnaissance International, 2008, pp. 1–10.
98. C.D. MacPherson and B.A. Hardwick, 'Optically variable devices, their production and use', *World International Property Organization*, no. WO2011130842, 2011.
99. A.C. Arsenault, D.P. Puzzo, I. Manners and G.A. Ozin, 'Photonic-crystal full-colour displays', *Nature Photonics*, vol. **1**, pp. 468–472, 2007.
100. S.-L. Kuai, G. Bader and P.V. Ashrit, 'Tunable electrochromic photonic crystals', *Applied Physics Letter*, vol. **86**, p. 221110, 2005.
101. D.A. Champion and C.S. Betrabet, 'Security device', U.S. Patent, no. US 7 599 109, 2009.
102. 'Nanochromics printed security solutions', *Advancing Microelectronics*, vol. **38**, pp. 14–20, 2011.
103. D. Corr, U. Bach, D. Fay, M. Kinsella, C. McAtamney, F. O'Reilly, S.N. Rao and N. Stobie, 'Coloured electrochromic 'paper-quality' displays based on modified mesoporous electrodes', *Solid State Ionics*, vol. **165**, pp. 315–321, 2003.
104. P.M.S. Monk, F. Delage and S.M.C. Vieira, 'Electrochromic paper: Utility of electrochromes incorporated in paper', *Electrochimica Acta*, vol. **46**, pp. 2195–2202, 2001.
105. B. Baloukas, J.-M. Lamarre and L. Martinu, 'From passive to active: Future optical security devices', in *Optical Interference Coatings*, Tucson, Arizona, USA, Optical Society of America, 2010.
106. B. Baloukas, J.-M. Lamarre and L. Martinu, 'Electrochromic interference filters fabricated from dense and porous tungsten oxide films', *Solar Energy Materials and Solar Cells*, vol. **95**, no. 9, pp. 807–815, 2011.
107. B. Baloukas and L. Martinu, 'Electrochromic interference filters based on WO_3 and composite SiO_2/WO_3 films', in *55th Annual Technical Conference of the Society of Vacuum Coaters*, Santa Clara, California, USA. Society of Vacuum Coaters, 2012.
108. B. Baloukas and L. Martinu, ' WO_3/SiO_2 composite optical films for the fabrication of electrochromic interference filters', *Applied Optics*, vol. **51**, no. 16, pp. 3346–3356, 2012.
109. J. Shi, Y. Zhu, X. Zhang, W.R.G. Baeyens and M. García-Campaña, 'Recent developments in nanomaterial optical sensors', *TrAC Trends in Analytical Chemistry*, vol. **23**, no. 5, pp. 351–360, 2004.
110. J. Volk, J. Balázs, A. L. Tóth and I. Bárszny, 'Porous silicon multilayers for sensing by tuneable IR-transmission filtering', *Sensors and Actuators B*, vol. **100**, no. 1–2, pp. 163–167, 2004.
111. A. Kovacs, P. Jonnalagadda, X.Y. Meng and U. Mescheder, 'Characterization of porous silicon based optical sensor system for biosensor applications', *Sensors, IEEE*, pp. 21–26, 2009.
112. J.J. Steele, 'Nanostructure engineering in porous columnar thin films: recent advances', *Journal of Materials Science: Materials in Electronics*, vol. **18**, no. 4, pp. 367–379, 2007.
113. D.-H. Chang, Y.J. Park and C. K. Hwangbo, 'Optical humidity sensor using a narrow band-pass filter prepared by glancing angle deposition', *Journal of Korean Physical Society*, vol. **53**, no. 5, pp. 2700–2704, 2008.

114. R. Messier, A.P. Giri and R.A. Roy, 'Revised structure zone model for thin film physical structure', *Journal of Vacuum Science & Technology A*, vol. **2**, no. 2, pp. 500–503, 1984.
115. R. Vernhes, O. Zabeida, J.E. Klemburg-Sapieha and L. Martinu, 'Single-material inhomogeneous optical filters based on microstructural gradients in plasma-deposited silicon nitride', *Applied Optics*, vol. **43**, no. 1, pp. 97–103, 2004.
116. R. Vernhes, A. Amassian, J.E. Klemburg-Sapieha and L. Martinu, 'Plasma treatment of porous SiN_x:H films for the fabrication of porous-dense multi-layer optical filters with tailored interfaces', *Journal of Applied Physics*, vol. **99**, no. 11, pp. 114315–1–12, 2006.
117. R. Vernhes, O. Zabeida, J.E. Klemburg-Sapieha and L. Martinu, 'Properties, growth, and filter applications of a-SiN_x:H alloys prepared in pulsed radiofrequency plasma', *OSA Topical Meeting on Optical Interference Filters*, Tucson, June 2007.
118. L. Martinu, J.E. Klemburg-Sapieha, O.M. Küttel, A. Raveh and M.R. Wertheimer, 'Critical ion energy and ion flux in the growth of films by plasma-enhanced chemical vapor deposition', *Journal of Vacuum Science & Technology A*, vol. **12**, no. 4, pp. 1360–1364, 1994.
119. R. Vernhes, J.E. Klemburg-Sapieha and L. Martinu, 'Fabrication and testing of nanoporous Si₃N₄ optical filters for gas sensing applications', *Sensors and Actuators B: Chemical*, vol. **185**, pp. 504–511, 2013.

Optical coatings for high-intensity femtosecond lasers

V. PERVAK, Ludwig-Maximilians-University,
Germany

DOI: 10.1533/9780857097316.4.664

Abstract: A dispersive mirror-based laser permits a dramatic simplification of high-power femto- and atto-second systems and affords promise for their further development towards shorter pulse durations, and higher peak and average powers with user-friendly systems. Design approaches, together with the existing modern deposition technology, pave the way for the manufacture of dielectric multilayer coatings capable of compressing pulses of tens of picoseconds duration down to a few femtoseconds. The result of the continuous development of dispersive optics permits pulse compression down to single cycle with pulse duration 2 fs.

Key words: dispersive optics, chirped mirrors, multilayer coating, ultrafast coating, femtosecond coating.

18.1 Introduction

The goal of generating short laser pulses down to the limit set by a single wave cycle of light has been pursued ever since the invention of lasers. Laser pulses consisting of only a small number of wave cycles allow more efficient exploitation of nonlinear optical effects¹ with implications as striking as the generation of single sub-femtosecond light pulses.² The controlled superposition of light frequencies extending over more than one octave together with carrier-envelope phase control^{3–5} pave the way for shaping the sub-cycle evolution of light fields in laser pulses.

Here, we provide an overview of dispersive multilayer optics⁶ offering high reflectivity and controlled group delay dispersion (GDD) over some 1.5 octaves spanning ultraviolet to near infrared frequencies. Nowadays, we cannot imagine ultrashort pulses being obtained without dispersive multilayer optics. A dispersive mirror (DM)⁶ is a multilayer optical interference coating with the controllable phase upon reflection, usually designed by optimizing the initial multilayer design. A DM is characterized by a certain

value of the group delay (GD) or GDD. GD is the first derivative of the phase shift with respect to the angular frequency:

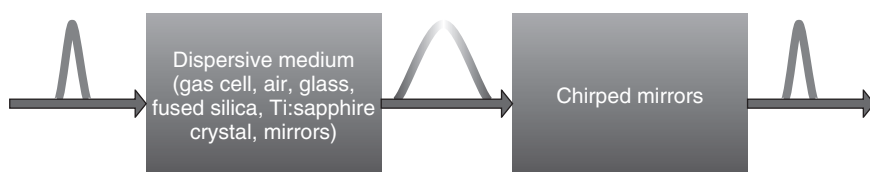
$$GD = \frac{d\varphi}{d\omega}, \quad [18.1]$$

where φ is the phase-shift obtained on reflection or transmission and ω is the angular frequency. GDD is the second derivative of the phase shift with respect to the angular frequency or is first derivative of the GD:

$$GDD = \frac{d(GD)}{d\omega} = \frac{d^2\varphi}{d\omega^2}. \quad [18.2]$$

The short pulse penetrating through dispersive medium becomes longer due to the introduced GD, as illustrated in Fig. 18.1. By introducing an inverse GD with a DM, the pulse can be compressed to its original pulse duration. In general, the GDD of the mirror should compensate the dispersion of the material (through which the initially short pulse passes) or the (nonlinear) chirp of the pulse. All mediums have dispersion of refractive index, that is, different wavelength components penetrate at different speeds. We can consider a short pulse as superposition of different frequencies matched in time. It is then obvious that the different frequencies, which penetrate through some dispersive medium, become mismatched in time and thus the pulse becomes longer. DM is supposed to match the different frequencies in time after the pulse penetrates through some dispersive medium.

The DM⁶⁻⁴⁰ is one of the key elements of most ultrafast (femtosecond) lasers. While being able to provide control of phase over unprecedented bandwidths and high efficiency, the DM technology suffers from unavoidable spectral oscillations of the phase. Reflection from the top layer of a multilayer structure introduces oscillations to the GDD curve due to interference between waves reflected from the top layer and waves which have penetrated and have been reflected from deeper layers. These oscillations may adversely affect the quality of the femtosecond laser pulses



18.1 Basic scheme of pulse compression.

which are being controlled with DMs. During design optimization the residual fluctuations usually drop down to a low level. The GDD oscillations can broaden the pulse and lead to energy transfer from the initial single pulse to satellites. The period of the ripples in the spectral domain determines the position of the satellite in the temporal domain, and the amplitude of these oscillations determines the amount of energy which is transferred to the satellites.

The manufacture of DMs can be as challenging as their design, as DMs are extremely sensitive to a discrepancy in layer thickness. In most cases, magnetron-sputtering and ion-beam sputtering technologies provide sufficient precision of the layer thickness control. Modern sputtering technology can provide sub-nm precision in controlling the layer thickness. Some applications such as highly dispersive mirrors^{28,32,40} require angstrom precision. The extreme sensitivity of the DM can then be overcome by applying a special, robust design algorithm.^{35,37}

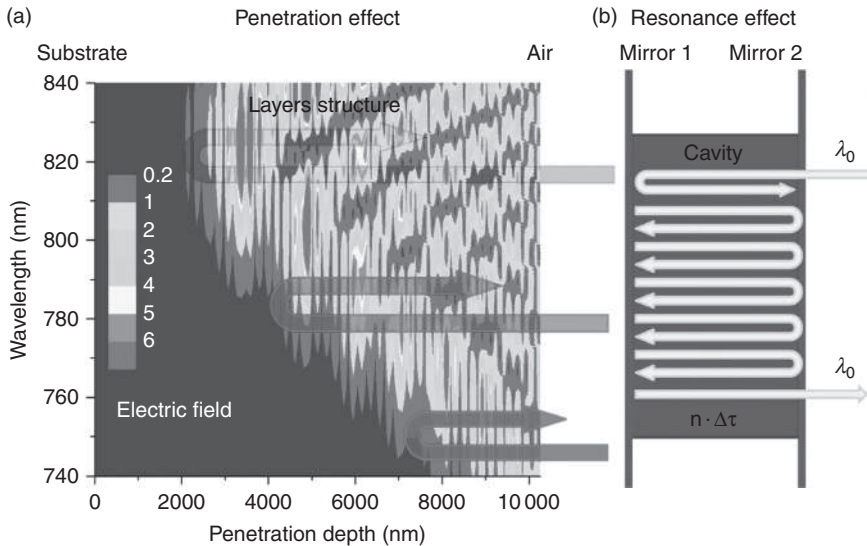
The result of the 20-year evolution of the design and fabrication of dispersive multilayers^{6–40} now allows the development of structures with low loss and high dispersion over a wide spectral range, and permits compression down to the theoretical limit of the pulse duration.

18.2 Mirror design approaches

The main problem of DM design concerns unavoidable phase oscillations which appear due to interface mismatch between the top layer of the multilayer structure and the external medium. The GDD oscillations lead to the destruction of the pulse shape. Several approaches have been devised for suppressing these undesirable oscillations: double-chirped mirrors,^{7,9} back-side-coated DMs,¹³ complementary pairs of DMs,^{8,14,17,24,25} tilted-front-interface DMs,¹⁵ ‘Brewster-angle’ DMs^{18,22} and double-angled DMs.³¹ Recently, a time-domain approach based on the direct optimization of the parameters of the compressed optical pulse was also reported.^{20,29,30}

18.2.1 Dispersive mirrors (DMs)

Chirped mirrors (CMs) rely on a multilayer structure with a gradual change in the optical thickness across the structure, resulting in a wavelength-dependent penetration depth of the incident radiation.⁶ A CM is characterized by a certain value of the GDD, see Fig. 18.2a. Alternatively, GD variation may be introduced by using resonant structures (or Gires-Tournois interferometer, GTI)^{11,12} employing a wavelength-dependent storage time of the incident radiation, see Fig. 18.2b. Both effects may co-exist in a single multilayer structure in order to improve the performance;^{28,32,40} in this case the multilayer mirrors should be called DMs.



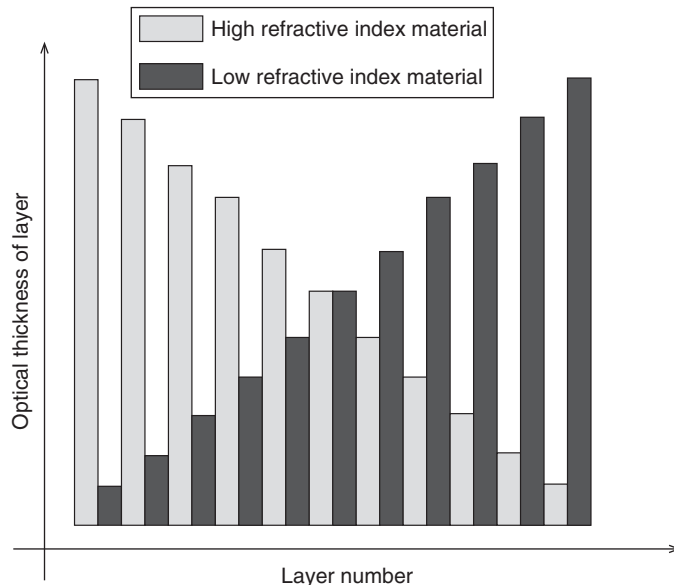
18.2 (a) Schematic explanation of the penetration effect. The optical thickness between different coating layers in the dielectric chirped mirror structure changes gradually. This causes different wavelengths to penetrate to a different extent and hence exhibit a GD. In this example, the shorter wavelengths are reflected near the surface of the multilayer mirror while the longer wavelengths penetrate deeper. (b) Schematic explanation of the resonance effect: When the optical thickness of the layers is close to half of the wavelength, they act as a cavity of a Fabry-Pérot interferometer.

Optimization software (such as Optilayer,⁴¹ TFCalc⁴² and Essential Macleod⁴³) can be used to design the DM. During design optimization, residual GDD oscillations can be reduced.

To demonstrate advantages and disadvantages for pulse compression of different design approaches of DMs which fulfill following specifications: (i) reflectance > 99.9% in bandwidth 600–1000 nm, (ii) GDD = -50 fs², the comparison of the compression performance of different approaches will be provided at the end of this section.

18.2.2 Resonant structure or Gires-Tournois interferometer mirror

Two interfaces separated by an optical distance corresponding to the half wavelength of the incident radiation resonantly enclose the impinging wave. Such nanoscale Fabry-Perot interferometers embedded in the multilayer structure can introduce large GDs at selected wavelengths, as shown in



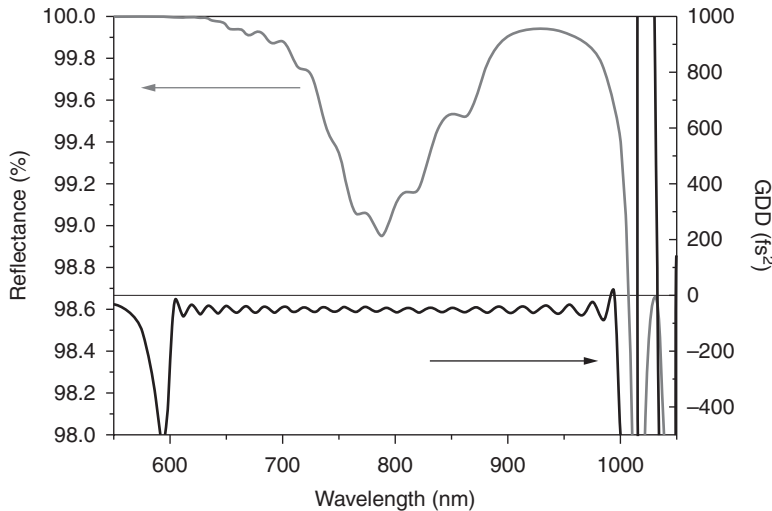
18.3 The layer structure of the double CM is depicted.

Fig. 18.2b. The GTI approach is realized by optimizing the last few layers in the symmetrical quarter-wave layer stacks that make the reflecting mirrors (or Bragg structure). A standard quarter-wave stack or Bragg structure has zero GDD at the center of its stop band with little variation over the entire high-reflectivity range. This results in a design exhibiting greater tolerance for manufacturing errors. The lower number of aperiodic layers means that this approach leads to a structure with smooth GDD that exhibits little sensitivity to deposition errors.

For a broader bandwidth, multi-GTI can be used.¹¹ The only difference between multi- and a single resonance effects is that a number of cavities are organized in a single multilayer structure. The multi-GTI mirror is characterized by a larger bandwidth and a large GDD value compared to a single GTI mirror. By using this approach, however it would be difficult to design a DM with a bandwidth of 600–1000 nm, because it will require tens of cavities. It would be hard to design and produce multilayer structures consisting of tens of cavities.

18.2.3 Double-chirped mirrors

The multilayer Bragg structure can be decomposed into a series of symmetric index steps, as is shown in Fig. 18.3. The depicted structure with an antireflection (AR) coating on the top can provide a smooth GDD characteristic



18.4 Calculated reflectivity (grey) and GDD (black) of Brewster-angle DM at angle of incidence of 55.6°.

allowing the compression of the pulse down to a duration of 6.5 fs.⁹ AR makes it possible to match an interface mismatch between the top layer and the external medium, resulting in oscillation-free GDD characteristics.

Double CM has its limitations, as does any approach. The main limitation is a relatively narrow operating bandwidth. To overcome this bandwidth limitation and to keep the GDD oscillations small, it is necessary to design broadband AR with a reflection below 0.1% over the entire bandwidth. The amount of light reflected by the AR coating mainly depends on the bandwidth and the maximal contrast of available coating materials. The number of materials is limited. The largest contrast in refractive indexes can be obtained with TiO₂ and SiO₂ (2.4 and 1.45 at 800 nm, respectively). The maximal bandwidth of AR with a reflectivity < 0.1%^{44–46} can be estimated to be ~300 nm. As a result, one individual double CM cannot be used for the full bandwidth wider than 300 nm.

18.2.4 Brewster-angle chirped mirror (CM)

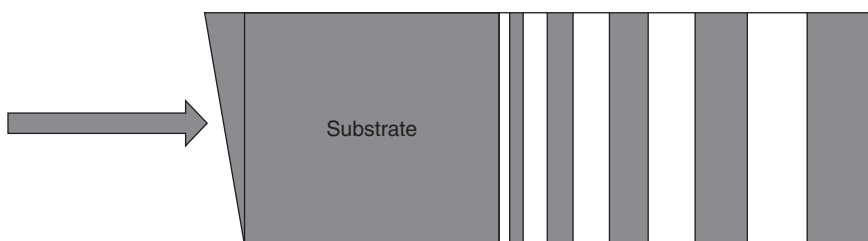
The elegant way of avoiding the cause of oscillations – due to interface mismatch – is to use p-polarized light at the Brewster angle.¹⁸ Placing a CM at the Brewster angle for the top layer ensures only a small amount of Fresnel-reflected light, resulting in oscillation-free GDD. Baum *et al.*²² report the compression of a broadband spectrum corresponding to a pulse duration of a few cycles. P-polarized light at large angles (the Brewster angle of fused

silica is $\sim 56^\circ$, for example) requires a significantly higher number of layers and greater total optical thickness. As a result, the manufacture of Brewster-angle mirrors with a reflectivity $> 99\%$ becomes a problem. In Fig. 18.4, we demonstrate a designed Brewster-angle mirror which has reflectance $> 99\%$ and $\text{GDD} = -50 \text{ fs}^2$ in bandwidth 600–1000 nm. This design consists of alternating of 135 layers of $\text{Nb}_2\text{O}_5/\text{SiO}_2$. The total physical thickness is $> 14 \mu\text{m}$. The design is characterized by smooth GDD and high sensitivity to angle of incidence. This mirror can be used in an extra-cavity application where an angle of 55.6° is easily achieved. Contrariwise, the intra-cavity beam bounces at a small incidence angle, which makes it unrealistic to use the Brewster-angle CM as a laser oscillator mirror.

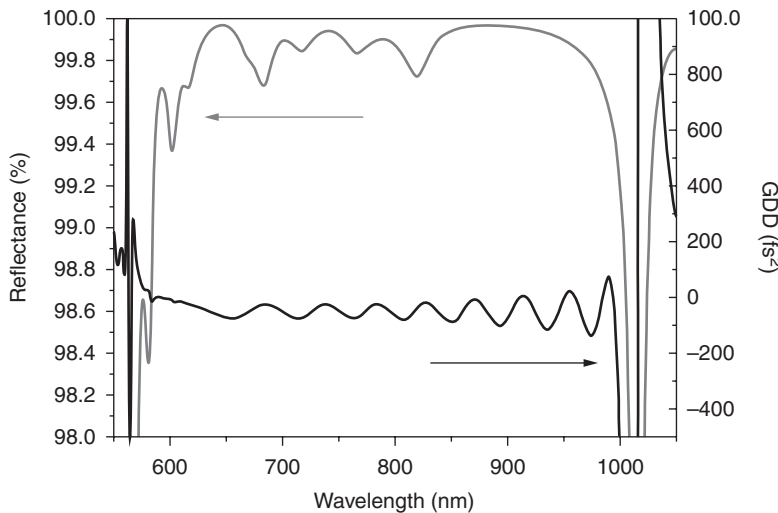
18.2.5 Back-side coated CM

In 2000, the back-side coated CM was proposed by Matuschek *et al.*¹³ The authors suggest using a one-side wedged substrate. The radiation penetrates through the wedged side of the substrate and interacts with a multi-layer structure, as shown in Fig. 18.5. The wedge spatially splits the Fresnel reflection from the top layer and the main part of the irradiation reflected from the inner layers. Such a design can be used to obtain a smooth GDD characteristic.

Unfortunately, the substrate has to be a few millimeters thick to stay flat with a relatively thick dielectric multilayer on the top. The delay caused by reflection from the multilayer structure is neglected due to the delay caused by the beam passing twice through the substrate. Again, back-side coated CM which covers 600–1000 nm, $R > 99\%$ and $\text{GDD} = -50 \text{ fs}^2$ can be designed. Reflectance and GDD is shown in Fig. 18.6. This design consists of alternating 60 layers of $\text{Nb}_2\text{O}_5/\text{SiO}_2$. Total physical thickness is $6.7 \mu\text{m}$. Back-side coated CM has relatively smooth GDD but it cannot be used for compression of a pulse due to the large path where the beam travels inside the substrate.



18.5 Sketch of the main principle of back-side-coated CM.



18.6 Calculated reflectivity (grey) and GDD (black) of back-side-coated DM at angle of incidence of 5°.

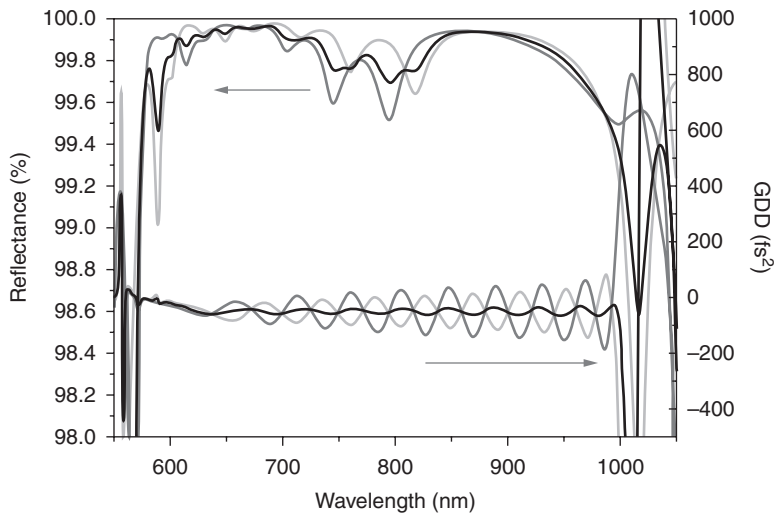
18.2.6 Tilted-front-interface CM

The back-side coated CM paved the way for the tilted-front-interface CM.¹⁵ To avoid Fresnel reflection from the top layer, we now attach the wedge on the top layer, see Fig. 18.5. The tilted-front-interface CM requires an additional AR coating on top of the wedge to minimize losses. The requirements for AR of the coating on the top of the tilted-front-interface CM are not as strict as for a double CM. The amount of Fresnel-reflected light brings only additional losses, but it has no influence on the GDD oscillation.

The weakest point in the tilted-front-interface CM is the technology for applying a wedge onto the top of the multilayer stack. As far as we know, a tilted-front-interface CM with only a small diameter (half an inch) was fabricated using the tilted-front-interface approach. Nevertheless, the tilted-front-interface approach will be developed further as soon as the technology provides a process for applying a high-quality wedge on top of the multilayer. The design performance of a tilted-front-interface CM looks identical to a back-side coated CM shown in Fig. 18.6.

18.2.7 Complementary pairs of CMs

Complementary pairs were mentioned for the first time by V. Laude⁸; later Kaertner *et al.*¹⁴ used two different mirrors for which the GDD curves have the same oscillations and are shifted by only half a period, so that



18.7 Calculated reflectivity and GDD of a pair of complementary pair of DMs. The grey curves represent one single mirror, the light grey curves the other single mirror of the pair. The black curve is the average of the grey and light grey curves per bounce.

the average GDD curve has oscillations which are as low as possible, see Fig. 18.7. For a pair of CMs covering less than one octave, such a design can be realized easily.

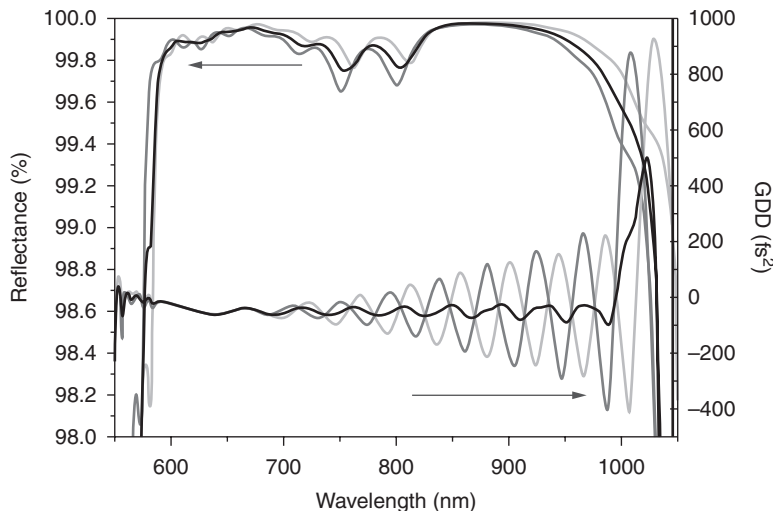
In Reference 25 the authors numerically and experimentally demonstrated a CM pair with controlled dispersion over 1.5 optical octaves. The complementary pair of such mirrors has average reflectivity >95% in a range between 400 and 1200 nm with a residual GDD oscillation <100 fs², as shown in Fig. 18.8. The mirror pair makes it possible to compensate a chirp of the corresponding spectrum (with a smooth phase), resulting in sub-3 fs pulses.

In order to design a complementary CM pair, the following merit function can be used²⁵:

$$F = \frac{1}{L} \sum_{j=1}^L \left(\frac{R_p(\lambda_j) - R^{(j)}}{\Delta R^{(j)}} \right)^2 + \left(\frac{\text{GDD}_p(\lambda_j) - \text{GDD}^{(j)}}{\Delta \text{GDD}^{(j)}} \right)^2, \quad [18.3]$$

where $R_p(\lambda_j)$ and $\text{GDD}_p(\lambda_j)$ are theoretical characteristics at wavelength λ_j , $R^{(j)}$ and $\text{GDD}^{(j)}$ are target values, $\Delta R^{(j)}$ and $\Delta \text{GDD}^{(j)}$ are corresponding tolerances and L is the number of selected wavelength points.

The currently available pulse limit of 1.5 optical cycles²⁵ can be pushed to a sub-optical cycle pulse by using broader DMs based on the complementary



18.8 Calculated reflectance and GDD of double-angle DM. Grey and light grey curves correspond to angles of incidence of 5° and 19°, respectively. Black curves show the average calculated reflectance and GDD.

approach. To reduce GDD oscillations one can use three, four and even more independent mirrors.

Here, a complementary pair of DMs which covers 600–1000 nm, $R > 99\%$ and $\text{GDD} = -50 \text{ fs}^2$ was designed. The reflectance and GDD are shown in Fig. 18.7. These designs consist of alternating of 58 layers of $\text{Nb}_2\text{O}_5/\text{SiO}_2$. The total physical thicknesses of the design pair are 5.95 and 6.1 μm , respectively.

18.2.8 The time-domain DM

A transform-limited short pulse, which can be calculated by the inverse Fourier transform of an arbitrary input spectrum, propagates in a dispersive medium or a set of dispersive materials (see Fig. 18.1). The pulse stretches in dispersive media due to the fact that the speed of light is different for different frequencies. A DM compressor can be employed to compensate this dispersion and thus compress the pulse. In femtosecond optics, the Fourier transform-limited pulse (FTLP) has the shortest possible pulse duration for a given spectrum with flat phase. Using ideal DMs for pulse compression will give us FTLP. In the conventional design approach, the ideal mirror dispersion has to be as close as possible to the dispersion of the laser elements but of the opposite sign. Usually DM has unavoidable GDD oscillations, which are the reason why the pulse becomes longer, and cannot be compressed to

its FTL. In the new time-domain design approach the algorithm needs structures which allow the best possible comparability of the pulse after passage through the dispersive medium and the DMs.

In publications^{20,29,30} the authors report the results of the realization, application and comparison of the two design approaches for sub-5 fs pulse compression. By changing the optimization parameters,²⁹ the pulse duration can be traded off against the energy concentration. The time-domain approach allows us to control the pulse duration directly. There are two experimental requirements: (i) optimize the design so that the shortest pulse is generated and (ii) optimize the design so that the maximum energy is concentrated in the main pulse (in this case the pulse duration can be 10% longer). The time-domain approach has greater flexibility in controlling the pulse duration, and the pulse energy concentration, compared to conventional approaches which use phase, GD, or GDD as target for optimization.

18.2.9 Double-angle DM

In their publication²⁴ the authors suggest a novel concept for suppressing GDD oscillations. It is based on identical DMs used at two different angles of incidence in combination (Fig. 18.8). The ‘double-angle’ DMs offer: (i) better manufacturing stability compared to the conventional complementary-pair approach^{8,13,14,19,20} and (ii) reduced manufacturing costs compared to the complementary-pair approach which requires two perfectly matched coating runs. By proper selection of incidence angles and application of a specialized version of the needle-optimization technique^{47,48} a double-angle DM has been designed, manufactured and characterized with very low overall GDD oscillations. To demonstrate the utility of the double angle approach, the mirrors were used for compressing pulses which had been spectrally broadened in a hollow fiber. Theoretical simulation shows that the pulse can be compressed to a duration of 4.3 fs, which is very close to their Fourier limit of 4.2 fs.

This time the double-angle DM approach has been used to design a DM which covers the range 600–1000 nm with $R > 99\%$ and $\text{GDD} = -50 \text{ fs}^2$. Resulting reflectance and GDD curves are shown in Fig. 18.8, for 5° and 19° as angle of incidence.

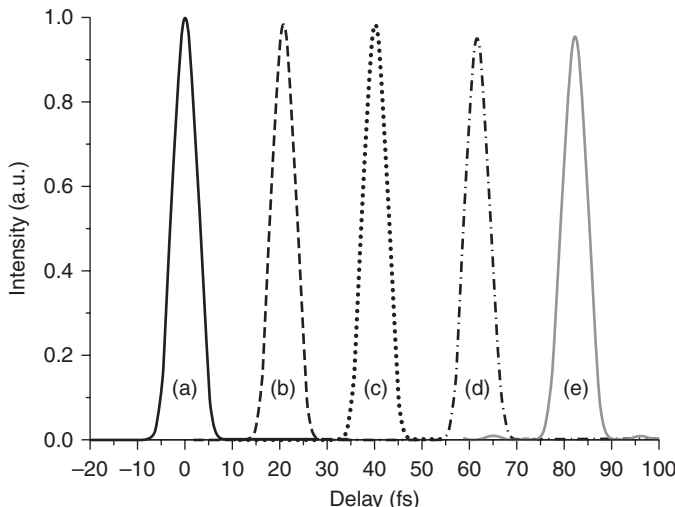
18.2.10 Pulse compression and analysis

In this section, we will compare the designed mirrors from the previous sections for the same virtual theoretical experiment. We have considered a hypothetical broadband dispersive delay line with the compensating GDD $+500 \text{ fs}^2$. A Gaussian pulse carried at a wavelength of 780 nm with a

Table 18.1 Summarized design parameters (number of layer and total physical thickness)

Design type	Pulse duration (fs)	Number of layers	Total physical thickness (nm)
Fourier transform limited pulse	5.86	–	–
Back-side-coated/tilt interface	6.09	60	6732
Brewster angle	5.94	135	14 738
Complementary pair	6.00	58	6109
		58	5947
Double-angle	5.98	58	6126

Note: Pulse durations obtained by using a certain mirror design approach in a virtual compression experiment after 10 bounces are shown.



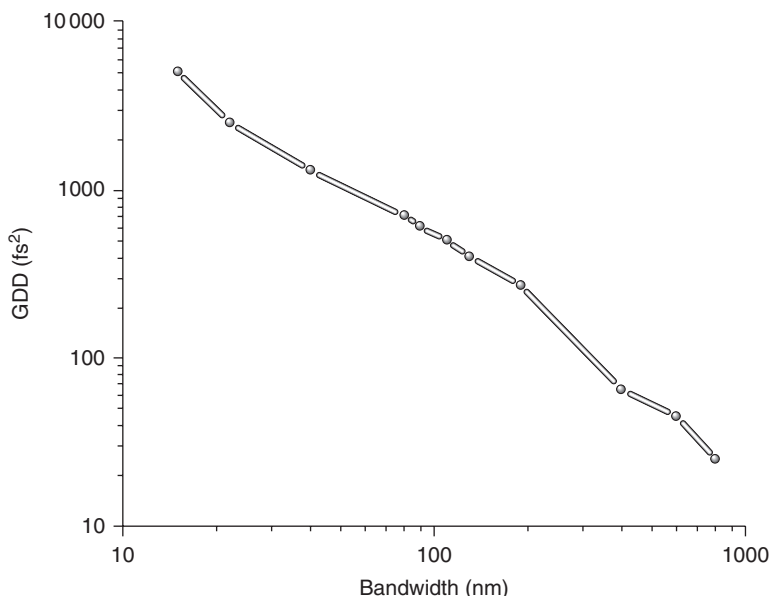
18.9 (a) Temporal analysis of the reflection of an incident Gaussian-shaped free-chirp 5.86 fs pulse. Pulse compressed by different design approaches: (b) double angle design approach, (c) complementary pair approach, (d) Brewster-angle approach, (e) back-side coated or tilted-front-interface approaches.

Fourier transform duration of 5.86 fs (FWHM) was sent through its optical delay line and calculated the temporal intensity profile of the pulse exiting the system. The results are summarized in Table 18.1 and in Fig. 18.9. The uncompensated spectral oscillations in the GDD curve of the mirror leads to a broadening of the pulse, accompanied by a decrease of the pulse energy. The results from the different approaches are similar, but still different. The shortest pulse has been obtained by using Brewster-angle mirrors. The largest pulse intensity was obtained by using double angle approach, see Fig. 18.9b. The difference in the results, obtained using the double angle

and complementary pair approaches is almost indistinguishable. The double angle design is robust and easier to produce. Usually, however, the complementary pair gives theoretically better results. All of the approaches have advantages and disadvantages. There is no universal solution, it depends on experimental requirements where one of the approaches demonstrate better performance for the certain laser system. For a broadband mirror with bandwidth > 300 nm, the best solution is double angle and complementary pair approaches.

18.3 The highest possible value of group delay dispersion (GDD)

During recent years, dispersive mirrors have made a quantum leap in their performance (reflectance and amount of the GDD), and now pave the way for purely dispersive-mirror compressors for different applications. Recently it has been revealed that the broader the spectrum for which the GDD must be controlled, the lower the nominal value of the GDD that can be achieved. In other words, relaxing the requirements on bandwidths allows higher values of the GDD. This finding has been inferred from the design



18.10 The highest absolute value of GDD as a function of the relative bandwidth, obtained at center design wavelength of about 800 nm. The sign of GDD presented here is negative, it can be positive as well. The lines connecting the points serve as a guide to the eye.

and manufacture of 11 different DMs, described in References 24, 25, 28, 30–32, 37, 38, 40, each of which represents the highest absolute value of the GDD obtained for a certain spectral width by using the same optimization technique, see Fig. 18.10.

The actual values of the points along the GDD axis depend on the central frequency, layer materials, and total thickness.

18.4 Production of dispersive mirrors

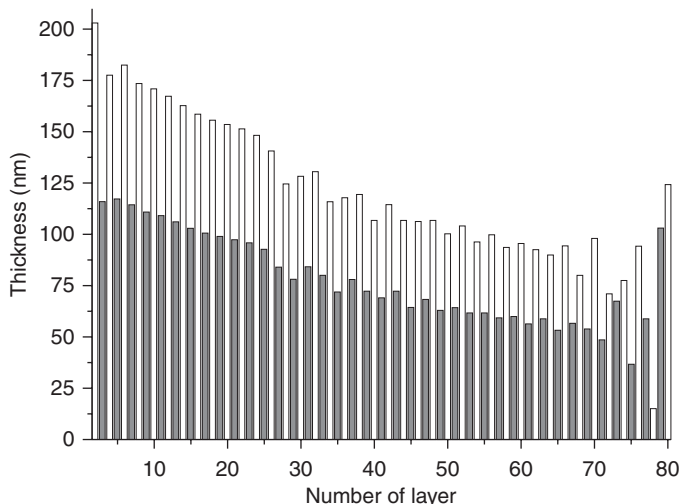
In order to produce the designed DM coatings, ion-beam sputtering or magnetron sputtering (for example Helios plant, Leybold Optics) using time monitoring or broadband monitoring⁴⁹ of layer thicknesses can be used. High quality dispersive mirrors with many dozens of layers were successfully deposited^{28–32,35–38,40} and the monitoring accuracy is estimated at 1–2 nm.^{28,31}

The Helios deposition plant is also equipped with the broadband monitoring (BBM) system.²⁹ Depending on the design of the coating time control, broadband monitoring or a combination of both can be used. The most frequently used high refractive index materials are Nb₂O₅, Ta₂O₅ (2.3 and 2.12 at 800 nm, respectively) and, for low refractive index, SiO₂ (1.47 at 800 nm). These materials offer optimum trade-off between low loss and high difference in the refractive indices for the wavelength range around 800 nm. The actual refractive indices of the coating materials should be determined just before the coating process is started in order to maximize the degree to which the designs can be produced in the manufacturing process. As an example, DMs produced with the magnetron-sputtering Helios machine (Leybold Optics) are considered. Helios is equipped with two of the proprietary TwinMags magnetrons and a plasma source for plasma/ion-assisted reactive middle-frequency dual-magnetron sputtering. The magnetrons were optimized for high sputtering rates and high optical layer performance. The system was pumped by turbo-molecular pumps to 1×10^{-6} mbar before deposition. Argon and oxygen were used for both magnetrons. In the magnetron cathodes, Nb, Ta and Si targets were used. The electric power of the Si cathode was 4500 W and the power of the Nb cathode was 3500 W. The power applied to the Nb and Ta cathode was not constant because it operated in the oxygen control (or lambda control) mode, which guaranteed stable process and film properties. The gas pressure was 1×10^{-3} mbar during the sputtering process. Oxygen was fed near the targets in order to oxidize the sputtering films. The distance from the targets to the substrates was 100 mm. The purity of the Si target was 99.999% and that of the Nb and Ta target, 99.9%. By changing the electric power applied to the cathode, it was possible to increase or decrease the sputtering rate. It was found that the film quality degrades at high rates and good film quality was achieved at a rate of around 0.5 nms⁻¹ for both materials. In the experiments BK7 and FS substrates were usually used.

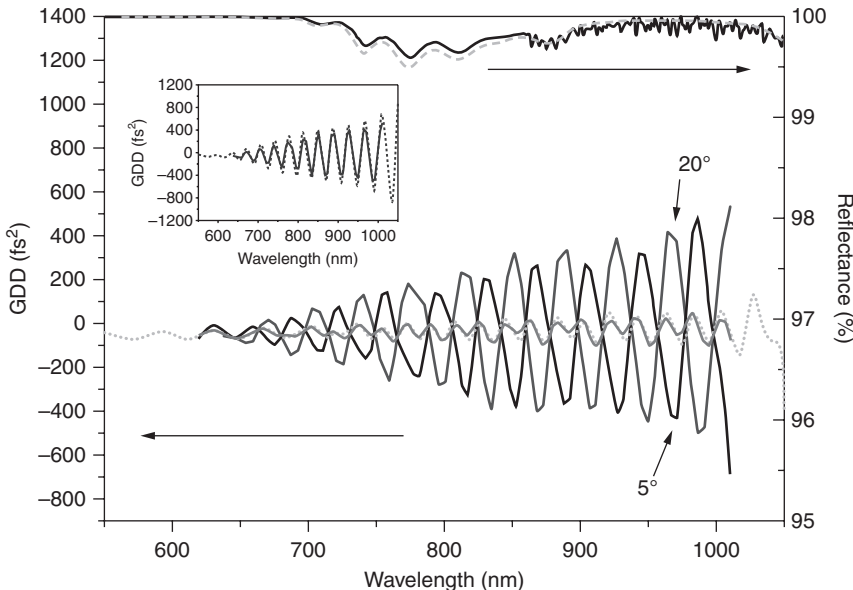
18.5 Pulse compression with dispersive mirrors

As an example for pulse compression of broadband spectrums, double-angle DMs can be considered. The design of double-angle DM consists of 80 alternating $\text{Nb}_2\text{O}_5/\text{SiO}_2$ layers, with a multilayer structure shown in Fig. 18.11. The thickness of both types of layers tends to decrease with increasing distance from the substrate, which resembles the design of ‘classical’ chirped mirrors.⁶ The physical thicknesses of the layers range from 13 to 210 nm. The successful fabrication of DMs can be as challenging as their design. The main problem is connected to the high sensitivity of GDD to even small errors in layer thicknesses. Therefore a high precision of the deposition process is mandatory for successful DM production. The GDD of the DMs was measured using a white-light interferometer.⁵⁰ The result is summarized in Fig. 18.12. In the inset of Fig. 18.12, a comparison of the measured and theoretical GDD of a double-angle DM³¹ for an angle of incidence of 5° is shown. Good agreement has been observed between the calculated and measured reflectance as well as the GDD values.

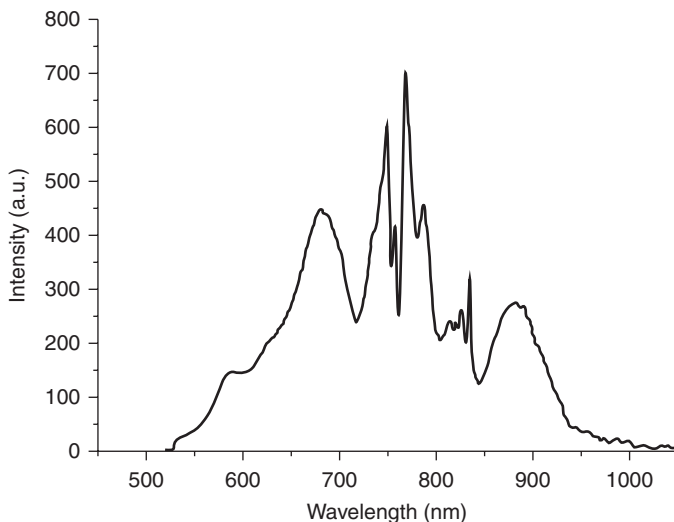
In order to check the implications of the residual oscillations of the effective GDD of the double-angle mirror, the propagation of an ideal transform-limited pulse having the frequency spectrum originating from a hollow-core fiber (see Fig. 18.13) was simulated through a simple optical system following the fiber. The hollow-core fiber was used to stretch the existing spectrum.



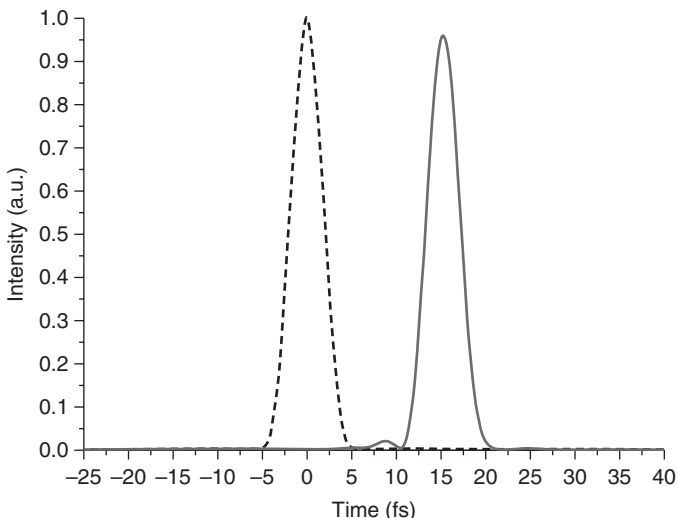
18.11 Physical thicknesses of layers in our prototypical double-angle DM design. Layers are numbered starting from the substrate. Empty and full bars correspond to low and high refractive index materials, SiO_2 and Nb_2O_5 , respectively.



18.12 Measured GDD and reflectance of our prototypical double-angle DM for an angle of incidence of 5° and 20° (full lines). GDD and reflectance of the theoretical design are shown by dashed lines. Gray curves correspond to angles of incidence of 5° and 20°. Black curves show the effective measured GDD and reflectance.



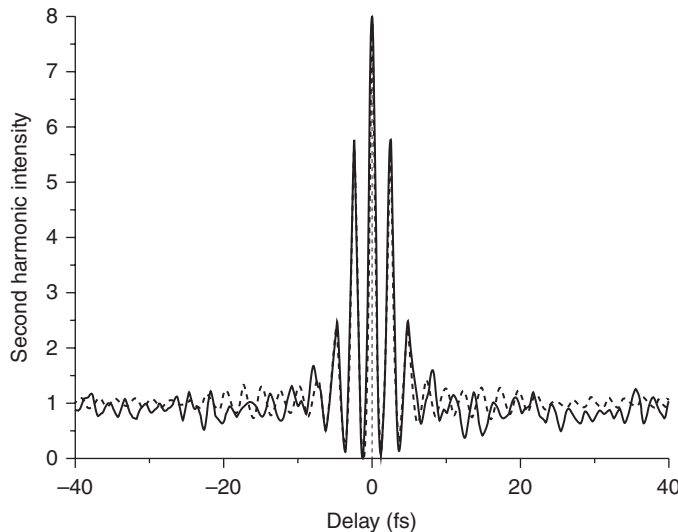
18.13 Spectrum of femtosecond pulses originating from our gas-filled hollow fiber. With constant or linearly-varying spectral phase, it allows the generation of 4.2-fs transform-limited pulses.



18.14 4.2-fs Fourier-limited pulse before (dashed line) and after (full line) propagation through dispersive material and our double-angle DM compressor.

After proper compression of the stretched spectrum in a hollow-core fiber using DM, sub-5 fs pulses could be obtained. Four bounces on our double-angle DMs at each of the two selected angles of incidence used to compensate GVD of a 3 mm path through fused silica and a 5 m path through air. As revealed by the dashed line in Fig. 18.14, the Fourier-limited input pulse with a duration of 4.2 fs measured as the full width at half maximum (FWHM), of the intensity profile (solid line in Fig. 18.14), suffers virtually no broadening, merely a small fraction (~5%) of its energy is scattered into the satellite pulses.

The double-angle DMs were tested in a hollow-core-fiber/dispersive-mirror compressor seeded by millijoule-scale, sub-25 fs pulses from a kilohertz-rate femtosecond Ti:sapphire laser. The hollow fiber with a length of ~1 m and a core diameter of 0.3 mm was filled with neon at a pressure of 2.2 bar and resulted in the output spectrum shown in Fig. 18.13. The pulses exiting the fiber traveled a distance of 1.7 m in air and 1.5 mm in fused silica and were passed through the double-angle DM compressor. The duration of the compressed pulse was measured by second-harmonic generation interferometric autocorrelation, utilizing a 5 μm thick, type-1 phase-matched BBO crystal (BaB_2O_4 – barium borate). The measured autocorrelation function is shown in Fig. 18.15 (full line) along with the one calculated from the measured spectrum (Fig. 18.13) under the assumption of the absence of spectral phase modulation (dashed line).



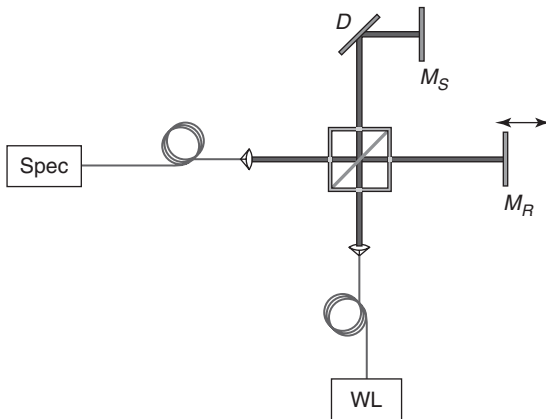
18.15 Dashed line: theoretical interferometric autocorrelation of a pulse with the frequency spectrum shown in Fig. 18.13 in the absence of spectral phase modulation. This Fourier-limited pulse has a duration (FWHM) of 4.2 fs. Full line: measured interferometric autocorrelation function of the pulses compressed with double-angle DM compressor, indicating a pulse duration of \sim 4.3 fs.

Interferometric autocorrelation measurement yields a near-bandwidth-limited pulse duration of 4.3 fs after the double-angle DM compressor. The autocorrelation trace has some small oscillations over a delay range of several tens of femtoseconds, indicative of small pre/post-pulsing as a consequence of the residual GDD oscillations in the compressor and incomplete high-order dispersion compensation.

For the purpose of further suppression of residual GDD oscillations or increasing bandwidth, while keeping the oscillations at the same level, the number of different angles of incidence can be increased, without compromising complexity and cost of manufacture.

18.6 Measurement of group delay with white light interferometer

A number of dispersion measurement devices, including white-light interferometers (WLIs) have been reported.^{51–58} A WLI is a powerful tool for measuring the GD wavelength dependence of optical elements in a broad spectral range.^{51,52} Usually the WLI is a Michelson-type interferometer of the scanning arm type with a broadband light source.^{51,52,54–56} That allows

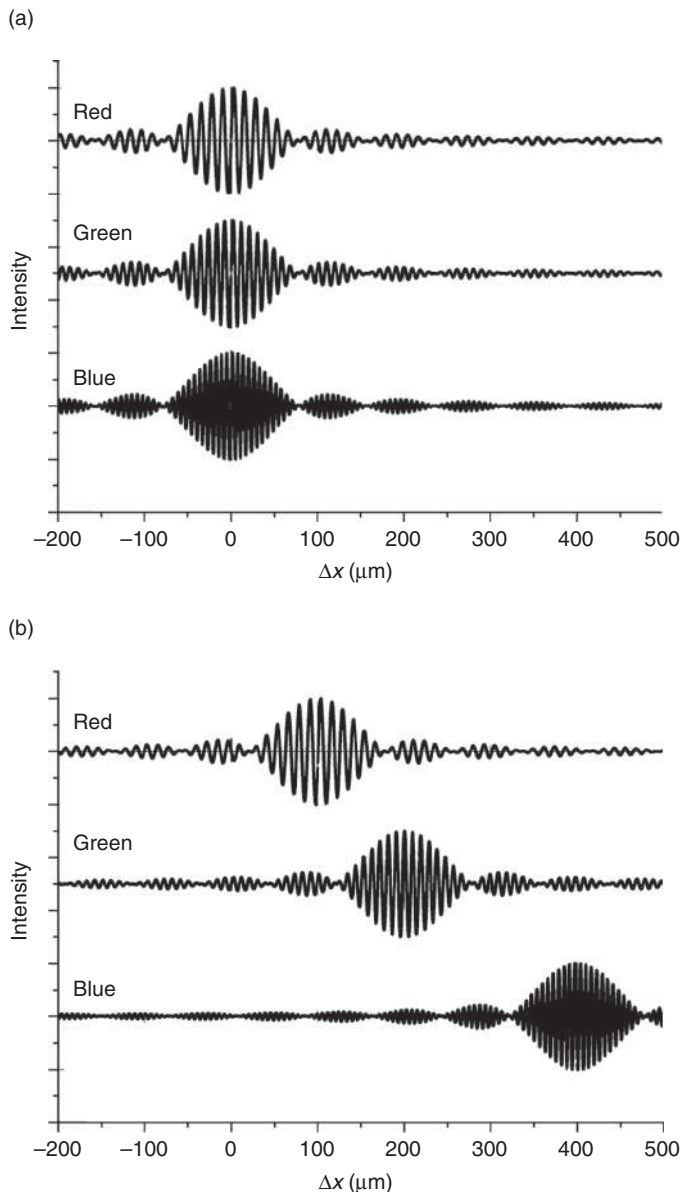


18.16 Diagram of the set-up. A broadband white light source (WL) couples into an optical fiber. After exiting the fiber the beam is collimated and divided by a beam splitter. The reference arm is terminated by a mirror (M_R) mounted on a linear stage. A dispersive sample such as a dielectric multilayer mirror (D) is inserted into the other arm. The superposed beams are collimated into a fiber and analysed by a spectrograph (Spec).

for group delay dispersion measurements from the UV to the IR range. The measurement scheme is shown in Fig. 18.16. More detailed description can be found in References 57 and 58.

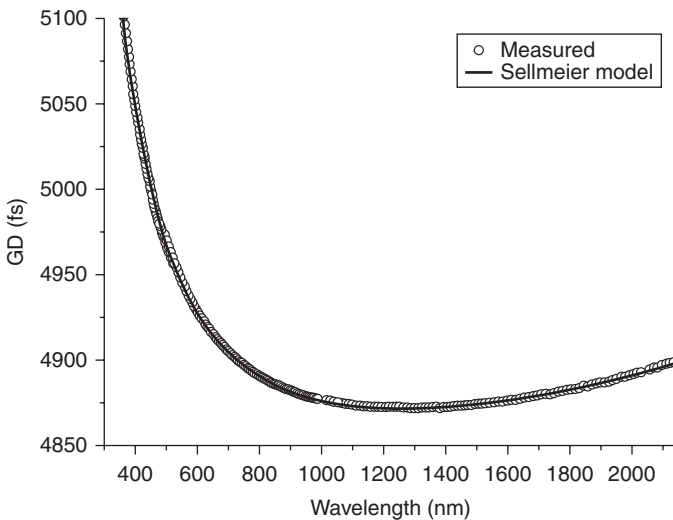
As is apparent from the sketch, the obtained spectra result from the overlap of the beams from the reference arm and from the sample arm. There are a number of ways in which this set-up can be used to measure the GD, but we need to consider the nature of the interference in the first place. Unlike interferometry with lasers, where coherence length is large (so that it can often be practically taken for granted). The white light interferometry essentially requires small differences in the optical path length, of both arms, which is the same to within a few micrometers. The relative delay of the two beams is then low enough for the short coherence time of the white light source. Spatial coherence is already achieved by using an optical fiber to propagate the beam into the interferometer. If the optical path lengths of both arms are perfectly balanced, then the two waves that recombine at the beam-splitter will have the same phase and will thus interfere constructively. If one mirror is moved slightly, then the optical path lengths are not equal and a phase difference between the two waves results. The detector registers an intensity which is given by the coherent interference.

In a dispersionless balanced interferometer all parts of the spectrum have the same optical pathlengths. Therefore the maxima of all interferograms will coincide for a particular geometric reference armlength Δx (Fig. 18.17a).



18.17 Positions of the interferograms with a balanced interferometer (a) and a dispersive sample inserted (b).

Now, if a dispersive substance is put into the sample arm the optical pathlength becomes wavelength dependent. This shift in pathlength must be compensated by a corresponding shift of the reference mirror in order to regain a maximum visibility. So the respective shift of a spectrally confined



18.18 Full-bandwidth measurement on fused-silica. The measurements overlap at 1500 shows mismatch within the resolution limit (10 nm).

interferogram (read out from the changed reference armlength Δx at the centre of an interferogram) reveals the respective group delay (Fig. 18.17b).

There are a number of different methods for retrieving the GD by using this set of measurement data: contour fringe shift interferometry,^{51,59,60} Fourier-Transform spectroscopy,^{54,61–64} phase locked interferometry,^{65,66} utilizing wavelet analysis,⁶⁷ and reconstruction of the precise distance between each measurement of the interference pattern.⁵⁰ All of these methods have advantages and disadvantages. Here, we will not discuss retrieving methods in detail, the interested reader can easily find all the details in References 50–67. It is important to note that, currently, Michelson interferometer set-ups allow GDD measurements of dispersive optics over the range 250–2150 nm comprising different independent evaluation methods mentioned above. As an example, in Fig. 18.18, the measurement of fused-silica substrate on transmission is shown. The figure consists of four independent measurements. They replicate the theoretical curve calculated from the Sellmeier model of fused-silica. One of the best results being achieved by a full-bandwidth-applicable phase tracking technique yielded a GD repeatability (standard deviation) of $GD = 0.2$ fs in a reference range 700–950 nm for a spectral resolution of 2.2 nm.⁵⁷

The data acquisition generally suffers from inaccuracies of various origins which provide space for further improvement. While setting up the interferometer a trade-off had to be made between practicality and precision. A higher spectral resolution could be achieved by better resolving gratings

and a spectrograph of longer focal length. However this would necessarily mean smaller bandwidths of the single measurements and consequently a higher number of measurements to be performed.

18.7 Application of dispersive mirrors in high-intensity lasers

At the moment there are a lot of ongoing research projects involving high intensity lasers. Such well-known projects are ELI (Extreme Light Infrastructure) (www.elaser.eu), CALA (Centre for Advanced Laser Applications) (http://www.attoworld.de/Documents/pdf/CALA-Flyer_englisch.pdf), APOLLON, EMINI, Vulcan and PFS (Petawatt Field Synthesizer).⁶⁸ All of these research activities will be based on an incremental development of the light sources to achieve unprecedented peak power performance, from tens of petawatts up to a fraction of an exawatt (10^{18} W).⁶⁸

The ELI project was selected in 2006 by the European Strategic Forum for Research Infrastructure (ESFRI) committee as one of the 37 major research infrastructure projects. ELI is now about to complete its Preparatory Phase (ELI-PP) funded by the EC, in which 13 EU countries and around 50 academic institutions have been involved (www.elaser.eu). The ELI will be the first facility in the world dedicated to laser-matter interaction in the ultra-relativistic regime ($>10^{24}$ W/cm²), providing unprecedented intensity levels. It will be the gateway to new regimes in physics. At the same time, it will also promote new technologies such as relativistic microelectronics with the development of compact laser accelerators. The ELI will be built with a joint international effort and form an integrated infrastructure comprised of at least three branches: Attosecond Science (in Szeged, Hungary) designed to make temporal investigation at the attosecond scale of electron dynamics in atoms, molecules, plasmas and solids. High Field Science will be mainly focused on producing ultra-intense and ultra-short sources of electrons, protons and ions, coherent and high energetic X-rays (in Prague, Czech Republic) as well as laser based nuclear physics (in Magurele, Romania) (www.elaser.eu).

The new Centre for Advanced Laser Applications (CALA) research facility expands laser science applications to biology and medicine. The unique spectrum of particle beam sources and ultrashort, intense light pulses will enable CALA to open up new fields of research in biochemistry, physics, medicine and material sciences to the universities involved in this excellence initiative – Ludwig-Maximilians-Universität München (LMU) and Technische Universität München (TUM). CALA will produce light pulses with properties that are unique in the world. They last just a few femtoseconds (10^{-15} s)

and yield an extremely high energy within this incredibly short length of time. When focused to very few thousandths of a millimetre, this unique concentration of light energy causes hitherto unattained forces to be exerted on charged particles. Electrons accelerated with this immense femtosecond light force can in turn produce extremely brilliant (i.e., intense and bunched) X-radiation as well as proton and ion beams. These can be enlisted to detect very fine structures, such as that of biomolecules, or to detect tumours in the earliest stage of growth and then eradicate them.⁶⁸

Most high intensity laser projects rely on so-called chirped-pulse amplification (CPA) concept.⁶⁹ CPA of ultrashort light pulses in solid-state lasers and parametric amplifiers has permitted the generation of optical pulses with multi-gigawatt to multi-terawatt peak powers and holds promise for scaling high-power laser technology far beyond the petawatt frontier.^{70–72} CPA systems constitute a pivotal research tool in nonlinear optics, ultrafast spectroscopy^{73,74} and high-field science.⁷⁰ Chirped-pulse amplifiers are seeded with low-energy ultrashort pulses temporally broadened in a dispersive pulse stretcher to permit for amplification without damaging the gain medium. The chirp of the amplified pulses is subsequently removed in a pulse compressor introducing a GDD of opposite sign. The pulse duration is thereby restored close to that of the input pulse. Conventional CPA systems rely on rather lossy, complex and alignment-sensitive systems of gratings^{75,76} and/or prisms⁷⁷ for pulse stretching and recompression, which have compromised the production efficiency and the spatio-temporal quality of the amplified pulses. When diffraction gratings or prisms are used in stretchers/compressors, their angular dispersion introduces the desired wavelength-dependent delay. The alignment sensitivity of these components poses a serious challenge in the day-to-day operation of CPA systems. Minute deviations from optimum prism and grating orientations lead to angular chirp and pulse front tilt. The consequence is the deterioration of the pulse profile in focus, both spatially and temporally,⁷⁸ which may be additionally impaired by thermal and nonlinear effects in these optical components. Moreover, their relatively large amount of uncompensated higher-order dispersion requires the use of additional dispersion management such as dispersive multilayer mirrors,^{77,79} or hybrid (prism-grating-material) stretcher-compressor systems⁸⁰ for bandwidth-limited pulse generation in broadband (10-fs-scale) amplifiers. Recently, a novel implementation of CPA that overcomes these problems by using dominantly dispersive multilayer mirrors for chirp control was reported.³²

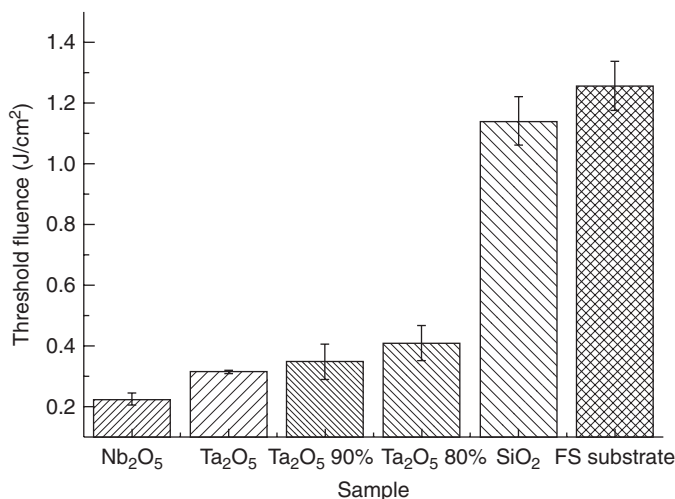
Dispersive mirrors offer the potential for eliminating these drawbacks owing to their capability of providing tailored dispersion over unprecedented bandwidths without spatial separation of spectral components. The wavelength-dependent delay originates from short propagation through virtually lossless, highly dispersive multilayered media. CPA implemented with dispersive mirrors is therefore intrinsically free from the angular chirp, pulse-front

tilt and nonlinear effects with the added benefit of higher-order dispersion control. They can be designed to provide GDD of either sign and hence compensate material dispersion both in the visible/near-infrared and the mid-infrared spectral range, where the dispersion of most materials changes its sign.

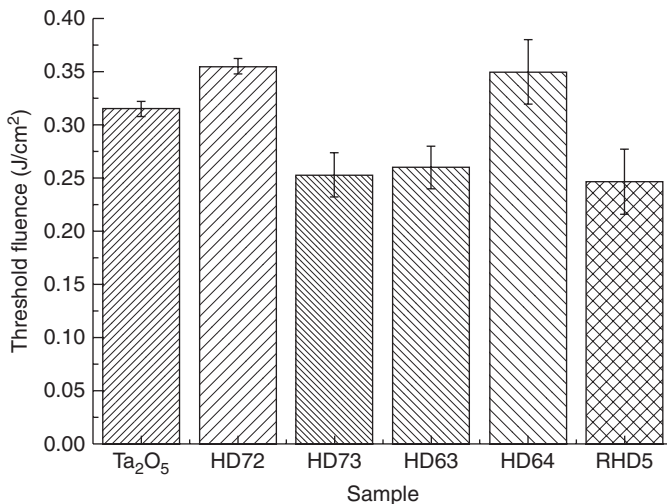
The exploitation of this potential calls for multilayer structures with high GDD and low loss (denoted by L) over a spectral range of several tens of THz. The figure of merit $FOM = |GDD|/L$ determines the loss at the expense of which a certain amount of dispersion for a certain stretching factor can be realized. The first generation of chirped multilayer mirrors has typically exhibited a GDD of several tens of fs^2 with a loss of a fraction of a percent. Stretching the duration of sub-50-fs pulses by a factor of ~ 1000 requires a GDD of the order of tens of thousands of fs^2 . This demand would have called for a prohibitively large number of bounces leading to excessive overall losses with early-generation chirped multilayers.

Recent progress in the design and manufacture of multilayer high-dispersive mirrors (HDM)^{32,35,37} has resulted in a quantum leap in enhancing the FOM, and opened the door for an all dispersive-mirror compressor for CPA.

All of the above mentioned projects rely on unique highly dispersive optics with high laser-induced damage threshold (LIDT). The generation of ultrashort pulses with large pulse energies is constrained by the LIDT of the dispersive optics. The LIDT of the dispersive optics is one of the bottlenecks in the development of high-power ultrafast systems. The optical breakdown thresholds of the single layer depositions are shown in Fig. 18.19.



18.19 Threshold fluencies of single layer deposition and fused silica substrate.



18.20 Comparisons between a single layer of Ta_2O_5 and dispersive coatings employing Ta_2O_5 as high and SiO_2 as low index materials.

The damage threshold of the single layer dielectric coatings was found to be dependent on the band gap of the material used. Dispersive coatings had damage thresholds close to that of a single layer of the high index material used for the respective coating, see Fig. 18.20. The LIDT measurements of dispersive mirrors^{81,84} confirmed previously reported band gap dependence of the laser-induced damage for ultrashort pulses.^{83,84} The dispersive mirrors consist of Ta_2O_5 and Nb_2O_5 , as high refractive index material have damage of $\sim 0.3 \text{ J}/\text{cm}^2$ ⁸¹ for Ti:Sapphire laser yielding 1 mJ, 30 fs pulses at 500 Hz repetition rate at 790 nm central wavelength. Increasing of current LIDT will make possible the femtosecond and attosecond applications to reach the higher intensity and energy levels.

18.8 Conclusion

Existing approaches are still not at their limit. Mentioned designing approaches can be successfully used for a certain application. There is no universal approach. Another material combination with higher refractive index contrast and better accuracy of the deposition process together with further development of the mathematical designing approaches could push the now existing frontier toward shorter pulse durations, higher peak powers and higher average powers. Another alternative for improving performance may be a combination of different approaches: for example, double-angle

DM approach with the time-domain optimization, or any other combinations. In the near future dispersive multilayers will continue to play a critical role in the field of ultrafast physics.

18.9 References

1. Brabec T and Krausz F, (2000), 'Intense few-cycle laser fields: Frontiers of nonlinear optics', *Rev Mod Phys*, **72**, 545.
2. Hentschel M, Kienberger R, Spielmann Ch, Reider G A, Milosevic N, Brabec T, Corkum P, Heinzmann U, Drescher M and Krausz F, (2001), 'Attosecond metrology', *Nature*, **414**, 509.
3. Jones D J, Diddams S A, Ranka J K, Stentz A, Windeler R S, Hall J L and Cundiff S T, (2000), 'Carrier-envelope phase control of femtosecond mode-locked lasers and direct optical frequency synthesis', *Science*, **288**, 635.
4. Apolonski A, Poppe A, Tempea G, Spielmann C, Udem T, Holzwarth R, Hänsch T and Krausz F, (2000), 'Observation of light-phase-sensitive photoemission from a metal', *Phys Rev Lett*, **85**, 740.
5. Baltuska A, Udem T, Uiberacker M, Hentschel M, Goulielmakis E, Gohle C, Holzwarth R, Yakovlev V S, Scrinzi A, Hänsch T W and Krausz F, (2003), 'Attosecond control of electronic processes by intense light fields', *Nature*, **421**, 611.
6. Szipočs R, Ferencz K, Spielmann C and Krausz F, (1994), 'Chirped multilayer coatings for broadband dispersion control in femtosecond lasers', *Opt Lett*, **19**, 201–203.
7. Kärtner F X, Matuschek N, Schibli T, Keller U, Haus H A, Heine C, Morf R, Scheuer V, Tilsch M and Tschudi T, (1997), 'Design and fabrication of double-chirped mirrors', *Opt Lett*, **22**, 831–833.
8. Laude V and Tournois P, (1999), 'Chirped mirror pairs for ultrabroadband dispersion control', in *Digest of Conference on Lasers and Electro-Optics (CLEO_US)* (Optical Society of America), 23–28 May 1999, Orlando, FL, USA, 187–188.
9. Matuschek N, Kärtner F X and Keller U, (1999), 'Analytical design of double-chirped mirrors with custom-tailored dispersion characteristics', *IEEE J Quantum Electron*, **35**, 129–137.
10. Sutter D H, Steinmeyer G, Gallmann L, Matuschek N, Morier-Genoud F, Keller U, Scheuer V, Angelow G and Tschudi T, (1999), 'Semiconductor saturable-absorber mirror assisted Kerr-lens mode-locked Ti:sapphire laser producing pulses in the two-cycle regime', *Opt Lett*, **24**, 631–633.
11. Szipočs R, Koházi-Kis A, Lako S, Apai P, Kovács A P, DeBell G, Mott L, Louderback A W, Tikhonravov AV and Trubetskov M K, (2000), 'Negative dispersion mirrors for dispersion control in femtosecond lasers: chirped dielectric mirrors and multi-cavity Gires-Tournois interferometers', *Appl Phys B*, **70**, S51–S57.
12. Golubovic B, Austin R R, Steiner-Shepard M K, Reed M K, Diddams S A, Jones D J and Van Engen A G, (2000), 'Double Gires-Tournois interferometer negative-dispersion mirrors for use in tunable mode-locked lasers', *Opt Lett*, **25**, 275–277.

13. Matuschek N, Gallmann L, Sutter D H, Steinmeyer G and Keller U, (2000), 'Back-side-coated chirped mirrors with ultrasmooth broadband dispersion characteristics', *Appl Phys B*, **71**, 509–522.
14. Kärtner F X, Morgner U, Ell R, Schibli T, Fujimoto J G, Ippen E P, Scheuer V, Angelow G and Tschudi T, (2001), 'Ultrabroadband double-chirped mirror pairs for generation of octave spectra', *J Opt Soc Am B*, **18**, 882–885.
15. Tempea G, Yakovlev V, Bacovic B, Krausz F and Ferencz K, (2001), 'Tilted-front-interface chirped mirrors', *J Opt Soc Am B*, **18**, 1747–1750.
16. Yakovlev V and Tempea G, (2002), 'Optimization of chirped mirrors', *Appl Opt*, **41**, 6514–6520.
17. Schibli T R, Kuzucu O, Kim J W, Ippen E P, Fujimoto J G, Kaertner F X, Scheuer V and Angelow G, (2003), 'Toward single-cycle laser systems', *IEEE J Sel Topics Quantum Electr*, **4**, 990–1001.
18. Steinmeyer G, (2003), 'Brewster-angled chirped mirrors for highfidelity dispersion compensation and bandwidths exceeding one optical octave', *Opt Express*, **11**, 2385–2396.
19. Morlens A, Balcou P, Zeitoun P, Valentin C, Laude V and Kazamias S, (2005), 'Compression of attosecond harmonic pulses by extreme-ultraviolet chirped mirrors', *Opt Lett*, **30**, 1554–1556.
20. Dombi P, Yakovlev V S, O'Keefe K, Fuji T, Lezius M and Tempea G, (2005), 'Pulse compression with time-domain optimized chirped mirrors', *Opt Express*, **13**, 10888–10894.
21. Steinmeyer G, (2006), 'Femtosecond dispersion compensation with multilayer coatings: toward the optical octave', *Appl Opt*, **45**, 1484–1490.
22. Baum P, Breuer M, Riedle E and Steinmeyer G, (2006), 'Brewster-angled chirped mirrors for broadband pulse compression without dispersion oscillations', *Opt Lett*, **31**, 2220–2222.
23. Wonisch A, Neuhäusler U, Kabachnik N M, Uphues T, Uiberacker M, Yakovlev V, Krausz F, Drescher M, Kleineberg U and Heinzmann U, (2006), 'Design, fabrication, and analysis of chirped multilayer mirrors for reflection of extreme-ultraviolet attosecond pulses', *Appl Opt*, **45**, 4147–4156.
24. Pervak V, Krausz F and Apolonski A, (2007), 'Dispersion control over the UV-VIS-NIR spectral range with $\text{HfO}_2/\text{SiO}_2$ chirped dielectric multilayers', *Opt Lett*, **32**, 1183–1185.
25. Pervak V, Tikhonravov A V, Trubetskov M K, Naumov S, Krausz F and Apolonski A, (2007), '1.5-octave chirped mirror for pulse compression down to sub-3 fs', *Appl Phys B*, **87**, 5–12.
26. Nohadani O, Birge J R, Kärtner F X and Bertsimas D J, (2008), 'Robust chirped mirrors', *Appl Opt*, **47**, 2630–2636.
27. Chen R, Wang F and Wang Z, (2008), 'Design of chirped Mo/Si multilayer mirror in the extreme ultraviolet region', *Chin Opt Lett*, **6**, 310–312.
28. Pervak V, Teisset C, Sugita A, Naumov S, Krausz F and Apolonski A, (2008), 'High-dispersive mirrors for femtosecond lasers', *Opt Express*, **16**, 10220–10233.
29. Trubetskov M, Tikhonravov A and Pervak V, (2008), 'Time-domain approach for designing dispersive mirrors based on the needle optimization technique. Theory', *Opt Express*, **16**, 20637–20647.

30. Pervak V, Ahmad I, Fulop J, Trubetskoy M K and Tikhonravov A V, (2009), 'Comparison of dispersive mirrors based on the time-domain and conventional approaches, for sub-5-fs pulses', *Opt Express*, **17**, 2207–2217.
31. Pervak V, Ahmad I, Trubetskoy M K, Tikhonravov A V and Krausz F, (2009), 'Double-angle multilayer mirrors with smooth dispersion characteristics', *Opt Express*, **17**, 7943–7951.
32. Pervak V, Ahmad I, Trushin S A, Major Zs, Apolonski A, Karsch S and Krausz F, (2009), 'Chirped-pulse amplification of laser pulses with dispersive mirrors', *Opt Express*, **17**, 19204–19212.
33. Rivera Ch A, Bradforth S E and Tempea G, (2010), 'Gires-Tournois interferometer type negative dispersion mirrors for deep ultraviolet pulse compression', *Opt Express*, **18**, 18615–18624.
34. Chen L, Chang G, Birge J R and Kärtner F X, (2010), 'Complementary chirped-mirror pair for broadband dispersion-free cavities', in *Optical Interference Coatings, OSA Technical Digest* (Optical Society of America), paper FB5.
35. Trubetskoy M K and Tikhonravov A V, (2010), 'Robust synthesis of multilayer coatings', in *Optical Interference Coatings, OSA Technical Digest* (Optical Society of America), paper TuA4.
36. Jinlong Z, Xinbin C, Zhanshan W, Hongfei J and Tao D, (2011), 'HfO₂/SiO₂ chirped mirrors manufactured by electron beam evaporation', *Appl Opt*, **50**, C388–C391.
37. Pervak V, Trubetskoy M K and Tikhonravov A V, (2011), 'Robust synthesis of dispersive mirrors', *Opt Express*, **19**, 2371.
38. Pervak V, (2011), 'Recent development and new ideas in the field of dispersive multilayer optics', *Appl Opt*, **50**, C55.
39. Hofstetter M, Schultz M, Fieß M, Dennhardt B, Guggenmos A, Gagnon J, Yakovlev V S, Goulielmakis E, Kienberger R, Gullikson E M, Krausz F and Kleineberg U, (2011), 'Attosecond dispersion control by extreme ultraviolet multilayer mirrors', *Opt Express*, **19**, 1767–1776.
40. Pervak V, Pronin O, Razskazovskaya O, Brons J, Angelov I B, Trubetskoy M K, Tikhonravov A V and Krausz F, (2012), 'High-dispersive mirrors for high power applications', *Opt Express*, **20**, 4503–4508.
41. Tikhonravov A V and Trubetskoy M K, OptiLayer Thin Film Software, <http://www.optilayer.com>
42. TFcalc Software, <http://www.sspectra.com>
43. Macleod A, Essential Macleod, <http://www.thinfilcenter.com/>
44. Dobrowolski J A, Tikhonravov AV, Trubetskoy M K, Sullivan B T and Verly P G, (1996), 'Optimal single-band normal-incidence antireflection coatings', *Appl Opt*, **35**, 644–658.
45. Tikhonravov A V, Trubetskoy M K, Amotchkina T V and Dobrowolski J A, (2008), 'Estimation of the average residual reflectance of broadband antireflection coatings', *Appl Opt*, **47**, 124–130.
46. Amotchkina T V, (2008), 'Empirical expression for the minimum residual reflectance of normal and oblique-incidence antireflection coatings', *Appl Opt*, **47**, 3109–3113.
47. Tikhonravov A V, Trubetskoy M K and DeBell G W, (1996), 'Application of the needle optimization technique to the design of optical coatings', *Appl Opt*, **35**, 5493–5508.

48. Tikhonravov A V, Trubetskoy M K and DeBell G W, (2007), 'Optical coating design approaches based on the needle optimization technique', *Appl Opt*, **46**, 704–710.
49. Ristau D, Ehlers H, Gross T and Lappschies M, (2006) 'Optical broadband monitoring of conventional and ion processes', *Appl Opt*, **45**, 1495–1501.
50. Amotchkina T V, Tikhonravov A V, Trubetskoy M K, Grupe D, Apolonski A and Pervak V, (2009), 'Measurement of group delay of dispersive mirrors with white-light interferometer', *Appl Opt*, **48**, 949–956.
51. Knox W H, Pearson N M, Li K D and Hirlmann C A, (1988), 'Interferometric measurements of femtosecond group delay in optical components', *Opt Lett*, **13**, 574–576.
52. Knox W H, (1994), 'Dispersion measurements for femtosecond-pulse generation and applications', *Appl Phys B*, **58**, 225–235.
53. Beck M and Walmsley I A, (1990), 'Measurement of group delay with high temporal and spectral resolution', *Opt Lett*, **15**, 492–494.
54. Gosteva A, Haiml M, Paschotta R and Keller U, (2005), 'Noise related resolution limit of dispersion measurements with white-light interferometers', *J Opt Soc Am B*, **22**, 1868–1874.
55. Naganuma K, Mogi K and Yamada H, (1990), 'Group-delay measurement using the Fourier transform of an interferometric cross correlation generated by white light', *Opt Lett*, **15**, 393–395.
56. Daddams S and Diels J C, (1996), 'Dispersion measurements with white-light interferometry', *J Opt Soc Am B*, **13**, 1120–1129.
57. Grupe D, (2008), 'Measuring group delay dispersion in the UV-VIS-IR range by white-light interferometry', Master thesis, Munich.
58. McFadden D, (2011), 'Operating a white light interferometer for the measurement of group delay in the ultraviolet range', Bachelor thesis, Munich.
59. Bruning J H, (1978), 'Fringe scanning interferometers', in Malacara, D. (ed.), *Optical Shop Testing*, 409–437, Wiley, New York.
60. Tateda M, Shibata N and Seikai S, (1990), 'Interferometric method for chromatic dispersion measurement in a single-mode optical fiber', *IEEE J Quantum Electron QE*, **17**, 404–407.
61. Naganuma K, Mogi K and Yamada H, (1990), 'Group-delay measurement using the Fourier transform of an interferometric cross correlation generated by white light', *Opt Lett*, **15**, 7.
62. Imran T, Hong K H, Yu T J and Nam C H, (2004), 'Measurement of the group delay dispersion of femtosecond optics using white-light interferometry', *Rev Sci Instrum*, **75**, 2266–2270.
63. Takeda M, Hideki I and Kobayashi S, (1982), 'Fourier-transform method of fringe pattern analysis for computer-based topography and interferometry', *J Opt Soc Am*, **72**, 156–160.
64. Nebel T, (2005), 'Measuring the group delay dispersion of optical elements', Diploma Thesis at Fakultaet fuer Physik der Ludwig-Maximilians-Universitaet, Munich.
65. Beck M and Walmsley I A, (1990), 'Measurement of group delay with high temporal and spectral resolution', *Opt Lett*, **15**, 492–494.
66. Beck M, Walmsley I A and Kafka J D, (1991), 'Group delay measurement of optical components near 800 nm', *IEEE QE*, **27**, 2074–2081.

67. Luo Z, Zhang S, Shen W, Xia C, Ma Q, Liu X and Zhang Y, (2011), 'Group delay dispersion measurement of a dispersive mirror by spectral interferometry: comparison of different signal processing algorithms', *Appl Opt*, **50**, C239–C245.
68. Chambaret J, Chekhlov O, Cheriaux G, Collier J, Dabu R, Dombi P, Dunne A M, Ertel K, Georges P, Hebling J, Hein J, Hernandez-Gomez C, Hooker C, Karsch S, Korn G, Krausz F, Le Blanc C, Major Zs, Mathieu F, Metzger T, Mourou L, Nickles P, Osvay K, Rus B, Sandner W, Szabo G, Ursescu D and Varjú K, (2010), 'Extreme Light Infrastructure: architecture and major challenges', SPIE Photonics Europe: High-Power Lasers, Brussels, Belgium, Proc SPIE, **7721**, 77211D.
69. Strickland D and Mourou G, (1985), 'Compression of amplified chirped optical pulses', *Opt Comm*, **56**, 219–221.
70. Mourou G, Tajima T and Bulanov S V, (2006), 'Optics in the relativistic regime', *Rev Mod Phys*, **78**, 309–371.
71. Perry M D and Mourou G, (1994), 'Terawatt to Petawatt subpicosecond lasers', *Science*, **264**, 917–924.
72. Gerstner E, (2007), 'Laser physics: Extreme light', *Nature*, **446**, 16–18.
73. Krausz F and Ivanov M, (2009), 'Attosecond physics', *Rev Mod Phys*, **81**, 163–234.
74. Brabec T and Krausz F, (2000), 'Intense few-cycle laser fields: frontiers of nonlinear optics', *Rev Mod Phys*, **72**, 545–591.
75. Treacy E B, (1969), 'Optical pulse compression with diffraction gratings', *IEEE J of Quan Electron*, **QE-5**, 454–458.
76. Pessot M, Maine P and Mourou G, (1987), '1000 times expansion compression of optical pulses for chirped pulse amplification', *Opt Comm*, **62**, 419–421.
77. Cheng Z, Krausz F and Spielmann C, (2002), 'Compression of 2 mJ kilohertz laser pulses to 17.5 fs by pairing double-prism compressor: analysis and performance', *Opt Comm*, **201**, 145–155.
78. Pretzler G, Kasper A and Witte K J, (2000), 'Angular chirp and tilted light pulses in CPA lasers', *Appl Phys B*, **70**, 1–9.
79. Cavalieri A L, Goulielmakis E, Horvath B, Helml W, Schultze M, Fieß M, Pervak V, Veisz L, Yakovlev V S, Uiberacker M, Apolonski A, Krausz F and Kienberger R, (2007), 'Intense 1.5-cycle near infrared laser waveforms and their use for the generation of ultra-broadband soft-x-ray harmonic continua', *New J Phys*, **9**, 242.
80. Tavella F, Nomura Y, Veisz L, Pervak V, Marcinkevičius A and Krausz F, (2007), 'Dispersion management for a sub-10-fs, 10 TW optical parametric chirped-pulse amplifier', *Opt Lett*, **32**, 2227–2229.
81. Angelov I B, von Conta A, Trushin S A, Major Zs, Karsch S, Krausz F and Pervak V, (2011), 'Investigation of the laser-induced damage of dispersive coatings', in Gregory J. Exarhos; Vitaly E. Gruzdev; Joseph A. Menapace; Detlev Ristau; M. J. Soileau, Editors, *Laser-Induced Damage in Optical Materials*, **8190**, 81900B, SPIE.
82. Von Conta A, (2011), 'Characterization of the laser induced damage threshold of mirrors in the ultra short pulse regime', Bachelor thesis, Hochschule Muenchen, Muenchen.
83. Mero M, Clapp B, Jasapara J C, Rudolph W, Ristau D, Starke K, Krüger J, Martin S and Kautek W, (2005), 'On the damage behavior of dielectric films

- when illuminated with multiple femtosecond laser pulses', *Opt Eng*, **44**(5), 051107.
84. Nguyen D, Emmert L A, Cravetchi I V, Mero M, Rudolph W, Jup e M, Lappschies M, Starke K and Ristau D, (2008), 'TixSi1-xO2 optical coatings with tunable index and their response to intense subpicosecond laser pulse irradiation', *Appl Phys Lett*, **93**(26), 261903.

Optical coatings for large facilities

C. GRÈZES-BESSET and G. CHAUVEAU,
Department of Thin Film Coatings, CILAS, France

DOI: 10.1533/9780857097316.4.695

Abstract: This chapter discusses the various fields of applications involving optical coatings for large facilities. A quick overview of the different technologies is given with their main advantages and drawbacks with a focus on large coating sputtering machine. Finally, we give highlights of two major programs involving sophisticated coatings.

Key words: large optical coatings, magnetron sputtering, ion beam sputtering, thin film uniformity.

19.1 Introduction

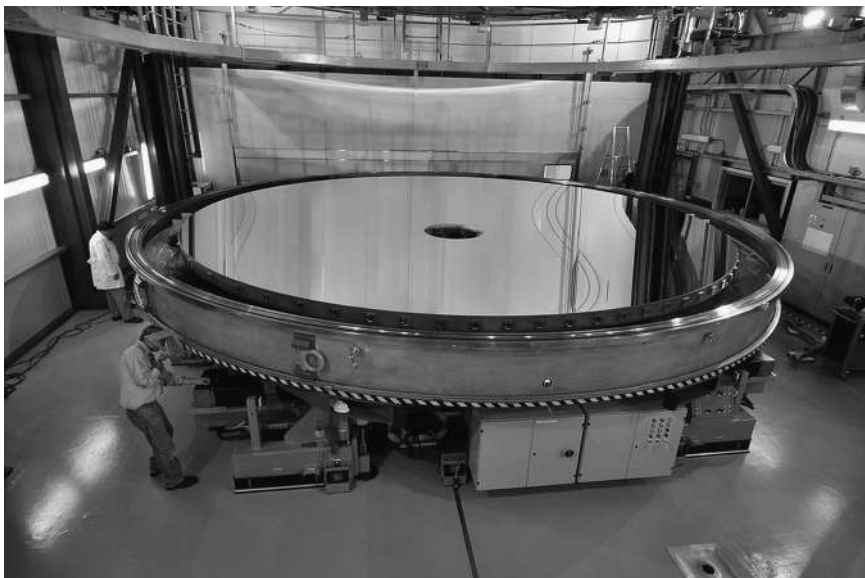
In the scope of this chapter we are dealing with the characteristics of coatings that are required for large facilities. In fact, it is necessary to consider both the industrial environment and the hard environmental conditions and also specific properties that are required for these components.

Moreover, in such facilities it is common to encounter optical components that present large dimensions and it is important to first define what is considered as large optics. In modern optical systems, progress in recent decades has led to dimensions in optics that now exceed 600 mm diameter that can be considered as large optics. As an example, mirrors for large telescopes commonly have a diameter greater than 1 m as presented in Fig. 19.1.

19.2 Domains of applications and major programs

Optical coatings have their use in large dimensions facilities and the coating technology is pushed to its limits due to the increasing demands on performances. The domains of applications of large optics may be split in different parts as the characteristics that are motivated are not the same; we will focus here on the following domains:

- Large scientific instruments,
- Laser,



19.1 The 8.2 m primary mirror of Yepun, Unit Telescope 4 of the European Southern Observatory (ESO) Very Large Telescope, after its recoating in early March (Credit: ESO/G. Huedepohl).

- Space,
- Astronomy,
- Solar.

19.2.1 Scientific large instruments

The first domain of applications concerns the Very Large Research Infrastructures (VLRI) for which cost of construction and use must be shared among several research organizations. Such VLRI allow the scientific community to access sophisticated installations and innovative technology that could not be supported by a lone laboratory. Major international collaborations between different countries are implemented to address fundamental experiments. Through such partnerships, it is thus possible to design, to develop and to maintain in operation very ambitious projects that could not have emerged alone; this is the case of international projects such as Virgo, for example, which will be presented in further detail.

Many facilities are implemented for many simultaneous users as is the case for the ESRF (European Synchrotron Radiation Facility) synchrotron in Grenoble, France, for example, dedicated to electromagnetic research intended for elementary particle acceleration and requiring multilayer

coatings for X-ray optical devices on substrates up to 100 cm long; another example is the Institut Laue-Langevin (ILL), which is an international research centre based in Grenoble, France, operating one of the most intense neutron sources in the world, which involves supermirrors based on several hundred layers of Ni/Ti coatings on large substrate surfaces.

On the other hand, facilities have also been established for a small number of simultaneous users such as big optical telescopes, or the forthcoming Extremely Large Telescope at ESO, and are also major specifiers of optical coatings. In this case, the sophisticated instruments installed in the telescopes require demanding spectral performances as well as environmental conditions. As an example, the ‘Planet Finder’ Instrument for the VLT, SPHERE (Spectro-Polarimetric High-contrast Exoplanet Research) involves many coatings and filters working at cryogenic temperature.^{1,2}

19.2.2 Laser

The large scale laser facilities that have been driven by laser fusion research are also huge users of optical coatings; we can quote some examples of current laser projects such as the National Ignition Facility (NIF) Project or the Laser Megajoule, for which very high fluences are the key driver of the optical components requirements.

Over about 50 years, many developments have led to reduced laser damage in optical coatings,^{3–8} involving the whole scientific community by the improvement of all the steps involved in the fabrication of coated components. Major works have been undertaken from the improvement of coating technologies to the implementation of post-processing steps by laser conditioning, where the optics are exposed to a progressively increasing fluence, allowing a large increase of the optic threshold of about a factor of two.

For these projects, many additional coatings are required such as reflective coatings, beam splitters and antireflection coatings on large substrate components and also small size components. As an example, the National Ignition Facility (NIF) – which is equipped with 192 laser beams and has been in operation since March 2009 – includes several thousands of large optics (1 m scale): mirrors, polarizers and transport mirrors, the size of which are compatible with the $40 \times 40 \text{ cm}^2$ beams and also smaller optics.⁹

Ambitious laser projects have been implemented around the world and we give hereafter a quick overview of these projects for which large optics are required:

- Upgrade of existing laser facility up to 10 PW: Vulcan is a 1015 W laser available to the UK and international research community. The Vulcan laser at the Rutherford Appleton Laboratory Central Laser

Facility in Oxfordshire, United Kingdom is constituted with 8 beams of 2.5 kJ each (~2 ns) pulse infrared neodymium glass laser. Vulcan is also capable of operating in frequency doubled mode where it can deliver about 1 kJ to a target at 532 nm in 2 ns pulses. One of the Vulcan beams is also available as an ultra-short pulse (~700 J in ~700 fs) ultra-high intensity beam using chirped pulse amplification called the ‘Vulcan petawatt’.

- HiPER: A new facility (High Power laser Energy Research facility) which will be a civilian facility whose main mission is to demonstrate that inertial fusion could be used as a future energy source.
- NIF: The largest and most powerful laser based in the US.
- LMJ: A laser facility (Laser Mégajoule) on a similar scale to NIF, based in France.
- ELI: A collaborative laser project (Extreme Light Infrastructure) based over several sites with the first in Romania.
- Orion: A new laser facility in Atomic Weapons Establishment (AWE), United Kingdom.
- XFEL: European free-electron laser project (X-ray Free-Electron Laser) based in Germany.
- Other projects currently ongoing in China, Japan, Russia and elsewhere.

Such complex projects require optical components of more than 900 mm diameter and 100 mm thickness coated with high reflective mirrors that must withstand more than 10 Jcm^{-2} at 1053 nm with pulse duration 1 ns. Requirements are also specified for wave front performance and sophisticated components are included in the laser systems involving adaptive optics systems.

As an example, we show here after a monomorph deformable mirror developed by CILAS for high intensity lasers (Fig. 19.2). In this case, the mirror is equipped with 63 actuators over an 85 mm useful aperture.

The ambitious collaborative European project ELI (Extreme Light Infrastructure) is a good example of the challenges posed by laser facilities. Optical coatings are considered as one of the bottlenecks of the project, which involves nearly 40 research and academic institutions from 13 EU Member States, forming a pan-European laser facility that aims to host the most intense lasers world-wide. It will require the production of large size optics and mirrors with dimensions of $250 \times 350 \text{ mm}$ with high damage threshold better than 1 Jcm^{-2} for 15 fs pulses; such mirrors require a 200 nm broad band of high reflectivity in the 700–900 nm spectral range.

Sophisticated coatings for gratings are also required, as is the case for the Apollon laser (150 J, 15 fs at 1 shot per min) currently under technological development at the Institut de Lumière Extrême (ILE) in Saclay, France. This laser uses the world’s largest ($940 \times 750 \text{ mm}^2$) gold gratings available at 800 nm wavelength for broadband spectrum from Livermore; these have been tested at a maximum fluence on gratings of 0.2 Jcm^{-2} .



19.2 Deformable mirror developed by CILAS for high intensity lasers.

A challenging goal is to increase the laser-induced damage threshold to a value of 1 Jcm^{-2} , as it would lead to avoiding one compressor and beam collimator in the laser. Thus research on coatings is in progress in order to meet this requirement; in particular, design and deposition processes are under development.¹⁰

Accurate wave front control is also necessary and deformable mirror development is considered as a technological leap as the ILE/ELI requirements are a useful aperture larger than 200 mm with hard dielectric coating for broadband femtosecond pulses.

19.2.3 Space

The Space industry, that has shown a tremendous growth of about ten percent per year in the last ten years, is another domain that requires complicated coated optics with strong environmental performance.

In this field of applications, a space-based observatory is considered as an attractive alternative solution to ground-based telescopes as it allows atmosphere turbulence to be overcome so that the limitation in angular resolution is only related to diffraction and also it permits work in the infrared and ultra-violet regions, which are strongly absorbed by the atmosphere. Moreover, due to the technological advances in reducing the weight of mirrors in particular, space telescopes have involved larger mirrors for several years.

With its 2.4 m aperture the Hubble telescope that was carried into orbit by a Space Shuttle in 1990 is one of the largest space telescopes. The Herschel Space Observatory of the European Space Agency, with its 3.5

meter diameter mirror, is the largest infrared space telescope ever launched, and has been in orbit since 2009. The protected mirror coating consisting of a 65 nm thick Al layer protected with a 25 nm thick MgF₂ layer has been achieved in one of the two coating facilities of the Calar Alto Observatory.

The James Webb Space Telescope (JWST), developed by NASA with the support of the European Space Agency and Canadian Space Agency, is intended to succeed the Hubble space telescope for infrared observation. The JWST will work at a low temperature of about 40 K in order to avoid the infrared emission from the telescope itself. It will include four instruments:

- NIRCam (Near-Infrared Camera), a wide field camera working in the near infrared (0.6–5 μm);
- NIRSpec (Near-Infrared Spectrometer), a multi-objects spectrometer working in the near infrared (1–5 μm);
- MIRI (Mid Infrared Instrument), a set constituted with a camera and a spectrometer working in the mid infrared (5–28 μm); and
- FGS (Fine Guidance System), an imaging system working over the range (0.6–5 μm).

The main scientific goals of the JWST are the first stars and galaxies in the universe just after the Big Bang. Planned for launch in 2018, the JWST will have a total mass of about 6200 kg.

The primary mirror, of 6.5 m diameter, is constituted with 18 individual hexagonal-shaped beryllium segments. The coating of the segments with a thin layer of gold, to be suited to infrared, is challenging but has been done successfully.¹¹

As an example of an international Japanese-led Japan Aerospace Exploration Agency (JAXA) European Space Agency (ESA) mission with collaboration including Canada, USA and South Korea, the SPICA mission (Space Infrared Telescope for Cosmology and Astrophysics), to be launched in 2022 for mid-infrared and far-infrared astronomy, is constituted with a cryogenically cooled telescope that involves a 3.5 m diameter primary mirror.

With the benefit of a large heritage from the Herschel program, the SPICA mission gathers the European industry and scientific community whose respective contributions are effective.

19.2.4 Astronomy

Generally, telescope mirrors are coated with a thin layer of highly reflecting material such as aluminum. It is common to install the coating plant next to the telescope for ease of refurbishing, which usually occurs at intervals

of some years due to normal ageing (oxidation and abrasion by airborne particles). In the case of the Very Large Telescope, this coating plant has a diameter of 9.4 m and is equipped with 8 cryo-pumps on the top of the vacuum chamber.

The Gemini Observatory, which consists of two 8.1 m diameter is located at Cerro Pachon in Chile; it should be noted that it is the first large telescope coated with a silver protective coating constituted of four layers. An advantage of a silver-based coating is that it leads to a reduction of the thermal infrared emission of the telescope by a factor of 2–3 compared to aluminum coatings. However, silver coating exhibits a lower reflectivity below 400 nm than aluminum coating though a higher reflectivity at wavelengths greater than 450 nm.

Generally, as large components are the result of a long and expensive process of fabrication, including molding, polishing and metrology before coating, it is necessary to guarantee a zero error coating process as far as possible. However, it is also necessary to provide a means to remove the coating in the case of major nonconformance encountered during this step or ageing effects due to environmental conditions. Processes involved in this operation are mainly based on immersion in chemical baths or under vacuum ion bombardment.

Very ambitious projects involving extremely large telescopes are in progress, and we can quote, for example, the Thirty-Meter Telescope, the Giant Magellan Telescope or the European Extremely Large Telescope (E-ELT); for the latter the primary mirror consists of nearly a thousand 1.4 m wide and 50 mm thick hexagonal segments. Adaptive mirrors are also incorporated into the optics of the telescope for the correction of the atmospheric turbulence that induces fuzziness in stellar observation from earth.

19.2.5 Solar plants

A solar furnace is a facility that gives out concentrated solar energy to produce very high temperatures. It is constituted by a complex optical and mechanical structure with automatically controlled systems, involving parabolic mirrors or heliostats that concentrate light onto a focal point at which the temperature may reach a value of 3500°C. The energy at the focal point is mainly used to generate electricity or to irradiate various materials for studying different effects (thermal, photonic, etc.)

The largest solar furnace is 54 m high and 48 m wide and opened in 1970 at Odeillo in the Pyrénées-Orientales in France, as the site presents clear skies up to 300 days a year; it is composed of 63 heliostats, plane mirrors which are automatically rotated depending on the direction of the sun that concentrate the solar rays onto a larger parabolic mirror constituted of

9500 square mirrors each 45 cm wide. Another solar furnace is located in Uzbekistan near Tashkent and with Odeillo these are the two largest solar furnaces in the world. Coatings of the mirrors consist of enhanced metallic mirror so that the efficiency in the blue region is optimized.

Other facilities are also available such as the high-flux solar furnace and xenon-high-flux solar simulator that are implemented at the Institute of Solar Research of the German Aerospace Center in Cologne, where irradiances of up to 5 MWm^{-2} and temperatures above 2000°C are achievable. The mirrors are made of float glass with a reflective layer of silver on their back side and coated on their front side with titanium oxide to guarantee the reflection of the UV spectrum of the solar radiation. Such systems are used for exploration and testing new technologies with concentrated sun-light and artificial light.

In terms of concentrating solar power collectors, the main challenges are increasing the lifetime of aluminum- or silver-based mirrors to exceed 10 years. The coating design and technology used have to allow low manufacturing cost. Different approaches are used in order to protect the metallic reflective layer. We can find, for example, thin glass mirrors which use 1 mm thick glass to protect against moisture, or adhesive polymer coated with a roll-to-roll technology using various techniques from sputtering to sol-gel.

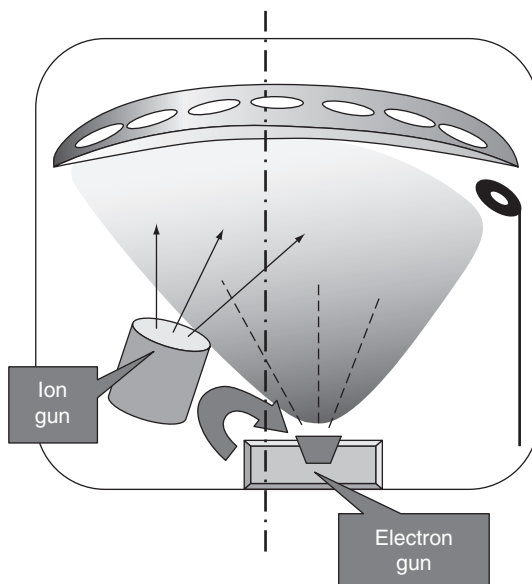
19.3 Review of technological solutions

Among the range of physical vapor deposition techniques that are available, the techniques that are mostly used for optical coatings are based on techniques of evaporation and sputtering.

19.3.1 Thermal and electron gun evaporation

Thermal evaporation under vacuum for which the material is evaporated from crucibles heated with electrical current and electron gun deposition under vacuum are the easiest physical vapor deposition techniques to implement. Such techniques allow the deposition of a large range of materials such as metals, semiconductors, or composite materials.^{12–15} Generally, as the energy of the ions impinging the surface of the substrate is very low, it is necessary to heat the substrate being coated to a high temperature of about 250°C up to 350°C . As a consequence, the deposited layers generally present a microstructure which is widely different from the bulk material evaporated.

Large area coating of protected or enhanced mirrors widely uses electron beam gun evaporation as this technology is easy to implement and the deposition speed is quite high. However, the microstructure of the deposited



19.3 Schematic of ion assisted deposition technique.

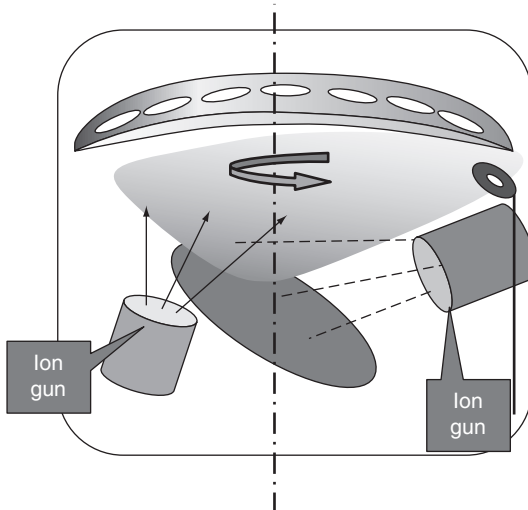
layers is known to be porous and this is a significant limitation for use in climatic environments.

To overcome these difficulties, we generally use assisted deposition by plasma or ion beams; in this case, as presented in Fig. 19.3, an ion beam gun is added inside the chamber, directed to the surface of the component to be coated, and it allows the density of the layer under construction to be increased while working at room temperature.¹⁶

19.3.2 Sputtering

Taking into consideration the environmental conditions to which the coatings will be exposed, it is necessary to use a coating technology that guarantees layer density is close to bulk.

Both ion beam sputtering (IBS) that uses one ion beam gun for sputtering a target or dual ion beam sputtering (DIBS) that uses a second one for compacting the sputtered material (Fig. 19.4) are particularly suited as the growth of the material is very close to bulk. The IBS technique has been widely studied by the French Laboratoire des Matériaux Avancés (LMA) in Villeurbanne for the production of low loss and low scattering mirrors involved in the Virgo project that will be presented later (see Section 19.6.2). The DIBS technique is the best technology for having very dense layers and high quality coatings. This technology is intensively used for manufacturing



19.4 Schematic of dual ion beam sputtering technique.

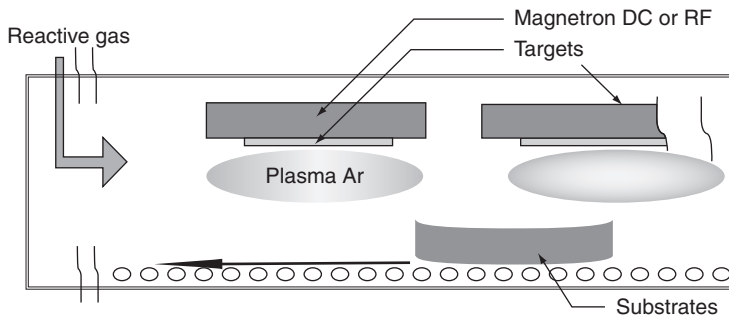
very narrow filters for the optical telecommunications market. The density of the deposited layer is very close to that of the bulk material and enables the optical functions to be nearly insensitive to environmental parameters. It enables very smooth interfaces too, that lead to a very low scattering level.

This is also an ideal technology for space applications as there is no measurable spectral shift between air and vacuum and with temperature variations, and because the coatings show very low ageing effects.

The second assisting ion beam is also used for cleaning the substrate before coating and leads to very good adhesion. The overall process is very stable and enables, together with optical monitoring system, excellent manufacturing yields.

Plasma sputtering technology has been widely used for several years^{17,18} as it allows high uniformity over large surfaces to be reached. A schematic of the magnetron sputtering technique is illustrated in Fig. 19.5. When the pressure inside the chamber is low enough (typically 5×10^{-3} mbar), the cathode is polarized at several hundred volts. This generates a plasma polarization – a mixture of ions, electrons and atoms – in the vicinity of the cathode. The magnets placed behind the cathode produce magnetic field lines and confine the plasma in the vicinity of the cathode. Sputtering takes place when the cathode material is bombarded with ions from the plasma. A major advantage of sputtering is the high deposition rates it is possible to obtain, particularly for metals.

Another interesting advantage is the energy with which the material is sputtered on the surface. Atoms or molecules collapse the substrate with



19.5 Schematic of an in-line magnetron sputtering technique.

a kinetic energy at least ten times greater than that of conventional evaporation. This produces denser layers and improves the mechanical attachment to the substrate. In addition, in comparison with the conventional evaporation, sputtering is extremely stable which allows for automation of deposition.

Figure 19.5 illustrates the main elements of a magnetron sputtering source, in the case of an in-line configuration. Rotative configurations are also available, and generally used for smaller components.

In order to produce uniform coatings on large optical components, it is necessary to optimize sputtering parameters in order to obtain a good level of uniformity, including the following main parameters which influence uniformity: magnetic field (which has to be adjusted regarding sputtered material), pumping speed uniformity, plasma power, target voltage, substrate potential, target-substrate distance and gas inlet position.

For reactive processes¹⁹ such as pulsed direct current (DC), radio frequency (RF) or mid frequency (MF), oxygen partial pressure is another important parameter which impacts the uniformity, both in terms of thickness and optical refractive index.

Fabrication technologies other than physical vapor deposition have to be mentioned as they are widely used in the optical thin film community. Examples are chemical vapour deposition (CVD) or sol-gel, although we will not discuss them in this chapter. For example the sol-gel process allows production of thin film, multilayer stacks constituted of nanoparticles of metal oxides (SiO_2 , ZrO_2 , TiO_2 , Ta_2O_5 , etc.) and is applied on large components for high laser flux resistance applications.²²

19.4 Thin film uniformity: key problem

When large components are involved or sophisticated optical functions are required, uniformity of performance of reflectivity and transmittance

is a key factor that has to be overcome. Further, directly linked to the uniformity of performance over the whole surface of the components, is the spatial distribution of thickness and refractive indices on the surface.

In fact, the effect of nonuniformity is directly connected to the complexity of the optical function to be performed. If some percentage of nonuniformity can be accepted in the case of standard antireflections, it will not be the same case for more complicated functions like narrow band filters. As the optical response is dependent on the optical thickness, the main parameters that must be mastered are uniformity of both thickness and refractive index for each material involved in the multilayer.

However, in the case of metallic mirrors, dielectric layers that are involved in the protection of the mirror or in the enhancement of the spectral response over a particular spectral range need to be precisely overcome.

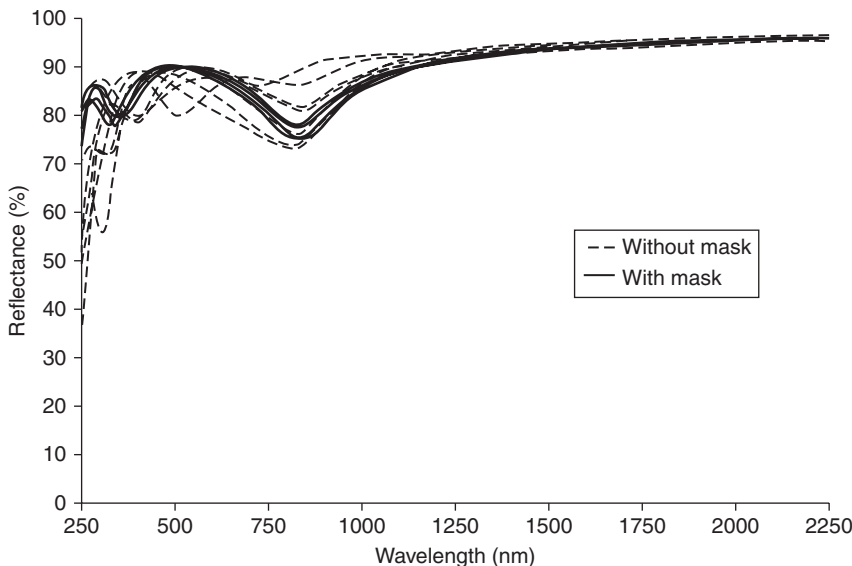
In the case of ion assisted deposition or sputtering, process parameters play a key role in the construction of the microstructure of the layers and a strict characterization of these parameters is necessary over the substrate holder to guarantee their stability.

Commonly, uniformity can be improved by the definition of a sample holder suited to the component and implementation of sophisticated masks of uniformity in the chamber can be necessary.^{23, 34} The problem may be very different depending upon the dimensions of the substrate. Although sometimes problematical, planetary or more complex movements can be implemented on smaller components which may not be possible for some to larger components.

Masking techniques are based on the fact that identical thickness repartition should be reached over the whole surface of the substrate. For this, a mechanical shape is positioned between the target and the substrates which aims to stop material deposition on some parts of the substrate and allow it on others. These techniques are commonly used in the thin film coating industry but some major drawbacks have to be managed: first, as the thickness repartition that will be reached will be close to the smallest thickness value deposited over the surface without mask, use of the mask may have a serious impact on the deposition rate, leading sometimes to a reduction greater than tenfold. Secondly, as the mask is located between the target and the substrate, coating is also deposited on the mask resulting in nonperfectly condensed material and greater thickness deposited on the mask, leading to potential pollution on the substrate.

However, as presented in the following paragraph, some significant improvements can be obtained to compensate sophisticated shapes on large components (Fig. 19.6) or to remarkably increase the uniformity on flat substrates.

In the case of large substrates, complex movements are difficult to implement related to parameters such as mass, inertia and size of the component; thus corrective masks could be a preferred solution. Improvement of deposition conditions also has to be implemented to achieve a uniformity curve



19.6 Improvement of uniformity obtained by masking technique on large concave reflectors (500 mm diameter, 200 mm high). Measurement of reflectivity with and without masking is undertaken on witnesses distributed over the reflectors.

which is as constant as possible, or at least characterization of this curve has to be undertaken so that it can be taken into account in the design synthesis of the stacks and their impact be assessed.

From a production point of view, the key parameters that play a major role during the process are the deposition rate, the partial pressure of oxygen, the temperature of the component and also the voltage and the current values of the ion beams and plasma that are responsible for the growth of the material on the surface of the component. However, and in most cases, it must be a trade-off between the process parameters and the production yield, as process conditions may have a direct impact on the deposition rate and consequently on the duration of the process.

19.5 Focus on large magnetron sputtering facility

In this section, we focus on the large deposition magnetron sputtering machine, known as PACA2M (PulvérisAtion CAthodique pour optiques de 2 Mètres), that CILAS has implemented for coating large optics up to 2 m, within a dedicated consortium, with the financial support of the French Department of Industry and of the local administrations, and with the help and the expertise of the French optical cluster (OPTITEC).

This innovative large size deposition machine (Fig. 19.7) has been developed to be able to coat large optical components, up to 2 m × 2 m, 40 cm



19.7 Two meter scale deposition sputtering chamber.

thick and 1.5 ton weight. It has been equipped with seven large planar magnetrons measuring 2.5 m, some of them can be polarized in DC or pulsed DC mode in order to coat metallic layers from a few tenths of a nanometer to hundreds of nanometers. Other pairs of magnetrons can be polarized in MF which allows the deposition of metals and also dielectric oxides under reactive atmosphere. An innovative 2.5 m long planar magnetron has been developed that can be polarized in RF mode in order to allow the deposition of dielectric oxides with or without a reactive atmosphere. In particular, it allows the realization of a dielectric oxide protective layer on silver.

An *in situ* analysis of the plasma emission is achieved with an optical device that monitors the gas flow rate and regulates the gas flow during reactive deposition.

Such a large coating machine is an in-line coating system in which the components to be coated are moving under the targets of the various materials. It is equipped with an automatic load lock system including a five position substrate holder stacker and a 9 m³ load lock chamber. It is possible to perform a glow discharge either under argon or oxygen to clean the component surface before coating, with the help of 2 m × 2 m electrodes positioned in the load lock chamber. Pumping down to 1×10^{-5} mbar of the load lock chamber can be achieved in 30 minutes. The main 14 m³ chamber is pumped down by 12 turbo pumps and a polycold® to reach a 10^{-7} mbar lower limit pressure.

With this sputtering system, it is then possible to produce optical coatings such as enhanced metallic mirrors, metal-dielectric absorbing coatings, or multi-dielectric coatings, deposited on different kinds of substrates. During the coating process, the substrate can be either polarized or at a floating potential.

Sputtering process optimization and characterization of plasma parameters can be implemented for different oxygen ratios, with the help of the ratio between optical amplitude of oxygen and argon rays emitted by the plasma, allowing the calibration of the required quantity of oxygen using a usual hysteresis curve (Fig. 19.8) which characterizes the two different operating modes of reactive magnetron sputtering (metallic mode and poisoned mode).²⁴

With such in-line configuration, non-uniformity is mainly parallel to the targets and can be optimized by tuning the sputtering parameters. In some cases, increasing the number of reactive gas inlets controlled with a dedicated plasma optical monitoring system could be also a way of improving coating uniformity. In a direction perpendicular to the magnetron, uniformity can be influenced by the modifications in the local geometry of the chamber due to the substrate movement that induces local changes in pressure, oxygen partial pressure, or target potential.

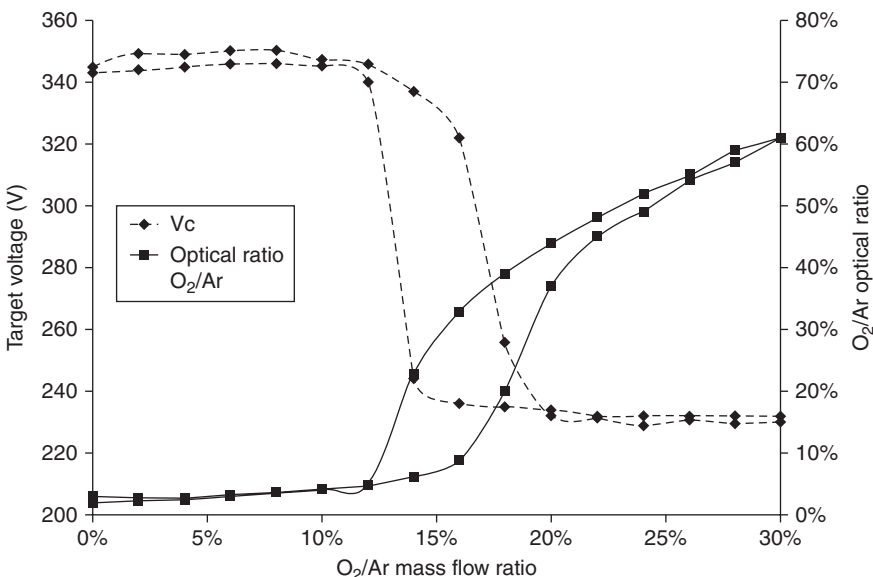
It has been shown that a uniformity value better than 5% can be achieved for various metallic and dielectric materials over 2 m × 2 m, and that it is possible to reach a value around 3% for non-reactive pulsed DC and RF sputtering and 1.5% over 1.5 m.

Production of metallic mirrors by magnetron sputtering technology is particularly well suited to severe environments as protected silver coatings can be fabricated with successful space qualification, including humidity tests and thermal cycling under vacuum.... Deposition on various types of substrates such as glass or silicon carbide is possible and additional dielectric materials can be used to enhance reflectivity.

For space projects, a major advantage of such a large coating chamber is that it allows production of flight model sets and spare sets in the same batch.

Moreover, this large coating machine has been equipped with an *in situ* broadband optical monitoring system that allows production of sophisticated spectral specifications on large optics, with a good agreement with theoretical design, such as multi-dielectric broadband antireflection or mirrors.²⁵

Specific optical systems have been developed for light beam entrance and exit inside the coating chamber, gathering emission and reception optics for transmission and reflection monitoring. Compatibility with the industrial environment is completed by the means of an all-fibered system equipped with 10 m long optical fibers; its all-fibered characteristics and its digital driving devices allow robust and fast processing over an extended spectral range from 280 to 2200 nm with a 10 000 high value signal-to-noise ratio that could be increased by increased averaging. However, with an in-line system, conventional continuous optical monitoring while the layer is growing is not achievable and intermittent monitoring has been carried out where the layer to be deposited is split in several steps at the end of which optical



19.8 Typical experimental hysteresis curve for SiO₂ reactive sputtering in pulsed DC.

measurement is done and monitoring of the next step is computed. With such a monitoring system, high spectral performances can be obtained, where production errors defined as the difference between *in situ* determined layer thickness and end-of-layer stop thickness set in the deposition strategy have a value less than 1% per layer. Moreover, accurate *in situ* refractive index characterizations and *in situ* thickness uniformity cartography on large surface coatings can be achieved due to the nine optical throughputs implemented at the top and the bottom of the large coating chamber.

Finally, due to the high stability of sputtering technology, deposition of layers of a few nanometers thickness is achievable with a good accuracy and metal-dielectric absorbers can be achieved accurately.

19.6 Highlights on two major programs

On the following paragraphs, we will now focus on two major programs that are demanding of complex and sophisticated coatings, as well for their size, shape, spectral performances or environmental conditions.

19.6.1 The Laser Megajoule (LMJ) project

The Laser Megajoule (LMJ) project led by the French nuclear agency is an experimental inertial confinement fusion (ICF) system located on the site

of CESTA (Centre d'Etudes Scientifiques et Techniques d'Aquitaine) near Bordeaux. The LMJ is 300 m long and will be one of the two most powerful lasers in the world. The system involves several thousands of high quality optical components, and has been dimensioned for 240 laser beams each producing an energy of 7500 J, which is focused on a 2 mm diameter target. A series of functions like mirrors, polarizers, transportation, or sealing is required and sophisticated coatings, most of them working in the infrared, are necessary to meet the requirements over a wide range of incidence.^{26–28}

Each laser beam consists of 40 large optics with demanding performance in terms of reflection or transmission, roughness, wave front quality, cosmetics, cleanliness, laser damage, etc., in order to guarantee the final performance of the laser and the lifetime of the components.

The laser chain is separated into several subsets the functions of which are, respectively, amplification, transport, frequency conversion and focus; at each stage, the requirements on the optics are different related in particular to beam dimensions and laser density.²⁹ Due to the square dimension of the beam, a major part of the optics is in the $400 \times 400 \text{ mm}^2$ dimensions.

Typical optical performances required on these components are a reflectivity higher than 99% for the mirrors, or a transmittance in p-polarization greater than 98.5% and lower than 1% in s-polarization for the polarizers.

The laser chains amplifiers, whose role is to increase the efficiency of the optical pumping, needs a high value of reflectivity. After the design phase, CILAS is in charge of the production of all the amplifiers, which are metallic reflective mirrors on large complex-shaped reflectors of about 1 m^2 dimensions, as presented in Fig. 19.9.

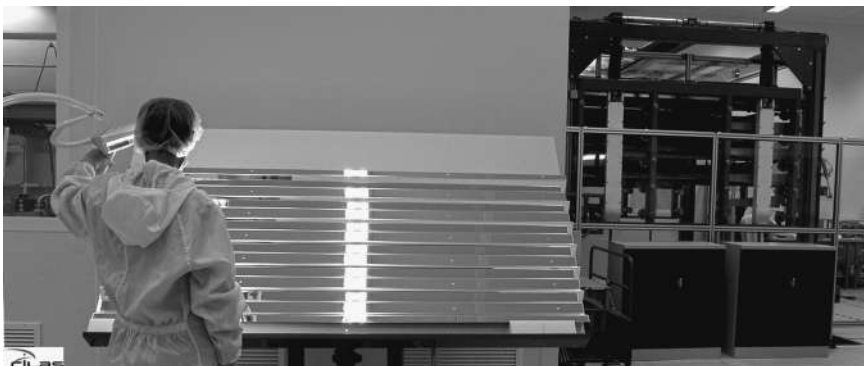
As mentioned above, coatings on large optics are mainly performed by evaporation techniques. As the magnetron sputtering technique leads to very dense layers close to bulk material, it is particularly well suited for applications that require environmental resistance, as it is the case for the LMJ program. Moreover, other properties that are required for the coatings are hardness, uniformity and also ability to clean it easily in an automatic washing system because the ultra-cleanliness of the LMJ hall of integration must be preserved.

The PACA2M magnetron sputtering machine that has been described above will produce the coating on more than 4000 m^2 of stainless steel substrates, some of them which are moreover not completely flat (Fig. 19.9).

In the framework of the LMJ program, such coating has been qualified on stainless steel and has been proven to resist thermal cycling ($-25^\circ\text{C}/+55^\circ\text{C}$).

19.6.2 The Virgo project

Another ambitious facility that implements large sophisticated optical components is the Virgo project in the field of gravitational wave interferometric detectors (GWIDs) located on the site of the European Gravitational



19.9 Complex-shaped, coated reflectors involved in the laser chains amplifier.

Observatory (EGO) in Italy.³⁰ An enhanced partnership has been established involving the teams from Virgo and also the others from similar projects such as LIGO (Laser Interferometer Gravitational Wave Observatory) constructed by the California Institute of Technology and Massachusetts Institute of Technology in the USA and German-British gravitational wave detector (GEO) in the UK and Germany.

This project is gathering a large number of experts from the international scientific community in a large variety of domains from optics to quantum physics and has driven advanced developments in the field of high reflectivity mirrors with very low losses as will be presented below.

The Virgo detector for gravitational waves consists of a Michelson laser interferometer that involves two orthogonal 3 km long arms, the optical length of each being stretched up to 120 km by the means of multiple reflections between mirrors located at the ends of each arm.

Key optical components are the large mirrors (diameter 35 cm, thickness 10–20 cm) developed by the French LMA in Villeurbanne that must be mastered in terms of optical shape imperfections, coating losses, mechanical losses, uniformity, etc. Exceptional characteristics of very low scattering and absorption are required for these mirrors and long-term developments at LMA have concentrated on ion beam sputtering (IBS) technology to enable the production of Ta_2O_5/SiO_2 multilayers to succeed. Such mirrors have been created on ultrapure fused silica substrates (Suprasil from Heraeus).³¹

A specific optical coating facility which is presented below (Fig. 19.10) has been built to produce these extremely high quality mirrors combining the highest reflectivity (over 99.999%), with nanometer surface control.

The cleanliness of the mirrors has also to be strictly overcome because it could induce losses that would result in a decrease of Virgo sensitivity due



19.10 Large $2.40 \times 2.40 \times 2.20\text{ m}^3$ IBS coater. (Courtesy of Laurent Pinard, Laboratoire des Matériaux Avancés—CNRS/IN2P3—France.)

to a thermal lensing effect. All the operations are thus performed in clean room laboratories with more than 500 m^2 of clean rooms available at LMA, involving 150 m^2 in ISO3.

As optical properties must be identical over the entire surface of the mirror, for reflection as well as for transmission, a very good uniformity of thickness is also essential.³⁴

Innovative thin film materials developments have been made at LMA to reduce the mechanical dissipation in the coatings which appears to be responsible for a limitation of mirror mechanical losses.³¹ In particular, such mechanical losses have been demonstrated to mainly occur in the high index material, and specific research has been focused on tantalum high index material. New alternative materials such as titania-doped tantalum pentoxide have been synthesized at LMA³² taking into account the optical absorption that has to be minimized in the coating.

For the next generation of interferometers (Virgo+), the symmetry between the two Fabry-Perot cavities becomes crucial and both mirrors have to be coated during the same coating run so that they could exhibit identical transmittance performances in both cavities. For this improvement, masking techniques have been considered and two masks for each material involved in the multilayer have been developed in order to control the coating thickness profiles on the rotating substrates.

A resulting value of 0.6% rms for the SiO_2 layer and 0.2% rms for the $\text{Ti}:\text{Ta}_2\text{O}_5$ layer, has been achieved, leading to a very low difference of 0.01% in transmission over 120 mm diameter between the two Virgo+ mirrors.^{33,35}

With such optimization of the high index material and implementation of doping the Ta_2O_5 with Ti atoms, a reduction of the extinction coefficient to a value of 4×10^{-8} at 1064 nm instead of 2×10^{-7} for non-doped Ta_2O_5 ³³ has been shown. Characterization of absorption by the photothermal deflection technique of low-transmission multilayer revealed an average value of 0.26 ± 0.05 ppm at 1064 nm over a diameter of 12 cm. This value has to be compared to 0.67 ppm with non-doped Ta_2O_5 high index material.³⁰

A perfect master of the shape of the mirrors is also needed as the imperfections may lead to additional losses in the cavities or reduction of contrast at interferometer output. It has been demonstrated that the substrate is a limitation as the multilayer coating replicates the initial surface. A corrective coating technique has thus been developed in order to lower the surface flatness by adding silica where it is needed and experimental results have been reported on an initial Virgo substrate down to less than 1 nm rms on 150 mm and less than 0.4 nm rms without astigmatism and residual curvature.³⁶

19.7 Conclusion

As a conclusion of this chapter dedicated to optical coatings for large facilities, we have seen that sophisticated coatings are involved in many different domains such as laser, astronomy, and space applications.

Optical coatings for large facilities become more and more crucial for major national or international programs. Successfully coating large areas involves challenges and risks first connected with substrate, polishing, flatness, cleaning and control. Durability, hardness and stability under severe environmental conditions are requirements which have to be fulfilled in regard to the growing demand of performances.

Recent progress in large coating technologies permits the management and optimization of major process parameters. Moreover, with the help of sophisticated monitoring systems, it is now possible to produce large scale components mastering key factors such as thicknesses, real indices and extinction coefficients, uniformity and stress.

In some situations, a compromise must be found between compacity and uniformity of films. Surely complete control of uniformity in the future will open the door to mass production of extremely complex filters.

19.8 References

1. J.L. Beuzit, M. Feldt, K. Dohlen, D. Mouillet, P. Puget, J. Antichi, A. Baruffolo, P. Baudoz, A. Berton, A. Boccaletti, M. Carbillet, J. Charton, R. Claudi, M.

- Downing, P. Feautrier, E. Fedrigo, T. Fusco, R. Gratton, N. Hubin, M. Kasper, M. Langlois, C. Moutou, L. Mugnier, J. Pragt, P. Rabou, M. Saisse, H.M. Schmid, E. Stadler, M. Turrato, S. Udry, R. Waters and F. Wildi, 'SPHERE: A 'Planet Finder' Instrument for the VLT', *The Messenger*, **125**, 29 (2006).
- 2. H. Krol, N. Valette, D. Torricini, C. Grèzes-Besset, K. Dohlen, D. Le Mignant, M. Saisse, G. Moreaux, M. Langlois, C. Moutou, A. Vigan and F. Lemarquis, 'IRDIS filters: from design to qualification', Advances in Optical Thin Films IV. Edited by Dobisz, Elizabeth A. and Eldada, Louay A. *Proceedings of the SPIE*, **8168**, 81680X–81680X-10 (2011).
 - 3. N. Bloembergen, 'Role of cracks, pores, and absorbing inclusions on laser induced damage threshold at surfaces of transparent dielectrics', *Applied Optics*, **12**(4), 661–664 (1973).
 - 4. J.O. Porteus and S.C. Seitel, 'Absolute onset of optical surface damage using distributed defect ensembles', *Applied Optics*, **23**(21), 3796–3805 (1984).
 - 5. M.R. Kozlowski and R. Chow, 'Role of defects in laser damage of multilayer coatings', Laser-induced damage in optical materials: 1993, in H.E. Bennett, L.L. Chase, A.H. Guenther, B.E. Newnam and M. J. Soileau, eds., *Proc. SPIE*, **2114**, 640–649 (1994).
 - 6. J.Y. Natoli, L. Gallais, H. Akhouayri and C. Amra, 'Laser-induced damage of materials in bulk, thin-film, and liquid forms', *Applied Optics*, **41**(16), 3156–3166 (2002).
 - 7. J. Neupert, D. Valla, J. Duchesne, P. Bouchut, L. Lamaignere, J. Bigarde and N. Daurios, 'Building high-damage-threshold surfaces at 351 nm', Optical fabrication, testing, and metrology, R. Geyl and L. Wangs, eds., *Proc. SPIE*, **5252**, 131–139 (2004).
 - 8. C. Amra, 'Endommagement laser dans les composants optiques interférentiels, Élaboration et caractérisation des cristaux massifs et en couches minces pour l'optique', © EDP Sciences (2005).
 - 9. C. Stoltz, C. Weinzapfel, G.T. Rogowski, D. Smith, A. Rigatti, J. Oliver and J. Taniguchi, 'Status of optical coatings for the national ignition facility', in *Optical Interference Coatings*, OSA Technical Digest Series (Optical Society of America, 2001).
 - 10. J.P. Chambaret (ILE/ ENSTA), 'The "10 PW Ti-Sapphire based" Lasers for the Romanian ELI NP Pillar. How far are we today from its availability?' ELI Executive committee Bucarest (2010).
 - 11. C. Childers, D. Patriarca, G. Sadkin and I. Stevenson, 'Gold coatings for the reflective optics on the JWST', Presentation given by I. Stevenson at Society of Vacuum Coaters (SVC) 2012 TechCon, Santa Clara, CA.
 - 12. L.I. Maissel and R. Glang, *Handbook of Thin Film Technology*, McGraw-Hill, New York (1970).
 - 13. R.F. Bunshah, *Deposition Technologies for Films and Coatings: Developments and Applications*, Noyes Publications, 2nd Ed., Park Ridge, New Jersey (1994).
 - 14. H.A. MacLeod, *Thin-Film Optical Filters*, Fourth Edition, CRC Press, Taylor and Francis Group, LLC (2010).
 - 15. P.W. Baumeister, *Optical Coating Technology* (SPIE Press Monograph Vol. PM137) ISBN 0-8194-5313-7, SPIE PRESS Bellingham, Washington USA.
 - 16. P.J. Martin, H.A. Macleod, R.P. Netterfield, C.G. Pacey and W.G. Sainty, 'Ion-beam-assisted deposition of thin films', *Applied Optics*, **22**(1), 178–184 (1983).

17. R. Hermann and G. Bräuer, 'DC and RF-magnetron sputtering', in *Handbook of Optical Properties: Thin Films for Optical Coatings*, R.E. Hummel and K.H. Guenther, eds., CRC Press, Boca Raton, Florida, Vol. 1, 135–187 (1995).
18. W.T. Pawlewicz, P.M. Martin, D.D. Hays and I.B. Mann, 'Recent developments in reactively sputtered optical thin films', *Proc. Soc. Photo-Opt. Instrum. Eng.*, **325**, 105–116 (1982).
19. W.D. Sproul, D.J. Christie and D.C. Carter, 'Control of reactive sputtering processes', *Thin Solid Films*, **491**(1–2), 1–17, Elsevier (2005).
20. G. Este and W.D. Westwood, 'A quasi-direct-current sputtering technique for the deposition of dielectrics at enhanced rates', *J. Vac. Sci. Technol.*, **A6**(3) (1988).
21. T. Rettich and P. Weidemuth, 'MF Sputtering- A powerful process tool for large area coating', 42nd Annual Technical Conference Proceedings of the Society of Vacuum Coaters, 147 (1999).
22. P. Belleville, P. Prené, C. Bonnin and Y. Montouillout, 'Use of sol–gel hybrids for laser optical thin films', *Mat. Res. Soc. Symp. Proc.*, **726** (2002).
23. L. Abel-Tibérini, F. Lemarquis and M. Lequime, 'Masking mechanisms applied to thin-film coatings for the manufacturing of linear variable filters for two-dimensional array detectors', *Appl. Opt.*, **47**, 5706–5714 (2008).
24. G. Chauveau, D. Torricini, C. Grèzes-Besset, D. Stojevski and M. Lequime, 'PACAA2M: magnetron sputtering for 2-meter optics', *Advances in Optical Thin Films IV*, Dobisz, E. A. and Eldada, L. A., eds. *Proceedings of the SPIE*, **8168**, 81680P-8 (2011).
25. D. Stojevski, M. Lequime, G. Chauveau, D. Torricini and C. Grèzes-Besset, 'Broadband optical monitoring for a 2-meter optics magnetron sputtering deposition machine', *Advances in Optical Thin Films IV*, Dobisz, E. A. and Eldada, L. A. *Proceedings of the SPIE*, **8168**, 81681G-8 (2011).
26. J. Daurios, 'Spécifications des grands composants lasers et métrologie optique associée', *Journée du Polissage Optique pour les Grands Instruments de la Physique et de l'Astronomie*, Bordeaux (2009).
27. B. Le Garrec, 'Lasers de puissance et composants optiques', *Journée du Polissage Optique pour les Grands Instruments de la Physique et de l'Astronomie*, Bordeaux (2009).
28. C. Chenais-Popovics and D. Vanderhaegen, 'Le Laser Mégajoule et la fusion inertielles', Laboratoire pour l'utilisation des lasers intenses, CNRS/Ecole polytechnique, CEA, from <http://www.cnrs.fr/publications/imagesdelaphysique>
29. L. Lamagnère, R. Courchinoux, J.C. Poncetta and H. Bercegol, 'L'endommagement des optiques du LMJ: problématique, mécanismes et métrologie', UVX 2010, 99–105 (2011), published by EDP Sciences (2011).
30. F. Beauville, F. Beauville, D. Buskulic, R. Flaminio, F. Marion, A. Masserot, L. Massonnet, B. Mouris, F. Moreau, J. Ramonet, E. Tournefier, D. Verkindt, O. Veziant, M. Yvert, R. Barille, V. Dattilo, D. Enard, F. Frasconi, A. Gennai, P. LaPenna, M. Loupias, F. Paoletti, L. Bracci, G. Calamai, E. Campagna, G. Conforto, E. Cuoco, I. Fiori, G. Guidi, G. Losurdo, F. Martelli, M. Mazzoni, B. Perniola, R. Stanga, F. Vetrano, A. Vicere, D. Babusci, G. Giordano, J.-M. Mackowski, N. Morgado, L. Pinard, A. Remillieux, F. Acerone, F. Barone, E. Calloni, R. De Rosa, L. Di Fiore, A. Eleuteri, L. Milano, K. Qipiani, I. Ricciardi, G. Russo, S. Solimeno, M. Varvella, F. Bondu, A. Brillet, E. Chassande-Mottin,

- F. Cleva, T. Cokelaer, J.-P. Coulon, B. Dujardin, J.-D. Fournier, H. Heitmann, C. N. Man, F. Mornet, J. Pacheco, A. Pai, H. Trinquet, J.-Y. Vinet, N. Arnaud, M. Barsuglia, M. A. Bizouard, V. Brisson, F. Cavalier, M. Davier, P. Hello, P. Heusse, S. Kreckelberg, C. Boccara, V. Loriette, J. Moreau, V. Reita, P. Amico, L. Bosi, L. Gammaitoni, M. Punturo, F. Travasso, H. Vocca, L. Barsotti, S. Braccini, C. Bradaschia, G. Celli, C. Corda, A. Di Virgilio, I. Ferrante, F. Fidecaro, A. Giazotto, E. Majorana, L. Holloway, R. Passaquieti, D. Passuello, R. Poggiani, A. Toncelli, M. Tonelli, L. Brocco, S. Frasca, C. Palomba, P. Puppo, P. Rapagnani and F. Ricci, 'Low loss coatings for the VIRGO large mirrors', *Proc. SPIE*, **5250**, 483 (2004).
31. D. Forest, P. Ganau, B. Lagrange, J.M. Mackowski, C. Michel, J.L. Montorio, N. Morgado, R. Pignard, L. Pinard and A. Remillieux, 'Ion beam sputtering coatings on large substrates: towards an improvement of the mechanical and optical performances', *Applied Optics*, **45**(7), 1436–1439 (1 March 2006).
 32. R. Flaminio, J. Franc, C. Michel, N. Morgado, L. Pinard and B. Sassolas, 'A study of coating mechanical and optical losses in view of reducing mirror thermal noise in gravitational wave detectors', *Class. Quantum Grav.*, **27**, 084030 (2010).
 33. L. Pinard, B. Sassolas, R. Flaminio, D. Forest, A. Lacoudre, C. Michel, J.L. Montorio and N. Morgado, 'Toward a new generation of low-loss mirrors for the advanced gravitational waves interferometers', *Optics Letters*, **36**, 1407–1409 (2011).
 34. B. Sassolas, R. Flaminio, J. Franc, C. Michel, J.L. Montorio, N. Morgado and L. Pinard, 'Masking technique for coating thickness control on large and strongly aspherical optics', *Applied Optics*, **48**(19), 3760 (2009).
 35. B. Sassolas, Q. Benoit, R. Flaminio, D. Forest, J. Franc, M. Galimberti, A. Lacoudre, C. Michel, J.L. Montorio, N. Morgado and L. Pinard, 'Twin mirrors for laser interferometric gravitational wave detectors', *Applied Optics*, **50**, 1894–1899 (2011).
 36. R. Bonnand, G. Cochez, J. Degallaix, R. Flaminio, L. Giacobone, B. Lagrange, F. Marion, C. Michel, B. Mours, P. Mugnier, E. Pacaud and L. Pinard, 'Improving the substrate flatness: the corrective coating technique', Gravitational Waves Advanced Workshop, Hawaii (May 2012).

Websites

<https://lasers.llnl.gov/about/nif/>
<http://www.clf.rl.ac.uk/Facilities>
<http://www-lmj.cea.fr/fr/lmj/index.htm>
<http://www.jwst.nasa.gov/>
<http://www.ligo.caltech.edu>
<http://www.ego-gw.it>

Optical coatings for automotive and building applications

C. H. STOESSEL, Southwall Technologies, USA

DOI: 10.1533/9780857097316.4.718

Abstract: This chapter describes the role of optical coatings in the design of energy-efficient glazing. The function of low-emissivity and spectrally selective coatings is well-established for architectural glazing, and is an emerging field in automotive applications, both increasingly defined by regulatory measures. The result is a broad range of coating solutions that respond to highly differentiated use requirements and need to be balanced with other glazing components for optimal performance.

Key words: energy-efficient glazing, low-emissivity coatings, spectrally selective coatings, passive house.

20.1 Introduction

Optical coatings provide important functionality in vehicles and architecture. Optical coatings can be found in countless applications such as rain sensors, headlight lens systems, lighting reflectors, rear view mirrors, motion detectors, or camera systems (to name just a few) that have been adopted from other application specialties. However, optical coatings in automotive and architectural glazing are a distinct application with specific market characteristics. Thus, this chapter focuses on the use of optical coatings on windows for use in vehicles and buildings.

Energy efficiency has become a prominent goal in western industrialized societies, particularly since the first 'oil crisis' in the 1970s, and is receiving renewed attention with the recognition of the role of energy consumption in the anthropogenic contribution to global warming. According to the United States Department of Energy,¹ fenestration influences approximately one third of all energy used in the USA, highlighting the role of energy-efficient glazing in vehicles and buildings. The impact of windows on energy consumption is various and complex, consequently many technical approaches have emerged for optical coatings to improve the performance of windows. Energy efficiency regulation increasingly shapes the requirements for architectural window coatings, while automotive window coating applications

are largely restrained by safety considerations imposed either by industry standards or government regulation.

After a discussion of the various use requirements and corresponding coating types for automotive and architectural glazing applications, the reader should have a good overview of coating options available today. An outlook on general industry trends from the perspective of the author will end this chapter.

20.2 The role of thermal control in glazing

Windows provide a visual connection between the contained (internal) environment and the external environment while maintaining a separation from the elements such as wind or precipitation. The desirable visible transparency of common commercial plate glass comes with a rather ‘transparent’ characteristic along a broader range of the electromagnetic spectrum, be it ultraviolet or infrared (IR) radiation. This transparency can result in a large energy transfer through windows that can result in undesirable heating of spaces from solar (daylight) radiation that require air conditioning to remove the built-up heat, or in excessive heat loss through windows by means of long-wavelength blackbody radiation that increases the heat load of an enclosed space.

The mitigation of thermal radiation transmission (either leaving or entering an enclosed structure) is an important function of windows. Optical coatings are just one means to accomplish this – well before the advent of optical coating technology, architects were adept at incorporating overhangs, louvers, storm windows, careful site selection, internal or external shading systems, and other design elements to achieve a comfortable built environment – so it is important to recognize that optical coatings compete with other techniques, and thus a thorough understanding of their costs and merits in a competitive marketplace is required. An awning or carefully designed external louver system in a south-facing window in a hot climate will doubtlessly be a simpler (and lower up-front cost) solution than an advanced switchable electrochromic window until specific design constraints or a more comprehensive energy analysis justify a coating-based solution. Fortunately, modern modeling tools (e.g., United States Department of Energy ‘EnergyPlus’) allow a very detailed analysis of the impact of various design options, and are routinely used by developers and architects that are conscious of the significant influence of a building on the long-term energy-efficient use of the built environment. Recent energy efficiency programs such as LEED (‘Leadership in Energy and Environmental Design’, developed in 1998 by the US Green Building Council), Energy Star in the USA or EnEV (‘Energieeinsparverordnung’) in Germany – to name just three of many national incentives and regulations – encourage the design of sustainable architecture, and recognize the role

of energy use in the overall ‘cradle-to-grave’ (life cycle) cost of a building, compared to the emphasis on low construction cost that tends to ignore opportunities to incorporate energy-efficient construction techniques that exceed basic construction code requirements.

Compared to architectural applications, thermal control in automotive glazing has historically been a niche market. This is largely due to the relatively small fraction of engine power required for cabin heating or cooling (and the fact that cabin heating is a convenient by-product of the classic internal combustion engine). Air conditioning in cars, however, is an ‘optional’ load, with a typical 400 W compressor load imposing added fuel consumption of at least 1 mile per gallon (mpg) (<http://www.nrel.gov/docs/fy00osti/28960.pdf>). However, since peak loads can be substantially higher and impose a much larger load on modern energy-efficient vehicles, studies identify air conditioning as the single most significant means to improve fuel economy (aside from the range of electric vehicles). Energy-efficient glazing employing thermal-control coatings is an effective means to reduce cabin soak temperatures and reduce air conditioning load.

20.2.1 Building window energy efficiency

For buildings in northern climate zones, thermal losses through poorly insulated windows are a significant source of wasted energy. Of the approximately 40% of the primary energy that was spent on buildings in the USA (<http://buildingsdatabook.eren.doe.gov/TableView.aspx?table=1.1.1>) in 2008, about a quarter (<http://buildingsdatabook.eren.doe.gov/TableView.aspx?table=1.2.5>) is spent on space heating. In view of the realistic prospect of ‘Zero-Energy’ buildings that eliminate the need for any external energy supply – to a large extent by efficiently harvesting the solar energy received through windows in the ‘passive house’ concept – adequate window coatings contribute significantly to energy conservation.

In the USA, the US Environmental Protection Agency (EPA) initiated the ‘Energy Star’ program in 1992 to promote energy-efficient products in order to reduce greenhouse gas emissions. In 1996, the EPA partnered with the US Department of Energy (DOE) to focus on certain products, and today the DOE maintains several laboratories and Government initiatives dedicated to energy efficiency. The DOE collaborates with industry and academia on defining voluntary goals and performance targets for energy-efficient products for the building envelope, including energy conservation targets and strategies for windows (<http://www.efficientwindows.org/>). For windows, the US Lawrence Berkeley National Laboratory (LBNL) develops thermal simulation software and maintains a database of glazing products (WINDOW) (<http://windows.lbl.gov/software/window/window.html>)

that allows modeling of the energy and visual characteristics of a wide range of window systems.

In Europe, the German ‘Energieeinsparverordnung’ (EnEV – law for the conservation of energy) is a leading example of energy efficiency legislation. In contrast to the promotional character of the US ‘Energy Star’ program, the EnEV mandates certain energy efficiency performance standards for windows (among many other products). EnEV regulates the total energy balance for buildings (with a targeted primary energy reduction by approximately 30% in 3-year intervals (http://www.bmu.de/fileadmin/bmu-import/files/pdfs/allgemein/application/pdf/klimapaket_aug2007.pdf, page 22 (in German))), and focuses on the energy transfer through the building envelope as a ‘system boundary’, thus taking the energy efficiency of windows into consideration.

In regions with intense solar radiation, a significant amount of energy is consumed to remove accumulating heat from buildings, mostly through air conditioning. Those regions are referred to as ‘cooling-dominated’. In commercial buildings with a higher window-to-wall ratio (compared to residential buildings), the cooling-dominated region even extends into moderate climate zones. Simple plate glass windows contribute heavily to the ‘greenhouse effect’ of trapping thermal energy. Along with the high energy transmission, glare is often a problem during sunny days in rooms with all but northern orientation, and shading is a common means to address these two issues. Well designed exterior shading fixtures such as awnings, louvers, or overhangs deliver excellent results (and are effective tools in the daylighting management toolbox of any architect), whereas interior shading fixtures (curtains, drapes, blinds) primarily address glare as they allow a significant amount of solar energy to enter the room without effective re-radiation of trapped heat.

Tinted glass is another common solution. However, most tinted glass is absorbing and becomes a significant source of radiant heat – for a simple single-pane of absorbing glass, 50% of the absorbed energy radiates into the room, whereas the exterior surface may get cooled from wind. The spectral performance of the absorbing glass plays another role – if it is absorbing primarily in the visible spectrum with little blocking of the infrared spectrum, the glare problem may be solved but the significant energy of solar infrared radiation will still heat up the room. Therefore, energy-efficient windows for cooling-dominated applications employ coatings to optimize the thermal performance.

Partially reflective coatings offer an effective approach for this application. In theory, sufficiently thick silver, gold, or copper coatings can reflect almost all of the solar radiation, and shading or glare control for the inhabitants is achieved by reducing the visible transmission to between 10% and 50%.

However, aesthetic demands often limit this approach – the high external reflectivity is often not desired, and architects often demand window designs that balance reflection and absorption to achieve a tolerable compromise between energy efficiency and design constraints. Laminated glass or multi-pane glazing opens up a myriad of possibilities by combining different glass types and coatings to achieve the desired effect and still be energy-efficient. More detail on design guidelines are given in Section 20.4.

Glare control typically is a ‘Comfort’ function of glazing in the visible solar spectrum, but the choice of glare attenuation can also affect the infrared portion of the spectrum, which often is an important consideration for the thermal performance of windows. Here, spectrally selective coating designs (explained in Section 20.3.2) allow de-coupling of glare and IR transmission functions.

20.2.2 Automotive window energy efficiency

As mentioned earlier, solar cabin heating of vehicles and the subsequent need for air conditioning has become a focus for energy conservation efforts in the automotive industry. The fundamental problem is similar to that of buildings in cooling-dominated regions, but the design constraints favor coating-based solutions – awnings and interior blinds are rarely options – and regulations mandate a minimum of visible transmission for windshields and front side windows in most countries. For example, in the United States, the minimum visible transmission of a windshield is 70%, and was only recently reduced from 72% in order to allow for more efficient dual-silver infrared-reflecting coatings that reduce solar heating of the cabin.

Thus, effective energy-efficient automotive windows have only been possible since the advent of spectrally selective coatings that allow a combination of the high visible transmission with the desired IR reflection. For cars, there also is a noticeable difference in cabin heating when parked or while driving – the moving air during motion can help cool absorptive windows, but the heat radiation of absorbing (often dark tinted) window glass contributes greatly to the cabin heat build-up of a parked car, illustrating how the shading function of tinted absorbing glass does not really present an effective means of energy conservation, contrary to common consumer perception.

20.3 Window coating types by functionality

In a window, energy travels primarily in three modes: conduction, convection, and radiation. Conduction is controlled by the conductivity of a glass pane, and is generally controlled by the thermal conductivity, k , of a bulk material.

Since optical window coatings are very thin compared to a glass pane, the conductive impact of window coatings is usually negligible. The conductive impact, however, becomes important when radiation control (transmission, reflections, absorption) comes into play. Convection plays a significant role in the energy efficiency of insulated glazing units (IGUs) that have one or more gas-filled cavities and the movement of the gas affects the heat transfer. Another convective contribution is how air movement (e.g., from wind in a building or a moving vehicle) affects the steady-state temperature of absorptive glass. In general, however, the biggest energy efficiency contributions in glazing come from controlling the radiative properties (emissivity) and spectral transmission properties of windows.

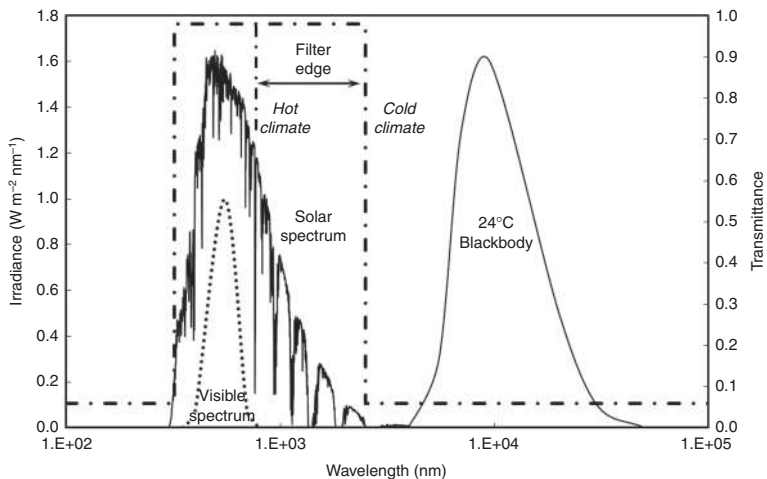
20.3.1 Low emissivity

While the control of transmission of electromagnetic radiation is important for windows, the role of thermal emissivity is a significant contributor to energy transfer as well. Any material surface will radiate energy at a given temperature, and the emissivity, ϵ , is defined as the ratio of energy emitted from a surface vs. a blackbody (perfect emitter) at the same temperature. For energy efficiency purposes, one seeks the smallest possible emissivity for a surface that is designed to minimize heat loss.

As a rule of thumb, highly glossy (reflective) or highly conductive materials have lower emissivity. Silver, in particular, is a preferred coating material for low-emissivity window coatings. While clear float glass has an emissivity of about 0.95, silver has an emissivity of about 0.02. Conductive tin oxide (SnO_2), along with similar materials of the group of transparent conductive oxides (TCOs), with an emissivity of 0.15–0.2 is another attractive low-emissivity material for windows. In Chapter 8 Carl-Gustav Ribbing explains the physics of emissivity. The physics and design characteristics of TCO coatings are described in detail by Clark Bright in Chapter 21.

20.3.2 Spectral selectivity (infra-red reflecting, ultra-violet blocking)

Spectral selectivity is another important concept in window coatings, as it allows customized transmission and rejection (either by reflection or absorption) of certain spectral ranges, such as in a bandpass filter. For windows, a common requirement is high transmission of the visible light (e.g., to allow occupants a clear view to the outside, or to enable daylighting of a room utilizing natural sunlight) while minimizing transmission of exterior solar heat or loss of long-range heat (infrared) energy from a room. Thus,



20.1 Graph of solar + blackbody spectrum with short/long pass.
(Source: Adapted from R. McCluney, 'Sensitivity of fenestration solar gain to source spectrum', *ASHRAE Transactions*, **10** (1996).)

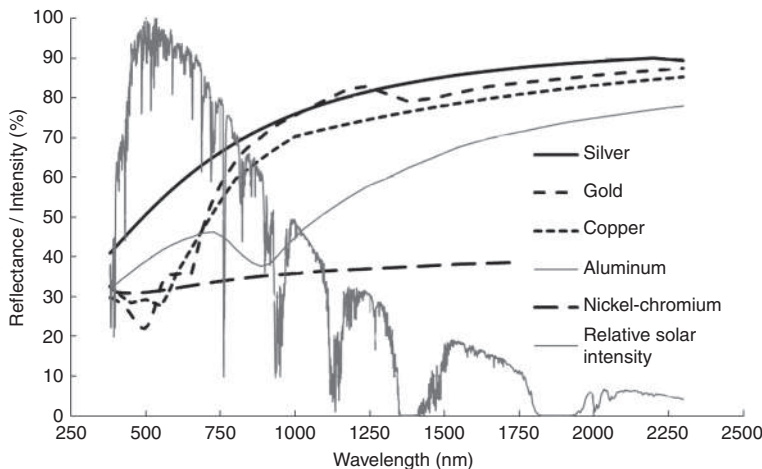
spectral selectivity applies to both heating- and cooling-dominated regions (Fig. 20.1).

As the solar spectrum delivers 52% of its total energy primarily in the (non-visible) infrared spectrum, blocking the IR portion of the solar spectrum (780–2300 nm) is an important function to suppress heat build-up in cooling-dominated regions. Ideally, this requires a very steep bandpass edge just past the visible spectrum.

Blocking longer-range IR radiation in the range of 2300 nm (the energy of a blackbody at $\sim 21^\circ\text{C}$ room temperature) is essential for conserving energy in a room in heating-dominated regions. Here, it is desirable to allow as much of the solar radiation to contribute to heating the building, while simultaneously suppressing the heat loss from room objects at room temperature by shifting the bandpass edge towards longer wavelengths.

In thin film form, most metals have a fairly uniform reflectivity across the solar spectrum, that is, they show no or moderate selectivity (Fig. 20.2). Copper and gold have the best selectivity² (especially compared to transition metals, which are essentially non-selective), and although not of optimum selectivity, in industrial practice silver is the preferred material as it combines practical selectivity with neutral reflected and transmitted color which is important for glazing aesthetics. The graph also shows the reflection properties of a nickel-chromium alloy, as an example for a material that is significantly more absorbing than noble metals.

The ratio of solar transmittance vs. visible transmittance for a thin film of silver is 1.2, and can be enhanced through the use of multilayer stacks,

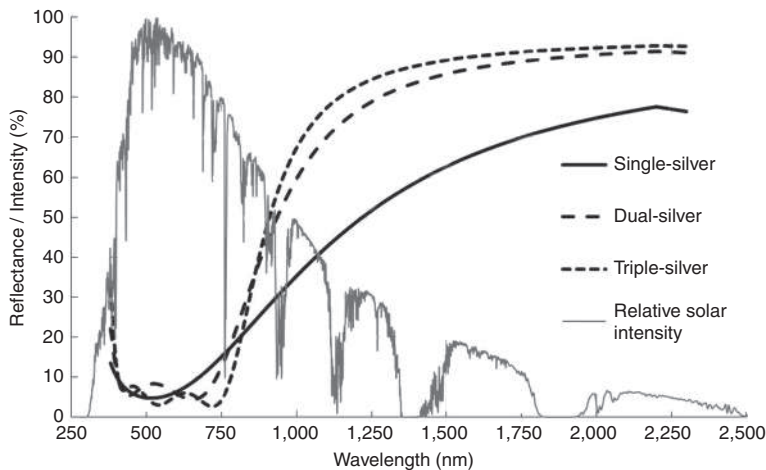


20.2 Graph of reflectivity of different metals at 15 nm thickness.

where the silver layers are separated by adequate dielectric layers of a thickness that effectively anti-reflects the entire stack as efficiently as possible. Such a stack design is known as an ‘induced transmission filter’. The dielectric layers in such a stack have the added benefit of protecting the sensitive metal layers. With this, the selectivity of a silver stack can be designed to approach the bandpass filter design indicated in Fig. 20.1, and with a much lower layer count than with a non-metal (i.e., all-dielectric). High-/Low-index Fabry–Perot filter, which might contain approximately 8–12 or more High-/Low-index pairs, and which is much thicker and more expensive to produce. Figure 20.3 shows the effect of single-, dual- and triple-silver stacks (each silver layer approximately 9 nm thick, and properly anti-reflection-coated for the visible spectral range). The resulting overall coating thickness (approximately 300 nm for a 2-silver stack) is significantly lower than what could be accomplished with a similarly performing all-dielectric filter stack.

20.3.3 Anti-glare

Avoiding the glare of bright sunlight is a common requirement in buildings and vehicles. By far the most common and cost-effective approach is the use of absorptive tinted glass. Glazing coatings can also be made absorptive, especially if suppression of excessive reflection in anti-glare applications is desired (however, if the coating becomes too thick it will become noticeably reflective, so this design approach has limits). Nickel-chrome (as shown in Fig. 20.2) is a typical example for this approach.



20.3 Graph of 30 nm silver stack – 1 × 30 nm, 2 × 15 nm, 3 × 10 nm, 4 × 7.25 nm.

Absorptive glazing solutions are notorious for their challenging thermal management properties. The absorbed light is converted to thermal energy, which heats up the respective component, and can lead to problems with stress build-up due to mismatch in the coefficient of thermal expansion (CTE). A hot, absorptive window also influences the thermal properties of the adjacent airspaces, and may require special considerations in the location of energy-efficient coatings by placing any reflective coatings as close to the heat source to minimize the absorptive heat load. This can result in a ‘mirror glass’ effect that building designers often try to avoid, preferring a more absorptive, anti-glare look, so the balance between aesthetics and thermal performance can result in some intricate glazing design compromises.

20.4 Glazing types: monolithic, laminated, and multi-cavity glazing designs

A glazing designer has three general window constructions available: monolithic glass, laminated glass, and multi-cavity glazing.

Monolithic glass consists of just a single window pane, coated or uncoated. In addition to any potential thin film coatings, monolithic glass comes in a vast array of clearness or absorptive tints (produced by adding minerals during the glass melt, and therefore distributed uniformly throughout the glass thickness), colors, transmissivity grades and glass types (e.g., borofloat glass, mid- or low-iron glass), all of which have different thermal and spectral characteristics. These glazing types are typically the building blocks for

more complex window structures, particularly laminated or insulated glazing units (IGUs).

Among the coated glass types, only the ‘hardcoat’ (pyrolytic) versions (e.g., for low-e glazing) are suitable for stand-alone, single-pane applications. TCOs (tin oxide, for example) are the prevalent candidates for such coatings. ‘Softcoat’ (sputtered) versions, especially those containing silver as a low-emissivity or spectrally selective component, require protection of the coating from the elements, and are suitable for laminated or IGU glazing.

Laminated glazings expand the application horizon by using two glass panes (or a glass plus an applied window film). Lamination of two glass panes requires an adhesive, which is typically polyvinyl butyral (PVB), or sometimes ethylene vinyl acetate (EVA), which is more expensive.

Laminated glass is often required for structural or safety reasons such as hurricane-resistant windows, intrusion protection in buildings, or impact resistance in automotive windshields, for example. Another common non-optical reason for laminated glass is sound attenuation. These requirements frequently dictate the thickness and type of PVB, but often allow integration of optical coatings, especially high-performing solar-selective coatings that may require protection from the elements (sputtered ‘softcoats’, especially) at the laminate interface. It is important to recognize that low-emissivity coatings lose their low-emissivity function when immersed in an adhesive (the thermal conductivity of the composite will prevail), but retain their IR-reflective function, and thus spectrally selective filtering can be integrated very effectively through adequate coatings.

20.5 Coatings on glass substrates

Most modern architectural glazing incorporates optical coatings for thermal and aesthetic functionality. Coating processes are often closely coupled to the glass float line (such as pyrolytic coatings), or in subsequent vacuum coating processes. They can provide the key functionalities of low emissivity (and spectral selectivity, with respective coating stacks) and glare reduction.

20.5.1 Low-emissivity coatings

Low-emissivity coatings on glass are divided into two families: pyrolytic ('hardcoat') and 'softcoat'. In Chapter 8, Carl-Gustav Ribbing explains the physics of emissivity.

Pyrolytic coatings are produced from CVD processes, and are all-dielectric materials, typically with indium tin oxide (ITO) as the functional low-e material (see also Chapter 21). The deposition process requires high temperatures to dissociate a gas-phase precursor for forming the coating, and is often implemented directly at a glass float line to take advantage of

the thermal energy from the cooling glass. Pyrolytic coatings can also be tempered and subjected to glass bending after the deposition process; they are hard, resilient and environmentally robust, and thus can be used on the glass exterior. This makes them an attractive option when a low-e surface is desired inside a room to boost energy efficiency of a multi-pane window, and the coating still tolerates user practices such as window cleaning. Modern pyrolytic coatings can also be combined with photocatalytic coatings (e.g., rutile titanium dioxide, TiO_2) to improve self-cleaning, or with hydrophobic window treatments that take advantage of rain to clean windows.

Softcoat low-e coatings have much lower emissivity in comparison to ITO-based coatings, due to the lower emissivity of silver that is part of the coating stack. Soft coatings are produced almost exclusively by magnetron sputtering, a vacuum-based physical vapor deposition (PVD) process that ensures optimum quality (thickness control, purity, and morphology) of the thin silver layers. The glass is usually coated in the form of large cut sheets in a semi-batch process to obtain the necessary high vacuum atmosphere required for best silver quality. The silver must be protected from tarnishing and degradation, and thus soft coats are more fragile compared to hard coats. Post-coating bending, forming, or tempering has only recently become possible, but is generally more problematic than for hardcoats. Softcoats cannot be used in exposed applications, and thus are typically found on the interior surfaces of IGUs where the noble gas fill and desiccant ensures a safe environment. In certain applications, it is also necessary to ‘cut back’ (grind off or edge-delete) the silver-containing coating stack at a glass edge to prevent deleterious environmental interactions with the softcoat stack at the edge of the glass.

20.5.2 Anti-glare

Anti-glare coatings aim at reducing reflective or transmissive glare, and are therefore almost always designed as absorptive coatings. For thin film coatings, metals such as chromium, nickel, or suitable alloys (nickel-chrome or even stainless steel in varying compositions) are the most typical materials. By choosing an appropriate coating thickness, the transmissive attenuation can be achieved rather easily, however usually at the cost of increased reflectivity, which can create aesthetic problems, and therefore it is typical to combine the metallic coating with tinted glass (or, in laminates, tinted PVB lamination adhesives or polymer films). Modifying the growth morphology of the metallic coating by creating a rough or porous coating can somewhat mitigate that effect but, in practice, it is not possible to achieve absorption that is lower than the resulting reflectivity (see the nickel-chrome profile in Fig. 20.2). Also, the aforementioned problem of absorptive heating and the responding thermal balance as well as stress build-up due to mismatch

in CTEs need to be taken into account. It is noteworthy that, for example, applying an absorptive tinted plastic window film to an IGU typically voids the warranty given by the IGU manufacturer because such windows are not designed for the thermal imbalance and the resulting stresses in the glass can lead to glass breakage.

20.6 Coatings on polymer substrates

Optical glazing coatings are very commonly applied to glass, but can also be deposited on thin, transparent, and flexible polymer films. The differences in coating substrates lead to differences in coating performance, applicable coating types, and coating process strategies for the two material groups.

The lower thermal budget of polymer films precludes them from use for hardcoat low-e coatings, and restricts them to vacuum thin film coated variants, especially magnetron sputtering, thermal evaporation, or low-temperature (e.g., plasma-assisted) variations of CVD, both in vacuum and atmospheric plasma. The lower tolerable coating temperatures also make it difficult to achieve the same coating quality as for glass (e.g., high-temperature deposited silver for improved nucleation and coating morphology, or post-tempering for post-oxidized indium tin oxide which is necessary to ensure optimum spectral and electrical/emissive functionality for this semiconductor material). The flexible substrate makes coatings more susceptible to stress effects such as curl. Proprietary additives in the polymer film may migrate and contaminate thin film coatings over time. Most polymer films have one side textured to prevent ‘blocking’ (the melding of coating wraps during storage or transport), and the surface roughness may degrade the nucleation and growth of an optimal solar control stack. Surface plasmon effects have been observed³ in high-performance low-e coatings, inducing absorption in the visible spectrum. High-index dielectric materials enhance the surface roughness effect, and leveling or smoothing layers or lower-index transition layers can mitigate the undesired effect.

Thin polymer substrates require special care and handling as they are prone to wrinkling, creases, can be difficult to clean, and can build up static charges, but they do provide a very cost-effective approach to delivering thin film coating stacks for glazing applications. Thicker substrates are more robust to handle in web winding and re-winding operations, and may be required for thicker coatings to control curl from the typically compressive sputter coating stack.

On the benefits side, coatings on thin polymer substrates have a significantly lower embodied energy when compared to glass, and enable reduced shipping, transportation, and installation costs. The capital investment required for a polymer film coating operation is much lower (at least half) when compared to a glass coating line of the same capacity, particularly for specialty applications as with the coating of curved substrates such as

automotive windshield glass. The possibility of incorporating functionally coated thin plastic films into glazing products through lamination or suspension significantly expands the design space for glazing designers.

The most common plastic type for glazing applications is polyethylene terephthalate (PET), a very ubiquitous plastic material. PET films for glazing are usually of the high-value variety (as compared to packaging PET) due to their superior optical clarity, well-controlled physical properties, and environmental stability. All major global PET suppliers (for example, DuPont, Teijin, ICI, Dow Chemical) sell high-grade PET films suitable for glazing applications. PET films can be impregnated with ultraviolet-blocking (absorbing) agents without degrading their optical, mechanical, or thermal properties to resist long-term yellowing, and to help protect against UV radiation damage. With proper material selection and application design, PET-based window products can easily exceed 30 years service life.

Another notable polymer substrate is ethylene tetrafluoroethylene (ETFE). Architects prefer this material for the design of clear tent structures due to its outstanding chemical robustness, radiation stability, and high temperature tolerance in combination with acceptable optical properties (clarity in the visible spectral range, neutral color) and acceptable cost. Recently, the use of this material in static or dynamic multilayer structures such as pneumatic cushions, that can be adjusted to meet changing seasonal or climatic thermal needs for a given structure, have received considerable interest⁴ and the material is suitable for enhancement with the same types of low-e or spectrally selective coatings as have been proven for PET films to improve the energy efficiency of resulting buildings. Since a cushion structure allows silver-containing softcoats to be protected from direct environmental impacts that would otherwise destroy the silver rather quickly, new concepts for the control of optical and thermal characteristics are conceivable. However, only very few such projects have been realized to date, and it remains to be seen how robust and reliable such coatings are over time.

20.6.1 Films for laminates

PET films with optical coatings can be found in many laminated glazing applications, particularly in the automotive or commercial architectural market where lamination is required for safety or other considerations. For such applications, it is important that the PET film and coating are compatible with the adjacent encapsulation materials (typically PVB, sometimes EVA). This covers chemical stability, mechanical integrity, and optical properties. Chemical compatibility requires that no additives that can potentially leak from the PET penetrate the top dielectric coating to degrade the silver. Mechanical integrity requires that the coating can tolerate the shear loads and thermal expansion mismatch that the lamination process imposes.

Optical compatibility requires that residual film stress does not result in excessive film waviness or optical distortion of the finished laminate, and may include the compliance of the film/coating structure to compound curvatures often found in automotive applications. In laminates with softcoated films, it is common to include a 'cutback' where the film is recessed from the glass edge by a few millimeters in order to embed the film edge in a seal of surrounding encapsulant to prevent any environmental degradation of the silver coating over time. Often, the cutback is obscured by printed perimeter patterns or the windshield adhesive or other window frame structures so that it is typically not noticed by the end user.

20.6.2 Films for multi-cavity glazing applications

Optically coated films also find applications in multi-cavity/multi-pane windows. They increase the thermal insulation achieved by adding additional cavities filled with noble gas (argon or krypton). The gas cavities can be separated by glass panes, or by suspending plastic films to create additional cavities.⁵ In such applications, one or more coated PET films are suspended in the space between the inner and outer glass pane, replacing what would typically be a glass pane for a triple- or quadruple-pane IGU. The benefit of using coated PET film is primarily a significant reduction in IGU weight (approximately 50% compared to an all-glass quadruple-pane IGU) as well as a thinner overall IGU thickness due to the thin film in comparison to the thicker glass, which helps accommodate multi-cavity glazing into traditional window frame dimensions. Silver-based low-e coatings perform very well in such applications as the noble gas environment and desiccant prevents long-term degradation (similar to soft-low-e coated glass panes), and the PET films usually preserve a more neutral color of the IGU as compared to the noticeable green tint imposed by additional soda-lime glass panes. The suspension systems for such PET films require special care to suppress distortion from wrinkles or other cosmetic blemishes.

20.6.3 Applied window film products for retrofit applications

Optically coated film products also enable retrofitting of existing windows for improved thermal efficiency by applying a flexible film to a window surface by use of adhesives. Aside from a few recent examples of low-e window films (which must expose the rather fragile softcoat to either the interior or exterior environment of a window in order to retain the low-emissivity functionality), the majority of these products aim at glare reduction (using absorptive/tinted films) and/or infrared reflection from suitable solar-selective coating stacks. Since silver is a typical component of most

high-performance solar control coatings, it must be protected from the environment, and is usually part of a laminate structure, resulting in a product that features an adhesive (for mounting to the glass surface, protected by a removable liner) and two PET films that encapsulate the silver-dielectric stack with the help of a suitable laminating adhesive. For added robustness, hardcoats or anti-fouling coatings can be added to the exterior laminate surface, improving scratch resistance and cleaning. Depending on additional use requirements (anti-glare, privacy), the laminate may include tinted absorptive PET or sputtered films.

20.7 Special considerations for applications

While the fundamental functionalities of glass, polymer films, and coatings described earlier constitute the common building blocks for windows, glazing applications for vehicles and buildings have distinct use constraints that influence the implementation of coatings.

20.7.1 Automotive applications

In comparison to architectural applications (which are subject to rather broad energy conservation requirements), the coating considerations for automotive applications face more complex regulatory and applications-related constraints. Windshields must meet requirements for both impact resistance as well as visible transmission, which extend to any coatings that are involved. Windshields must sustain impacts without penetration from exterior objects (into the cabin) as well as passenger ejection resistance (such as a head impact during an accident) that are qualified with rigorous tests in the industry, and require any coatings to maintain the mechanical integrity of the windshield laminate. This is particularly critical for laminated PET films, as the additional interfaces may introduce additional failure points. Since the impact resistance is primarily delivered from the plastic deformation of the PVB laminating adhesive, it is critical that the embedded PET film and coating stack does not diminish the structural properties of the laminating adhesive.

Automotive windshields have strict requirements regarding the minimum visible transmission (T_{vis}). For example, Europe⁶ requires a T_{vis} of at least 75% for windshields and at least 70% for sidelights and backlights, the US⁷ and Japan require a T_{vis} of at least 70% for automotive glazing. In practice, the 75% limit allows for just a single-silver IR-reflective coating, whereas the 70% limit can accommodate a more spectrally selective dual-silver coating.

Coating-based window heating applications

The permitted visible transmission limits have also allowed the introduction of resistive heating into windshields. While the most common technical approach is the use of microwires, sufficiently thick direct-coated ITO films

have been used in the past as well (see also Chapter 21). The thickness of the coatings is largely dictated by the required sheet resistance for the film, which itself is a function of the window dimensions, the contacting/termination approach, and the supply voltage applied. In the common 12 V systems, the resulting ITO film thickness will have a considerable reddish color in reflection (and particularly at angle), which is aesthetically undesirable. However, thin film based windshield systems avoid the 'starburst' phenomenon typical for microwire solutions, where the diffraction of the light from the headlights of an oncoming vehicle at night creates an irritating diffraction pattern in the driver's eye.

Perceived passenger comfort vs. energy conservation

The spectral property of an automotive window is only one of many factors that determine passenger comfort, and thus makes for a complex discussion. The IR radiation into the cabin can increase the absolute cabin temperature, but even at a moderate cabin temperature, sun exposure (whether with a high or low IR dosage) onto bare skin generates a different temperature perception. In addition, the radiated heat from absorptive surfaces (dashboard, tinted windows) further adds to the radiative heat load that alters the perceived temperature. Finally, the influence of forced or natural air circulation in the cabin can be significant, is more user-controllable through ventilation controls, and thus the improvement of air circulation (even at the expense of added fans and electrical load) competes with improved thermal control coatings in the automotive sector.

Dimmable windows/sun roofs

A few luxury vehicles also feature dynamic glazing in the form of electrochromic windows for privacy and shading control. Such coatings can mostly be found on sunroofs but also on some rear sidelights. These electrochromic coatings are directly derived from similar products in the architectural markets, and thus have similar performance characteristics and operating constraints. In automotive applications, integration into the control system based on a 12 V operating voltage is a particular hurdle, which is often solved by designing the window surfaces into sufficiently small segments so that the overall electrical resistance of the coating and the resulting operating voltage are acceptable.

An often-voiced concern about the use of electrically conducting coatings in motor vehicles is the potential attenuation of radio signals. It has indeed been shown⁸ that the use of metallic spectrally-selective coatings attenuates the signal of cellular phones, global positioning system (GPS) receivers (and possibly also toll collection transceivers and garage door openers), but technological alternatives such as the use of deletion zones (e.g., near the rear view mirror, where rain sensors or other sensors are already placed) or exterior

antennas (already common for satellite radio or pre-installed GPS receivers) are available and can resolve the ‘Faraday Cage’ effect while still enabling the energy-conservation benefits of implementing solar-selective coatings that can reduce carbon emissions in automobiles. Another approach to resolve the RF signal attenuation of conductive coatings is the substitution with all-dielectric (non-conductive) coatings stacks. However, such Fabry–Perot filters require very thick overall coating designs, significantly higher layer counts, show a high sensitivity to color variations when viewed at angle, and thus are complex and expensive and not a realistic solution.

Modern glass forming capabilities have extended the design envelope for automotive glazing, and it is now common to include complex curvatures in car windows. Beyond simple cylindrical glass bending, so-called ‘cross-curvatures’ (biaxial bending of glass over a 3-dimensional mold) allow for more refined contour integration. Bent glass poses a significant challenge for glass coaters. Among common thin film coating processes, only some CVD coating processes are truly omnidirectional (and allow the coating of virtually any geometry, including hollow structures), but solar control coatings are predominantly deposited with magnetron sputtering, which is highly directional. Therefore, the shape of the substrate directly influences the coating thickness uniformity. Coating uniformity can be modeled fairly well for a given deposition process, and some process variables can be adjusted to extend the capability range, but generally, windows with any significant curvature are difficult to coat without noticeable color gradations (the result of non-uniform film thickness).

One solution to the problem of applying spectrally selective coatings on curved glass is to coat the glass prior to bending with a coating that tolerates the subsequent bending temperatures. Pyrolytic coatings are the best candidates for this process. Another solution is the lamination of a plastic film that is coated with a spectrally selective coating. The latter approach lends itself especially to the manufacture of windshields, which need to be laminated anyway for safety regulation compliance, so including the plastic film and a second layer of PVB lamination adhesive can be accommodated rather easily. Pyrolytic coatings as well as plastic films allow a certain degree of cross-curvature.

20.7.2 Building applications

In architectural glazing, a specific coating or glazing solution is constrained by market conditions that quickly go beyond the simple question of which coating type or spectral performance is optimal to satisfy a certain application profile. It is important to understand the additional motivations or constraints the market imposes on a certain glazing solution.

The purpose of a building determines many aspects of its glazing solution. A big distinction is the difference between commercial and residential dwellings, or the difference in motivation whether the building is owned by the operator or leased/rented.

In an unregulated market, the owner/operator distinction highlights the different motivations of owners and operators: owners want to minimize construction cost whereas operators want to minimize operating cost. The resulting discrepancy between minimizing glazing cost and choosing an energy-efficient window is increasingly being resolved by regulatory requirements for energy efficiency, or – as is the case in Germany, for example – the need for a landlord to disclose the energy consumption of a rental building (especially residential).

Another application related distinction between commercial and residential construction is the size of individual windows. Residential windows tend to be smaller and of much more varied size and operator type compared to commercial construction which tends to be more standardized for a given building, and generally of larger size.

Another distinguishing concept of commercial buildings is the trend towards ‘curtain wall’ construction (especially in high-rises), which has a very different mounting system (the windows can become load-bearing members, so the structural integrity is important), and usually are fixed (non-opening). Commercial windows can also incorporate design elements where the exterior glass pane extends beyond the window opening to cover structural elements of the curtain wall structure or spandrels, which requires special window manufacturing techniques to accommodate the large setbacks (for multi-pane windows, removal of silver-containing low-e coatings, or additional printed aperture frames). Residential windows, in comparison, still follow the ‘hole-in-the-wall’ paradigm, are smaller, and typically require being opened for ventilation by the use of slider or turn/tilt operator types. It is important to recognize that the frame-to-aperture ratio influences the thermal properties of the overall window – multi-pane glazing can achieve significantly higher thermal insulation than common window frame systems, and for passive house windows that rely on large apertures, larger windows are desirable. This may sometimes create design conflicts – sliding windows typically have higher frame cross-sections than turn/tilt windows of similar window aperture, or historicizing muntins or grids that are embedded inside multi-pane cavities add to shadowing and can create undesirable thermal bridges that negate the benefits of advanced energy-efficient glazing coatings.

Integration of coatings into multi-functional glazing requirements

A recent trend in window technology diversification is the combination of glazing with additional functionality such as photovoltaics or dimmable/switchable glazing.

Building-integrated photovoltaics (BIPV) offer many opportunities to utilize the building envelope for solar electricity generation.⁹ The combination of photovoltaic (PV) structures with (typically semi-) transparent glazing is a niche technology that is often a compromise between the desire for solar energy generation and design goals, most often shading (but possibly also infrared-blocking – from the transparent conductors in a PV element – and UV-blocking from the use of suitable laminating adhesives) because a semi-transparent solar cell will not utilize the full amount of available photons for energy conversion. Amorphous and crystalline silicon are the most common PV elements, and dye-sensitized cells (DSCs) may have future potential but currently show very small conversion efficiencies. Considering the significant ‘balance of system’ expense and infrastructure for converters and wiring, a strong architectural design justification is typically driving such implementation, while a more conversion-efficient PV function can be obtained with opaque building components (some curtain wall structures may combine clear non-PV windows with adjacent opaque PV panels). Another design constraint for BIPV windows is the lack of standardized window sizes, as the solar panels are very difficult and expensive to build in custom formats. Therefore, installations tend to favor curtain wall designs that take advantage of the standardized formats of the PV cells but demonstrate the creative potential, e.g., by laminating with colored and screen-printed glass (for example a semi-transparent amorphous silicon solar panel in a office building staircase façade).¹⁰

Switchable glazing (or ‘smart windows’) is an attractive way to dynamically control the spectral properties of windows, and resolve the changing optical requirements during the day or the seasons.^{11,12} Although the fundamental concept of electrochromism is well established, development into robust, reliable, and lasting consumer products has been hampered by technical hurdles (mostly reliability for the two leading technical embodiments, thin film solid-state devices, and electrolyte exchange polymer-based devices), which translates into relatively high consumer prices that have moved little, and relegates electrochromic windows to niche applications. The need for electrical controls and thus supply of electrical power to windows is another hurdle that hinders broad adoption. Electrochromic windows, with their multilayer structures of transparent conductors, allow easy integration of several energy-efficiency functions beyond just-switchable shading (which primarily affects the visible spectrum), such as infrared reflection or ultraviolet blocking.

20.8 Conclusion

Optical coatings play a significant role in the design of modern windows for buildings and automobiles. The important contributions of low-emissivity

and solar selective coatings have long been implemented to improve the energy efficiency of windows in the building envelope, and a broad range of options of how coatings can be integrated into windows allows architects to adapt to regional climate conditions, additional functional building requirements as well as design preferences. The integration of ‘active’ functionalities such as electrochromics or building-integrated photovoltaics is emerging, but is currently confined to a high-cost niche market.

For automotive applications, optical window coatings have been implemented on a much smaller scale compared to architectural glazing, primarily due to design constraints (e.g., visibility requirements for windshields, coating curved window surfaces), but also a different cost/benefit profile for the implementation of energy-saving coatings in vehicles. Only recently have there been some regulatory efforts to promote the broader adoption of spectrally selective (IR-reflective) coatings (along with other approaches to improve energy efficiency by reducing air conditioning loads).

It is expected that regulatory conditions will increase the demand for low-emissivity and spectrally selective coatings to improve the energy efficiency, not only for buildings (where it is a well-established part of modern code requirements), but also in the automotive sector where it is relatively new.

20.9 Future trends

Improvements in energy efficiency will continue to be a primary motivator for the development of optical coatings for glazing. Emerging economies are expected to adopt energy-efficient glazing technologies much sooner and faster through regulation than has historically been demonstrated by developed countries. China, for example, is setting rather ambitious energy conservation goals for buildings in the recent 5-year plan that calls for a 20% reduction in energy intensity through various initiatives,¹³ with a large focus on new construction and building retrofits. This will force adoption of modern coating technologies, expansion of production capacity, and cost reduction, similar to what has resulted from energy efficiency regulation in Europe and the United States. The shift from energy efficiency as an optional/high-end product function to a mandated, broadly adopted standard will continue to drive the competition between competing technologies, and those that cannot realize major cost reduction will be left behind. One example might be electrochromic windows which, despite significant capacity expansion and government support in the United States, have not been able to demonstrate significant end-consumer price reductions, and may stand the risk of losing the ‘adoption race’ against, for example, a combination of improved insulating windows in combination with the replacement of incandescent lighting with energy-efficient lighting which responds to the energy-efficiency goal

of dynamic glazing. The urgency of cost reduction for broad adoption of new technologies is likely to increase due to regulatory mandates. Modern energy modeling programs already enable a thorough analysis of the complete energy footprint of a specific building, and the case scenario with the most attractive adoption cost will become more transparent.

For automotive glazing, it remains to be seen if energy conservation standards translate into direct regulation of the thermal performance of windows. Although eventually not implemented, the recent Californian ‘Cool Cars’ initiative¹⁴ called for a solar control function in car windows starting with the 2012 model year, but until the 2015 model year, only the windshield might have an IR-reflective coating in response to concerns about electromagnetic signal transmission, and subsequent implementation stages allowing for various glazing solutions. This is an example for the more complex balance of functionalities in automotive glazing resulting in less stringent regulatory mandates. Another market motivation may come from the electric vehicle sector – if the driving range reduction that results from the energy consumption to heat and cool an electric vehicle becomes a notable argument, it may indirectly drive the demand for energy-efficient vehicle glazing.

A specific hurdle for ‘active’ glazing components (electrochromic or BIPV glazing) that will need to be overcome is the market expectation for customized window formats and short lead times. Especially in the residential window market, this calls for innovative fabrication and interconnect techniques that compete with the practice in passive glazing of single-day turnaround for IGUs and fully automated manufacture of freely definable window sizes and configurations.

20.10 Sources of further information and advice

- US Department of Energy Efficient Windows Initiative: <http://www.energystar.gov/windows>
- National Fenestration Rating Council (NFRC): www.nfrc.org
- National Glass Association: www.glass.org
- European Glass and Glazing Association (UEMV): www.uemv.org
- Insulating Glass Industry Association (IGMA): www.igmaonline.org
- Glass Association of North America (GANA): www.glasswebsite.com
- American Architectural Manufacturers Association (AAMA): www.aamanet.org
- ‘Residential Windows: A Guide to New Technologies and Energy Performance (Third Edition)’ by Dariush Arasteh, John Carmody, Lisa Heschong and Stephen Selkowitz (2007), W. W. Norton & Company, ISBN 978–0393732252

- ‘Window Systems for High-Performance Buildings’ by Dariush Arasteh, John Carmody, Eleanor S. Lee and Stephen Selkowitz (2004), W. W. Norton & Company, ISBN 978-0393731219
- Glasstec trade show, Düsseldorf, Germany: www.glasstec-online.com
- Glass Processing Days trade show/conference: www.gpd.fi

20.11 Acknowledgements

I want to thank my colleagues and especially Rich Wipfler for sharing their insights and expertise in the area of optical coatings for glazing applications.

20.12 References

1. US Department of Energy: ‘Recovery Act: Advanced Energy Efficient Building Technologies’, Funding Opportunity Announcement DE-FOA-0000115 (2009).
2. E. Valkonen, B. Karlsson and C-G. ‘Solar optical properties of thin films of Cu, Ag, Au, Cr, Fe, Co, Ni and Al’, *Ribbing Solar Energy*, Volume **32**, Issue 2, 1984, 211–222.
3. R. Kleinhempel, A. Wahl, T. Böhme and R. Thielsch, ‘Einfluss der Oberflächenmorphologie auf die Performance von Low-E Schichtsysteme’ [Influence of surface morphology on the performance of low-e coating systems, in German], *Vakuum in Forschung und Praxis*, Volume **23**, Issue 1, 35–39, February–March 2011.
4. H. Poirazis, M. Kragh and C. Hogg, ‘Energy modelling of ETFE membranes in building applications’, Proc. 11th International IBPSA Conference, Glasgow, Scotland, 23–30 July 2009.
5. R. Lizardo and R. O’Shaughnessy, ‘Method of manufacturing a multiple-pane insulating glass unit’, United States Patent 4,335,166 (1982).
6. Standard UN/ECE R-43, ‘Uniform provisions concerning the approval of safety glazing materials and their installation on vehicles’, available at http://treaties.un.org/Pages/ViewDetails.aspx?src=TREATY&mtdsg_no=XI-B-16-43&chapter=11&lang=en European Standard ECE R-43.
7. US Federal Motor Vehicle Safety Standard 205 (49 C.F.R Part 571.205), SAE ANSI Z26.1–1996.
8. ‘Evaluation of electromagnetic interference due to automotive reflective glazing’, California Air Resources Board, Emission Research Section, Mobile Source Control Division, El Monte, California, November 2009.
9. M. Pagliario, R. Ciriminna and G. Palmisano, ‘BIPV: merging the photovoltaic with the construction industry’, *Prog. Photovolt. Res. Appl.*, Volume **18**, 61–72 (2010).
10. T. Massek, ‘Transparent Amorphous Silicon PV-Façade as part of an integrated concept for the energetic rehabilitation of an office building in Barcelona’, Proc. 20th European Photovoltaic Solar Energy Conference, 6–10 June 2005, Barcelona, Spain.

11. C. Lampert, 'Smart switchable windows for solar energy and daylighting control', *Solar Energy Materials and Solar Cells*, Volume **52**, 207–221 (1998).
12. N. R. Lynam and A. Agrawal, 'Automotive applications of chromogenic materials', in *Large Area Chromogenics: Materials & Devices for Transmittance Control*, C. M. Lampert and C. G. Granquist (editors),, Optical Engineering Press, Bellingham, Washington (1990).
13. M. Levine, L. Price, N. Zhou, D. Fridley, N. Aden, H. Lu, M. McNeil, N. Zheng, Q. Yining and P. Yowargana, 'Assessment of China's energy-saving and emission-reduction accomplishments and opportunities during the 11th five year plan', publication LBNL-3385E http://china.lbl.gov/sites/china.lbl.gov/files/LBNL_3385E.Ace_Study_Report_FINAL.pdf
14. California Environmental Protection Agency Air Resources Board: 'Cool Cars and Reflective Glazing', <http://www.arb.ca.gov/cc/cool-cars/cool-cars.htm>

DOI: 10.1533/9780857097316.4.741

Abstract: Transparent conductive thin films (TCTF) are widely used in electronic devices, and are of growing interest for devices on flexible substrates. Tin doped indium oxide (ITO), is the most used of the TCTF, but because of high cost and availability concerns with indium, there is considerable interest in alternative transparent conductive oxides (TCO). This chapter discusses ITO, alternative TCO and optically enhanced metallic thin films, which exhibit excellent flexibility and optical/electrical properties. The chapter focuses on TCTF properties and use in applications. Conductivity fundamentals, doping, optical properties related to conductivity and control of optoelectronic properties, are all discussed. Many traditional, recent and future TCTF applications are described.

Key words: indium tin oxide (ITO), transparent conductive oxides (TCO), metallic thin films, transparent conductive materials, transparent electrode (TE).

21.1 Introduction

Transparent conductive thin films (TCTFs) are widely used in electronic devices by almost everyone. Smartphones, tablets, computer displays and TVs are just a few examples of devices with TCTF. Tin doped indium oxide (ITO) is the most commonly used of the TCTF and is one of a family of materials called transparent conductive oxides (TCOs). There is considerable interest in alternative TCO to replace or be an alternative to ITO because of the high cost of ITO (indium) and concerns about the availability of indium (Schwarz-Schampera and Herzig, 2002). This chapter will discuss ITO, alternative TCO and some other TCTF alternatives. One non-TCO example of TCTF discussed in this chapter is optically enhanced (matched) metallic thin films. These antireflected metallic thin films can exhibit excellent optical/electrical properties, and can be very flexible (Bright, 2010b).

Examples of transparent conductive materials not discussed in this chapter are graphene, nanotubes, nanowires and conductive polymers. While there is considerable interest in universities and elsewhere in these alternatives

they are still emerging technologies and considered beyond the scope of this chapter.

There is growing interest in and demand for thin films and electronic and optoelectronic devices on flexible substrates. This chapter will focus on the electrical and optical properties obtainable with TCTF on flexible substrates and their applications. However, the properties of TCTF obtained on temperature tolerant substrates, which are often rigid, for example, glass, will be discussed for benchmarking what is achievable and for comparison with the properties achieved on temperature sensitive substrates, such as plastics. In addition, often little or no information is available in scientific publications for these TCFT and applications on temperature sensitive substrates, particularly plastics. TCTF on metal foil substrates will not be discussed here. Generally, they are considered ‘bendable’ but not ‘flexible’, and, of course, they are not transparent. TCTF on ‘flexible glass’ substrates will also not be discussed in this chapter; it too is considered ‘bendable’ but not ‘flexible’, and results on rigid glass substrates are included as appropriate. Because of the chosen focus on optical and electrical properties and applications, mechanical properties of TCTF and plastic substrates are not discussed. A limited discussion of the mechanical properties of TCTF and references to other work in this area can be found in Bright (2007, 2006), Cairns *et al.* (2000) and Leterrier *et al.* (2003).

21.1.1 Transparent conductive oxides (TCO)

Transparent conductive oxides are a class of materials, which have the unusual capability of being both transparent and electrically conductive. Today, there are no rules for identifying which metal oxides can be TCO (there are some empirical rules of thumb for dopants). Rather, TCO have been identified experimentally over many years. Examples of binary metal oxide compounds shown to be TCO when doped by defects, either extrinsic or intrinsic, are indium oxide (In_2O_3), tin oxide (SnO_2), cadmium oxide (CdO) and zinc oxide (ZnO). These hosts have been shown to be acceptable TCO with many different dopants and have been widely discussed (see for example, Ginley and Bright, 2000). Table 21.1, lists many TCO and dopants, which achieved good performance including these classic binary metal oxide hosts. The most widely known of these binary TCO is $\text{In}_2\text{O}_3:\text{Sn}$, commonly known as ITO. Doping of TCO is discussed in Section 21.2.

The optical and electrical (O/E) performance achieved by ITO with high and low temperature processes is summarized in Table 21.2. The values listed are typical values that can be achieved in industry with volume production, not the best values that can be achieved in the laboratory on small samples. Because ITO is the most widely used of the TCO, its performance will be

Table 21.1 TCO semiconductors for thin-film transparent electrodes

Material	Dopant or compound
SnO_2	Sb, F, As, Nb, Ta
In_2O_3	Sn, Ge, Mo, F, Ti, Zr, Hf, Nb, Ta, W, Te
ZnO	Al, Ga, B, In, Y, Sc, F, V, Si, Ge, Ti, Zr, Hf
CdO	In, Sn
ZnO-SnO_2	Zn_2SnO_4 , ZnSnO_3
$\text{ZnO-In}_2\text{O}_3$	ZnIn_2O_5 , $\text{Zn}_3\text{In}_2\text{O}_6$
$\text{In}_2\text{O}_x\text{-SnO}_2$	$\text{In}_4\text{Sn}_3\text{O}_{12}$
CdO-SnO_2	Cd_2SnO_4 , CdSnO_3
$\text{CdO-In}_2\text{O}_3$	CdIn_2O_4
MgIn_2O_4	
GaInO_3 , $(\text{Ga, In})_2\text{O}_3$	Sn, Ge
CdSb_2O_6	Y
$\text{ZnO-In}_2\text{O}_3\text{-SnO}_2$	$\text{Zn}_2\text{In}_2\text{O}_5\text{-In}_4\text{Sn}_3\text{O}_{12}$
$\text{CdO-In}_2\text{O}_3\text{-SnO}_2$	$\text{CdIn}_2\text{O}_4\text{-Cd}_2\text{SnO}_4$
$\text{ZnO-CdO-In}_2\text{O}_3\text{-SnO}_2$	

Source: Manami (2005).

Table 21.2 Typically achieved electrical and optical properties for ITO: (90% In_2O_3 /10% SnO_2)

	High temperature process (glass)	Low temperature (RT) process (plastic)
Resistivity (ρ) (ohm-cm)	$1\text{--}2 \times 10^{-4}$	$5\text{--}8 \times 10^{-4}$
%T Visible transmittance	$\geq *85\text{--}88\%$	$\geq *80\text{--}85\%$

*Includes substrate losses, 'Transmission' often given without these losses

Source: Bright (1995a–2012).

used as the comparison baseline for alternative TCO. Notice in the table the significant volume resistivity difference (~4×) between high temperature and low temperature processed ITO; the reason for this difference will be discussed in Section 21.2.2 on doping. Table 21.3 shows typical values of sheet resistance and the corresponding optical transmittance for ITO made by high and low temperature processes. Generally, the O/E performance of other binary host TCO, even with the preferred dopant, at best, may equal the performance of ITO but is generally inferior.

Less well known, are ternary and multicomponent TCO, which also have been investigated, typically by blending known binary TCO with or without defect dopants. Most often a mixture results but occasionally 'new' compounds are formed (see Table 21.1). Some of these compounds are excellent TCO while others are poor TCO. For example, cadmium stanate (Cd_2SnO_4), CTO, is an excellent TCO (Haack, 1976) comparable or

Table 21.3 Typically achieved sheet resistance and optical transmittance for ITO: (90%In₂O₃/10%SnO₂)

	High temperature process (glass)	Low temperature process (plastic)
Sheet resistance (R_s) ≈	10 ohms/square	50 ohms/square
Physical thickness, $d \approx$	128 nm ($\lambda/2$ optical thickness)	135 nm ($\lambda/2$ optical thickness)
$T \approx$	*85–88% luminous transmittance	*80–85% luminous transmittance

*Includes substrate losses.

Source: Bright (1995a–2012).

superior to ITO; while zinc stannate (Zn₂SnO₄) is a poor TCO. Another zinc stannate compound identified is ZnSnO₃, but its O/E properties are inferior even to those of the other zinc stannate compound, Zn₂SnO₄ (Minami, 1999). Another cadmium stannate compound (CdSnO₃) is also known but it is inferior to CTO. Conversely, certain mixtures of indium oxide and zinc oxide have produced TCO with good performance including a zinc indate compound (Zn₂In₂O₅) and related compounds, with equal atomic percentages of Zn and In (Minami *et al.*, 1996).

Multicomponent TCO have been made from mixtures of multiple binary or ternary TCO and sometimes with additional metal oxides for example, gallium oxide (Ga₂O₃) and magnesium oxide (MgO). The most successful multicomponent TCO to date, are made from the following systems:

- Zn-In-Sn-O,
- Zn-Ga-Sn-O,
- In-Ga-Zn-O and
- these three systems with various dopants.

Some of these multicomponent TCO, particularly IGZO, will be discussed in more detail when transparent oxide electronics applications are discussed. Multicomponent materials have, so far, become more important as semiconducting materials than TCO.

21.1.2 Transparent metallic thin films

Metals are highly conductive and when deposited as a very thin film, can be semitransparent to highly transparent. Noble metals and alloys, particularly silver (Ag)-based, are widely used as TCTF. Single layer metallic thin films like Ag and Au are typically semitransparent with significant reflectance. However, when antireflection by a high index layer on either side of the metallic thin film, the three-layer stack produces an optically enhanced metallic thin film, which is highly transparent. This three-layer construction

Table 21.4 Optical/electrical performance summary for ultra-transparent conductive materials (U-TCM): polymer/metal/polymer design on plastic film

ID	O/n	% T_{lum}	%* R_i μm	% T_{ave} (450– 650 nm)	% T_{ave} (400– 700 nm)	%* R_{ave} (450– 650 nm)	Color	
							x	y
2817 Ag	10.20	87.20	5.37	86.90	85.60	5.60	0.311	0.331
2810 Ag/Au	30.30	88.60	5.70	88.39	87.60	5.82	0.313	0.331
2690A Ag/Au	36.66	91.41	3.75	91.19	90.25	3.72	0.313	0.331
2703B Ag	23.71	91.62	4.10	91.15	90.81	4.11	0.313	0.331

Notes: Transmittance values include PET substrate losses.

*The spectrometer-measured reflectance values are intermediate between the first surface (coating) and total (2 surfaces) values.

Source: Bright (2010).

was originally called an induced transmission filter (Berning and Turner, 1957), and more information about their designs can be found in Macleod (2001). More current literature often refers to these constructions as dielectric-metal-dielectric (DMD), insulator-metal-insulator (IMI) or by listing the metal oxide used, whether it is an insulator or TCO, for example, ITO-Ag-ITO, or similar. Metallic thin films with enhanced nucleation can result in excellent O/E properties, and the stack can be very flexible, as reported recently by Bright (2010b), when (high index) polymers are used as the matching layers in a DMD design (Table 21.4).

21.2 Conductivity fundamentals

The classical free electron model explains the properties of metals based on the motion, that is, the kinetic properties, of the conduction electrons. As will be shown later, some optical properties of metals can be successfully explained with the classical theory. However, classical physics is unable to explain all the interaction of electrons with electromagnetic waves. Understanding these interactions is important to explaining the dependence of some optical properties (e.g., the bandgap) on the conductive properties of metals and TCO. Both the classical and quantum theory models are used in the following discussion.

21.2.1 Metals

The electrical properties of a metal are fundamentally related to its atomic structure. Highly conductive metals like copper, silver and gold, have a single free electron per atom. For copper, it is a 4s electron, in silver it is a 5s electron and in gold a 6s electron, where the number represents the principal quantum number (n). In these metals their conduction band is formed by these ns electrons. Recall that (Bright, 1995a–2012)

by definition, in a metal, the highest energy band, the conduction band, is only partly filled with electrons. The highest filled energy state in the conduction band is called the Fermi Level (E_F). The conduction band wavefunction is formed from the separate ‘s-state’ electron wavefunctions of the atom; hence, these metals are often called ‘s-band metals’. In a noble metal there is also a filled ‘d-band’, where the electrons are bound. The bound electrons of the metal ion core cannot carry an electrical current. This filled band below the conduction band is called the valence band.

Other effects, which occur, include broadening of the energy bands caused by disorder in the atomic structure of the solid, and excitation of an electron into the empty ‘p-band’ (the band above the conduction band) by absorption, i.e., interaction with an electromagnetic wave (EM).

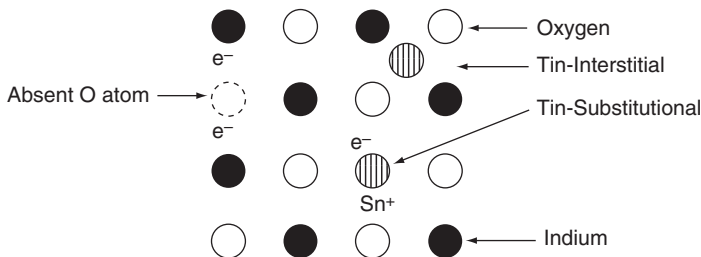
In metals electrical conductivity, σ , or its reciprocal resistivity, ρ , is a function of just two variables: the carrier (electrons) concentration per unit volume, N , and the mobility of the carriers, μ . However, the mobility is frequency (wavelength) dependent and therefore so is the conductivity (resistivity). The conductivity can be represented by the following equations (Bright, 1995a–2012):

$$\sigma(\omega) = Ne\mu(\omega) \text{ and for DC} (\omega = 0), \quad \sigma = Ne\mu = \frac{Ne^2\tau}{\epsilon_0 m^*} = \omega_p^2 \tau \quad [21.1]$$

where ω is angular frequency, N is the number density of electrons, e is the electronic charge, τ is the electron scattering time, ϵ_0 is the dielectric constant of free space, m^* is the electron effective mass and ω_p is the plasma angular frequency. The plasma frequency will be discussed further when the optical properties of TCO are discussed. From Equation [21.1] is clear that the mobility is directly proportional to the scattering time and is inversely proportional to the electron effective mass.

21.2.2 Doping

While metals have a partially filled conduction band and a filled valence band, by definition semiconductors have an empty conduction band and a filled valence band. However, when semiconductors are doped, an electron can be promoted from the valence band into the conduction band. In heavily doped semiconductors the valence band overlaps the conduction band, and the conduction band contains many free electrons. When this occurs, a semiconductor is called degenerate. Degenerate n -type semiconductors behaved electrically like metals. Because all highly conductivity TCO are degenerate n -type semiconductors, the expression for σ in TCO is the same as that for metals shown above in Equation [21.1].



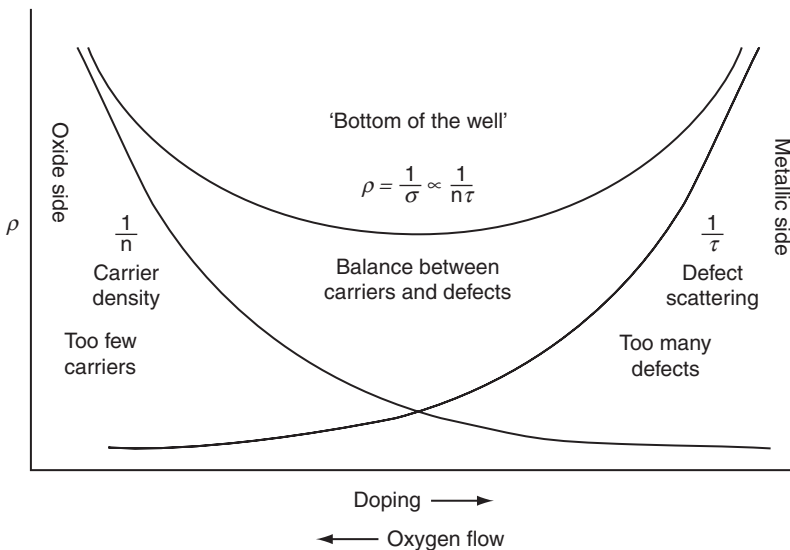
21.1 Basic physics of transparent conductive coatings. Over-simplified crystal structure and doping model for indium tin oxide. (Source: Adapted from Granqvist, 1989.)

In a semiconductor, the conduction electrons are created by impurity doping or by a lack of stoichiometry (defects). The typical TCO is a degenerate semiconductor, so it behaves electronically like a metal. For ITO and other TCO there is a threshold growth temperature required to activate an impurity metal dopant (~150°C for Sn in ITO). Most industrial ITO deposition processes for temperature tolerant substrates like glass, use substrate temperatures of $\geq 200^\circ\text{C}$ to promote Sn replacing In substitutionally in the indium oxide lattice (see Fig. 21.1). However, even in ITO, the conduction electrons are usually created *primarily* ($\geq 2:1$) by oxygen deficiencies ('vacancies' and tin interstitials) not tin doping (substitutional) (Fraser and Cook, 1972).

Deposition of ITO or other TCO on temperature sensitive substrates like plastics, at or near room temperature, results in virtually all of the conduction electrons being created by oxygen deficiencies, and virtually none by Sn substitutional doping. An oversimplified schematic drawing for these two doping processes is shown in Fig. 21.1. Because oxygen deficiency is the major cause of conductivity (and absorption) and its control during deposition and any postprocessing, is critical.

For any given TCO deposition process, there is a resistivity minimum. At low doping levels, the film resistivity is increased by a lack of conduction electrons. At high doping levels, the resistivity is increased by electron scattering from oxygen 'vacancies' and tin ions (ionized impurity scattering), reducing mobility. The minimum resistivity occurs when scattering caused by doping is comparable to scattering caused by all other mechanisms (Bright, 1995a–2012; Bright, 2012a).

A plot of resistivity vs doping will generate a curve demonstrating this relationship, which has been named the 'resistivity-well' (Bright, 1995a–2012; Bright, 2010a), Fig. 21.2. The resistivity-well will be discussed much further in Section 21.2.3 and used extensively in the discussion on control of optoelectronic properties.



21.2 Resistivity vs doping and the origin of the ‘resistivity-well’. TCO deposition process (Bright, 1995a–2012).

21.2.3 Optical properties related to conductivity

Of course, the optical properties of a material are related fundamentally to its atomic structure. A given material, for example, an insulating metal oxide, will absorb in selected wavelength regions because of its structure. The absorption coefficient, $\alpha(\lambda)$ or for convenience simply α , varies with wavelength, and is given by:

$$\alpha = \frac{4\pi k}{\lambda} \quad [21.2]$$

where k is the extinction coefficient and λ is the wavelength.

TCO

However, if this same metal oxide is doped and becomes electrically conductive additional wavelength regions of selective absorption occur. Therefore, in TCO some optical properties are related to the conductivity. In the near infrared (NIR) the optical properties are related to the conductivity, and can be modeled using classical Drude theory by the following equations. The plasma frequency is related to the conductivity as shown above by the equation:

$$\sigma = Ne\mu = \frac{Ne^2\tau}{\epsilon_0 m^*} = \omega_p^2 \tau \quad [21.1], \quad \text{then} \quad \omega_p^2 = \frac{Ne^2}{\epsilon_0 m^*} \quad [21.3]$$

$$\text{and } \omega_p = \frac{(Ne^2)^{1/2}}{(\epsilon_0 m^*)^{1/2}} \quad [21.4]$$

$$\text{or } \lambda_p = 2\pi c \frac{(\epsilon_0 m^*)^{1/2}}{(Ne^2)^{1/2}} \quad [21.5]$$

λ_p is the plasma (linear) wavelength and c is the speed of light in vacuum.

The free carriers needed for conduction in TCO will absorb incident EM radiation. The NIR absorption of photons by free-carriers (A_e) is given by:

$$A_e = \frac{\lambda^2 e^3 N d}{4\pi^2 c^3 n m^{*2} \mu} \quad [21.6]$$

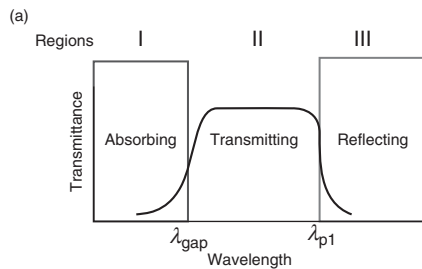
where d is the film thickness and n is the real part of the refractive index. A_e is directly and linearly proportional to the carrier concentration (Chopra *et al.*, 1983); however, free carrier absorption is also inversely and linearly proportional to the mobility (μ). Because conductivity is directly proportional to the product of N and μ but absorption is inversely proportional to μ it is better optically to increase conductivity by increasing μ rather than increasing N (Cotts *et al.*, 2000). Equation [21.6] demonstrates that the characteristic spectral optical properties of TCO are inherently related to its conductivity.

A schematic representation of the optical properties of TCO in three regions is shown in Fig. 21.3. The discussion above applies near the plasma wavelength and to the region shown as ‘Reflecting’ beyond the plasma wavelength. The spectral region shown as ‘Transmitting’ is typically the visible wavelength region, and the spectral region shown as ‘Absorbing’ is typically in the ultraviolet spectral region. The Absorbing region is a function of the TCO bandgap.

The spectral transmittance and reflectance for ITO determined by optical modeling for different N values is shown in Fig. 21.4. As shown in the figure the location of the plasma wavelength, determined by Equation [21.6], moves to shorter wavelengths with increasing N values. The location of the absorbing region due to the bandgap of ITO also moves to shorter wavelengths due to the Bernstein–Moss effect (Burstein, 1954).

Metals

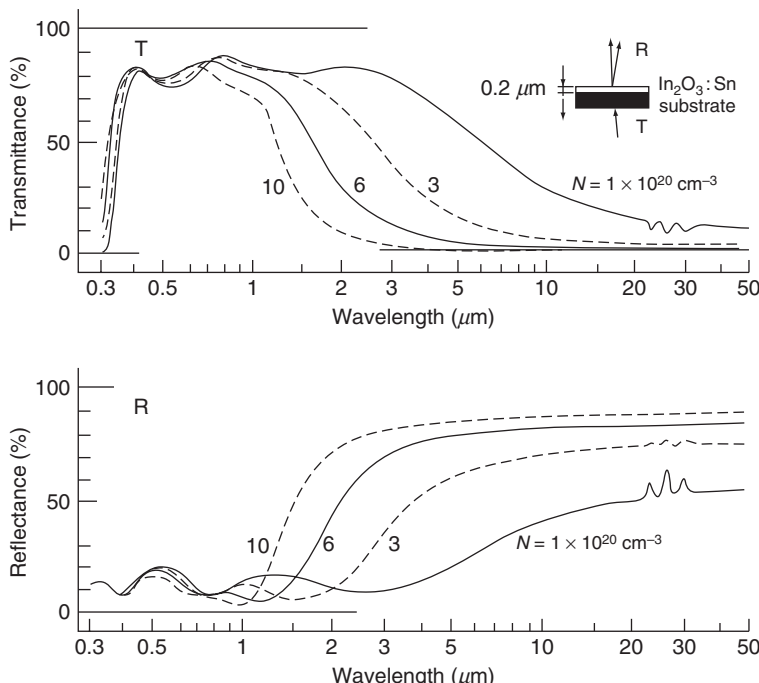
Similarly, the optical properties of metals are determined by its atomic structure. Also the optical properties of metals are described by Equations



(b)

- I $\omega > \omega_{\text{gap}}$ ($\lambda < \lambda_{\text{gap}}$) $k \gg n$ Like silicon in visible (high absorption)
- II $\omega > \omega_p$ ($\lambda < \lambda_p$) $n \gg k$ Like a dielectric (low absorption)
- III $\omega < \omega_p$ ($\lambda > \lambda_p$) $k \gg n$ Like a noble metal (high reflectance)

21.3 Basic physics of transparent conductive coatings. (a) Optical properties related to conductivity (classical Drude theory). (Source: Adapted from Simonis *et al.*, 1979.) (b) Three optical regions (Bright, 1995a–2012).



21.4 Optical properties related to conductivity: optics of TCO (ITO) thin films. Graphs showing change in spectral properties of ITO at bandgap and plasma wavelengths as a function of carrier density (N) (Granqvist, 1989).

[21.1–21.6] as discussed for TCO. However, in a metal the carrier concentration, N , is roughly two orders of magnitude greater than in TCO. Consequently, the plasma wavelength is located in the visible or ultraviolet regions. For example, gold has its plasma wavelength located in mid-visible causing the characteristic color of the metal. For silver, the plasma wavelength is located in the ultraviolet and it reflects highly over the entire visible (and infrared regions) with a neutral ‘silver’ color. A major difference between metals and TCO is that metals have a fixed N value but the N value for TCO are determined by the doping (deposition process), that is, TCO are engineered materials whose optical properties are controlled by their electrical properties.

Thin film metals exhibit the optical characteristics of their material; however, the optical properties can be modified by interference effects due to film thickness or interference effects of the optical construction, for example, the three layer stack described previously. Of course, TCO films can exhibit interference effects as well, even as a single layer.

Because the optical properties of TCO and metals are related to their conductivity, a compromise is always required, between high optical transmittance and high conductivity (low resistivity). TCO, for example ITO, or metals, have optical transmittance that is fundamentally limited by absorption and the amount of visible absorption depends on carrier concentration. As explained above, the visible transmittance and reflectance of conductive thin films are wavelength dependent (dispersive). Further, the optical performance can be generalized by conductor type (i.e., metal, TCO or semiconductor) and by waveband (UV, Vis, NIR, midwave IR and longwave far IR).

21.3 Control of optoelectronic properties

Process conditions have the largest effect on the O/E properties of TCO for example, ITO films. For a typical vacuum deposition process, the most important process variable is oxygen partial pressure (flow rate) because this will control the amount of doping by oxygen deficiency, that is, ‘vacancies’ (Zunger, 2003). As explained previously oxygen deficiency is the major reason for free carrier generation.

Substrate temperature during deposition is also a very important process parameter. As previously discussed in Section 21.2.2, substitutional doping with an impurity cation requires an activation energy which is typically achieved by heating.

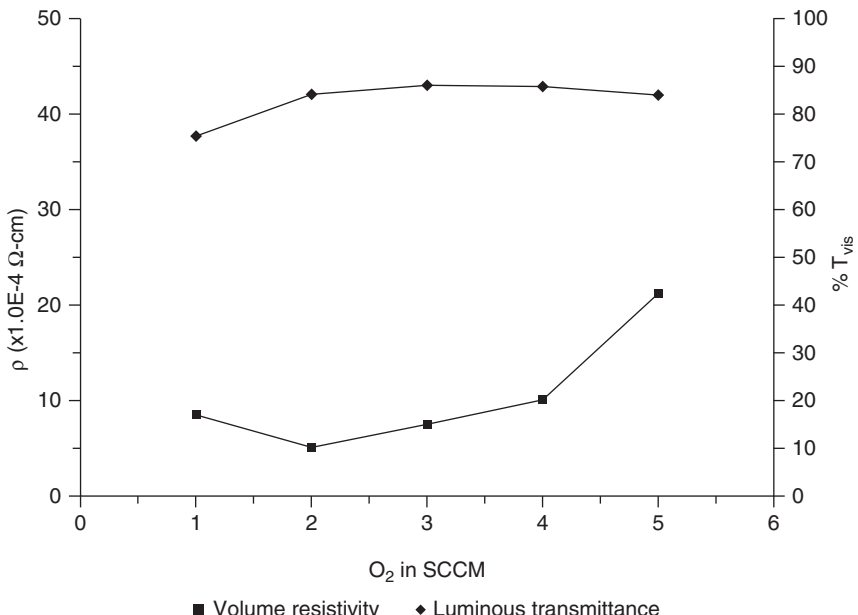
Of course, all of the typical process parameters that are important in thin film deposition such as deposition rate, vacuum level (pressure), gas or plasma conditions and deposition geometry, all influence film properties. But they do not directly affect the electrical and optical properties except in

terms of the film quality for example, crystallinity or microstructure, as they would for a dielectric thin film.

As explained in Section 21.2.2, for any given TCO deposition process, there is a resistivity minimum; at low doping levels, the film resistivity is increased by lack of conduction electrons and at high doping levels, the resistivity is increased by electron scattering from oxygen vacancies and dopant ions. The minimum resistivity occurs as was shown in Fig. 21.2, when scattering caused by doping is comparable to scattering caused by all other defects.

Consider for example the magnetron sputter deposition of an ITO film onto a plastic film substrate held at a temperature near room temperature in a roll-to-roll deposition process. After determining the sputter deposition conditions in argon, oxygen is added to the plasma. The oxygen flow rate is varied to create the resistivity-well as shown in Fig. 21.5. The O/E properties for the samples made with differing oxygen flow conditions are measured and plotted. By overlaying the O/E values on the resistivity-well chart the functional relationship between the optical properties, for example, percent transmittance, % T , vs doping (oxygen flow rate) can be determined, Fig. 21.5.

These optical and electrical relationships versus oxygen flow rate are very useful in controlling the deposition process to achieve the desired trade-off between electrical and optical properties of the TCO. Of course one can repeat the generation of these curves with different starting sputtering



21.5 Optical and electrical properties relationship of ITO thin films versus oxygen flow rate.

conditions to produce TCO thin films of differing thickness and sheet resistance (ohms per square).

While a vacuum sputter deposition process, which is most common for TCO, was described the same principles apply for other PVD, CVD or solution deposition processes but the control of the variables, for example, oxygen may be different and even indirect (Bright, 1995a–2012; Bright 2010a).

21.4 Beyond optoelectronic properties

While the optoelectronic properties of TCO are of paramount importance in many applications, other characteristics of the film also may be required. For example, in applications where the film will be deposited on flexible substrates and flexibility is required in the application, clearly the mechanical properties of the TCO are important. In some applications, for example organic light emitting diodes (OLEDs), the work function of the transparent electrode is critical for efficient charge injection. In some applications, durability for example, abrasion resistance and resistance to humid conditions of the TCO may be required. In such applications the selection, design and deposition of the TCO must accommodate these requirements. In the next section, applications of TCO will be discussed and the requirements of each application both optoelectronic and other requirements, will be addressed.

21.5 Traditional applications

There are a surprisingly large and growing number of applications for TCTF. In the next three sections many applications are described, which for context are divided in three categories: Traditional (21.5), Recent (21.6) and Future (21.7). The format of the discussion in the text is to provide an overview and methodology for designing a TCTF for each application. An associated Example ('figures/tables') demonstrates the detailed design of a TCTF meeting the specific Example's requirements. This format provides the reader with a 'handbook' of TCTF coating application examples, yet allows the reader to quickly focus on the details of an application of current interest.

21.5.1 Heaters

One of the earliest significant applications of TCO was for electrical heating of aircraft windshields during World War II. Doped tin oxide, $\text{SnO}_2\text{:Sb}$, was produced from a tin chloride solution containing antimony by pyrolysis on heated glass substrates (McMaster, 1947). Electrical heating of windshields and windows in aircraft and other vehicles is still a significant application of TCO today.

The pertinent design parameters for heated windows are the terminal resistance R_T , the power density W , the voltage V and the optical transmittance $\%T$. Formulae useful for designing a heated window are summarized in

- Power, $P = W \times A$, where W , is the power density (watts/in²) and A , is the total heated area
- $P = \frac{V^2}{R_T}$, where V is the applied voltage and R_T is the resistance of the heater coating and $R_T = R_{sheet} \frac{S}{L}$
- $A = A_{TRI} + A_{RECT}$ where $A_{TRI} = \frac{1}{2}[L1x(S2-S1)]$ and $A_{RECT} = [L1 \times S1]$
- S' is effective bussbar spacing and L' is the projected bussbar length
- $R'_{sheet} = \frac{V^2}{W(s')^2}$ and $S' = \frac{A}{L'}$ or if uncurved, $S' = \frac{s1+s2}{2}$
- the sheet resistance at any location, X , $R_{x,sheet} = R'_{sheet} \times \left(\frac{s1}{s_x}\right)^2$ and the power density is $W = \frac{V^2}{R_{sheet}S^2}$

21.6 Basic heater formulae (Bright, 1995a–2012).

Fig. 21.6. A design example for a heated window, using a low voltage source, to provide deicing/defogging capability and transmitting at several wave bands is summarized in Example 21.1. As shown, once the voltage source is known, the terminal resistance can be calculated to achieve the required power density. From the terminal resistance and the window geometry, the resistance of the coating sheet, either TCO or thin metal film, can be determined. Knowing the sheet resistance the corresponding optical transmittance must be achieved by selecting the coating type and by deposition process control. The measured electrical and optical performance for the window of the design example is shown in Example 21.2 (Bright, 1995a–2012; Bright 2010a) on page 756.

21.5.2 Electromagnetic interference shielding

Electromagnetic interference (EMI) shielding is another traditional application of TCTF. Any active electronic device which has a display is a likely candidate for an EMI shield. Because the display must have some type of transparent opening or window for viewing, radiation can escape from or be incident through this aperture. The rest of the device can, typically, be contained in an opaque conductive enclosure. To form a ‘Faraday cage’ shielding the device by some type of transparent conductive material must cover the viewing aperture. Often a TCTF-like ITO or a metallic thin film is chosen for the EMI shield.

The equations for far field EMI shielding effectiveness (SE) are shown in Fig. 21.7. As shown the SE is proportional to the logarithm of the inverse of the sheet resistance. Therefore, the lower the resistance or the higher the conductivity, the higher is the shielding. A design example for a device requiring 20 dB of SE and visible transmittance of $\geq 85\%$ is summarized in Example 21.3 on page 757. From the calculation of SE the required sheet resistance is ≤ 20 ohms per square. Any TCTF of 20 ohms per square or less and a corresponding transmittance of 85% or greater can meet the design requirements (Bright, 1995a–2012; Bright 2010a).

(a) Requirements:

- Heater specifications:

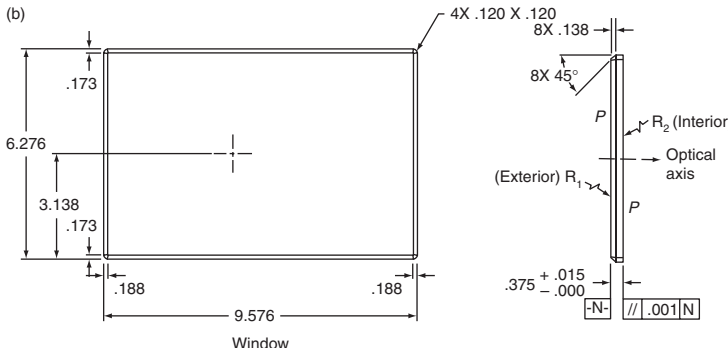
Power density of 1.4 watts/in² from a 25 volts, DC power source

- Coated window transmittance:

T visible	>84% from 525 nm to 625 nm
T average	>83% between 700 nm and 900 nm
T laser	>82% at 1070 nm

- Laser damage resistant (36 mw/cm², 20 ns FWHM, 20 pps)
- Durability to Mil-C-48497

(b) Explanatory diagram



(c) Approach:

- Choose Materials And Deposition Process For High Durability (Metal Oxides And High Temperture)
- Try two layer ITO/SiO₂ coating design to meet optical requirements
- Use halfwave (or multiples) SiO₂ thickness to minimize laser damage
- Adjusted optical design for electric field control at interfaces
- Select ITO thickness for optical requirements
- Adjust ITO deposition process parameters to produce nominal sheet resistance at thickness determined by optics

(d) Determining coating parameters:

- From window drawing, requirements and basic formulae
- The separation (*S*) between bussbars is 6.0" (bussbar width of 0.138")
- The total heated area, *A* = *S* × *L* = 6.0" × 9.20" = 55.2 in²
- With a power density, *W* = 1.4 watts/in² and *A* = 55.2 in², the power is *P* = *W* × *A* = 77.3 watts
- The nominal sheet resistance is given by
- $R_{\text{SHEET}} = \frac{V^2}{WS^2} = \frac{(25)^2}{1.4 \times (6.0)^2} = 12.4 \Omega/\square (+/- 1.8 \Omega/\square = 10.6 - 14.2 \Omega/\square)$
- *R_T* is the resistance of the heater coating and $R_T = R_{\text{Sheet}} \frac{S}{L}$
- $R_T = \frac{12.4 \times 6.0''}{9.20''} = 8.1 \text{ ohms} (+/- 1.2 \text{ OHMS} = 6.9 - 9.3 \text{ ohms})$

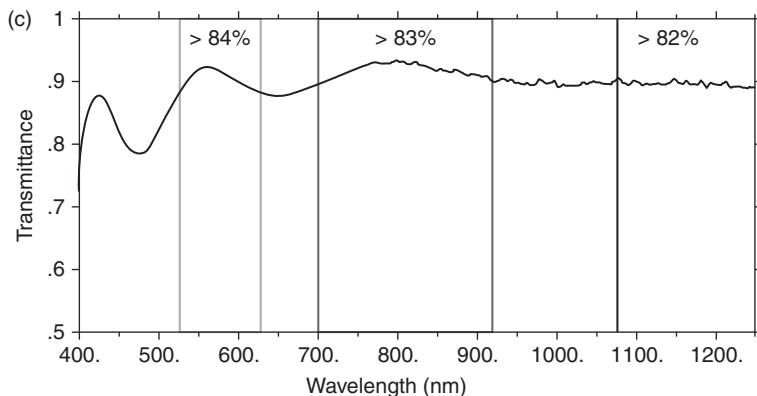
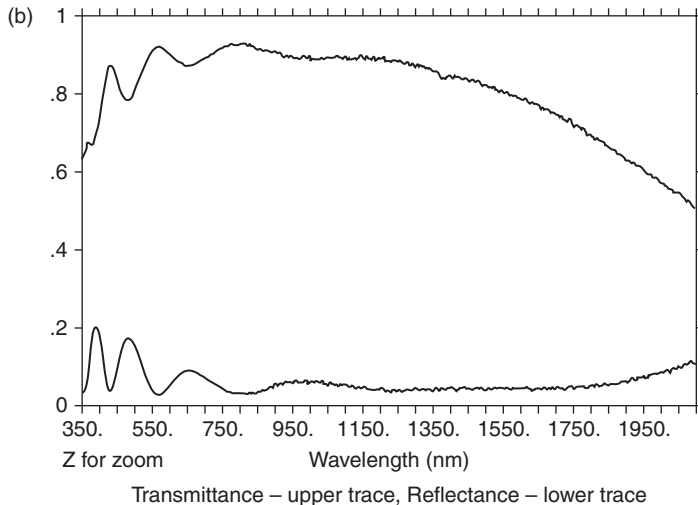
Example 21.1 A design example for anti-icing of TV laser window: (a) requirements; (b) explanatory diagram; (c) approach; (d) determining coating parameters (Bright, 1995a–2012).

(a)

- Heater coating resistance = 79 ohms (6.9 – 9.3 ohms)
- Coating sheet resistance = $11.3 \Omega/\square$ ($10.6 - 14.2 \Omega/\square$)
- Window transmittance

T visible	525–625 nm	=	88%	(> 84%)
T average	700–910 nm	=	92%	(> 83%)
T laser	1070 nm	=	89%	(> 82%)

- Passed laser damage testing at 22.5 to 36.0 mw/cm²
- Passed durability tests of Mil-C-48497



Example 21.2 Measured electrical and optical performance for the window of the design example: (a) measured TCO performance and (requirements); (b) graph showing measured spectral reflectance and transmittance performance with a resistive heater coating for anti-icing TV and laser window; (c) graph showing measured optical performance for coated anti-icing TV and laser window versus waveband requirements (Bright, 1995a–2012).

- Shielding effectiveness (SE) is a figure-of-merit for the performance of a shield in reducing interfering incident electromagnetic radiation
- Shielding effectiveness (SE) can be defined as the reduction in (transmitted) field intensity by losses (e.g., reflections) which occur after inserting the shield
- $SE = -20 \log_{10} E_{\text{TRANS}} / E_{\text{INC}}$ in same medium (impedance), where E_{TRANS} is the transmitted electric field and E_{INC} is the incident electric field
- $SE = 20 \log_{10}[1 + \eta_0 / 2R_{\text{FILM}}] = 20 \log_{10}[1 + 188.5/R_{\text{FILM}}]$ where $\eta_0 = (\mu_0 \epsilon_0)^{1/2} = 377$ ohms (free space)
- (This formula assumes the substrate is one-halfwave, or multiples, in optical thickness or a free standing film)

21.7 Basic formulae for far field EMI shielding effectiveness (Klein, 1990).

(a) Requirements:

- shield effectiveness (SE) of 20 dB minimum (far field)
- transmittances of $\geq 80\%$ at both 1.06 μm and 1.54 μm
- laser damage resistant
- mil-spec durability

(b) Basic EMI formulae (far field): $SE = 20 \log_{10}[1 + 188.5 / R_{\text{film}}]$

Shielding effectiveness (dB)	R_{film} ohms/square
4.2	300
9.2	100
13.5	50
20.4	20
26.0	10
31.8	5
45.6	1

(c) Approach:

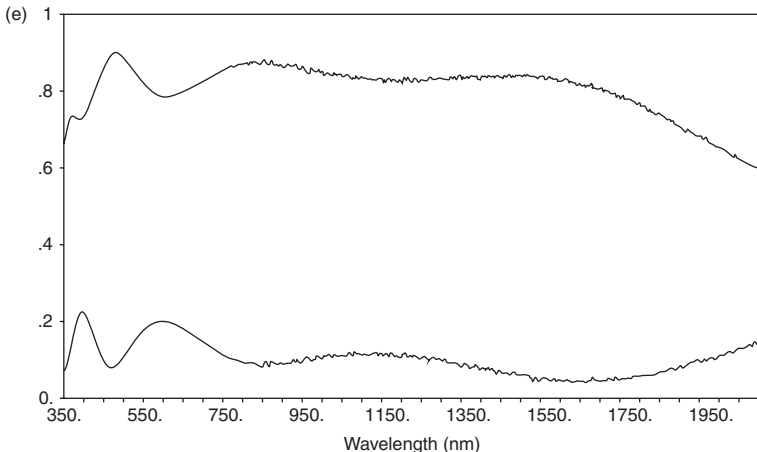
- SE requires coating surface resistivity ≤ 20 ohms/square
- Plasma wavelength must be longer than near infrared wavelength (1.54 μm) for required transmittance
- Use **indium oxide** (IO) low loss TCO on heated glass substrate ($\geq 250^\circ\text{C}$) coating process for low optical loss, laser damage resistance and durability
- Use deposition process (oxygen flow) to control carrier concentration and locate plasma wavelength beyond longest wavelength (1.54 μm)
- Assure TCO minimum thickness meets coating surface resistivity (sheet resistance) requirement
- Adjust TCO optical thickness to locate halfwave-multiples at laser wavelengths (1.06 μm and 1.54 μm) to achieve transmittance

Example 21.3 EMI shield for dual laser (1.06 and 1.54 μm) range finder window: (a) requirements; (b) basic EMI formulae (far field); (c) approach; (d) determining coating parameters; (e) measured TCO performance; (f) measured TCO performance: requirements (Bright, 1995a–2012).

(d) Determining coating parameters:

- Determine carrier concentration to locate plasma wavelength beyond $1.54 \mu\text{m}$, $N \sim 3 \times 10^{20}$
 $(\sigma = N e \mu, \omega_p = [Ne^2/\epsilon_0 m^*]^{1/2}, \lambda_p = 2\pi c[\epsilon_0 m^*/Ne^2]^{1/2})$
- Calculate minimum **IO** thickness to meet coating surface resistivity requirement, assume μ , from process data, or find empirically μ , then $\rho(1/\sigma)$ is known, find $d = \rho/r$
- Calculate **IO** optical thickness to locate halfwave-multiples at laser wavelengths ($1.06 \mu\text{m}$ and $1.54 \mu\text{m}$), $(x)\lambda/2$ and $(x-1)\lambda/2$
- Surface resistivity $\leq 20 \Omega/\square$ requirement
- $\sigma = N e \mu, N \sim 3 \times 10^{20} \text{ cm}^{-1}, \mu \sim 48.7 \text{ cm}^2/\text{V-s}, \rho = 4.3 \times 10^{-4} \Omega\text{-cm}, d = 242 \text{ nm}, r = \rho I d, r = 17.7 \Omega/\square$

(e) Measured TCO performance



(f) Measured TCO performance: requirements

- Surface resistivity = $17.7 \Omega/\square$ ($\leq 20 \Omega/\square$)
- Shield effectiveness = $\geq 21.3 \text{ dB}$ ($\geq 20 \text{ dB}$)
- Transmittance at $1.54 \mu\text{m}$ = 83.5% ($\geq 80\%$)
 (without adding AR layers)
- Transmittance at $1.06 \mu\text{m}$ = 83.5% ($\geq 80\%$)
- Passed laser damage resistance
- Passed durability requirement of Mil-C-48497

Example 21.3 Continued

21.5.3 Antistatic films

Another early application of TCTF was as an antistatic film. The function of an antistatic film is the non-destructive discharge of a static electric charge. Therefore, the electrical requirement on the film is for a ‘leaky’ film rather than a highly conductive film. One early application for this type of film was to bleed off the static charge created on cathode ray tube (CRT) displays by the scanning electron beam. The resistance to ground of the coating

can be high and still achieve adequate discharge—often in the kilohm or megaohm region. Because the coating ohms/square value can be high and easily achieved, the primary TCTF requirement is usually an attendant high transmittance (Bright, 1995a–2012; Bright 2010a).

21.5.4 Transparent electrodes

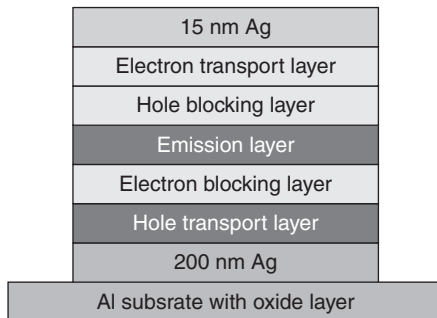
Type I

Today, the most common use of TCO is as a transparent electrode (TE) for a display device. Every device with an electrical flat-panel display uses one or more TE. The most common type of display today is a liquid crystal display, LCD, and most LCD devices have an ITO electrode. Because a LCD is an electric field effect device, it requires an electric field for operation but current drawn is very low. This type of transparent electrode is defined here as Type I. Another example of devices using Type I TE is electrophoretic displays like that made by E ink™. Type II transparent electrodes defined here are for current-carrying devices and will be discussed in the next section.

For field effect display devices the requirements for the TE are for very high transmittance, but a relatively high ohm per square value is acceptable. Typical coatings like ITO on glass would transmit near 90% in the visible with the corresponding sheet resistance of 1000 ohms per square or greater. For small devices the sheet resistance can easily be in the high kilohms per square. Thus, the technical requirements on TCO for a LCD are not demanding; often, cost considerations are paramount.

Type II

A Type II TE is required in current-carrying devices such as OLEDs or photovoltaic (PV) cells. Because current-carrying is required, the ohms per square value must be low to avoid electrical losses and nonuniformity. Common requirements for the TE in a small display are for a sheet resistance of ≤ 10 ohms per square with a transmittance of $\geq 85\%$. Depending on the type and size of the device, the required sheet resistance may be even lower. Thus, the O/E requirements on the Type II TEs are technically much more challenging than for the Type I TE. Example 21.4 shows a cross-sectional schematic drawing of an OLED emissive display. The requirements for a TE for this generic OLED device are listed in Example 21.5. The electrical requirements for the TE can vary depending on the type of addressing scheme used for the OLED display. Today, most displays use an active matrix (AM) addressing method, particularly for larger displays, which mitigates somewhat the requirements for a very low resistance TE. A high carrier concentration, $\sim 10^{21} \text{ cm}^{-3}$, for the chosen TCO, will typically be



Example 21.4 Transparent electrodes –Type IIA; current devices (injecting). Cross-sectional schematic drawing of an organic light emitting device (OLED) display. (Source: Adapted from C. May, S. Mogck and J. Amelung, Roll-to-Roll Deposition for OLED Lighting Devices, 52nd SVCTechCon, pp. 701–704, 2009.)

(a) Requirements:

- Low surface resistivity (sheet resistance) ≤ 10 ohms/square
- High transmittance (T_{vis}) $\geq 85\%$
- Low surface roughness (rms and peak) \leq few nm
- Match organic layer work function

Approach:

- Single layer ITO coating
- ITO anode work function should match (homo) organic (hole) layer
- High carrier density ($\sim 10^{21} \text{ cm}^{-3}$) for low surface resistivity (≤ 10 ohms/square)
- ITO thickness of halfwave (or multiple) for high visible transmittance

(b) Deposition process parameters:

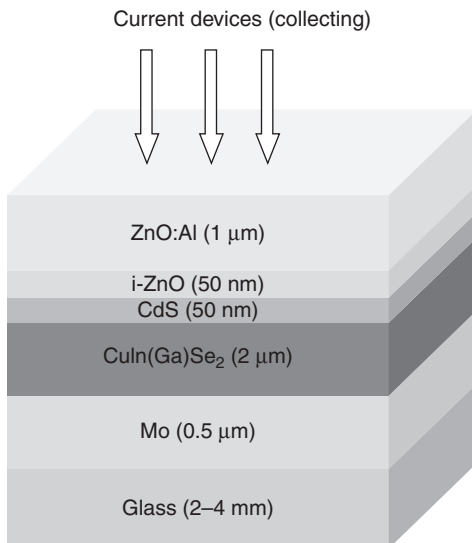
- Magnetron sputter deposit ITO from ceramic target (low defects)
- High substrate temperature for tin doping and high durability
- Control oxygen flowrate (partial pressure) near ITO resistivity-well minimum for high conductivity (low surface resistivity) but maintaining high transmittance
- Control sputtering parameters for smooth ITO surface
- Oxygen plasma or UV surface post-treatment for high ITO work function

Example 21.5 Charge injecting transparent electrode (anode) for OLED device: (a) requirements and approach; (b) deposition process parameters (Bright, 1995a–2012).

used to achieve low sheet resistance. Corresponding visible transmittance should be as high as possible while achieving the required low sheet resistance. Typical values for visible transmittance of the chosen TCO on a thin glass substrate are $\geq 85\%$. Generally ITO is the selected candidate from the TCO for OLED applications (Bright, 1995a–2012; Bright 2010a).

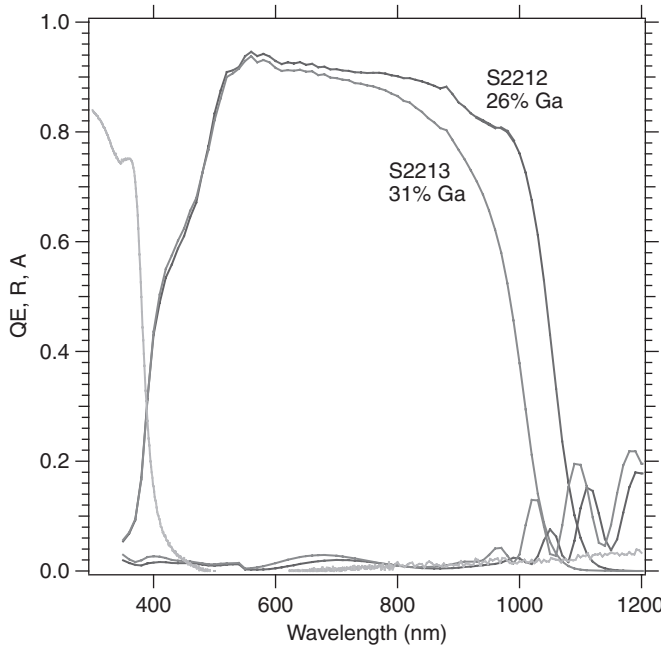
There are several requirements of the TE beyond the O/E requirements for OLED devices. For example, the TE surface roughness must be very low, typically less than a nanometer, because very thin layers are deposited on it to make the OLED. Also, generally the TE work function must be matched to the neighboring organic layer for proper charge injection. The TE is typically the anode in an OLED, and to match common organic materials used, a work function of about 5.0 eV is desired. ITO can achieve a work function near this value (Kim *et al.*, 1999).

Another example of a device with a Type II TE requirement is shown in Example 21.6, a cross-sectional schematic view of a thin film PV cell. In this example, a TE for a CIGS ($\text{Cu}(\text{In},\text{Ga})\text{Se}_2$) cell is selected. The electrical requirement for the TE in this PV cell is typically specified as ≤ 10 ohms per square. However, a lower sheet resistance is desirable, particularly in larger area cells, but the requirement must be a compromise with the optical requirement. The transmittance requirement is based on the absorption characteristics of the active material in the PV cell. The spectral absorption characteristics of CIGS cells of two compositions are shown in Example 21.7. From the example it is seen that the spectral transmittance of the TE must be from about 400 to 1100 nm. This broad spectral transmittance band will put limits on the allowed carrier concentration. The calculation of the



CIGS ($\text{Cu}(\text{In},\text{Ga})\text{Se}_2$) Type thin film solar cell stack

Example 21.6 Cross-sectional schematic view of a thin film PV cell: another example of a device with a Type II transparent electrode requirement (Ochs *et al.*, 2009).



Example 21.7 Transparent electrode for photovoltaic (PV) device; properties of high efficiency CIGS thin film solar cells. (Source: From NREL Invited Presentation, 2004.)

- Locate plasma wavelength, $\lambda_p \geq 1100$ nm for high transmittance to solar cell
- Calculate maximum allowed AZO carrier density, N , from

$$\lambda_p = 2\pi c \frac{(\epsilon_0 m^*)^{1/2}}{(N e^2)^{1/2}} \quad (\text{see Section 21.2.3})$$

- maximum $N \leq 6 \times 10^{20} \text{ cm}^{-3}$ needed for $\lambda_p \geq 1100$ nm
- for low surface resistivity (sheet resistance) and high transmittance, high mobility, μ , desirable ($\geq 20 \text{ cm}^2/\text{Vs}$)
- calculate AZO minimum thickness, d , for surface resistivity, $r \leq 10 \text{ ohms/square}$,
[using $\sigma = n e \mu, \rho = 1/\sigma \text{ ohm-cm}, r = \rho/d$]
 - $\sigma = 6 \times 10^{20} \text{ cm}^{-3} \times 20 \text{ cm}^2/\text{Vs} \times e = 1920 \text{ S/cm}$, then $\rho \approx 5 \times 10^{-4} \text{ ohm-cm}$
 - $d = 500 \text{ }\mu\text{ohm-cm}/10 \text{ ohms/sq} = 5 \times 10^{-5} \text{ cm} = 500 \text{ nm}$

Example 21.8 Transparent electrode for CIGS PV device: AZO film requirements (Bright, 1995a–2012).

allowed plasma wavelength (see Section 21.2.3) and the corresponding N is shown in Example 21.8 along with the other required characteristics of the TE. In this example, zinc oxide doped with aluminum, commonly called AZO, was selected. The result is a TCTF with $N \leq 6 \times 10^{20} \text{ cm}^{-3}$, a mobility of

$20 \text{ cm}^2\text{V}^{-1}\text{s}^{-1}$ and a thickness of $\geq 500 \text{ nm}$ for $\leq 10 \text{ ohms per square}$ (Bright, 1995a–2012; Bright 2010a).

21.5.5 Energy efficient windows

Energy efficient windows are also addressed in Chapters 8 and 20 and the reader is referred to these chapters for more detailed discussions related to controlling thermal radiation from surfaces and in automotive and building glazing. The purpose of the brief discussion here is to provide sufficient understanding of the application requirements so that the appropriate TCTF can be selected and designed (see Sections 21.2.3 and 21.3).

Low emissivity windows

There are, fundamentally, two types of energy efficient coatings for window applications. The first type of coating is for energy conservation windows where the dominant concern is to conserve heat loss from the interior and to harvest solar heating. These TCTF coatings are sometimes called ‘winter films’ because they are most useful in cold climates. When the temperature on the outside of the window is lower than that on the inside of the window, heat is radiated out from the interior of the building. To reduce this heat loss a low emissivity or ‘low-e’ coating can be applied to the window. Recall that over a spectral interval, the sum of the transmittance (T), reflectance (R) and absorption (A) must equal one, that is,

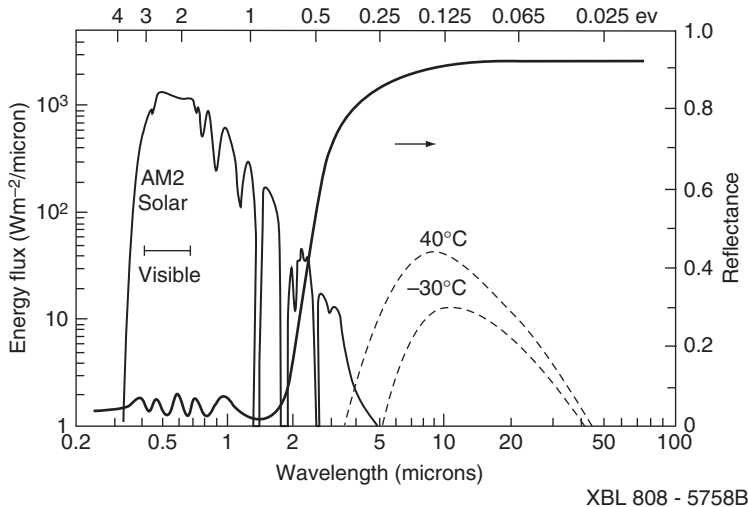
$$T + R + A = 1 \text{ or rearranging } A = 1 - R - T \quad [21.7]$$

and by Kirchhoff’s law, $A = e$, where epsilon or ‘e’ is the emissivity. Further, for metallic thin films and TCO on glass in the far infrared (FIR) because $T \approx 0$, then

$$e = 1 - R \quad [21.8]$$

Therefore, low-e (or more commonly called ‘low-e’) properties can be accomplished with a TCTF having high FIR reflectance.

To also achieve heating of the interior requires that the visible and near infrared solar energy be transmitted by the low-e coating and window. This concept is illustrated in Fig. 21.8 showing the solar spectral energy distribution and the desired spectral characteristics of the low-e coating. Solar heat gain is better achieved with TCO than with most metallic thin films. The spectral characteristics of the metallic thin films are determined primarily by the choice of metal that is, by its atomic structure, whereas with TCO these characteristics can be controlled by doping. By suitable doping of TCO



21.8 Low ϵ 'winter film' window with TCO coating (Lampert, 1981).

Requirements:

- Solar transmittance ($\leq 2 \mu\text{m}$) (TE) $\geq 50\%$
- Low emissivity in FIR waveband ($\lambda \geq 5 \mu\text{m}$), for $\epsilon \leq 0.20$, $R \geq 1 - \epsilon = 0.80 = 80\%$
- visible (eye weight) transmittance (T_{vis}) $\geq 70\%$

Approach:

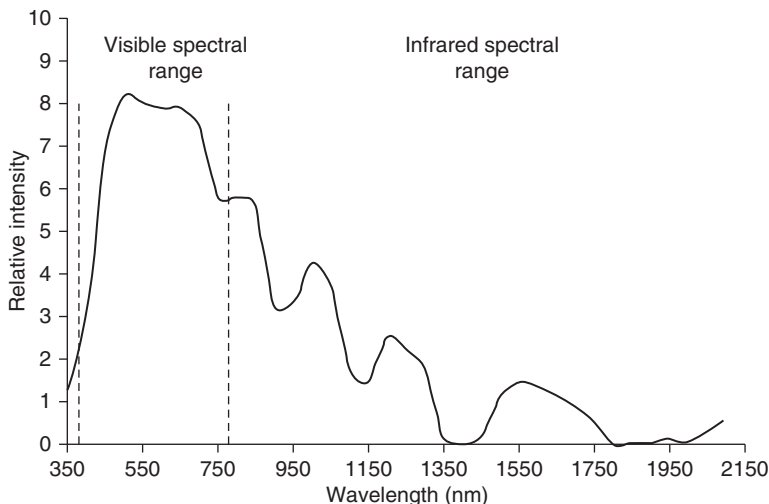
- TCO with low carrier concentration
- Fluorine doped tin oxide TCO for high mobility ($\text{SnO}_2:\text{F}$)
- Pyrolytic deposition process, low cost and high durability

Determine coating parameters:

- Single layer tin oxide coating doped for low carrier density, $\sim 3 \times 10^{20} \text{ cm}^{-3}$, to locate plasma wavelength for high NIR transmittance
- High mobility $\geq 40 \text{ cm}^2/\text{Vs}$ for steep slope in IR reflectance
- Low surface resistivity for high ($\geq 80\%$) FIR reflectance
- Minimum thickness \geq skin depth of $\sim 200 \text{ nm}$ ($0.2 \mu\text{m}$) at $20 \mu\text{m}$ wavelength, for high IR reflectance (low emissivity)
- Thickness multiple of halfwave for visible transmittance

Example 21.9 Design of low- ϵ winter films.

the plasma wavelength can be located at the desired wavelength for the change from transmittance to reflectance. An example of the design process for matching the low- ϵ application requirements is detailed in Example 21.9 (Bright, 1971; Bright, 1995a–2012).



21.9 'Summer film' window with metal coating (American Society for Testing and Materials (ASTM), www.astm.org).

Solar control coatings

The second type of energy efficient coatings for windows is called solar control coatings. These coatings are used in hot regions to reject solar energy entering through the window to the interior. These types of TCTF coating are also called 'summer films'. Figure 21.9 shows a plot of the solar spectral energy distribution. An ideal solar control coating would transmit all the visible spectral range (dashed area in Fig. 21.9) and reflect all of the infrared spectral range. To reject the maximum amount of nonvisible solar radiation the plasma wavelength of the TCTF should be located at the long wavelength extreme of the visible that is, about 700 nm. Because of the short wavelength required for the plasma wavelength, thin film metals are generally superior to TCO for this application. TCO cannot generally achieve a carrier concentration greater than about 10^{21} cm^{-3} whereas noble metals typically have N values of about 10^{23} cm^{-3} .

If additional heat rejection is desired some reduction of visible light will be required. Almost half of the incident solar energy is in the visible, so a compromise will be required between achieving greater heat rejection and maintaining transparency. Typical values of visible transmittance for reflecting solar control films are from about 40% to 75% T. A detailed example of the design of a solar control film is given in Example 21.10 (Bright, 1971; Bright, 1995a–2012) on page 766.

(a) Design of solar control ‘summer’ film

Requirements:

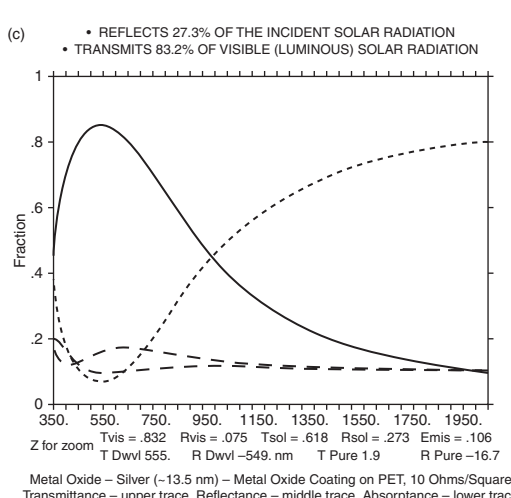
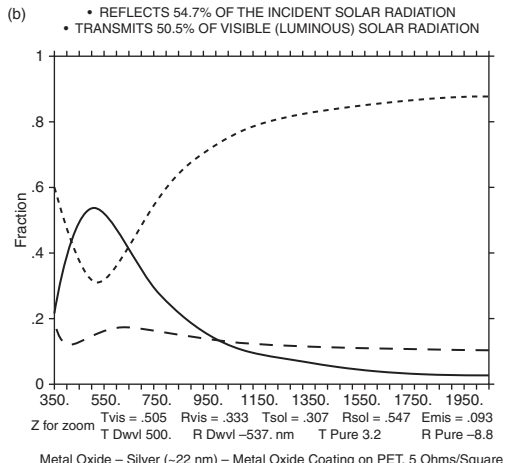
- Solar control ‘summer film’ for existing window
- Visible transmittance $\geq 75\%$ (coated film only)
- Solar reflectance $\geq 25\%$ (\sim solar IR reflectance $\geq 50\%$)

Approach:

- Optically enhanced metal on plastic film
- Indium oxide – silver – indium oxide coating stack
- Magnetron sputter indium oxide and silver layers in roll-to-roll (web) coating process

Determine coating parameters:

- Computer optical design program for layer thickness
- Trade-off required between visible transmittance and solar IR reflectance
- Silver surface resistivity (thickness) controls solar IR reflectance
- Surface resistivity ≤ 10 ohms/square (see figures)



Example 21.10 Detailed example of the design of a solar control film: (a) design of solar control ‘summer’ film; (b) optically enhanced silver (5 ohms/square); (c) optically enhanced silver (Bright, 1995a–2012).

21.6 Recent applications

21.6.1 Conductive antireflection

Antireflection (AR) thin films are widely used in optical displays, eyeglasses, smartphones and tablets, and much more. Today, most AR coatings are multilayer thin film stacks based on optical interference designs. Additional functionality can be incorporated in AR coatings by using TCTF. Including one or more TCTF in the AR stack can provide antistatic, EMI shielding or if patterned, touch sensing capability. The use of TCTF for touch sensing applications will be discussed in Section 21.6.2.

Because the eye is not equally sensitive to all visible wavelengths, one important set of parameters for displays are eye-weighted that is, photopic or luminous, transmittance and reflectance values. However for color displays, transmittance and reflectance values over a broad band in the visible often are used also for performance specifications. A common spectral band specified is the wavelength region from 450 to 650 nm. The optical requirements for a conductive AR coating on a flexible plastic substrate for use with displays are summarized in Example 21.11.

In addition to meeting difficult optical requirements, a wide range of other requirements must be met by the conductive AR coatings including abrasion resistance, chemical and environmental durability, antistatic and EMI shielding performance. In addition it must be produced at low-cost. These requirements are also summarized in Example 21.11.

A four layer optical coating design with alternating layers of ITO as the high index material and SiO_2 as the low index material was chosen for meeting the requirements of this example. An optical design program was used to optimize the layer thicknesses. The preferred thicknesses are shown in the cross-section schematic drawing (Example 21.12).

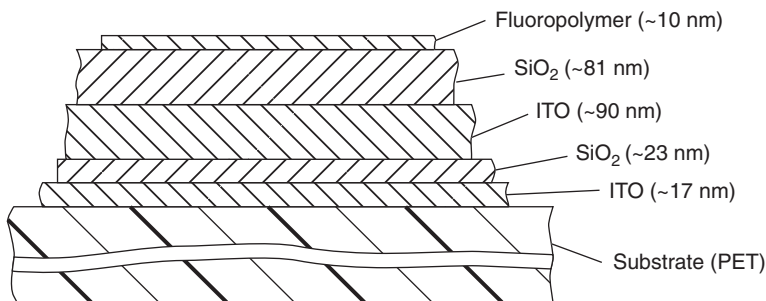
Optical requirements:

- Average reflectance from 450–650 nm: $\leq 0.7\%$
- Maximum reflectance at 450 nm and 650 nm: 2.0%
- AR bandwidth: ≥ 1.4
(long wavelength \div short wavelength for $R = 1.0\%$)
- Luminous reflectance: $\leq 0.6\%$

Other requirements:

- Abrasion resistant to 3H (1000 g) pencil, mechanical pencil (200 g) and #0000 steel wool (200 g/cm^2)
- Chemical and environmental (temperature/humidity) durability
- Antistatic and moderate EMI shield ($\leq 200 \text{ ohms/square}$)
- Low cost (few dollars/square feet)

Example 21.11 Requirements for conductive AR coating for displays (Bright, 1995).



Example 21.12 Cross-section schematic of conductive AR coating (Bright *et al.*, 1998).

- Average reflectance (450–650 nm) 0.46%
- Maximum reflectance (450 nm, 650 nm) 1.1%, 0.3%
- Bandwidth (1% wavelengths) 1.5
- Luminous reflectance 0.44%
- Surface resistivity 200 ohms/square

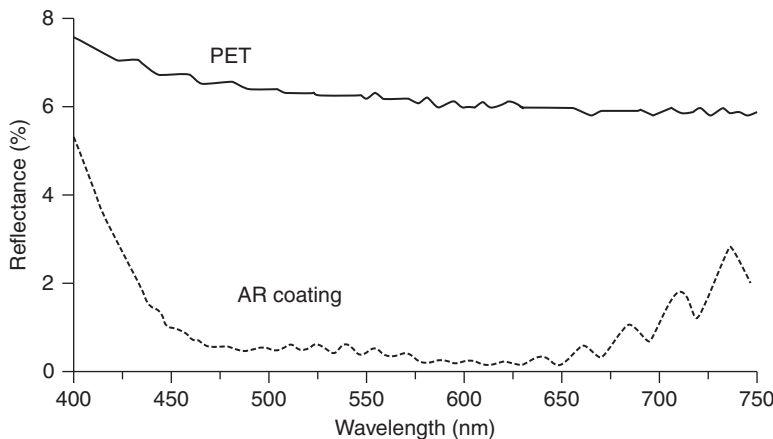
Example 21.13 Conductive AR coating for displays: typical measured optical and electrical performance (Bright, 1995b).

An AR coating exceeding the requirements was produced by the roll-to-roll (web) coating method using a PET plastic film substrate with an organic SiO₂ particle loaded hardcoat. DC magnetron sputtering was used for the ITO layers and AC dual magnetron sputtering for the SiO₂ layers. A liquid fluorocarbon coating was applied to the AR stack to provide anti-fingerprint capability and increased scratch resistance. Typical optical and electrical performance for the four-layer coating is summarized in Example 21.13 and spectral performance is shown graphically in Example 21.14. Durability requirements are summarized in Example 21.15. For more detail on the optical design, deposition process, performance and testing see Bright (1995) and Bright (1998).

21.6.2 Touch sensors

Analog resistive

There are many different types of touch sensor technologies; however, only two mainstream technologies will be described. The first type is analog resistive touch, which has been used for many years, and is based on having two conductive coatings, at least one of which is applied to a flexible substrate. When the flexible coated film is touched ('pushed'), it makes physical (electrical) contact with the opposite conductive coating, say on glass,



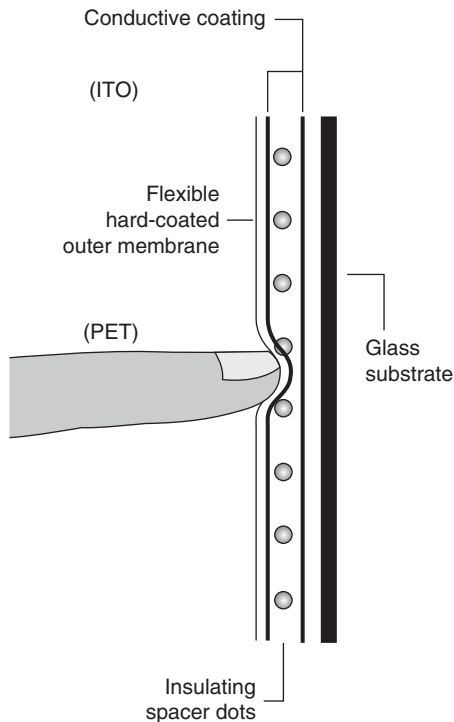
Example 21.14 Conductive AR coating for displays: typical measured spectral optical performance (Bright *et al.*, 1998).

- 3H pencil hardness ≥ 1 kg load
- Mechanical pencil resistant at ≥ 200 g load
- Steel wool (#0000) 30 cycles at 200 g/cm^2 load
- Resists ‘all’ common household and office chemicals
- Passes 48 hours at 50°C and 98% humidity
- Unaffected by temperature cycling from -40°C to 71°C (5 cycles)

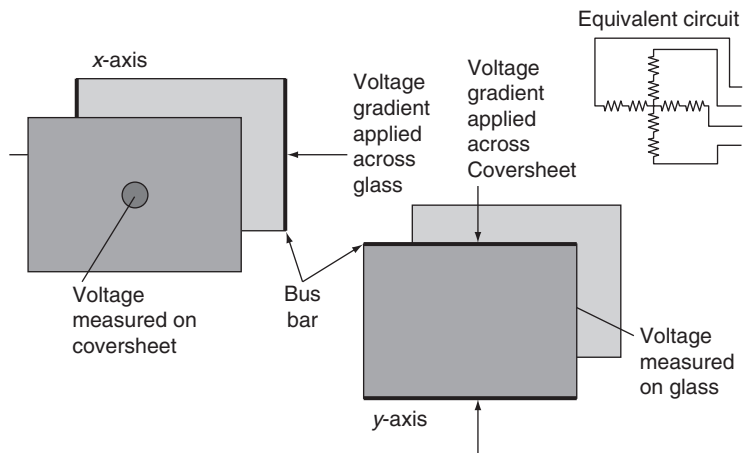
Example 21.15 Conductive AR coating for displays: typical measured durability performance (Bright, 1995b).

see Fig. 21.10 (Walker, 2010). This electrical contact completes a circuit and allows sensing of that location.

For example, the voltage applied across the (second) conductive coating on glass could be in the x -direction and because of the resistance of that coating, a voltage gradient is created. When the conductive coating on the flexible substrate touches the coating with the voltage gradient, it measures the voltage at that location and therefore senses the x -direction. Similarly, a voltage across the flexible conductor could be applied in the y -direction and because of the resistance of that coating a voltage gradient is again created. When the voltage gradient is across the conductive coating on the flexible substrate (y -direction) and it comes in contact with (touches) the coating on the glass, the voltage of the coating on the flexible substrate is measured and the location sensed. Now both the x and y directions at the point of touch are known. This method of resistive touch screen sensing (4-wire) is shown in Fig. 21.11 (Walker, 2010). For display applications where the touch sensor is in the field of view, of course, both of the conductive coatings and their substrates must be transparent.



21.10 Resistive touch (Walker, 2010).

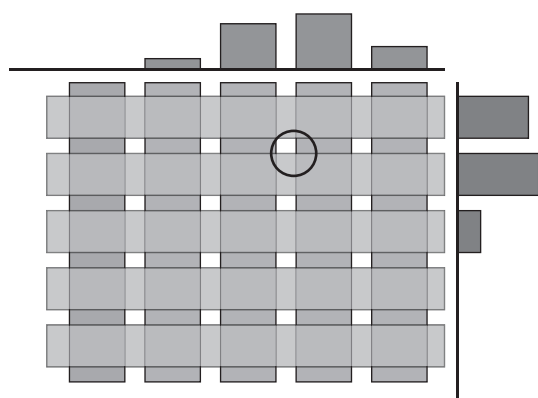


21.11 4-Wire resistive touch sensing (Walker, 2010).

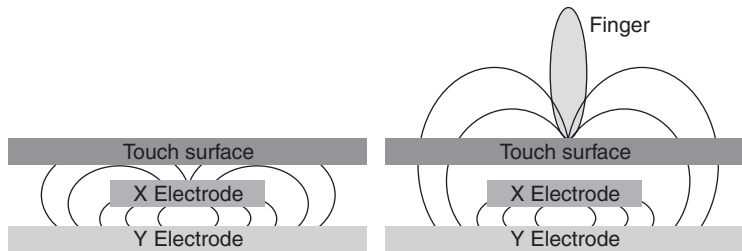
For resistive touch applications the sheet resistance of the TCTF is relatively high, typically 200–500 ohms per square so that a significant voltage drop, that is, gradient, is produced across the coating. Because sensing is based on this voltage gradient the conductive coatings must be very uniform in resistance to cause a very linear voltage drop to correlate accurately with location. The contact resistance between the two conductive coatings upon touching should be low and constant at all locations to avoid introducing sensing errors. Durability against contact, ‘abrasion resistance’, for the two TCTF coatings is also a requirement for resistive touch sensing applications. ITO is most commonly used for resistive touch sensing and display applications, and because of this durability requirement, crystalline ITO is preferred.

Projected capacitive

Projected capacitive touch technology is the fastest growing touch sensor method since Apple introduced the iPhone in 2007. Apple was not the first to use this touch sensor method but it has added many capabilities to the original technology and popularized its use. Like resistive touch technology, projected capacitive touch uses two conductive coatings for sensing, one for the *x*-direction and one for sensing the *y*-direction; however, there is no physical contact between the two coatings for sensing. Also, the two coatings are patterned typically in some type of a grid-line structure (magnified, not to scale) as shown in Fig. 21.12. Typically the two coatings are of ITO and may be deposited on both sides of a single substrate or on one side of the two substrates. The space between the two patterned coatings is a dielectric and thus a capacitor is formed wherever the two coatings separated by a



21.12 Schematic grid-line structure for *x* and *y* sensing (Walker, 2010).



- A finger ‘steals charge’ from the X-electrode, changing the capacitance between the electrodes
- E-field lines are ‘projected’ beyond the touch surface when a finger is present

21.13 Projected capacitive sensor (Walker, 2010).

dielectric overlap each other. Usually another substrate, which is touched with a finger by the user, is placed above the sensor substrate(s). When a voltage is applied to the two patterned ITO coatings an electric field is generated between them, which extends beyond the conductive grid-line into the space between lines and further into the insulating touch substrate as shown in Fig. 21.13. When a finger touches the surface of the insulating substrate, charge is drawn to the finger (to ground) from the nearest conductive patterned area, changing the capacitance between the X and Y electrodes in that area. This change in capacitance is sensed by electronic circuitry to identify the touched area. There are many different schemes for sensing this touch and for applying the voltage to the X and Y electrodes but all rely on the electric field being projected beyond the electrodes and interacting with the finger causing a change in capacitance.

The requirements on the TCTF are for high transmittance and low reflectance so that the patterned electrodes are not readily visible, the ability to be patterned accurately, and having an appropriate sheet resistance such that the resistance of a grid-line does not reduce the signal significantly before electronic processing. The actual value of sheet resistance required will depend on the construction details and the electronics of the device; however, a typical value for handheld devices like smartphones is a sheet resistance of about 100 ohms per square for the ITO (Bright, 1995a–2012; Bright 2010a).

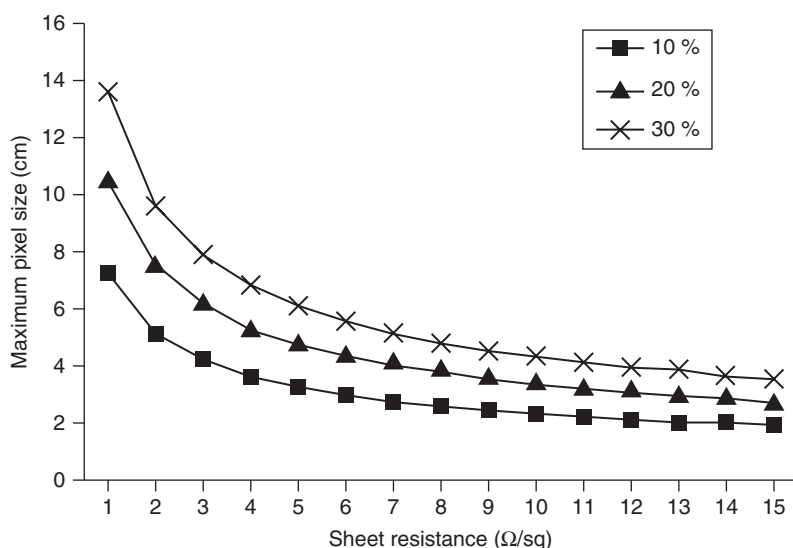
21.6.3 OLED lighting

Technically the use of a TCTF for OLED lighting is also a Type II, current-carrying, transparent electrode application as discussed for OLED displays. However, OLED lighting is an emerging application and has some differences in requirements compared with active matrix displays, that is,

AMOLED. For example, an OLED lamp is in essence a single pixel display. Thus, there is no need for a patterned TE and a method of driving the x and y addressing lines as in a display. However, the TE must be capable of supplying significant current without significant voltage drop across the entire OLED lamp. If the resistance (sheet resistance) of the TE is too high the voltage drop across the lamp will cause a drop in the illumination spatially across the lamp, which will be detected by the human eye. In fact, today the size of an OLED lamp is limited by the TE electrode resistance, as shown in Fig. 21.14 (Ma *et al.*, 2011). Prototype OLED lamps typically use ITO as the TE; however, the resistance is higher than desired and the cost of the ITO is a concern. Alternative TE solutions including hybrid electrodes, for example, a wiremesh plus a TCO or conductive polymer, are being sought for this application in particular. As in the OLED display example, all the additional non-O/E requirements apply to OLED lighting, but the major requirements are low resistance and low cost for which no preferred TE solution has yet been found.

21.6.4 Transparent oxide electronics

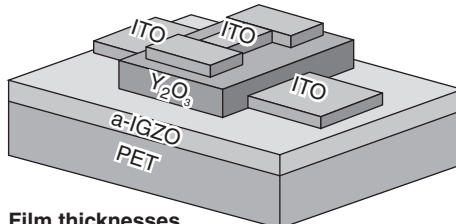
Transparent oxide electronics represents both a traditional and a new use for TCO. (Facchetti and Marks, 2010). The traditional application of TCO is as a TE or transparent contact. The new TCO use is as a semiconductor. As



21.14 Percentage non-uniformity as a function of pixel size and TE (TCTF) ohms/square (Ma *et al.*, 2011).

explained earlier in Section 21.2.2, all common high performance TCO are *n*-type degenerate semiconductors, that is, electrically equivalent to metals. In this application transparent semiconductive oxides (TSO) are used for the channel of a thin film transistor (TFT), that is, a field effect transistor (FET).

A typical TFT (FET) structure is shown in Fig. 21.16. In a typical TFT (FET), current flows from the source through the channel to the drain when the gate electrode is activated. TFTs are widely used as ‘switches’ in AM, addressing electronics for displays. Nomura *et al.* (2004) demonstrated the first transparent TFT (TTFT) deposited on a flexible substrate, PET. ITO was the selected TCO used as a TE for the source, gate and drain (Fig. 21.15). The TSO used for the semiconducting channel was amorphous indium gallium zinc oxide, a-IGZO. This TSO is currently the preferred material for the channel of TTFT because of its high field effect mobility and amorphous structure. Many TCO materials have been used to make TSO channel layers



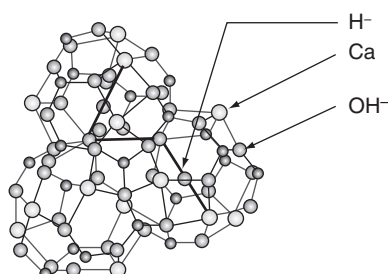
Film thicknesses

a-IGZO active layer : 30 nm

Y_2O_3 gate : 140 nm

ITO electrode : 40 nm

21.15 Structure of first TTFT deposited on a flexible substrate (Nomura *et al.*, 2004).



Crystal structure of H-doped $12\text{CaO} \bullet 7\text{Al}_2\text{O}_3$
(only three of the 12 cages in the unit cell are shown)

21.16 Example of cage structure materials of $12\text{CaO} \bullet 7\text{Al}_2\text{O}_3$: Crystal structure of H-doped $12\text{CaO} \bullet 7\text{Al}_2\text{O}_3$ (only three of the 12 cages in the unit cell are shown) (Medvedeva, 2006).

in TFT and TTFT. However, there are significant issues with making TSO from binary and ternary TCO materials, particularly on low temperature substrates like plastics (Bright, 2010a). The interesting history of TFT and TTFT is reported in a recent book (Fortunato, 2010). Oxide electronics applications are growing rapidly and their use is expected in the next generation of pad/tablet devices from a major manufacturer.

21.7 Future applications

21.7.1 Beyond TFT

While current transparent oxide electronics are entering industry, and the use of TFT and TTFT will be very large because of the display industry, *p*-type TCO and TSO are needed to make *p-n* junction type devices. Much progress has been made in recent years in developing crystalline *p*-type TCO and TSO, and some *p-n* junction type devices have been demonstrated (Kudo *et al.*, 1999; Kawazoe *et al.*, 2000). However, to make practical electronic devices beyond TFT and TTFT ‘switches’ much work is needed. New and improved *p*-type materials must be found and developed with superior O/E properties.

The breakthrough, which caused the Renaissance search for *p*-type semiconducting materials, occurred in 1997 (Kawazoe *et al.*, 1997) with the investigation of copper aluminum oxide, CuAlO₂. This success spawned investigation of many other delafossites and then spinel materials. Several materials have been found which demonstrate *p*-type properties, for example, copper gallium oxide, CuGaO₂, and strontium copper oxide, SrCu₂O₂. Also, copper indium oxide, CuInO₂, was developed as a *p*-type material (Yanagi *et al.*, 2001). The first transparent bipolar *p-n* homojunction (CuInO₂;Mg/CuInO₂;Sn) was fabricated based on this material (Yanagi *et al.*, 2001).

After the success with delafossites, chalcogenide materials with copper were also investigated and *p*-type semiconductors demonstrated, for example, α -BaCu₂S₂. However, the chalcogenide materials will not have high transparency in the visible. Next chalcogenide oxide (and fluoride) materials were investigated for wider bandgaps. These materials have a stacked, alternating two-layered structure, which exhibits two-dimensional like electronic properties. Degenerate *p*-type conduction was exhibited in LaCuOSe doped with magnesium with mobility of \sim 4 cm² V⁻¹ s⁻¹. All of the *p*-type materials discussed in this section have been epitaxially grown. The performance of polycrystalline or amorphous samples where attempted, has been much poorer.

Another *p*-type discovered, which operates fundamentally differently (polarons) than these copper-based materials is nickel cobalt oxide, NiCo₂O₄; this material has demonstrated some quite interesting properties including IR transmittance and the ability to be magnetic (Exarhos, 2007).

Binary *p*-type oxides of copper (Cu_2O) and nickel ($\text{NiO}:\text{Li}$), have been known for decades but the O/E performance is too low. Of course, there have been many efforts attempting to make *p*-type materials from known binary *n*-type TCO such as zinc oxide. Generally, this has been unsuccessful or controversial although there have been some convincing reports of making ZnO *p*-type material (Ryu *et al.*, 2003; Tsukazki *et al.*, 2005).

However, none of these materials has demonstrated *p*-type performance comparable to elemental semiconductors, adequate for a *p*-channel layer or comparable with *n*-type TCO (see Section 21.8 for more discussion of *p*-type materials).

21.7.2 Transparent OLED

Transparent displays are expected to enter the market in 2012. This new application for displays, for example, OLED, LCD and PDP, is predicted to grow rapidly to an \$87.2 billion market in 2025 (Displaybank, 2012).

The use of TCO as a TE for OLED displays was discussed previously in Section 21.5.4 and for lighting in Section 21.6.3. A future application is using more than one TCTF with OLED to produce a transparent display or lamp. The same general O/E requirements and considerations as discussed previously would apply for this new application; however, now two TEs would be required. In fact, transparent OLEDs have already been demonstrated (Gu *et al.*, 1996). However, the performance and TE characteristics were not optimized for an intended application. Simply choosing to make an OLED with two ITO single layer electrodes, will not make an efficient device because for ohmic contacts the work function of the TE should match the work function of the organic layers, separately for electron and hole injection. Clearly, different work functions are required for the two cases.

Traditionally, the cathode electrode is metallic whereas the anode is typically ITO (TCO). Generally, metal layers used as electrodes are opaque but thin layers can be made semitransparent. Transparent OLEDs of this type have been demonstrated but the percentage transmittance of the full structure is not adequate for most applications (Gu *et al.*, 1997; Riedl, 2010). For example, for either display or lighting applications high light transmittance is required for efficient operation. Therefore, a different approach is needed which will meet the electrical requirements while also satisfying the demanding optical requirements. There have been many attempts to use TCO, particularly ITO, as the cathode for an OLED (Dobbertin *et al.*, 2003; Kowalsky *et al.*, 2007) by adding additional layers to better match the work function of the organic layer. However, the preferred deposition process for ITO, sputtering, is well known as being damaging to organic layers. Therefore adding a very thin buffer layer, which will protect the organic layer during

sputtering yet have acceptable hole injection, and which can be deposited by a low energy evaporation process has been attempted. This approach has been demonstrated successfully using transition metal oxides, for example, tungsten oxide, WO_3 , as the buffer layer. However, the added layers and processes brings additional complexity and cost concerns for such a device construction, particularly in large areas of application (Riedl, 2010).

Another possibility for the cathode TE is to use a very thin metallic film between optical matching layers (see Section 21.2.1). As recently demonstrated by Bright (2010b), these constructions can have very high transmittance and high conductivity. Perhaps the optical matching layers could be thin enough to allow charge injection yet still increase transmittance. Alternatively, the matching layers could be made of transition metal oxides or organic materials with known, good hole injection properties.

Once a practical construction for transparent OLEDs is demonstrated it can be combined with transparent oxide electronics, for example, TTFT, to enable large area transparent displays.

21.7.3 Transparent PV (solar) cells

The idea of having a transparent solar cell at first seems contradictory. One would think that collecting the maximum amount of solar radiation to which the cell is sensitive would be a requirement, and typically it is for opaque cells. However, even though almost half of the energy arriving from the sun is at visible wavelengths, solar control coatings for windows, which allow significant transmittance of visible light for viewing and reject infrared radiation, are still energy efficient and very useful (see Section 21.5.5). Similarly, a transparent solar cell used as a window can provide dual use as an energy-efficient compromise between energy generation and energy conservation. Actually, this idea is not new and was proposed at least as early as the 1970s by Bright in a patent application, and perhaps earlier.

There are multiple ways to implement a transparent PV cell. One way is to use an inorganic thin film PV cell construction like CIGS, cadmium telluride (CdTe) or amorphous or polycrystalline silicon; alternatively, organic polymer photovoltaic (OPV) device constructions could be used (Huang *et al.*, 2010). Conceptually, even dye-sensitized solar cells could be used. For the compromise in visible transmittance, basically the absorbing layer of the PV cell is made thinner to achieve the desired transmittance.

The spectral transmittance band for the two required TEs will depend on the type of cell chosen and its spectral sensitivity, which will set the limit on the allowed carrier concentration, N . The calculation of the allowed carrier concentration for a CIGS PV cell was described previously in Section 21.5.4.

For all of these implementations, two TCTFs (or alternatives) will be required as TEs for the transparent PV cell. The choice of TCTF, for example TCO or metallic thin film, will depend on several factors. Because the transparent PV is a current device the TE electrical requirements will be determined in a similar way to that previously described for a Type II PV. Because of the very large size of windows, for example in commercial buildings, some types of very high conductivity bussbars will be needed periodically to collect current from the PV window to avoid unacceptable losses occurring in the TCTF. This situation also occurs in standard opaque photovoltaic solar cell modules. It is also similar to the voltage drop problem discussed for OLED lighting. Because of this issue early implementations of transparent PV windows may look more like a ‘French door’ with mutton bars between what appears to be individual small windows. Smaller size windows and skylights are also candidates for transparent PV cells.

21.7.4 Transparent electrochromic windows

Another application incorporating TCTFs and expected to find commercial use in the future is electrochromic (EC) windows. EC devices can vary the optical properties between a clear transmitting state and a darkened state achieved by either reflection or absorption or both. One of the primary applications foreseen for EC devices is in active energy efficient windows, that is, ‘smart windows’. The application of TCTF in passive energy efficient windows was described in Section 21.5.5. The benefits of having an active EC window are that the transmittance and reflectance/absorption of the window can be modified as appropriate for interior lighting needs, the time of day or season of the year, resulting in reduced energy usage for lighting, heating and cooling.

Modern EC cells are typically based on metal oxide EC materials. Obviously for a transparent EC device two TEs are required. In addition, one electrode must be in contact with an EC material and the other TE must be in contact with an ion storage layer, which also may be an EC material. In addition an ion transport layer must be in between these layers. In operation, when a voltage is applied, charge is transported between the EC material and the ion storage material which causes the change in optical transparency. The full transparency can be restored by reversing the voltage polarity (Granqvist, 2010).

Current EC technology has advanced to being compatible with roll-to-roll fabrication wherein each ‘half’ of the cell is deposited on a separate plastic substrate then laminated together with polymer layers used for the ion transport (see Granqvist, 2010 and references therein). This flexible laminate could then be installed or laminated between two pieces of glass. Of

course the application of EC technology is not limited to architectural glazing or even auto glazing but these two applications are very likely.

The basic function of the TCTF for EC applications would again be a TE. However, for EC applications the function of the TE is neither purely Type I nor Type II. Electrically, an EC cell is similar to a battery. When the EC cell is switched on there is current flow and the requirements of the TE are similar to Type II. However, when the EC cell is in the darkened or the transparent state no current flow is required to maintain that state (assuming no leakage). This condition is not exactly like either Type I or Type II functionally. Because of the large area covered in many window applications the same size related concerns discussed in Section 21.7.3 for transparent PV cells in window applications would apply for transparent EC windows. Spectral consideration for the TEs will depend on the specifics of the application and also the ability of the chosen EC technology to modulate not only visible transmittance but also infrared reflectance and emissivity properties.

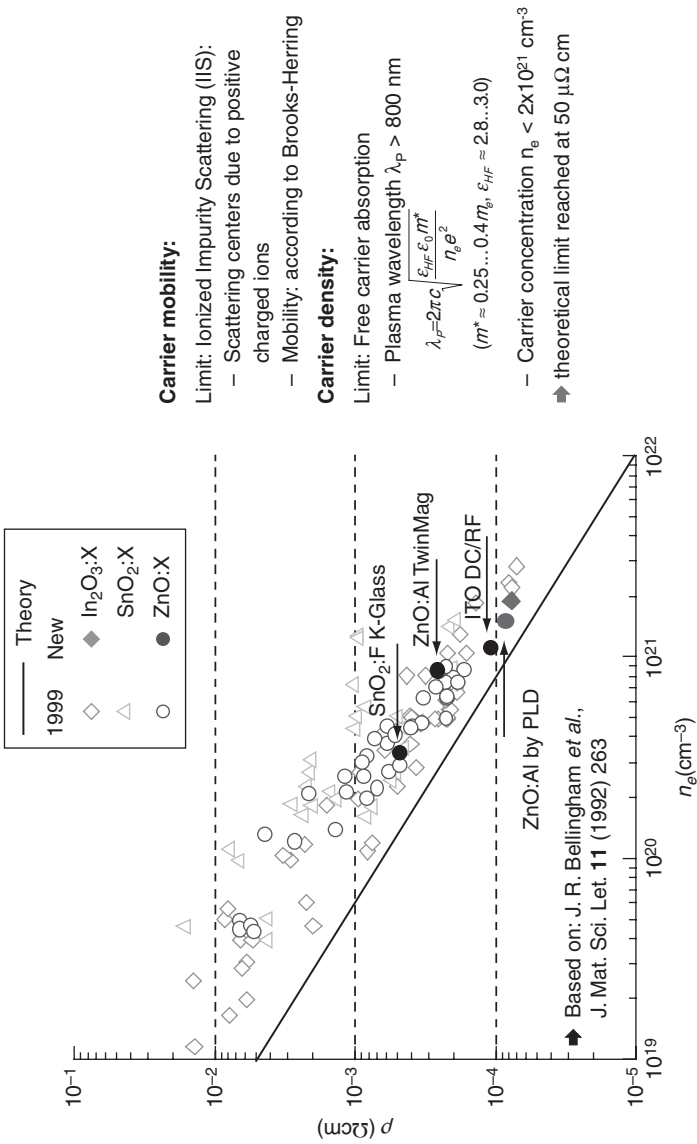
One can envision combining several of the applications discussed, for example, transparent photovoltaic and transparent EC characteristics in a given window application, or one or both of these along with passive solar control or energy efficient coatings. A multifunctional window might also have display capabilities. Future applications for TCTF will likely be quite varied and challenging optically and electrically but also requiring many other features and attributes both technology and business related.

21.8 Conclusion

The section has three subsections. Because of the large difference in the state of development and the underlying physics, *n*-type and *p*-type TCTF are discussed separately. The first subsection addresses *n*-type TCTF, followed by the *p*-type TCTF discussion. Because of the specialized nature of the TCTF topic, there is not a single or few obvious sources for information; therefore, the final subsection provides some advice on sources of further information. The intent of Section 21.8 is to provide some perspective for expectations of future developments, rather than provide conclusions, *per se*. Further, there always may be some surprising developments, which alter the performance expectations discussed here and even the character of future TCTF.

21.8.1 Future developments and outlook for *n*-type TCTF

Recently, Bright (2007) discussed the outlook for improved O/E properties in (*n*-type) TCO. Today that discussion is still relevant and is paraphrased and quoted here, but updated where experimental advances or improved knowledge have occurred. The ‘theoretical limit’ for conductivity (resistivity) in classical TCO was calculated following Bellingham *et al.* (1992).



21.17 Intrinsic performance limits for TCO (Szymzka, 2006).

Using nominal values for the ITO material properties an estimated resistivity value of $\sim 4 \times 10^{-5}$ ohm centimeters was calculated as the ‘theoretical limit’. Figure 21.17 shows the calculated theoretical resistivity limit, plotted with the measured performance reported, at that time, for various TCO and updated by Szyszka (2006).

However, two exceptions to the assumptions by Bellingham, which could allow further improvement in the resistivity of certain TCO, were reviewed by Bright (2007). The first exception is that some ‘multicomponent TCO with layered structures achieve spatial separation of the carrier donors and carrier transport layers; thus, alleviating scattering on the dopants’ (Kawazoe *et al.*, 1994). To the extent that scattering of ionized impurities is reduced beyond standard theory, a commensurate reduction in the theoretical limit for resistivity would be allowed. On the contrary, however, to date no multicomponent TCO of any type, has achieved experimentally, equal or better conductivity than classical binary TCO, for example, ITO.

The second exception is that ‘using transition metals, magnetically mediated dopants, with new or traditional binary TCO hosts can reduce the ‘traditional TCO theoretical limit’ by a factor of 2× (Medvedeva, 2006a), to $\sim 2 \times 10^{-5}$ Ohm·cm, because conduction electrons of only one spin direction are scattered. To date this approach has resulted in high mobility TCO with good O/E performance. But a resistivity of $\sim 10^{-5}$ ohm cm has not been demonstrated because, even though the mobility is high, carrier concentrations achieved by transition metal doping are in the low $\times 10^{20}$ cm $^{-3}$.

Cage-structured materials have been suggested as a new class of TCO with the possibility of not compromising optical properties to achieve good conductivity (Hayashi *et al.*, 2002). Theoretical band structure analysis (Medvedeva, 2006a, 2006b) supports this possibility although experimental results to date have not achieved this goal. Examples of cage structured materials are the CaO-Al₂O₃ family, in particular, 12CaO•7Al₂O₃, abbreviated C12A7 (see Fig. 21.16) (Hosono, 2010). The unit cell can be represented by the chemical formula [Ca₂₄Al₂₈O₆₄]⁴⁺ + 2O²⁻. The bracketed quantity represents the ‘cage framework’ and the two additional oxygens are considered ‘free oxygen ions’. The nanostructure of these cage-structured materials leads to unique doping opportunities (Hosono, 2010 and references therein). Substitution of hydrogen ions (H⁻) for the free oxygen ions created a hydrogen doped material (C12A7:H⁻). However, this doped material remained an electrical insulator until irradiated with UV light, causing conductivity as high as 1 S cm $^{-1}$ but which also created new absorption bands imparting a green color to the previously colorless material. Further experiments were able to replace all of the free oxygen in the cages with electrons by a reduction process (Hosono, 2010 and references therein). This material is considered an ‘electride’ and has achieved conductivity as high as 1000 S cm $^{-1}$, without requiring UV illumination radiation. The new material with

complete replacement of the free oxygen ions can be represented by the chemical formula $[\text{Ca}_{24}\text{Al}_{28}\text{O}_{64}]^{4+} + 4\text{e}^-$, and is considered a ‘new type of inorganic electrode’ with metallic conduction and mobilities from about $\sim 0.1\text{--}4 \text{ cm}^2 \text{ V}^{-1} \text{ s}^{-1}$ with strong dependence on the electron carrier concentrations (Hosono, 2010 and references therein). Cooling the material to very low temperatures (0.2–0.4 K) causes a metal to superconductor transition at ambient pressure; a first for an s-metal material (Hosono, 2010 and references therein).

Bright (2007), also suggested ‘for developing TCO with improved E/O properties (versus ITO), systematic exploration of the full periodic table should be undertaken, rather than limiting studies to (host) materials in neighboring columns IIB and IIIA (except for Sn in IVA, which isn’t a high performance TCO host).

‘The surprise discovery of $\text{TiO}_2:\text{Nb}$ (Furubayashi *et al.*, 2006) shows the value of a broader investigation (column IVB), rather than “mixing” of the known binary TCO.’ These single crystalline films of anatase $\text{TiO}_2:\text{Nb}$ (TNO) were grown by pulsed laser deposition (PLD) and achieved resistivity of $2\text{--}3 \times 10^{-4} \text{ ohm-cm}$, with an internal transmittance of 97%, that is, 3% absorption. Since that discovery considerable work has been performed on this material system at several laboratories and achieved similar performance for epitaxial films. In all cases the rutile phase of TiO_2 shows significantly poorer O/E properties than the anatase phase (Zang, 2007). The growth temperature was high ($\sim 600^\circ\text{C}$) for all of these TNO epitaxial films. More recently magnetron sputtered films were deposited on unheated glass or 150°C heated glass but were subsequently post-annealed at 500°C or 600°C in a hydrogen atmosphere (Hitoguri *et al.*, 2008; Sato *et al.*, 2008). Polycrystalline films on glass have exhibited a resistivity of about 4.5×10^{-4} to $1.5 \times 10^{-3} \text{ ohm-cm}$. Clearly, after only a few years of study with a new material, achieving this type of O/E performance is very promising.

21.8.2 Future developments and outlook for *p*-type TCTF

Since the discovery of *p*-type copper aluminum oxide, CuAlO_2 , substantial progress has been made in developing new *p*-type oxide materials. Conductivities as high as 900 S cm^{-1} , mobility near $10 \text{ cm}^2 \text{ V}^{-1} \text{ s}^{-1}$ and high visible transmittance all have been achieved (Tate and Keszler, 2010). However, this level of performance requires epitaxial films, typically grown at very high temperatures. It is desirable to have polycrystalline or even more preferable to have amorphous *p*-type materials which are processable on glass or ideally on flexible plastic substrates.

For fabrication it is very desirable to have a bipolar material for making *p-n* junction devices but to date only CuInO_2 (*p-n*) and co-doped ZnO

(also *p-i-n type*) materials have been used successfully, and neither has the characteristics desired for transistor- or TFT-type devices (Hosono, 2010; Tate and Keszler, 2010). Even for heterojunction-type devices no satisfactory *p*-type transparent oxide material suitable for practical use has been found. Further, no *p*-type materials have been demonstrated which could be satisfactory as a *p*-channel in TFT and TTFT devices (Tate and Keszler, 2010). If a transparent material adequate for *p*-channel TTFT devices could be found, complementary metal–oxide–semiconductor (CMOS) field effect devices could be developed. For *p*-type semiconductor materials, developing suitable transparent oxide contacts, that is, *p*-type TCO, to achieve proper hole injection with an ohmic contact, or at least a low injection barrier, is another requirement.

The challenges in developing *p*-type, wide bandgap semiconductors, that is, *p*-TSO, are different than those for *n*-TSO. Because for holes carrier movement is in the valence bands, carriers have inherently lower mobility in comparison to electrons in a conduction band generated by diffuse and spherical s orbitals. Valence bands are typically highly directional p or d orbitals and are narrower with less spatial overlap of atomic orbitals. Because of this inherent lower mobility higher doping is needed to achieve a high carrier concentration for a given amount of conductivity, which leads to higher ionized impurity scattering (Tate and Keszler, 2010). Further, obtaining high carrier concentrations is not always possible due to development of ‘killer defects’ causing ‘pinning’ of the Fermi level (Zunger, 2003). Maintaining transparency of the material by avoiding causing absorption at visible wavelengths when doping in the valence band, also is very challenging. Clearly, there are many difficult hurdles to be overcome for achieving satisfactory transparent *p*-TSO and *p*-TCO (Tate and Keszler, 2010).

21.8.3 Other review articles

Today, with access to so much information sometimes it is hard to know where to start. Here are some suggested sources of further information based on my personal knowledge. Certainly this list is far from inclusive but represents some sources I am aware of and which are generally useful to me. Of course, the usual thin film journals such as Thin Solid Films (TSF) and the Journal of Vacuum Science and Technology (JVST) and many others are appropriate but cover many topics. Occasionally, journals will have a special issue, which covers the TCTF topic. For example, the MRS Bulletin, August 2000 issue focused on Transparent Conductive Oxides and is still recommended. Other examples are special issues of TSF and JVST, which document selected papers from focused conferences.

Excellent sources of information on TCTF are review articles. Of course, by their nature they represent the knowledge base relevant to the time of

the article. However, even quite old review articles still can be quite useful and authoritative. For example, the review by Chopra *et al.* in 1983 is still recommended as a good way to efficiently review prior work on TCTF. It is particularly strong in reviewing solution-coated TCO. Already mentioned is the MRS bulletin of August 2000, which is based on a TCO workshop with contributors from many different countries and representing universities, institutes and industry. More recent, recommended TCTF reviews are the reviews by Granqvist and Hultaker (2002) and Granqvist (2007) and the review by Exarhos (2007).

Similarly, there are many good conferences to attend such as American Vacuum Society (AVS) held annually in November and the Materials Research Society (MRS) held in spring and fall, but these are very large conferences and, again, cover many topics. The content in these two conferences are also heavily weighted towards academic presentations. If you are looking for the latest research results from a university or institution these could be good sources.

Alternatively, if you are looking for thin film results representative of industry and technology applied on a large scale, the Society of Vacuum Coaters (SVC) conference is suggested. In addition to the excellent technical conference there is an associated exhibit with companies representing most major and specialty vacuum and thin film equipment, materials and related services. SVC has a few parallel sessions, which cover several technology and market segments of vacuum and thin film coatings. TCTF papers may be in more than one session including for example, Large Area Coatings, for example, glass and glazing and Web Coating for roll-to-roll coating primarily on plastics. In addition, there will be one or two annual theme topics which focuses on papers in a particular area like Photovoltaic and Clean Technologies.

Another good US conference, which includes TCTF on flexible substrates, is FlexTech Alliance, previously called the United States Display Consortium (USDC), conference focused on flexible displays and electronics and held annually in February.

Specialty conferences for TCTF include the biannual TOEO (Symposium on Transparent Oxide Thin Films for Electronics and Optics) held in even numbered years in Japan, and the Symposium on Transparent Conductive Materials, TCM20XX, conference, formerly Symposium on Transparent Conductive Oxides, TCO20XX, held in Crete, Greece in even numbered years.

Finally, of course there are many websites with helpful information on TCTF; the websites for the professional societies and conferences previously mentioned are recommended as well as the websites of universities, institutes and companies active in TCTF work. In the US, National Laboratory websites may also be useful, for example the National Renewable Energy

Laboratory (NREL), at www.nrel.gov. Also one should not forget patents and patent applications as a source of detailed TCTF information. Both the United States patent office (USPTO) and the European patent office (EPO) are excellent sources of information available online, as are patent offices of other countries.

21.9 Sources of further information and advice

- Granqvist, C.G., (2007) 'Transparent conductors as solar energy materials, A panoramic review', *Sol Eng Mat & Solar Cells*, **91**, 13, 1529–1598.
- Granqvist, C. G. and Hultaker, A., (2002), 'Transparent and conducting ITO films: new developments and applications', *Thin Solid Films*, **411**, 1–5.
- Dawar, A. L. and Joshi, J. C., (1984) 'Review – Semiconducting transparent thin films: their properties and applications', *J Mat Sci*, **19**, 1–23.

21.10 References

- Bellingham, J. R., Phillips, W. A. and Adkins, C. J. (1992) 'Intrinsic performance limits in transparent conducting oxides', *J. Mat. Sci. Lett.* **11**, 263.
- Berning, P. H. and Turner, A. F. (1957) 'Induced transmission in absorbing films applied to band pass filter design', *J. Opt. Soc. Am.*, **47**, 230–239.
- Bright, C. (1971) 'Solar shielding performance of sierracin coating', Sierracin Corporation, Sylmar, CA., RDR-13–71, 1971.
- Bright, C. (1995b) 'Conductive antireflection coatings on plastic films', AVS, Southern California Chapter, Vacuum Coating Workshop, 1995.
- Bright, C. (2008) 'Alternative Transparent Conductive Oxides (TCO) to ITO', 51st Annual Technical Conference Proceedings of the Society of Vacuum Coaters, pp. 840–850
- Bright, C. I. (1995a–2012), 'ITO and other transparent conductive coatings: fundamentals, deposition, properties, and applications', Class C-304, Annual Technical Conference of the Society of Vacuum Coaters.
- Bright, C. I., (2006) 'Fundamental Issues with TCO on Plastic Substrates,' 1st International Symposium on Transparent Conductive Oxides, Crete, Greece, Conference Proceedings, C6, 62 (2006).
- Bright, C. I. (2007) 'Review of Transparent Conductive Oxides (TCO)', in Mattox and D. Harwood-Mattox, V., *50 Years of Vacuum Coating Technology and the Growth of the Society of Vacuum Coaters*, Albuquerque, New Mexico, U.S.A., Society of Vacuum Coaters, 42–50.
- Bright, C. I. (2010a) 'Deposition and performance challenges of transparent conductive oxides on plastic substrates', in Facchetti, A. and Marks, T. J., *Transparent Electronics from Synthesis to Applications*, Chichester, Wiley.
- Bright, C. I. (2010b) TCM 2010, 3rd International Symposium on Transparent Conductive Materials, 17–21 October 2010, Analipsi, Hersonissos, Crete, Greece.
- Bright, C. I., Woodard, F. E., Pace, S. J. and Kozak, J. G. (Southwall Technologies Inc) (1998) 'Antireflective coatings comprising a lubricating layer having a specific surface energy', US patent 5,744,227, 28 April 1998.

- Burstein, E. (1954) 'Anomalous optical absorption limit in InSb', *Phys. Rev.*, **93**, 632.
- Cairns, D. R., Witte II, R.P., Sparacin, D.K., Sachsman, S.M., Paine, D.C., Crawford, G. P. and Newton, R. R' (2000), 'Strain-dependent electrical resistance of tin-doped indium oxide on polymer substrates', *Appl. Phy. Lett.*, **76**, 1425.
- Chopra, K. L., Major, S. and Pandya, D. K. (1983) 'Transparent conductors – a status review', *Thin Solid Films*, **102**, 1–46.
- Coutts, T. J., Young, D. L. and Li, X. (2000) 'Characterization of transparent conducting oxides', *MRS Bulletin*, 25 August 2000.
- Displaybank, I. H. S. (2012) 'Transparent display technology and market forecast', San Jose, CA, USA, Available from: http://www.displaybank.com/_eng/research/report_view.html?id=768&cate=6 [Accessed 19 November 2012].
- Dobbertin, T., Werner, O., Meyer, J., Kammoun, A., Schneider, D., Riedl, T., Becker, H., Johnnes, H. and Kowalsky, W. (2003) 'Inverted hybrid organic light-emitting device with polyethylenedioxythiophene-polystyrene sulfonate as an anode buffer layer', *Appl. Phy. Lett.*, **83**, 5071.
- Exarhos, G. J. and Zhou, X.-D. (2007) 'Discovery-based design of transparent conducting oxide films', *Thin Solid Films*, **515**, 7025–7052.
- Facchetti, A. and Marks, T. J., Editors (2010) *Transparent Electronics from Synthesis to Applications*, Chichester, Wiley.
- Fortunato, E., Barquinha, P., Goncalves, G., Pereira, L. and Rodrico Martins (2010) 'Oxide semiconductors: from materials to devices', in Facchetti, A. and Marks, T. J., *Transparent Electronics from Synthesis to Applications*, Chichester, Wiley.
- Fraser, D.B. and Cook, H. D., (1972) 'Highly conductive transparent films of sputtered $\text{In}_2\text{-xSn}_x\text{O}_3\text{-y}$ ', *J. Electrochem. Soc.*, **119**, 1368.
- Furubayashi, Y., Hitosugi, T., Yamaoto, Y., Hirose, Y., Kinoda, G., Inaba, K., Shimada, T. and Hasegawa, T. (2006) 'Novel transparent conducting oxide: Anatase $\text{Ti}_{1-x}\text{Nb}_x\text{O}_2$ ', *Thin Solid Films*, **496**, 157–159.
- Ginley D. S. and Bright, C. I. (2000) 'Transparent conducting oxides', Guest Editors, *MRS Bulletin*, 25 August 2000.
- Granqvist, C. G. (1989) 'Spectrally selective surfaces for heating and cooling applications', Tutorial Texts in Optical Engineering, Volume TT 1, Bellingham, Washington, USA, SPIE optical engineering press, SPIE – The International Society for Optical Engineering.
- Granqvist, C. G. (2010) 'Oxide-based electrochromics', in Facchetti, A. and Marks, T. J., *Transparent Electronics from Synthesis to Applications*, Chichester, Wiley.
- Gu, G., Bulovic, V. and Forrest, S. R. (1996) 'Transparent organic light-emitting devices', *Appl. Phys. Lett.*, **85**, 3911.
- Haacke, G. (1976) 'New figure of merit for transparent conductors', *J. Appl. Phys.*, **47**(9), 4086–
- Hayashi, K., Matsuishi, S., Kamiya, T., Hirano, M. and Hosono H. (2002) 'Light-induced conversion of an insulating refractory oxide into a persistent electronic conductor', *Nature*, **419**, 462.
- Hitosugi, T., et al. (2008) 'Electronic band structure of transparent conductor: Nb-doped anatase TiO_2 ', *Appl. Phys. Express*, **1**, 111203.
- Hosono, H. (2010) 'Transparent oxide semiconductors: Fundamentals and recent progress', in Facchetti, A. and Marks, T. J., *Transparent Electronics from Synthesis to Applications*, Chichester, Wiley.

- Huang J., Li, G., Li, J-H., Chen, L-M. and Yang, Y. (2010) 'Transparent solar cells based on organic polymers', in Facchetti, A. and Marks, T. J., *Transparent Electronics from Synthesis to Applications*, Chichester, Wiley.
- Kawazoe, H., Yanagi, H., Ueda, K. and Hosono, H. (2000) 'Transparent p-type conducting oxides: Design and fabrication of p-n heterojunctions', *MRS Bull.*, **25**, 28–36.
- Kawazoe, H., Ueda, N., Un'no, H., Omata, T., Hosono, H. and Tanoue, H. 'Generation of electron carriers in insulating thin film of MgIn₂O₄ spinel by Li⁺ implantation' *J. Appl. Phys.*, **76**, 7935 .
- Kawazoe, H., Yasukawa, M., Hyodo, H., Kurita, M., Yanagi, H. and Hosono, H. (1997) 'P-type electrical conduction in transparent thin films of CuAlO₂', *Nature (London)*, **389**, 939–942.
- Kim, J. S., Cacialli, F., Granstrom, M., Friend, R. H., Johanson, N., Salaneck, W. R., Daik, R. and Feast, W. J. (1999) 'Characterisation of the properties of surface-treated indium-tin oxide thin films' *Synth. Met.*, **101**, 111.
- Klein, C. (1990) 'Microwave shielding effectiveness of EC coated dielectric slabs', *IEEE Trans. Microwave Theory Tech.*, **38**, 3 March 1990, 321–324.
- Kowalsky, W., Gorrn, P., Meyer, J., Kroger, M., Johannes, H. and Riedl, T. (2007) 'See-through OLED displays', *Proc. SPIE*, **6486**, 64860L.
- Kudo, A., Yangi, H., Hosono, H., Kawazoe, H. and Yano, Y. (1999) 'Fabrication of transparent p-n heterojunction thin film diodes based entirely on oxide semiconductors', *Appl. Phys. Lett.*, **75**(18), 2851–2853.
- Lampert, C. M. (1981) 'Heat mirror coatings for energy conserving windows', *Solar Energy Mat.*, **6**, 1.
- Leterrier, Y., Medico, L., Demarco, F., Manson, J.-A.E., Bouten, P.C.P., de Goede, J. and Nisato, G. (2003) 'Mechanical properties of transparent functional thin films for flexible displays,' 46th Annual Technical Conference Proceedings of the Society of Vacuum Coaters, May 3–8, 2003 San Francisco, CA, 169–174.
- Ma, R., Levermore, P.A., Mandlik, P., Pang, H. and Brown, J.J. (2011) 'Technology gap analysis of vacuum coated materials for flexible OLED display and lighting applications', Society of Vacuum Coaters, 54th Annual Technical Conference Proceedings, Chicago, IL, USA, 16–20 April 2011.
- Macleod, H. A. (2001) *Thin-Film Optical Filters*, Third edition, Bristol and Philadelphia, Institute of Physics Publishing.
- McMaster, M. A. (Libby-Owens-Ford) (filed 5 October 1942) U.S. Patent 2,429,420, issued 21 October 1947, (see other McMaster US and British patents too).
- Medvedeva, J. E. (2006a) 'Unconventional approaches to combined optical transparency with electrical conductivity', 1st International Symposium on Transparent Conductive Oxides, Crete, Greece, Conference Proceedings, FC4–1–FC4–2.
- Medvedeva, J. E. (2006b), 'Magnetically mediated transparent conductors: In₂O₃ doped with Mo', *Phys. Rev. Lett.*, **97**, 086401.
- Minami, T. (1999) 'Transparent and conductive multicomponent oxide films prepared by magnetron sputtering', *J. Vac. Sci. Technol.*, **A 17**(4), 1765.
- Minami, T. (2005) 'Transparent conducting oxide semiconductors for transparent electrodes', *Semicond. Sci. Technol.*, **20**, D35–S44.
- Minami, T., Sonohara, H., Kakumu, T. and Takata, S. (1995) 'Highly transparent and conductive Zn₂In₂O₅ thin films prepared by RF magnetron sputtering', *Jpn. J. Appl. Phys.*, Part 2, **34**, L971–L974 .

- Nomura, K., Ohta, H., Takagi, A., Kamiya, T., Hirano M. and Hosono, H. (2004) 'Room-temperature fabrication of transparent flexible thin-film transistors using amorphous oxide semiconductors', *Nature*, **432**, 488–492.
- Noufi, R., Romero, M.J., Jiang, C.-S., Yan, Y., Abu-shama, J., Ramanathan, K. NREL Invited Presentation (2004) 'Why do CIGS-based solar cells have superior performance? Insight into the properties of grain boundaries and the surface as influenced by the growth dynamics', European MRS Meeting, Thin Film Chalcogenide Symposium O.
- Ochs, D., Rozanski P. and Ozimek, P. (2009) Progressive DC Power for TCO Deposition, 52nd Annual Technical Conference Proceedings, Santa Clara, CA, 9–14 May 2009, P60–63.
- Riedl, T. (2010) 'Transparent OLED displays', in Facchetti, A. and Marks, T. J., *Transparent Electronics from Synthesis to Applications*, Chichester, Wiley.
- Ryu, Y.R., Lee, T. S., Leem, J. H. and White, H. W. (2003) 'Fabrication of homostructural ZnO p–n junctions and ohmic contacts to arsenic-doped p-type ZnO', *Appl. Phys. Lett.*, **83**, 4032.
- Sato, Y., Akizukia, H., Kamiyamab, T. and Shigesatoa, Y. (2008) 'Transparent conductive Nb-doped TiO₂ films deposited by direct-current magnetron sputtering using a TiO_{2-x} target', *Thin Solid Films*, **516**, 5758–5762.
- Schwarz-Schampera, U. and Herzig, P. M. (2002) *Indium-Geology, Mineralogy and Economics*, Springer.
- Szyszka, B., Ruske, F., Sittinger, V., Pflug, A., Werner, W., Jacobs, C., Ulrich, S. and Kaiser, A. (2006), 'Transparent conductive oxides for large area applications by in-line magnetron sputtering', 1st International Symposium on Transparent Conductive Oxides, 23–25 October 2006, FORTH Crete, Greece.
- Tate, J. and Keszler, D. A. (2010) 'p-type wide-band-gap semiconductors for transparent electronics', in Facchetti, A. and Marks, T. J., *Transparent Electronics from Synthesis to Applications*, Chichester, Wiley.
- Tsukazaki, A., Ohtomo, A., Omuma, T., Ohtani, M., Makino, T., Sumiya, M., Chichibu, S., Fuke, S., Segawa, Y., Ohno, Koizumi, H. and Kawasaki, M. (2004) 'Repeated temperature modulation epitaxy for p-type doping and light-emitting diode based on ZnO', *Nature Mater.*, **5**, 42.
- Walker, G. (2010) 'Touch Technologies Tutorial', 2010 Flexible Electronics & Displays Conference, Phoenix Arizona, USA, 1–4 February 2010.
- Yanagi, H., Hase, T., Ibuki, S., Ueda, K. and Hosono, H. (2001) 'Bipolarity in electrical conduction of transparent oxide semiconductor CuInO₂ with delafossite structure', *Appl. Phys. Lett.*, **78**, 1583–1585.
- Yanagi, H., Ueda, K., Ohta, H., Orita, M., Hirano, M. and Hosono, H. (2002) 'Fabrication of all oxide transparent p-n homojunction using bipolar CuInO₂ semiconducting oxide with delafossite structure', *Solid State Commun.*, **121**, 15–17.
- Zhang, S. X., Kundaliya, D. C., Yu, W., Dhar, S., Young, S. Y., Salamanca-Riba, L. G., Ogale, S. B., Vispute, R. D. and Venkatesan, T. (2007) 'Niobium doped TiO₂: Intrinsic transparent metallic anatase versus highly resistive rutile phase', *J. Appl. Phys.*, **102**, 013701.
- Zunger, A. (2003) 'Practical doping principles', *Appl. Phys. Lett.*, **83**, 1, 7, 57–59.

Optical coatings in the space environment

D. WERNHAM, The European Space Agency,
The Netherlands

DOI: 10.1533/9780857097316.4.789

Abstract: The following chapter describes the main impacts of the space environment on optical coatings giving examples of the degradation of the performance of the physical properties of the coatings. This includes the impact of the space vacuum and the radiation emitted by the sun, along with the temperature extremes that optics have to survive. This is followed by a brief description of the basic product assurance and verification activities that are undertaken on coatings that are to be used in the space environment.

Key words: space, satellite, optics, coatings.

22.1 Introduction

The environment in space is a particularly harsh one for optical coatings. For porous coatings, the space vacuum causes a spectral shift, and a change in stress due to water release. Atomic oxygen present in Low Earth Orbits causes erosion of coatings. Space also has a harsh radiation environment which can cause absorptive losses in optics due to colour centre activation or polymerisation of organic contaminants of the surface of optics. Coatings exposed to solar radiation are subject to UV fixation of outgassing contaminants. Similarly, high power laser irradiation of coatings in the presence of contaminant outgassing sources results in laser-induced contamination, high absorption and, in the worst case, laser damage. An important effect for high power laser optics is the reduction of the laser-induced damage thresholds of porous coatings in vacuum. An additional factor is the often high thermal excursion coatings can experience in space, typically ranging from -50°C to $+80^{\circ}\text{C}$, notwithstanding deep space missions involving cryogenic temperatures, where coatings have to withstand -270°C and missions to the inner planets, or solar missions where coatings may have to survive temperatures in excess of 300°C . This chapter attempts to give a general overview of the effects of the space environment on optical coatings giving some examples from tests carried out on European Space Agency missions.

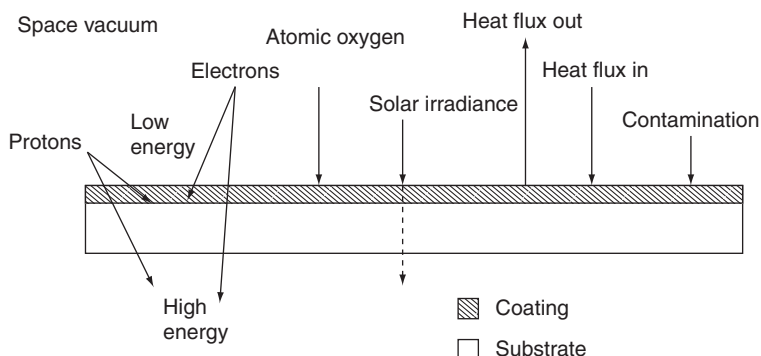
22.2 The space environment

The space environment is a particularly harsh environment for optical coatings, which are exposed to high energy particulate and electromagnetic radiations, high energy atomic oxygen, high vacuum and large temperature excursions simultaneously. The schematic of Fig. 22.1 below gives an overview of the main environmental components of space that can have an impact on optical coatings and their performance.

Each of the space environment effects are briefly described in the following sections along with some examples of the impacts that they can have on space optics. A good overview of the space environment is given by Fortescue *et al.*¹ and in the relevant European Co-operation for Space Standardisation (ECSS) standard.²

22.2.1 General overview of optics in space

Optics are used extensively on spacecraft, not only for optical instrumentation, where almost all conceivable coating types are utilised. These range from the very large – for example the primary mirrors of space-borne telescopes such as the Hubble Space Telescope, Herschel and Planck satellites, which can be several metres in diameter – to the very small – for example laser optics, which can be a few millimetres in diameter, necessarily minimised due to the severe weight and volume constraints placed on satellite payloads. Coverglasses protect solar cells from the harsh solar environment, the main form of power generation on most satellites. Optical solar reflectors (second surface mirrors) on radiators and the outer surfaces of the satellite, form the key means of thermal control of the satellite via radiative



22.1 The schematic gives an overview of the main environmental components of space that can have an impact on optical coatings and their performance.

heat exchange with space. In these cases, the optical function is to have a high emissivity of the heat conducted from the satellite to space, while minimising absorptance of radiation sources impinging upon the satellite. Multi-layer insulation (MLI) is used in order to thermally isolate sensitive equipment from heat sources or to keep equipment temperatures high enough for proper operation via alternating low emissivity metal coatings and low thermal conductance between the layers. Telescopes which look at the very cold universe have reflective coatings which minimise emissivity in order to increase measurement sensitivity.

A recent development in Europe has been high power laser optics for LIDAR instruments such as the ALADIN and ATLID, payloads on the ADM-Aeolus and EarthCARE satellites, respectively, which have presented their own, unique challenges. Not only do they need sufficient margins with respect to laser damage threshold, but they are particularly sensitive to optical degradation via the mechanism of laser-induced contamination, particularly at the short laser wavelengths they are to utilise (355 nm).

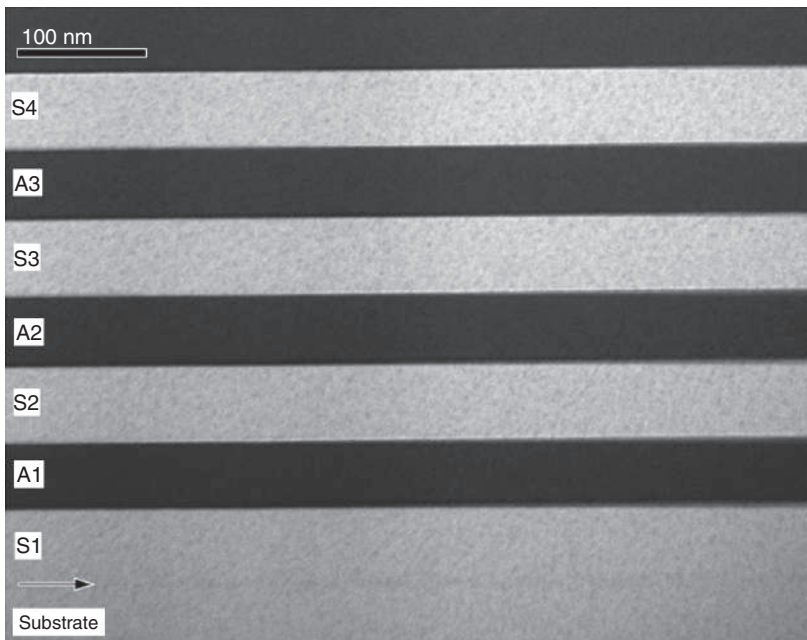
One of the major issues surrounding space optics is that if degradation does occur, there is usually no way to fix the problem in-orbit (a famous exception to this was the Hubble Space Telescope but even then, there were very large cost and mission downtime implications). Hence, the basic approach is that prevention is better than cure. The above necessitates a very high level of functional performance testing on-ground in order to guarantee the performance in orbit. As typical satellite mission durations range from 3 to 15 years, there is also a fundamental problem in testing for sufficient durations in order to make proper predictions on the End of Life (EOL) performance. This has necessitated forms of accelerated testing which may not be completely representative. Another issue is the synergistic effect when multiple space environment effects are present at the same time. Good examples of this are the presence of contaminants together with UV radiation or high intensity laser radiation.

22.2.2 Impact of space vacuum

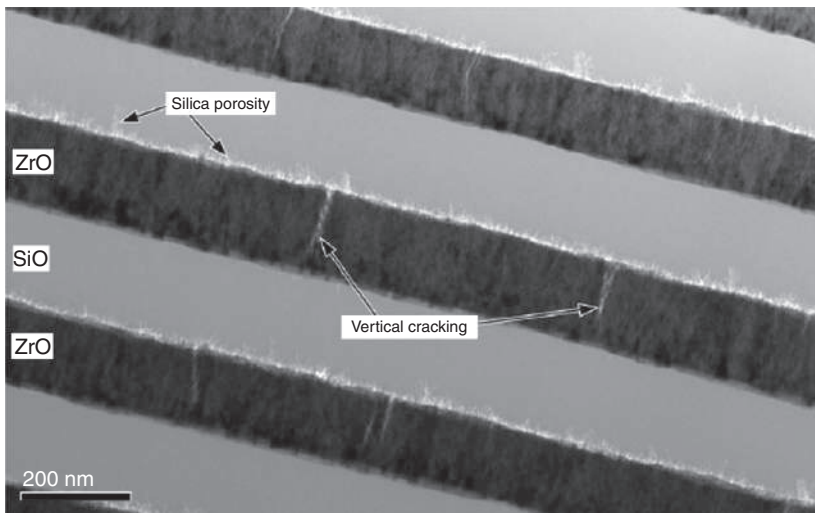
Space vacuum involves pressures below 10^{-8} torr for a typical satellite Low Earth Orbit (LEO) environment and pressures lower than this for higher orbits and planetary missions. Planetary landing missions for bodies such as Mars or Titan, which have atmospheres, will have different operational constraints.

For a highly densified coating, vacuum has little impact but for porous coatings we see the classical shift of the spectral response of the coating to lower wavelengths. Despite the fact that this is a well-known phenomenon, we continue to find that porous coatings are present in many of the

(a)



(b)



22.2 (a) Cross-sectional Transmission Electron Micrograph (TEM) of a fully dense coating deposited using an assisted sputtering technique; (b) corresponding TEM for a conventional electron beam evaporated coating.

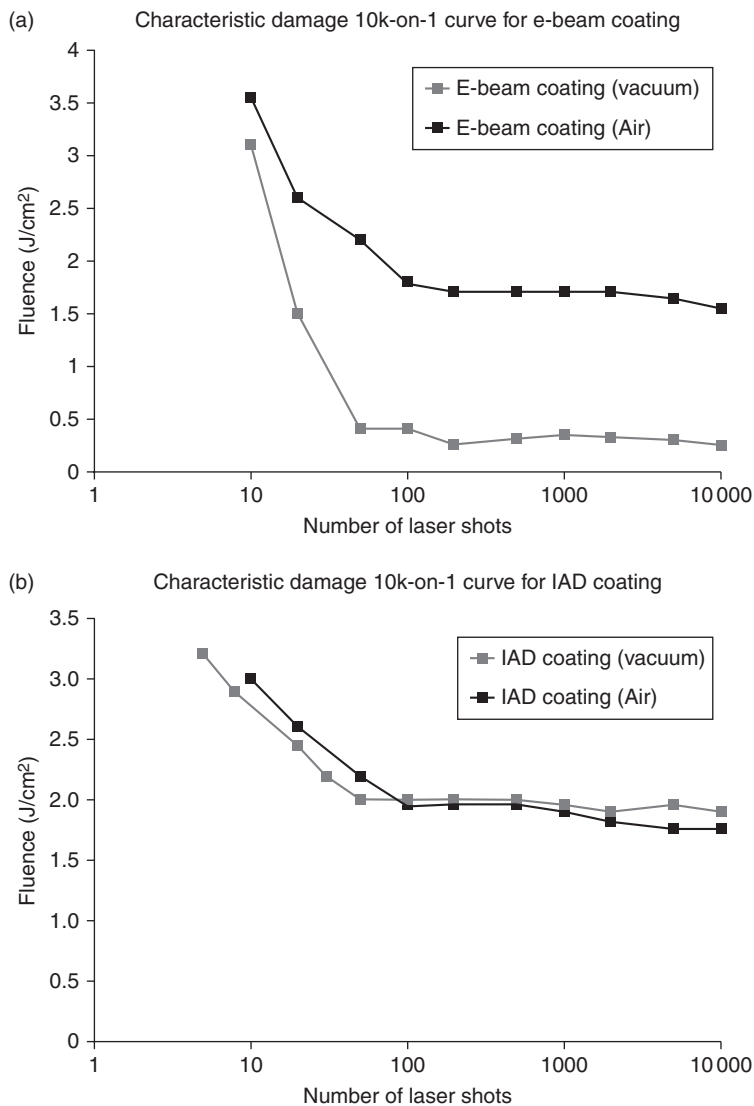
instruments being manufactured today. Figure 22.2a shows the cross sectional Transmission Electron Micrograph (TEM) of a fully dense coating deposited using an assisted sputtering technique. The corresponding TEM for a conventional electron beam evaporated coating is shown in Fig. 22.2b. It is clear from a comparison of the micrographs of the two coatings that the sputtered coating has a much less porous structure. Conversely, the classical unassisted e-beam evaporated coating clearly shows a large degree of porosity, particularly at the interfaces and within the high index material. Air to vacuum spectral shifts of a dense and porous coating are shown in Plates V and VI (see colour section between pages 404 and 405), respectively.

The impacts on instrument performance caused by the air-vacuum shift can be significant. In the case of the ALADIN laser, the air-vacuum shift of a dielectric polariser within the master oscillator of the laser, caused a complete failure due to an increase in the passive losses of the laser cavity. It is clear that coatings in space should be fully densified to avoid this effect, in addition to allowing representative performance testing on-ground that can be related to in-orbit performance. The lesson learned in this case is to test the air-vacuum shift on the coatings that will be exposed to space vacuum, and not to simply accept from the manufacturer that coatings are vacuum compatible. Special attention has to be given to narrow band coatings, edge filters and dielectric polarisers where small vacuum shifts can have a large impact on the coating and instrument performance.

Another impact of the loss of water from porous coatings is the change in the overall stress of the coatings. In general, we observe a change in stress from compressive to tensile. For instruments containing alignment-sensitive focal planes, this can cause an unacceptable level of defocusing due to the induced deformation of the substrate.

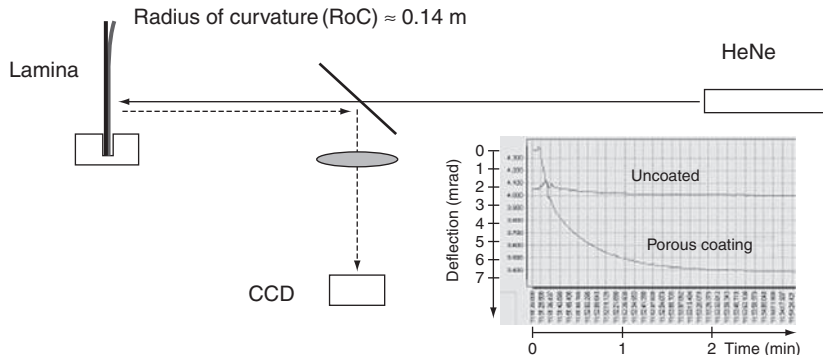
There is also an impact of water release on the laser damage threshold for laser coatings where a decrease in the laser-induced damage threshold (LIDT) in tests performed under vacuum conditions compared to tests of the same samples in air is observed.³ This is analogous to the toughening of glass where a thin compressively stressed layer is induced at the surface, either thermally or chemically in order to increase the fracture toughness, at the expense of more tensile stresses in the bulk. Figure 22.3a shows the results of an S-on-1 test on a coating sample prepared by conventional, unassisted electron beam evaporation in air and in vacuum. For comparison, air and vacuum LIDT test results for a fully densified coating are shown in Fig. 22.3b. The results of the test show a significant reduction in the LIDT of the porous coating of approximately a factor of $\times 5$.

We only observe this decrease on coatings which have a significant level of porosity. In the case of dense coatings, there is no decrease in the LIDT from air to vacuum. In order to demonstrate that this effect was due to the release



22.3 (a) Results of an S-on-1 test on a coating sample prepared by conventional, unassisted electron beam evaporation in air and in vacuum; (b) air and vacuum LIDT test results for a fully densified coating.

of water and the resulting increase in the tensile stress of the coating, Riede *et al.* used a thin coverglass lamina substrate and measured the deflection of the coating in vacuum. The results of the test are shown in Fig. 22.4. The deflection is fully reversible when going from air to vacuum and back again.



22.4 Results of a test using a thin coated lamina measuring the deflection in vacuum.

Tests of uncoated lamina did not show any bend, isolating the effect to the porous coating. Tests conducted in He atmospheres gave similar results to N₂, indicating that the thermal conductance was not a major effect.⁴

22.2.3 Thermal cycling in vacuum

As well as the vacuum effects described above, coatings in space are often cyclically subjected to large thermal excursions. Generally speaking, optical instruments, especially those which are alignment sensitive, are contained within environments which are thermally controlled by means of heaters and radiators in order to minimise the impact of thermal variations. Optics are still however, subjected to non-operational thermal cycles during orbit acquisition, and when the satellite goes into safe mode as a result of an operational failure. This will typically involve eight or more thermal cycles in the range of -40°C to +50°C for the qualification of optics operating in a LEO. Solar array coverglasses are designed to be directly exposed to the sun and are thus exposed to 1 solar constant, sometimes referred to as Air Mass Zero (1 AM0) amounting to some 1375 Wm⁻² of solar flux. This typically means that they will be exposed to thermal cycles between -40°C and +120°C. Coatings that are on inner planet or solar missions can experience much higher thermal excursions as they are exposed to up to 20 solar constants (several hundred °C) and extremely low temperatures during eclipses (-150°C). Optics that are designed to look into deep space, or cryogenic detectors, have coatings which have to operate at even lower temperatures.

Failures of coatings due to vacuum thermal cycles occur frequently, due to the change in stress caused by water release as well as the stresses caused by the different coefficients of thermal expansion of the materials which make up the layers of the coating and the substrate. A typical failure due to vacuum thermal

(a)



(b)



22.5 (a) Typical failure due to vacuum thermal cycle of a space optic; (b) high magnification image of the failure, indicating that this was a stress failure.

cycle of a space optic is shown in Fig. 22.5a. A high magnification image of the failure is shown in Fig. 22.5b, indicating that this was a stress failure. The key for these coatings is to ensure that they are qualified with sufficient margins (generally $\pm 10^\circ\text{C}$ of the nominal values), paying attention to the potential rate of change of the thermal cycles in addition to the actual temperature levels.

It is important to differentiate between thermal cycling in vacuum and thermal cycling carried out under ambient pressure conditions, as coatings that survive in the latter can often fail under vacuum testing. It is still common practice for suppliers to test thermal cycling under ambient pressure nitrogen conditions to save costs, only to find there are failures during sub-system or satellite level vacuum thermal cycle tests where the rectification

of the problem is far more costly. Coatings that are designed to operate in vacuum should be tested in vacuum.

22.2.4 Solar irradiance

The main impact from the solar spectrum comes from the higher energy UV wavelengths which can cause darkening of coatings due to colour centre formation or polymerisation of organic contaminants. The general characteristic of the degradation is that there is typically an increase of the absorption of the coatings at the UV end of the spectrum which becomes less prevalent at longer wavelengths.

This degradation in performance is particularly serious for solar cell coverglasses and optical solar reflectors used in radiators. In the former case, there can be a significant reduction in the conversion efficiencies of the cells and a resulting loss in power generation of the array, potentially leading to parts of the satellite payload being shut down before its nominal mission lifetime has been reached. In the latter, there is a loss in the efficiency of the radiator resulting in excessive heating and potential loss of the thermal control of the satellite. Degradation of a solar cell coverglass tested with UV irradiation in vacuum is shown in Plate VII (see colour section between pages 404 and 405). Note that the optic has been placed on an aluminium mirror in order that both reflective and transmissive losses could be measured during the test. There is an annealing effect which can reverse the degradation caused by UV exposure in vacuum when the optics are re-exposed to ambient conditions. This, of course, does not happen in space, meaning that performance degradation effects can easily be underestimated if an *in situ* measurement is not used during testing. It should be noted that great care is required in performing vacuum testing for space optics where chamber contamination due to outgassing has to be minimised as far as possible, as this can cause a similar degradation in the spectral performance.

For optical solar reflectors, degradation leads to an increase in the solar absorptance, α_s , of the coating, meaning that the radiative efficiency (directly proportional to α/ϵ , where ϵ is the emissivity) is degraded leading to an overall increase in the temperature of the satellite.

22.2.5 Particulate radiations

For optics in space, we are mainly concerned with protons and electrons which we qualitatively define as low energy (< 1 MeV) and high energy (> 1 MeV). For coatings, we are mostly concerned with low energy particulate radiations as the energy from these can be completely absorbed within the thin coating layers whereas higher energy radiations are only partially absorbed and are more of a problem for the substrate. Protons with energies

< 240 keV can cause particularly severe degradation due to the fact that the majority of damage occurs where the protons stop in the material.

The degradation effects caused by particulate radiations are generally similar to those caused by UV degradation inasmuch as there is typically more degradation in optical performance at shorter wavelengths which gets gradually less as we move to longer wavelengths. As with the UV performance degradations described above, there is an annealing affect, which reverses the degradation when optics are re-exposed to ambient conditions. Thus the optical performance should be measured *in situ* during the test, in order to make a proper evaluation of the in-orbit performance. An example of degradation of an optic exposed to various equivalent doses of low energy protons (240 keV) is shown in Plate VIII (see colour section between pages 404 and 405). Note that the optic has been placed on an aluminium mirror during the test in order that both reflective and transmissive losses could be measured during the test. Electrons show similar degradation effects although care has to be taken to ensure that the proper dose is applied to the test article due to the much larger stopping distances of electrons compared to protons.⁵ The susceptibility to particulate radiation-induced degradations can be mitigated by suitable dopants. An example is the cerium doping used in solar cell coverglasses or radiation resistant glasses where the glass is protected by the redox reaction of Ce³⁺ being converted to Ce⁴⁺ and vice versa.⁶ Unprotected glasses such as BK7 show rapid darkening if they are not properly doped and should generally be avoided for use in space applications.⁷

22.2.6 Atomic oxygen

Atomic oxygen (ATOX) is the main atmospheric component present in LEOs up to altitudes of 700 km. The main effect of ATOX is reactive sputtering and erosion of surfaces, particularly those surfaces which contain elements that react with oxygen. The main effect of atomic oxygen is the erosion caused by the relative velocity of approximately 8 km⁻¹ between the oxygen atoms and the spacecraft due to the orbital velocity of the spacecraft. Thus, the main impact occurs in the RAM direction of the spacecraft. Silver is particularly prone to ATOX degradation⁸ and is sometimes used as reflector coating on satellite telescope optics. Although protective layers are usually applied, care should be taken due to the presence of pinholes and other defects in the protective coating layers, and testing should always be carried out for any optics which are exposed to ATOX.

22.3 Contamination

Contamination is a major concern for satellite optical payloads, especially those which have multiple surfaces. The contamination can come from the

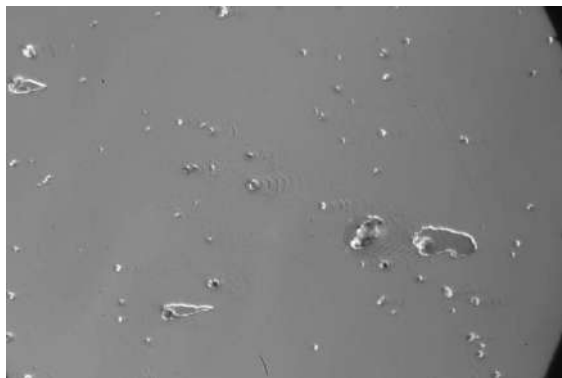
assembly process, during integration, during verification testing, from the launch and in-orbit, over the mission lifetime of the instrument. This section gives a brief introduction to the various contamination sources that typically effect space optics.

22.3.1 Terrestrial contamination

Terrestrial contamination is an ever-present problem for optical components being sent into space. The main contributors are particulate contamination and molecular contamination. The general guidelines of contamination control are similar to those employed for radiation protection for personnel who work with radioactive materials, that is, time, distance, shielding and monitoring. Good practice is to minimise the time for which the parts are exposed to any contaminant sources, maximise the distance from sensitive items to contamination sources, use physical barriers, for example, protective covers or positive pressure gas purges to shield sensitive items, and always monitor the contamination levels. The contamination control methodologies to be used for space equipment are described in detail in the relevant ECSS standard.⁹

The main source of particulate contamination in clean rooms is usually from people working in the proximity of the optics, from dead skin flakes, fibres from clothing and contamination transferred from footwear. It is thus important to have appropriate contamination controls in place and, in particular, to have a clear demarcation between ‘clean’ and ‘dirty’ areas, to define the acceptable levels of particle contamination, and to monitor the contamination levels during the production of the optics. Typical methods of monitoring contamination are to place a clean witness sample which follows the optics through the entire assembly, integration and testing phases. In addition to this, periodic particle counting should be performed in order to determine if a contaminating event has occurred and to check the levels against the required values.

The general particulate contamination monitoring in cleanrooms relies upon airborne measurements of the particle concentrations. It should be noted that for space optics, we are more concerned with the particle ‘fallout’ that is those particles which are heavy enough to fall under the influence of gravity onto the sensitive surfaces. Only a small quantity of these particles are detected by airborne particle counters which are thus regarded as a warning system for potential contaminating events. It is also worth noting that a vertical surface will generally have a factor of $\times 10$ less contamination than a horizontal one. Particle contamination can be particularly severe for laser optics where it can cause a significant reduction of the laser-damage threshold, or in optical systems which are very sensitive to stray light. In general, it is a sensible precaution to have a qualified cleaning procedure that can be used on optics in the event that the contaminant levels are deemed



22.6 An example of the impact of high particulate contamination levels causing laser damage on an optic.

to be outside the required levels. Figure 22.6 shows the impact of high particulate contamination on a laser optic which has been irradiated. From the figure it can be seen that standing waves have been ‘written’ into the coated surface from the interference generated by the particles.

The main source of molecular contamination on optical surfaces is generally from the offgassing of organic materials, that is, the release of volatile, low molecular weight species under ambient pressure conditions. It is important to avoid organic contamination on optics, which could subsequently darken due to the polymerisation of the contaminants in the space environment caused by UV and proton irradiation. As with particulate contamination, a contamination budget should be defined beforehand, and monitored with a witness sample which follows the flight optics and is periodically measured. The typical contaminants encountered are hydrocarbons, silicones and esters which can usually be identified from their infrared absorption spectrum. There is a dedicated ECSS standard¹⁰ which describes how the monitoring of organic contamination is performed for space optics. As with particulate contamination, it pays to have a qualified cleaning process in order to mitigate an unacceptable level of molecular contamination.

Another source of contamination is when the optics are incorporated into component-, system- or satellite-level vacuum bake-outs or tests. Here the vacuum chamber, along with supporting ground support equipment within it, can often be the source of contaminants. In this case it is always best practice to check the vacuum compatibility of materials within the chamber, to incorporate a cold trap and to perform a quartz crystal monitored bake-out of the vacuum chamber along with the ground support equipment at elevated temperature. This should be followed by a quartz crystal monitored blank test of the chamber at the test temperature prior to the flight optics being installed. Care should be taken when re-pressurising the vacuum

chamber. The chamber should be re-pressurised with dry nitrogen prior to cold traps or shrouds being warmed-up in order to prevent re-deposition of contaminants onto the sensitive optics.

There are also contaminants which can be present as part of the actual manufacturing of the optic itself which can have a severe impact when the optic is exposed to the space environment. Small concentrations of impurities in optical glasses and optical coatings, particularly metals with multiple oxidation states, can form colour centres which can be subsequently activated by radiation in space. Care has to be taken with the purity of the substrates and raw materials used for the manufacture of optical coatings to be used for space and they should always be linked to a dedicated certificate of composition from the supplier and, if necessary, periodically checked by techniques sensitive to trace contaminant levels such as inductively coupled plasma mass spectroscopy (ICPMS), secondary ion mass spectroscopy (SIMS) or X-ray photoelectron spectroscopy (XPS). Contaminants can also be introduced in the coating process itself which could have an impact on the performance of the optic in space such as the incorporation of crucible materials in the coatings for electron beam evaporated coatings or contaminants caused by arcing during sputtered coating deposition.

22.3.2 Space contamination effects

The vacuum of space causes the efficient outgassing of non-metallic materials which are unavoidably used in the construction of spacecraft. Some examples of these are adhesives; multi-layer insulation (MLI) used for spacecraft thermal control; carbon fibre reinforced plastic (CFRP) used for structures; cable insulation on electrical harnesses; and potting compounds and conformal coatings applied to electronics, to name a few. Great care is usually taken to reduce the outgassing levels of these materials as far as practically possible via the use of high temperature, vacuum bake-outs of materials, subsystems and at satellite level, prior to flight. However, some long-term outgassing flux will still remain which can accumulate over the many years of a typical satellite lifetime. There are standard methods for the screening of materials to be used in space vacuum which are described in the relevant ECSS standard.¹¹

Outgassing is particularly hazardous for cold space optics, where the efficiency of condensation of outgassing contaminants is significantly increased. There have been examples of water-ice condensation leading to performance degradations in-orbit for detectors which are below -150°C .^{12,13} Of course, even if extensive vacuum bake-outs have been undertaken, it is almost impossible to prevent re-adsorption of atmospheric moisture on the materials used in the satellite. The main preventative methods are

therefore good instrument design (ensuring that view factors of the sensitive optics are restricted as far as possible from outgassing sources) and ensuring that the cold detector optics are the last ones to be cooled down. Lastly heaters are often installed which allow recovery of performance via re-evaporation.

UV fixation of contaminants

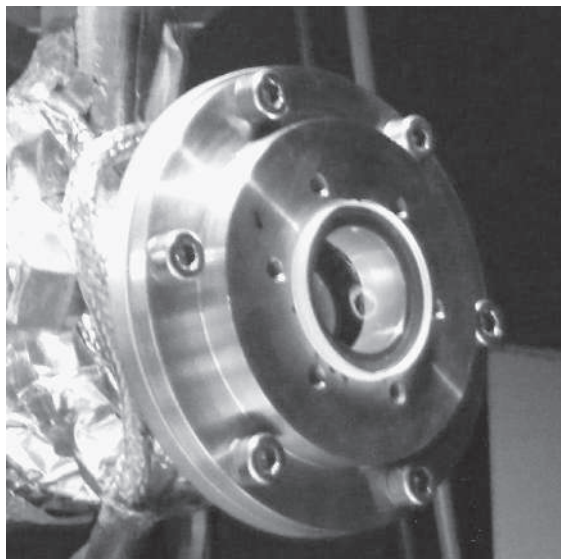
The fixation of contaminants on surfaces which are also exposed to UV radiation, has been studied by a number of groups^{14,15} who have shown that the deposition of outgassing contaminants on optical surfaces is greatly increased compared to the deposition rate when no UV is present. This is due to UV-activated polymerisation of contaminants, an increase in the molecular weight and a consequent increase in the residence time on the surface of the optic. This effect highlights the sometimes insidious, synergistic effects that can occur in space, which are not always properly accounted for in qualification test campaigns.

Laser-induced contamination

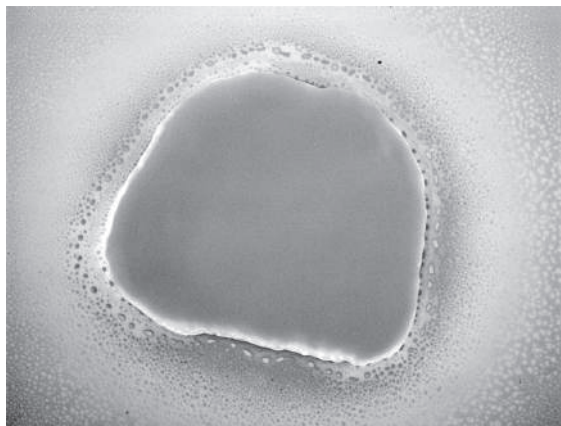
A similar example to the UV fixation of contaminants is laser-induced contamination (LIC), where highly absorbing deposits are formed in the areas of laser optics exposed to the high intensity irradiation in non-oxidising environments.¹⁶ This has been studied extensively for the ALADIN and ATLID instruments (payloads for the ADM-Aeolus and EarthCARE satellites, respectively) which both contain high intensity lasers operating at 355 nm.^{17,18} An example of a fluorescing LIC deposit formed during a laser test is shown in Fig. 22.7a. A microscope image of an LIC deposit is shown in Fig. 22.7b. The degradation in performance can be dramatic. During a vacuum test of an ALADIN laser, the energy dropped by a factor of $\times 2$ in 6 hrs due to LIC on the UV optics. LIC has also been implicated in the failure of the GLAS lasers on ICESAT, and the rapid degradation observed on the LITE instrument which flew on the space shuttle.¹⁹

Normal methods of mitigation against LIC such as screening of ‘bad actor’ materials, high temperature vacuum bake-outs, reduction of view factors by baffling, and molecular absorbers, are only partially successful in eliminating LIC. One mitigation method which has proved to be successful was the implementation of a low pressure oxygen environment which will now be used on the ALADIN instrument.²⁰ A much better method is to ensure that high power lasers are pressurised and that the number of vacuum exposed optics surfaces is minimised, which is the approach now adopted for the ATLID laser and has been successfully implemented on CALIPSO.

(a)



(b)



22.7 (a) example of a fluorescing LIC deposit formed during a laser test; (b) microscope image of an LIC deposit.

22.4 Product assurance for space coatings

The general principles of space product assurance relevant to space optics are to properly define and control the materials and processes used in the manufacture, assembly, integration and test of the components; to verify that the component meets its operational requirements with sufficient margins

to account for any uncertainties ensuring performance over lifetime; and to formally track any non-conformances and ensure that these do not have an unacceptable impact on the final performance. These are usually defined beforehand in a dedicated product assurance plan for the deliverable item.

22.4.1 End to end traceability

It is of particular importance for space equipment that the quality chain from source materials to finished product remains unbroken and includes all of the materials and processes in between. The main principle behind this is that, if a problem does occur during subsequent testing phases, or in orbit, that this problem is traceable and the root cause for any anomaly can be determined and corrected efficiently (or at the very least not repeated). Thus all of the materials used for the manufacture of optics and coatings should have a valid certification of composition which is traceable to the batch used. This is usually tracked with a declared materials list (DML) which is supplied to the customer along with the finished optics. This should include materials which are used in the manufacture and then removed such as waxes, rosins, pitch and polishing compounds used in the formation of optical substrates, along with the solvents used to remove them. It is also important to review the packaging materials used for the transportation and containment of space optics to ensure that these are compatible, particularly given the long durations that optics often reside in the packaging container prior to being integrated into instrument or satellite assemblies.

Residual contaminants from organic compounds, if not properly removed can result in subsequent failure of the optics in humidity, thermal vacuum and adhesion tests. They can also darken in the space environment via the interaction with the radiations described previously. Residual polishing compounds such as cerium dioxide can have a detrimental effect on the damage threshold of high power laser optics especially at shorter wavelengths where they can have significant absorption. It is often the case that materials which are used in the manufacturing process and which are subsequently removed are omitted from the DML, only to be found later on during an anomaly investigation.

Certain materials are not permitted for use in space due to their incompatibility with the vacuum environment. These include mercury, cadmium and zinc due to their propensity to evaporate in vacuum, PVC which contains a large proportion of plasticisers which are released in vacuum and pure tin which can grow tin whiskers in space. Silicones should generally be avoided for space optics due to the fact that they are very difficult to remove and will darken if exposed to UV or low energy proton radiation.

It is usually the responsibility of the goods receiving party, for example coating manufacturer receiving a substrate, to have the same level of product

assurance in their supply chain, and so on. For example, if there is a delamination failure of a coating, it is all too often the case that the failure cannot be attributed to problems at the coating manufacturer or the substrate supplier, because the quality chain has been broken and both the substrate and the coating are potentially implicated in the failure.

22.4.2 Process control

The DML is usually cross-referenced with a declared process list (DPL), which uniquely identifies all of the processes used for the manufacture of the optics. This includes cleaning processes and measurement and verification processes. Log books and plant maintenance files are complementary documents to the DML and the DPL. Some of the most important aspects to track are engineering changes, which are often implemented by experienced coating engineers, in order to stabilise or rectify drifts in coating plant performance. It is often the case that the materials are defined by the coating manufacturer in a process identification document (PID) and the various processes and measurements performed are recorded in a ‘traveller’ which follows the product through its entire manufacturing life cycle. These documents can often take the place of the DPL.

22.4.3 Non-conformance control

Non-conformances, defined as any breach of a requirement, either from the customer-defined specification of the delivered product, or from the internal specifications defined by the manufacturer for the manufacturing processes, should be traced and subjected to formal processing. Generally speaking, non-conformances are divided into major and minor depending on their degree of severity. Major non-conformances should be reported to the supplier as they are usually in a better position to make an assessment of the potential impacts at system level and judge whether they are acceptable or not. The non-conformance process usually comes under the responsibility of the quality assurance or product assurance department, who raise a non-conformance report (NCR) and then chair the subsequent non-conformance review boards (NRBs) until the issue is closed. For space products, any non-conformances associated with a product are considered to be an inherent part of its configuration. Thus, all NCRs are usually reviewed at the point of the delivery of the product, as part of the overall acceptance process.

The non-conformance control process should be regarded by the supplier as beneficial, inasmuch as it often provides valuable inputs for improvements to manufacturing processes, and eventual yield of good quality components, along with efficient identification and rectification of recurring manufacturing problems.

22.4.4 Space qualification

Qualification is the verification that the equipment meets its requirements with sufficient margins. Qualification can be by design; by analysis; by test; via similarity to components made using the same design, materials and processes, as one that has a demonstrated space heritage; or a combination of the above. The majority of space optics are qualified by test and similarity. It should be noted that in the latter case, it is often difficult to obtain direct performance data of optics from operational satellites due to the fact that the performance is often not directly measured, that the performance degradation cannot easily be traced to a single cause, and that satellite operators often do not provide detailed performance degradation data. In addition, depending on the particular satellite mission and orbit, any qualification by similarity argument has to ensure that the operation environment, for example orbit and mission lifetime, for the component is completely enveloped by the heritage satellite. The fact that optics are flying on a particular satellite is not a demonstration that they are performing to requirements applicable to another mission, and therefore that cannot be used as an argument for qualification in isolation. Thus a certain amount of verification testing should be performed in order to augment the heritage argument and ensure that there have been no process or material changes in the interim period which could affect the performance.

For optical coatings, witness samples are often used for qualification testing. Care has to be taken that these witness samples are not ‘hostile’ and are truly representative of the actual flight optic that will be produced. There have been several cases where witness samples have passed tests, only for the flight optic to subsequently fail. Common differences are geometry, for example when the witness sample is planar and the flight optic is curved; that the thermal environments in the coating plant are different between the witness sample and the flight optic due to geometry or tooling differences; in materials and processing, where different processes or materials are used for the witness sample and the flight optic; or that the witness sample is in a different coating run to that of the flight optic. For space optics, qualification is preferably at coating lot level unless there is evidence of process stability over a statistically significant number of coating runs. For critical components which can cause a single point failure for the satellite instrument, such as those for high power lasers; or where a small number of failures randomly distributed with a large number of components, can have a large overall impact on system performance, for example solar cell assemblies for solar arrays; qualification at coating lot level is even more important. Clearly the qualification methodology should be based upon an assessment of the potential severity of the eventual performance impacts at system level and be agreed between the customer and supplier beforehand.

22.5 Conclusion

The general impact of the space environment on optics has been briefly described in the preceding text along with a brief description of the product assurance principles that are applied to space optics. Clearly, space is a harsh environment for optics with many physical interactions leading to potentially severe degradation of optical performance. The main lessons learned are summarised below:

- In almost all cases, it is not possible to repair the degradation of optics in orbit. This necessitates a comprehensive terrestrial test campaign, and product assurance process for space optics, in order to guarantee their eventual performance. Space optics should always be presumed ‘guilty’ until proven ‘innocent’.
- Testing of space optics should be as representative as possible to the actual environment they will be exposed to. *In situ* performance measurements during testing should be implemented where possible in order to ensure that performance degradations are not missed due to annealing effects. In other words: ‘test as you fly’.
- Coatings used for space optics should be highly densified in order to reduce a number of degradation effects caused by porosity such as optical performance changes due to water release and the resulting changes in the stress of the coatings.
- A careful and detailed assessment of the risk and impacts of contamination on space optics should always be carried out, especially if the optics are exposed to UV or high power laser irradiation, and if the optics are cold compared to their surroundings. Coatings which are operated at temperatures below -150°C , and thus subject to water-ice contamination in vacuum, should be cooled down after the rest of the satellite, and heating should be implemented in order to decontaminate if necessary.
- Better test facilities are needed in order to investigate the synergisms of space environmental effects on space optics as performance degradation can be significantly underestimated if only individual effects are tested.
- The impacts of accelerated tests need to be compared with the data from long term exposure tests in order to construct better predictions of in-orbit performance.

22.6 Acknowledgements

The success of a satellite programme is, by necessity, the result of a high degree of collaboration, and I am deeply indebted to many of my colleagues, both in ESA and in industry for their contributions to the summary above. In particular, I would like to thank the ALADIN Project teams, the D-TEC

technical support directorate at ESTEC and the Laser Risk Reduction Group, from which much of the above has been taken. It is through constructive collaboration and the dissemination and understanding of many different test results that a successful satellite mission is made possible. I have attempted to introduce the most important effects that the space environment has on space optics but it is by no means a comprehensive review of a rather vast topic. I thus apologise for any omissions I may have made.

22.7 References

1. P. Fortescue, J. Stark, G. Swinerd Ed. *Spacecraft Systems Engineering*, 3rd Edition, Wiley, ISBN 0-471-61951-5 (2004).
2. ECSS-E-ST-10-04C 'Space Engineering – Space Environment', 15 November 2008, ECSS Secretariat, ESA-ESTEC, Requirements & Standards Division, Noordwijk, The Netherlands (available to download from: www.ECSS.nl).
3. W. Riede, P. Allenspacher and D. Wernham, *Laser qualification testing of space optics*, 38th Annual Boulder Damage Symposium 2006, Boulder, CO, USA (2006).
4. P. Allenspacher, W. Riede, D. Wernham, A. Capanni and F. Era, Vacuum laser damage test bench, *Proc. SPIE*, **V5991**, 599128–6 (2005).
5. J. Russell and G. Jones, *Radiation testing of coverglasses and second surface mirrors*, Proc. 9th International Symposium on Materials in a Space Environment, Noordwijk, The Netherlands, 16–20 June 2003 (ESA SP-540 Sept 2003).
6. G. Haynes, *Effect of radiation on cerium-doped solar-cell coverglass*, NASA TN D-6062, National Aeronautics and Space Administration, Washington D.C. 20546 (December 1970).
7. A. Gusarov, D. Doyle, L. Glebov and F. Berghmans, Comparison of radiation-induced transmission degradation of borosilicate crown optical glass from four different manufacturers, *Opt. Eng.*, **46**, 043004 (10 April 2007).
8. A. De Rooij, *The degradation of metal surfaces by atomic oxygen*, Proc. 3rd European Symposium on Spacecraft Materials in Space Environment, ESA SP-232 (1985).
9. ECSS-Q-ST-70-01C (15 November 2008) Space product assurance, Cleanliness and contamination control.
10. ECSS-Q-ST-70-05C (6 March 2009) Space product assurance, Detection of organic contamination of surfaces by infrared spectroscopy.
11. ECSS-Q-ST-70-02C (15 November 2008) Space product assurance, Thermal vacuum outgassing test for the screening of space materials.
12. D. Smith, *Impact on the performance of the ATSR instruments due to Condensation*, Contamination of Optical Equipment Workshop, ESTEC, Noordwijk, The Netherlands, 11–12 December 2003.
13. R. Hoogeveen, G. Lichtenberg and M. Wuttke, *The ice problem on Sciamachy: Origin and Solutions*, Contamination of Optical Equipment Workshop, ESTEC, Noordwijk, The Netherlands, 11–12 December 2003.
14. A. C. Tribble and J. W. Haffner, Estimates of photochemically deposited contamination on the GPS satellites, *J. Spacecraft*, **28**, 222–228, No. 2 (1991).

15. A. Pereira, J-F. Roussel, M. van Eesbeek, J. M. Guyt, O. Schmeitzky and D. Faye, *Study of the UV enhancement of contamination*, Proc. 9th International Symposium on Materials in a Space Environment, Noordwijk, The Netherlands, 16–20 June 2003 (ESA SP-540 Sept 2003).
16. F. Hovis, B. A. Shepherd, C. T. Radcliffe, A. L. Bailey and W. T. Boswell, Optical damage at the part per million level, *SPIE*, **2114**, 145–153 (1994).
17. W. Riede, P. Allenspacher, H. Shroder, D. Wernham and Y. Lien, Laser-induced hydrocarbon contamination in vacuum, *SPIE*, **5991**, 59910H-1 to H-13 (2005).
18. Adrian P. Tighe, Federico Pettazzi, Jorge Alves, Denny Wernham, W. Riede, H. Schroeder, P. Allenspacher and H. Kheyrandish, Growth mechanisms for laser induced contamination on space optics in vacuum, *Proc. SPIE* **7132**, **71321L** (2008).
19. D. M. Winker, R. H. Crouch and M. P. McCormick, An overview of LITE: NASA's lidar in-space technology experiment, *Proc. IEEE*, **84**, 164–180, No. 2 (February 1996).
20. D. Wernham, J. Alves, F. Pettazzi and A.P.Tighe, Risk mitigation for laser-induced contamination on the ADM-Aeolus satellite, *Proc. SPIE*, **7842**, 78421E-1 to E-12 (2010).

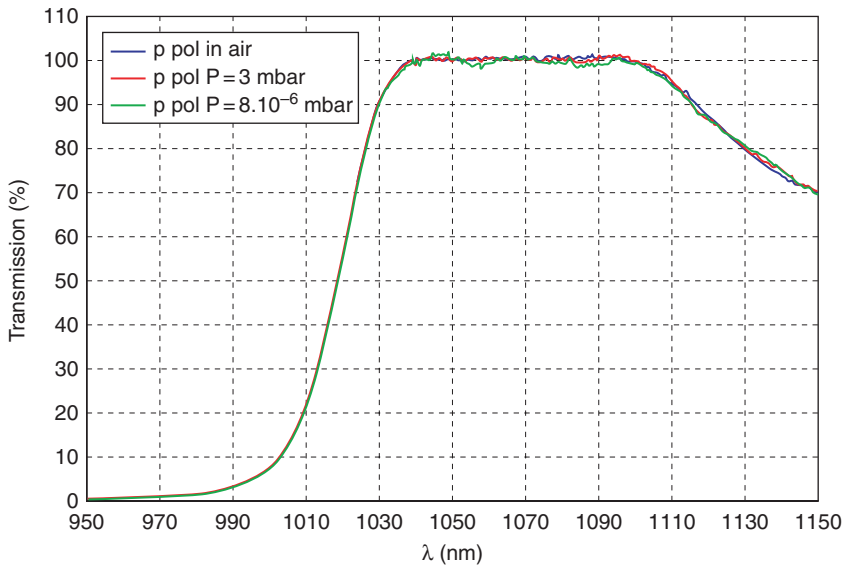


Plate V (Chapter 22) Air to vacuum spectral shift of a dense coating.

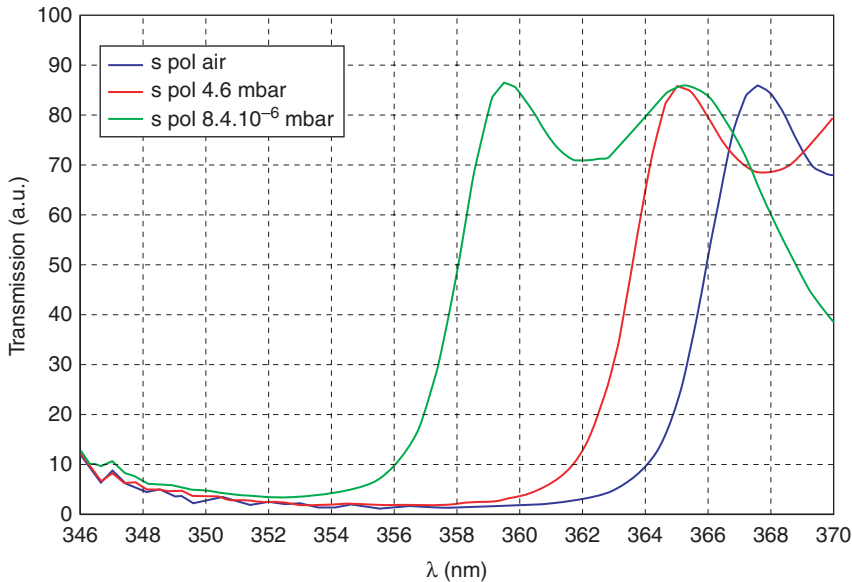


Plate VI (Chapter 22) Air to vacuum spectral shift of a porous coating.

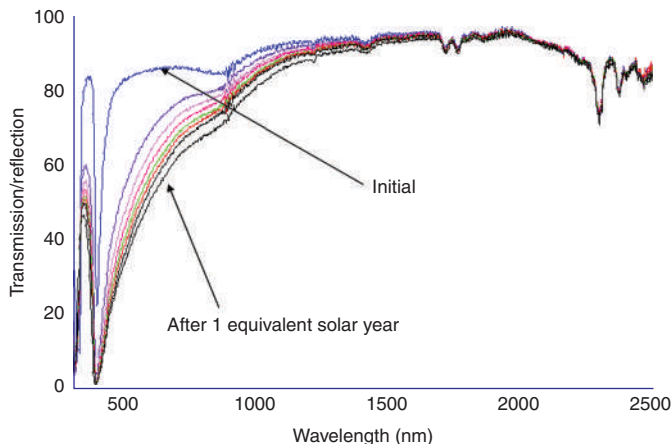


Plate VII (Chapter 22) Degradation of a solar cell coverglass tested with UV irradiation in vacuum.

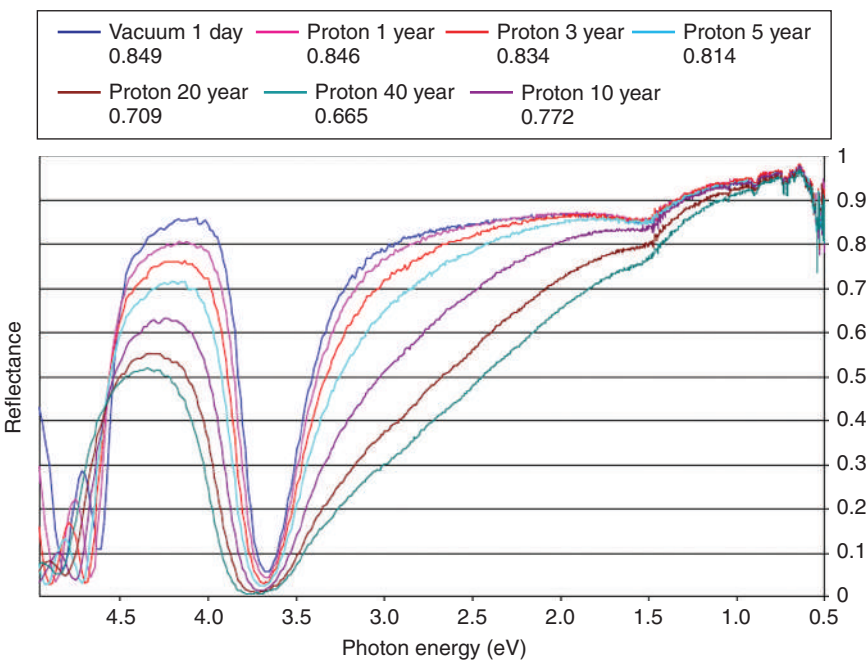


Plate VIII (Chapter 22) An example of degradation of an optic exposed to various equivalent doses of low energy protons (240 keV).

- a,b-band-emittance, 364
Abney's law, 404
absorption, 504–6
 absorbances of PMMA layers
 including TiO₂ anatase
 nanocrystal, Plate IV
 water, 525–7
absorption edge, 306
acceptor-like material, 47
active device, 650–3
 application, 650–1
 electrochromic devices, 651–3
 active metamerич interference
 security image structure, 650
active glazing, 736
active monochromatic monitoring
 strategies, 73–82
expected levels of errors in thickness
 of layers of the 40-layer hot
 mirror, 78, 80
monitoring signal for a coating layer
 with several signal extrema, 81
monitoring signal for the first eight
 layers of 40-layer hot mirror, 76,
 79
monitoring signal for the first eight
 layers of 42-layer hot mirror, 75
monitoring spreadsheet for the
 40-layer hot mirror design, 76
monitoring spreadsheet for the
 42-layer hot mirror design, 74
spectral transmittance and layer
 optical thickness of 40-layer hot
 mirror design, 73
spectral transmittance and layer
 optical thickness of 42-layer hot
 mirror design, 73
adhesion, 547–9
 improvement by plasma treatment,
 443
 plasma treatment, 443
all-dielectric filters, 635–6
reflectance spectra at various angles
 (unpolarised light), 636
alternating ion plating, 14
Ampère-Maxwell equation, 458
Anderson localisation, 145
angular selection filter (ASF), 574, 579
anti-glare coating, 565, 725–6, 728
antireflection
 optical coatings on plastic, 519–34
 coatings, 528–33
 transparent polymer materials,
 520–2
 vacuum coating processes, 522–8
antireflection coating, 31, 528–33, 565
antireflective structures (ARS), 530–2
reflectance and transmission
 spectra of plasma-etched plastic
 sheet, 531
SEM showing PMMA and Zeonex
 surfaces, 531
vacuum deposited antireflective-
 coatings, 528–9
AR-hard design principle, 529
reflection R and transmission T of
 scratch resistant AR-hard layer,
 529
wet-chemical AR coatings on plastics,
 532–3
antireflective structures (ARS), 530–2
antistatic film, 758–9
aperture mode, 403
AR-hard design, 528–9

- architectural coating, 376
 aspecular angle, 415
 ASTM D1003, 551
 asymmetric single split ring resonator (ASR), 140
 atmospheric windows, 380
 atomic force microscopy (AFM), 152
 atomic layer deposition (ALD), 18–19
 atomic oxygen (ATOX), 798
 atomic scattering factors, 304–7
 authentication devices
 optical coatings, 631–56
 active devices, 650–3
 basic principles and structures, 633–41
 film functionality and structurally controlled optical coatings, 653–5
 optical effects, 641–50
- back-side coated chirped mirror, 670–1
 band pass filter, 574
 bandgap, 300
 baricentric coordinated, 406
 Bayer test, 545–6
 beam splitter, 585
 Beer-Lambert law, 294, 318
 Bergman-Milton representation, 156
 Bernstein–Moss effect, 749
 Bethe-Salpeter equation, 179, 246–50, 258, 259, 269
 bidirectional reflectance distribution function (BRDF), 414
 bidirectional transmittance distribution function (BTDF), 415
 birefringence, 334
 black chrome, 372
 black silicon, 601
 blackbody, 358
 blackbody radiation, 359–63
 spectral radiance from blackbody as function of frequency, 360
 spectral radiance from blackbody as function of wavelength, 362
 boiling test, 548–9
 Boltzman’s distribution, 36
 Bose-Einstein distribution, 359
 bottom-up techniques, 530
 boundary condition, 196, 201
 Bragg structure, 668
 Bragg’s law, 311, 325
 Brandsealing, 640
 Brewster angle, 334
 Brewster-angle chirped mirror, 669–70
 broad band monitor (BBM), 65, 95, 96, 98, 101–5, 114, 125
 broadband wide-angle AR coating (BBAAR), 40
 building-integrated photovoltaics (BIPV), 736
 bulk-heterojunction materials, 48
 bulk plasmon, 133
 cadmium sulphide (CdS), 615
 cadmium telluride (CdTe), 597
 calibration factors, 66
 cathodic arc evaporation, 16
 Cauchy principal value, 316
 Centre for Advanced Laser Applications (CALA), 685
 ceramic matrix
 embedded metal nanostructures, 137–46
 composites of random elements, 144
 materials and quantum dots, 138–9
 metamaterials, 139–43
 small random disorders and imperfection in metamaterials, 143–4
 thin and ultrathin metal coatings and metamaterials, 144–6
 cermet, 372
 characteristic material parameters (CMP), 158
 charge coupled device (CCD), 64, 102
 charge separation, 609
 charge transport, 609
 chemical colours, 391
 chemical vapour deposition (CVD), 17–18, 432
 chiral sculptured thin film, 455
 chirped mirrors, 666
 chirped-pulse amplification, 686
 ChromaFlaire, 641
 chromaticity diagram, 404
 CIELAB, 412
 CIELUV, 412

- closed field magnetron sputtering, 14, 522
 clustering, 37
 coarse wavelength demultiplexing (CWDM) filter, 26
 coating-based window heating, 732–3
 coating design, 551–5
 glass substrate, 551–2
 multi-functional coatings, 553, 555
 numerical simulation, 553
 polycarbonate, 552–3
 schematic design of coating stack with gradient adjustment, 553
 coatings
 glass substrate, 551–2, 727–8
 polycarbonate, 552–3
 polymer substrates, 729–32
 films for laminates, 730–1
 films for multi-cavity glazing applications, 731
 window film products for retrofit applications, 731–2
 coherent backscattering, 263–9
 enhancement, 261
 random medium with random rough interfaces, 266–9
 cross-section of a slab with an effective permittivity, 270
 incoherent cross-sections for random slab, 269
 random medium with two planar interfaces, 264–6
 TM-TM scattering coefficient, 268
 total incoherent cross-section of a layer with dielectric scatterers, 266
 total incoherent cross-section of a layer with metallic scatterers, 267
 semi-infinite medium, 264
 incoherent bistatic cross-section for the co-polarised and cross-polarised scattering, 265
 coherent bistatic matrix, 228, 229, 235
 coherent potential approximation (CPA), 250, 252
 cold-cathode fluorescent lamp (CCFL), 567
 colour-appearance colorimetry, 413
 colour constancy, 411
 colour filters, 566
 colour-matching-functions (CMF), 404
 colour stimulus, 403
 colorimetry
 basic colorimetry, 402–13
 CIE 1931 and CIE 1964
 chromaticity diagrams, 408
 CIE 1931 and CIE 1964 colour-matching functions, 408
 colour-matching functions in fundamental reference frame, 404
 perspective view of tristimulus space, 405
 psychometric colorimetry, 411–13
 psychophysical colorimetry of colour stimuli, 403–9
 psychophysical colorimetry of light sources and non-self-luminous surfaces, 409–11
 colour in optical coatings, 391–422
 development of the understanding of interference colour, 392–402
 Auguste Michel-Lévy (184–1911), 399–400
 Brewster's diagram, 399
 David Brewster (1781–1868), 397–9
 Isaac Newton (1642–1727), 393–5
 J. F. Gabriel Lippmann (1845–1921), 400
 lens optical coatings, 401
 Leopoldo Nobili (1784–1835), 397
 Newton's representation of colours reflected and transmitted lights, 394
 Nobili's metallocromia colour gamut, 398
 soap bubbles, 401
 thin film anti-counterfeiting coatings, 401–2
 Thomas Young (1773–1829), 395–7
 optical coating colorimetry, 413–22
 CIE 31 chromaticity coordinated produced by equal-energy illuminant, 419
 CIE 1931 chromaticity diagram, 421

- colorimetry (*cont.*)
 geometry for the definition of
 bidirectional transmittance and
 reflectance spectral distribution
 function, 414
 gonio-apparent colour
 measurement, 414–16
 multi-angle spectrophotometry, 415
 optical coating colour, 416–22
 representation on the incidence
 plane of system of three media,
 416
 spectral reflectance for a glass with
 refractive index $n_2 = 1.6$, 418
 spectral reflectance related to
 polarisation p and s , 420
 columnar thin film (CTF), 455
 complementary colour, 393
 Compton scattering, 312
 conduction band, 300
 conductive antireflection, 767–8
 coating cross section, 768
 coating requirements, 767
 measured optical and electrical
 performance, 768
 conductivity, 745–51
 doping, 746–7
 metals, 745–6
 optical properties, 747–51
 cone activation, 403
 continuous refractive index, 117–25
 material mixtures production, 118–22
 comparison of results for selected
 effective media theories, 120
 laser induced damage thresholds,
 121
 measured transmittance spectrum,
 123
 principle of Ion sputtering process,
 120
 rugate filters deposition control,
 122–5
 contour fringe shift interferometry, 684
 conventional thermal evaporation, 98
 ‘Cool Cars’ initiative, 738
 cooling-dominated region, 721
 copper, 370
 copper indium gallium diselenide thin
 film solar cells, 612–23
 Ga composition depth profile, 615
 novel absorbers, 619
 schematics of CIGS devices and SEM
 cross section of efficient CIGS
 solar cell, 618
 state of the art technologies at
 industry level, 618–19
 vacuum free deposition, 619–23
 electrodeposition, 620–1
 printing and doctor blade, 622–3
 ultrasonic spray, 622
 core polarisability, 136
 crack onset strain (COS), 428, 547
 critical angle, 319
 Croce model, 297
 cross-section, 241–6
 decomposition of the wave vectors,
 243
 random volume with rough
 boundaries, 245
 scattering of an incident plane wave
 with a wave vector, 243
 scattering operators, 244
 cumulative effect of thickness errors, 78
 cutoff, 301
 3D time-of-flight laser radar, 273
 dark exciton, 507
 dark mirror, 370
 de Broglie wavelength, 494
 declared materials list (DML), 804
 density-functional theory (DFT), 598
 deposition
 optical thin films and coatings, 3–21
 atomic layer deposition (ALD),
 18–19
 cathodic arc evaporation, 16
 chemical vapour deposition
 (CVD), 17–18
 energetic processes, 6–16
 etching, 20
 processes, 4–6
 pulsed laser deposition (PLD), 17
 Sol-gel processes, 19–20
 dichroic beam splitters, 569
 dielectric coatings, 5
 dielectric constant, 194, 202, 295
 dielectric film
 scattering of light, 212–19

- mean differential reflection coefficient, 217
- dielectric filters, 33
- dielectric function, 135
- dielectric-metal-dielectric (DMD), 745
- dielectrics, 384
- differential reflection coefficient, 184, 203, 204, 210, 216
- differential transmission coefficient, 203, 204
- diffraction Bragg reflector (DBR), 588
- digital light processing (DLP), 572
- digital micromirror device (DMD), 572
- dimmable window, 733–4
- DIN EN ISO 2409, 548
- DIN ISO 9211–3, 545
- DIN ISO 9211–4, 545
- DIN standard 52347, 545
- DIN standard 52348, 546
- direct broad band optical monitoring, 82–5
- expected levels of errors in thickness of the 40-layer hot mirror, 84
- direct on-line correction, 110–11
- dispersive mirrors (DM), 664, 666–7
- application in high-intensity lasers, 685–8
- production, 677
- pulse compression, 678–81
- femtosecond pulses spectrum originating from gas-filled hollow fibre, 679
- Fourier-limited pulse before and after propagation, 680
- measured GDD and reflectance of prototypical double angle DM, 679
- physical thicknesses of layers in prototypical double-angle DM design, 678
- theoretical and measured interferometric autocorrection pulse, 681
- displays
- optical coatings for lighting, 564–91
 - automobiles head up display (HUD), 584–7
 - flat panel display (FPD), 565–7
 - LEDs, 587–9
- projector using light emitting diode (LED) light source, 573–84
- projectors, 567–73
- doctor blade deposition, 622–3
- donor-like material, 47
- doping, 746–7
- physics of transparent conductive coatings, 747
 - vs. resistivity and origin of the ‘resistivity well,’ 748
- double-angle dispersive mirror, 674
- double-chirped mirrors, 668–9
- Drude model, 303, 378
- dual ion beam sputtering (DIBS), 703
- Dyakonov-Tamm waves, 456, 484
- Ebanol, 370
- effective medium approximation (EMA), 155, 158–9
- effective medium theory (EMT), 530
- effective permittivity, 250–1
- ‘eggshell’ effect, 552
- electrically conducting coatings, 272
- electrochemical appearances, 397
- electrochemical etching, 654
- electrochromic devices, 651–3
- electrodeposition, 620–1
- electromagnetic field, 182, 234
- electromagnetic interference shielding, 754–8
- basic formulae for far field EMI shielding effectiveness, 757
- determining coating parameter, 758
- EMI shield for dual laser, 757–8
- measured electrical and optical performance for window, 756
- measured tco performance, 758
- wideband conductive AR coating for anti-icing of TV laser window, 755
- electron-beam-evaporated oxide layers, 523–4
- electron energy loss spectroscopy, 320
- electron gun evaporation, 702–3
- ion assisted deposition technique, 703
- electron transporting material, 47
- ellipsometry, 319
- embossing *see* bottom-up techniques
- emulsion polymerisation, 532

- energy conservation, 733
 energy efficiency
 automotive window, 722
 building window, 720–2
 energy efficient windows, 763–6
 coatings, 368
 enhanced backscattering peak, 206, 216, 218
 enhanced transmission peak, 206
 erbium doped fibre amplifiers (EDFA), 40
 error self-compensation effect, 67–72, 70, 83–4
 19-layer Fabry-Perot filter
 transmittance *vs.* optical thickness, 68
 122-layer four-cavity WDM filter
 error sensitivity analysis, 72
 four-cavity WDM filter transmittance *vs.* optical thickness, 72
 multi-cavity narrow band pass filter, 69
 schematic diagram, 71
 error sensitivity, 39
 Essential Macleod, 667
 etching *see* bottom-up techniques
 ethylene vinyl acetate (EVA), 727
 EUV lithography (EUVL), 323
 exciton diffusion, 608, 609
 Exner's coefficients, 407
 Extended X-ray Absorption Fine Structure spectroscopy (EXAFS), 309
 external electrode fluorescent lamp (EELF), 567
 external quantum efficiency (EQE), 508, 612
 extinction coefficient, 294
 extinction ratio, 569–70
 Extreme Light Infrastructure (ELI), 685, 698
 extreme ultraviolet (EUV), 291
 Fabry-Perot filter, 68, 431
 Fabry-Perot interferometer, 667
 Fabry-Perot-like structures, 636
 Fano waves, 484
 far infrared, 140
 far ultraviolet (FUV), 291
 Faraday equation, 458
 fast Fourier transform, 210
 Feynman diagram, 258, 261
 films
 laminates, 730–1
 multi-cavity glazing applications, 731
 Fine Guidance System (FGS), 700
 finite-difference time domain (FDTD), 157
 Fits of easy Reflexion, 393
 Fits of easy Transmission, 393
 flat fluorescent lamp (FFL), 567
 flat panel display (FPD), 565–7
 Floquet-Bloch theorem, 183
 Floquet harmonics, 467
 Floquet-Lyapunov theorem, 458
 Floquet-type representation, 156
 Fluorescence Spectroscopy, 299
 forward atomic scattering factor, 305
 Fourier coefficient, 184
 Fourier transform (FT), 28–33, 181, 190, 233, 258
 designed and measured transmittance of a rugate filter, 32
 Fourier transform-limited pulse (FTLP), 673–4
 Fourier-transform spectroscopy, 684
 free-carriers, 749
 free-electron-like film, 377
 free electron metals, 303–4
 free oxygen ions, 781
 free-space radiation mode, 43
 Fresnel reflection, 671
 Fresnel's coefficient, 295, 417
 Fresnel's laws, 401, 416
 Fresnel's reflectance, 419
 full width at half maximum (FWHM), 577, 578
 gain flattening filters, 41
 gamma-ray interaction processes, 313–14
 gamma rays, 292
 gas flow sputtering (GFS), 558
 gas modified filter, 588
 Gauss-Legendre method, 260
 Gaussian pulse, 674
 Gaussian random process, 181, 205, 213, 220

- genetic algorithm, 37, 40
 Gires-Tournois interferometer, 666,
 667–8
 glancing-angle deposition (GLAD), 654
 glass substrate, 551–2
 glazing
 integration of coating into multi-
 functional requirements, 735–6
 role of thermal control, 719–22
 automotive window energy
 efficiency, 722
 building window energy efficiency,
 720–2
 global optimisation, 36–8
 gonio-apparent colour, 392, 414
 gonio-spectrophotometer, 415
 gravitational wave interferometric
 detector (GWID), 711
 Green function, 241–2, 246–7, 248, 254
 Green tensor, 255–63
 backscattering enhancement, 263
 contribution to the first order, 261
 contribution to the second order, 262
 scattering processes for the ladder
 approximation, 257
 group delay dispersion (GDD), 664
 highest possible value, 676–7
 relative bandwidth function
 obtained at centre design
 wavelength of 800 nm, 676
- Hagen-Rubens relation, 370
 halogen lamp, 567–8
 hard X-rays (HXR), 292
 hardcoat *see* pyrolytic coating
 hardness, 547
 haze, 551
 head up display (HUD), 584–7
 heat mirror, 370
 heaters, 753–4
 basic formulae, 754
 Helios, 677
 Helmholtz equation, 221
 hexamethyldisiloxane (HMDSO), 438
 hexane diol diacrylate, 431
 high-intensity femtosecond lasers
 dispersive mirrors application, 685–8
 single layer Ta_2O_5 vs dispersive
 coating, 688
- threshold fluencies of single layer
 deposition and fused silica
 substrate, 687
 optical coatings, 664–89
 dispersive mirrors production, 677
 group delay measurement with
 white light interferometer, 681–5
 highest possible value of group
 delay dispersion (GDD), 676–7
 mirror design approaches, 666–76
 pulse compression with dispersive
 mirrors, 678–81
- high power impulse magnetron
 sputtering (HIPIMS), 15
- high power pulse magnetron sputtering
 (HPPMS), 552
- high reflection coating, 588
- highest occupied molecular orbital
 (HOMO) band, 608
- hole-transporting material, 47
- hollow cathode activated deposition
 (HAD), 557
- homogenisation theory, 509
- hot cathode fluorescent lamp (HCFL),
 567
- Huygens-Fresnel principle, 648
- illuminants, 409
- impurity potential operator, 247
- incoherent bistatic matrix, 228, 229, 235
- incoherent intensity, 255–63
 backscattering enhancement, 263
 scattering processes for the ladder
 approximation, 257
- indentation elasticity, 547
- indirect optical monitoring strategies,
 85–90
 layer optical thickness of the 18-layer
 filter, 87
 monitoring spreadsheet for the
 40-layer hot mirror design, 86
 predicted and actually measured
 transmittance of witness chip, 88
 theoretical transmittance of the
 18-layer filter, 88
 traces of monitoring signal for the
 first four witness chips, 87
- witness chips for monitoring different
 filter layers, 88

- induced transmittance filters, 145
 inertial confinement fusion (ICF),
 710–11
 infrared radiation, 543
 inhomogeneous refinement, 33–5
 broadband, wide-angle, non-polarizing AR coating, 34
 initiated chemical vapour deposition (iCVD), 442
 inorganic nanostructures, 599–606
 light trapping and photo-carrier collection, 601–2
 design of a radial pn junction in nanorod, 602
 new concepts of solar cells, 600
 quantum dots and nanowires in thin film solar cells, 602–6
 silicon tandem solar cells, 604
 theoretical calculation of conversion efficiency of tandem solar cells, 605
 Institut Laue-Langevin (ILL), 697
 instrumental colour measurement, 392
 instrumental reference frame, 405
 insulator-metal-insulator (IMI), 745
 integration operator, 235
 intensity operator, 251–5
 particle scattering in an infinite medium and volume, 253
 interference coatings, 145
 interference colour, 391, 414
 development of understanding of, 392–402
 Interference Colour Chart, 399
 reproduction of the original chart, Plate II
 interference colour photography, 400
 interference term, 232
 interferometers, 713
 interferometry, 319
 Interval of its Fits, 393
 inverse Fourier transform, 673
 inverse wavelength, 29
 ion assisted deposition (IAD), 7–9, 111
 schematic diagram, 7
 ion assisted filtered cathodic arc evaporation (IFCAD), 16
 ion beam sputtering (IBS), 15, 96, 98–9,
 101, 119, 703, 713
 ion plating, 9–11
 reactive low-voltage ion plating, 10
 ionised impurity scattering, 747
 iridescence phenomenon, 400
 iridescent, 397
 Jahoda-Velicky dispersion relation, 316
 James Webb Space Telescope (JWST),
 700
 Kirchhoff's law, 363, 364
 Kramers-Krönig relation, 316, 509
 Kretschmann configuration, 476
 Kretschmann-Raether configuration, 476
 Krönig-Penney model, 499
 Lambertian, 409
 laminated glass, 727
 laminated glazing, 726–7
 laser cross-section, 273
 laser imagery, 272
 laser-induced contamination (LIC),
 802–3
 fluorescing LIC deposit, 803
 laser-induced damage threshold (LIDT), 121–2, 687, 793
 laser Megajoule (LMJ) project, 710–11
 complex-shaped coated reflectors, 712
 laser radar, 273
 Lexan, 523
 light emitting diode (LED), 573–84,
 587–9
 band pass filter spectrum used in colour gamut-enhanced DLP, 574
 CIE 1931 chromaticity diagram, 575
 daylight simulation coating of LEDs by adding GDF, 589
 experimental spectrum of ASF at different incident angles, 581
 increasing colour gamut by adding red LD in regular DLP, 573
 LEDs and X-plate used in projector, 583
 luminance with and without ASF measured at different output angles, 581
 ODR coating structure, 588

- phosphor colour wheel and red LED
to produce red, green and blue
colours, 575
- phosphor colour wheel to produce
red, green and blue colours, 582
- reflectance at 460 nm vs angle of
ODR reflector, 588
- reflectance of green light 525 nm by
WAR filter at different incident
angle, 582
- simulation and experiment of
FWHM at incident angle from 0°
to 60°, 580
- simulation and experiment of
spectrum shift at incident angle
from 0° to 60°, 579
- simulation of FWHM at incident
angle from 0° to 60°, 579
- simulation of spectrum shift at
incident angle from 0° to 60°, 578
- simulation spectrum of ASF at
different incident angles, 580
- spectra of blue and red reflection
filter of X-plate, 583–4
- transmittance of green light 525 nm
by ASF at different incident
angles, 576
- light trapping, 601–2, 609–12
electromagnetic field distribution, 610
- implementation of periodic structures
in multilayer stack, 610–11
- absorption of P3HT:PCBM blend
active layer vs photonic crystal,
611
- plasmons for increasing absorption in
OSCs, 611–12
- device fabricated with thin silver
film deposited onto ITO, 612
- lighting
optical coatings for displays, 564–91
automobiles head up display
(HUD), 584–7
- flat panel display (FPD), 565–7
- LEDs, 587–9
- projector using light emitting diode
(LED) light source, 573–84
- projectors, 567–73
- lightness, 412
- Lippmann-Schwinger equation, 247
- Lippmann photography, 400
- Liquid Crystal on Silicon technology,
569
- lithium fluoride (LiF), 291
- lithographic technology, 566
- localised surface plasmon resonance
(LSPR), 138
- localised surface plasmons (LSP), 137–8
- long wavepass filter, 573–4
- Lorentz oscillator model, 150
- Lotus effect, 532
- low- ϵ coatings
windshield, 555–7
- ITO coating on glass after
annealing and bending, 556
- uncoated glass vs ITO coating
on glass pane under same
weathering conditions, 557
- low emissivity coating, 376, 723, 727–8
- low emissivity windows, 763–4
design of low ϵ winter film, 764
- low ϵ ‘winter film’ window with TCO
coating, 764
- lowest unoccupied molecular orbital
(LUMO) band, 608
- luminance, 406
- macula lutea, 402
- magnetic films, 645, 647
- magnetic colour shifting pigments
exposed to magnetic field of
cylindrical magnet, 647
- magnetron sputtering, 12
- magnetron sputtering facility, 707–10
2 m scale deposition sputtering
chamber, 708
- hysteresis curve for SiO₂ reactive
sputtering, 710
- Makrolon, 523
- many-body perturbation theory, 180
- masking technique, 706
- mass attenuation coefficient, 307
- matrix assisted pulse laser evaporation
(MAPLE), 434
- matrix integral equation, 213
- Maxwell-Garnett formula, 250
- Maxwell-Garnett theory, 155, 509
- Maxwell’s equation, 209, 213, 416, 509
- melamine, 433

- metal-based multilayer, 377
 metal-dielectric filters, 636–40
 reflection and transmission spectra at normal incidence of filter with three colour shifts, 639
 various configurations of Fabry-Perot-like metal-dielectric filters, 638
 metallic mirrors, 706
Metallocromia, 397
 Nobili's piece of art, Plate I
 metals, 745–6, 749, 751
 metamaterials (MM), 134, 135, 162–3
 metal nanoclusters in periodic arrays, 139–43
 classification of materials based on their dielectric and magnetic properties, 143
 transmission of MM-based isoindex filters for microwaves and NIR, 142
 small random disorders and imperfection, 143–4
 thin and ultrathin metal coatings, 144–6
 metamerism, 404, 641–5
 Dutch 250 guilder banknote, 642
 examples of all-dielectric metameric filters, 646
 metameric pairs based on metal-dielectric Fabry-Perot-like filters, 643
 methyl methacrylate (MMA), 438
 Michel-Lévy Table of Birefringence, 399
 Michelson-type interferometer, 681–2
 mid-frequency sputtering, 13
 Mid Infrared Instrument (MIRI), 700
 mid ultraviolet, 291
 mirror design approaches, 666–76
 back-side coated chirped mirror, 670–1
 calculated reflectivity and GDD at angle of incidence of 5°, 671
 main principal sketch, 670
 Brewster-angle chirped mirror, 669–70
 complimentary pairs of chirped mirror, 671–3
 calculated reflectance and GDD of double-angle DM, 673
 calculated reflectivity and GDD, 672
 dispersive mirrors (DMs), 666–7
 schematic explanation of penetration and resonance effect, 667
 double-angle DM, 674
 double-chirped mirrors, 668–9
 calculated reflectivity and GDD of brewster angle DM, 669
 layer structure, 668
 pulse compression and analysis, 674–6
 summarised designed parameters, 675
 temporal analysis of reflection of a Gaussian pulse, 675
 resonant structure or Gires-Tournois interferometer mirror, 667–8
 tilted-front-interface chirped mirror, 671
 time-domain DM, 673–4
 molybdenum, 613
 monochromatic monitoring (MM), 65
 monolithic glass, 726
 monolithic glazing, 726–7
 moth eye effect, 117
 Mueller bistatic cross section, 242
 Mueller matrix, 227–30
 multi-angle spectrophotometers, 415
 multi-cavity glazing, 726–7
 multi-dielectric broadband antireflection, 709
 multi-functional coatings, 553, 555
 multi-layer insulation (MLI), 791
 multilayer high-dispersive mirrors, 687
 multiple exciton generation (MEG), 605
 multiple surface-plasmon-polariton (SPP) waves, 450
 nano velour structure, 493
 nanoparticles (NP), 134, 137–8
 nanowires, 602–6
 National Ignition Facility (NIF), 697
 National Institute for Standards and Technology (NIST), 315
 near-infrared, 141

- Near-Infrared Camera (NIRCam), 700
 Near-Infrared Spectrometer (NIRSpec),
 700
 near ultraviolet (NUV), 291
 needle method, 35
 Newton-Raphson method, 460
 Newton rings, 393
 N,N-di(1-naphthyl)-N,N'-diphenyl-1,1'-
 diphenyl-1,4'-diamine (NPD),
 434
 non-conformance, 805
 non-conformance report (NCR), 805
 non-conformance review board (NRB),
 805
 non-iridescent material (NIM), 644–5
 non plasma activated chemical vapour
 deposition, 440–3
ns electrons, 745
 numerical simulation, 553
 experimental results of indentation
 and bending tests from diverse
 coatings, 554
 simulation and experimental result
 for critical condition under
 diverse cases, 554
 stress distribution of simulation
 example two coating systems,
 555
- OLED lighting, 772–3
 percentage non-uniformity, 773
 omnidirectional reflecting coating
 (ODR), 588
 optical absorbtivity, 363
 optical and electrical (O/E) properties,
 742–3, 752
 optical broad band monitoring, 99–105
 arrangement, 100
 specification, 101
 transmittance spectrum of a
 multilayer system, 103
 optical coating
 automobiles head up display (HUD),
 584–7
 chromatic discrimination ellipse of
 white light and beam splitter, 587
 optical design of beam splitter, 586
 R1/R2 for s- and p-polarisation,
 586
- schematic architecture, 585
 transmittance spectra with
 different wavelengths for
 simulation and fabricated films,
 587
 automotive and building applications,
 718–39
 coatings on glass substrates, 727–8
 coatings on polymer substrates,
 729–32
 future trends, 737–8
 glazing types, 726–7
 role of thermal control in glazing,
 719–22
 special considerations, 732–6
 window coating types by
 functionality, 722–6
- basic concept, 96–9
 production cycle for coated optical
 components, 97
- basic principles and structures,
 633–41
 multiple reflections in thin film of
 index and thickness, 633
- colour, 391–422
 basic colorimetry, 402–13
 development of the understanding
 of interference colour, 392–402
 optical coating colorimetry, 413–22
- deposition control with continuous
 refractive index variation, 117–25
- deposition techniques, 3–21
 atomic layer deposition (ALD),
 18–19
 cathodic arc evaporation, 16
 chemical vapour deposition
 (CVD), 17–18
 energetic processes, 6–16
 etching, 20
 processes, 4–6
 pulsed laser deposition (PLD), 17
 Sol-gel processes, 19–20
- design, 26–51
 hybrid, 41–50
 manufacturing, 38–41
 measured transmittance of triple
 band CWDM, 27
 numerical thin film synthesis
 techniques, 28–38

- optical coating (*cont.*)
 design stability in production
 processes, 111–17
 process monitored by a
 simultaneous application of all
 presented tools, 117
 process monitored by BBM-
 system, 114
 process monitored by BBM-
 system after a VDP parameter
 refinement, 116
 process monitored by BBM-system
 with a direct on-line correction
 tool, 116
 process monitored by hybrid
 combination of a BBM-system
 and quartz crystal, 115
 theoretical transmittance target
 spectrum of design 1, 112
 theoretical transmittance target
 spectrum of design 2, 113
 direct on-line correction tools, 110–11
 displays and lighting, 564–91
 high resolution multi-band coating
 technology without crosstalk,
 590
 LEDs, 587–9
 micro-projector schematic drawing,
 591
 domains of applications and major
 programs, 695–702
 astronomy, 700–1
 deformable mirror, 699
 lasers, 697–9
 scientific large instruments, 696–7
 solar plants, 701–2
 space, 699–700
 flat panel display (FPD), 565–7
 high-intensity femtosecond lasers,
 664–89
 basic scheme of pulse compression,
 665
 dispersive mirrors application,
 685–8
 dispersive mirrors production, 677
 group delay measurement with
 white light interferometer, 681–5
 highest possible value of group
 delay dispersion (GDD), 676–7
 mirror design approaches, 666–76
 pulse compression with dispersive
 mirrors, 678–81
 large facilities, 695–714
 large magnetron sputtering facility,
 707–10
 major programs, 710–14
 manufacturing monitoring strategies,
 62–91
 classification, 65–7
 direct broad band optical
 monitoring, 82–5
 indirect optical monitoring
 strategies, 85–90
 passive and active monochromatic
 monitoring strategies, 73–82
 turning point optical monitoring
 and error self-compensation
 effect, 67–72
 mirrors for large telescopes, 696
 optical broad band monitoring,
 99–105
 plastic for antireflection purposes,
 519–34
 antireflection coatings, 528–33
 basic problems for vacuum coating,
 520
 transparent polymer materials,
 520–2
 vacuum coating processes, 522–8
 production strategies, high-precision,
 94–127
 projectors, 567–73
 DLP project system schematic
 drawing, 571
 DLP project system with three
 DMDs schematic drawing, 572
 ER of PBS spectrum at 31° and
 45°, 570–1
 LCOS projector using colour
 wheel schematic drawing, 572
 light emitting diode (LED) light
 source, 573–84
 reflection type using LCOS, 568
 reflection type using three LCOSS,
 570
 transmission type with liquid
 crystal panel, 568
 UV-IR cut filter spectrum, 569

- security and authentication devices, 631–56
 active devices, 650–3
 film functionality and structurally controlled optical coatings, 653–5
 optical effects, 641–50
 space environment, 789–07
 atomic oxygen, 798
 contamination, 798–803
 environment components of space, 790
 overview, 790–1
 particulate radiations, 797–8
 product assurance for space coatings, 803–6
 solar irradiance, 797
 space vacuum, 791–5
 thermal cycling in vacuum, 795–7
 technological solutions, 702–5
 thin film uniformity, 705–7
 improvement obtained by masking technique, 707
 virtual deposition system, 105–9
 optical coating colorimetry, 413–22
 optical coating colour, 416–22
 optical conductivity, 295
 optical effects, 641–50
 combining interference and diffraction, 647–9
 light diffraction, 648
 magnetic films, 645, 647
 metamerism, 641–5
 other colour shifting technologies, 650
 optical filters, 634–5
 optical interference coatings (OIC), 37, 40, 51
 optical monitoring strategies
 classification, 65–7
 subdivisions, 65
 direct broad band optical monitoring, 82–5
 indirect optical monitoring strategies, 85–90
 optical coating, 62–91
 passive and active monochromatic monitoring strategies, 73–82
 turning point optical monitoring and error self-compensation effect, 67–72
 optical solar reflectors, 797
 optical spectroscopy, 550
 optical surfaces
 protective coatings, 540–60
 application examples, 555–60
 coating design, 551–5
 testing methods, 545–51
 optical thin film
 analytical methods scattering from a three-dimensional film with randomly rough surface, 219–40
 scattering matrix, 220–3
 small-slope approximation and the small perturbation method, 224–30, 230–9
 applications, 270–80
 air-to-ground scenario and full 3D reconstruction with intensity voxel, 276
 air-to-ground scenario and full 3D reconstruction with isodensity voxel, 277
 computation of a non-polarised 2D laser image of a vehicle, 276
 vehicle visible and a 2D laser image, 275
 blackbody radiation, 359–63
 spectral radiance from blackbody as function of frequency, 360
 spectral radiance from blackbody as function of wavelength, 362
 complex materials with plasmonic effects, 133–63
 alternative materials, 146–51
 ceramic matrix with embedded metal nanostructures, 137–46
 novel material characterisation, 152–62
 novel material physics, 135–6
 containing quantum dots, 493–513
 characterisation of thin films containing quantum dots, 503–9
 modelling the electronic properties of multiple quantum wells, 497–8
 numerical results, 498–502
 quantum dots applications, 494–7
 realisation of thin films containing quantum dots, 502–3

- optical thin film (*cont.*)
 refractive index of layers
 containing quantum dots and of
 quantum dots alone, 509–12
 controlling thermal radiation, 357–87
 importance of correct
 light chopping in a
 spectrophotometer, 358
 deposition techniques, 3–21
 atomic layer deposition (ALD),
 18–19
 cathodic arc evaporation, 16
 chemical vapour deposition
 (CVD), 17–18
 energetic processes, 6–16
 etching, 20
 processes, 4–6
 pulsed laser deposition (PLD), 17
 Sol–gel processes, 19–20
 emissivity, 363–8
 radiometric determination of the
 band-emittance, 367
 relationship between thermal
 emission from a real body and
 that from a blackbody, 364
 use of conventional infrared
 spectrophotometer in emittance
 mode, 366
 material behaviour over the
 spectrum, 291–3
 k and $\delta = 1 - n$ of SiC in broad
 spectral range, 293
 names and limits of ranges in
 electromagnetic spectrum, 292
 methods for scattering of polarised
 light from randomly rough
 interfaces and random media,
 240–70
 coherent backscattering, 263–9
 effective permittivity, 250–1
 expression for incoherent intensity
 and Green tensor, 255–63
 expression of the intensity
 operator, 251–5
 specific intensity and Bethe–
 Salpeter equations, 246–50
 specific intensity and cross-section,
 241–6
 numerical synthesis techniques, 28–38
- Fourier transform method, 28–33
 global optimisation, 36–8
 inhomogeneous refinement, 33–5
 needle methods, 35
 optical constants of materials at short
 wavelengths, 299–315
 absorption coefficient at Fe K-edge
 of FeO showing XAFS spectrum,
 310
 absorption edges, 307–11
 contributions to the total measured
 cross section in carbon over
 photon energy range 10–100
 GeV, 315
 $\delta = 1 - n$ of Pr from experimental
 k data using Kramers-Krönig
 analysis, 308
 Fe K-edge XANES spectrum of Fe
 metal and several Fe compounds,
 311
 free electron metals, 303–4
 gamma-ray interaction processes,
 313–14
 interaction mechanisms between
 photons and matter, 299–300
 k from the infrared to SXR for
 metal Sc, 301
 optical properties at higher
 energies, 311
 plasma wavelength of alkali metals,
 304
 temperature dependence of the
 transmission cutoff of various
 fluorides and oxides, 302
 tightly bound electrons: atomic
 scattering factors, 304–7
 total-reflection critical angle for Si
 and W, 307
 transparency cutoffs of dielectrics,
 300–2
 XANES and EXAFS regions of
 Ti K-edge XAS spectrum of
 PbTiO₃, 309
 optical properties at short
 wavelengths, 290–343
 experimental determination of
 optical constants, 317–20
 link between n and k : Kramers–
 Krönig analysis, 316–17

- optically selective coatings, 368–87
 coatings for control of radiative exchange with the atmosphere, 380–7
 coatings for thermal solar collectors, 368–76
 energy efficient window coatings, 376–80
- reduced Rayleigh equation for p-and s-polarised light, 192–207
- reduced Rayleigh equation for scattering of light, 179–92, 208–12
- reflection and transmission in absorbing materials, 294–9
 normal incidence reflectance of Al, 298
 roughness and scattering, 296–9
- scattering of light from a dielectric film, 212–19
- scattering properties of random structures, 177–289
- specifics of optical coatings at short wavelengths, 320–42
 3-mirror and 4-mirror polariser configurations, 338
 calculated reflectance as function of wavelength of Mo/Si MLs, 328
 high-reflectance coatings, 321–2
 HR coatings spanning the EUV and SXR, 323
 linear polarisers and phase retarders, 332–42
 measured reflectance of SQWM, 331
 optical constants of many materials at 30.4 nm, 332
 phase retardation on transmission, 340–1
 reflectance enhancement measured for MLs, 333
 reflectance of Au calculated for parallel and perpendicular polarisation, 335
 reflectance of materials used for single-layer mirrors in long EUV:Ir, 330
 R_s and R_s/R_p calculated at 45° for prospective ML polarisers, 337
- transmission filters, 320–1
 transmission properties of several materials, 322
 transmittance expected for commonly used filter materials, 322
- surface multiplasmonics with periodically non-homogeneous thin films, 450–86
 canonical boundary-value problem, 456–65
 grating-coupled configuration, 466–75
 historical development, 451–3
 periodically non-homogeneous dielectric materials, 453–6
 Turbadar-Kretschmann-Raether (TKR) configuration, 476–82
- optically selective coating, 368–87
 coatings for control of radiative exchange with the atmosphere, 380–7
 calculated and measured near-normal reflectance spectra for double-layer Si/SiO₂, 386
 measured and calculated reflectance spectra for Si/BeO, 385
 MODTRAN calculated transmittance spectrum, 380
 radiance functions computed according to mid-latitude winter model, 381
 reflectance spectra for evaporated SiO films on an Al substrate, 383
 reststrahlen bands of BeO and SiO₂, 384
 coatings for thermal solar collectors, 368–76
 dark mirror and heat mirror, 371
 DC magnetron sputtering unit, 375
 reflectance spectra for different samples of black chrome, 373
 reflectance spectrum for co-evaporated graded Ni/Al₂O₃ cermet coating on silver backing, 374
 two blackbody radiance curves on log-lin axes, 369

- optically selective coating (*cont.*)
 energy efficient window coatings,
 376–80
 idealised reflectance and
 transmittance spectra for
 window coatings, 377
 optically variable ink (OVI), 640
 optically variable pigments, 640–1
 example of micro-structured, square
 shaped magenta to green, 641
Opticks, 393
 Optilayer, 667
 optoelectronic properties, 751–3, 753
 indium tin oxide ceramic target, 752
 organic light emitting diode (OLED),
 428, 432, 753
 organic optical coating, 427–45
 composites, 443–5
 co-evaporated TiO₂-polyamide-
 composite thin films, 444
 co-sputtered Ta₂O₅-PTFE-
 composite thin films, 444
 sputtering set-up for organic-
 inorganic composites, 445
 deposition techniques, 432–43
 adhesion improvement by plasma
 treatment, 443
 crack onset strain and hardness as
 function of ratio of oxygen to
 HMDSO, 439
 deposition rate for different plasma
 powers, 440
 deposition rate of sputtered PTFE
 and sputtered tantalum in argon
 atmosphere, 436
 deposition set-up for poly-para-
 xylylene, 442
 evaporation set-up, 433
 heating cartridge with quartz
 crucible, 434
 influence of oxygen on refractive
 and absorption index of RF
 sputtered fluorocarbon layers,
 436
 IR-ATR spectra for PECVD
 made layers with C₄F₈ as
 precursor, 440
 non plasma activated chemical
 vapour deposition, 440–3
 physical enhanced chemical vapour
 deposition, 437–40
 polymerisation process of poly-
 para-xylylene, 441
 PTFE sputter target and sputtered
 fluorocarbon layer on glass
 substrate, 435
 refraction and absorption indices
 at 500 nm for different plasma
 powers, 439
 RF sputtering, 435–7
 sketch of PECVD coating set-up,
 438
 thermal evaporation, 433–5
 optical coatings with organic layers,
 431–2
 specific properties of organic layers,
 428–31
 crack onset strain of various layer
 materials on polycarbonate
 substrates, 430
 refractive and absorption indices
 of various deposited layer
 materials, 430
 set-up for crack onset strain
 determination, 429
 organic photovoltaic systems (OPV),
 432
 organic thin film solar cells, 606–12
 light trapping strategies, 609–12
 electromagnetic field distribution,
 610
 implementation of periodic
 structures in multilayer stack,
 610–11
 plasmons for increasing absorption
 in OSCs, 611–12
 working principles, 607–9
 charge transport, 609
 exciton diffusion, 608
 exciton diffusion or charge
 separation, 609
 photon absorption, 608
 traditional and inverted structure,
 607
 oxygen flow rate, 752
 p-polarisation, 182, 183, 188, 195–200,
 218, 295

- pair production, 312
 particle swarm optimisation (PSO), 38
 particulate radiations, 797–8
 degradation of an optic exposed to
 equivalent doses of low energy
 protons, Plate VIII
 parylene, 429, 431, 441
 parylene AF-4, 441
 parylene C, 441
 parylene D, 441
 parylene N, 441
 passenger comfort, 733
 passive monochromatic monitoring
 strategies, 73–82
 expected levels of errors in thickness
 of layers of the 40-layer hot
 mirror, 78, 80
 monitoring signal for a coating layer
 with several signal extrema, 81
 monitoring signal for the first eight
 layers of 40-layer hot mirror, 76,
 79
 monitoring signal for the first eight
 layers of 42-layer hot mirror, 75
 monitoring spreadsheet for the
 40-layer hot mirror design, 76
 monitoring spreadsheet for the
 42-layer hot mirror design, 74
 spectral transmittance and layer
 optical thickness of 40-layer hot
 mirror design, 73
 spectral transmittance and layer
 optical thickness of 42-layer hot
 mirror design, 73
 Patinal WR5, 434
 percentage luminance factor, 409
 Percus-Yevick correlation
 function, 255
 Percus-Yevick distribution, 250–1
 perfect reflecting diffuser, 409
 PET film, 730, 731
 phase locked interferometry, 684
 phase retarders, 339
 photo-carrier collection, 601–2
 photoelectric absorption, 312
 photometry, 406
 photon absorption, 608
 photonic crystals, 493, 651
 photopic vision, 402
 physical enhanced chemical vapour
 deposition (PECVD), 437
 physical vapour deposition (PVD),
 134–5, 454, 541
 Planck function, 360, 363
 Planck theory, 360
 Planck's Law, 359
 'Planet Finder' Instrument, 697
 plasma enhanced chemical vapour
 deposition (PECVD), 542, 557
 plasma frequency, 303
 plasma impulse chemical vapour
 deposition (PICVD), 18, 542
 plasma ion assisted deposition, 522, 541–2
 plasma sputtering, 704
 plasmon polariton (PP), 133
 plasmonic materials
 alternative materials, 146–51
 absorption spectra of copper and
 silver, 147
 alloys and intermetallics, 146–9
 extinction spectra of silver and
 gold, 147
 semiconductors, 149–51
 ceramic matrix with embedded metal
 nanostructures, 137–46
 novel material characterisation,
 152–62
 attenuated total reflectance
 measurement, 153
 complex materials and ultrathin
 metals, 158–62
 ellipsometric spectra of two AZO/
 Ag/AZO samples, 161
 local properties of nanostructured
 materials, 154–5
 macroscopic parameters, 155–8
 measured and theoretical
 dependence of cosine of
 ellipsometric angle, 162
 optical characterisation techniques,
 152–4
 refractive index and extinction
 coefficient of silver ultrathin
 layers, 160
 novel material physics, 135–6
 carrier concentration and mobility
 with interband transition, 136
 optical thin film applications, 133–63

- plastic optics
 coatings and antireflection purposes, 519–34
 antireflection coatings, 528–33
 transparent polymer materials, 520–2
 vacuum coating processes, 522–8
- plateau problem, 401
- pleochroism, 399
- polarisation beam splitters, 569
- polariser, 333
- poly-bisphenol-A-carbonate, 523
- poly(3,4-ethylenedioxothiophene):poly(styrene sulfonate) (PEDOT:PSS), 607
- poly-para-xylylene (parylene), 441
- polyamide (PA), 433
- polycarbonate, 428, 540, 552–3
 auto-motive glazing, 557–60
 optimised adhesion of functional coating, 560
- sputtered UV protective coating, 558
 breaking edge of ZnO, 559
 UV absorption edge of lacquers, ZnO and ZnO, 558
- polychrome recording, 400
- polyethylene, 433, 435
- polyethylene terephthalate (PET), 729–30
- poly(glycidyl methacrylate) (PGMA), 442
- polyimide, 433, 435
- poly(methyl methacrylate) (PMMA), 431, 442, 530
- polytetrafluoroethylene (PTFE), 435
- polyvinyl butyral (PVB), 727
- porous films, 654
- potassium gold (KAu), 148
- power conversion efficiency (PCE), 50
- power spectrum, 185, 187, 215, 218
- Poynting vector, 461
- printing, 622–3
- prismatic colours, 391
- process identification document (PID), 805
- projectors, 567–73
- protective coatings
 optical surfaces, 540–60
- abrasive performance of float glass, ITO, HIPIMS, ITO dc and SnO₂F coatings, 544
- application examples, 555–60
- coating design, 551–5
- potential application of functional thin film coatings in automotive sector, 542
- testing methods, 545–51
- thin film application in architectural glazing, 541
- pseudo-Brewster angle, 335, 336
- psychometric colorimetry, 392, 411–13
- psychophysical colorimetry, 392
 colour stimuli, 403–9
 light sources and non-self-luminous surfaces, 409–11
- pulsed laser deposition (PLD), 17
- pyrolytic coating, 727
- Q-function, 30–1
- quantum dots (QD), 138–9, 493–513, 602–6
 applications, 494–7
 discrete energy levels, excitation and relaxation processes, 496
- characterisation of thin films
 containing quantum dots, 503–9
 absorption and luminescent spectra of PMMA layer, 508
 absorption spectrum of PMMA layers, 505
 evolution of the average value of luminescence, 507
 luminescence of quantum dot layers, 506–9
 luminescence spectra of PMMA layers, 507
- photoluminescence intensity variations of 550 nm luminescence band, 508
- TEM images of CdSe/ZnS QDs, 504
- transmission electronic microscopy, 503–4
- transmittance, reflectance and absorption, 504–6
- transmittance spectrum of CdSe/ZnS QDs, 504

- modelling the electronic properties of multiple quantum wells, 497–8
- numerical results, 498–502
- density of probability of electrons in non-periodic structure, 501
 - distribution of discrete energy levels of ZnO QDs, 499
 - electron probability density of lowest energy in the structure, 501
 - energy levels of electrons for three coupled identical quantum wells, 499
 - highest energy level of electrons in a single well, 500
- realisation of thin films containing quantum dots, 502–3
- absorption spectra of pure silica glass and silica glass coated with PMMA, Plate III
- realisation process of PMMA layers including different QDs concentrations, 503
- refractive index of layers containing quantum dots and of quantum dots alone, 509–12
- normalised EQE for Si solar cell with silica substrate coated with pure PMMA layer, 510
- refractive index dispersion of PMMA layers including QDs, 511–12
- refractive index measured by m-line technique, 510, 511
- quantum wells (QW), 494
- quantum yield (QY), 494
- quarterwave, 325
- quartz crystal microbalance, 104
- quasi-crystalline approximation (QCA), 250
- quasi-crystalline coherent potential approximation (QC-CPA), 250, 251
- quasi rugate filter, 118
- radiative cooling, 381
- radical assisted sputtering (RAS), 14
- radio frequency signal, 652
- radiofrequency identification (RFID), 652
- random measurement errors, 77
- rapid thermal annealing, 623
- Rayleigh equation
- numerical solution for scattering of light from two-dimensional randomly rough penetrable surface, 208–12
 - mean differential reflection coefficients, 211
- scattering of light from dielectric films with one-dimensional rough surfaces, 179–92
- scattering of p-and s-polarised light, 192–207
- contribution to the mean differential reflection coefficient, 206, 207
 - p-polarisation, 195–200
 - results, 203–7
 - s-polarisation, 200–2
 - scattering system, 195
- reactive evaporation, 8
- reactive low-voltage ion plating, 10
- reactive pulse magnetron sputtering, 522
- reactive sputtering, 12–13
- refinement, 27
- reflectance, 296
- reflectance/transmittance extrema, 63
- reflective polarisers, 336, 337
- refraction, 319
- refractive index, 28, 29, 294
- decrement, 306
- relative spectral power distribution, 409
- relativistic quantum theory, 315
- resistivity-well, 747
- reststrahlen band, 384
- retarder, 333
- RF sputtering, 435–7
- rigorous coupled-wave analysis (RCWA), 468, 483, 530
- Rochon prisms, 334
- root-mean-square (RMS), 31, 35
- rugate filter, 29
- deposition control, 122–5
 - theoretical and realised spectrum for laser protection goggles, 124
- Rushton's univariance principle, 403

- s-polarisation, 182, 183, 189, 200–2, 218, 295
 s-polarised light, 179–80, 185, 187, 190, 192–207, 203, 204, 208, 211, 212
 sand trickling, 546, 556
 Sarid configuration, 452
 satisfaction yield, 196
 scanning near-field optical microscopy (SNOM), 152
 scanning probe microscopy (SPM), 152
 scanning tunnelling microscopy (STM), 152
 scattering amplitude, 182, 183, 188, 189, 197, 198, 201, 209, 213, 233, 249
 scattering matrix, 220–3, 223, 224, 232
 incident wave, 221
 scattering vectors, 222
 Schrödinger equation, 407, 497
 scratch test, 546–7, 556
 schematic illustration, 546–7
 sculptured nematic thin film (SNTF), 450, 452, 455
 sculptured thin film (STF), 452
 security devices
 optical coatings, 631–56
 active devices, 650–3
 basic principles and structures, 633–41
 film functionality and structurally controlled optical coatings, 653–5
 optical effects, 641–50
 combining interference and diffraction, 647–9
 magnetic films, 645, 647
 metamerism, 641–5
 Sellmeier model, 684
 semi-infinite media, 230
 Incoherent components as functions of the scattering angle, 231
 sequential algorithm, 110
 Shockley-Queisser limit, 495, 600
 short wave infrared (SWIR), 272
 short wavelength radiation, 522
 SICON, 438
 sinusoidal grating, 45
 small-amplitude perturbation theory, 180
 small perturbation method (SPM), 178, 219–20
 slabs with randomly rough boundaries, 230–40
 components VH and HV, 231
 formulation, 230–6
 two-dimensional rough surface, 224–30
 cross-section and the Mueller matrices computation, 227–30
 formulation, 224–7
 randomly rough surface between two semi-infinite media, 230
 small-slope approximation (SSA), 178–9, 219–20
 slabs with randomly rough boundaries, 230–40
 applications, 236–9
 components VH and HV, 231
 formulation, 230–6
 incoherent components VH and HV, 237, 238
 incoherent components VV and HH, 238, 239
 two-dimensional rough surface, 224–30
 cross-section and the Mueller matrices computation, 227–30
 formulation, 224–7
 randomly rough surface between two semi-infinite media, 230
 smart windows, 736
 Snell's law, 294, 416, 417, 637
 soft coat *see* sputtered coating
 soft X-rays (SxR), 292
 Sol-gel technique, 19–20, 543, 566
 solar cells, 46–50
 absorption simulation, 48
 effect of changing the active layer thickness on the measured short circuit current, 49
 solar control coatings, 765–6
 design of a solar control film, 766
 ‘summer film’ window with metal coating, 765
 solar irradiance, 797
 degradation of a solar cell coverglass tested with UV in vacuum, Plate VII
 solar photon absorption (SPA), 49–50
 solar screen, 376

- solar selective, 368
 solar thermal absorbers, 368
 solar transmittance, 724–5
 space coatings
 product assurance, 803–6
 end to end traceability, 804–5
 non-conformance control, 805
 process control, 805
 space qualification, 806
 space contamination, 801–3
 UV fixation, 802
 space vacuum, 791–5
 air to vacuum spectral shift of a dense coating, Plate V
 air to vacuum spectral shift of a porous coating, Plate VI
 S-on-1 test and air and vacuum LIDT test, 794
 TEM of a fully dense coating and electron beam evaporated coating, 792
 thermal cycling, 795–7
 thin coated lamina test, 795
 spacer, 323
 spacer layer, 68
 spatial harmonic analysis (SHA), 158–9
 special-effect colour, 392, 414
 specific intensity, 241–6, 246–50
 decomposition of the wave vectors, 243
 random volume with rough boundaries, 245
 scattering of an incident plane wave with a wave vector, 243
 scattering operators, 244
 spectral reflectance factor, 409, 410
 spectrophotometer version, 357
 spectroscopic ellipsometry, 159
 split ring resonator (SRR), 140
 sputtered coating, 727, 728
 sputtering, 11–16, 703–5
 arrangement of source and treatment stations in alternating ion plating, 14
 dual ion beam sputtering technique, 704
 in-line magnetron sputtering technique, 705
 planar magnetron cathode, 12
 stearic acid, 433
 Stefan-Boltzmann equation, 362
 Steven's power law, 413
 Stokes parameters, 333
 stokes shift, 495
 stress effects, 524–5
 structural colours, 391
 structured coatings, 43–6
 narrow-band reflectance spectrum of a silicon, 46
 planar grating diffraction model, 44
 wideband reflectance spectrum of two Ge/SiO₂ resonant grating, 47
 sub-quarterwave MLs (SQWMs), 330
 sun roof, 733–4
 supermirror, 327, 329
 surface enhanced Raman spectroscopy (SERS), 152
 surface height autocorrelation function, 205
 surface-height correlation functions, 220
 surface multiplasmonics
 canonical boundary-value problem, 456–65
 metal/rugate filter interfaces, 460–3
 metal/SNTF interface, 463–5
 real and imaginary parts of κ as functions of ψ for SPP wave propagation, 464
 solutions of the dispersion equation computed using the Newton-Raphson method, 462
 theoretical formulation, 456–60
 variations of components of $P(x,z)$ with z along the line, 465
 variations with z of the Cartesian components of $P(x,z)$, 463
 grating-coupled configuration, 466–75
 absorptances A_p and A_s vs θ in the grating-coupled configuration, 474
 absorptances as functions of incidence angle in the grating-coupled configuration, 469
 metal/rugate filter interface, 466–72
 metal/SNTF interface, 472–5
 relative wave numbers of Floquet harmonics, 470

- surface multiplasmonics (*cont.*)
 relative wave numbers of possible
 SPP waves, 470
 schematic of grating-coupled
 configuration, 466
 variation of the x- and
 y-components of the time-
 averaged Poynting vector, 475
 variation of the x-component of the
 time-averaged Poynting vector,
 471
 historical development, 451–3
 periodically non-homogeneous
 dielectric materials, 453–6
 rugate filters, 453–4
 sculptured nematic thin films,
 454–6
 periodically non-homogeneous thin
 films, 450–86
 Turbadar-Kretschmann-Raether
 (TKR) configuration, 476–82
 absorptance A_p as function of the
 incidence angle, 478
 absorptance A_s as function of the
 incidence angle, 480
 metal/rugate filter interface, 476–81
 metal/SNTF interface, 481–2
 relative wavenumbers of SPP
 waves, 479
 schematic, 477
 values of incidence angle and
 relative wavenumbers, 478
 values of incidence angles and the
 relative wavenumbers, 479
 variations of the x- and
 z-components of time-averaged
 Poynting vector, 481
 surface plasmon frequency, 297
 surface plasmon polariton (SPP), 133,
 137
 surface plasmons (SP), 133–4, 135, 137
 surface profile function, 185, 194
 surface roughness, 190
 susceptibility χ , 295
 switchable glazing, 736
- Taber abrasion test, 545–6, 556
 tandem solar cell, 603
- TCP/IP-interface, 107
 terrestrial contamination, 799–801
 impact of high particulate
 contamination causing damage
 on optic, 800
 testing methods, 545–51
 adhesion, 547–9
 surface damage by crosshatch
 cutter, 548
 crack onset strain, 547
 four point bending test for
 measuring the strain at failure
 COS, 548
 hardness and indentation elasticity,
 547
 haze, 551
 optical properties characterisation,
 550–1
 transmission and reflection of
 low-e, solar control coating and
 uncoated glass, 550
 sand trickling, 546
 scratch test, 546–7
 Taber abrasion test, 545–6
 schematic diagram, 545
 weathering, 549
 tetramethylsilane (TMS), 438
 TFCalc, 667
 thermal control
 role in glazing, 719–22
 automotive window energy
 efficiency, 722
 building window energy efficiency,
 720–2
 thermal cycling
 vacuum, 795–7
 failure, 796
 thermal effects, 524–5
 thermal evaporation, 21, 433–5, 702–3
 thermal heating, 543
 thermal radiation
 controlling from surfaces in optical
 thin films, 357–87
 blackbody radiation, 359–63
 emissivity, 363–8
 optically selective coatings, 368–87
 thermal radiation transmission, 719
 thin film cells, 46–7

- thin film photovoltaic cells
 innovative approaches, 596–624
 copper indium gallium diselenide
 thin film solar cells, 612–23
 inorganic nanostructures, 599–606
 organic thin film solar cells, 606–12
 record conversion efficiencies of
 thin film solar cells, 598
- thin film transistor (TFT), 775–6
- thin island film (TIF), 161
- Thomas-Reiche-Kuhn sum rule, 305, 317
- tilted-front-interface chirped mirror, 671
- time-domain dispersive mirror, 673–4
- tin doped indium oxide (ITO), 741,
 742–3, 745, 746–7
- Tinuvin 360, 434
- TiO₂, 533
- TM (transversal magnetic), 295
- total electron yield, 320
- total-internal-reflection ellipsometry
 (TIRE), 153
- touch sensors, 768–72
 analog resistive, 768–71
 4-wire resistive touch sensing, 770
 resistive touch, 770
 projected capacitive, 771–2
 grid-line structure for x and y
 sensing, 771
 projected capacitive sensor, 772
- tracing algorithm, 108
- transition metal nitrides, 151, 379
- transition operator, 247
- transmission amplitude, 199, 202, 203
- transmission coefficient, 29
- transmission electron microscopy
 (TEM), 598
- transmission filters, 320–1
- transmittance, 296
- transmittance polarisers, 338
- transparent conductive coating, 566–7
- transparent conductive oxides (TCOs),
 615–16, 742–4, 746–7, 748–9
 electrical and optical properties, 743
 optical properties related to
 conductivity, 750
- physics of transparent conductive
 coatings, 750
- semiconductors for thin-film
 transparent electrodes, 743
- sheet resistance and optical
 transmittance, 744
- transparent conductive thin films
 (TCTF), 741–84
 conductivity fundamentals, 745–51
 future applications, 775–9
n-type, 779–82
 intrinsic performance limits for
 TCO, 780
 optoelectronic properties, 751–3, 753
p-type, 782–3
 recent applications, 767–75
 traditional applications, 753–66
 antistatic film, 758–9
 electromagnetic interference
 shielding, 754–8
 energy efficient windows, 763–6
 heaters, 753–4
 transparent electrodes, 759–63
 transparent conductive oxides
 (TCO), 742–4
 transparent metallic thin films, 744–6
- transparent electrochromic windows,
 778–9
- transparent electrodes, 759–63
 type I, 759
 type II, 759–63
 charge injecting transparent
 electrode for OLED device, 760
 CIGS PV device, 762
 photovoltaic (PV) device, 762
 schematic diagram, 760
 thin film PV cell, 761
- transparent metallic thin films, 744–5
 optical/electrical performance, 745
- transparent OLED, 776–7
- transparent oxide electronics, 773–5
 cage structure materials of
 12CaO•7Al₂O₃, 774
- structure of first TTFT deposited on a
 flexible substrate, 774
- transparent polymer materials
 optics, 520–2
 properties of important
 thermoplastics for optics, 521
- transparent PV (solar) cells, 777–8

- transversal electric (TE), 295
 triangular algorithm, 110
 Tribrid, 520
 trichomacy, 403
 tris-(8-hydroxyquinolinolato) aluminium (Alq₃), 433
 tristimulus space, 403
 tristimulus values, 403, 404
 Trivex, 520
 Turbadar-Kretschmann-Raether (TKR) configuration, 451
 turning point optical monitoring, 67–72
 19-layer Fabry-Perot filter
 transmittance vs. optical thickness, 68
 122-layer four-cavity WDM filter
 error sensitivity analysis, 72
 arrangement, 67
 four-cavity WDM filter transmittance vs. optical thickness, 72
 multi-cavity narrow band pass filter, 69
 ultrahigh pressure mercury lamp, 567–8
 ultrasonic spray, 622
 utilising wavelet analysis, 684
 UV-BBM-system, 101
 vacuum coating processes, 522–8
 general considerations, 527–8
 interaction with emissions from plasma, 522–4
 antireflection coating providing UV-protection to polycarbonate substrate, 524
 polar component of surface energy of PMMA, Makrolon and Zeonex, 523
 thermal and stress related effects, 524–5
 residual stress of TiO₂-coatings on silicon and plastic, 525
 tensile stress cracking and buckling defects, 526
 water absorption and desorption, 525–7
 coated and uncoated polycarbonate, 527
 water content of polymers depending on storage time, 526
 vacuum deposited antireflective-coatings, 528–9
 vacuum-dielectric interface
 deposited on one-dimensional randomly perfect conducting surface, 188–92
 contribution of mean differential reflection coefficient, 191
 scattering system, 188
 deposited on planar surface of perfect conductor, 181–7
 contribution to the mean differential reflection coefficient, 186
 scattering system, 181
 vacuum free deposition, 619–23
 electrodeposition, 620–1
 electrochemical phase diagram, 621
 printing and doctor blade, 622–3
 ultrasonic spray, 622
 valence band, 300
 Very Large Research Infrastructures (VLRI), 696
 Virgo+ mirrors, 713–14
 Virgo project, 711–14
 IBS coater, 713
 virtual deposition process (VDP), 96, 105–9, 112–13, 115, 126
 application, 108–9
 spectra of a broadband anti-reflection coating, 109
 deposition system, 106–7
 on-line measurement system, 107
 process tracing algorithm, 108
 schematic diagram, 106
 visible transmittance, 724–5
 volumic pixel, 276
 water desorption, 525–7
 waveguide coatings, 41–3
 schematic diagram, 42
 wavelength division multiplexing (WDM), 63, 69, 70, 71, 91
 weak localisation effect *see* coherent backscattering enhancement
 weathering, 392, 549
 wet-chemical coatings, 532–3

- white light interferometer
group delay measurement, 681–5
full-bandwidth measurement on
fused-silica, 684
positions of interferograms, 683
set-up diagram, 682
wide angle reflection filter, 581
'Wien peak' position, 361
Wiener bounds, 145
Wien's displacement law, 360
window
coating types by functionality, 722–6
30 nm silver stack, 726
anti-glare, 725–6
low emissivity, 723
solar + blackbody spectrum with
short/long pass, 724
spectral selectivity, 723–5
energy efficiency, automotive, 722
energy efficiency, building, 720–2
- windshield, 732
Wood filters, 304
- X-cube prism, 567
X-radiation, 686
X-ray Absorption Fine Structure
(XAFS), 309
X-ray Absorption Near-Edge
Spectroscopy (XANES), 309
X-ray Absorption Spectroscopy (XAS),
309
- X-ray Photoelectron Spectroscopy
(XPS), 299, 309
- X-rays, 292
- Zeonex, 523, 530
- zero-order diffraction gratings (ZODs),
649
- ZnO-NC, 50
- zone melting approach, 37

